STATE OF CALIFORNIA • DEPARTMENT OF TRANSPORTATION

TECHNICAL REPORT DOCUMENTATION PAGE

TR0003 (REV 10/98)

ADA Notice

For individuals with sensory disabilities, this document is available in alternate formats. For information call (916) 654-6410 or TDD (916) 654-3880 or write Records and Forms Management, 1120 N Street, MS-89, Sacramento, CA 95814.

1. REPORT NUMBER	2. GOVERNMENT ASSOCIATION NUMBER	3. RECIPIENT'S CATALOG NUMBER
CA14-2424		

4. TITLE AND SUBTITLE

Title: Development of a Rational Design Method for Shear Keys at In-Span Hinges in Multi-Frame Highway Bridges

Subtitle: Part-1: A Rational Seismic Analysis Method for In-Span Hinge Shear Keys

5. REPORT DATE

09/22/2014

6. PERFORMING ORGANIZATION CODE

7. AUTHOR

Masoud Mehr and Arash E. Zaghi

8. PERFORMING ORGANIZATION REPORT NO.

NG-MRIL 14-01

9. PERFORMING ORGANIZATION NAME AND ADDRESS

University of Connecticut
Civil & Environmental Engineering
261 Glenbrook Road, Unit 3037
Storrs, CT 06269-3037

10. WORK UNIT NUMBER

11. CONTRACT OR GRANT NUMBER

12. SPONSORING AGENCY AND ADDRESS

California Department of Transportation
Division of Research, Innovation and System Information
P.O. Box 942873
Sacramento, CA 94273-0001

California Department of Transportation
Division of Engineering Services
1801 30th Street, MS #9-2/5I
Sacramento, CA 95816

13. TYPE OF REPORT AND PERIOD COVERED

Final Report

14. SPONSORING AGENCY CODE

15. SUPPLEMENTARY NOTES

Part-2 of this report is published as a separate document.

16. ABSTRACT

Long concrete box-girder bridges are often constructed in multiple frames separated by in-span hinges in their superstructure. Shear key members are placed at in-span hinges to connect adjacent frames in transverse direction, while allowing for the longitudinal relative movement of the frames. The shear keys ensure seismic integrity of the frames. Seismic transverse response of multi-frame bridges has not been comprehensively studied. No reliable method exists for estimating the design force demands of in-span shear key elements. In this study, OpenSees simulation tool was used to conduct approximately 7,700 nonlinear response history analyses on high-fidelity models of two-, three-, four-, and five-frame bridges with single-column and two-column bents, and different valley shapes. These prototypes were carefully designed in accordance to the Caltrans Seismic Design Criteria (SDC v1.7). The major findings of this study are: 1) higher in-plane modes of vibrations of superstructure significantly contribute to shear key force response; 2) the ratio of the periods of adjacent frame does not have a major effect on the magnitude of shear key forces; 3) transverse impacts, due to closure of gaps on the sides of shear keys, increase shear forces by an average factor of 2.5; 4) non-uniform ground motions along the bridge length may increase shear key forces by a factor of approximately 1.25; and 5) the maximum shear key force does not exceed the 75% of the transverse capacity of the weaker adjacent frame. It was established that modal shear key forces shall be modified separately by the corresponding modal displacement ductility values to account for the nonlinear behavior of system. This concept enables reliable estimation of force demands of in-span shear key elements. It was used as basis to develop an analysis methodology for obtaining the elastic shear force demands in multi-frame bridges.

17. KEY WORDS	18. DISTRIBUTION STATEMENT	
Multi-Frame Bridge, In-Span Hinge Shear Key, Seismic Design, Transverse Response, Pipe Seat Extender	No restrictions. This document is available to the public through the National Technical Information Service, Springfield, Virginia 22161	
19. SECURITY CLASSIFICATION *(of this report)*	**20. NUMBER OF PAGES**	**21. COST OF REPORT CHARGED**
None	491	

DISCLAIMER STATEMENT

This document is disseminated in the interest of information exchange. The contents of this report reflect the views of the authors who are responsible for the facts and accuracy of the data presented herein. The contents do not necessarily reflect the official views or policies of the State of California or the Federal Highway Administration. This publication does not constitute a standard, specification or regulation. This report does not constitute an endorsement by the Department of any product described herein.

For individuals with sensory disabilities, this document is available in alternate formats. For information, call (916) 654-8899, TTY 711, or write to California Department of Transportation, Division of Research, Innovation and System Information, MS-83, P.O. Box 942873, Sacramento, CA 94273-0001.

NG-MRIL
Next-Generation Multihazard Resilient Infrastructure Laboratory

UCONN
UNIVERSITY OF CONNECTICUT

Development of a Rational Design Method for Shear Keys at In-Span Hinges in Multi-Frame Highway Bridges (Part-1)

Caltrans Contract: 65A0464

Masoud Mehr
Department of Civil and Environmental Engineering
University of Connecticut

Arash E. Zaghi, PhD, PE
Department of Civil and Environmental Engineering
University of Connecticut

NG-MRIL 14-01
August, 2014

Development of a Rational Design Method for Shear Keys at In-Span Hinges in Multi-Frame Highway Bridges

Part-1 A Rational Seismic Analysis Method for In-Span Hinge Shear Keys

Prepared for:

CALIFORNIA DEPARTMENT
OF TRANSPORTATION

Division of Engineering Service

DISCLAIMER STATEMENT

This document is disseminated in the interest of information exchange. The contents of this report reflect the views of the authors who are responsible for the facts and accuracy of the data presented herein. The contents do not necessarily reflect the official views or policies of the State of California or the Federal Highway Administration. This publication does not constitute a standard, specification or regulation. This report does not constitute an endorsement by the Department of any product described herein.

For individuals with sensory disabilities, this document is available in Braille, large print, audiocassette, or compact disk. To obtain a copy of this document in one of these alternate formats, please contact: the Division of Research and Innovation, MS-83, California Department of Transportation, P.O. Box 942873, Sacramento, CA 94273-0001.

ACKNOWLEDGEMENT

The research presented in this report was funded by the California Department of Transportation (Caltrans) Contract number: 65A0464. Special thanks are due Dr. Charles Sikorsky, the Caltrans Research Program Manager, for his strong support and his advices through the course of this project. Dr. Daryoush Tavatli, Mr. Marc Friedheim, Dr. Toorak Zokaie, Dr. Mark Mahan, Mr. Tom Ostrom and Mr. Mike Keever of Caltrans are thanked for their critical feedbacks, comments and suggestions. Dr. Saad El-Azazi is thanked for his support at early parts of the projects.

The strong support of Dr. Saiid Saiidi of the University of Nevada, Reno, and Dr. Mike Accorsi, Dr. Richard Christenson, and Dr. Sarira Motaref of the University of Connecticut is highly appreciated. UConn students Mr. Kevin Zmetra, Mr. Dylan Allen, Ms. Emma Burris-Janssen and Ms. Alicia Echevarria, are thanked for their assistance. Thanks are also due Ms. An-Wen Chen of Computers and Structures, Inc. for the generous donation of the license for SAP2000.

This report is part of a PhD dissertation by the first author supervised by the second author.

ABSTRACT

Long cast-in-place post-tensioned (CIP/PS) and reinforced concrete (RC) box-girder bridges are often constructed in multiple frames separated by in-span hinges in the superstructure. The multi-frame design simplifies construction by facilitating the post-tensioning of the superstructure and lowering the effects of creep deformations in long bridges; and allows for longitudinal thermal expansion and contraction. In-span shear keys are structural elements connecting adjacent frames in the transverse direction. Shear keys shall preserve the transverse integrity of frames. To date, no rational method is available for estimating design forces of in-span shear keys. In the absence of data on the transverse response of multi-frame bridges, Caltrans allows for shear transfer between two frames only if the periods of the stand-alone frames are comparable.

This project is conducted to improve understanding on seismic response of multi-frame bridges in transverse direction and present a data-driven, reliable, yet simple method that allows bridge design engineers calculate force demands for seizing shear keys. The objectives of this project are: formulating the dynamic characteristics of the multi-frame bridge system in the transverse direction; understanding the nonlinear response of this bridge system; developing a rational method for calculating force demands to minimize seismic damage to shear keys. A comprehensive analytical study is performed to achieve the objectives. OpenSees simulation software is used to conduct approximately 7,700 nonlinear response history analyses on high-fidelity models of a large set of prototype bridges. 52 two-, three-, four-, and five-frame bridges with single extended pile-shaft and two-column bents are considered. The set included a variety of realistic valley shapes. The prototype bridges are carefully designed in accordance to Caltrans Seismic Design Criteria v1.7. A suite of thirty-three ground motions, representing design ARSs, is used for NTH analyses.

The findings of this study are as follow. 1) Higher in-plane modes of vibrations of superstructure significantly contribute to shear key force response. 2) The ratio of the periods of adjacent frame does not have a major effect on the magnitude of shear key forces. 3) Spectral analysis reasonably estimate shear key force demands only if modal forces are modified individually by the corresponding modal displacement ductility values, 4) Transverse impacts, due to closure of gaps on the sides of shear keys, increase shear forces by an average factor of 2.5. 5) A non-uniform ground motion along the bridge length may increase shear key forces by a factor of approximately 1.25. 6) The maximum shear key force does not exceed the 75% of the transverse overstrength shear of the weaker adjacent frame. 7) The proposed analysis method accurately and effectively estimates the elastic shear force demands in multi-frame bridges.

TABLE OF CONTENT

LIST OF FIGURES

LIST OF TABLES

GLOSSARY

ARS:	Acceleration Response Spectra
CQC:	Complete Quadratic Combination
Two-Column:	A bridge substructure system composed of two columns in a bent
EDA:	Elastic Dynamic Analysis
In-Span Hinge:	A joint between adjacent frames in multi-frame bridges
Multi-Frame Bridge:	A bridge composed of multiple frames connecting at hinges by shear keys
MEDA:	Modified EDA method
MCE:	Maximum Considered Earthquake
NTH:	Nonlinear Time History
NUBE:	Non-Uniform Base Excitation
Pipe Seat Extender:	A steel pipe connecting adjacent frames at in-span hinges
PS:	Post tensioned concrete
PGA:	Peak Ground Acceleration
PGV:	Peak Ground Velocity
RC:	Reinforced Concrete
SDC:	Caltrans Seismic Design Criteria
SDOF:	Single Degree-of-Freedom
Shear Key:	A structural member connecting adjacent frames in transverse direction
Single-Column:	A bridge substructure system made of a single extended pile-shaft.
SRSS:	Square Root of Sum of Squares
UBE:	Uniform Base Excitation

1 Introduction

1.1 MULTI-FRAME BRIDGES WITH IN-SPAN HINGES

In this study, the transverse seismic response of multi-frame bridges is comprehensively investigated. The main objective of this study is to develop a rational method for assessing force demands for the seismic design of in-span hinge shear keys to ensure elastic response.

According to National Bridge Inventory (FHWA, 2013), 25,000 (4%) of the bridges in the United State are located in the State of California. Figure 1.1 shows the demography of California's bridges. Approximately 8,000 (32%) of California's bridges are concrete box girder bridges.

Long cast-in-place post-tensioned (CIP/PS) and reinforced concrete (RC) box girder bridges are often constructed in multiple frames separated by in-span hinges in their superstructure.

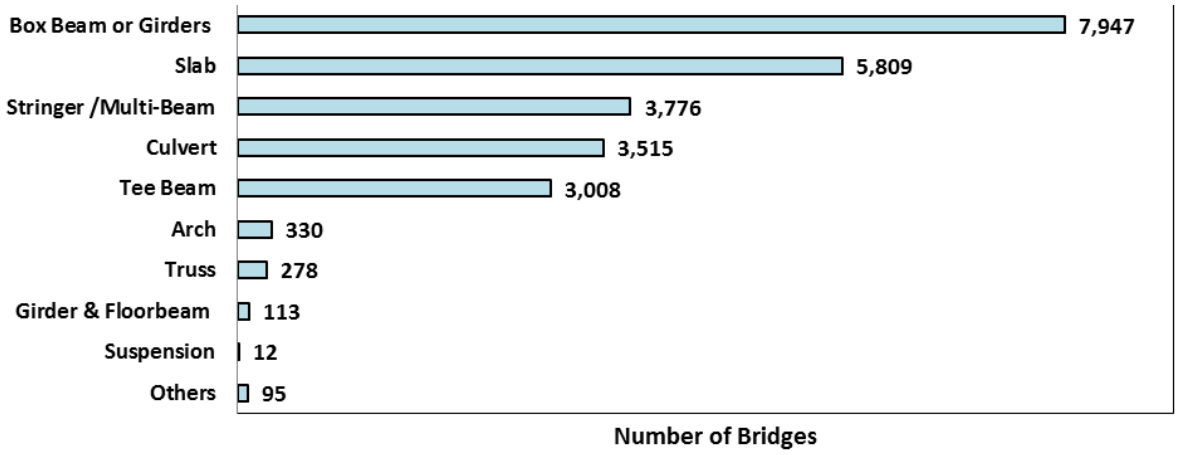

Figure 1.1 California Bridge Distribution Based on Super Structural Type (FHWA, 2013)

The schematic of a typical multi-frame bridge is shown in Figure 1.2. A multi-frame bridge system is composed of the following components: 1) frames that act individually under service loads; 2) intermediate or in-span hinges performing as longitudinal expansion joints that allow for longitudinal expansion and contraction of the superstructure; and 3) abutments that support the reaction of the end spans (DesRoches & Fenves, 1998). The multi-frame design simplifies construction by facilitating the post-tensioning of the superstructure and lowering the adverse effects of creep deformations in long bridges. It also allows for the longitudinal thermal expansion and contraction of the superstructure without inducing large forces in supporting columns (Hube & Mosalam, 2008). In addition, the multi-frame bridge system simplifies the design by allowing for the independent responses analysis of subsystems of a long bridge.

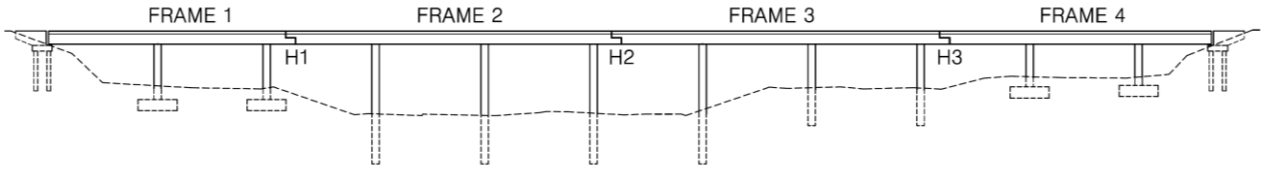

Figure 1.2 Schematics of a Multi-Frame Bridge

An in-span hinge detail is composed of end diaphragms, a concrete seat, bearings, and shear key/s. In-span hinges allow for the relative longitudinal movement of adjacent frames; at the same time, the transverse seismic integrity of the bridge needs to be preserved using one or more shear keys within the hinge to transfer lateral loads. These shear keys are typically constructed in the form of concrete blocks (Figure 1.3a). As a new practice in construction of concrete bridges in California, xx-Strong steel pipes (Figure 1.3b) are being used as in-span shear keys and as a measure to prevent seismic unseating (Yashinsky, 2013).

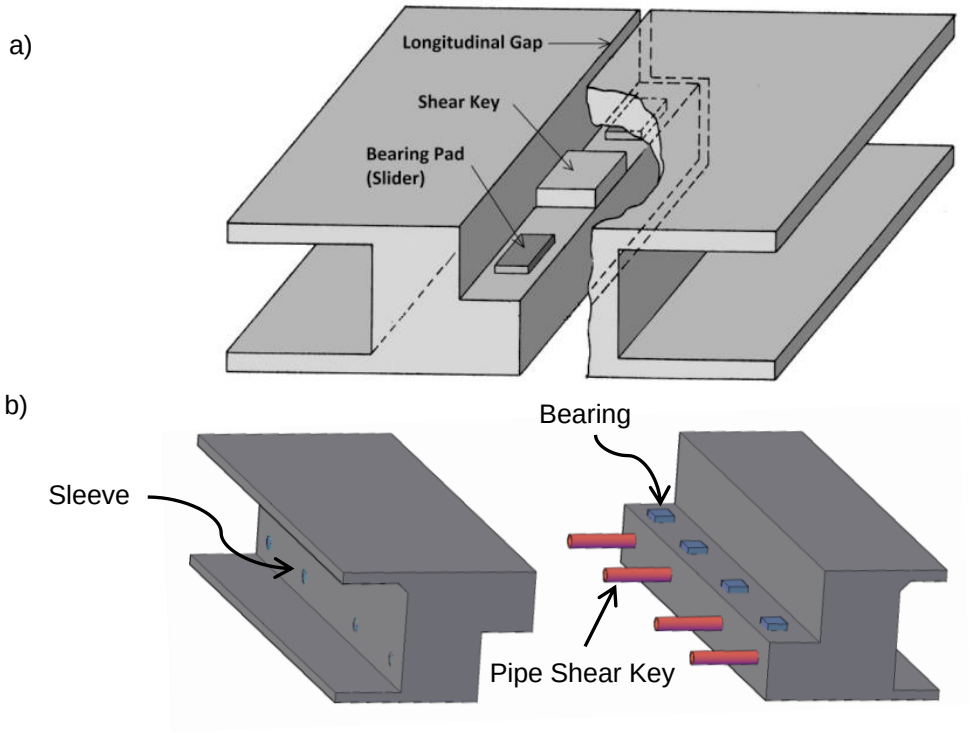

Figure 1.3 Typical Components of In-Span Hinges a) with Concrete Block Shear Key b) with Pipe Seat Shear Key

Figure 1.4 Left) In-Span Hinge in a Highway Interchange, Oakland, California (Courtesy of Godden), top right) Interstate 580 connector, San Rafael (Hube & Mosalam, 2008), bottom right) Interstate 80 connector, Albany (Hube & Mosalam, 2008)

The in-span hinges are typically positioned at or near the point of contraflexure of a continuous span superstructure under dead loads and, occasionally, in other places along the length (Figure 1.4).

1.2 BACKGROUND AND PROBLEM STATEMENT

Section 7.2.5 of the Seismic Design Criteria (SDC 1.7) (Caltrans, 2013) indicates that shear keys in in-span hinges are expected to transmit the lateral shear forces under small earthquakes and service loads. It also suggests that determining the seismic force demand on shear keys is a complex task because shear key forces are dependent on the magnitude of the relative displacement of the adjacent frames. There is no simple analytical method for the calculation of in-span shear key force. It is understood that the elastic dynamic analysis (EDA) method (i.e. response spectrum analysis) leads to a significant overestimation of shear key force demands and shall not be used to size shear keys. The Caltrans SDC allows for shear transfer between adjacent frames if the ratio of the fundamental periods of vibration of the stiffer frame to that of the more flexible frame, in transverse direction, is larger than 0.7, assuming a synchronized vibration of frames. While no specific design force for in-span shear keys is recommended, the force demand is limited to the sum of the columns overstrength shear (typically defined as M_o^{col} / L, SDC Sec. 2.3.2) in the weaker of the adjacent frames. In cases where the ratio of the period of adjacent frames is smaller than 0.7, it is suggested that the capacity of in-span shear keys is limited to prevent transfer of large lateral forces to the stiffer frame. In a simplistic approach, shear keys are designed as a capacity-protected member for a portion of the maximum of the overstrength shear in the neighboring bents (Caltrans project committee, personal communication, 2012).

1.3 LITERATURE REVIEW

After the collapse of several bridges in the 1971 San Fernando earthquake due to hinge unseating, the application of cable restrainers was considered for the seismic retrofitting of existing bridges (DesRoches & Fenves, 1998). The failure of some of these restrainers in the 1989 Loma Prieta and the 1994 Northridge earthquakes led studies to focus mainly on the longitudinal seismic response of multi-frame bridges. The goal of these studies was to determine the minimum gap size and seat width required to avoid significant pounding and unseating due to the out-of-phase movement of adjacent frames (Fenves & Ellery, 1998; Hao & Chouw, 2008; Singh, 1994; DesRoches & Muthukumar, 2004; Shrestha, et al., 2013). Some others focused on the design of hinge restrainers as a retrofit measure for bridges with inadequate seat width

(DesRoches & Fenves, 2001; DesRoches & Fenves, 1998; Trochalakis, et al., 1997; Tegos & Markogiannaki, 2014).

A dissertation titled “Earthquake Analysis of Multi-Frame Bridges” (Singh, 1994) includes the basic results of the elastic transverse response analysis of multi-frame bridges with no assessment of shear key demands. This work presents that the gap size between adjacent frames affects the transverse response and the coupling of longitudinal and transverse responses. Concerning the transverse seismic analysis of a multi-frame bridge, Priestly et al., 1996 state that it is essential for hinges to be modeled by their exact geometry, because the hinges open and close in a non-uniform fashion. They also suggest that the deck of the bridge is assumed rigid in plane (Figure 1.5). The in-plane rigidity of the superstructure allows the system to be statically determinate, making the shear key force easily obtainable (Priestly, et al., 1996).

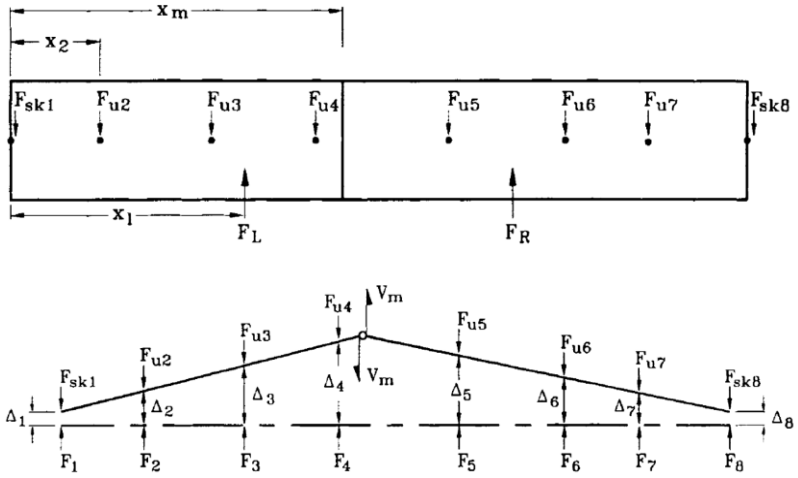

Figure 1.5 The Concept of a Simple Model for Calculating the Force Demand of In-Span Shear Key (Priestly, et al., 1996)

Bozorgzadeh (2007) showed that concrete shear keys are stronger than anticipated, so a new modular shear key has been designed to enable the capacity protection of bridge abutments (Bozorgzadeh, et al., 2007).

A review of the technical literature reveals that there is a lack of understanding of the transverse seismic response of multi-frame bridges and the parameters affecting that response. In addition, the role of in-span shear keys in the seismic performance of multi-frame bridges is unknown, and the current bridge seismic design codes do not include detailed provisions for determining the lateral force demands on in-span hinge shear keys. This study will address this gap by investigating the transverse response of multi-frame bridges, with a particular focus on developing a method that enables the shear force demands in in-span hinge shear key force to be assessed.

1.4 MOTIVATION AND OBJECTIVES

Caltrans has an acute interest in using multi-frame systems for the construction of long bridges because of the advantages this system offers. However, the lack of a reliable method for finding the force demand on in-span shear keys may lead to unrealistic and cost-prohibitive shear key designs. Although a similar natural frequency of the adjacent frames support the in-phase longitudinal vibration of the frames, it does not ensure a synchronous transverse seismic response of the frame. The transverse dynamic response of multi-frame bridges is more complicated than its longitudinal equivalent. This is because the transverse vibration of individual frames is compounded by the rotational modes of the frames' vibration and the in-plane vibration of the superstructure (Priestly, et al., 1996). Likewise, non-simultaneous lateral yielding of bents and abutment shear keys, as well as the transverse pounding of the frames, adds further complexity to the problem.

The main goal of this study is to develop a simple rational method for determining reliable design force demands for sizing in-span hinge shear keys. The results of the proposed study will benefit the safety of the design of in-span shear keys by offering an easy-to-implement guideline that is built on the EDA method and application of Caltrans ARSs (acceleration response spectrums) (Caltrans, 2013). This method eliminates the need for conducting sophisticated and computationally expensive nonlinear response history analyses for design purposes.

The specific objectives of this study are presented below:

- Demonstrate the dynamic transverse response characteristics of a multi-frame bridges system making use of the governing equation of motion and simplified analytical models.
- Develop high-fidelity three-dimensional nonlinear models for a suite of prototype bridges that enables performing a large number of nonlinear dynamic analyses.
- Examine the effects of several geometric and design parameters on the seismic response of multi-frame bridges and force demands on in-span shear keys.
- Develop a rational method for the reliable estimation of in-span shear key force demands as well as a realistic upper bound design force.
- Investigate the significance of in-span shear keys to the seismic performance of multi-frame bridges by studying bridge systems with ductile shear keys.

The results of this study are expected to expand the application of multi-frame bridges by addressing the lack of knowledge regarding the transverse seismic response of these systems.

1.5 METHODOLOGY

Figure 1.6 presents the overall design of the study. This study is consisted of two components: 1) understanding the dynamic characteristics of multi-frame bridge systems in transverse direction, and 2) conducting extensive analytical study on prototype bridges to generate the analytical data needed for the development of the method.

An analytical approach was taken to achieve these objectives. Approximately 7700 nonlinear time history (NTH) analyses were conducted on prototype bridges designed in accordance with Caltrans' seismic design practices. A suite of thirty-three earthquake ground motions is utilized in these analyses. In consultation with bridge design experts at Caltrans, a set of 56 box-girder prototype bridges with a span length of 110 and 200 ft was defined. The prototype models are comprised of multi-frame bridges with single-column of extended pile shaft and pinned-base two-column bents. To study the effect of the number of frames, sets of two-, three-, four-, and five-frame bridges are considered. The frame lengths vary from 440 to 720 ft as a practical length for post-tensioned superstructures. Prototype models with different realistic valley shapes are included in each set.

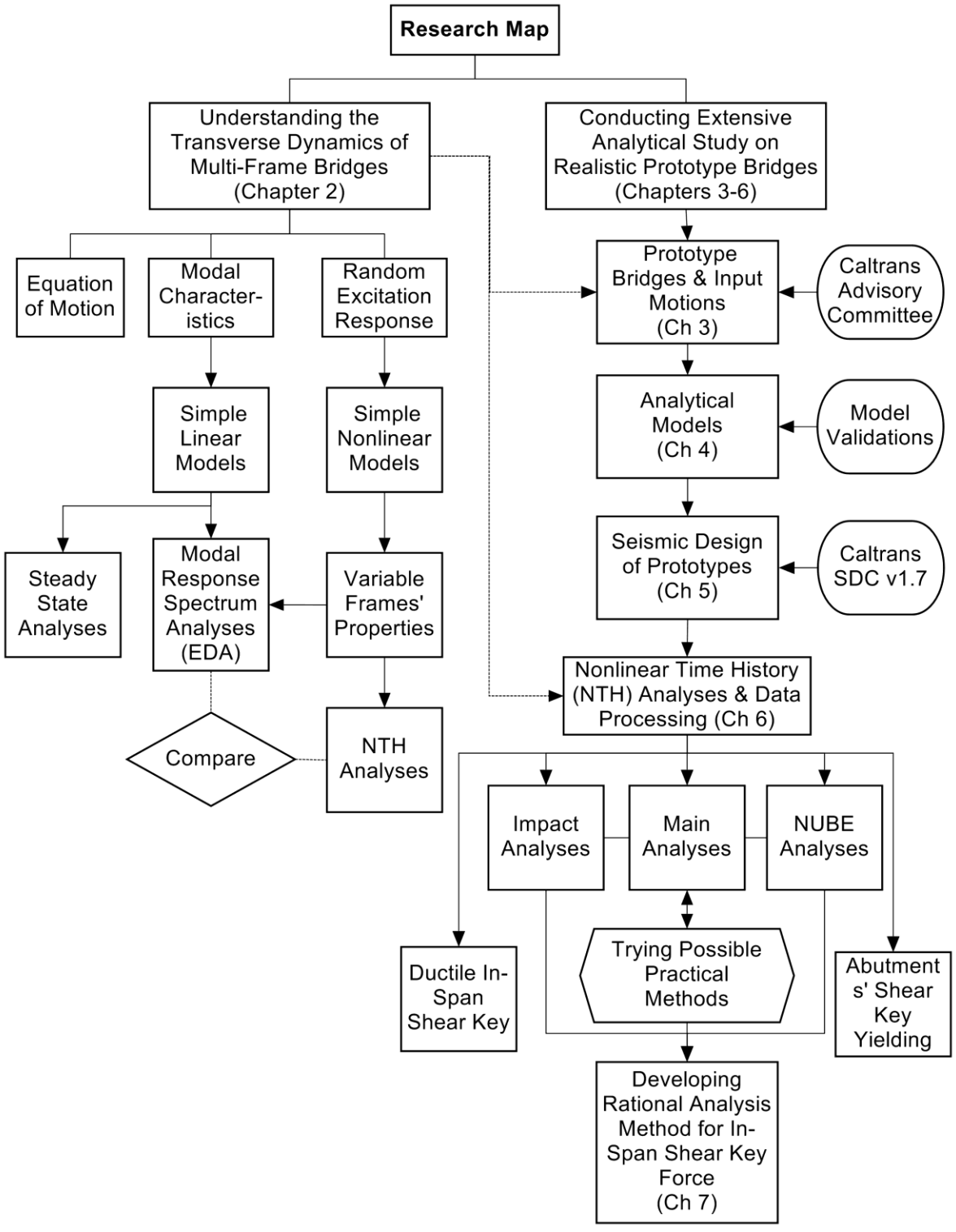

Figure 1.6 Research Map

Understanding the Dynamic Characteristics of Multi-Frame Bridge Systems: The dynamic response characteristics, unique to this bridge system, are investigated by performing steady state and modal analyses on two elastic bridge models. Nonlinear properties are assigned to the same models, and a limited number of time history analyses are performed to quantify the isolated effects of different system properties, such as period ratios of adjacent frames, on the seismic response of this bridge system.

Developing Refined Analytical Models: For the main body of the analytical studies, the spine modeling method (Caltrans, 2014; Aviram, et al., 2008) is used to develop the three-dimensional analytical model of each prototype bridge in OpenSees 2.4.4 (McKenna & Fenves, 2014). These analytical models are used in the design of the prototype bridges and for conducting the response history analyses. The elastic frame elements are used for the deck, diaphragms, and bent caps. The columns are modeled by the inelastic beam-column elements with fiber sections. For the single-column bridges, soil parameters are considered to locate the depth of fixity and the location of the plastic hinge. For the Two column bents, plastic hinges are assigned to the top of the column elements. Abutments and in-span hinges are explicitly modeled. Their assembly is composed of elements representing diaphragms, bearings, shear keys, gaps, backwall, and backfill soil.

The inelastic response of an individual column model is verified using the data from shake table experiments previously performed in UNR (Zaghi & Saiidi, 2010). The system level response of a sample OpenSees model was compared to that of the same model obtained from SAP2000 v15.1 (CSI, 2011). A series of sensitivity analyses are performed to define the modeling parameters of shear keys and transverse impact.

A robust OpenSees (McKenna & Fenves, 2014) script with over 10000 lines was developed in this research to generate and design the analytical models. This OpenSees code is used to perform gravity loading; EDA to find displacement demand; moment curvature analysis to find the effective section property; pushover analysis of subsystem column bents to calculate yield displacement and local ductility capacity; and pushover analysis of the entire structure to check the global displacement capacity.

Designing the Prototype Models: A suite of eleven ARSs is used for the seismic design of each prototype model according to Caltrans SDC v1.7 (Caltrans, 2013). The following five criteria are considered in designing each prototype: 1) the minimum local displacement ductility capacity of the bents; 2) the maximum displacement ductility demands of the bents; 3) the global displacement capacity of bridge; 4) the minimum lateral load capacity of the bents; and 5) the maximum permissible P-Delta effects.

Defining Seismic Hazard Levels and Ground Motions: Three seismic hazard levels of moderate, large, and severe are defined for this project. The corresponding

ARS's are obtained from Appendix B of SDC (Caltrans, 2013) for four soil types of B, C, D, and E for the hazard levels. The Pacific Earthquake Engineering Research Center (PEER) NGA ground motion database (PEER, 2011) is used to select and scale eleven sets of three biaxial ground acceleration histories. Each set is selected from sites with a soil type, moment magnitude, and intensity level compatible with one ARS. SeismoMatch software (Seismosoft, 2011) is used to match the scaled ground motions to the target ARS.

Performing a Nonlinear Time History (NTH) Analysis on the Prototype Models: Each prototype model is subjected to ground accelerations that is corresponded to its design ARS. Because each set of the ground accelerations are compatible with the ARS used to design the prototype bridges, the nonlinear response history analyses are expected to be proportional to the design and result in a realistic estimation of the force demands in in-span shear key. In addition to the "main analyses", a subset of analyses are conducted to investigate the effects of the following parameters on shear keys forces: gap closure and pounding of adjacent frames, yielding of abutment shear keys, and spatial variations in the base excitation along the length of the bridge. In addition, responses of the system with ductile in-span shear keys - as opposed to elastic shear keys - on the seismic performance of multi-frame bridge system is investigated.

Approximately 180GB of raw data was generated in this study. Multiple post-processing codes are developed using MATLAB 2012a (Mathworks, 2012) to develop the statistical distributions of the different responses, as well as the relationships between the shear key forces and the other response parameters. Responses such as the maximum displacement and acceleration at hinges, base shear, column ductility, period ratios of standalone frames, EDA forces, and pushover forces among several others are studied. Correlations between different response parameters and the relationships between the maximum shear key forces and multiple possible analysis methods are presented and discussed.

Developing a Rational Analysis Method and Presenting the Design Examples: The maximum shear key forces, obtained from the NTH analyses, are considered as the reference to develop a rational method for determining the design force demands for in-span hinge shear keys. In the proposed method, forces obtained from spectral analysis (i.e. EDA) are modified to account for the transverse yielding of the bridge. Factors are proposed to adjust the base force for the effects of the transverse pounding of frames and non-uniform base excitation. In addition, a rational upper bound force is defined to cap the shear key design force demand. Finally, a set of examples are presented to facilitate the implementation of the proposed method by bridge designers.

1.6 ORGANIZATION OF REPORT

This report comprises nine chapters and three appendices. This chapter is followed by an explanation of the fundamentals of multi-frame bridge system dynamics. Chapter 2 presents the transverse dynamics of this bridge system and provides the results of steady state analyses of elastic systems and response history analyses of simplified inelastic systems.

Chapter 3 provides information on the geometry of prototype bridges, seismic hazard levels, and the selection and spectrum matching of input ground motions.

Chapter 4 is allocated to the detailed description of the analytical modeling method. The assumptions used for developing elastic and inelastic models in OpenSees are presented in this chapter. This chapter also includes the results of the sensitivity analyses on modeling parameters.

In Chapter 5, the procedure for the seismic design of the prototype bridges based on SDC v1.7 is discussed in detail.

Chapter 6 presents the results obtained from the analyses of the prototype bridges. It presents the correlations, statistical distributions, observations, and interpretations of the analytical data. Correlations between different response parameters and the relationships between the maximum shear key forces and multiple possible analysis methods are also presented and discussed in this chapter.

Chapter 7 describes the proposed rational method. This is followed by some design examples.

A summary of this report and a list of observations and important conclusions are presented in Chapter 8.

Three appendices (A, B, and C) are included in the document to present the design of the ground motions and the spectrums, a summary of the design results of the prototype bridges, and graphs presenting the important analytical results, respectively.

2 Transverse Dynamics of Multi-Frames

A generalized equation of motion for the transverse vibration of a multi-frame bridge system is discussed in this chapter. The response of elastic systems is studied through steady state analyses of simple elastic models. Subsequently, the dynamic response of inelastic systems is investigated by performing nonlinear time history (NTH) analyses of the same models after implementing nonlinear elements. This chapter also investigates the effects of stiffness and the capacity ratios of adjacent frames on the dynamic response of the system. Finally, the results of the elastic dynamic analysis (EDA) are compared to the nonlinear results for the simple model.

2.1 EQUATION OF MOTION FOR THE MULTI-FRAME BRIDGE SYSTEM

Figure 2.1 provides a schematic of a three-frame bridge, as well as a free-body diagram of the effective forces on each frame. In this system, the superstructure is assumed to be composed of an articulated and flexible superstructure that is supported by a series of springs representing the transverse stiffness of the columns. The forces acting on the bridge superstructure are shown through a consideration of the shear key and column forces as external loads on each frame and the inertial forces as internal actions.

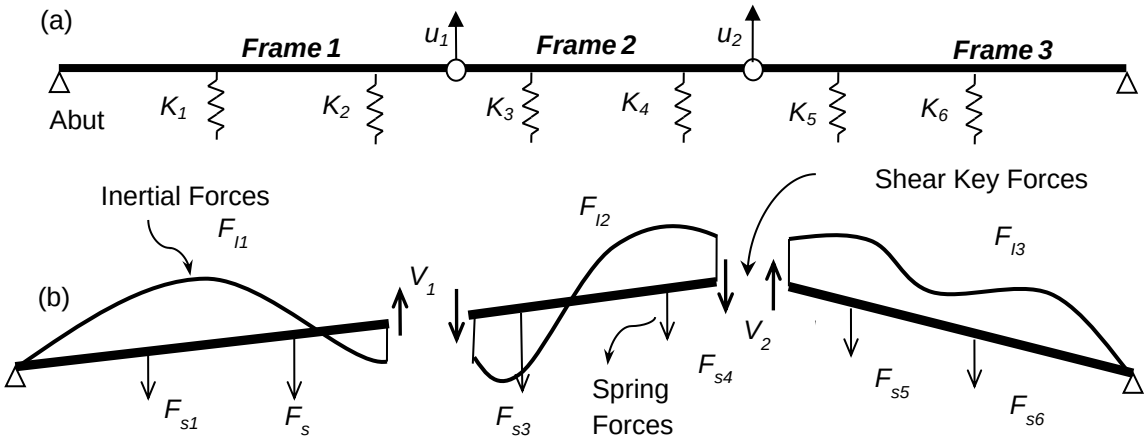

Figure 2.1 Schematic of a Multi-Frame Bridge and Dynamic Free Body Diagram of Frames

The inertial forces on the middle frame are shown in Figure 2.2 with a nonuniform distribution because of the flexibility of the superstructure and a nonuniform distribution of accelerations. The effects of the flexibility of the deck will be discussed in detail later in this chapter. Damping forces are not shown in this free-body diagram.

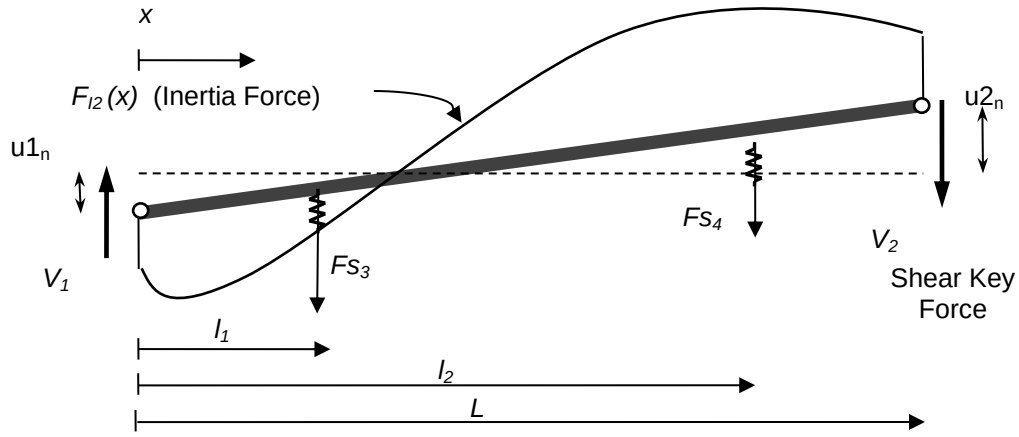

Figure 2.2 Free-Body Diagram of the Middle Frames

The equations of dynamic equilibrium for this frame are presented as Eq. 2.1 and 2.2. The equations are split into frames while they are coupled via shear key force. For each frame, two equations govern the equilibrium of transverse forces and the equilibrium of moments about the left end (in-span hinges).

$$\sum F = 0\,; \quad \int_0^l F_{I2}(x)\,dx + \sum Fs + V_1 + V_2 = 0 \qquad \text{Eq. 2.1}$$

$$\sum M = 0\,; \quad \int_0^l F_{I2}(x).x\,dx + Fs_3.l_1 + Fs_4.l_2 + V_2.L = 0 \qquad \text{Eq. 2.2}$$

By observing the equations of motion, it is clear that the shear key force stems from the difference between inertial and stiffness forces within individual frames. These forces are also affected by the interaction of frames with each other due to the continuity of displacements (the continuity of rotations does not exist because of the in-span hinges). On the other hand, if the frames are laterally isolated (zero shear key force is present) then the stiffness and inertial forces are in equilibrium. Applying compatibility of displacement or acceleration between adjacent frames at the hinges enables for solving the equation of equilibrium for the entire system.

2.2 MULTI-FRAME BRIDGES AND "PERIODIC STRUCTURES"

From a different point of view, long multi-frame bridges may be considered a finite periodic structure. An example of a periodic structure is shown in Figure 2.3. A periodic structure is a structure that is made up of similar sub-systems, which are connected end to end (Mead, 1996). Each sub-system is made up of two parts: The first is a group of point masses connected one after the other by massless springs; in the case of multi-frame bridges, the tributary mass is set on the column nodes. The second consists of elements that hold up a group of connected masses; for bridges, this is presented by the flexural stiffness of the superstructure.

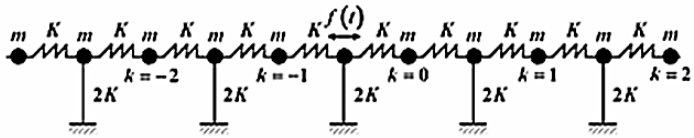

Figure 2.3 A Typical Periodic Structure (Zhang, et al., 2012)

A periodic structure undergoing a forcing function experiences wave propagation within its length (Mead, 1996). These waves move through each frame of a periodic structure. Based on the theory of wave propagation, a wave is reflected and transferred when it reaches a discontinuity. In multi-frame bridges, the presence of in-span hinges causes discontinuity in the rotation of the superstructures about the vertical axis. Thus, the in-plane flexural waves are reflected once they reach an in-span hinge. Due to the presence of these reflections, a form of explicit time history analysis capable of simulating the wave propagations is needed to obtain the exact response of the superstructure. Wave propagation deals with a transient response at a local level. Thus, the modal analysis method may provide slightly different results as the time-dependent effects are not captured**.**

Modal analysis is based on the theory that the response of a structure can be modeled by a combination of a set of harmonic modes referred to as the natural modes of vibration. The natural modes of vibration are inherent to the structure and depend only on physical characteristics such as stiffness, mass, and damping as well as the

spatial coordinates of each characteristic (He & Fu, 2001). Because the modal analysis cannot capture the transient (time-dependent) local effects, it ignores the presence of a wave's reflection. One should be mindful of this limitation of analysis methods - that time varying local responses are not explicitly simulated.

2.3 DYNAMIC CHARACTERISTICS OF ELASTIC SYSTEMS

2.3.1 Modal Characteristics of Multi-Frame Bridge Models

In order to understand the dynamic characteristics of multi-frame bridges, a series of modal and steady state analyses are performed on two simple elastic multi-frame bridge models shown in Figure 2.4. The shear key force, in-span hinge displacements, and in-span hinge accelerations are selected as structural responses. The excitation was applied as a base acceleration. For this purpose, two-dimensional stick models are developed in SAP2000 v15.1.0 (CSI, 2011) for the two- and four-frame bridges shown in Figure 2.4 . The span length is selected as 200 ft and the in-span hinges are located at one-fifth of the span. The superstructure is modeled by elastic frame elements with a realistic cross section shown in Figure 2.4. Each span is divided into five segments to capture the effect of the higher modes. To be able to read the shear key force responses, a 5-ft frame is used to connect the adjacent frames. The moment at one end of the connector element is released to account for the hinge action. The columns are simply modeled by linear springs with an elastic stiffness value of 100 kip/in. Abutments are modeled as pinned supports. Translational masses and rotational masses are assigned to each node. These masses are calculated based on the tributary length for each node.

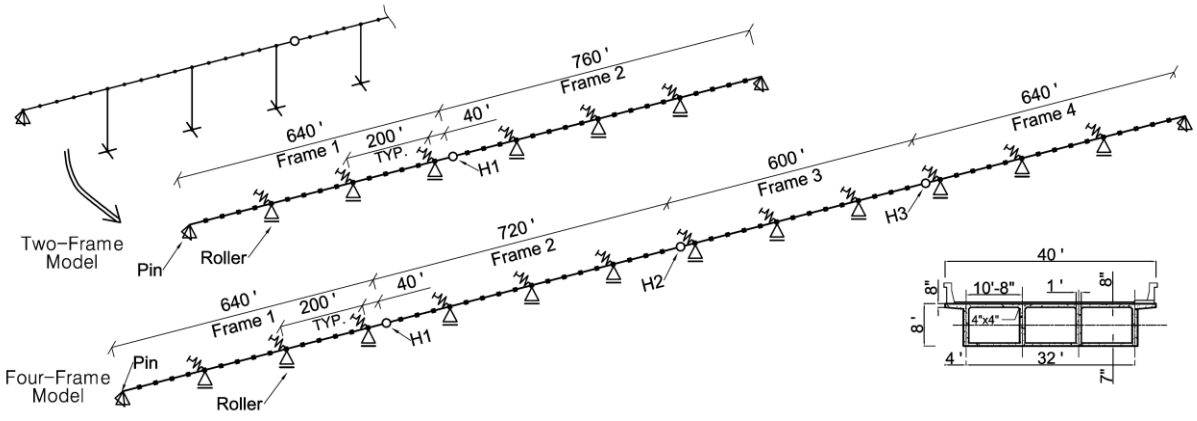

Figure 2.4 Two- and Four-Frame Bridge Models for Dynamic Characterization Studies

The rationale for defining two- and four-frame models is to study the effects of the number of frames on the responses of the hinge/s. As such, comparing the results between hinge H1 in the two-frame model and hinges H1, H2, and H3 in the four-frame

model allows for the consideration of different frame numbers and different frame boundary conditions. The first ten transverse mode shapes of the two- and four-frame models and their corresponding natural frequencies are presented in Table 2.1 and Table 2.2, respectively. The dashed line shows the locations of in-span hinges. The mode shapes are obtained from two-dimensional models with only transverse and rotational DOFs. In a three-dimensional model of a bridge, the longitudinal and vertical modes may fall between the transverse modes.

The modal shapes with spread out frequency values indicate the dynamic effects of the in-plane flexibility of the superstructure. The first and the first three modes of vibration in the two- and four-frame models, respectively, may be considered as “rigid superstructure” modes since the flexural deformations of the superstructure do not appear to be defining the modal shapes. Another important observation from Table 2.3 is the close frequencies of the first three natural modes of the four-frame model.

It is notable that individual frames experience the same modal shapes one at a time but at different frequencies. The number of zero-crossings (or the number of points of contraflexure) within one frame is an identifier of the modal shape. Therefore, a multi-frame bridge with *n* frames is composed of *n* dynamic subsystems. As an example, for the two-frame model, mode shapes #2 and #3 differ because Frame 1 goes from its first inter-frame mode to the second one. Similarly, in mode shapes #3 and #4, Frame 2 goes from its second to third inter-frame modes. This is a well-understood phenomenon in periodic structures, which is discussed in Sec. 2.2. For the same reason, the rule that “the mode number is equal to the number of zero-crossings + 1” can be violated in multi-frame bridge systems. As an example, the 9^{th} and 10^{th} natural mode of the four-frame model have 9 and 10 zero-crossings, respectively.

The significance of this phenomenon, with respect to the forces in the shear keys at different hinges, is that each shear key is influenced by the mode shapes of the adjacent frames. There will be mode shapes that do not contribute to the shear key forces. This distinct modal characteristic of multi-frame bridges necessitates the inclusion of the participation of a large number of modes in order to accurately estimate the maximum shear key forces at all the hinges.

Table 2.1 Two-Frame Transverse Modal Properties

Mode No.	Freq. (Hz)	Mode Shape Frame-1 Frame-2
1	0.57	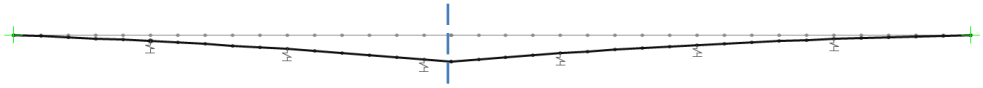
2	0.69	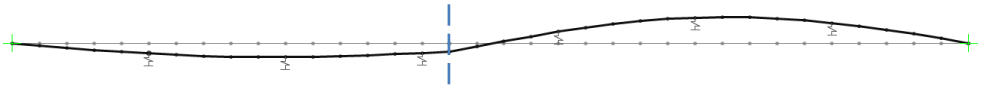
3	0.81	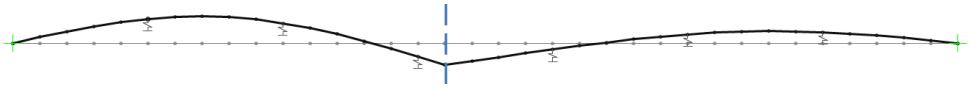
4	1.45	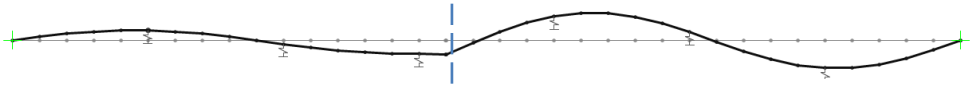
5	1.96	
6	2.90	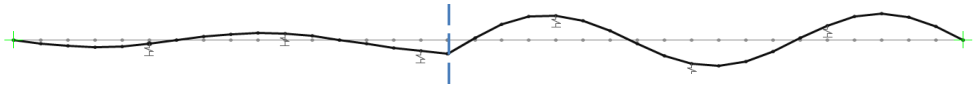
7	3.89	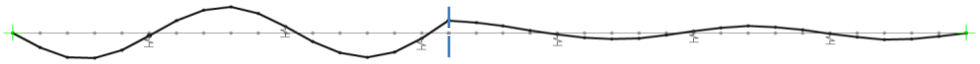
8	4.80	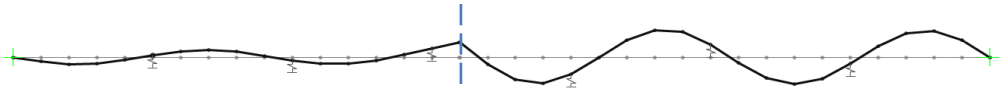
9	6.50	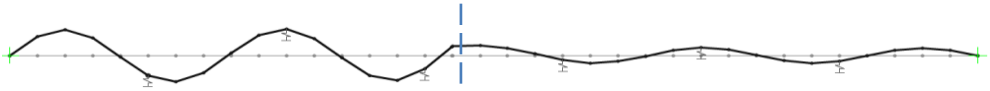
10	7.15	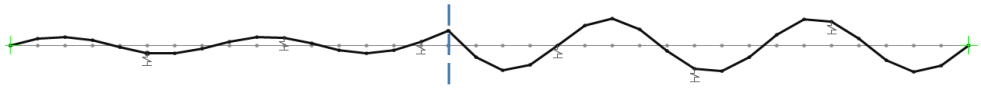

Table 2.2 Four-Frame Transvese Modal Properties

Mode No.	Freq. (Hz)	Mode Shape
		Freme-1 / Frame-2 / Farme-3 / Frame-4
1	0.56	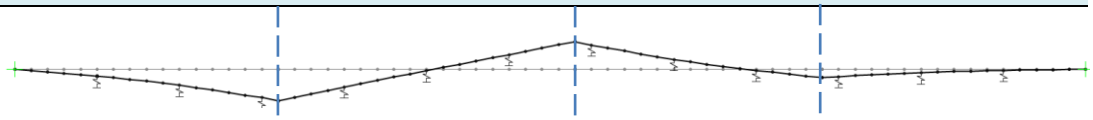
2	0.58	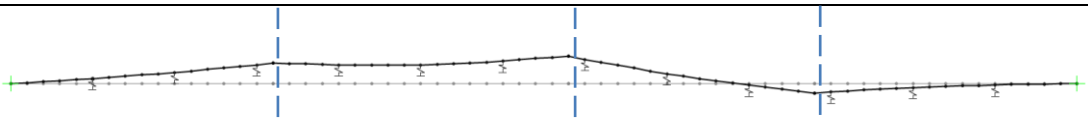
3	0.63	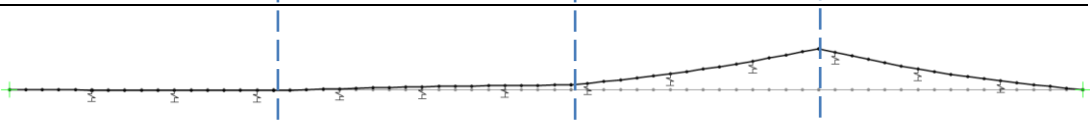
4	0.73	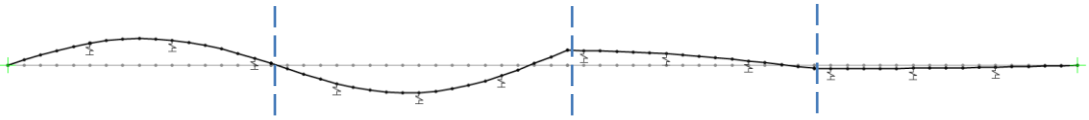
5	0.82	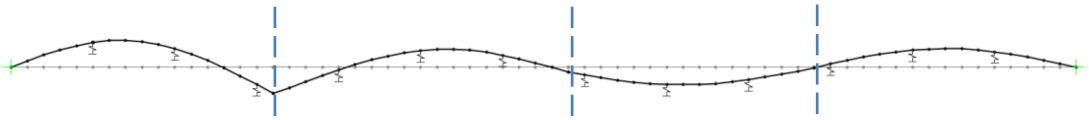
6	0.86	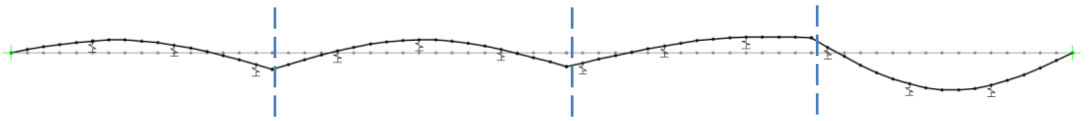
7	1.05	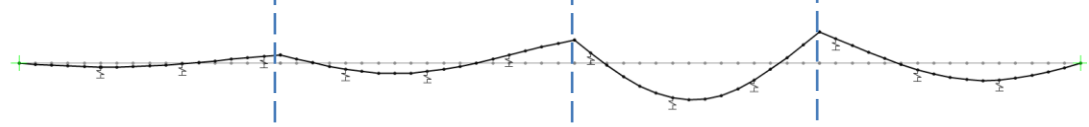
8	1.67	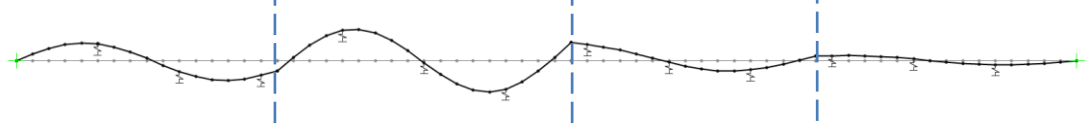
9	1.99	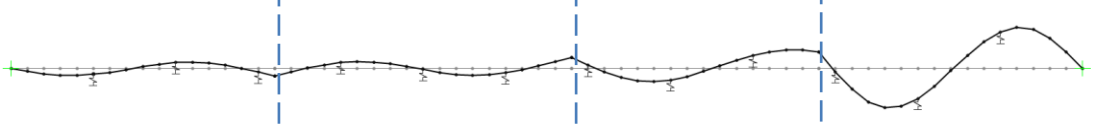
10	2.10	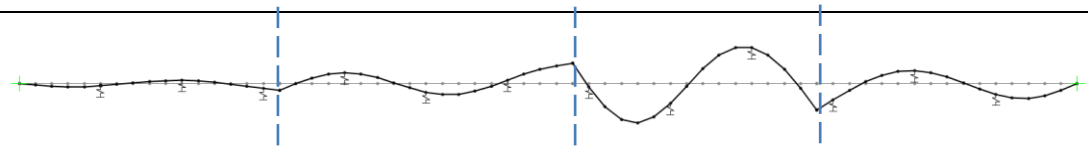

2.3.2 The Concept of Steady State Response

When a harmonic force is applied to a structural system, it will typically reach a steady state after going through some transient behavior. The steady state analysis is a common method used for studying the response of elastic structures to harmonic excitations at different frequencies (Rao, 2010). If the support of a spring-mass-damper system with mass, stiffness, and damping coefficients of *m*, *k,* and *c* undergoes harmonic displacement excitation at the base (as shown in Figure 2.5a), the equation of motion (Eq. 2.3) can be obtained from the free body diagram shown in Figure 2.5b.

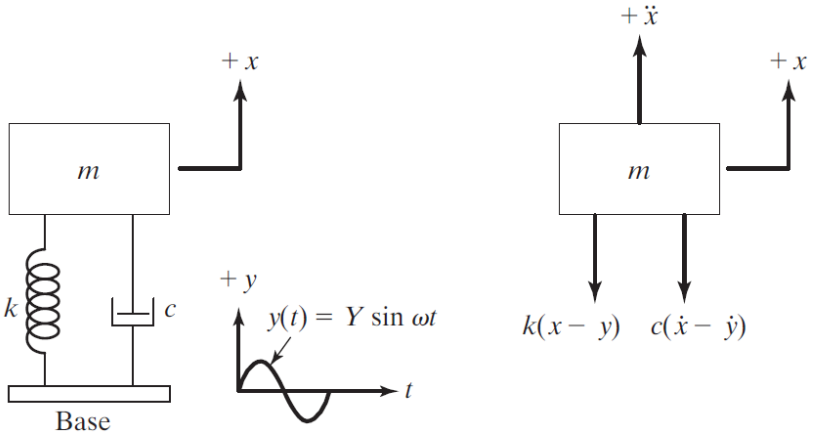

Figure 2.5 Base Excitation on a Mass-Spring System (Rao, 2010)

The steady state displacement response of the mass, $x_p(t)$, can be expressed as Eq. 2.4.

$$m\ddot{x} + c(\dot{x} - \dot{y}) + k(x - y) = 0 \qquad \text{Eq. 2.3}$$

$$x_p(t) = X\sin(\omega t - \phi) \qquad \text{Eq. 2.4}$$

Where ω and ϕ are the frequency of the base excitation and phase angle respectively, and *X* is the amplitude of the response. The ratio of the amplitude of the response, $x_p(t)$, to that of the base motion, $y(t)$, i.e. *X/Y*, is called the displacement transmissibility (named as steady state response). The magnitude and phase of the steady state response can be presented as a function of ω as expressed in Eq. 2.5 and 2.6, respectively.

$$\frac{X}{Y} = \left[\frac{1+(2\zeta\omega/\omega_n)^2}{\left[1-(\omega/\omega_n)^2\right]^2+[2\zeta\omega/\omega_n]^2}\right]^{\frac{1}{2}} \qquad \text{Eq. 2.5}$$

$$\phi = tan^{-1}\left[\frac{2\zeta(\omega/\omega_n)^3}{1+(4\zeta^2-1)(\omega/\omega_n)^2}\right] \qquad \text{Eq. 2.6}$$

where ω_n is the natural frequency of the dynamic system and ζ is the critical damping ratio. The amplitude of the steady state response and phase angle can be plotted for different frequencies of excitation as shown in Figure 2.6.

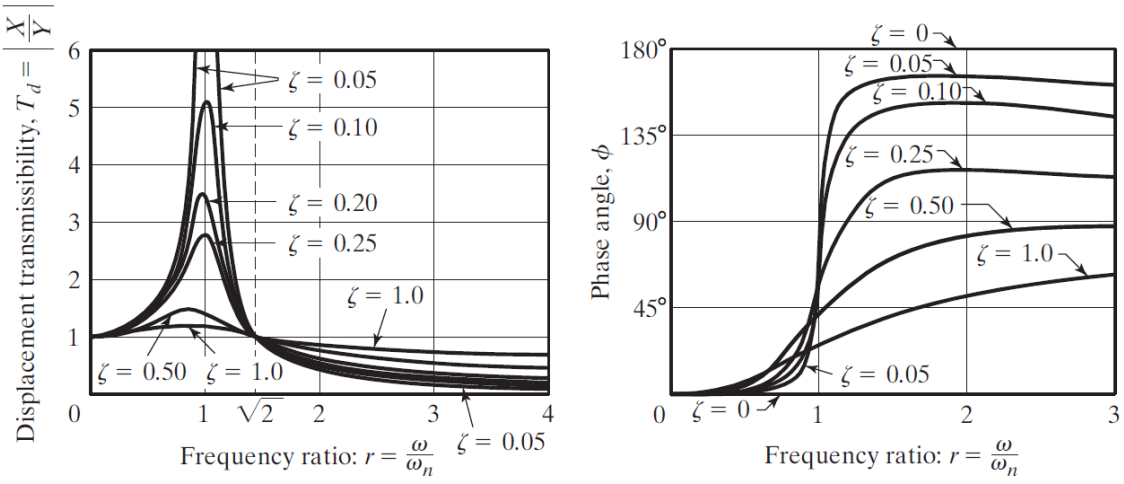

Figure 2.6 Steady-State Displacement Response Functions (Rao, 2010)

Steady state relationships can be obtained for any given excitation and response measures of a structure, such as displacements, accelerations, and forces. The steady state analyses can be performed on any complex multi-degree of freedom structural system using structural analysis software packages, such as SAP2000 (CSI, 2013). In a more complex multi-support system under non-uniform base excitation, the excitation frequencies must be kept the same.

2.3.3 Steady State Response Analysis of Simple Bridge Models

The two models introduced in Sec. 2.3.1 are used for the steady state analyses. The steady state analysis is performed using a base acceleration with frequencies ranging from 0.0Hz to 3Hz at 0.01Hz intervals. The steady state responses of the in-span hinges are obtained for the key forces, in-span hinge transverse displacements, and in-span hinge transverse accelerations. The unit of a steady state response curve is equivalent to that of the response divided by that of the excitation. Yet, in order to be able to compare the effects excitations with different frequencies on the response of the system, the magnitudes of the response curves are normalized with their maximum values. The steady state relationships for in-span hinges are shown in Figure 2.7 for the two-frame system. The same response is shown in a logarithmic scale in Figure 2.8. The response of hinges H1, H2, and H3 of the four-frame bridge model are shown in Figure 2.9, Figure 2.10, and Figure 2.11, respectively. The natural frequencies and the mode numbers are presented by the vertical dot lines.

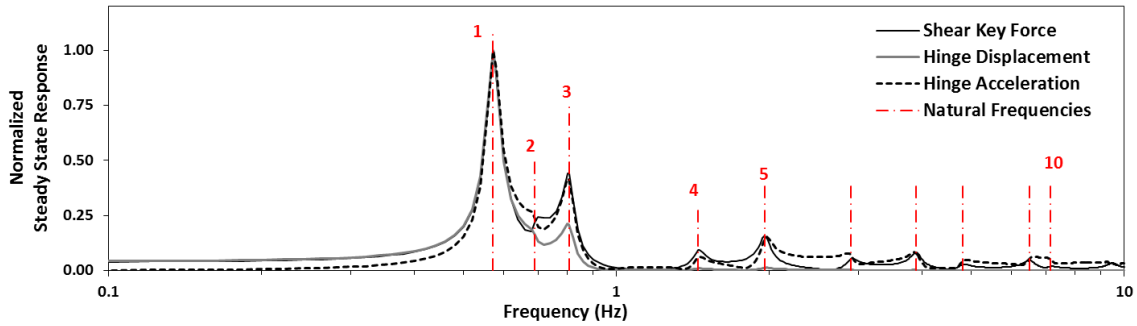

Figure 2.7 The Normalized Steady State Responses of the In-Span Hinge H1, Two-Frame Model

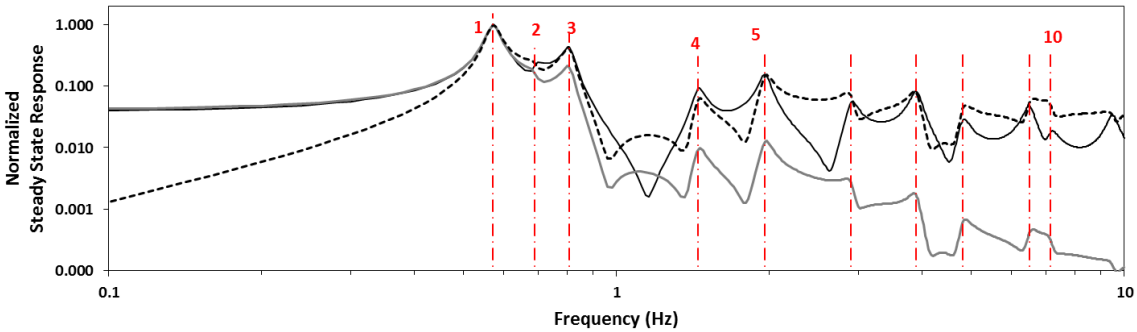

Figure 2.8 The Same as Figure 2.8, Logarithmic Scale

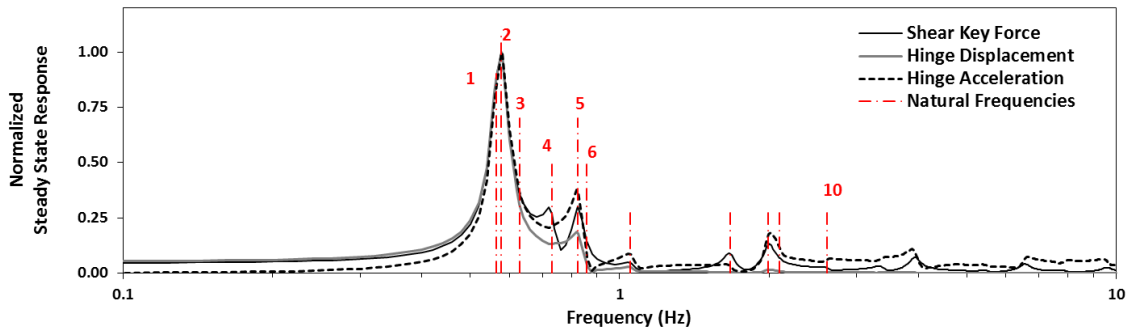

Figure 2.9 The Normalized Steady State Responses of the In-Span Hinge H1, Four-Frame Model

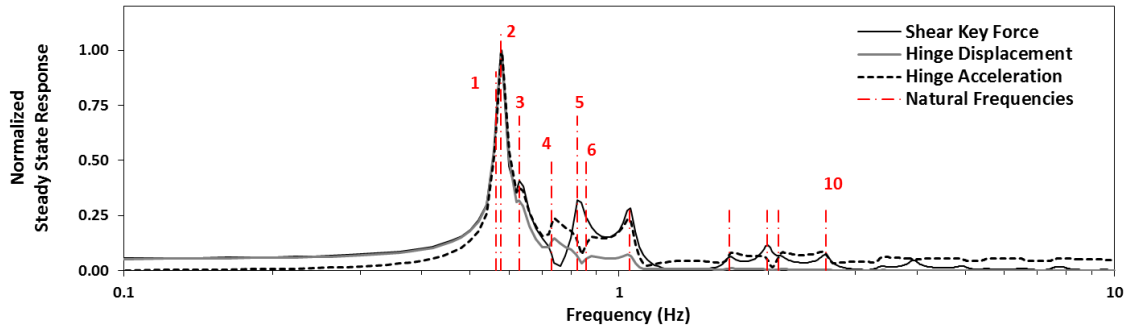

Figure 2.10 The Normalized Steady State Responses of the In-Span Hinge H2, Four-Frame Model

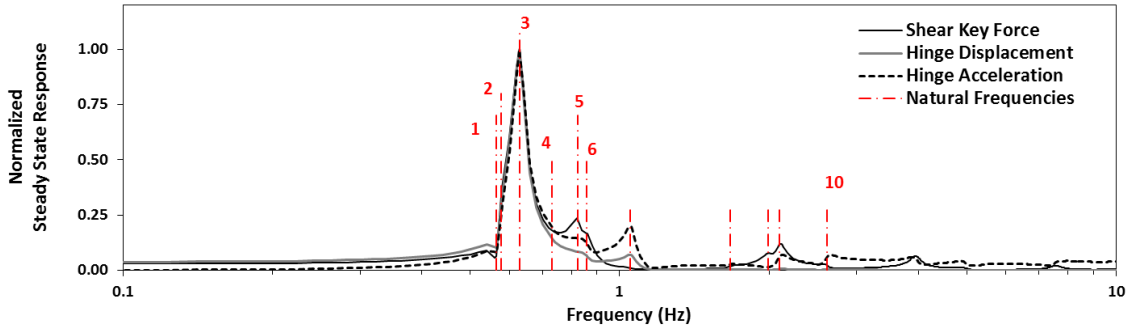

Figure 2.11 The Normalized Steady State Responses of the In-Span Hinge H3, Four-Frame Model

It should be noted that in this steady state analysis, the amplitude of the base excitation is constant over the studied range of frequencies; hence, the relative amplitude of the steady state response curve is directly related to the relative maximum responses at different frequencies of excitation.

A study of these curves indicates that the displacement responses at in-span hinges are not significantly affected by the higher modes. In contrast, the higher natural modes contribute significantly to the accelerations and shear key forces. In general, the shear key force responses often follow a pattern similar to that of the acceleration for frequencies larger than the first mode's frequency. The input frequencies that have an impact on the acceleration response of the hinges are those that contribute to the shear key force responses.

For the two-frame model, the first mode of vibration has the largest contribution to the three response parameters. The hinges in the four-frame model do not respond similarly to the excitation of the different modes. In this model, hinges H1 and H2 are controlled by the second mode of vibration, while the response of hinge H3 is governed by the third mode. This confirms the multi-subsystem response characteristics of multi-frame bridges as discussed in Section 2.3.1.

2.3.4 Analysis of Subsystem Models

To investigate the effect of the dynamic responses of the far frames on the force responses of an in-span hinge, a separate set of analyses are conducted on the four-frame model. In these analyses, three subsystems, each comprised of only two of the adjacent frames of the four-frame model, are analyzed. These subsystem models include Frame 1-Frame 2, Frame 2-Frame 3, and Frame 3-Frame 4 to study the H1, H2, and H3 hinges, respectively. Three steady state shear key force response curves are generated as shown in Figure 2.12 to Figure 2.14. These figures show that an approximate shear key force response may be obtained from the analysis of a subsystem of the two adjacent frames in isolation. This is more evident for the case of H3. This may be a result of the isolated dynamic response of this hinge, while the

responses of the other two hinges are closely coupled because of their close natural frequencies. This can be observed by comparing the modal shape of the four-frame bridge in Table 2.2.

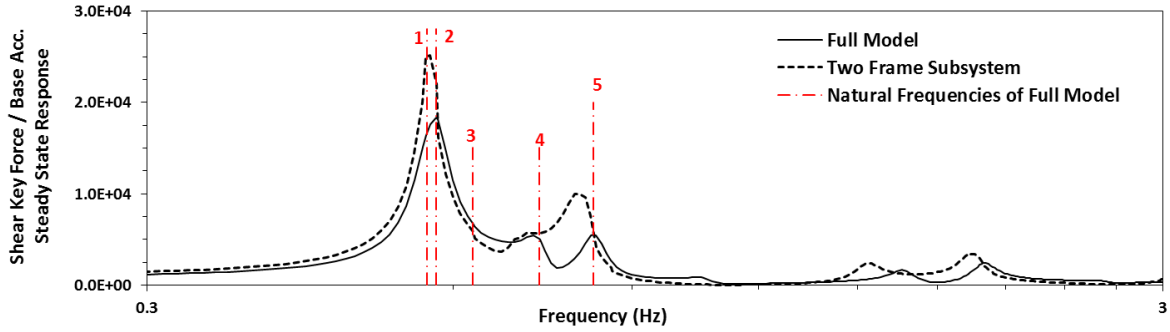

Figure 2.12 Steady State Responses of Hinge H1 from the First Subsystem of Four-Frame Model

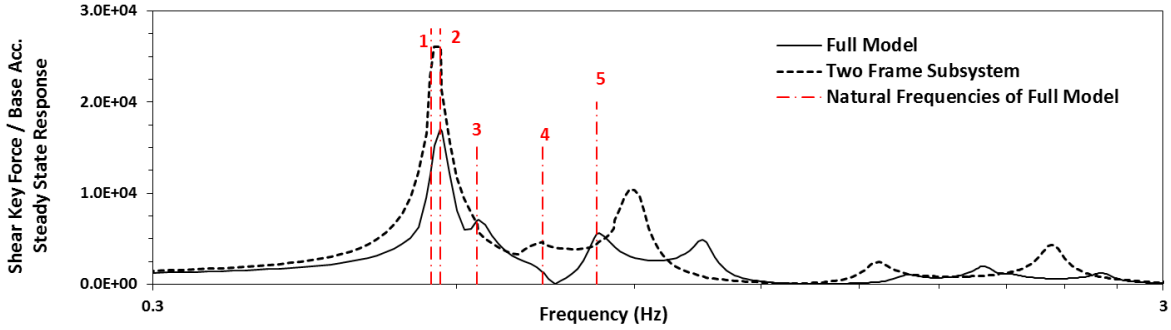

Figure 2.13 Steady State Responses of Hinge H2 from the Second Subsystem of Four-Frame Model

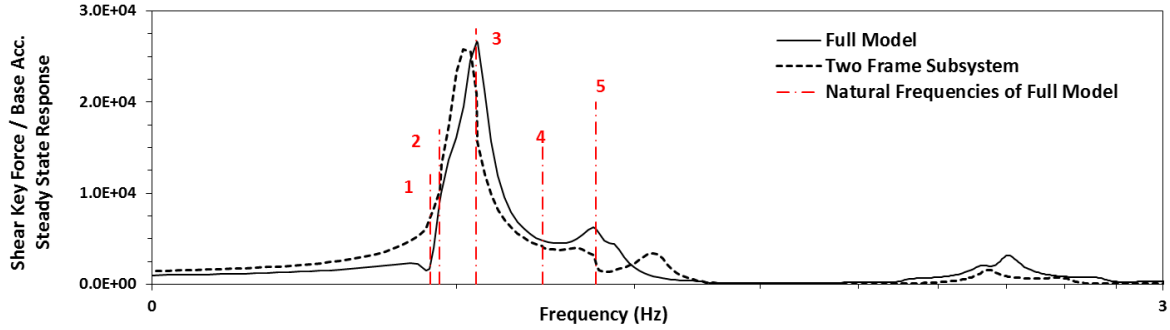

Figure 2.14 Steady State Responses of Hinge H3 from the Third Subsystem of Four-Frame Model

2.3.5 Effect of the Rigidity of the Superstructure

Finally, to study the significance of the flexibility of the superstructure on the force response of the shear key, the two-frame model is analyzed after the superstructure

was made 100 times stiffer. Figure 2.15 shows the steady state responses obtained from the models with flexible and stiff superstructures. It is evident that only the effect of the first mode of vibration can be captured accurately, which may result in an under prediction of the shear key forces. The model shows some higher mode effects because the superstructure is not completely rigid. This is a clear indication that, even in the case of unrealistically stiff superstructures (100 times stiffer), the higher modes may form and contribute to the force due to the large length of the superstructure. Thus, to obtain the maximum shear key forces, the modal analyses shall include modes with frequencies that are typically larger than those sufficiently used for finding the maximum displacements.

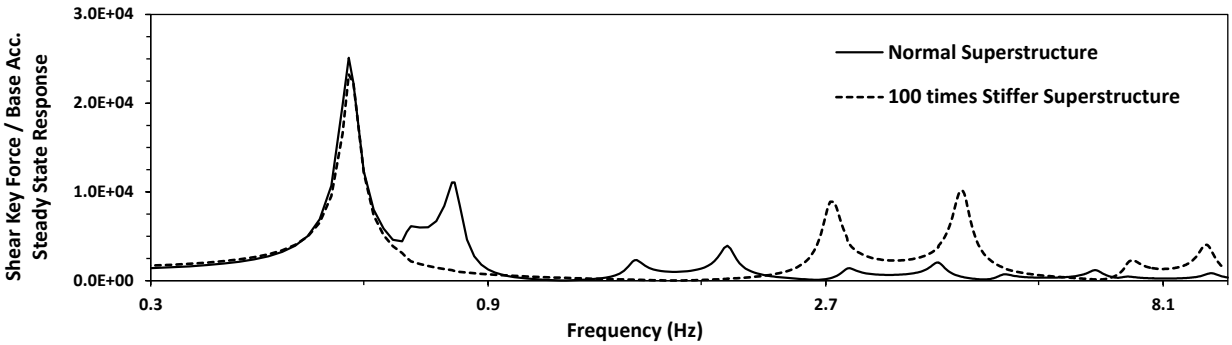

Figure 2.15 Effect of Superstructure Flexibility on Shear Key Force Response

2.4 DYNAMIC RESPONSE CHARACTERISTICS OF INELASTIC SYSTEMS

2.4.1 Modeling Assumptions

To investigate the dynamic response characteristics of an inelastic multi-frame system and study the effects of basic system properties, a number of response history analyses are performed on the same bridge models illustrated in Figure 2.4. This time, an elasto-plastic force-displacement relationship was assigned to the support springs. For nonlinear response history analyses, OpenSees 2.4.3 (McKenna & Fenves, 2014) is employed in place of SAP2000 because of the simplicity it offers for the execution of the parametric studies that will be presented later in this chapter.

The deck is modeled using “elasticBeamColumn” elements with the transverse stiffness of the cross section shown in Figure 2.4. Each span is broken into five segments and the same masses used in the elastic models are assigned to the nodes. For modeling the in-span hinge, “zeroLength” elements with uniaxial material “Elastic” with large shear stiffness are used to connect the end nodes of adjacent frames. The support springs are modeled by “zeroLength” elements with the inelastic material “Steel02” assigned to them (OpenSees Wiki, 2014). This material has a bilinear force-

displacement relationship. The elastic stiffness is set equal to 100 kip/in, the yield capacity was taken to be 300 kips, and the post-elastic stiffness of the springs was assumed to be 3% of the elastic stiffness. The yield force is based on an approximate seismic design for the acceleration response spectrum (ARS) for soil type C, a magnitude of 7.0-7.5, and a PGA of 0.4g per Caltrans SDC (Caltrans, 2013). A damping ratio of 5% is assigned to the first and third modes using the Rayleigh formulation (Chopra, 2001).

The ground motion number NGA#782, which was obtained from the PEER database (PEER, 2011), is utilized as the base excitation. The ground motion is matched to the design spectrum. Figure 2.16 shows the design ARS and the acceleration spectrum of the matched acceleration history.

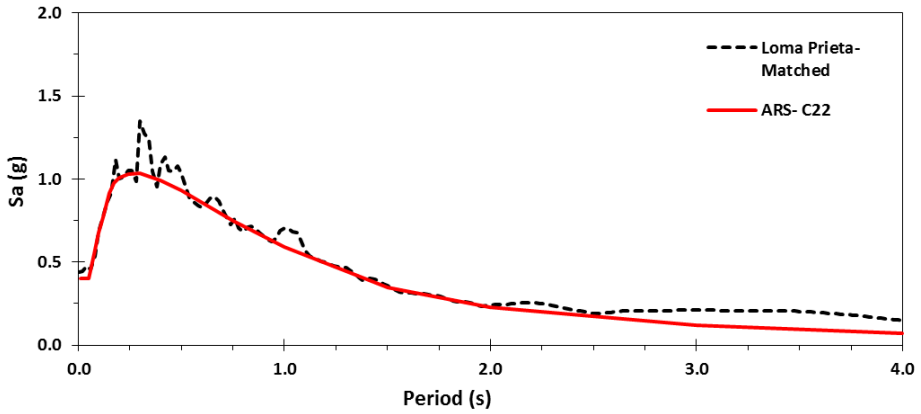

Figure 2.16 Acceleration Response Spectrum of the Design and Matched Ground Motion

2.4.2 Responses and Observations

The response histories of the shear key force, in-span hinge displacement, and acceleration responses are normalized with their maximum values and plotted in the same graphs as shown in Figure 2.17 for the two-frame model. Figure 2.18 to Figure 2.20 are the same graphs but for H1, H2, and H3, respectively, for the four frame model. Only the portion of the response that is comprised of the large intensity responses is presented.

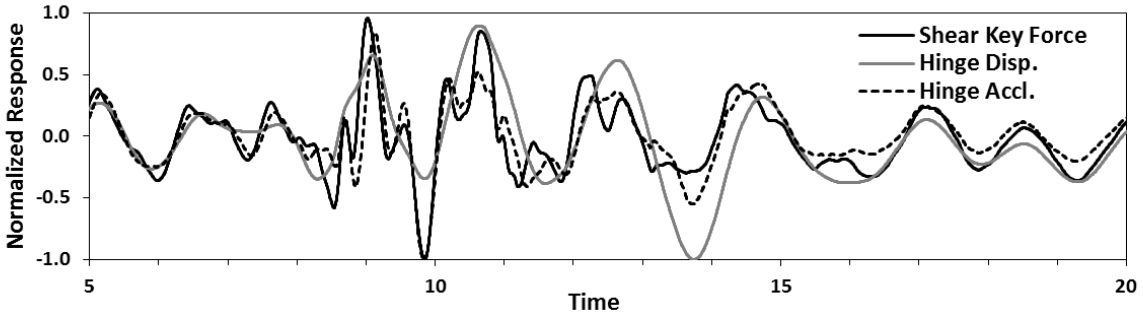

Figure 2.17 Normalized Response Histories of Hinge in Two-Frame Model

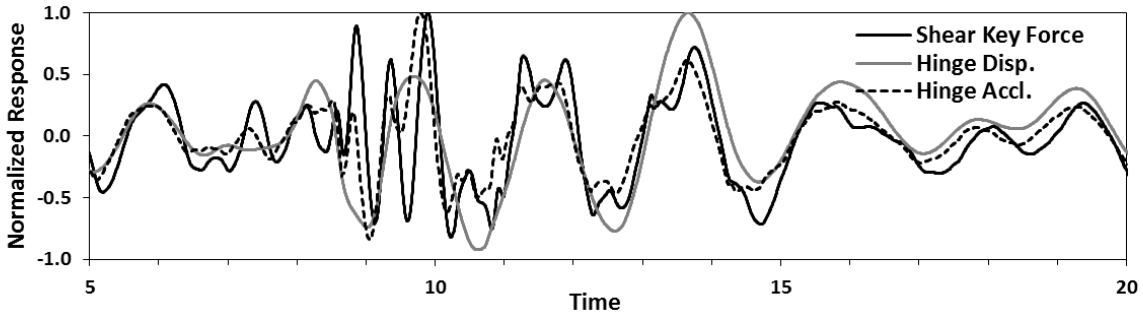

Figure 2.18 Normalized Response Histories of Hinge H1 in Four-Frame Model

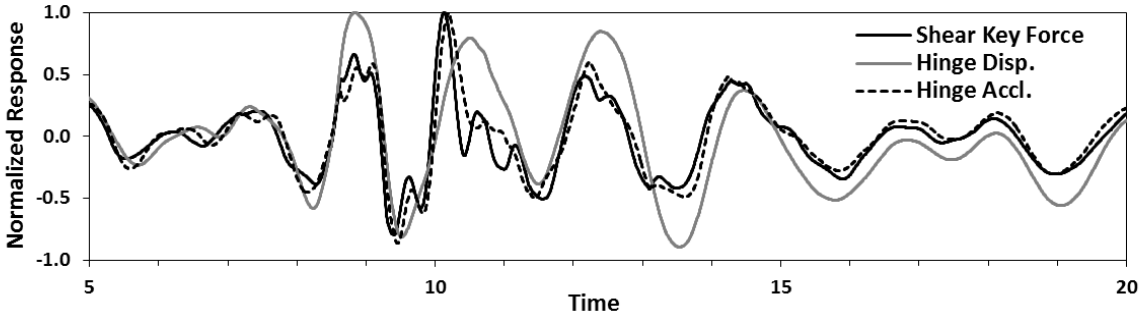

Figure 2.19 Normalized Response Histories of Hinge H2 in Four-Frame Model

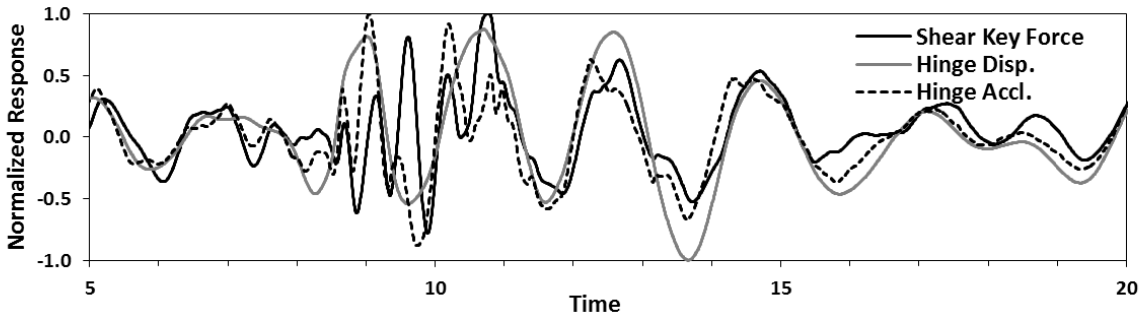

Figure 2.20 Normalized Response Histories of Hinge H3 in Four-Frame Model

The general observation drawn from the figures shown above is that the shear key force profile approximately follows that of the hinge acceleration. Careful comparison of the shear key force histories, the hinge acceleration histories, and the hinge displacement histories confirms that the first two responses have larger high frequency contents. The maximum shear key force may not happen simultaneously with the maximum displacement or acceleration. These observations are consistent with the findings of the steady state analyses, thus demonstrating that the dynamic transmissibility of the system is similar to the shear key force and the hinge acceleration responses. The steady state graphs and response history results clearly indicate that higher modes play a significant role in maximizing the shear key force. On the other hand, these higher modes do not contribute significantly in the displacement response of a multi-frame bridge system.

Figure 2.21 to Figure 2.24 show the relationship between shear key force and hinge displacement, velocity, acceleration, and the base shear values. No clear relationship exists between displacement and shear key force.

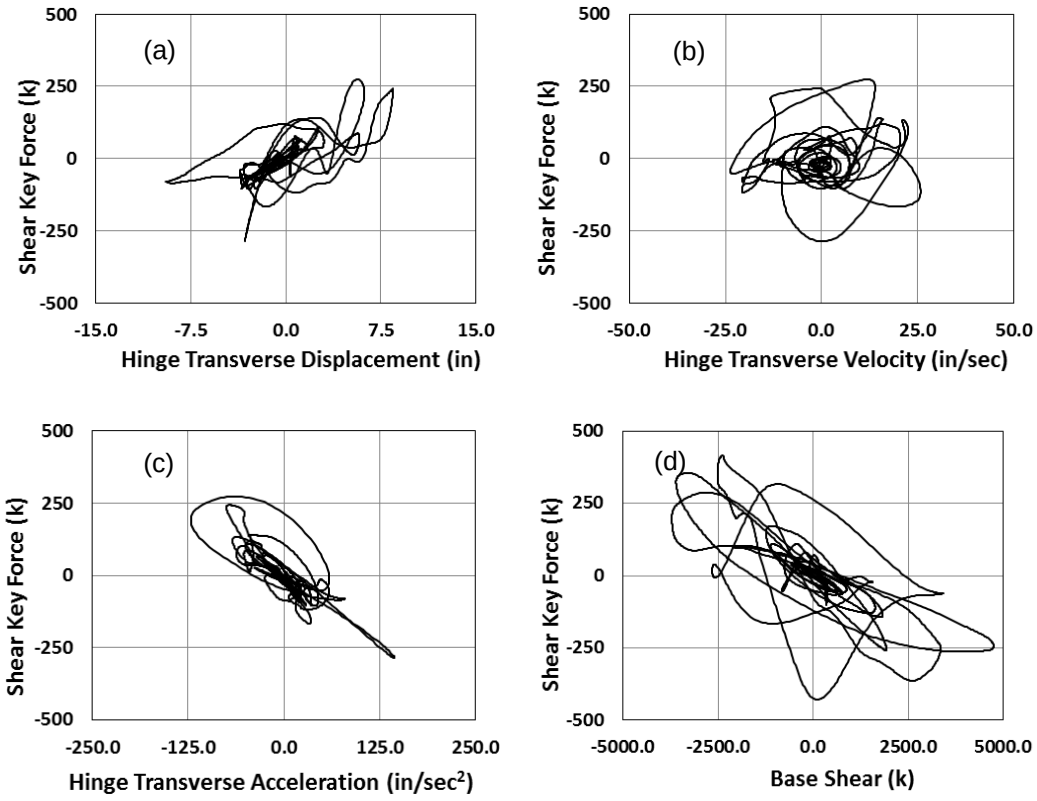

Figure 2.21 Two-Frame Model, Relationship of Shear Key Force with a) Hinge Displacement, b) Hinge Velocity, c) Hinge Acceleration, and d) Base Shear

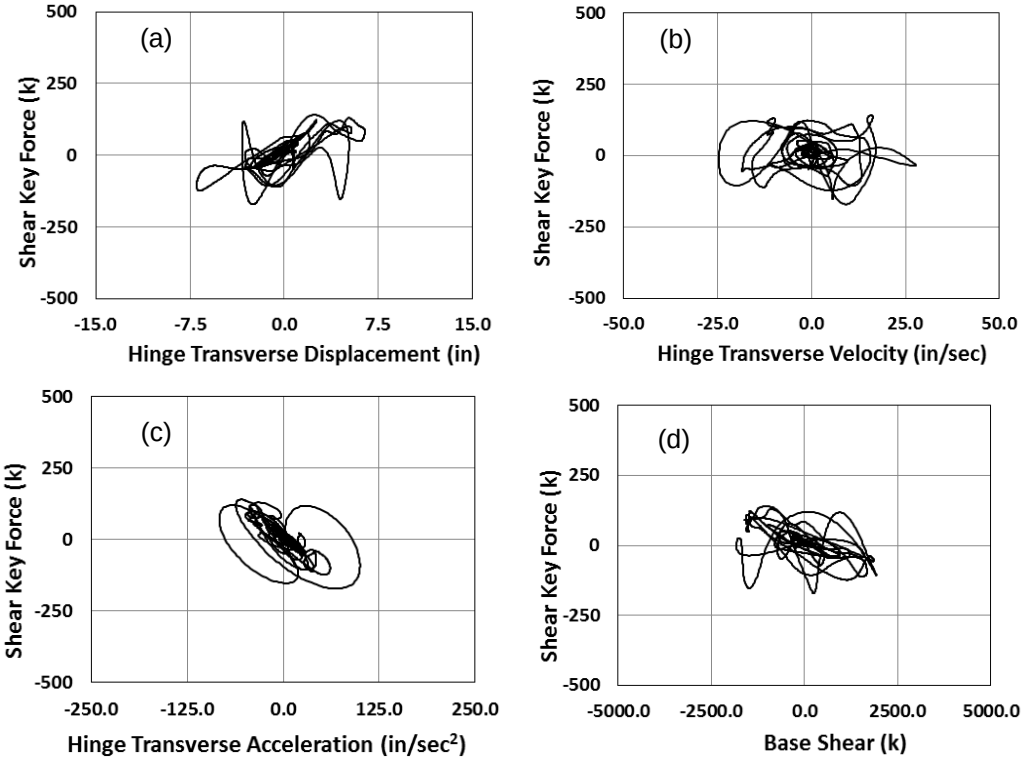

Figure 2.22 Four-Frame Model, Hinge H1, Relationship of Shear Key Force with a) Hinge Displacement, b) Hinge Velocity, c) Hinge Acceleration, and d) Base Shear

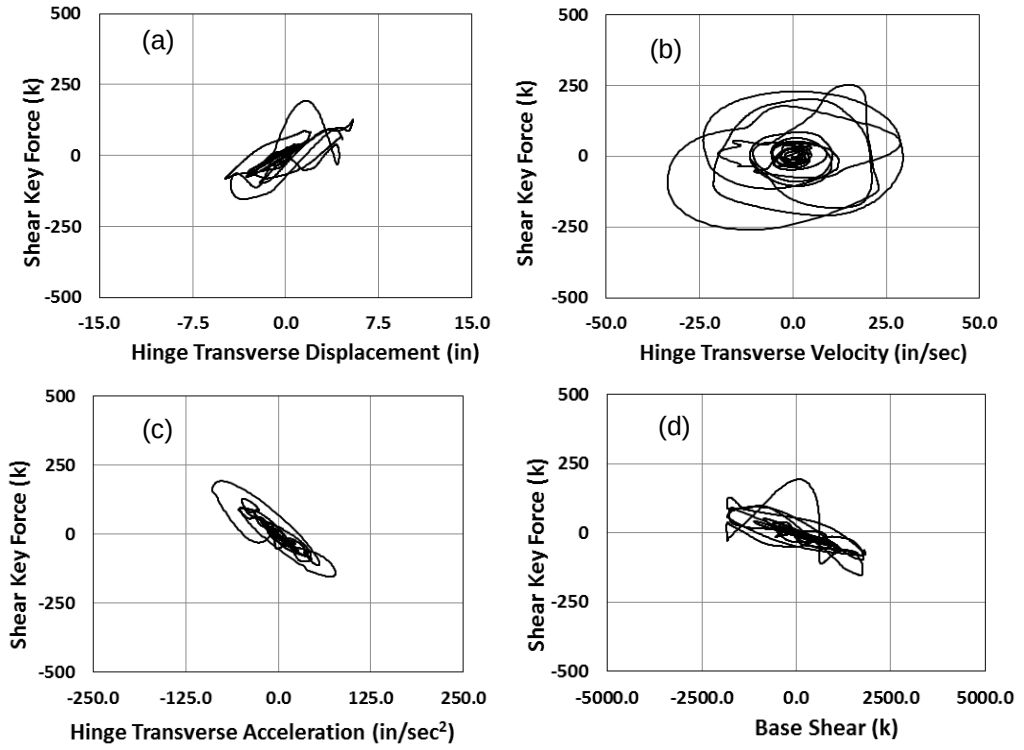

Figure 2.23 Four-Frame Model, Hinge H2, Relationship of Shear Key Force with a) Hinge Displacement, b) Hinge Velocity, c) Hinge Acceleration, and d) Base Shear

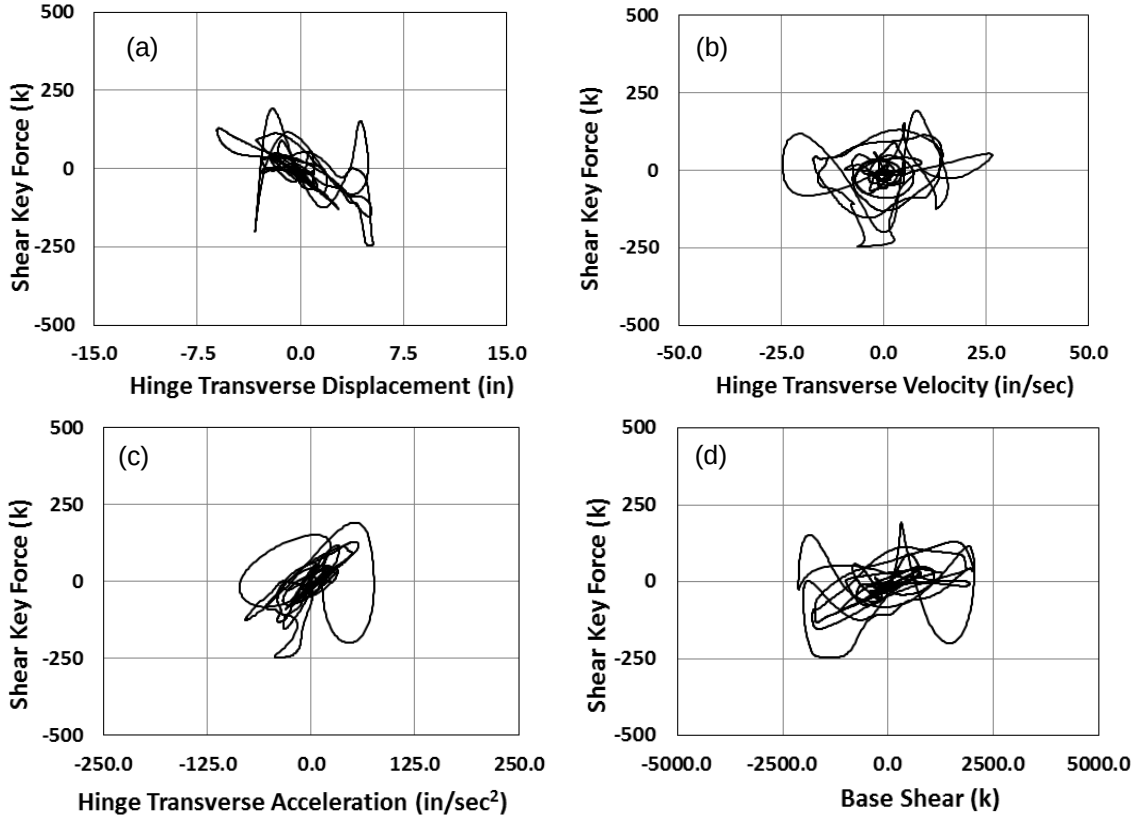

Figure 2.24 Four-Frame Model, Hinge H3, Relationship of Shear Key Force with a) Hinge Displacement, b) Hinge Velocity, c) Hinge Acceleration, and d) Base Shear

The snapshots of displacement and acceleration profiles along the length of the two-frame and four-frame prototypes are shown in Figure 2.25 through Figure 2.28. The in-span shear key with the maximum shear force is indicated by a solid black dot. These Figures show that, when the maximum shear key force happens, the superstructure is highly deformed transversely. It reveals that the transverse flexibility of the superstructure plays a substantial role in the force response of the shear keys. Consequently, assuming a rigid body transverse displacement and rotation of the individual frames may lead to significant errors in the estimation of shear key forces.

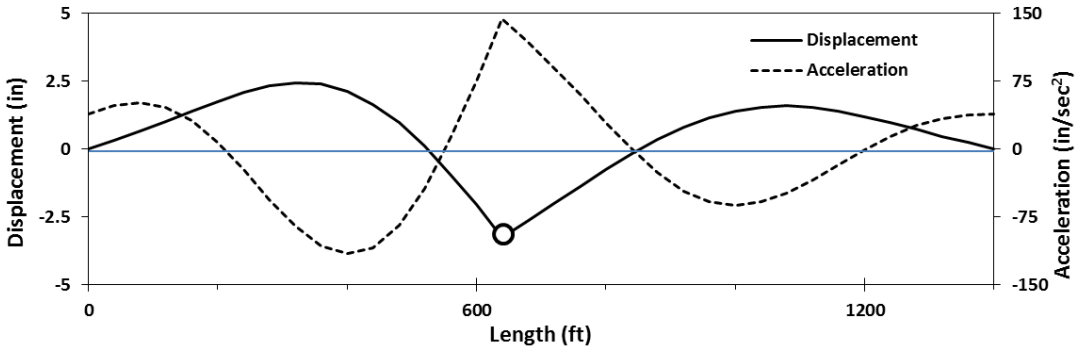

Figure 2.25 Two-Frame Model, System State at the Time of Maximum Shear Key Force

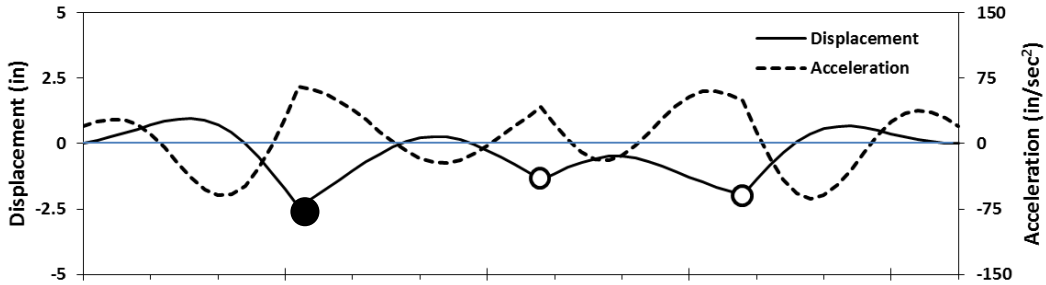

Figure 2.26 Four-Frame Model, System State at the Time of Maximum Shear Key Force at H1

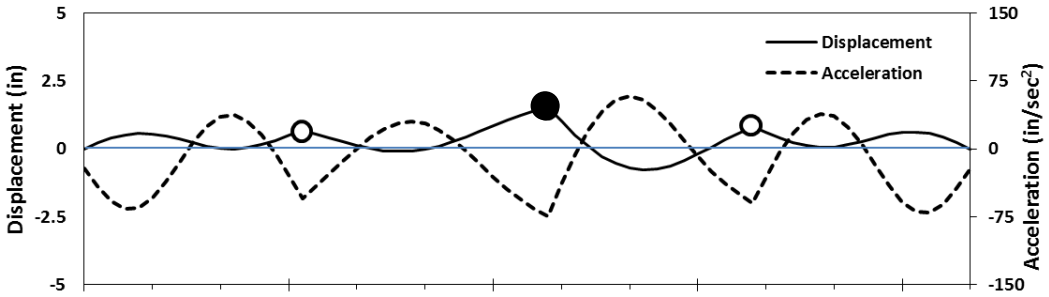

Figure 2.27 Four-Frame Model, System State at the Time of Maximum Shear Key Force at H2

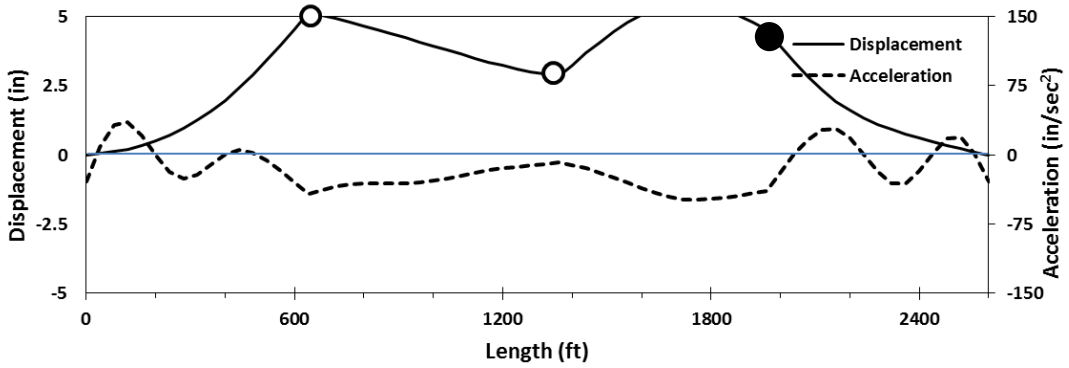

Figure 2.28 Four-Frame Model, System State at the Time of Maximum Shear Key Force at H3

2.5 EFFECTS OF THE ADJACENT FRAMES' RELATIVE PROPERTIES

To examine the effect of adjacent frames' stiffness and capacity on shear key force demand, three cases of parametric analysis are performed (indicated in Table 2.3). The K1 and C1 represent the stiffness and the capacity of the nonlinear springs of the frame with the short cantilever, respectively, while K2 and C2 represent that of the frames with the long cantilever. The ratios are varied between 0.1-1.0. In Case A, only stiffness varies while the capacities of the frames are kept constant. Case B is the opposite of Case A; and, in Case C, both stiffness and capacity vary at the same rate.

Table 2.3 Parametric Study

Case	Stiffness Ratio K1/K2	Capacity Ratio C1/C2
A	0.1 to 10	1.0
B	1.0	0.1 to 10
C	0.1 to 10	0.1 to 10

Although stiffness and capacity usually change relatively, three cases are studied to isolate different effects. In the four-frame model, only the properties of the adjacent frames are considered. The same inelastic models introduced in Sec. 2.4 are used. They have been analyzed under the Loma Prieta ground motion at three PGA intensity levels: 0.18g, 0.36g, and 0.72g to achieve different levels of nonlinear response.

The results are shown in Figure 2.29 to Figure 2.31. For the hinge in the two-frame model and hinge H1 in the four-frame, when either of these ratios increases from 0.1 to approximately 0.6, the shear key force decreases. After that point, it starts increasing. Shear key force is not very sensitive to the ratios of frame properties larger than 4. The minimum forces are not correlated with the same ratio. In other words, adjacent frames with similar stiffness or capacities do not necessarily generate the smallest shear key values.

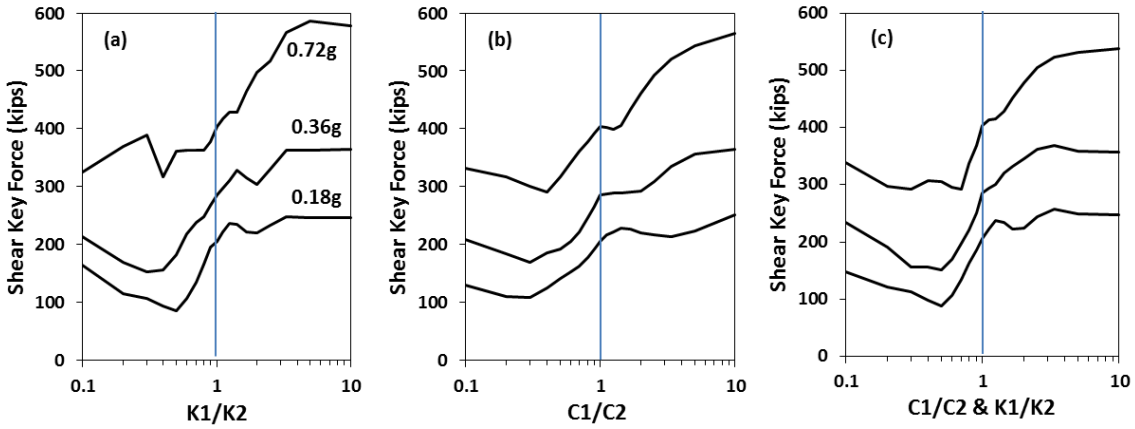

Figure 2.29 Frame Property Ratio Effect, Two-Frame Models, a) Case A, b) Case B, and c) Case C

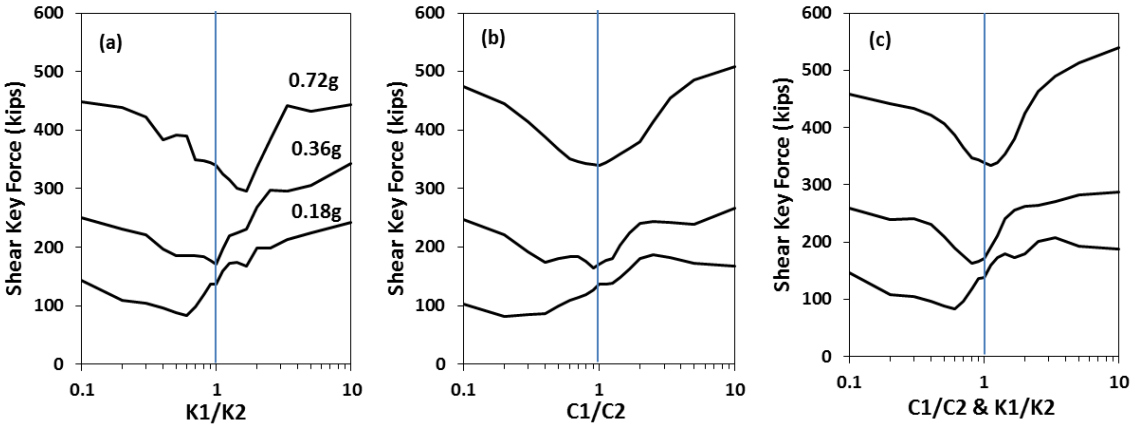

Figure 2.30 Frame Property Ratio Effect, Four-Frame Models, Hinge1, a) Case A, b) Case B, and c) Case C

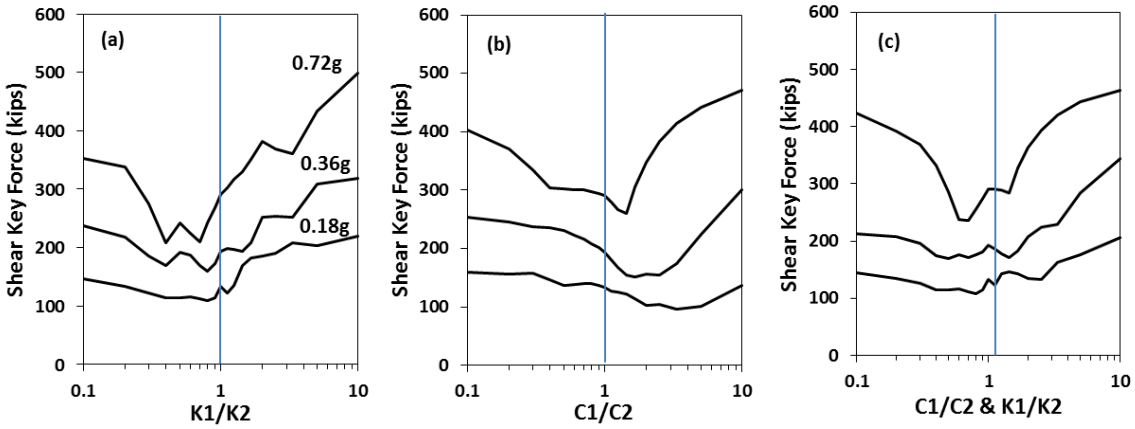

Figure 2.31 Frame Property Ratio Effect, Four-Frame Models, Hinge2, a) Case A, b) Case B, and c) Case C

2.6 ELASTIC DYNAMIC ANALYSIS (EDA)

According to SDC, the design displacement demand may be estimated using EDA. For this purpose, a spectral analysis is typically used. However, forces are over predicted in the EDA method. The EDA analysis results were compared with that of the nonlinear time history (NTH) analysis to examine their difference in terms of shear key force. This was done by using the same models in each of the relative property ratios presented in Table 2.3. Different graphs comparing the shear key force from EDA with NTH are presented in Figure 2.32 to Figure 2.37. Dashed lines show the EDA results, and solid lines show NTH ones. The EDA shear key force is constant for all C1/C2 ratios because the capacity does not change the modal properties.

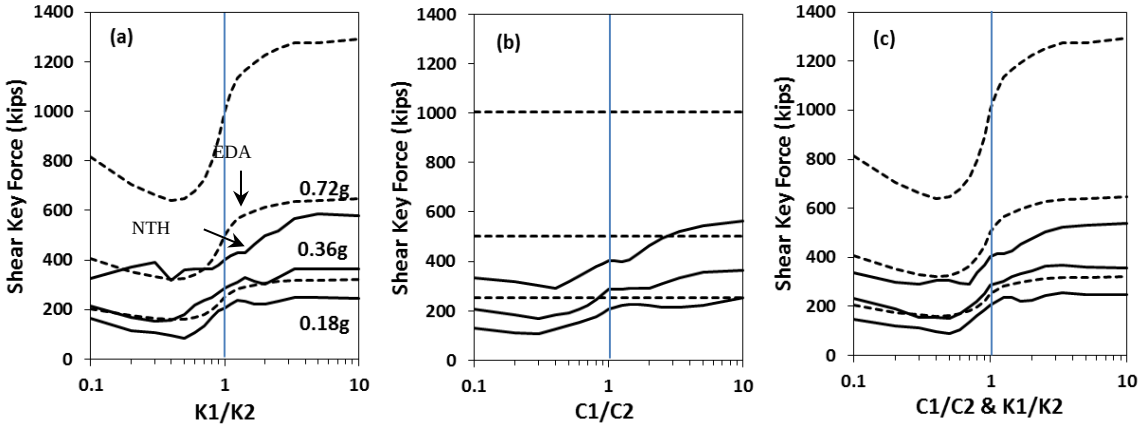

Figure 2.32 Comparing EDA with NTH Shear Key Force, Two-Frame Model a) Case A, b) Case B, and c) Case C

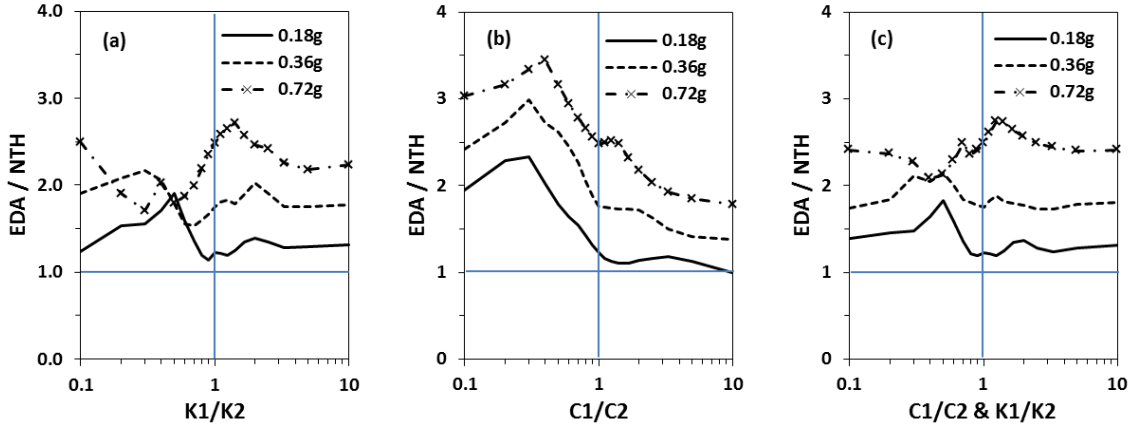

Figure 2.33 Ratio of EDA/NTH Shear Key Force, Two-Frame Model a) Case A, b) Case B, and c) Case C

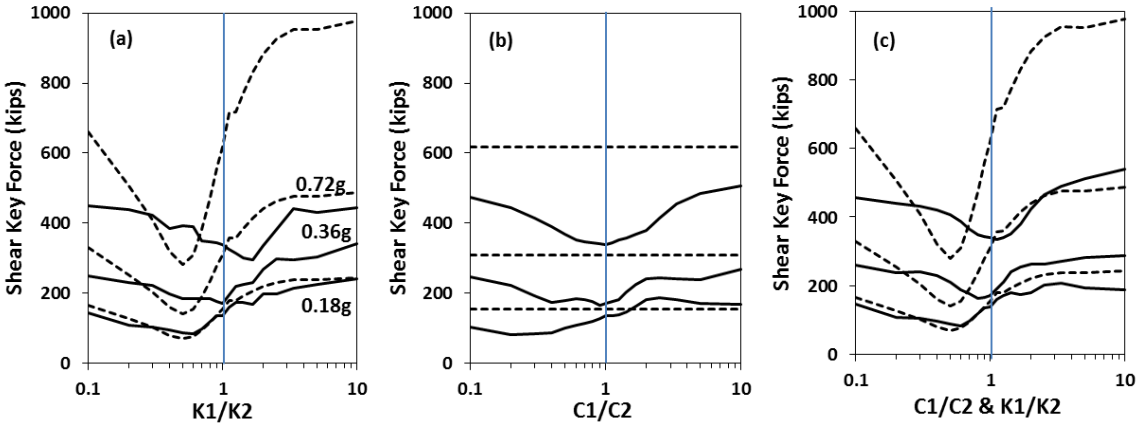

Figure 2.34 Comparing EDA with NTH Shear Key Force, Four-Frame Model, Hinge H1 a) Case A, b) Case B, and c) Case C

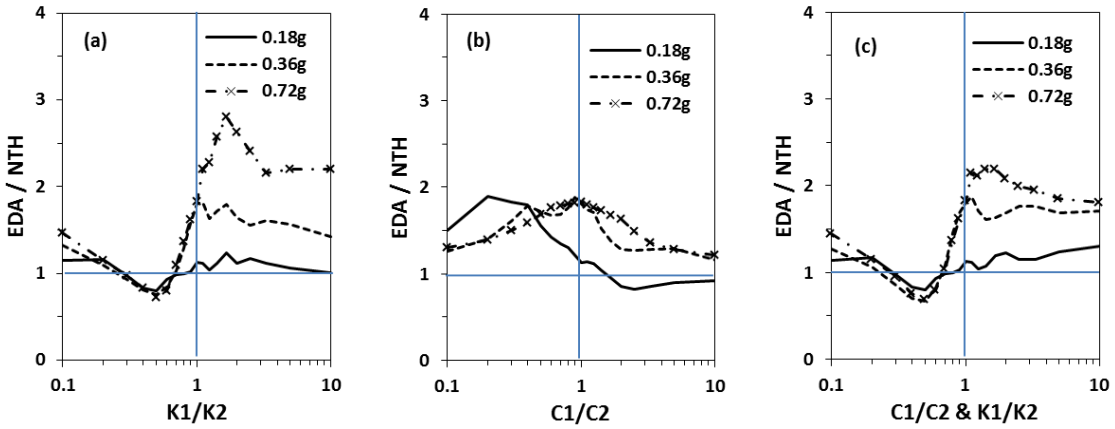

Figure 2.35 Ratio of EDA/NTH Shear Key Force, Four-Frame Model, Hinge H1 a) Case A, b) Case B, and c) Case C

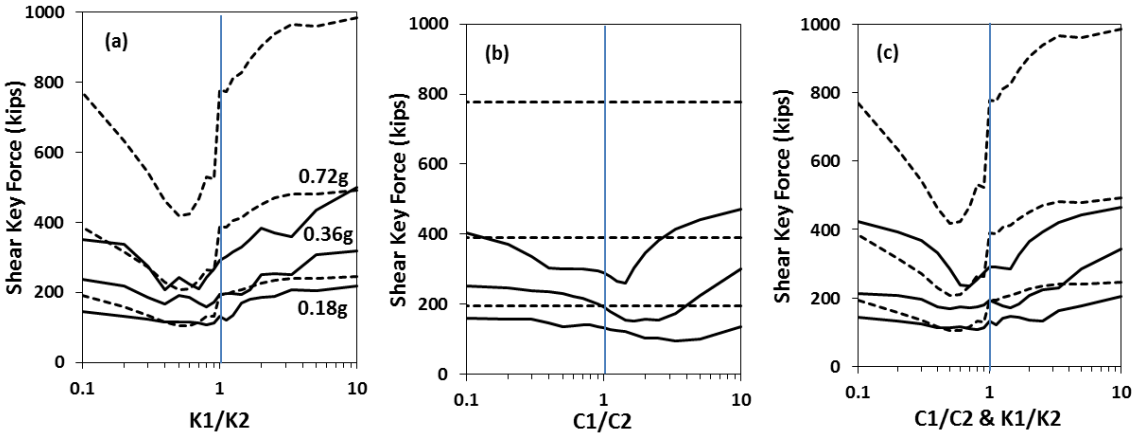

Figure 2.36 Comparing EDA with NTH Shear Key Force, Four-Frame Model, Hinge H2 a) Case A, b) Case B, and c) Case C

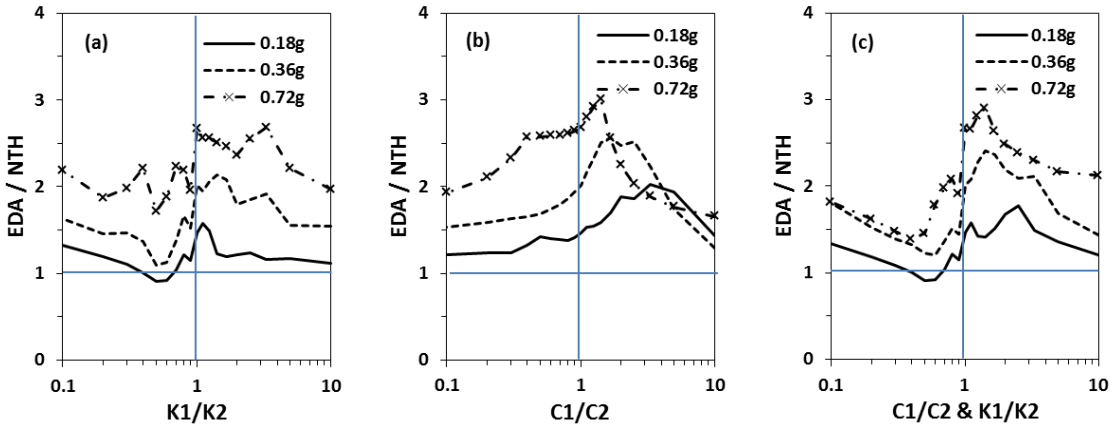

Figure 2.37 Ratio of EDA/NTH Shear Key Force, Four-Frame Model, Hinge 2 a) Case A, b) Case B, and c) Case C

The EDA results follow the pattern of those from NTH. However, its accuracy is highly variable for different frame property ratios. As expected, three intensity levels of motion show different behaviors due to nonlinear behavior. In the four-frame model, the EDA is underestimating the force by up to 50%.

Surprisingly, the maximum discrepancy of the results from EDA and NTH methods belongs to the models with comparable frame stiffness. This may be due to the fact that the system loses its symmetry after yielding. It can be concluded that the difference of the EDA and NTH forces not only depends on the ground motion intensity, but also on the stiffness and capacity ratio of the frames adjacent to the hinge.

3 Prototype Bridges and Input Motions

To develop a methodology for determining the design force demands on in-span shear keys, an extensive analytical study is performed on a large number of multi-frame bridges models. This chapter includes information regarding the selection of prototype bridges and the input motions used for the nonlinear response history analyses. Earthquake hazard levels used for the design and analysis of prototypes are also introduced in this chapter. In addition, the variables that are considered for the parametric study analyses are introduced and discussed.

3.1 BRIDGE PROTOTYPES

3.1.1 Geometry of the Prototype Bridges

In consultation with bridge design professionals at Caltrans, a suite of fifty-six multi-frame bridges including two-, three-, four-, and five-frame models are selected. Each bridge is considered with two substructure systems: single-column extended pile-shaft (single-column) and two-column bents. Two span lengths of 110-ft and 200-ft are selected as short-span and long-span constructions, respectively. However, this study is mainly focused on long-span prototypes. The span length of 200 ft is selected as a practical span length for post-tensioned box girder bridges. The short span bridges with the span length of 110 ft may represent superstructures without post-tensioning. The prototypes are expected to represent a wide variety of realistic multi-frame bridge geometries. Only straight bridges with no skew are included in this study. These

prototypes were carefully designed according to the Caltrans Seismic Design Criteria (SDC 1.7) (Caltrans, 2013) for three hazard levels and four soil types. The seismic design of these prototypes will be discussed further in Chapter 5.

The configurations of the long- and short-span prototype bridges are shown in Figure 3.1 and Figure 3.2, respectively. The total length of two-, three-, four-, and five-frame bridges are 1400, 2000, 2600, and 3200 ft for the long-span and 1210, 1760, 2310, and 2860 ft for the short-span prototypes, respectively. The in-span hinges are positioned at one-fifth of the span lengths, which is a distance of 40 ft and 22 ft from the adjacent column in the long- and short-span prototypes, respectively. This location is near the point of contraflexure under the dead loads.

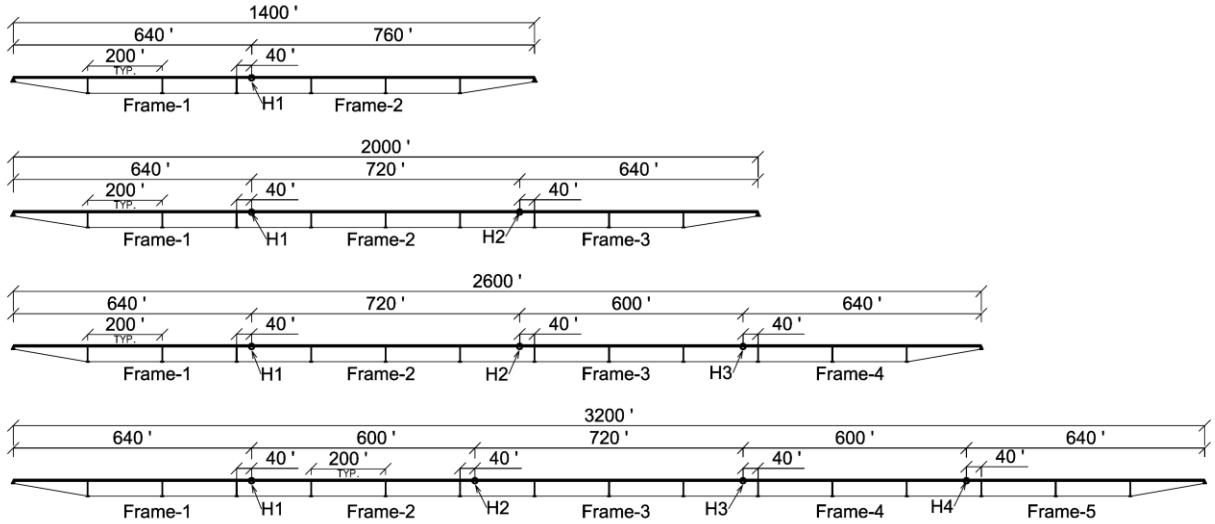

Figure 3.1 Long-Span Prototype Bridges (200-ft Span Length)

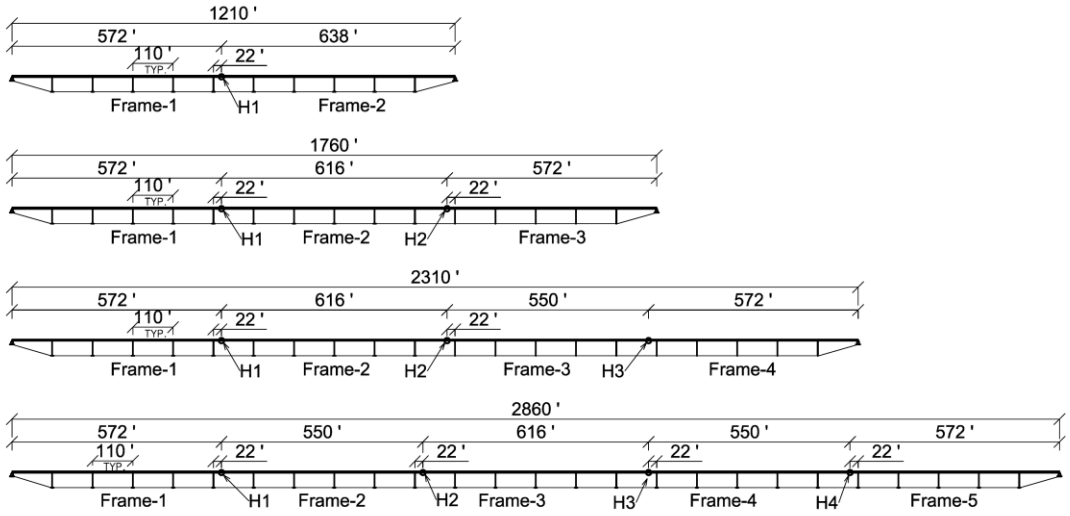

Figure 3.2 Short-Span Prototype Bridges (110-ft Span Length)

The average frame length for the long-span bridges is approximately 650 ft., and the frame length is limited to 760 ft. Each frame is supported by three columns. In the short-span bridges, the average frame length is approximately 550 ft; thus, each frame has four or five columns. It is expected that the diverse valley shapes of the prototype bridges allow for capturing the possible effects of asymmetric geometries on shear key forces. In addition, altering the number of columns within a frame could significantly increase the number of prototype and computational expenses.

Table 3.1 presents the valley shapes selected for the long-span prototypes. The in-span hinge/s is indicated using a flag. The number of valley shapes in two-, three-, four-, and five-frame prototypes are four, five, seven and ten, respectively. For short-span bridges, only uniform valley shapes are considered.

One bridge from each group has a non-uniform column height within its frame/s to account for effects of large eccentricity of the center of stiffness and mass. The shallow, intermediate, and deep valleys are 20 ft, 30 ft and 40 ft, respectively. These heights are the distance between the ground and the bottom the superstructure.

A labeling scheme in the form of Fx-Vy is used to name these prototypes. The letters “F” and “V” stand for Frame and Valley, respectively. Variables “x” and “y” define the number of frames and an arbitrary valley shape tag, respectively. For example, F3-V4 is a three-frame prototype with valley tag 4. The array of numbers in curly braces presents the valley depth for each frame. Using “Var.” indicates that the length of the columns is linearly varied within that frame. Symmetric shapes are excluded (F2-V2 and F2-V3 are not the same because the location of the hinge).

Table 3.1 Valley Shapes for Long-Span Prototypes

2 Frames	Valley Shape Tag **1** {20, 20}	Valley Shape Tag **2** {30, 20}
	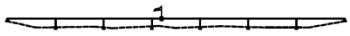	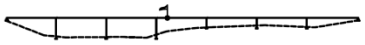
	Valley Shape Tag **3** {20, 30}	Valley Shape Tag **4** {40, Var.}
		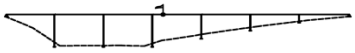
3 Frames	Valley Shape Tag **1** { 20, 20, 20}	Valley Shape Tag **2** {30, 20, 20}
	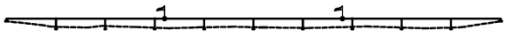	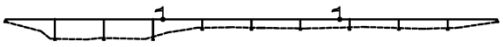
	Valley Shape Tag **3** {20, 30, 20}	Valley Shape Tag **4** {30, 40, 20}
	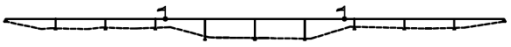	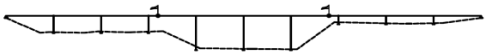
	Valley Shape Tag **5** {Var., 40, Var.}	
	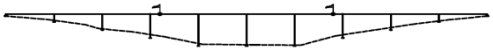	
4 Frames	Valley Shape Tag **1** {20, 20, 20, 20}	Valley Shape Tag **2** {30, 20, 20, 20}
	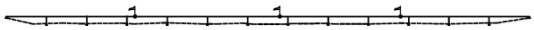	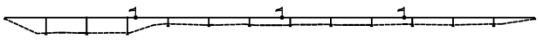
	Valley Shape Tag **3** {20, 30, 20, 20}	Valley Shape Tag **4** {30, 30, 20, 20}
	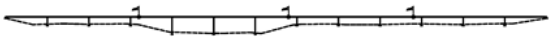	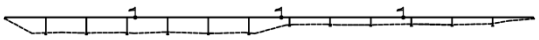
	Valley Shape Tag **5** {20, 30, 30, 20}	Valley Shape Tag **6** {30, 30, 40, 20}
	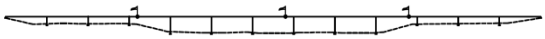	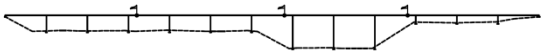
	Valley Shape Tag **7** {30, Var., 40, Var.}	
		
5 Frames	Valley Shape Tag **1** {20, 20, 20, 20, 20}	Valley Shape Tag **2** {30, 20, 20, 20, 20}
	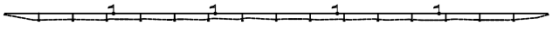	
	Valley Shape Tag **3** {20, 30, 20, 20, 20}	Valley Shape Tag **4** {20, 20, 30, 20, 20}
		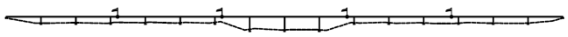
	Valley Shape Tag **5** {30, 30, 20, 20, 20}	Valley Shape Tag **6** {20, 30, 30, 20, 20}
		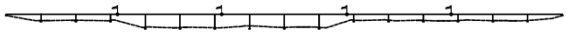
	Valley Shape Tag **7** {30, 30, 40, 20, 20}	Valley Shape Tag **8** {20, 30, 30, 40, 20}
	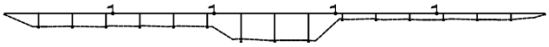	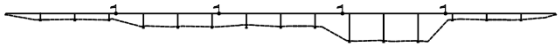
	Valley Shape Tag **9** {30, 30, 30, 40, 20}	Valley Shape Tag **10** {20, 30, Var., 40, Var.}
		

* Column Clearance Height in ft

3.1.2 Superstructure System

The type of superstructure commonly used in multi-frame bridge construction is a cast-in-place, post-tensioned, multi-cell, concrete box-girder. This superstructure system is also used for the prototype bridges. Two superstructure widths of 40 ft and 64 ft are used that correspond to three- and five-lane bridges, respectively (Figure 3.3a, b). For the short-span prototypes, only a 40-ft wide superstructure is used (Figure 3.3c). The geometric proportions of each superstructure and the thickness of the deck slab, web, and soffit are determined according to MTD-10-20 (Caltrans, 2008) for the two span lengths of 110 ft and 200 ft. The total dead weight including overlay and barriers per linear foot of the superstructures are 11.18, 13.56, and 20.78 kip/ft for cross sections shown in Figure 3.3a, b, and c, respectively. In the same way, the transverse moments of inertia of these cross sections are 1.493e8, 1.979e8, and 7.934e8 in^4.

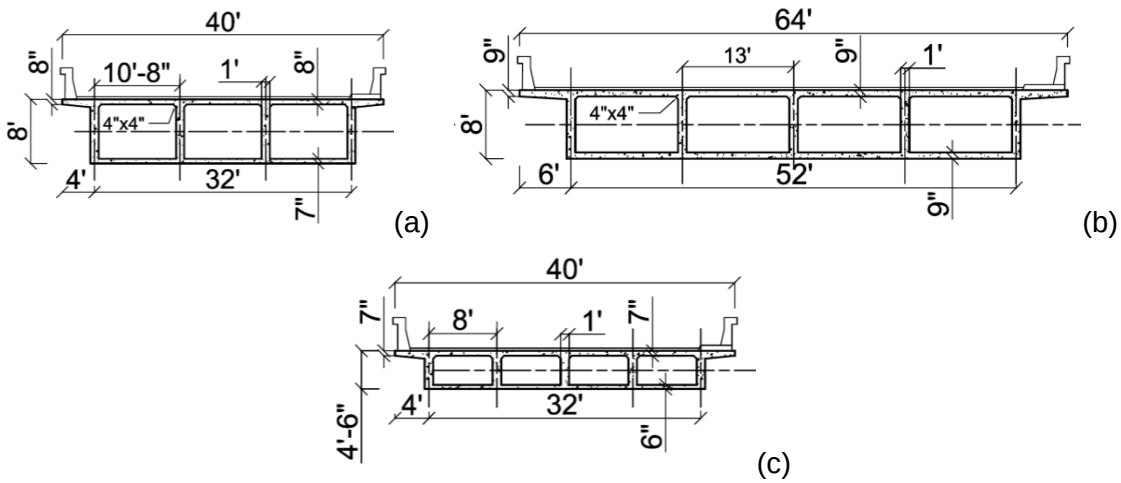

Figure 3.3 Superstructure Sections, a) Long-Span, Three-Lane, b) Long-Span, Five-Lane, and c) Short-Span, Three-Lane

The components of a standard in-span hinge are shown in Figure 3.4. The diaphragm width is 6.5 ft on each side. Four and six “pipe extender/shear key” elements are assumed to serve as in-span hinge shear keys in the 40-ft and 64-ft superstructures, respectively. The “pipe extender/shear key” detail is shown in Figure 3.5.

The size of the longitudinal gaps at in-span hinges and at the abutments is assumed 2.0 in. The gap size is calculated using a spreadsheet that Caltrans provided for the research team, which was developed according to AASHTO provisions (AASHTO, 2012). This gap size accommodates thermal movements for a temperature variation of 70ºF. The weight of a 2.0-in asphalt overlay and two standard barriers of Type 732 (AASHTO, 2012) are added to the weight of the superstructure.

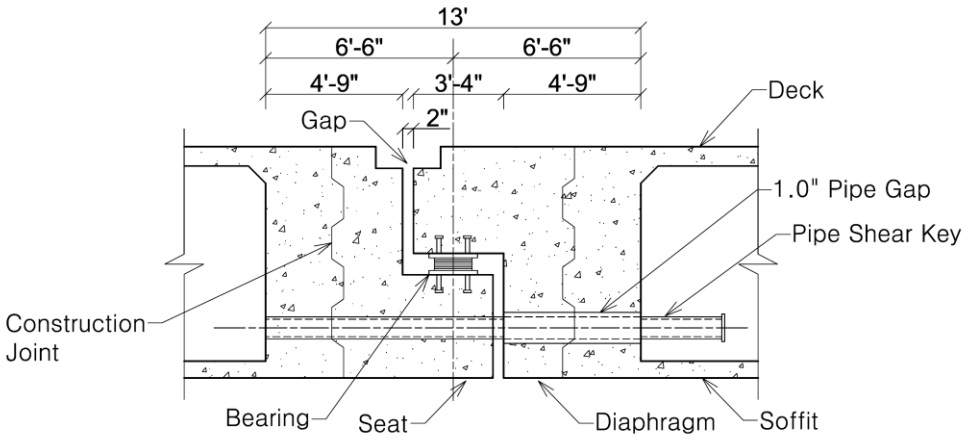

Figure 3.4 In-Span Hinge Detail

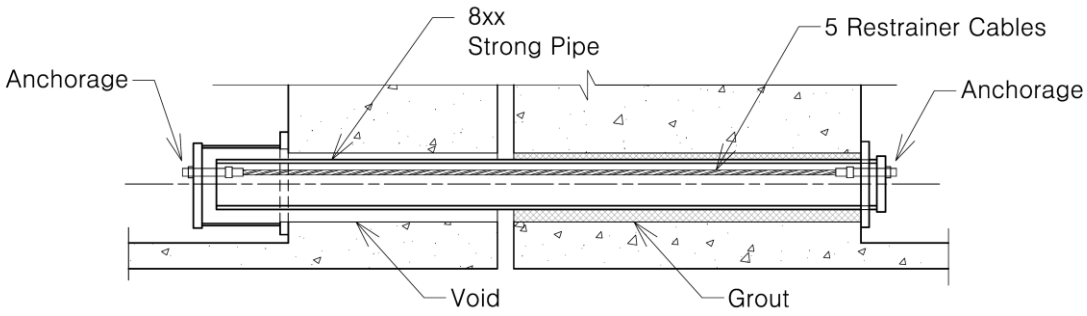

Figure 3.5 Pipe Extender/Shear Key Detail

3.1.3 Substructure System

Two substructure systems are studied: the single-column (single extended pile-shaft) that is used for short- and long-span bridges (shown in Figure 3.6a and b) and the pinned base two-column bent (shown in Figure 3.6c). The two-column bent substructure is only used for long-span prototypes. In both systems, the columns are circular. The diameter of the columns is defined in the design. For the two-column bent, the height is extended by 5 ft below the ground surface.

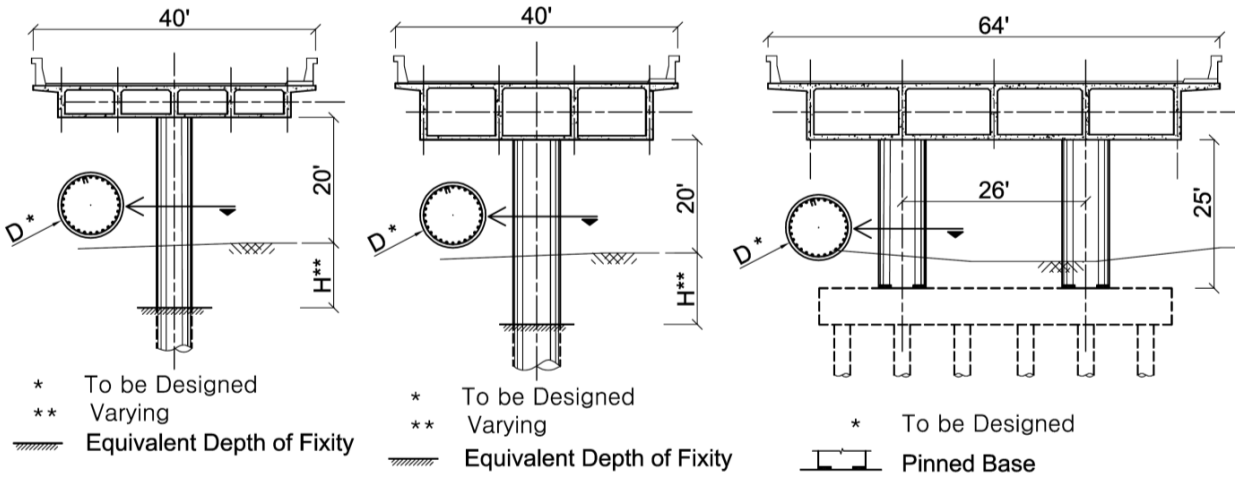

(a) (b) (c)

Figure 3.6 a) Single-Column for Short-Span Prototypes, b) Single-Column for Long-Span Prototypes, and c) Two-Column Bent for Long-Span Prototypes

Columns are integrated into the superstructure through the solid cap-beams shown in Figure 3.7. The width of the cap-beam is determined after the diameter of the column is defined. This cap-beam extends along the width of the soffit.

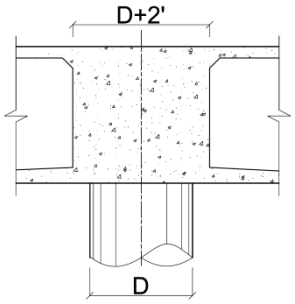

Figure 3.7 Solid Concrete Cap-Beam (Caltrans, 2013)

The reason for studying both single- and two-column substructure systems is that, under seismic loading, they deflect in different ways, as demonstrated in Figure 3.8. The single-column system allows for horizontal translation and torsion of the superstructure about the longitudinal axis of the bridge. In contrast, a superstructure supported by a two-column bent only allows horizontal translations. Because of the different ways the superstructures displace under seismic loading, the inertial forces developed in these two bridge systems are different. For a single-column bridge, both torsional and translational masses participate in the seismic response, while, for a two-column bridge, only translational masses work. In addition, bridges that are supported on single-column bents are in general softer than the two-column ones. Other substructure systems such as multiple-column bents, fixed-base columns, or multiple extended pile-shafts are also practical in bridge design. However, it is expected that the results from the studied prototype is applicable to other types.

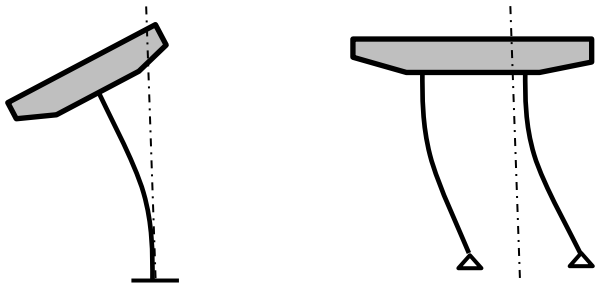

Figure 3.8 Transverse Deformation of Single-Column and Two-Column Bent Bridges

3.1.4 Abutment System

A seat-type abutment system is used in prototype bridges models. Figure 3.9 shows the main components of this abutment system. A weak backwall with a shear-off joint is commonly used in this type of abutment to avoid transferring large forces to the abutment piles (Caltrans, 2013). In the transverse direction, two exterior ductile shear keys are used. These shear keys are designed to fail in shear, or yield in flexure (Bozorgzadeh, et al., 2007). In this study, a flexural behavior is assumed for these shear keys. Gap sizes of 2.0 in and 1.0 in are used between the superstructure and the abutments in longitudinal and transverse directions, respectively.

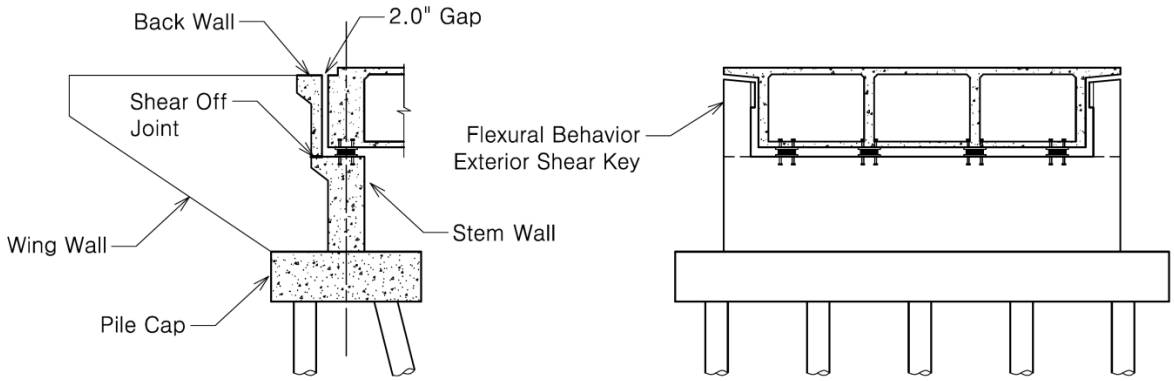

Figure 3.9 Seat-Type Abutment System

3.2 HAZARD LEVELS AND DESIGN SPECTRUMS

According to Section 2.1 of SDC 1.7 (Caltrans, 2013) for structural design applications, seismic demand should be determined using an elastic 5%-damped acceleration response spectrum (ARS) corresponding to the largest of:

1) A probabilistic spectrum for a hazard level of 5% in 50 years (975-year return period);

2) A deterministic spectrum based on the largest median response resulting from the maximum rupture of any fault in the vicinity of the bridge site (corresponding to M_{Max});

(3) A statewide minimum spectrum, defined as the median spectrum, that is generated by M=6.5 earthquake on a strike-slip fault located 12 kilometers from the bridge site.

Beginning in 2013, Caltrans launched a web-based calculator for generating acceleration response spectrum (ARS) (Caltrans, 2014). This source calculates both deterministic and probabilistic acceleration response spectra for any location in California based on the criteria mentioned earlier. In addition to the online ARS calculator, SDC contains a wide range of ARS's for soil types B, C, D, and E, each for three magnitude ranges (M_w) and different peak ground acceleration (PGA) levels ranging from 0.1g to 0.7g. SDC is one of few seismic design codes to provide different design response spectra for different magnitudes. Mohraz (1978) showed that ground acceleration amplification, for earthquakes of magnitudes 6.0<M<7.0 is more than that for earthquakes with a magnitude within 5.0<M<6.0. The peak ground acceleration also depends on the earthquake magnitude and epicenteral distance (Mohraz, 1978). The effect of the duration of strong motion on the shapes of spectrums was studied by (Peng, et al., 1989). They showed that ground accelerations of larger earthquakes have longer period contents.

To ensure that the findings of this study are applicable to different hazard levels and site specifications, a diverse set of ARS's are selected. This set includes three hazards levels of moderate, large, and severe, each for soil types B, C, and D. Only two hazard levels of moderate and large are considered for soil type E. Thus, the number of spectrums used in this study totals 3x3+2=11. The shear wave velocity for soil types B, C, D, and E are defined as 1500-760, 760-360, 360-180, <180 m/sec., respectively (Caltrans, 2013).

Table 3.2 summarizes the magnitude-intensity-soil type combinations selected for this study. A labeling scheme in the form of "Xyz" is used to name the selected ARS's. The first letter indicates the soil type. The second variable, "y", is 1, 2, or 3 and specifies a magnitude level of 6.25-6.75, 7.0-7.5, and 7.75-8.25, respectively. The third variable, "z", takes the value of 1, 2, or 3 representing the intensity levels of 0.2g, 0.4g and 0.6g, respectively. For example, B22 refers to the ARS for soil type B, magnitude level 2 (7.0-7.5), and PGA level 2 (0.4g).

Table 3.2 Selected Hazard Levels and ARS Lables

	Intensity Level (PGA)		
Magnitude Level (M_w)	**1 (0.2g)**	**2 (0.4g)**	**3 (0.6g)**
1 (6.25-6.75)	B11, C11, D11, E11 (Moderate Hazard)		
2 (7.00-7.75)		B22, C22, D22, E22 (Large Hazard)	
3 (7.75-8.25)			B33, C33, D33 (Severe Hazard)

The corresponding pseudo spectral accelerations of the selected spectrums are shown in Figure 3.10. These spectrums served two purposes: to design the prototype bridge models, and to spectrum match the ground accelerations used in nonlinear time history (NTH) analyses of the prototype models.

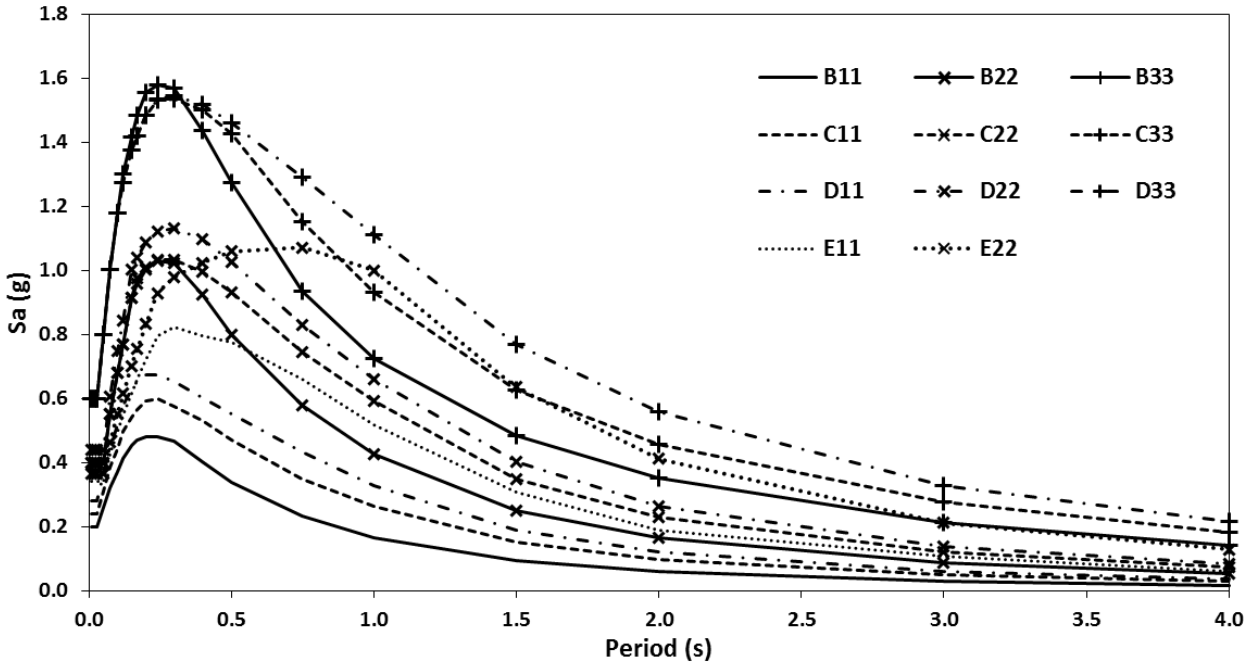

Figure 3.10 Selected ARSs Used for Design and Analysis of Prototype Bridges

3.3 GROUND MOTIONS

3.3.1 Selection of the Ground Motions

The NGA ground motion database of the Pacific Earthquake Engineering Research Center (PEER, 2011) is used to select 11 sets of three ground motions compatible with each ARS presented in Table 3.3. Each set contains three biaxial ground motions with

a soil type, magnitude, and intensity level that are “approximately” similar to that of the corresponding ARS. In addition, special care is taken to select motions with spectral shapes comparable to the target spectrum in the period range of 0.1-2.0 sec. These motions are scaled using the PEER-NGA search engine such that the difference of the ground motion spectrum with the target ARS is minimized. The ground motion spectrum is taken as geometric mean of two horizontal components (PEER, 2010). The scale factor was limited to 0.5 and 2.0. Several combinations of motions are considered to ensure each set includes one or two pulse motions, with the exception of moderate hazard level (i.e. B11, C11, D11, and E11 spectrums).

3.3.2 Spectral Matching

SeismoMatch software (Seismosoft, 2011) is used to generate a library of 33 ARS-matched biaxial acceleration histories. SeismoMatch software utilizes a wavelet-based algorithm to match acceleration histories to a target response spectrum. This method conserves the time-energy characteristics of acceleration histories, while their spectral accelerations are matched to target spectrums. To avoid distorting the non-stationary characteristics of the ground motions, the number of iterations was limited to five. For the same reason, the spectrum misfit tolerance between periods 0.1 and 2.0 sec. is defined as large as 30%. The upper bound period value of 2.0 sec. is defined to preserve the pulse characteristics of the motions. Two samples original and matched ground motions for non-pulse and pulse-like motions are shown in Figure 3.11 and Figure 3.12, respectively. It is evident in both figures that the distortions of acceleration and velocity histories are minimal, while the shape of the spectrum of the matched motions resembles the target spectrum.

Figure 3.12 shows that the velocity pulse is preserved during the matching. Comparing the spectrums of the matched and unmatched motions demonstrates that the long-period effect of the pulse remains unchanged.

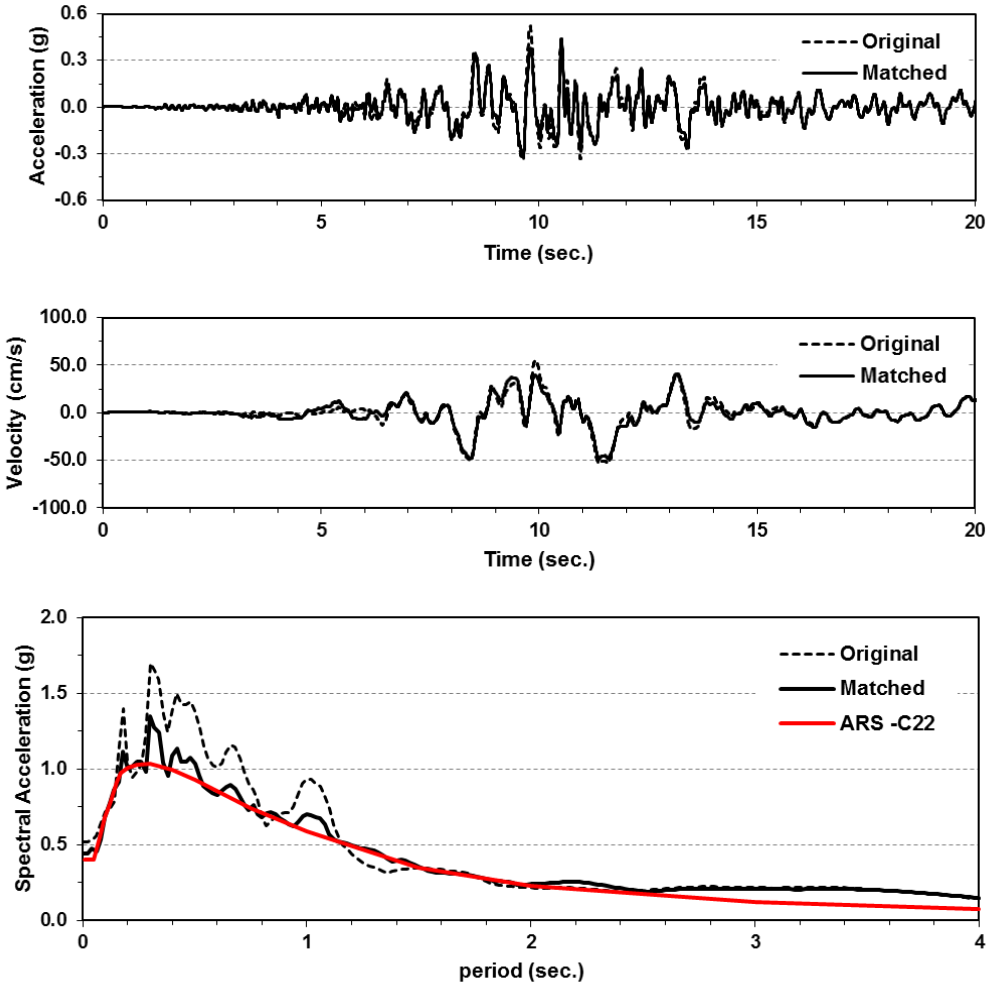

Figure 3.11 Original and Matched Acceleration History, Velocity History, and Acceleration Spectrum for ARS-C22 (Non-Pulse Motion)

Detailed information on the final ground motions used for the nonlinear time history analyses is summarized in Table 3.3. PGA-1, PGA-2, PGV-1, and PGV-2 define the peak ground accelerations and velocities of the two normal components of the ground motion.

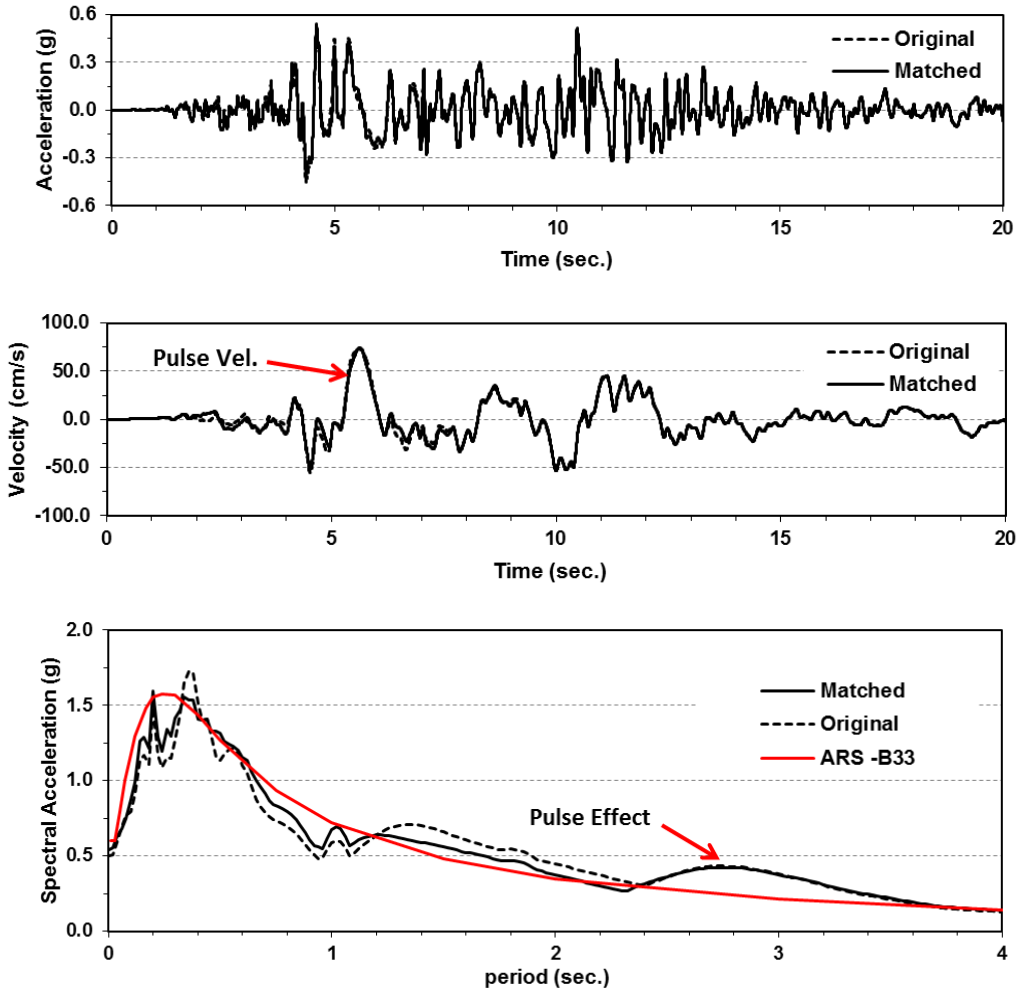

Figure 3.12 Original and Matched Acceleration History, Velocity History, and Acceleration Spectrum for ARS-B33 (Pulse-Like Motion)

3.3.3 Application of Ground Motions into Analysis

The horizontal components of the motions are randomly assigned to the longitudinal and transverse directions of the bridge models. The sets of three motions developed for each ARS include both non-pulse and pulse motions. In near fault sites, bridges are designed for 1.2 times ARS (Caltrans, 2013). To avoid multiple prototype designs for each ARS, instead of magnifying the design ARS, a reduction factor of 1/1.2 is applied to pulse motions that are used for the NTH analyses. The acceleration spectrums of the entire set of matched ground motions are presented in Figures A.1 to A.33 of Appendix A. Each graph includes the target ARS and two spectrums for the components of matched ground motions.

Table 3.3 Matched Ground Motions Properties

ARS	No.	NGA #	Event	Year	Station	M_w	V30 (m/s)	Rupture Mech.	Pulse	Dist. (km)	PGA-1 (g)	PGA-2 (g)	PGV-1 (cm/s)	PGV-2 (cm/s)
B11	1	1091	Northridge-01	1994	Vasquez Rocks Park	6.69	996.4	Reverse	**0 0**	23.6	**0.183**	**0.221**	14.9	11.3
	2	1011	Northridge-01	1994	LA - Wonderland	6.69	1222.5	Reverse	**0 0**	20.3	**0.167**	**0.171**	15.8	14.2
	3	957	Northridge-01	1994	Burbank - Howard Rd.	6.69	821.7	Reverse	**0 0**	16.9	**0.178**	**0.199**	15.3	13.7
B22	4	143	Tabas- Iran	1978	Tabas	7.35	766.8	Reverse	**0 0**	2.0	**0.426**	**0.337**	44.7	56.5
	5	292	Irpinia- Italy-01	1980	Sturno	6.9	1000	Normal	**1 1**	10.8	**0.362**	**0.389**	45.0	60.5
	6	1091	Northridge-01	1994	Vasquez Rocks Park	6.69	996.4	Reverse	**0 0**	23.6	**0.419**	**0.335**	39.4	25.1
B33	7	1521	Chi-Chi-Taiwan	1999	TCU089	7.62	680	Reverse-Oblique	**0 0**	8.9	**0.618**	**0.509**	60.3	64.2
	8	1511	Chi-Chi-Taiwan	1999	TCU076	7.62	615	Reverse-Oblique	**1 0**	2.8	**0.526**	**0.663**	110.0	96.8
	9	292	Irpinia- Italy-01	1980	Sturno	6.9	1000	Normal	**1 1**	10.8	**0.542**	**0.618**	74.0	98.4
C11	10	164	Imperial Valley	1979	Cerro Prieto	6.53	659.6	Strike-Slip	**0 0**	15.2	**0.206**	**0.189**	14.2	18.7
	11	1005	Northridge-01	1994	LA - Temple & Hope	6.69	376.1	Reverse	**0 0**	31.5	**0.198**	**0.249**	17.1	24.5
	12	2714	Chi-Chi-04	1999	CHY046	6.2	442.1	Strike-Slip	**0 0**	38.1	**0.295**	**0.218**	21.1	20.2
C22	13	963	Northridge-01	1994	Castaic - Old Ridge Route	6.69	450.3	Reverse	**0 0**	20.7	**0.400**	**0.426**	46.8	38.1
	14	787	Loma Prieta	1989	Palo Alto - SLAC Lab	6.93	425.3	Reverse-Oblique	**0 0**	30.9	**0.376**	**0.441**	67.5	48.8
	15	1085	Northridge-01	1994	Sylmar -	6.69	370.5	Reverse	**1 0**	5.2	**0.574**	**0.388**	71.9	49.3
C33	16	779	Loma Prieta	1989	LGPC	6.93	477.7	Reverse-Oblique	**1 1**	3.9	**0.640**	**0.787**	126.9	62.7
	17	1508	Chi-Chi-Taiwan	1999	TCU072	7.62	468.1	Reverse-Oblique	**0 0**	7.0	**0.601**	**0.505**	75.2	64.7
	18	802	Loma Prieta	1989	Saratoga - Aloha Ave	6.93	370.8	Reverse-Oblique	**1 0**	8.5	**0.853**	**0.687**	71.7	99.2
D11	19	949	Northridge-01	1994	Nordhoff Fire Station	6.69	297.7	Reverse	**0 0**	8.7	**0.286**	**0.254**	33.4	25.1
	20	1082	Northridge-01	1994	Sun Valley - Roscoe Blvd	6.69	308.6	Reverse	**0 0**	10.1	**0.232**	**0.349**	19.5	25.4
	21	988	Northridge-01	1994	LA - Century City CC North	6.69	278	Reverse	**0 0**	23.4	**0.288**	**0.246**	23.6	25.9
D22	22	949	Northridge-01	1994	Nordhoff Fire Station	6.69	297.7	Reverse	**0 0**	8.7	**0.538**	**0.449**	61.7	54.2
	23	1048	Northridge-01	1994	Northridge - 17645Saticoy	6.69	280.9	Reverse	**0 0**	12.1	**0.367**	**0.409**	44.3	47.0
	24	1119	Kobe- Japan	1995	Takarazuka	6.9	312	Strike-Slip	**1 0**	0.3	**0.487**	**0.444**	45.9	48.2
D33	25	1119	Kobe- Japan	1995	Takarazuka	6.9	312	Strike-Slip	**1 0**	0.3	**0.709**	**0.644**	79.1	79.0
	26	1085	Northridge-01	1994	Sylmar -	6.69	370.5	Reverse	**1 0**	5.2	**0.877**	**0.648**	129.5	96.0
	27	803	Loma Prieta	1989	Saratoga - W	6.93	370.8	Rev.-Ob.	**1 1**	9.3	**0.684**	**0.683**	102.5	139.1
E11	28	728	Superstition Hills-02	1987	Westmorland Fire Station	6.54	193.7	Strike-Slip	**0 0**	13.0	**0.293**	**0.300**	40.9	40.3
	29	721	Superstition Hills-02	1987	El Centro Imp. Co. Cent	6.54	192.1	Strike-Slip	**1 0**	18.2	**0.399**	**0.417**	50.5	51.0
	30	175	Imperial Valley-06	1979	El Centro Array #12	6.53	196.9	Strike-Slip	**0 0**	17.9	**0.301**	**0.255**	40.9	50.4
E22	31	182	Imperial Valley-06	1979	El Centro Array #7	6.53	210.5	Strike-Slip	**1 1**	0.6	**0.515**	**0.549**	69.9	94.3
	32	758	Loma Prieta	1989	Emeryville -	6.93	198.7	Rev.-Ob.	**0 0**	77	**0.464**	**0.496**	67.6	55.6
	33	759	Loma Prieta	1989	Foster City -	6.93	116.3	Reverse-	**0 0**	43.9	**0.422**	**0.425**	52.1	64.1

Dist: Closest distance to rupture plane, **Pulse**: 0=Non-pulse, 1=Pulse, related to Fault Normal and Fault Parallel Components.

4 Development of Analytical Models

This chapter describes the analytical models (previously defined in Chapter 3) that were developed for the prototype multi-frame bridges. Modeling provisions established by the Caltrans Seismic Design Criteria (SDC 1.7) (Caltrans, 2013), Bridge Design Practice Manual, Chapter 4 (Caltrans, 2014), and the Guidelines for Nonlinear Analysis of Bridge Structures in California (Aviram, et al., 2008) are presented as general modeling considerations. Refinements that are made to these guidelines are discussed. This chapter addresses the following topics: material models, fibers section analyses, modeling assumptions for elastic elements and inelastic elements, impact simulations, mass assignments, and defining of base excitation.

4.1 SCOPE OF THE ANALYTICAL MODELING

Two analytical models are created for each prototype bridge: 1) an elastic (linear) model for seismic design purposes (as outlined in SDC 1.7) and for elastic dynamic analyses (modal analyses), and 2) an inelastic (nonlinear) model for pushover and time history analyses. Because the configurations of both models are identical, the nonlinear model is explained first, and then differences between the linear and the nonlinear models are addressed.

4.2 ANALYTICAL SIMULATION PLATFORM

OpenSees v2.4.4 (McKenna & Fenves, 2014) is used for the analytical simulations. OpenSees is a software framework used to simulate the performance of structural and geotechnical systems subjected to earthquakes. This software was developed for computational simulation in earthquake engineering. OpenSees has advanced capabilities to model and analyze the nonlinear response of systems using a wide range of material models, elements, and solution algorithms. The software is designed for parallel computing to allow for scalable simulations on high-end computers or for parametric studies. This platform utilizes the capabilities of Tcl (Tool Command Language), a very powerful yet easy to use programming language. In this study, the basic control structures (if, while, and for loops) enable the development of programing scripts to automatize the geometric modeling and design of prototypes, as well as parametric studies and iterative analyses.

4.3 GENERAL MODELING INFORMATION

4.3.1 Coordinate System

There are three global directions defined in the bridge model (Figure 4.1). The global 1-axis is in the direction of the chord connecting the abutments, which is denoted as the longitudinal direction, while the global 2-axis is orthogonal to the chord in the horizontal plane, representing the transverse direction. Finally, the global 3-axis defines the vertical direction of the bridge.

4.3.2 Modeling Scheme

A three-dimensional spine model with line elements located at the centroid of the cross section following the alignment of the bridge is implemented. This geometric modeling scheme is shown in Figure 4.1. The spine models provide a good balance between computational efficiency and accuracy. Detailed multi-component models are developed for the abutment and the in-span hinges. The superstructure, diaphragm, and cap beams are modeled as elastic frame elements, while the columns are modeled by nonlinear beam-column frame elements.

For all the prototype models, the superstructure is discretized to equal length segments for better precision. This discretization helps approximate the distributed mass of the bridge components with lumped masses at the nodes between segments. The additional assignment of rotational mass of the superstructure as well as of the columns is required when a global torsional mode is excited under certain dynamic conditions (Aviram, et al., 2008). The use of fewer elements, even for the linear elastic superstructure element, could result in a loss of accuracy in capturing the effects of

higher modes. Masses are assigned to nodes for all the six degrees-of-freedoms (DOFs), corresponding to the tributary mass associated with each node.

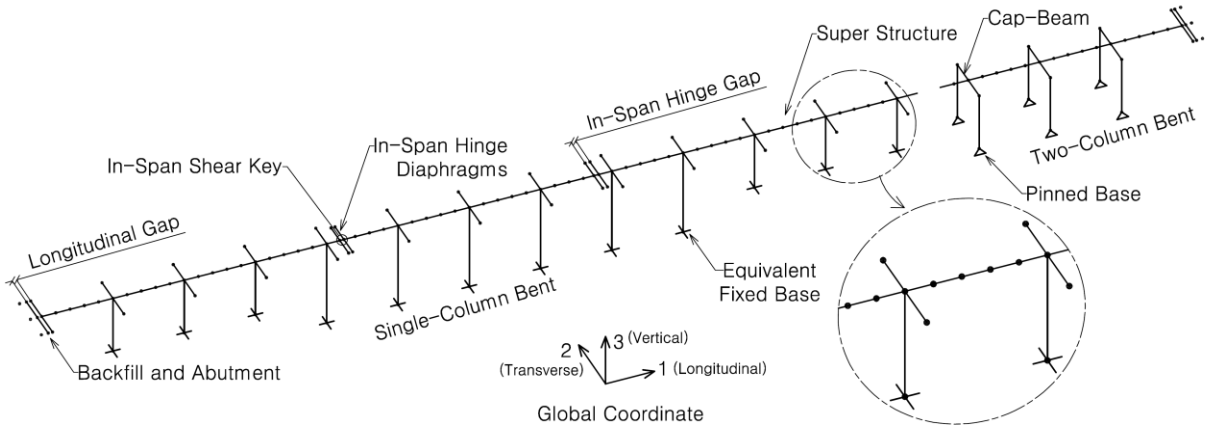

Figure 4.1 Generic Spine Model Developed for Multi-Frame Bridges

4.3.3 Nodal Masses

The dead load includes the self-weight of the superstructure, the weight of 2.0 in. of asphalt overlay with a density of 35 lb/ft^2, and two barriers with a density of 0.53 lb/ft each. No live load is included in masses, which is a common practice for seismic modeling and analyses of highway bridges. Masses are calculated by dividing the dead weights by the gravitational constant, g=386 in/sec^2.

The translational mass of all the line elements in the three global directions of the bridge (longitudinal, transverse, and vertical) are calculated based on the weight of the tributary lengths, and are assigned as a lumped mass to each node.

Rotational masses (mass moment of inertia) are assigned to each node. The assignment of rotational mass helps the model capture the accurate dynamic responses, especially for single-column bridges. Ignoring rotational masses about the vertical axis leads to an inaccurate calculation of higher modes. In the spine models, the rotational mass about the longitudinal axis (m_{r1}) must be added because the width of the superstructure is not explicitly modeled. The effects of the other two rotational masses (m_{r2} ,m_{r3}) can be accurately captured in the spine models only if a large number of segments exist in the model of the superstructure. Rotational masses can be calculated from Eqs. 4.1 to 4.3:

$$m_{r1} = \frac{m\left(w^2+d^2\right)}{12}$$ (Rotational Mass about Longitudinal Axis-1) Eq. 4.1

$$m_{r2} = \frac{m\left(l^2+d^2\right)}{12}$$ (Rotational Mass about Transverse Axis-2) Eq. 4.2

$m_{r3} = \frac{m\,(w^2+l^2)}{12}$ (Rotational Mass about Vertical Axis-3) Eq. 4.3

where *m* is the translational mass of the segment, *w* is the superstructure width, *d* is the superstructure depth, and l is the segment of the superstructure length. The translational and rotational masses of cap-beams, diaphragms, and columns are added to their corresponding nodes. For the abutments, the masses of the backwall and a 45° wedge of backfill soil are assigned to the frame element representing the backwall (abutment model is discussed in Section 4.4.3).

4.3.4 Pounding Effects (Impact)

The presence of gaps in structures causes a sudden change in stiffness and exerts a significant force upon the gap's closure at the contact surface, which is due to the momentum of the colliding masses. The impact phenomenon is complex and depends on mass, speed, and the contact surface of the two objects (Muthukumar & DesRoches, 2006; He, 2010). The pounding effects have a high intensity but a short duration. In a multi-frame bridge system, closure of the gaps may affect the global response of the structure (Figure 4.2). However, the impact forces do not directly affect the overall response of the system due to their localized effect and short duration.

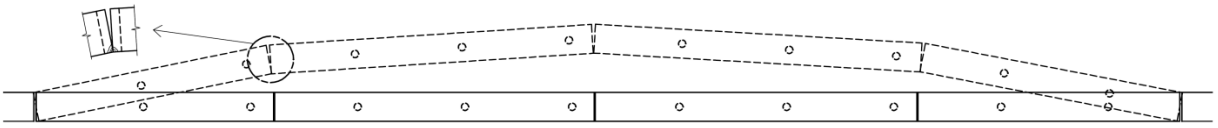

Figure 4.2 The Exaggerated Transverse Displacement of a Multi-Frame Bridge Showing Gap Opening and Gap Closure in an In-Span Hinge

Effects of the closure of longitudinal and transverse gaps should be considered for an accurate response analysis of multi-frame bridge models. It is necessary to capture the impact effects in this study in order to estimate the impact forces on shear keys. In the multi-frame bridge system, the longitudinal gaps include the spacing between the superstructures of adjacent frames at in-span hinges, as well as the gap between the abutment backwall and the superstructure (Figure 4.1). Transverse gap is the gap between the main and female portions of the in-span hinge shear key, as well as the gap between the abutment shear key and the end diaphragm. These gaps are explicitly simulated in the model provided below (Figure 4.3).

OpenSees v2.4.4 (McKenna & Fenves, 2014) is capable of simulating the gap closure and of capturing impact effects. It includes an impact material object, named "ImpactMaterial", which implements the inelastic collision and the Hertz theory of impact (Muthukumar & DesRoches, 2006). To provide a better estimation of the pounding force, the impact material object is implemented as a compression-only gap, which accounts for the dissipated energy at the contact surface during impact. Figure 4.3

shows the load-displacement relationship defined for this material. This differentiates it from the simple gap element, "ElasticPPGap", which does not realistically model the energy dissipation. The forming parameters of "ImpactMaterial" are defined in Eqs. 4.4 through 4.8 (OpenSees Wiki, 2014):

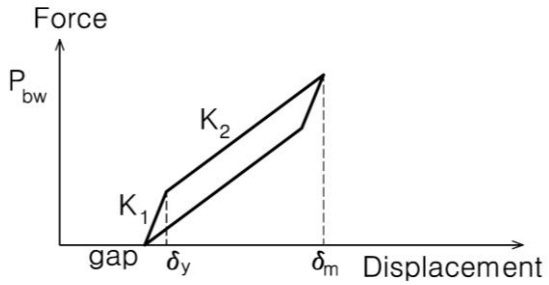

Figure 4.3 Impact Material Model

$K_1 = K_{eff} + \frac{E}{0.1 \times \delta_m{}^2}$ (Initial Stiffness) Eq. 4.4

$K_2 = K_{eff} - \frac{E}{0.9 \times \delta_m{}^2}$ (Secondary Stiffness) Eq. 4.5

$E = \frac{K_h}{2.5}\ \delta_m{}^{2.5}(1 - e^2)$ (Dissipated Energy) Eq. 4.6

$K_{eff} = K_h \sqrt{\delta_m}$ (Effective Stiffness) Eq. 4.7

$\delta_y = 0.1\ \delta_m$ (Yield Penetration Displacement) Eq. 4.8

e = Coefficient of Restitution with typical values from 0.6-0.8

where δ_m is the maximum penetration during the pounding event and K_h is the impact stiffness parameter. In this study, K_h was assumed the larger of the stiffnesses of colliding elements. Combining the above relationships yields the following:

$K_1 = 3.0 \sqrt{\delta_m}\ K_h$ Eq. 4.9

$K_2 = 0.25\ K_1$ Eq. 4.10

These parameters are uniquely set for modeling different gaps in the analytical model and are discussed in the in-span hinge modeling and abutment modeling sections of this chapter.

4.4 SUPERSTRUCTURE

4.4.1 Box-Girder Superstructure

The box-girder superstructures introduced in Chapter 3 are modeled by an elastic beam column element using “elasticBeamColumn” in OpenSees. It is expected that the superstructure elements remain elastic. Other elements such as the columns and abutments are designed to undergo inelastic excursions, while the superstructure is protected by a capacity design and is expected to remain in the elastic range.

Given the significant effects of the higher dynamic modes of the superstructure and of the in-span hinge shear key forces (demonstrated in Chapter 2), the section properties of the superstructures must be precisely calculated. Incorrect specification of the moment of inertia (about the vertical axis), shear area, and torsional constant (for the superstructure) will significantly alter the modes of deformation of the superstructure.

The values of the cross-sectional area, A_g; torsional constant, J_g; moment of inertia about the strong and weak axes, I_g; and the corresponding shear areas, A_v, are determined using the “superstructure Section” module of CSi Bridge software v15.2.0 (CSI, 2013). Figure 4.4 shows the built-in generic concrete box-girder section in CSi Bridge. Figure 4.5a, b, and c show the cross-section properties calculated for the superstructures of long-span prototypes with single-column, long-span prototypes with two-column bents, and short-span prototypes with single-column, respectively.

The value of the torsional constant, J_g, is compared to the value obtained using BRIGE STRUDL Manual, Appendix C (Caltrans, 1973).

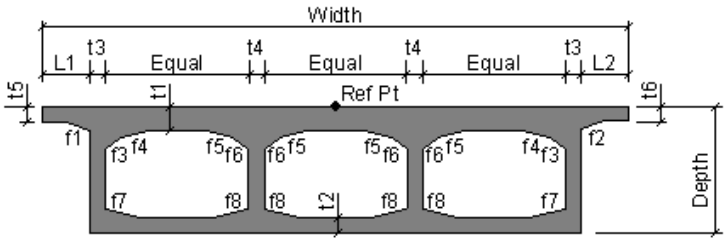

Figure 4.4 Generic Concrete Box-Girder in CSi Bridge

A	17644.
J	80133515
I33	26601791
I22	7.934E+08
I23	0.
AS2	5876.7829
AS3	11824.138
S33(+face)	599533.
S33(-face)	515247.5
S22(+face)	2066075.9
S22(-face)	2066075.9
Z33	643704.6
Z22	3215868.
r33	38.8291
r22	212.051
Xcg	384.
Ycg	51.6291
Xpna	384.
Ypna	60.6333

(a)

A	10716.
J	41219380
I33	15152695
I22	1.979E+08
I23	0.
AS2	4619.2115
AS3	6333.7436
S33(+face)	351194.7
S33(-face)	286690.4
S22(+face)	824462.1
S22(-face)	824462.1
Z33	371453.3
Z22	1273510.7
r33	37.6035
r22	135.886
Xcg	240.
Ycg	52.8539
Xpna	240.
Ypna	60.875

(b)

A	8428.
J	11136892
I33	3596874.
I22	1.493E+08
I23	0.
AS2	3363.2135
AS3	5571.6499
S33(+face)	149686.72
S33(-face)	120013.2
S22(+face)	622266.8
S22(-face)	622266.8
Z33	159976.6
Z22	965052.
r33	20.6586
r22	133.1164
Xcg	240.
Ycg	29.9707
Xpna	240.
Ypna	36.6333

(c)

Figure 4.5 Superstructure Section Properties, a) Long-Span Prototypes with Single-Column Bent, b) Long-Span Prototypes with Two-Column Bents, and c) Short-Span Prototypes with Single-Column

The stiffness values are obtained based on the properties of un-cracked cross sections of the superstructure. Multi-modal analyses are incapable of capturing the variations in flexural stiffness caused by moment reversal (Aviram, et al., 2008). Therefore, no flexural stiffness reduction is recommended for post-tensioned concrete box-girder sections ($I_{eff}=I_g$), as specified by Section 5.6.1.2 of SDC (Caltrans, 2013). Per Section 5.6.2 of SDC, a reduction of the torsional moment of inertia is not required for bridge superstructures because the prototype models meet the Ordinary Bridge requirements in Section 1.1 of SDC.

To obtain the module of elasticity of concrete, a compressive strength, f'_c, equal to 5.0 ksi is assumed for the superstructures. The weight of normal concrete, w_c, is specified by SDC Section 3.2.6 to be approximately 144 lb/ft^3. Equation 3.2.6-1 in SDC 1.7 (Caltrans, 2013) is used to determine the modulus of elasticity of concrete, E_c, which was obtained as approximately 4000 ksi.

4.4.2 Cap-Beam

In both the single-column and the two-column bent models, the cap-beam is explicitly modeled by an elastic beam column element at each side of the superstructure axis with a concrete solid rectangular section. The cap-beam width is D_{col} + 2 ft, and the depth is equal to the depth of the superstructure. D_{col} is the diameter of the column as determined in the design of the prototypes.

For the single-column models, the cap-beam elements are modeled for the accurate placement of mass (or weight). However, in the two-column bent models, it is important to model the cap-beam with accurate stiffness values. Since the concrete

superstructure and cap-beam are integrated, the superstructure's flexural stiffness enhances the torsional stiffness of the cap-beam. The actual dimensions of the cap-beam-superstructure system resisting torsion and in-plane bending are larger than the cross-sectional dimensions of the cap-beam element exclusively. Because the spine model does not make this realization, the bridge stiffness in the longitudinal direction is underestimated, as shown in Figure 4.6. To handle this issue, the effective torsional constant, J_{eff}, and effective moment of inertia about the vertical axis, $I_{z\text{-}eff}$, were increased by a factor of 100 and 5, respectively, as indicated in Eqs.4.11 and 4.12 (Aviram, et al., 2008):

$$J_{eff} = 100 \times J_g \qquad \text{Eq. 4.11}$$

$$I_{Z-eff} = 5 \times I_{z-g} \qquad \text{Eq. 4.12}$$

where J_g is the gross section torsional constant and $I_{z\text{-}g}$ is the gross section moment of inertia about the vertical axis. It should be noted that using equal constraints or slave nodes for this purpose might lead to unrealistic results because the nodes are constrained in the global axis. In the transverse direction, the cap-beam interacts with a portion of the superstructure and soffit of the superstructure; therefore, the cap-beam's bending stiffness increases. However, cracking due to bending will reduce its stiffness. These two effects approximately negate each other; therefore, no modification was applied on the out of plain bending stiffness of the cap-beam elements.

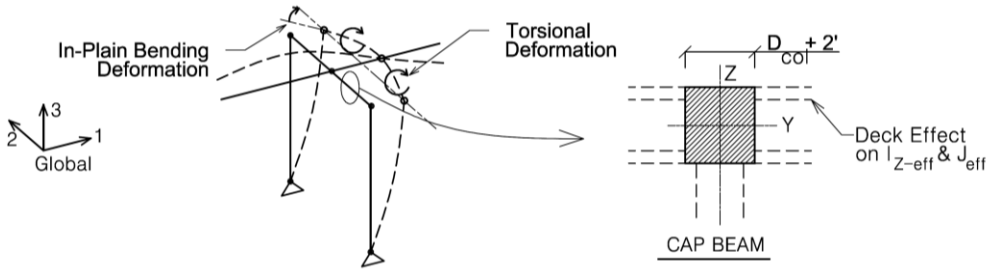

Figure 4.6 Twisting and In-Plane Bending of Cap-Beam under Longitudinal Loads

4.4.3 Seat-Type Abutment

A refined form of the abutment model proposed by Mackie and Stojadinovic (2006) is used in this study (Aviram, et al., 2008). Figure 4.7 shows the schematic of the abutment model and its components. The end diaphragm and backwall are modeled using elastic-beam column element objects, "elasticBeamColumn", with solid rectangular sections of D_s×5 ft and D_s×1 ft, respectively where D_s is the depth of the superstructure. The effective flexural moment of inertia of the end diaphragm, about the vertical axis ($I_{z\text{-}eff}$) was increased by a factor of five because of the presence of the superstructure on one side. Nodes connecting the backwall elements were restrained in the vertical direction. For the transverse direction, only the middle node was fixed to

avoid binding when the backwall rotates about the vertical axis. A set of zero length element objects “zeroLength“ are used to model the backfill, impact, abutment shear keys, and bearing as discussed below.

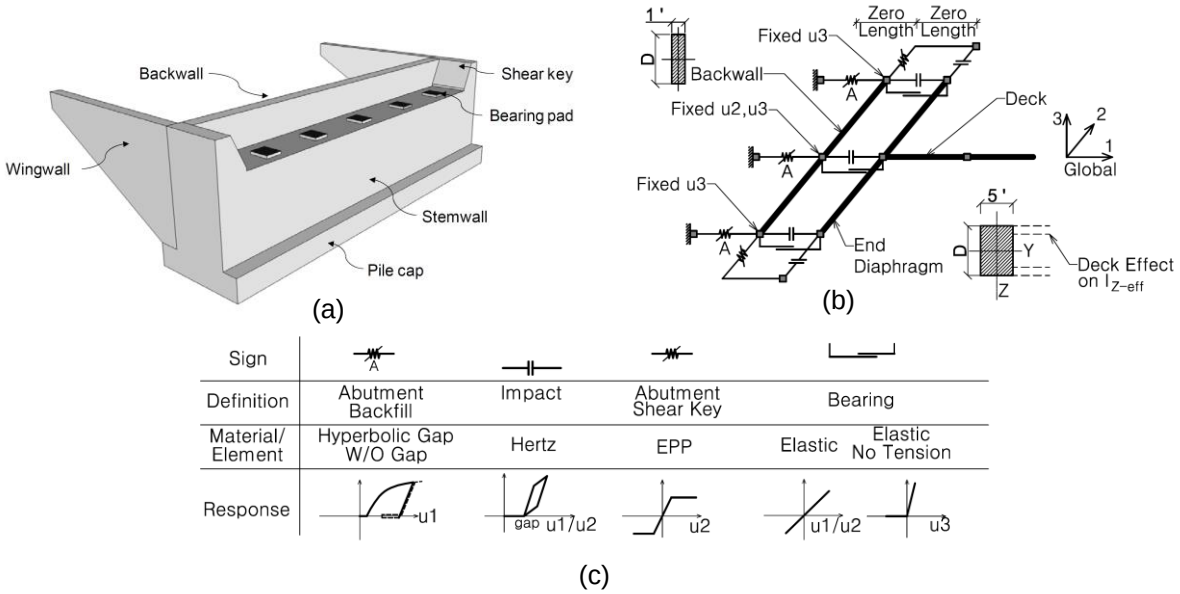

Figure 4.7 a) Seat-Type Abutment Configuration (Kaviani, et al., 2014), b) Abutment Modeling Scheme, and c) Zero Length Elements

I. Backfill

The longitudinal response of the backfill at the abutments is modeled using the uniaxial hyperbolic gap material, “HyperbolicGapMaterial”. This is a compression only material that is developed specifically for modeling abutment backfill because it accumulates plastic damage in unloading-reloading cycles as shown in Figure 4.8. The values of initial stiffness, K_{Abut}, and the ultimate passive force, P_{bw}, are calculated according to SDC 1.7 Sec. 7.8.1 for seat-type abutments (Eq.4-13 and 4-14):

$$K_{Abut} = K_i \frac{k/in}{ft} \times w \times \frac{h}{5.5\ ft} \text{ (kip/in)} \qquad \text{Eq. 4.13}$$

where K_i = 50 kip/in/ft, w and h denote the backwall’s width and height, respectively. w is the superstructure’s width, and h is assumed to be 13 ft:

$$P_{bw} = A_e \times 5.0\ ksf \times \frac{h_{bw}}{5.5} \text{ (kip)} \qquad \text{Eq. 4.14}$$

$$A_e = h_{bw} \times W_{bw} \text{ (in}^2\text{)} \qquad \text{Eq. 4.15}$$

where h_{bw} is the effective height of the backwall and W_{bw} is the width of the backwall. These parameters are assumed to be equal to the superstructure’s depth and the superstructure’s soffit width, respectively.

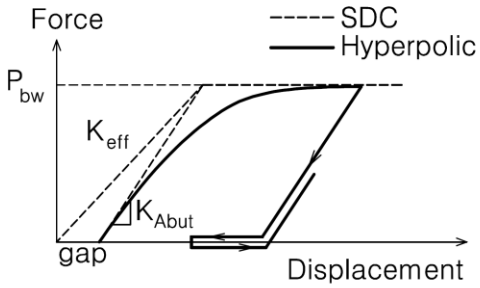

Figure 4.8 Abutment Backfill Material Model

The initial stiffness and the ultimate passive force calculated for the entire width of the backwall are proportionally assigned to the middle and side nodes based on their tributary widths. The initial gap was set to zero for the backfill elements because the gap was modeled in the impact element introduced below.

II. Longitudinal Gap (Impact)

The impact material introduced in Sec. 4.3.4 is used to model the gap between the end diaphragm and the backwall. In accordance with (Muthukumar & DesRoches, 2006) study on the effects of longitudinal impact on the response of multi-frame bridges, the maximum penetration displacement at the contact surface, δ_m, is assumed to be 0.5 in. The impact stiffness parameter, K_h, is assumed equal to the longitudinal (axial) stiffness of the superstructure as defined in Eq. 4.16:

$$K_h = \frac{E_c A_{sup.}}{L} \qquad \text{Eq. 4.16}$$

where E_c is the concrete modulus of elasticity, $A_{sup.}$ is the cross-section area of the superstructure, and L is the average length of the frames in the models, which is taken to be 600 ft.

For the main analysis, the longitudinal gaps were opened in order to avoid the noises in the shear key forces due to the longitudinal impacts. A set of supplemental analyses is conducted, specifically to study the impact effects. In those models, a 2.0-in. gap was implemented.

III. Abutment Shear Keys

According to SDC 1.7, the abutment shear key should be designed as a fuse (either sacrificial or ductile) to limit the force demands on the foundation. Its capacity is prescribed to be equal to αP_{dl} where P_{dl} is the superstructure's dead load reaction at the abutment and $0.5 < \alpha < 1.0$. The exterior shear key shows a ductile load-displacement behavior when it yields in flexure (Bozorgzadeh, et al., 2007). In this study, an elasto-plastic model is used for the force-displacement relationship. To this end, the "Steel02"

material model shown in Figure 4.9 is used in series with the impact material (Figure 4.3) to simulate the behavior of the shear key. One shear key assembly is modeled on each side of the end diaphragm to replicate the two exterior abutment shear keys.

The yield force is αP_{dl} and the elastic stiffness is approximately $K_e=2000\alpha^{1.5}$ kip/in, which is found through a moment curvature analysis of the generic shear key shown in Figure 4.9. For the Main Analyses, α is assumed 1.0. Upon the yielding of the abutment, shear key(s), the end boundary condition of the model changes. To examine this effect on the force demands for in-span shear keys, two other values of 0.5 and 2.0 are also considered for α (only for uniform valley shape prototypes). This parametric analysis allows studying the effect of the yielding of abutment shear key(s) on in-span shear keys.

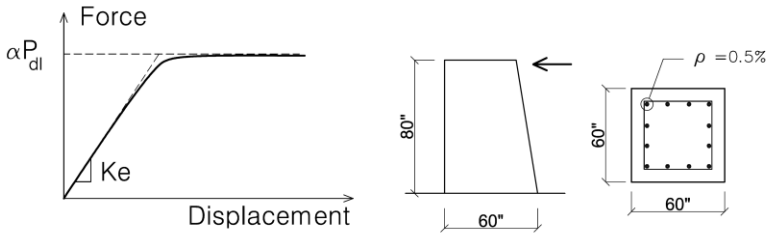

Figure 4.9 Abutment Shear Key Model

To model the transverse gap between the superstructure and the abutment shear key, the impact element is used. This is modeled by implementing an axillary node that connects the shear key and impact elements. The approximate mass of the shear key (0.01 kip.s^2/in) is assigned to this auxiliary node to help with the numerical stability of the model. This makes it possible to assign mass-proportional damping to the element. To find the impact parameters (similar to the backwall), δ_m was assumed 0.5 in. The impact stiffness parameter (K_h) is taken to be equal to the elastic stiffness of the shear key. The transverse gaps were considered closed in the main analysis. A gap size of 1.0 in. is used in the models to study the effects of impact.

IV. Bearings

Steel-reinforced elastomeric bearing type is used for the prototype bridges. The bearings are modeled by an elastic material in both the longitudinal and transverse directions. In the vertical direction, the bearings are modeled using an elastic no-tension material called “ENT,” which allowed for corner uplift. The bearings’ sizes, axial stiffness, and shear stiffness are determined according to the Caltrans Bridge Design Specifications, Sec.14.6.5.3 (Caltrans, 2008). The required bearing area, A_b, was determined using Eq. 4.17a, and the bearing shear stiffness, K_s, was calculated using Eq. 4.17b:

$$A_b = \frac{P}{\sigma_{all}} \quad \text{Eq. 4.17a}$$

$$K_s = \frac{G_r A_b}{t_r} \quad \text{Eq.4-17b}$$

where P is the dead load reaction on each bearing, σ_{all} is the allowable compressive stress of the bearing, which was assumed to be 1.6 ksi. G_r is the shear modulus of the elastomer, which was taken to be 0.12 ksi. t_r is the total thickness of the rubber layers, which was taken to be two times the longitudinal gap size to accommodate for the transverse displacements of the superstructure.

4.4.4 In-Span Hinges and Shear Keys

The in-span hinge model is developed using a concept similar to the one used for modeling the abutments. The in-span hinge model is shown in Figure 4.10. The in-span diaphragms were modeled using the elastic beam column elements "elasticBeamColumn" with a solid L-shape cross section. The effective flexural moment of inertia of the diaphragms about the vertical local axis ($I_{z\text{-}eff}$) was increased by a factor of five because of the presence of the superstructure. This is because the spine model does not incorporate the rigidity of the superstructure on the diaphragm. Bearings and longitudinal impact elements were modeled with properties similar to those of the abutments.

One shear key model is incorporated in the in-span hinge assembly. This element is placed at the center, which is on the same line as the superstructure elements. To model the in-span shear keys, a uniaxial elastic material "Elastic" is defined and assigned to the shear direction of a zero length element "zeroLength". To model the transverse gap (clearance around the shear key) and impact, two zero length elements with impact material "ImpactMaterial" are defined in series on the two sides of the shear key element. An axillary node is implemented to connect the shear key and the impact elements. An infinitesimal translational mass of 0.01 kip.s^2/in is assigned to the auxiliary node.

The concrete block shear key, shown in Figure 4.10a, is the standard type of in-span shear key for modeling purposes. As in Section 3.1.2, Caltrans has developed a new detail called the "pipe extender/shear key" which is available in Bridge Standard Detail Sheets, xs-7-80 (Caltrans, 2014). This detail is being used in new multi-frame bridges as an alternative for concrete shear keys. The shear key type only reflects itself in the value of the shear stiffness of the shear key element. The stiffness calculation of the in-span shear keys is explained in the following section. The effect of varying the shear key stiffness based on its force response is examined through sensitivity analysis, which is discussed later in Section 4.8.

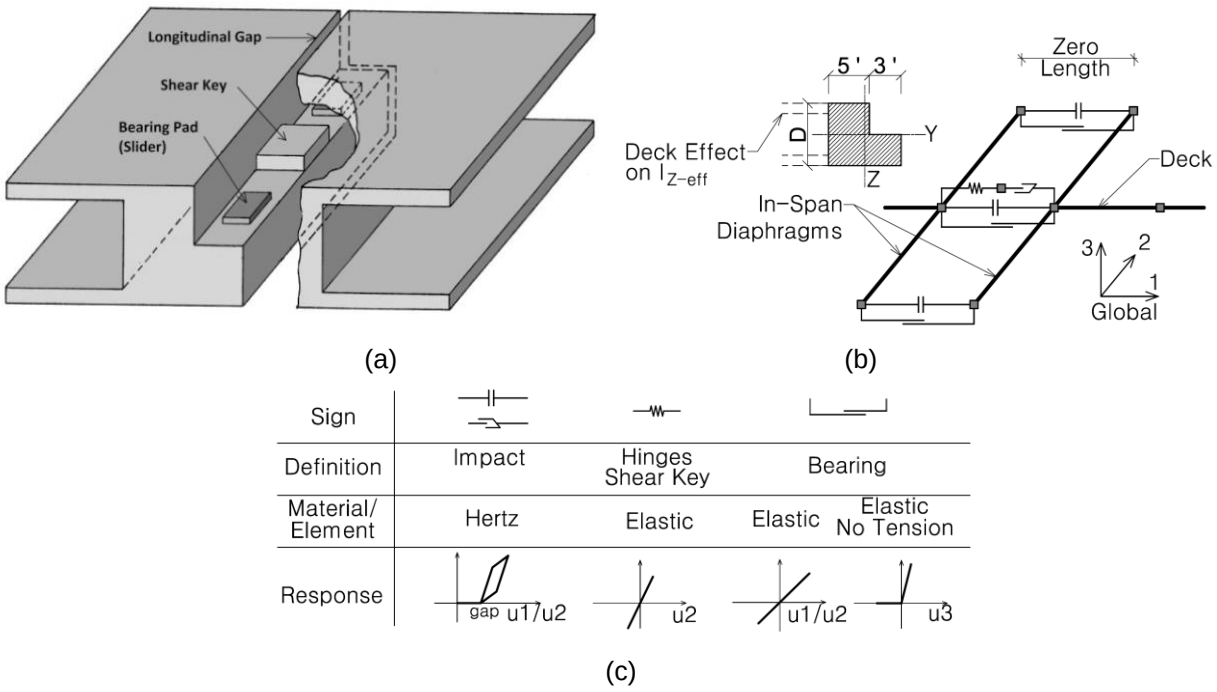

Figure 4.10 a) In-Span Hinge Configuration, b) In-Span Hinge Modeling Scheme, and c) Zero Length Elements

Stiffness of Concrete Block Shear Keys: Megalley proposed an empirical force-shear deformation relationship for interior concrete block shear keys, which is shown in Figure 4.11 and presented in Eqs. 4.18 and 4.19 (Megalley, et al., 2002).

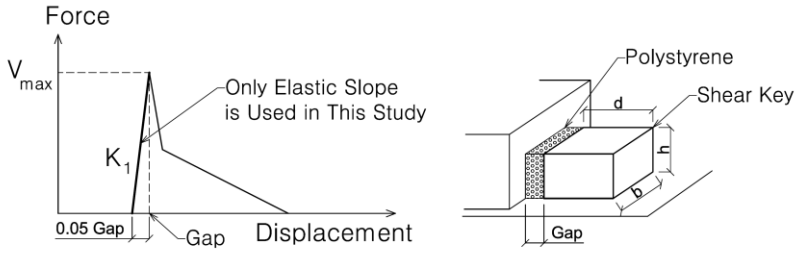

Figure 4.11 Interior Concrete Shear keys Model (Bozorgzadeh, et al., 2007)

Assuming a 30 in x 45 in (*b* x *d*) concrete block with f'_c=4 ksi and a 1.0-in gap size, the elastic stiffness is determined to be 22500 kip/in:

$$V_{max} = 11.3\sqrt{f_c'} \times b \times d = 11.3\sqrt{4000} \times 45 \times 35 = 1125\ (kip) \qquad \text{Eq. 4.18}$$

$$K_1 = \frac{V_{max}}{0.05\ Gap} = \frac{1125}{0.05 \times 1.0} = 22500\ (kip/in) \qquad \text{Eq. 4.19}$$

Stiffness of Pipe Extender/Shear Key: There is no technical reference on the capacity and stiffness of steel pipe shear keys. Thus, the behavior of this element is studied as part of this study through refined finite element (FE) simulations using

ABAQUS 6.11-1 (Dassault Systems, 2011). The details of these FE simulations are explained in Part 2 of this report. The maximum elastic stiffness of one pipe when the longitudinal gap is closed is found to be approximately 1000 kip/in, as shown in Figure 4.12. This value corresponds to zero longitudinal gap size. Because the pounding on shear keys may happen at other longitudinal gap sizes as well, 80% of this value is used (800 kip/in). Four and six pipe extender/shear keys are assumed for the single-column prototypes (40-ft wide superstructure) and two-column bent prototypes (64-ft wide superstructure), respectively. The total shear stiffness for these two models is calculated accordingly as 3200 kip/in and 4800 kip/in, respectively.

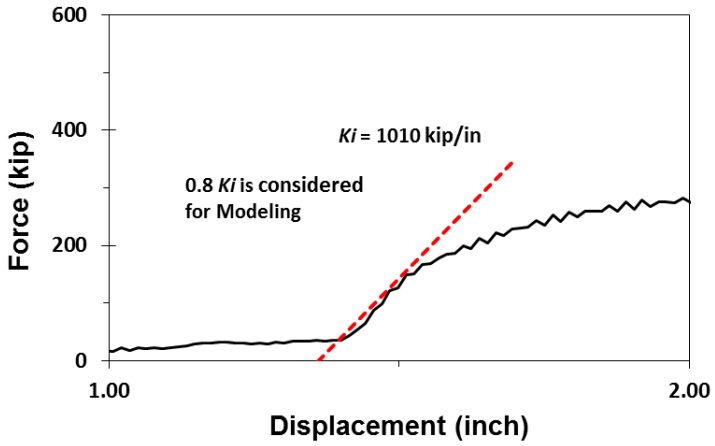

Figure 4.12 Force-Displacement Relationship for One Standard Pipe Extender/Shear Key Detail with Zero Longitudinal Gap from Finite Element Analysis

The results show that a concrete shear key is stiffer than a set of multiple pipe extender/shear keys. To understand the effect of shear key stiffness on maximum shear key force, a set of sensitivity analyses is performed and their results are discussed in Section 4.8. The stiffness value of the pipe extender/shear key is used in the models since the pipe extender/shear key offers several construction benefits over the concrete block shear key.

One of the objectives of this research is to study the seismic performance of multi-frame bridges with ductile in-span shear keys. In the separate set of models used for this purpose, the “Elastic” material model was replaced with “Steel02” material to simulate the yielding of the shear keys. Figure 4.13 shows the force-shear deformation represented by the inelastic material. The elastic stiffness of the pipe seat extenders is used. The post-elastic hardening is 0.5% of the elastic stiffness. The yield capacity was assumed equal to the lateral load capacity of the adjacent bent with a 20% over strength factor.

Figure 4.13 Material Model for Ductile In-Span Shear Key

For the two impact elements, the maximum penetration displacement (δ_m) was assumed 0.5 in. The impact stiffness parameter (K_h) was taken as the transverse stiffness of the shorter superstructure acting as a cantilever ($3EI/L^3$). For the main analyses, the transverse gaps are closed as they are for the abutments. For the models used to study the effects of impact, a 1.0 in. gap is considered on both sides.

4.5 COLUMNS

Unlike building structures, bridge columns are designed to yield under strong ground motions. The columns of the prototype bridges are carefully modeled to capture the accurate inelastic responses.

The columns in the two-column bent prototypes are modeled as pinned base cantilevers. For the single-column bent, two modeling methods have been developed and used by researchers. In the first approach, linear or nonlinear soil is explicitly modeled using a series of springs, called p-y springs. In the second method, an equivalent depth of fixity is defined under the ground level to replicate the lateral stiffness of the soil-pile system. In the latter method, soil effects are indirectly accounted for. The first approach is not used in this study for the following reasons: 1) to avoid the complexities and uncertainties involved in selecting the proper p-y relationships (values of the equivalent depth of fixity are simply presented in design standards like Sec. 10.7.3.13.4 of AASHTO LRFD (AASHTO, 2012)), and 2) because explicit modeling of a nonlinear p-y spring is computationally demanding. With the large number of prototype models and ground motions, using the second approach is more practical.

The plastic hinging of the columns is modeled using the fiber section definition. The following sections present the modeling details of the columns, including the definition of inelastic material, the fiber section properties, the moment-curvature analyses, and the distribution and location of inelastic behavior along the length.

4.5.1 Material Properties and Models

The characteristics of concrete and reinforcing steel are defined in accordance with SDC1.7 Sec. 3.2 (Caltrans, 2013).

Unconfined Concrete: The specified and expected strengths of unconfined concrete are assumed to be f'_c = 5.0 ksi and f'_{ce} = 6.5 ksi, respectively. The strain at the maximum strength and the ultimate strain are ε_{co}=0.002 and ε_{sp}=0.005, respectively. The tensile strength of concrete and the modulus of elasticity are f_t = 0.6 ksi and E_c = $57000 \times \sqrt{f'_{ce}}$ for normal weight concrete. The constitutive model for unconfined concrete is shown in Figure 4.14a.

Confined Concrete: The strength (strain at maximum stress) and the ultimate strength of the confined concrete core are determined based on Mander model, which is defined in Eq. 4.20 to 4.22 (Mander, et al., 1988):

$$f'_{cc} = f'_c[-1.254 + 2.254\sqrt{1 + \frac{7.94f'_c}{f'_c} - \frac{2f'_l}{f'_c}}] \quad \text{Eq. 4.20}$$

$$\varepsilon_{cc} = \varepsilon_{c0}[1 + 5\left(\frac{f'_{cc}}{f'_c} - 1\right)] \quad \text{Eq. 4.21}$$

$$\varepsilon_{cu} = \varepsilon_{sp} + 1.4\,\frac{\rho_s f_{yh}\,\varepsilon_{suh}}{f'_{cc}} \quad \text{Eq. 4.22}$$

where f'_l is the effective confining pressure and ρ_s is the transverse steel ratio. f_{yh} is the strength of transverse reinforcement and ε_{suh} is the ultimate strain of the transverse hoops, which are assumed 60 ksi and 0.12, respectively.

This formulation is implemented in the OpenSees script in order to automatically update the material properties based on the design results for each column diameter and transverse reinforcement ratio. Both confined and unconfined concrete were modeled by using “Concrete04” uniaxial material, as shown in Figure 4.14b. This uniaxial material model is based on Popovics concrete material object with degraded linear unloading/reloading stiffness and tensile strength with exponential decay. This is all according to the work of Karsan-Jirsa (OpenSees Wiki, 2014).

Longitudinal Reinforcing Steel: The longitudinal reinforcing bar was considered as A706 (Grade 60) with a module of elasticity E_s= 29000 ksi, expected yield stress f_{ye}= 68 ksi, ultimate stress f_{su}= 95 ksi, ultimate strain ε_{su}= 0.09, and tangent at initial strain hardening E_{sh}= 0.04E_s= 11600 ksi. The “ReinforcingSteel” material, shown in Figure 4.14c, is used to model the longitudinal steel.

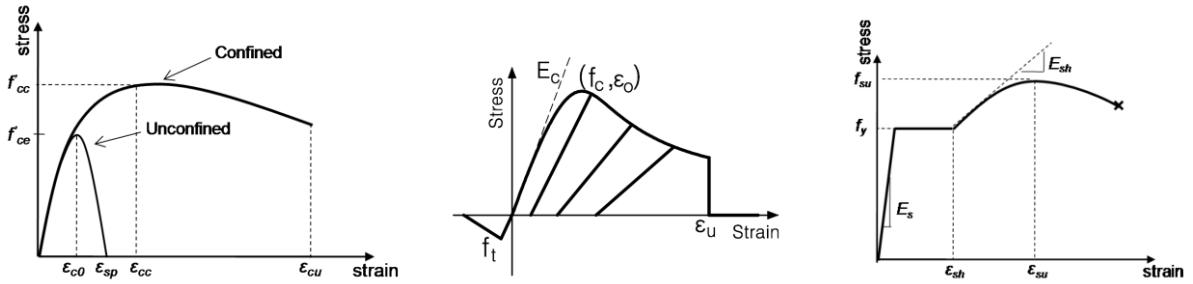

(a) (b) (c)

Figure 4.14 Materials Models a) Confined and Unconfined Concrete, b) "Concrete04" Material, and c) "ReinforcingSteel" Material

4.5.2 Element Type and Geometric Specifications

Each column is modeled by a single nonlinear force-based beam column element "forceBeamColumn" with seven and six integration points for the single-column and two-column respectively (shown in Figure 4.15). The formulation with mid-distance integration points is selected because this option allows for the user-specified location of the integration points and the integration weights (Scott, 2011). The associated integration weights are defined as being equal to the distance between the adjacent integration points. The force-deformation response at each integration point is defined by different section properties.

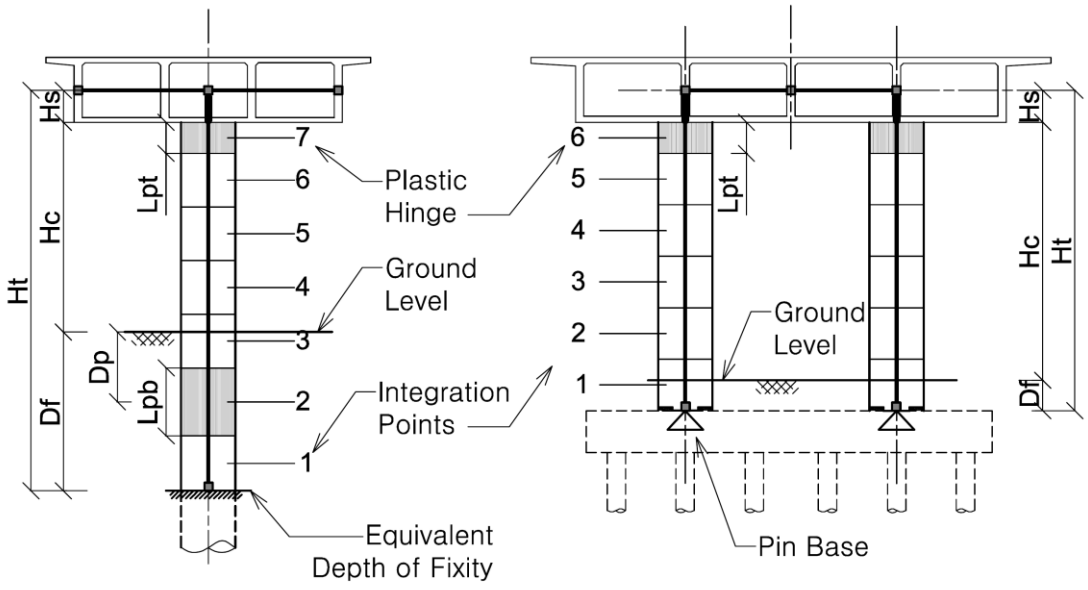

Figure 4.15 Column Modeling Scheme and Integration Points for Single-Column and Two-Column Bents

To define the proper location of the integration points for each column, the following parameters are defined.

Column Height: The total column height (H_t) is defined as clearance height (H_c) plus the depth of fixity (D_f) and the superstructure centroid height (H_s), as defined in Figure 4.15. H_s is one half of the superstructure depth. For Two-column bents, D_f is assumed to be a constant value of 5 ft, while, for the single-column, the equivalent depth of fixity is varied based on soil stiffness and column diameter. According to AASHTO LRFD 2012 Sec. 10.7.3.13.4 (AASHTO, 2012), the equivalent depth of fixity, D_f, for sandy soils is defined as:

$$D_f = 1.8 \times \sqrt[5]{E_p\, I_{eff}/n_h} \qquad \text{Eq. 4.23}$$

where E_p is the modulus of elasticity of the pile in ksi, I_{eff} is the effective moment of inertia for the pile in ft^4, and n_h is the rate of increase of soil modulus with depth in ksi/ft. Table C10.4.6.3-2 of AASHTO (AASHTO, 2012) presents the values of 0.471, 1.11 and 2.78 for loose, medium, and dense sand, respectively. As discussed in Section 3.2, the design acceleration response spectrums (ARSs) used in this study are defined for the four soil types of B, C, D, and E. To find the proper value for n_h, a correlation is developed between the seismic soil type, soil density, and the value of n_h. These values are presented in Table 4.1.

Plastic Hinge Location: Figure 4.16 to Figure 4.18 show the distribution of bending forces and the expected locations for plastic hinges. In the Two-column bents, the plastic hinge forms only at the top of the columns because of the inverse cantilever behavior of the columns (Figure 4.16). The location of the center of the plastic hinge region can be assumed to be at half of the plastic hinge length below the superstructure soffit. For the single-column, however, two plastic hinges are permissible. In the transverse direction, the location of the point of contraflexure is typically close to the superstructure (Figure 4.17). Consequently, the magnitude of the moment at the top of the column is smaller than that generated at the base. This being said, one plastic hinge may form below the ground's surface. In the longitudinal direction, two plastic hinges may form, one at each end of the column, due to the frame action of the column-superstructure (Figure 4.18). The location of the center of the top plastic hinge is similar to that of the two-column bents. The bottom plastic hinge forms at the point of maximum bending moment, which is between the depth of fixity and the ground surface. It should be noted that, in some cases, the torsional restraining of the superstructure provided by the abutments and large torsional stiffness of the superstructure might cause double curvature bending. In such cases, under transverse loading, plastic hinges may form at both the top and the bottom of single-column (Aviram, et al., 2008).

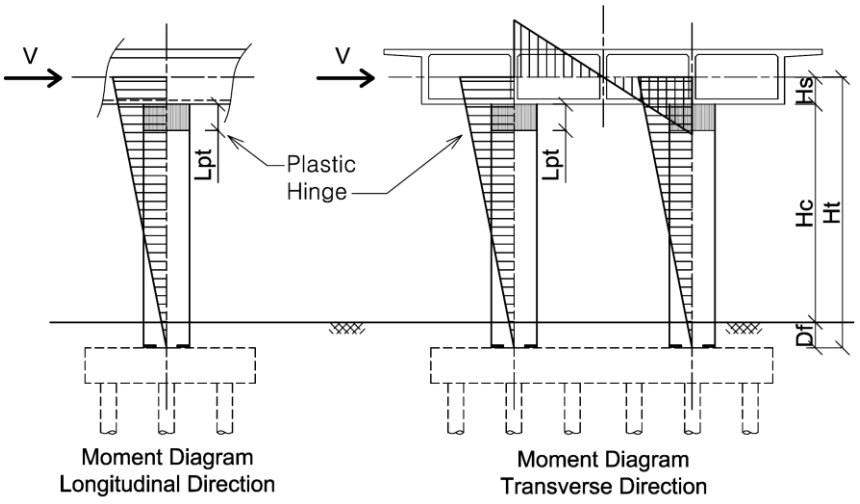

Figure 4.16 Plastic Hinge Locations for Two-Column Bents

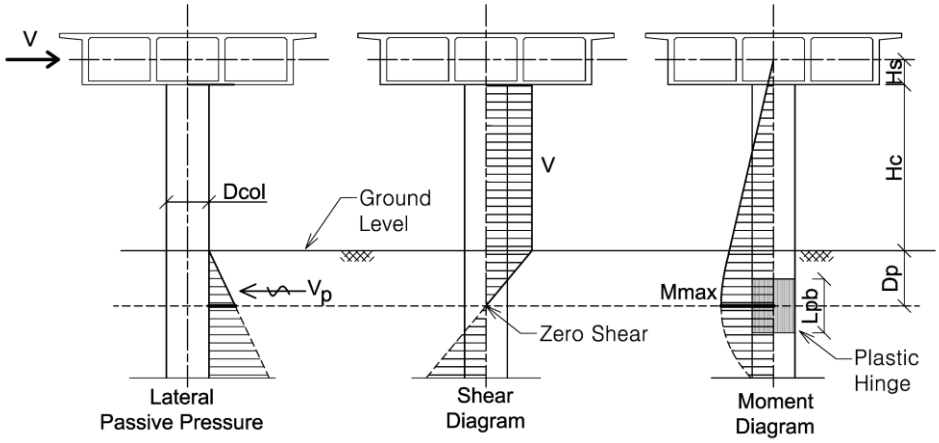

Figure 4.17 Plastic Hinge Location in Single-Column under Transverse Loads

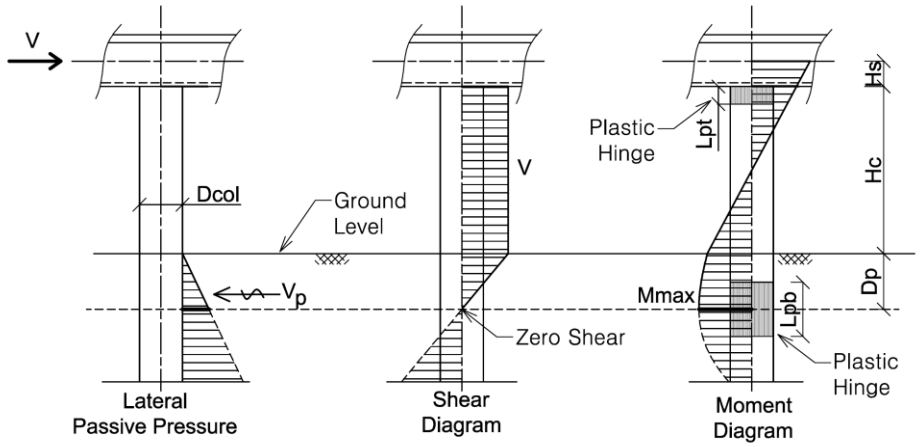

Figure 4.18 Plastic Hinge Location in Single-Column under Longitudinal Loads

An analytical approach is developed in this study to find the depth of the maximum moment (D_p) under the ground surface for a single-column, based on the equilibrium of the passive soil pressure, internal moment, and lateral load. The moment equilibrium at the point of maximum moment gives:

$$M_{max} = V(H_c + H_s) - \frac{1}{3} V_p D_p \quad \text{Eq. 4.24}$$

where V is the shear force and V_p is the passive soil pressure resultant force. H_c and H_s are column length and half of the superstructure depth, respectively. At the point of maximum moment, the internal shear force is zero. Thus:

$$V - V_p = 0 \quad \text{Eq. 4.25}$$

Combining Eqs. 4.24 and 4.25 results in Eq. 4.26:

$$M_{max} = V_p \left(H_c + H_s + \frac{2}{3} D_p\right) \quad \text{Eq. 4.26}$$

Assuming the linear distribution for passive soil pressure drives the resultant passive force as demonstrated in Eq. 4.27. The ultimate passive pressure for piles is assumed to be three times the passive pressure (Hutchinson, et al., 2002):

$$V_p = \frac{3}{2} \times \gamma_s \times K_p \times D_{col} \times {D_p}^2 \quad \text{Eq. 4.27}$$

where γ_s is the soil density and K_p is the passive pressure coefficient. These values are presented in Table 4-2 for the four ARS soil types. D_{col} is the diameter of the column. Combining Eqs. 4.26 and 4.27 gives the maximum moment:

$$M_{max} = \frac{3}{2} \gamma_s K_p D_{col} ({D_p}^2 (H_c + H_s) + \frac{2}{3} {D_p}^3) \quad \text{Eq. 4.28}$$

It can be assumed that M_{max} is equal to the plastic moment of the column (M_p). Finally, Eq. 4.28 can be solved for D_p.

Table 4.1 Assumed Soil Properties

Soil Type	V_s ft/sec (m/s)	γ_s (lb/ft^3)	$\varphi°$	K_p	n_h (ksi/ft)
B	3750 (1130)	125	45	5.8	2.7
C	1850 (557)	120	40	4.6	1.5
D	900 (271)	112	35	3.7	1.0
E	500 (150)	105	30	3.0	0.4

Vs: Average Shear Wave Velocity
Kp: Soil Passive Pressure Coefficient
n_h: rate of increase of soil modulus with depth

Plastic Hinge Length: Plastic hinge length is found according to SDC 1.7 Sec. 7.6.2 (Eq. 4.29). The length of the top plastic hinge for the single-column and the two-column bent is:

$$L_{pt} = 0.08\,L + 0.15 f_{ye} d_{bl} \geq 0.3 f_{ye} d_{bl} \quad \text{(in, ksi)} \qquad \text{Eq. 4.29}$$

where d_{bl} is the longitudinal bar diameter and was taken to be 1.25 in. (bar #10) for all cases, and L is the length from the point of maximum moment to the point of contraflexure. The length, L, for the longitudinal action of a single-column and a two-column bent are defined in Eq. 4.30 and Eq. 4.31, respectively:

$$L = {}^{1}/_{2}\,(H_c + D_p) \quad \text{(For single-column, under longitudinal loads)} \qquad \text{Eq. 4.30}$$

$$L = H_c + D_f \quad \text{(For two-column bents)} \qquad \text{Eq. 4.31}$$

Because the pile-shafts have frame action in the longitudinal direction, the contra-flexure point is located at the mid-distance of the top and bottom plastic hinges.

The length of the bottom plastic hinge for the single-column under transverse loads is indicated by Eq. 4.32 based on (Caltrans, 2013):

$$L_{pb} = D_{col} + 0.08 H_{o-max} \quad \text{(For single-column under transverse loads)} \qquad \text{Eq. 4.32}$$

where $H_{o\text{-}max}$ is the length of the column from the point of the maximum moment to the point of contraflexure above the ground (Eq.4.33):

$$H_{o-max} = H_s + H_c + D_p \qquad \text{Eq. 4.33}$$

It should be noted that $H_{o\text{-}max}$ is approximately half of the length of that in Eq. 4.33 because of the double curvature action in the longitudinal direction. Because of the limitations in the assignment of modeling parameters of the columns, this difference between plastic hinge lengths in orthogonal directions is ignored, and Eq. 4.29 is used as a basis for the calculation of the bottom plastic hinge length in the single-column bent.

Location and Weight of Integration Points: Figure 4.15 schematically shows the distribution and the numbering of the integration points along the length of the columns. The location and the weight of the integration points are set according to the plastic hinge location and length discussed earlier.

For the single-column, seven integration points are used. This includes two points for plastic hinges (#2 and #7), four points that are uniformly distributed between the two plastic hinges (#3 to #6), and one integration point that is defined below the bottom plastic hinge (#1). For the two-column piers, six integration points are implemented. This includes one point for the plastic hinge at the top (#6) and five points equally

distributed over the remaining length (#1 to #5). The weight assigned to the integration points representing the plastic hinges is equal to the ratio of the plastic hinge length to the total length of the element. For the intermediate integration points, the assigned weight is equal to the ratio of the tributary length to the total length of the element. In all cases, the summation of the integration weights must be equal to one. The rigid end zone at the column-cap beam connection was considered using the joint offset option with a length equal to half of the superstructure depth. The flexibility of the joint is not considered in the models.

4.5.3 Section Properties

A nonlinear fiber section is used for all the integration points except for the first integration point of the single-column. The fiber section configuration used in this study is shown in Figure 4.19. The section is divided into twelve circumferential and five radial subdivisions (fibers). The number of circumferential subdivisions in the central part is reduced to eight, while the size of the radial fibers is increased. This helps with the analysis time without adversely affecting the accuracy because the stresses and plastic strains, at the center of the section, are smaller than those of the exterior portions. The unconfined concrete material, confined concrete material, and steel material discussed earlier, are assigned to the concrete cover, the concrete core, and the longitudinal bar fibers, respectively.

Because the single-column bents are modeled with an equivalent depth of fixity, the maximum moment occurs at the base of the column; however, Eq. 4.28 shows that the bottom plastic hinge forms at a location between the base and the ground surface. To cope with this issue, an elastic fiber section is assigned to the first integration point (Figure 4.15). The configuration of the elastic fiber section is the same as that of the nonlinear section, but elastic material is used for steel, while an elastic compression only material is used for concrete. The moduli of elasticity of these materials are taken as the elastic moduli used in the constitutive material models. This elastic fiber section is assigned to the lowest integration point in order to capture the cracked stiffness of the section in nonlinear response history analyses. At the same time, it must remain elastic and preserve the formation of the plastic hinge at the expected location.

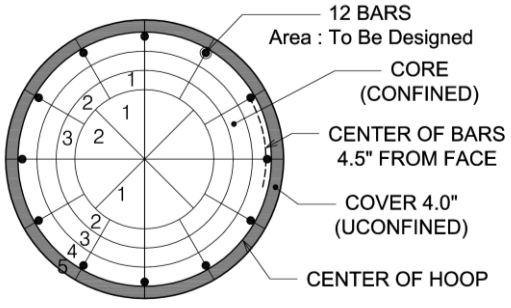

Figure 4.19 The Column Fiber Section

For the inelastic and elastic fiber sections, the section aggregator command "Aggregator" is used to combine the torsional stiffness of the column section with the fiber section. An elastic section with a torsional stiffness of $0.2xG_cxJ_{col}$ was aggregated with the fiber sections, where G_c and J_{col} are the concrete shear modulus and the torsional constant, respectively. The reduction factor of 0.2 is based on Sec. 5.6.2 of SDC 1.7 and accounts for the torsional cracking of the columns section.

4.5.4 Verification of Column Model

To ensure that the definition of the material, fiber section, and integration points allow for an accurate estimation of the hysteresis behavior of the reinforced columns (RC), data from a shake table experiment on a 1:5 scaled RC column performed at the University of Nevada, Reno (Zaghi & Saiidi, 2010) are used for validation. Figure 4.20 shows a comparison of the experimental results and those obtained from a model of a single cantilever column constructed in this study using the modeling assumptions discussed in Section 4.5. A reasonable agreement between the analytical and experimental data confirms the accuracy of the modeling assumptions.

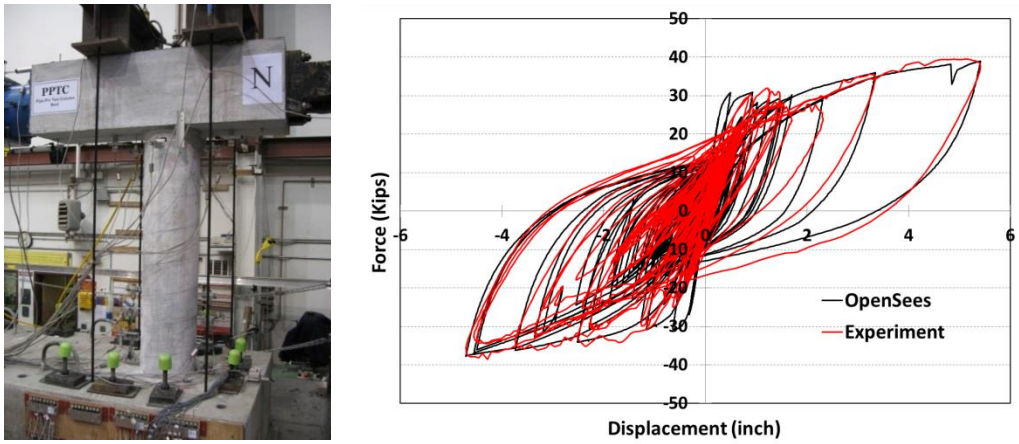

(a) (b)

Figure 4.20 a) Shake Table Test Specimen, b) Lateral Force-Displacement Hysteresis (Zaghi & Saiidi, 2010)

4.6 LOADING AND ANALYSIS

4.6.1 Gravity Loading

The self-weight of the line elements plus the additional superstructure dead loads (as mentioned in Sec. 4.3.3) are applied on the frame elements as a linearly distributed load. Static analysis with a load control integrator was used for the gravity analysis.

4.6.2 P-Delta Effects

P-Delta effects are considered using the “PDelta” coordinate transformation object for all the frame elements. This object performs a linear geometric transformation of the beam stiffness and the resisting force from the basic system to the global coordinate system, considering second-order P-Delta effects. This transformation only considers P large Delta (P-Δ) effects and does not include P small delta (P-δ) effects due to inter-element deformation (OpenSees Wiki, 2014). Because each column was modeled by a single element, P- δ effects are not captured in the analyses.

4.6.3 Damping

Mass and stiffness proportional damping is utilized in the model according to the Rayleigh method that is formulated in Eqs. 4.34 to 4.36 (Chopra, 2001). The Rayleigh equations specify the classical damping matrix *C* (uniform distribution of damping) as the linear combination of proportioned mass, *M,* and current (tangent) stiffness, *K*:

$$C = \alpha M + \beta K \qquad \text{Eq. 4.34}$$

$$\alpha = \frac{2\xi\omega_i\omega_j}{\omega_i+\omega_j} \qquad \text{Eq. 4.35}$$

$$\beta = \frac{2\xi}{\omega_i+\omega_j} \qquad \text{Eq. 4.36}$$

In these equations, ξ is the critical damping ratio, and ω_i and ω_j are the two separate frequencies at which the damping value is set. The Rayleigh damping command of OpenSees defines the damping based on parameters α and β. Special caution is needed when the proportional damping is used to avoid artificial damping (Charney, 2008). In this study, the ratio of critical damping ξ = 5% at the periods of 2.0 and 0.5 sec. (corresponding to the use of ω_i =2.51 and ω_j =12.56 rad/sec). These periods are selected such that approximately uniform damping is obtained over a wide range of periods of vibration, as shown in Figure 4.21. The reason for targeting the periods of higher modes is that the effects of the local modes of vibration of the superstructure are not artificially damped. It is demonstrated in Chapter 2 that these significantly contribute to the in-span shear key force.

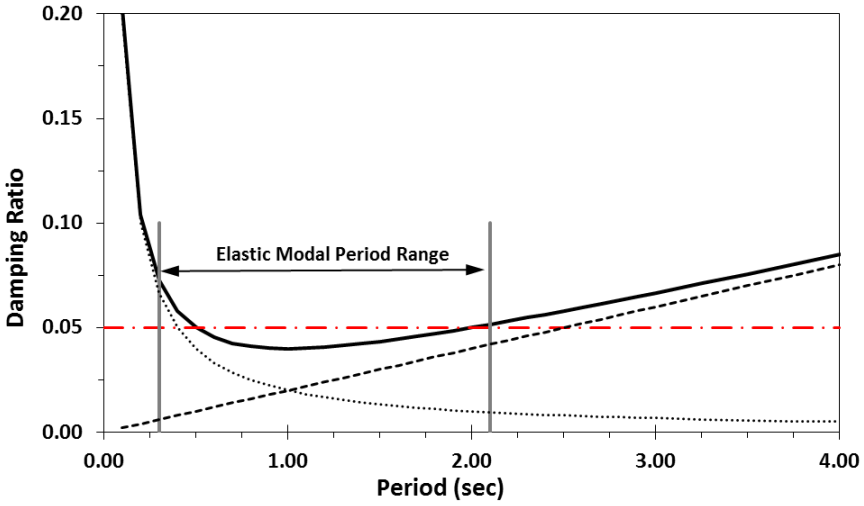

Figure 4.21 Implemented Rayleigh Damping

4.6.4 Time History Analysis

A step-by-step direct integration method was used for the nonlinear time history analyses. The Newmark's time integration method with $\gamma = 0.5$ *and* $\beta = 0.25$ is implemented. In the case of a convergence problem, the Central Difference, Hilber-Hughes-Taylor, and TRBDF2 methods are automatically tried. The maximum time step is set as 0.005 sec. and, in the case of convergence problems, the time step is reduced by a factor of 0.5. This is done until convergence is achieved, while other integration methods were tried instantaneously. Once a stable converged step is achieved, the integration method and the time step are automatically reset to their original settings.

4.7 SYSTEM-LEVEL VERIFICATION OF THE MODEL

In addition to the element level verification of the column model using experimental data, the modeling method is verified using the results of an analogous model developed in SAP2000 Ver. 15.1 (CSI, 2011). The prototype model F3-V1 single-column (Section 3.1) is used for this purpose. Figure 4.22 shows a comparison of the lateral and longitudinal displacements of the midpoint of the bridge and the shear key force obtained from these two models under the input motion D22 (Section 3.3). In spite of using a lumped plasticity formulation to model the nonlinear behavior of columns in the SAP2000 model, an acceptable agreement is achieved between the OpenSees and SAP2000 simulation results. The minor differences may be related to the different hysteresis models incorporated in OpenSees and SAP2000.

The agreement between the system-level responses obtained from the two different structural analysis software platforms confirms the correctness of the analytical model in OpenSees.

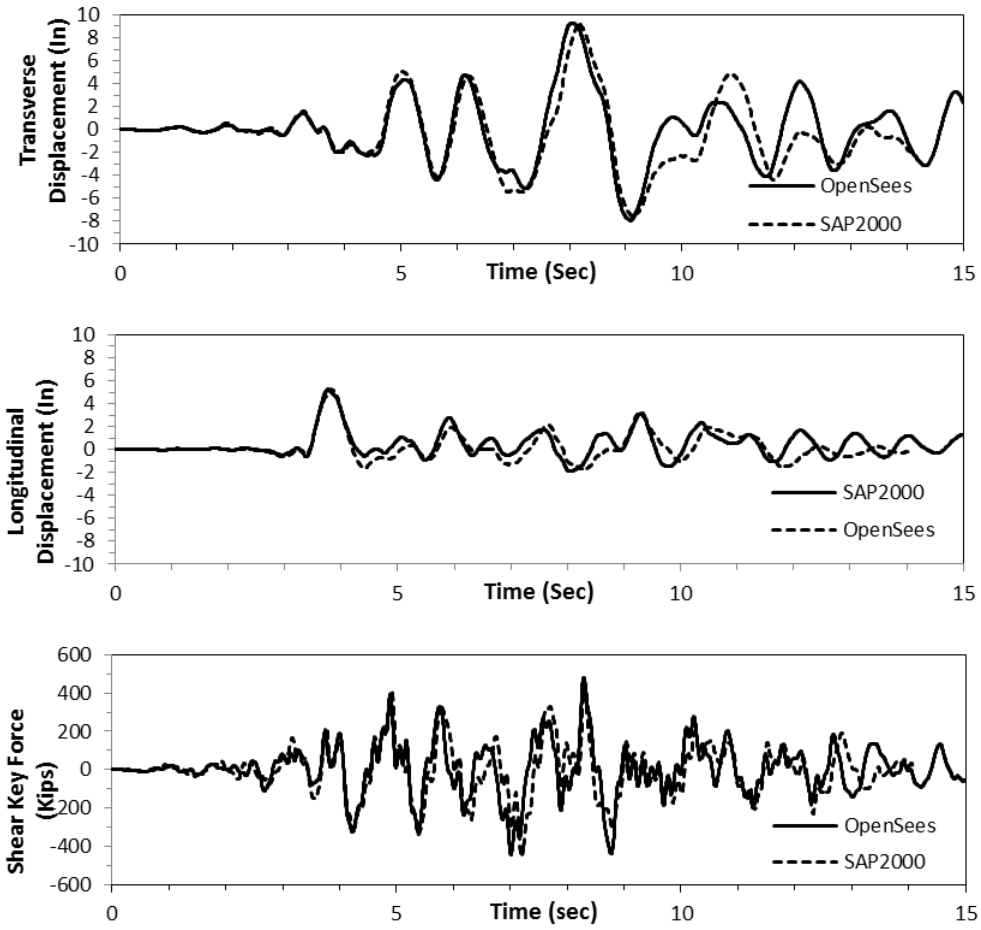

Figure 4.22 Comparison of SAP2000 and OpenSees Results for System-Level Modeling Verification

4.8 SENSITIVITY TO MODELING PARAMETERS

To validate the modeling assumptions for the in-span shear key, a brief sensitivity analysis is performed on the parameters with uncertain values. The designated parameters are the elastic stiffness of the shear key element and the yield penetration displacement (δ_y) used for the impact modeling (Section 4.3.4). Note that $\delta_y = 0.1\ \delta_m$. These parameters are varied one-at-a-time to investigate the sensitivity of the shear key force response to the variation of these parameters. For this purpose, the value of each parameter is first doubled and then halved from the initial parameter. The single-column prototype model F3-V4 is subjected to the suite of B33 and D22 ground motions (six motions).

The effect of the shear key stiffness is examined in two cases: 1) one with no transverse gap and 2) one with a 1.0-in transverse gap. Figure 4.23 shows that shear key stiffness does not have a pronounced effect on maximum shear key force when the transverse gap is closed. If a transverse gap exists, then shear key stiffness affects the impact forces. Figure 4.24 shows that a 100% change in stiffness yields - on average -

a 15% change in the maximum shear key force. This implies that the impact forces are not too sensitive to shear key stiffness values. Thus, the assumption of shear key stiffness being 3200 kip/in is appropriate.

The effect of yield penetration displacement (δ_y) for the impact material used in modeling the transverse gaps is shown in Figure 4.25. It is shown that, on average, a 100% variation in the parameter leads to less than an 8% change in the shear key force, rendering the initial assumption of 0.05 inappropriate.

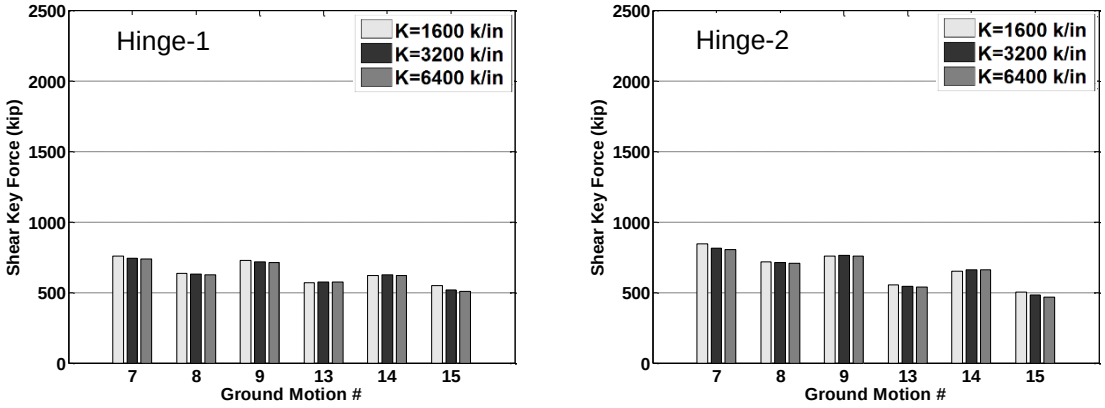

Figure 4.23 Effect of Shear Key Stiffness on the Maximum Shear Key Force (with Closed Transverse Gap)

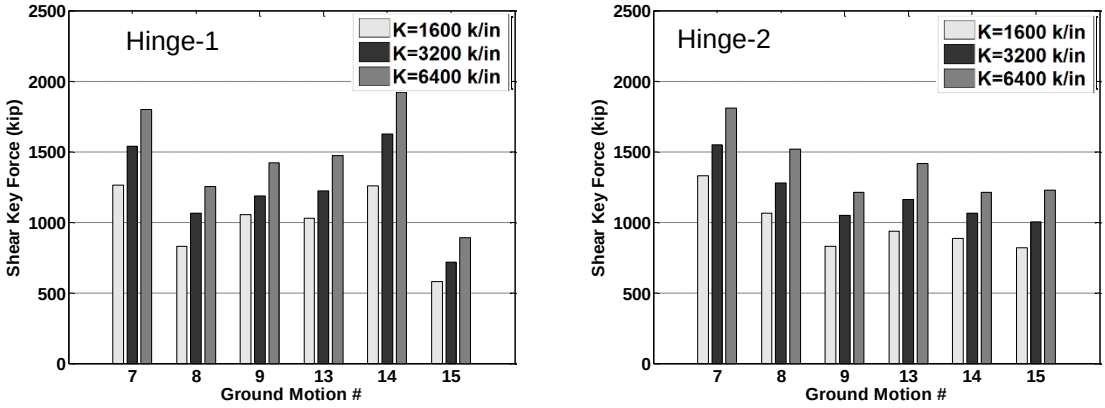

Figure 4.24 Effect of Shear Key Stiffness on the Maximum Shear Key Force (with Transverse Gap)

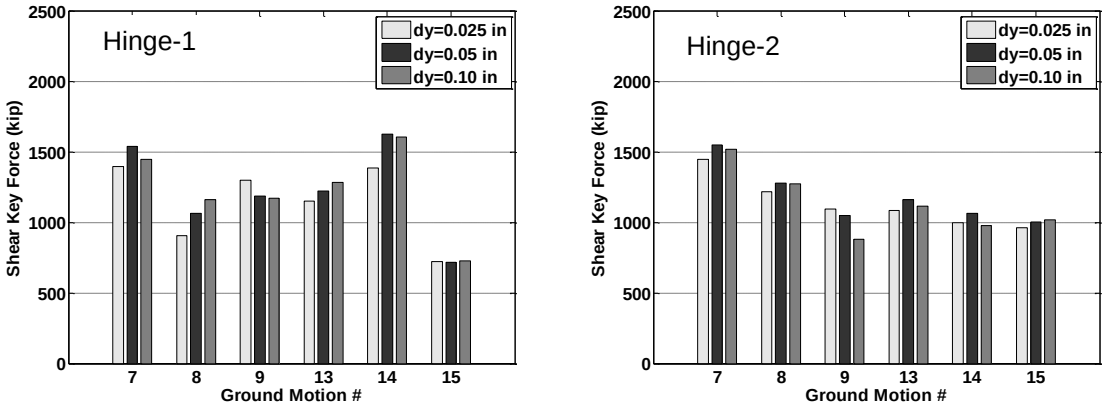

Figure 4.25 Effect of Yield Penetration Parameter ($\bar{\delta}_y$) on the Maximum Shear Key Force

4.9 LINEAR MODEL

4.9.1 Complete Model

A set of linear models are built for the purposes of seismic design, in accordance with the modeling criteria of Sec. 5.2.2, SDC 1.7. The configuration of the linear model is similar to that of the nonlinear model with a few exceptions stated below:

- Columns are modeled by the elastic beam column element with an effective moment of inertia over the entire height of the column.
- Each column is divided into four segments.
- All transverse gaps are closed
- All longitudinal gaps, including abutments, are released.
- End diaphragms were fixed in the transverse direction.

4.9.2 Stand-Alone Model

The frames of the prototype bridges are also modeled individually. These models are used to find the transverse period of vibration and stiffness of the stand-alone frames and are not used for the purposes of design. Each model was extracted from a complete model, and, for the side frames, the abutment was considered as a transverse fixed support.

5 Seismic Design of Prototype Bridges

This chapter presents the seismic design procedure for prototype bridges. The implementation of related SDC provisions to the prototypes' design is described here.

5.1 SDC V1.7 SEISMIC DESIGN PHILOSOPHY

The SDC classifies bridges into two categories for seismic design purposes: standard and non-standard bridges. Some of the standard bridges in SDC Sec.1.1 are listed as bridges with spans smaller than 300 ft., bridges with regular geometry, and bridges with a fundamental period larger than 0.7 sec. All other bridges with irregular geometry, unusual framing, and unusual geological conditions are classified as non-standard (MTD-20-1) (Caltrans, 2010).

In addition, SDC categorizes bridges as ordinary and important. An important bridge is defined by the following criteria: 1) it is required to provide post-earthquake life safety, 2) the time taken for the restoration of its functionality after closure would be a major economic impact, and 3) it is formally designated as critical by local emergency plans (Caltrans, 2010). All other bridges are considered "ordinary." Table 5.1 lists the seismic performance criteria for ordinary and important bridges.

Table 5.1 Seismic Performance Criteria, (Caltrans, 2010)

Bridge Category	Seismic Hazard Evaluation Level	Post Earthquake Damage Level	Post Earthquake Service Level
Important	Functional	*Minimal*	*Immediate*
	Safety	*Repairable*	*Limited*
Ordinary	Safety	*Significant*	*No Collapse*

The scope of SDC V1.7 is limited to ordinary standard bridges. It requires that project-specific criteria for ordinary non-standard bridges be defined to address non-standard features. These criteria shall be approved by the Caltrans Office of Structural Design. Standard ordinary prototypes were studied in this research; therefore, the prototypes were designed according to SDC V1.7 provisions.

The seismic design philosophy of the SDC is based on the equivalent displacement method. According to this method, elastic analysis is used to estimate the expected displacement demand on the bridge due to design seismic hazards (Figure 5.1). Later, the displacement demand is compared to the displacement capacity of the structure. The bridge design is satisfactory if the displacement capacity exceeds the displacement demand and several other criteria are met (Chen & Duan, 2014). The design will be a process of trial and error since displacement demand depends on member properties.

Structural members are identified as either ductile or capacity-protected in ordinary bridges. A ductile member can deform inelastically for several cycles without a significant degradation of strength or stiffness under the design earthquake. Columns are the most critical ductile members in ordinary bridges. The capacity-protected members of a bridge are expected to remain essentially elastic.

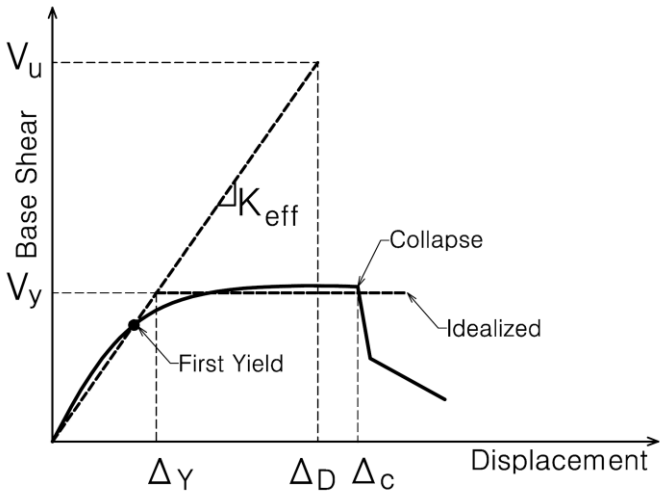

Figure 5.1 Displacement Based Design Method

The SDC defines two types of component performances: local and global. Individual local components or subsystems perform independently from adjacent components, subsystems, or boundary conditions. The term “global” describes the overall behavior of the component, subsystem, or bridge system and includes the effects of adjacent components, subsystems, or boundary conditions (Caltrans, 2013). Further details of the displacement-based method are explained extensively in Sections 5.3 to 5.5.

5.2 ASSUMPTIONS FOR THE DESIGN OF PROTOTYPE BRIDGES

California’s seismic design criteria were used to design the prototype bridges in this study. In this study, the following assumptions are made in the prototype design process:

- The column diameter is the same in each bridge.
- The column reinforcement ratio is the same in each frame. The column reinforcement ratios may be variable in different frames where the column’s height varies due to the shape of valley. Variable reinforcement ratios in different frames allows for the realistic distribution of demand and capacity along the bridge.
- Prototypes are designed only in the transverse direction of the bridge. It is expected that the bridge details will be the same when it is designed either in the transverse direction or in the longitudinal direction.

5.3 DESIGN FLOWCHART

A design flowchart is developed, as shown in Figure 5.2. This flowchart is programed in OpenSees to design each prototype model automatically.

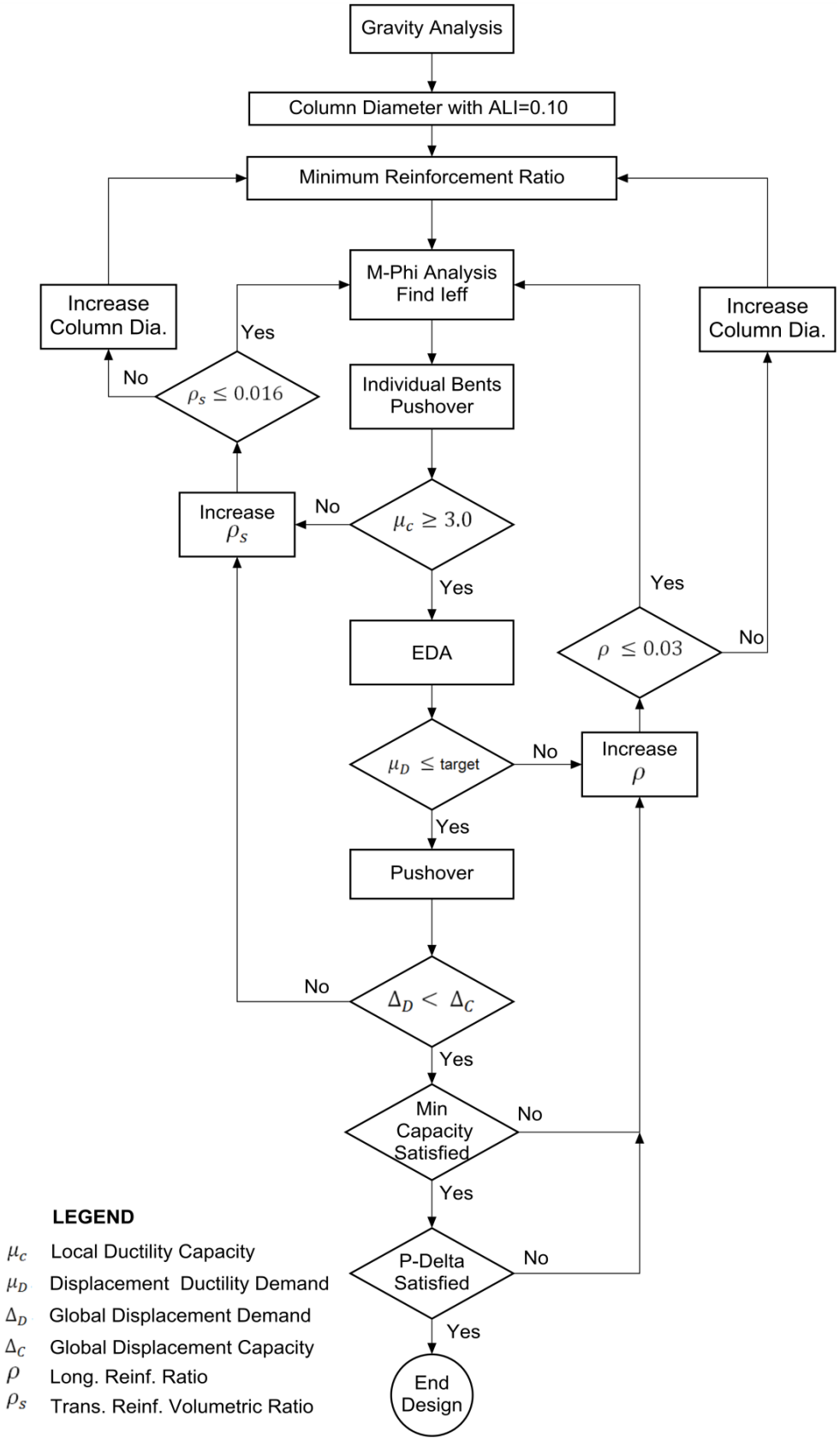

Figure 5.2 Seismic Design Flowchart

5.4 DESIGN DISPLACEMENT DEMAND

Elastic static analysis (ESA) or elastic dynamic analysis (EDA) can be utilized to determine the global displacement demand (Δ_D) of bridges using the effective section properties for columns (Caltrans, 2013). Components attributed to the flexibility of the foundation, bent cap, and ductile members should be considered in the global displacement demand.

5.4.1 Modeling

The linear model explained in Sec. 4.9 was used to determine the prototypes' displacement demand. This model includes detailed frames including effective section properties.

5.4.2 Initial Design Parameters

An initial column diameter and reinforcement ratio was selected to start the analysis and to determine the displacement demand. An Axial Load Index (ALI) of 0.1 was assumed to calculate the initial column section diameter (Eq. 5.1).

$$ALI = {P_{dead}}/{A_g \times f'_c} \qquad \text{Eq. 5.1}$$

The longitudinal reinforcement ratio (ρ) (Eq. 5.2) and the transverse reinforcement volumetric ratio (ρ_s) (Eq. 5-3) were 1% in the initial design:

$$\rho = {A_s}/{A_g}; \qquad 0.01 \leq \rho \leq 0.03 \qquad \text{Eq. 5.2}$$

$$\rho_s = {4\,A_b}/{D'S}; \quad 0.01 \leq \rho_s \leq 0.016 \qquad \text{Eq. 5.3}$$

where A_s and A_g are the longitudinal steel area and the column gross section area, respectively. A_b is the transverse reinforcement area of an individual hoop or spiral. *D'* and *S* are the outer diameter of the hoop or spiral and spacing of transverse reinforcement, respectively. An increment of 0.002 was considered for ρ and ρ_s up to the maximum amounts indicated in Eq. 5-2 and 5-3.

5.4.3 Effective Section Properties

Eq. 5.4 is used to determine the column effective moment of inertia SDC Sec. 5.6.1 (Caltrans, 2013). A moment curvature analysis of the fiber section is conducted to determine the yielding moment and the yielding curvature. The average axial load of the columns is applied to the section in the moment curvature analysis:

$$I_{eff} = {M_y}/{E_c \times \varphi_y} \qquad \text{Eq. 5.4}$$

M_y is the moment capacity of the section at the first yielding of the reinforcing steel, and φ_y is the corresponding first yield curvature (Figure 5.3). E_c is the concrete modulus of elasticity. The ratio of the effective torsional constant of the columns section to the gross sections is 0.2.

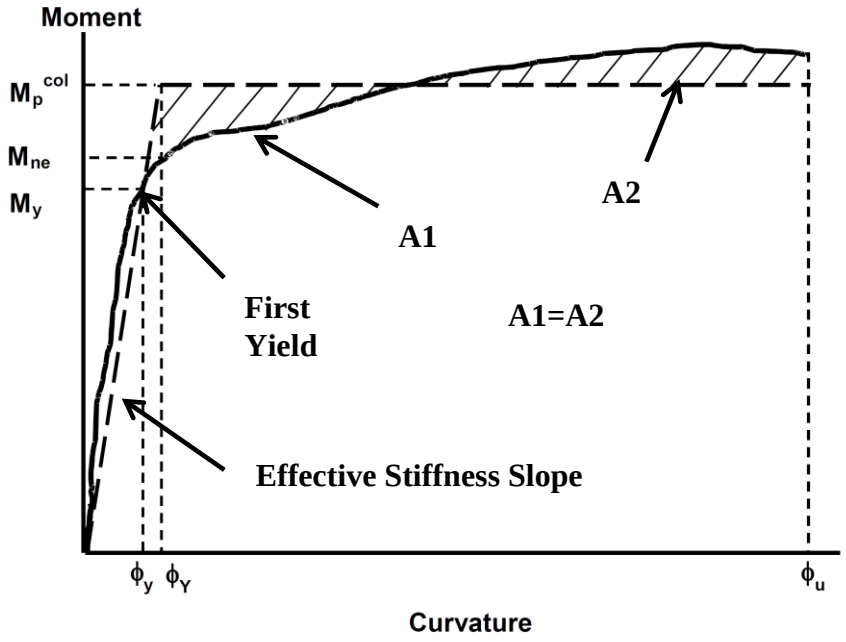

Figure 5.3 Moment Curvature Curve, Effective Stiffness and Idealized Plastic Moment (Caltrans, 2013)

5.4.4 Elastic Dynamic Analysis (EDA)

The EDA method is used to calculate the displacement demands. OpenSees is able to solve eigenvalue problems to find the natural frequencies and mode shapes; however, it does not perform EDA. Thus, a code is developed in OpenSees to perform the matrix operations for spectral analysis. These operations are shown in Eqs. 5.5 to 5.10:

$$M^* = \Phi^T M \Phi \qquad \text{Eq. 5.5}$$

$$L = M \Phi \qquad \text{Eq. 5.6}$$

$$\Gamma = {L}/{M^*} \qquad \text{Eq. 5.7}$$

$$F = \Gamma M \Phi S_a \qquad \text{Eq. 5.8}$$

$$\gamma = \Gamma L \,/\, Total\ Mass \qquad \text{Eq. 5.9}$$

$$\Delta_D = \left[\sum_{i=1}^{N}\sum_{j=1}^{N} C_{ij}\,\Delta_{D,i}\Delta_{D,j}\right]^{1/2} \quad \text{Eq. 5.10}$$

where

Φ = Mode shape matrix.

M = Mass matrix.

*M** = Modal mass matrix.

Γ = Modal participation factor.

F = Equivalent force vector.

S_a= Spectral acceleration obtained from ARS.

Υ= Modal mass participation ratio.

$\Delta_{D,i}$ and $\Delta_{D,j}$ =Global displacement of the i^{th} and j^{th} mode.

C_{ij}= Modal response correlation coefficient between modes *i* and *j*, which is used for CQC method. In the SRSS method, C_{ij}=0 for $i \neq j$ and C_{ij}=1 for $i = j$.

N= Number of total modes.

The CQC method is used in this study. The displacement obtained for each node is considered as the global displacement demand (Δ_D). Dynamic modes mobilizing 97% of the total mass are included in the EDA analysis.

5.4.5 Displacement Ductility Demands

The displacement ductility demand (μ_D) is a measure of the imposed post-elastic deformation on a member, which is indicated by Eq. 5.11.

$$\mu_D = {}^{\Delta_D}/_{\Delta_Y} \quad \text{Eq. 5.11}$$

where Δ_D is the estimated global displacement demand at subsystem (bent) discussed in section 5.4.4. Δ_Y is the idealized yield displacement of the subsystem (bent) that can be calculated using the following two methods:

1) Estimating Δ_Y from the yield curvature of the section using the Priestley method (Eq. 5.12):

$$\Delta_Y = \varphi_Y \times {}^{L_{col}^2}/_{3} \quad \text{Eq. 5.12}$$

where L_{col} is the length of the column.

2) Estimating Δ_Y from the bi-linear force-displacement curve achieved from the pushover analysis of the subsystem (Figure 5.4).

The second method is used to calculate yield displacement in this study. The pushover analysis is performed for individual models of a representative bent within each frame. The modeling assumption of the bent is similar to the global model explained in Sec. 4.5. The individual bent models are subjected to axial dead loads and are pushed in the bridge's transverse direction until they collapse. This analysis does not include the P-Delta effect. The P-Delta effect will be considered as an additional provision for local member capacity later in the analysis. SDC Sec.3.1.3 allows this assumption with the first simplified method (Caltrans, 2013).

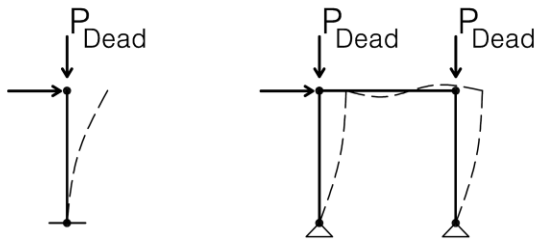

Figure 5.4 Pushover of Individual Bent Models for Single-Column and Two-Column Bents

5.5 DESIGN LIMIT STATES

SDC defines local member capacity and global system capacity in the design procedure. The local member displacement capacity (Δ_c) is the member displacement capacity prior to collapse, considering the member's individual elastic and plastic flexibility regardless of the flexibility of other adjacent members. A global system's displacement capacity (Δ_C) is the reliable capacity of a bridge or subsystem as it approaches a collapse limit state. In global systems, the flexibility of all the members, such as the foundation and the cap beam, shall be included.

5.5.1 Local Member Displacement Ductility Capacity

The local displacement ductility (μ_c) of a member is calculated by Eq. 5.13 for the cantilever columns shown in Figure 5.5. μ_c should be equal or larger than 3.0 (Eq. 5.14):

$$\mu_c = {}^{\Delta_c}/_{\Delta_Y} \qquad \text{Eq. 5.13}$$

$$\mu_c \geq 3.0 \qquad \text{Eq. 5.14}$$

Δ_c is the local displacement capacity before collapse. The collapse limit state occurs when the core of the concrete reaches its ultimate compressive strain or its reinforcement reaches its ultimate tensile strain. Whichever is smaller controls the capacity. The local displacement capacity is independent of the displacement demand and is only related to member specifications. The confinement by transverse reinforcements can effectively increase the displacement capacity of the columns.

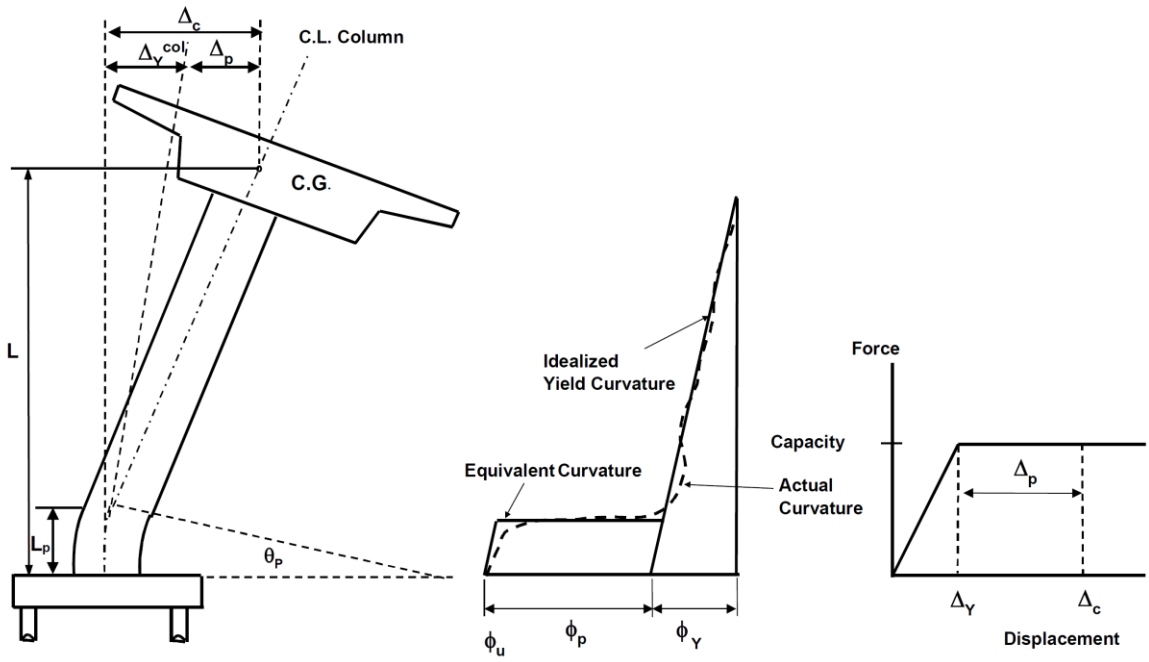

Figure 5.5 Local Displacement Capacity of Cantilever Column (Caltrans, 2013)

A pushover analysis of individual bent models is conducted to calculate and verify the displacement ductility capacity. The yield displacement is estimated from the bi-linearized force-displacement curve. The capacity displacement is determined upon reaching collapse. The transverse reinforcement (ρ_s) is increased to satisfy the minimum displacement ductility capacity. It should be noted that, by increasing the longitudinal reinforcement ratio, there is an adverse effect on the displacement ductility capacity. That is, it increases the yield displacement, Δ_Y, while the capacity displacement (Δ_c) remains the same.

5.5.2 Global Displacement Capacity

Per the SDC, bridges shall satisfy global displacement capacity (Eq. 5.15):

$$\Delta_D < \Delta_C \qquad \text{Eq. 5.15}$$

where Δ_C is the bridge or frame displacement capacity when the first ultimate capacity is reached by any plastic hinge, and Δ_D is the displacement demand along the local principal axes of a ductile member.

To check this criterion, a pushover analysis of bridge model was performed using the nonlinear model explained in Chapter 4. Every single node of the bridge model was pushed to the corresponding displacement demand by the displacement control method. To satisfy Eq. 5.15, transverse reinforcement was increased, if needed, and, if still not satisfied, the column diameter was increased.

5.5.3 Controlling for Target Displacement Ductility

The SDC limits the maximum displacement ductility demand of columns to the target values listed below:

For Single-Column Bents $\mu_D \leq 4.0$

For Multiple-Column Bents $\mu_D \leq 5.0$

where μ_D is defined in Eq. 5.11. To satisfy this criterion, longitudinal reinforcement was increased if needed and, if still not satisfied, the column's diameter was increased.

5.5.4 Checking the Minimum Lateral Capacity

The SDC defines a minimum lateral flexural capacity based on expected material properties by Eq. 5.16:

$$M_P \geq 0.1 \times P_{dl} \times L_c \qquad \text{Eq. 5.16}$$

where

M_P = section's idealized moment capacity (Figure 5.3)

L_c = column length

P_{dl} = tributary dead load applied at the center of gravity of the superstructure.

To satisfy this criterion, longitudinal reinforcement was increased if needed.

5.5.5 Consideration of P-Delta Effects

The SDC defines a criterion to account for the P-Delta effect by controlling Eq. 5.17. This criterion should be checked only if a nonlinear time history analysis is not performed for the design.

$$P_{dl} \times \Delta_r \leq 0.20 \times M_P \qquad \text{Eq. 5.17}$$

where

M_P = section's idealized moment capacity (Figure 5.3)

P_{dl} = tributary dead load applied at the center of gravity of the superstructure

Δ_r= the relative offset between the point of contraflexure and the base of the plastic hinge (Figure 5.6).

For a single-column bent $\Delta_r = \Delta_D - \Delta_s$ and can be approximately equal to Δ_D.

Longitudinal reinforcement is increased to satisfy Eq. 5.17, if needed. This conservative criterion mostly governs the design.

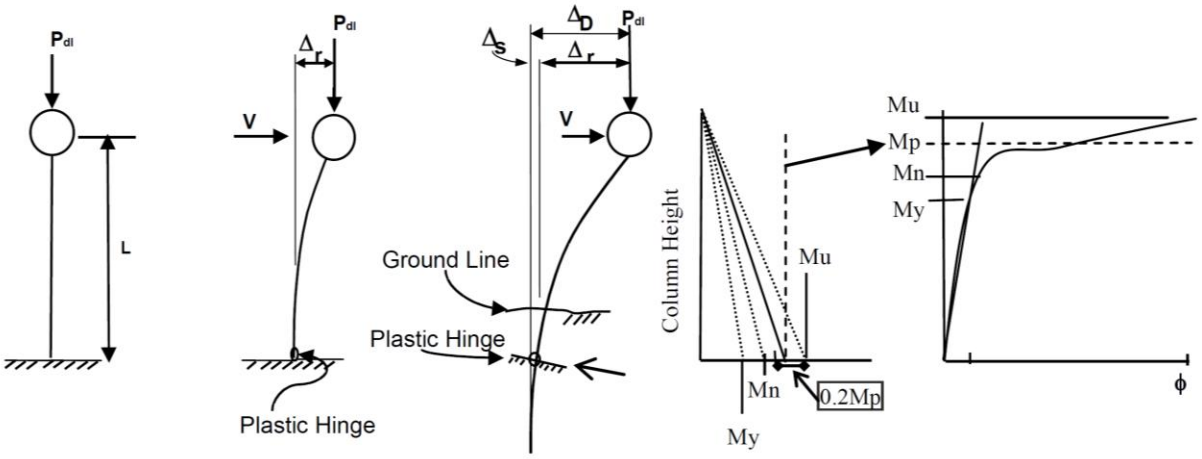

Figure 5.6 P-Delta Effect on Bridge Columns (Caltrans, 2013)

5.5.6 Capacity Protected Components

Non-ductile members/actions, including bent beams, joints, foundations, and the shear in columns, should have a nominal expected capacity larger than the capacity of the connecting ductile members' considering a 20% over strength. This criterion was not controlled for the studied prototype bridges because all components were assumed elastic as explained in Chapter 4.

5.5.7 Design Requirements for Stand-Alone Frames

A stand-alone analysis of frames shall be performed to quantify the strength and ductility capacity of individual frames (SDC reference). This criterion was not checked in the design of this study's prototype bridges, but, in a few analysis cases, it did not govern the design. Meanwhile, frame stand-alone analyses were performed only to find individual periods of frames, as noted in Sec. 4.9.2.

5.6 DESIGN RESULTS

The prototype bridges' design results - including column diameter and reinforcement ratio are presented in Appendix B in the form of bar graphs. Figure 5.7 shows an example from Appendix B, which belongs to single-column, F3-V4 prototype. The first graph shows the design of the prototype bridge for the eleven ARSs. The wide bars show the column diameter on the left axis. The solid bars show the longitudinal reinforcement of the column on the right axis. A transverse reinforcement ratio of 0.01 is sufficient for all the prototypes and is not presented in the results. The second graph in each figure shows the design ductility demand of the frame for the eleven ARSs.

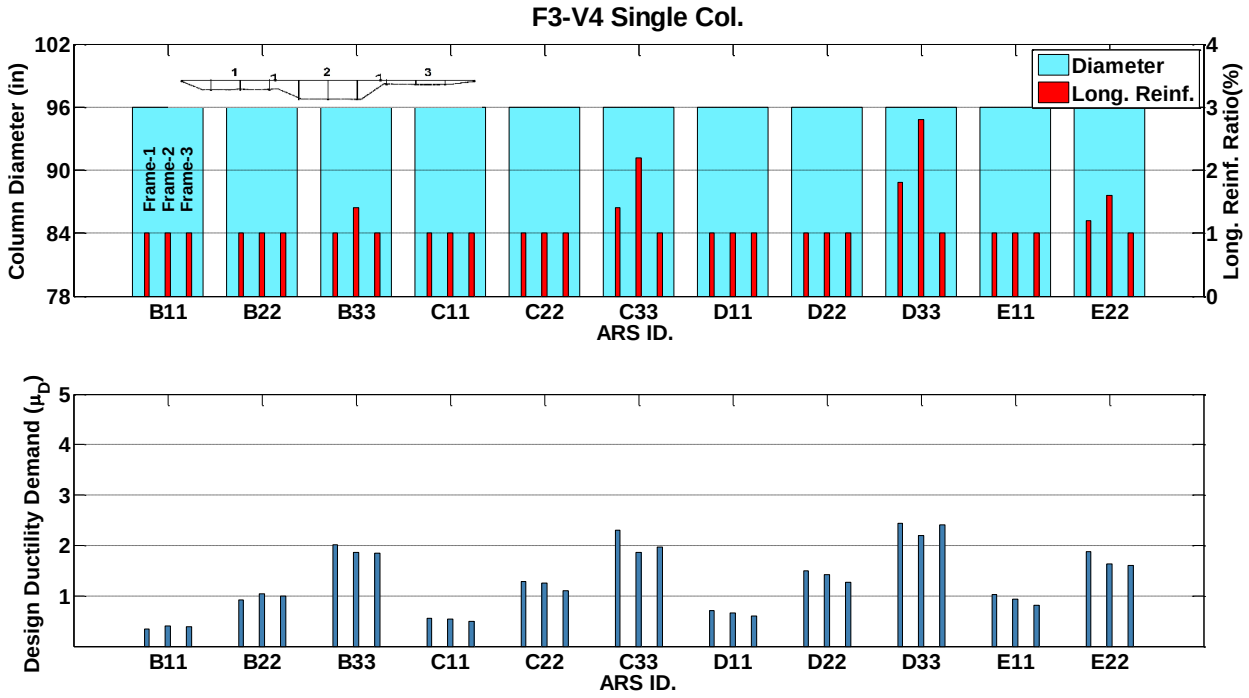

Figure 5.7 Seismic Design Results of Prototype F3-V4, Single-Column

6 Analysis Results and Observations

The results obtained from the analyses of the prototypes introduced in Chapter 3 are presented and discussed in this chapter. The results of the NTH analyses, EDA, and pushover analyses are presented in this chapter. These data are summarized in the form of scatter plots, bar charts, distributions of responses along the length, and hysteresis relationships. The correlations of the in-span hinge shear key force demands with other response parameters are presented and discussed in this chapter. The analysis methods developed to estimate the shear key forces are explained and evaluated. This chapter presents the background information that is the basis for the rational analysis method presented in the next chapter. The effect of parameters such as the yielding of abutment shear keys, gap closure and impact, non-uniform base excitation, and the yielding of the in-span shear keys are also investigated in this chapter. The data set from the NTH analyses are presented in Appendix-C.

6.1 ANALYSIS CATEGORIES

Prototype bridges are analyzed in the seven categories listed in Table 6.1, which reflect the study's objectives. The specific considerations for each category are indicated in this table. The purpose of the analysis category labeled as "Main Analyses" is to find the maximum shear key forces from NTH analyses, when the effects such as impacts due to longitudinal and transverse gap closure under biaxial motions are

excluded. The Reference Shear Key Forces from NTH analysis are the bases for the development of the rational analysis method. In the "Main Analyses", all transverse gaps are set to be closed, the size of the longitudinal gap in the "ZeroLength" elements is defined as 20.0 in to avoid impact, and the bridge is subjected to only transverse motions.

Each prototype is subjected to the thirty-three ground motions introduced in Section 3.3. The total number of analyses for all the categories is 7,656 as indicated in Table 6.1.

Table 6.1 Analysis Categories

	Description	Remarks	Single-Column Models (Analyses)	Two-Column Models (Analyses)
1	**Main Analyses**	Zero Transverse Gap, Only Transverse Ground Motion	26 (858)	26 (858)
2	**Effect of Abutment Shear Key Capacity on In-Span Shear Key Force**	Same as Main Analyses	8 (264) Uniform Valleys	8 (264) Uniform Valleys
3	**Impact Analyses**	1.0-in Transverse Gap, 2.0-in Longitudinal Gap, Biaxial Ground Motion	26 (858)	26 (858)
4	**Ductile In-Span Shear Key Analyses**	Similar to Impact Analyses	26 (858)	26 (858)
5	**Non-Uniform Base Excitation Analyses**	Similar to Main Analyses	26 (858)	26 (858)
6	**Short-Span Prototypes**	Similar to Main Analyses	4 (132) Uniform Valleys	-
7	**Impact Analyses of Short-Span Prototypes**	Similar to Impact Analyses	4 (132) Uniform Valleys	-
	Total Number of Analyses		**232 (7,656)**	

6.2 DATA COLLECTED FROM THE ANALYSES

6.2.1 Nonlinear Time History (NTH) Analyses

The data recorded from the nonlinear time history (NTH) analyses includes: base accelerations and column base reactions in the transverse, longitudinal, and vertical directions; longitudinal and transverse displacements at the top of the columns; transverse accelerations on the top of the columns; longitudinal and transverse displacements on the diaphragm nodes; in-span hinge transverse accelerations; in-span shear key forces and in-span shear key deformations; transverse and longitudinal impact forces; and longitudinal and transverse abutment forces.

6.2.2 Elastic Dynamic Analyses (EDA)

The data collected from the elastic dynamic analyses (EDA) includes: modal periods; three-dimensional mode shapes; spectral accelerations for each mode; modal participation factors; modal mass participation; modal base shears; modal displacements; modal shear key forces; and modal periods of standalone frames.

6.2.3 Pushover Analyses

The data collected from the pushover analyses includes base reactions of the columns; displacements at the top of the columns; force reactions at the hinges; and shear forces in the superstructure elements next to the in-span hinges.

6.3 DATA PROCESSING AND PRESENTATION OF RESULTS

MATLAB R2012a/7.14.0.739 (Mathworks, 2012) is used for the processing of 180GB of data by extracting maximum values from response histories, generating plots, and calculating the statistical values. The general algorithm and MATLAB scripts that are used for summarizing the data are presented in Appendix-D. In addition to MATLAB, Excel 2010 (Microsoft, 2010) is used in places to generate some of the graphs. The mass data presented in the form of bar charts, time history responses, and hysteresis responses are incorporated in Appendix-C for the completeness of the report. Appendix-C includes 446 figures.

6.3.1 Presentation Formats

Processed data is presented in one of the following formats:

Bar Charts: The bar charts are made up of columns. The columns are positioned over a range of values, or definitive parameters. The height of the bars indicates the size of the group. The values for the “median” and “mean” of data are presented on the graph. The “median” is the numerical value separating the higher half of the data from the lower half, while the “mean” is the arithmetical mean, also known as the average. The total number of data points is also indicated on the graph. A theoretical lognormal distribution curve is fitted to bar charts, using Eq. 6.1 (Mathworks, 2012). The theoretical and data driven lognormal cumulative distribution functions (CDF) are plotted next to the bar charts. The CDF plots give the probability of exceeding a given value, such as displacement, force, etc. These graphs are intended to provide an illustrative presentation of the statistical distributions of a specific parameter.

$$f(x|\mu,\sigma) = \frac{1}{x\sigma\sqrt{2\pi}} \exp\left[-(lnx-\mu)^2 \Big/ 2\sigma^2\right]; x > 0 \qquad \text{Eq. 6.1}$$

Scatter Plots: These plots present the degree of correlation between two different data sets in a summarized format. To quantify the correlation, the Pearson product-moment correlation, known as correlation coefficient is calculated and presented on the scatter plots. This factor is obtained using Eq. 6.2 (Montgomery, et al., 2010) and is shown as CC on the scatter plots. This factor is a measure of the strength and direction of the linear relationship between two variables.

$$CC = {cov(X,Y)}/{\sigma_X \sigma_Y} \qquad \text{Eq. 6.2}$$

where *cov(X,Y)* is covariance and σ is the standard deviation. Correlation coefficients of several schematic scatter plots are shown in Figure 6.1.

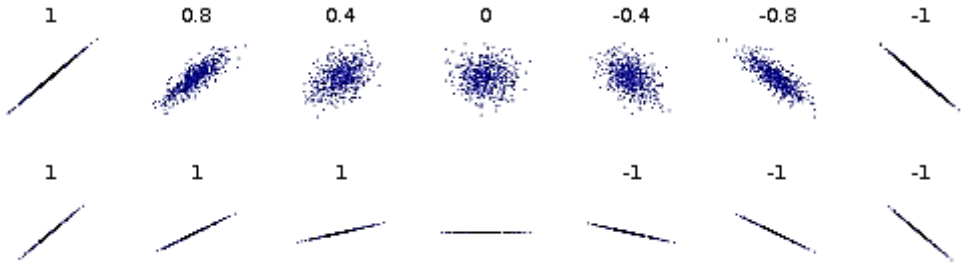

Figure 6.1 Correlation Coefficient for Several Scatter Configurations (Wikipedia, 2014)

The scatter data points are separated for the three hazard levels of moderate, large and severe, which are shown using cyan, red and black, respectively. The corresponding correlation coefficients are also indicated separately on the graphs. In addition, the total number of data points is indicated on the graph.

Hysteresis Plots: These plots present a pictorial representation of the relationship between two response parameters, such as shear key forces and hinge displacements, through the duration of the base excitation. If the two presented parameters are perfectly synchronized, a hysteresis plot simply shows a line in the first and third, or second and third quadrants. Any other form occurs purely because of a time lag between the two responses parameters.

System State Graphs: These graphs show a snapshot of the distribution of a parameter along the length of the bridge. They show the transverse displacements and transverse accelerations of the superstructure at the occurrence of the maximum force. These graphs illustrate what the value of accelerations and displacements are at different locations on the bridge when either one of the shear keys is at its maximum force.

6.4 GLOBAL RESPONSES

6.4.1 Maximum Global Displacements

Figure 6.2 and Figure 6.3 show the correlation between the transverse displacements from the EDA and the maximum transverse displacements from the NTH analyses for long-span and short-span prototypes, respectively. These figures present the transverse displacement of the superstructure at the top of the columns and in-span hinges. For consistency, the exact acceleration spectrums of the ground motions used in the NTH analyses are used for the EDA. Each figure contains four graphs, which are related to the two-, three-, four-, and five-frame prototypes. In general, there is a reasonable correlation between the design and NTH analyses, especially for the ground motions corresponding to moderate and large hazards.

For the ground motions of the severe hazard level, the displacements are overestimated using EDA. This is more pronounced for the four- and five-frame bridges. For a few ground motions, the NTH displacements are larger than that of the EDA, usually in the cases of pulse motions. The scatter in these figures signifies that a certain level of error is inherent in the EDA method, even where the global response of the structure is of a concern.

Figure 6.4 shows the statistical distribution and cumulative distribution function (CDF) for the maximum transverse displacements from the Main Analyses. It should be noted that the maximum transverse displacements typically happen at one of the in-span hinges not the column nodes. Larger transverse displacements are expected in the single-column prototypes. The median displacement in the single-column prototypes is 11.85 in, while, in the two-column prototypes, the same value is 9.18 in. The maximum displacement in both systems is approximately 40 in.

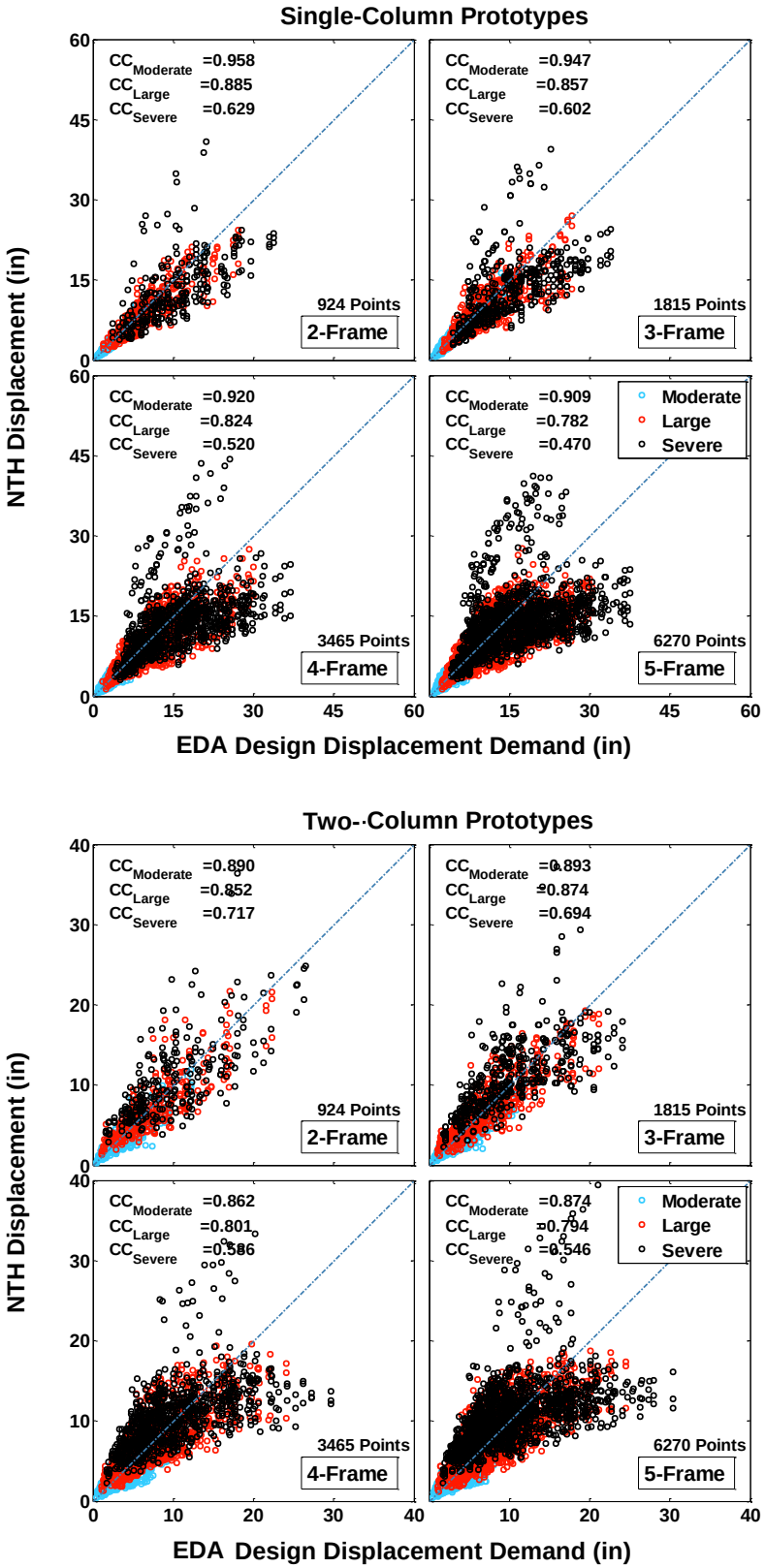

Figure 6.2 Correlation of the Transverse Design Displacement Demands from EDA and NTH Displacements, Long-Span Prototypes

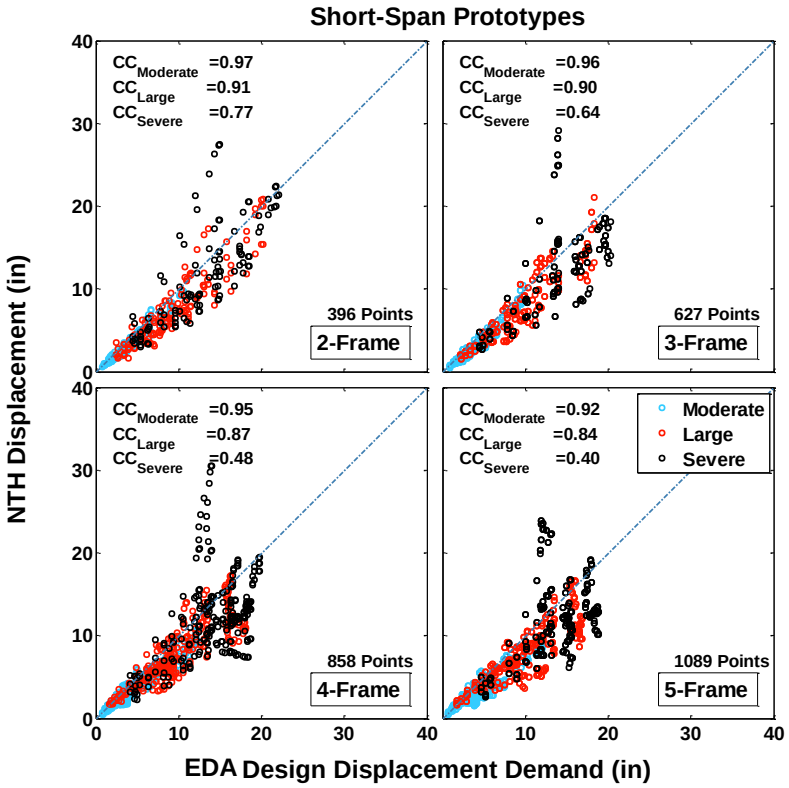

Figure 6.3 Correlation of the Transverse Design Displacement Demands from EDA and NTH Displacements, Short-Span Prototypes

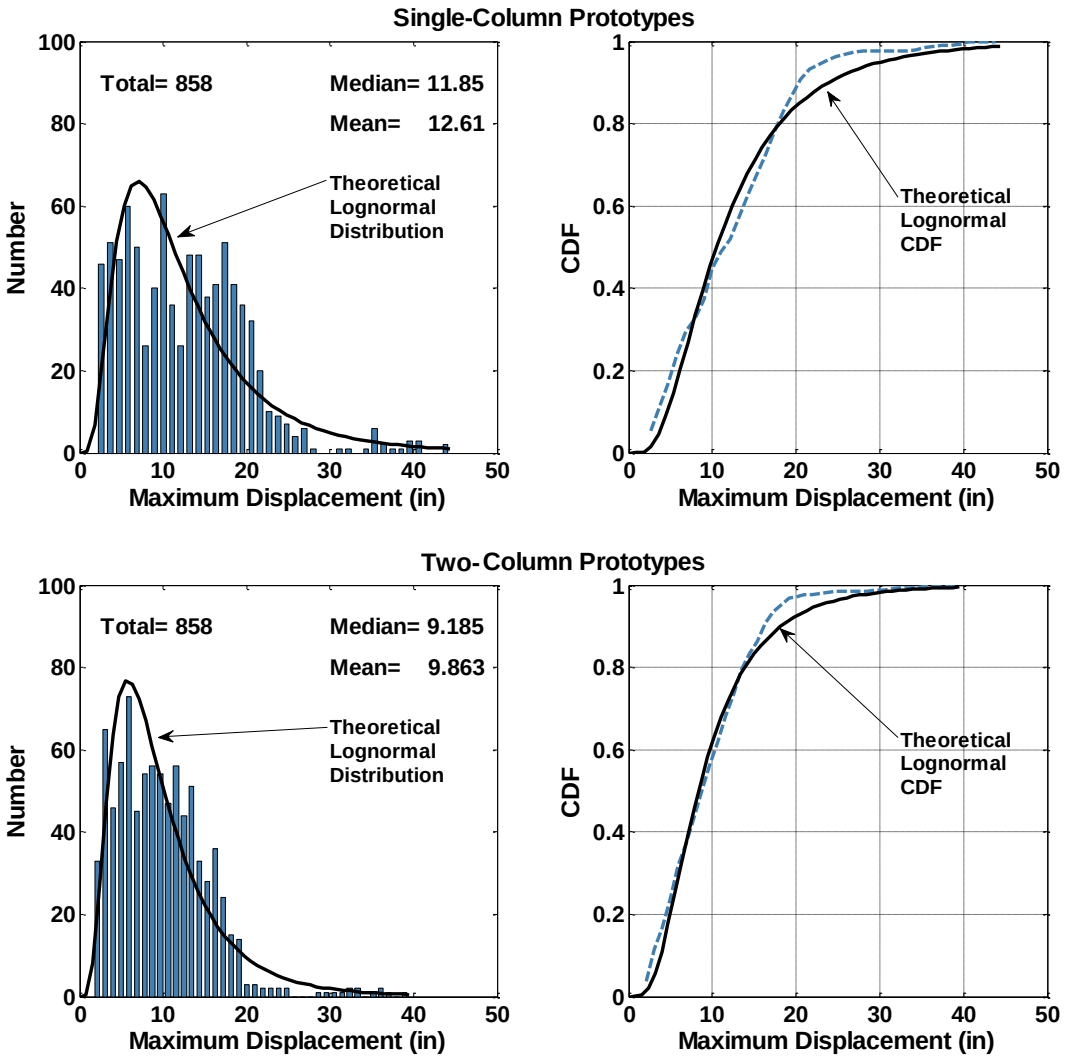

Figure 6.4 Distribution and CDF of the Maximum NTH Transverse Displacements along the Bridge, Long-Span Prototypes

6.4.2 Maximum Ductility Demands

Figure 6.5 presents the correlation between the design ductility ratios for all of the columns and the maximum column ductility values from the NTH analysis. The design ductility demand is not the same as the target design ductility (Sec. 5.4.5 and 5.5.3); it is defined as EDA displacements normalized by the yield displacement. The ductility values from NTH analyses are obtained by dividing the maximum column displacement by the yield displacement defined in Sec 5.4.5. These figures are comparable with the displacement data, but the design ductility values and the NTH ductility values present an improved correlation for the severe hazard. The saturation of the design ductility for the two-column bridges is because the design ductility was limited to the target design ductility in the design process. Although a notable scatter is visible in these figures, the linear correlation confirms the concept of displacement design.

Per SDC 1.7, the values of target design ductility are 4.0 and 5.0 for the single- and two-column bents, respectively. With a few exceptions, the maximum ductility values from the NTH analyses of the single-column prototypes were less than 4.0. In approximately 20% of the NTH analyses of the two-column prototypes, the NTH ductility exceeded the target design ductility of 5.0, while bridges are designed with the expectation that columns' ductility do not exceed the target design ductility.

The statistical distribution and CDF of the maximum NTH ductility ratios for all of the columns are shown in Figure 6.6. Unlike the statistical distribution of the maximum displacements, there is a notable difference between the distributions of the NTH ductility demands for single- and two-column prototypes. This can be attributed to smaller yield displacements in the pinned base columns (two-column bents) in comparison with the extended pile-shafts (the single-column bent). In single-column bents, the flexibility of the extended pile-shaft results in a larger yield displacement, and consequently smaller ductility values.

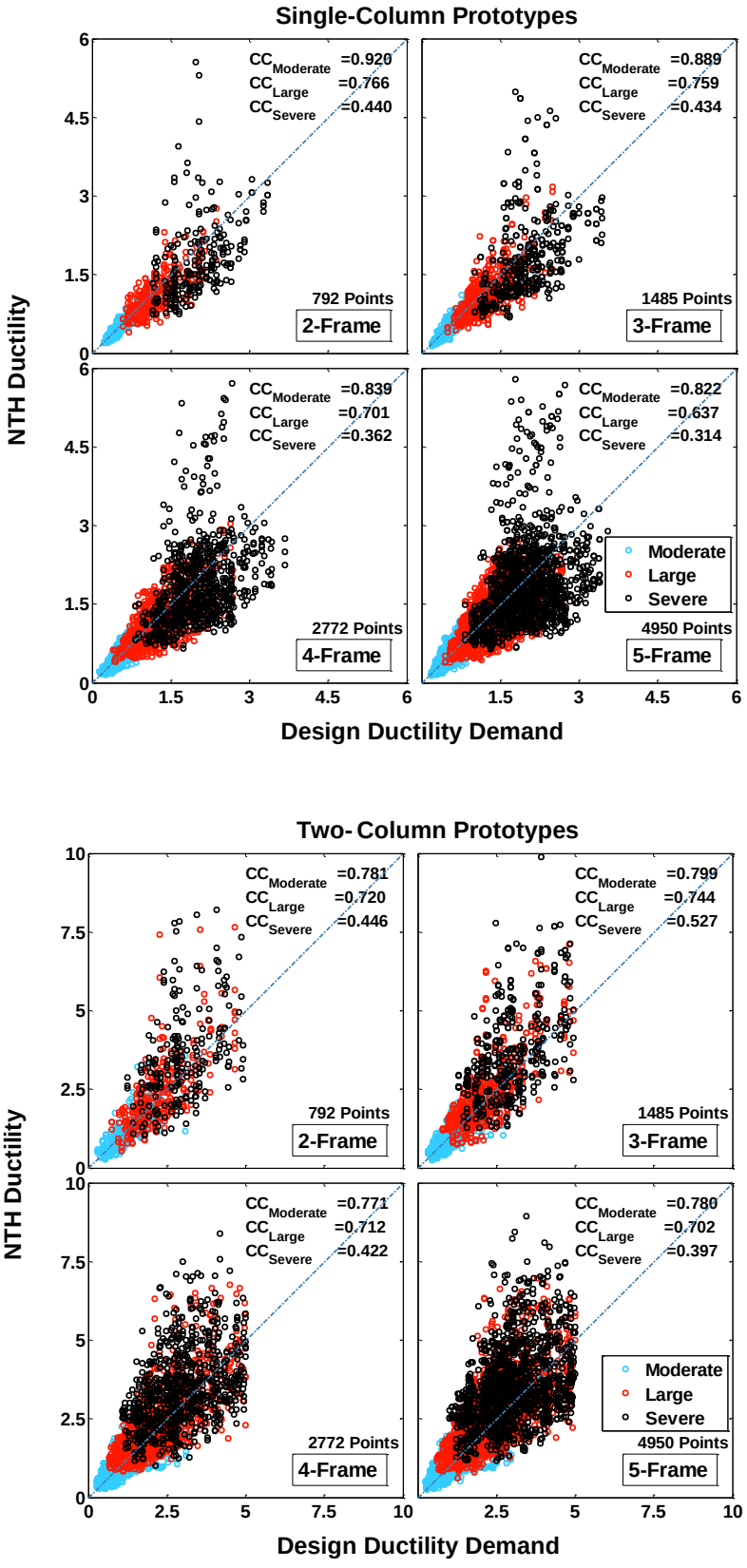

Figure 6.5 Correlation of the Transverse Design Displacement Ductility Demand with NTH Ductility Demand, Long-Span Prototypes

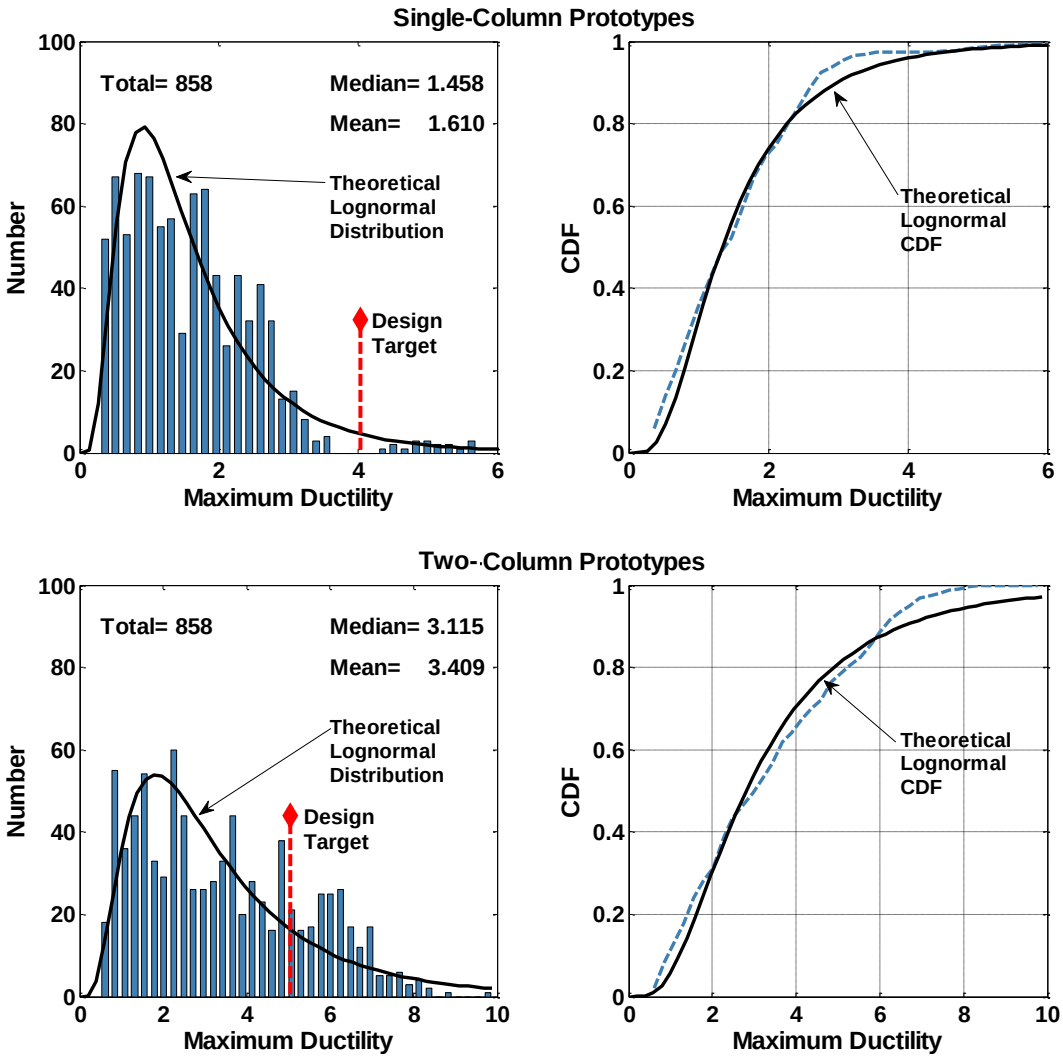

Figure 6.6 Distribution and CDF of the Maximum NTH Displacement Ductility Demand of All Columns, Long-Span Prototypes

6.5 MAXIMUM IN-SPAN SHEAR KEY FORCES

The maximum shear key forces for every in-span hinge shear key for all of the prototype bridges under thirty-three ground motions are shown in the Part 1 of Appendix-C. These graphs show the data from the Main Analyses. They are presented in the form of bar charts where horizontal axis indicating the ground motion numbers, ranging from 1 to 33 (refer to Table 3.3) and vertical axis showing the Reference Shear Key Forces. The name of the prototype and the hinge numbers are indicated in the graph titles. Hinge numbers start from the left end. These charts present the complete picture of the in-span shear key force responses.

6.5.1 Definition of "NTH Shear Key Forces" and "Reference Shear Key Force"

Each ARS group includes three ground motions as indicated in Chapter 3. The maximum shear key force values, from the "Main Analysis" series, for individual ground motions are called the "NTH Shear Key Forces". The value of the geometric mean of the three shear key forces, for each ARS, is named as "Reference Shear Key Force" (Eq. 6.3). This terminology will be used throughout this chapter. The geometric averaging of the values from the three motions is expected to eliminate some of the uncertainties attributed to the non-stationary response characteristics.

$$\text{Reference Shear Key Force} = [F_1 \times F_2 \times F_3]^{1/3} \quad \text{Eq. 6.3}$$

To investigate the variation of the NTH Shear Key Forces within each set of three ground motions two methods are utilized. In the first method, the difference between the maximum and minimum NTH Shear Key Forces within each set of three motions is normalized by the geometric mean of the three values. These values are presented in Figure 6.7. The coefficient of variation (Eq. 6.4), defined as the ratio of the standard deviation to the mean (Montgomery, et al., 2010), is used as the second measure of variation of the forces within each set of three motions. Figure 6.8 shows the values of the coefficient of variation. The relatively small values of these two measures of variation within the set of three motions confirm that NTH Shear Key Forces obtained from the three motions are comparable.

$$CV = {}^{\sigma}/_{\mu} \quad \text{Eq. 6.4}$$

where σ and μ are the standard deviation and the mean, respectively.

Because each set of motions is matched to one of the design ARSs, the geometric mean of the responses from the three motions may be related to the response obtained from EDA when the associated ARS is used. In addition, demands will be proportional to the capacity of the prototype bridge that leads to viable and consistent results.

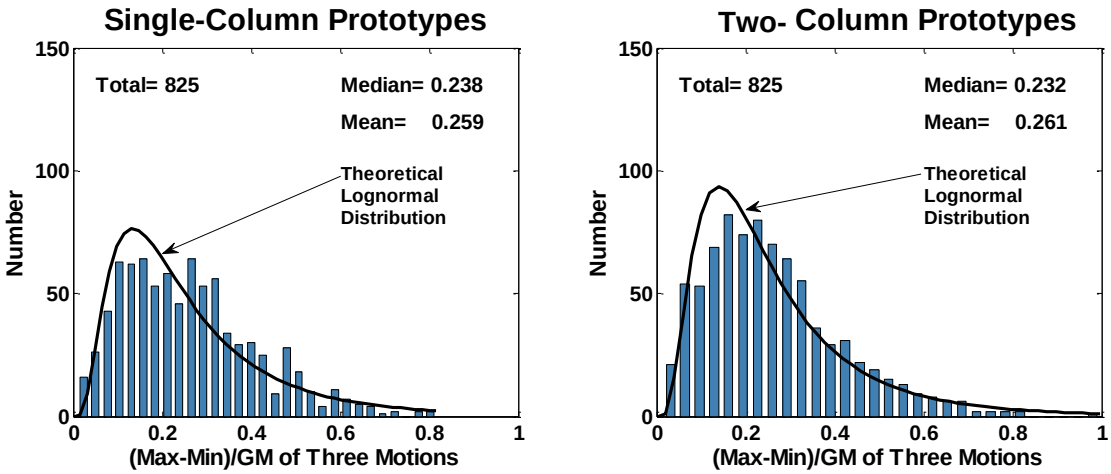

Figure 6.7 Normalized Variation of the NTH Shear Key Forces from Three Motions

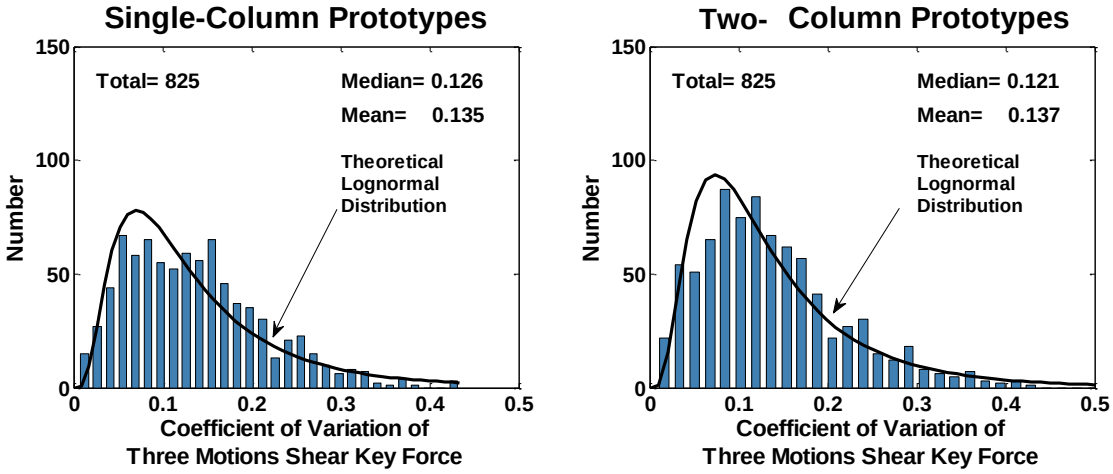

Figure 6.8 Coefficients of Variation (CV) of the NTH Shear Key Forces within the Three Motions of each ARS

6.5.2 Statistical Distribution of "NTH Shear Key Forces"

The statistical distribution and CDF of NTH Shear Key Forces is shown in Figure 6.9. The shear key forces are between 100 kip and 1,000 kip, for single-column prototypes, and 200 kip and 2,000 kip, for the two-column prototypes. The mean and median values for these prototypes are 378 kip and 763 kip; and 358 kip and 723 kip, respectively. This implies that the shear key forces in two-column prototypes were twice that of the single-column ones.

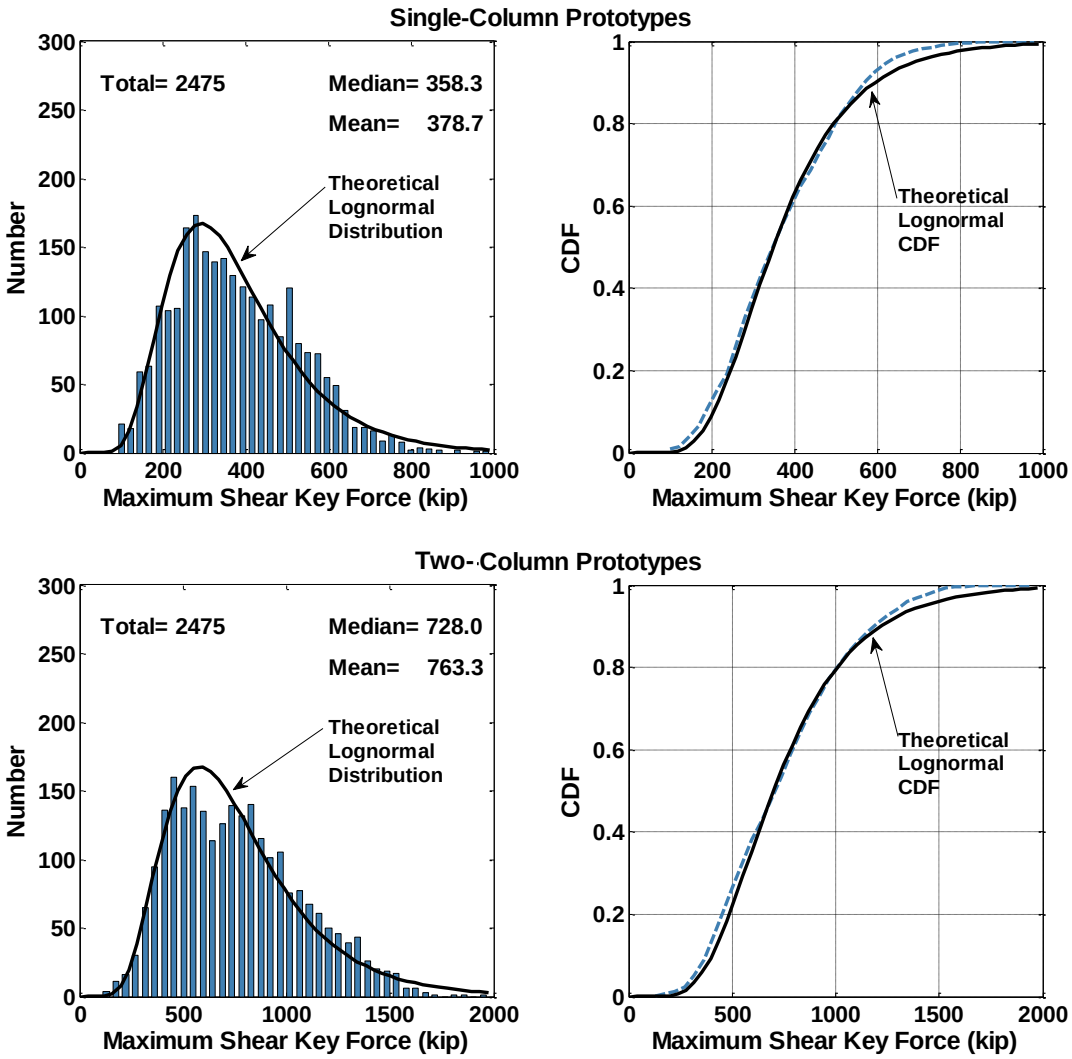

Figure 6.9 Distribution and CDF of "NTH Shear Key Forces" from the Main Analyses

6.5.3 Correlation of the NTH Shear Key Forces with Motion Characteristics

Correlations of the NTH Shear Key Forces with the peak ground acceleration (PGA) and the peak ground velocity (PGV) values of the input motion are presented in Figure 6.10 and Figure 6.11, respectively. In general, the motions with larger PGA and PGV values generate larger shear key forces. The relationship between the NTH Shear Key Force and PGV becomes nonlinear after the PGV of 20 in/sec. Increasing the PGVs after this value does not generate larger shear key forces. This shows that pulse type motions do not necessarily generate larger shear key forces. The Reference Shear Key Force remains relatively proportional to PGA. This confirms the contribution of the higher dynamic modes that are not typically suppressed by the yielding of the structure.

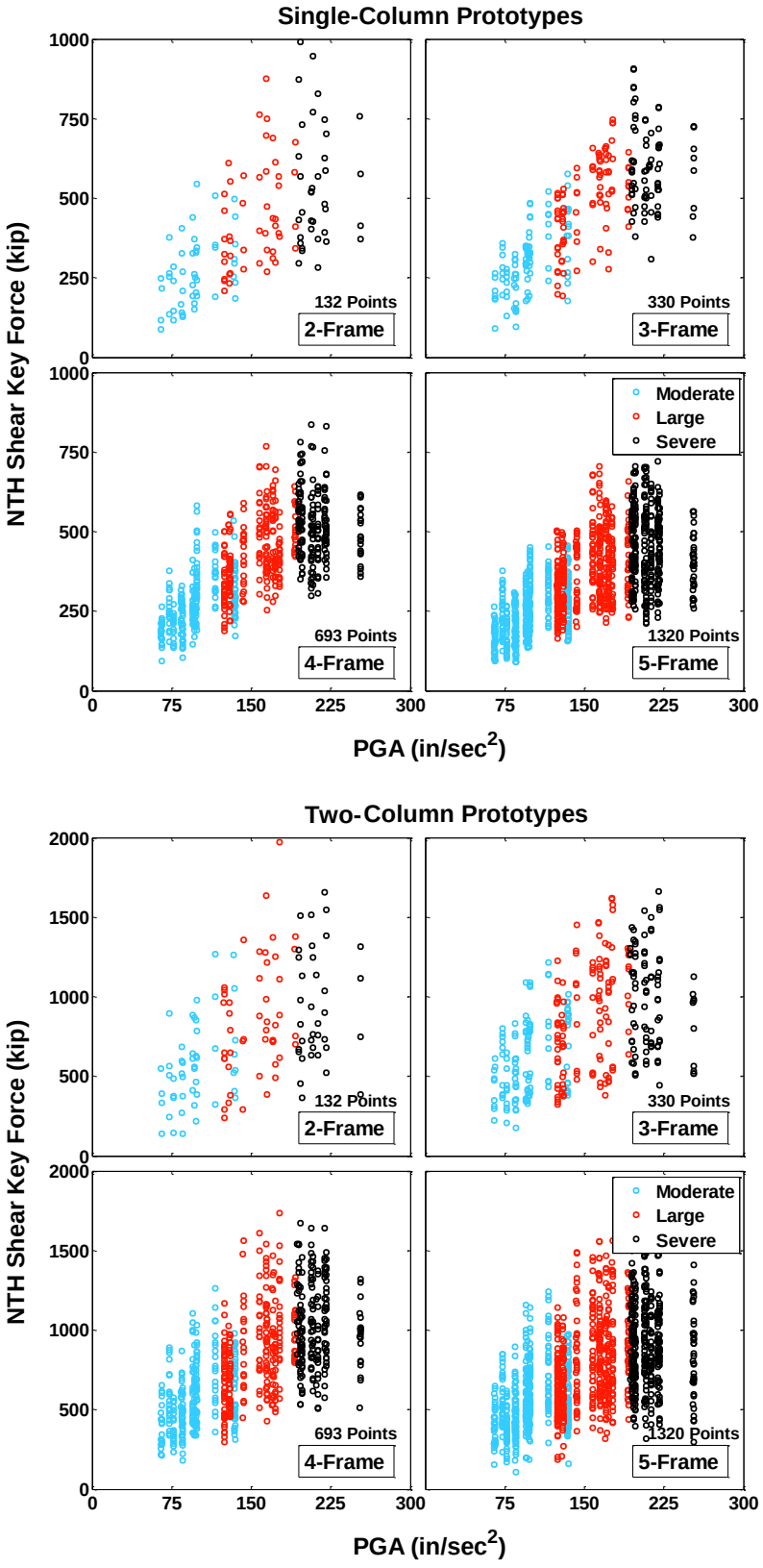

Figure 6.10 Correlation of Peak Ground Acceleration (PGA) with the NTH Shear Key Forces

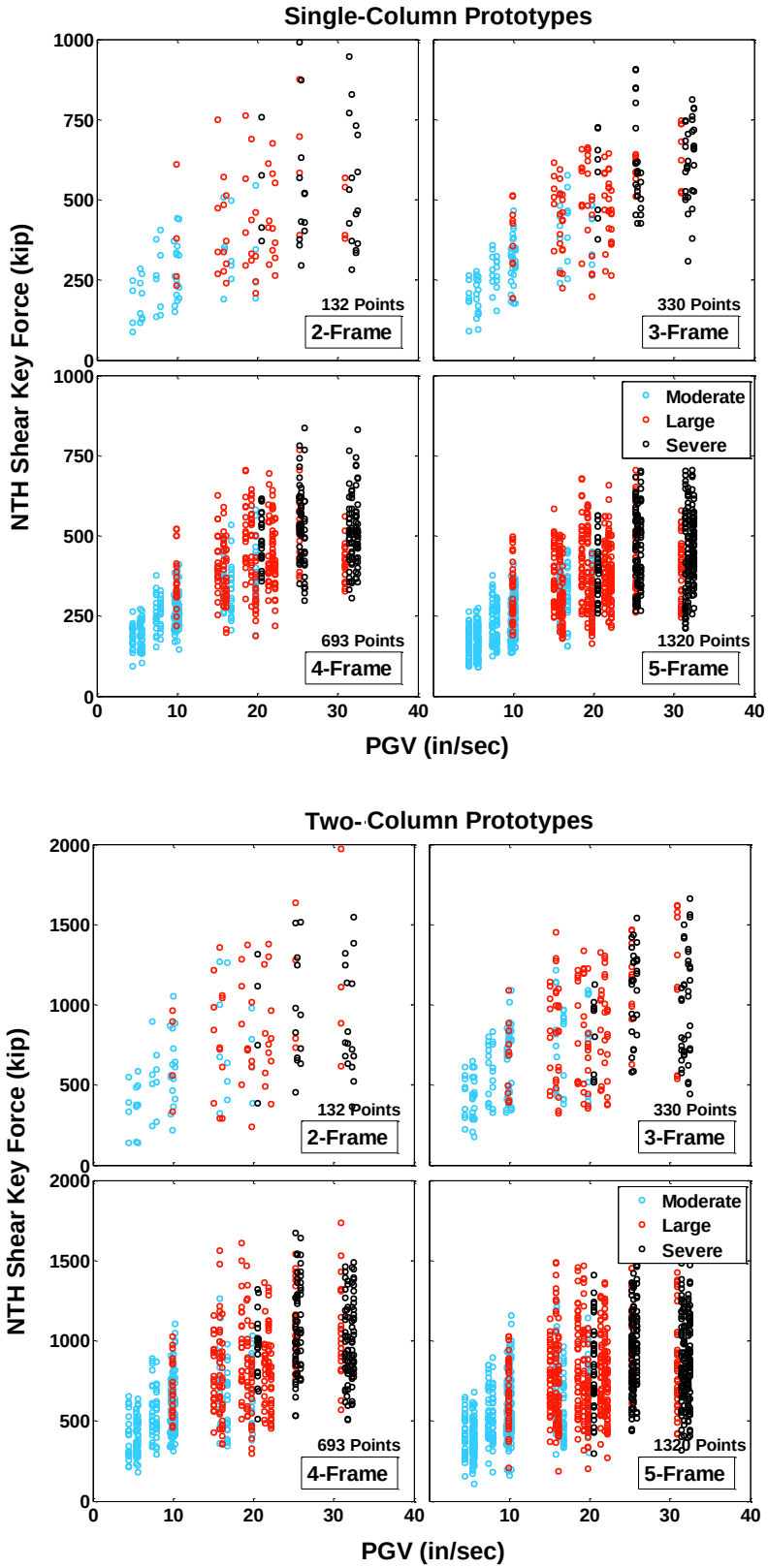

Figure 6.11 Correlation of Peak Ground Velocity (PGV) with the NTH Shear Key Forces

6.5.4 Effect of Valley Shapes on the Reference Shear Key Forces

This section presents the variation of the shear key forces in each prototype for different valley shapes. In Figure 6.12 to Figure 6.15, each bar shows the mean of NTH Shear Key Forces for all the in-span hinges. The standard deviation of the values is also indicated by error-bars. A table is presented below the bar charts, which illustrates the shape of the valleys and the columns' clearance height in each frame. The in-span hinge with the maximum NTH Shear Key Force is indicated by a circle in the tables, except in the case of the two-frame and symmetric prototypes. The presence of two circles on a prototype means that both hinges have almost equal demands. Results for all prototypes show that "balanced" condition is achieved when the stiffness of the left column divided by the distance of the hinge from the left column is comparable with that of the right column. In-span hinges with balanced adjacent frames have smaller forces in comparison to the hinges with unbalanced frames. This implies that the closer the hinge is to the stiffer columns, the larger the shear key force demand. For instance, valley shapes V3 and V2 of the two-frame prototype have significantly different shear key demands because in V2, the hinge is located to the softer column, but in V3 it is closer to stiffer. This is more pronounced in the two-column prototypes, which is probably due to their stiffer superstructure in the transverse direction. From another perspective, the non-uniform valley shapes do not necessarily increase the shear force. In the two-frame prototypes, valley shapes V2 and V4 have less demand compared to valley shape V1. However, for the three-, four- and five-frame prototypes, the uniform valley shape leads to the least shear key forces. Therefore, where possible in design practice, it is suggested that the in-span hinge be placed close to the softer of the adjacent columns.

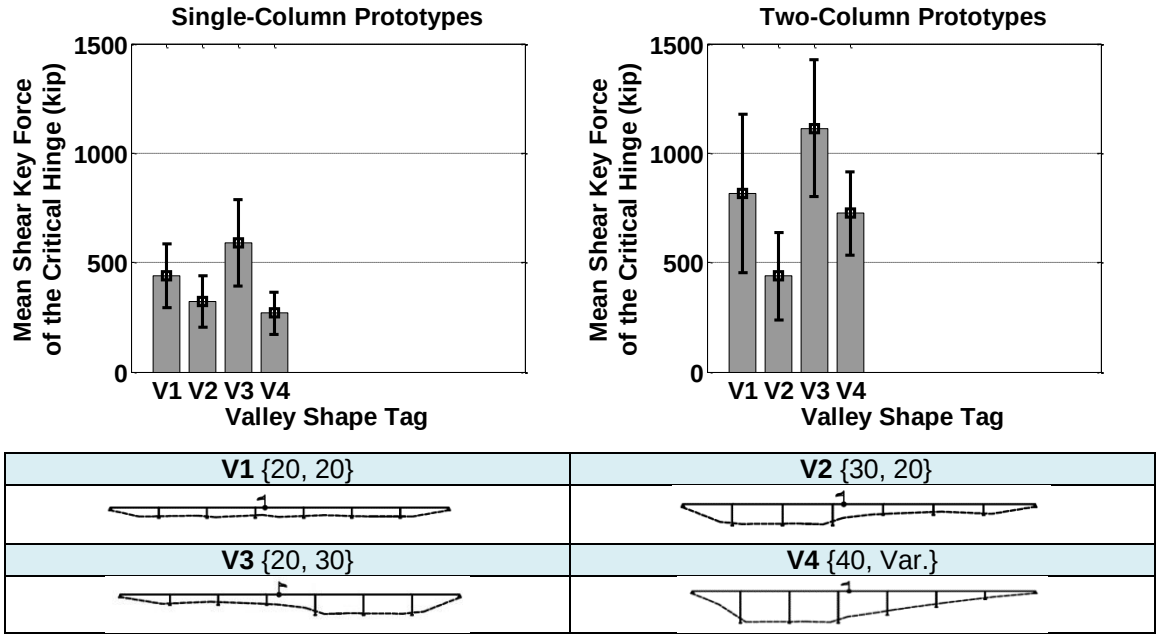

Figure 6.12 Effect of Valley Shape on Shear Key Force, two-Frame Prototypes

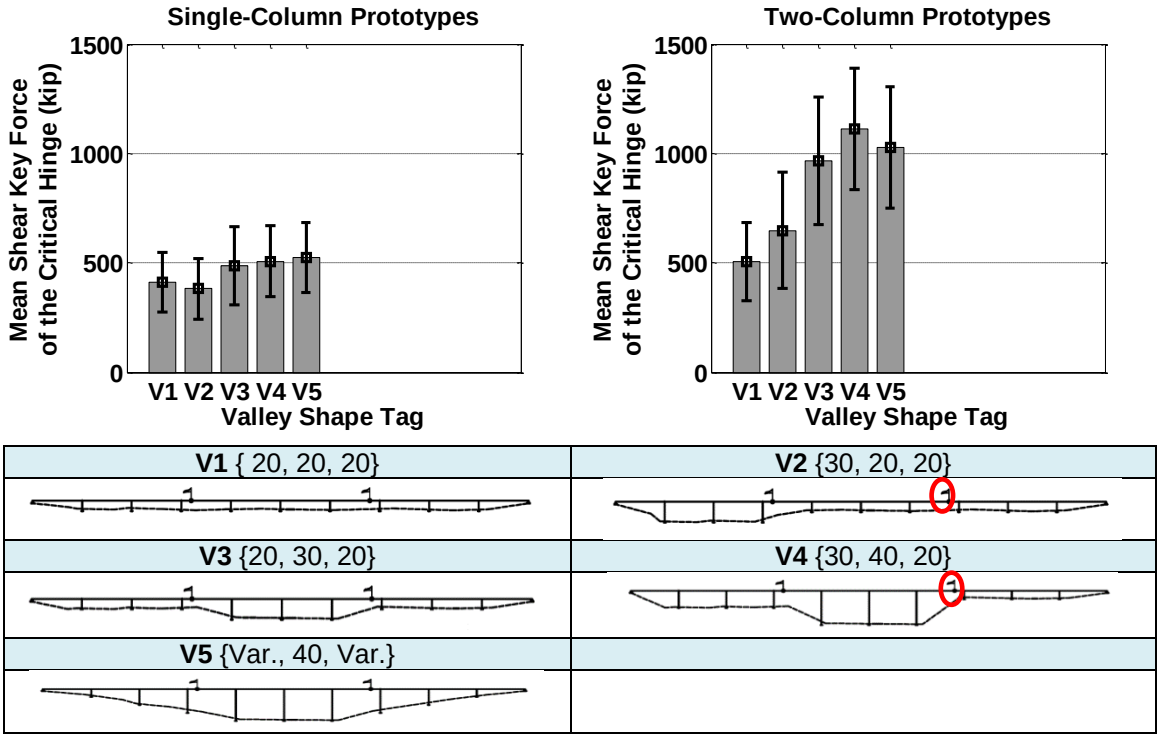

Figure 6.13 Effect of Valley Shape on Shear Key Forces, Three-Frame Prototypes

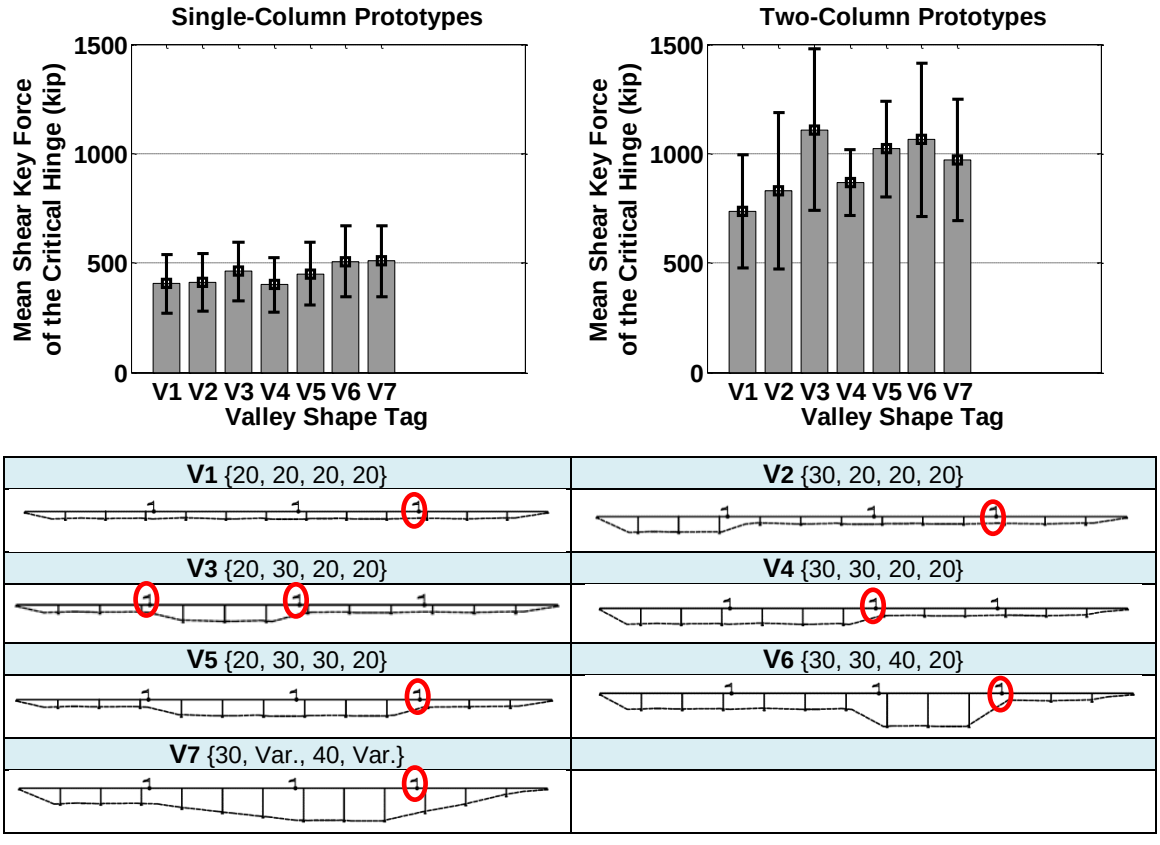

Figure 6.14 Effect of Valley Shape on Shear Key Forces, Four-Frame Prototypes

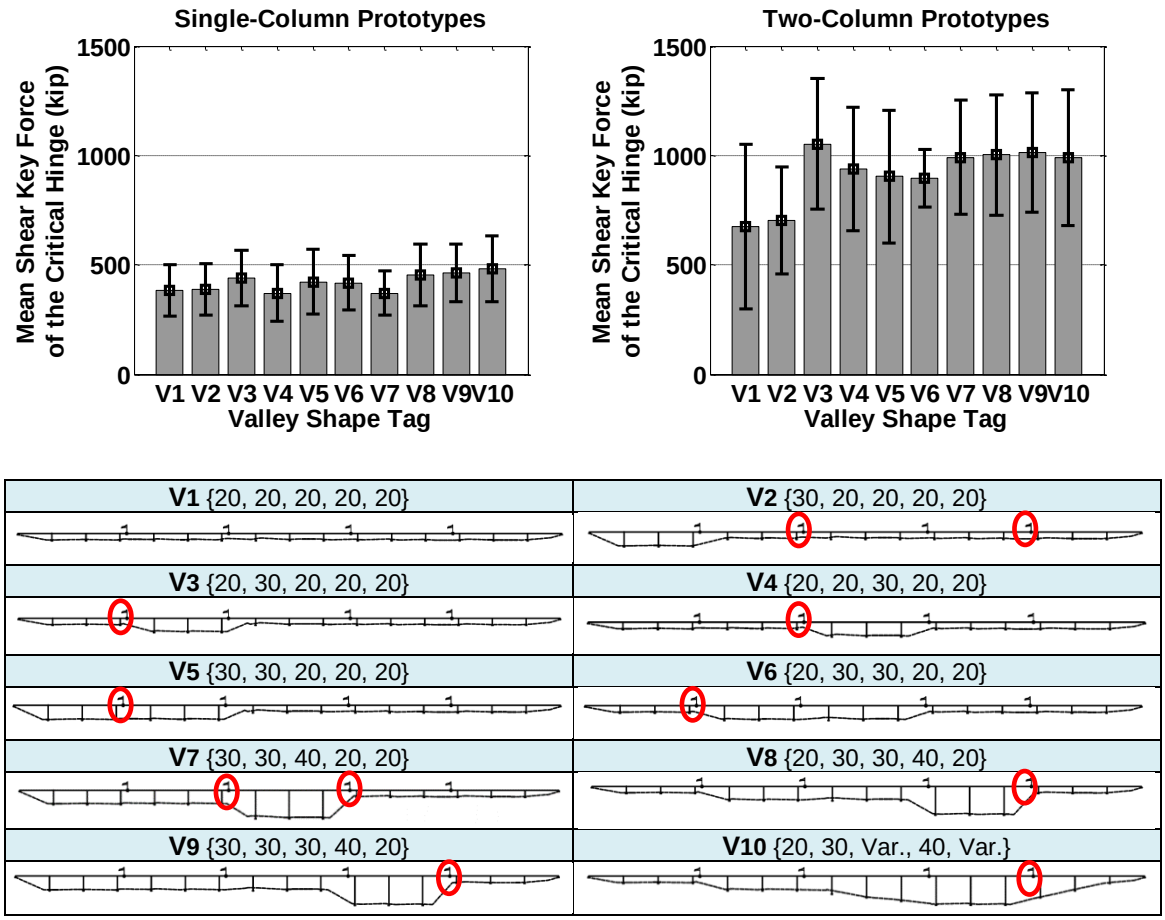

Figure 6.15 Effect of Valley Shape on Shear Key Forces, Five-Frame Prototypes

In the four- and five-frame prototypes, the effect of the non-uniform valley shape on the shear key force is less significant. The reason is that, in long bridges with a large number of frames, there are often one or two hinges close to a stiff column, which governs the force as the critical hinge. For instance, for the five-frame prototype, valley shape V8 has a very different shape when compared to V3. However, the end hinge is critical in both of them, of almost equal forces.

6.5.5 Effect of Adjacent Frame Properties on Shear Key Force

The Sec. 7.1.2 of SDC 1.7 defines the balance condition as Eq. 6.5

$$T_i / T_j \geq 0.7 \qquad \text{Eq. 6.5}$$

where T_i is the natural period of the less flexible stand-alone frame and T_j is that of the more flexible frame. SDC states that there is a greater likelihood for the out-of-phase responses of adjacent frames when the stand-alone periods are significantly different. To examine this criterion with respect to the magnitude of the shear key forces, the correlation of the mean NTH Shear Key Forces for each hinge with the value of *T1/T2* is

shown in Figure 6.16, where *T1* is the fundamental transverse period of the stand-alone frame with a shorter cantilever (closer to the hinge), and *T2* is that of the frame with a longer cantilever (further from the hinge). This definition is slightly different than the SDC's. Thus, Eq. 6.5 is always less than 1.0, while *T1/T2* can be larger than 1.0. The reason for the updated definition is that it was found that the closer bent has more effect on the hinge response.

Although Figure 6.16 shows a poor correlation, it is seen that shear key forces decreases with an increase in *T1/T2*. This means that, the stiffer the closer column, the larger the shear key force.

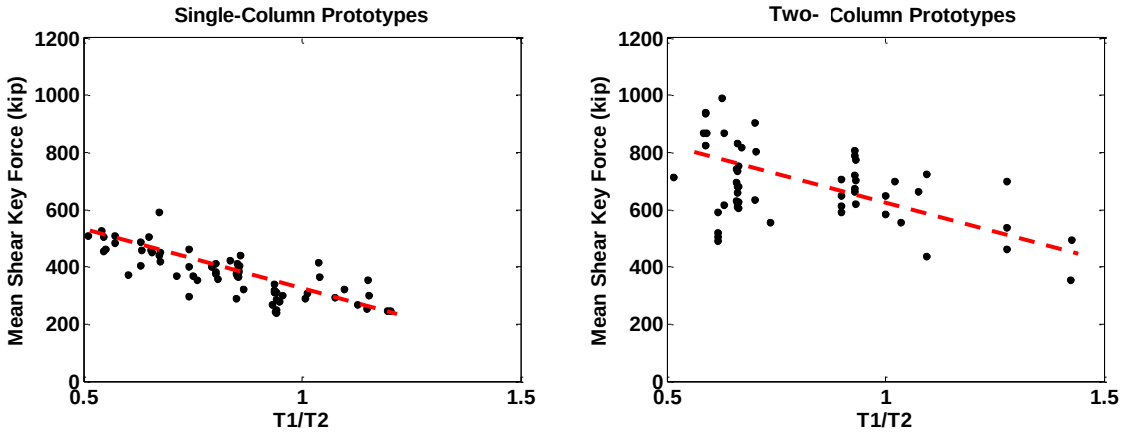

Figure 6.16 Correlation of Stand-Alone Frames Period Ratio (*T1/T2*) with the Mean NTH Shear Key Forces

6.6 RESPONSE OF IN-SPAN HINGES

6.6.1 Shear Key Force, Displacement, and Acceleration Responses

The response histories of the in-span shear key forces, transverse displacements at the in-span hinges, and accelerations at the in-span hinges are normalized to their corresponding maximum values and plotted together in a single graph for each in-span hinge. These plots are presented in Appendix-C Part-2a and Part-2b for the single- and two-column prototype bridges, respectively. Only the large intensity portions of the responses are presented. These multi-graphs allow for tracking the variations of these responses through time. For brevity's sake, these results only include prototypes F2-V1, Hinge 1 of F3-V3, Hinge 2 F4-V4, and Hinge 2 of F5-V5 as samples for different valley shapes, frame numbers, and hinge locations.

6.6.2 Correlations of Shear Key Forces with Displacements and Accelerations

The correlations of the maximum displacements and maximum accelerations with the Reference Shear Key Forces are plotted in Figure 6.17 and Figure 6.18, respectively. A large scatter is visible in these plots. The Reference Shear Key Forces and the maximum accelerations present a better correlation compared to the correlation of the Reference Shear Key Forces and the maximum displacements.

The relationship of the NTH Shear Key Forces with hinge displacements becomes nonlinear as the displacements become larger. However, the shear key force and hinge accelerations remain proportional even under larger ground motions. This is strong evidence that the accelerations that generate large shear key forces are not affected by structural yielding. This suggests that these accelerations are associated with higher modes of vibration that do not contribute to the displacement response.

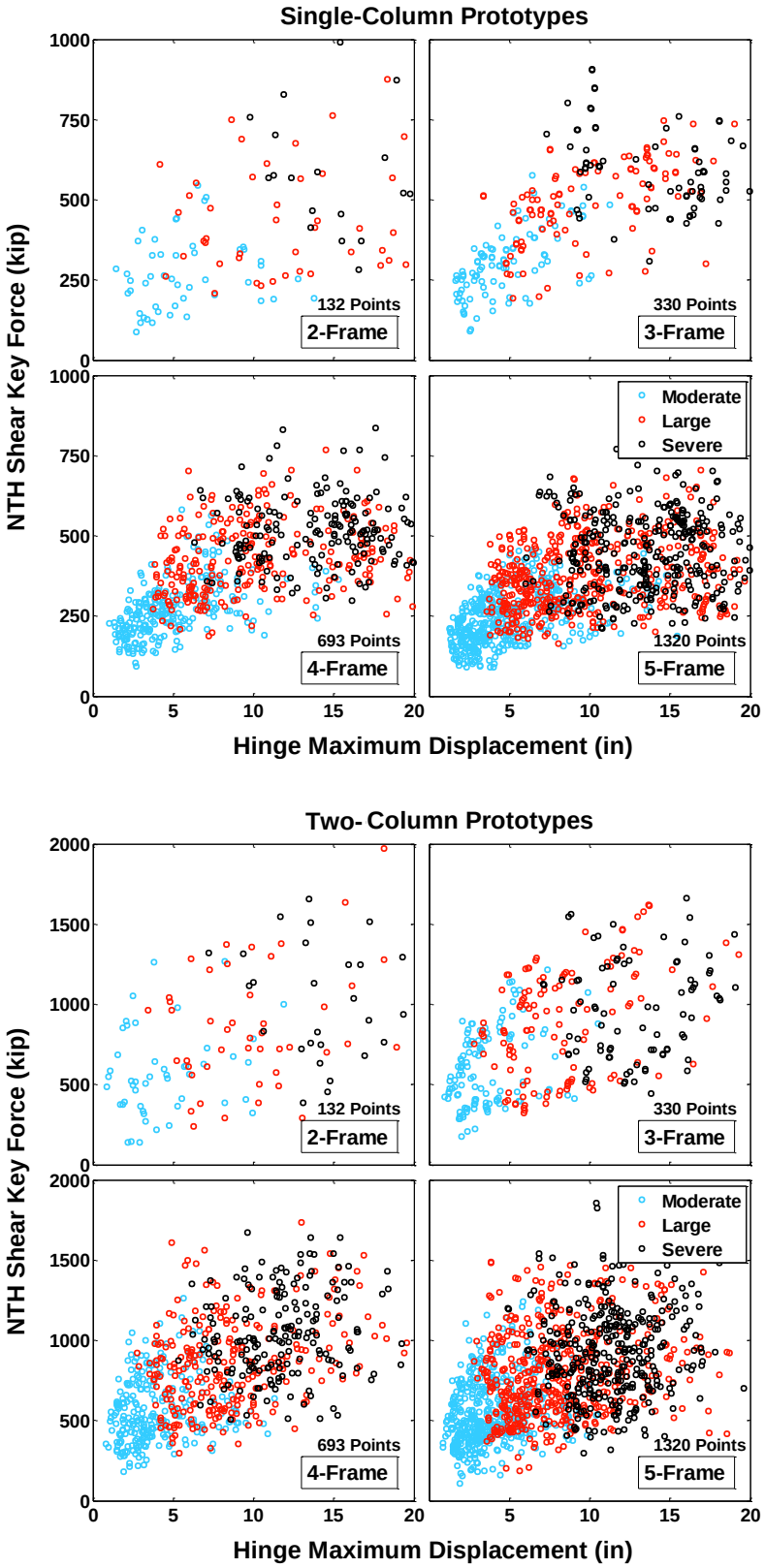

Figure 6.17 Correlation of the Maximum Transverse Displacement at Hinge with NTH Shear Key Force

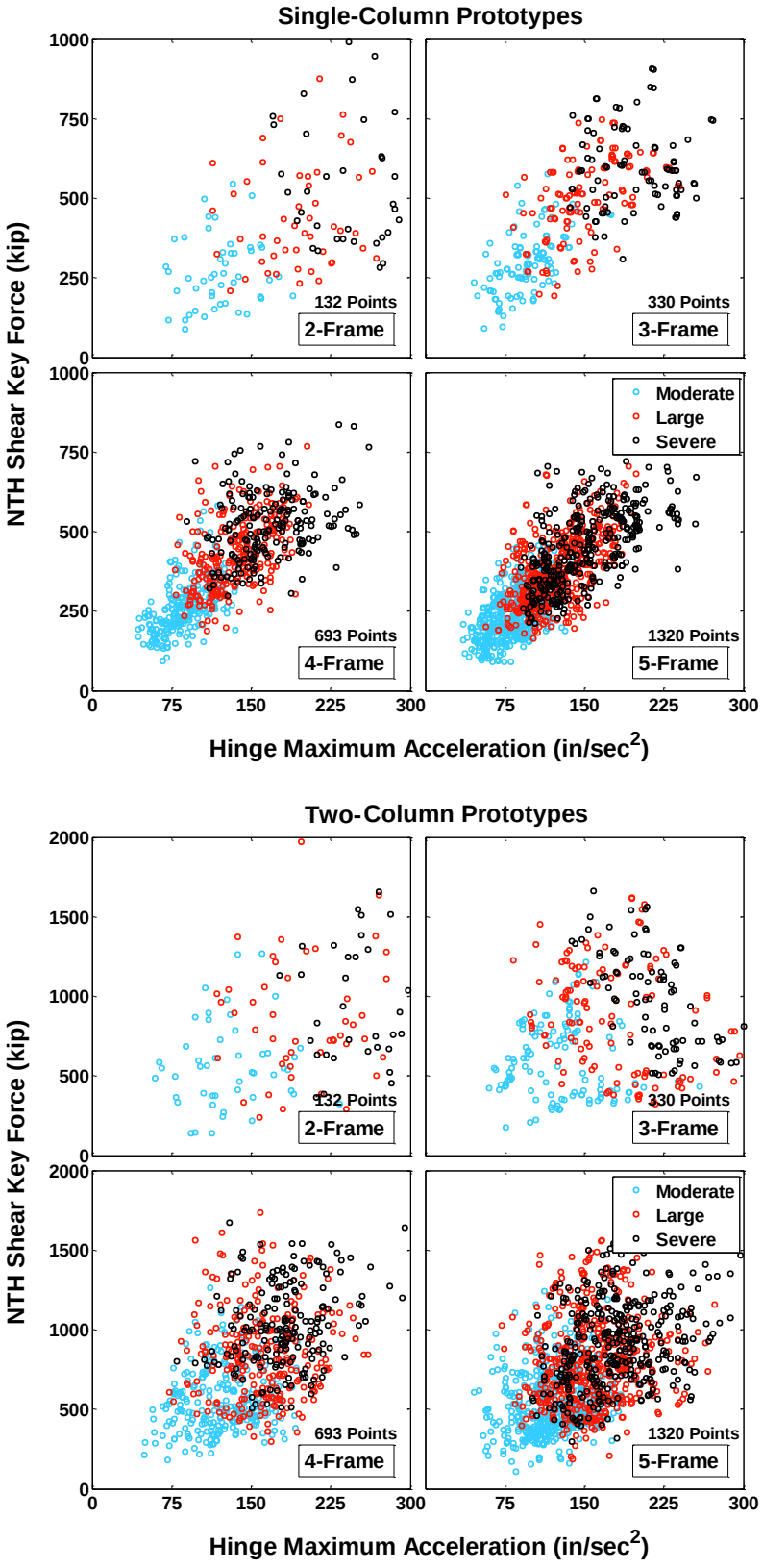

Figure 6.18 Correlation of the Maximum Transverse Acceleration at Hinge with NTH Shear Key Force

6.6.3 Hysteresis Relationship of Reference Shear Key Force with Hinge Displacement and Acceleration

The relationship between the shear key forces and the hinge displacement, as well as the shear key forces and hinge accelerations are presented in Appendix-C, Parts 3a and 3b in the form of hysteresis plots. Each figure includes three force-displacement relationships and three force-acceleration relationships (one relationship for each ground motion). Figure 6.19 is presented as a sample. The maximum forces happen at different hinge displacements or accelerations, while their values remain approximately the same. These figures show that the maximum shear key forces do not necessarily occur when the maximum displacements or accelerations of the hinge happen.

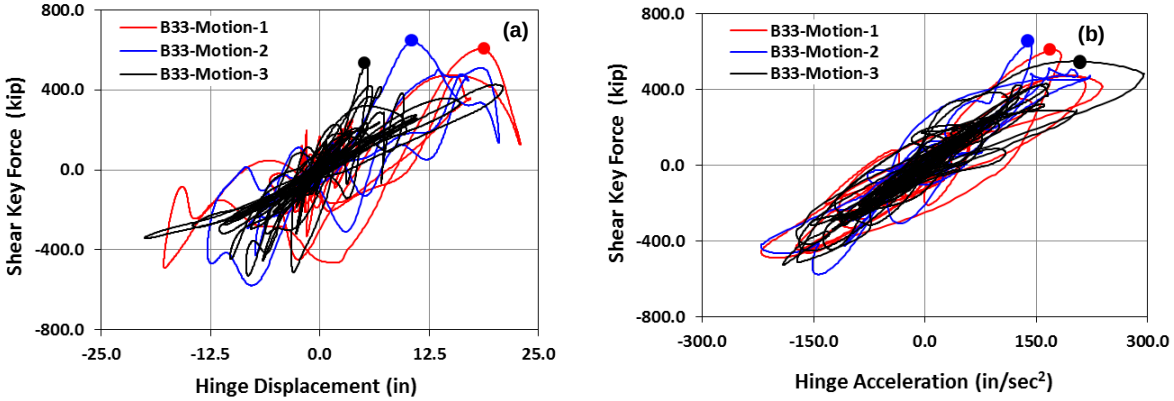

Figure 6.19 Sample Hysteresis Plot for a) Shear Key Force-Hinge Displacement Relationship and b) Shear Key Force-Hinge Acceleration Relationship

6.6.4 Coincidence of Peak Shear Key Forces, Displacements, and Accelerations

The statistical distribution of the ratios of displacement at the maximum shear key force to the maximum value of displacement is shown Figure 6.20 for both the single- and two-column prototype bridges. The same is plotted for accelerations in Figure 6.21. These figures suggest that, for the single-column prototypes, the values of the displacements at the maximum shear key forces tend to be closer to the maximum displacements.

From another perspective, Figure 6.22 illustrates the statistical distribution of the ratios of shear key force at the maximum displacements to the maximum value of shear key forces. Similarly, Figure 6.24 shows the same distribution, but for acceleration. The relatively uniform statistical distributions demonstrate that the maximum shear key force may happen at different hinge displacements or levels of acceleration.

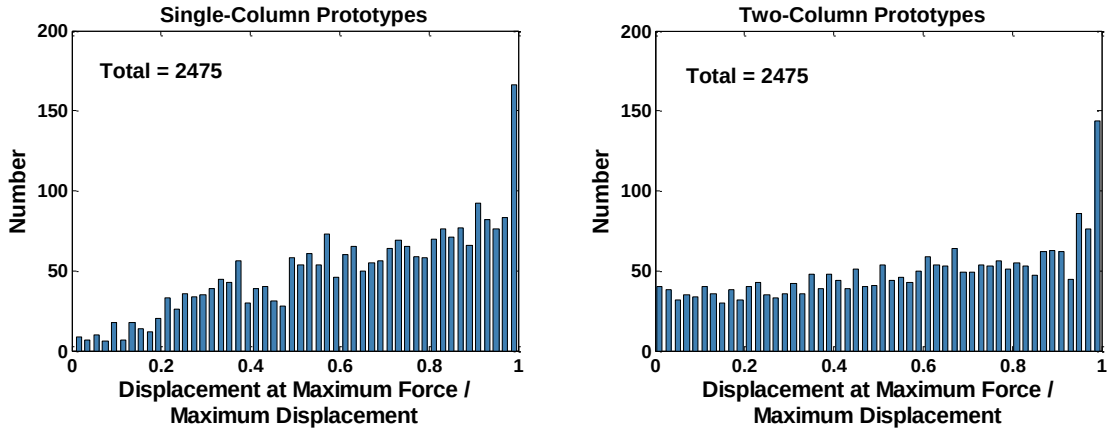

Figure 6.20 Distribution of "the Ratios of Displacement at the Instant of Maximum Shear Key Force to the Maximum Displacements"

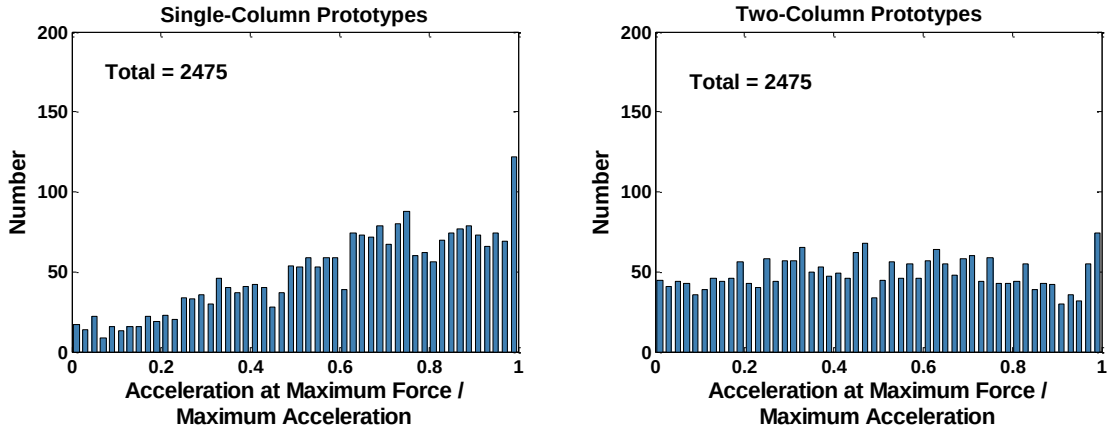

Figure 6.21 Distribution of "the Ratios of Accelerations at the Instant of Maximum Shear Key Force to the Maximum Value of Accelerations"

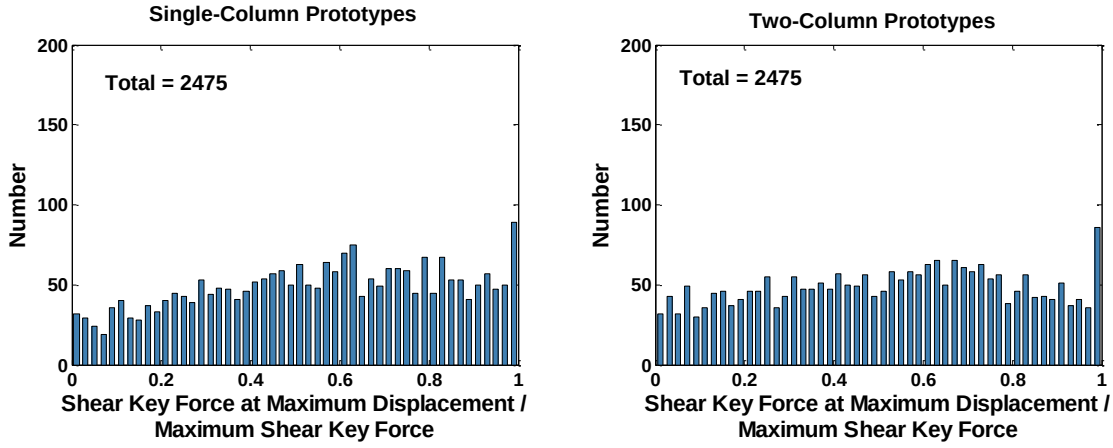

Figure 6.22 Distribution of "the Ratios of the Shear Key Forces at the Instant of the Maximum Displacements to the Reference Shear Key Forces"

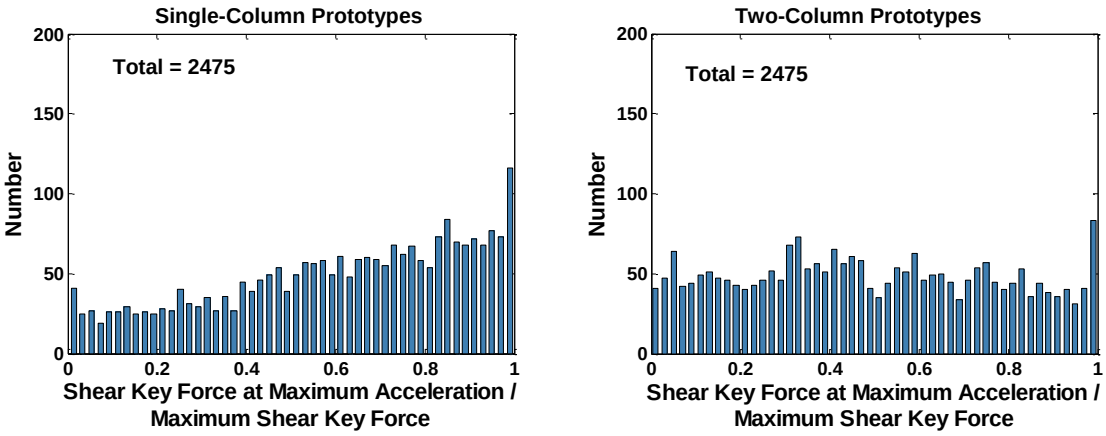

Figure 6.23 Distribution of "the Ratios of the Shear Key Forces at the Instant of the Maximum Acceleration to the Reference Shear Key Forces"

6.7 SYSTEM STATE AT THE PEAK SHEAR KEY FORCE

The state of the systems at the instant of peak shear key force in one of the in-span hinges is presented in Appendix-C Parts 4a and 4b. Two sample figures are shown in Figure 6.24 and Figure 6.25.

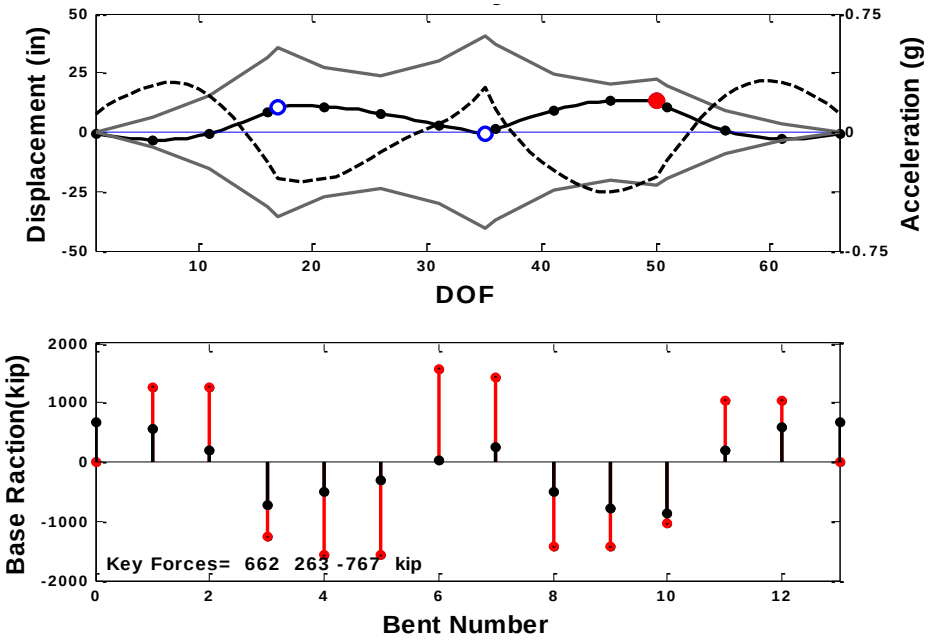

Figure 6.24 System State of Prototype F4-V3, at the Instant of Maximum Force in the 3rd Shear Key, Ground Motion 25, Single-Column

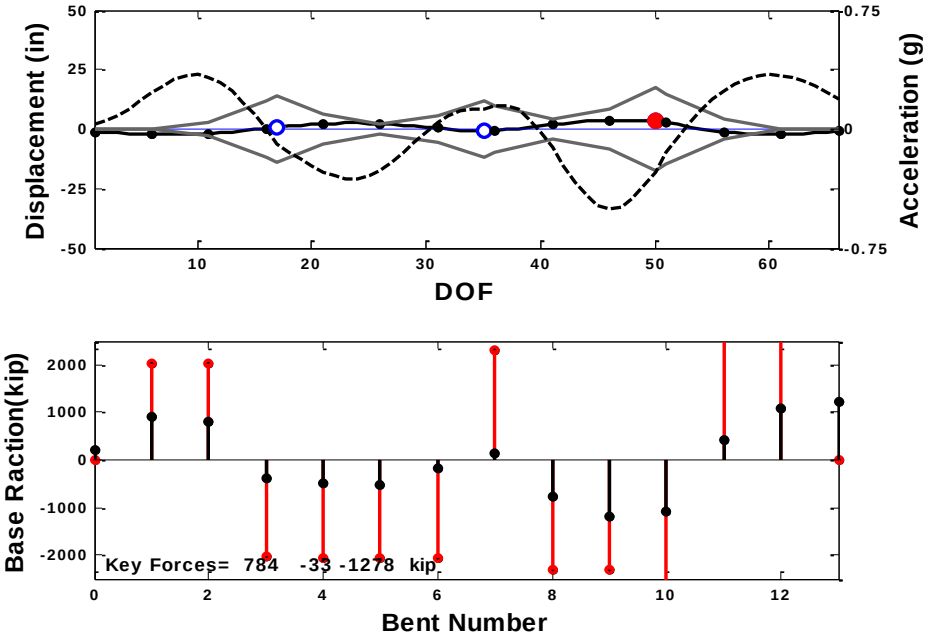

Figure 6.25 System State of Prototype F4-V3, at the Instant of Maximum Force in the 3rd Shear Key, Ground Motion 25, Two-Column

Each figure includes two graphs. The top graph shows the profiles of the displacements and acceleration, using solid black and dashed lines, respectively. The gray line shows the profile of the design displacements per SDC 1.7. The left and right vertical axes show the scale for displacements and accelerations, respectively. The hinges with the maximum forces are indicated with a red dot, and the other hinges are shown with blue dots. The horizontal axis shows the node numbers. The bottom graphs show the base reactions of the column in the transverse direction with a black stem, and their corresponding over strength shear demand with a red stem.

The shape of the displacement and acceleration profiles, at the instant of the maximum shear key force resembles the response of the bridge in its higher modes. The large flexural deformations in the superstructure suggest that assuming rigid movement of the individual frames in multi-frame bridges is not correct. In addition, the base reactions of the columns at the instant of maximum shear key force are typically smaller than their yield forces.

6.8 POSSIBLE METHODS FOR ESTIMATION OF SHEAR KEY FORCES

A correlational study is performed to determine the relationship between the Reference Shear Key Force, and those calculated from several other analysis methods. The correlational studies enable the identification of methods with a consistent performance for the entire set of prototype models.

The general analysis methods that are investigated in the correlation studies are as follows: 1) the nonlinear static analysis or pushover analysis, 2) the modal analysis or spectral analysis, and 3) the rigid modal analysis. For some of these analysis methods, a few variations are also investigated.

With the insight gained on the strengths and weaknesses of each analysis method, a set of modifications is proposed and the degree of improvement of the modified analysis method is investigated. To this end, the correlations of the shear key forces predicted by the modified analysis method with the Reference Shear Key Forces are evaluated. Two major criteria are considered in the evaluation of the suitability of each method: **reliability** and **accuracy**. Reliability refers to the consistency of the results when the method is utilized for different prototype models and hazard levels. The accuracy refers to the degree of the correlation of the predicted force with Reference Shear Key Forces.

The modified analysis methods that are studied are the following: 1) the pushover method combined with inertial effects, 2) the rigid dynamic method, 3) the combined pushover and rigid dynamic method, 4) the modal analysis method with inelastic spectrum, 5) the modal analysis method modified with displacement ductility, and 6) the modal analysis method with modification of multiple modes. Some of these methods are examined with different assumptions and refinements. The 1st, 2nd, 4th, and 5th methods are well established for the seismic analysis of structures, while the 3rd and 6th methods are developed in this study.

6.8.1 Pushover Methods

Conventional force-based pushover analyses use a uniform load pattern or load patterns obtained from the combination of multiple modes. Refined pushover analysis methods, like adaptive pushover or spectral pushovers, implement a varying load pattern during the analysis or a sophisticated combination of multiple pushovers (Wilson, 2010).

The shear key forces obtained from a force- or displacement-based pushover analysis, where all the nodes along the length of the bridge are pushed, is not realistic because of the equilibrium of the column forces and the push forces. Therefore, in accordance with the concept of capacity design, only the nodes of the in-span hinges are pushed to their corresponding design displacements, as shown in Figure 6.26. The pushover shear key forces are obtained using two methods: 1) the difference of the

absolutes of the difference of the shear forces in the left and right neighboring frame elements, i.e. |*V1*|-|*V2*|; and 2) the quarter of the absolutes of these two values, which is equal to the push force divided by four, i.e. *P/4*= (|*V1*|+|*V2*|)/4.

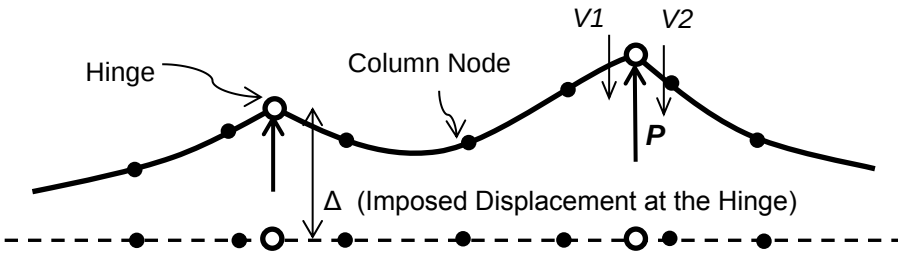

Figure 6.26 Defining Pushover Forces

The correlations of |*V1*|-|*V2*| and the Reference Shear Key Forces are shown in Figure 6.27. Similar scatter plots with the *P/4* are presented in Figure 6.28. It is evident that the method based on |*V1*|-|*V2*| lacks reliability, as it fails in the case of the two-column prototypes. It is because |V1|-|V2| leads to small values when the left and right shear forces are comparable.

The second method, based on *P/4*, is more reliable but is not always accurate. The observation that the Reference Shear Key Forces are comparable with *P/4* is supported by the data shown in Sec. 6.14, which demonstrates that the shear key force is correlated to one-half of the plastic shear demand of its adjacent column. The value of *P* approximates the summation of the plastic shear demands of the two adjacent columns.

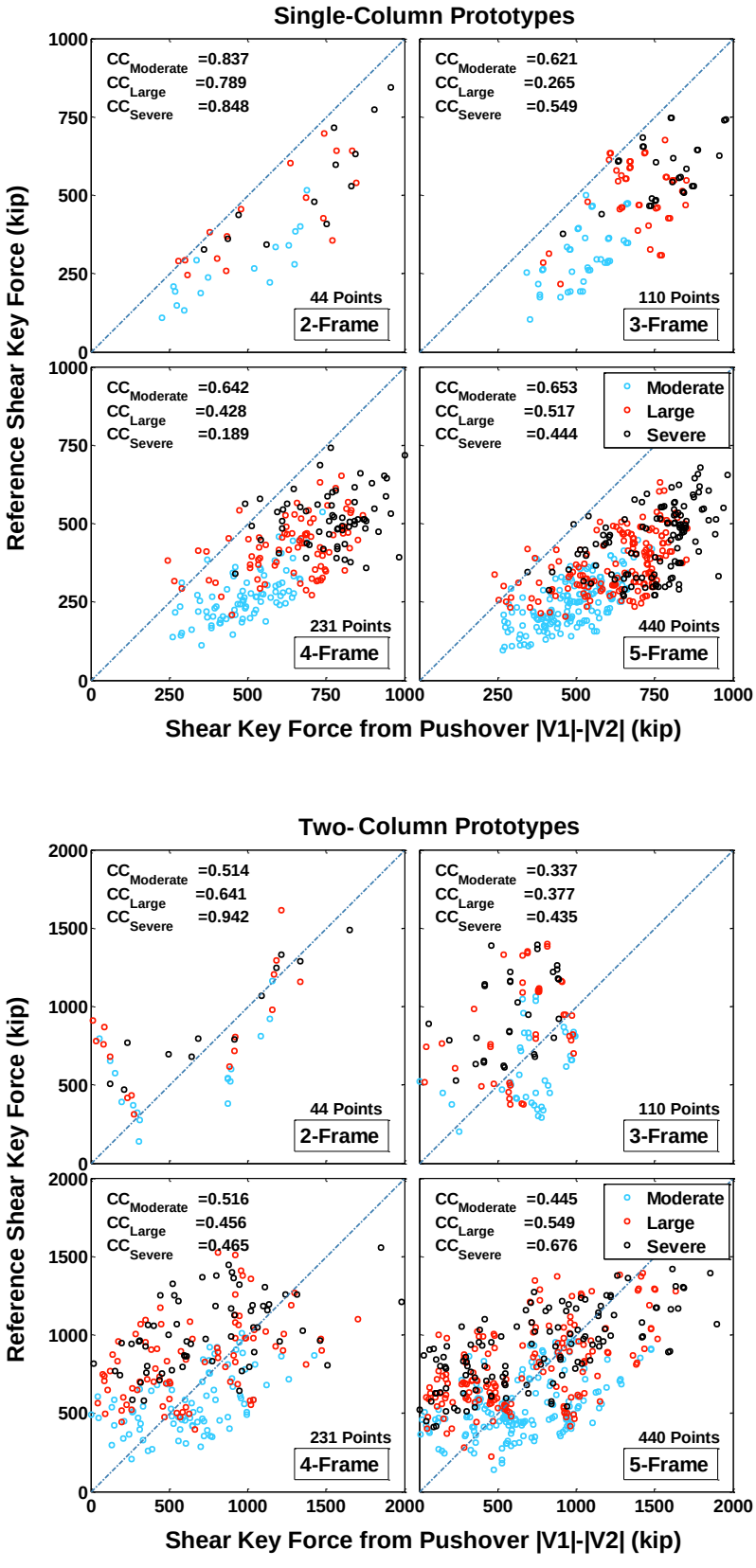

Figure 6.27 Correlation of |*V1*|-|*V2*| from Pushover Analyses with the Reference Shear Key Force

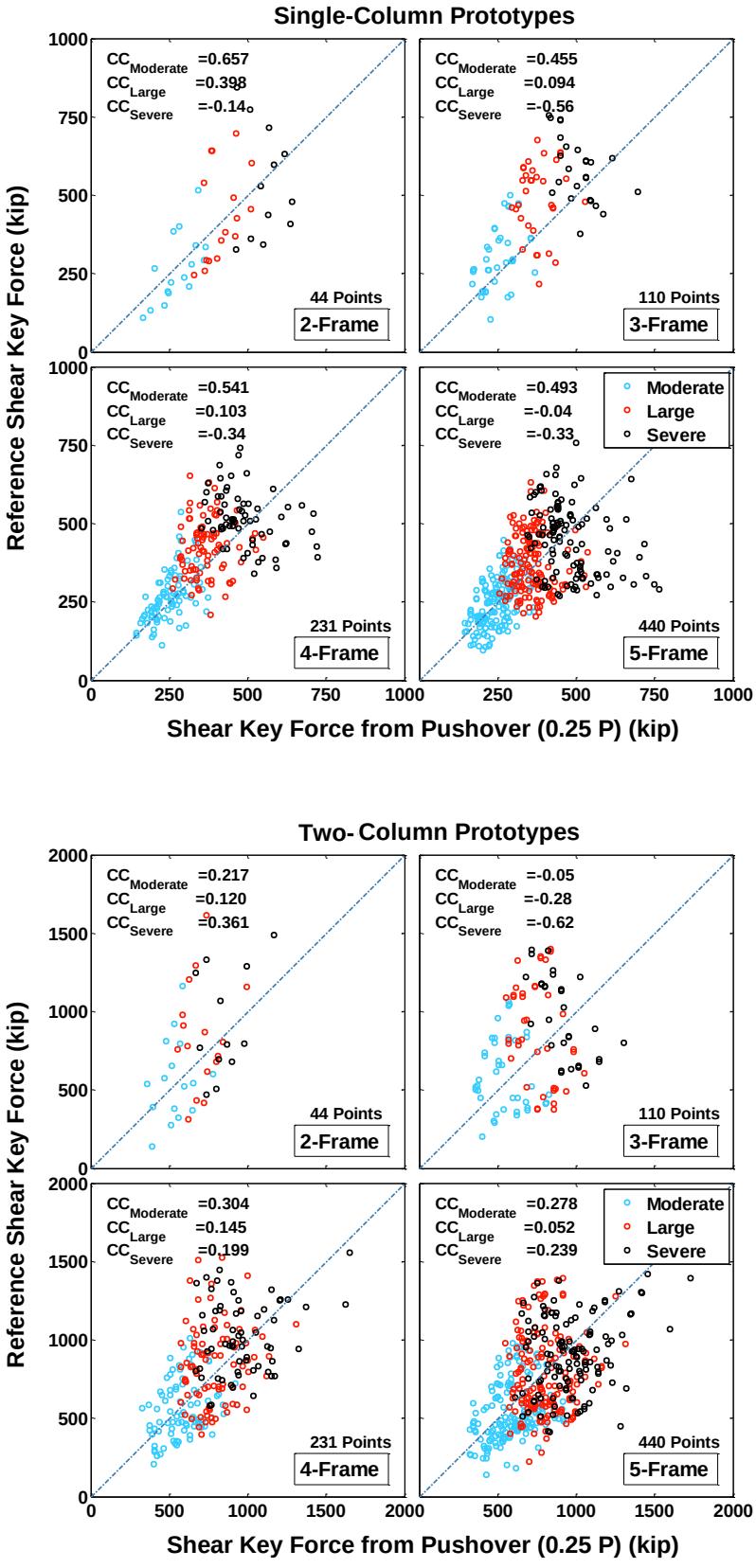

Figure 6.28 Correlation of (*P/4*) from Pushover Analyses with the Reference Shear Key Force

6.8.2 EDA Method

The correlation between the shear key force from the elastic dynamic analyses (EDA) and the Reference Shear Key Forces are presented in Figure 6.29. The ground motion specific spectrums are used to find the values of spectral accelerations instead of ARSs. The complete quadratic combination (CQC) method is used to combine the modal responses. The EDA method offers the advantage of including the effects of higher modes of vibration. It is established in Chapter 2 that these modes, most of which are related to the in plane deformations, of the superstructure, significantly contribute to the in-span shear force response. However, one should be aware that all methods utilized to combine spectral responses of individual modes only provide an approximation of response values, which are not exact when compared to a time history method.

For low amplitude motions, there is a relatively good correlation between EDA and NTH results. In this range, the models remain elastic or undergo minimal plastic deformations. On the other hand, under large amplitude motions, the shear key forces derived from NTH analyses are significantly smaller than those values derived from the EDA because NTH suppresses the forces and accelerations due to yielding. The figures show that the EDA method may over predict the maximum shear key forces by 300%.

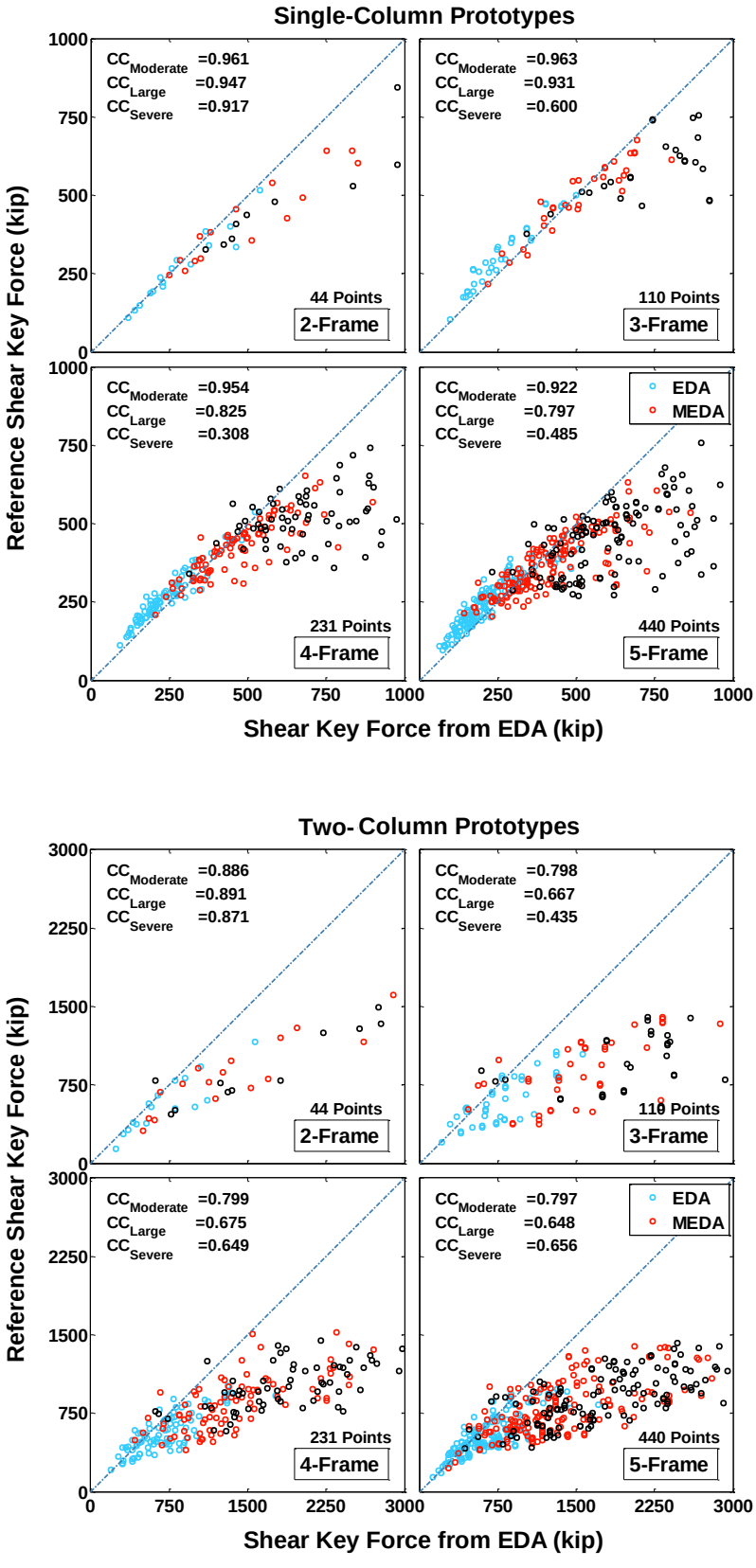

Figure 6.29 Correlation of Force from EDA with the Reference Shear Key Force

The statistical distribution of the cumulative mass participation ratio needed to achieve more than 90% of the total shear key force is shown in Figure 6.30. The total shear key force is obtained by combining a large number of modes of vibration (over 50 modes). A similar statistical distribution is plotted in Figure 6.31 for the cumulative mass participation ratio needed to mobilize more than 90% of the total displacement. These figures show that, on average, the contribution of the natural modes, which make up 95% of the total mass, should be included in the EDA for mobilizing a relatively precise estimation of the shear key forces. Two general observations can be made based on Figure 6.30 and Figure 6.31: 1) A dynamic mode that does not participate in the displacement response may significantly participate in the total shear key force, and 2) the effect of the modes mobilizing 90% of the mass participation ratio may not be adequate for an accurate estimation of the elastic shear key forces. Especially in the two-column bridges, there are modes that have small mass participation ratios but mobilize large shear key forces.

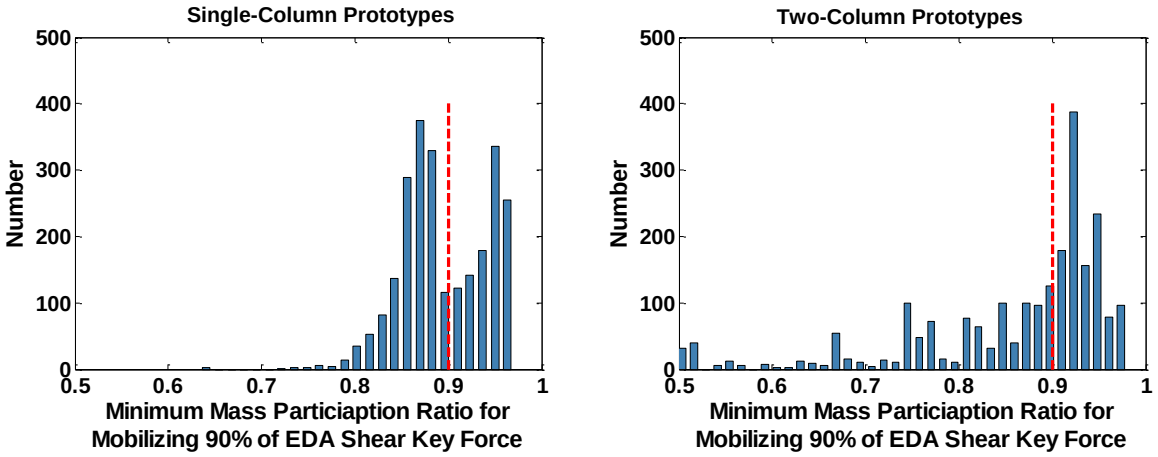

Figure 6.30 Distribution of the Mass Participation Ratios for Mobilizing 90% of the Total Shear Key Force

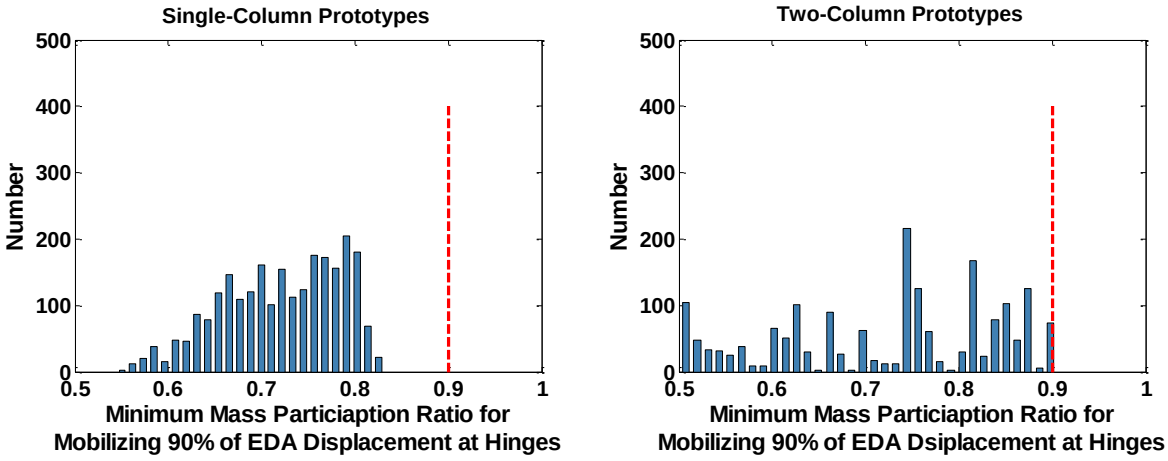

Figure 6.31 Distribution of the Mass Participation Ratios for Mobilizing 90% of the Total Displacement at Hinges

The increase in the mobilized shear key forces achieved by including higher modes is plotted in Figure 6.32. This figure demonstrates that modes with frequencies as high as 10 Hz and 15 Hz should be considered in single- and two-column bridges to mobilize a large percentage of the shear key force.

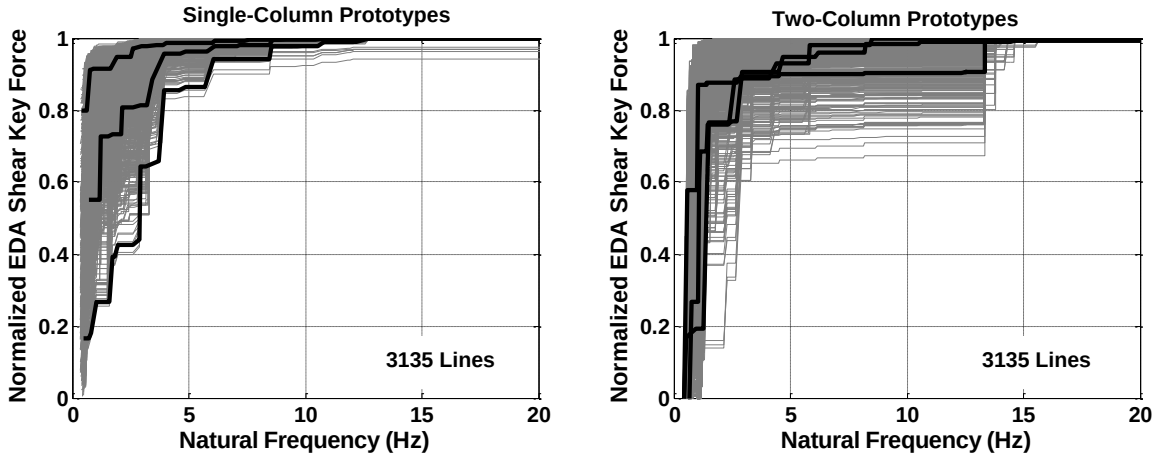

Figure 6.32 The Relationship of Modal Frequency and the Participation in Shear Key Force

6.8.3 Rigid Dynamic Method

It is generally accepted that the responses in modes having frequencies greater than the rigid frequency (modes in the constant acceleration region of the spectrum at high frequencies) are almost perfectly correlated with the input acceleration history and, therefore, are mutually and perfectly correlated (Gupta, 1984). Higher modes can be assumed to respond in phase with the PGA and with each other. Hence, these modes are combined algebraically. This is equivalent to a pseudo static response to the inertial forces from these higher modes excited by PGA. The pseudo static shear key forces associated with inertial forces at the two sides of a hinge are equal to (*M1-M2*) x PGA. The values of *M1* and *M2* are dependent on superstructure flexibility. Figure 6.33 and Figure 6.34 show how these masses are defined. *M1* is the mass of 0.75 and 0.625 of the length of the longer cantilevers for single- and two-column bridges, respectively. Similarly, *M2* is the mass of the 0.5 length of the shorter cantilever in both bridge systems. These values are found by trial and error to get the best correlation in results. Therefore, the values of the differential masses at in-span hinges (i.e. *M1-M2*) are 3.5 kip.sec^2/in and 4.48 kip.sec^2/in for single- and two-column bridges, respectively. The inertial effects are subtracted because the masses experience the same acceleration. Thus, the shear key force is equal to the difference of these inertial forces. This is illustrated in Figure 6.35.

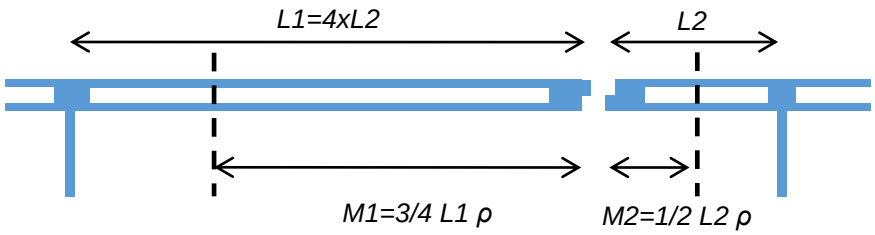

Figure 6.33 Participating Mass of Superstructure, Single-Column Prototypes

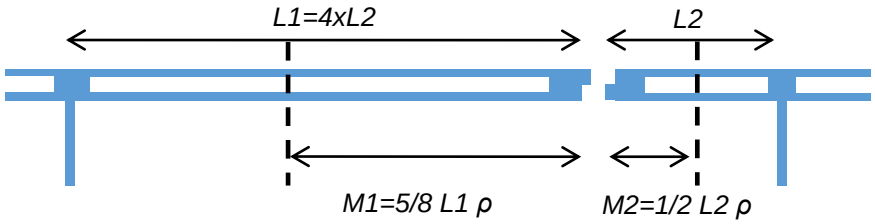

Figure 6.34 Participating Mass of Superstructure, Two-Column Prototypes

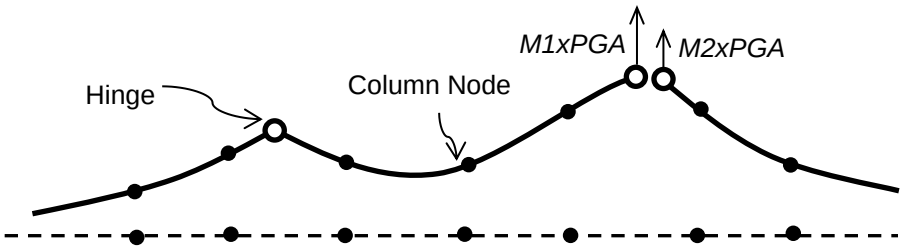

Figure 6.35 The Inertial Forces in Rigid Dynamic Method

Figure 6.36 shows the correlation of the forces obtained by this method with the Reference Shear Key Forces. This method presents a reliable approach, but, in this simple form, it lacks the accuracy. It should be emphasized that this approach only considers the inertial effects, which means that no stiffness forces are accounted for.

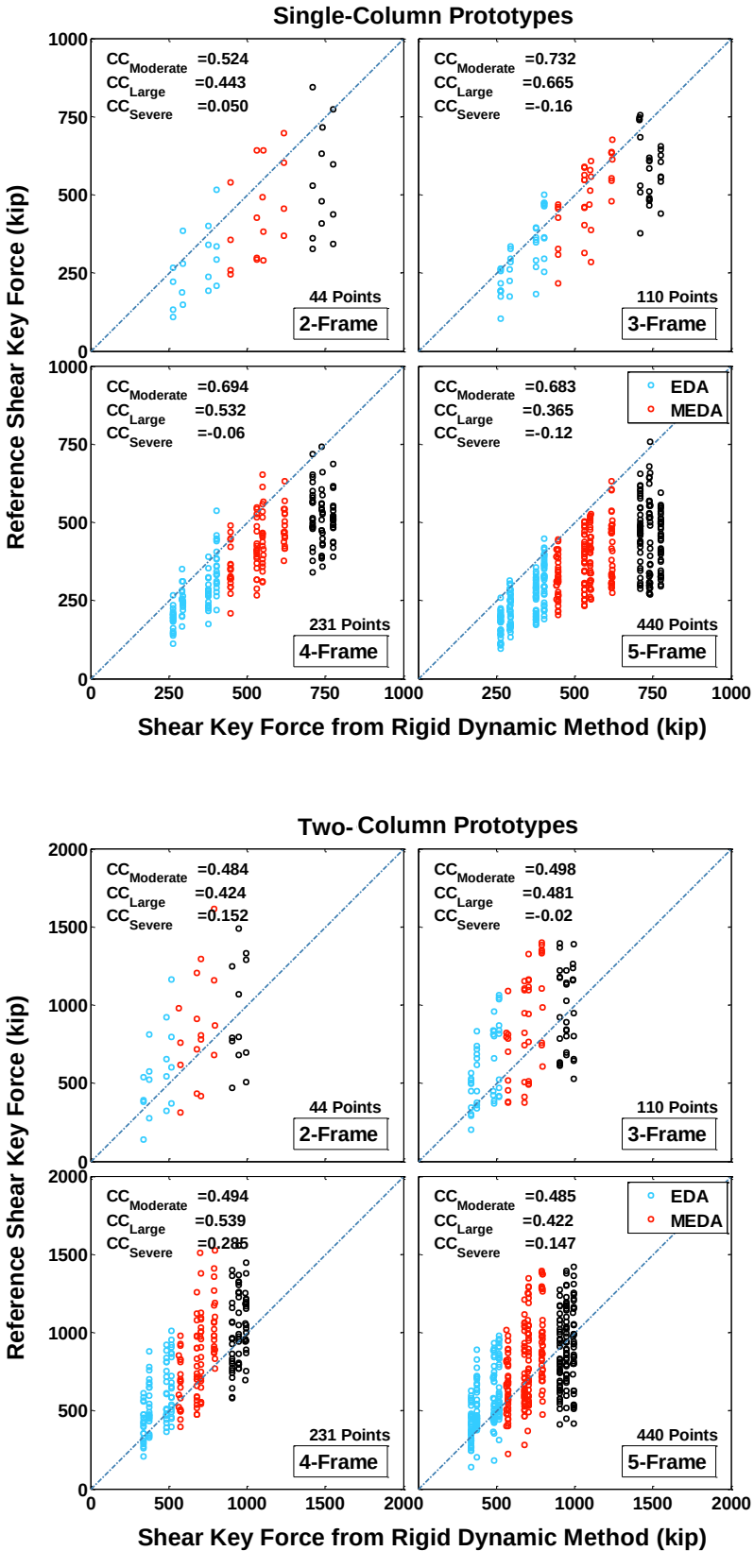

Figure 6.36 Correlation of Force from Rigid Mode Method with the Reference Shear Key Force

6.8.4 Combination of Pushover and Inertial Effects

The major deficiency of the static nonlinear analysis (pushover) method is that it ignores the higher modes' inertial effects. To address this, a simple approach is developed during this study to combine pushover and inertial forces. It is done by combining the shear key forces, from the pushover analysis, i.e. 0.25*P*, with the inertial forces from the rigid dynamic method, i.e. (*M1-M2*) x PGA. This combination is called the "M-V" analysis method where "M" is related to inertial force and "V" represents shear key force from the pushover analysis. These values are combined using the root mean square (RMS) method presented in Eq. 6.6. Some other combination methods including the arithmetic mean (Eq. 6.7), the geometric mean (Eq. 6.8), and SRSS (Eq.6.9) were examined; however, the RMS equation was found to be the best:

$$V_{RMS}^{Sk} = \sqrt[2]{0.5 \times [(0.25P)^2 + (M1 - M2)^2 \times PGA^2]} \quad \text{Eq. 6.6}$$

$$V_{AM}^{Sk} = 0.5 \times [(0.25P) + (M1 - M2) \times PGA] \quad \text{Eq. 6.7}$$

$$V_{GM}^{Sk} = \sqrt[2]{(0.25P) \times (M1 - M2)PGA} \quad \text{Eq. 6.8}$$

$$V_{SRSS}^{Sk} = \sqrt[2]{(0.25P)^2 + (M1 - M2)^2 \times PGA^2} \quad \text{Eq. 6.9}$$

The correlation between the shear key forces obtained from the "M-V" method and the Reference Shear Key Forces are shown in Figure 6.37. This method has a decent reliability but large scatters are still visible in the data.

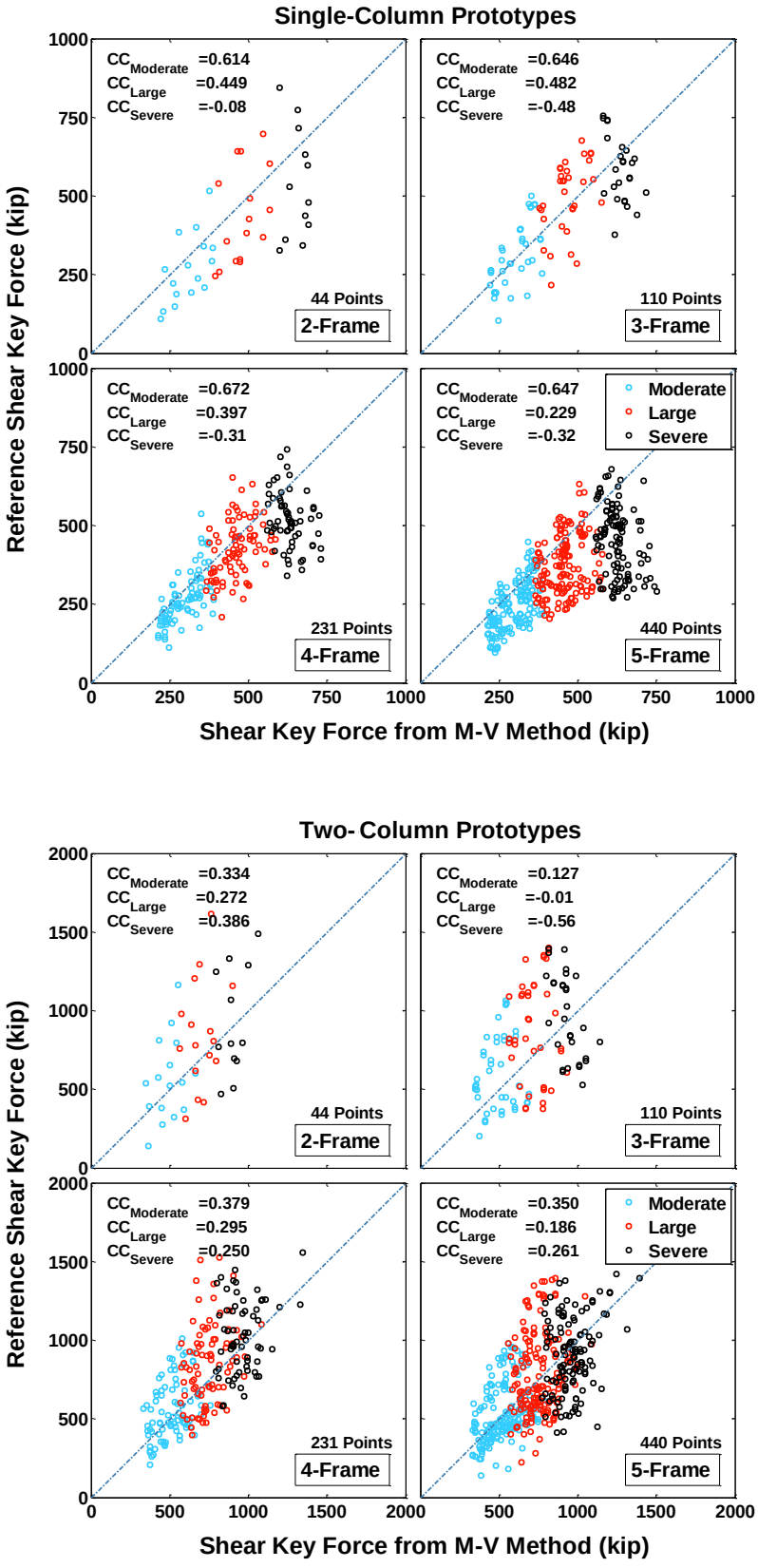

Figure 6.37 Correlation of Force from M-V Method with the Reference Shear Key Force

6.8.5 EDA Method with Inelastic Spectrum

To address the over prediction of the shear key forces by the EDA method under large ground motions, the elastic spectrum is replaced with a constant-ductility inelastic spectrum. The inelastic spectrums are constructed for each ground specific spectrum by applying the modification factor R_y presented as Eqs. 6.7 and 6.8. (Krawinkler & Nassar, 1992). The elastic response spectrums of the ground motions are divided by this reduction factor to obtain the inelastic spectrums.

$$R_y = [c(\mu - 1) + 1]^{1/c} \qquad \text{Eq. 6.10}$$

where

$$c(T, a) = {T^a}/{(1 + T^a)} + {b}/{T} \qquad \text{Eq. 6.11}$$

The numerical coefficients *a* and *b* depend on the post-elastic stiffness ratio (hardening slope) of the bilinear force-displacement relationship. In this study these parameters are assumed as *a*=1.0 and *b*=0.37, corresponding to a hardening slope of 2%. The parameter *T* is the fundamental period of the structure and μ is the displacement ductility ratio, which was taken as the design displacement ductility demand, μ_D.

The correlation of the results from this method and the Reference Shear Key Forces are given in Figure 6.38. While the inelastic spectrum method corrects the overprediction of the shear key force by EDA, the correlation of the data is poor. This method may significantly under predict the shear key forces. The reason is that the higher modes of vibration that mainly contribute to the shear key forces are mostly elastic modes, and using a constant-ductility inelastic spectrum suppresses the effects of these modes.

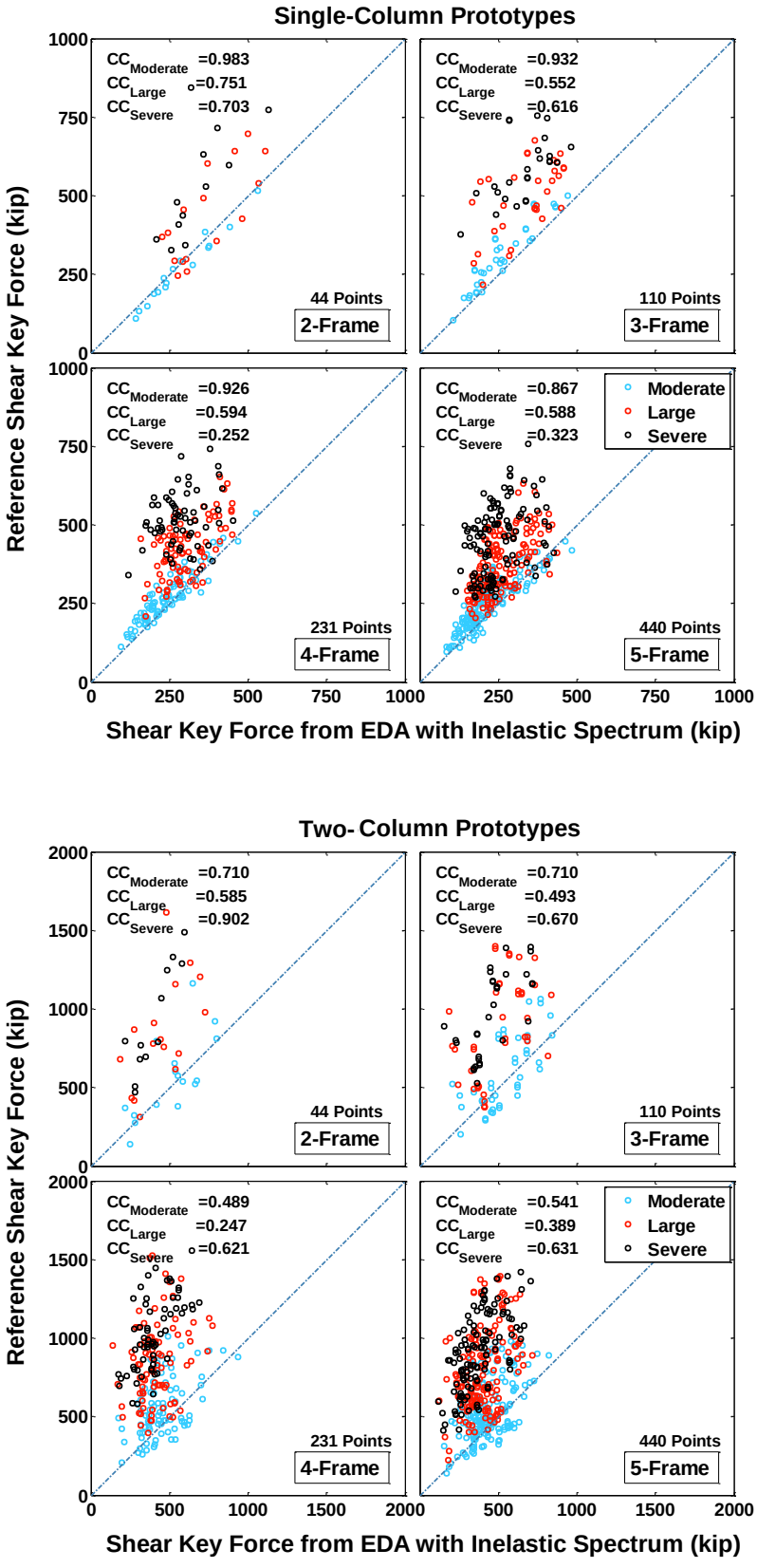

Figure 6.38 Correlation of Force from EDA with Inelastic Spectrum with Reference Shear Key Force

6.8.6 EDA Method Modified by Ductility

The concept of equal displacements is based on the assumption that forces are linearly proportional with the displacements for ductility ratios smaller than approximately 4.0. This concept is used in the displacement-based design method adopted by SDC 1.7 (see Figure 5.1).

In an effort to account for the nonlinear response of the model under strong motions, the total elastic shear key forces obtained from the EDA method (Sec. 6.8.2) are divided by the maximum column displacement ductility ratio, μ_D. The ductility ratios that were smaller than 1.0 were set to be 1.0. The displacement ductility is the maximum of column ductility values. Since the EDA forces are found using the spectrum of ground motions, to preserve the consistency, the ductility values are also obtained from NTH analysis. The correlation of the results from this method with the Reference Shear Key Forces is shown in Figure 6.39. This method lacks reliability and accuracy.

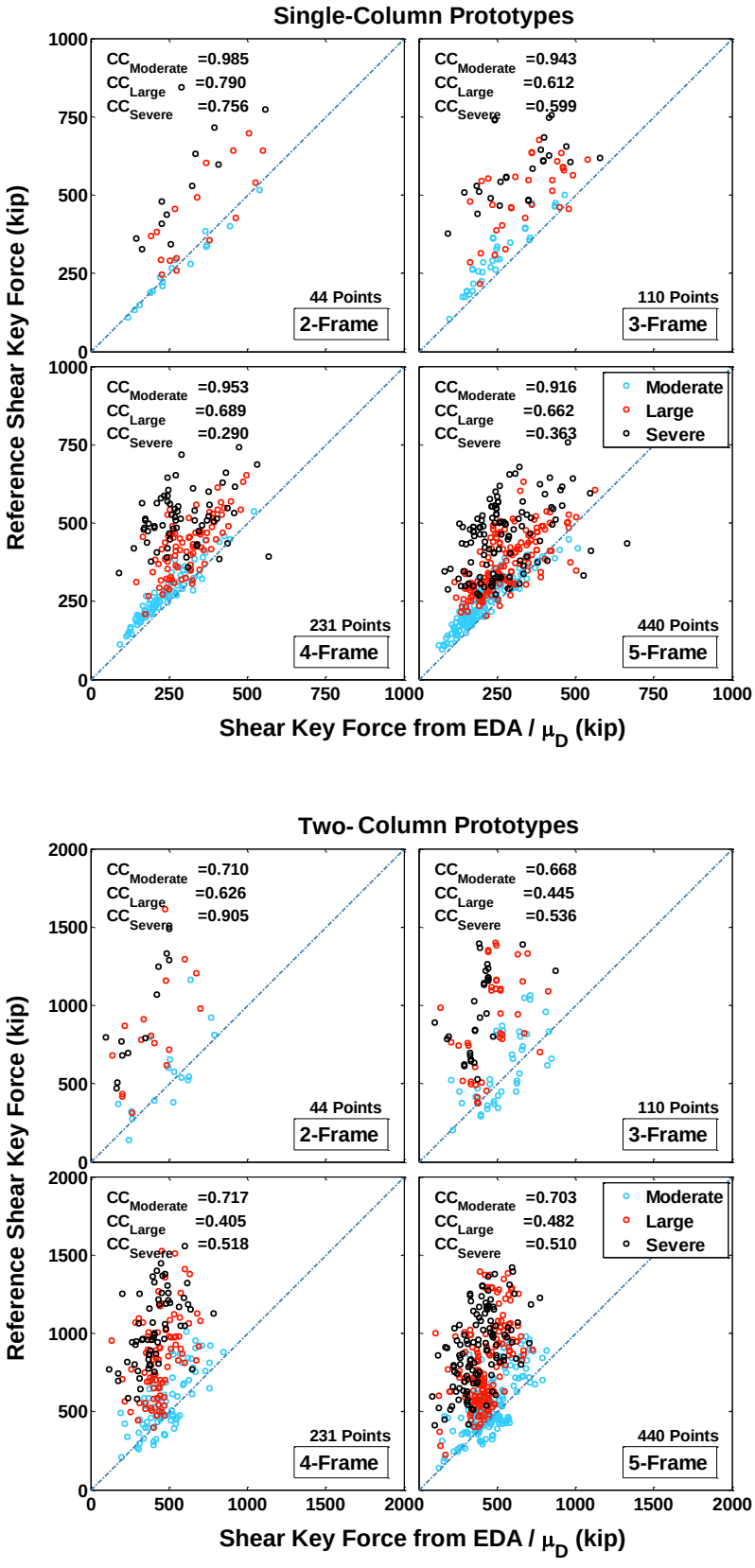

Figure 6.39 Correlation of Force from EDA Modified by Ductility with Reference Shear Key Forces

6.9 EDA SHEAR KEY FORCE WITH MODIFICATION OF MULTIPLE MODES

Results of the two previous methods showed that the uniform modification of modal shear key forces leads to significant errors. A refined method is developed in this study to target the reducing effects of the nonlinearities at certain modes.

6.9.1 Modal Displacement Ductility

Recent research studies for building types of structures have shown that they typically become inelastic at the first mode of vibration and remain elastic at higher modes. Therefore, applying a reduction factor to the effects of the higher mode can lead to the under prediction of responses. Thus, it has been proposed that the reduction factor, R, only be applied to the effects of the first mode of building structures (NIST, 2012).

For this study, reducing the effects of the first mode does not yield accurate results. This is due to the unique dynamic characteristics of multi-frame bridges that are explained in Chapter 2. In multi-frame bridges, the higher modes can generate inelastic displacements that are even with or larger than the inelastic displacements due to the first mode. To address this difference, the concept of modal displacement ductility is developed in this study as a new concept for bridges. The displacement ductility of the system is defined by, $\mu_{D,n}$, where n is defined as the equivalent mode to the largest displacement ductility in the columns under the n^{th} modal displacement.

The ductility values calculated for each mode are plotted in Figure 6.40. In the single-column models, the 1st to 4th modes show inelastic deformations, while, in the two-column prototypes, modes as high as 22nd become inelastic. It should be mentioned that these mode numbers include the lateral, longitudinal, and vertical modes of vibration.

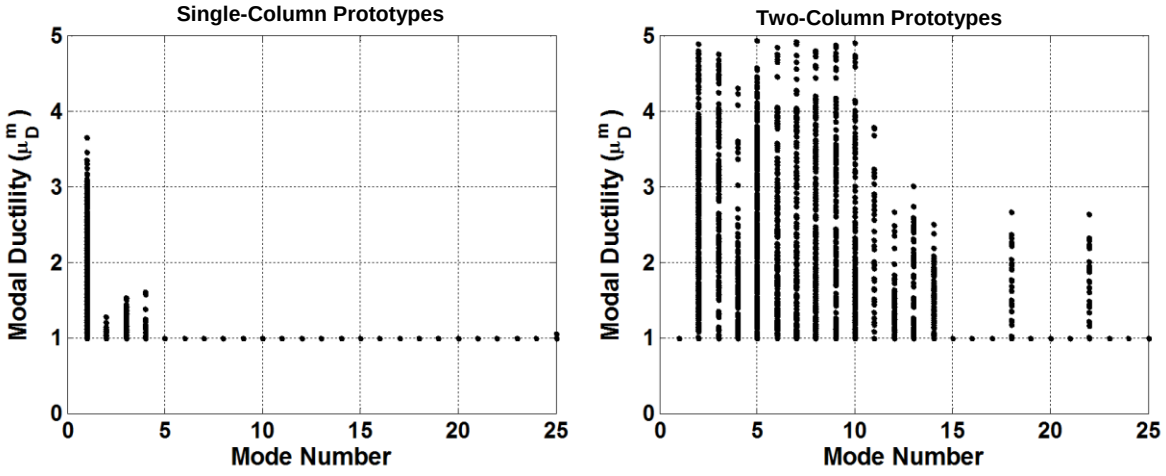

Figure 6.40 Transverse Modal Ductility Ratios for Different Modes

Figure 6.41 shows the modal ductility values versus the modal periods. For a single-column system, the inelastic modes have periods between 1.0 sec. and 2.8 sec., while, in a two-column system, they happen between 0.5 sec. to 2.2 sec. with some exceptions.

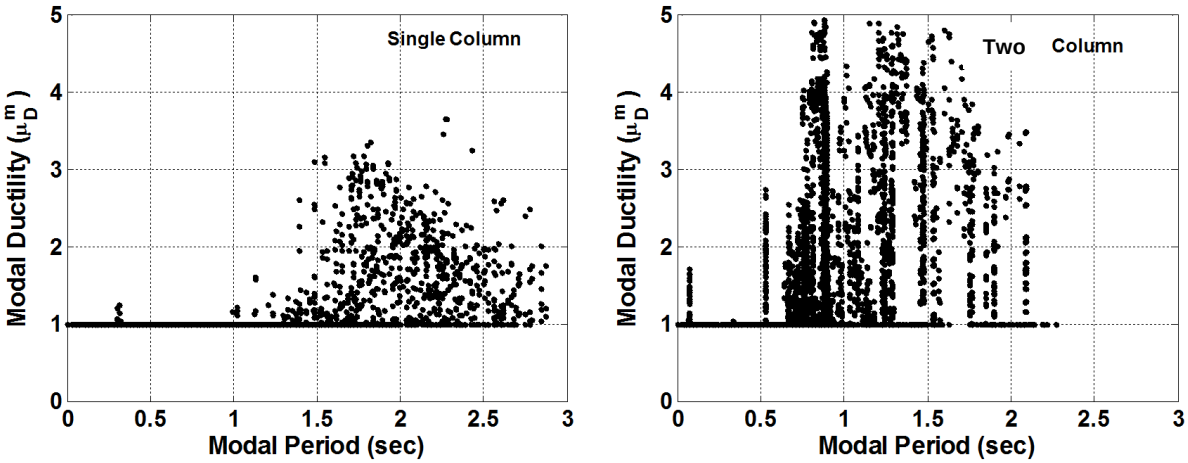

Figure 6.41 Transverse Modal Ductility Ratios versus Modal Periods

6.9.2 EDA with Modification of Multiple Modes

This data demonstrates the importance of treating each mode separately for the effects of nonlinearities. The approach of the proposed EDA method with modification of multiple modes is to modify the participation of each mode in shear force by the ductility of the same mode. The modified modal forces are then combined using CQC.

Figure 6.42 compares the results of the EDA method and the proposed modified EDA method, named MEDA with respect to the Reference Shear Key Force. The modification of the individual modes has a significant effect in reducing the elastic forces to realistic levels. This is more pronounced in the two-column systems. Figure 6.44 presents the performance of the MEDA method for three hazard levels. Acceptable values of correlation coefficients demonstrate the accuracy of this method. The MEDA is found to be a reliable and accurate method.

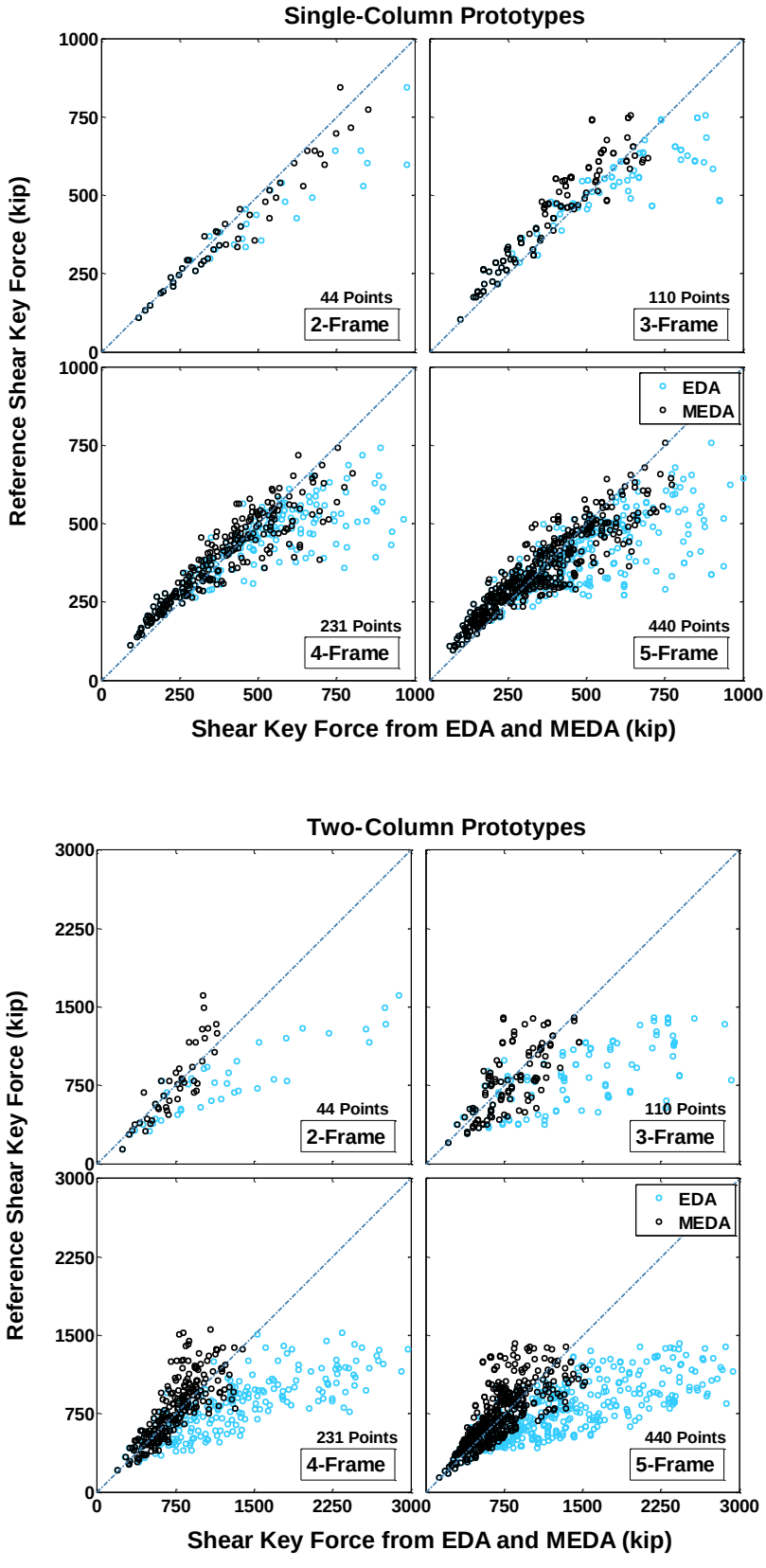

Figure 6.42 Comparing the Results of EDA and EDA with Modification of Multiple Modes (MEDA)

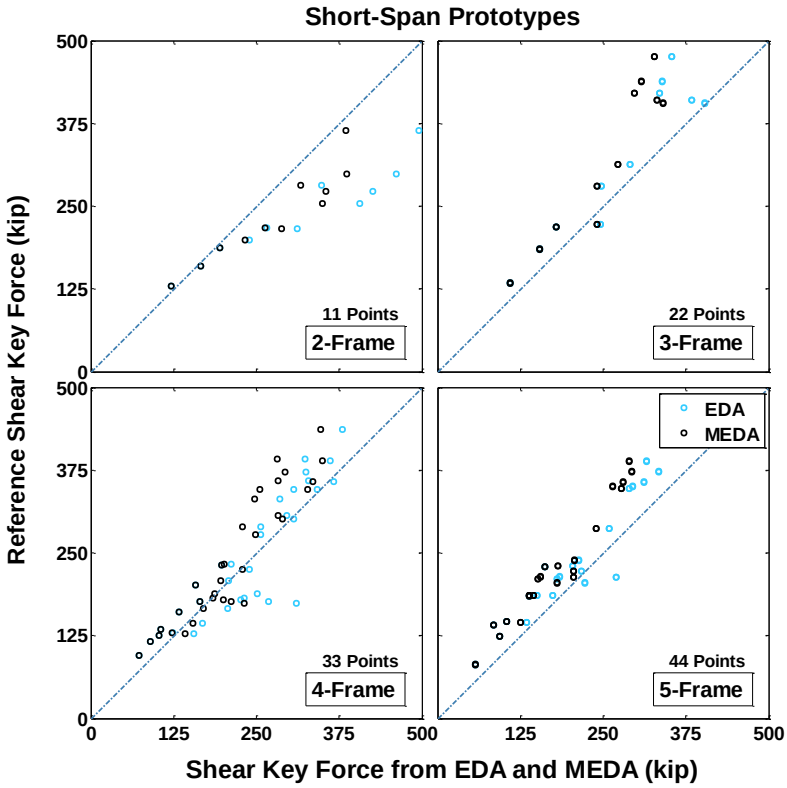

Figure 6.43 Comparing the Results of EDA with EDA with Modification of Multiple Modes (MEDA) for Short-Span Prototypes

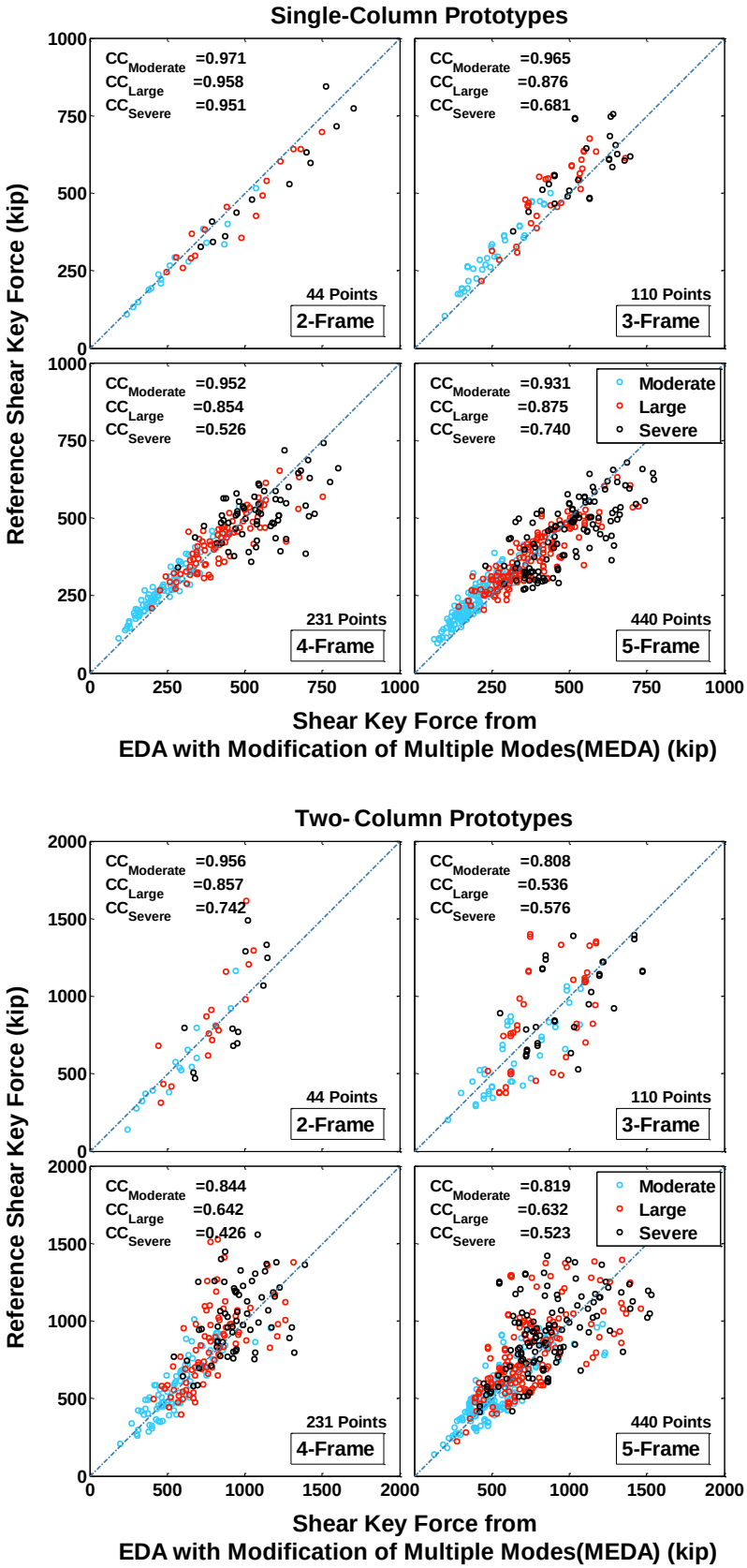

Figure 6.44 Performance of MEDA Method

The results of the MEDA method for all long-span prototypes are condensed in Figure 6.45. The same results for all short-span bridges are shown in Figure 6.46.

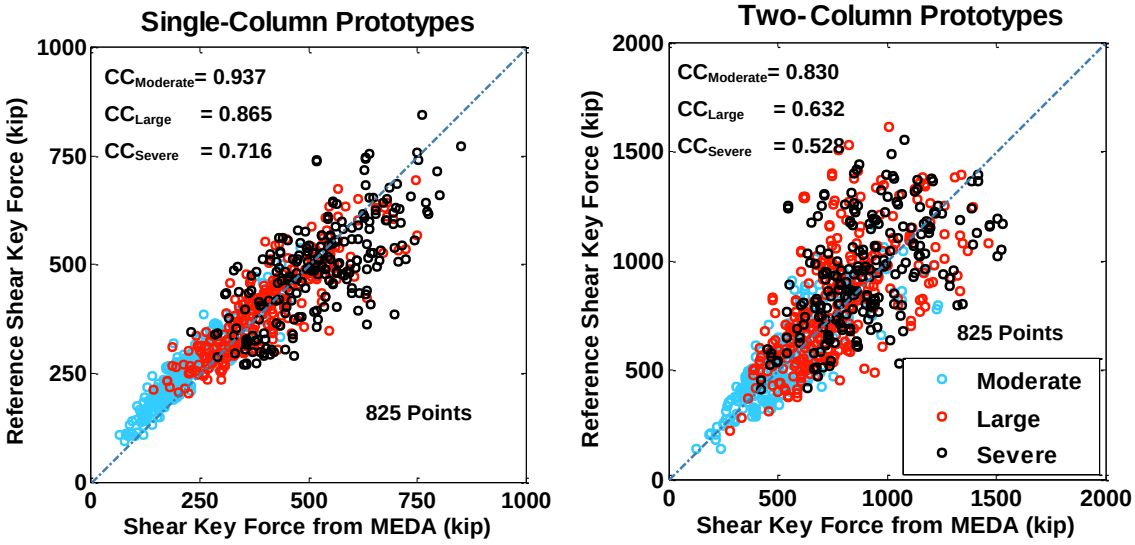

Figure 6.45 Performance of MEDA for All Long-Span Prototypes

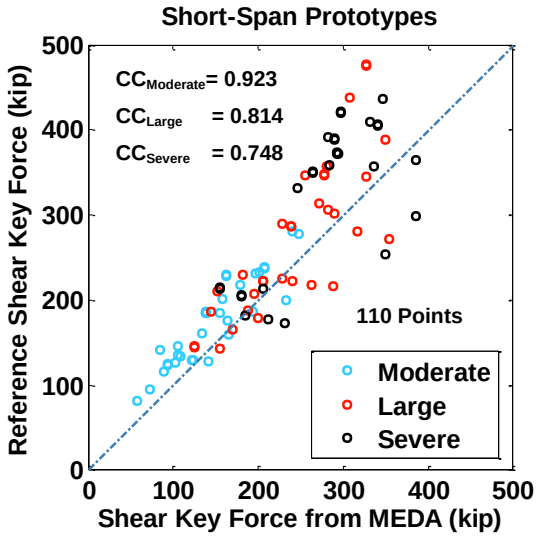

Figure 6.46 Performance of MEDA for All Short-Span Prototypes

The proposed MEDA method is adopted as the preferred analysis method for the estimation of the shear key force demand. This method is easy to implement once the values of the force and ductility values are known for each mode.

6.9.3 Sources of Error in MEDA

The differences between the results from the NTH analysis and MEDA may be associated with the following factors. 1) The spectral analysis method is formed around theories of random vibration and is expected to present an approximate estimation for

maximum response values. 2) In a seismic event, a multi-column bridge will be subjected to multi-support excitation. Even for a uniform support excitation, the non-uniform yielding of the columns generates changes in the relative stiffness of the frames. This effect may not be captured by the EDA method. 3) Non-transient dynamic effects of the base excitation in the form of wave propagation in the superstructure cannot be seen when implicit methods like spectral analysis are used.

6.10 EFFECTS OF YIELDING OF ABUTMENT SHEAR KEYS

Per the SDC, abutment shear keys are designed as sacrificial or ductile elements. The yielding of abutment shear keys changes the end boundary conditions, and consequently the response of the system. This section examines the effect of the design capacity of abutment shear keys on the in-span shear key responses.

6.10.1 Inelastic Transverse Displacements at Abutments

The abutment shear keys are modeled with bilinear behavior. Their capacities are equal to the abutment dead load reaction. The abutment shear key design force is 1,300 kip and 2,000 kip for the single-column and two-column systems, respectively. Figure 6.47 shows the total transverse displacement at the abutments as a function of PGA. The transverse gap is not included in the Main Analyses. However, after the shear key capacity is exceeded, the gap forms due to the one-way yielding of the abutment. At this point, transverse pounding begins to participate.

In the single-column system, the abutment shear keys start yielding when PGA exceeds approximately 0.35g. In the two-column system, the abutment shear keys yield under smaller ground motions with a PGA of approximately 0.2g. For the two-column bridges, displacements as large as 5.0 in may be expected. The reason for the larger extent of yielding in the two-column systems is a stiffer and heavier superstructure compared to the single-column models. It can be concluded that, in the two-column system, the boundary conditions at the abutments are more prone to changing during the earthquake.

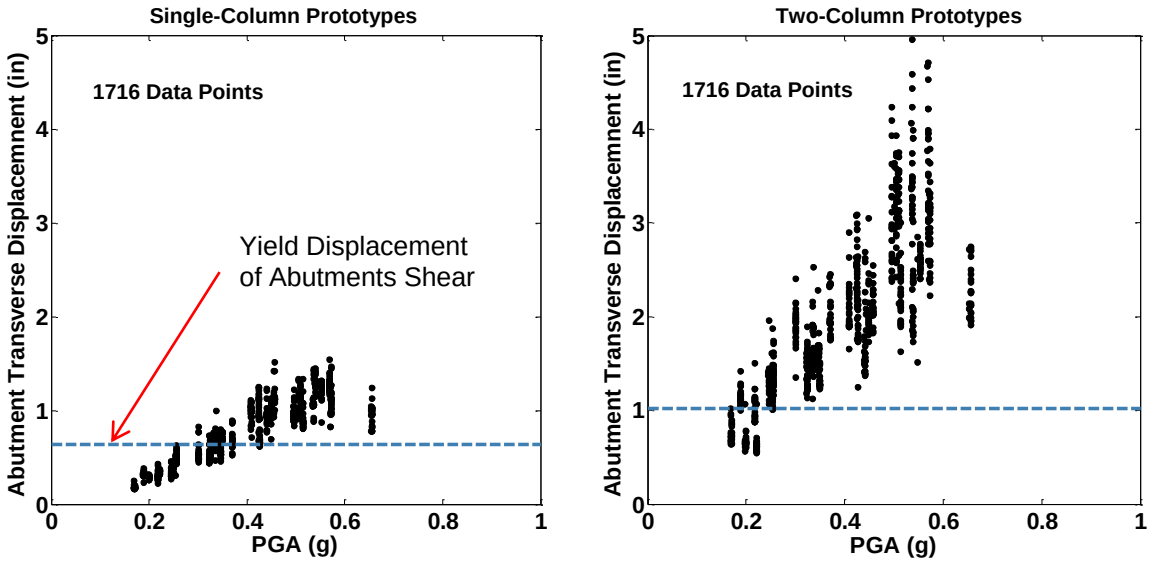

Figure 6.47 Transverse Displacement at Abutments

6.10.2 Effects of the Yielding of Abutments Shear Keys on the In-Span Hinges

Two cases are studied to understand the effect of yielding of the abutment shear keys on the in-span shear key forces. A strong and weak abutment shear key with a capacity equal to 2.0 and 0.5 times the abutment dead load reaction respectively are studied. These analyses were performed only for the prototypes with uniform valley shape. The results are shown in Figure 6.48 and Figure 6.49. They show the statistical distribution of the ratio of the in-span shear key force to the Reference Shear Key Force for weak and strong abutment shear keys, respectively.

The change in the capacity of the abutment shear keys may increase or decrease the in-span shear key forces due to the changing of the boundary conditions. The over strength of the abutment shear keys slightly increase the in-span shear key forces in the two-column models while it has almost no effect on the single-column models. A weaker abutment shear key may lead to smaller in-span shear key forces in both systems, which is more pronounced in the two-column models.

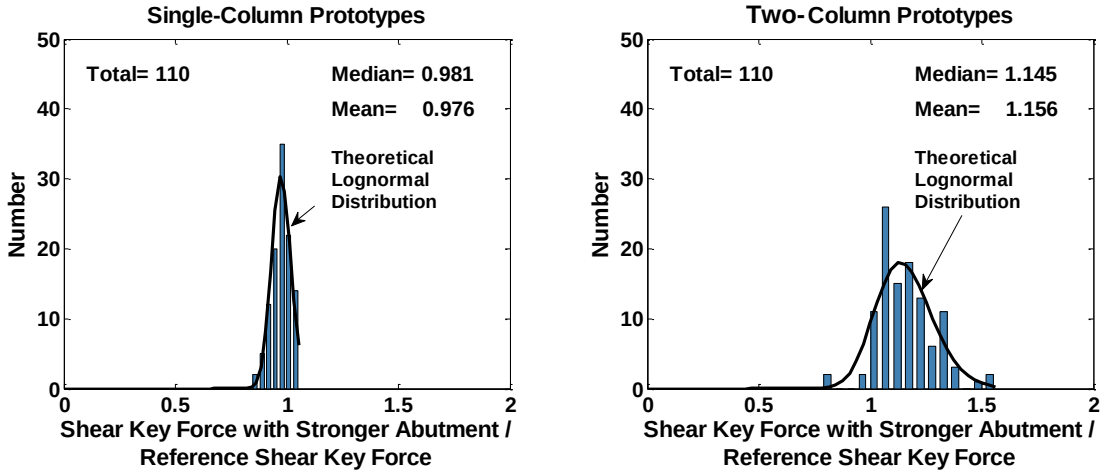

Figure 6.48 Effect of Stronger Abutment Shear Key (Capacity of 2.0 Dead) on In-Span Shear Key Force

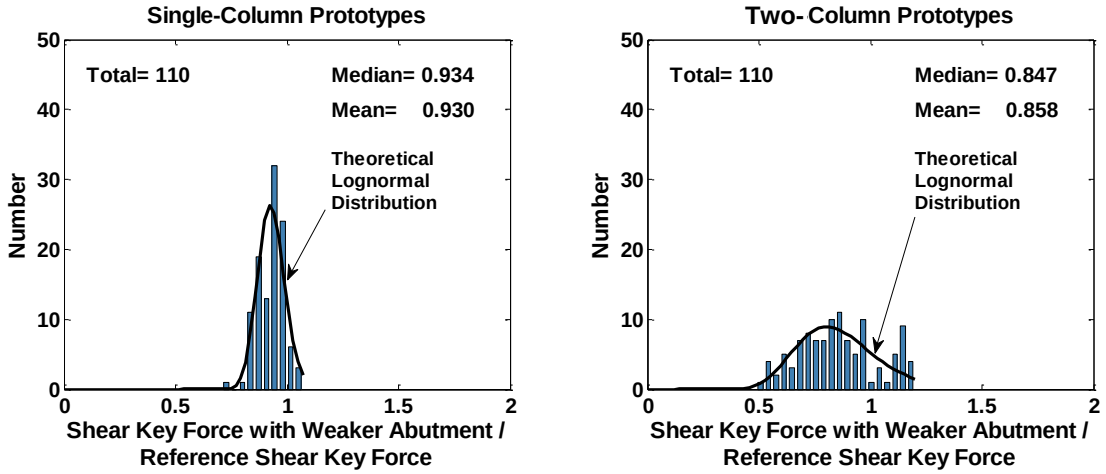

Figure 6.49 Effect of Weaker Abutment Shear Key (Capacity of 0.5 Dead) on In-Span Shear Key Force

6.11 EFFECT OF IMPACT BEETWEEN FRAMES

As mentioned earlier, the Main Analysis is performed with closed transverse gaps, extended longitudinal gaps, and only transverse motion is applied. To investigate the full dynamic response and the dynamic amplification on shear key force due to gap closure, all prototypes are analyzed with a 1.0-in transverse gap and a 2.0-in longitudinal gap under biaxial ground motion. This set of analyses is called the "Impact Analysis." The results of this analysis are shown in Appendix-C Part 5a (single-column) and 5b (two-column). The shear key force response histories from the Main Analysis and the Impact Analysis are plotted together. Only results of prototypes with uniform valley shape are presented in here.

Figure 6.50 shows the impact factor with respect to the Reference Shear Key Force. The impact factor is the ratio of shear key force from the impact analysis to that of the Main Analyses (no gap). It can be seen that the impact factor decreases as the shear key force increases. The reason for this is the increase in damping at the contact surface due to an increase in penetration. The distribution and CDF of the impact factor is shown in Figure 6.51 and Figure 6.52 for long-span and short-span prototypes, respectively. The mean and median impact factor in all three systems is approximately 2.5.

The impact phenomenon that results from the transverse gap in multi-frame bridges is a complex problem which is affected by many parameters, including: 1) torsional displacement of the frames about the vertical axis upon the gap closure and non-uniform change in momentum; 2) longitudinal gap closure and friction in the transverse direction at the hinge contact surface; 3) shear wave velocity along the frame deck; 4) contact surface conditions and the coefficient of restitution; 5) ground motion frequency and pulse content; and 6) non-uniform base excitation. In addition, the dynamics of a discrete system with gaps is completely different from the dynamics of a continuous system, such that, before gap closure, the vibration modes are related to the stand-alone frames.

The individual correlation between the impact factor and some parameters, including PGA, PGV; the maximum acceleration at the hinge, the maximum velocity, spectral acceleration, spectral velocity, and columns' ductility are studied. However, no traceable relationship was found that addresses the complexity of the problem. Therefore, a straightforward analytical solution for the impact problem in the transverse direction of multi-frame systems cannot be developed.

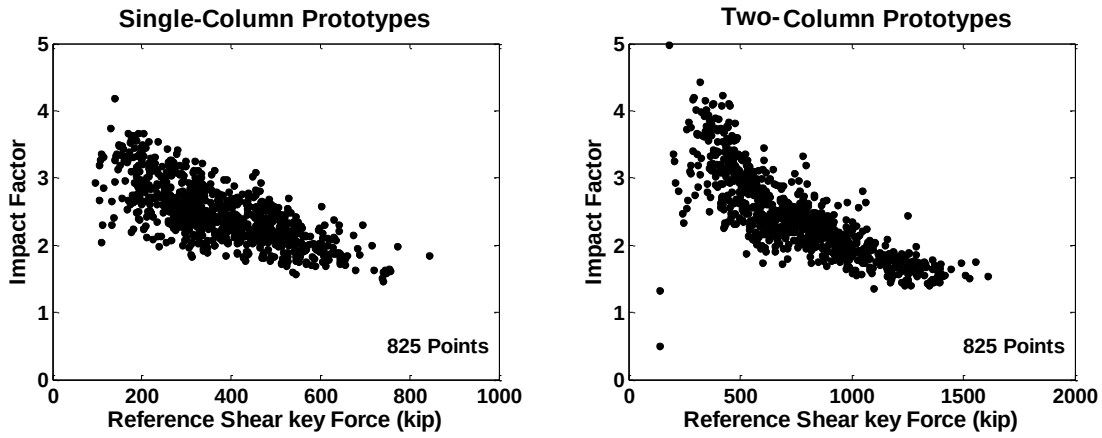

Figure 6.50 Impact Factor with Respect to Reference Shear Key Force

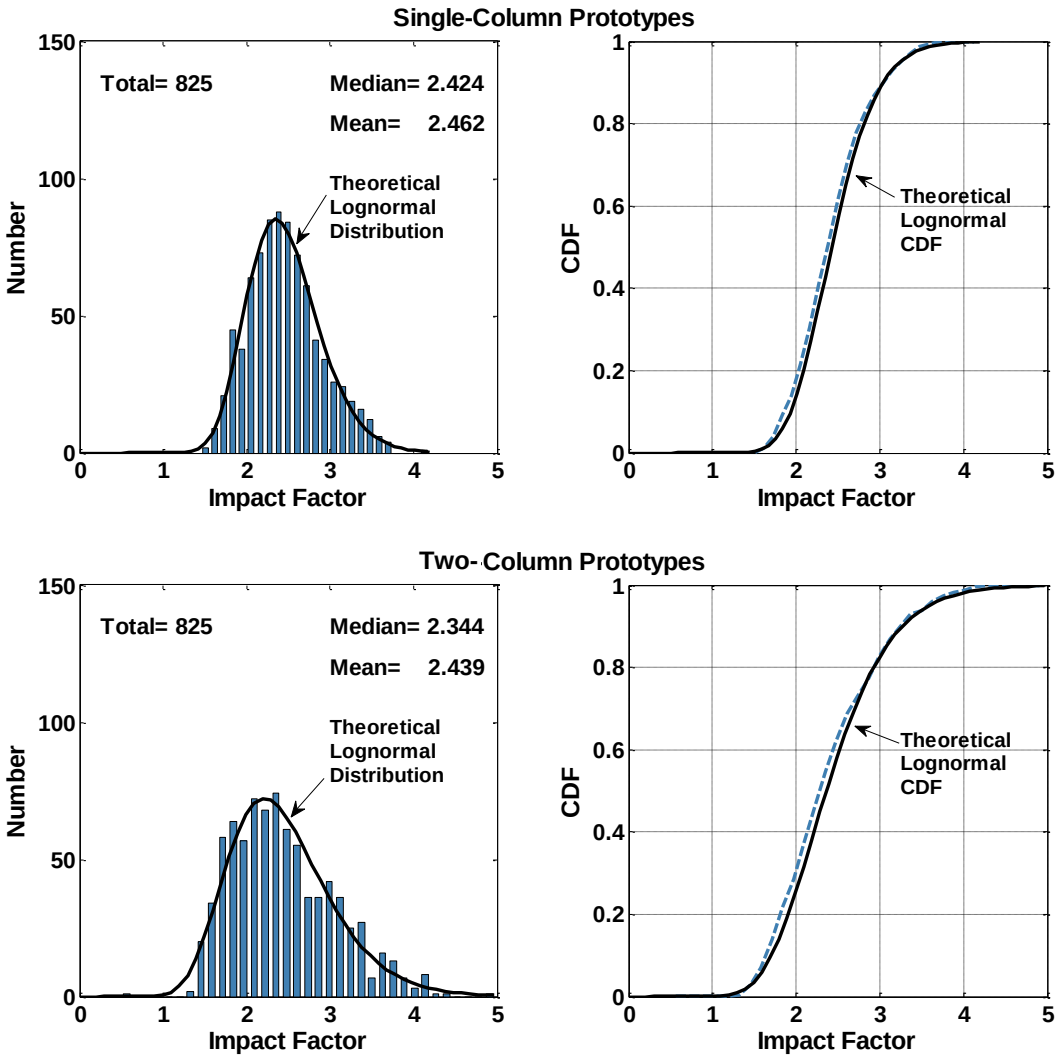

Figure 6.51 Distribution and CDF of the Impact Factor, Long-Span Prototypes

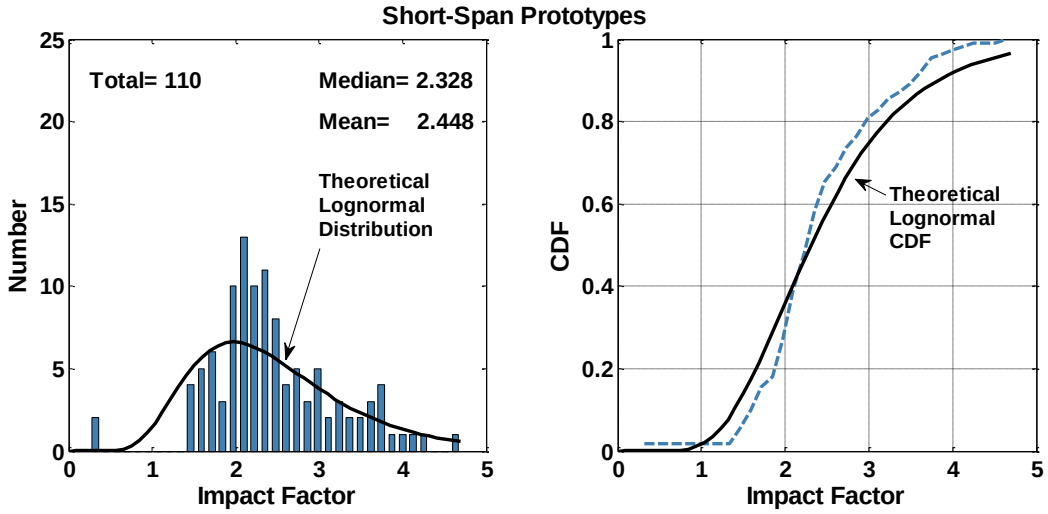

Figure 6.52 Distribution and CDF of the Impact Factor, Short-Span Prototypes

6.12 EFFECT OF NON-UNIFORM BASE EXCITATION

Long bridges, including multi-frames, are prone to be excited non-uniformly at different supports due to the traveling speed of seismic waves. To study this phenomenon on the shear key force response, all of the main analyses are repeated with non-uniform base excitations (NUBE). For this purpose, each support is excited with a time lag proportioned to the ratio of the distance from the left abutment to the shear wave velocity of the soil. The velocity of the shear wave is assumed as an average of the velocity range for soil types B, C, D, and E. According to recommendations found in the OpenSees users' forum, the displacement history of ground motion is applied instead of acceleration. The displacement history is obtained from the double integration of the acceleration history. To ensure that the method of analysis is working properly, it is checked for a uniform base excitation (UBE).

The results in Figure 6.53 show the distribution of the shear key amplification ratio. The amplification ratio is the ratio of shear key force with non-uniform base excitation to the Reference Shear Key Force. Each graph is related to one of the following soil types: B, C, D, and E.

It can be seen that, for all cases, the effect of NUBE may increase the shear key force by 200%-300% or decrease it by 50%. This effect for soil type B is negligible because of the high velocity of the shear wave. However, for the other soils, the effect of NUBE is more visible. Figure 6.54 shows the median ratio of NUBE/Reference Shear Key Force for different soil types and compares the single-column with the two-column bent system. Almost no change is seen in the shear key force of soil type B while the increase in the shear key force for other soils is 20%-30%. This happened consistently, except in the single-column prototype for soil type D, which showed, on average, a 75% increase in force. The reason for this sudden change is not known.

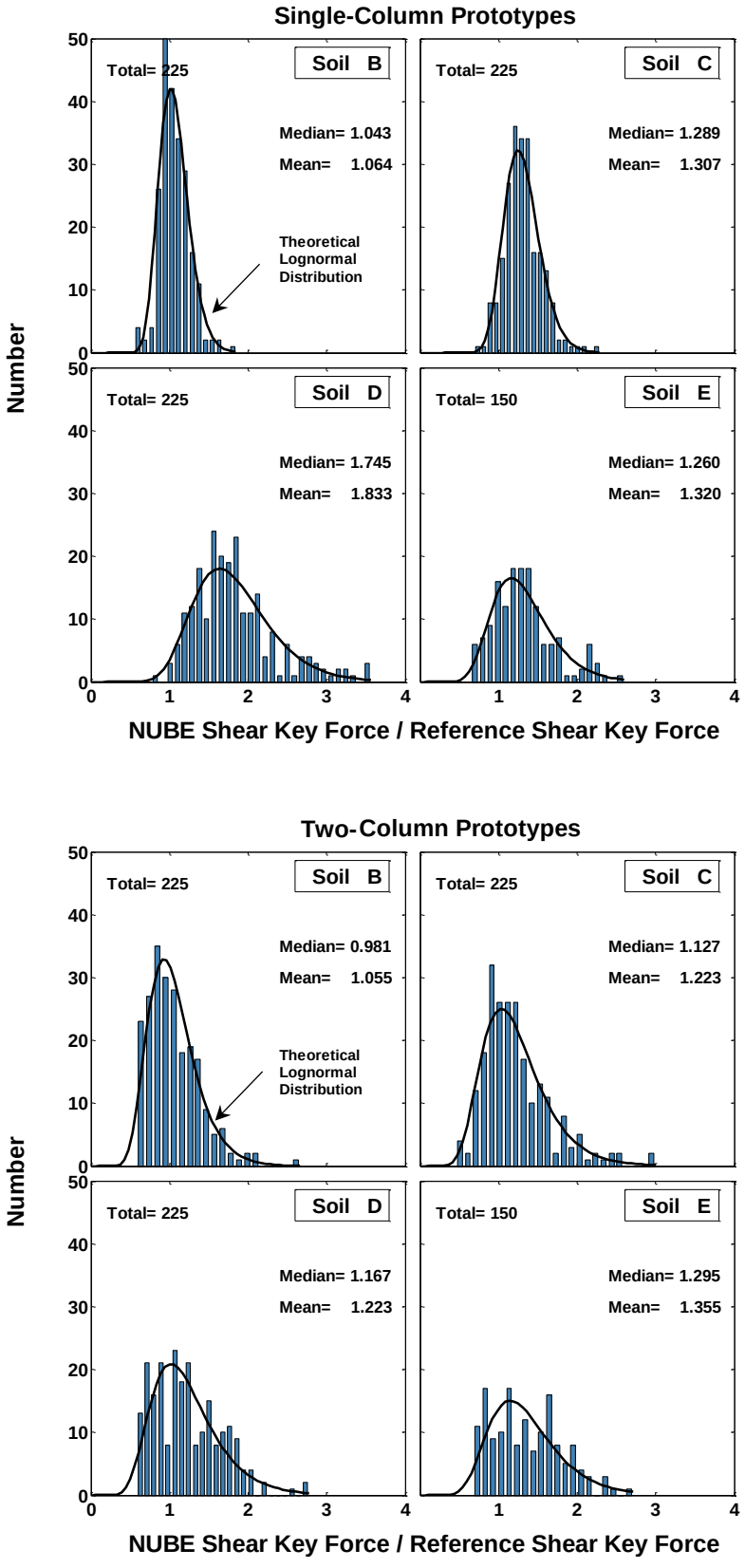

Figure 6.53 Effect of Non-Uniform Base Excitation on Shear Key Force

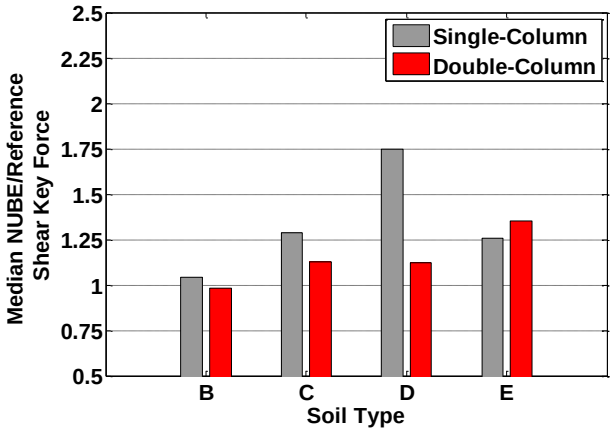

Figure 6.54 Effect of Non-Uniform Base Excitation on Shear Key Force for Different Soil Types

6.13 DUCTILE SHEAR KEY DESIGN FOR IN-SPAN HINGES

In contrast with the elastic shear key design that ensures the shear key remains elastic in the event of the design earthquake, a ductile shear key design allows for yielding of the shear keys. For ductile shear keys, the performance measure may be in terms of the maximum relative displacement of the adjacent frames and the residual relative displacements. Currently two approaches are implemented for the design of multi-frame bridges. 1) Frames are designed assuming a full transverse integrity of the frames. For that, the shear key needs to be designed to remain intact. 2) Frames can be designed as individual structures ignoring the shear key and transverse integrity. This approach is suggested by SDC when T1/T2 < 0.7 sec. For the latter case, a nominal shear key may be provided to preserve the integrity only under service level seismic events. In this study, only the first approach has been considered.

The concept of the ductile shear key is briefly studied through the analysis of all of the prototypes with yielding shear keys, open gaps, and biaxial ground motions. The yielding capacity of the shear key was taken to be equal to the maximum of the adjacent bents' capacities (overstrength shear). The modeling of the ductile shear key was explained in Chapter 4. In Sec. 6.11, it was demonstrated that the median ratio of the maximum shear key force to the plastic shear demand of the adjacent is approximately 0.9 and 0.8 for the single-column and two-column systems, respectively. Therefore, it can be expected that more than 50% of shear keys remained elastic in the recent analysis. Figure 6.55 shows a representative sample of the response of the ductile shear keys for single-column prototype F1-V1 under ground motion #27 (D33). To assess the bridge performance with ductile shear keys, three matrices are studies: 1) the maximum relative displacement at the hinges; 2) the residual relative displacement at the hinges; and 3) the displacement ductility demands of the columns.

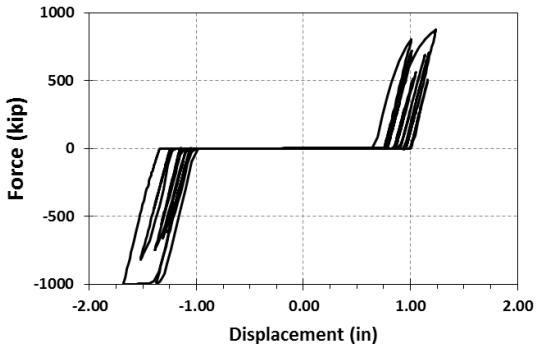

Figure 6.55 Force-Displacement Response of Ductile Shear Key

The distribution of the maximum relative transverse displacement at the hinges is shown in Figure 6.56. The median relative displacement is approximately 1.35 in, where 1.0 in. of this displacement is the initial gap opening, and the remaining 0.35 in. is related to the maximum plastic deformation of the ductile shear key. This is a reasonable and small deformation.

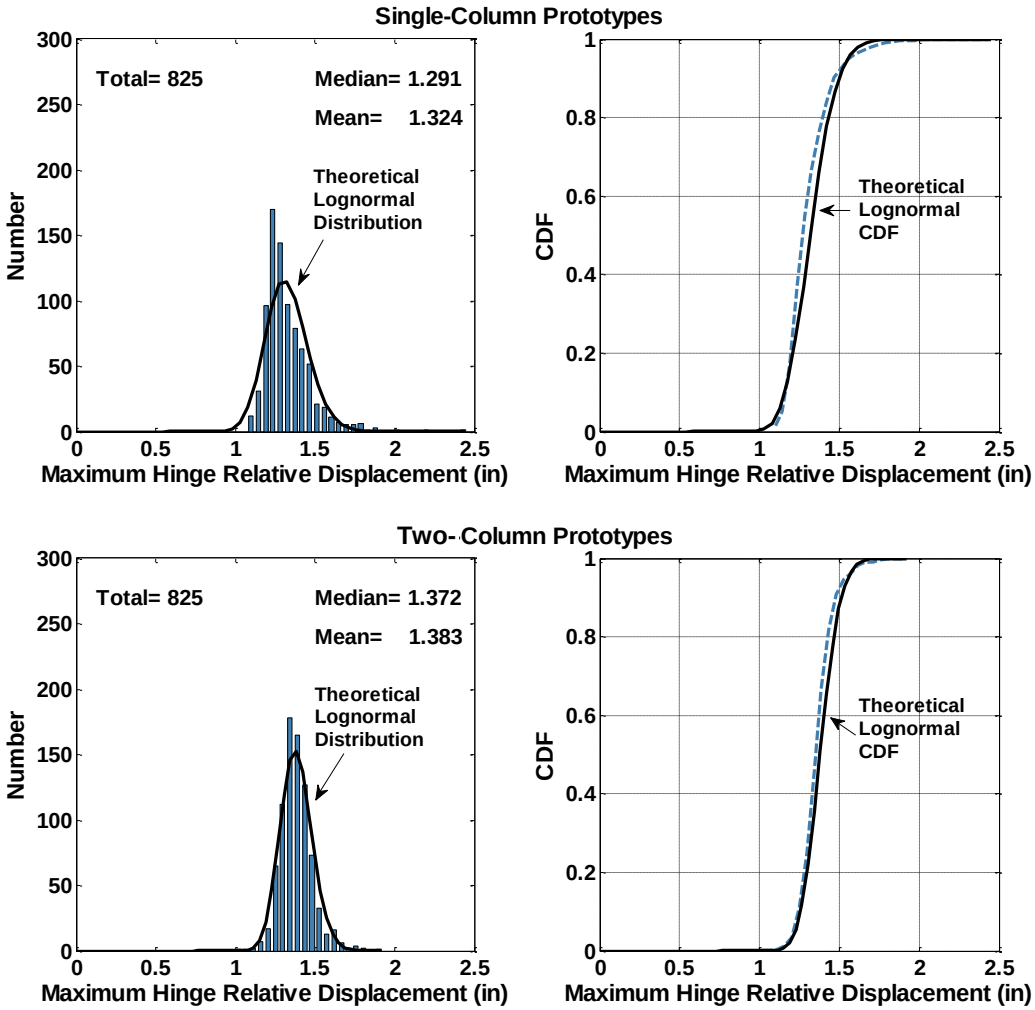

Figure 6.56 Distribution and CDF of the Maximum Hinge Relative Displacement with Ductile Shear Key

The distribution of the residual relative displacement at the hinges is shown in Figure 6.57. To find this value, the analysis was continued 2.0 sec. after the end of the ground motion duration. The residual transverse deformations in the hinges are acceptable in terms of post-earthquake repair. Only a few cases have residual displacements larger than 1.0 in.

Finally, the maximum displacement ductility demand of the columns, in models with ductile shear keys, is compared with the results of the impact analysis. The change in the ductility demand was smaller than 10%. This can be attributed to the small plastic deformation of the shear keys and the correspondingly small change in the displacement of the columns. It can be concluded that a ductile shear key with a capacity equal to the adjacent bent's overstrength shear is able to preserve the integrity of the frames without any considerable change in bridge performance during and after an earthquake.

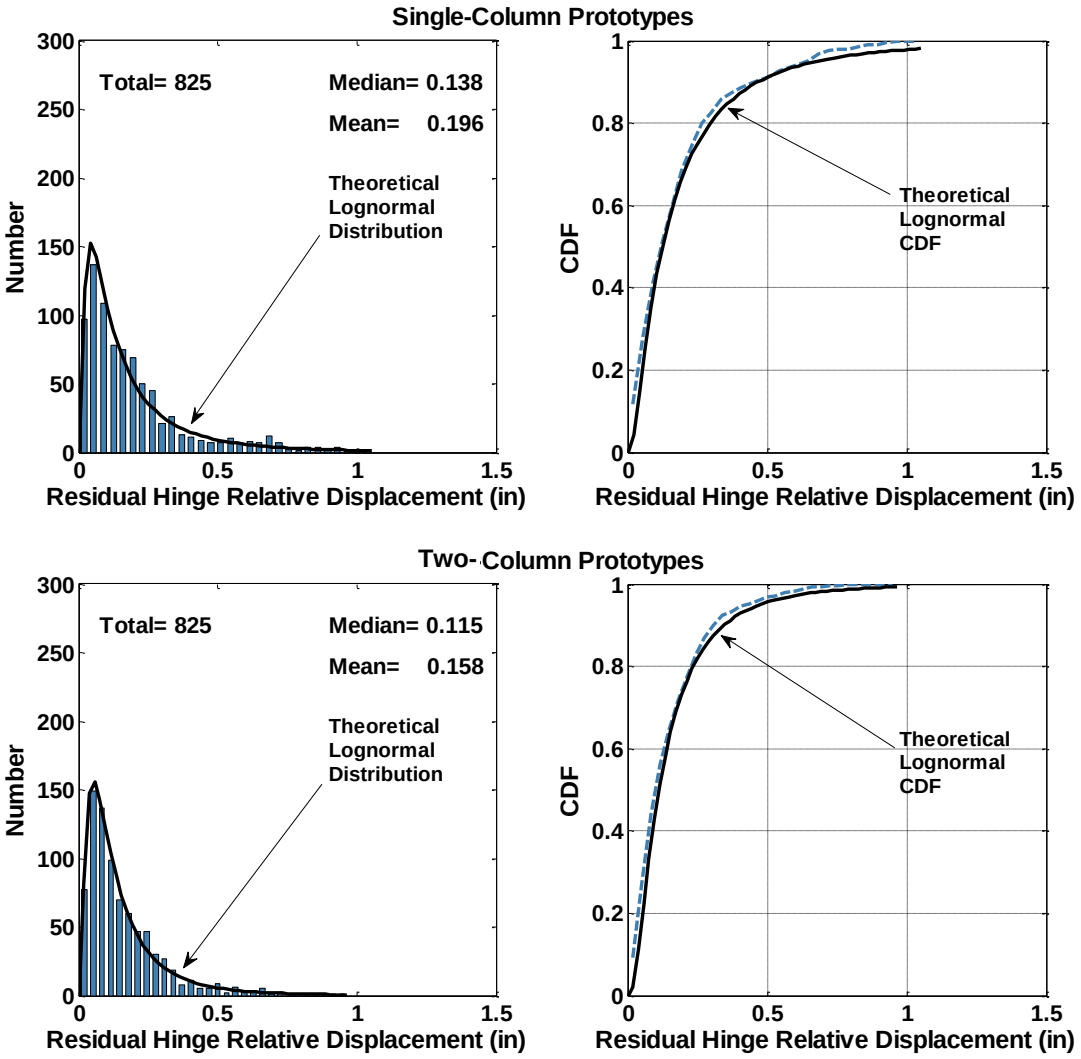

Figure 6.57 Distribution and CDF of Residual Hinge Transverse Relative Displacement with Ductile Shear Key

6.14 UPPER BOUND SHEAR KEY FORCE

As a simple design approach, in-span hinge shear keys are currently designed for a portion of the maximum expected transverse capacity (also known as the column overstrength shear, $V_o^{co\ l}$ in SDC, typically defined as M_o^{col} / L, SDC Sec. 2.3.2) of the two adjacent bents to the hinge. For the two-column bents, the bent capacity is the summation of the individual columns' capacities in the bent. The column overstrength shear is $1.2M_p^{col}$ divided by the length of the column, where M_p^{col} is the plastic moment of the column obtained from the bilinear moment-curvature relationship. For the single-column bents, the length of columns is the distance between the superstructure centroid and the mid-point of the plastic hinge.

The statistical distribution of the ratios of the NTH Shear Key Forces to the maximum overstrength shear of the two adjacent bents is presented in Figure 6.58. The medians of the data sets are approximately 0.9 and 0.8 for the single- and two-column bent prototypes with 200-ft spans, respectively. For these prototypes, the maximum shear key forces, including the impact effect, do not exceed two times the overstrength shear of the bent. However, for the 110-ft span prototypes the median ration is 1.5 and the maximum ratio may be as high as 3.5. Thus, the capacity of the bent may not be used to define the upper bound design force.

Figure 6.59 shows the distribution and CDF of the ratio of the maximum shear key force to the transverse overstrength shear of the weaker of the two adjacent frames. The distributions are fairly similar for all the prototypes. The median ratios are approximately 0.33 and the maximum ratios are approximately 0.8. The CFD graphs show that with a confidence higher than 95%, the ratio of the maximum shear key force to the transverse overstrength shear of the weaker frame is less than 0.75. In other words with a high level of confidence, it may be assumed that the maximum shear key force does not exceed 75% of the transverse overstrength shear of the weaker frame. Therefore, this matric may be suggested as an upper bound value for shear key force demands.

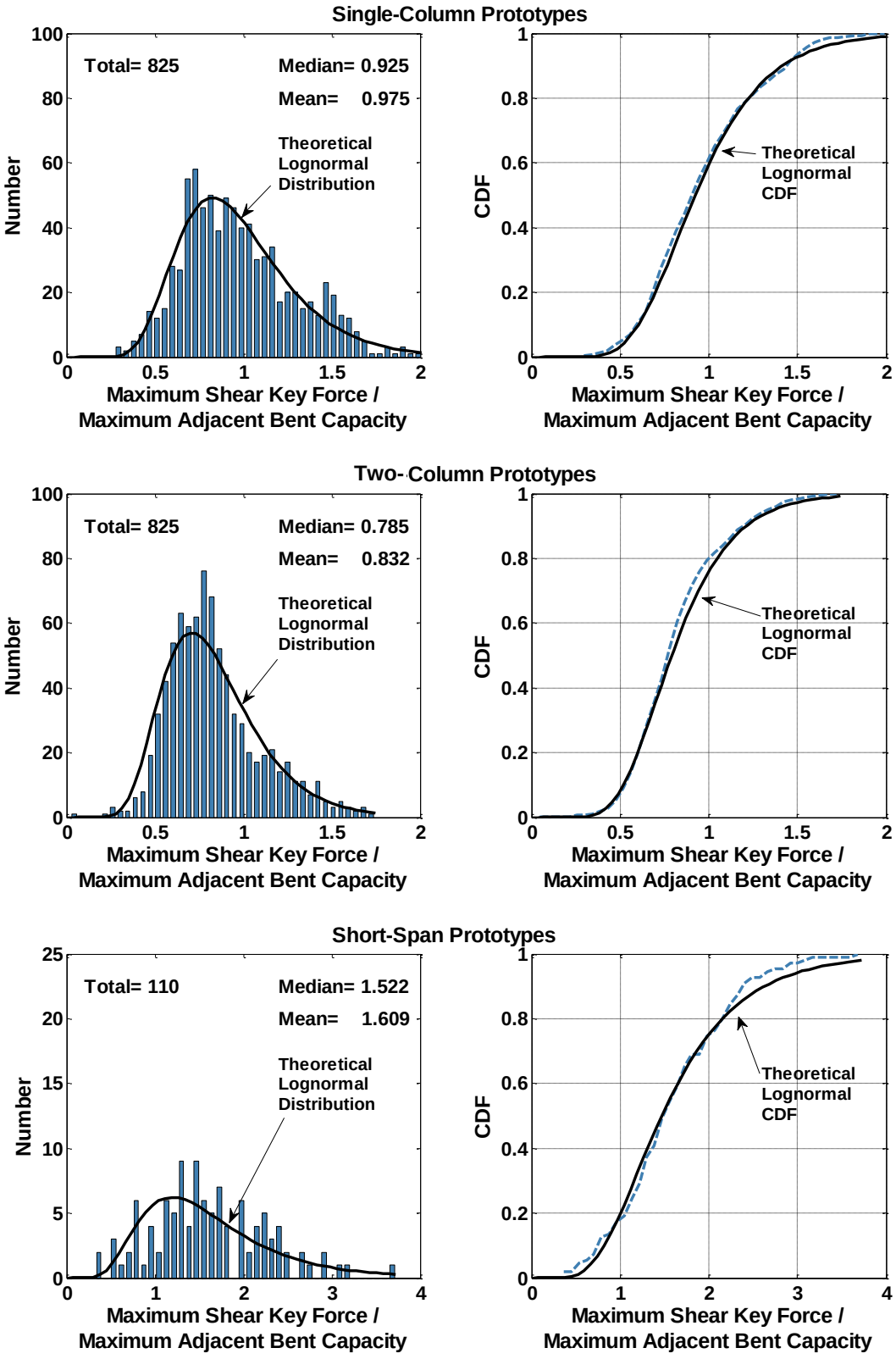

Figure 6.58 Distribution and CDF of the Ratio of the Reference Shear Key Force with Impact Effect to Capacity of the Bent Adjacent to the Hinge

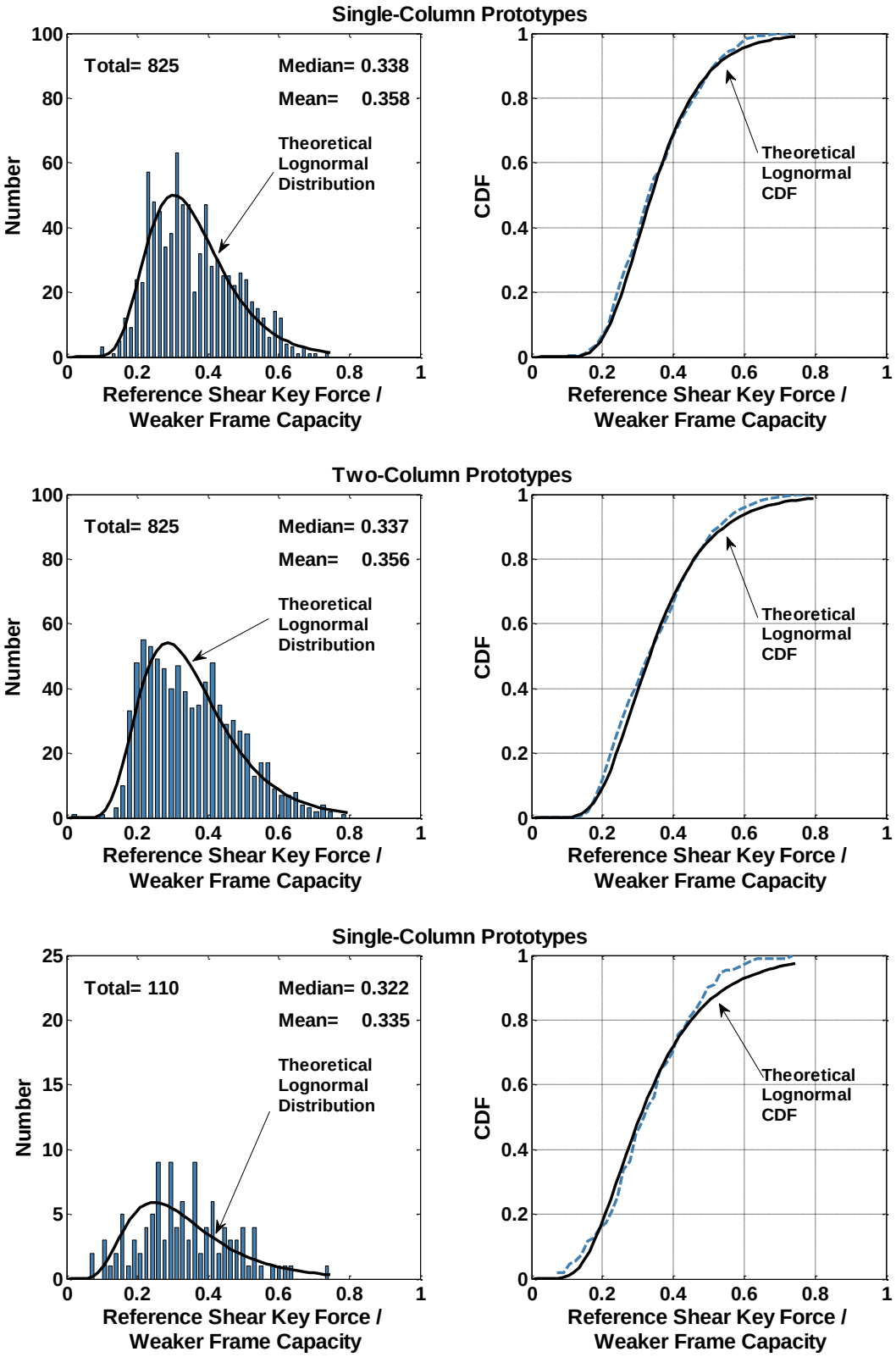

Figure 6.59 Distribution and CDF of the Ratio of Reference Shear Key Force with Impact Effect to the Transverse Capacity of the Weaker of two Adjacent Frames

6.15 DISPLACEMENTS OF LONGITUDINAL GAPS

It was discussed in Chapter 4 that transverse and longitudinal gaps are explicitly modeled. The opening/closure of the longitudinal gaps and the relative rotation of the adjacent frames about the vertical axis at the instant of peak shear key force are obtained. In addition, the maximum hinge opening regardless of shear key force is also obtained. All results are extracted from the "Impact Analysis," which incorporates active gaps and biaxial motion. The geometric mean of the results of three motions is considered as the Reference Responses.

The purposes of this investigation are as follows. 1) In Part 2 of this report it is shown that the capacity of the shear key varies by changing the longitudinal gap size. In order to estimate a reasonable longitudinal gap for which the capacity of the pipe shear key should be obtained. 2) To estimate the maximum longitudinal relative displacement at the hinge that shall be accommodated by bearings. Figure 6.60 demonstrates the maximum gap size along with the width of the superstructure (g_{max}), the minimum gap size along the width of the superstructure (g_{min}), and the rotation angle (α) at the in-span hinges. The initial gap size is selected as 2.0 in. for the abutments and the in-span hinges.

The statistical distributions of g_{max} and g_{min} are shown in Figure 6.61 and Figure 6.62, respectively. The mean g_{max} for both single-column and two-column systems is approximately 2.0 in., which is equal to the initial gap size, and the maximum value may be as large as 6.0 in. Figure 6.64 shows the statistical distribution of the relative rotations at the in-span hinges. The rotation in the two-column system is notably smaller than the rotation in the single-column system, which is mostly due to the presence of a wider superstructure. The maximum hinge rotation measured in both systems is approximately 0.004 rad. It should be noted that these results correspond to the instance of peak shear key force. The maximum values of hinge deformations are much larger. It should be remembered that, in Sec. 6.5.4, it was discussed that the peak shear key force does not necessarily occur at the maximum displacement. The absolute maximum hinge opening, regardless of shear key force, is given in Figure 6.64. The median displacement is approximately 5.0 in. and may be as large as 15 in. This relatively large displacement shall be considered in the design of the bearing systems.

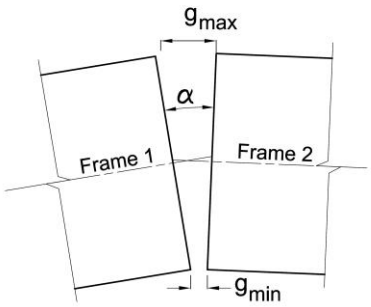

Figure 6.60 Hinge Deformation Plan at the Time of Peak Shear Key Force

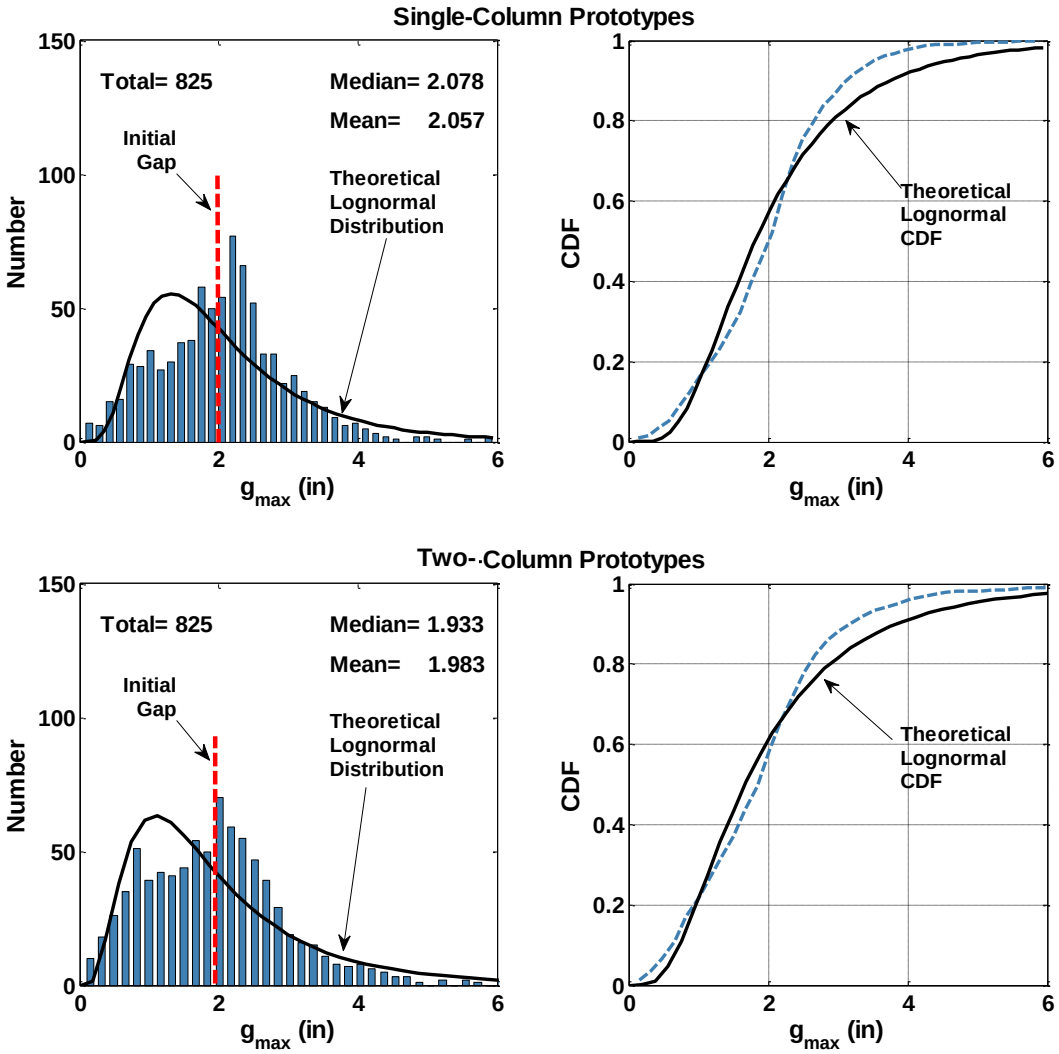

Figure 6.61 Distribution and CDF of Reference Hinge Maximum Opening at the Time of Peak Shear Key Force

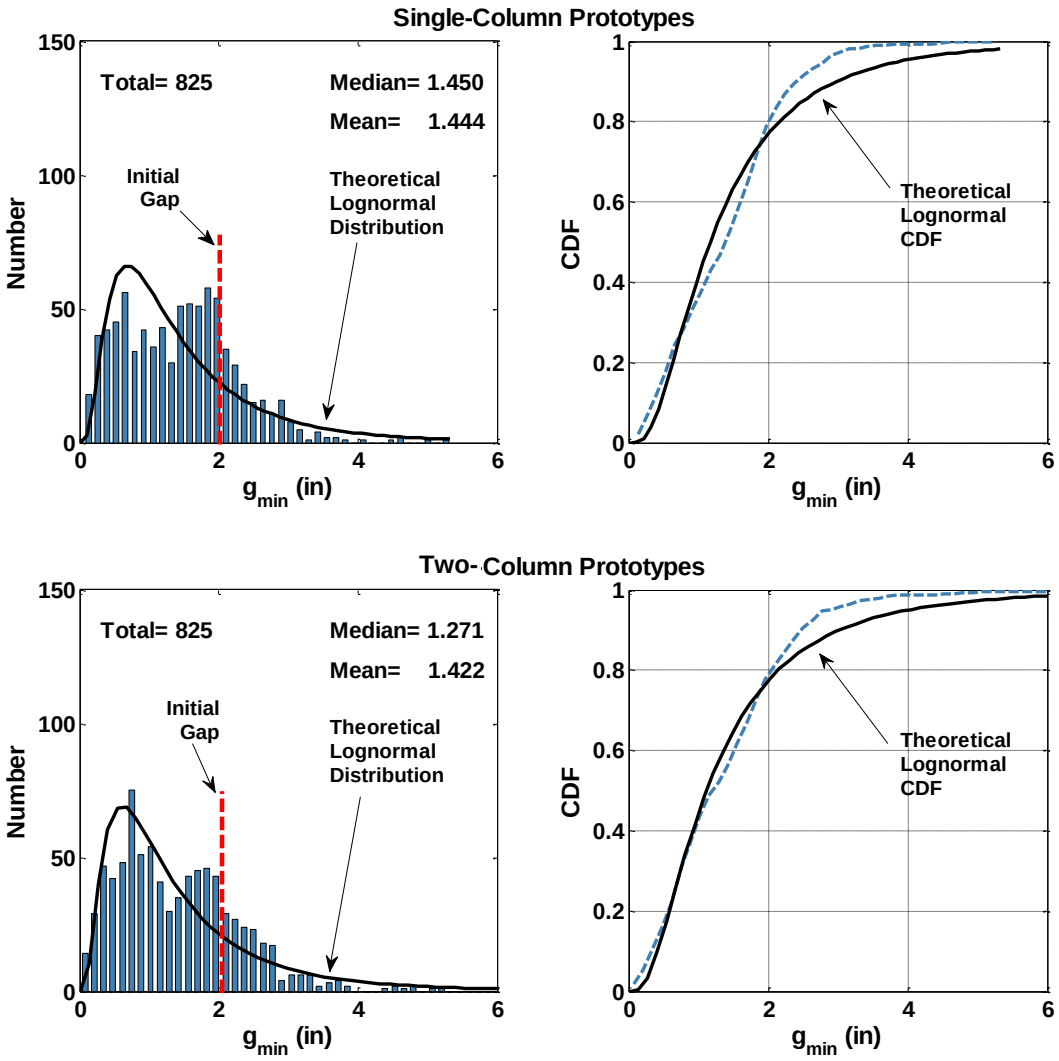

Figure 6.62 Distribution of Reference Hinge Minimum Opening at the Time of Peak Shear Key Force

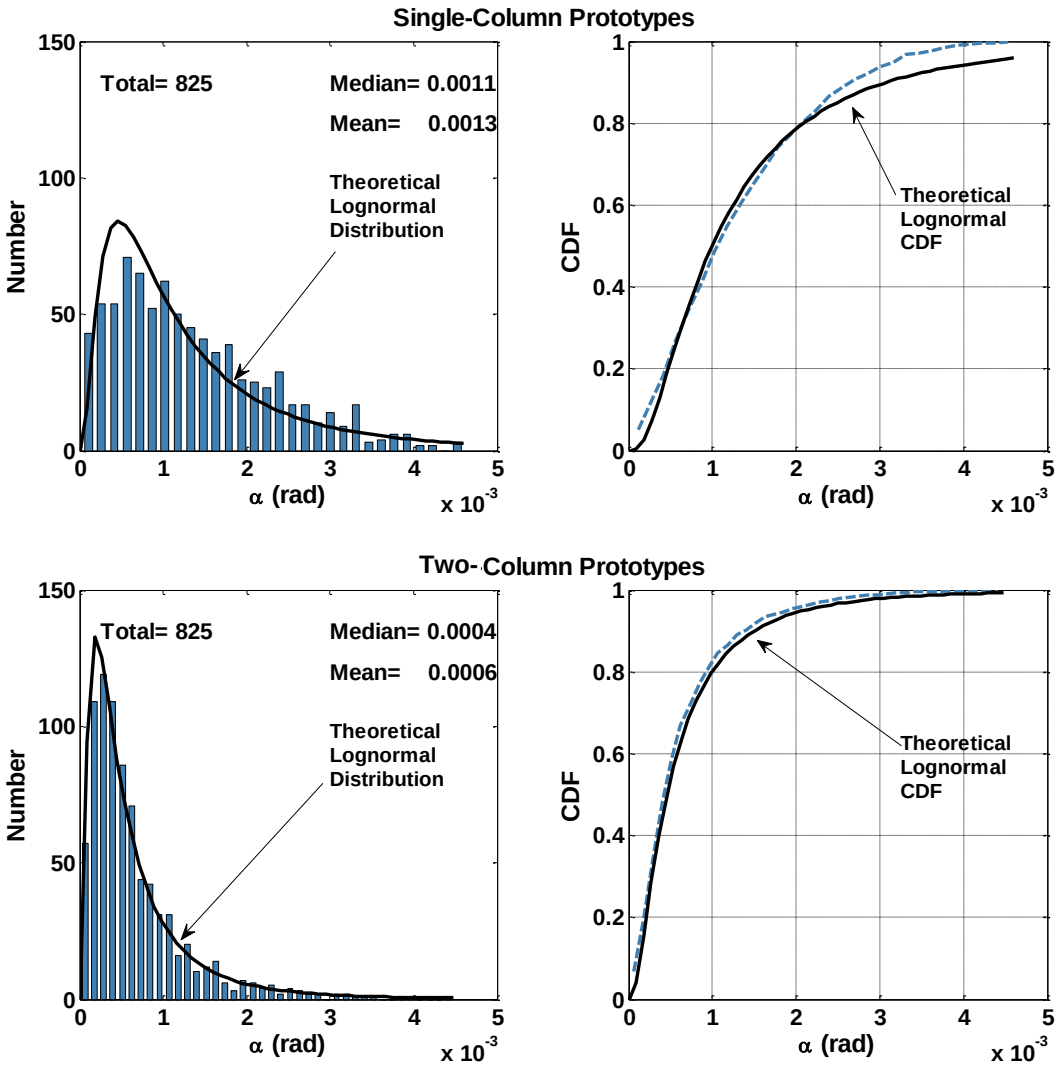

Figure 6.63 Distribution and CDF of Reference Hinge Rotation at the Time of Peak Shear Key Force

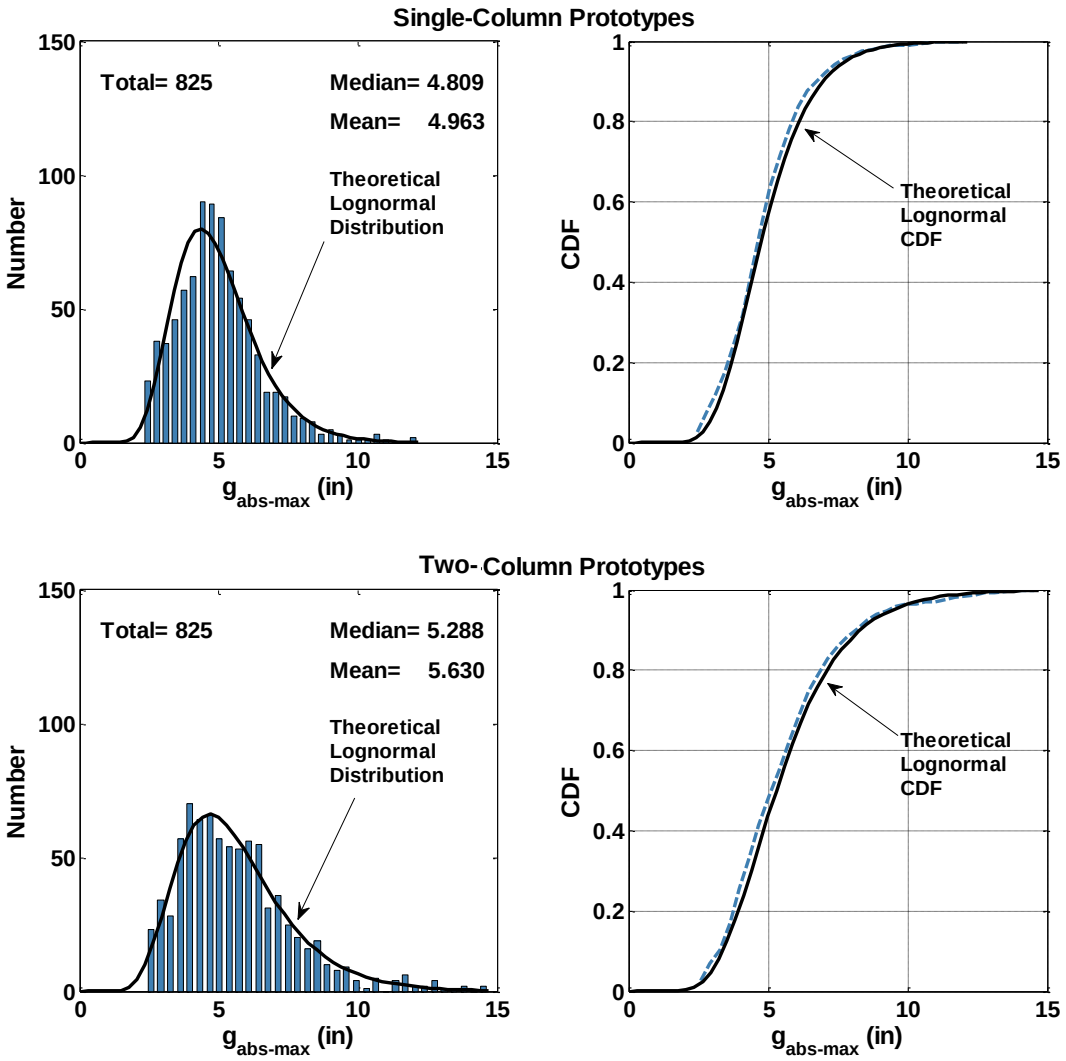

Figure 6.64 Distribution and CDF of Hinge Absolute Maximum Opening

7 Rational Analysis Method

A rational analysis method is proposed for the calculation of the seismic design forces of in-span shear keys in multi-frame bridges. This method is developed based on the concept of EDA. A methodology is advanced to modify elastic forces to account for nonlinear behavior in the transverse. The components of this method are presented in this chapter. The modification factors that are proposed to account for the effects of impact and non-uniform base excitation are discussed. An upper bound force is suggested. The final form of the proposed analysis method is presented in a format that is consistent with SDC V1.7. The bridge modeling considerations for the proposed method are presented. This chapter includes two comprehensive design examples.

7.1 GENERAL FORM OF THE PROPOSED ANALYSIS METHOD

The higher modes of vibration may participate significantly in shear key force demand. Thus, an analysis method that does not include effect of higher modes may yield inaccurate shear key force demands. Several possible analysis methods are studied through this research project. This study proposes a reliable method for modifying the EDA forces. This method is named as “MEDA” or Modified EDA. Compared to other analysis approaches, MEDA yields accurate shear key forces. It is proposed that the ultimate seismic force demands on in-span shear keys (V_u^{sk}) are calculated using the relationship given in Eq. 7.1.

$$V_u^{sk} = \text{Factor 1} \times \text{Factor 2} \times V_{MEDA}^{sk} \quad \text{Eq. 7.1}$$

where:

Factor 1*:* Impact Factor

Factor 2: Non-uniform Base Excitation Factor

V_{MEDA}^{sk}*:* Shear Key Force from MEDA Method

7.2 THE MEDA ANALYSIS METHOD

In Chapter 6, it was discussed that the modification of EDA force with a single scalar or using a nonlinear design spectrum leads to an unreliable and non-conservative estimation of the shear key force demands. Therefore, the concept of MEDA proposes modification of modal forces individually. In this method, the modal shear key forces are modified by the displacement ductility ratio of the corresponding mode. Modified modal shear key forces are then combined using conventional modal combination methods.

7.2.1 Modal Ductility

The concept of modal displacement ductility ($\mu_{D,n}$) is developed in this study to enable the estimation of forces in a nonlinear system. It considers the nonlinear responses at higher modes. Eq. 7.2 is proposed for the values of modal ductility.

$$\mu_{D,n} = max\left|\Delta_{(i)D,n}/\Delta_{(i)Y}^{col}\right| \geq 1.0 \quad \text{Eq. 7.2}$$

where $\Delta_{(i)D,n}$ is the contribution of the ***n*th mode of vibration** to the global displacement of the ***i*th column,** in the transverse direction. $\Delta_{(i)Y}^{col}$ is the transverse yield displacement of the *i* th column (SDC Sec. 2.2.4). These parameters are illustrated in Figure 7.1. Where $\Delta_{(i)D,n}$ is smaller than $\Delta_{(i)Y}^{col}$, modal displacement ductility shall be taken as 1.0.

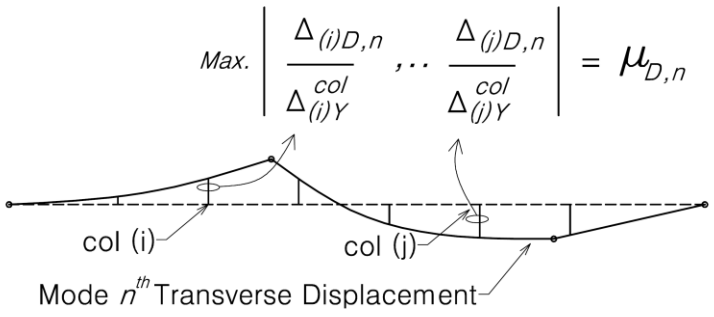

Figure 7.1 Obtaining the Value of Modal Displacement Ductility

7.2.2 Modified Modal Shear Key Force

Elastic modal shear key force is divided by the corresponding modal displacement ductility to obtain the modified modal shear key force. The concept of reducing elastic forces with displacement ductility ratio is consistent with the concept of the equivalent displacement method (EDM). For mid-range period structures, the force reduction factor is assumed proportional to the inverse of the displacement ductility ratio. The equivalent displacement method is valid for bridges with a fundamental period of vibration between 0.7 sec. and 3.0 sec. (Caltrans, 2010).

7.2.3 Modal Combination of Modified Modal Forces

Modified modal shear forces shall be combined to obtain the MEDA shear key force, V_{MEDA}^{sk}. Both SRSS and CQC methods are studied. The CQC method is more accurate. The SRSS method is still acceptable as an easy to implement method. It is found that modes of vibration with frequencies as high as 10Hz to15 Hz may contribute to the shear key force. Thus, the minimum number of considered modes, *m*, is suggested to be the number of the modes with a period smaller than 0.05 sec.

7.2.4 Validation of the Results with the NTH Method

Figure 7.2 and Figure 7.3 show a comparison of the shear key forces estimated using the MEDA method, V_{MEDA}^{sk}, and the Reference Shear Key Forces obtained from the nonlinear time history analyses of all the prototype bridges. V_{MEDA}^{sk} is obtained using the design ARS spectrum. The correlation coefficient of approximately 0.9, is comparable with the values obtained for the correlation of EDA displacements and NTH displacements, as discussed in Sec 6.4.1. This confirms that the accuracy of the proposed method in estimating the shear key force demands is comparable with the accuracy of the EDA method in estimating the global displacement demands.

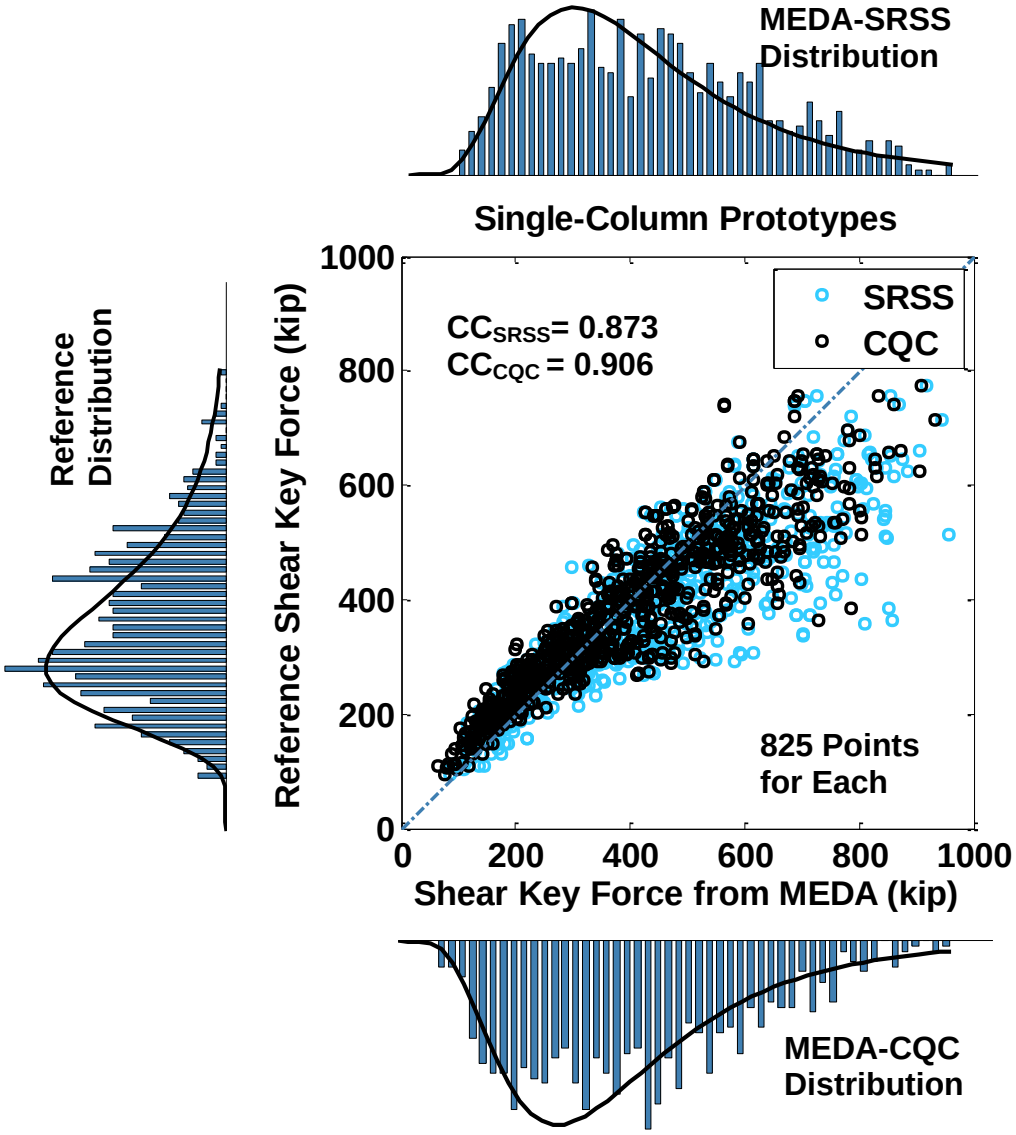

Figure 7.2 Distribution and Correlation of MEDA Forces using Design ARS with Reference Shear Key Forces for All Single-Column Prototypes

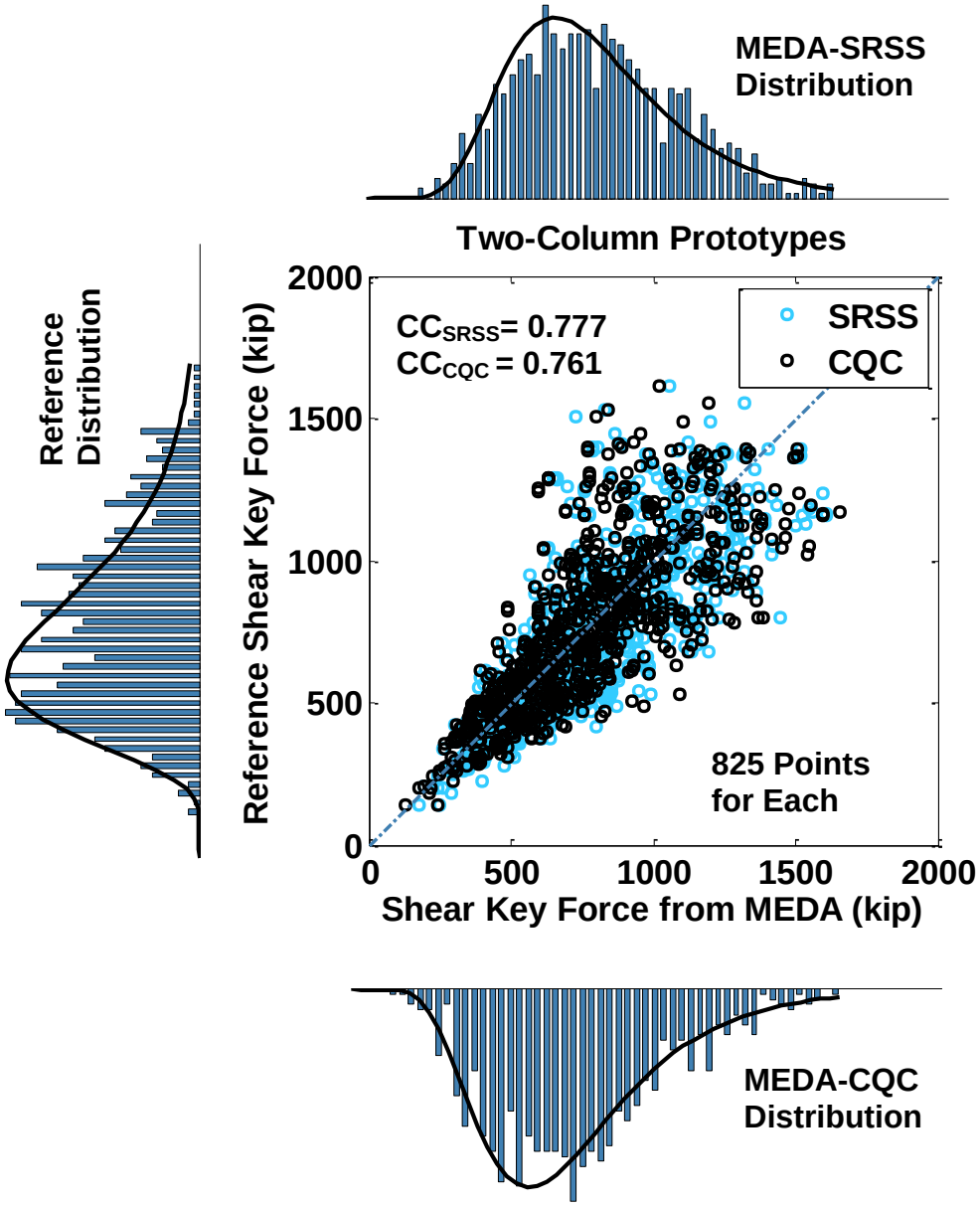

Figure 7.3 Distribution and Correlation of MEDA Forces using Design ARS with Reference Shear Key Forces for All Two-Column Prototypes

7.3 MODIFICATION FACTORS

Two modification factors are proposed in the analysis formulation. Factor 1 accounts for the increase in shear key forces due to the transverse and longitudinal pounding. Factor 2 include the amplifying effects of non-uniform base excitation.

7.3.1 Effect of Pounding

The discussion on the impact forces caused by transverse gap closure is presented in Sec. 6.11. Because of the complexity of the impact phenomenon, developing an exact formulation to estimate the impact forces is impractical. Based on the results from the NTH analysis, an impact factor equal to 2.5 is proposed for the single pile-shaft and the two-column long-span bridges, as well as for the short-span bridges. Figure 7.4 shows the correlation of the amplified V_{MEDA}^{sk} with the Reference Shear Key Forces from impact analysis. The design ARS's are used in the MEDA method.

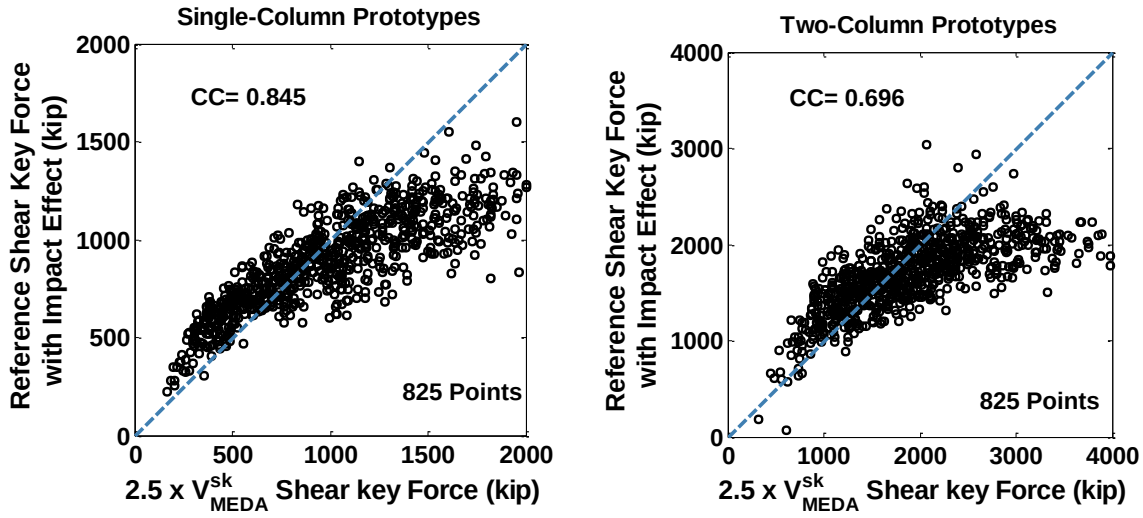

Figure 7.4 Correlation of Design Force with NTH Shear Key Force Including Impact Effect

7.3.2 Non-Uniform Base Excitation

The effect of non-uniform base excitation on shear key forces is discussed in Sec. 6.12. Amplification factors of 1.0 for soil Type A and B and 1.25 for soil Type C, D, and E are suggested to be applied to V_{MEDA}^{sk}.

7.4 UPPER BOUND FORCE

According to SDC 1.7, the upper bound force for in-span shear keys is equal to the smaller of the transvers capacities of the adjacent frames. This study presented that the maximum shear key forces, including the impact effect, do not exceed 75% of the

transverse capacity of the weaker of the adjacent frames. The 75% of the capacity of the weaker proposed as an upper bound for the shear key design force.

7.5 PROPOSED ANALYSIS METHOD

The ultimate seismic shear demand for in-span hinge shear keys shall be calculated using Eq. 7.3.

$$V_u^{sk} = \text{Factor 1} \times \text{Factor 2} \times V_{MEDA}^{sk} \leq V_{up}^{sk} \qquad \text{Eq. 7.3}$$

$$V_{MEDA}^{sk} = \left[\sum_{n=1}^{m}\left(V_n^{sk}/\mu_{D,n}\right)^2\right]^{1/2} \quad \text{(SRSS Method)} \qquad \text{Eq. 7.4a}$$

or

$$V_{MEDA}^{sk} = \left[\sum_{n=1}^{m}\sum_{l=1}^{m} C_{nl}\left(V_n^{sk}/\mu_{D,n}\right) \times \left(V_l^{sk}/\mu_{D,l}\right)\right]^{1/2} \quad \text{(CQC Method)} \qquad \text{Eq.7.4b}$$

where V_n^{sk} is the modal shear key force obtained from the n^{th} mode of vibration using the design ARS, m is the mode number associated with the period of 0.05 sec, and C_{nl} is the modal response correlation coefficient between modes n and l, in the CQC method.

$$\mu_{D,n} = max\left|\Delta_{(i)D,n}/\Delta_{(i)Y}^{col}\right| \geq 1.0 \qquad \text{Eq. 7.5}$$

where $\Delta_{(i)D,n}$ is the global system displacement of the i^{th} column in the transverse direction due to the n^{th} mode of vibration, $\Delta_{(i)Y}^{col}$ is the idealized yield displacement of the i^{th} column (SDC Sec. 2.2.4).

$$\text{Factor 1} = 2.5 \qquad \text{Eq. 7.6}$$

$$\text{Factor 2} = \begin{cases} 1.0 & \text{Soil Type A , and B} \\ 1.25 & \text{Soil Type C, D, and E} \end{cases} \qquad \text{Eq. 7.7}$$

$$V_{up}^{sk} = 0.75 \times min\left(V_o^{Left\ Frame}, V_o^{Right\ Frame}\right) \qquad \text{Eq. 7.8}$$

where V_o^{frame} is the summation of the transverse over strength shear capacities (SDC Sec. 2.3.2.1) of the columns in each frame.

7.6 MODELING AND ANALYSIS CONSIDERATIONS

To calculate shear key force demands based on the proposed design method, the following structural modeling and analysis requirement should be considered. The modeling and analysis method is consistent with the SDC provisions; however, some minor modifications are needed.

Modeling of Bridge Structure: An elastic model similar to what is used for estimating design displacements may be used for the MEDA method with the following considerations:

1) The superstructure shall be divided into a minimum of five segments in each span in order to capture higher mode effects.
2) To read the shear key forces, a short-length “dummy element” needs to be modeled connecting adjacent frames. A flexural and axial hinge shall be assigned to one end of this element, while torsion and shear stiffnesses remain engaged. The modal shear force outputs from this element are used in the proposed method. **The shear force values read from the adjacent superstructure segments cannot be used because of the inertial forces on diaphragms.**
3) Masses shall be assigned to the nodes for the six degrees of freedom. Ignoring the rotational and torsional masses of the superstructure leads to incorrect estimation of shapes and frequencies of higher modes. The diaphragms and bent caps are massive members. They largely affect the shear key force response. The mass of the diaphragms should be assigned to the nodes at each end of the dummy element.
4) For bridges with more than five frames, sub models with boundary frames may be used in accordance with SDC Sec.5.3.
5) Effective section properties according to SDC Sec.5.6 shall be assigned to column and superstructure elements.
6) The abutments shall be modeled as transversely restrained. Modeling the abutments as springs (per SDC 1.7 Sec. 7.8.2) may lead to non-conservative in-span shear key forces.

Analysis of Bridge Structure Model: Elastic Dynamic Analysis (EDA), in accordance with SDC1.7 Sec. 5.2.2, shall be performed in the transverse direction with the following considerations:

1) All the modes of vibration with periods larger than 0.05 sec. shall be considered for modal analysis. The target mass participation of 90% is not adequate for estimating shear key force demands.

2) Both the shear key forces and displacements associated with all the modes shall be extracted from the model to enable implementation of the method.

7.7 DESIGN EXAMPLES

Two examples are presented in this section to demonstrate the proposed analysis method. The configurations of the example bridges are different from the prototypes used in the analytical studies for cross-referencing validation.

7.7.1 Example Bridges Configurations

Both examples are three-frame bridges, shown in Figure 7.5. Column heights are different for each frame. Example 1 is a single-column and Example 2 is a two-column bent bridge, as shown in Figure 7.6. Columns heights are given in Table 7.1 for both example bridges. All other specifications, including the superstructure dimensions, the location of in-span hinges, hinge and abutment details, bent caps, as well as dead loads are assumed the same as those of the prototype bridges explained in Chapter 3.

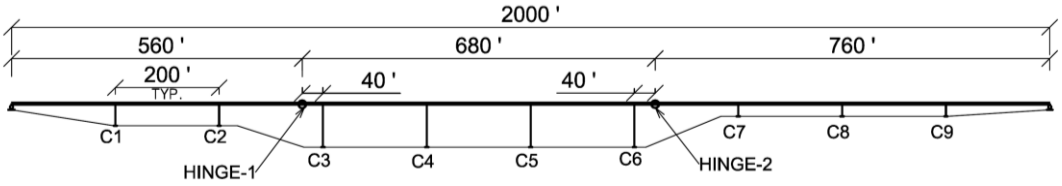

Figure 7.5 Elevation for Example Bridges

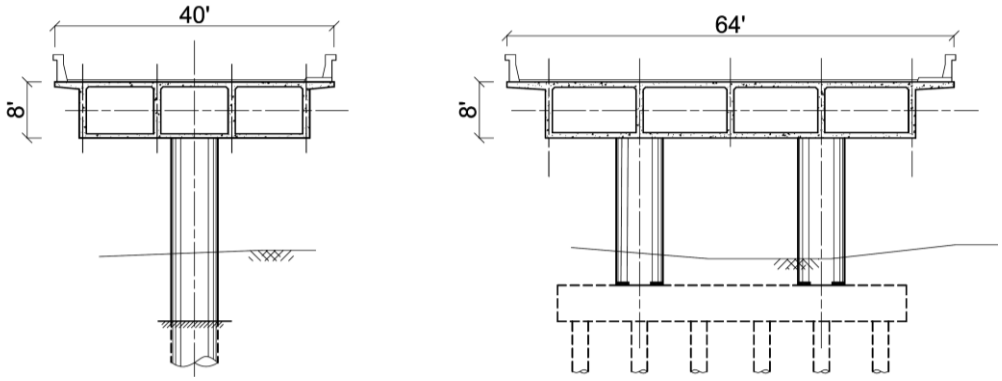

Figure 7.6 Sections a) Example 1and b) Example 2

Table 7.1 Example Bridges Columns Height (feet)

#	Frame 1	Frame 2	Frame 3
Example 1	30* (66.6)**	40 (78.75)	20 (55.1)
Example 2	30 (39)	40 (49)	20 (32)

* Clearance height

** Total Height from the mid-height of the superstructure to the base or point of fixity

7.7.2 Hazard Level and Design Spectrum

The design spectrum is ARS-C33, which represents a severe hazard level. This spectrum represents magnitude of 7.75-8.25 (Level 3) and a PGA of 0.6g on soil Type C. The design spectrum and the spectrums of the three matched ground motions are shown in Figure 7.7. The bridges are designed for the specified ARS following SDC. These motions are implemented for the NTH analyses of the example bridges. The ARS spectrum is used in the MEDA methods. The shear key force obtained using the proposed analyses method is compared with the average of the values from the three NTH analyses. The specifications of the ground motions are presented in Table 3.3.

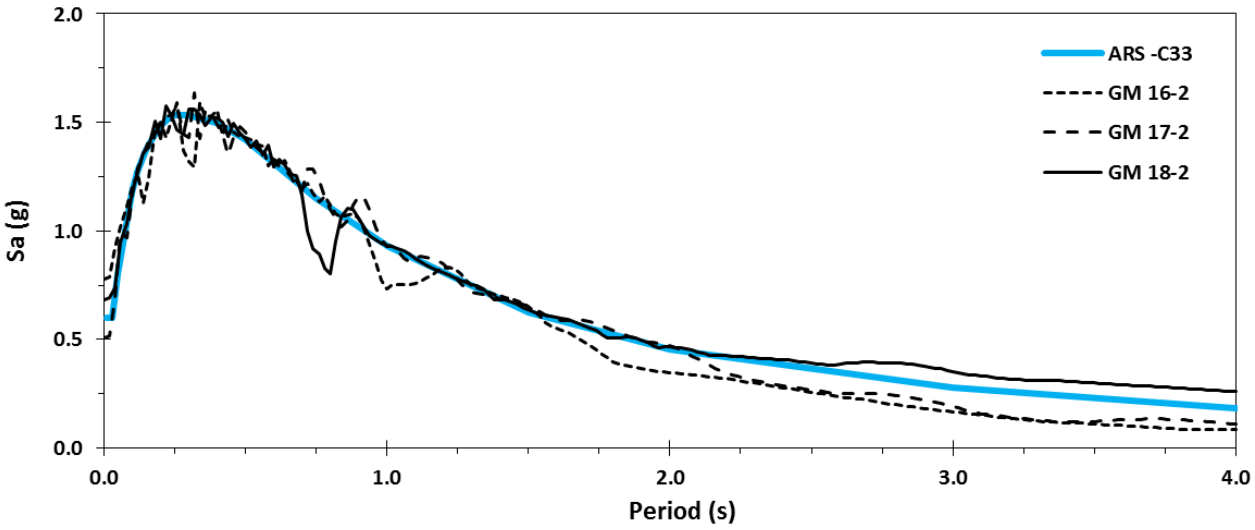

Figure 7.7 Design and Three Ground Motions Response Spectrums

7.7.3 Example 1

The bridge is designed according to SDC V1.7 with the same method discussed in Chapter 5. The design results are summarized in Table 7.2.

Table 7.2 Columns Design, Example 1

Description	Frame 1	Frame 2	Frame 3
Diameter (in)	102	102	102
Longitudinal Reinforcement Ratio (%)	1.4	2.8	1.0
Transverse Reinforcement Ratio (%)	1.0	1.0	1.0
I_{eff} / I_g	0.364	0.540	0.311
D_Y^{col} **(in)**	15.71	22.83	10.32
Design Ductility Demand	2.3	1.65	1.80
V_o^{frame} **(kip)**	1972	5084	2928

SAP2000 15.1.0 (CSI, 2011) is used for modeling and conducting the EDA analysis of the example bridges (Figure 7.8). The modeling and analysis considerations of Sec. 7.6 are incorporated. The three analysis cases are defined in the following ways: 1) Dead, 2) Modal, and 3) Response Spectrum, which are named as “DEAD”, “MODAL” and “EDA-ARS-D33”, respectively.

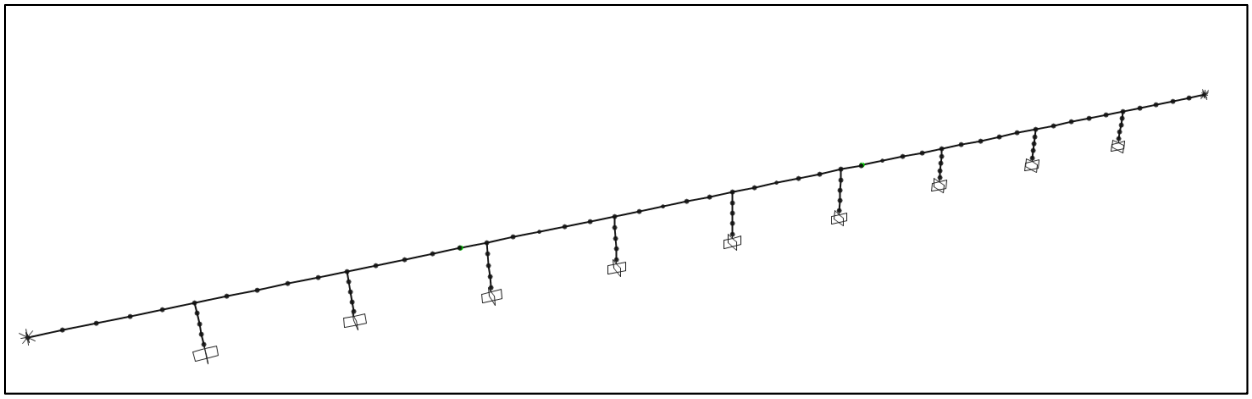

Figure 7.8 Analytical Model of Example1 using SAP2000

After running the analyses, the first step is finding the modal ductility values. For this purpose, the nine column nodes are selected. Using the “Show Tables…” tab from the “Display” menu, two result tables of “Joint Displacements” and “Response Spectrum Modal Information” are recalled, as illustrated in Figure 7.9.

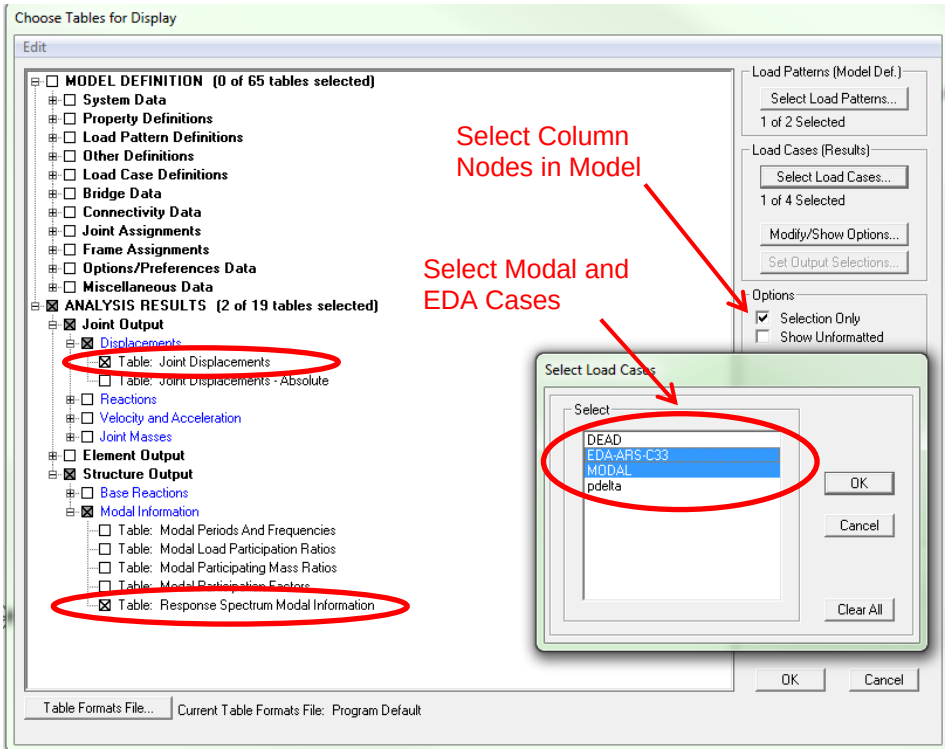

Figure 7.9 Extracting Modal Displacements from SAP2000 "Show Tables" Tab

From the "Joint Displacements" table, normalized mode shapes in the transverse direction (U2) are exported to a spreadsheet and organized as Table 7.3. This value is indicated by "$\boldsymbol{\varphi_D}$" in the table. Then, from the "Response Spectrum Modal Information" table, illustrated in Figure 7.9, the "U2Amp" for all modes is extracted and inserted into Table 7.3. This parameter is the same for all the nodes in the transverse direction. The global modal displacement demands of the i^{th} column are found using Eq. 7.9. This equation is based on the definition of the parameters in SAP2000 (CSI, 2013). The mode shape values, $\boldsymbol{\varphi_D}$, are unit-less and shall be multiplied by "U2Amp" scalar to obtain the modal displacements. Then modal ductility is calculated using Eq. 7.5, given the yield displacement for each column.

$$\Delta_{(i)D,n} = \text{U2Amp} \times \phi_D \qquad \text{Eq. 7.9}$$

Table 7.3 Finding Modal Ductilities, Example1

			Col. 1		Col. 2		Col. 3		Col. 4		Col. 5		Col. 6		Col. 7		Col. 8		Col. 9	
Mode	Period (sec)	U2Amp	φ_D	$\mu_{D,n}$	φ_D	$\mu_{D,n}$	φ_D	$\mu_{D,n}$	φ_D	$\mu_{D,n}$	φ_D	$\mu_{D,n}$	φ_D	$\mu_{D,n}$	φ_D	$\mu_{D,n}$	φ_D	$\mu_{D,n}$	φ_D	$\mu_{D,n}$
1	2.49	211.6	-0.05	0.64	-0.10	1.37	-0.15	**2.04**	-0.15	1.40	-0.14	1.33	-0.13	1.19	-0.08	1.65	-0.04	0.88	-0.02	0.39
2	2.09	16.72	0.06	0.07	0.12	0.13	0.15	0.16	0.04	0.03	-0.07	0.05	-0.17	0.12	-0.13	0.20	-0.07	0.12	-0.03	0.06
4	1.48	53.65	0.07	0.24	0.09	0.31	0.04	0.12	-0.11	0.26	-0.13	0.31	-0.03	0.07	0.11	0.58	0.18	0.95	0.14	0.70
...	**Other Modes are Elastic**																			

In this example, only the first mode is inelastic with a modal ductility of 2.04, and the other modes remain elastic. The next step is finding the modal shear key forces. For this purpose, the two shear key elements in the model are selected. This piece of data is obtained from the "Element Forces - Frames" table in SAP2000, as shown in Figure 7.10.

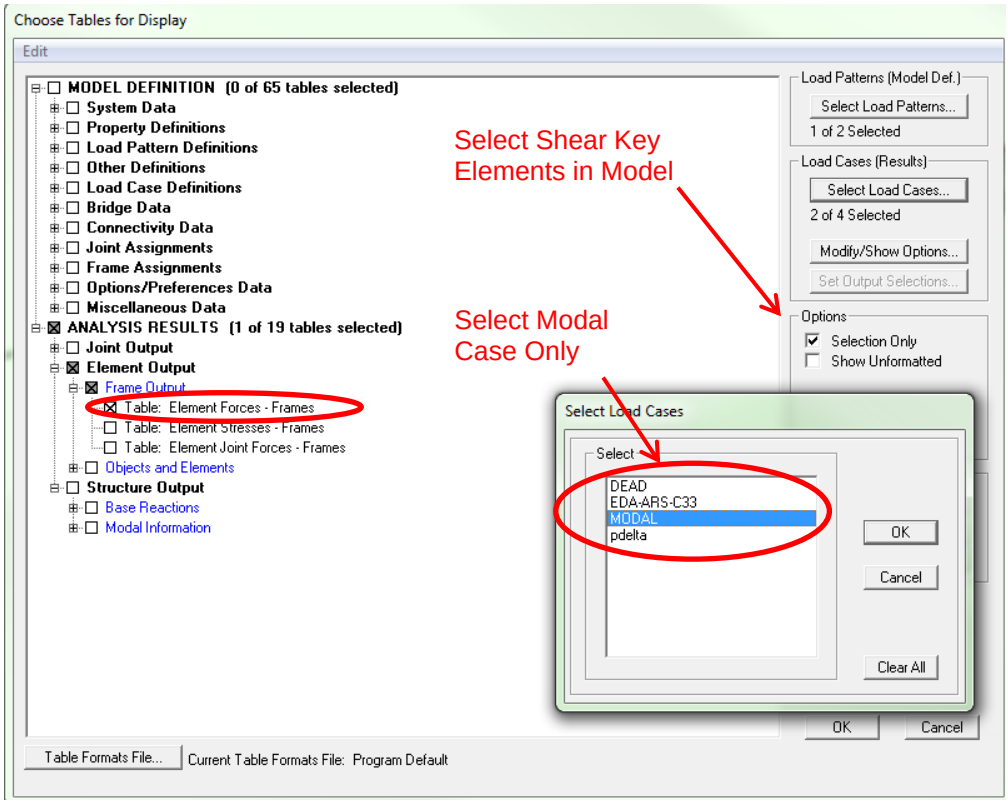

Figure 7.10 Extracting Modal Forces from SAP2000 "Display Tables" Menu

Then the "V3" response (transverse shear) for each shear key is exported to another spreadsheet and indicated by "$\boldsymbol{\varphi_V}$" in Table 7.4. Again, one should note that $\boldsymbol{\varphi_V}$ is unit-less. Modal shear key forces, V_n^{sk}, are calculated using Eq. 7.10, in which "U2Amp" is the same value that is obtained in the previous step (this value is applicable to both displacement and force responses in transverse direction (CSI, 2013)).

$$V_n^{sk} = \text{U2Amp} \times \phi_V \qquad \text{Eq. 7.10}$$

The value of V_{MEDA}^{sk} is calculated using SRSS method to combine the modified spectral shear key forces. Finally, the ultimate design force of the shear keys, V_u^{sk}, is calculated in Table 7.5 for in-span Hinges 1 and 2.

Table 7.4 Modal Shear Key Forces, Example 1

			Hinge 1			Hinge 2		
Mode	**U2Amp**	$\mu_{D,n}$	φ_V	V_n^{sk} (kip) (U2Amp×φ_v)	$V_n^{sk}/\mu_{D,n}$	φ_V	V_n^{sk} (kip) (U2Amp×φ_v)	$V_n^{sk}/\mu_{D,n}$
1	211.7	2.04	-1.7	-353.1	**-173.2**	0.3	64.1	**31.5**
2	16.7	1.0	-3.8	-63.7	**-63.7**	-2.0	-34.0	**-34.0**
4	-53.7	1.0	7.6	-407.6	**-407.6**	-6.4	344.6	**344.6**
6	5.2	1.0	11.8	61.9	**61.9**	-6.0	-31.7	**-31.7**
8	23.3	1.0	1.6	37.5	**37.5**	10.3	240.8	**240.8**
11	6.3	1.0	13.6	85.6	**85.6**	39.5	248.4	**248.4**
15	-3.5	1.0	-64.8	228.3	**228.3**	-42.0	147.7	**147.7**
19	-2.4	1.0	87.9	-212.4	**-212.4**	-35.6	86.1	**86.1**
22	-1.5	1.0	-11.6	17.8	**17.8**	108.4	-165.8	**-165.8**
23	4.6	1.0	20.4	93.4	**93.4**	-39.6	-181.3	**-181.3**
24	-0.5	1.0	-32.2	17.3	**17.3**	-15.8	8.5	**8.5**
27	0.5	1.0	-14.0	-6.9	**-6.9**	-14.6	-7.3	**-7.3**
28	0.1	1.0	177.6	12.7	**12.7**	-178.2	-12.7	**-12.7**
29	-0.1	1.0	-36.6	2.3	**2.3**	-0.9	0.1	**0.1**
30	0.2	1.0	20.8	4.4	**4.4**	1.3	0.3	**0.3**
31	-0.6	1.0	155.8	-91.9	**-91.9**	246.7	-145.4	**-145.4**
32	0.1	1.0	-16.2	-1.0	**-1.0**	-18.4	-1.1	**-1.1**
33	0.3	1.0	-288.5	-87.3	**-87.3**	-24.7	-7.5	**-7.5**
37	-0.1	1.0	-119.8	15.6	**15.6**	-171.5	22.3	**22.3**
39	0.1	1.0	-228.4	-32.7	**-32.7**	-295.5	-42.4	**-42.4**
46	0.0	1.0	16.2	-0.4	**-0.4**	75.2	-2.0	**-2.0**
48	-0.1	1.0	130.0	-17.1	**-17.1**	-392.9	51.7	**51.7**
50	-0.1	1.0	-745.8	82.6	**82.6**	235.3	-26.1	**-26.1**
55	0.0	1.0	-161.9	-1.8	**-1.8**	353.0	4.0	**4.0**
56	0.0	1.0	-198.5	-3.4	**-3.4**	510.7	8.7	**8.7**
58	0.1	1.0	-174.1	-9.5	**-9.5**	-531.0	-29.0	**-29.0**

Note: Modes with zero participation are excluded from table

Table 7.5 Design Shear Keys Forces from MEDA Method, Example 1

Description	**Shear Key at Hinge 1 (kip)**	**Shear Key at Hinge 2 (kip)**
V^{sk}_{MEDA} (Eq. 7.4a)	586	599
Factor 1 (Eq. 7.6)	2.5	2.5
Factor 2 (Eq. 7.7)	1.25	1.25
Factor 1 x V^{sk}_{MEDA}	1465	1498
Ultimate Design Force (Eq. 7.3)	**1831**	**1872**
Upper Bound Force (Eq. 7.8)	**1480 (governs)**	**2196**

For the NTH analysis and the cross checking of the EDA results for Example 1, OpenSees 2.4.4 is used. The modeling assumptions are the same as they were in Chapter 4. The mean shear key forces from the NTH analysis are indicated in Table 7.6. The shear key force without impact is comparable with V_{MEDA}^{sk} in the above table. The NTH analysis is performed with a uniform base excitation; hence, the design forces without Factor 2 are compared to the NTH forces.

Table 7.6 Comparing NTH and the Method Results, Example 1

Case	Hinge 1 Shear Key Force (kip)		Hinge 2 Shear Key Force (kip)	
	NTH	Method	NTH	Method
without Impact	527	586	460	599
with Impact	1155	1465	1002	1498

Note: Values do not include effect of NUBE (Factor 2)

7.7.4 Example – 2

A procedure similar to the one used for Example 1 is repeated for Example 2. Thus, only the calculation tables are presented.

Table 7.7 Column Design Results, Example 2

Description	Frame 1	Frame 2	Frame 3
Diameter (in)	90	90	90
Longitudinal Reinforcement Ratio (%)	1.2	2.0	1.0
Transverse Reinforcement Ratio (%)	1.0	1.0	1.0
I_{eff} / I_g	0.327	0.430	0.301
D_Y^{col} **(in)**	4.54	7.72	2.44
Design Ductility Demand	4.28	3.72	3.34
V_o^{frame} **(kip)**	3232	7108	5877

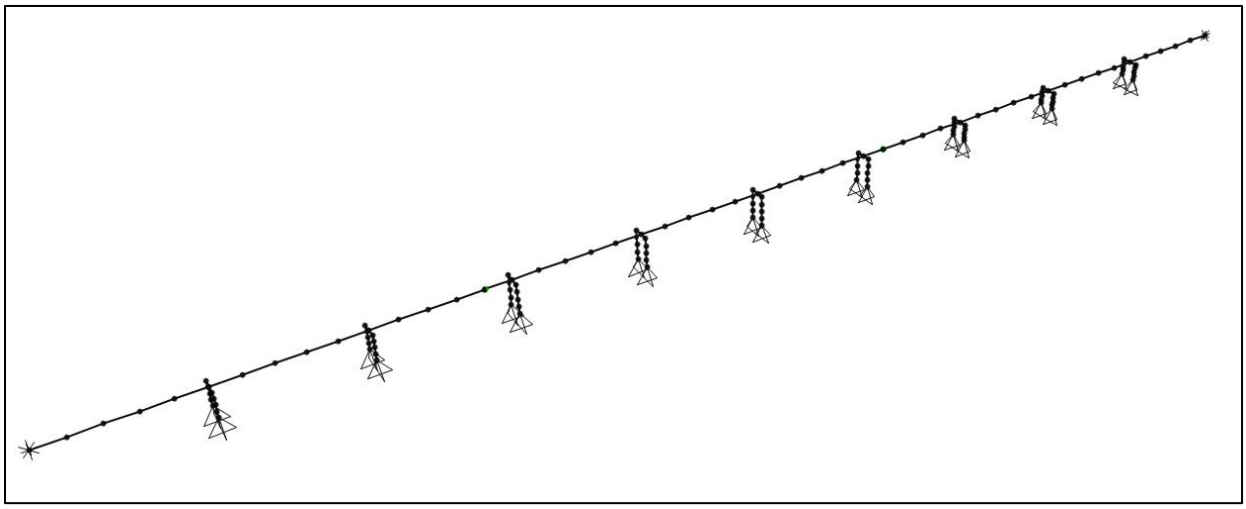

Figure 7.11 Analytical Model of Example-2 Using SAP2000

Table 7.8 Finding Modal Ductility, Example 2

			Col. 1		Col. 2		Col. 3		Col. 4		Col. 5		Col. 6		Col. 7		Col. 8		Col. 9	
Mode	**Period (sec)**	**U2Amp**	φ_D	$\mu_{D,n}$	φ_D	$\mu_{D,n}$	φ_D	$\mu_{D,n}$	φ_D	$\mu_{D,n}$	φ_D	$\mu_{D,n}$	φ_D	$\mu_{D,n}$	φ_D	$\mu_{D,n}$	φ_D	$\mu_{D,n}$	φ_D	$\mu_{D,n}$
3	1.745	152.31	-0.05	1.67	-0.12	**3.96**	-0.18	3.55	-0.13	2.61	-0.08	1.57	-0.02	0.43	0.00	0.27	0.00	0.03	0.00	0.03
4	1.529	-71.33	-0.03	0.42	-0.06	0.89	-0.06	0.56	0.05	0.45	0.13	1.24	0.19	1.73	0.09	**2.56**	0.01	0.34	-0.01	0.22
6	1.007	42.32	-0.10	0.94	-0.11	1.04	-0.02	0.09	0.13	0.73	0.10	0.56	-0.09	0.52	-0.10	**1.68**	-0.05	0.91	-0.02	0.38
7	0.871	38.27	0.06	0.51	0.04	0.37	-0.02	0.12	-0.03	0.16	0.00	0.01	0.05	0.27	-0.09	1.33	-0.19	**3.01**	-0.15	2.39
9	0.773	-23.58	0.18	0.93	0.08	0.39	-0.13	0.41	0.04	0.13	0.08	0.25	-0.05	0.16	-0.03	0.24	0.04	0.37	0.05	0.44
...	**Other Modes are Elastic**																			

Table 7.9 Finding Modal Shear Key Force, Example 2

			Hinge 1			Hinge 2		
Mode	**U2Amp**	$\mu_{D,n}$	φ_V	V_n^{sk} (kip) (U2Amp×φ_v)	$V_n^{sk}/\mu_{D,n}$	φ_V	V_n^{sk} (kip) (U2Amp×φ_v)	$V_n^{sk}/\mu_{D,n}$
3	152.31	**3.96**	-3.13	-476.72	**-120.39**	-0.71	-107.38	**-27.12**
4	-71.33	**2.56**	-4.94	352.52	**137.50**	8.61	-614.24	**-239.58**
6	42.32	**1.68**	-39.37	-1666.44	**-989.40**	20.43	864.82	**513.46**
7	38.27	**3.01**	18.12	693.32	**230.40**	12.34	472.29	**156.95**
9	-23.58	1.00	21.56	-508.37	**-508.37**	22.28	-525.53	**-525.53**
16	-3.41	1.00	42.13	-143.70	**-143.70**	134.51	-458.84	**-458.84**
20	-2.00	1.00	-195.12	390.51	**390.51**	-120.50	241.15	**241.15**
24	1.28	1.00	269.88	344.88	**344.88**	-105.09	-134.30	**-134.30**
25	0.03	1.00	3.87	0.12	**0.12**	-1.98	-0.06	**-0.06**
28	-0.04	1.00	0.47	-0.02	**-0.02**	-7.86	0.29	**0.29**
29	-1.03	1.00	42.24	-43.40	**-43.40**	-339.38	348.66	**348.66**
46	-0.28	1.00	383.63	-106.97	**-106.97**	667.78	-186.20	**-186.20**
47	0.01	1.00	-16.63	-0.17	**-0.17**	-29.34	-0.29	**-0.29**
48	-0.01	1.00	14.57	-0.08	**-0.08**	16.46	-0.09	**-0.09**
49	-0.16	1.00	773.51	-124.15	**-124.15**	47.58	-7.64	**-7.64**
55	0.07	1.00	716.06	52.38	**52.38**	903.04	66.06	**66.06**
62	0.07	1.00	-292.38	-19.28	**-19.28**	1010.12	66.60	**66.60**

Note: Modes with Zero Participation are Excluded from Table

Table 7.10 Finding Shear Keys Design Forces, Example 2

Description	**Shear Key at Hinge 1 (kip)**	**Shear Key at Hinge 2 (kip)**
V^{sk}_{MEDA} (Eq. 7.4a)	1287	1037
Factor 1 (Eq. 7.6)	2.5	2.5
Factor 2 (Eq. 7.7)	1.25	1.25
Factor 1 x V^{sk}_{MEDA}	3217	2592
Ultimate Design Force (Eq. 7.3)	**4021**	**3240**
Upper Bound Force (Eq. 7.8)	**2424(governs)**	**4407**

For Hinge 1, the design force is exceeding the upper bound, thus the upper bound is considered as a design force.

Table 7.11 Comparing NTH and the Method Results, Example 2

Case	**Hinge 1 Shear Key Force (kip)**		**Hinge 2 Shear Key Force (kip)**	
	NTH	**Method**	**NTH**	**Method**
without Impact	930	1287	1197	1037
with Impact	1920	2424	2063	2592

Note: Values do not include effect of NUBE (Factor 2)

8 Summary and Conclusions

8.1 SUMMARY

This study was conducted to: 1) demonstrate the transverse dynamic response characteristics of a multi-frame bridges, to examine the effects of geometric and design parameters on the seismic response of multi-frame bridges and force demands on in-span shear keys, 2) investigate the significance of in-span shear keys to the seismic performance of multi-frame bridges, and 3) develop a rational method for the reliable estimation of in-span shear key force demands as well as a realistic upper bound design force. The proposed method is intended to be used for determining seismic force demands for elastic design of in-span shear keys. An analytical approach was taken to achieve these objectives.

Approximately 7700 nonlinear time history (NTH) analyses were conducted on a set of 56 box-girder prototype bridges that were designed in accordance to the seismic design practices of Caltrans. Prototype bridges were comprised of multi-frame bridges with single-columns of extended pile shaft, and pinned-base two-column piers with 200-ft long spans. To study the effect of the number of frames, sets of two-, three-, four-, and five-frame bridges were considered. The frame lengths vary from 600 ft to 760 ft as a practical length for post-tensioned superstructures. Prototype models with different realistic valley shapes are included in each set. Four 110-ft long span bridge models with a uniform valley shapes were also studied as short-span models. A suite of thirty-three spectrum matched ground motions were used for the nonlinear time history analyses.

The dynamic response characteristics, unique to the multi-frame bridge system, were first investigated by performing steady state and modal analyses on two simple bridge models. A limited number of time history analyses were performed to quantify the isolated effects of different system properties, such as stiffness and strength ratios of adjacent frames, on the seismic response of this bridge system.

For the main body of the analytical studies, three-dimensional spine models of the prototype bridges were developed using OpenSees 2.4.4. These analytical models are used to design the prototype bridges and conduct the response history analyses. The elastic frame elements are used for the superstructure, diaphragms, and bent caps. The columns are modeled using the inelastic beam-column elements with fiber sections. For the single column bridges, soil parameters are considered to locate the depth of fixity and define the depth and length of the plastic hinge. For the two-column bents, the plastic hinges are assigned to the top of the column elements. The abutments and in-span hinges are explicitly modeled. Their assembly is composed of elements representing diaphragms, bearings, shear keys, gap and impact, backwall, and backfill soil. A series of sensitivity analyses were performed to define the modeling parameters of shear keys and transverse impact elements. The inelastic response of an individual column model is verified using the data from shake table experiments. The system level response of a trial OpenSees model is compared to that of the same model obtained from SAP2000 v15.1.

A suite of eleven ARSs was selected for the seismic design of each prototype model according to Caltrans SDC v1.7. Three seismic hazard levels of moderate, large, and severe are defined for this project. The corresponding ARS's are obtained from Appendix B of SDC for four soil types of B, C, D, and E for the three hazard levels. Five design criteria are controlled when designing each prototype: 1) the minimum local displacement ductility capacity of the bents, 2) the maximum displacement ductility demands of the bents, 3) the global displacement capacity of bridge, 4) the minimum lateral load capacity of the bents, and 5) the maximum permissible P-Delta effects.

The Pacific Earthquake Engineering Research Center (PEER) NGA ground motion database was used to select and scale eleven sets of three biaxial ground acceleration histories. Each set of motions was selected to have a soil type, moment magnitude, and intensity level compatible with the target ARS. SeismoMatch software is used to match the scaled ground motions to the target ARS. Each prototype model is subjected to the three compatible ground acceleration histories that corresponded to its design ARS. Because of the compatibility of the design demands with the input motions, the nonlinear response history analyses are expected to be proportional to the design, and present a realistic estimation of the force demands in in-span shear keys.

In addition to the “Main Analyses”, a subset of analyses are conducted to investigate effects of the following parameters on shear keys forces: 1) gap closure and pounding of adjacent frames in transverse and longitudinal directions, 2) yielding of abutment shear keys, and 3) variation of the base excitation along the length of the bridge. In addition, effects of limited yielding of ductile shear keys on seismic performance of multi-frame bridge systems were investigated.

Statistical distributions of different responses were presented. The correlations between shear key forces and other response parameters, including the maximum displacement and acceleration at hinges, base shears, displacement ductility of column, ratios of the periods of the standalone frames, elastic design forces, and pushover forces were extracted from NTH analyses results. The maximum shear key forces, obtained from the NTH analyses, are considered as the reference force. Several possible analysis methods were investigated including pushover method, rigid dynamic method, and spectral analysis method (i.e. EDA) to predict shear key force demands.

Finally, a refined EDA method is developed, where the effect of the nonlinear behavior is accounted for by modification of multiple modal forces. Factors are proposed to adjust the elastic shear key force for the effects of transverse impact of frames and non-uniform excitation at the base of columns along the length of the bridge. In addition, a rational upper bound force is defined to cap the shear key design force demands. At the end, two examples are presented to facilitate the implementation of the proposed method by bridge designers.

8.2 OBSERVATIONS AND CONCLUSIONS

The following present the observations and the conclusions that are made based on the comprehensive analytical simulations:

1. The design displacements that are determined in accordance with Caltrans SDC are comparable to the maximum displacements obtained from the nonlinear time history analyses. The same is true for the displacement ductility ratios of columns.
2. The in-plane vibration of the superstructure significantly contributes to the shear key forces; thus, assuming that superstructure is rigid in-plane yield inaccurate estimation of shear key force demands.
3. In transverse directions, it is possible to obtain the modal characteristics of a multi-frame bridge system from the modal characteristics of its two-frame subsystems.
4. In general, the maximum shear key force does not coincide with the maximum transverse displacement or acceleration at the corresponding in-span hinge, and/or the maximum base shear.

5. At the instance of the maximum shear key force, the profile of accelerations along the length of superstructure - and consequently inertial forces - is a high-order polynomial. Thus, the equation of equilibrium of column forces, inertial forces, and shear key forces may not be easily solved.
6. Shear key force demands increase approximately linearly, with the increase in the peak ground acceleration (PGA). In contrast, increase in the peak ground velocity (PGV) beyond 20 in/sec. does not generally increase shear key force demands. This confirms that pulse frequencies in pulse-type motions do not excite the local/higher modes of superstructure. Therefore, pulse-type motions do not generate shear key forces larger than that of non-pulse motions with the same amplitude.
7. The average of the shear key force demands obtained from the analyses of the two-column bent bridges is approximately two times that of the single-column bent bridges. This ratio is comparable to the ratio of the average plastic shear of two-column bents to that of single column bents.
8. As a general observation, the scatter of the seismic responses, including the maximum shear forces, is larger for the two-column bent bridges. This may be associated with the larger transverse stiffness and mass of the superstructure in two-column bent bridges.
9. The shear key force demands in bridges with a non-uniform valley shape are not always larger than the shear key force demands in bridges with a uniform valley shape.
10. Shear key force demands are roughly proportional with the ratio of the overstrength shear (typically defined as M_o^{col} / L, SDC Sec. 2.3.2) of the closer bent divided by the distances of the closer bent from the hinge, to that of the farther bent. This becomes more pronounced for bridges with stiff superstructures.
11. For bridges with a large number of frames (e.g. more than three frames), shear key force demands in all in-span hinges are comparable. As a result, shear keys of a bridge with a large number of frames may be sized for a single force demand, independent from valley shapes.
12. Only a weak correlation exists between the maximum shear key forces and the ratio of the periods of the adjacent frames.
13. Standard pushover method fails to estimate shear key force demands. However, when only in-span hinges are pushed to their design displacement demands, individually or together, a quarter of the pushover force at each hinge is comparable to the shear key force demand in the hinge.

14. Elastic dynamic methods significantly over predict the shear key forces as it ignores the de-amplification of elastic forces due to nonlinear response. Under severe base excitations, the shear key force may be over predicted approximately three and four times for single- and two-column bent bridges, respectively. EDA shear key forces shall not be directly used for designing and sizing shear keys.
15. In EDA, the mass participation ratio necessary for accurate estimation of elastic shear key forces is much larger than that needed for estimating displacements. Modes with frequencies as high as 15 Hz (period of 0.06 sec.) should be included in spectral analysis for mobilizing 90% of the total shear key force. For that, approximately 10 transverse modes should be considered. If the number of longitudinal and vertical modes is included, the total number of modes will be approximately 30. However, these numbers may be different for different prototypes; hence, the modal frequency is a more reliable measure for defining the number of required modes. It should be noted that including modes with a total mass participation of 90% of the total mass is not adequate for estimating shear key forces.
16. Using inelastic response spectrum or modifying EDA forces with one response factor to account for the nonlinear behavior leads to significant under prediction of shear key forces. This is because nonlinear behavior does not affect shear key forces generated by the higher modes.
17. It is found that the effect of yielding should only be applied to modal forces that generate large displacement ductility ratios. A modification of multiple modes present the most reliable and consistent results. In order to modify individual elastic modal forces, they should be divided by the ductility ratio of the corresponding mode (modal ductility ratio).
18. The displacement ductility ratios of higher modes (up to 15^{th} mode) may be as large as five for the two-column bent bridges with a large number of frames. For single-column bent bridges, large modal ductility ratios are limited to the first few modes (up to 4^{th} mode).
19. Abutment shear keys, designed for forces equal to the dead load reactions at the abutments (SDC v1.7, Eq. 7.8.4-4), may extensively yield under large motions. The transverse displacements at the abutments may be as large as 5.0 in. in two-column bent bridges with relatively stiff superstructure. However, if the abutment shear keys are designed per SDC 1.7, Eq. 7.8.4-1, smaller displacements are expected. For instance for the shear key capacity of twice the dead load the maximum displacement does not exceed 2.0 in.
20. The impact forces due to the closure of the transverse gap between the shear key and insert/sleeve may increase the forces by a factor of four under moderate levels

of seismic excitation. Under large earthquakes, the impact factor falls under 2.0. The median value of the impact factor across the range is determined as 2.5.

21. The median value of the ratios of the shear key force demands to the overstrength shear of the closer bent is approximately 0.9 and 0.8 for the single- and two-column bent prototypes with 200-ft spans, respectively. For these prototypes, the maximum shear key forces, including the impact effect, do not exceed two times the overstrength shear of the bent. However, for the 110-ft span prototypes the median ratio is 1.5 and the maximum ratio may be as large as 3.5.

22. The median value of the ratios of the shear key force demands to the transverse overstrength shear of the weaker of the two adjacent frames is fairly similar for all the prototype bridges. This median ratio is approximately 0.33. The maximum ratio is approximately 0.8.

23. With a confidence higher than 95%, the ratio of the maximum shear key force to the transverse overstrength shear of the weaker frame is less than 0.75. In other words, 75% of the transverse overstrength shear of the weaker frame is an upper bound value for shear key force demands.

24. Effect of non-uniform base excitations may increase the shear key forces. For soil Types C, D, and E, the mean increase factor was approximately 1.25. For soil Type B, the increase in shear key forces due to non-uniform excitation was negligible.

25. When the shear key was modeled as a ductile element (ductile shear key) with a transverse yield strength equal to the overstrength shear of the closer bent, the maximum inelastic deformation of the shear key was approximately 1.5 in.

26. In models where ductile shear key elements with a yield strength equal to the overstrength shear of the adjacent bent are implemented, the residual relative transverse displacement at in-span hinges were found to be smaller than 1.0 in. The residual relative displacements in bridges with ductile shear keys with a yield strength that is notably smaller than what was assumed in this study might be larger. In order to study the seismic response of bridges when large plastic deformations are expected in shear keys, a comprehensive understanding of the cyclic load-deformation relationship of the ductile shear key elements is necessary.

27. The median of relative longitudinal displacements at hinges at the instance of peak shear key force was approximately 2.0 in (the initial longitudinal gap size was 2.0 in). The median of maximum relative longitudinal displacements of adjacent frames was 5.0 in. The absolute maximum separation did not exceed 15.0 in.

28. If shear key members are allowed to go to failure and large relative transverse displacement at hinges are permitted, the shear key force can be assumed to be 0.25 times the overstrength shear of the adjacent bent.

This Page Intentionally Left Blank

This Page Intentionally Left Blank

REFERENCES

AASHTO, 2012. *AASHTO LRFD Bridge Design Specifications.* Fifth ed. Washington, DC: American Association of State Highway and Transportation Officials.

Aviram, A., Mackie, K. R. & Stojadinovic, B., 2008. Effect of Abutment on the Seismic Response of Bridge Structures. *Eartquake Engineering and Engineering Vibration,* 7(4), pp. 395-402.

Aviram, A., Mackie, K. R. & Stojadinovic, B., 2008. *PEER 2008/03: Guidelines for Nonlinear Analysis of Bridge Structures,* California, Berkeley: Pacific Earthquake Engineering Research Center (PEER).

Bozorgzadeh, A., Megalley, S. H., Ashford, S. & Restrepo, J. I., 2007. *Seismic Response of Sacrificial Exterior Keys in Bridge Abutments,* La Jolla, CA: Department of Structural Engineering, University of California, San Diego.

Caltrans, 1973. *BRIDGE STRUDL Manual.* Sacramento, CA: California Department of Transportation.

Caltrans, 2008. *Bridge Design Specifications.* Sacramento, CA: California Department of Transportation (Caltrans).

Caltrans, 2008. *Memo to Designers 10-20: Deck and Soffit Slabs.* Sacramento, CA: California Department of Transportation (Caltrans).

Caltrans, 2010. *Memo to Designers 20-1: Seismic Design Methodology.* Sacramento, CA: California Department of Transportation (Caltrans).

Caltrans, 2013. *Caltrans Seismic Design Criteria Version 1.7.* Sacramento, CA: Califionia Department of Transportation (Caltrans).

Caltrans, 2014. *Bridge Design Practice Manual.* Sacramento, CA: California Department of Transportation (Caltrans).

Caltrans, 2014. *Caltrans ARS Online.* [Online]

Available at: http://dap3.dot.ca.gov/ARS_Online/

Caltrans, 2014. *xs7-070: Restrainer Details for Pipe Extender/Shear Key (New).* Sacramento, CA: Bridge Standard Detail Sheets, Division of Engineering Services (DES).

Charney, F. A., 2008. Unintended Consequences of Modeling Damping in Structures. *Journal of Structural Engineering-ASCE,* 134(4), pp. 581-592.

Chen, W. F. & Duan, L., 2014. *Bridge Engineering Handbook, Seismic Design.* 2nd ed. Northwestern: Taylor & Francis Group.

Chopra, A. K., 2001. *Dynamics of Structures.* 2nd ed. New Jersey: Printce Hall.

CSI, 2011. *SAP2000 Ver.15.1.0.* Berkeley, California: Computers and Structures, Inc..

CSI, 2013. *Analaysis Reference Manual for SAP2000, ETABS, SAFE and CSIBridge.* Berkeley, California: Computers and Structures Inc.(CSI).

Dassault Systems, 2011. *Abaqus 6.11-1 User's Manual.* Paris: Dassault Systems.

DesRoches, R. & Fenves, G. L., 1998. *MCEER-0013: Design Procedures for Hinge Restrainers and Hinge Seat Width for Multiple-frame Bridges,* Berkeley, California: Multidisciplinary Center for Earthquake Engineering Research (MCEER), University at California, Berkeley.

DesRoches, R. & Fenves, G. L., 2001. Simplified Restrainer Design Procedure for Multi-Frame Bridges. *Earthquake Spectra,* 17(4), pp. 551-567.

DesRoches, R. & Muthukumar, S., 2004. Implications of Seismic Pounding on the Longitudinal Response of Multi-Span Bridges - an Analytical Perspective. *Earthquake Engineering and Engineering Vibration,* 3(1), pp. 57-65.

Fenves, G. L. & Ellery, M., 1998. *PEER 1998/08: Behavior and Failure Analysis of a Multiple-Frame Highway Bridge in the 1994 Northridge Earthquake,* Berkeley, California: Pacific Earthquake Engineering Research Center (PEER).

FHWA, 2013. *strtyp13.xlsx: Bridges by Structure Type.* s.l.:National Bridge Inventory, Federal Highway Administration.

Gupta, A. K., 1984. *Modal Combination in Response Spectrum Method*. San Francisco, Eighth World Conference on Earthquake Engineering.

Hao, H. & Chouw, N., 2008. Seismic Design of Bridges for Prevention of Girder Pounding. *EJSE,* pp. 133-141.

He, J. & Fu, Z. F., 2001. *Modal Analysis.* Oxford: Butterworth-Heinemann.

He, W., 2010. *Numerical Calculation Method for Beam-Shear Key Pounding Based on Wilson-θ Method.* China, ASCE.

Hube, M. A. & Mosalam, K. M., 2008. *PEER 2008/103: Experimental and Computational Evaluation of Current and Innovative In-Span Hinge Details in Reinforced Concrete Box-Girder Bridges,* Berkeley, California: Pacific Earthquake Engineering Center (PEER).

Hutchinson, T. C., Boulanger, R. W., Chai, Y. H. & Idriss, I. M., 2002. *PEER 2002/14: Inelastic Seismic Response of Extended Pile Shaft Supported Bridge Structures,* Berkeley, California: Pacific Earthquake Engineering Research Center (PEER).

Kaviani, P., Zareian, F. & Taciroglu, E., 2014. *PEER 2014/01: Performance-Based Seismic Assesment of Skewed Bridges,* Berkeley, California: Pacific Earthquake Engineering Research Center (PEER).

Krawinkler, H. & Nassar, A. A., 1992. Seismic design based on ductility and cumulative damage demands and capacities. *Elsevier Applied Science, New York.*

Mander, J. B., Priestley, M. J. & Park, R., 1988. Theoritical Stress-Strain Model for Confined Concrete. *Journal of Structural Engineering,* 114(8).

Mathworks, 2012. Massachusetts: Mathworks.

McKenna, F. & Fenves, G. L., 2014. *Open System for Earthquake Simulation Framework (OpenSees) Ver. 2.4.4.* Berkeley, California: Pacific Earthquake Engineering Research Center (PEER), University of California, Berkeley.

Mead, D., 1996. Wave Propagation in Continuous Periodic Structures: Research Contributions From Southhampton. *Journal of Sound and Vibration,* 190(3), p. 496.

Megalley, S. H., Silva, P. F. & Seible, F., 2002. *Seismic Response of Sacrificial Exterior Keys in Bridge Abutments,* La Jolla, CA: Department of Structural Engineering, University of California, San Diego.

Microsoft, 2010. Redmond, Washington: Microsoft.

Mohraz, B., 1978. *Influences of the magnitude of the earthquake and the duration of strong motion onearthquake response spectra.* San Salvadore, Central Ameriac Conference on earthquake Eng.

Montgomery, D. C., Runger, G. C. & Hubele, N. F., 2010. *Engineering Statistics.* Fifth ed. s.l.:John Wiley & Sons.

Muthukumar, S. & DesRoches, R., 2006. A Hertz contact model with non-linear damping for pounding simulation. *Earthquake Engng Struct. Dyn.,* Issue 35, pp. 811-828.

NIST, 2012. *GCR12-917-20: Tentative Framework for Development of Advanced Seismic Design Criteria for New Buildings,* Gaithersburg, MD: National Institute of Standards and Technology (NIST), U.S. Department of Commerce.

OpenSees Wiki, 2014. [Online]
Available at: http://opensees.berkeley.edu/wiki/index.php/Main_Page

PEER, 2010. *Technical Report for the PEER Ground Motion Database Web Application,* Berkeley, CA: Pacific Earthquake Engineering Research Center (PEER).

PEER, 2011. *Pacific Earthquake Engineering Research Center, Ground Motion Database.* [Online]
Available at: http://peer.berkeley.edu/peer_ground_motion_database/spectras/new

Peng, M. H., Elghadamsi, F. E. & Moheaz, B., 1989. A Simplified Procedure for Constructing Probabilistic Response Spectra. *Earthquake Spectra,* 5(2), pp. 393-408.

Priestly, M. J. N., Seible, F. & Calvi, G. M., 1996. *Seismic Design and Retrofit of Bridges.* 1 ed. New York: John Wiley & Sons, Inc.

Rao, S. S., 2010. Harmonically Excited Vibration. In: *Mechanical Vibrations Fifth Edition.* New Jersey: Prentice Hall, pp. 259-362.

Scott, M. H., 2011. *Numerical Integration Options for the Force-Based Beam-Column Element in OpenSees.* Corvallis, OR: Oregon State University.

Seismosoft, 2011. Pavia: Seismosoft.

Shrestha, B., Hao, H. & Bi, K., 2013. *Pounding and Unseating Damage Mitigation on Bridge Structures subjected to Spatially Varying Ground Motions using Restrainers and Rubber Bumpers.* Tasmania, Australian Earthquake Engineering Society.

Singh, S. P., 1994. *Earthquake Analysis and Response of Multi-Frame Bridges.* Berkeley, CA: PhD dissertation, University of California, Berkeley.

Tegos, I. A. & Markogiannaki, O. G., 2014. *Analytical Investigation on the use of FRP Materials as Seismic Restrainers in Concrete Bridges.* Istanbul, Bridge Conference.

Trochalakis, P., Eberhard, M. O. & Stanton, J. F., 1997. Design of Seismic Restrainers for In-Span Hinges. *Journal of Structural Engineering,* 123(4), pp. 469-478.

Wikipedia, 2014. *Pearson product-moment correlation coefficient.* s.l.:Wikipedia.

Wilson, E. L., 2010. *Static and Dynamic Analysis of Structures.* Berkeley, California: Computers and Structures, Inc.(CSI).

Yashinsky, M., 2013. *Recent Change to Seismic Design Practice in California.* Sacramento, CA: Caltrans Office of Earthquake Engineering.

Zaghi, A. E. & Saiidi, M. S., 2010. *CCEER-10-01: Seismic Design of Pipe-Pin Connections in Concrete Bridges,* Reno, Nevada: Center for Civil Engineering Earthquake Research (CCEER).

Zhang, Y. W. et al., 2012. A General Symplectic Method for thr Response Analysis of Infinitely Periodic Structures Subjected to Random Excitations. *Latin American Journals of Solids and Structures,* 1(11), p. 8.

This Page Intentionally Left Blank

This Page Intentionally Left Blank

This Page Intentionally Left Blank

This Page Intentionally Left Blank

APPENDIX A.
RESPONSE SPECTRUMS OF THE GROUND MOTIONS

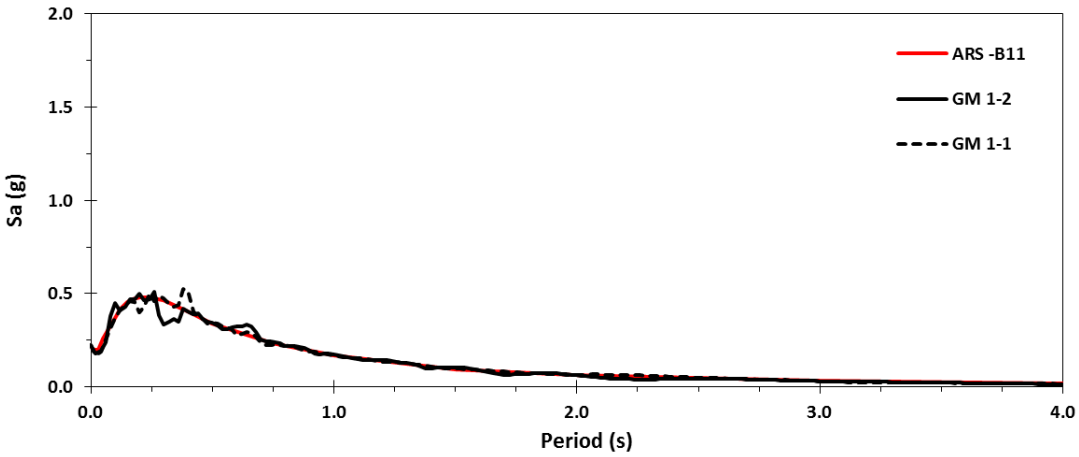

Figure A.1 Response Spectrums of the Horizontal Components of Ground Motion No.1

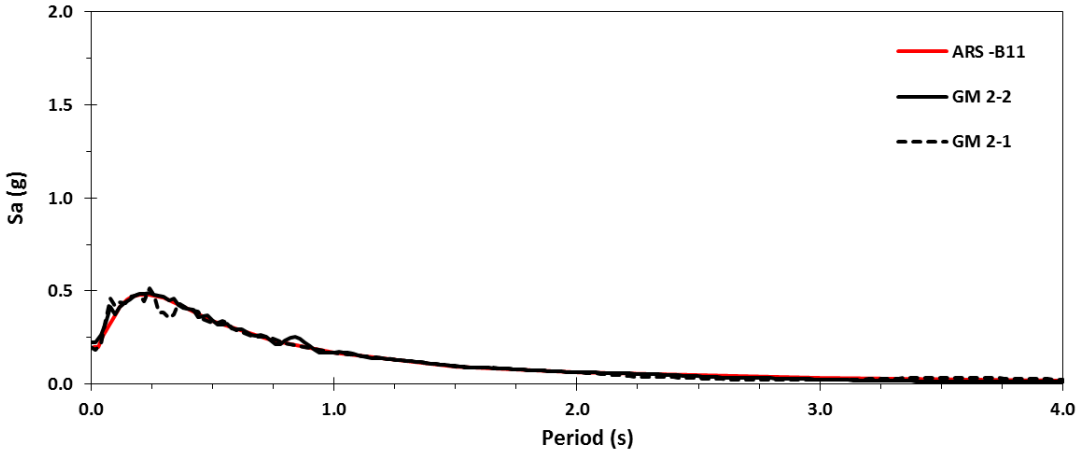

Figure A.2 Response Spectrums of the Horizontal Components of Ground Motion No.2

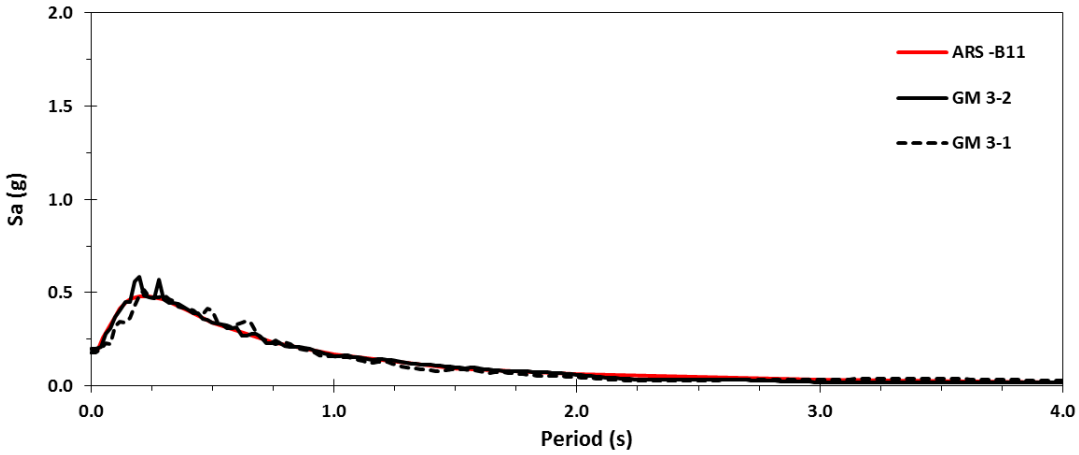

Figure A.3 Response Spectrums of the Horizontal Components of Ground Motion No.3

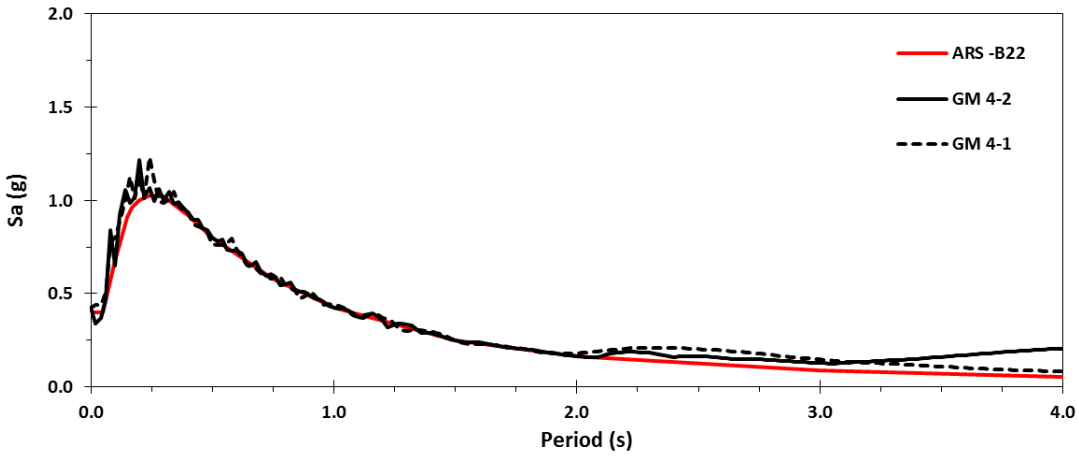

Figure A.4 Response Spectrums of the Horizontal Components of Ground Motion No.4

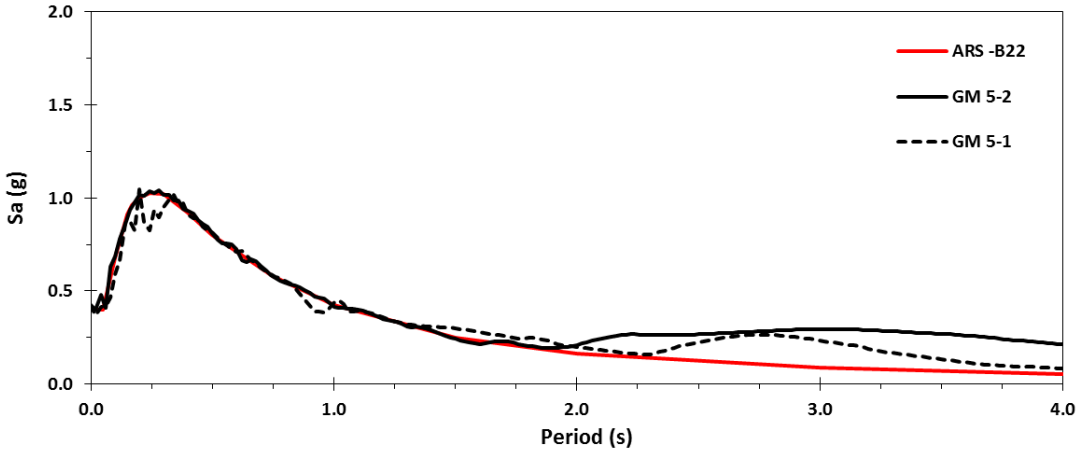

Figure A.5 Response Spectrums of the Horizontal Components of Ground Motion No.5

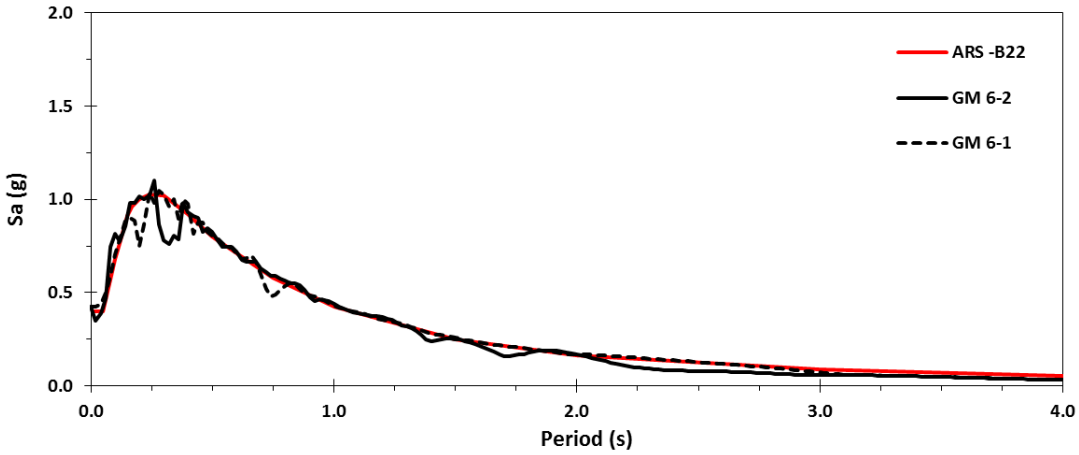

Figure A.6 Response Spectrums of the Horizontal Components of Ground Motion No.6

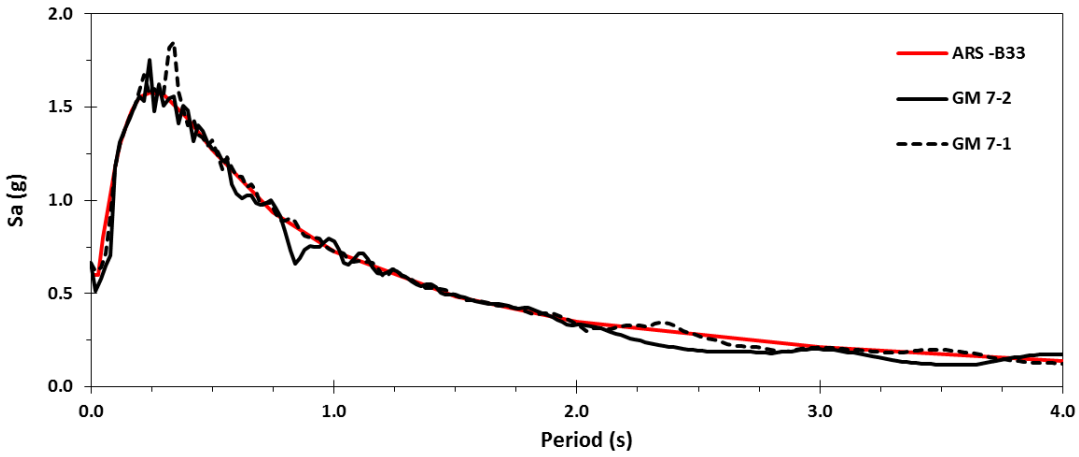

Figure A.7 Response Spectrums of the Horizontal Components of Ground Motion No.7

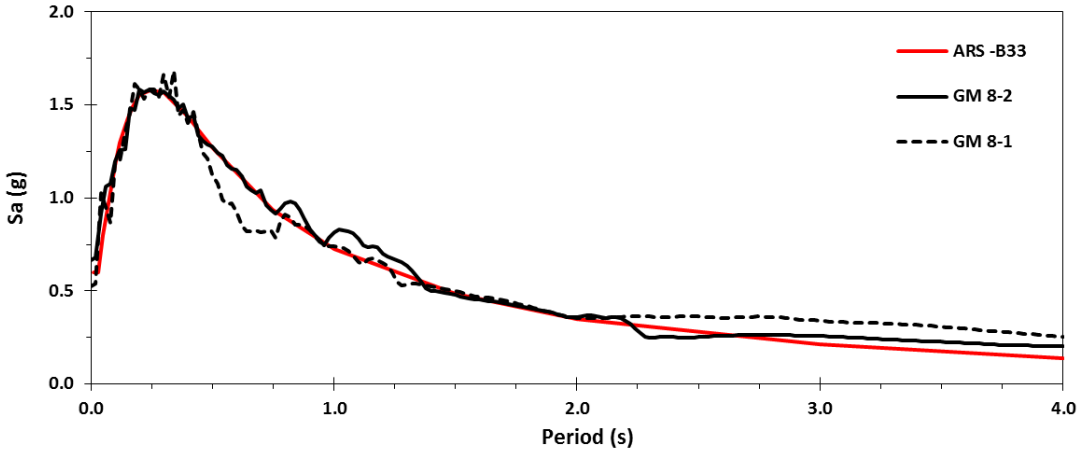

Figure A.8 Response Spectrums of the Horizontal Components of Ground Motion No.8

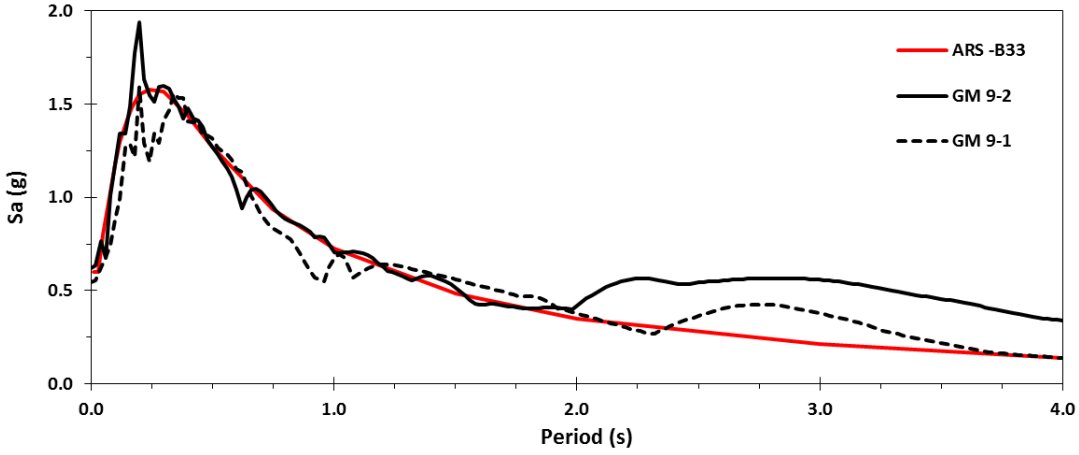

Figure A.9 Response Spectrums of the Horizontal Components of Ground Motion No.9

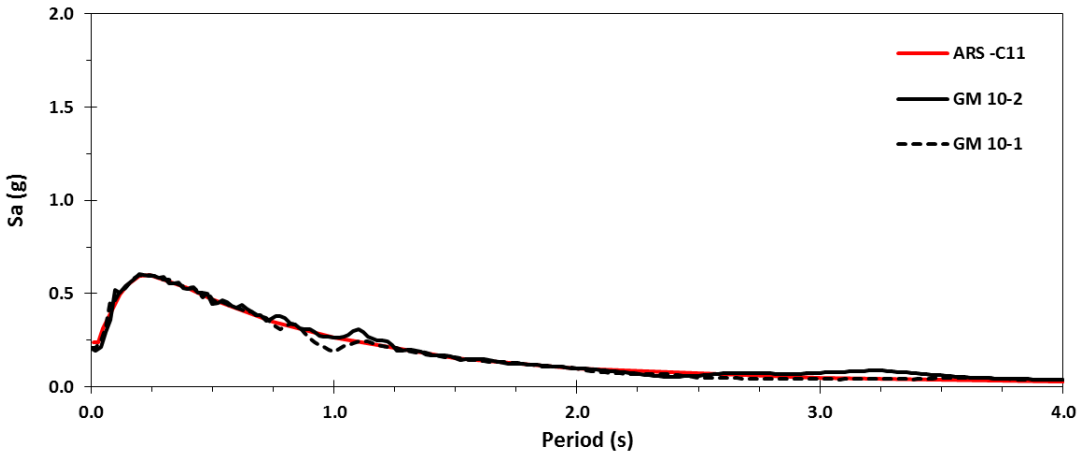

Figure A.10 Response Spectrums of the Horizontal Components of Ground Motion No.10

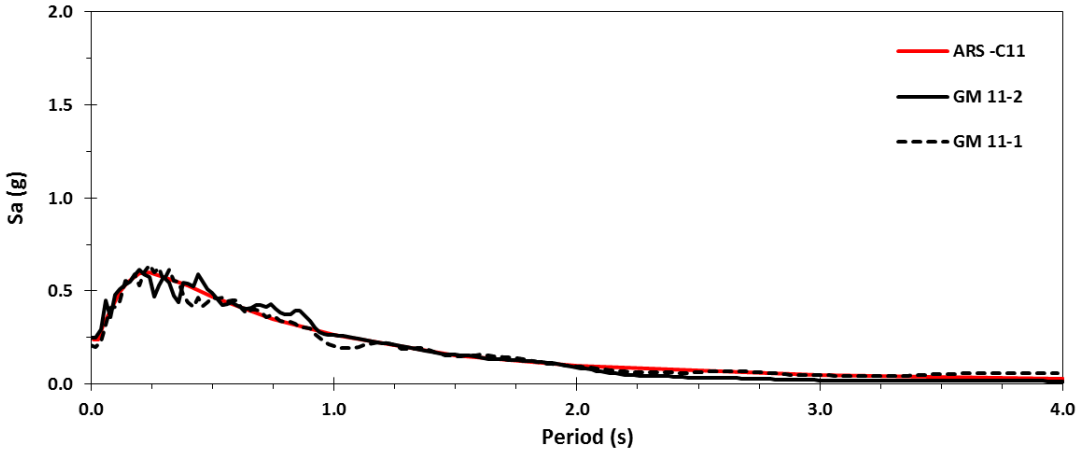

Figure A.11 Response Spectrums of the Horizontal Components of Ground Motion No.11

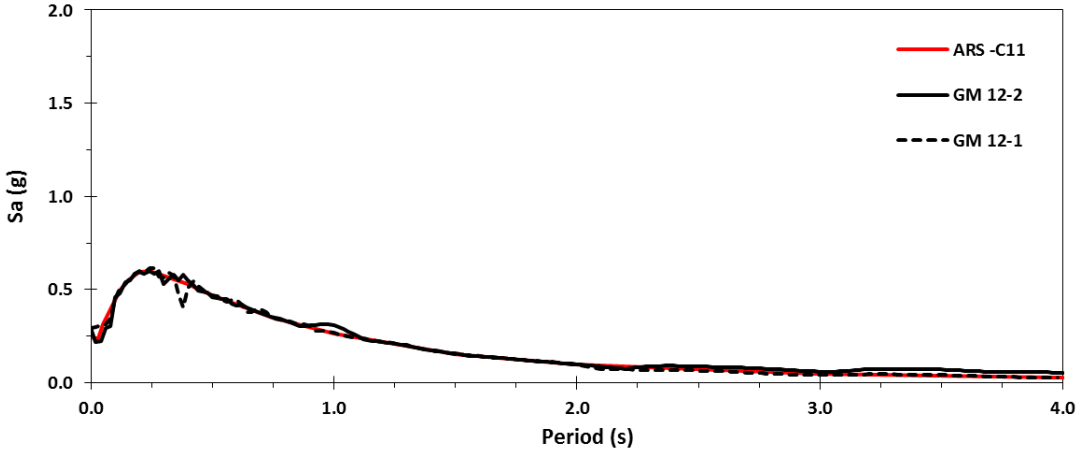

Figure A.12 Response Spectrums of the Horizontal Components of Ground Motion No.12

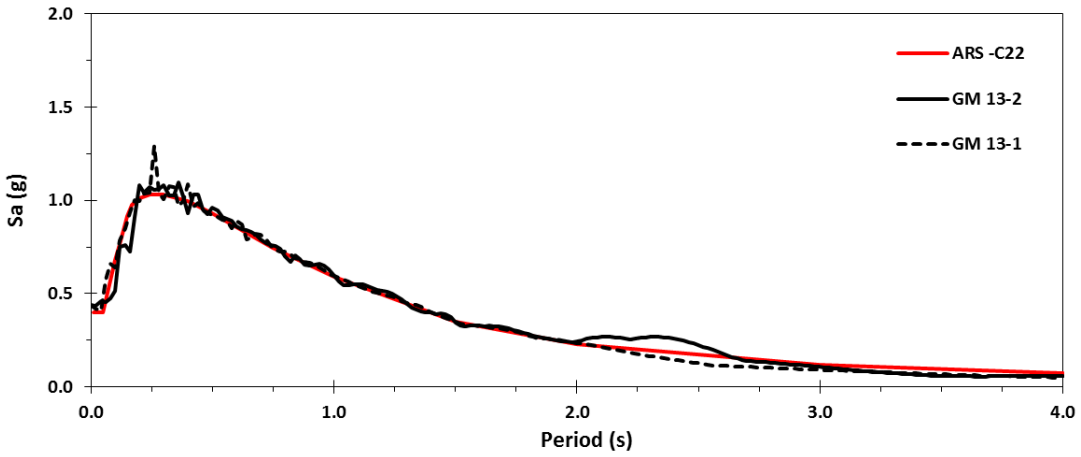

Figure A.13 Response Spectrums of the Horizontal Components of Ground Motion No.13

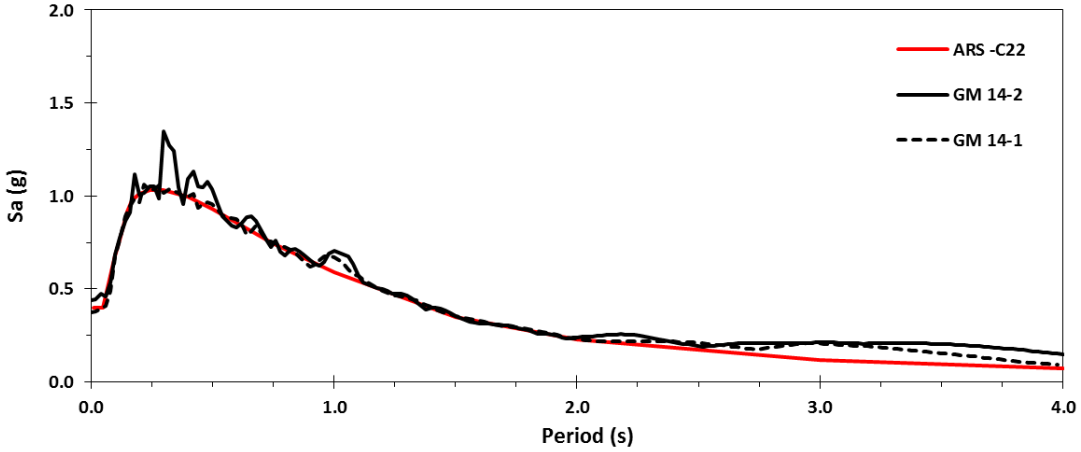

Figure A.14 Response Spectrums of the Horizontal Components of Ground Motion No.14

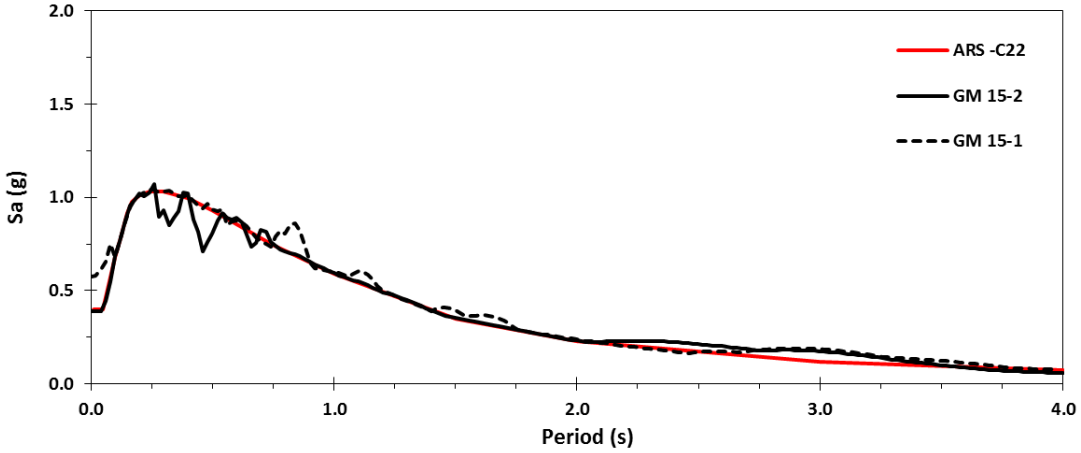

Figure A.15 Response Spectrums of the Horizontal Components of Ground Motion No.15

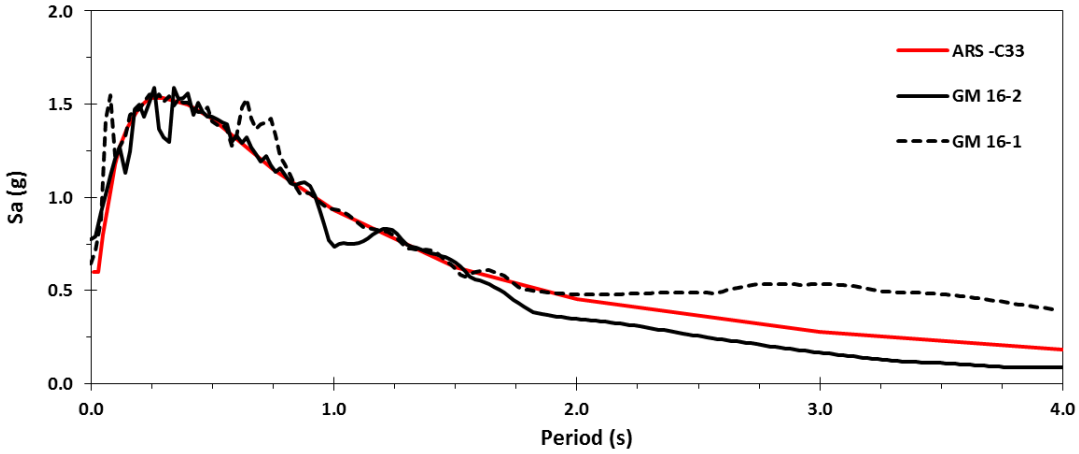

Figure A.16 Response Spectrums of the Horizontal Components of Ground Motion No.16

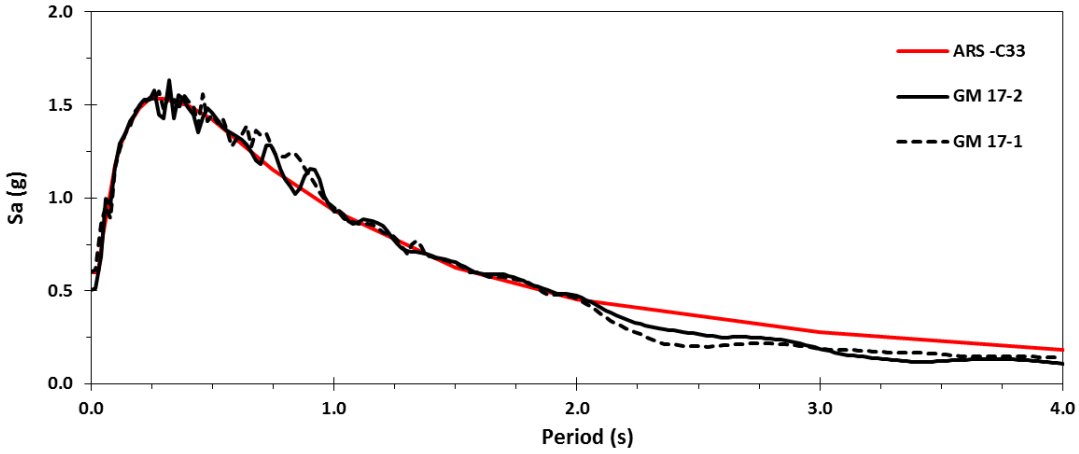

Figure A.17 Response Spectrums of the Horizontal Components of Ground Motion No.17

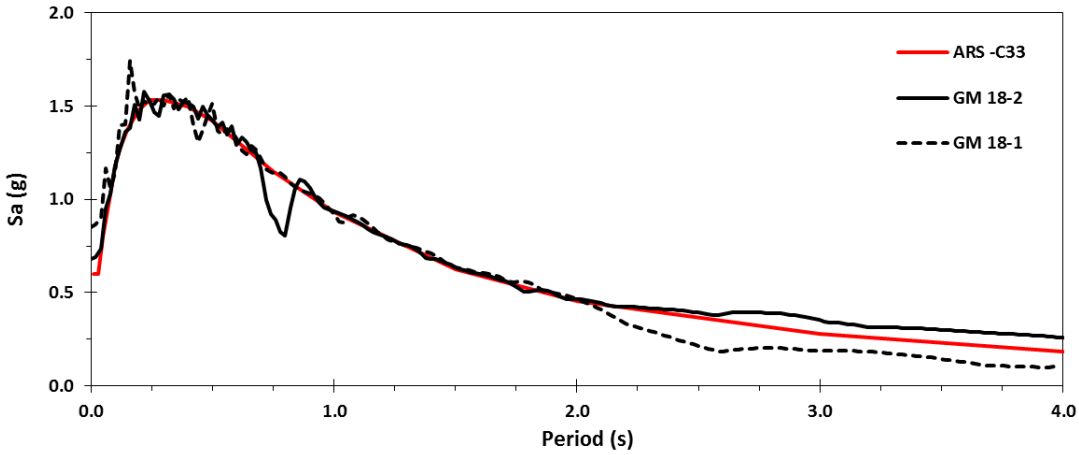

Figure A.18 Response Spectrums of the Horizontal Components of Ground Motion No.18

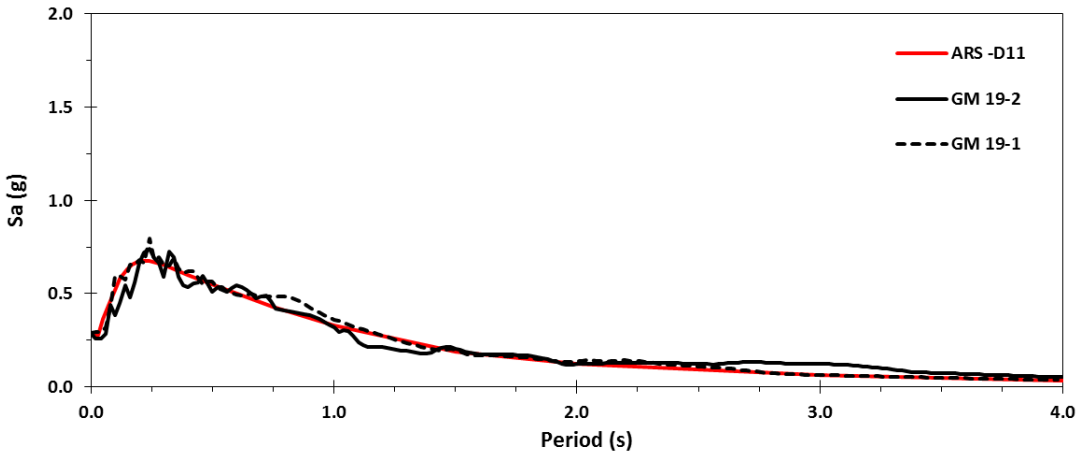

Figure A.19 Response Spectrums of the Horizontal Components of Ground Motion No.19

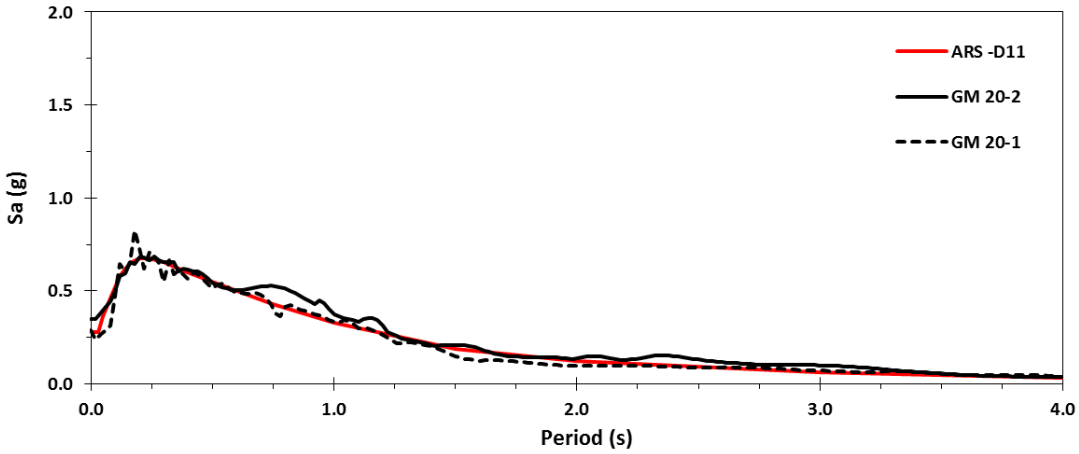

Figure A.20 Response Spectrums of the Horizontal Components of Ground Motion No.20

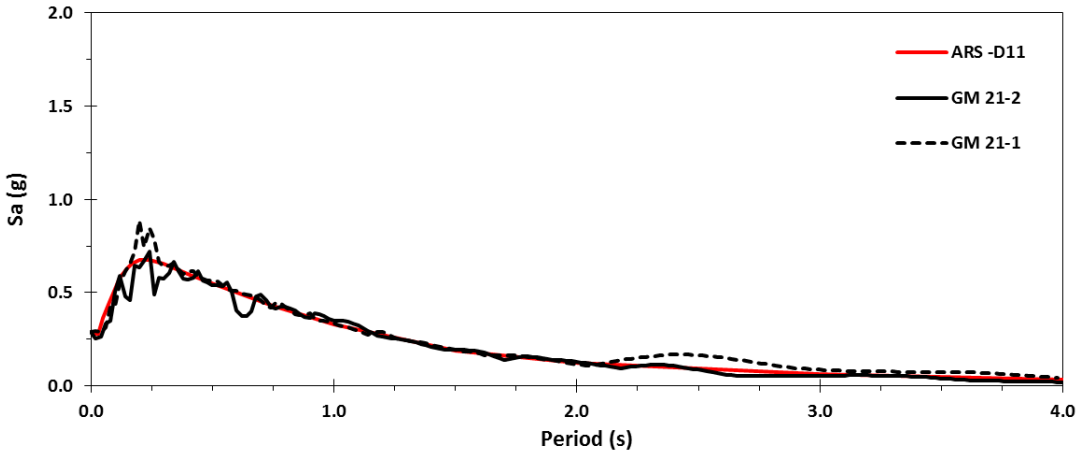

Figure A.21 Response Spectrums of the Horizontal Components of Ground Motion No.21

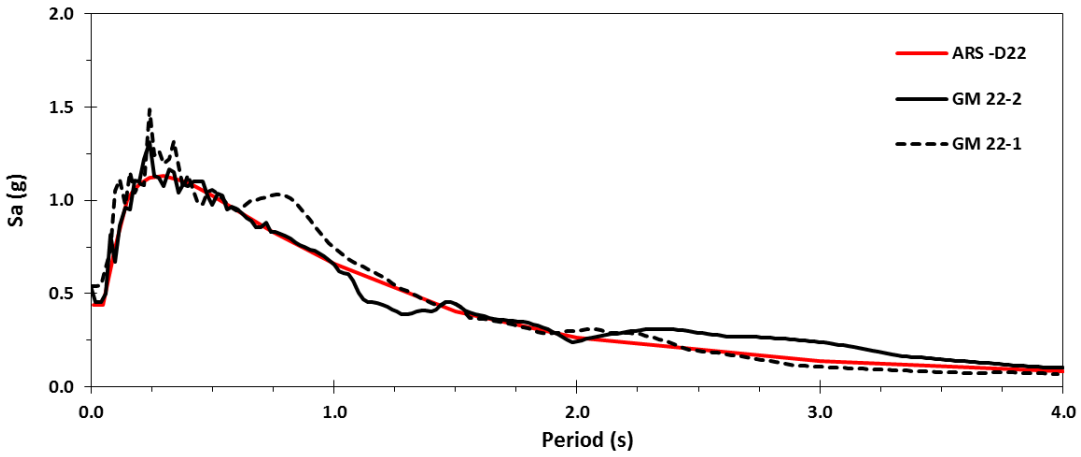

Figure A.22 Response Spectrums of the Horizontal Components of Ground Motion No.22

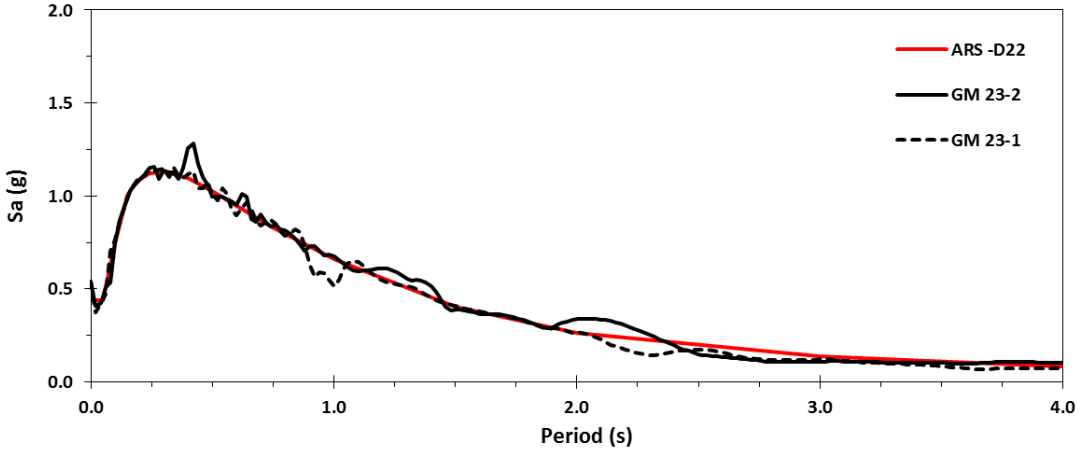

Figure A.23 Response Spectrums of the Horizontal Components of Ground Motion No.23

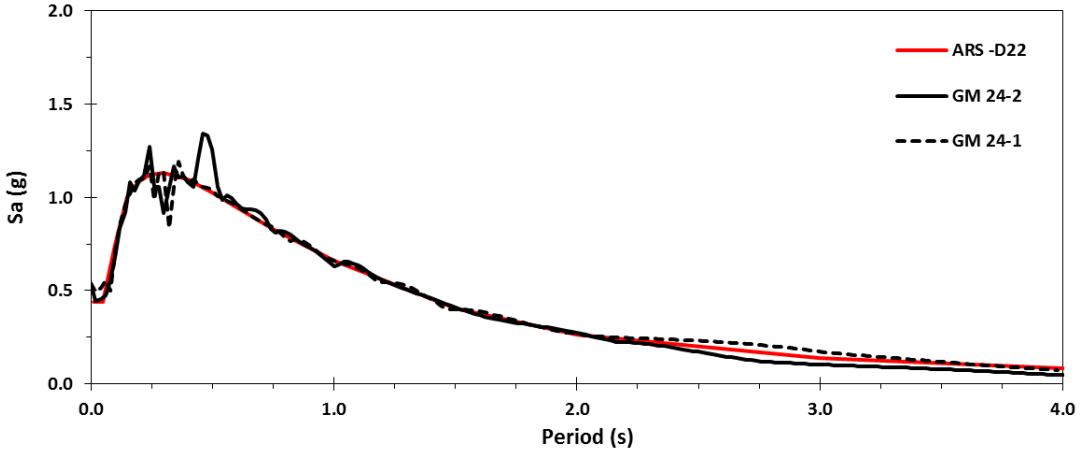

Figure A.24 Response Spectrums of the Horizontal Components of Ground Motion No.24

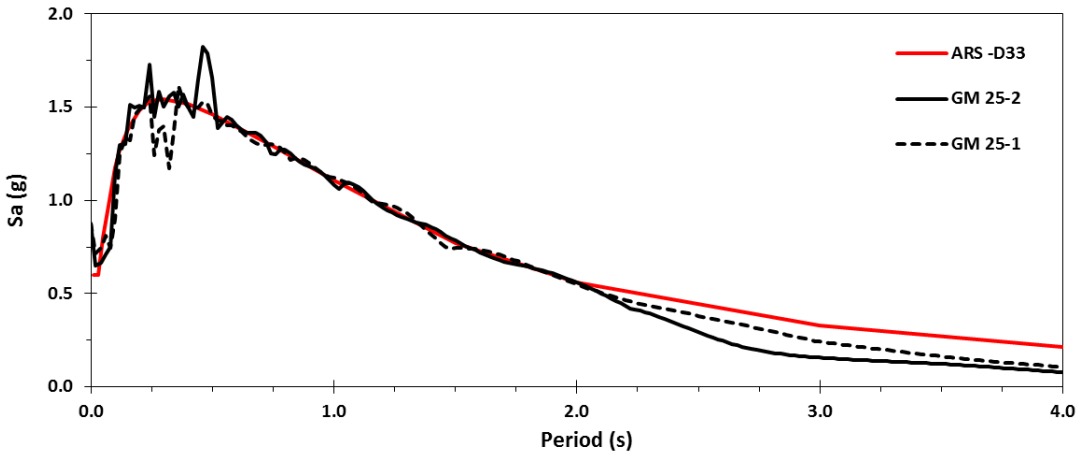

Figure A.25 Response Spectrums of the Horizontal Components of Ground Motion No.25

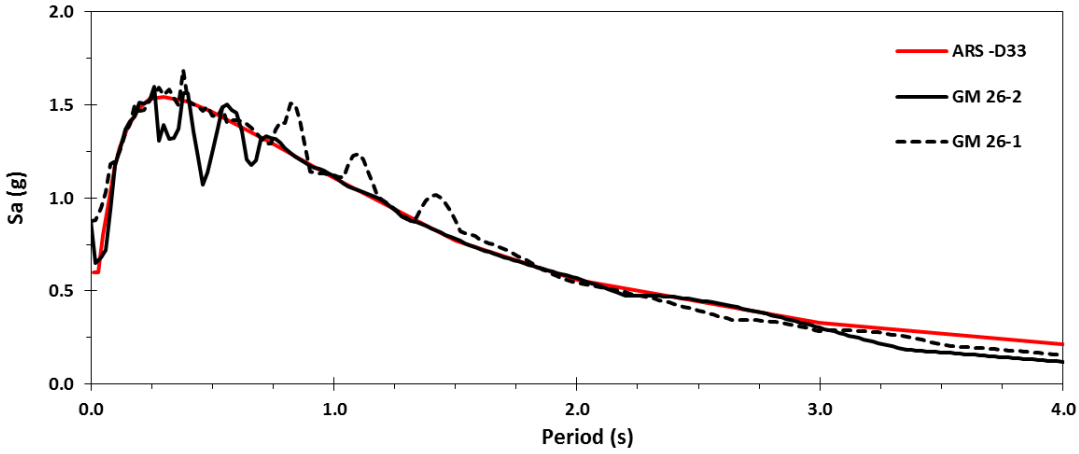

Figure A.26 Response Spectrums of the Horizontal Components of Ground Motion No.26

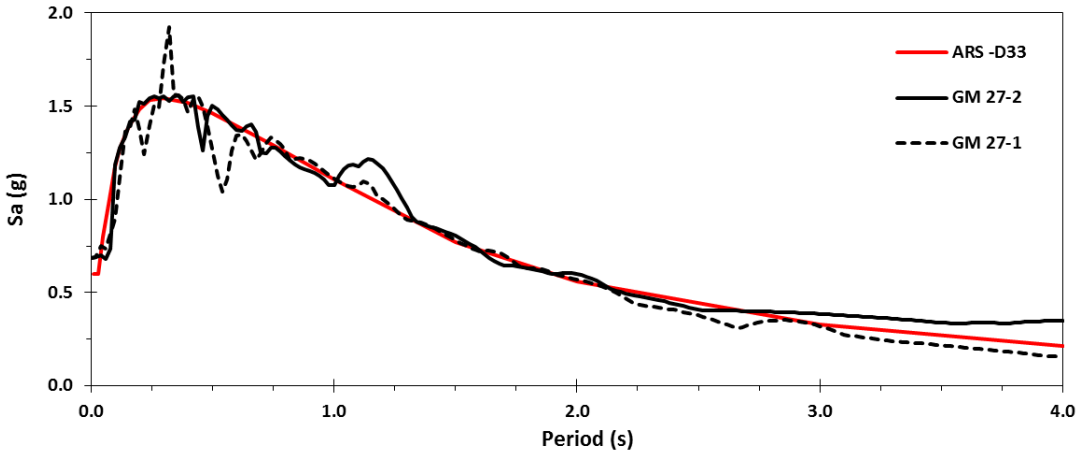

Figure A.27 Response Spectrums of the Horizontal Components of Ground Motion No.27

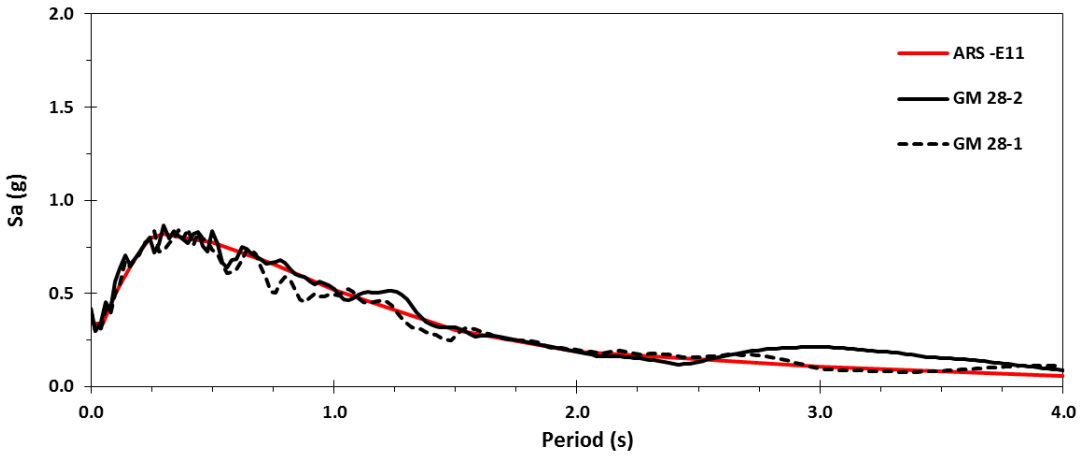

Figure A.28 Response Spectrums of the Horizontal Components of Ground Motion No.28

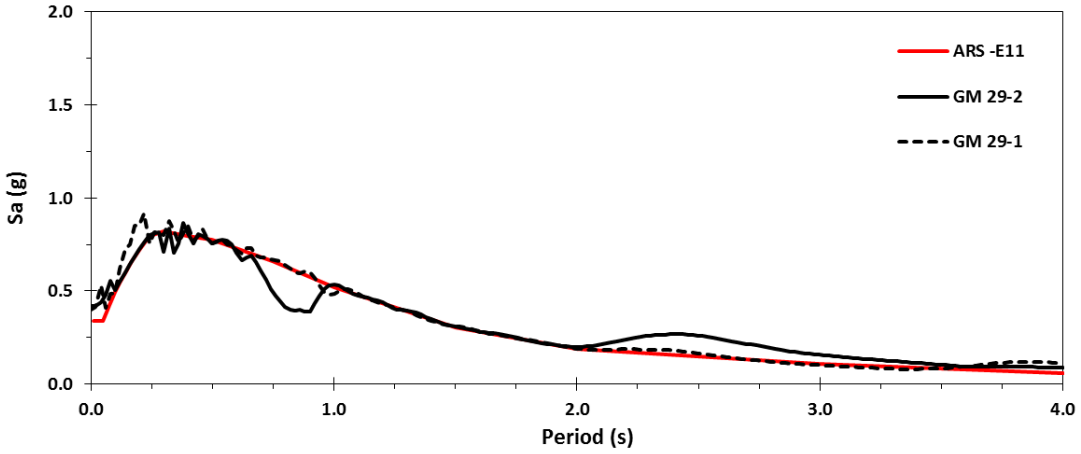

Figure A.29 Response Spectrums of the Horizontal Components of Ground Motion No.29

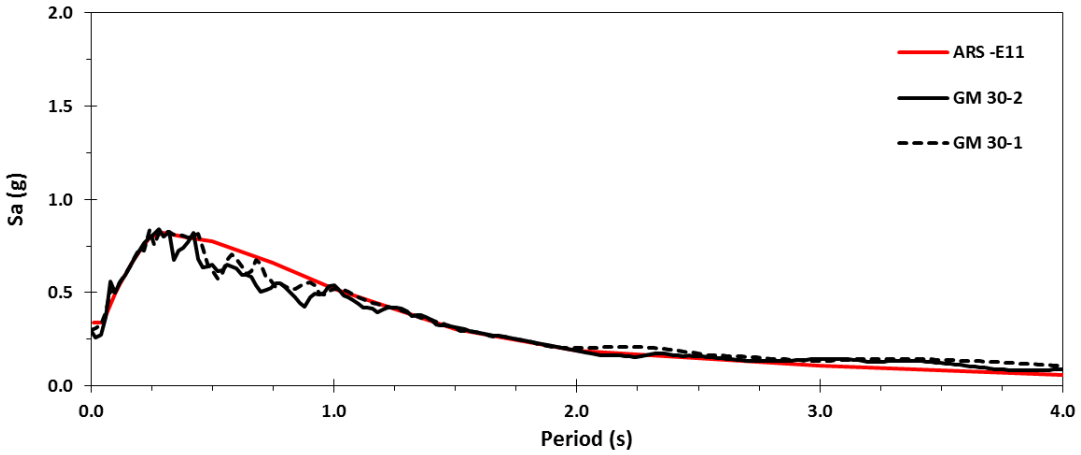

Figure A.30 Response Spectrums of the Horizontal Components of Ground Motion No.30

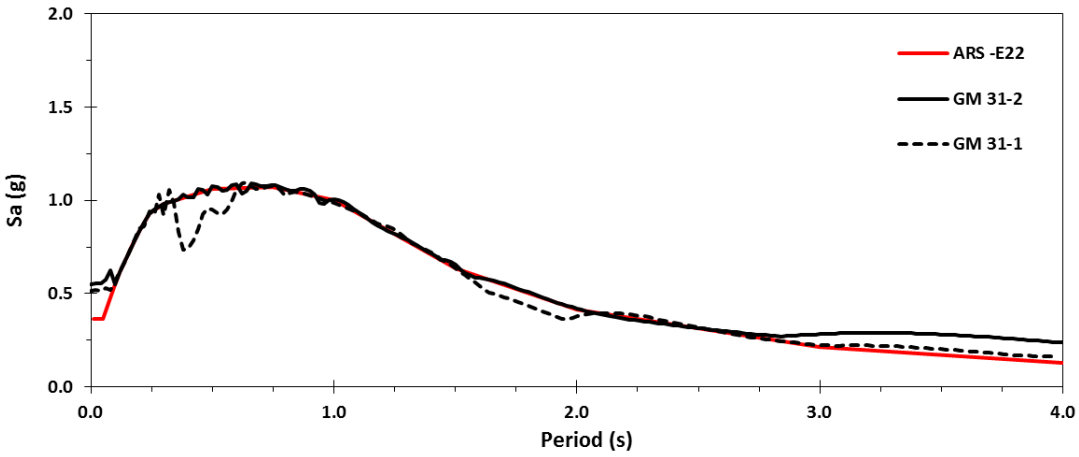

Figure A.31 Response Spectrums of the Horizontal Components of Ground Motion No.31

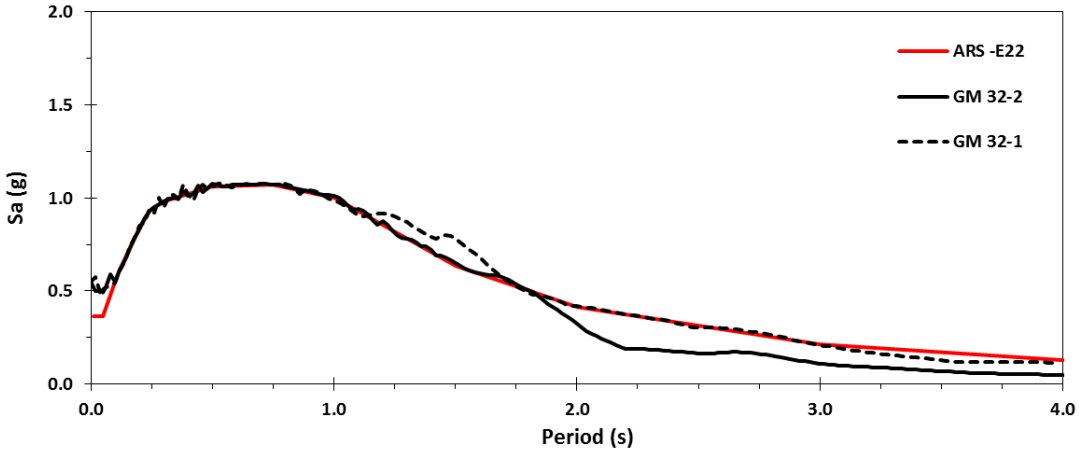

Figure A.32 Response Spectrums of the Horizontal Components of Ground Motion No.32

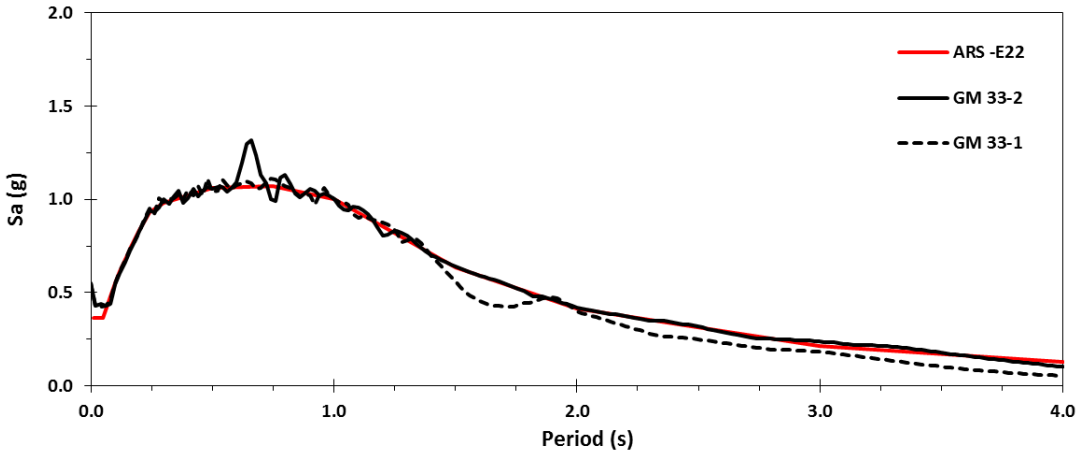

Figure A.33 Response Spectrums of the Horizontal Components of Ground Motion No.33

APPENDIX B.
SEISMIC DESIGN RESULTS OF PROTOTYPE BRIDGES

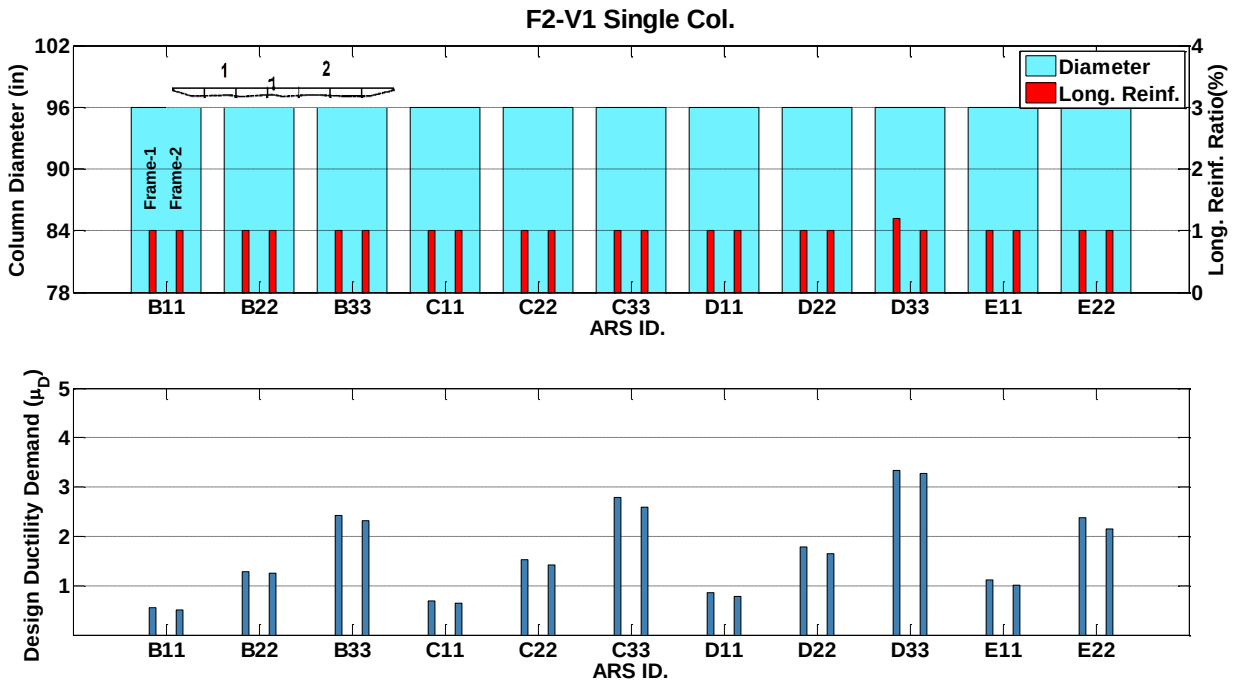

Figure B.1 Seismic Design Results of Prototype F2-V1, Single-Column

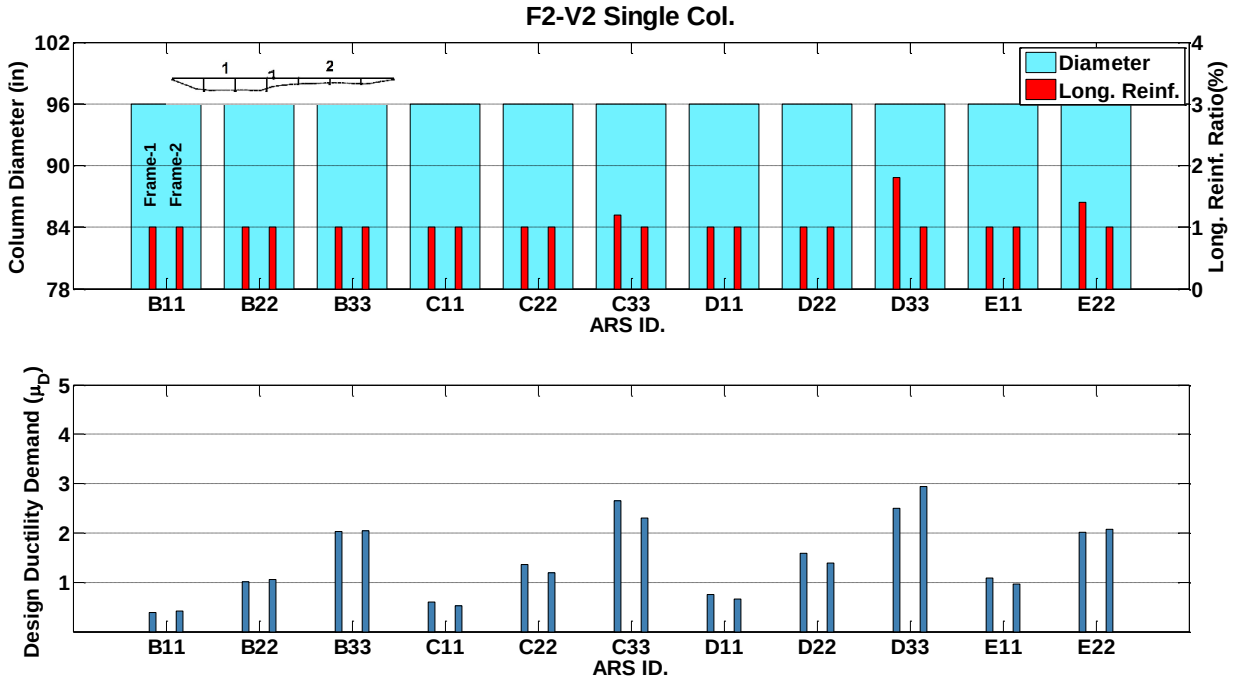

Figure B.2 Seismic Design Results of Prototype F2-V2, Single-Column

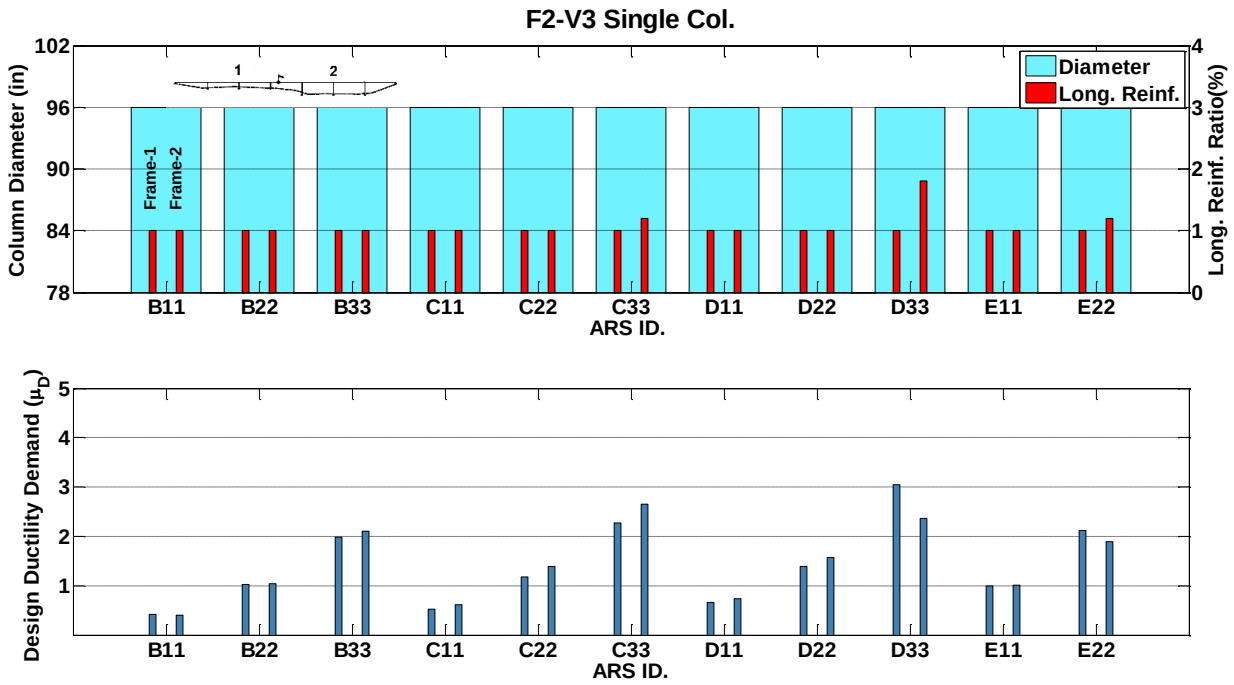

Figure B.3 Seismic Design Results of Prototype F2-V3, Single-Column

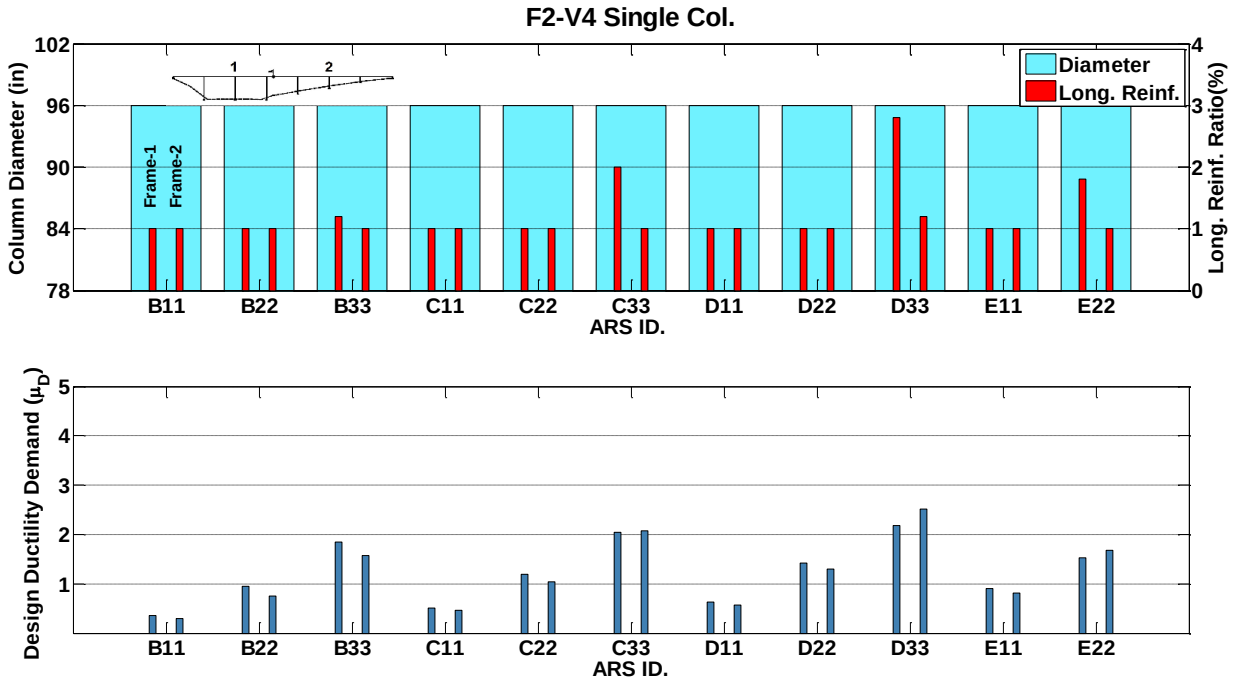

Figure B.4 Seismic Design Results of Prototype F2-V4, Single-Column

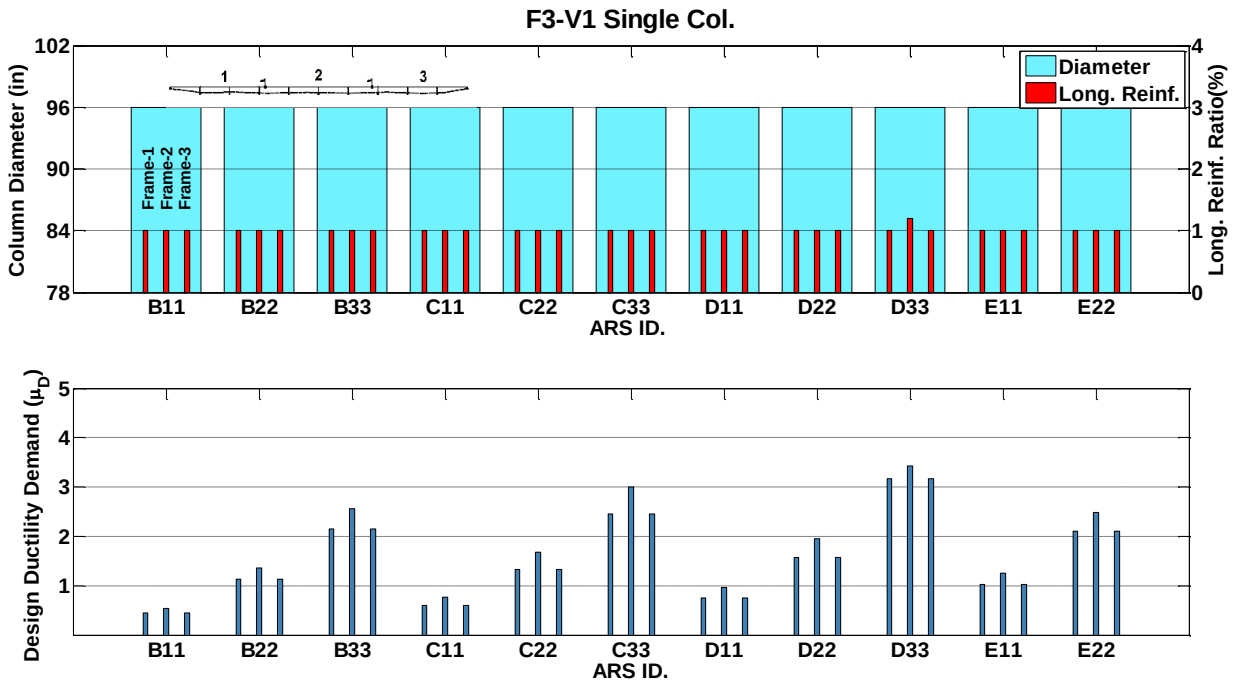

Figure B.5 Seismic Design Results of Prototype F3-V1, Single-Column

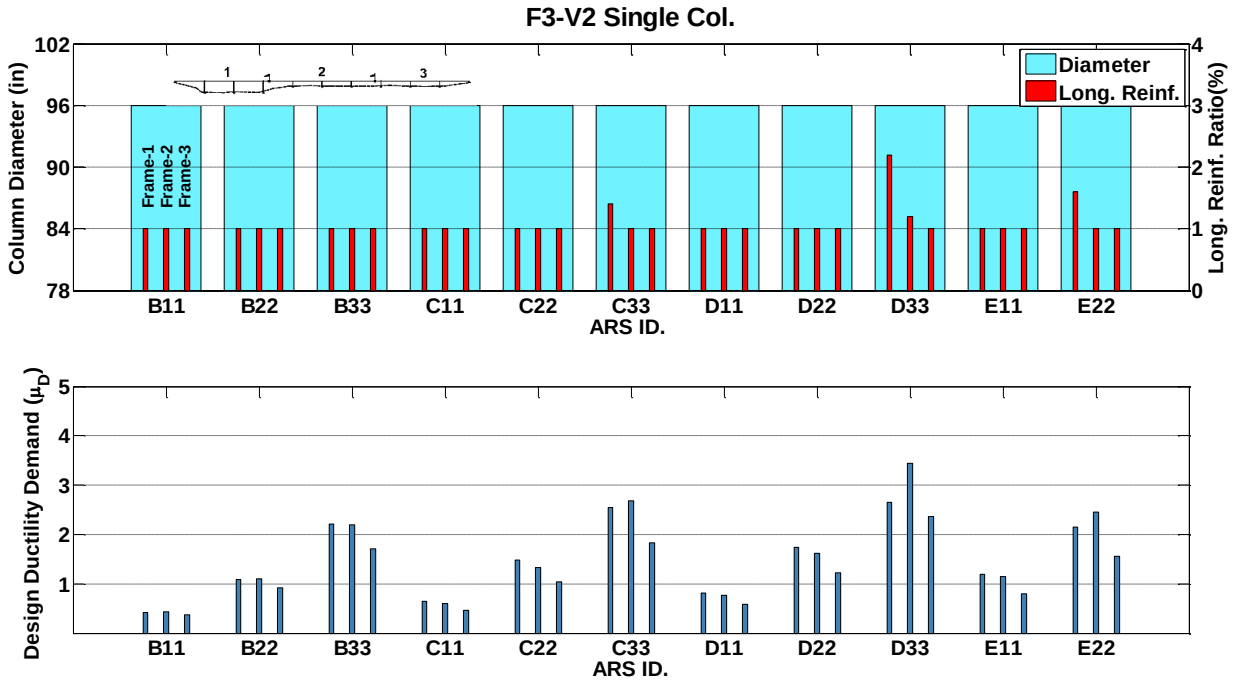

Figure B.6 Seismic Design Results of Prototype F3-V2, Single-Column

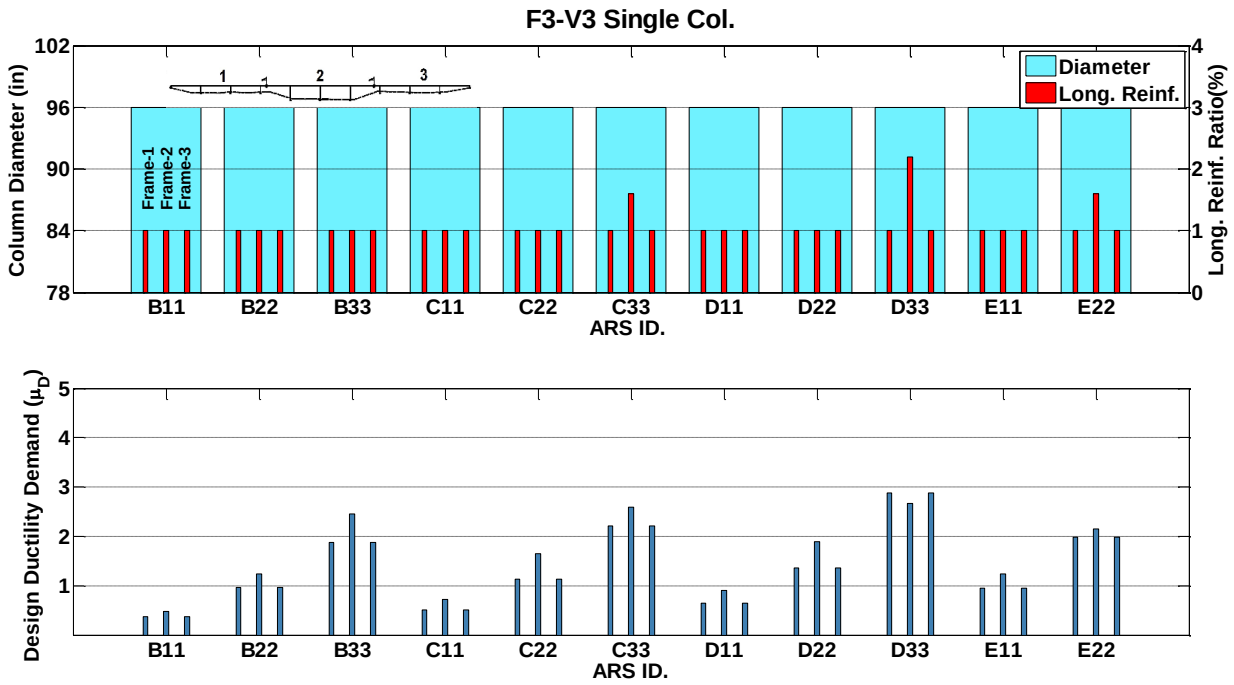

Figure B.7 Seismic Design Results of Prototype F3-V3, Single-Column

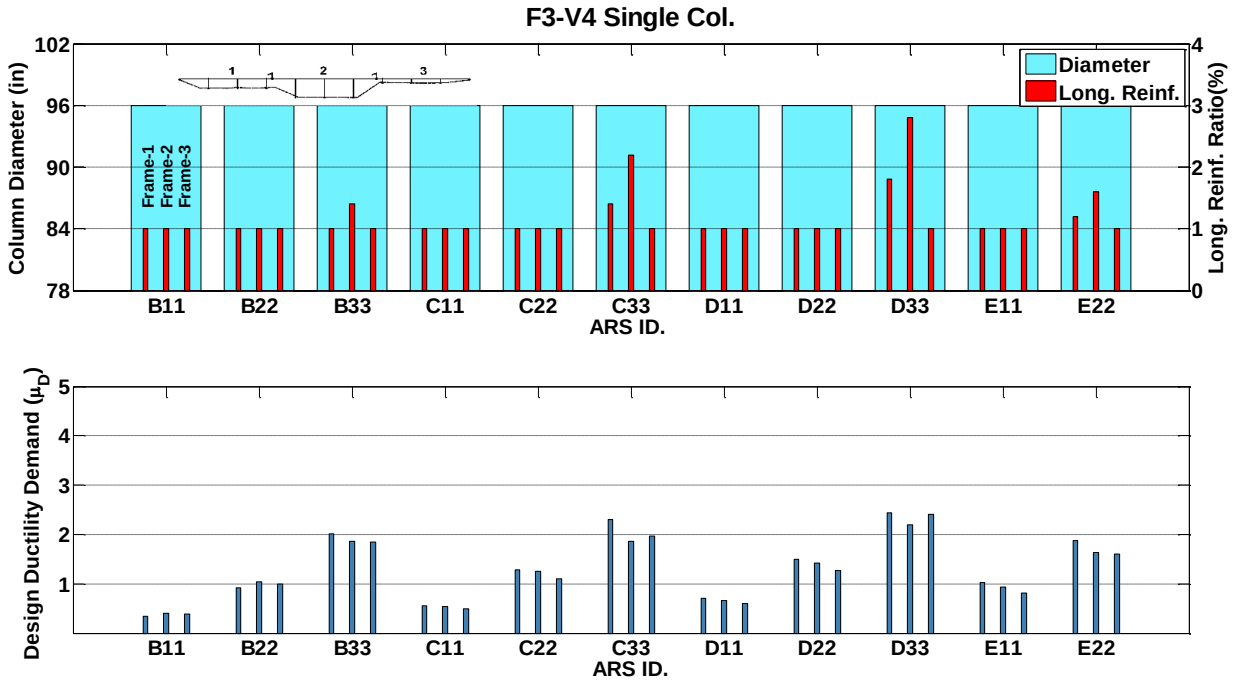

Figure B.8 Seismic Design Results of Prototype F3-V4, Single-Column

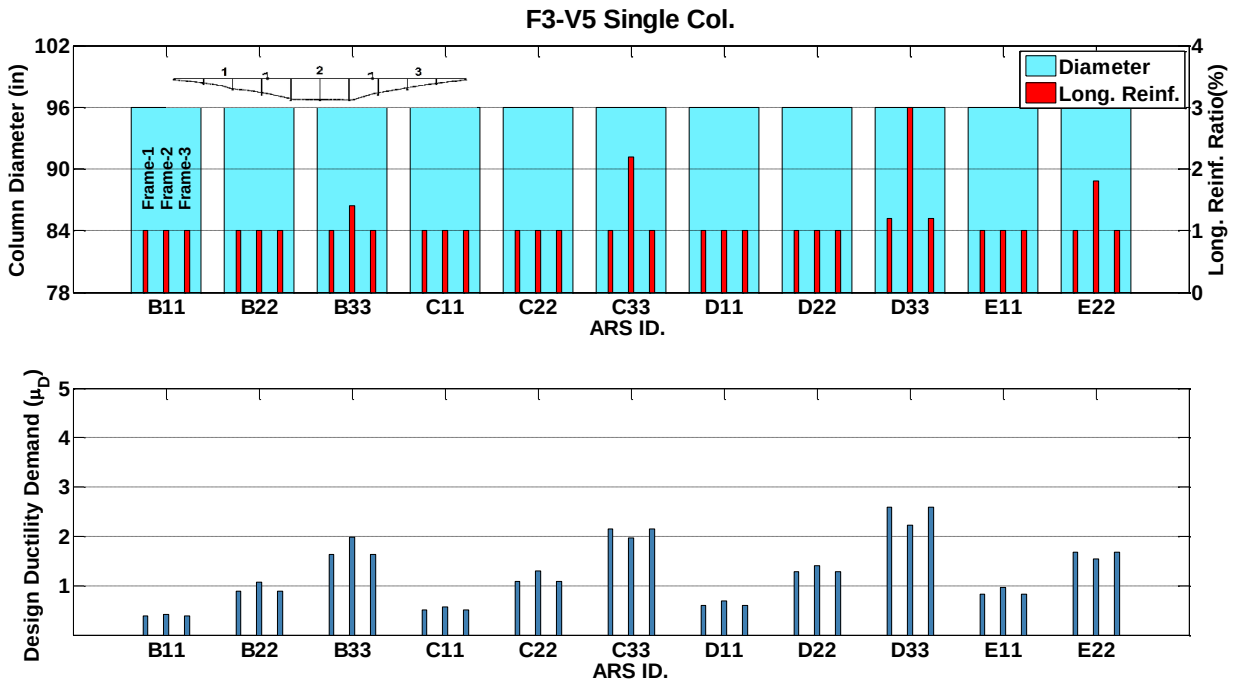

Figure B.9 Seismic Design Results of Prototype F3-V5, Single-Column

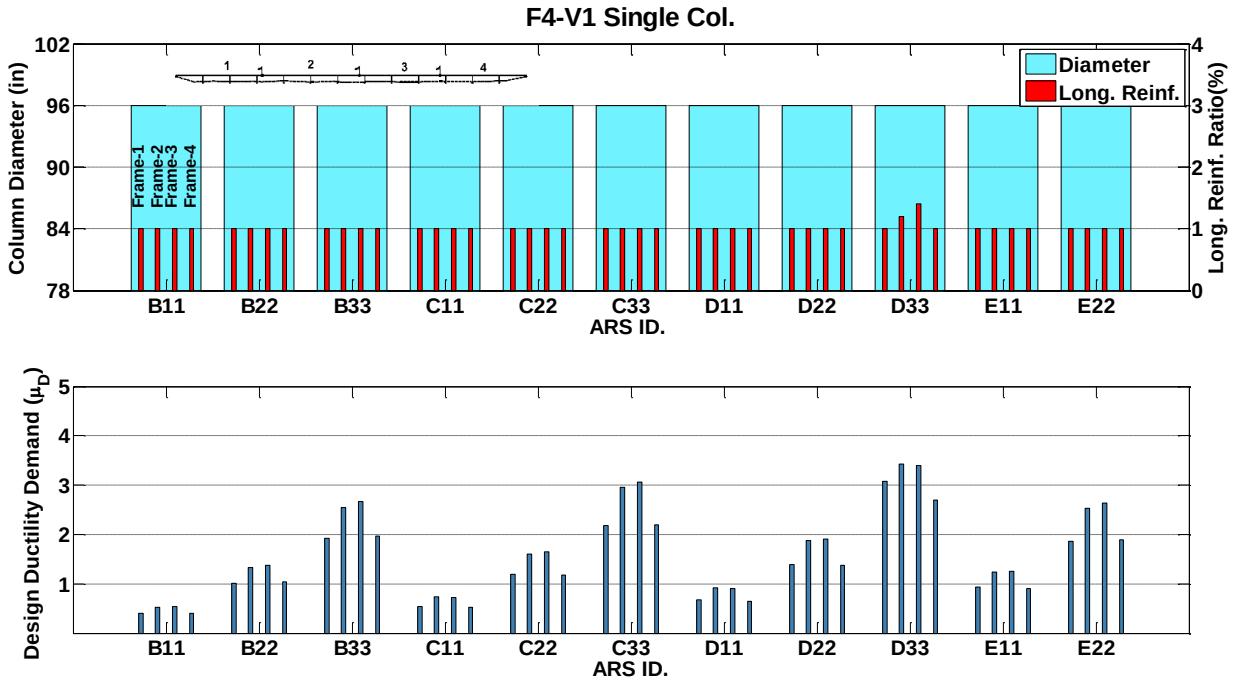

Figure B.10 Seismic Design Results of Prototype F4-V1, Single-Column

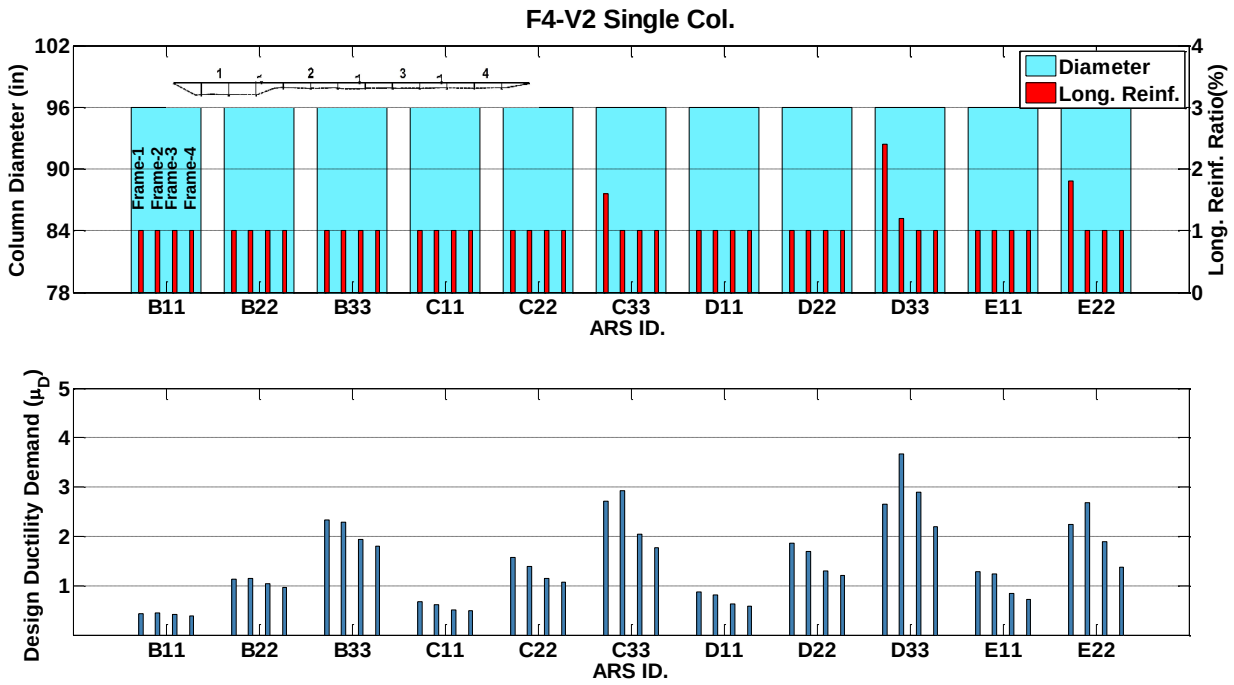

Figure B.11 Seismic Design Results of Prototype F4-V2, Single-Column

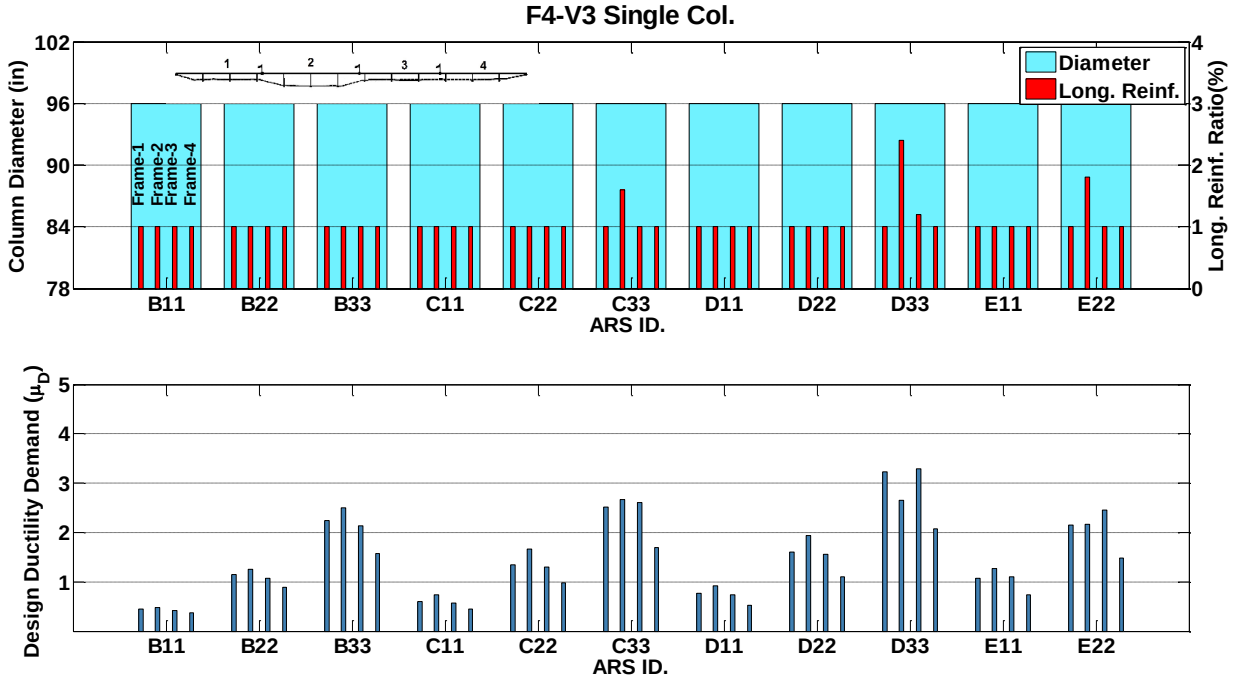

Figure B.12 Seismic Design Results of Prototype F4-V3, Single-Column

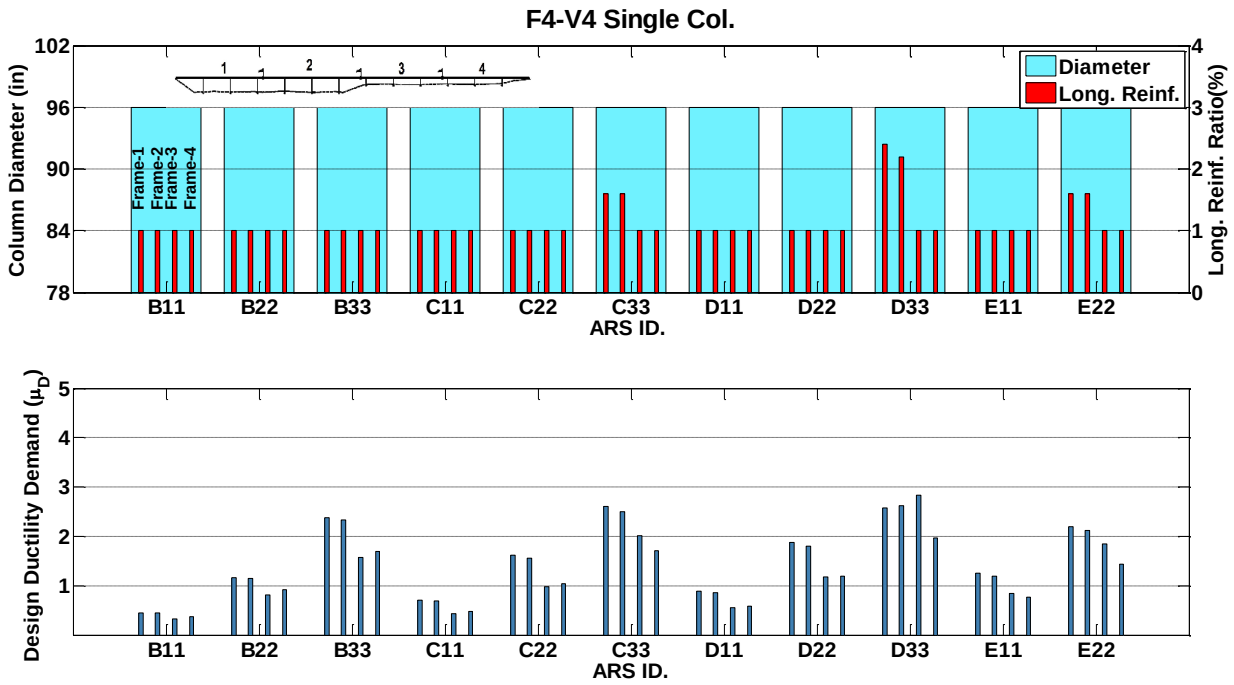

Figure B.13 Seismic Design Results of Prototype F4-V4, Single-Column

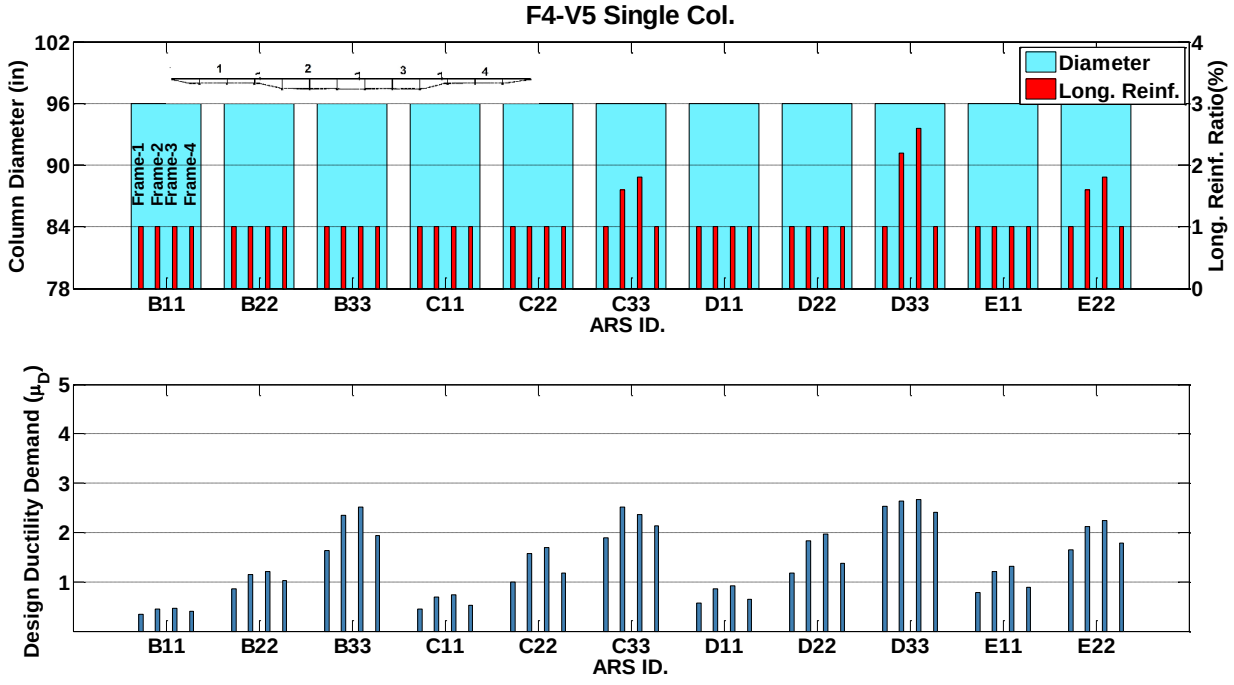

Figure B.14 Seismic Design Results of Prototype F4-V5, Single-Column

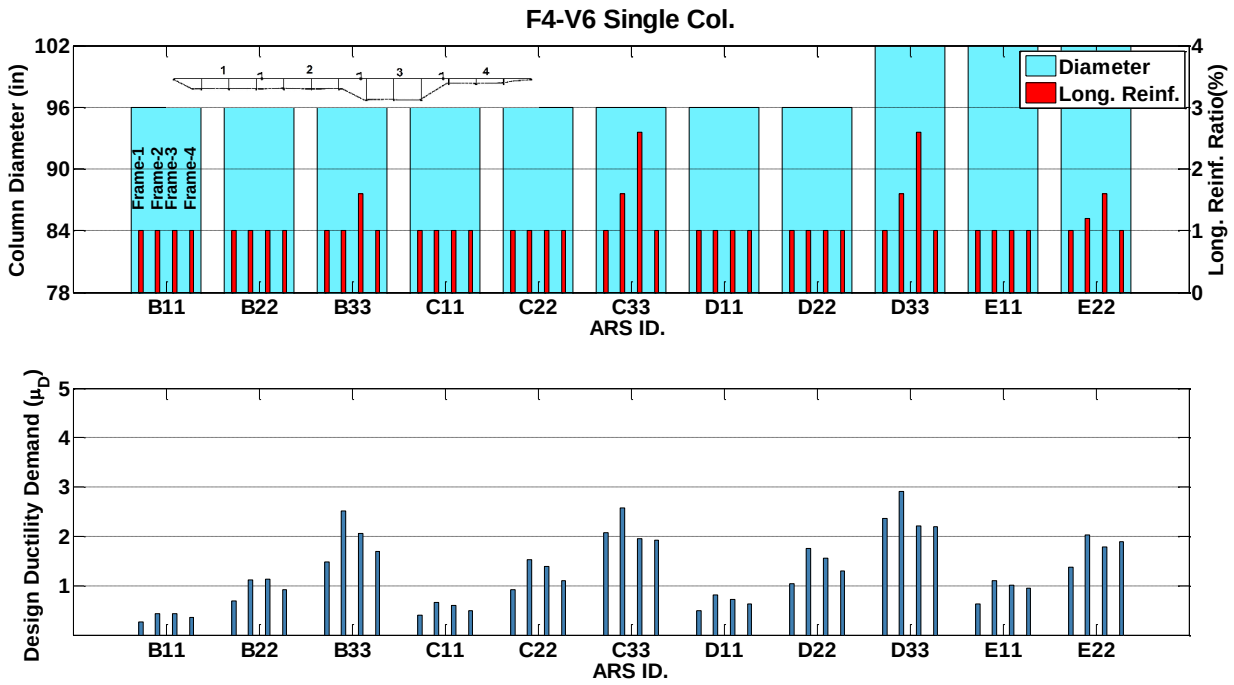

Figure B.15 Seismic Design Results of Prototype F4-V6, Single-Column

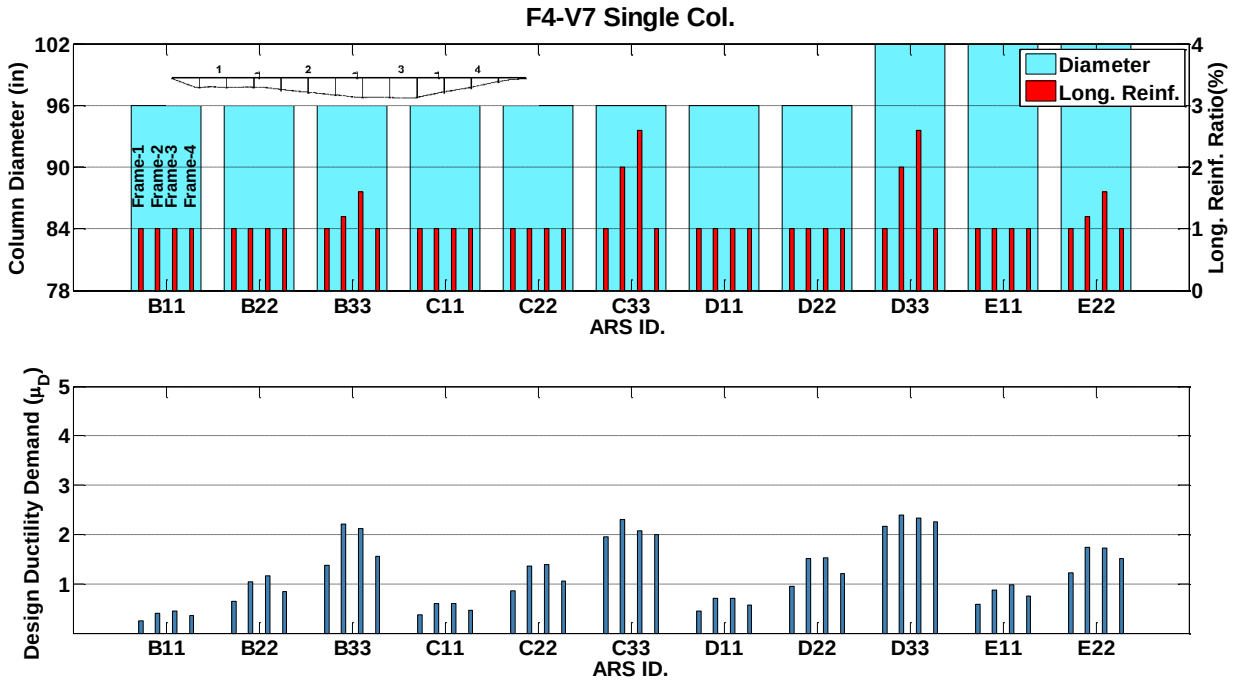

Figure B.16 Seismic Design Results of Prototype F4-V7, Single-Column

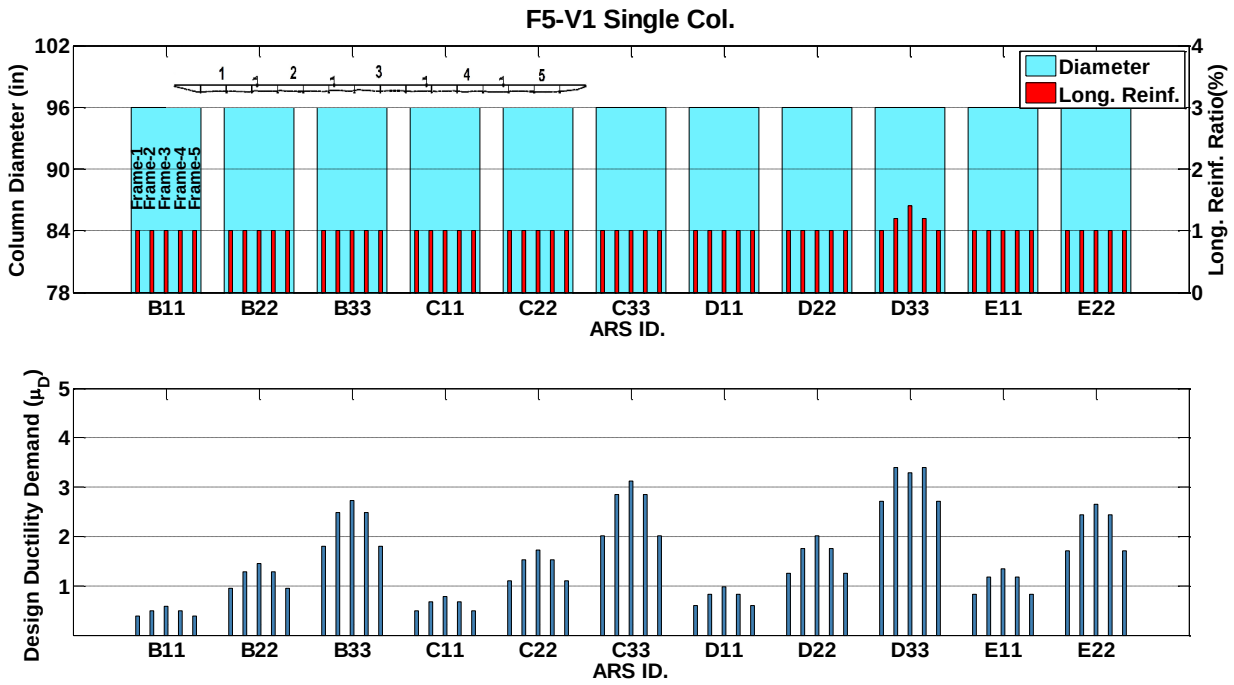

Figure B.17 Seismic Design Results of Prototype F5-V1, Single-Column

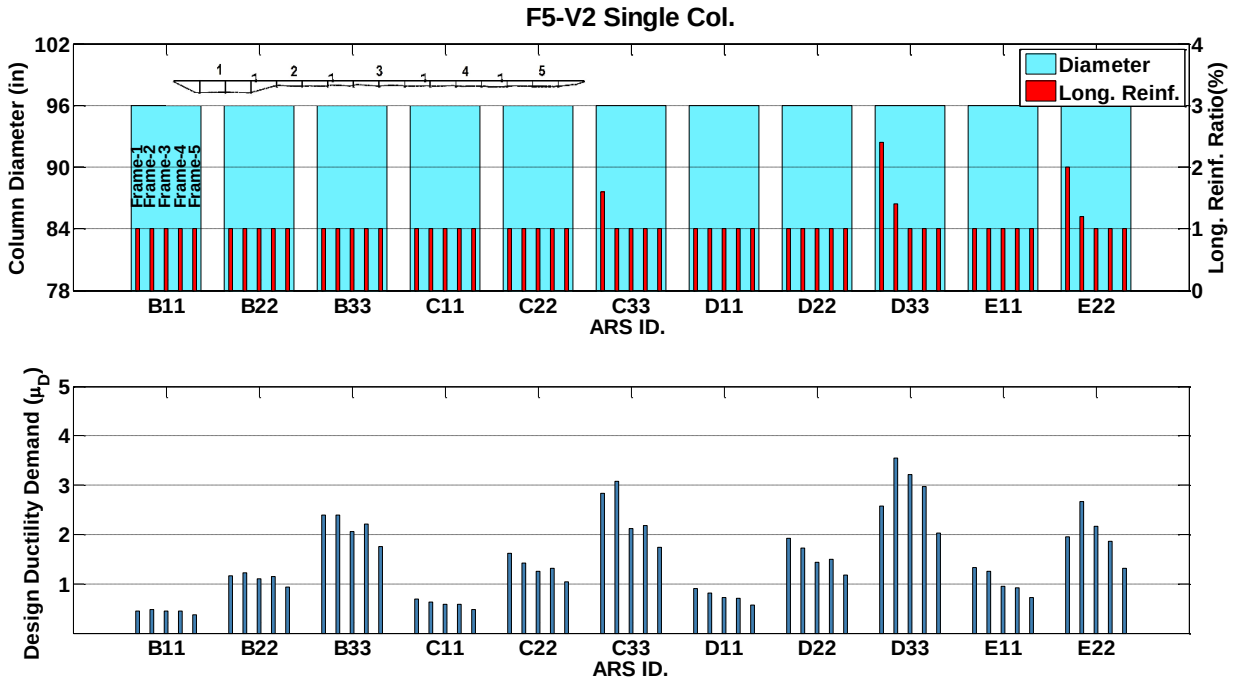

Figure B.18 Seismic Design Results of Prototype F5-V2, Single-Column

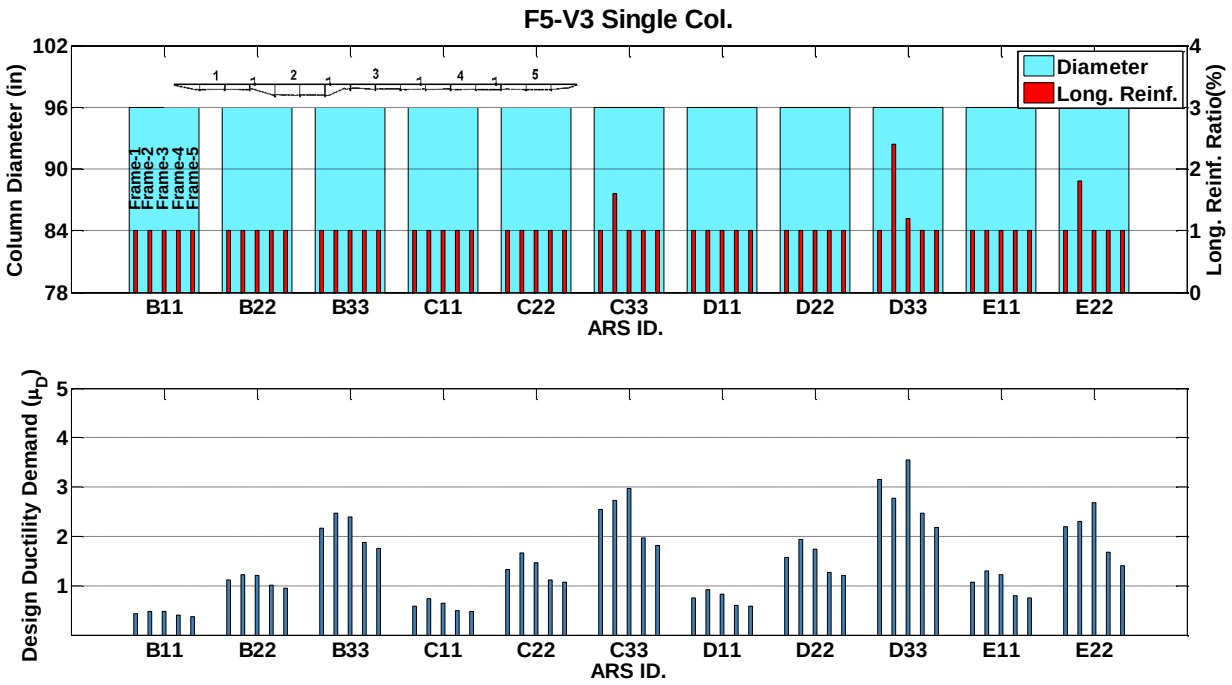

Figure B.19 Seismic Design Results of Prototype F5-V3, Single-Column

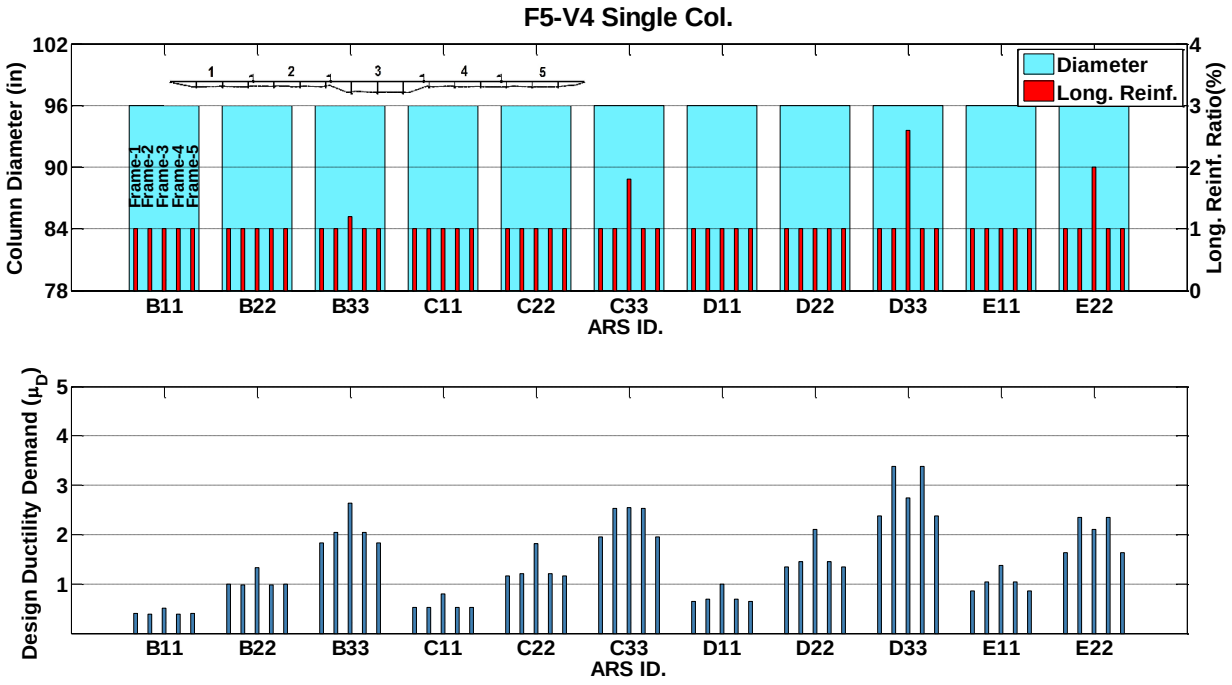

Figure B.20 Seismic Design Results of Prototype F5-V4, Single-Column

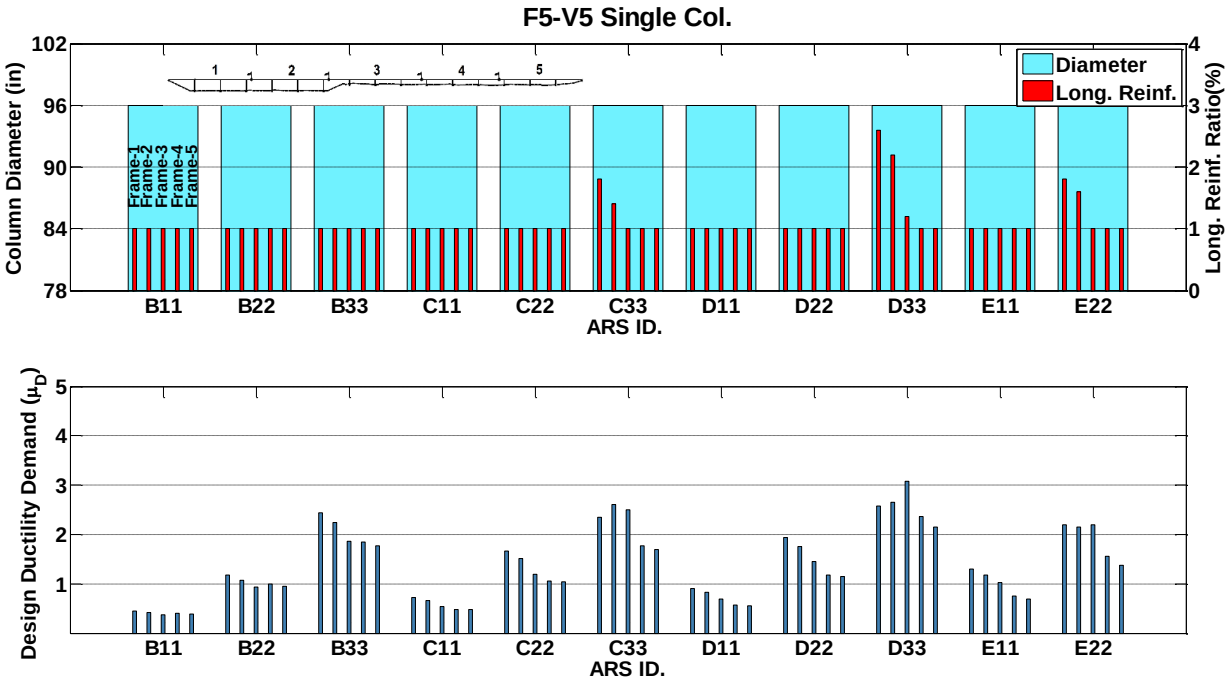

Figure B.21 Seismic Design Results of Prototype F5-V5, Single-Column

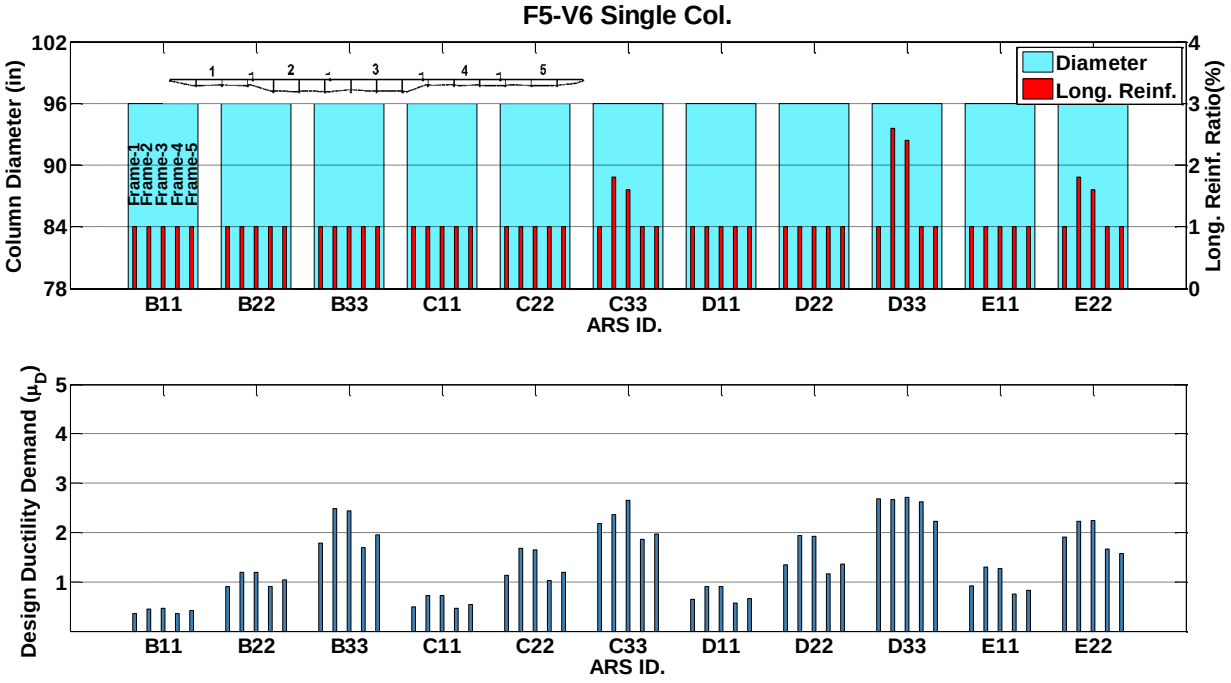

Figure B.22 Seismic Design Results of Prototype F5-V6, Single-Column

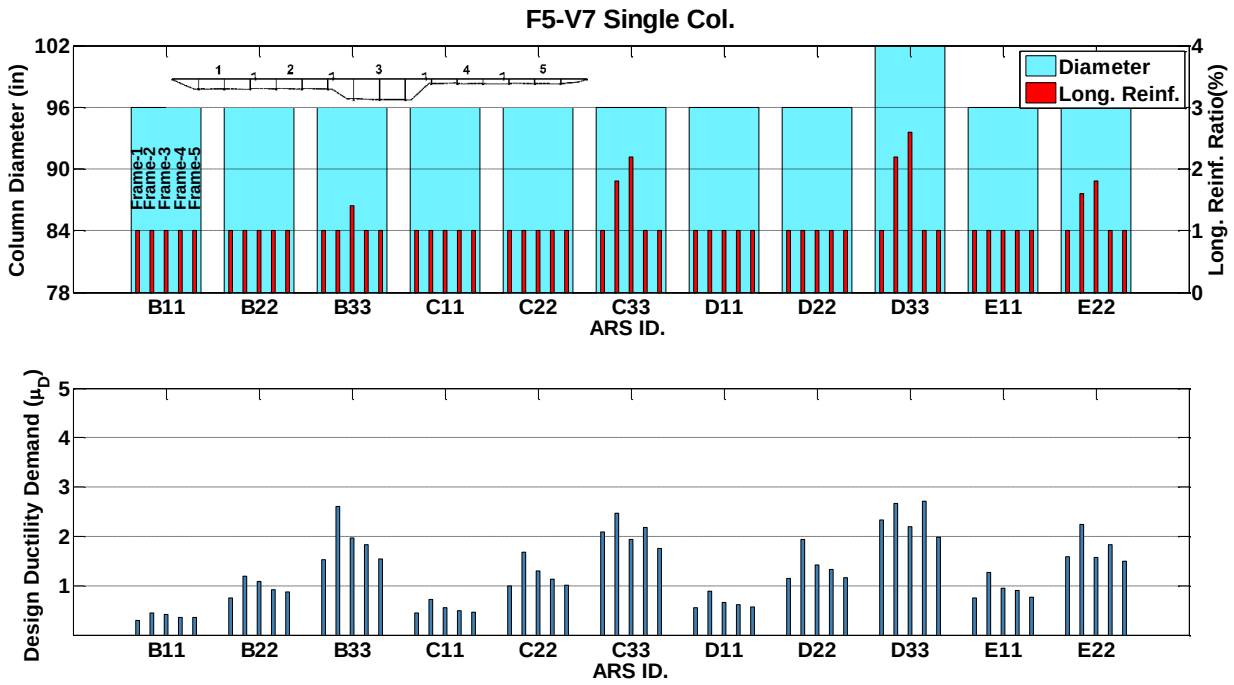

Figure B.23 Seismic Design Results of Prototype F5-V7, Single-Column

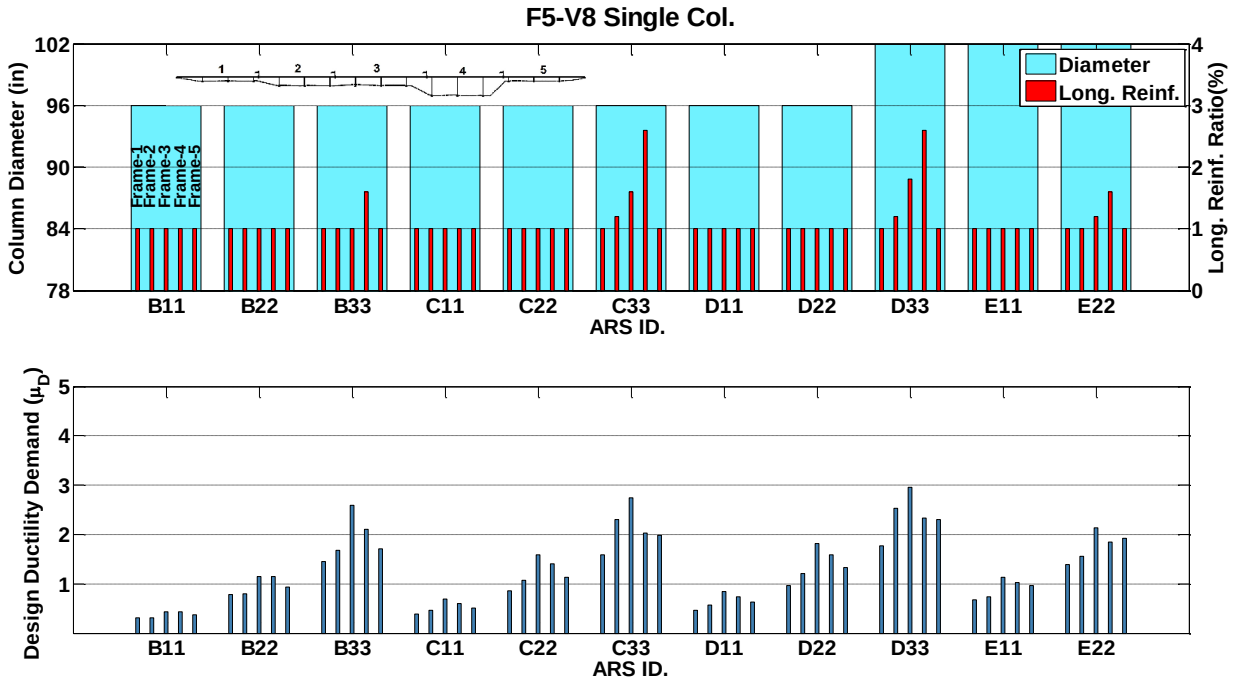

Figure B.24 Seismic Design Results of Prototype F5-V8, Single-Column

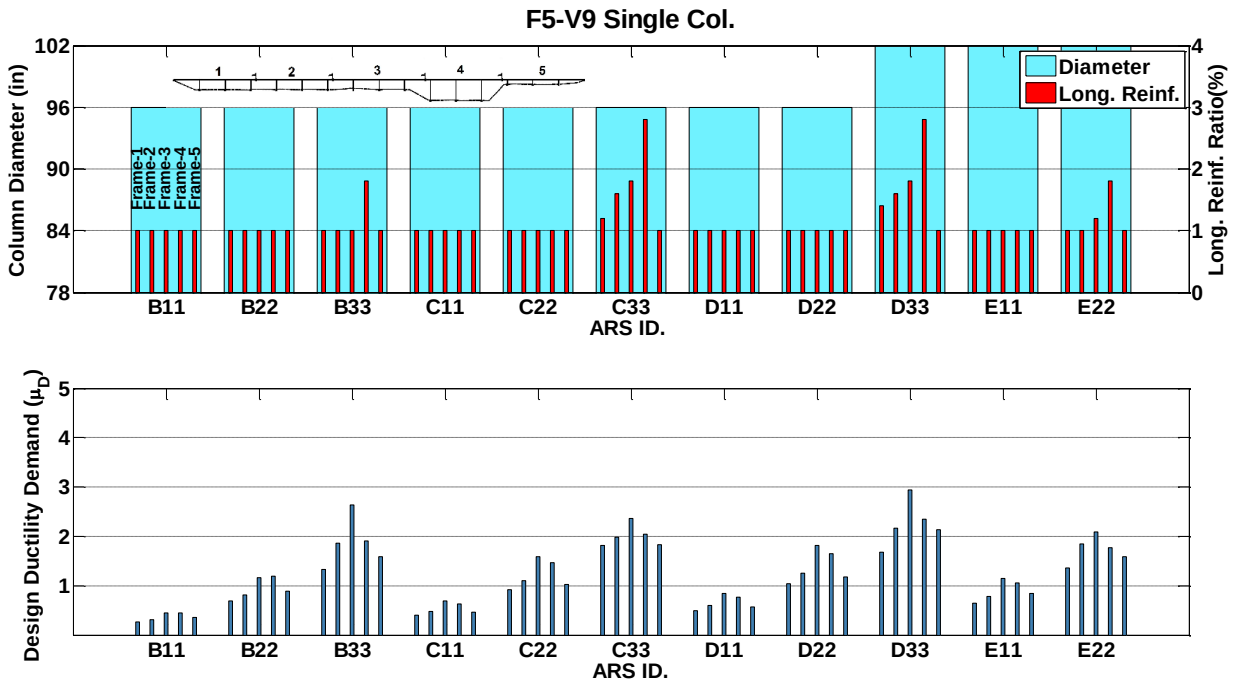

Figure B.25 Seismic Design Results of Prototype F5-V9, Single-Column

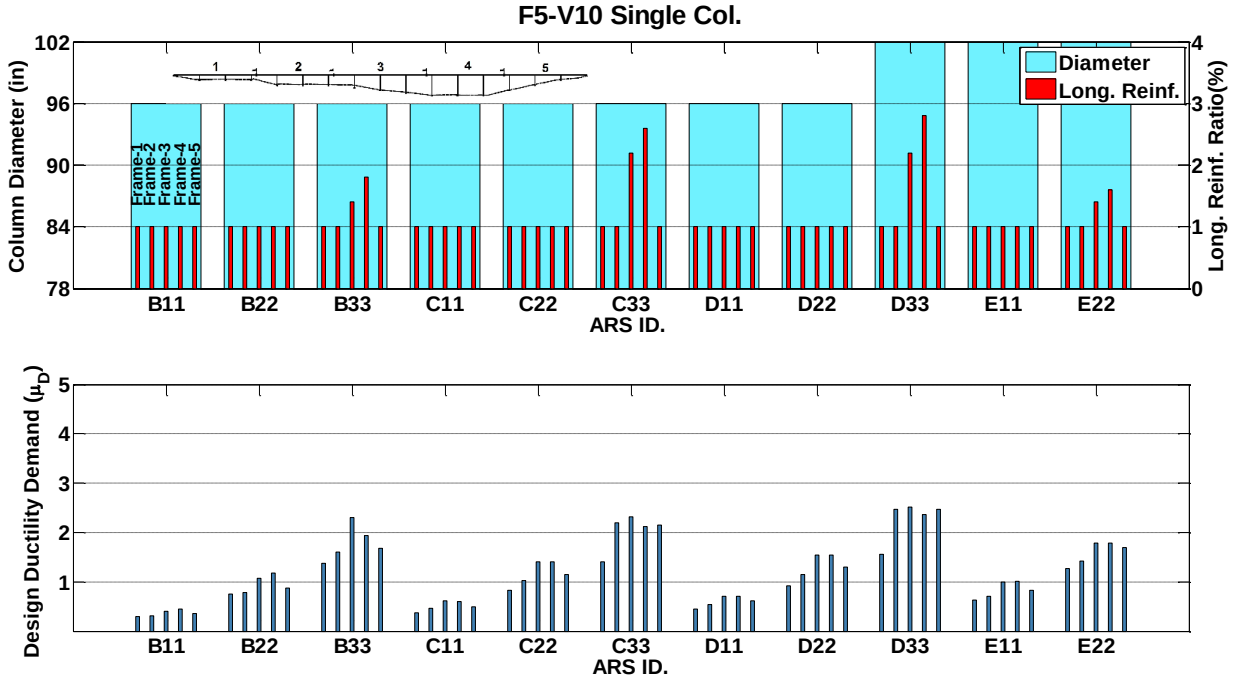

Figure B.26 Seismic Design Results of Prototype F5-V10, Single-Column

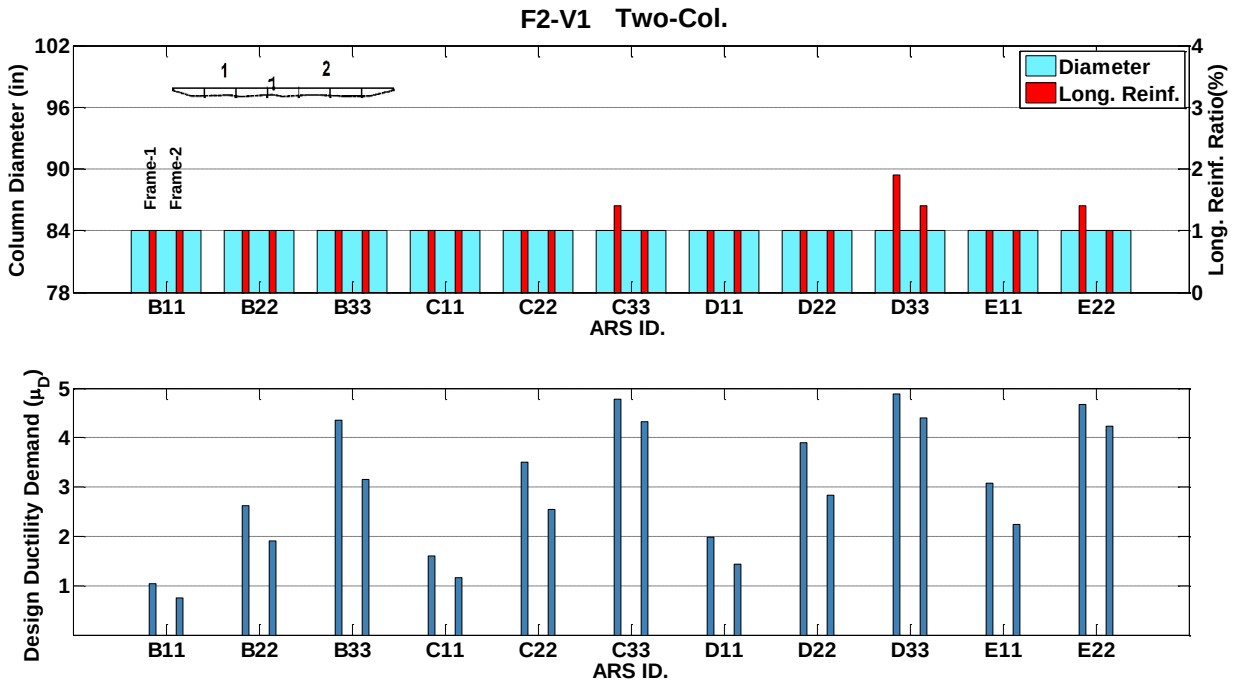

Figure B.27 Seismic Design Results of Prototype F2-V1, Two-Column

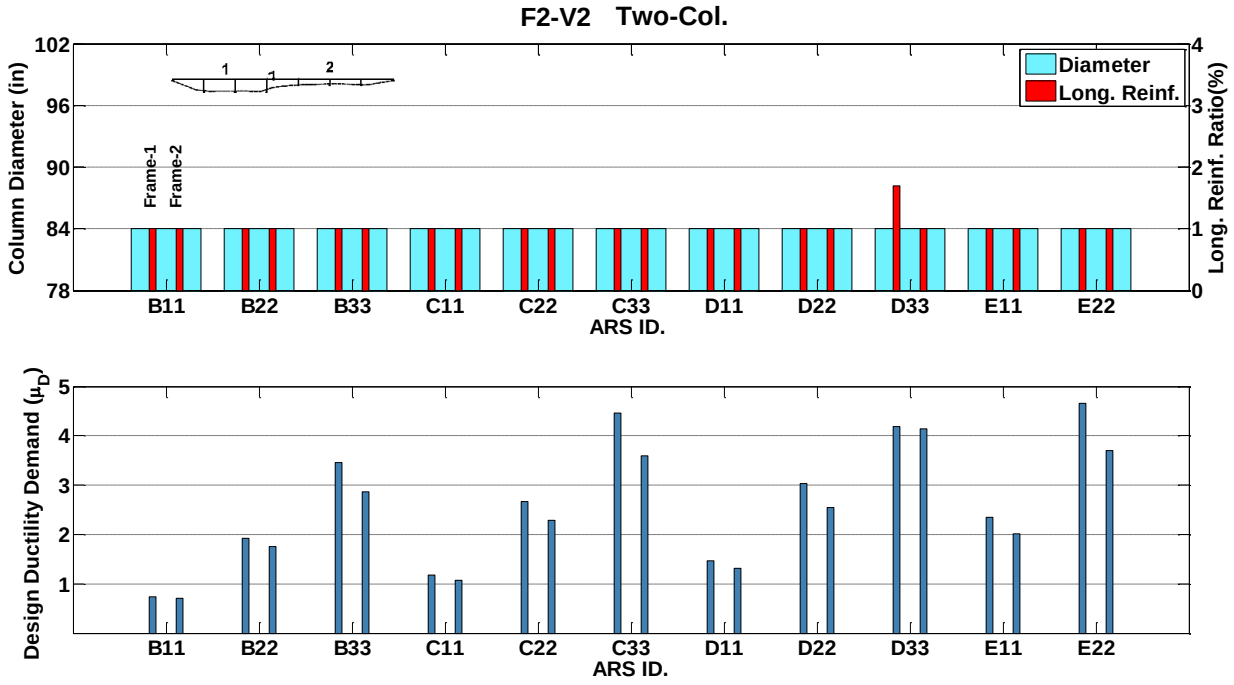

Figure B.28 Seismic Design Results of Prototype F2-V2, Two-Column

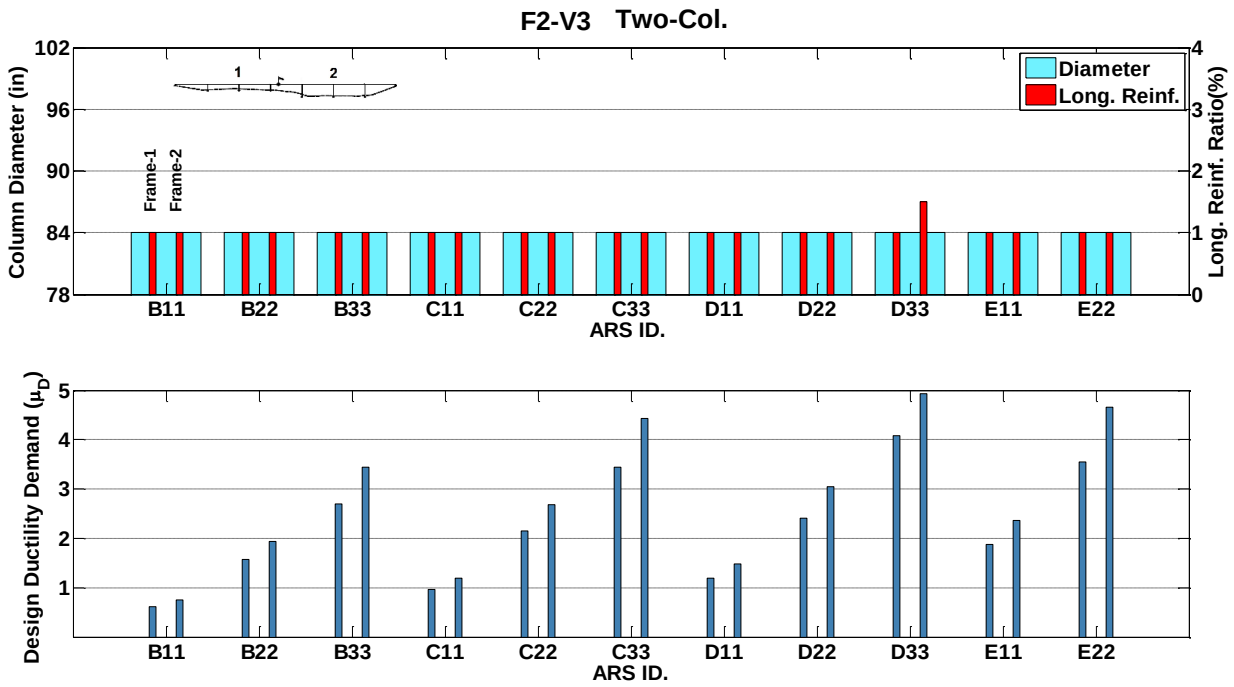

Figure B.29 Seismic Design Results of Prototype F2-V3, Two-Column

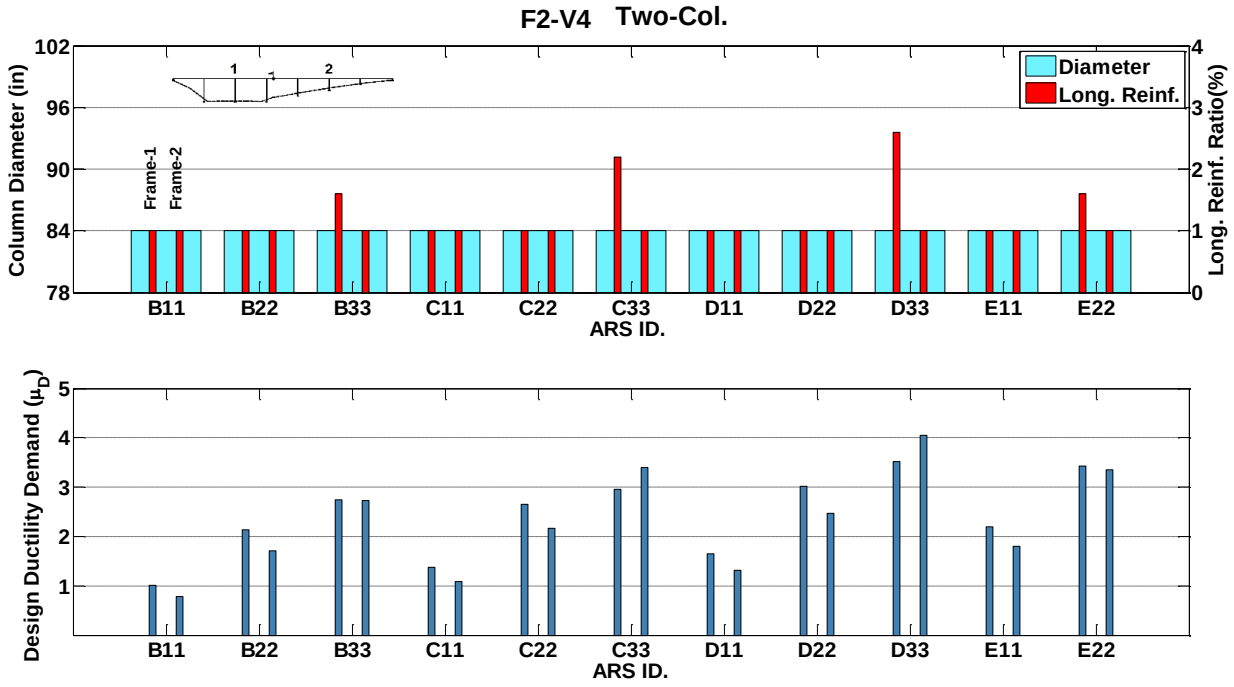

Figure B.30 Seismic Design Results of Prototype F2-V4, Two-Column

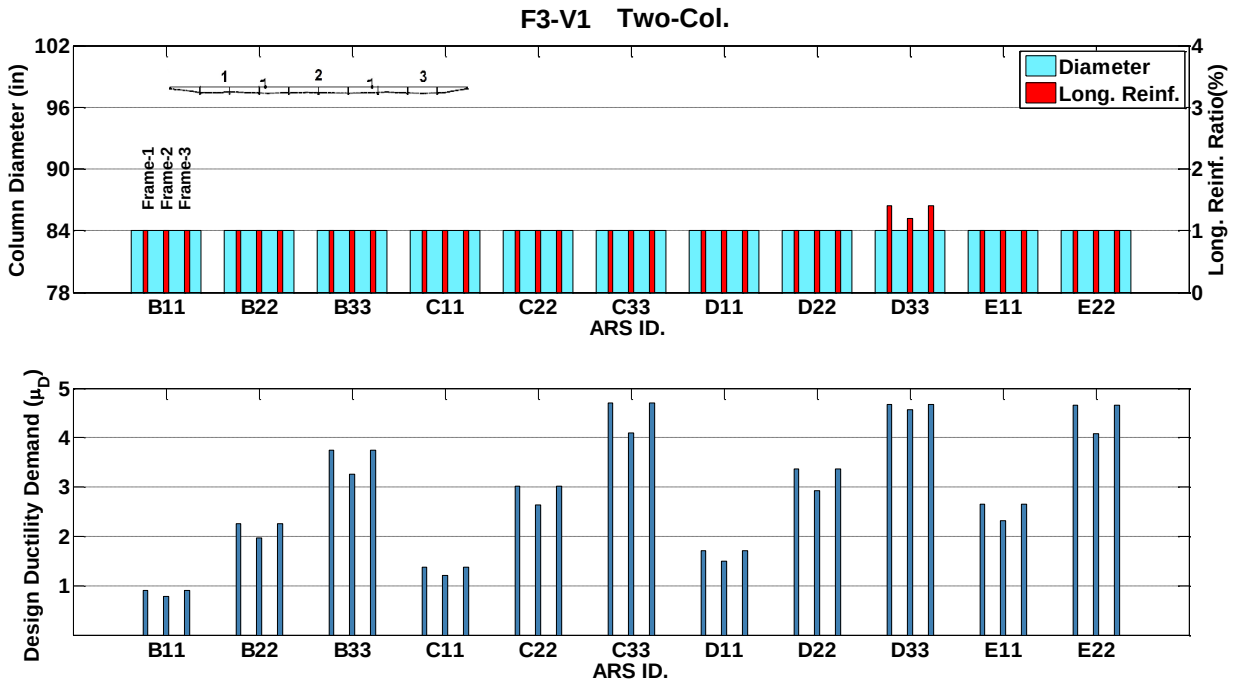

Figure B.31 Seismic Design Results of Prototype F3-V1, Two-Column

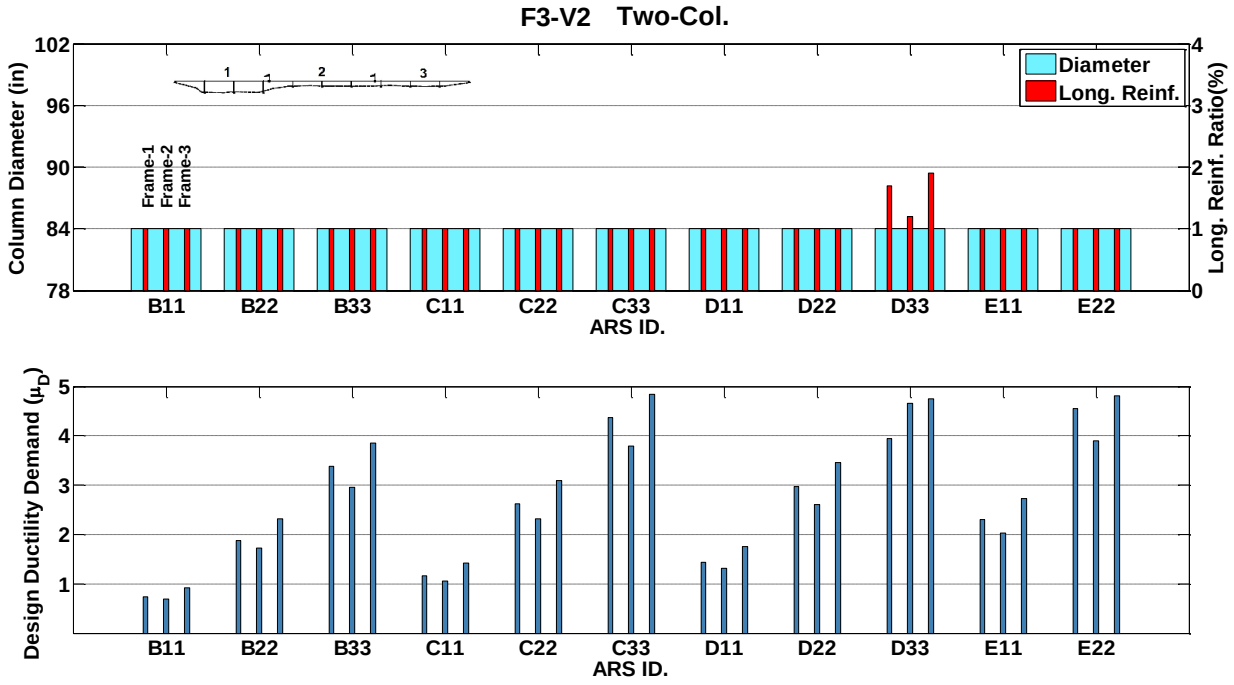

Figure B.32 Seismic Design Results of Prototype F3-V2, Two-Column

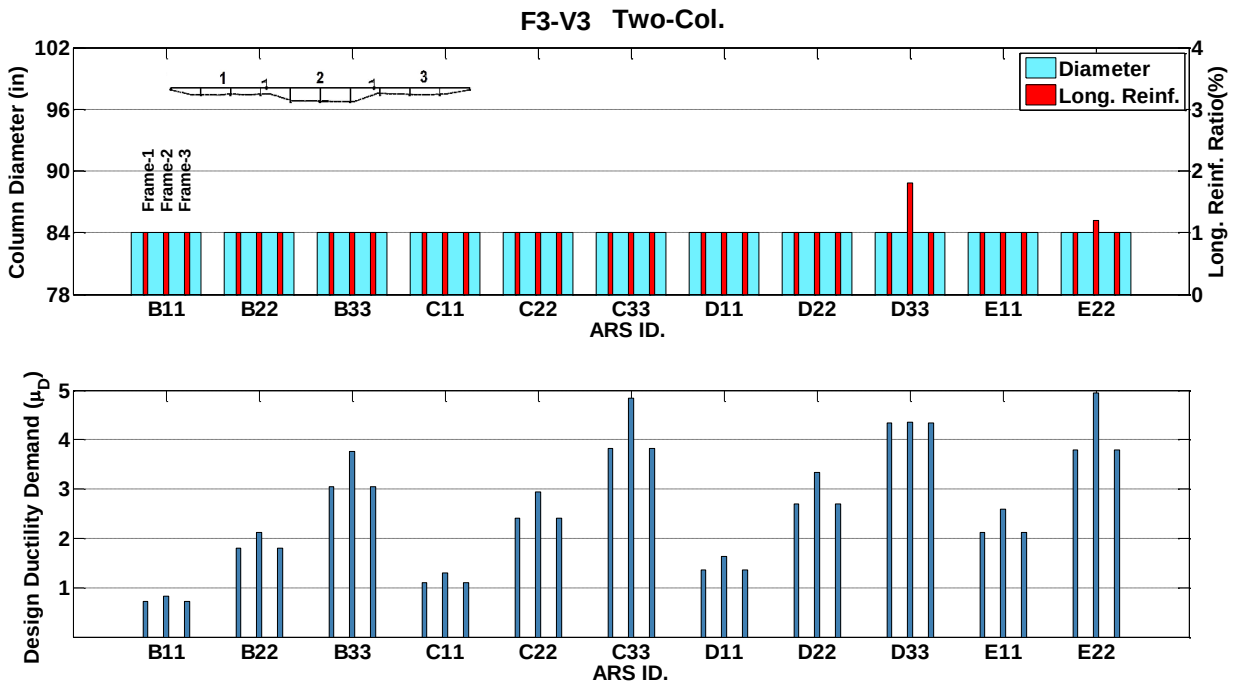

Figure B.33 Seismic Design Results of Prototype F3-V3, Two-Column

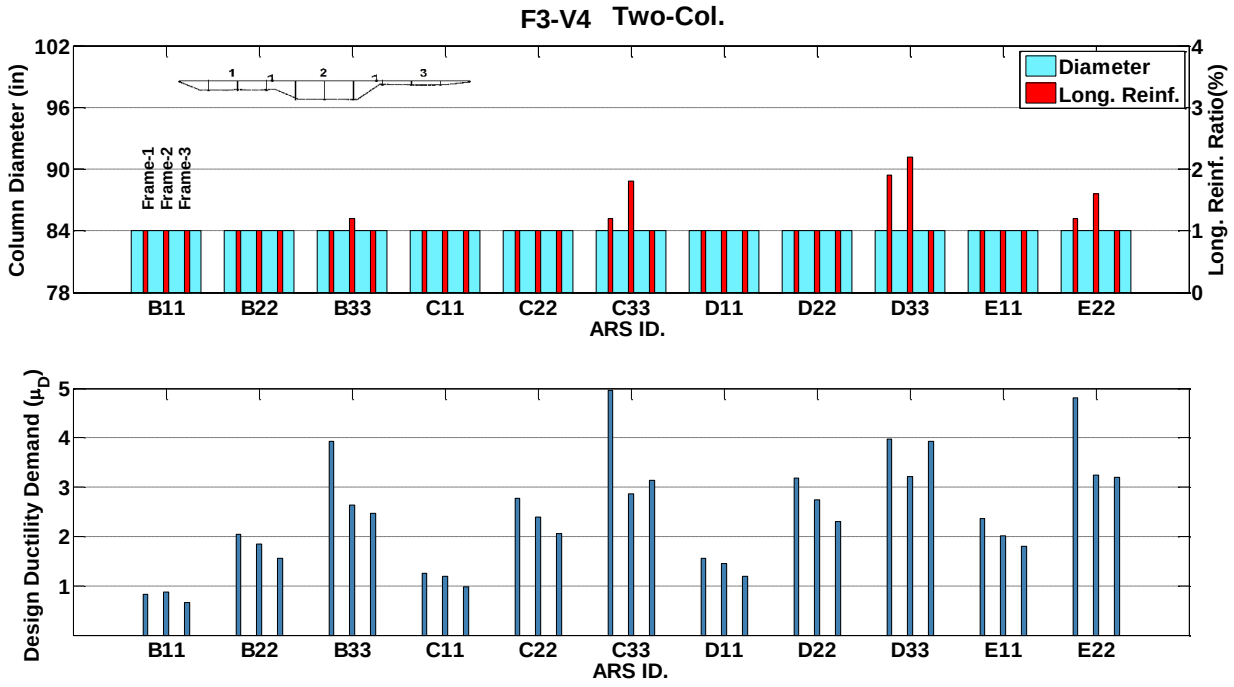

Figure B.34 Seismic Design Results of Prototype F3-V4, Two-Column

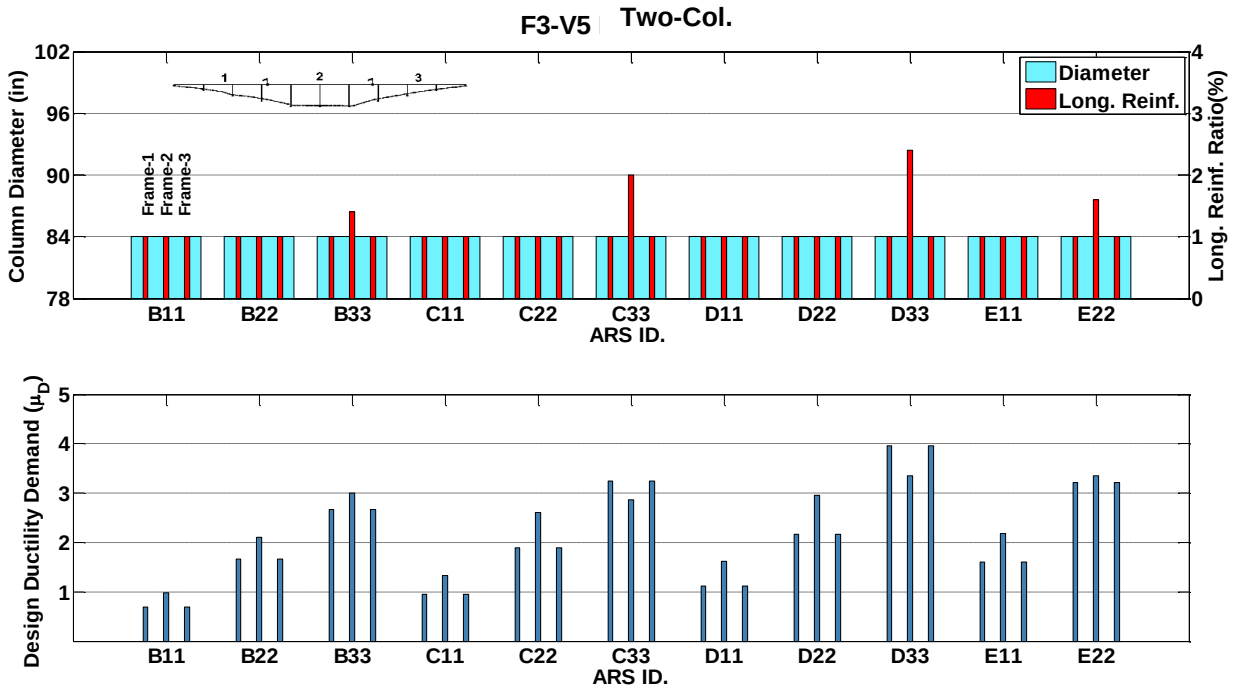

Figure B.35 Seismic Design Results of Prototype F3-V5, Two-Column

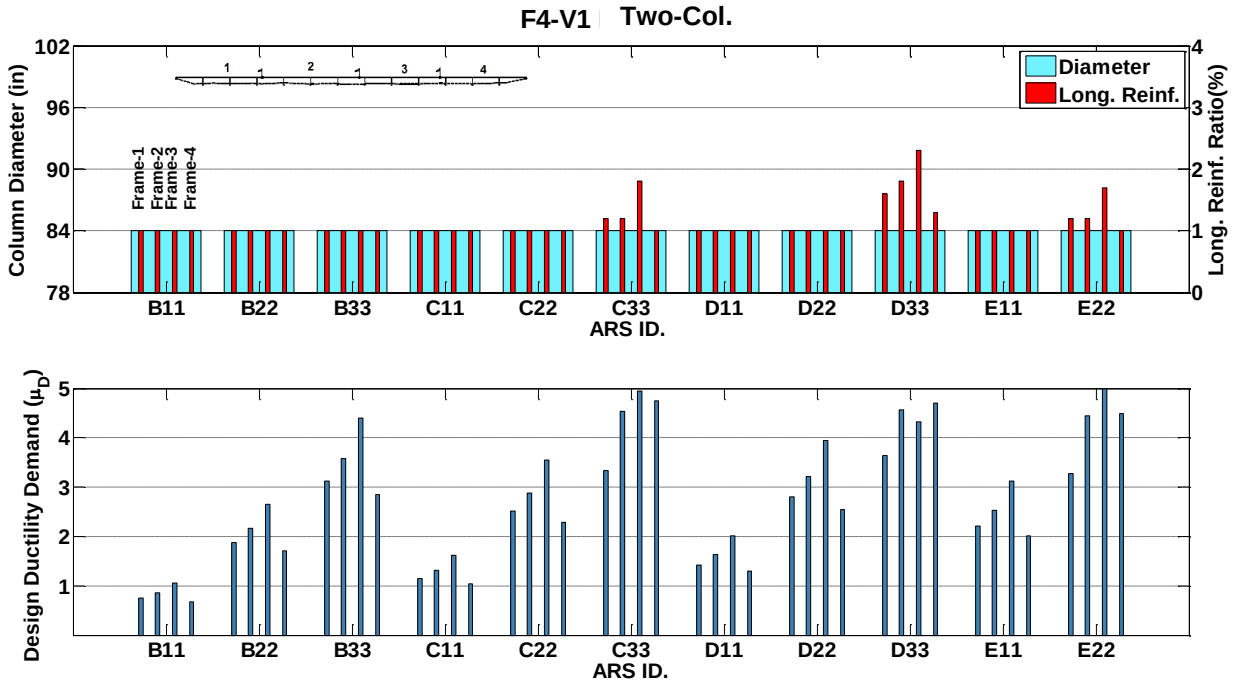

Figure B.36 Seismic Design Results of Prototype F4-V1, Two-Column

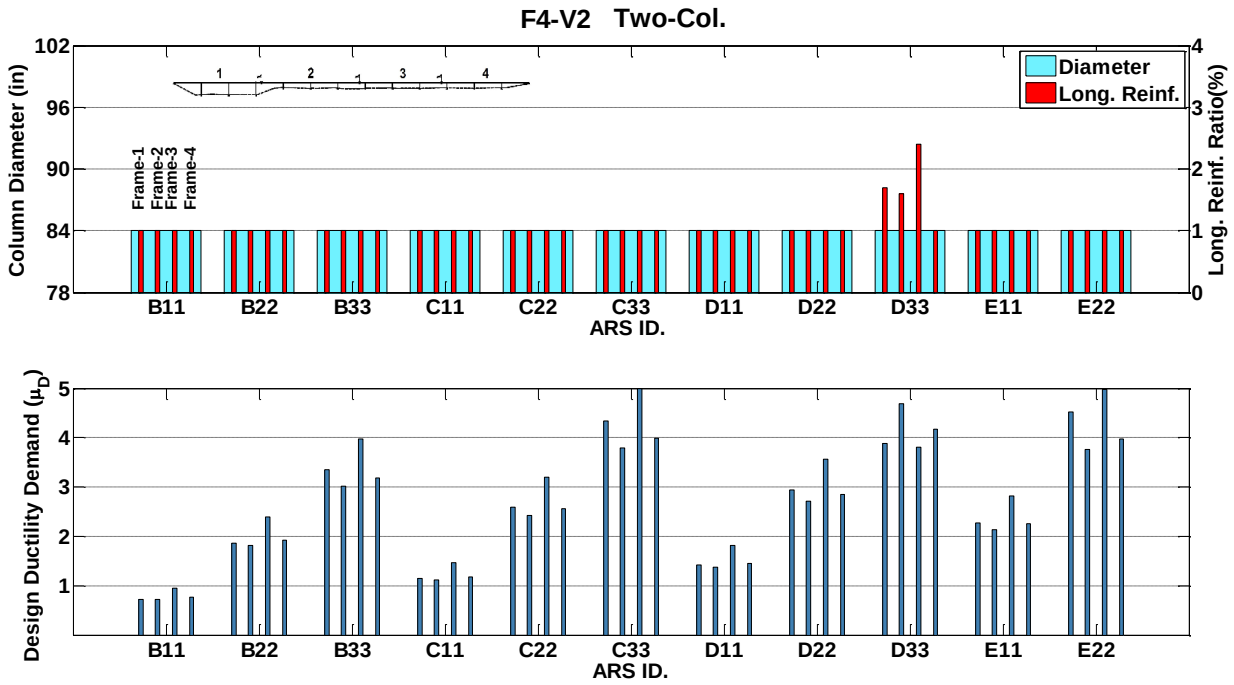

Figure B.37 Seismic Design Results of Prototype F4-V2, Two-Column

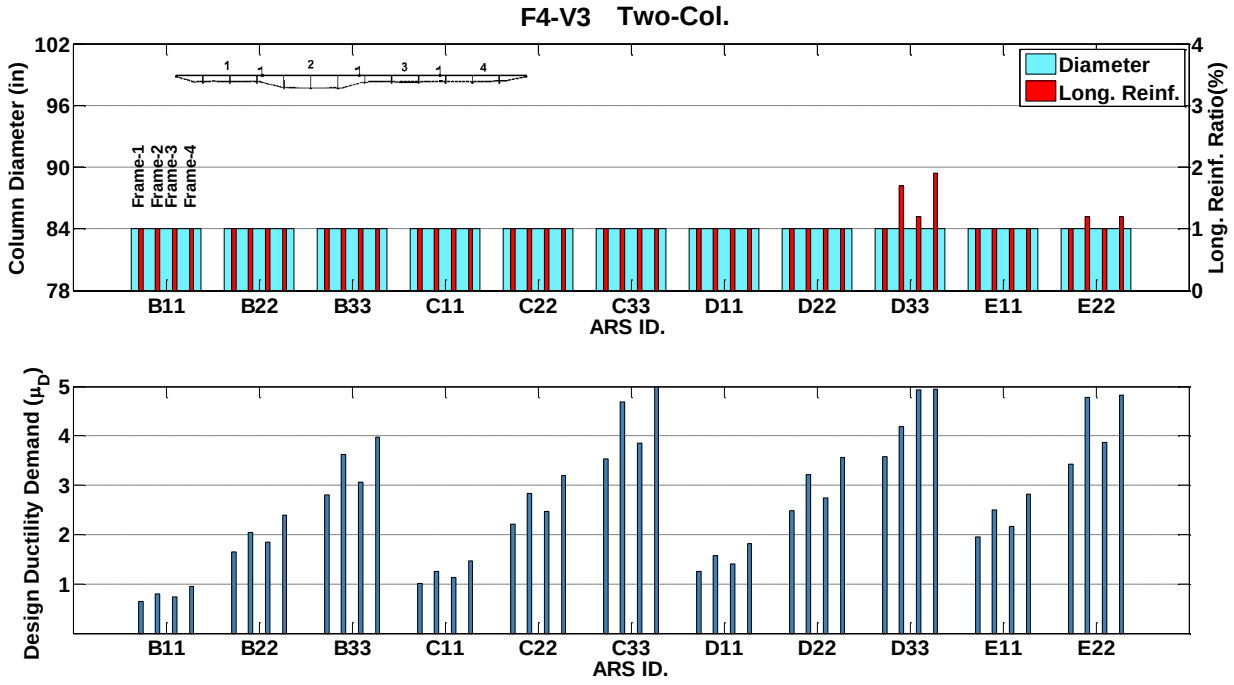

Figure B.38 Seismic Design Results of Prototype F4-V3, Two-Column

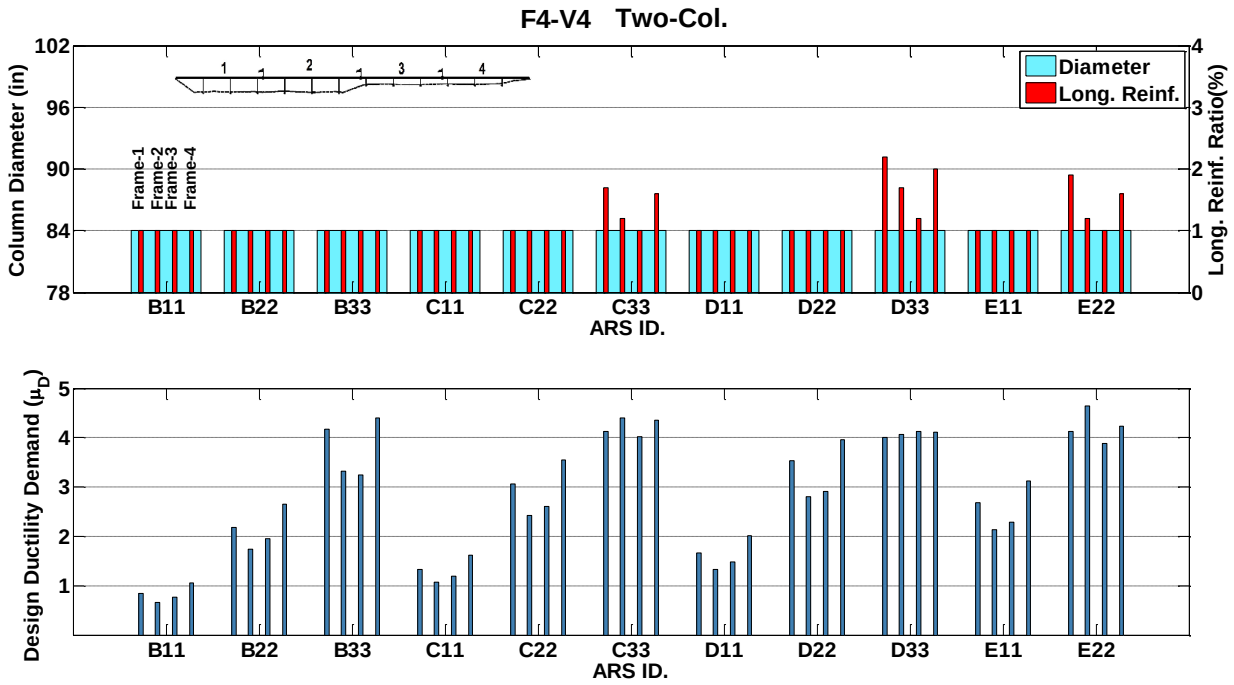

Figure B.39 Seismic Design Results of Prototype F4-V4, Two-Column

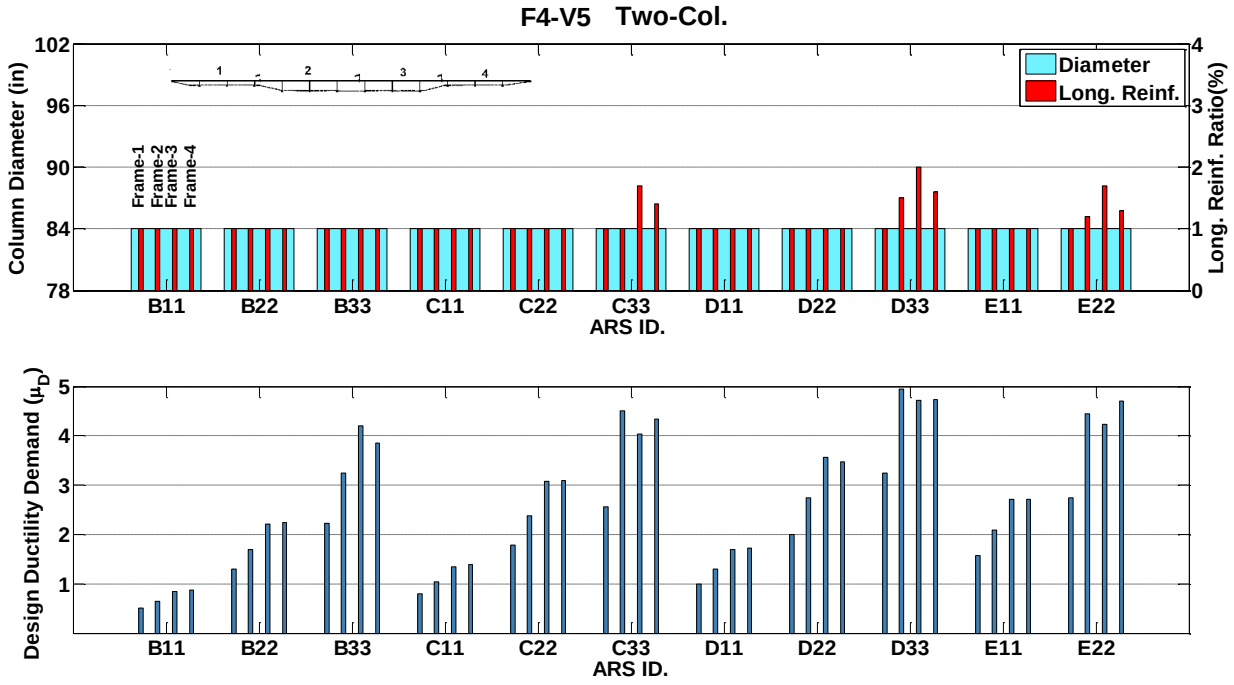

Figure B.40 Seismic Design Results of Prototype F4-V5, Two-Column

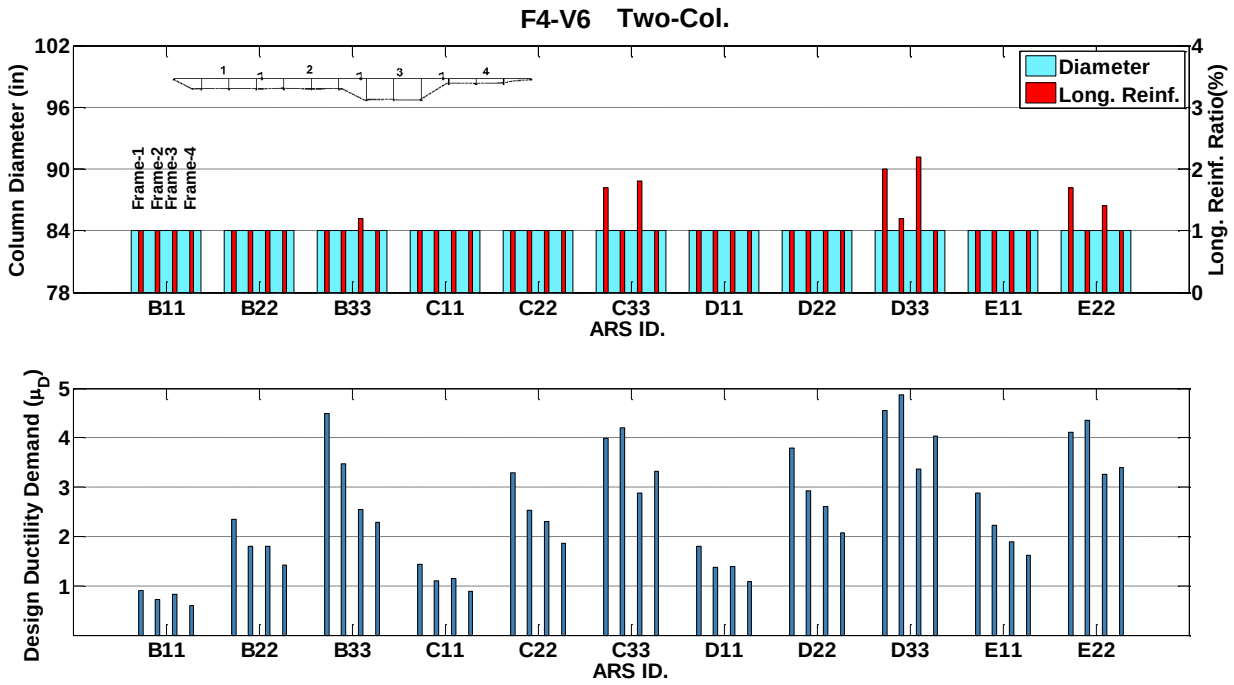

Figure B.41 Seismic Design Results of Prototype F4-V6, Two-Column

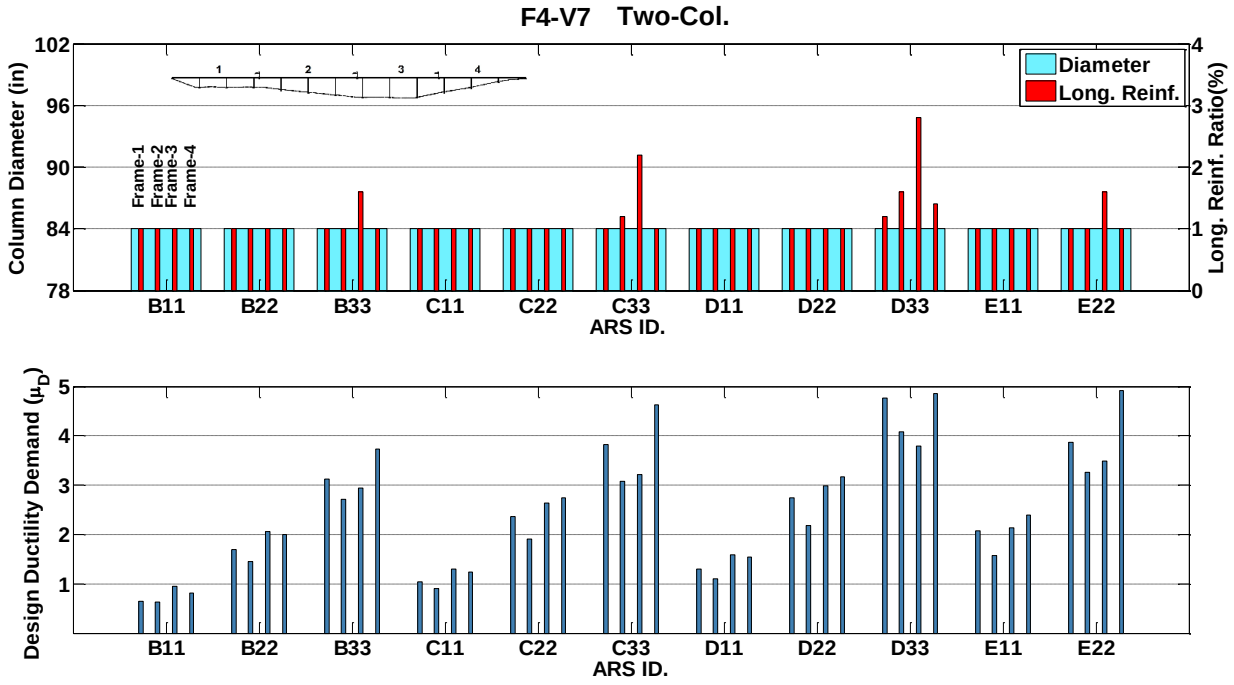

Figure B.42 Seismic Design Results of Prototype F4-V7, Two-Column

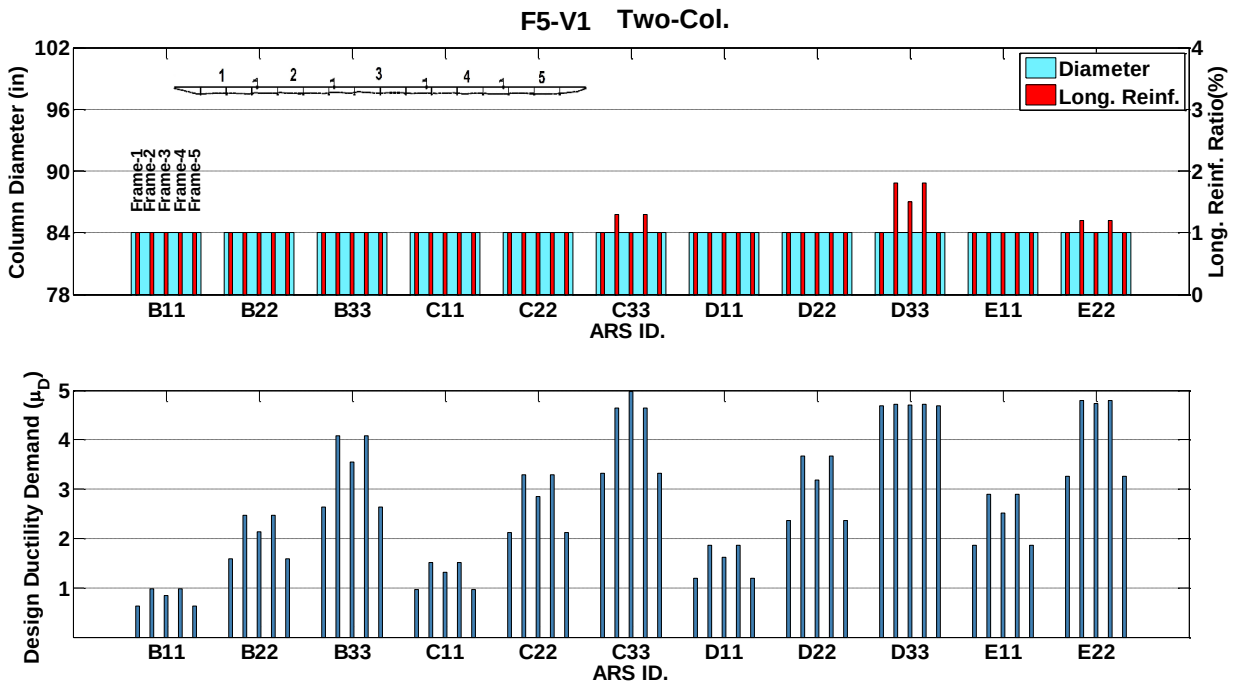

Figure B.43 Seismic Design Results of Prototype F5-V1, Two-Column

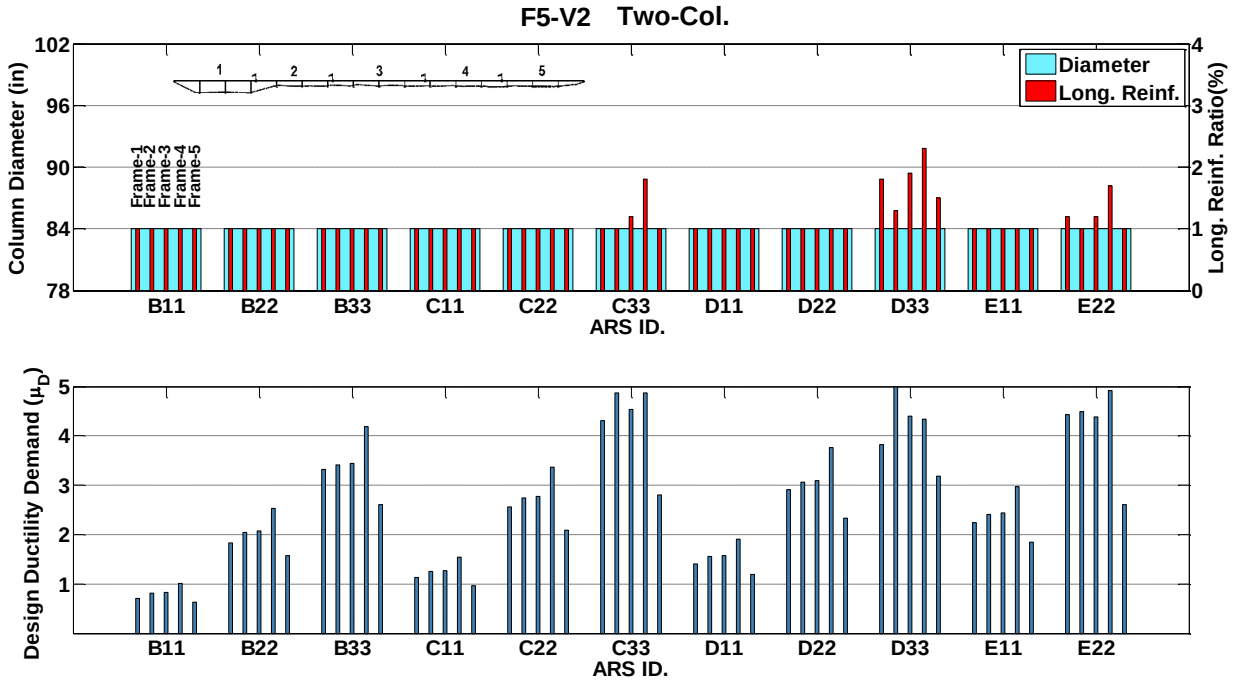

Figure B.44 Seismic Design Results of Prototype F5-V2, Two-Column

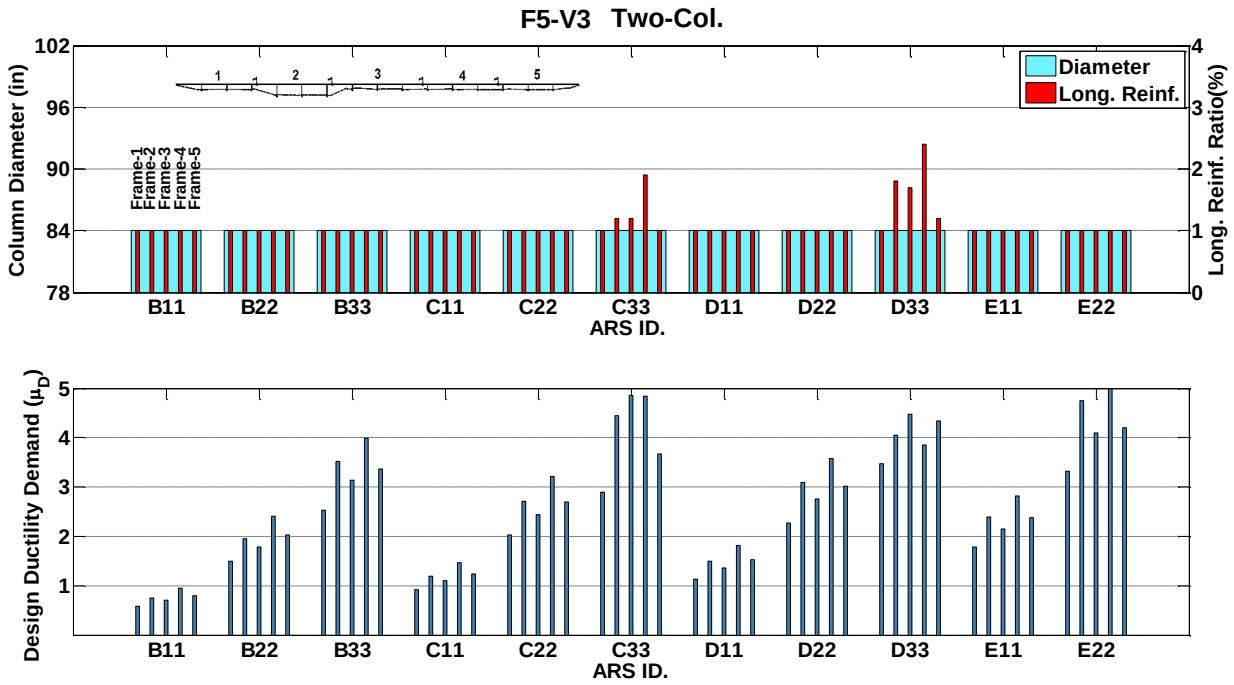

Figure B.45 Seismic Design Results of Prototype F5-V3, Two-Column

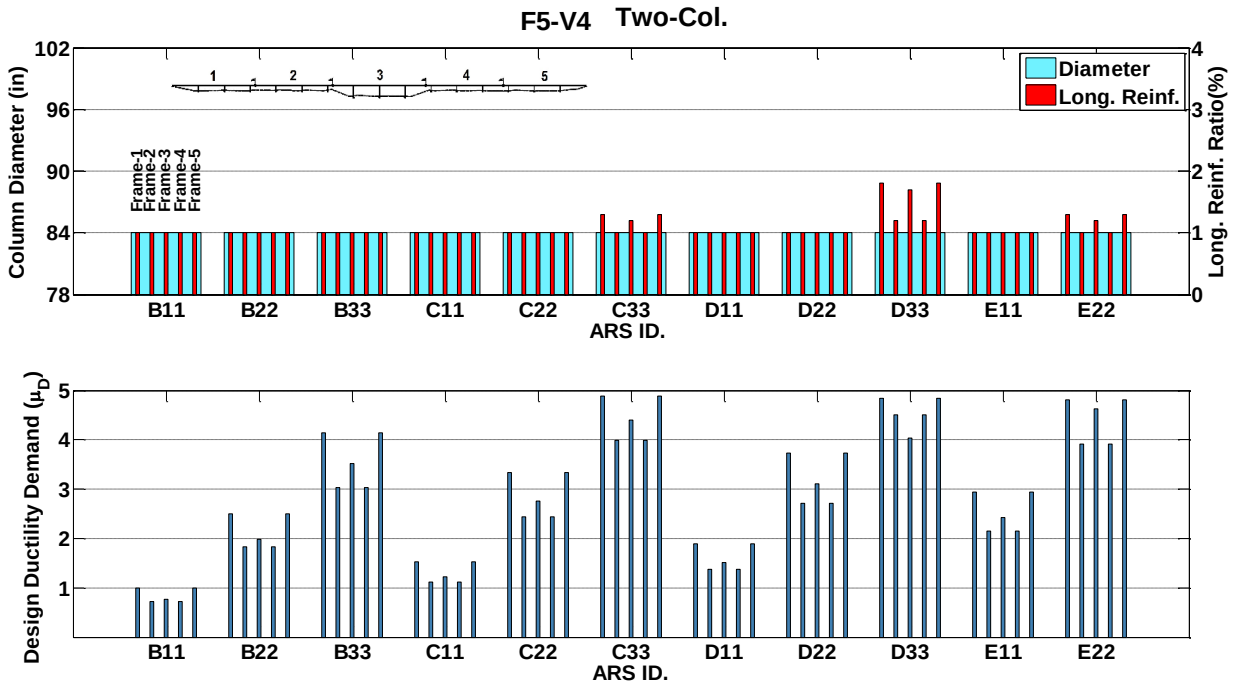

Figure B.46 Seismic Design Results of Prototype F5-V4, Two-Column

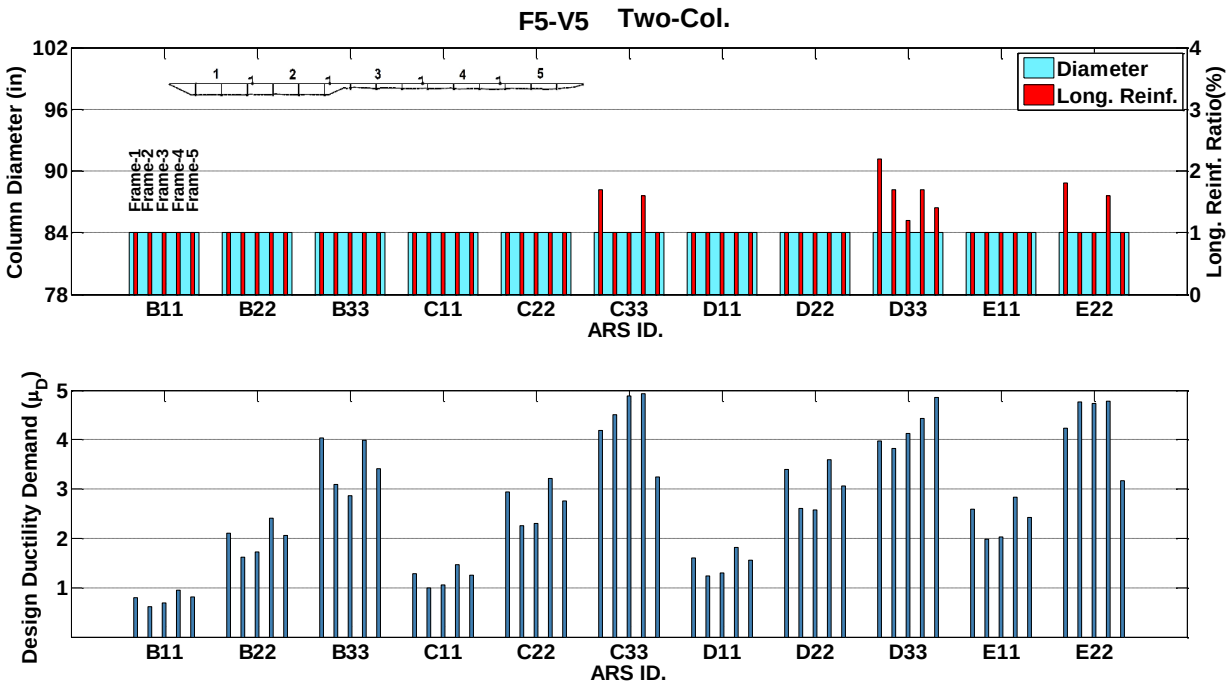

Figure B.47 Seismic Design Results of Prototype F5-V5, Two-Column

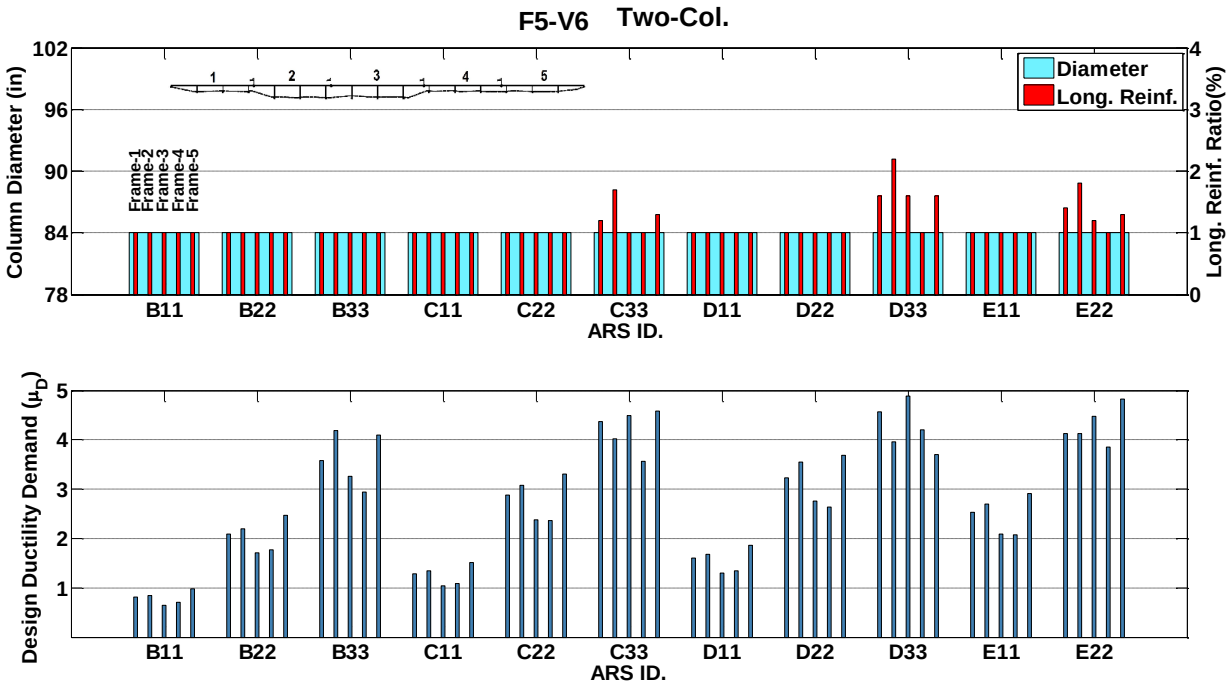

Figure B.48 Seismic Design Results of Prototype F5-V6, Two-Column

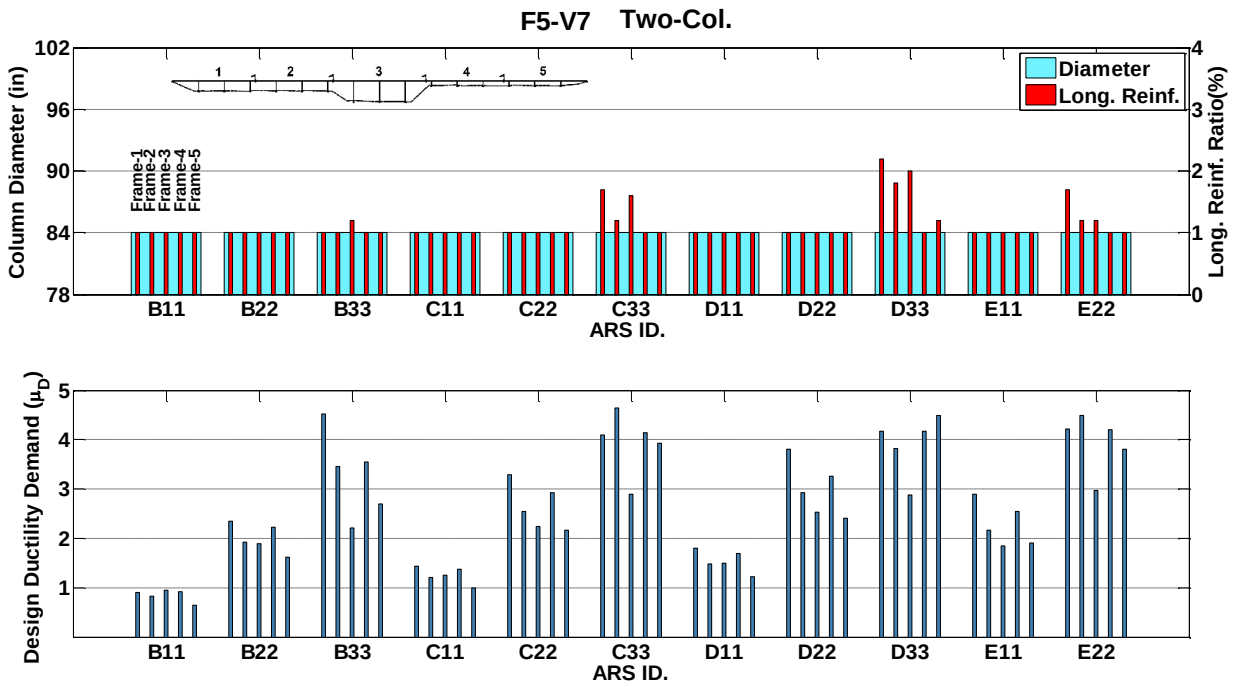

Figure B.49 Seismic Design Results of Prototype F5-V7, Two-Column

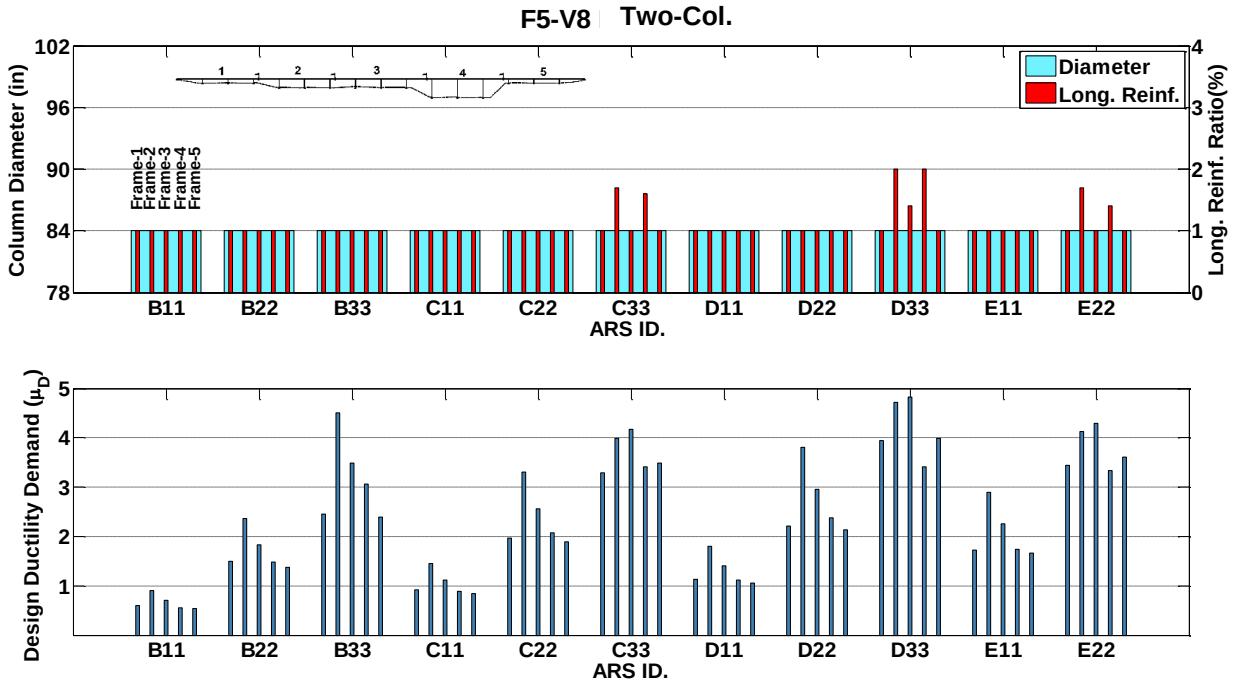

Figure B.50 Seismic Design Results of Prototype F5-V8, Two-Column

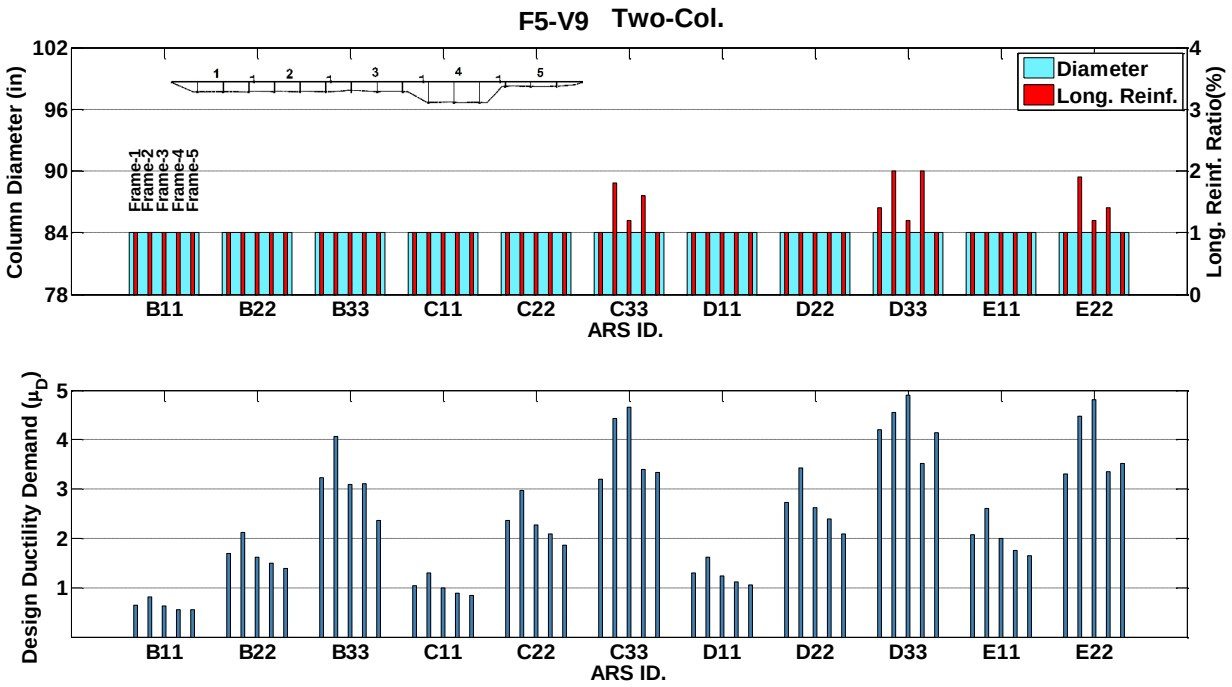

Figure B.51 Seismic Design Results of Prototype F5-V9, Two-Column

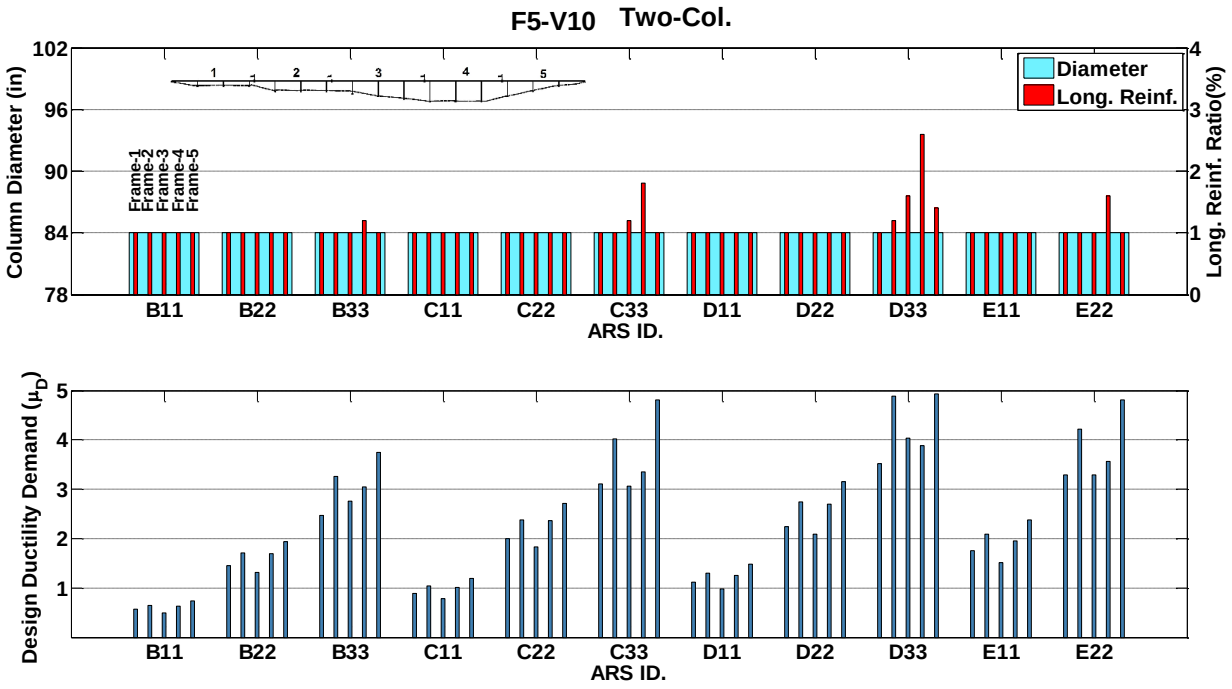

Figure B.52 Seismic Design Results of Prototype F5-V10, Two-Column

APPENDIX C.
SELECTED ANALYSIS RESULTS

PART-1: Maximum Shear Key Forces

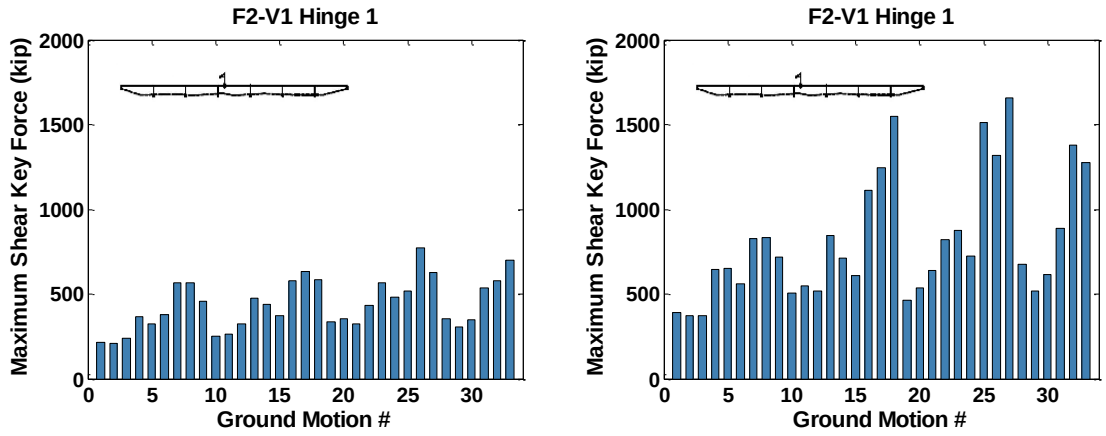

(a) (b)

Figure C.1 Maximum Shear Key Forces, Prototype F2-V1, Hinge 1, for a) Single-Column b) Two-Column

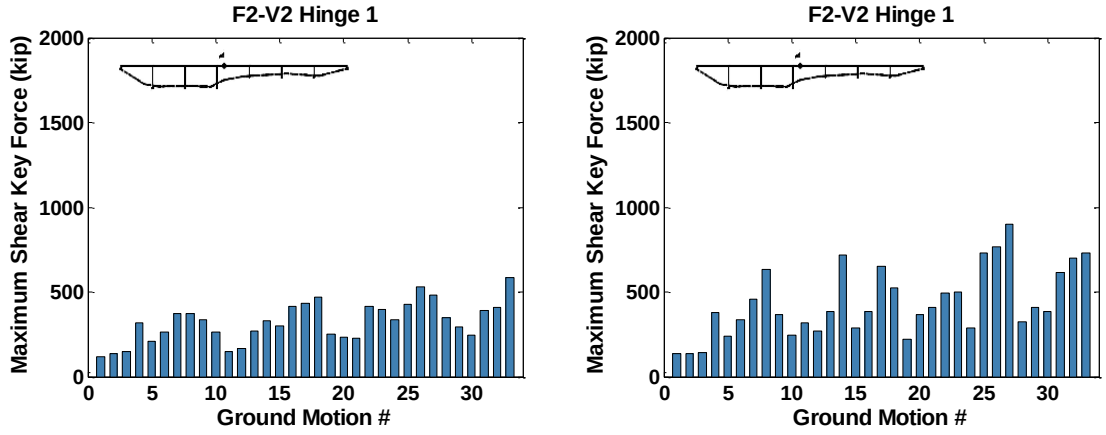

(a) (b)

Figure C.2 Maximum Shear Key Forces, Prototype F2-V2, Hinge 1, for a) Single-Column b) Two-Column

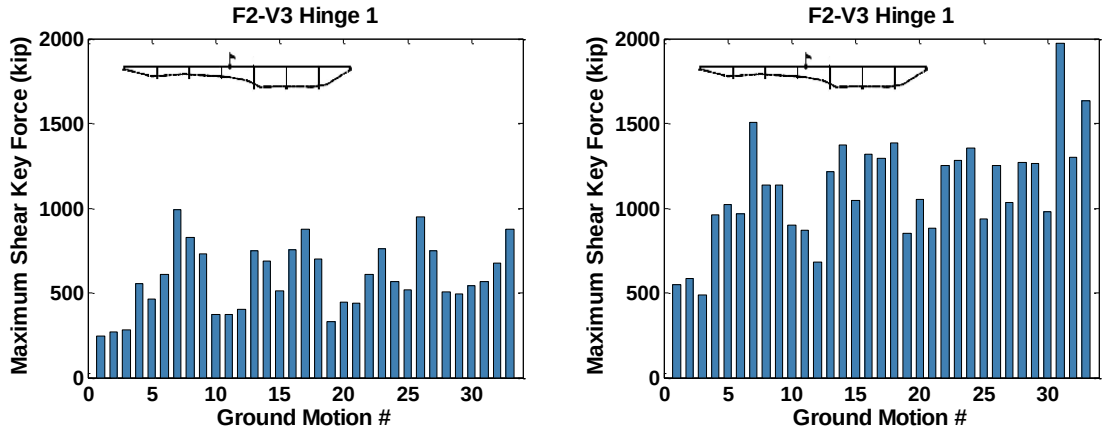

(a) (b)

Figure C.3 Maximum Shear Key Forces, Prototype F2-V3, Hinge 1, for a) Single-Column b) Two-Column

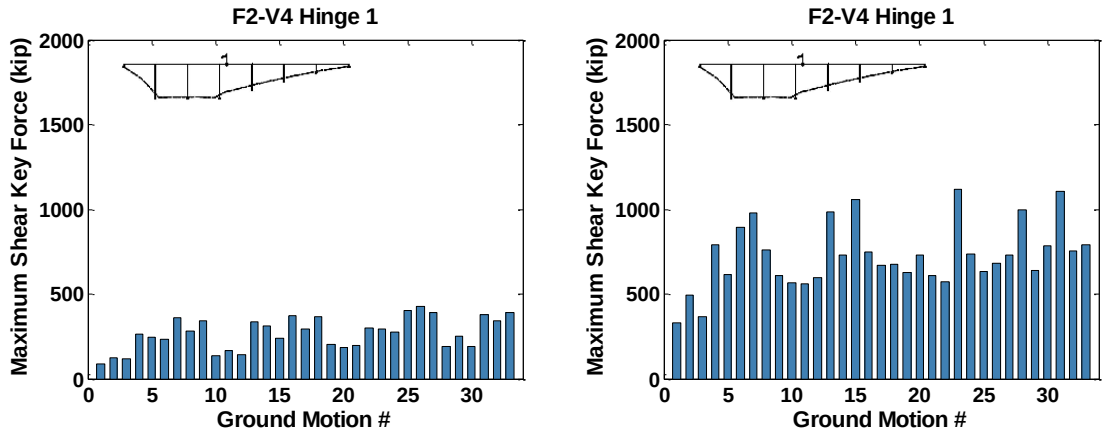

(a) (b)

Figure C.4 Maximum Shear Key Forces, Prototype F2-V4, Hinge 1, for a) Single-Column b) Two-Column

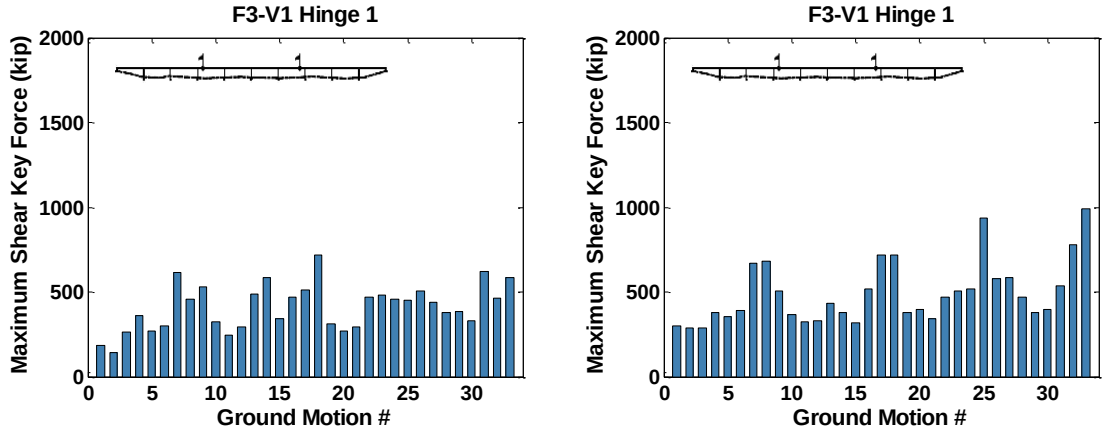

(a) (b)

Figure C.5 Maximum Shear Key Forces, Prototype F3-V1, Hinge 1, for a) Single-Column b) Two-Column

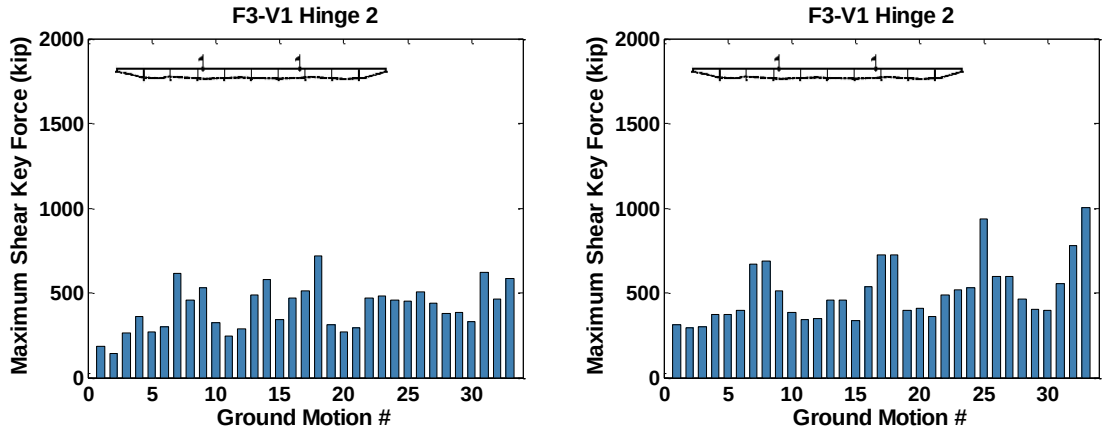

(a) (b)

Figure C.6 Maximum Shear Key Forces, Prototype F3-V1, Hinge 2, for a) Single-Column b) Two-Column

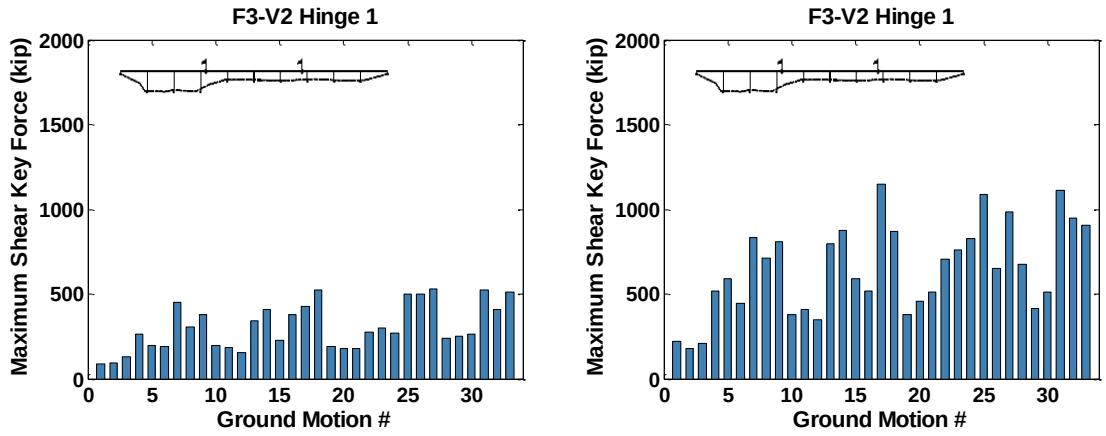

(a) (b)

Figure C.7 Maximum Shear Key Forces, Prototype F3-V2, Hinge 1, for a) Single-Column b) Two-Column

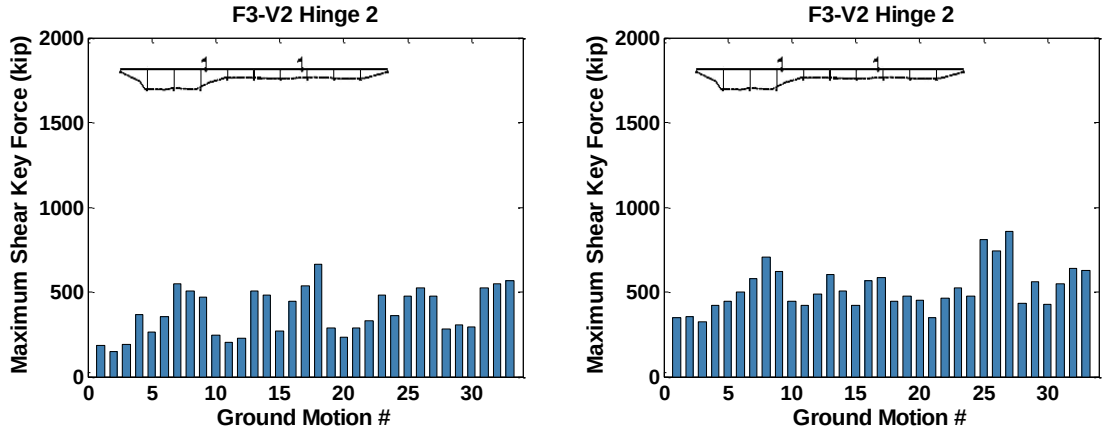

(a) (b)

Figure C.8 Maximum Shear Key Forces, Prototype F3-V2, Hinge 2, for a) Single-Column b) Two-Column

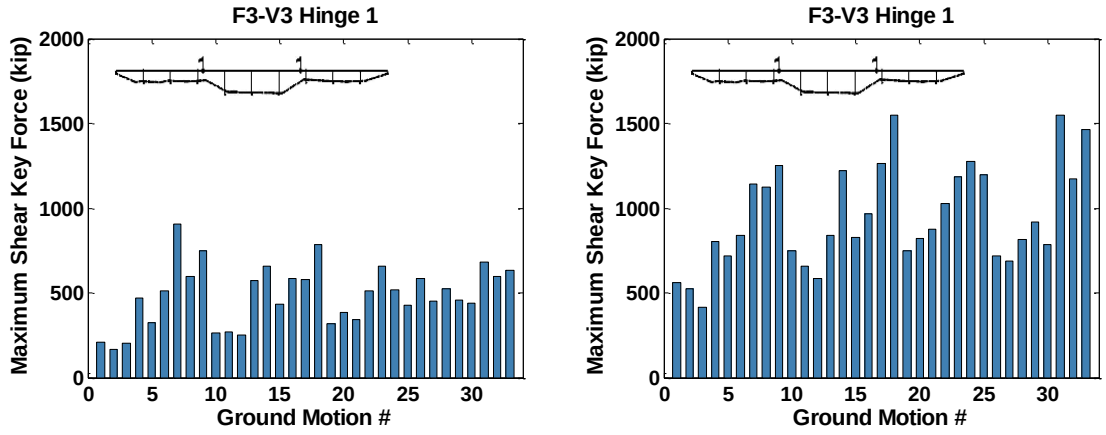

(a) (b)

Figure C.9 Maximum Shear Key Forces, Prototype F3-V3, Hinge 1, for a) Single-Column b) Two-Column

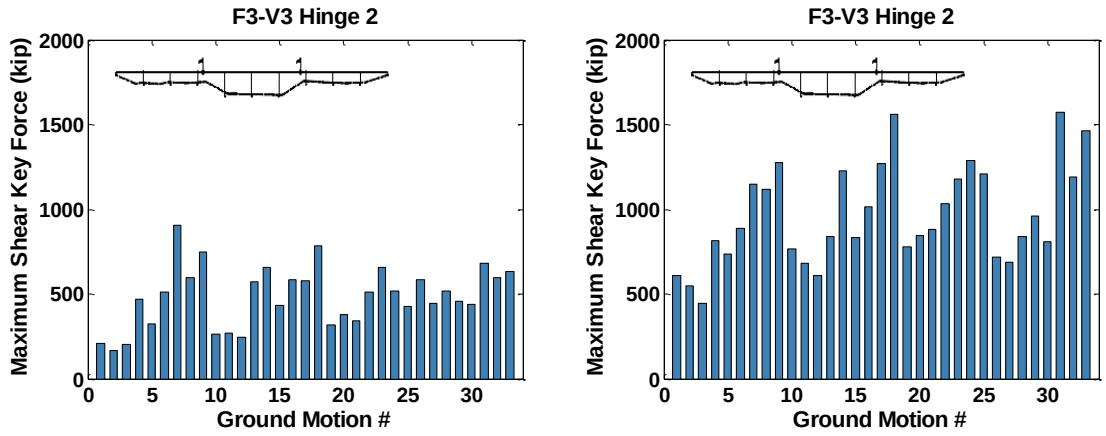

(a) (b)

Figure C.10 Maximum Shear Key Forces, Prototype F3-V3, Hinge 2, for a) Single-Column b) Two-Column

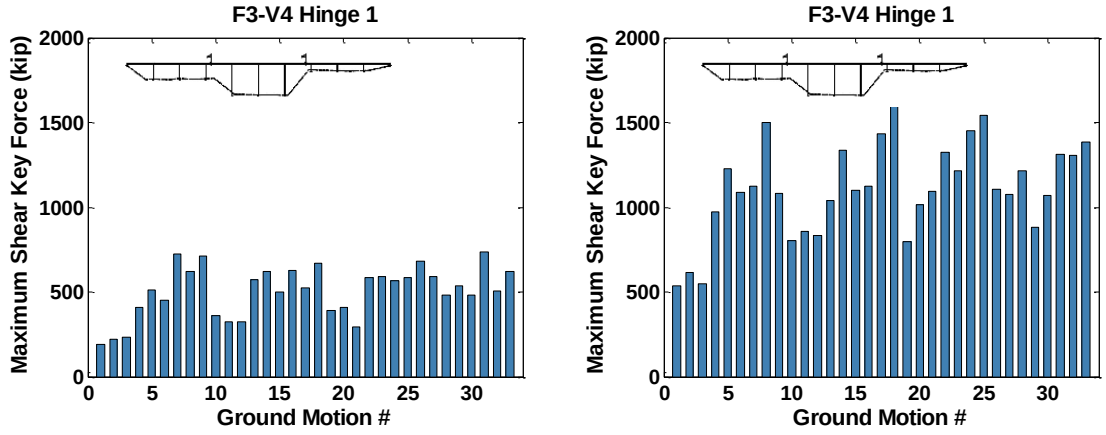

(a) (b)

Figure C.11 Maximum Shear Key Forces, Prototype F3-V4, Hinge 1, for a) Single-Column b) Two-Column

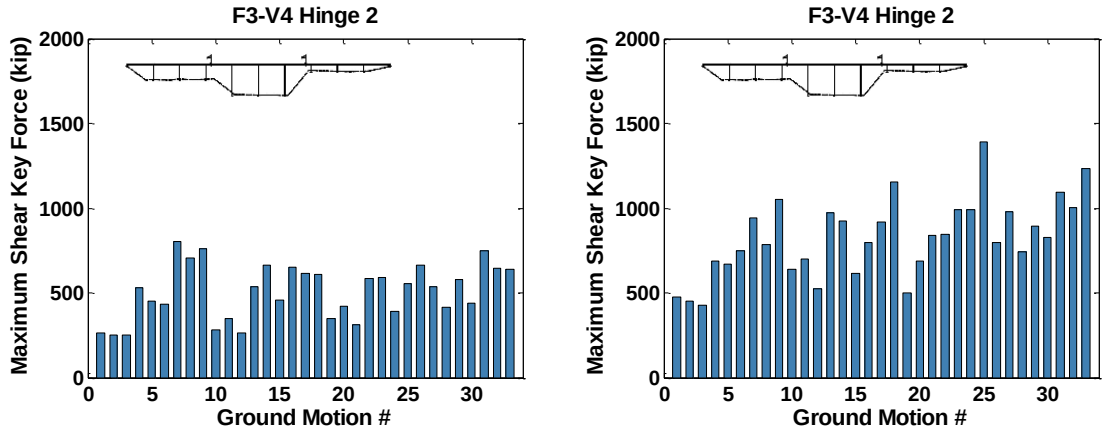

(a) (b)

Figure C.12 Maximum Shear Key Forces, Prototype F3-V4, Hinge 2, for a) Single-Column b) Two-Column

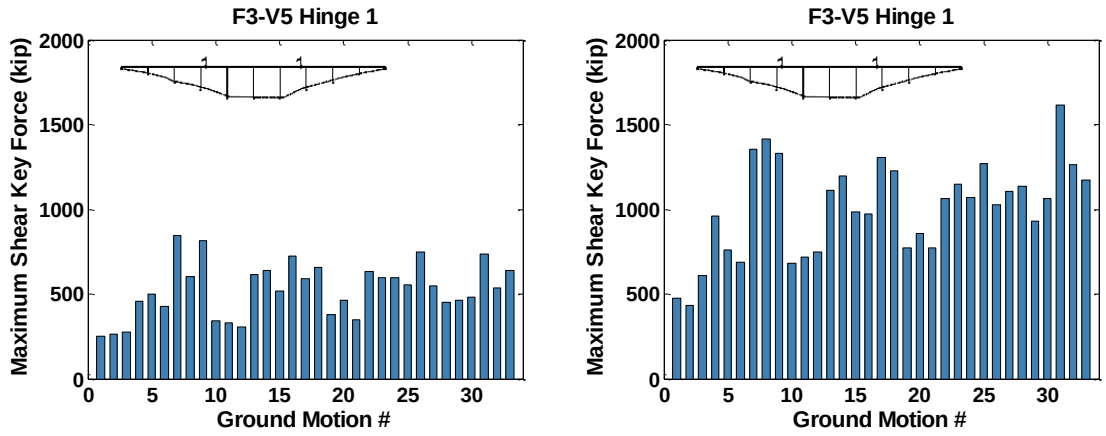

(a) (b)

Figure C.13 Maximum Shear Key Forces, Prototype F3-V5, Hinge 1, for a) Single-Column b) Two-Column

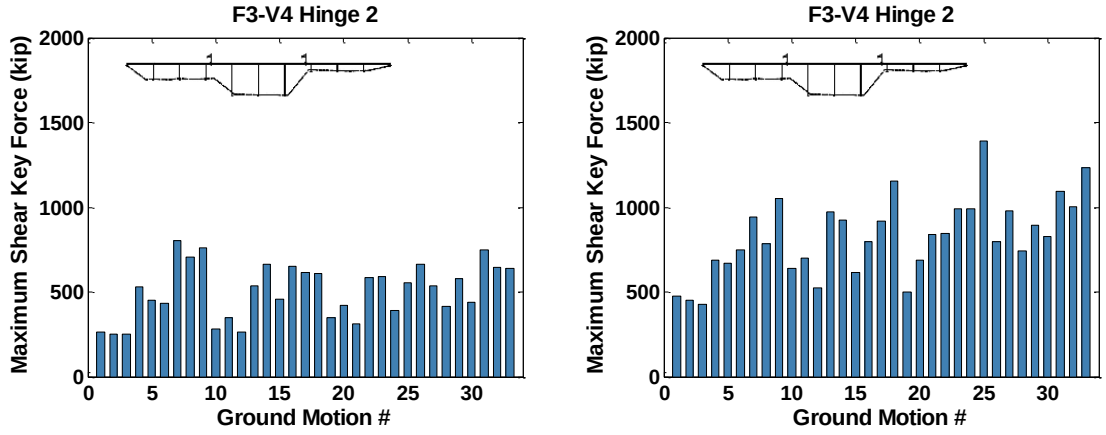

(a) (b)

Figure C.14 Maximum Shear Key Forces, Prototype F3-V4, Hinge 2, for a) Single-Column b) Two-Column

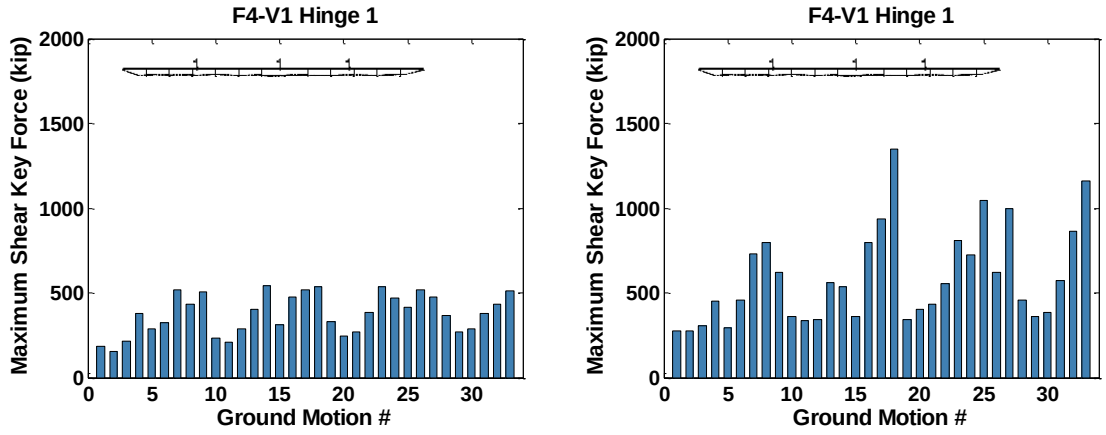

(a) (b)

Figure C.15 Maximum Shear Key Forces, Prototype F4-V1, Hinge 1, for a) Single-Column b) Two-Column

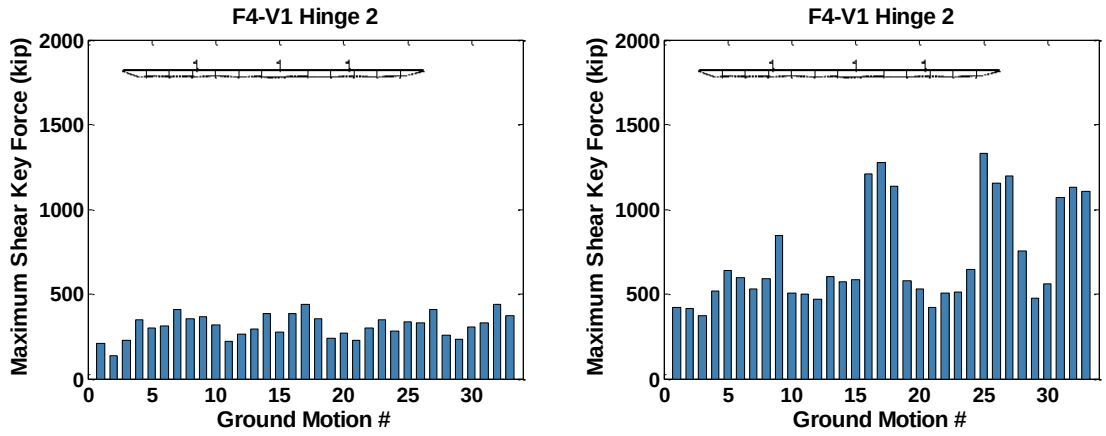

(a) (b)

Figure C.16 Maximum Shear Key Forces, Prototype F4-V1, Hinge 2, for a) Single-Column b) Two-Column

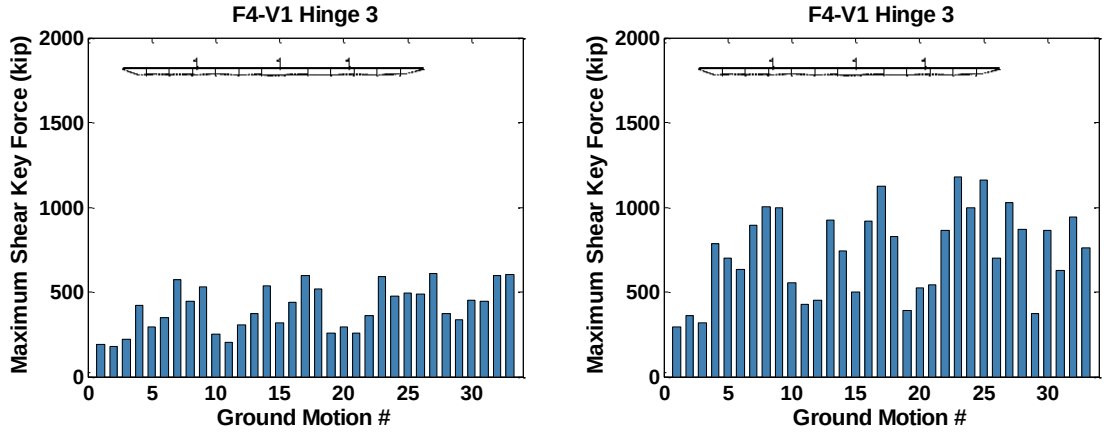

(a) (b)

Figure C.17 Maximum Shear Key Forces, Prototype F4-V1, Hinge 2, for a) Single-Column b) Two-Column

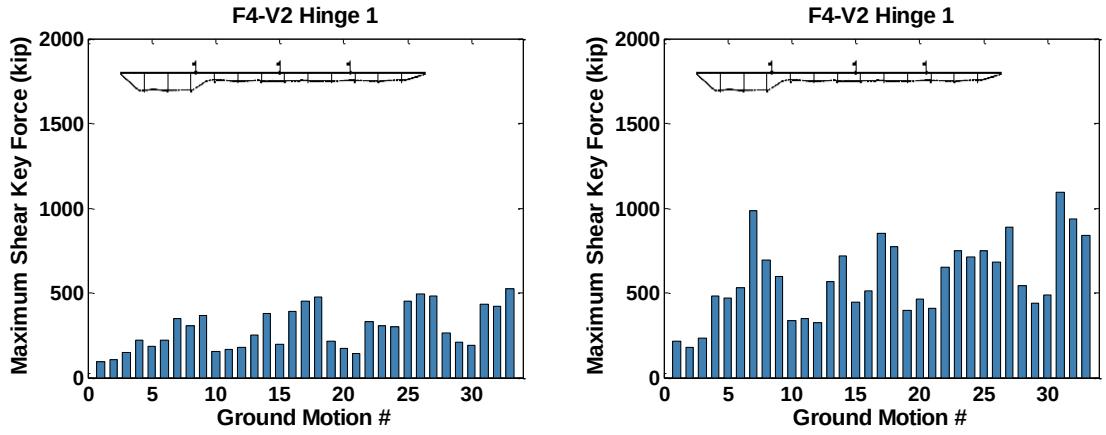

(a) (b)

Figure C.18 Maximum Shear Key Forces, Prototype F4-V2, Hinge 1, for a) Single-Column b) Two-Column

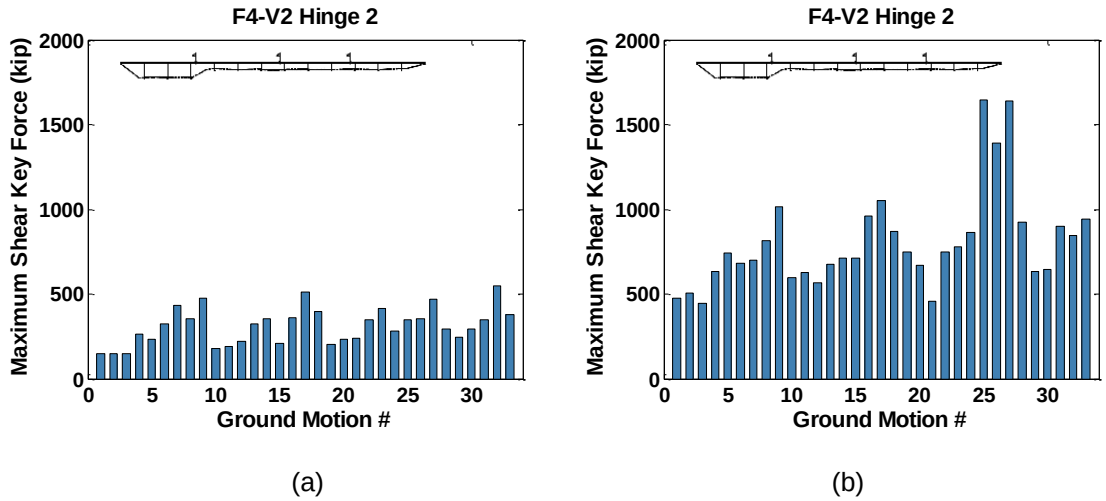

(a) (b)

Figure C.19 Maximum Shear Key Forces, Prototype F4-V2, Hinge 2, for a) Single-Column b) Two-Column

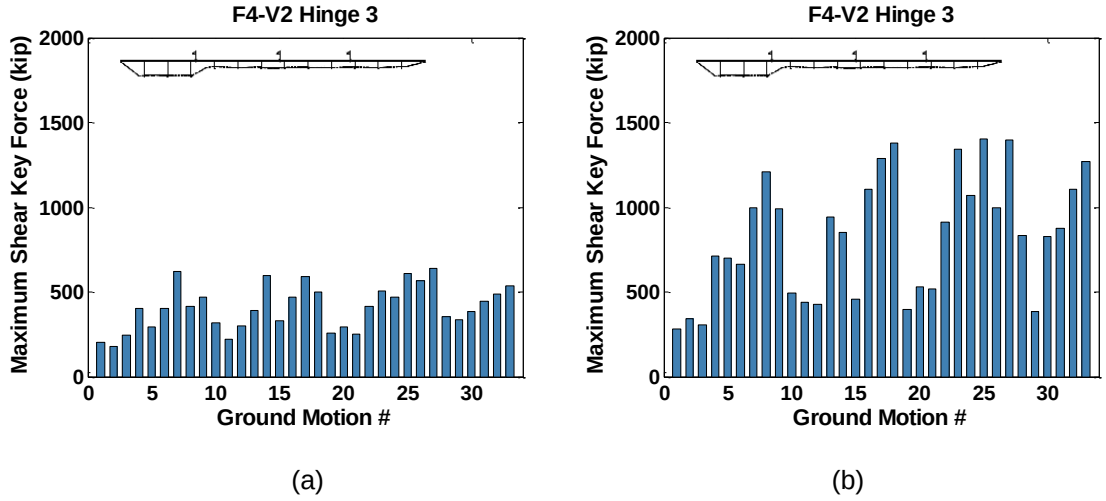

(a) (b)

Figure C.20 Maximum Shear Key Forces, Prototype F4-V2, Hinge 3, for a) Single-Column b) Two-Column

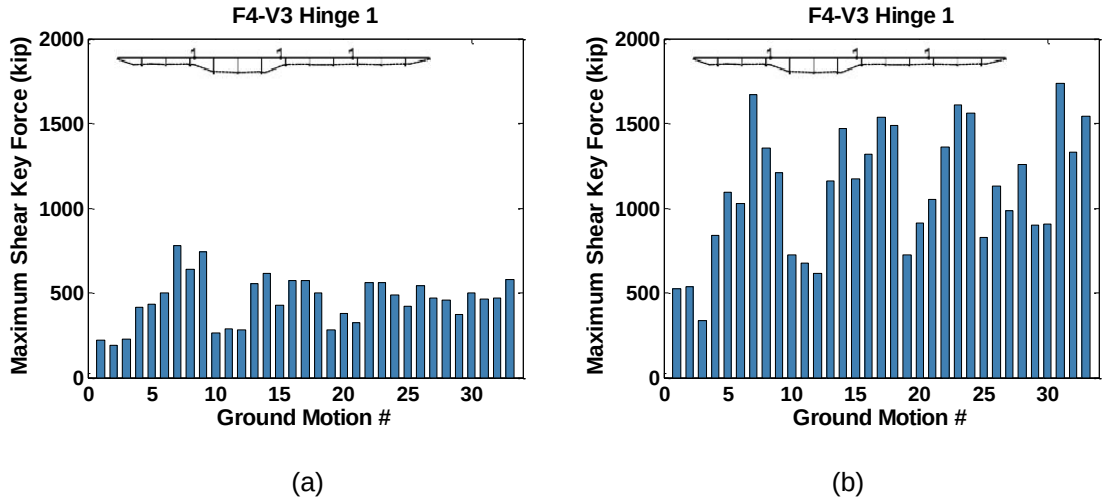

(a) (b)

Figure C.21 Maximum Shear Key Forces, Prototype F4-V3, Hinge 1, for a) Single-Column b) Two-Column

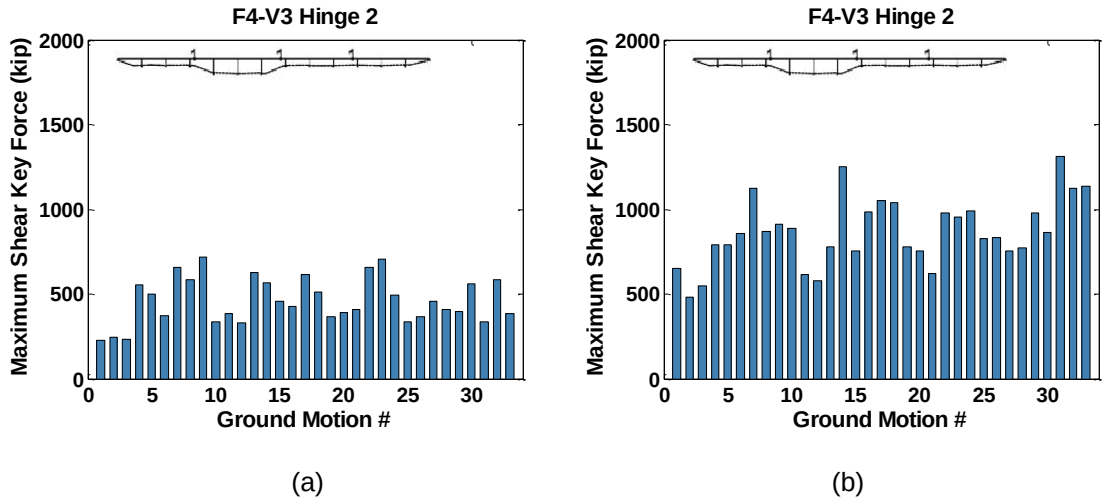

(a) (b)

Figure C.22 Maximum Shear Key Forces, Prototype F4-V3, Hinge 2, for a) Single-Column b) Two-Column

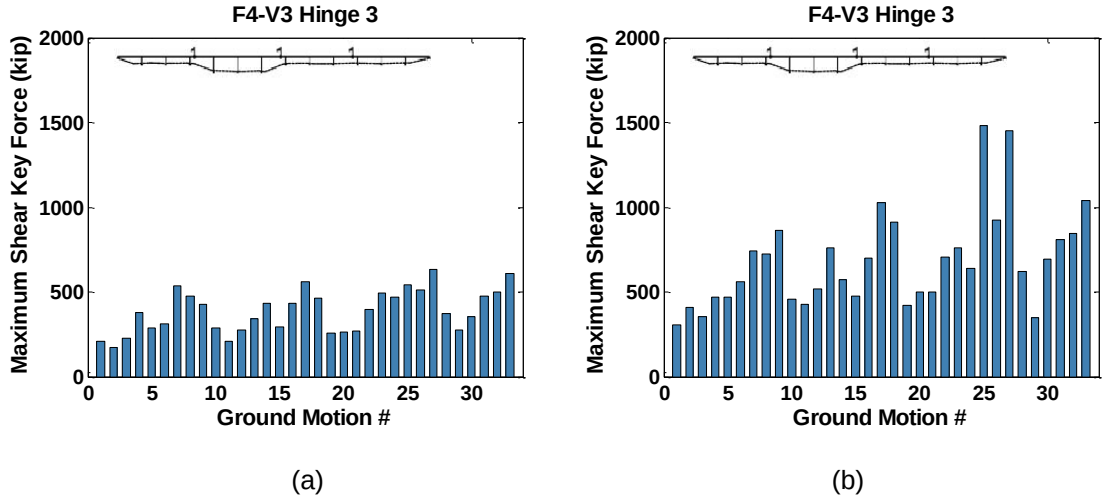

(a) (b)

Figure C.23 Maximum Shear Key Forces, Prototype F4-V3, Hinge 3, for a) Single-Column b) Two-Column

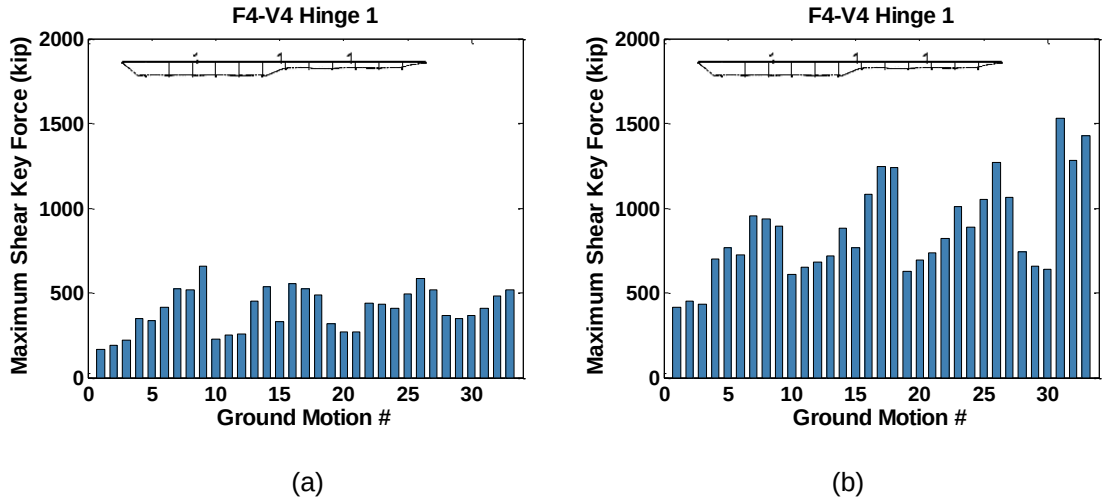

(a) (b)

Figure C.24 Maximum Shear Key Forces, Prototype F4-V4, Hinge 1, for a) Single-Column b) Two-Column

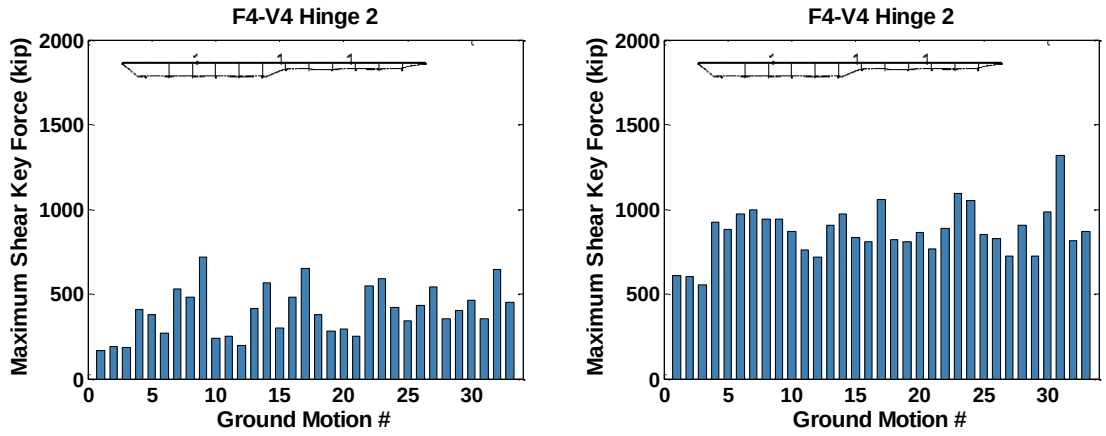

(a) (b)

Figure C.25 Maximum Shear Key Forces, Prototype F4-V4, Hinge 2, for a) Single-Column b) Two-Column

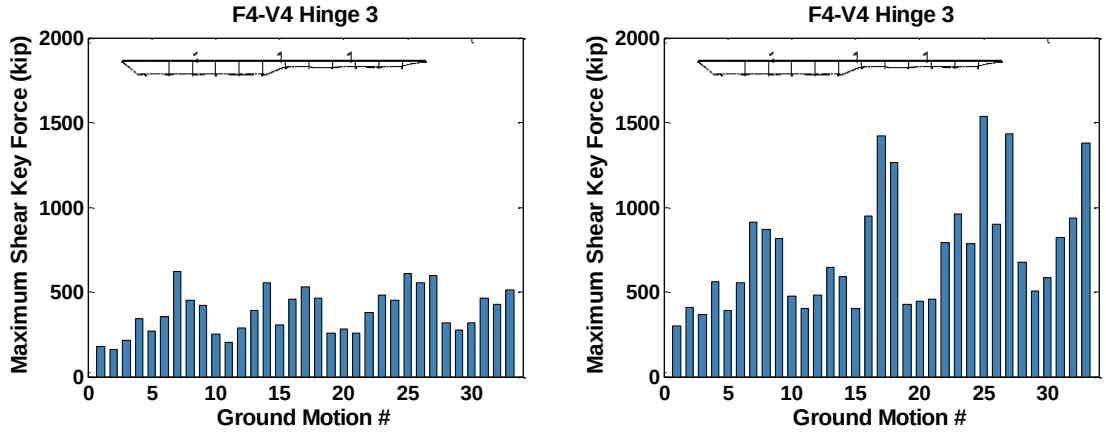

(a) (b)

Figure C.26 Maximum Shear Key Forces, Prototype F4-V4, Hinge 3, for a) Single-Column b) Two-Column

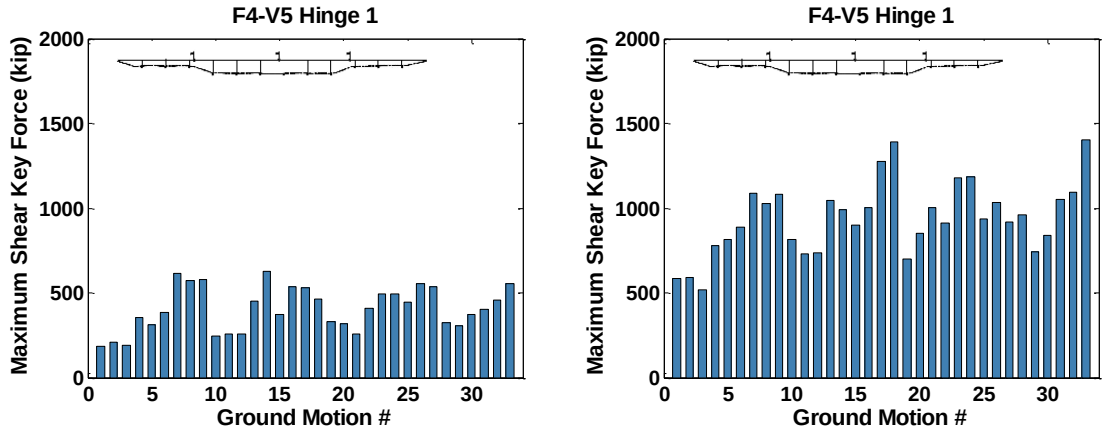

(a) (b)

Figure C.27 Maximum Shear Key Forces, Prototype F4-V5, Hinge 1, for a) Single-Column b) Two-Column

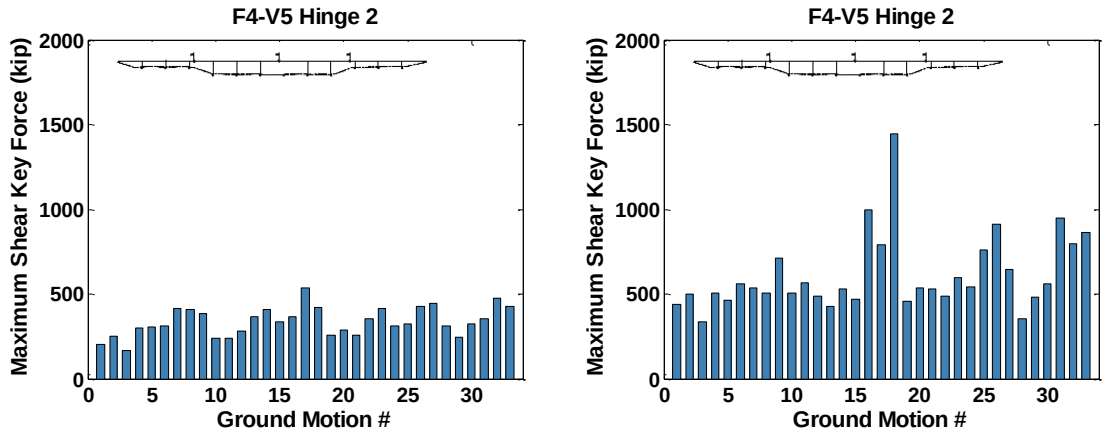

(a) (b)

Figure C.28 Maximum Shear Key Forces, Prototype F4-V5, Hinge 2, for a) Single-Column b) Two-Column

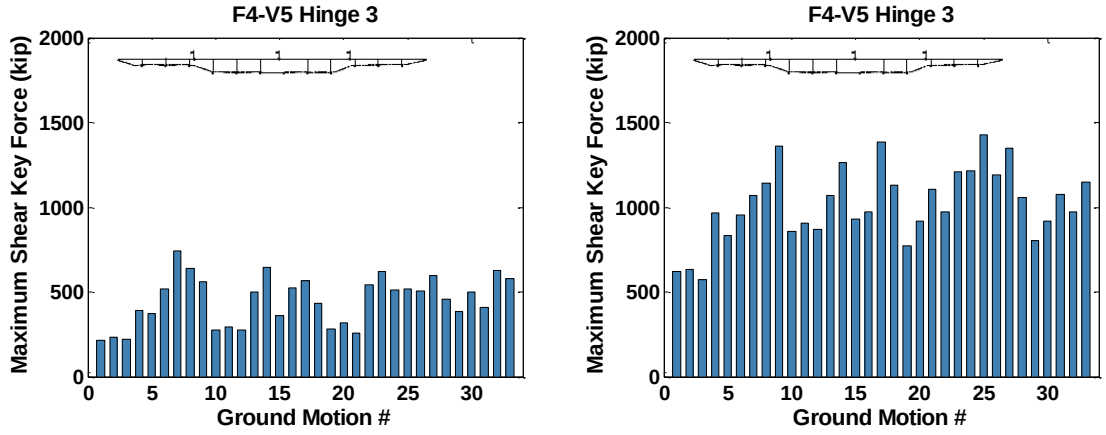

(a) (b)

Figure C.29 Maximum Shear Key Forces, Prototype F4-V5, Hinge 3, for a) Single-Column b) Two-Column

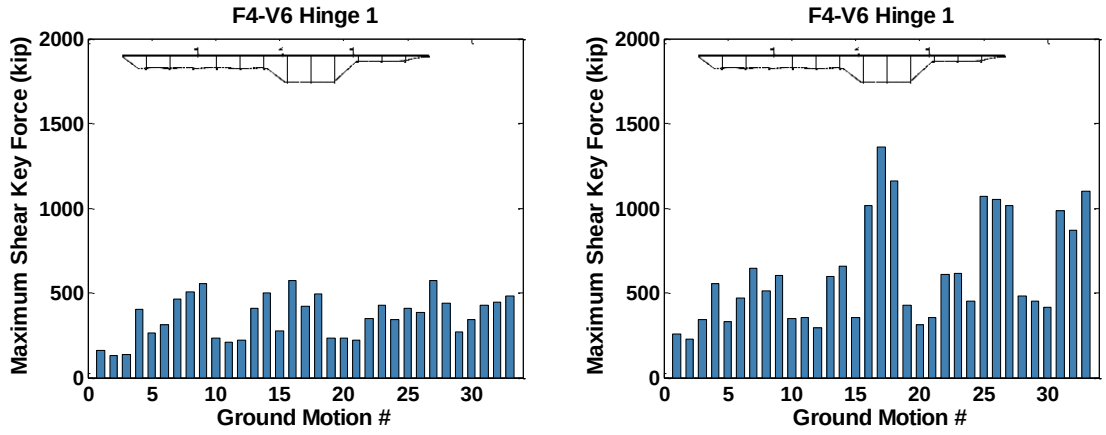

(a) (b)

Figure C.30 Maximum Shear Key Forces, Prototype F4-V6, Hinge 1, for a) Single-Column b) Two-Column

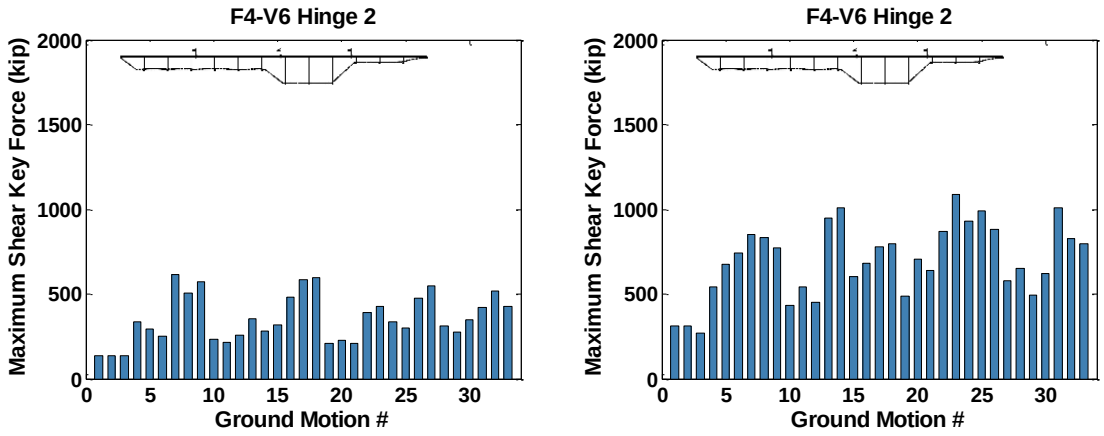

(a) (b)

Figure C.31 Maximum Shear Key Forces, Prototype F4-V6, Hinge 2, for a) Single-Column b) Two-Column

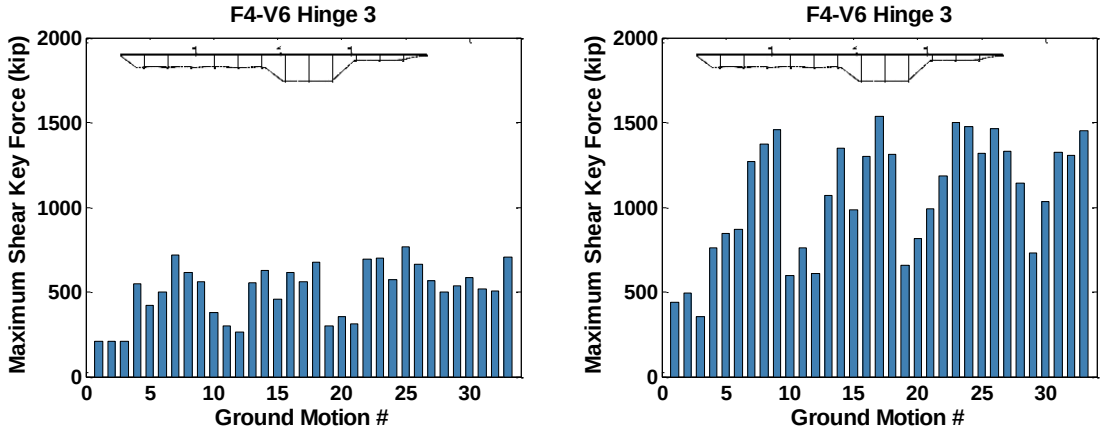

(a) (b)

Figure C.32 Maximum Shear Key Forces, Prototype F4-V6, Hinge 3, for a) Single-Column b) Two-Column

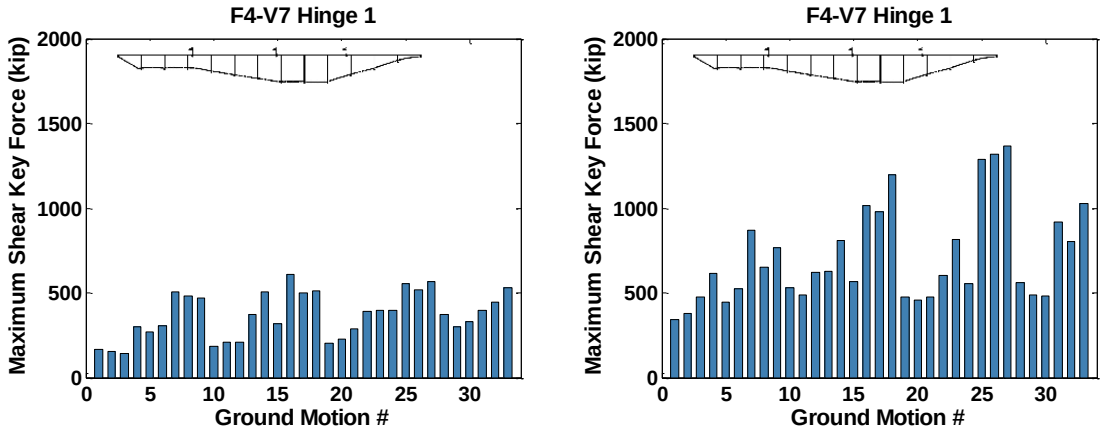

(a) (b)

Figure C.33 Maximum Shear Key Forces, Prototype F4-V7, Hinge 1, for a) Single-Column b) Two-Column

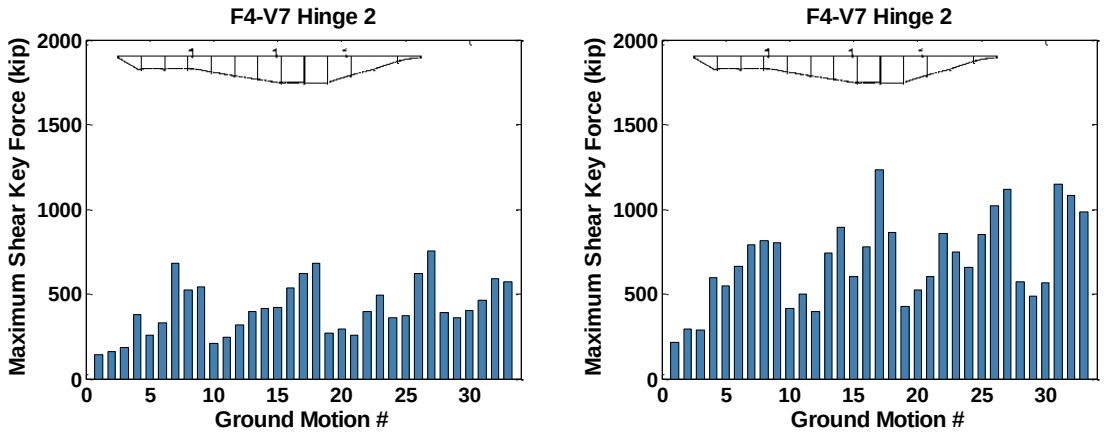

(a) (b)

Figure C.34 Maximum Shear Key Forces, Prototype F4-V7, Hinge 2, for a) Single-Column b) Two-Column

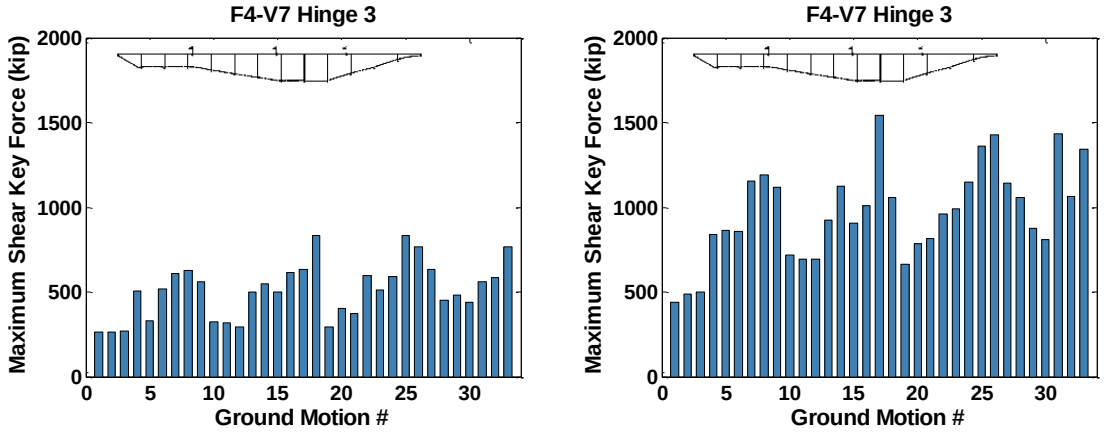

(a) (b)

Figure C.35 Maximum Shear Key Forces, Prototype F4-V7, Hinge 3, for a) Single-Column b) Two-Column

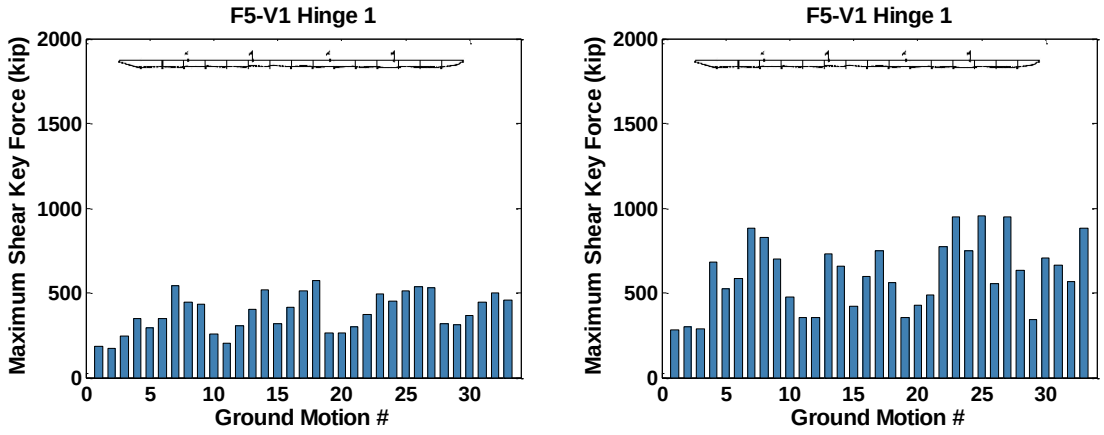

(a) (b)

Figure C.36 Maximum Shear Key Forces, Prototype F5-V1, Hinge 1, for a) Single-Column b) Two-Column

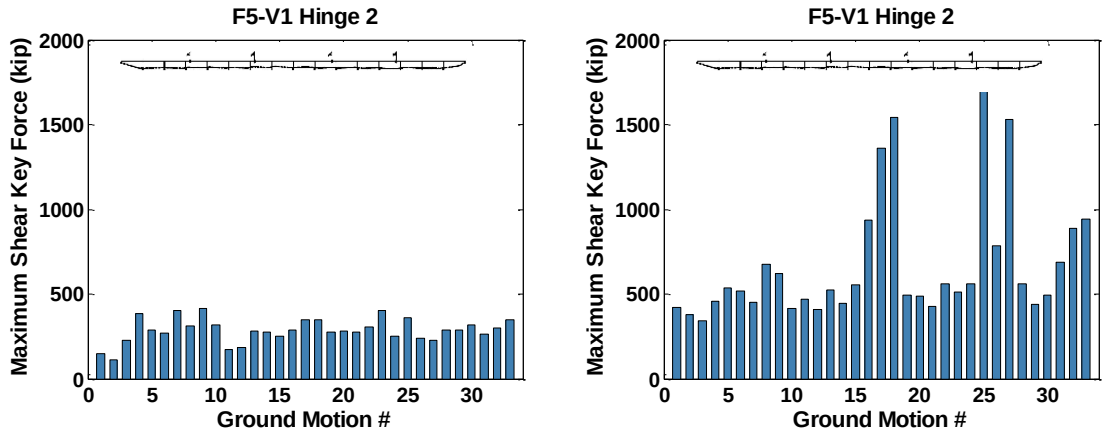

(a) (b)

Figure C.37 Maximum Shear Key Forces, Prototype F5-V1, Hinge 2, for a) Single-Column b) Two-Column

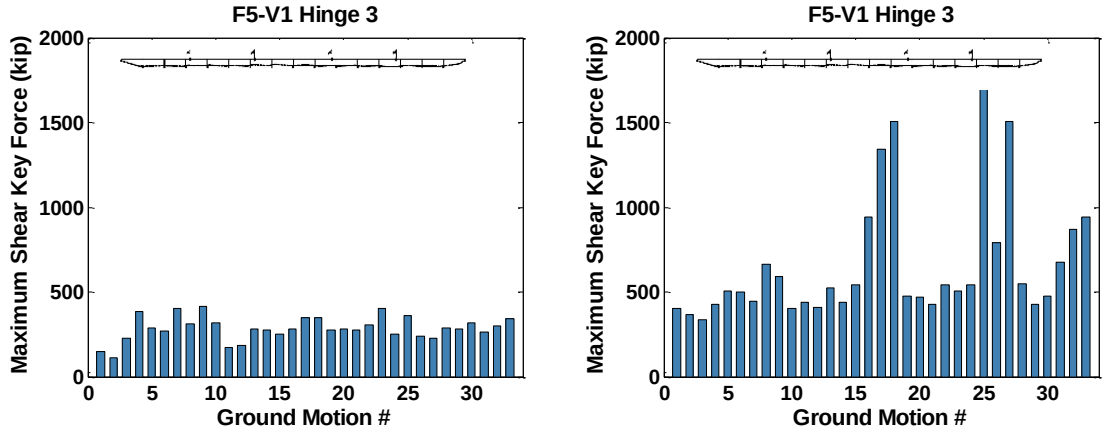

(a) (b)

Figure C.38 Maximum Shear Key Forces, Prototype F5-V1, Hinge 3, for a) Single-Column b) Two-Column

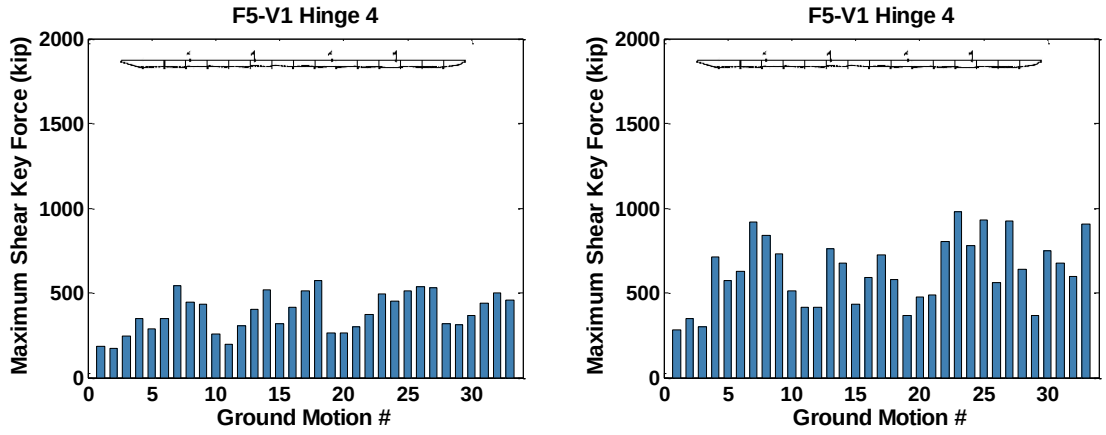

(a) (b)

Figure C.39 Maximum Shear Key Forces, Prototype F5-V1, Hinge 4, for a) Single-Column b) Two-Column

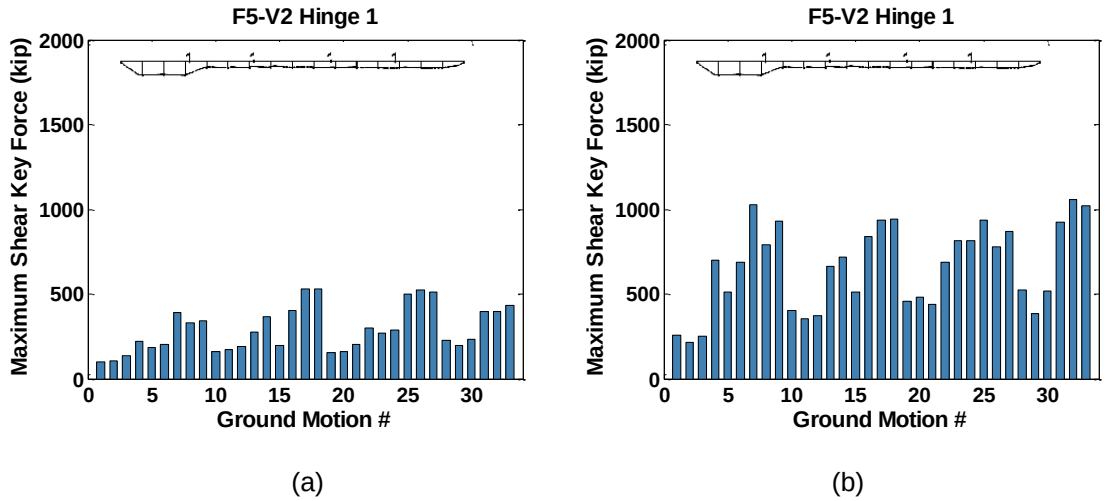

(a) (b)

Figure C.40 Maximum Shear Key Forces, Prototype F5-V2, Hinge 1, for a) Single-Column b) Two-Column

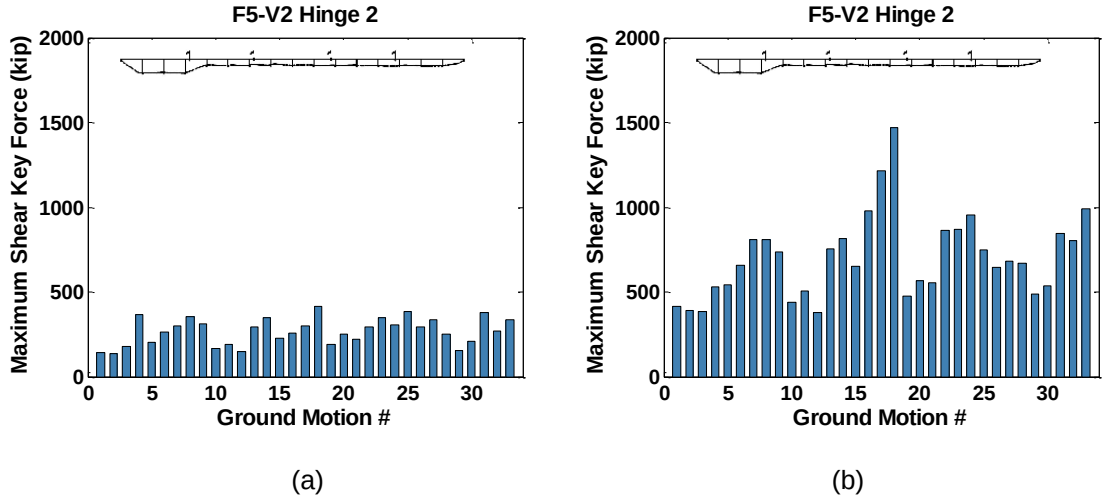

(a) (b)

Figure C.41 Maximum Shear Key Forces, Prototype F5-V2, Hinge 2, for a) Single-Column b) Two-Column

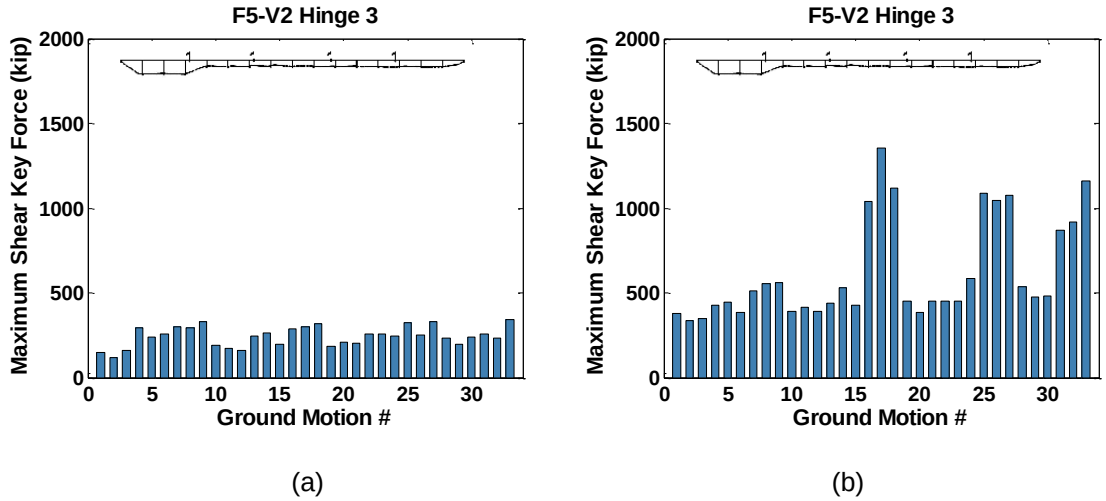

(a) (b)

Figure C.42 Maximum Shear Key Forces, Prototype F5-V2, Hinge 3, for a) Single-Column b) Two-Column

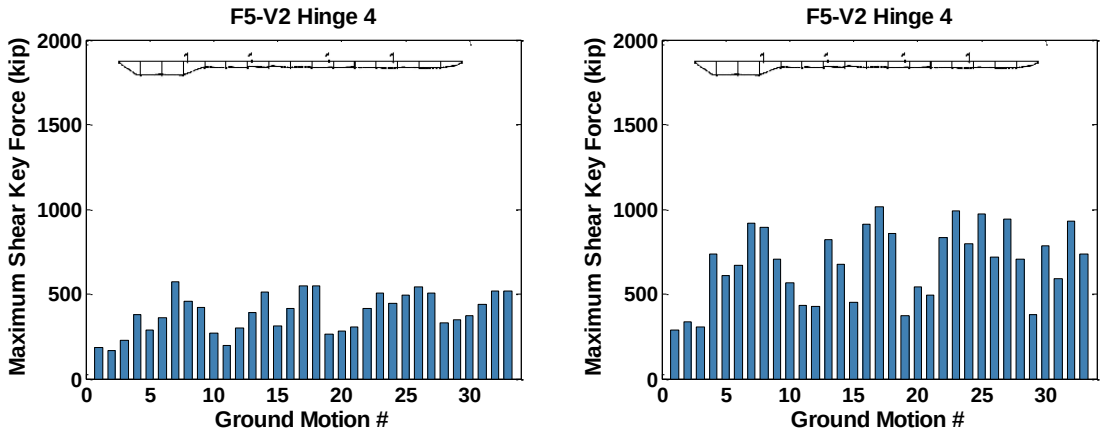

(a) (b)

Figure C.43 Maximum Shear Key Forces, Prototype F5-V2, Hinge 4, for a) Single-Column b) Two-Column

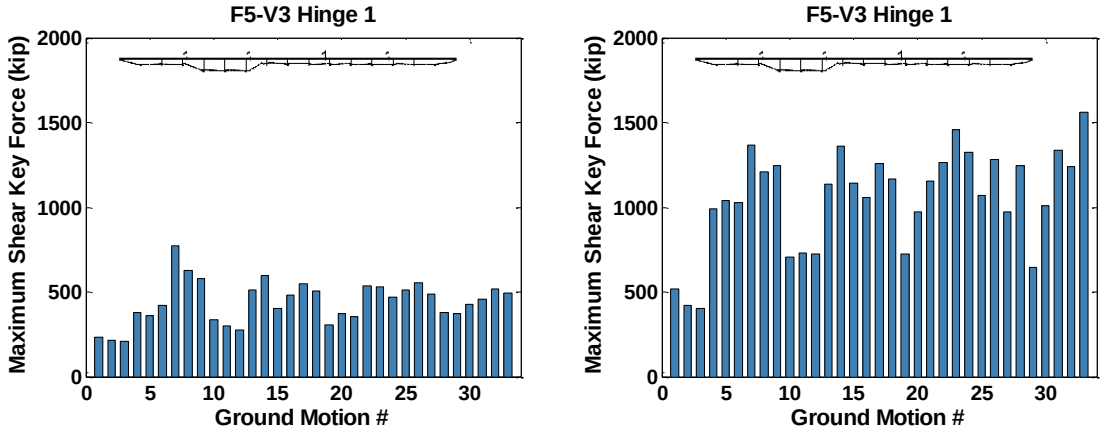

(a) (b)

Figure C.44 Maximum Shear Key Forces, Prototype F5-V3, Hinge 1, for a) Single-Column b) Two-Column

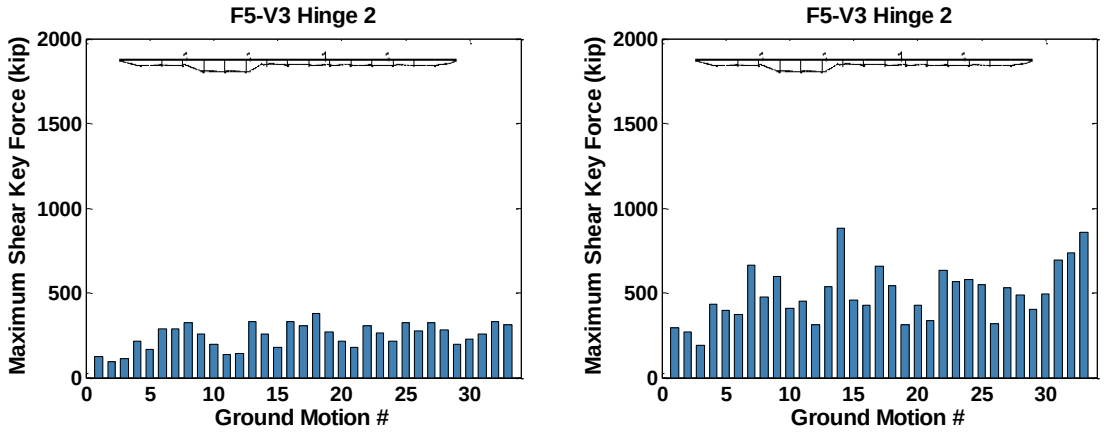

(a) (b)

Figure C.45 Maximum Shear Key Forces, Prototype F5-V3, Hinge 2, for a) Single-Column b) Two-Column

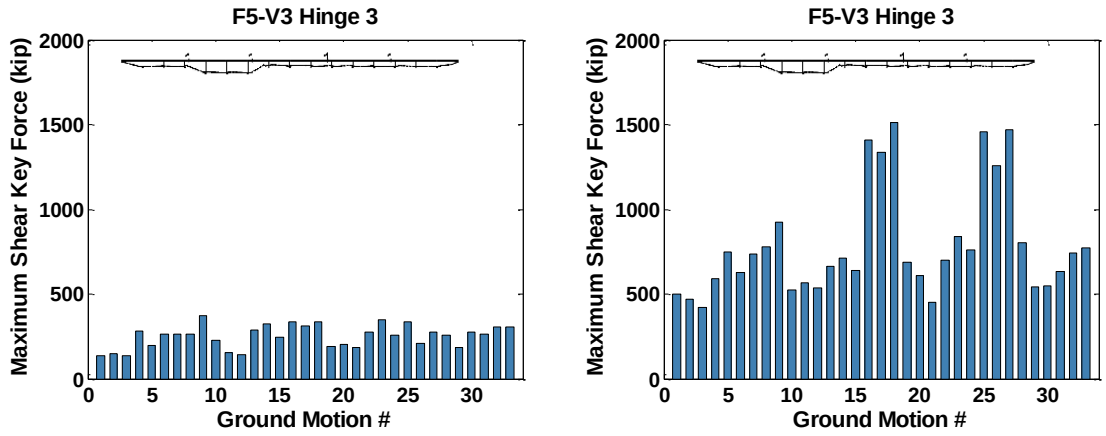

(a) (b)

Figure C.46 Maximum Shear Key Forces, Prototype F5-V3, Hinge 3, for a) Single-Column b) Two-Column

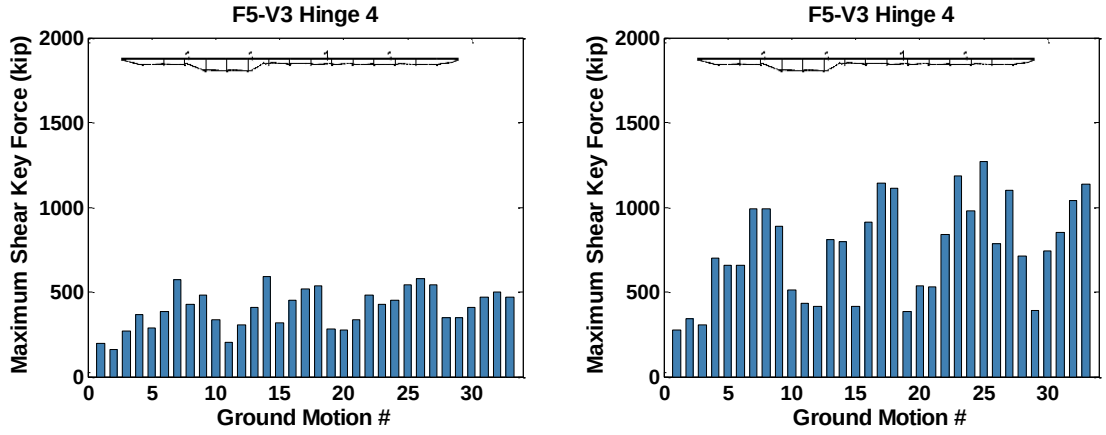

(a) (b)

Figure C.47 Maximum Shear Key Forces, Prototype F5-V3, Hinge 4, for a) Single-Column b) Two-Column

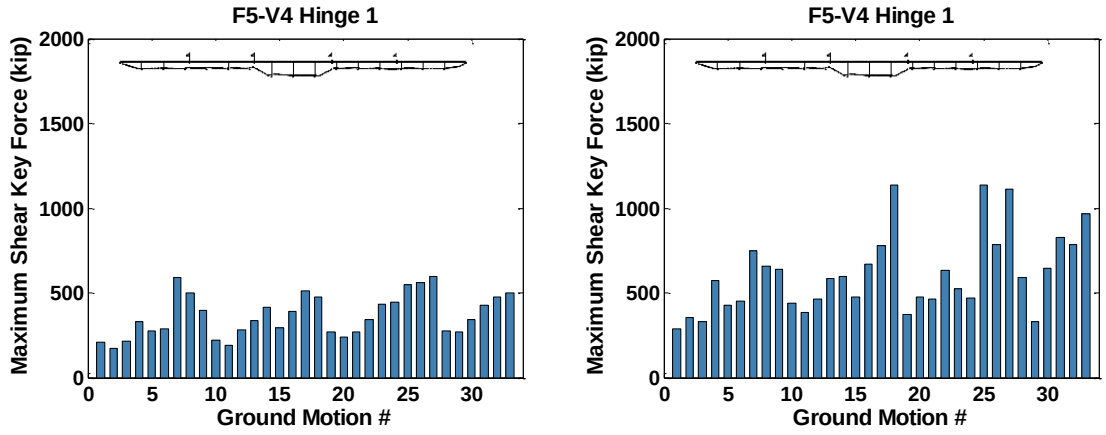

(a) (b)

Figure C.48 Maximum Shear Key Forces, Prototype F5-V4, Hinge 1, for a) Single-Column b) Two-Column

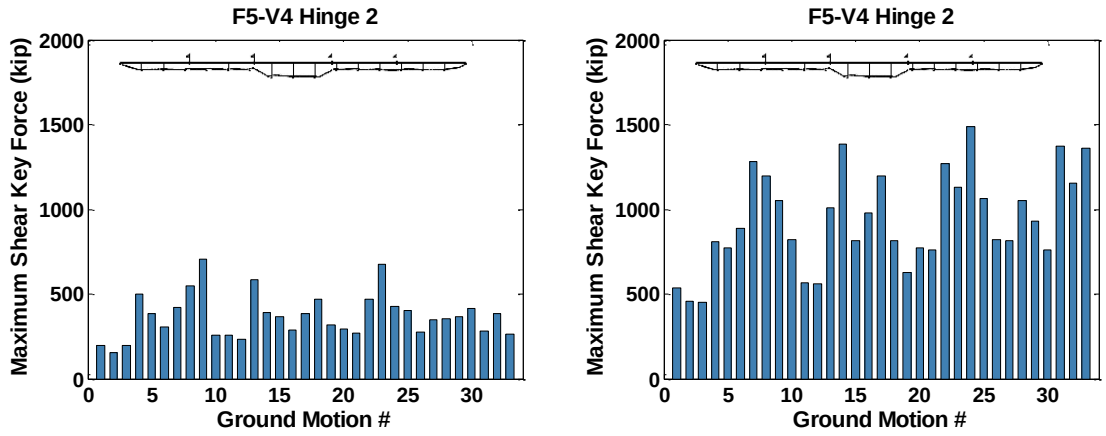

(a) (b)

Figure C.49 Maximum Shear Key Forces, Prototype F5-V4, Hinge 2, for a) Single-Column b) Two-Column

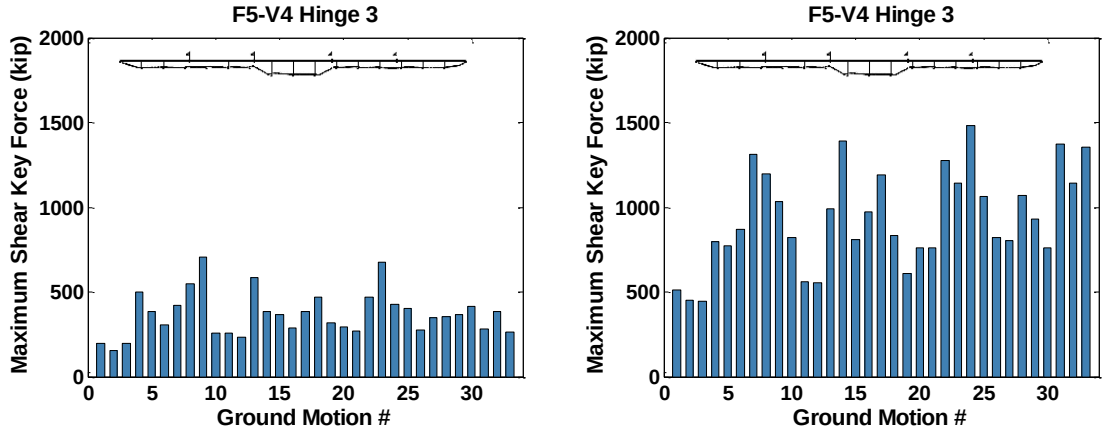

(a) (b)

Figure C.50 Maximum Shear Key Forces, Prototype F5-V4, Hinge 3, for a) Single-Column b) Two-Column

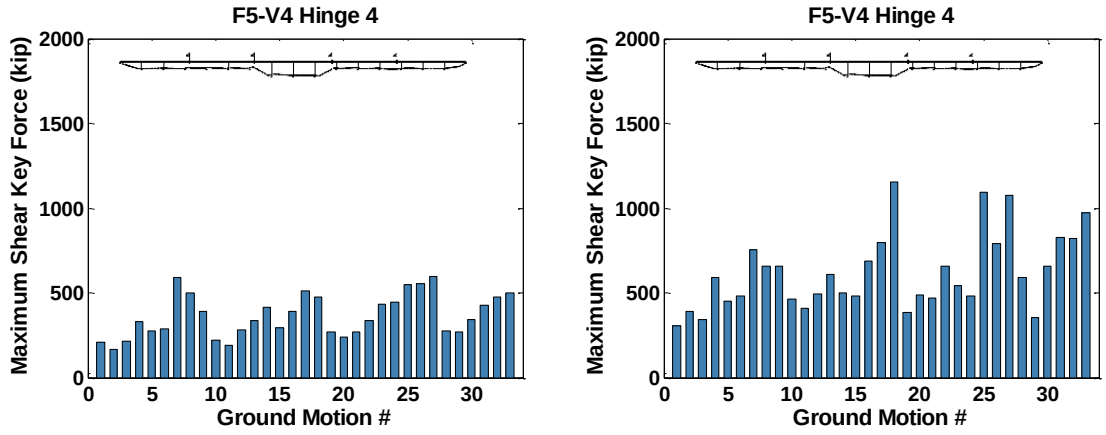

(a) (b)

Figure C.51 Maximum Shear Key Forces, Prototype F5-V4, Hinge 4, for a) Single-Column b) Two-Column

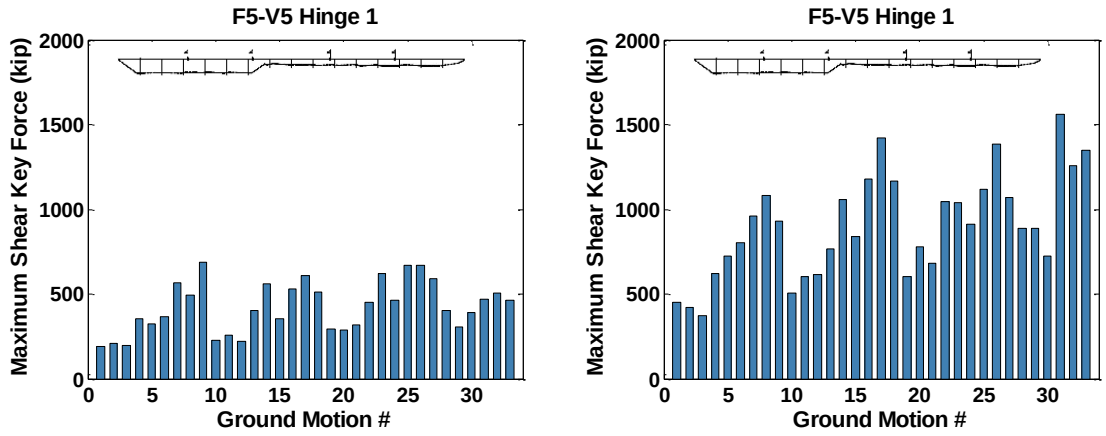

(a) (b)

Figure C.52 Maximum Shear Key Forces, Prototype F5-V5, Hinge 1, for a) Single-Column b) Two-Column

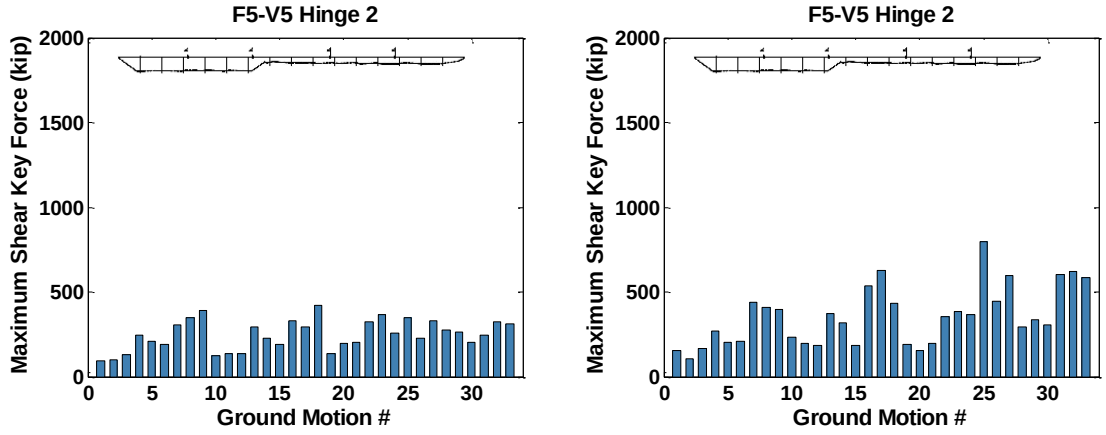

(a) (b)

Figure C.53 Maximum Shear Key Forces, Prototype F5-V5, Hinge 2, for a) Single-Column b) Two-Column

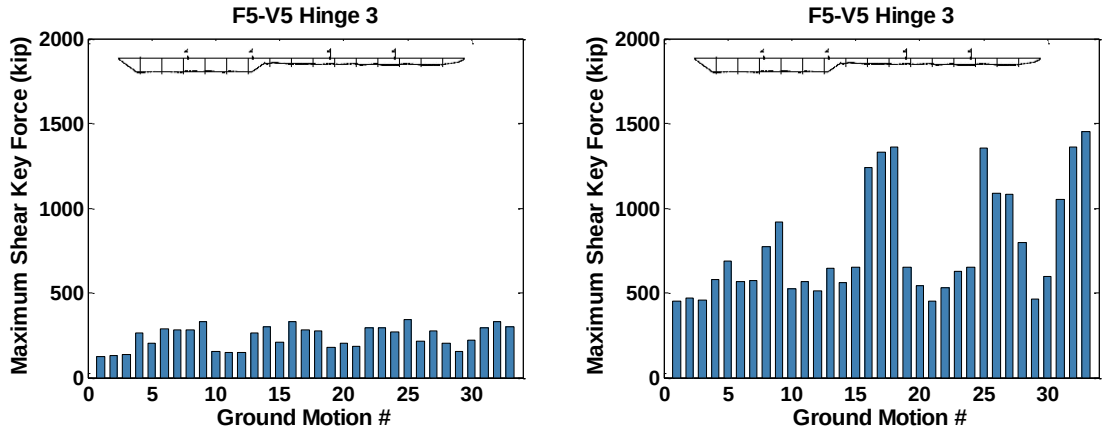

(a) (b)

Figure C.54 Maximum Shear Key Forces, Prototype F5-V5, Hinge 3, for a) Single-Column b) Two-Column

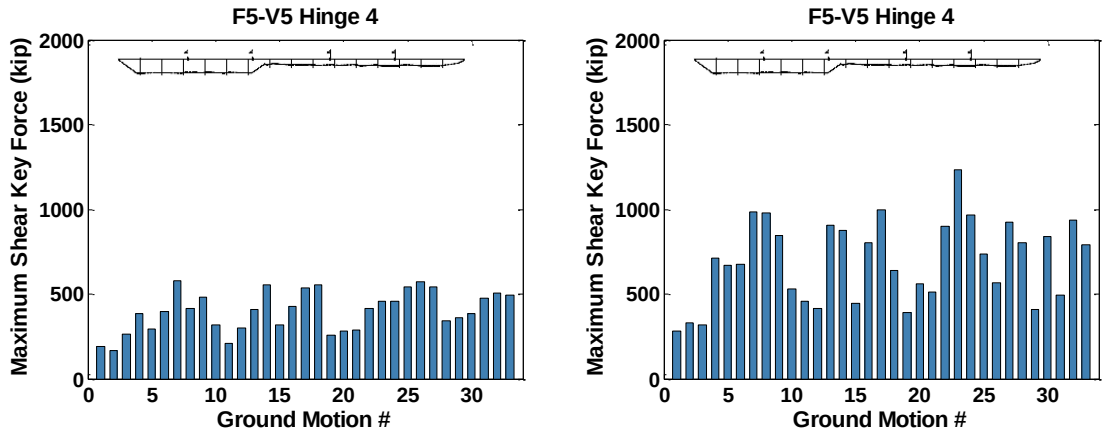

(a) (b)

Figure C.55 Maximum Shear Key Forces, Prototype F5-V5, Hinge 4, for a) Single-Column b) Two-Column

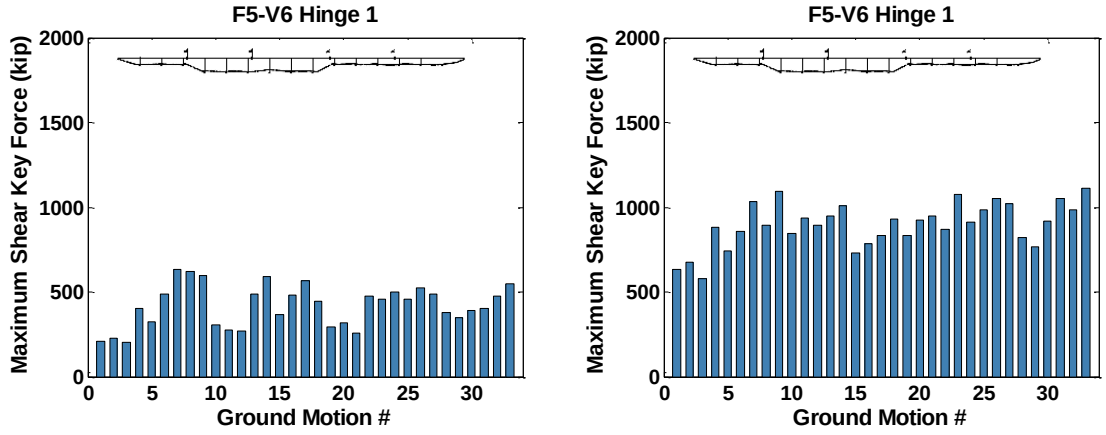

(a) (b)

Figure C.56 Maximum Shear Key Forces, Prototype F5-V6, Hinge 1, for a) Single-Column b) Two-Column

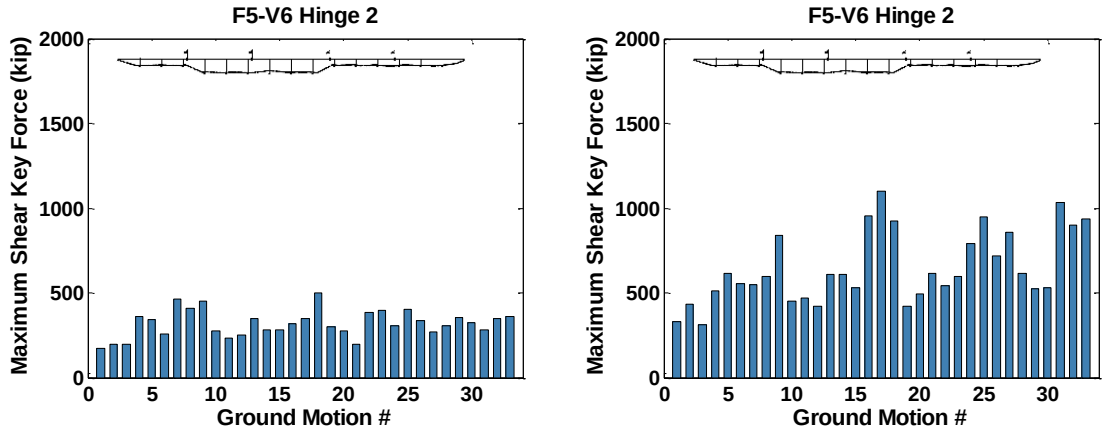

(a) (b)

Figure C.57 Maximum Shear Key Forces, Prototype F5-V6, Hinge 2, for a) Single-Column b) Two-Column

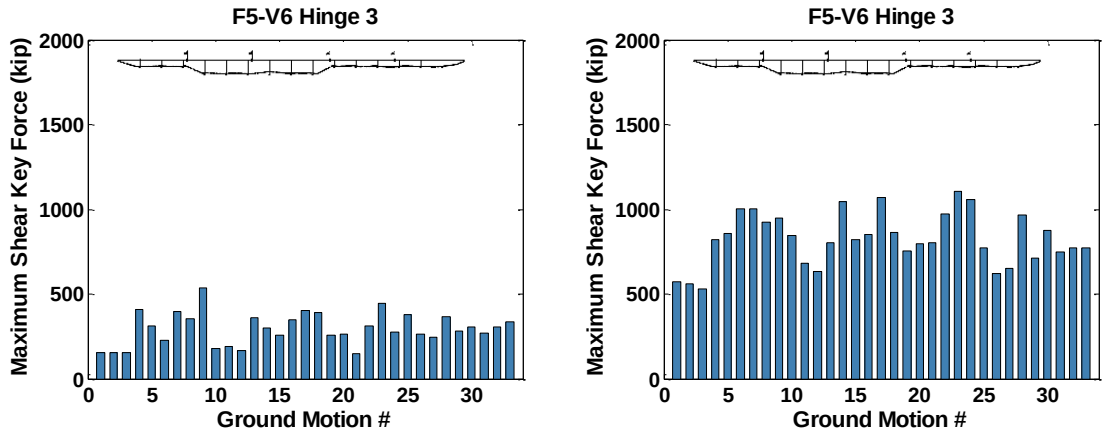

(a) (b)

Figure C.58 Maximum Shear Key Forces, Prototype F5-V6, Hinge 3, for a) Single-Column b) Two-Column

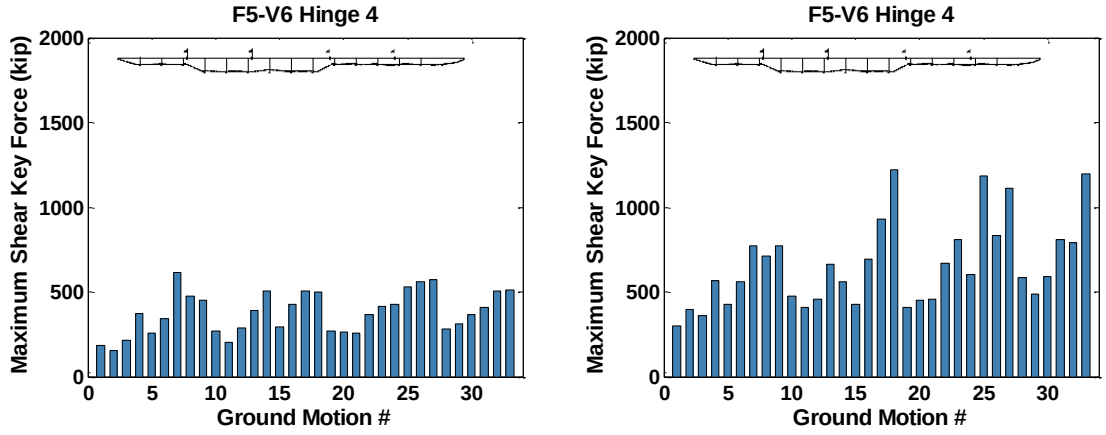

(a) (b)

Figure C.59 Maximum Shear Key Forces, Prototype F5-V6, Hinge 4, for a) Single-Column b) Two-Column

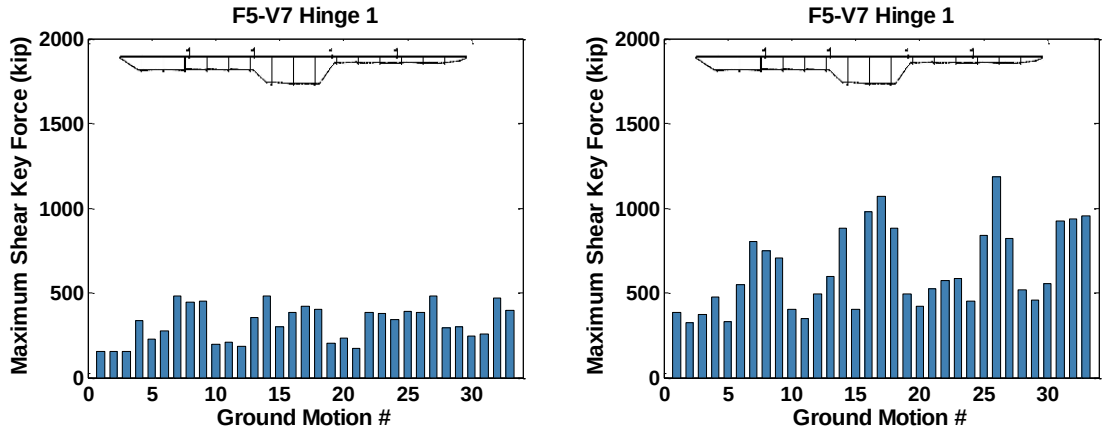

(a) (b)

Figure C.60 Maximum Shear Key Forces, Prototype F5-V7, Hinge 1, for a) Single-Column b) Two-Column

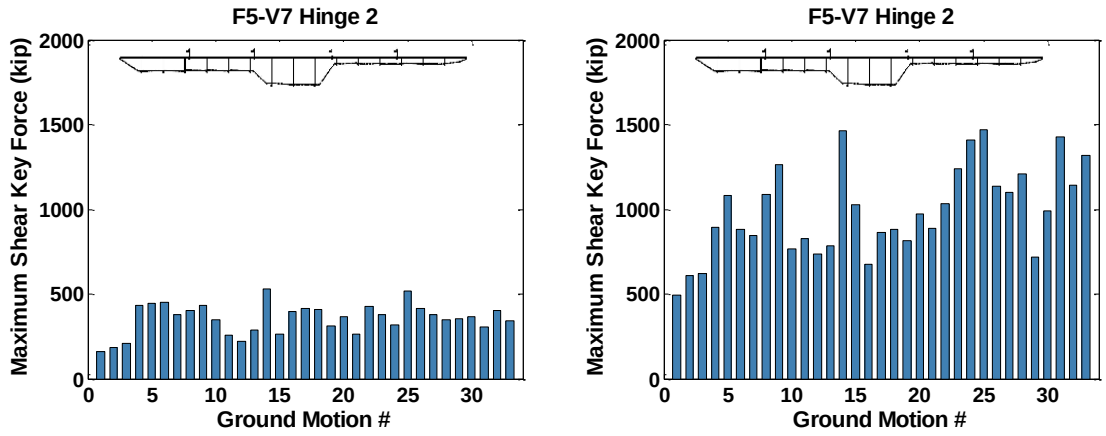

(a) (b)

Figure C.61 Maximum Shear Key Forces, Prototype F5-V7, Hinge 2, for a) Single-Column b) Two-Column

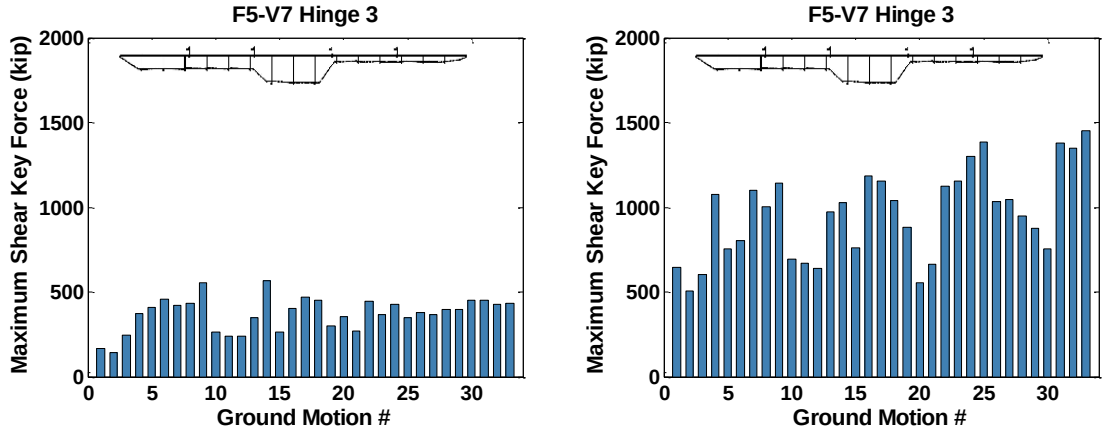

(a) (b)

Figure C.62 Maximum Shear Key Forces, Prototype F5-V7, Hinge 3, for a) Single-Column b) Two-Column

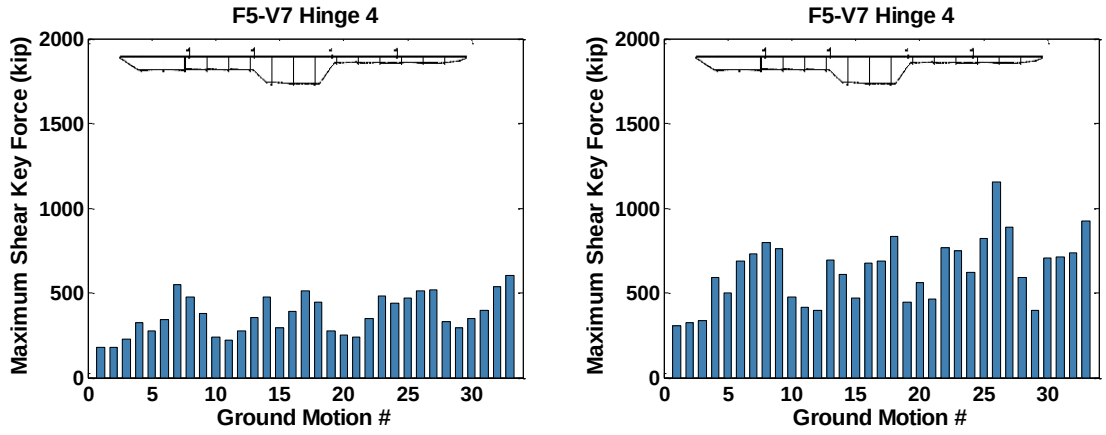

(a) (b)

Figure C.63 Maximum Shear Key Forces, Prototype F5-V7, Hinge 4, for a) Single-Column b) Two-Column

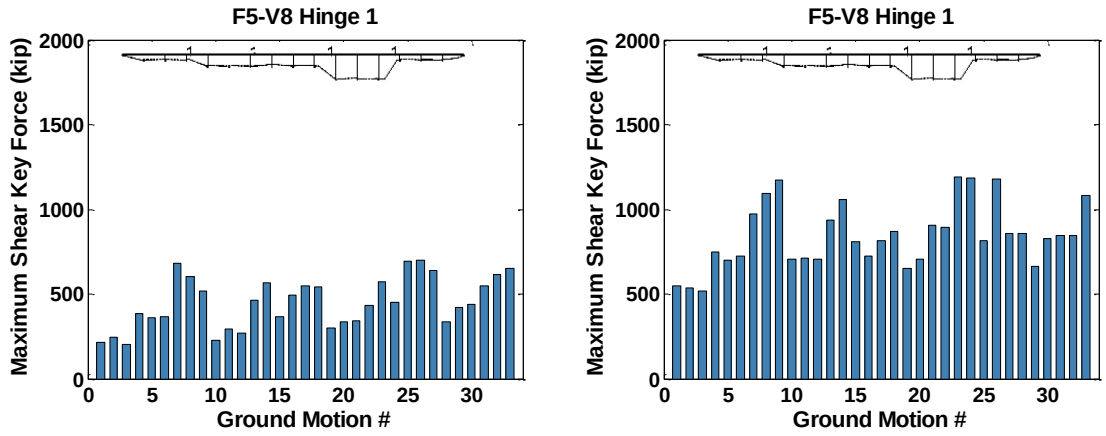

(a) (b)

Figure C.64 Maximum Shear Key Forces, Prototype F5-V8, Hinge 1, for a) Single-Column b) Two-Column

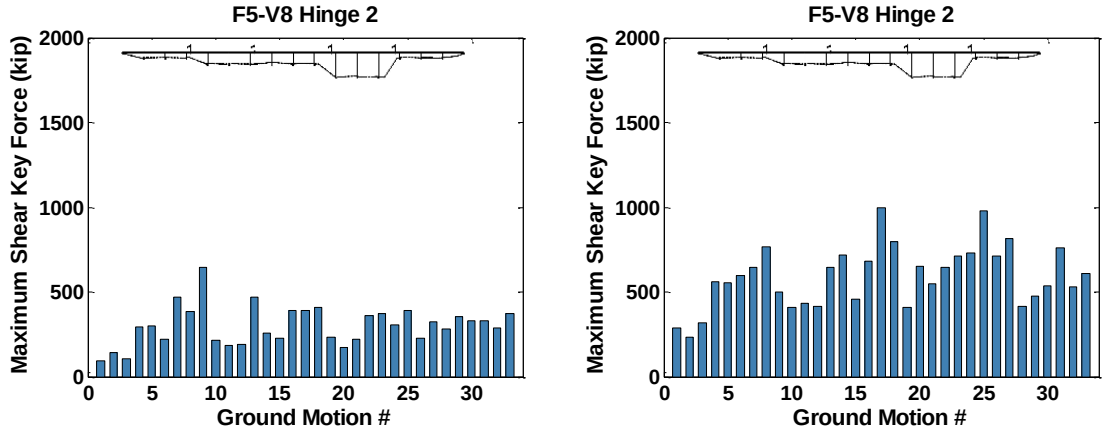

(a) (b)

Figure C.65 Maximum Shear Key Forces, Prototype F5-V8, Hinge 2, for a) Single-Column b) Two-Column

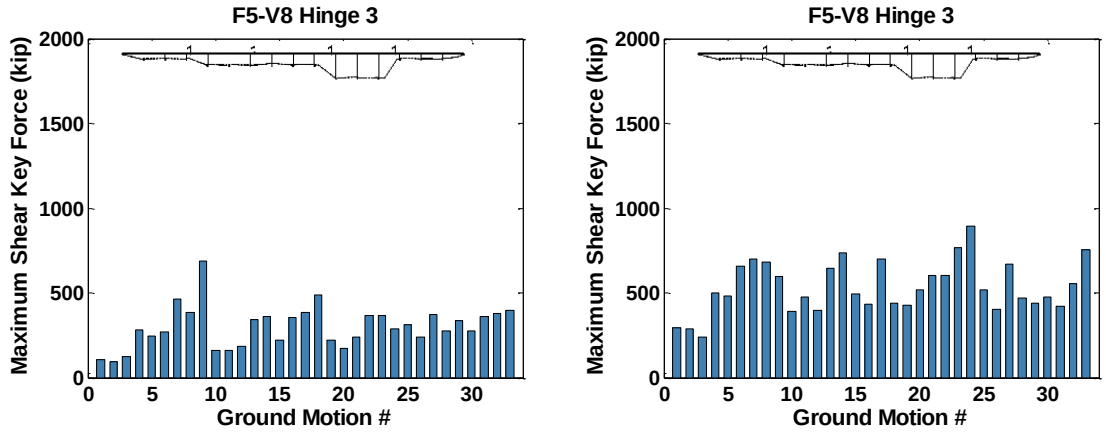

(a) (b)

Figure C.66 Maximum Shear Key Forces, Prototype F5-V8, Hinge 3, for a) Single-Column b) Two-Column

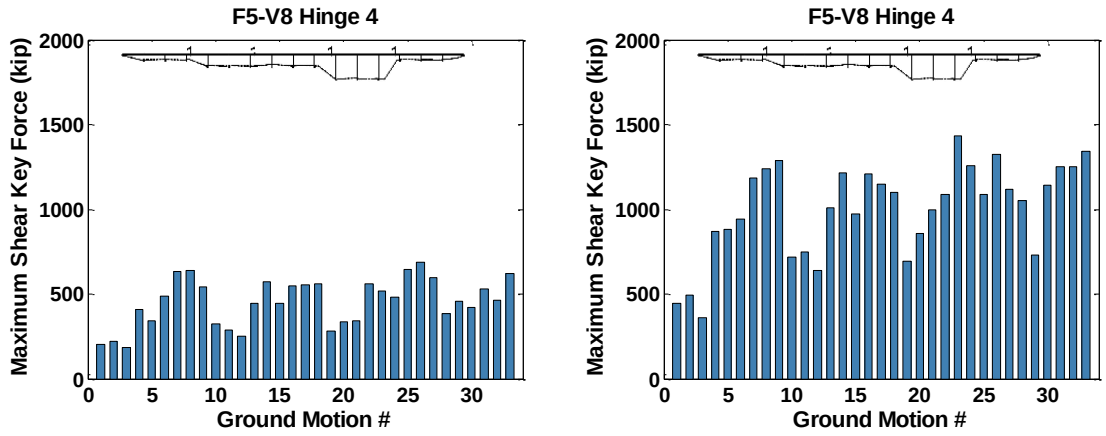

(a) (b)

Figure C.67 Maximum Shear Key Forces, Prototype F5-V8, Hinge 4, for a) Single-Column b) Two-Column

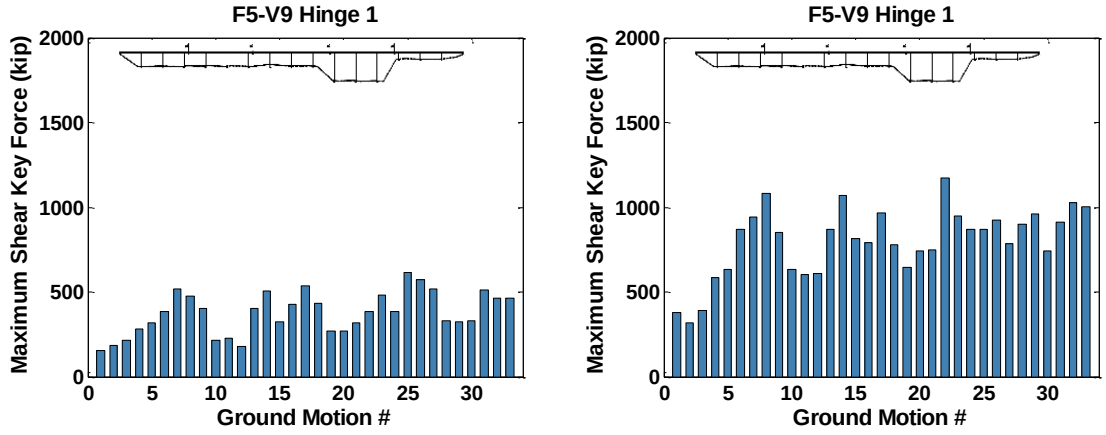

(a) (b)

Figure C.68 Maximum Shear Key Forces, Prototype F5-V9, Hinge 1, for a) Single-Column b) Two-Column

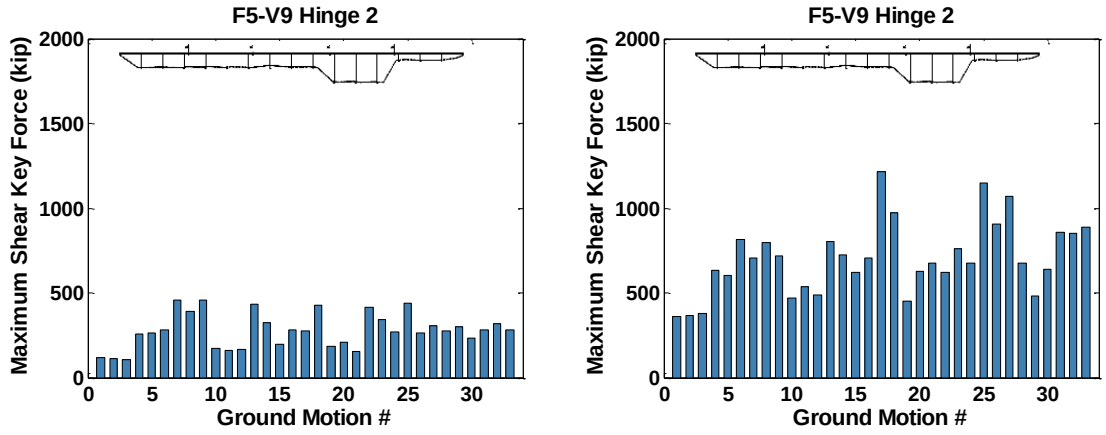

(a) (b)

Figure C.69 Maximum Shear Key Forces, Prototype F5-V9, Hinge 2, for a) Single-Column b) Two-Column

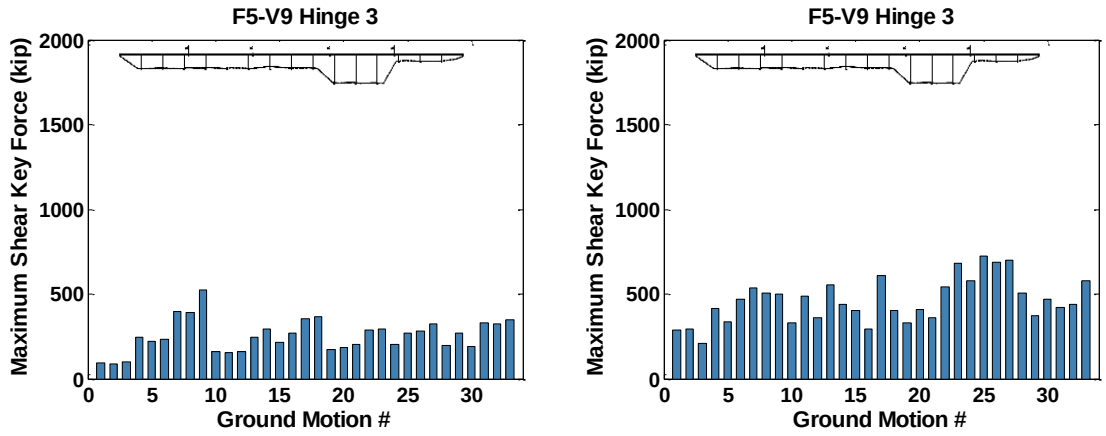

(a) (b)

Figure C.70 Maximum Shear Key Forces, Prototype F5-V9, Hinge 3, for a) Single-Column b) Two-Column

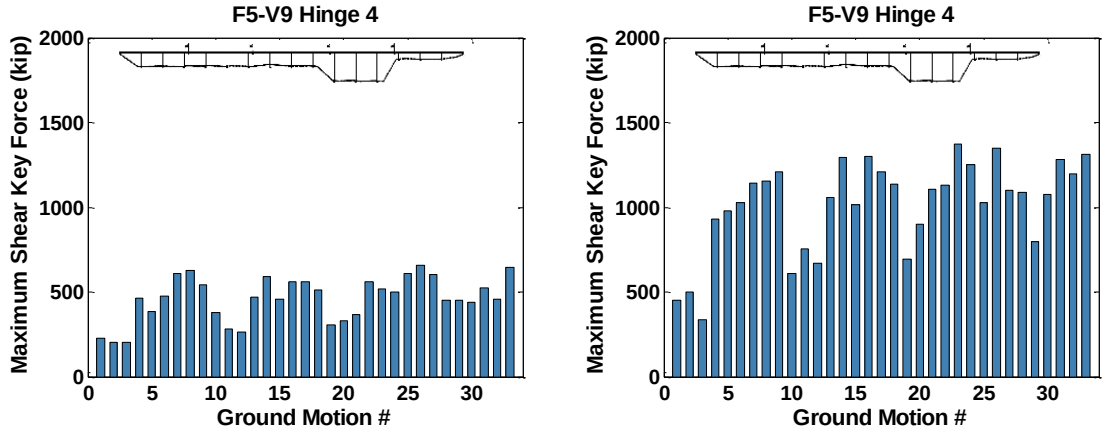

(a) (b)

Figure C.71 Maximum Shear Key Forces, Prototype F5-V9, Hinge 4, for a) Single-Column b) Two-Column

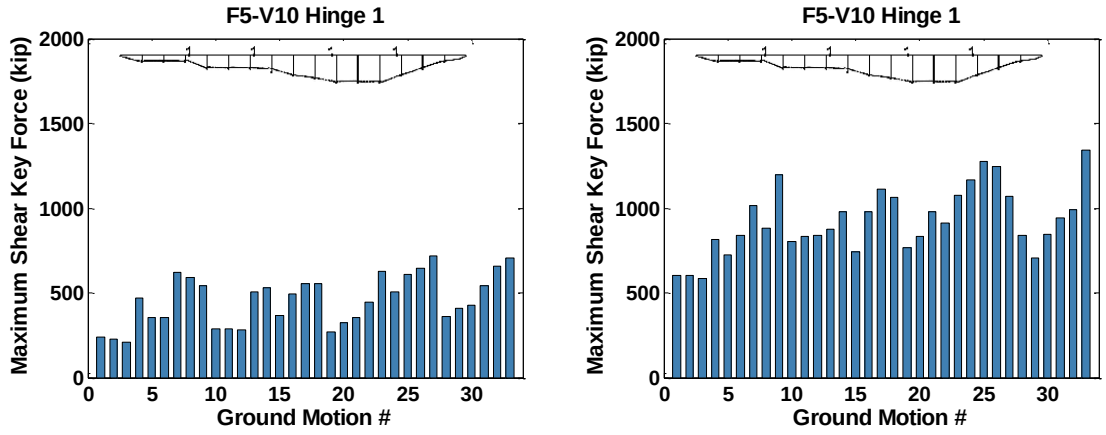

(a) (b)

Figure C.72 Maximum Shear Key Forces, Prototype F5-V10, Hinge 1, for a) Single-Column b) Two-Column

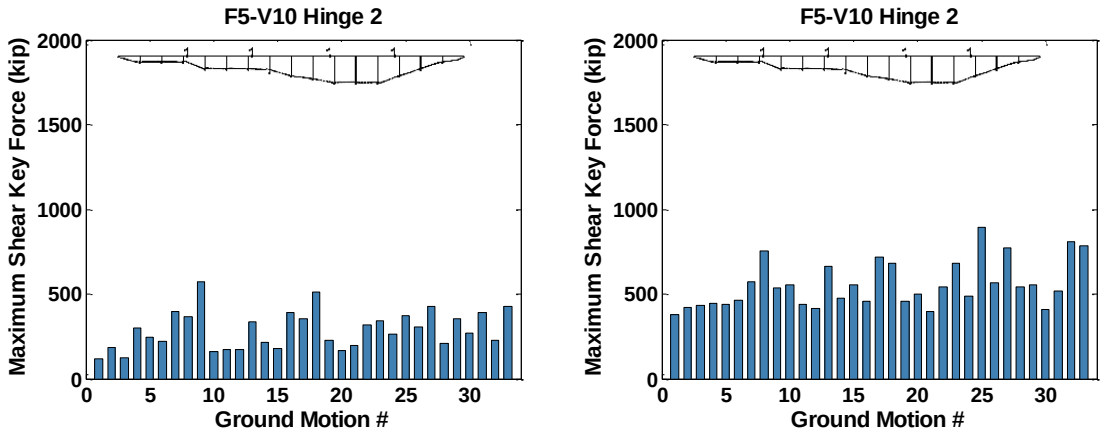

(a) (b)

Figure C.73 Maximum Shear Key Forces, Prototype F5-V10, Hinge 2, for a) Single-Column b) Two-Column

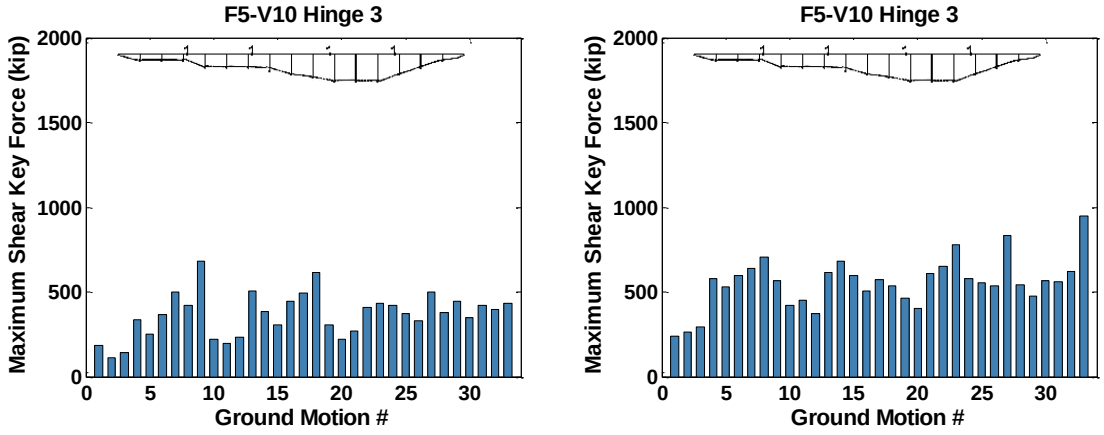

(a) (b)

Figure C.74 Maximum Shear Key Forces, Prototype F5-V10, Hinge 3, for a) Single-Column b) Two-Column

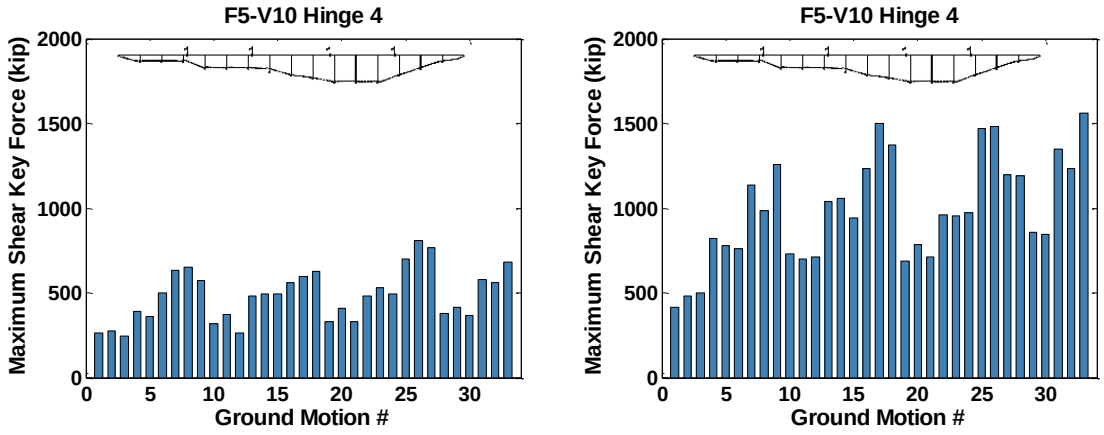

(a) (b)

Figure C.75 Maximum Shear Key Forces, Prototype F5-V10, Hinge 4, for a) Single-Column b) Two-Column

PART-2a: Single-Column Bent Prototypes
Time History of Shear Key Forces,
Time History of Transverse Displacement at Hinges, and
Transverse Acceleration at hinges.

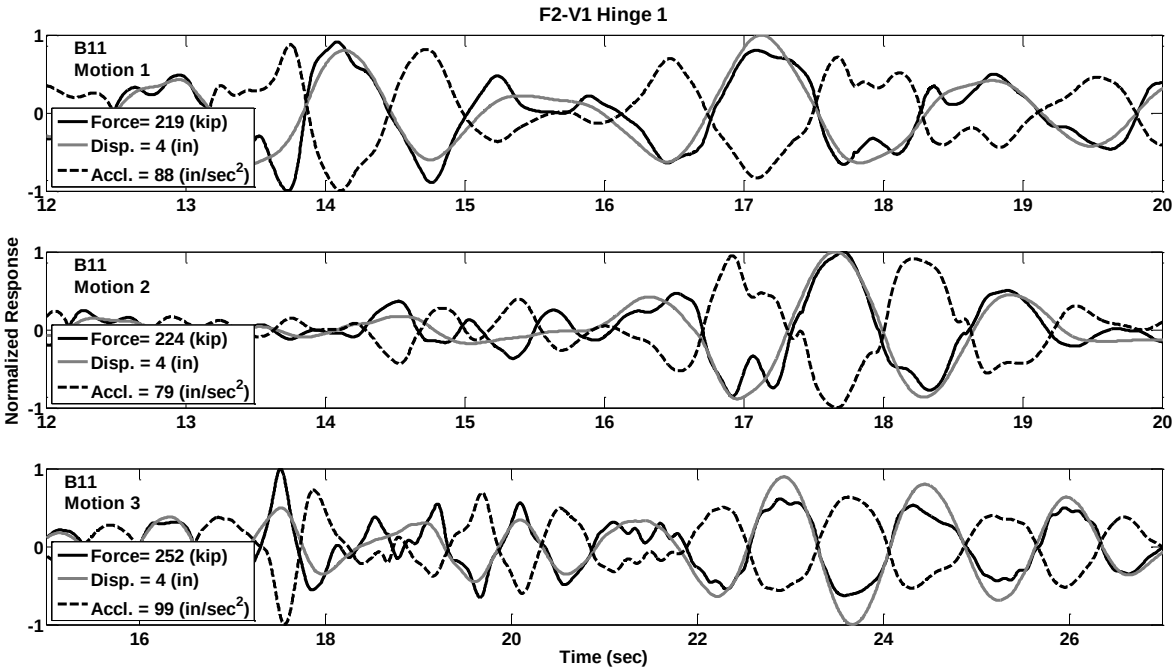

Figure C.76 Response Histories of Prototype F2-V1, Hinge 1, Motions B11

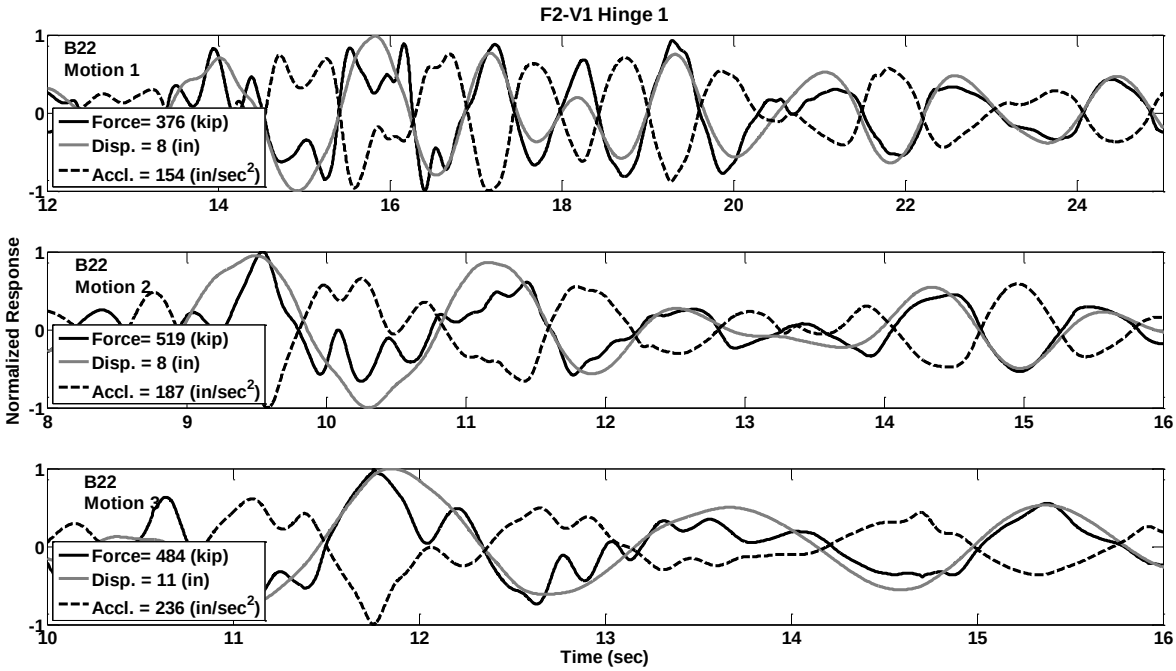

Figure C.77 Response Histories of Prototype F2-V1, Hinge 1, Motions B22

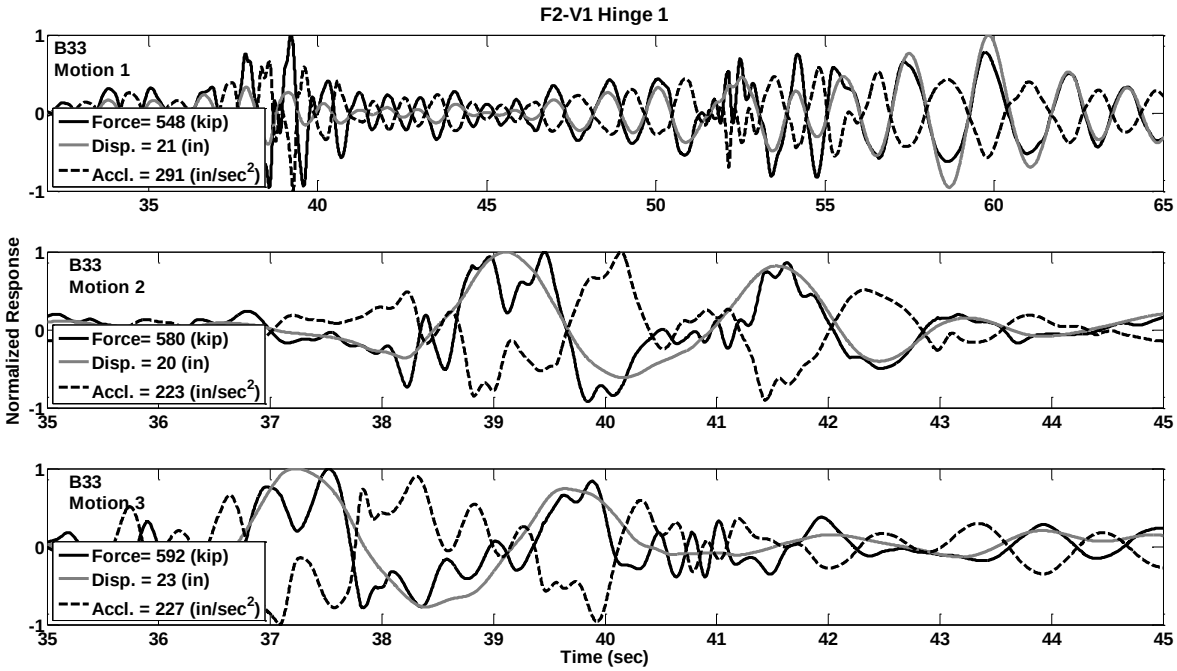

Figure C.78 Response Histories of Prototype F2-V1, Hinge 1, Motions B33

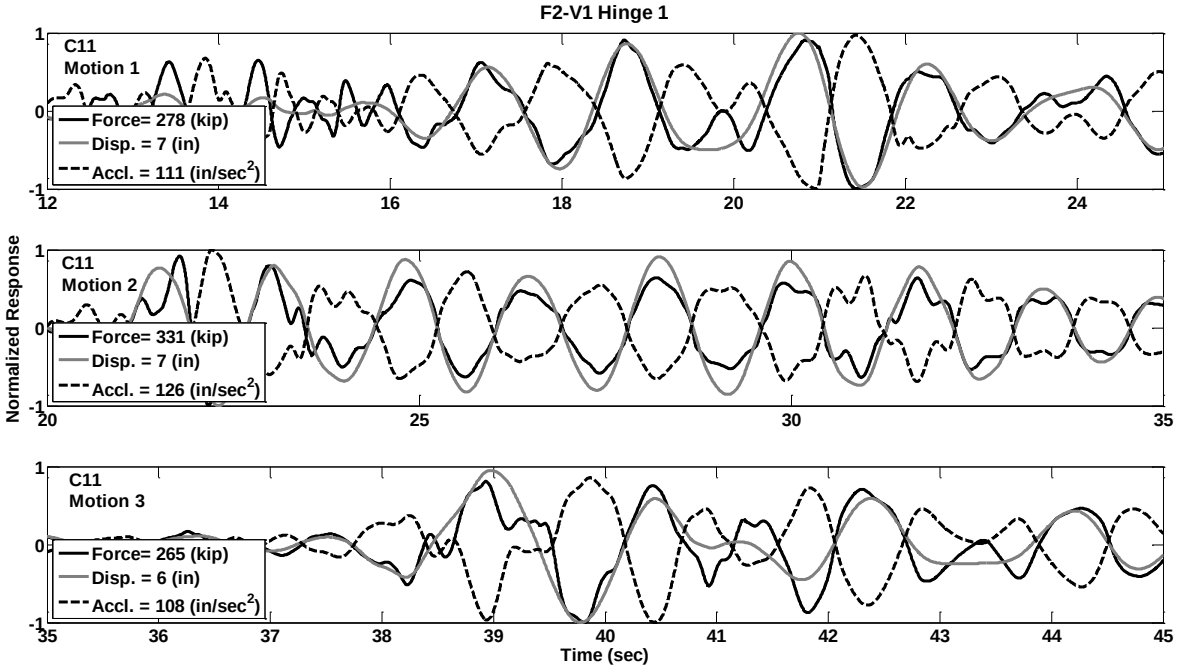

Figure C.79 Response Histories of Prototype F2-V1, Hinge 1, Motions C11

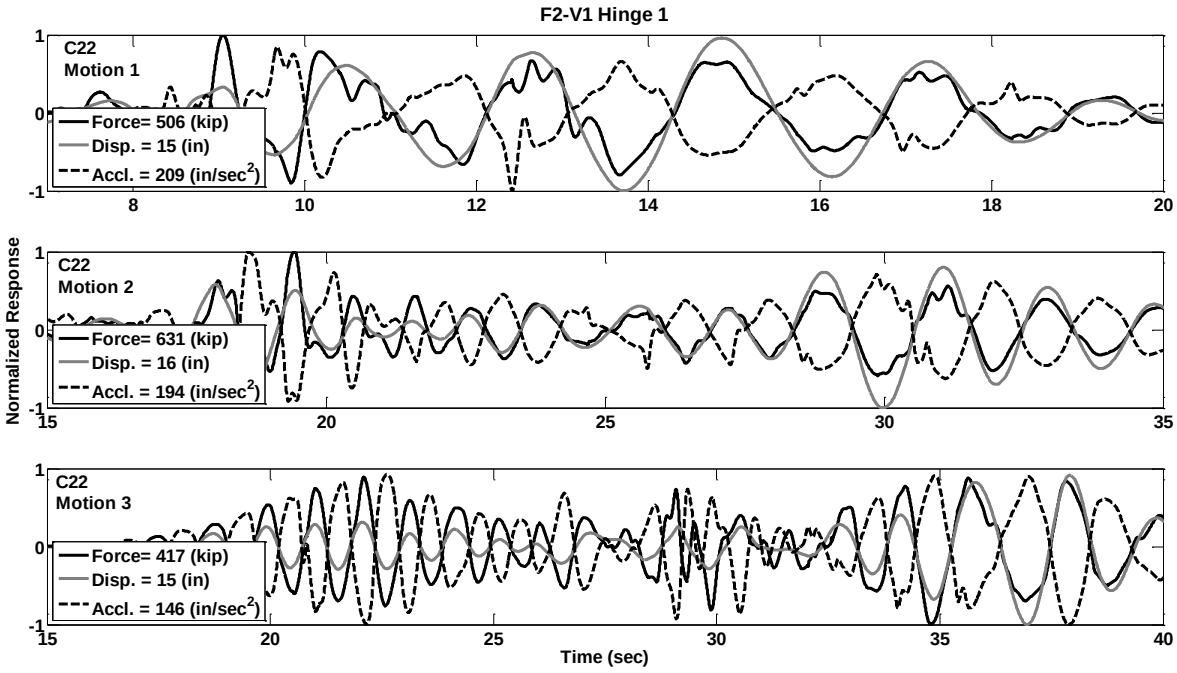

Figure C.80 Response Histories of Prototype F2-V1, Hinge 1, Motions C22

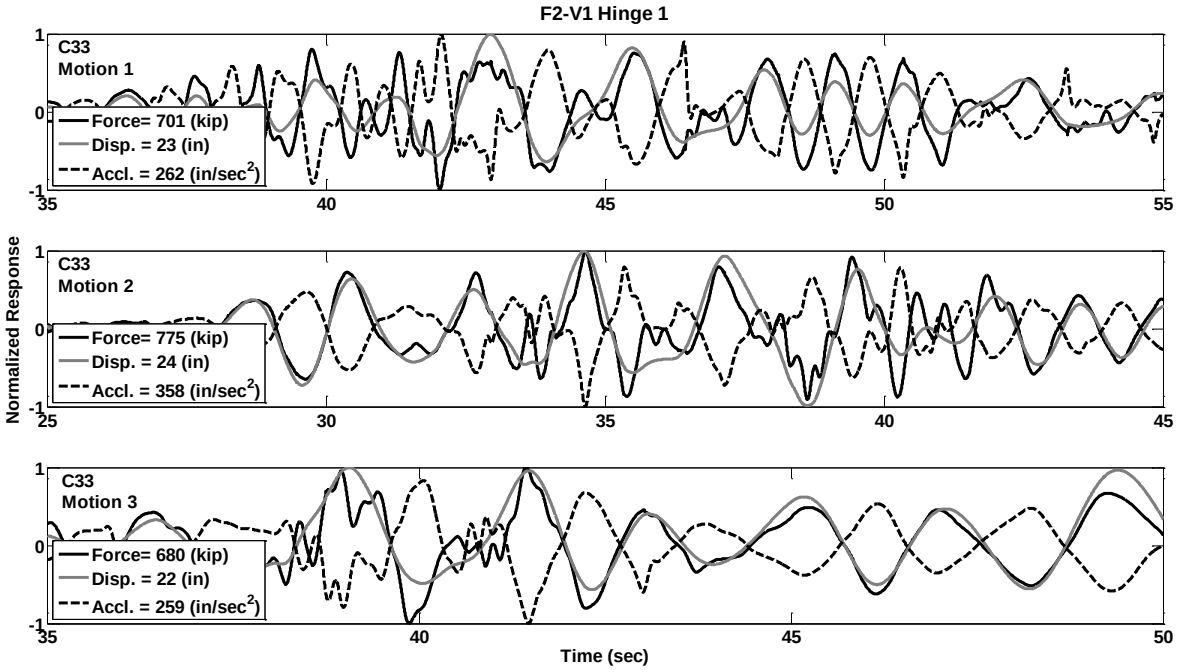

Figure C.81 Response Histories of Prototype F2-V1, Hinge 1, Motions C33

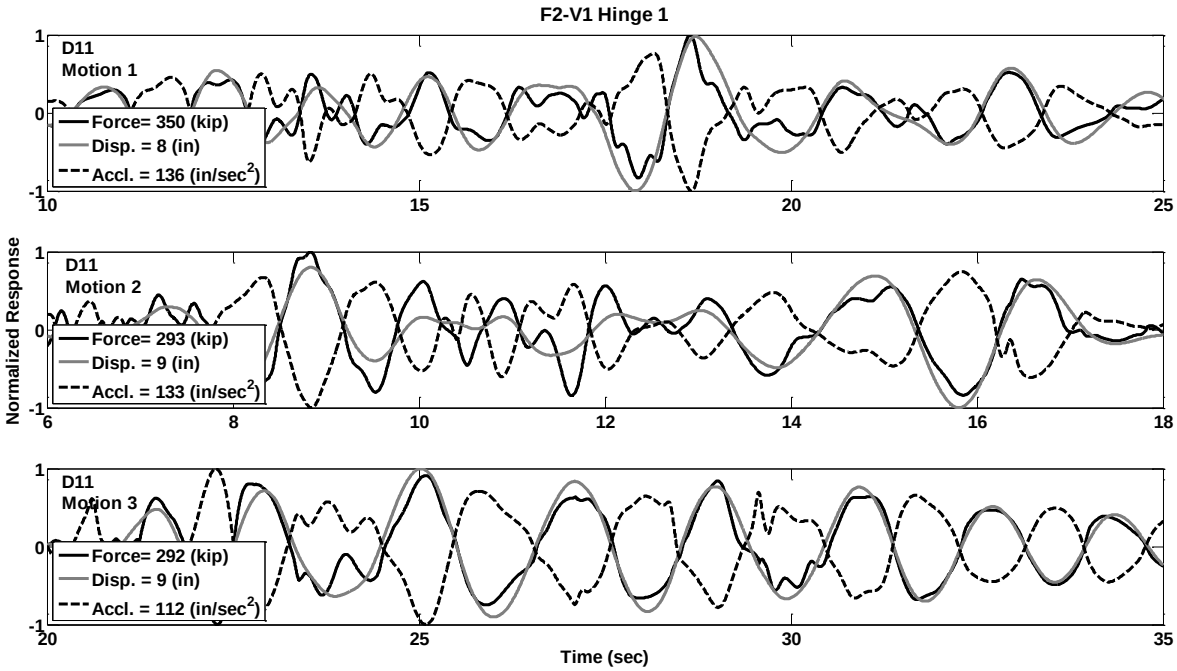

Figure C.82 Response Histories of Prototype F2-V1, Hinge 1, Motions D11

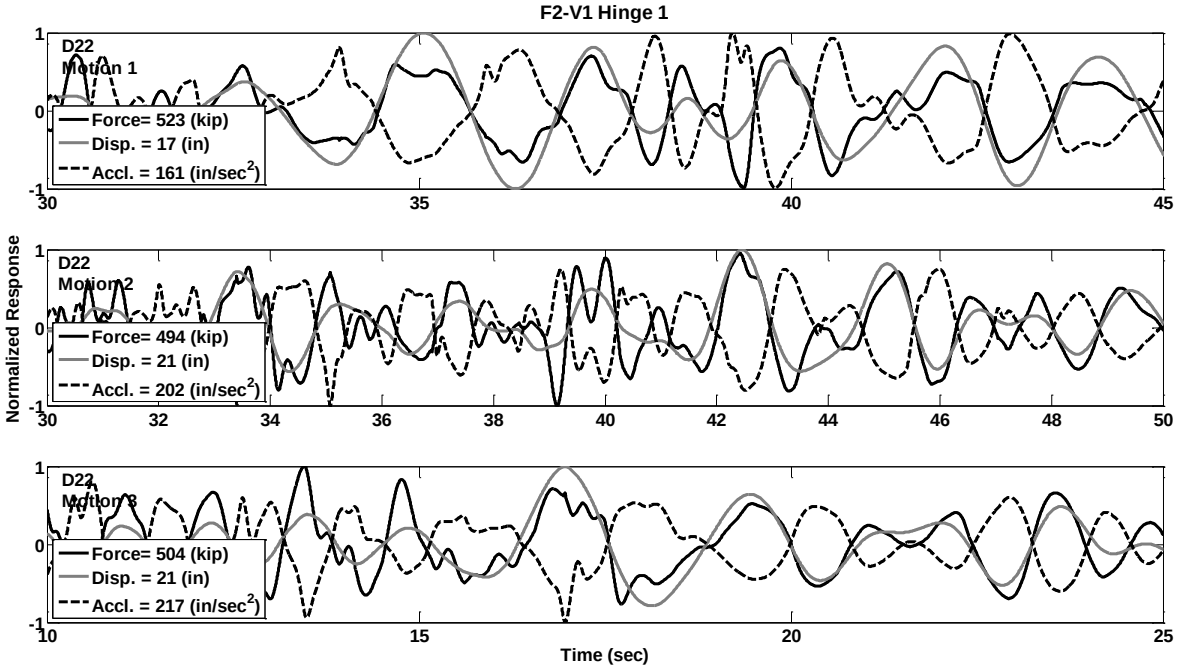

Figure C.83 Response Histories of Prototype F2-V1, Hinge 1, Motions D22

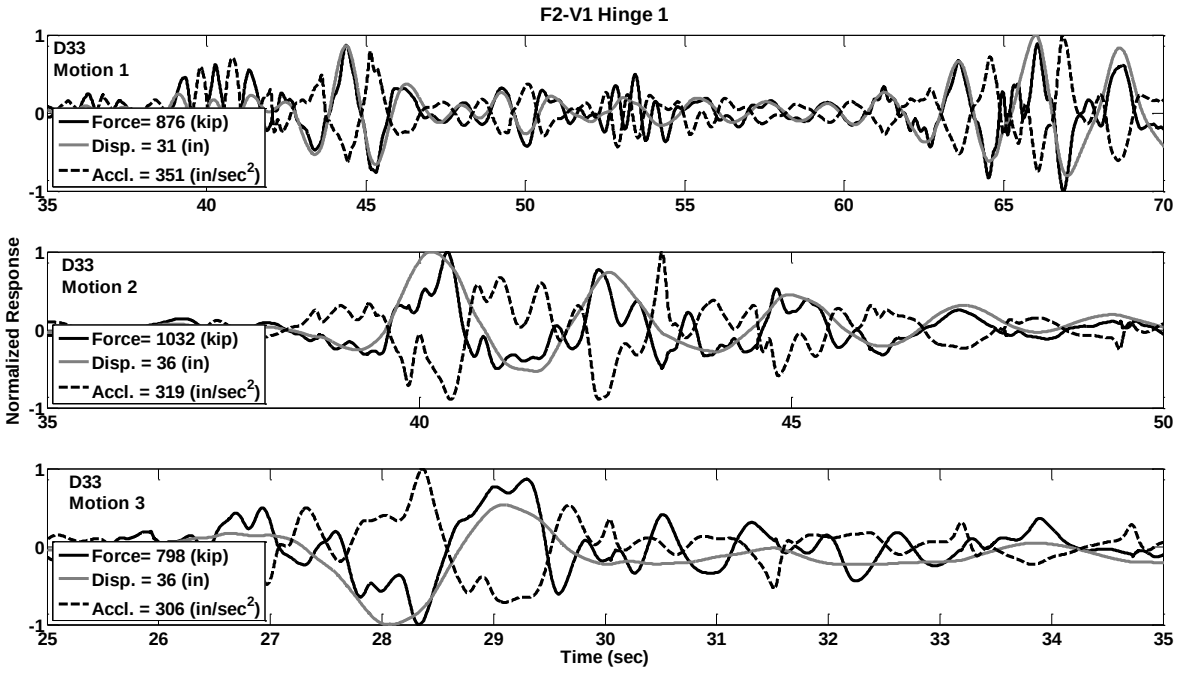

Figure C.84 Response Histories of Prototype F2-V1, Hinge 1, Motions D33

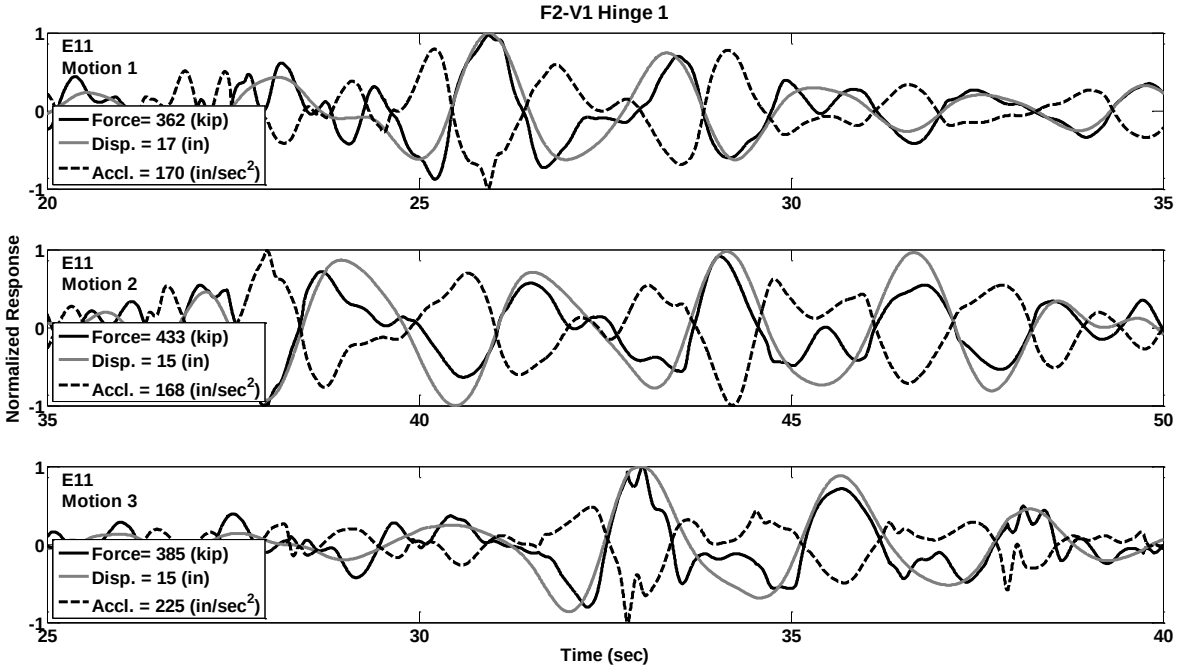

Figure C.85 Response Histories of Prototype F2-V1, Hinge 1, Motions E11

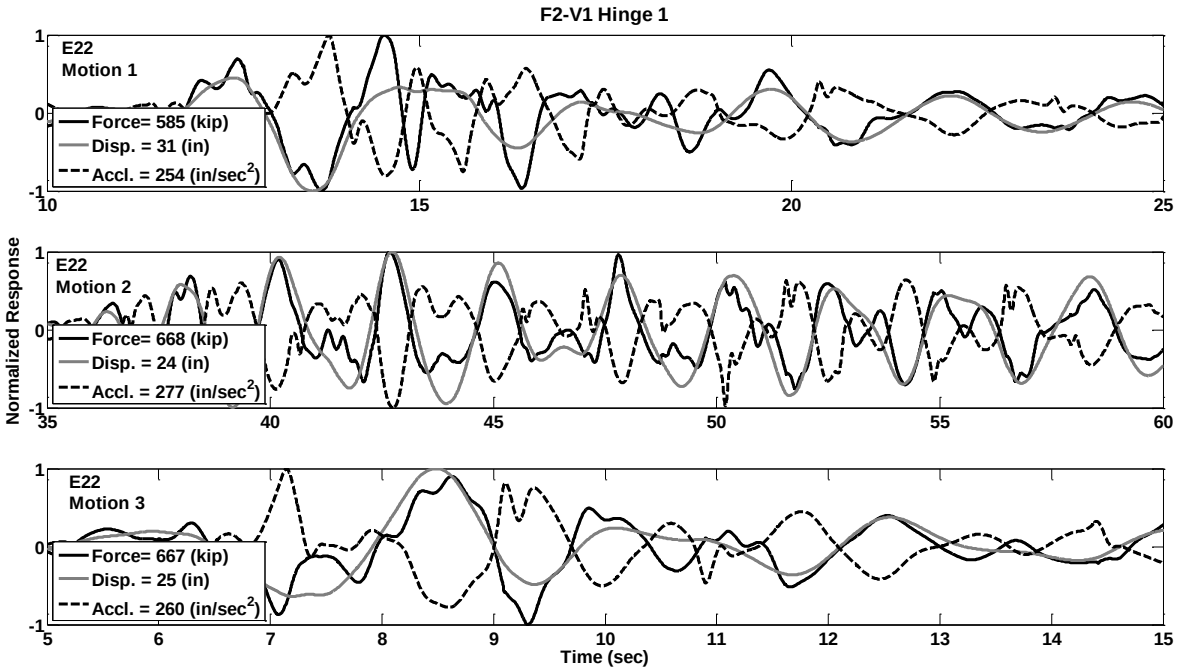

Figure C.86 Response Histories of Prototype F2-V1, Hinge 1, Motions E22

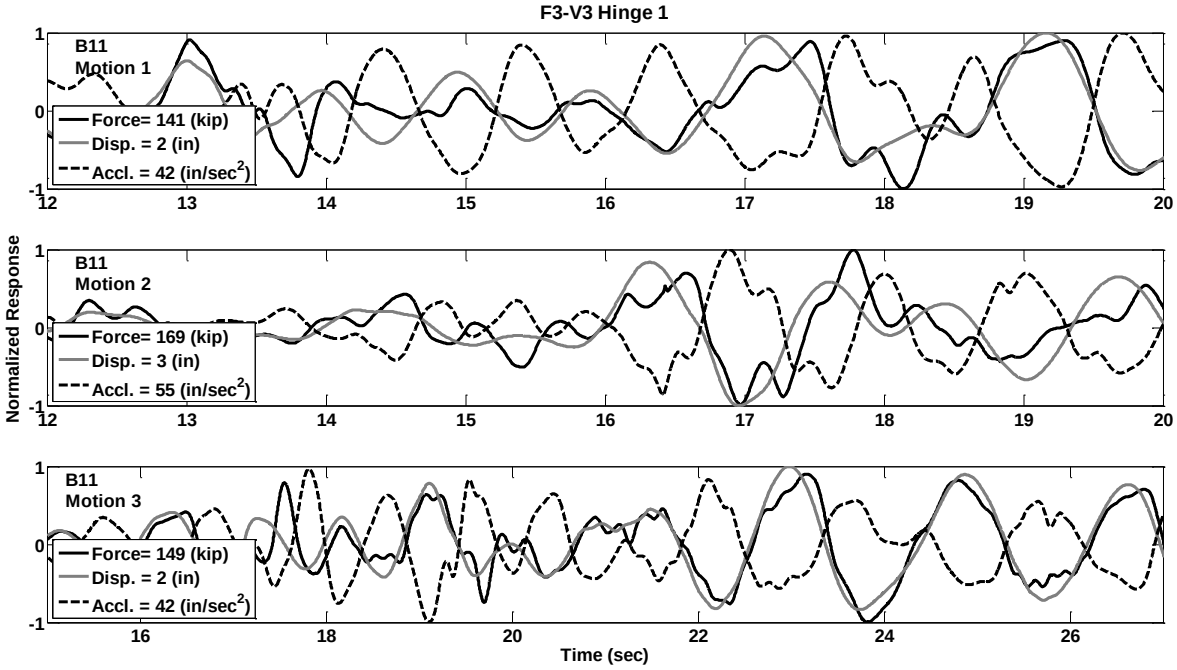

Figure C.87 Response Histories of Prototype F3-V3, Hinge 1, Motions B11

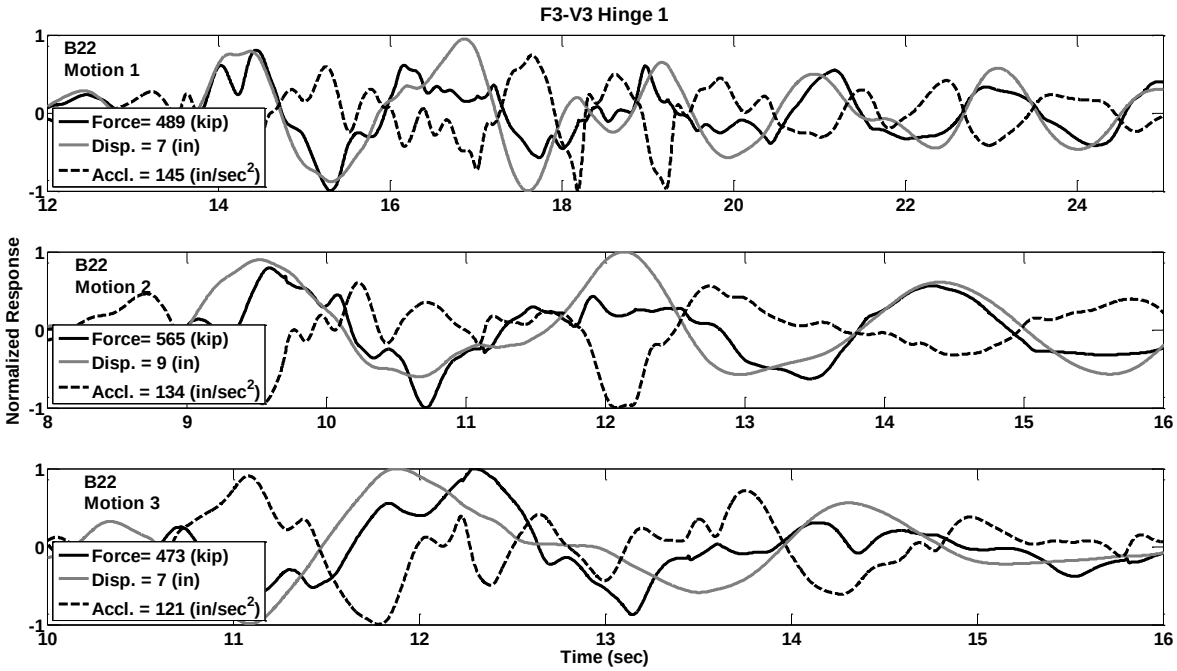

Figure C.88 Response Histories of Prototype F3-V3, Hinge 1, Motions B22

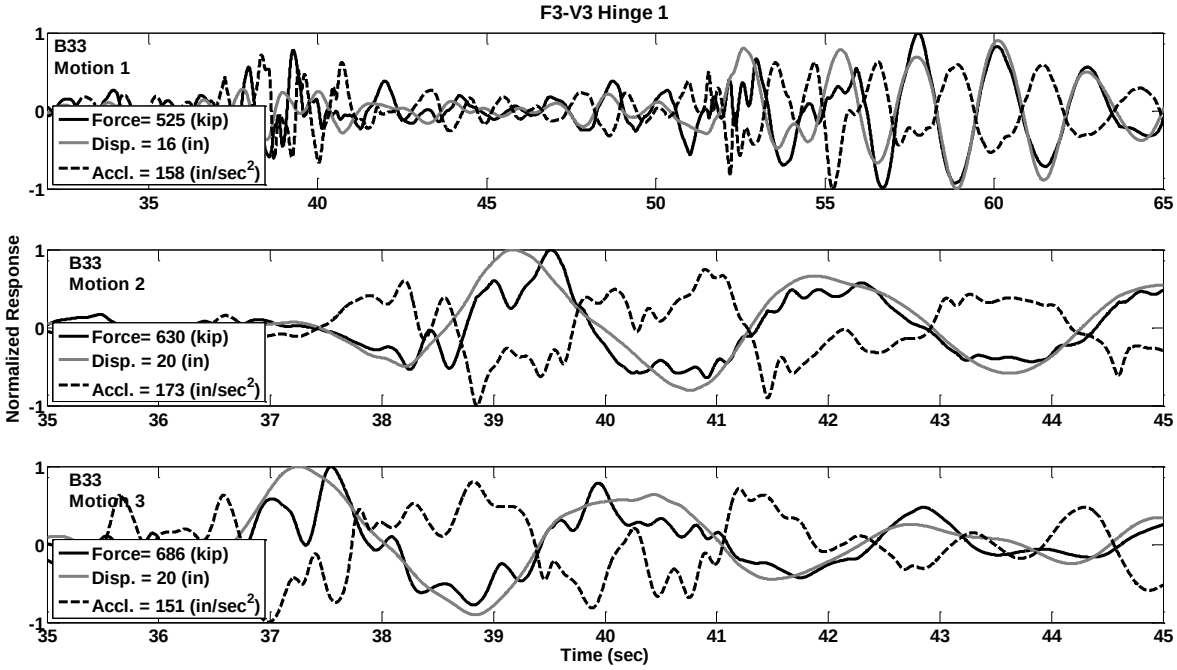

Figure C.89 Response Histories of Prototype F3-V3, Hinge 1, Motions B33

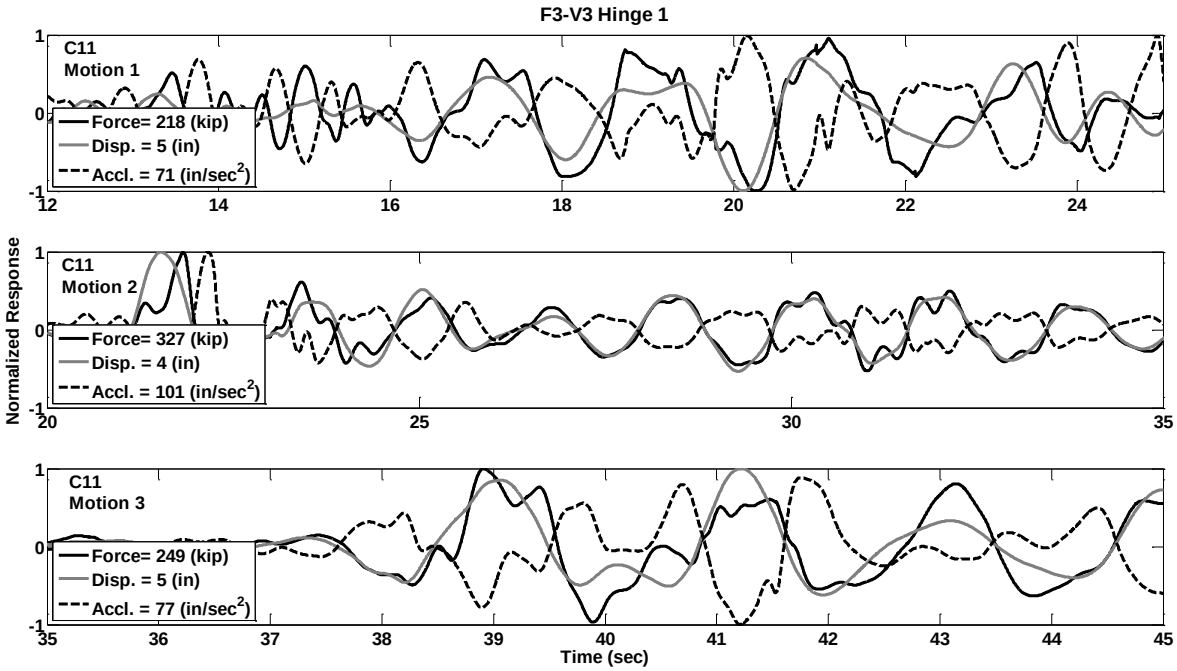

Figure C.90 Response Histories of Prototype F3-V3, Hinge 1, Motions C11

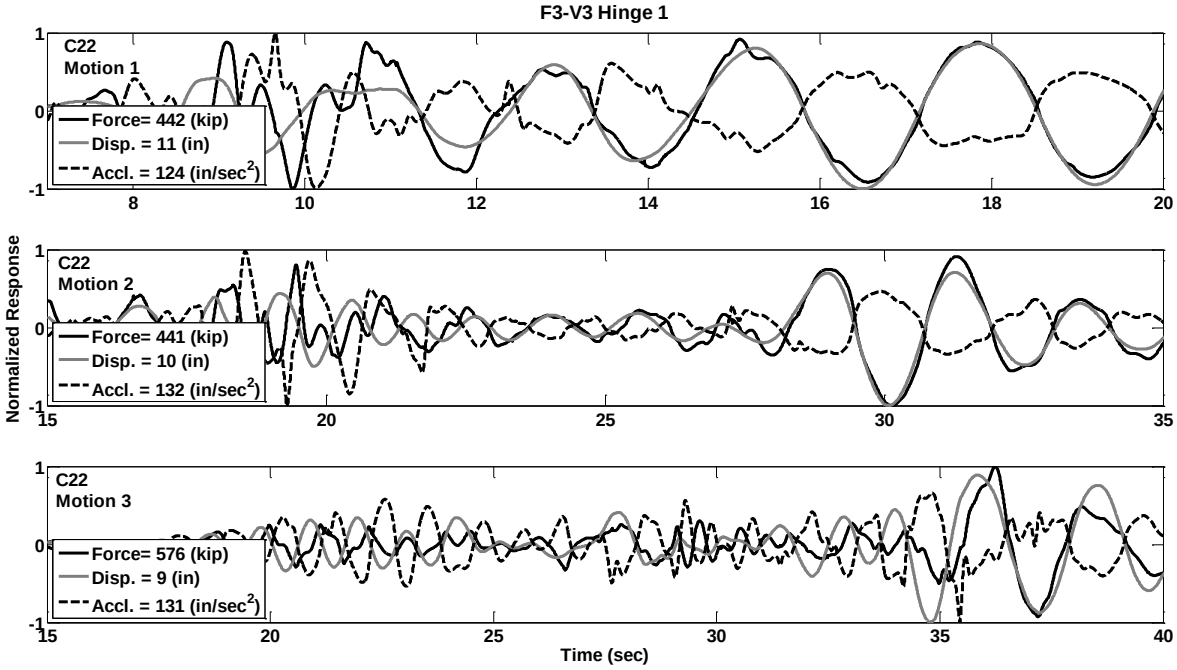

Figure C.91 Response Histories of Prototype F3-V3, Hinge 1, Motions C22

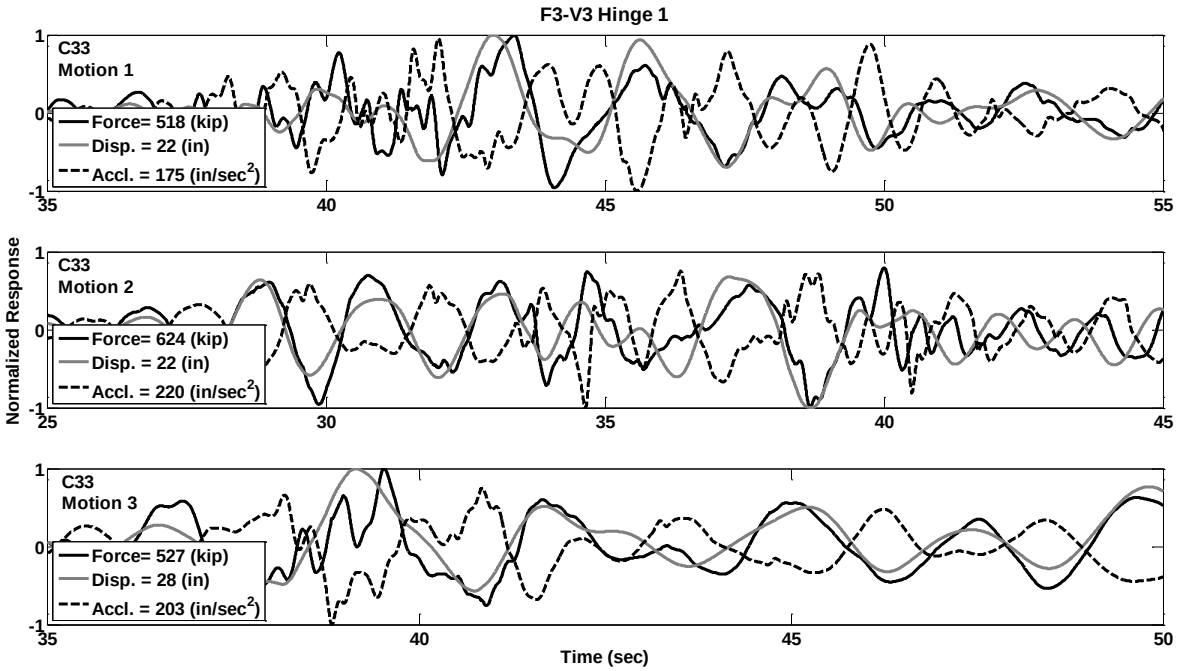

Figure C.92 Response Histories of Prototype F3-V3, Hinge 1, Motions C33

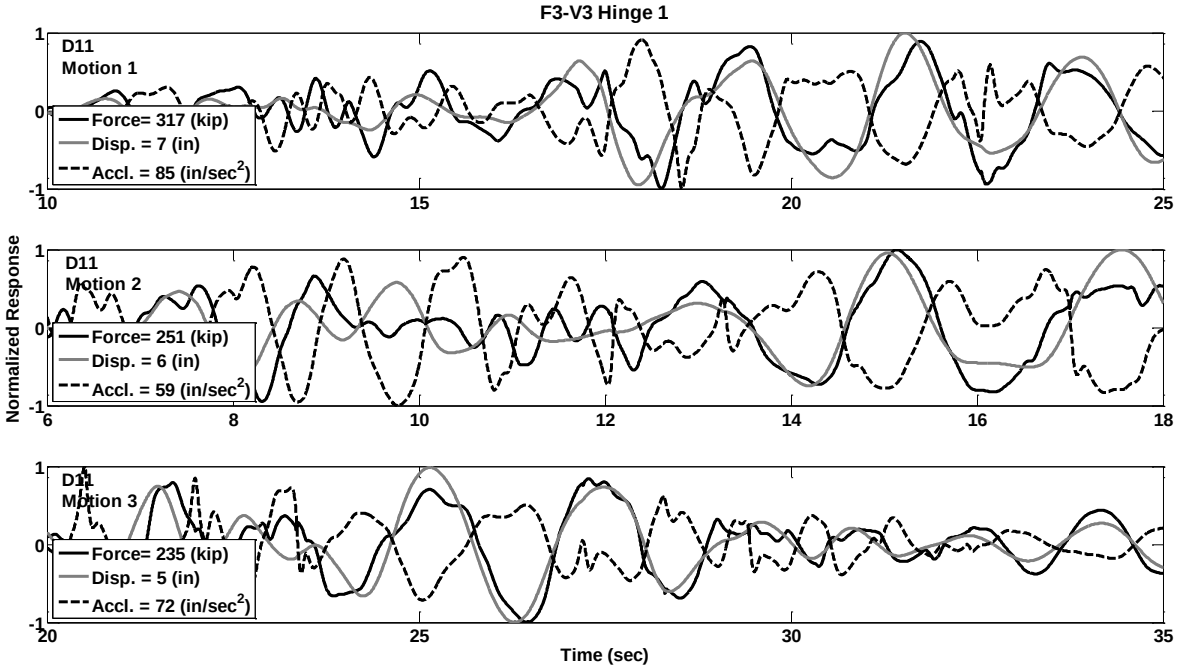

Figure C.93 Response Histories of Prototype F3-V3, Hinge 1, Motions D11

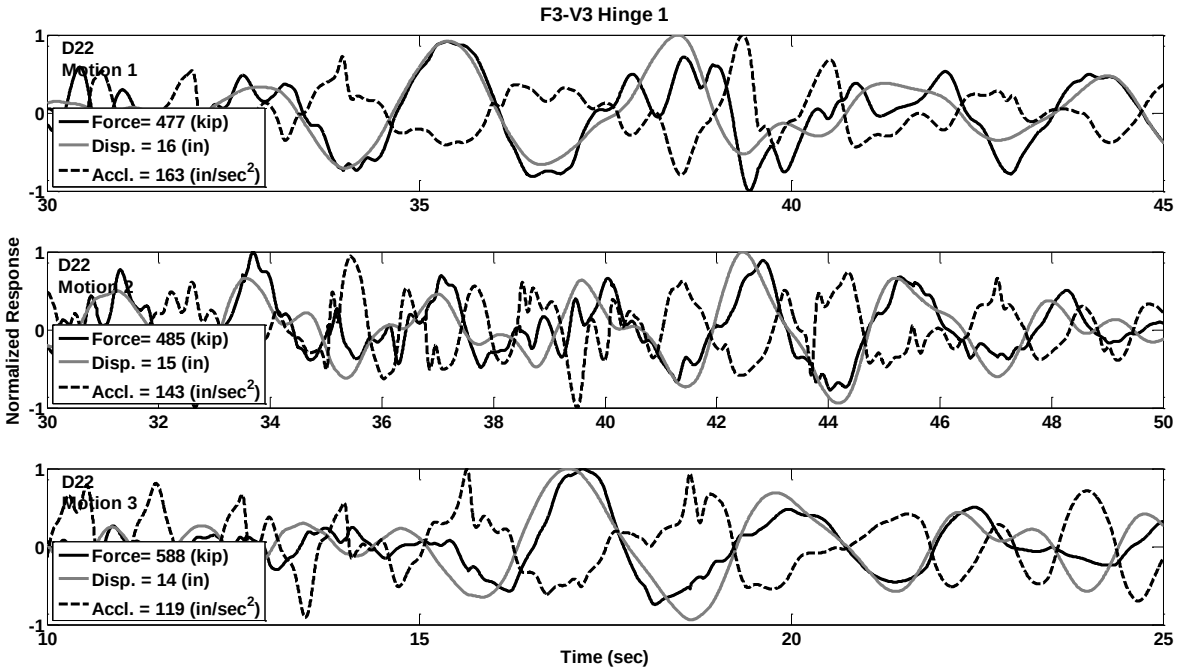

Figure C.94 Response Histories of Prototype F3-V3, Hinge 1, Motions D22

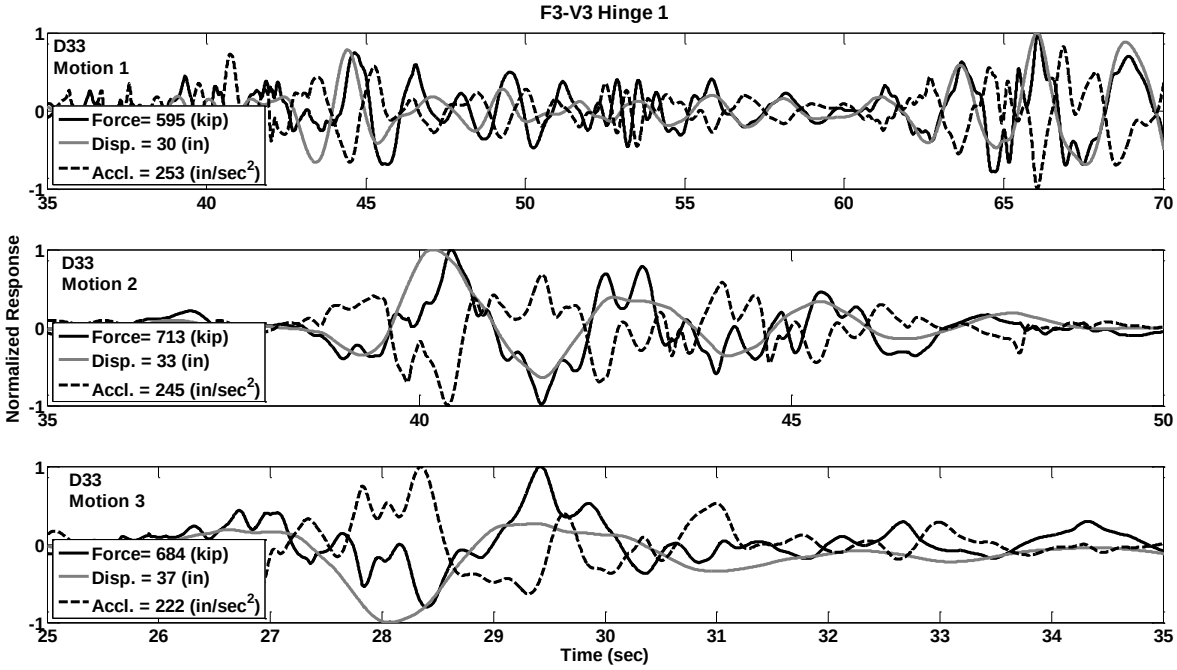

Figure C.95 Response Histories of Prototype F3-V3, Hinge 1, Motions D33

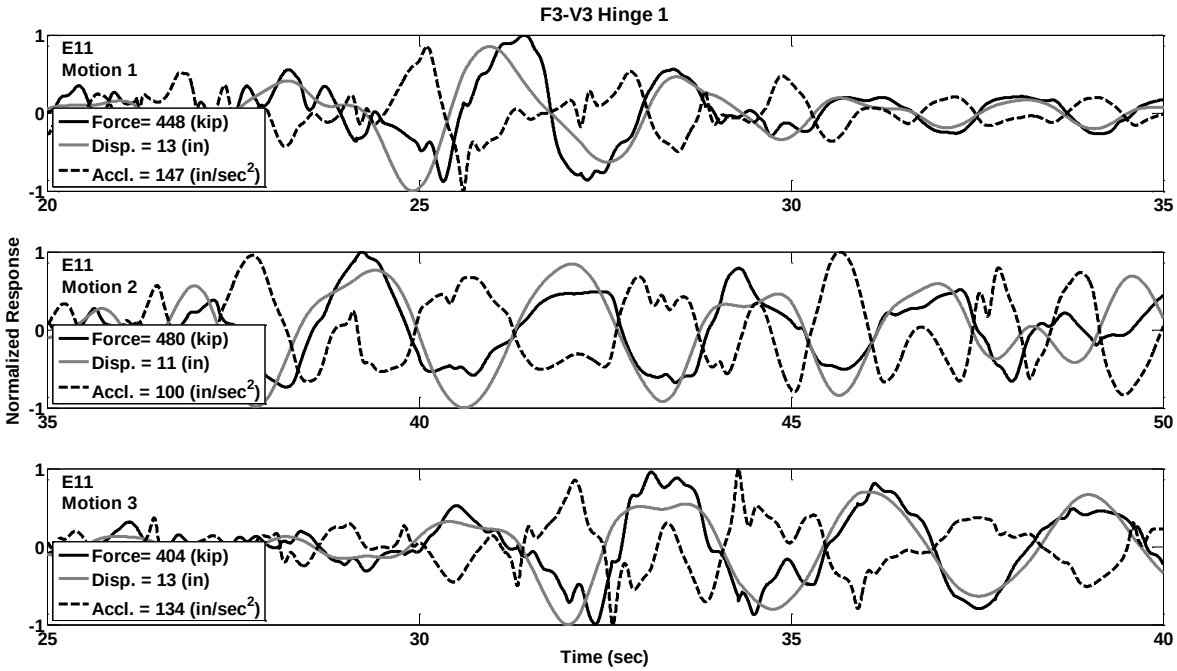

Figure C.96 Response Histories of Prototype F3-V3, Hinge 1, Motions E11

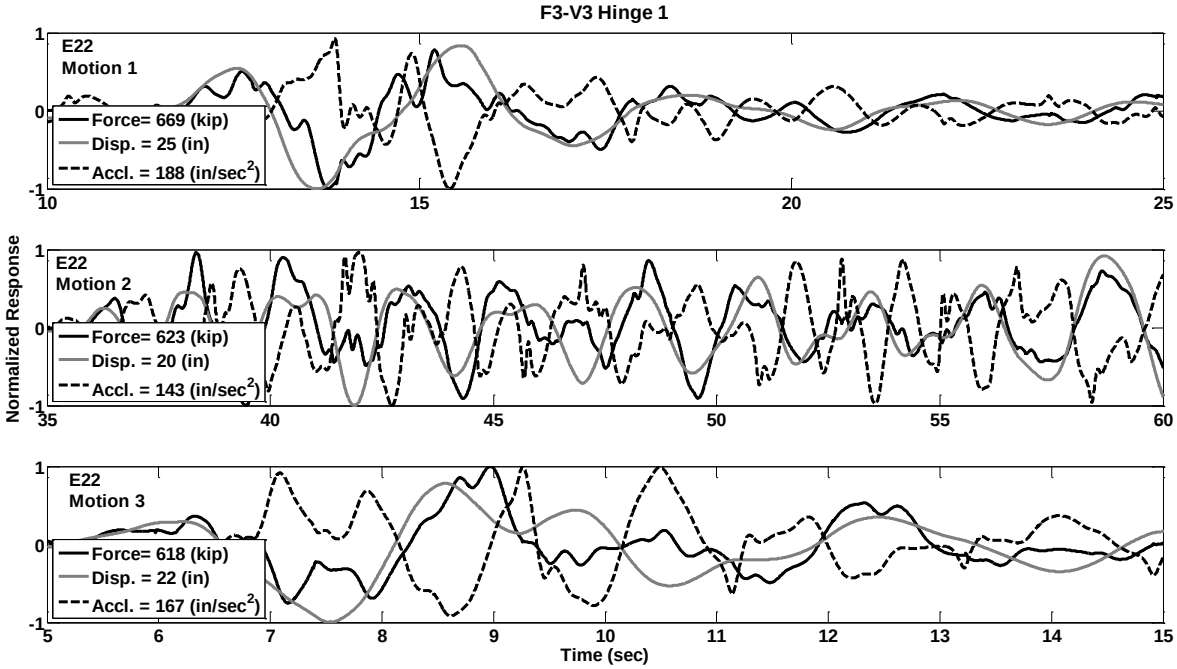

Figure C.97 Response Histories of Prototype F3-V3, Hinge 1, Motions E22

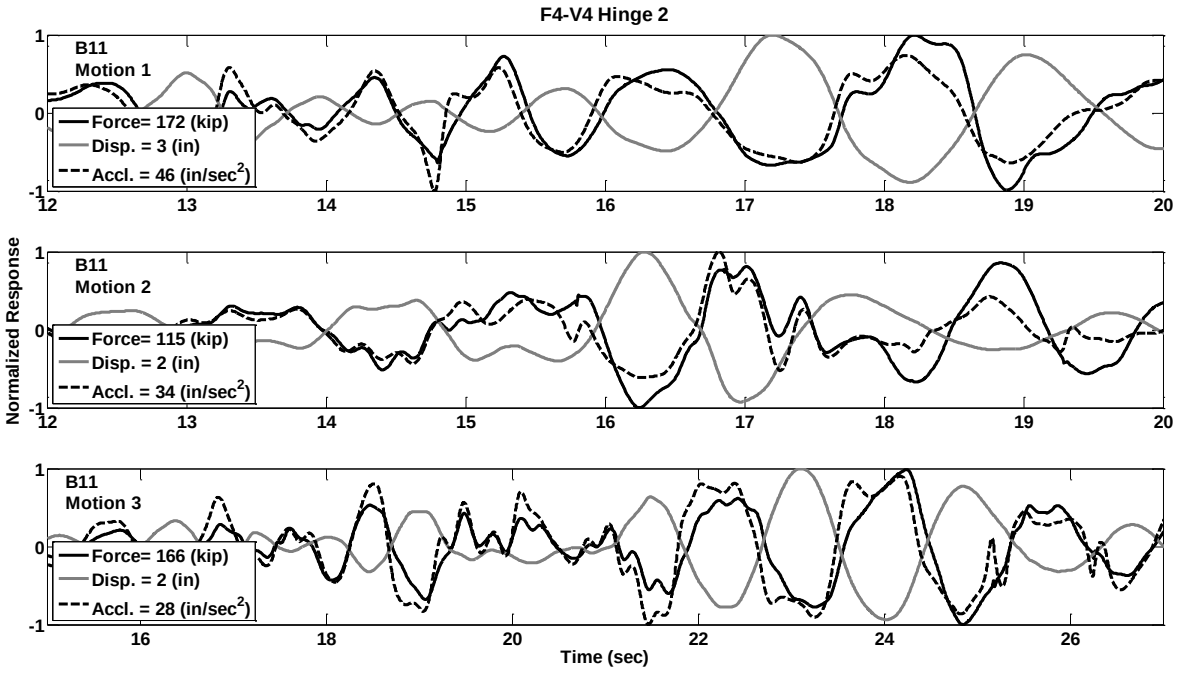

Figure C.98 Response Histories of Prototype F4-V4, Hinge 2, Motions B11

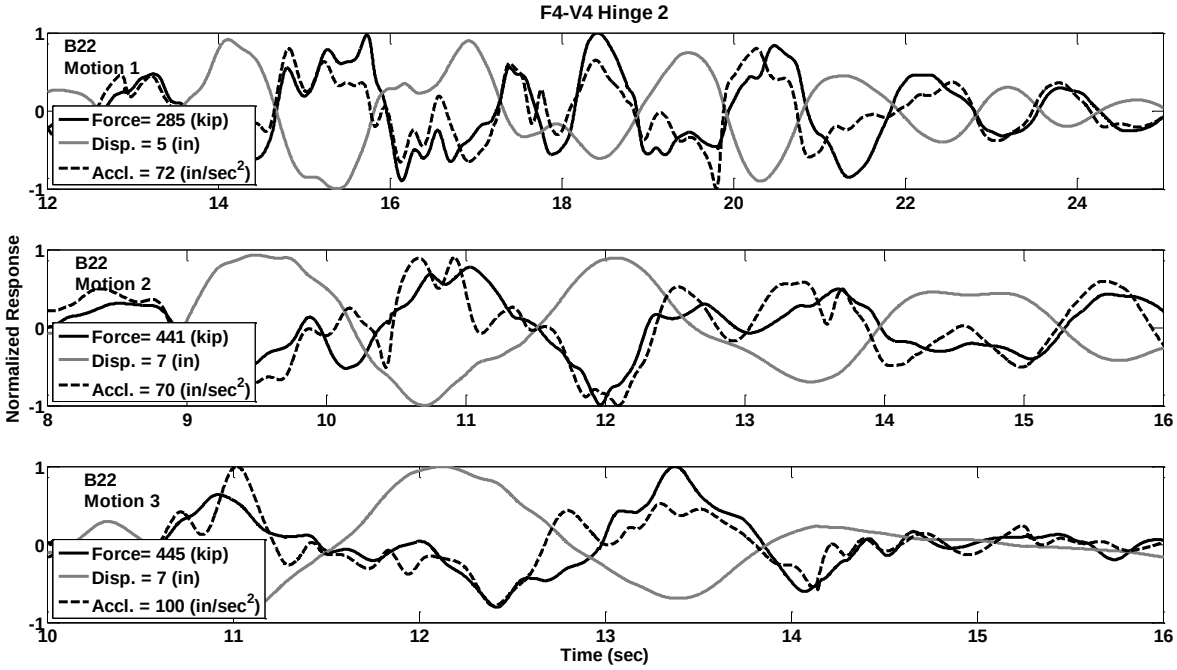

Figure C.99 Response Histories of Prototype F4-V4, Hinge 2, Motions B22

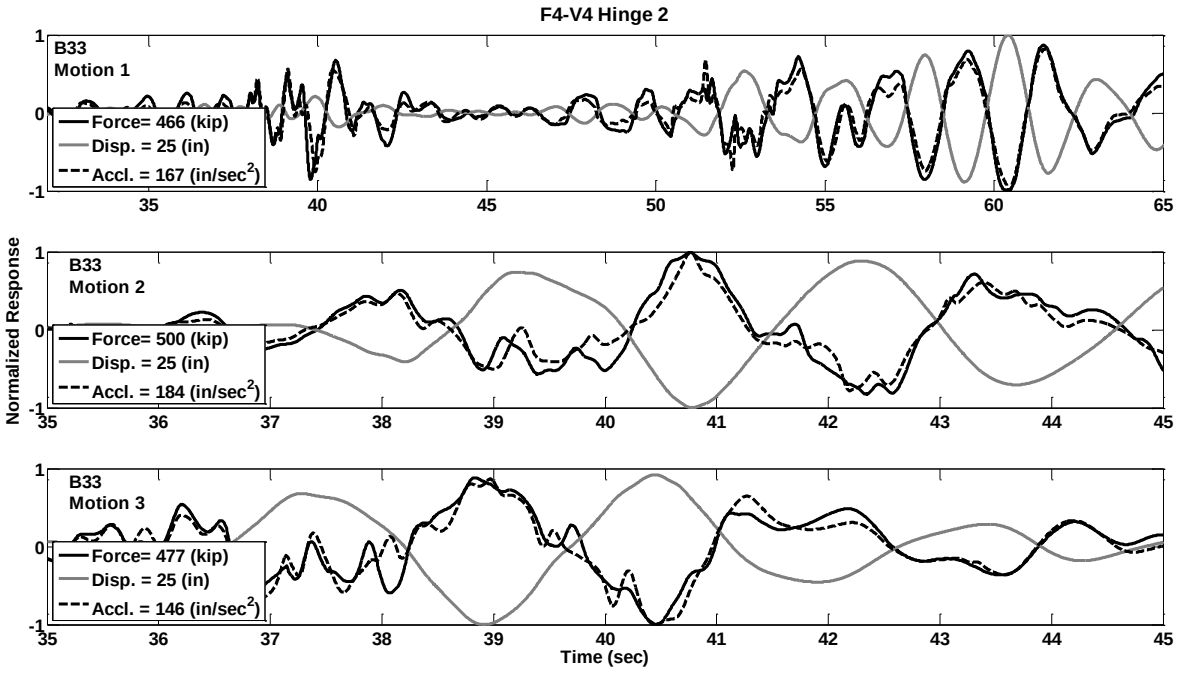

Figure C.100 Response Histories of Prototype F4-V4, Hinge 2, Motions B33

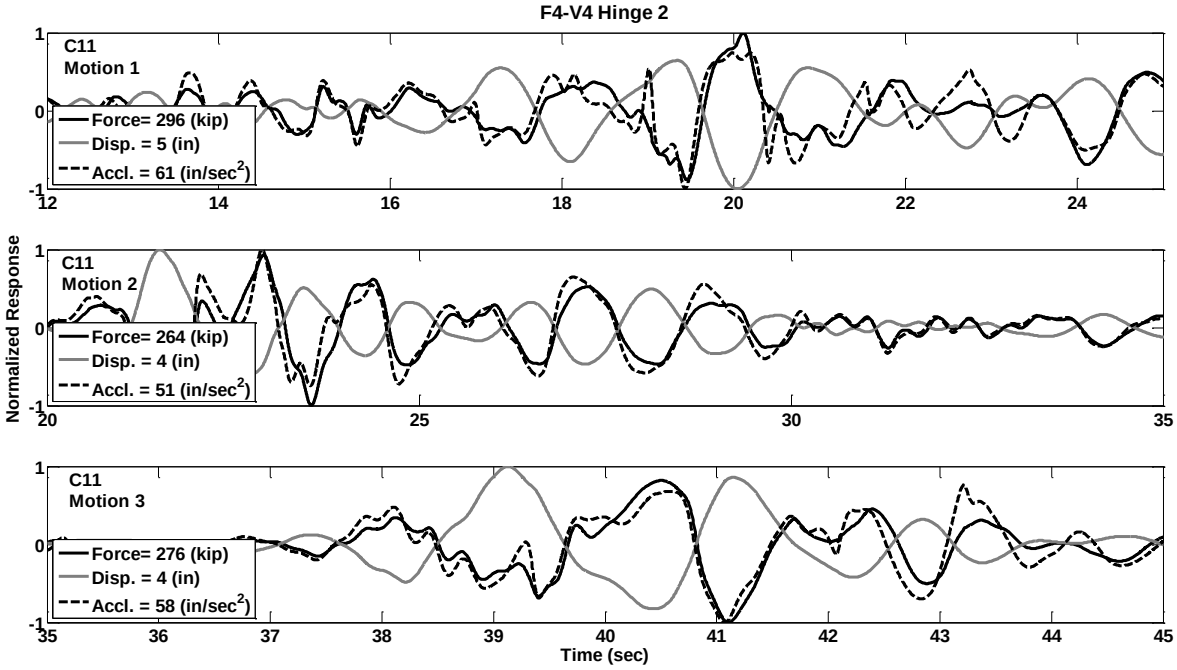

Figure C.101 Response Histories of Prototype F4-V4, Hinge 2, Motions C11

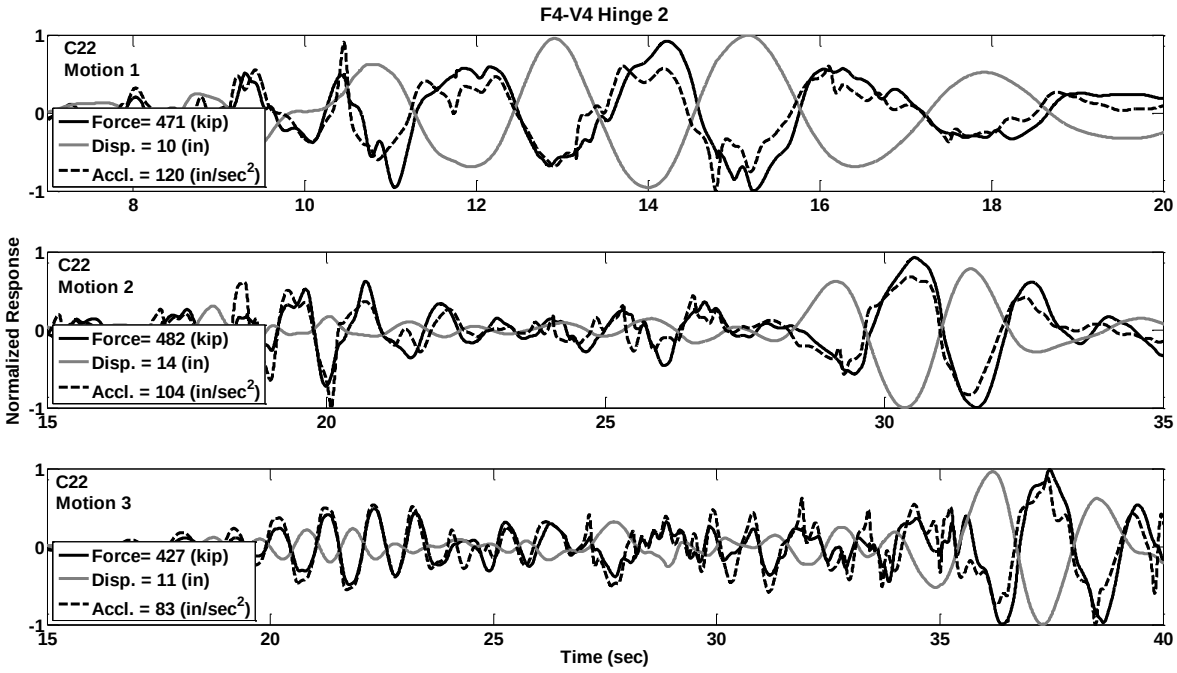

Figure C.102 Response Histories of Prototype F4-V4, Hinge 2, Motions C22

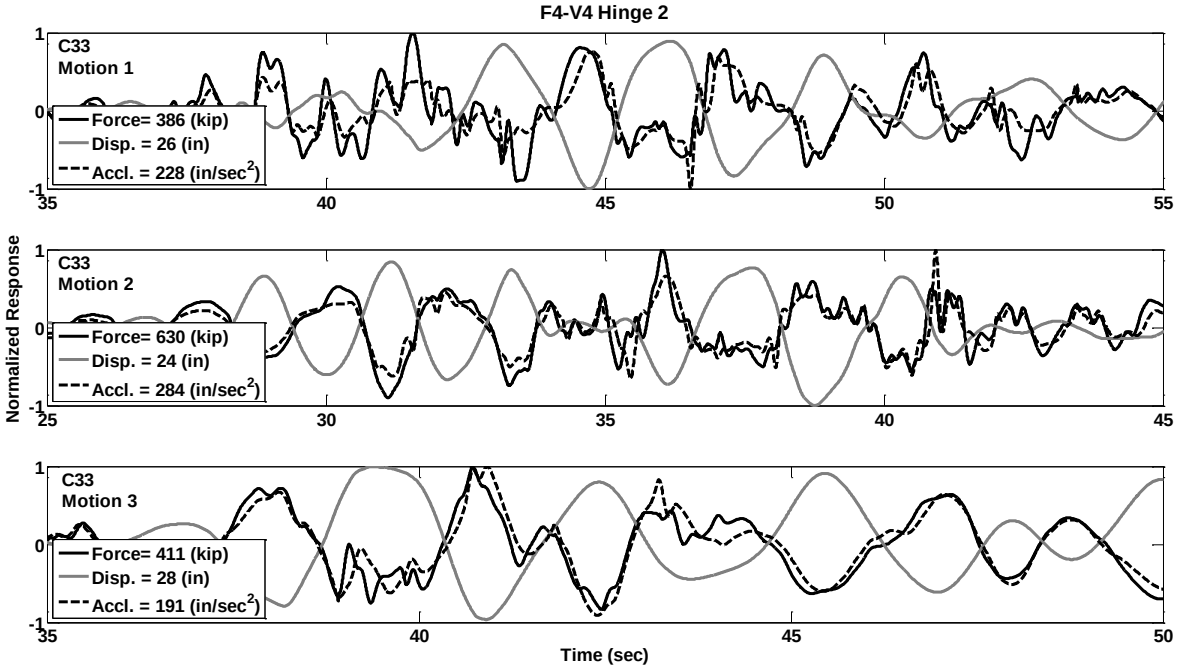

Figure C.103 Response Histories of Prototype F4-V4, Hinge 2, Motions C33

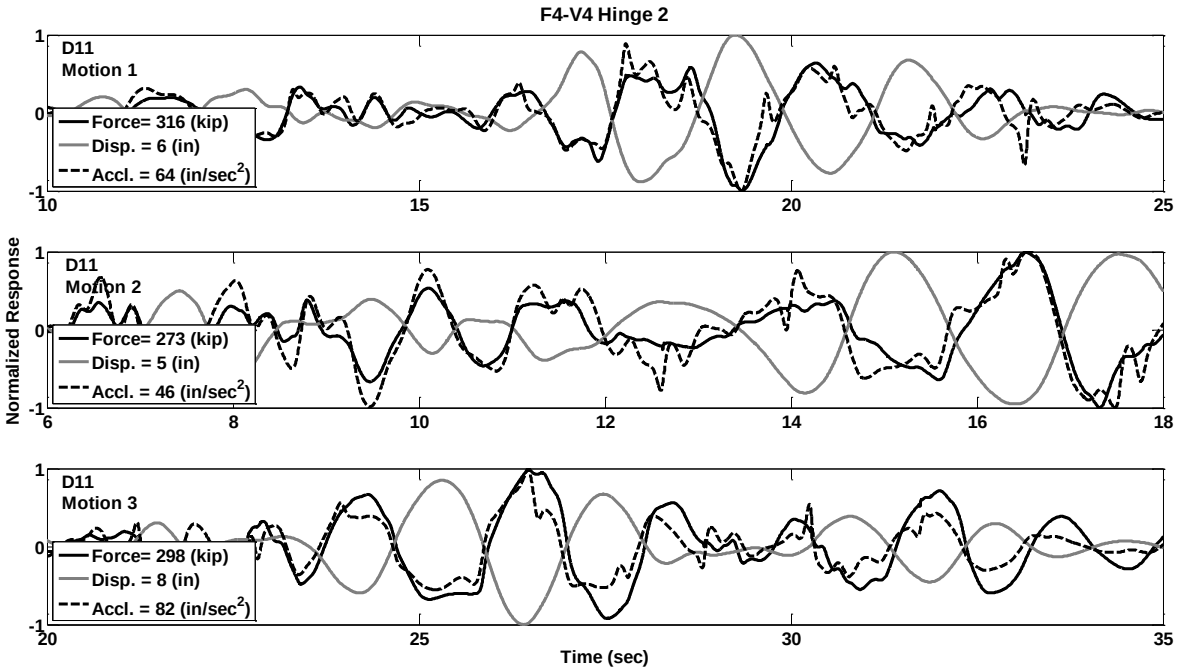

Figure C.104 Response Histories of Prototype F4-V4, Hinge 2, Motions D11

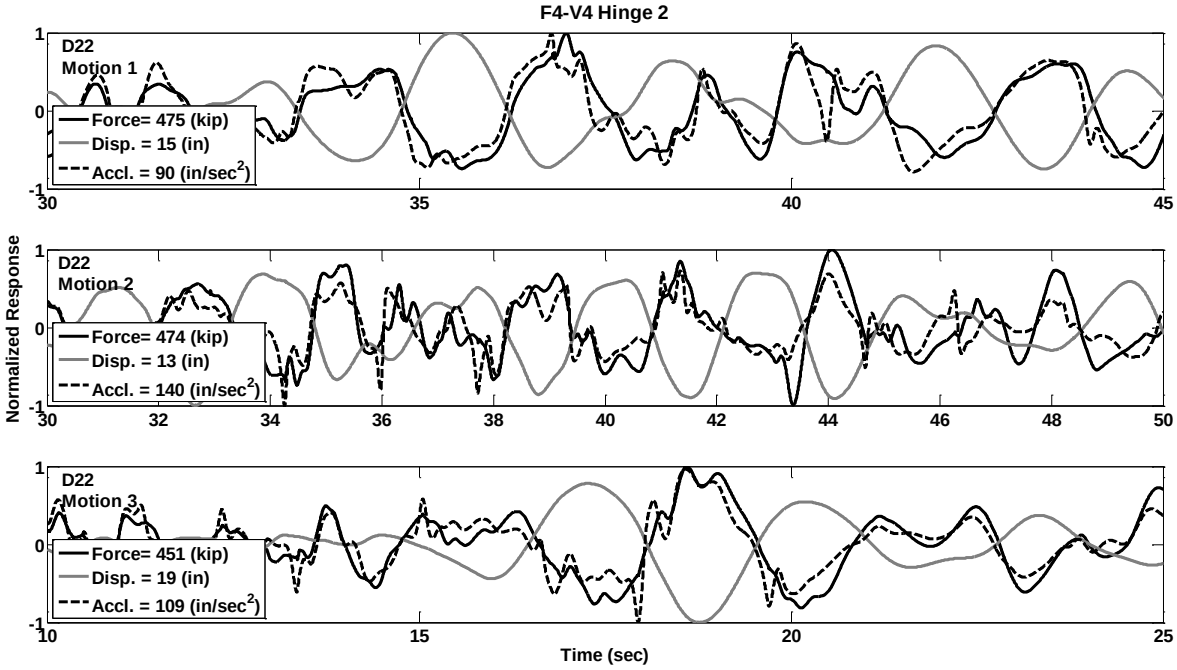

Figure C.105 Response Histories of Prototype F4-V4, Hinge 2, Motions D11

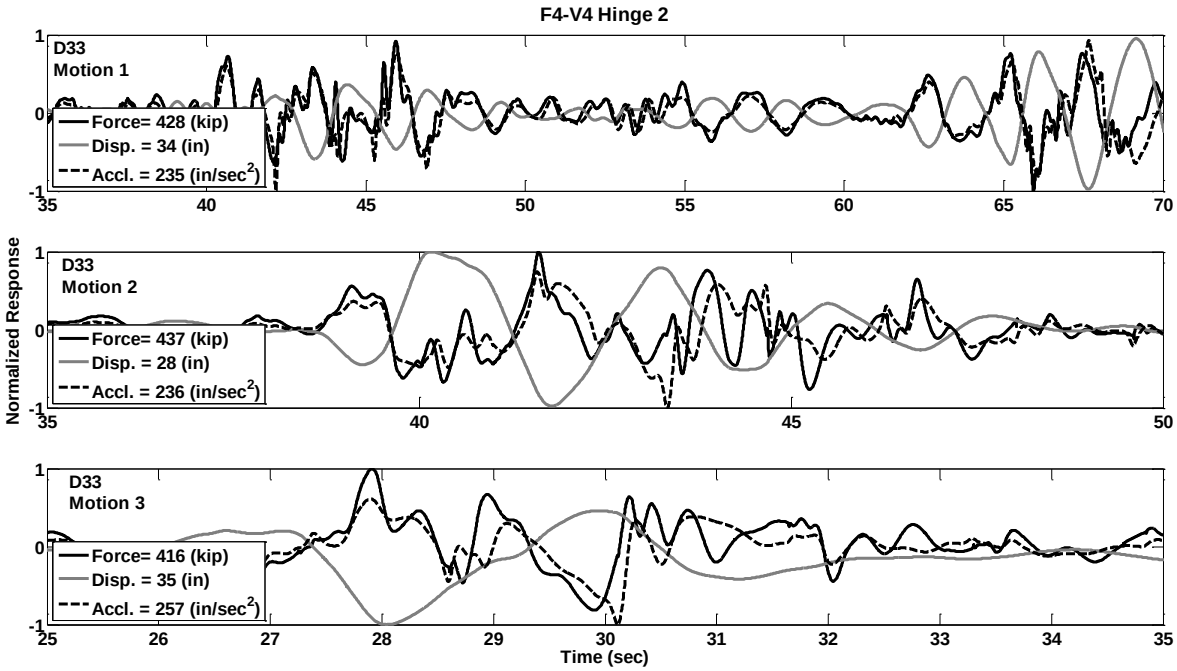

Figure C.106 Response Histories of Prototype F4-V4, Hinge 2, Motions D33

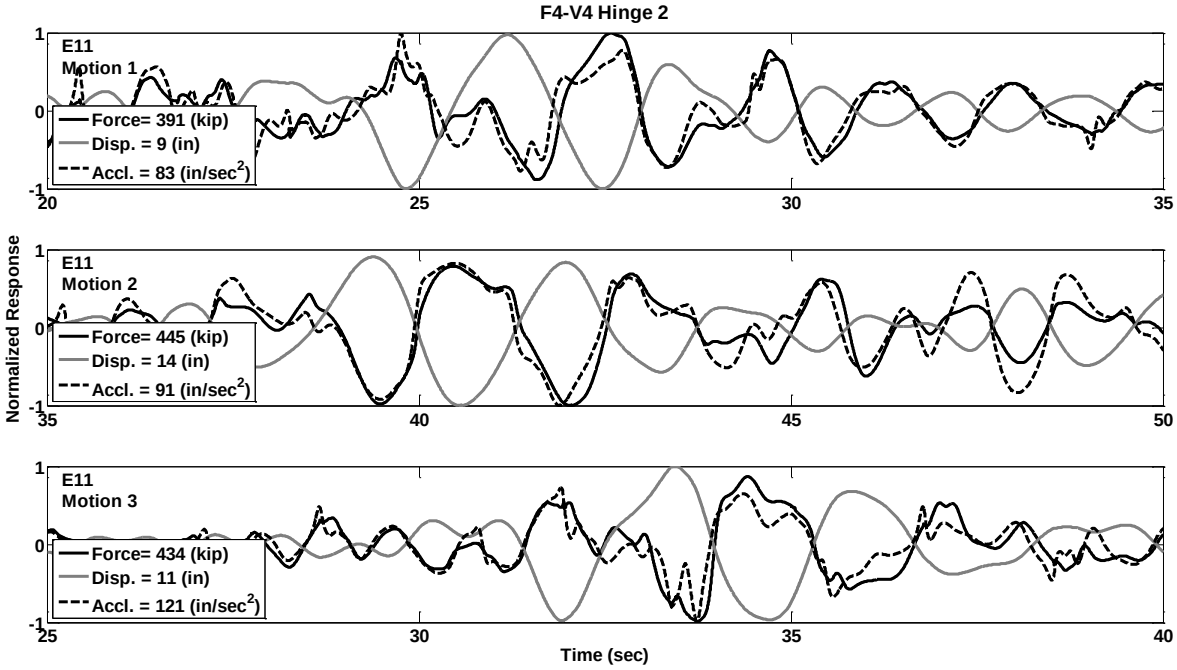

Figure C.107 Response Histories of Prototype F4-V4, Hinge 2, Motions E11

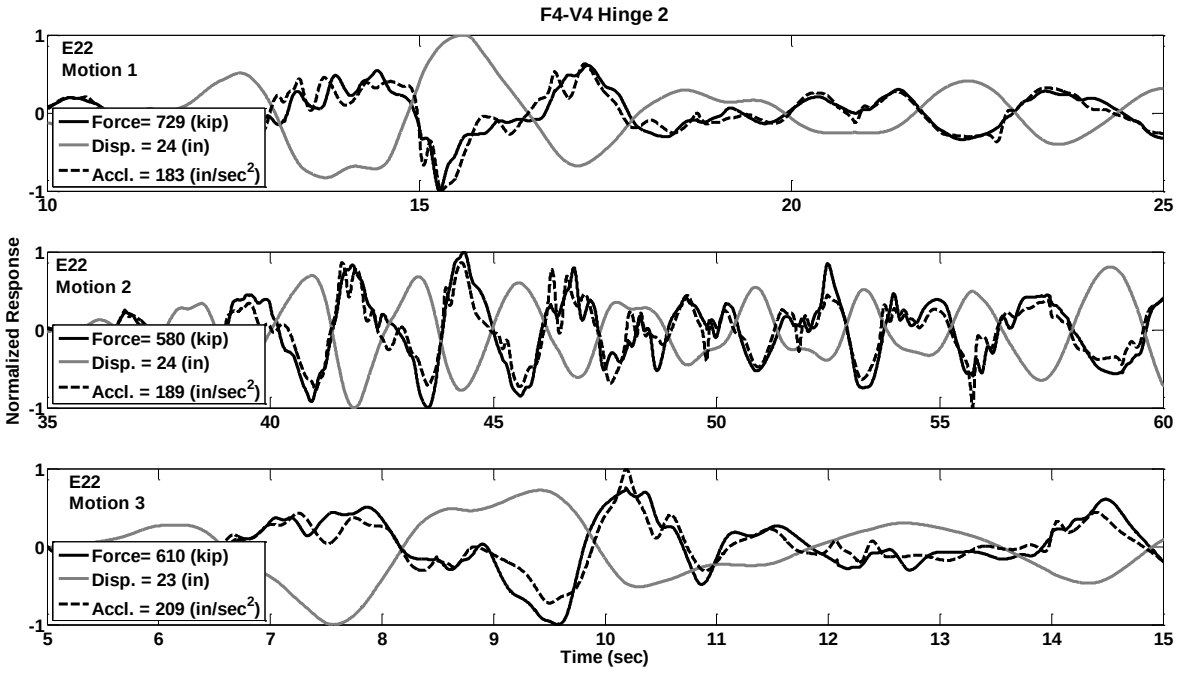

Figure C.108 Response Histories of Prototype F4-V4, Hinge 2, Motions E22

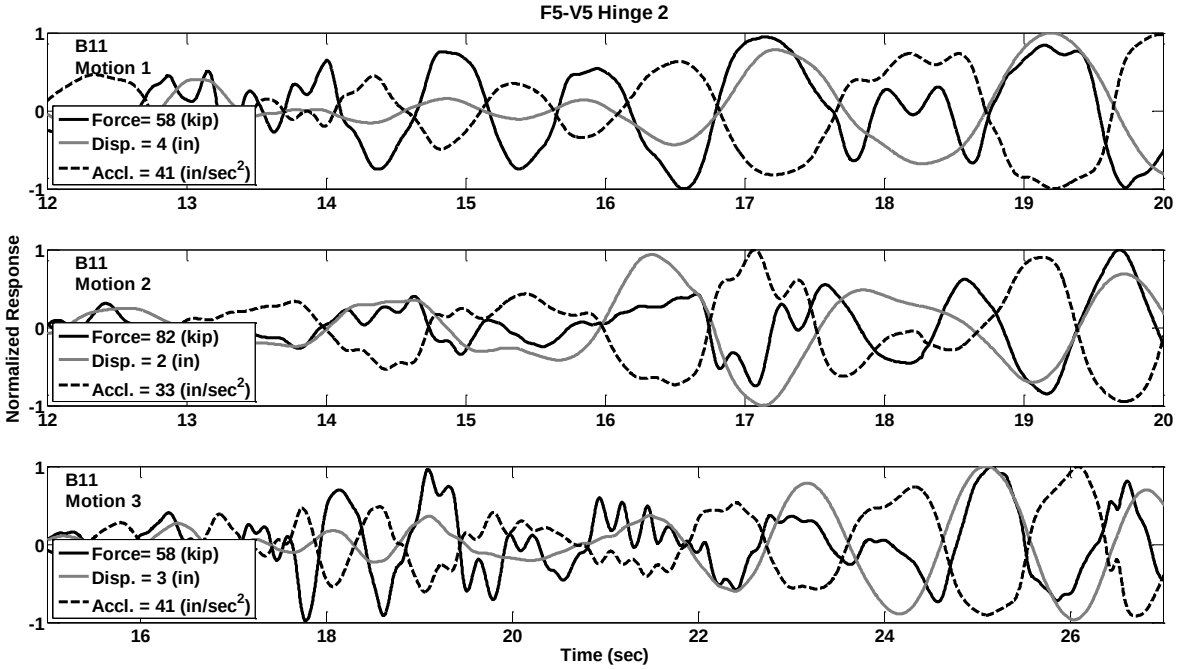

Figure C.109 Response Histories of Prototype F5-V5, Hinge 2, Motions B11

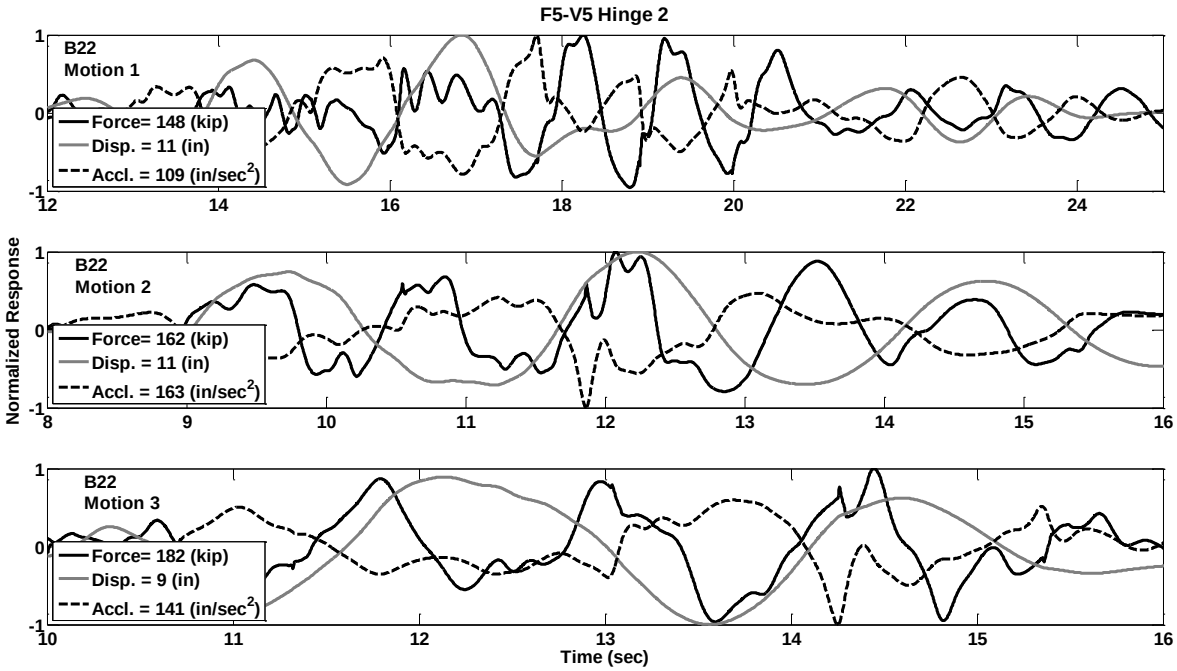

Figure C.110 Response Histories of Prototype F5-V5, Hinge 2, Motions B22

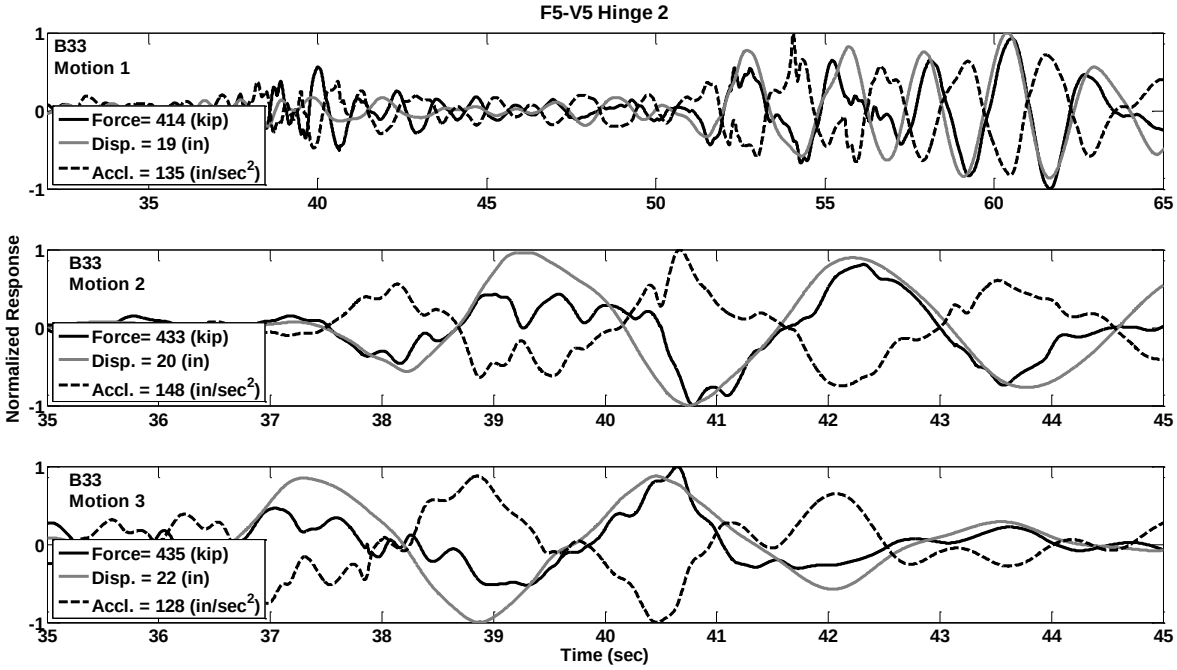

Figure C.111 Response Histories of Prototype F5-V5, Hinge 2, Motions B33

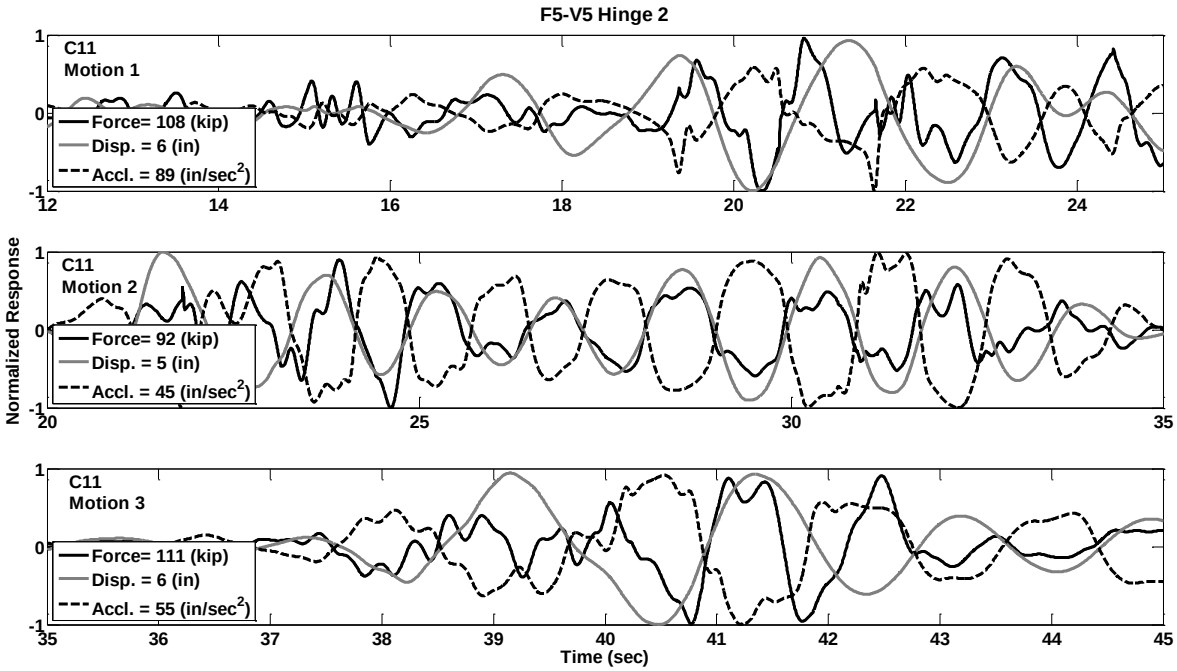

Figure C.112 Response Histories of Prototype F5-V5, Hinge 2, Motions C11

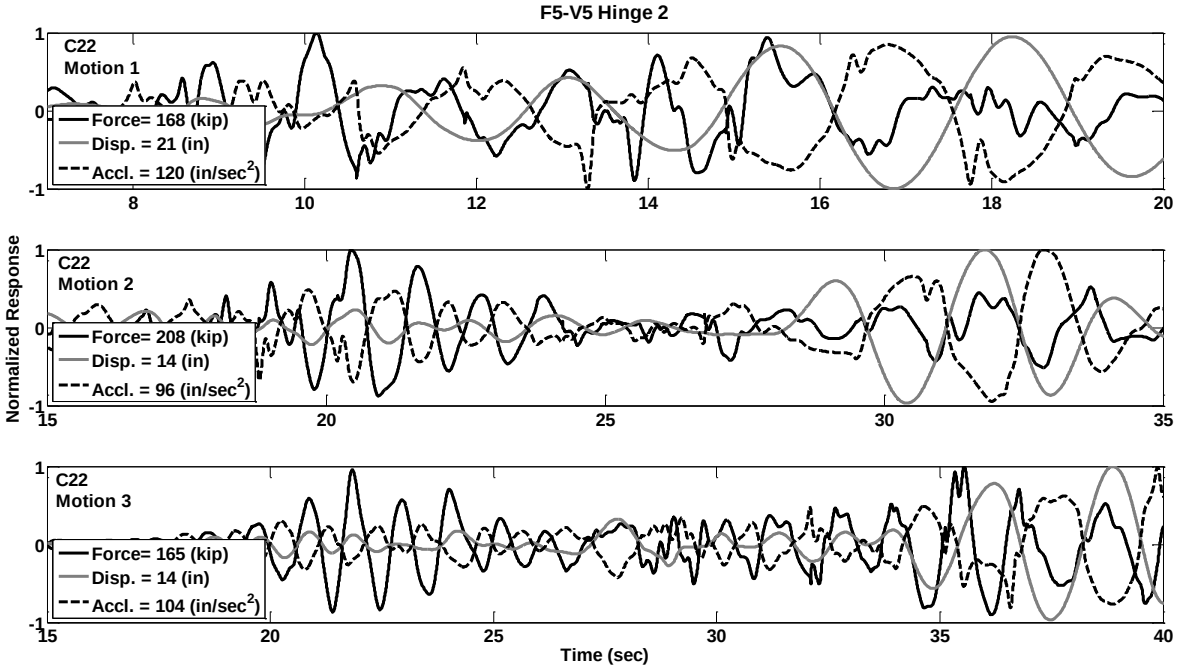

Figure C.113 Response Histories of Prototype F5-V5, Hinge 2, Motions C22

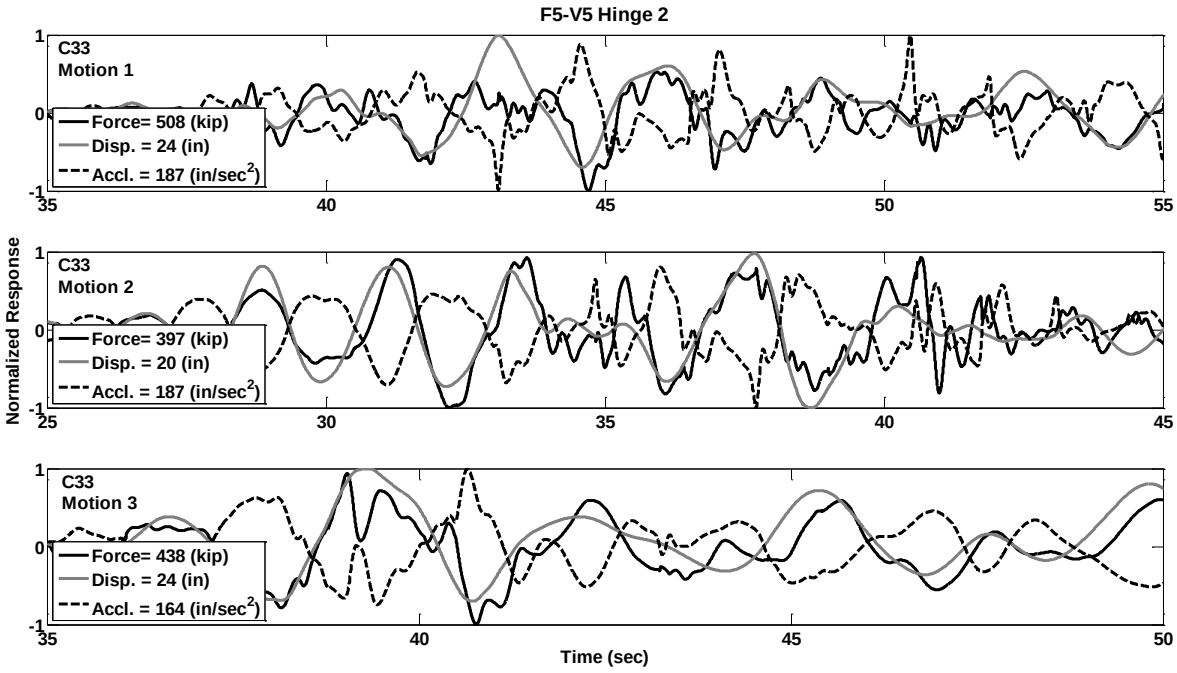

Figure C.114 Response Histories of Prototype F5-V5, Hinge 2, Motions C33

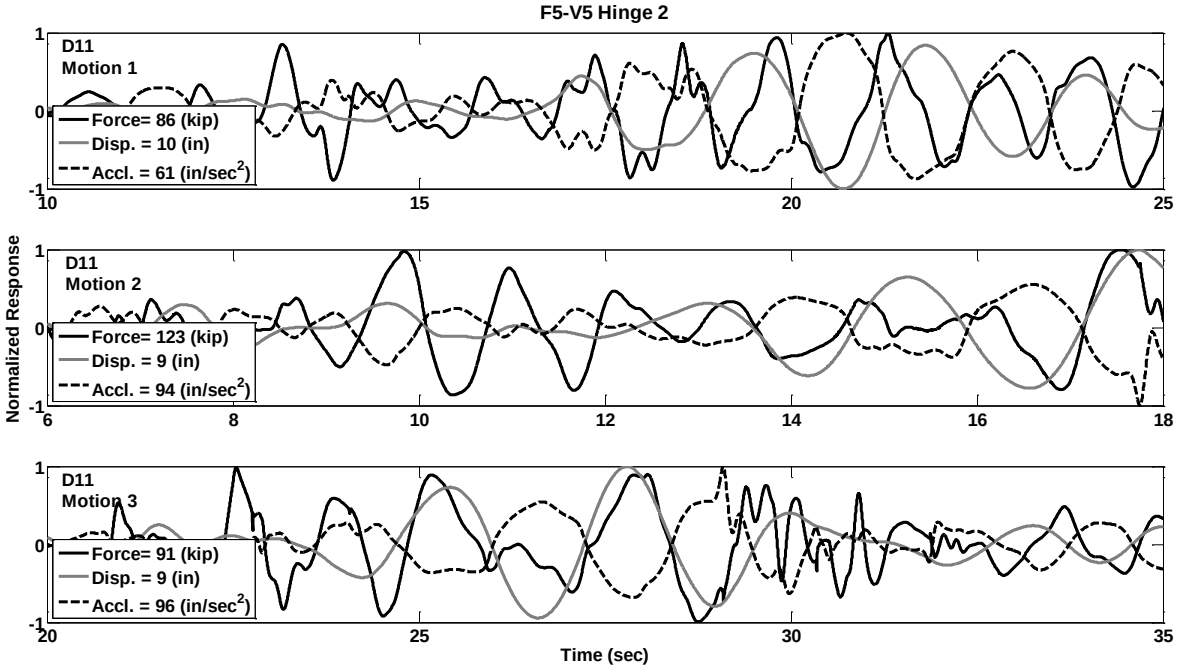

Figure C.115 Response Histories of Prototype F5-V5, Hinge 2, Motions D11

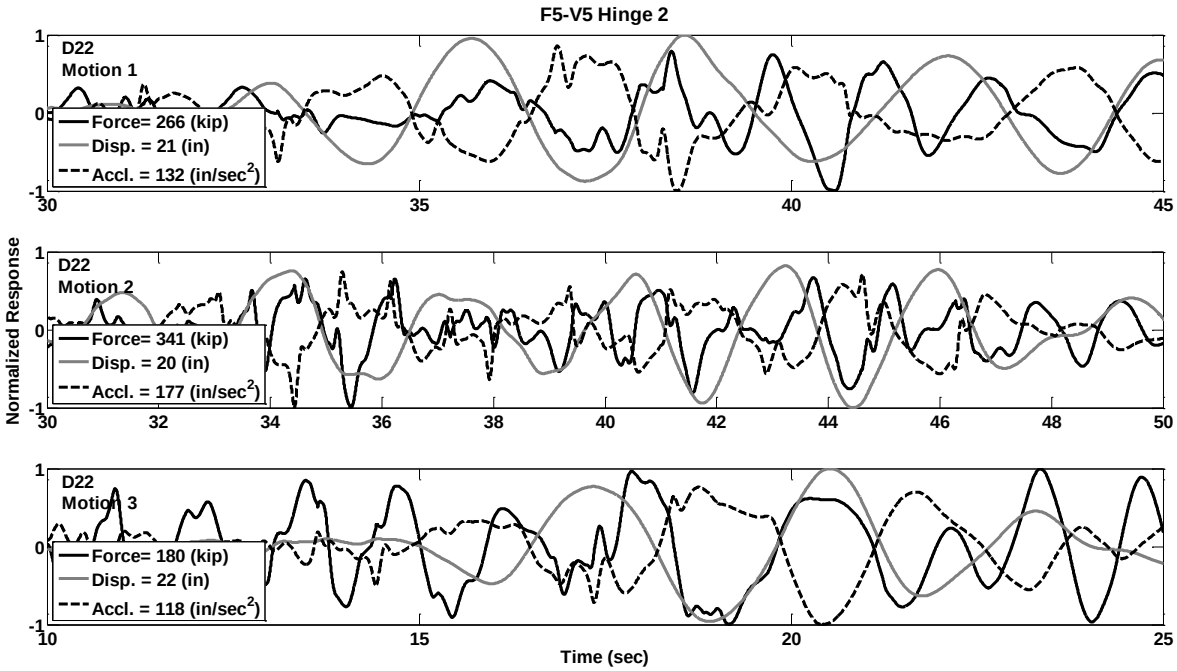

Figure C.116 Response Histories of Prototype F5-V5, Hinge 2, Motions D22

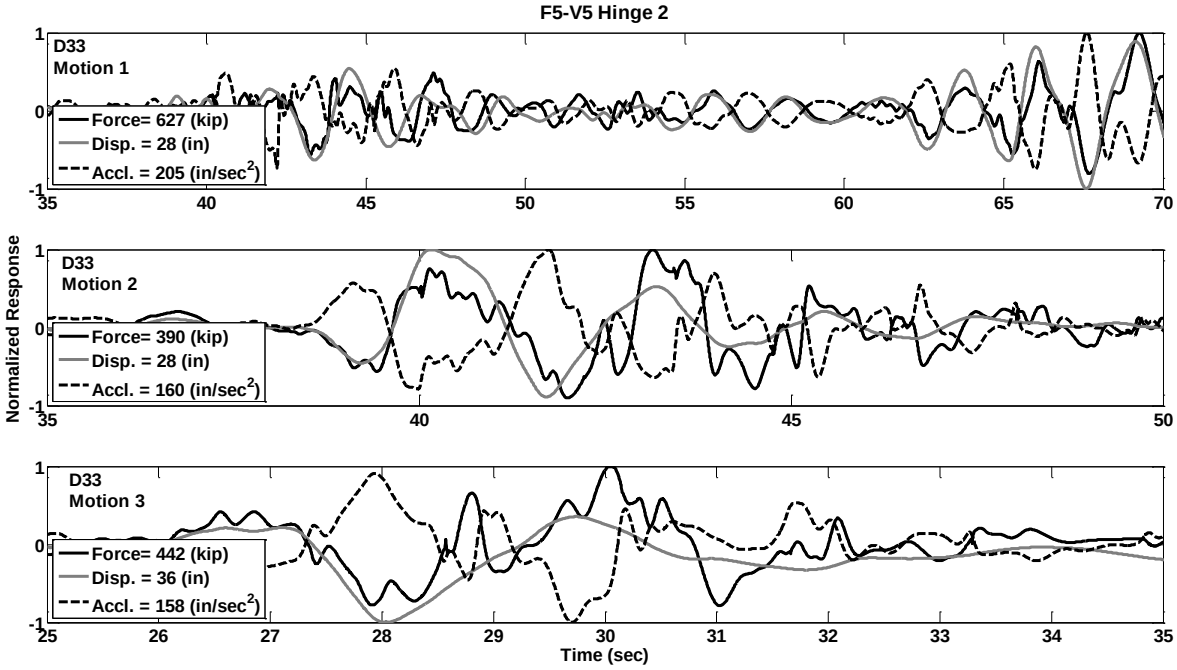

Figure C.117 Response Histories of Prototype F5-V5, Hinge 2, Motions D33

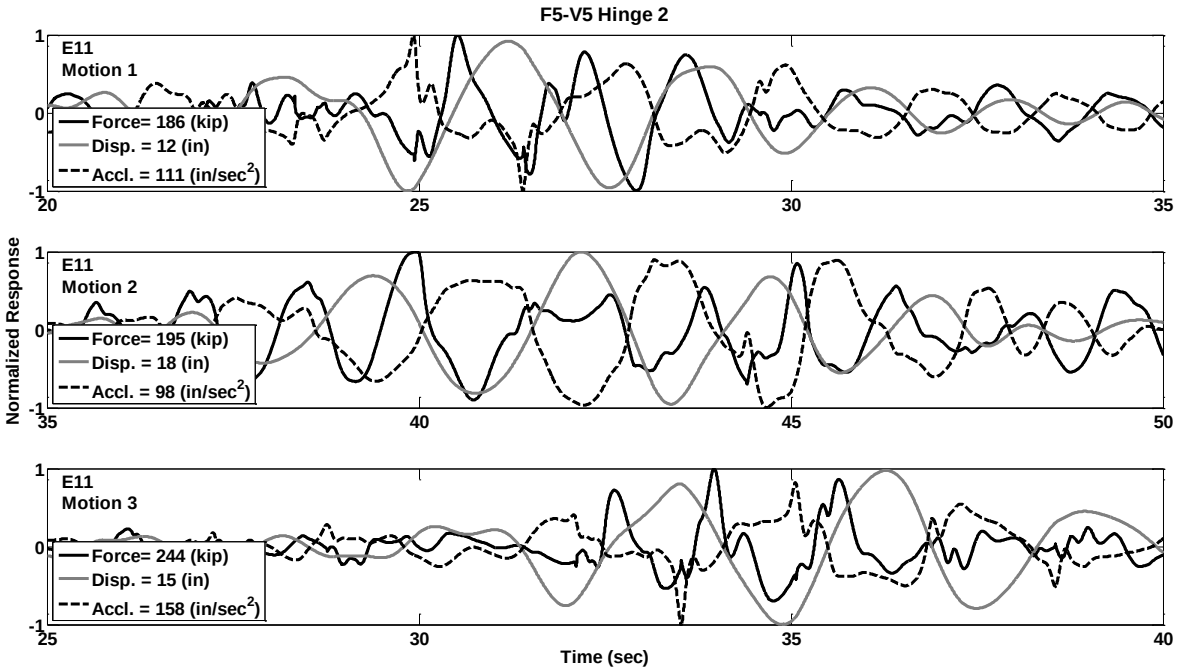

Figure C.118 Response Histories of Prototype F5-V5, Hinge 2, Motions E11

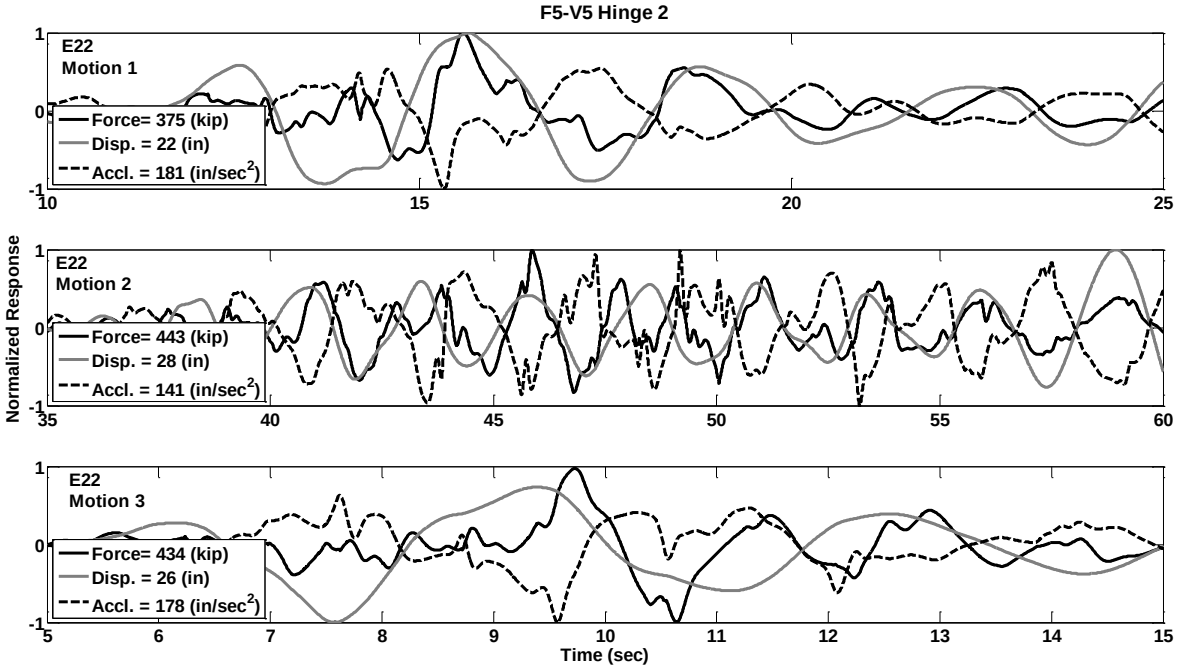

Figure C.119 Response Histories of Prototype F5-V5, Hinge 2, Motions E22

PART-2b: Two-Column Bent Prototypes
Time History of Shear Key Forces,
Time History of Transverse Displacement at Hinges, and
Time History of Transverse Acceleration at hinges.

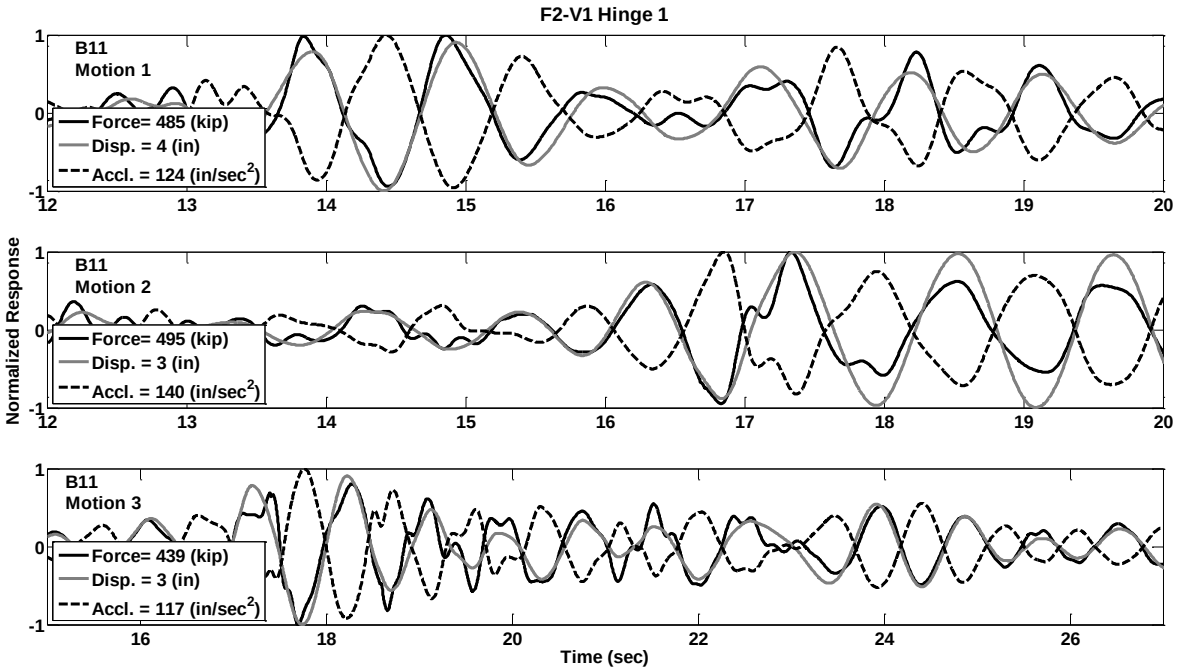

Figure C.120 Response Histories of Prototype F2-V1, Hinge 1, Motions B11

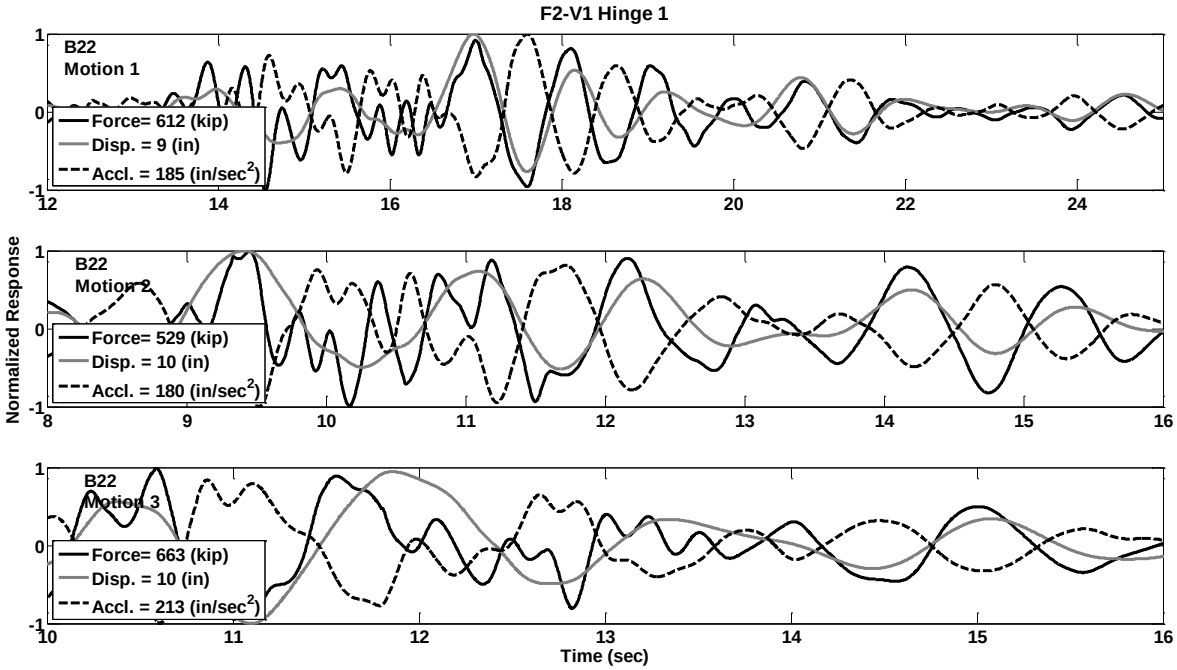

Figure C.121 Response Histories of Prototype F2-V1, Hinge 1, Motions B22

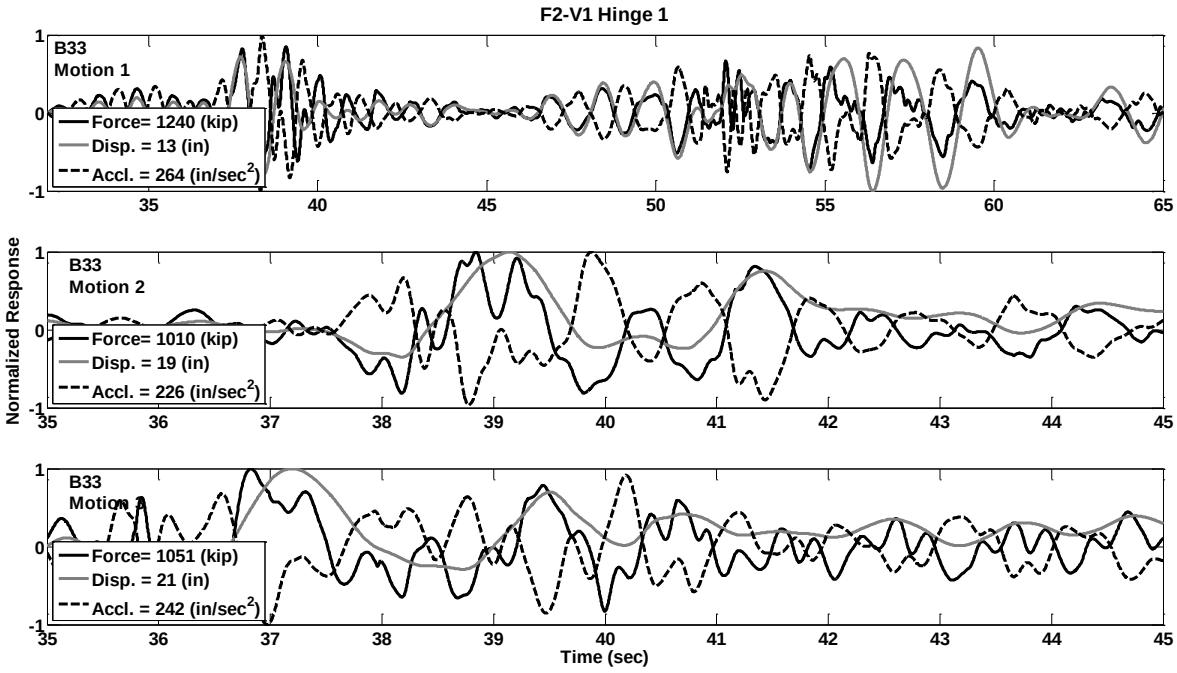

Figure C.122 Response Histories of Prototype F2-V1, Hinge 1, Motions B33

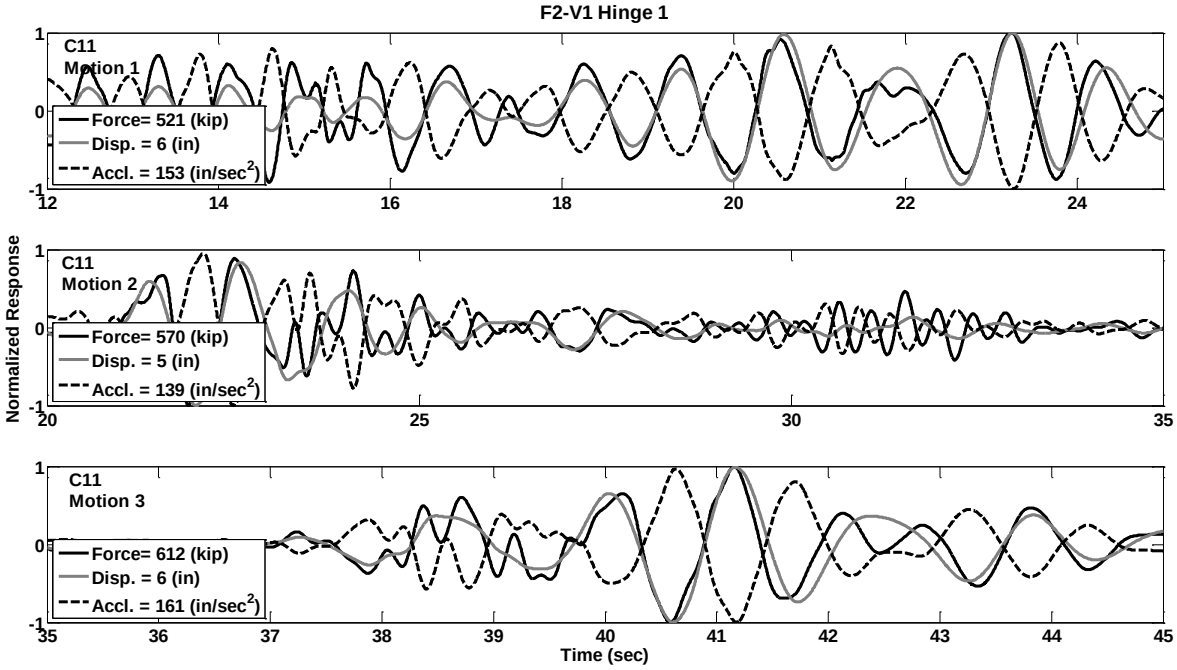

Figure C.123 Response Histories of Prototype F2-V1, Hinge 1, Motions C11

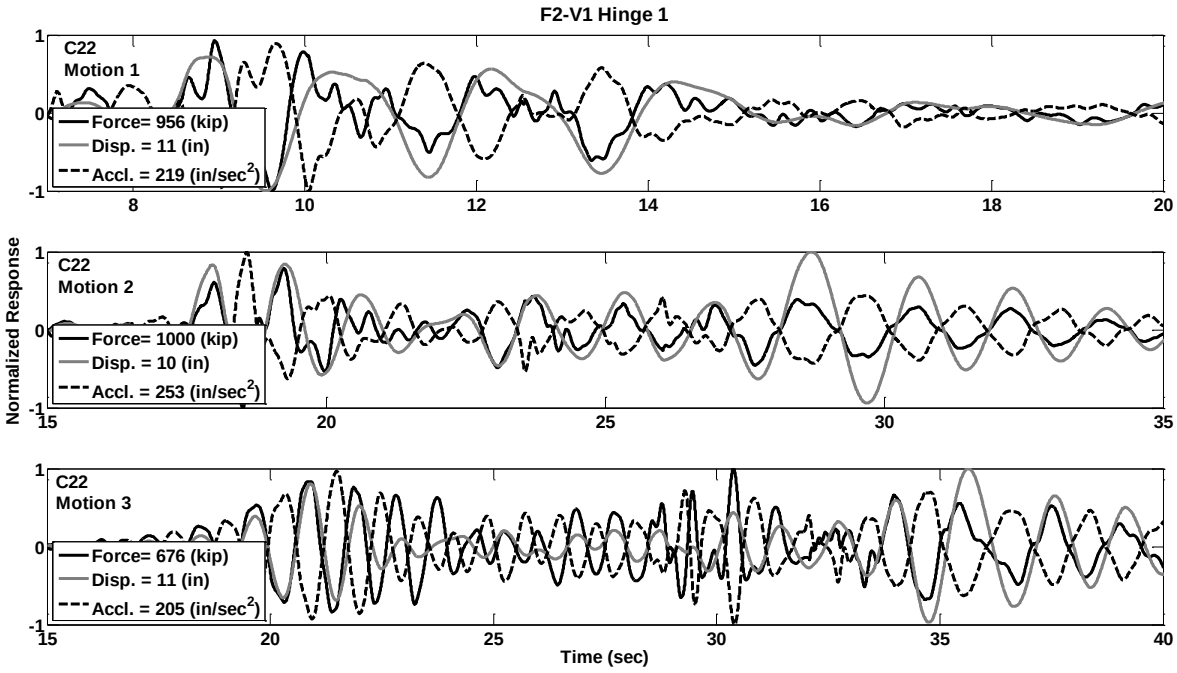

Figure C.124 Response Histories of Prototype F2-V1, Hinge 1, Motions C22

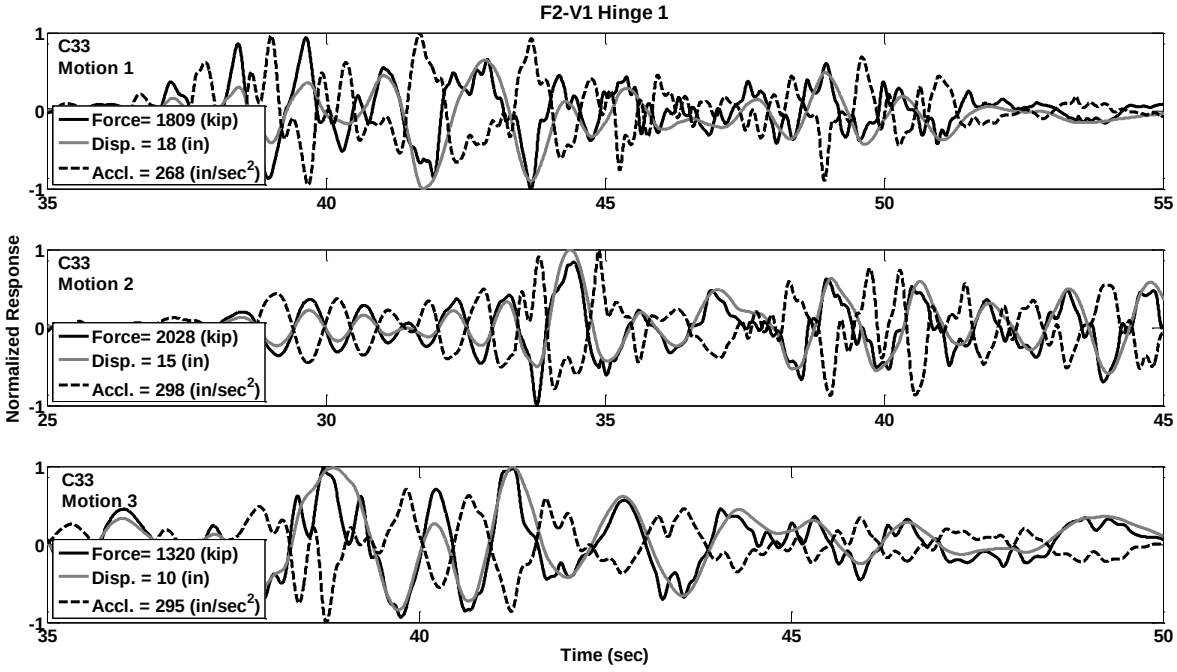

Figure C.125 Response Histories of Prototype F2-V1, Hinge 1, Motions C33

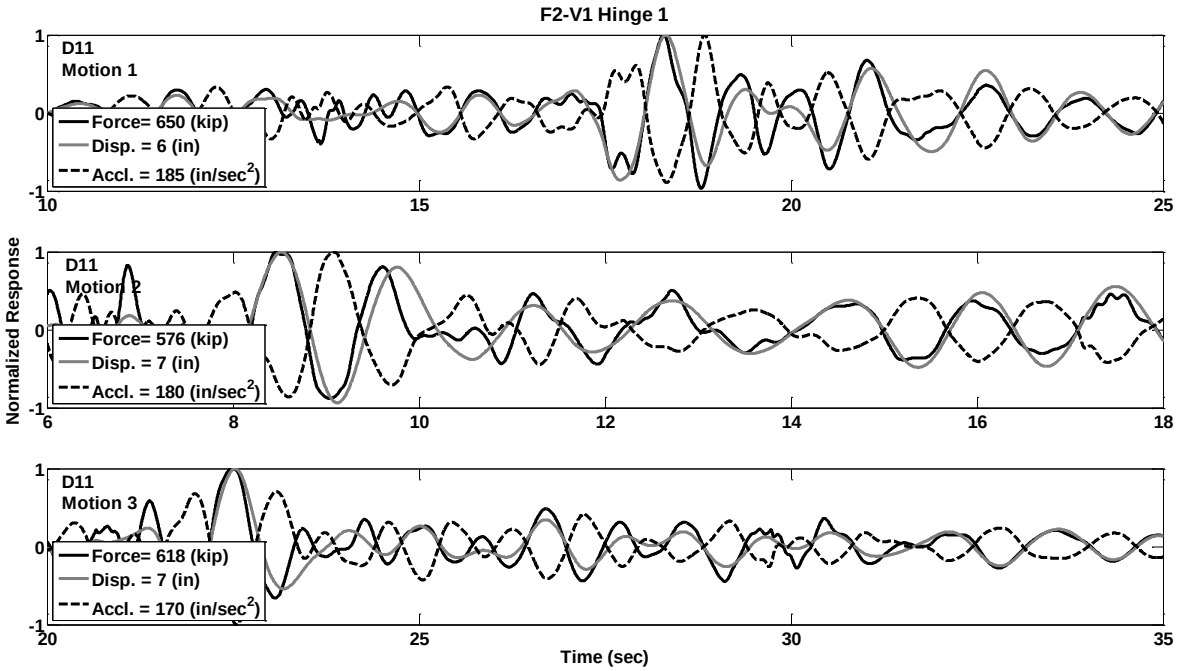

Figure C.126 Response Histories of Prototype F2-V1, Hinge 1, Motions D11

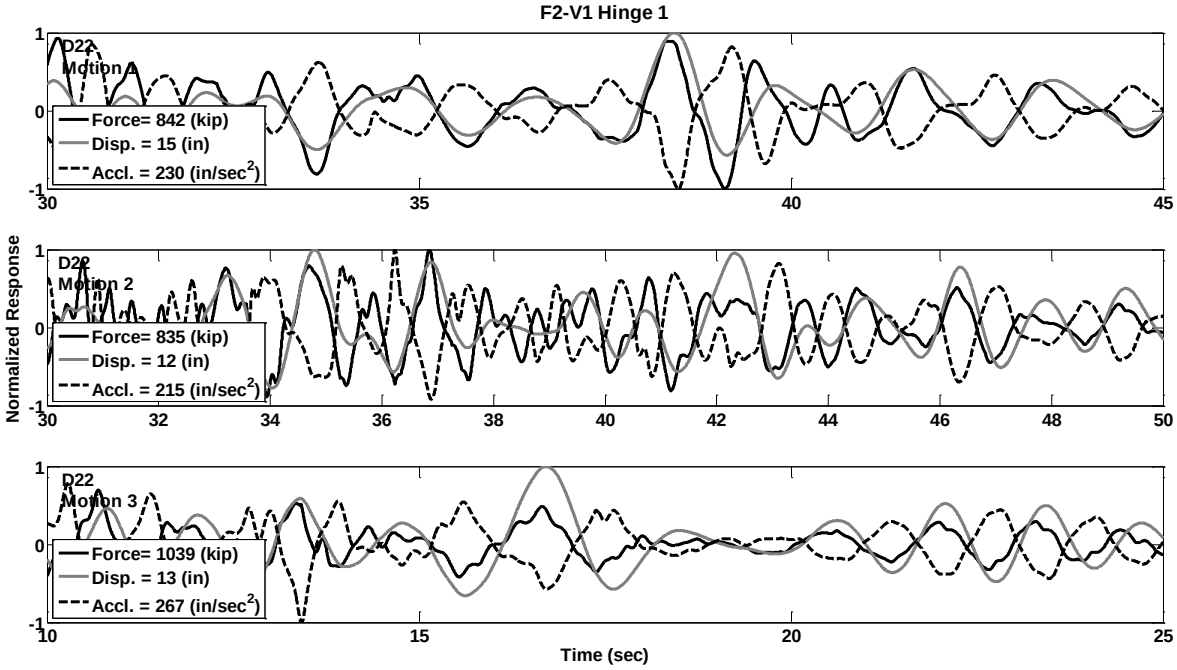

Figure C.127 Response Histories of Prototype F2-V1, Hinge 1, Motions D22

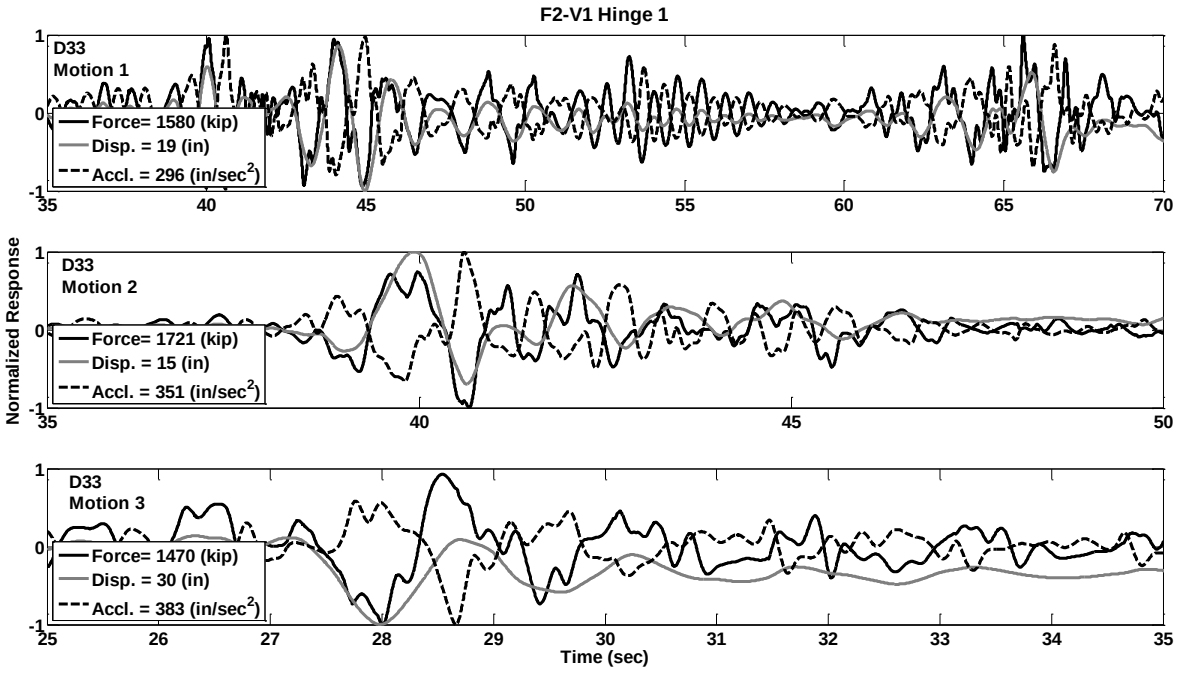

Figure C.128 Response Histories of Prototype F2-V1, Hinge 1, Motions D33

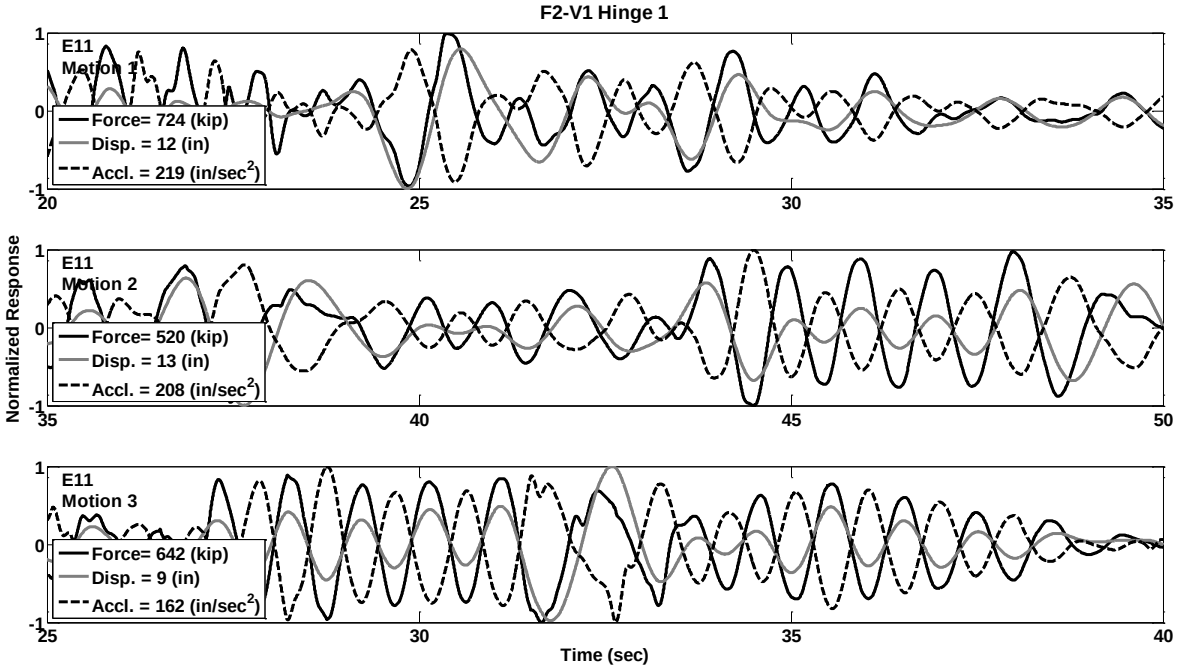

Figure C.129 Response Histories of Prototype F2-V1, Hinge 1, Motions E11

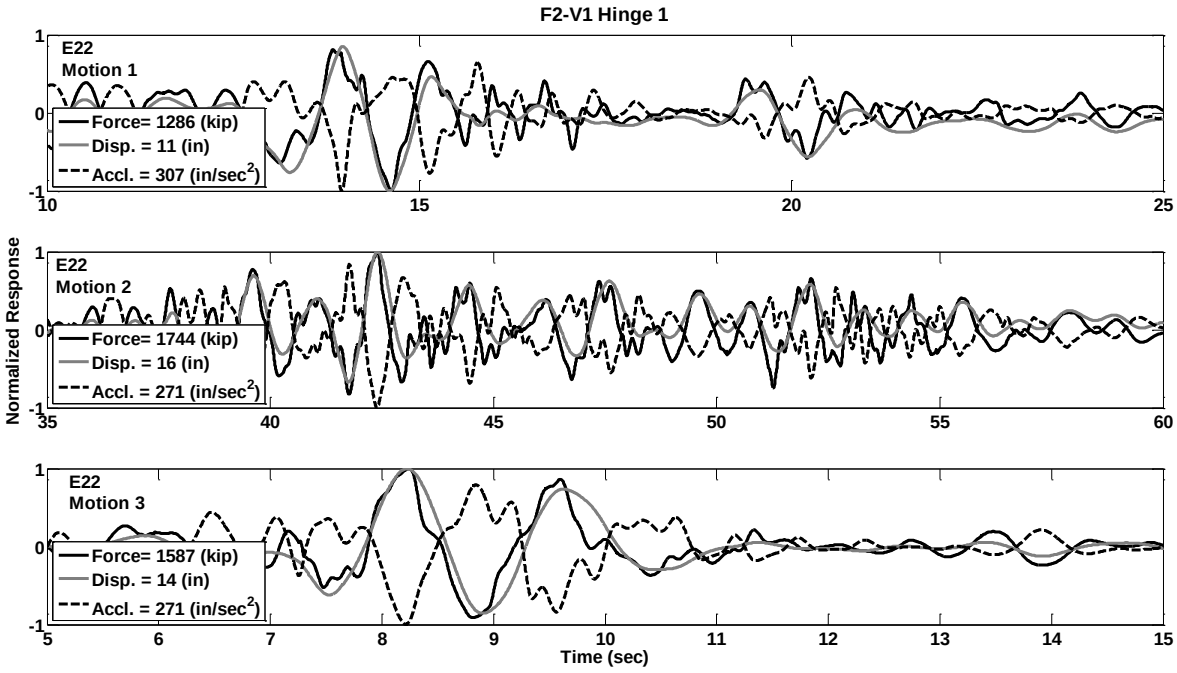

Figure C.130 Response Histories of Prototype F2-V1, Hinge 1, Motions E22

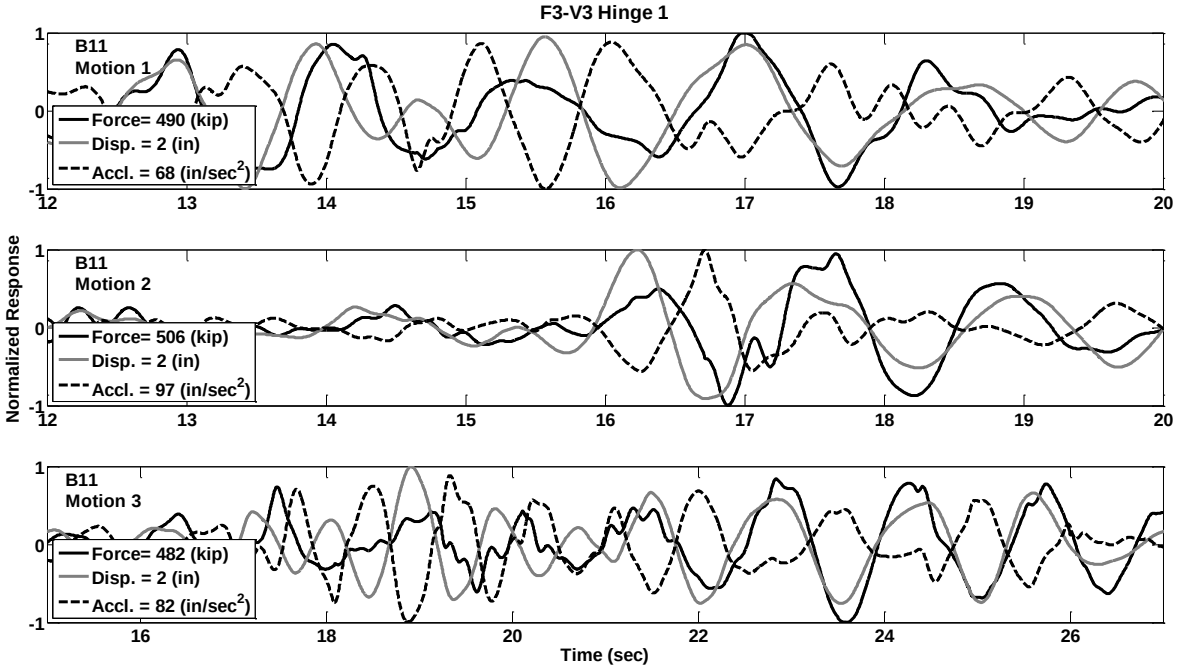

Figure C.131 Response Histories of Prototype F3-V3, Hinge 1, Motions B11

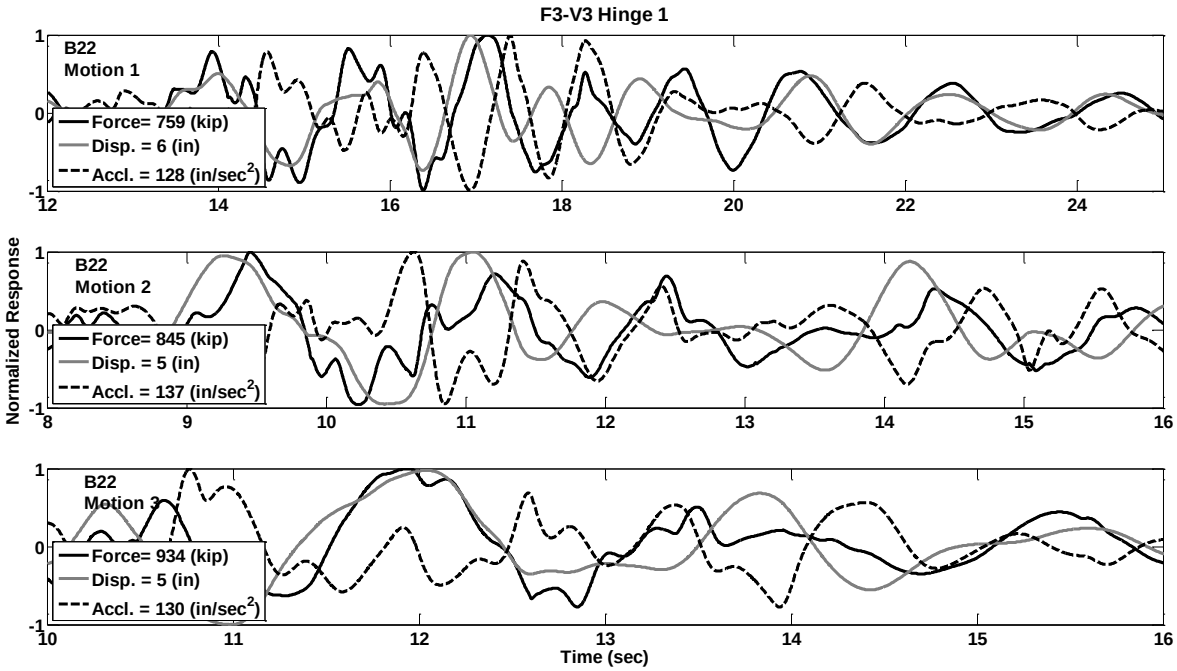

Figure C.132 Response Histories of Prototype F3-V3, Hinge 1, Motions B22

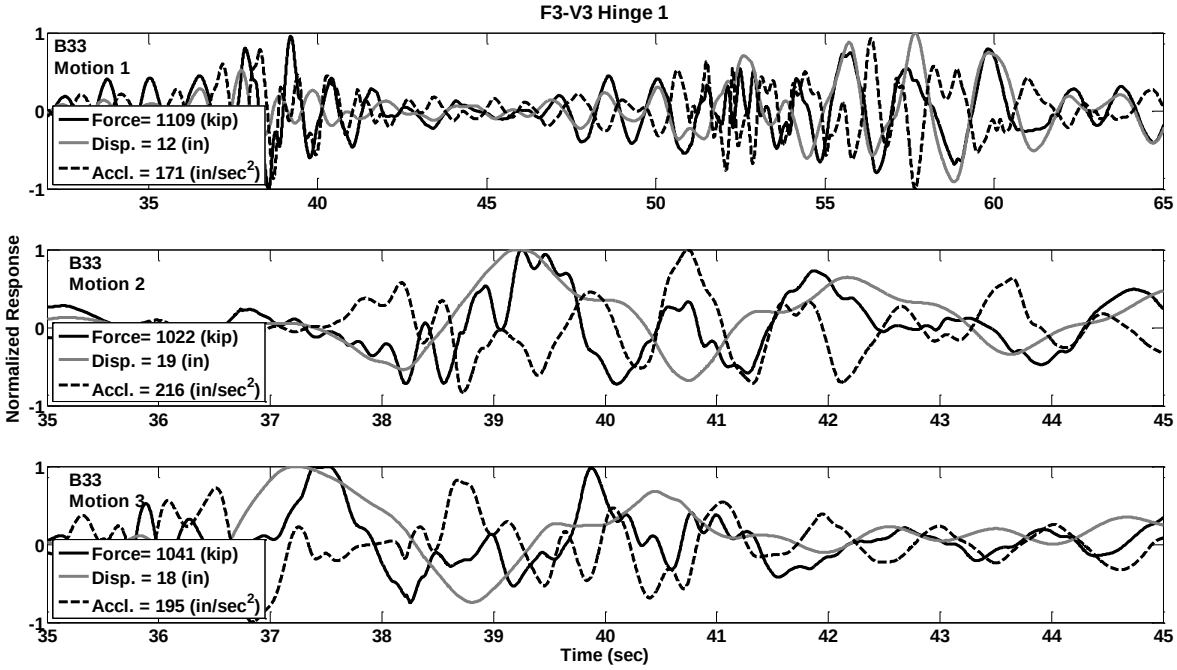

Figure C.133 Response Histories of Prototype F3-V3, Hinge 1, Motions B33

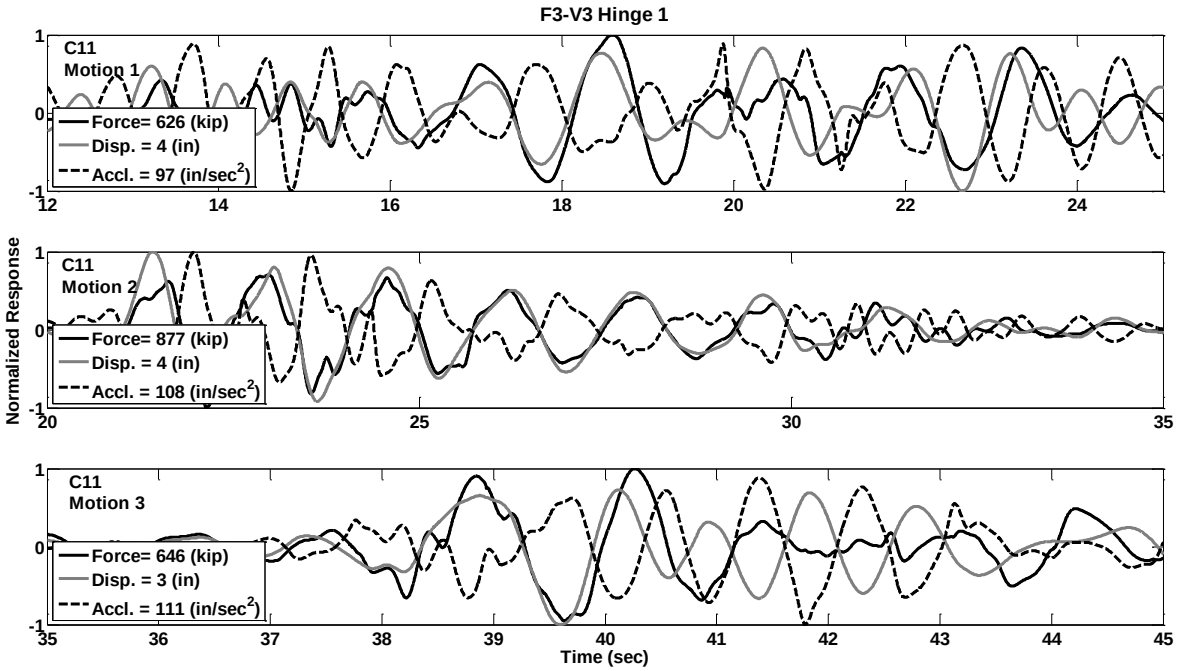

Figure C.134 Response Histories of Prototype F3-V3, Hinge 1, Motions C11

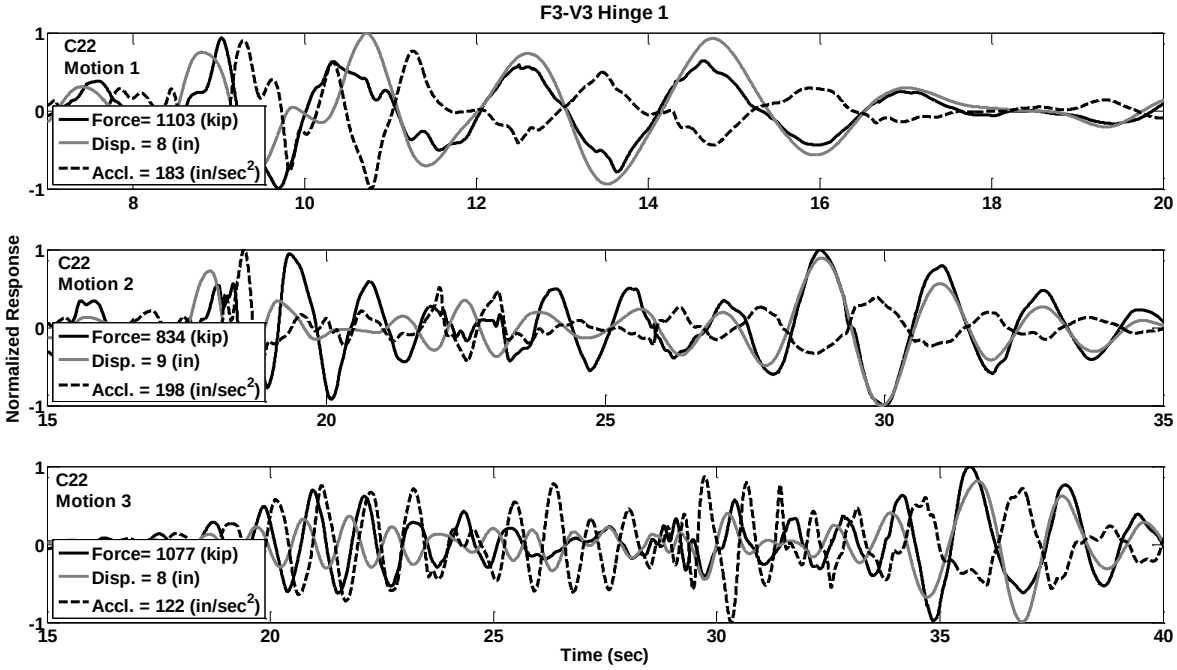

Figure C.135 Response Histories of Prototype F3-V3, Hinge 1, Motions C22

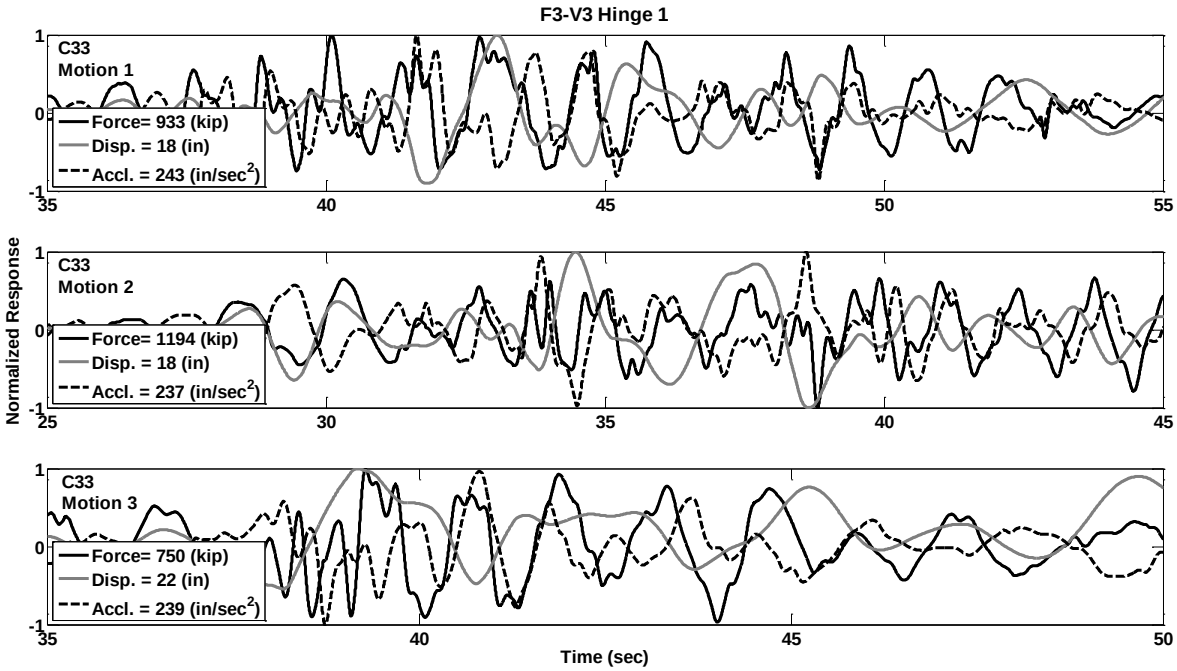

Figure C.136 Response Histories of Prototype F3-V3, Hinge 1, Motions C33

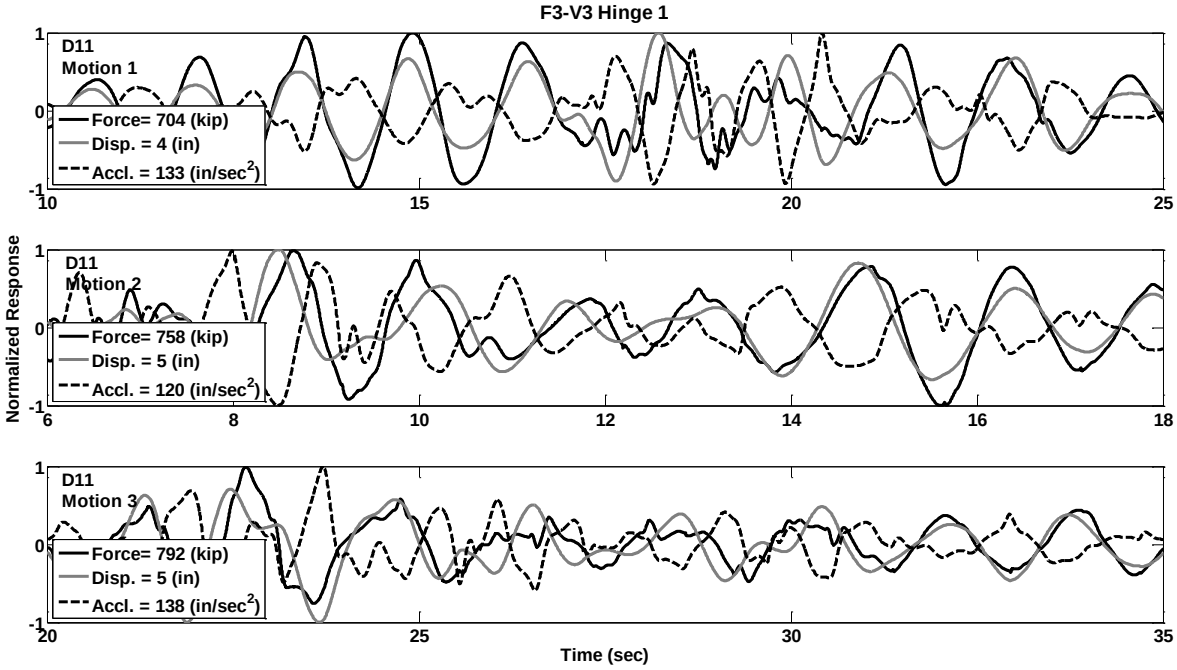

Figure C.137 Response Histories of Prototype F3-V3, Hinge 1, Motions D11

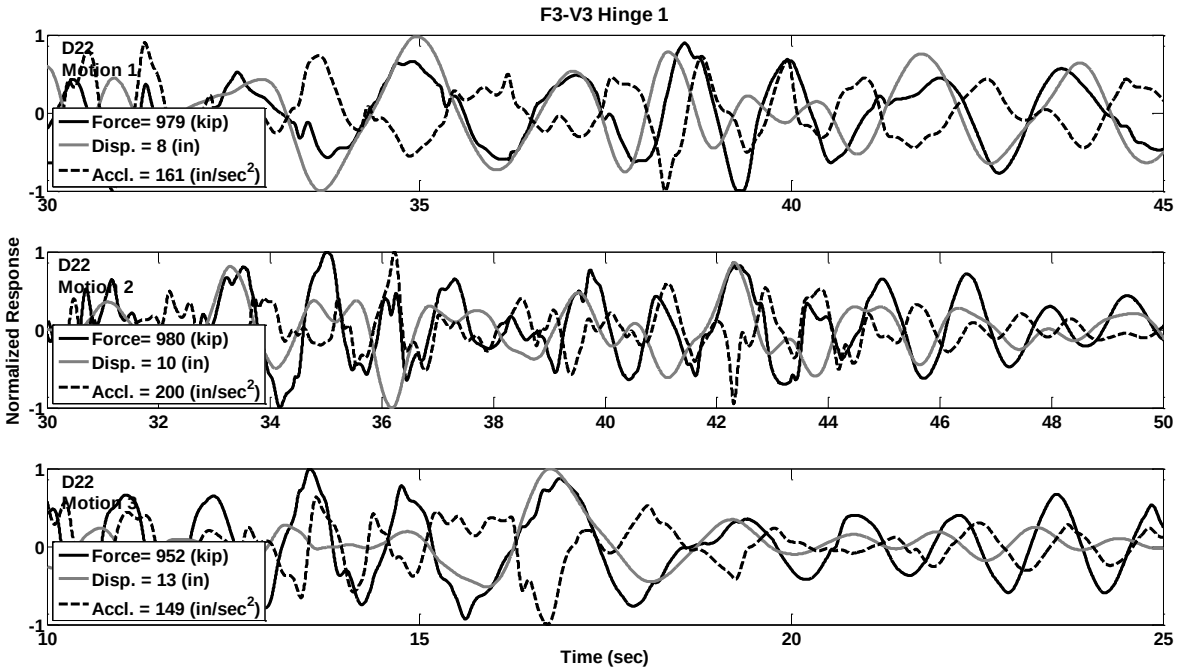

Figure C.138 Response Histories of Prototype F3-V3, Hinge 1, Motions D22

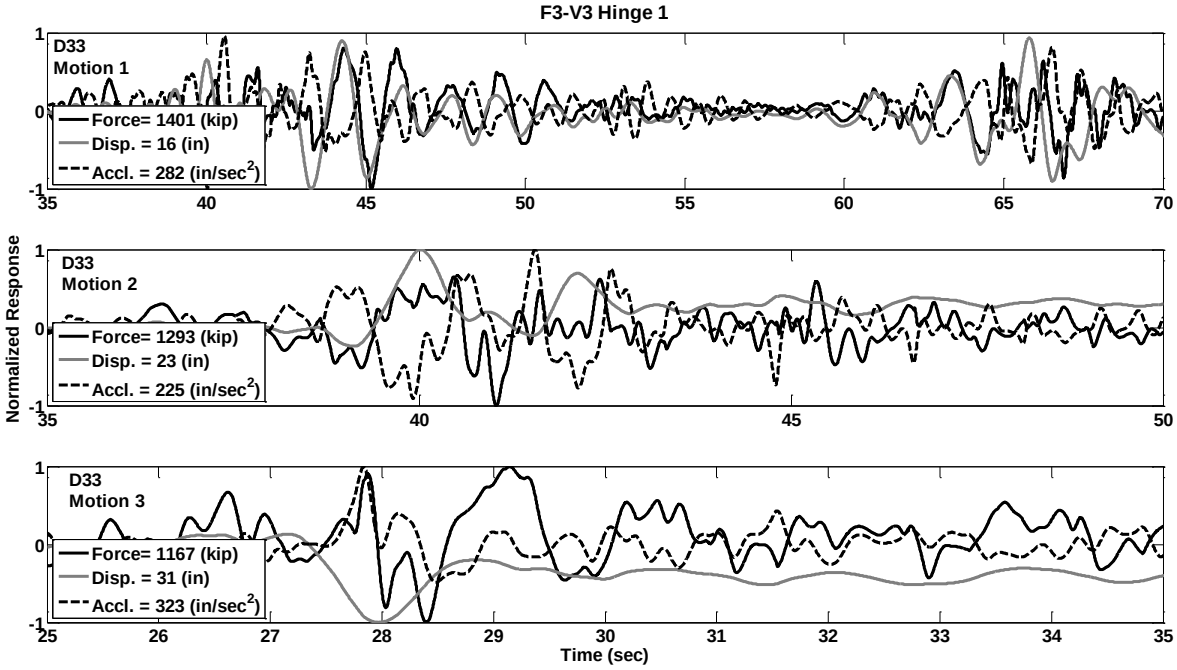

Figure C.139 Response Histories of Prototype F3-V3, Hinge 1, Motions D33

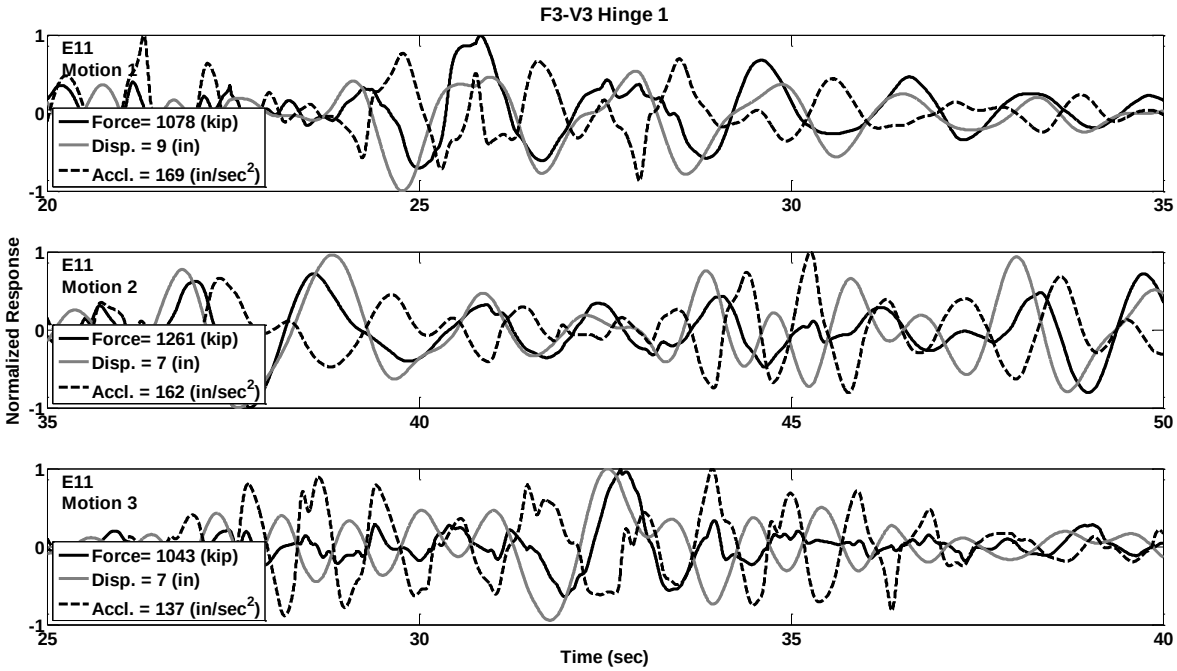

Figure C.140 Response Histories of Prototype F3-V3, Hinge 1, Motions E11

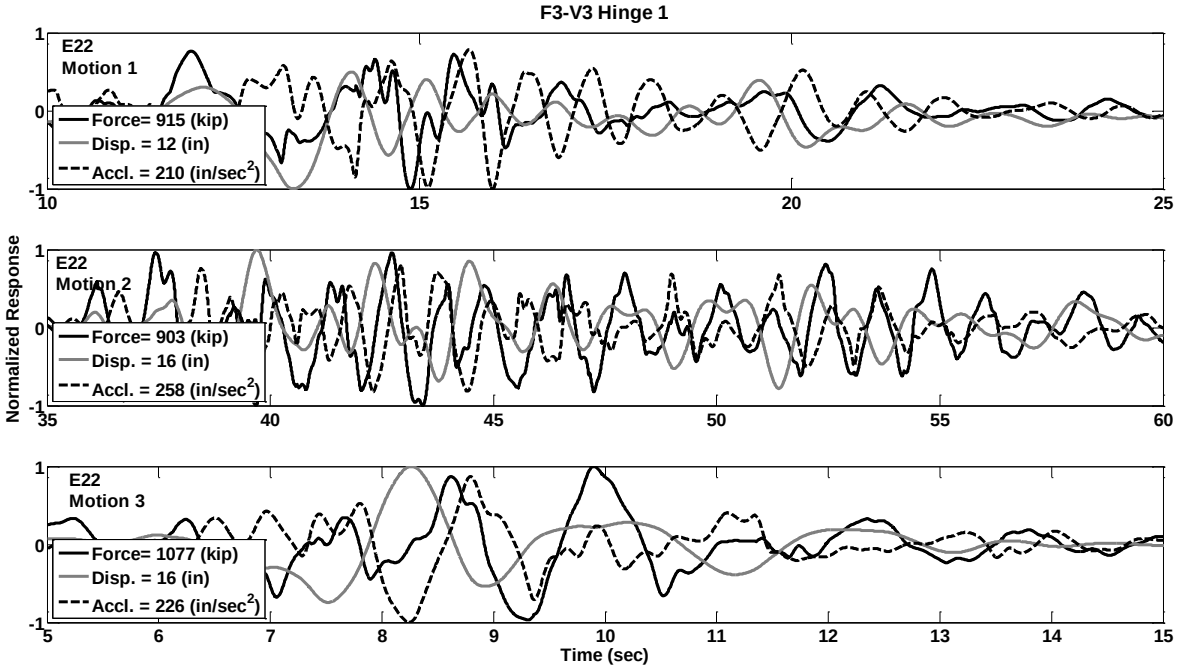

Figure C.141 Response Histories of Prototype F3-V3, Hinge 1, Motions E22

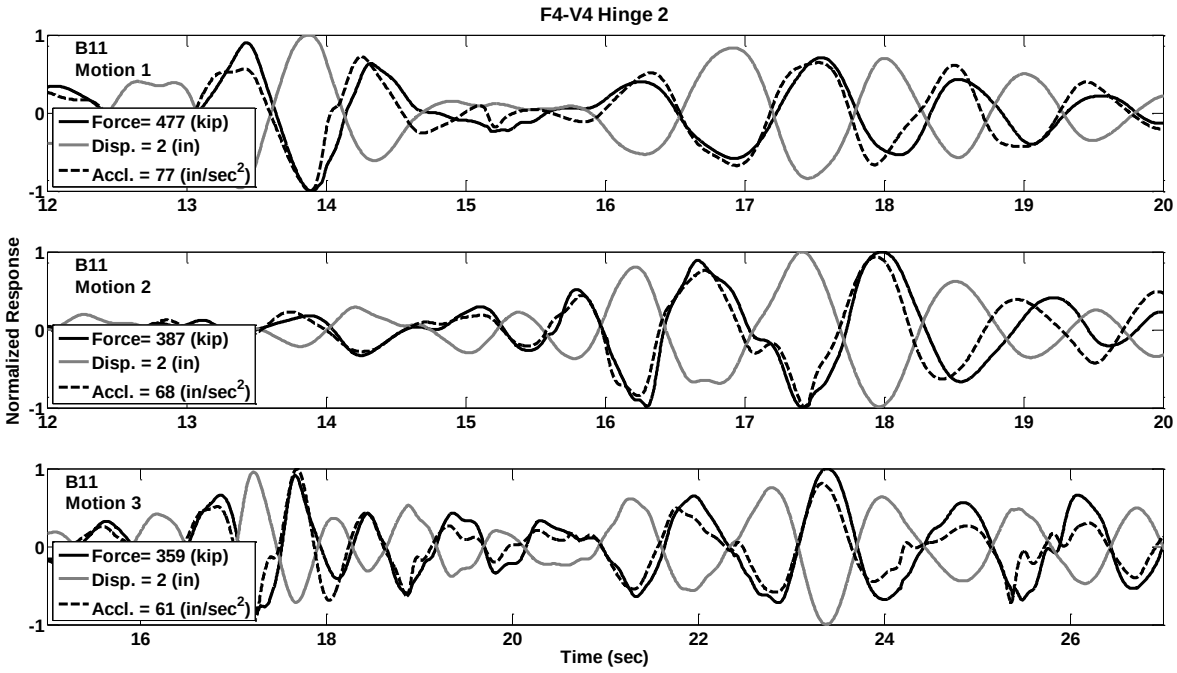

Figure C.142 Response Histories of Prototype F4-V4, Hinge 2, Motions B11

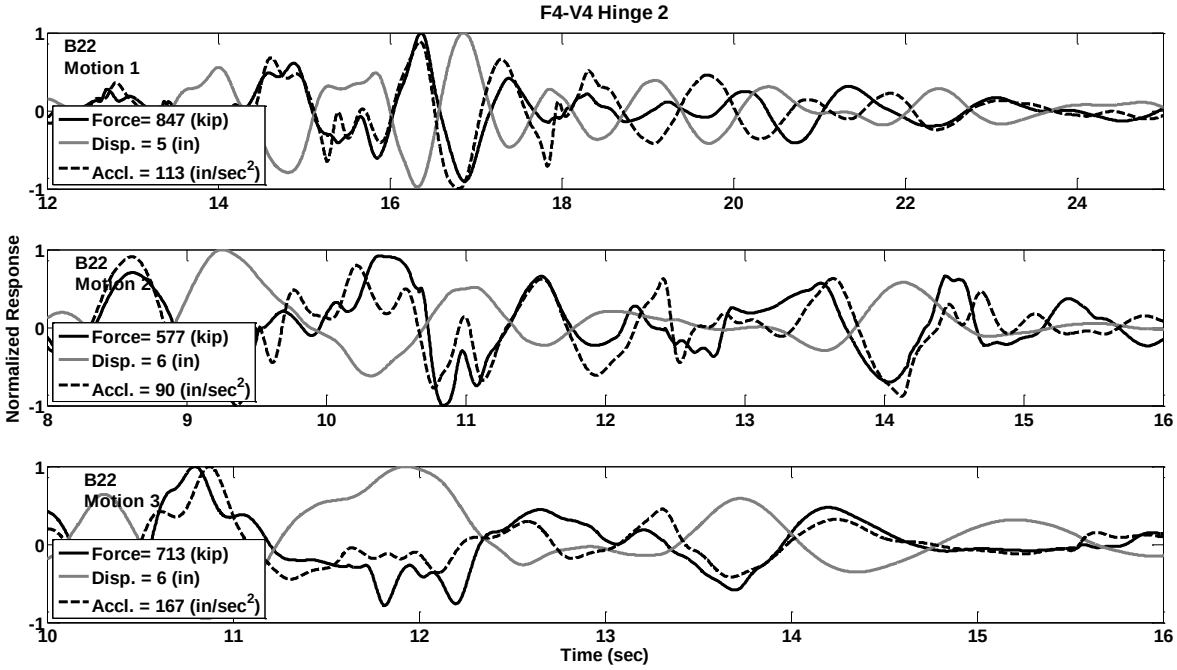

Figure C.143 Response Histories of Prototype F4-V4, Hinge 2, Motions B22

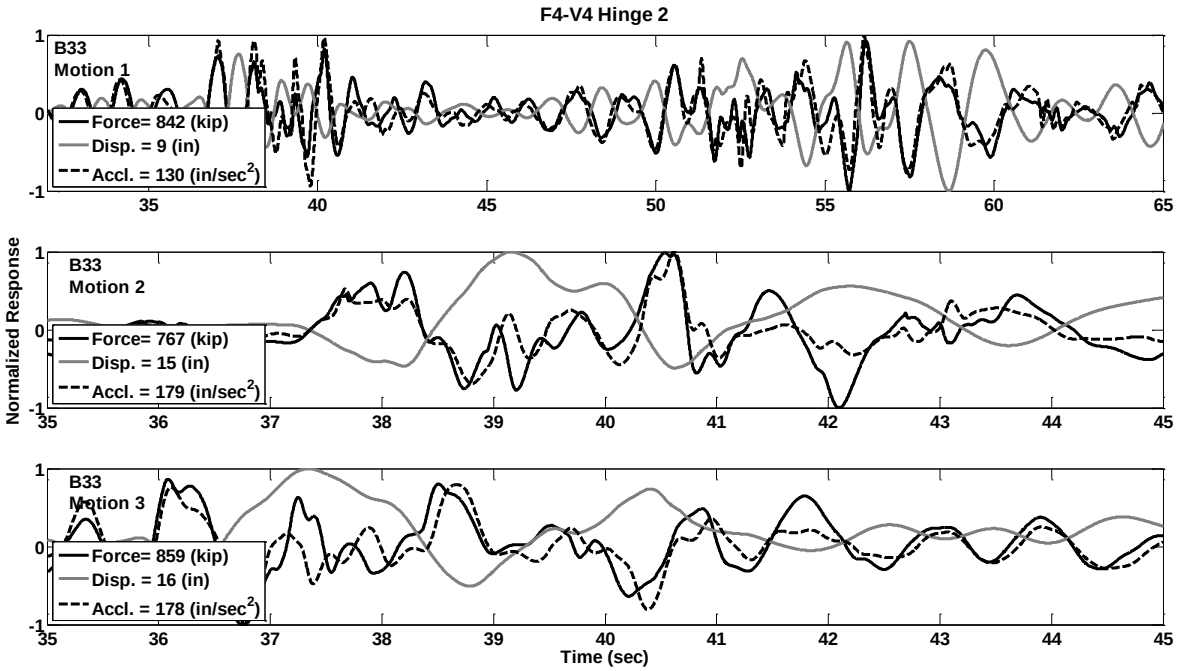

Figure C.144 Response Histories of Prototype F4-V4, Hinge 2, Motions B33

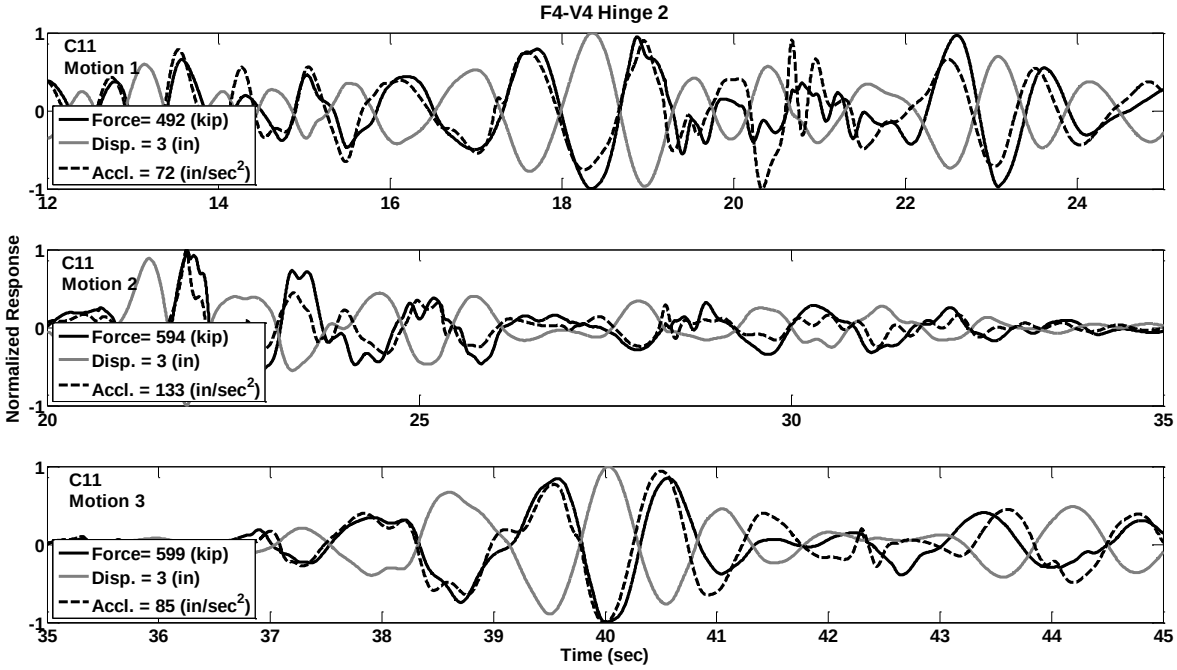

Figure C.145 Response Histories of Prototype F4-V4, Hinge 2, Motions C11

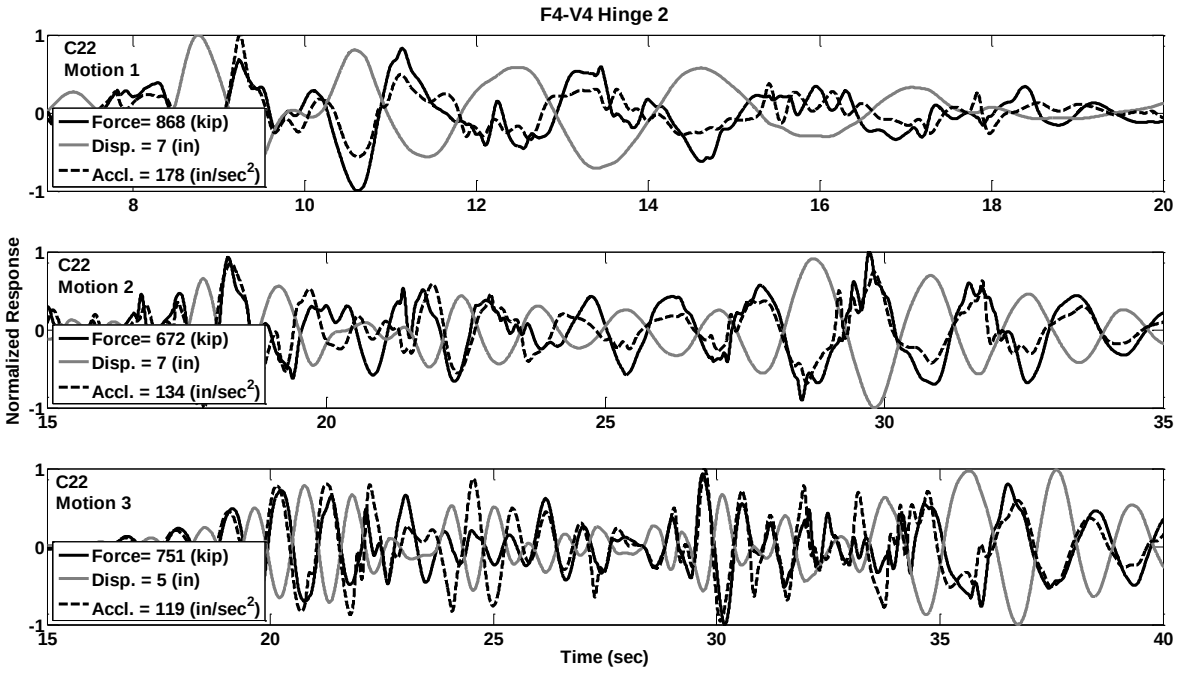

Figure C.146 Response Histories of Prototype F4-V4, Hinge 2, Motions C22

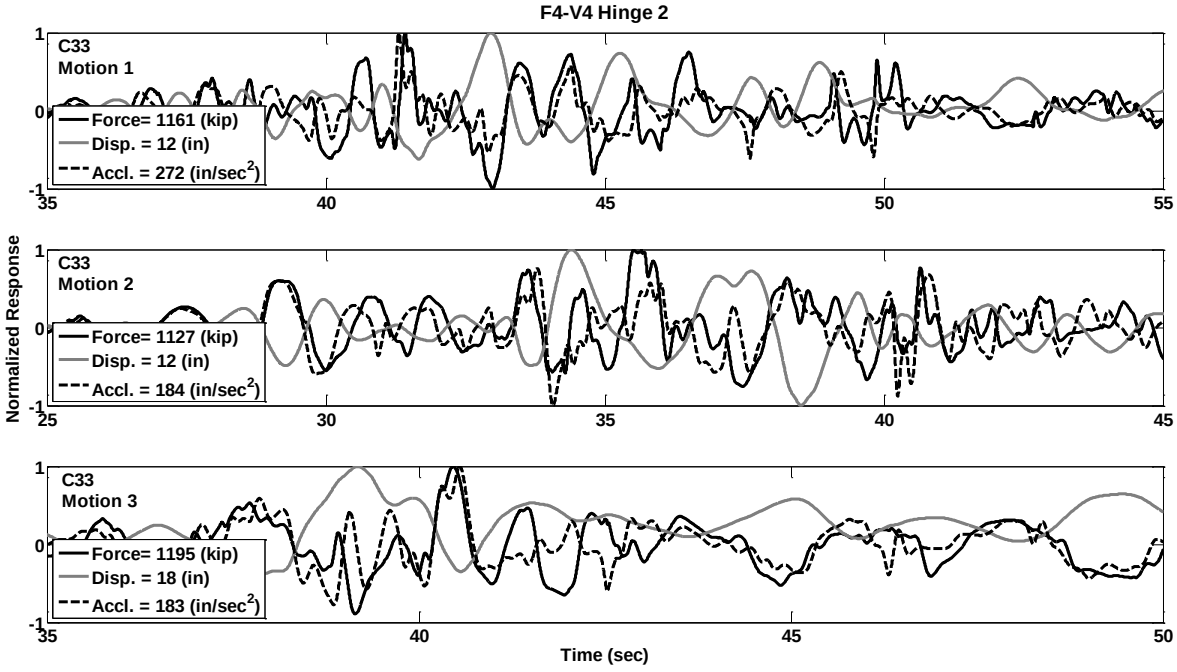

Figure C.147 Response Histories of Prototype F4-V4, Hinge 2, Motions C33

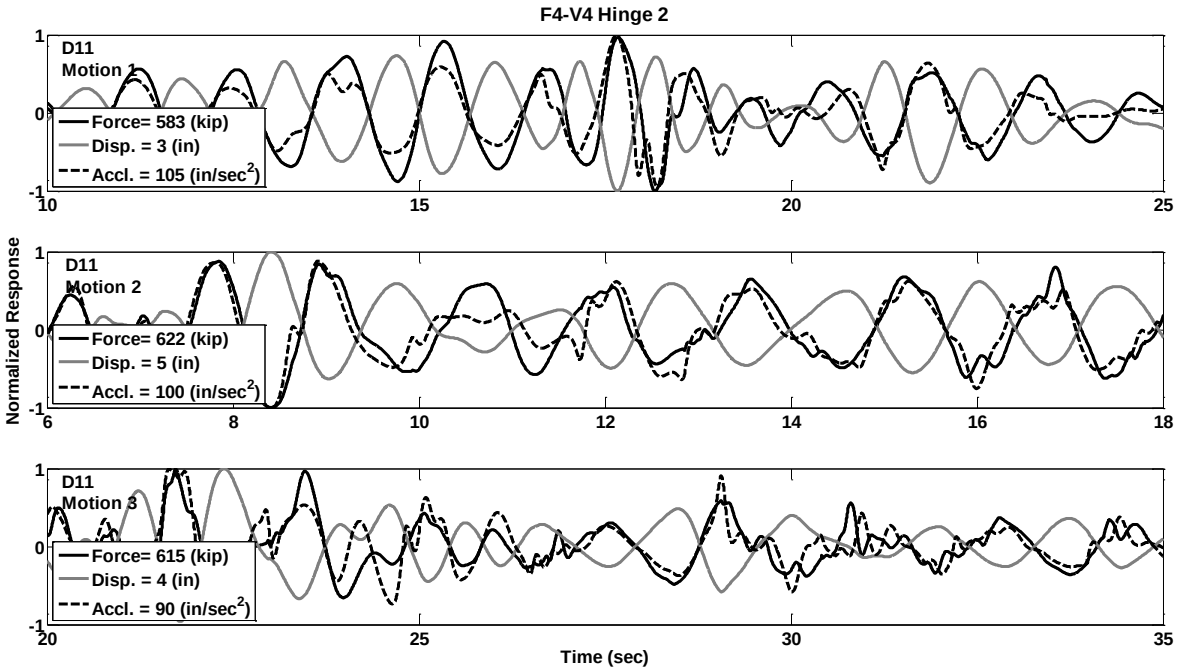

Figure C.148 Response Histories of Prototype F4-V4, Hinge 2, Motions D11

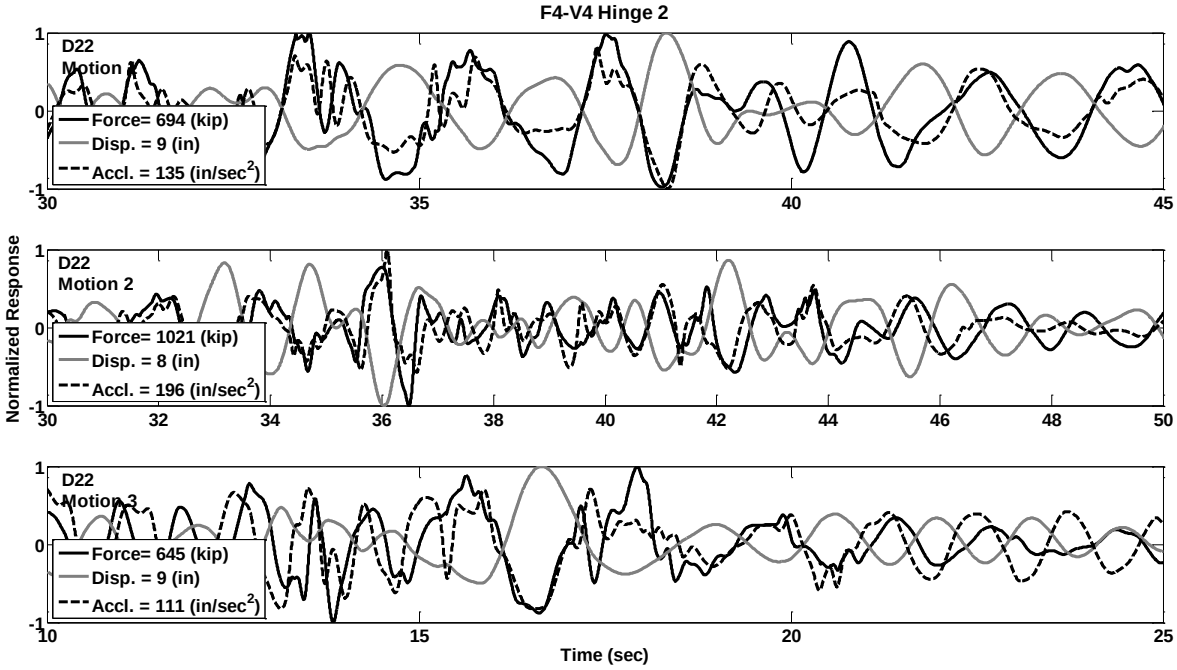

Figure C.149 Response Histories of Prototype F4-V4, Hinge 2, Motions D22

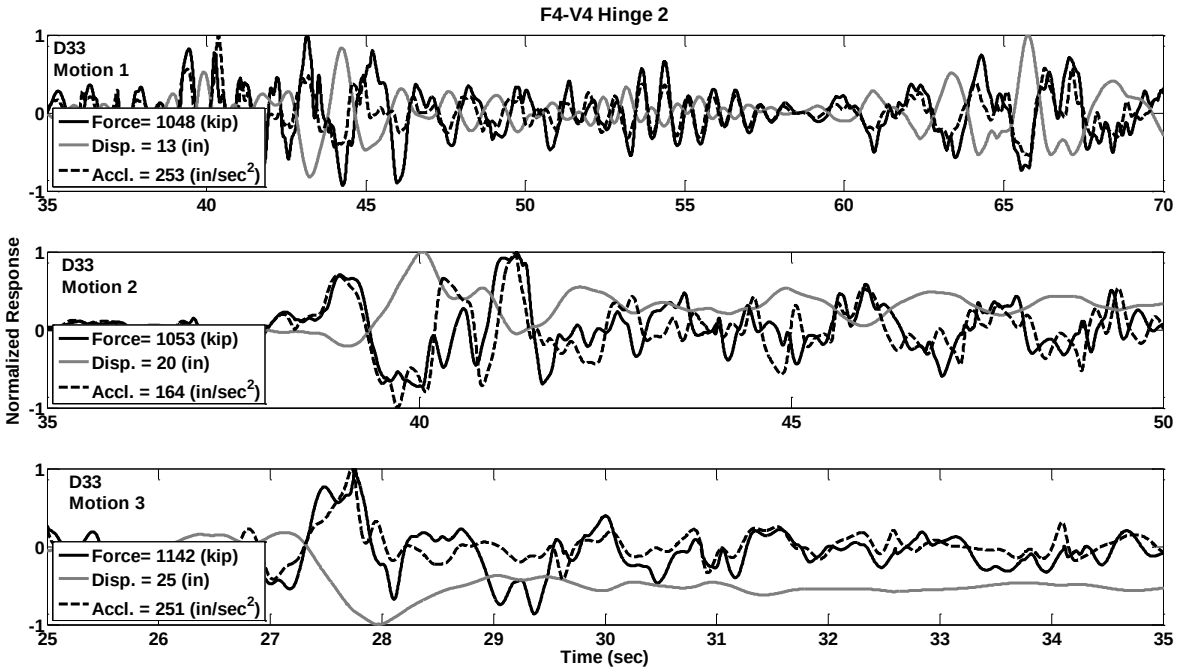

Figure C.150 Response Histories of Prototype F4-V4, Hinge 2, Motions D33

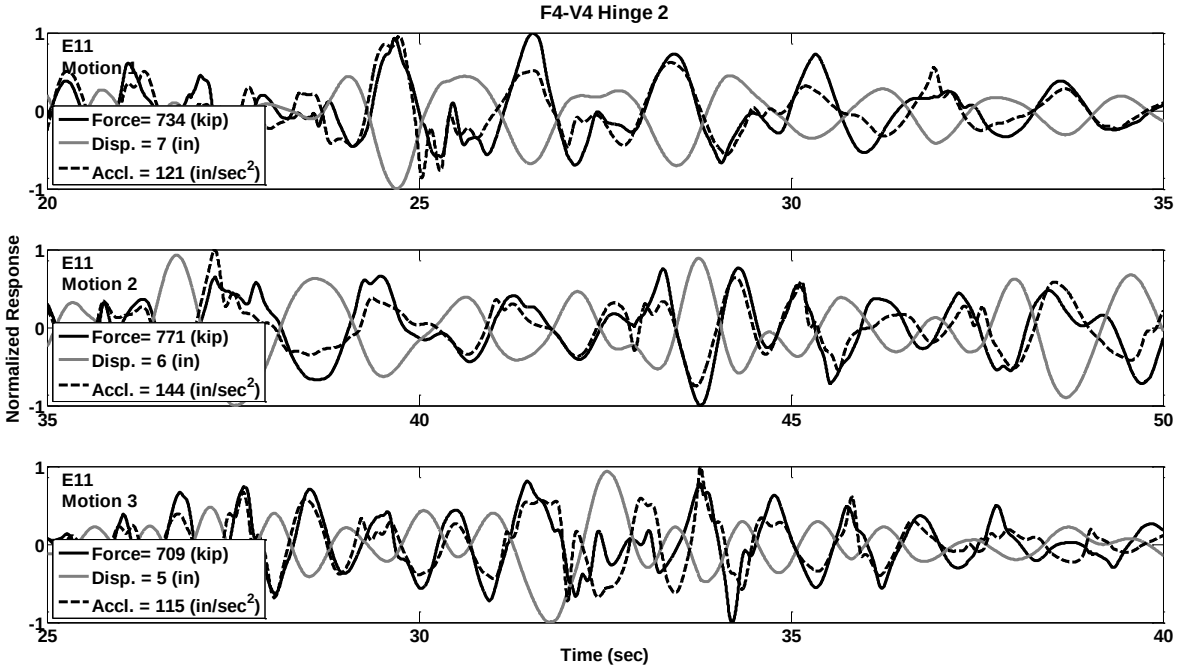

Figure C.151 Response Histories of Prototype F4-V4, Hinge 2, Motions E11

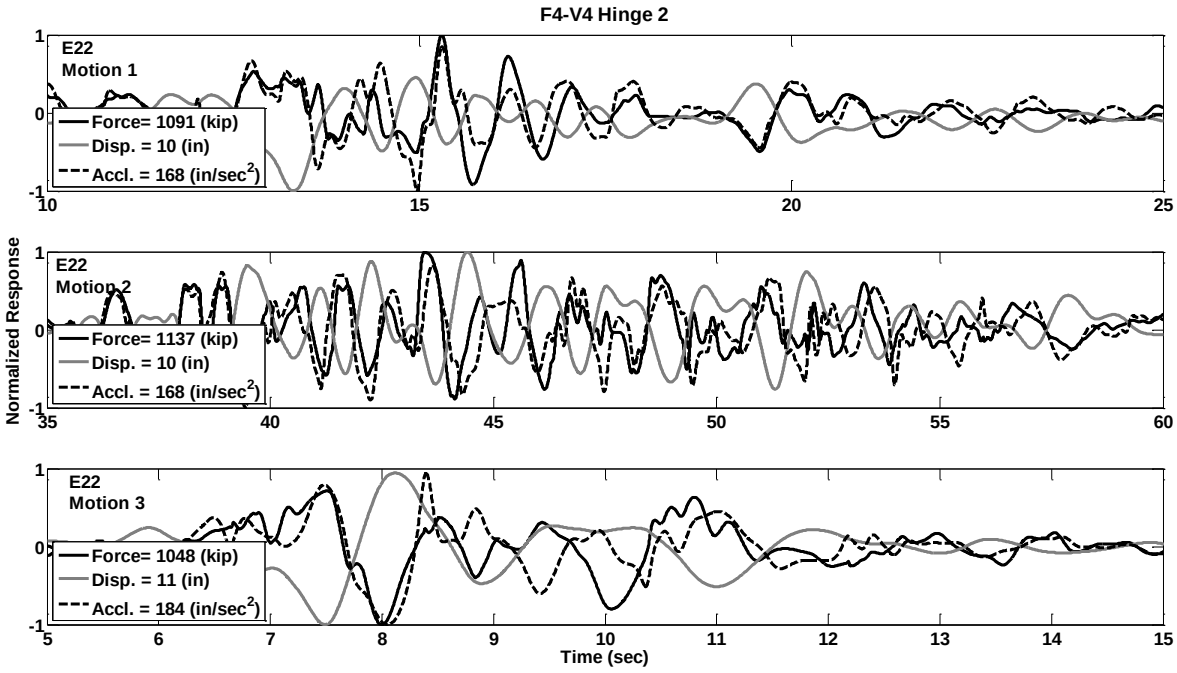

Figure C.152 Response Histories of Prototype F4-V4, Hinge 2, Motions E22

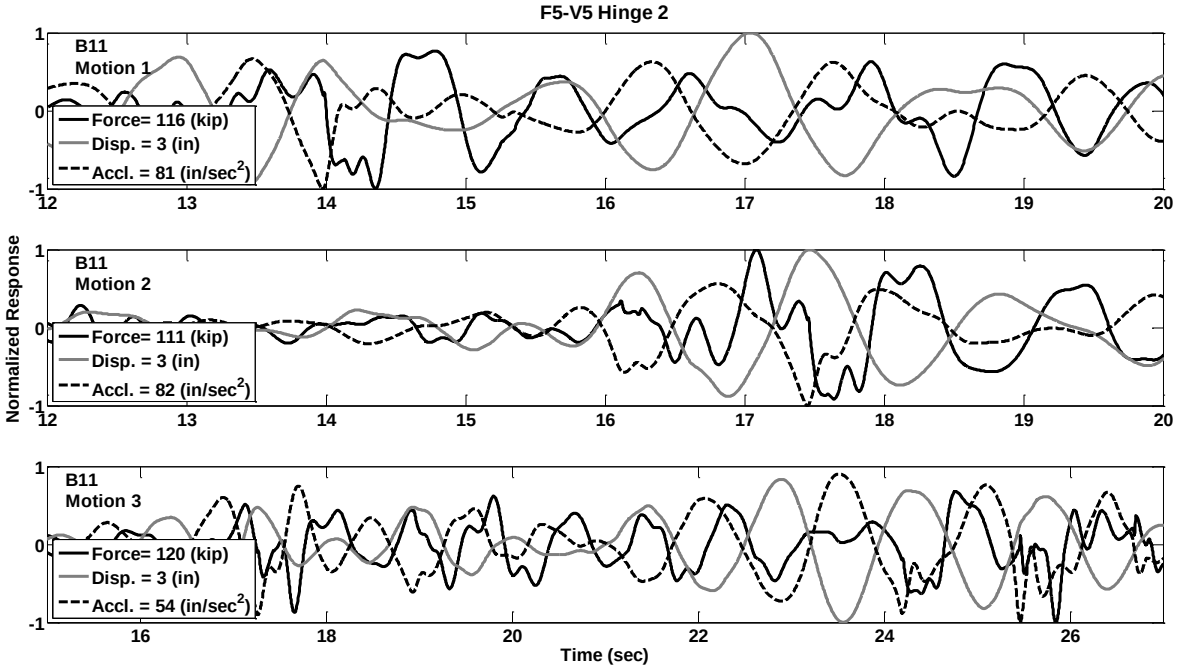

Figure C.153 Response Histories of Prototype F5-V5, Hinge 2, Motions B11

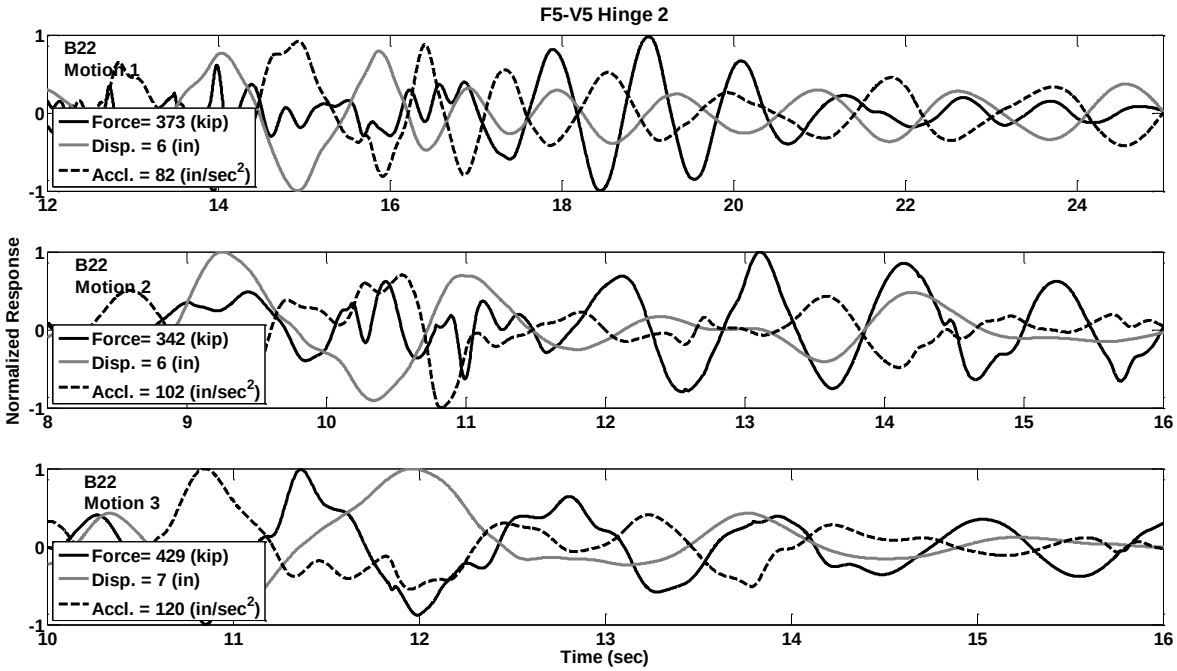

Figure C.154 Response Histories of Prototype F5-V5, Hinge 2, Motions B22

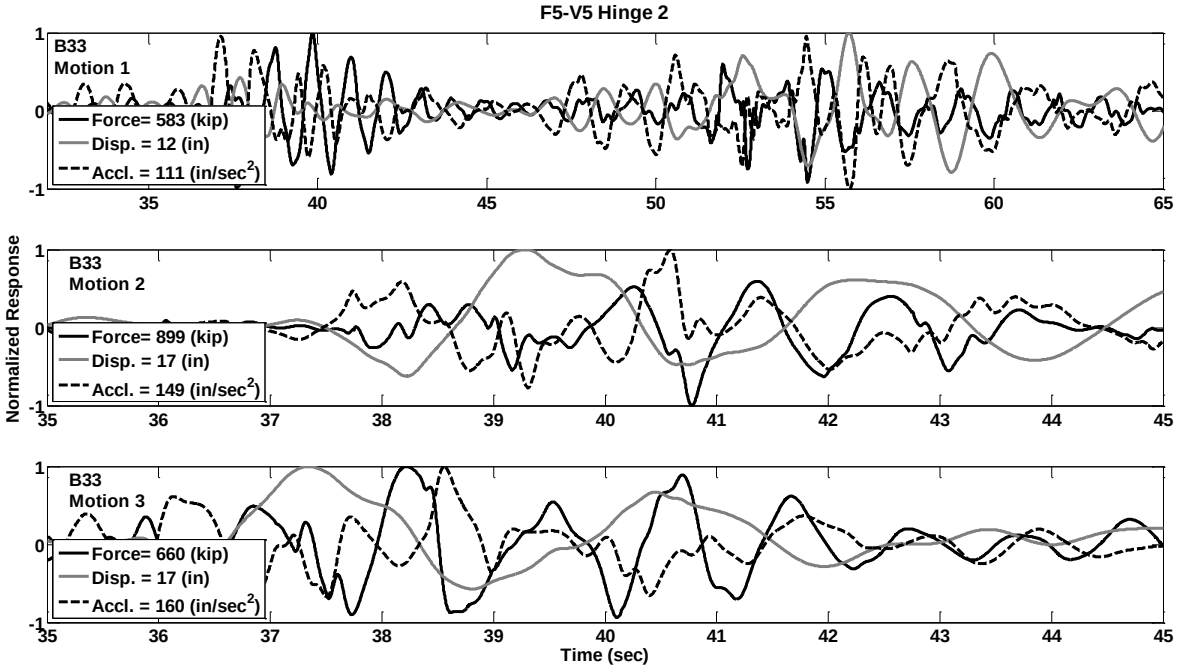

Figure C.155 Response Histories of Prototype F5-V5, Hinge 2, Motions B33

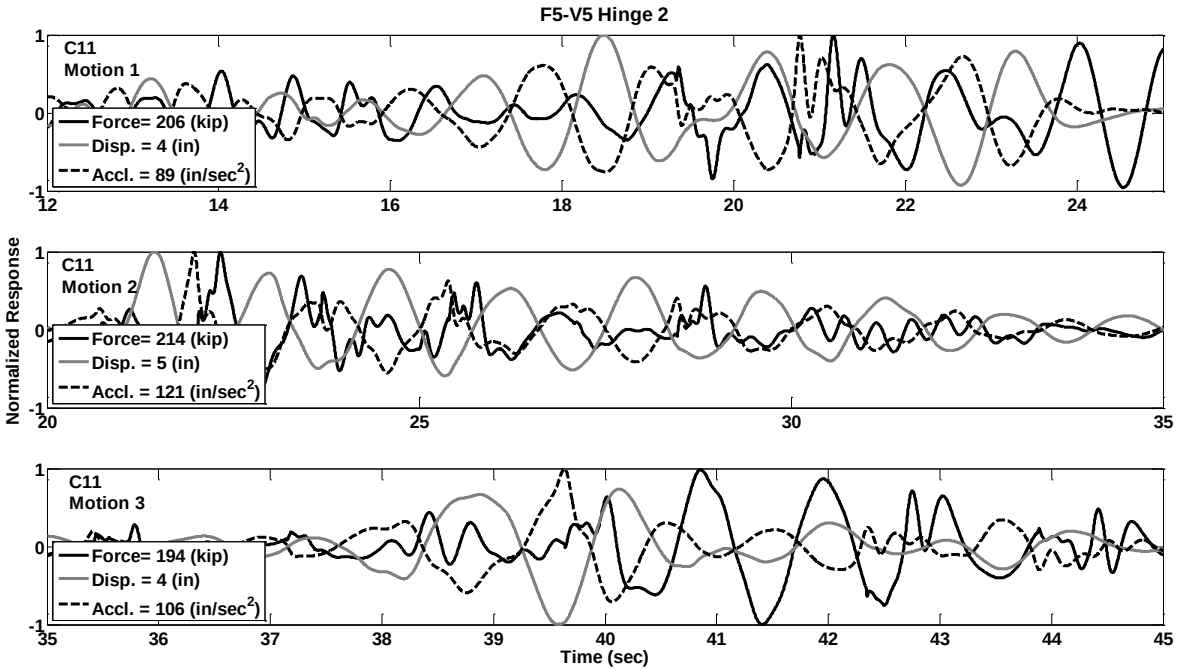

Figure C.156 Response Histories of Prototype F5-V5, Hinge 2, Motions C11

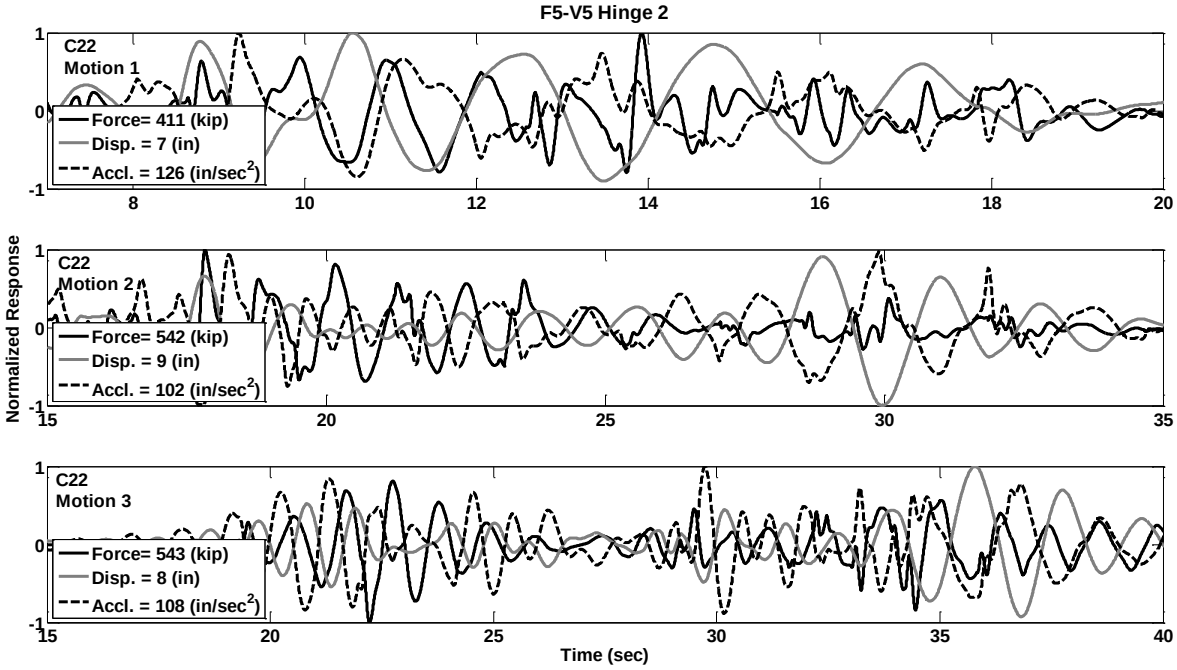

Figure C.157 Response Histories of Prototype F5-V5, Hinge 2, Motions C22

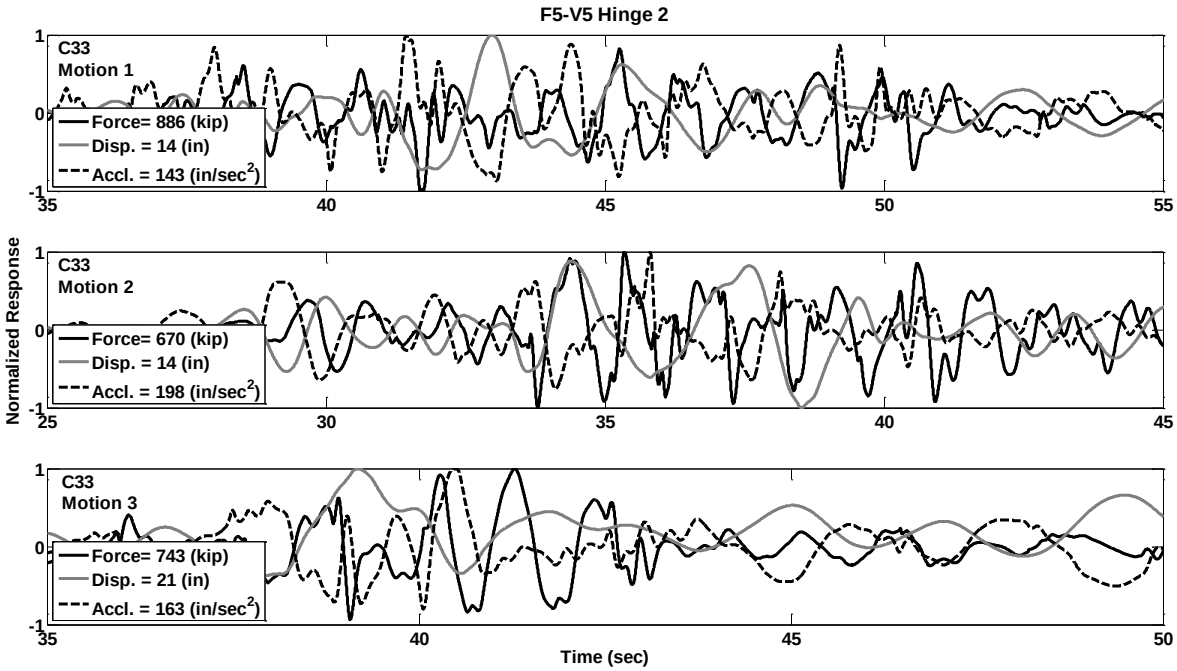

Figure C.158 Response Histories of Prototype F5-V5, Hinge 2, Motions C33

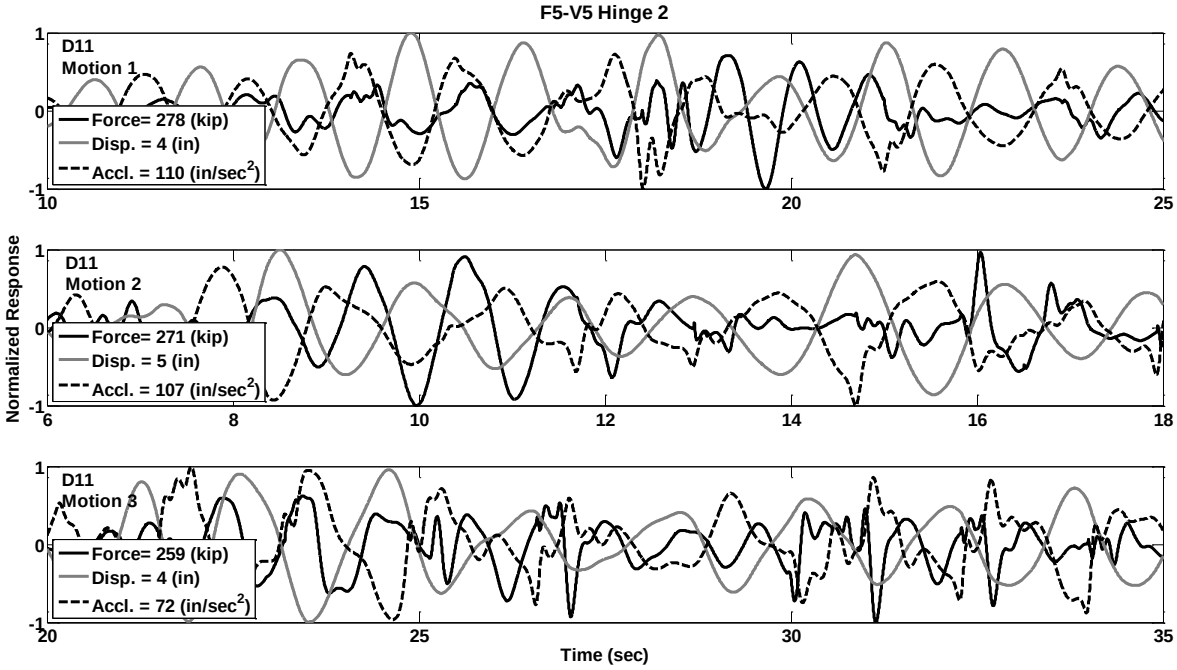

Figure C.159 Response Histories of Prototype F5-V5, Hinge 2, Motions D11

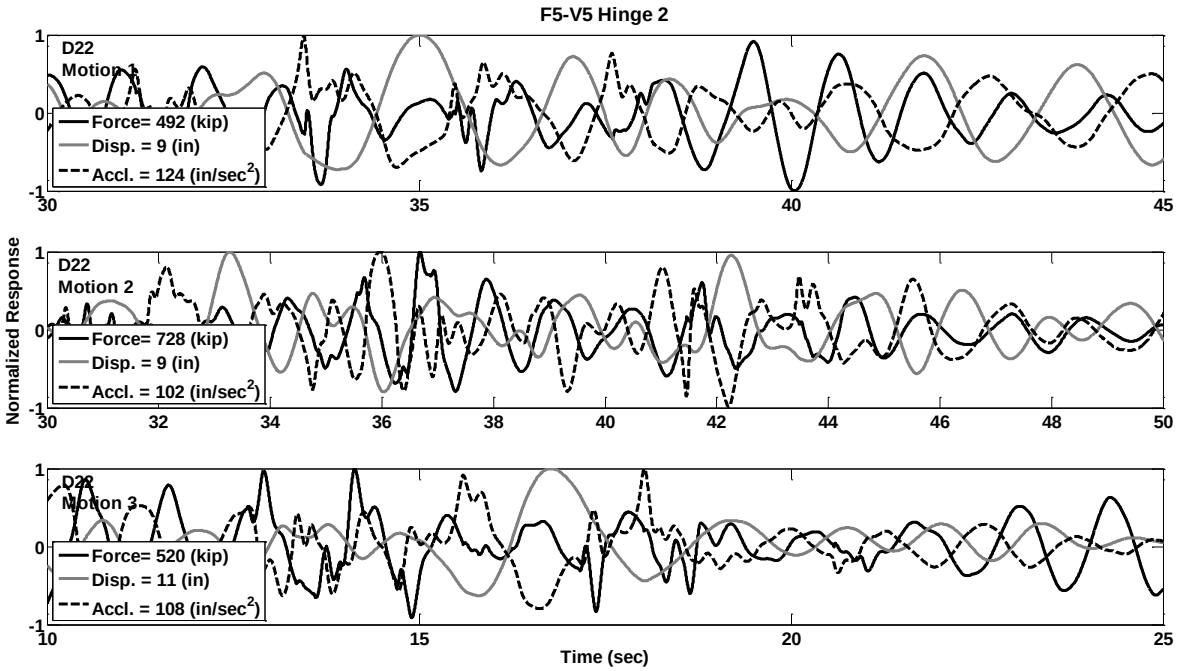

Figure C.160 Response Histories of Prototype F5-V5, Hinge 2, Motions D22

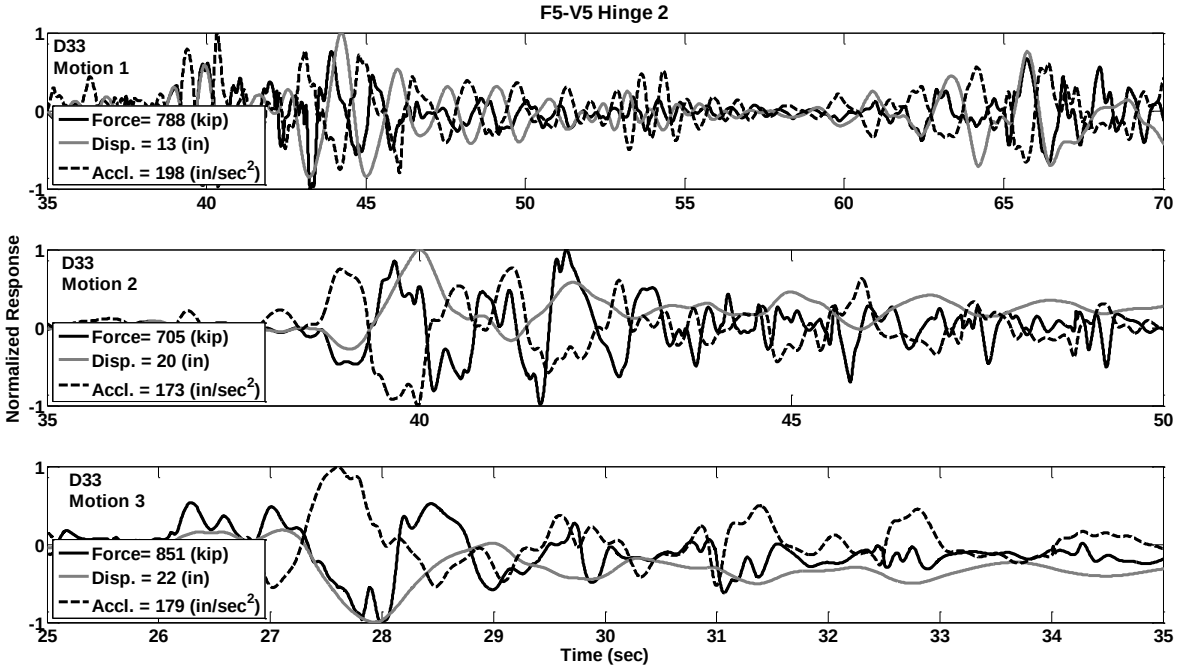

Figure C.161 Response Histories of Prototype F5-V5, Hinge 2, Motions D33

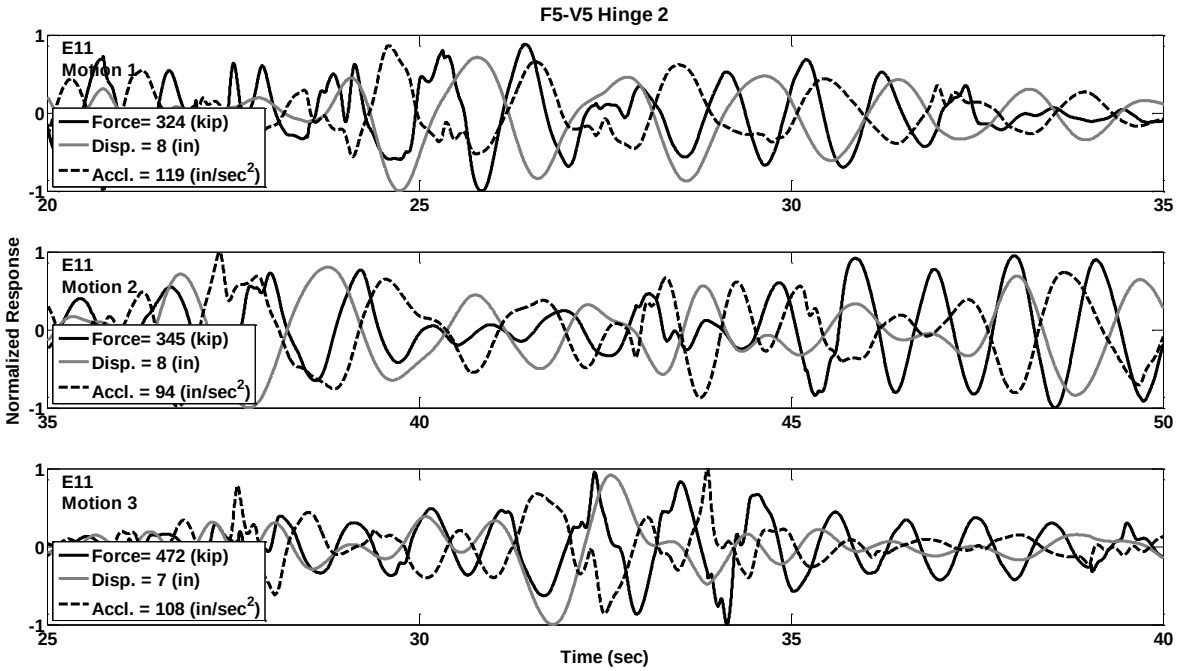

Figure C.162 Response Histories of Prototype F5-V5, Hinge 2, Motions E11

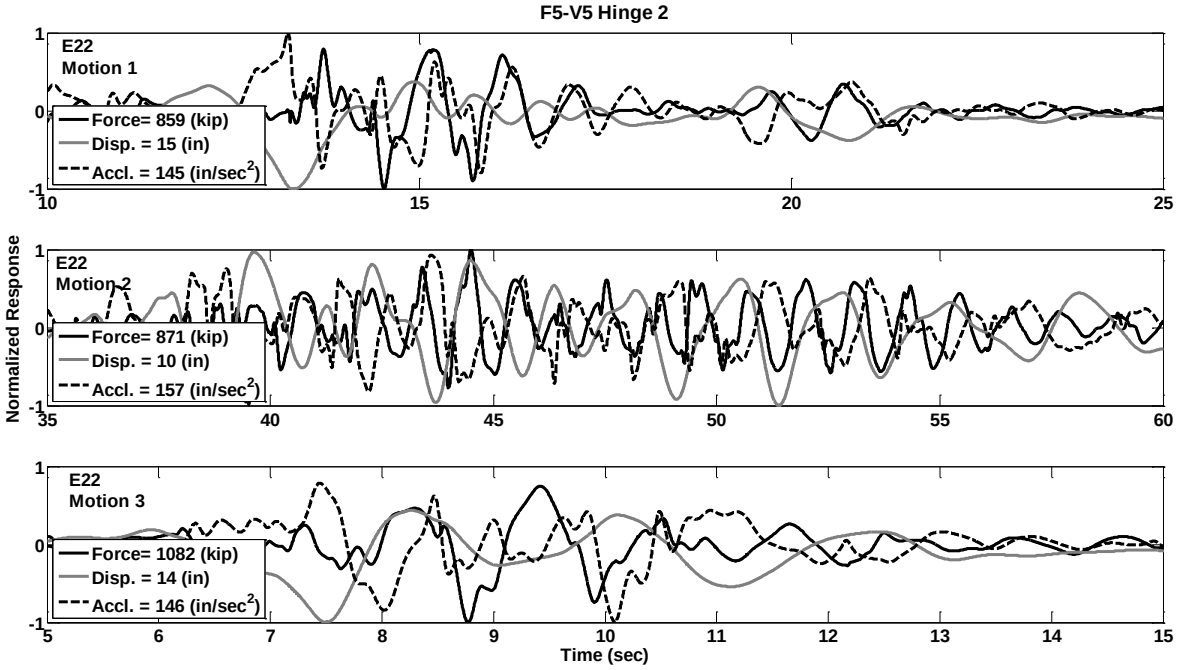

Figure C.163 Response Histories of Prototype F5-V5, Hinge 2, Motions E22

PART-3a: Hysteresis Curves for Single-Column Bent Prototypes

Shear Key Force vs. Transverse Displacement and Shear Key Force vs. Transverse Acceleration.

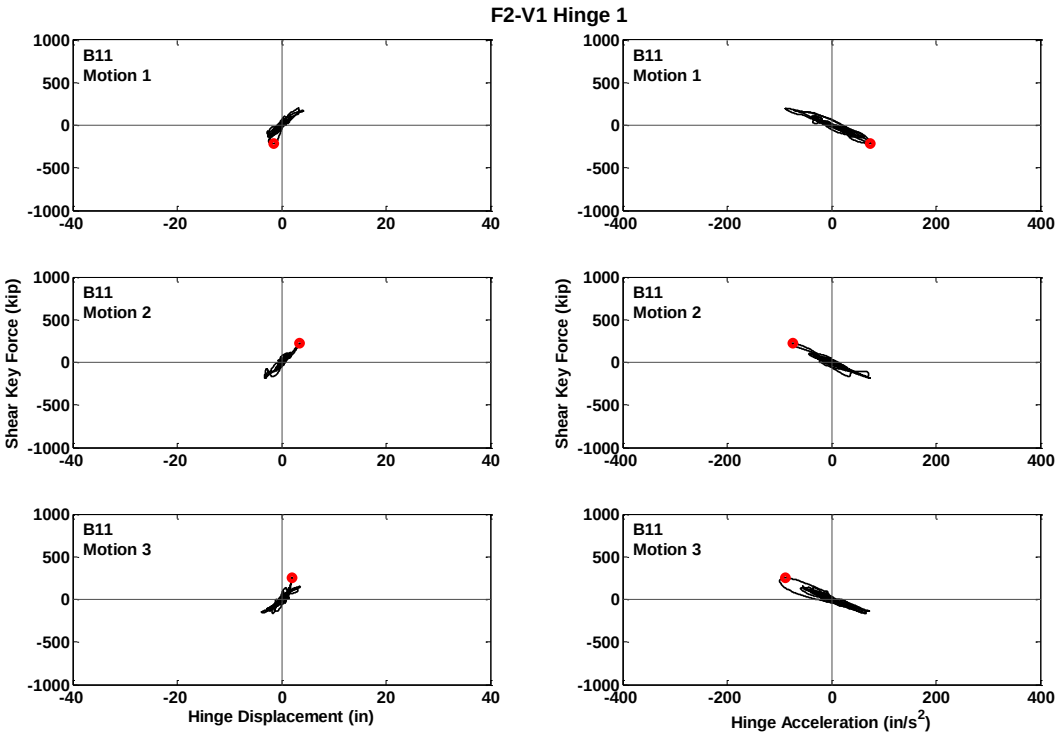

Figure C.164 Hysteresis Curves for Prototype F2-V1, Hinge 1, Motions B11

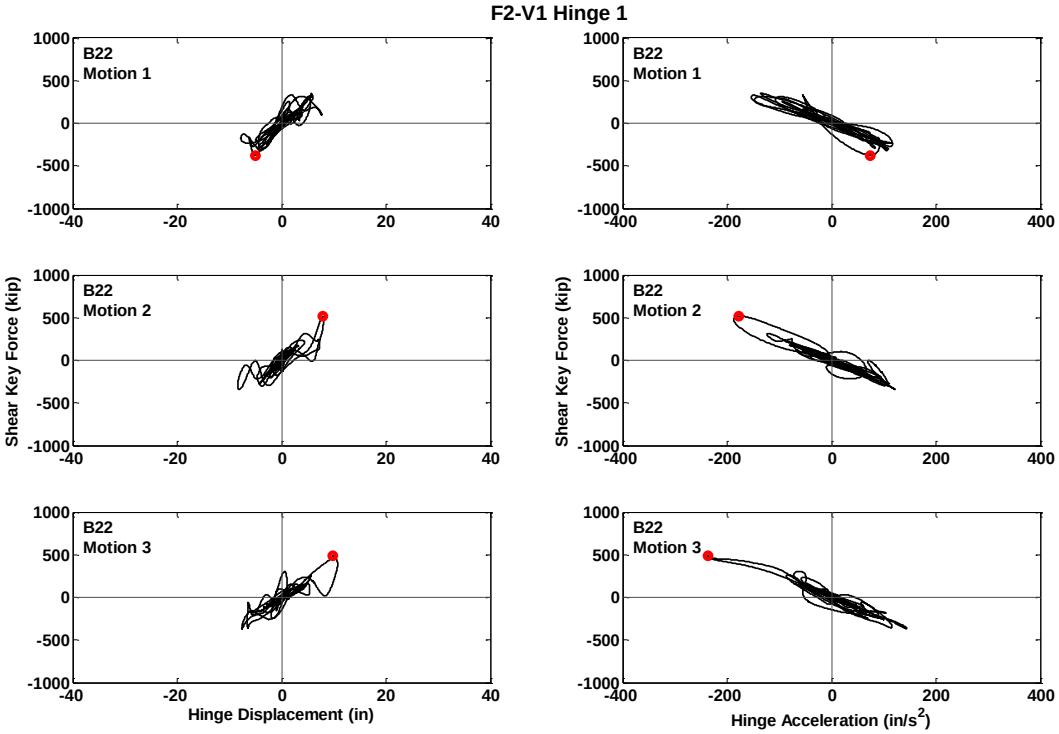

Figure C.165 Hysteresis Curves for Prototype F2-V1, Hinge 1, Motions B22

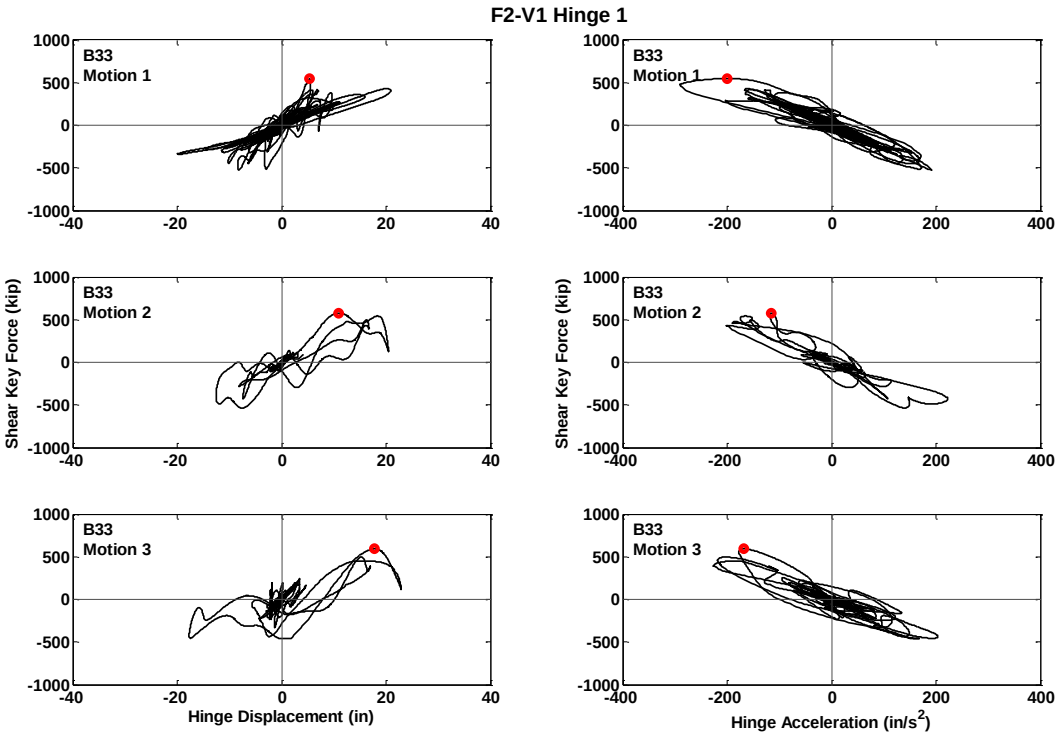

Figure C.166 Hysteresis Curves for Prototype F2-V1, Hinge 1, Motions B33

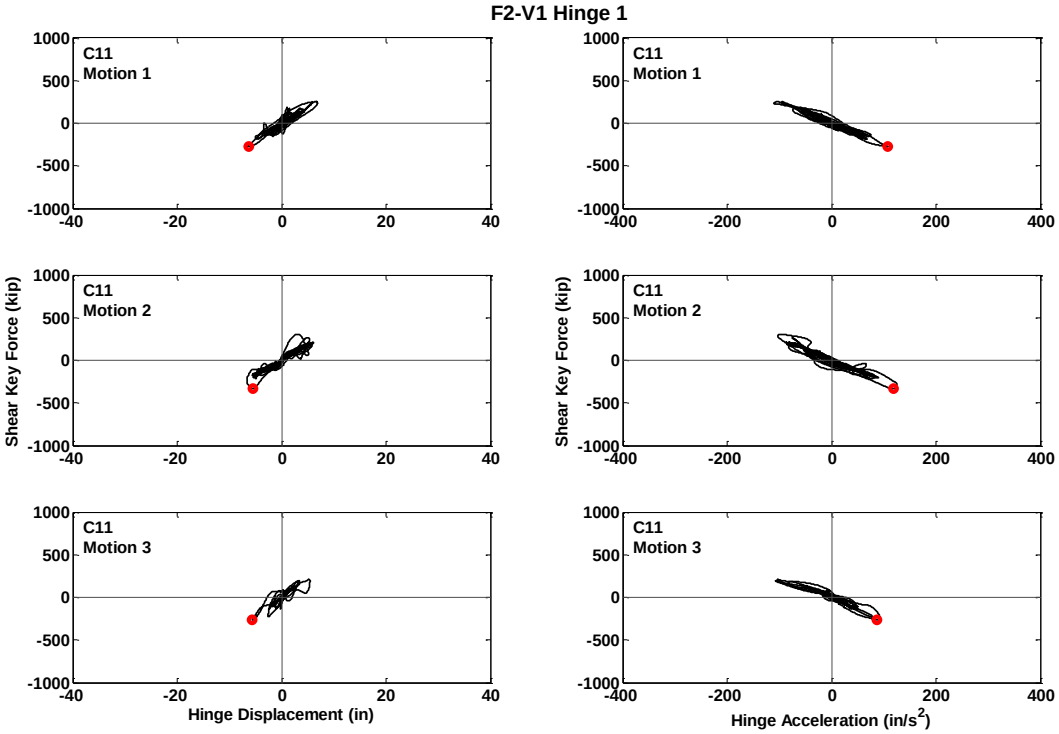

Figure C.167 Hysteresis Curves for Prototype F2-V1, Hinge 1, Motions C11

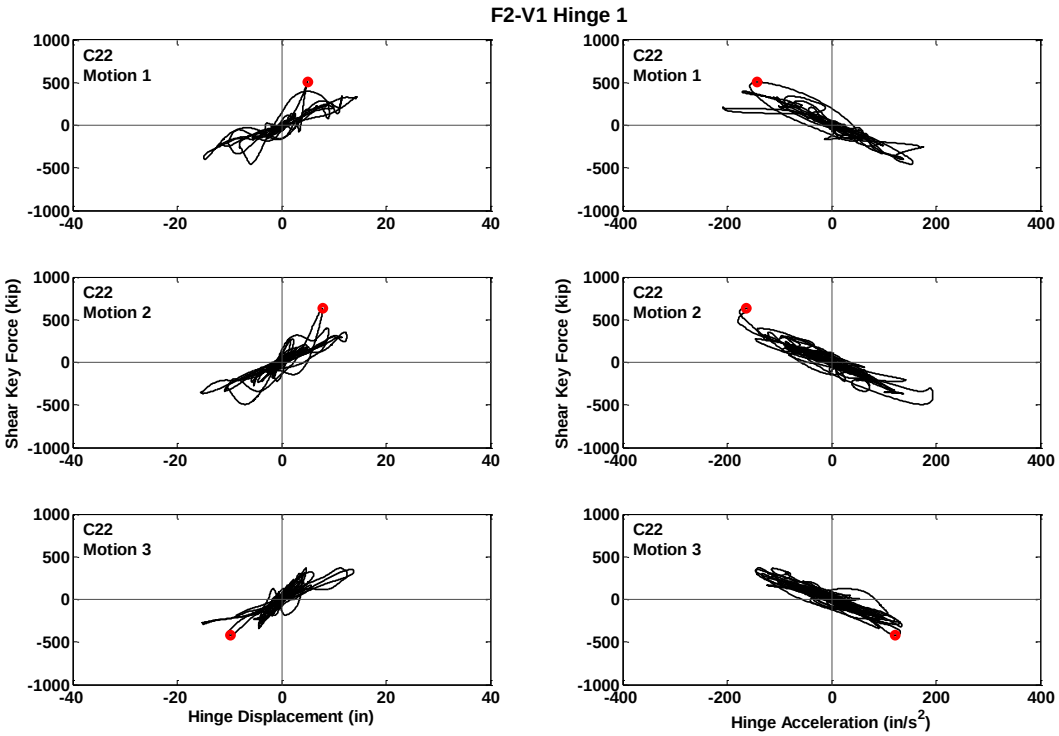

Figure C.168 Hysteresis Curves for Prototype F2-V1, Hinge 1, Motions C22

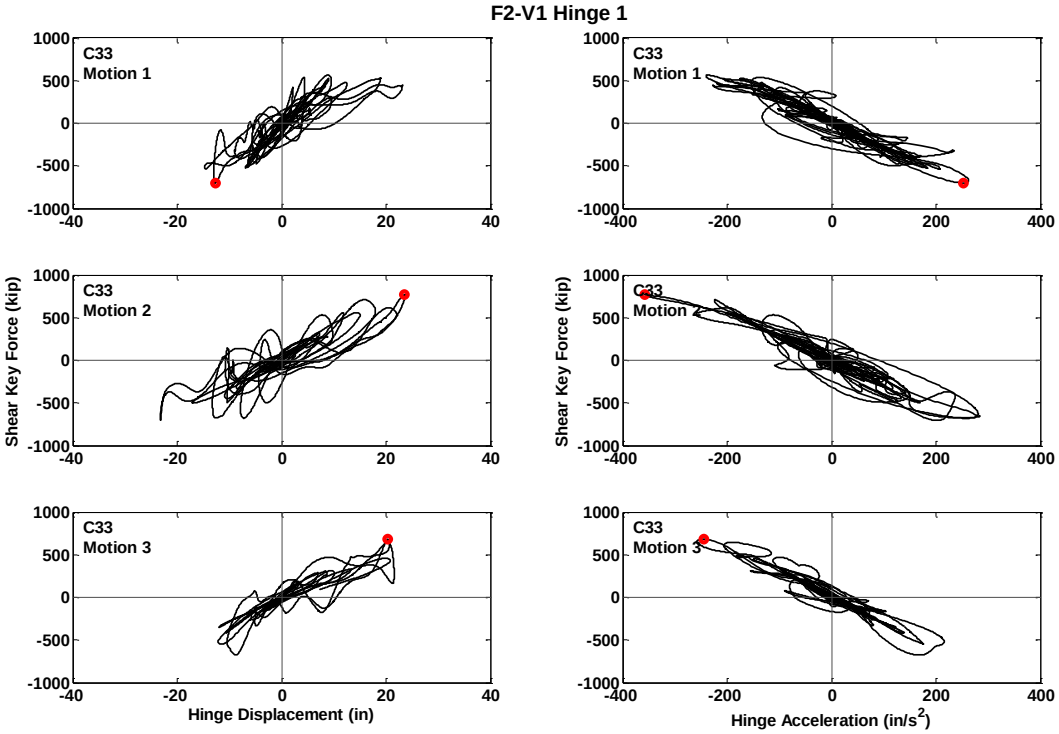

Figure C.169 Hysteresis Curves for Prototype F2-V1, Hinge 1, Motions C33

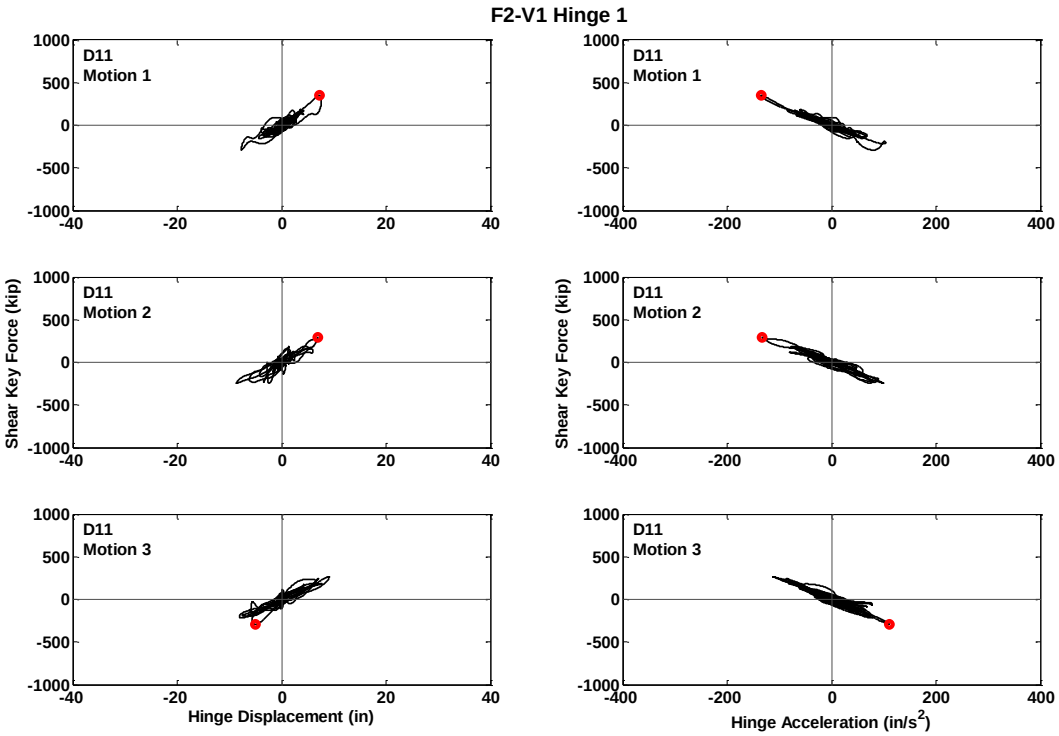

Figure C.170 Hysteresis Curves for Prototype F2-V1, Hinge 1, Motions D11

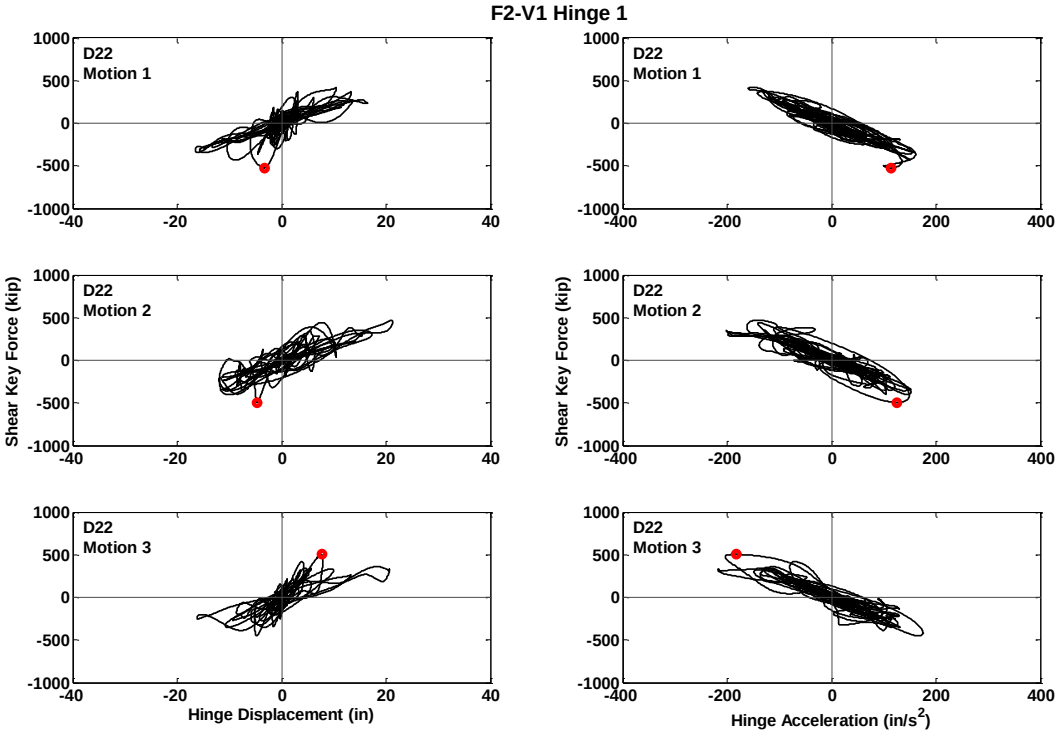

Figure C.171 Hysteresis Curves for Prototype F2-V1, Hinge 1, Motions D22

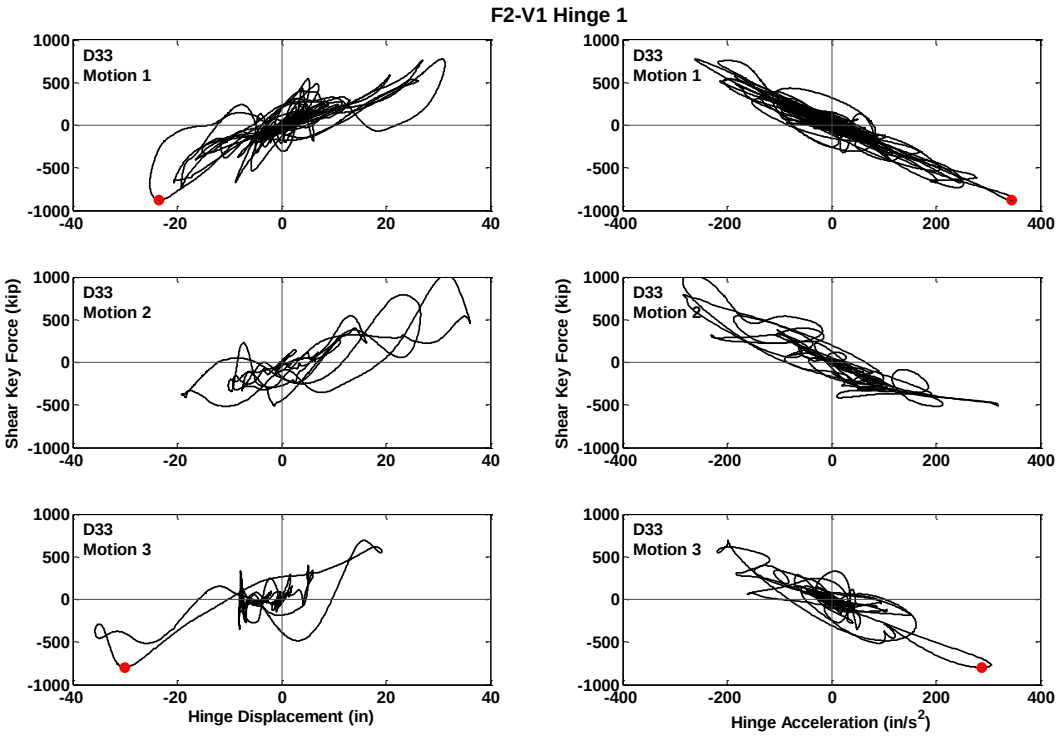

Figure C.172 Hysteresis Curves for Prototype F2-V1, Hinge 1, Motions D33

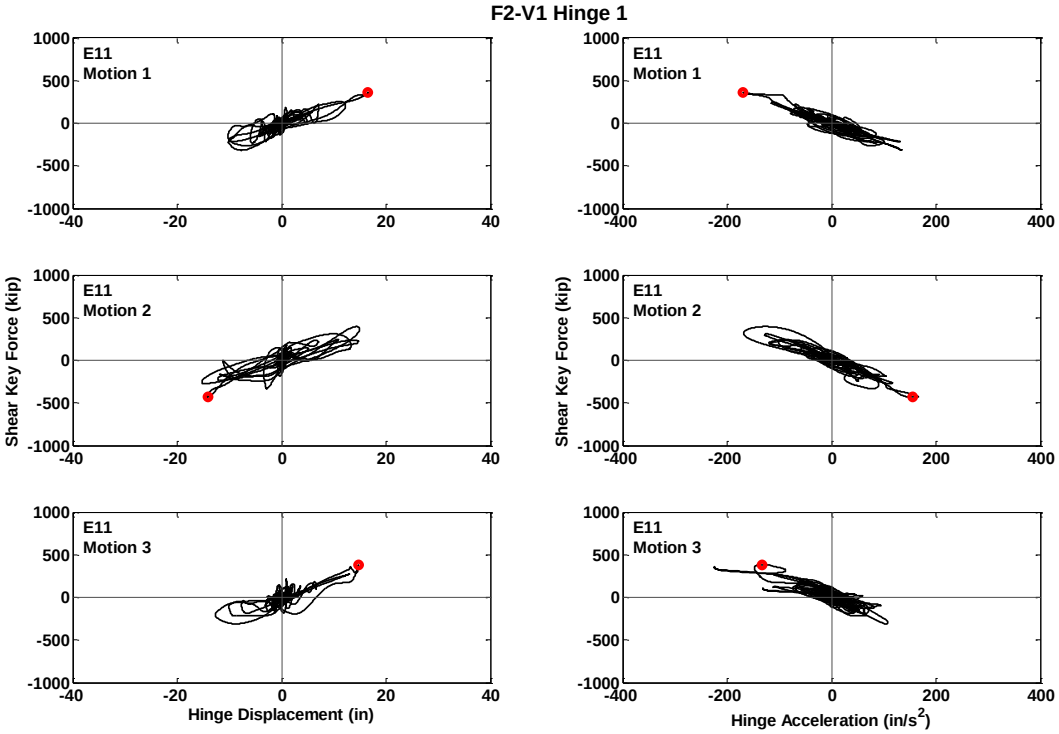

Figure C.173 Hysteresis Curves for Prototype F2-V1, Hinge 1, Motions E11

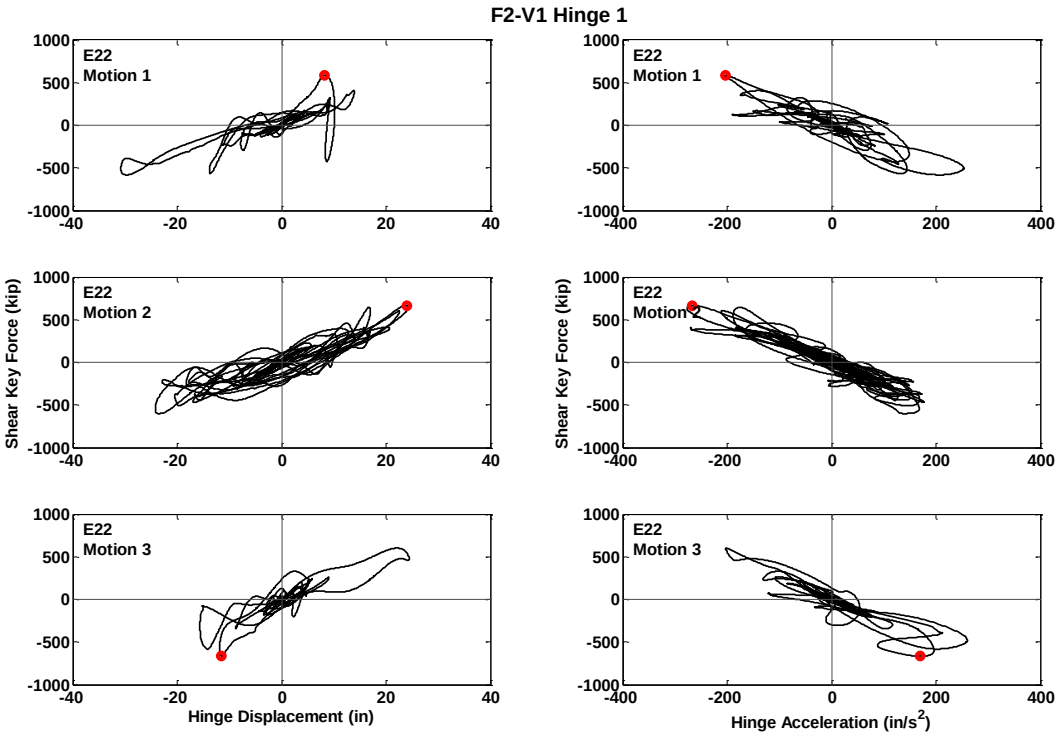

Figure C.174 Hysteresis Curves for Prototype F2-V1, Hinge 1, Motions E22

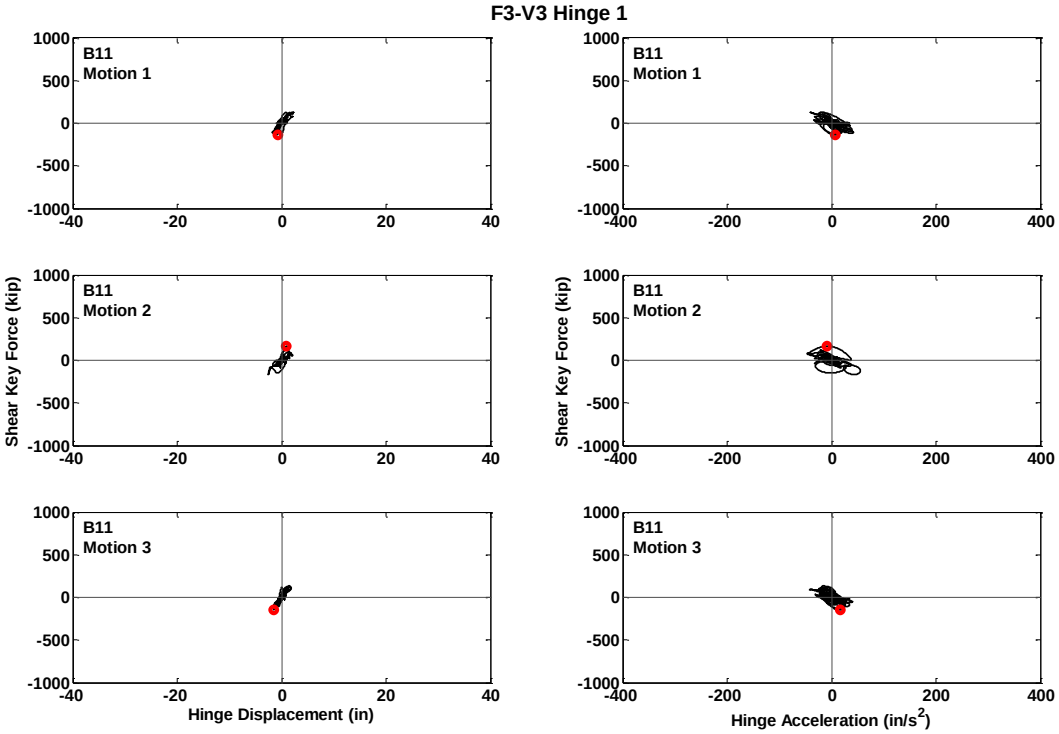

Figure C.175 Hysteresis Curves for Prototype F3-V3, Hinge 1, Motions B11

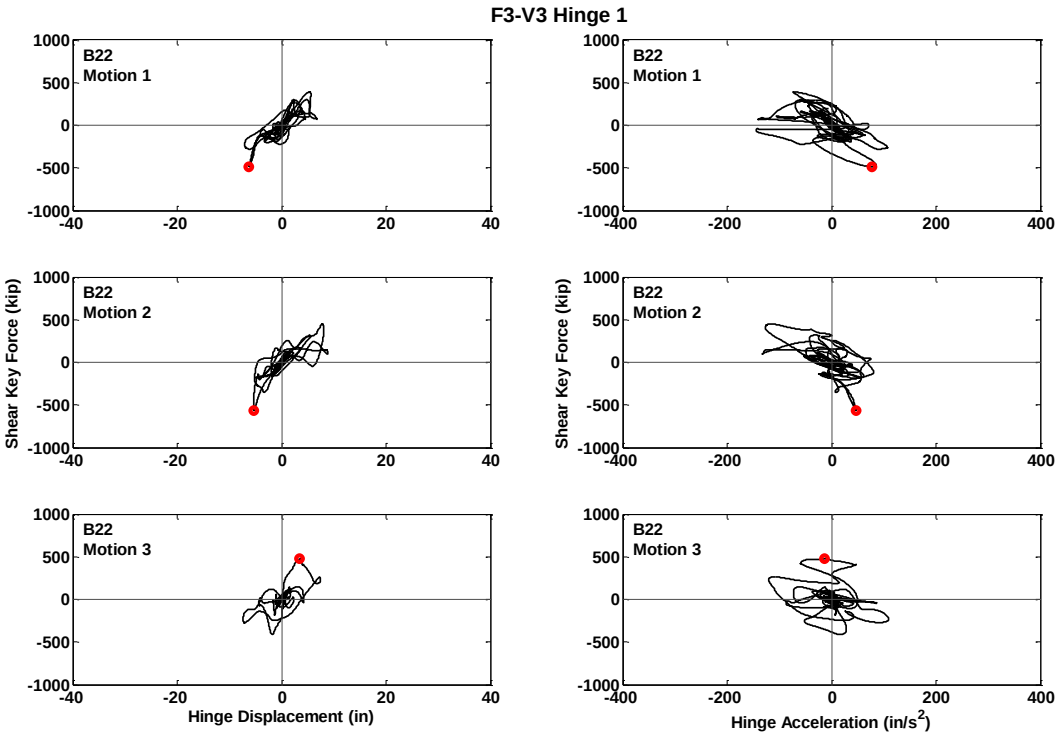

Figure C.176 Hysteresis Curves for Prototype F3-V3, Hinge 1, Motions B22

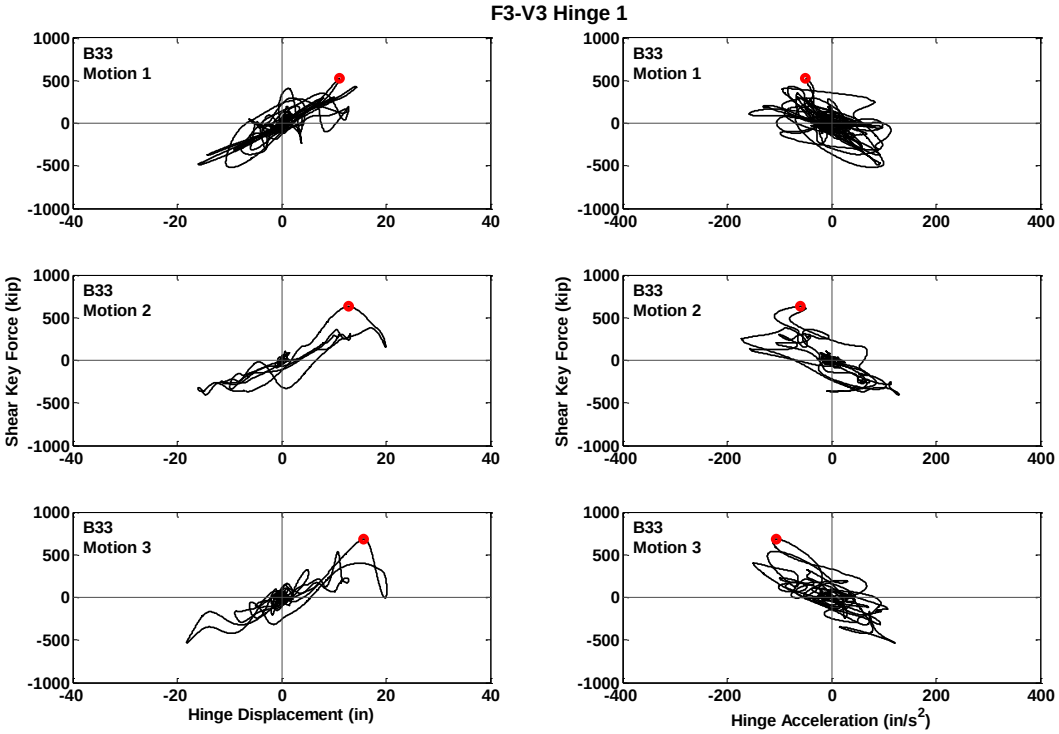

Figure C.177 Hysteresis Curves for Prototype F3-V3, Hinge 1, Motions B33

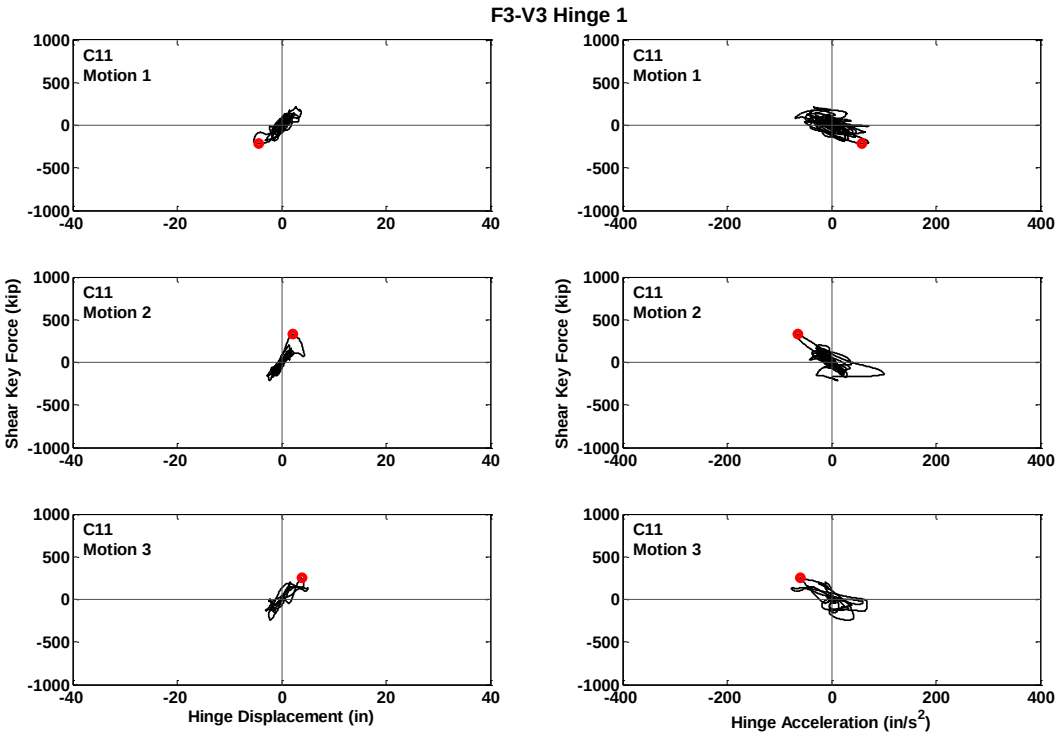

Figure C.178 Hysteresis Curves for Prototype F3-V3, Hinge 1, Motions C11

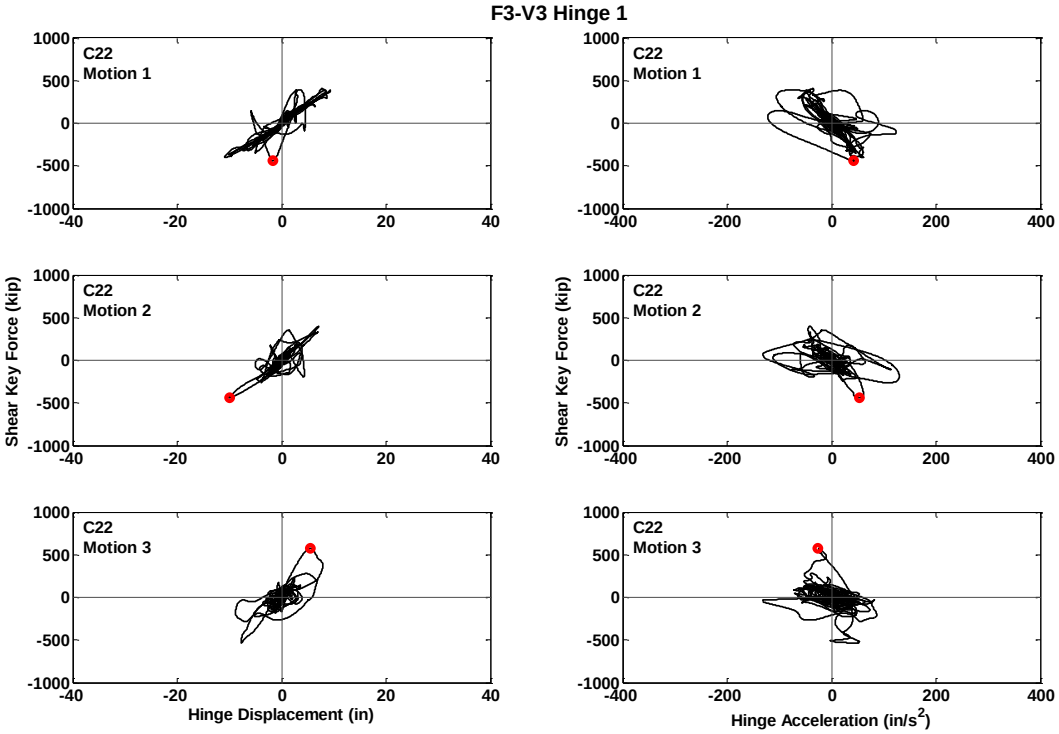

Figure C.179 Hysteresis Curves for Prototype F3-V3, Hinge 1, Motions C22

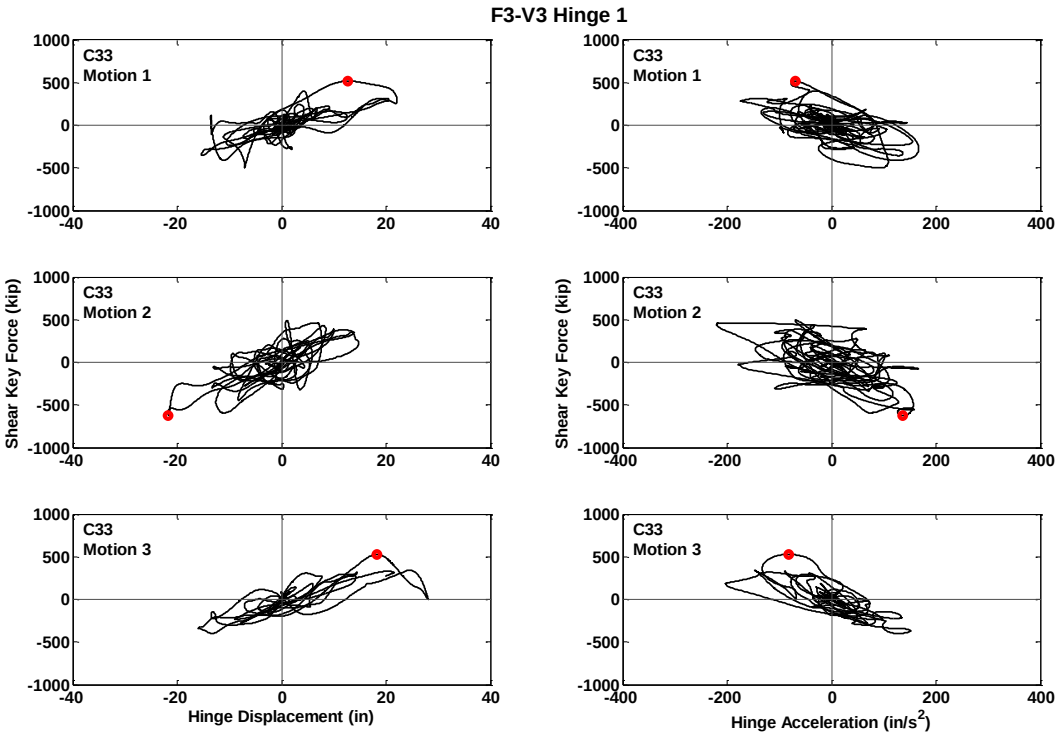

Figure C.180 Hysteresis Curves for Prototype F3-V3, Hinge 1, Motions B11

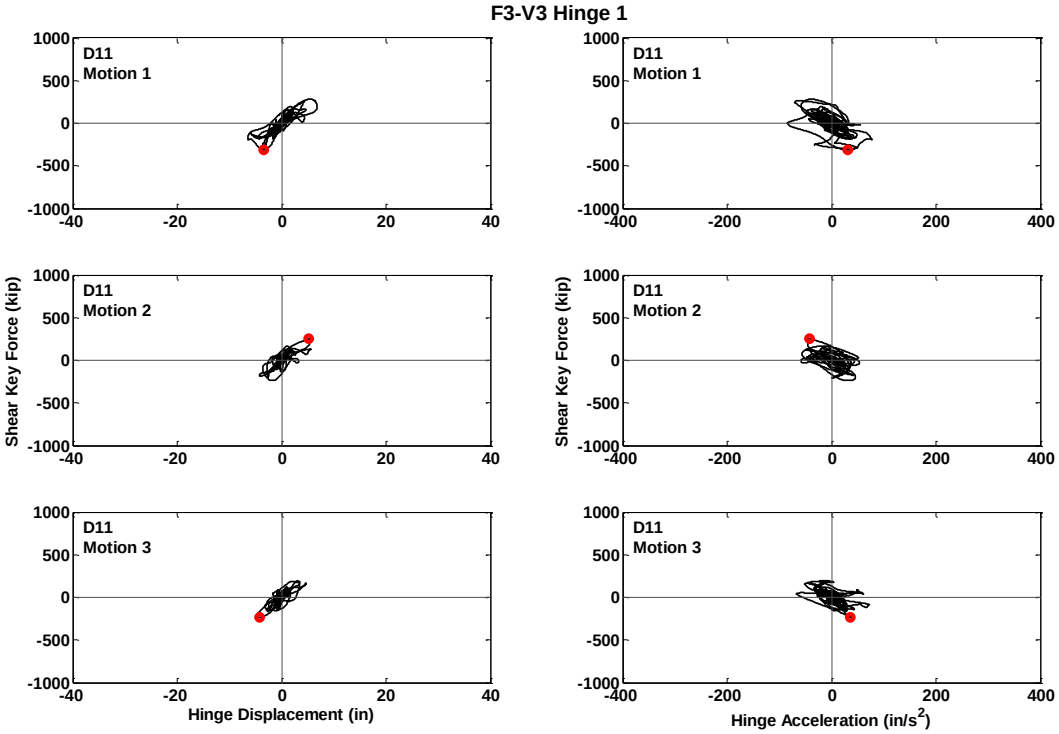

Figure C.181 Hysteresis Curves for Prototype F3-V3, Hinge 1, Motions D11

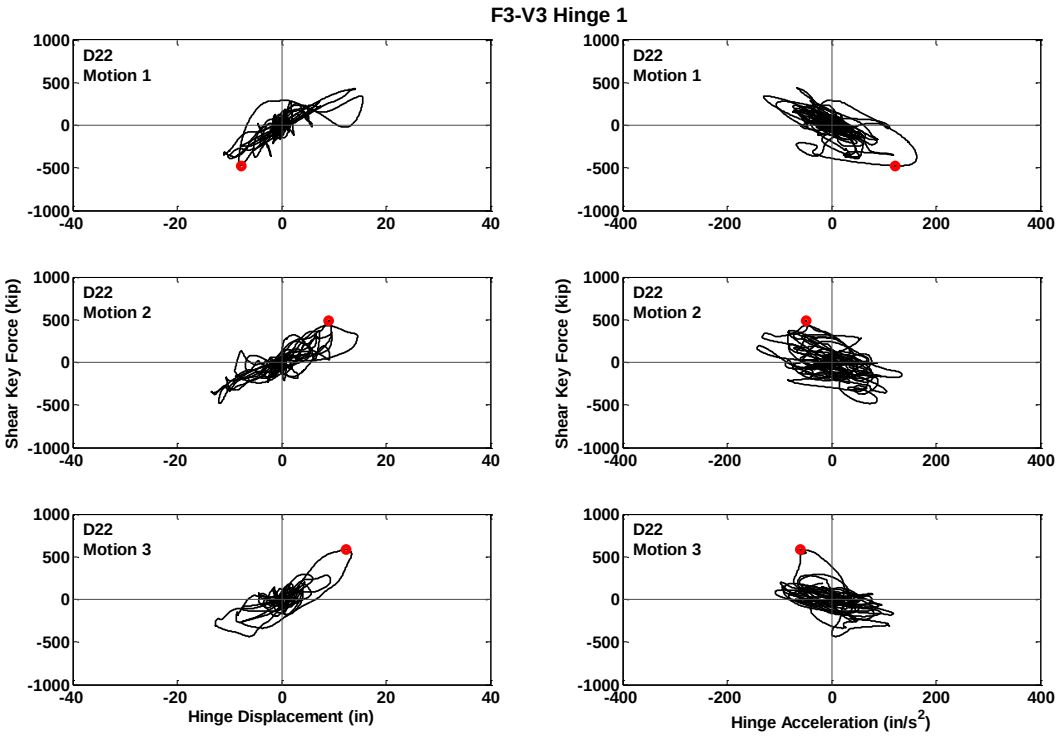

Figure C.182 Hysteresis Curves for Prototype F3-V3, Hinge 1, Motions D22

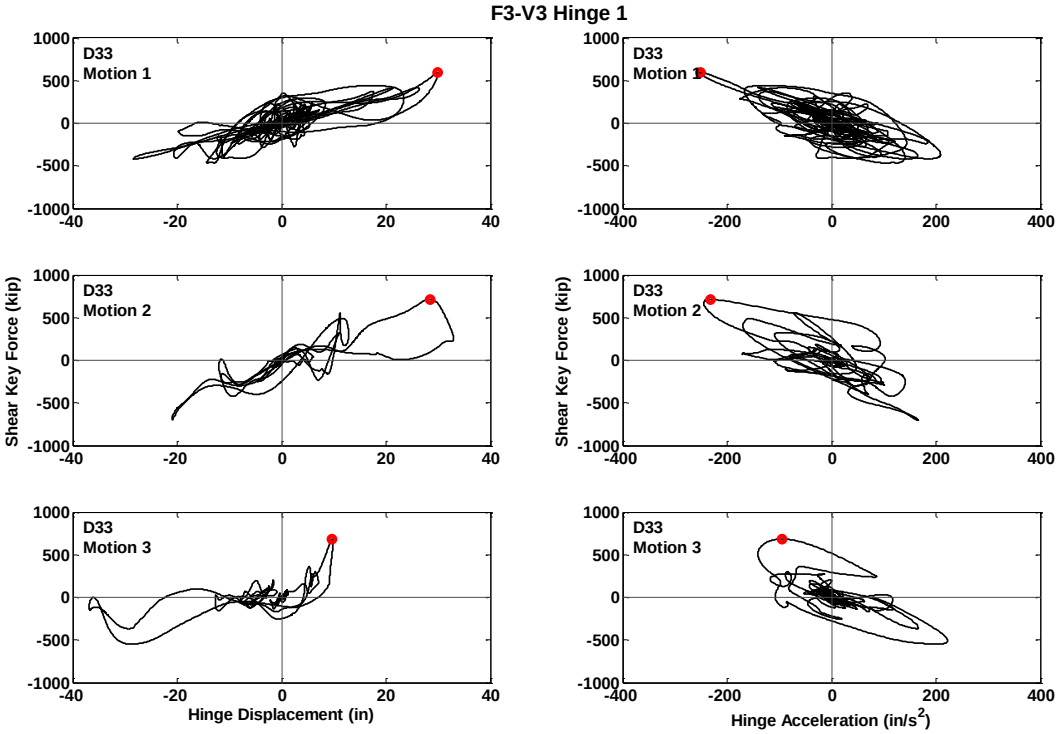

Figure C.183 Hysteresis Curves for Prototype F3-V3, Hinge 1, Motions D33

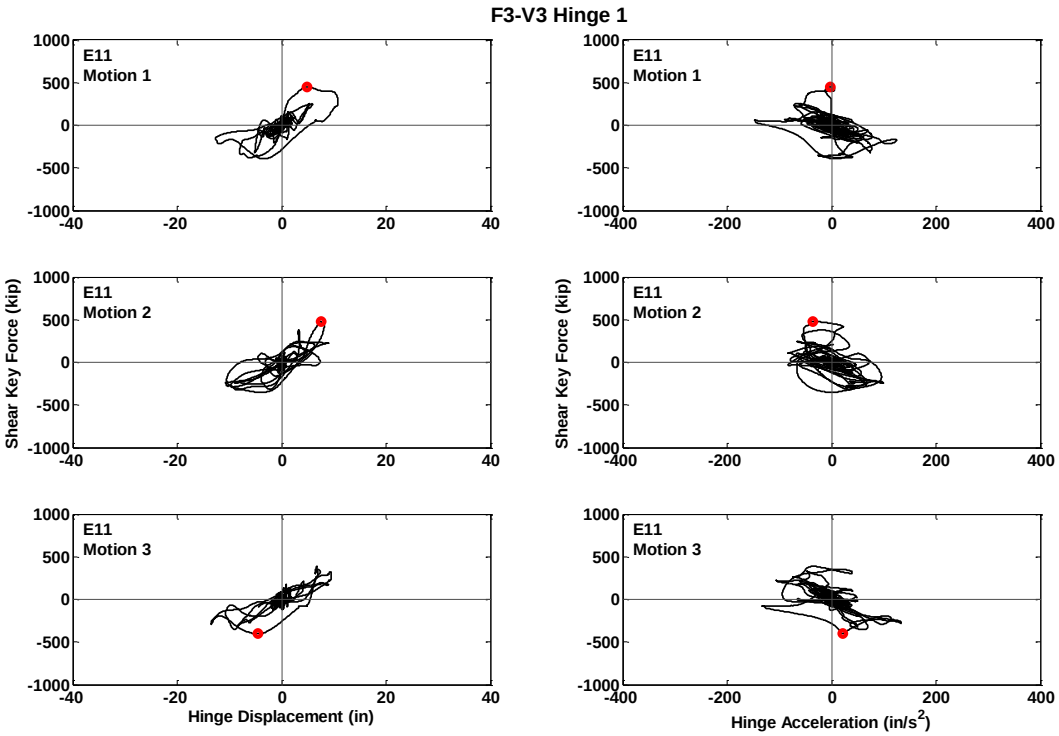

Figure C.184 Hysteresis Curves for Prototype F3-V3, Hinge 1, Motions E11

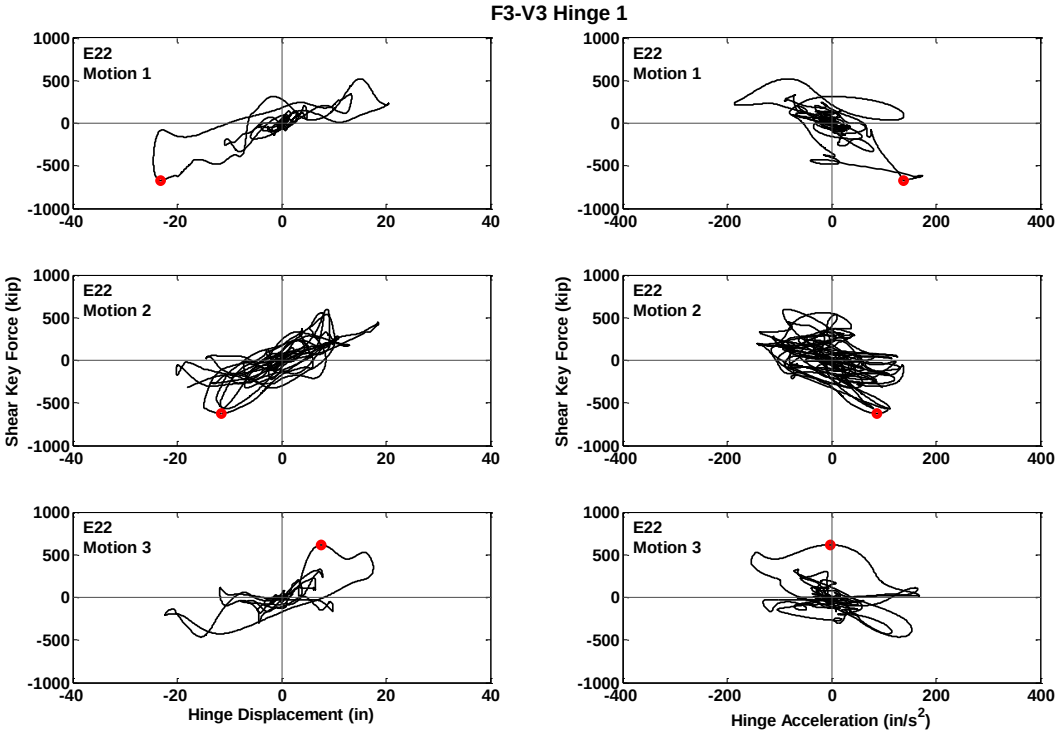

Figure C.185 Hysteresis Curves for Prototype F3-V3, Hinge 1, Motions E22

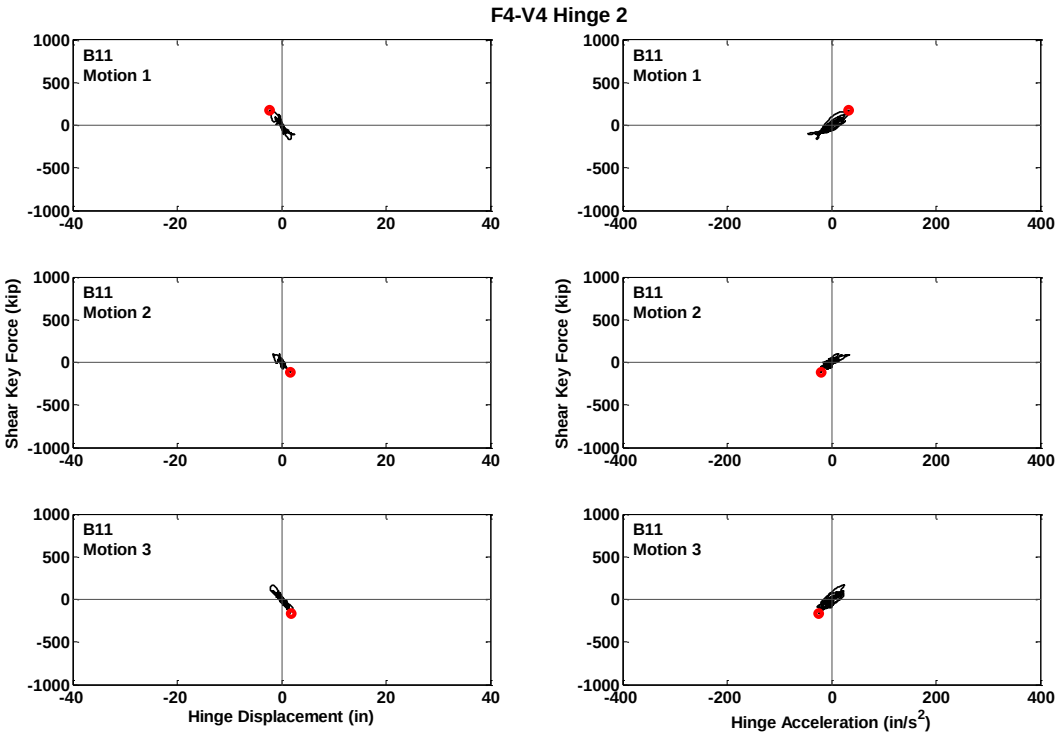

Figure C.186 Hysteresis Curves for Prototype F4-V4, Hinge 2, Motions B11

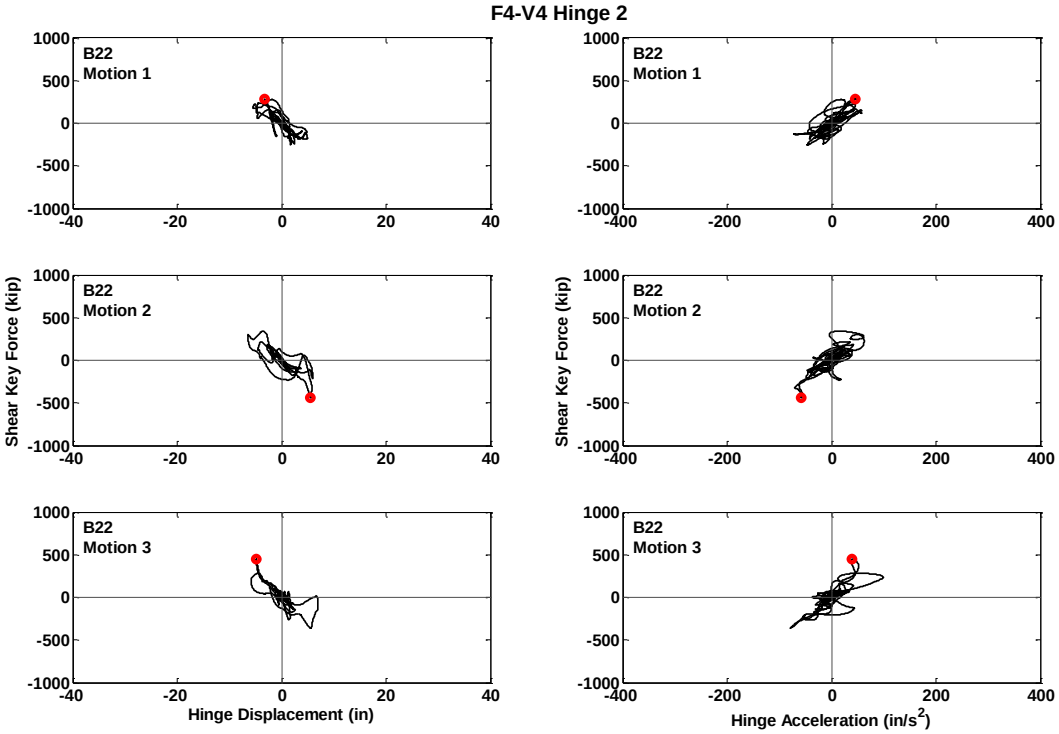

Figure C.187 Hysteresis Curves for Prototype F4-V4, Hinge 2, Motions B22

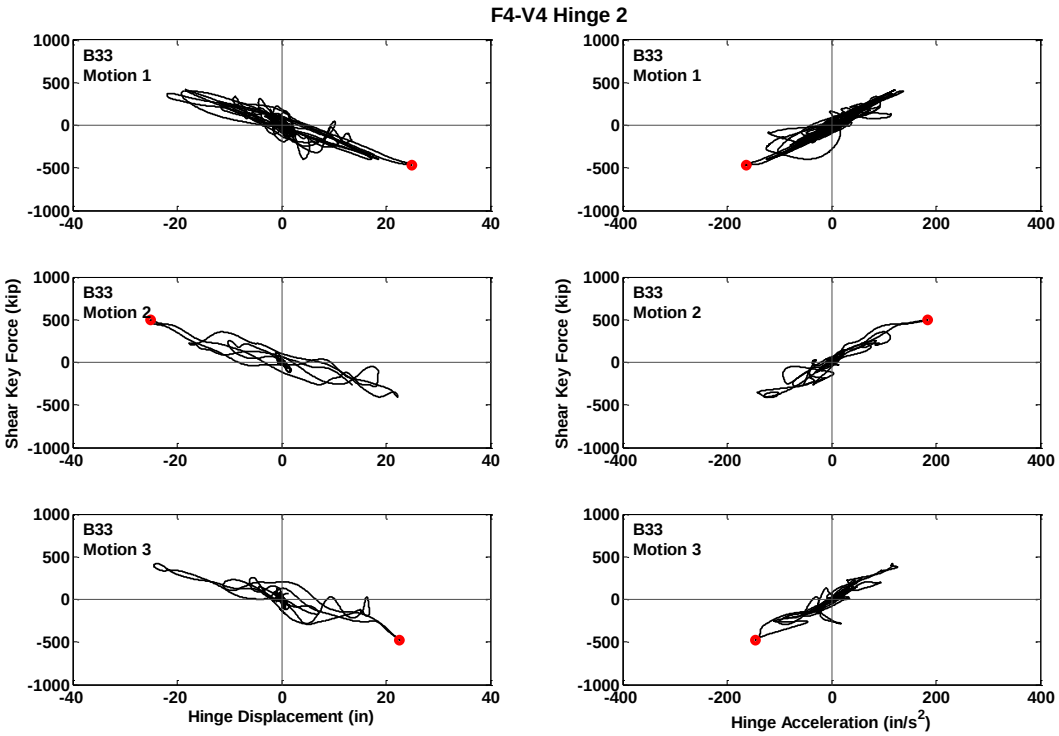

Figure C.188 Hysteresis Curves for Prototype F4-V4, Hinge 2, Motions B33

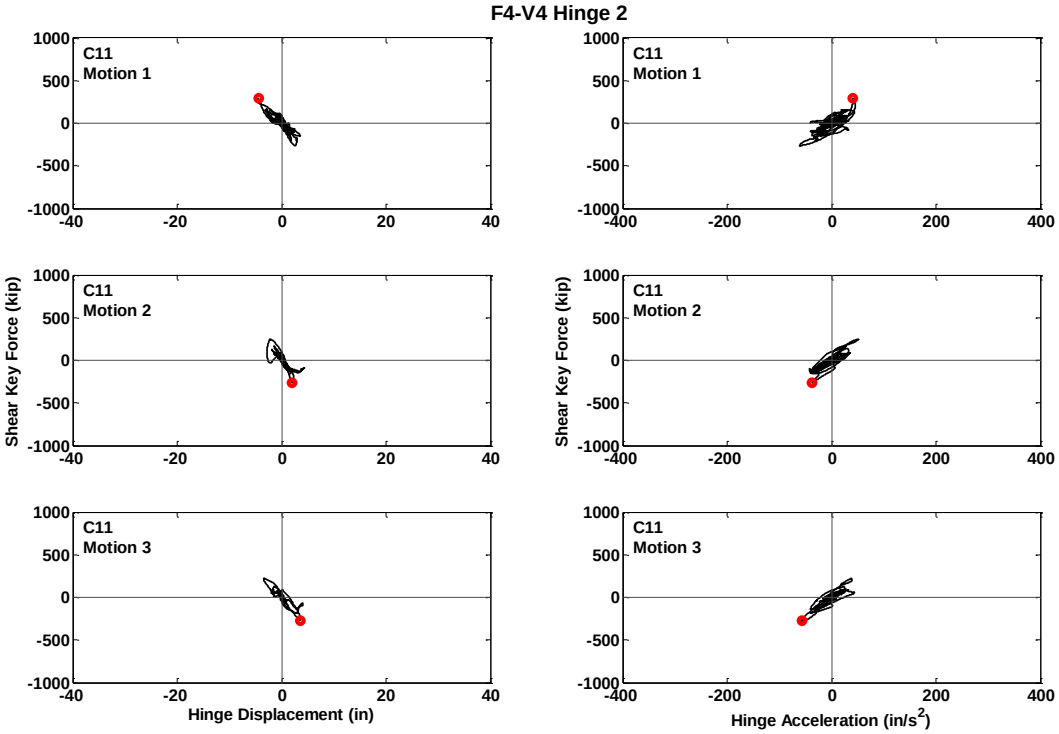

Figure C.189 Hysteresis Curves for Prototype F4-V4, Hinge 2, Motions C11

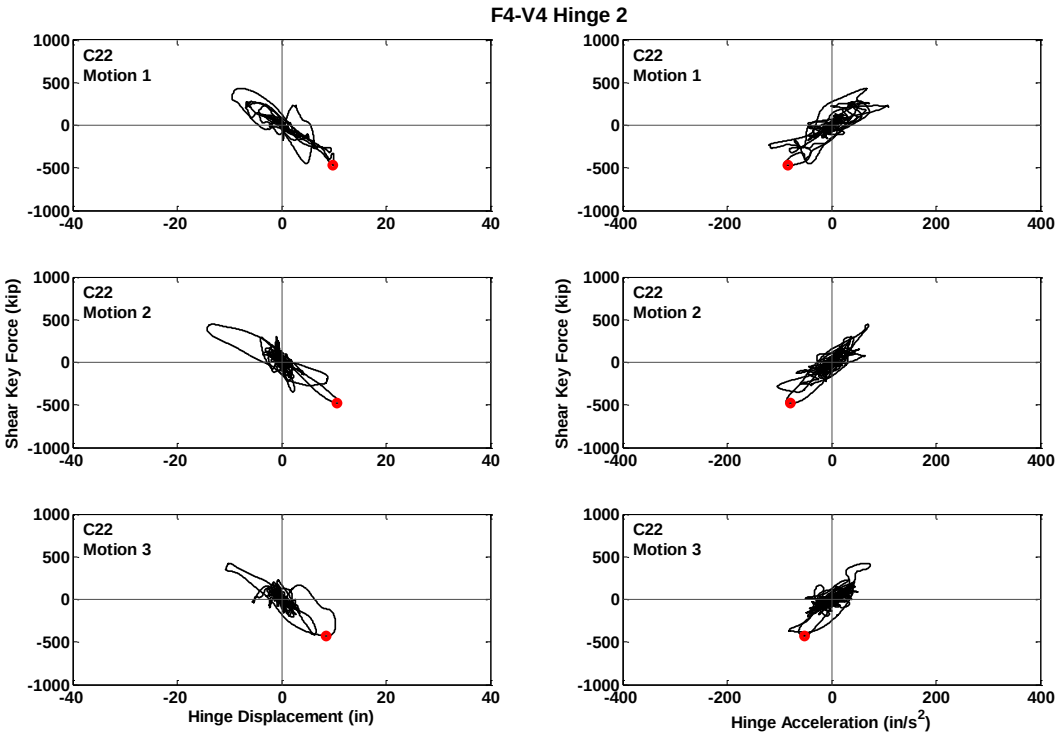

Figure C.190 Hysteresis Curves for Prototype F4-V4, Hinge 2, Motions C22

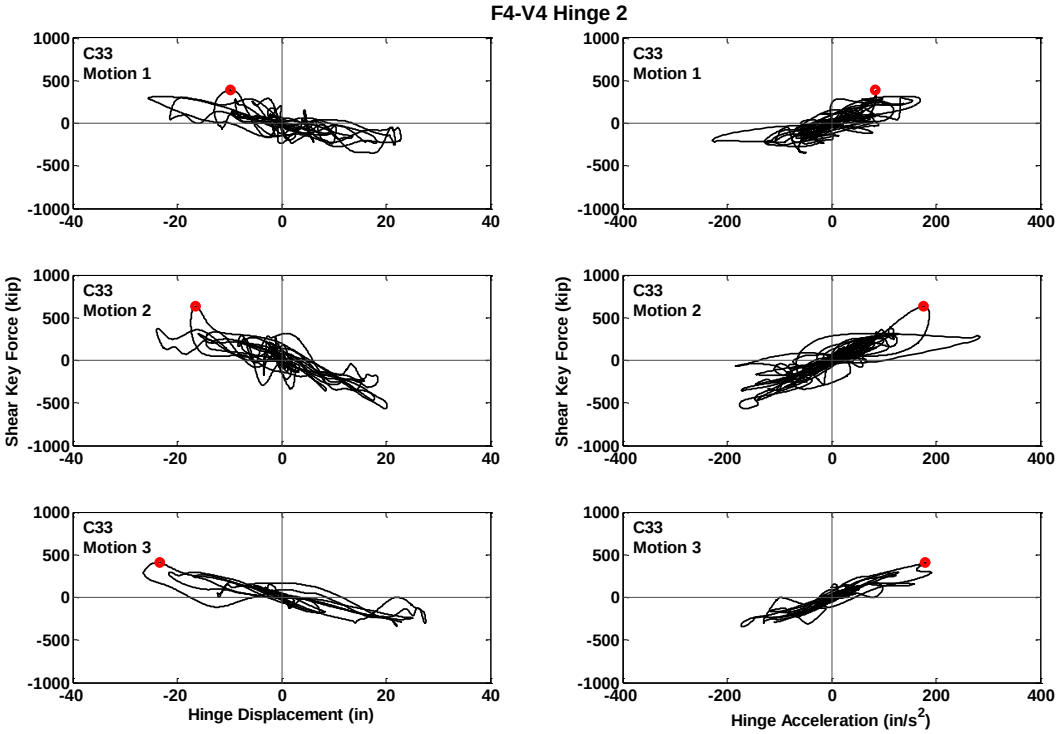

Figure C.191 Hysteresis Curves for Prototype F4-V4, Hinge 2, Motions C33

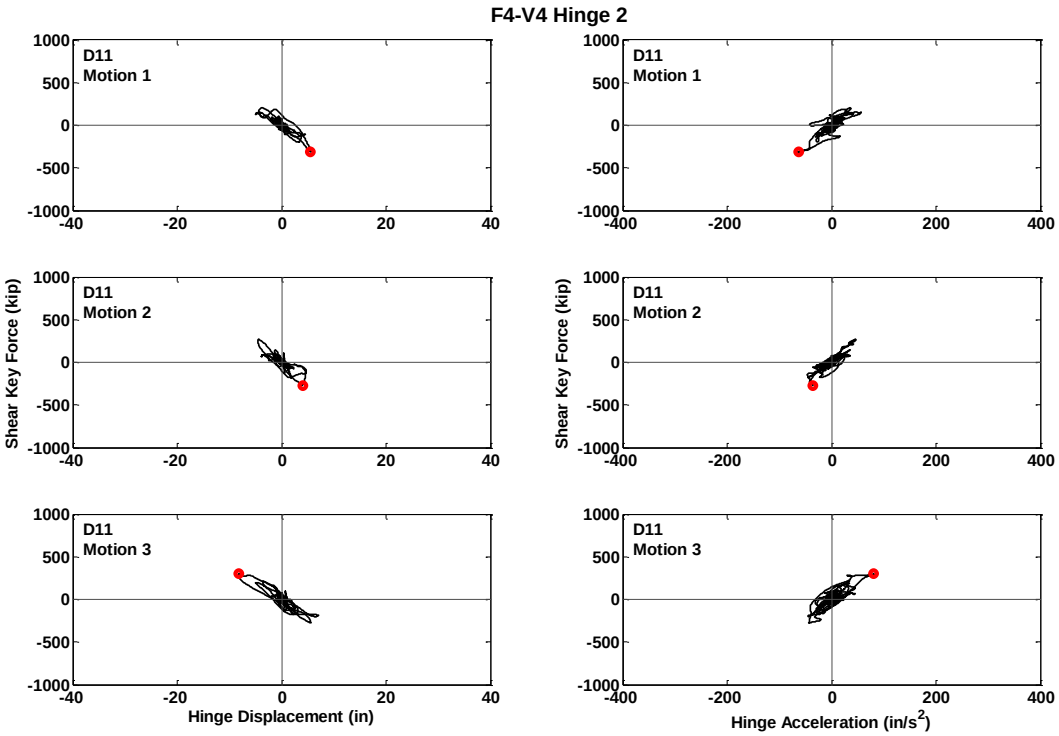

Figure C.192 Hysteresis Curves for Prototype F4-V4, Hinge 2, Motions D11

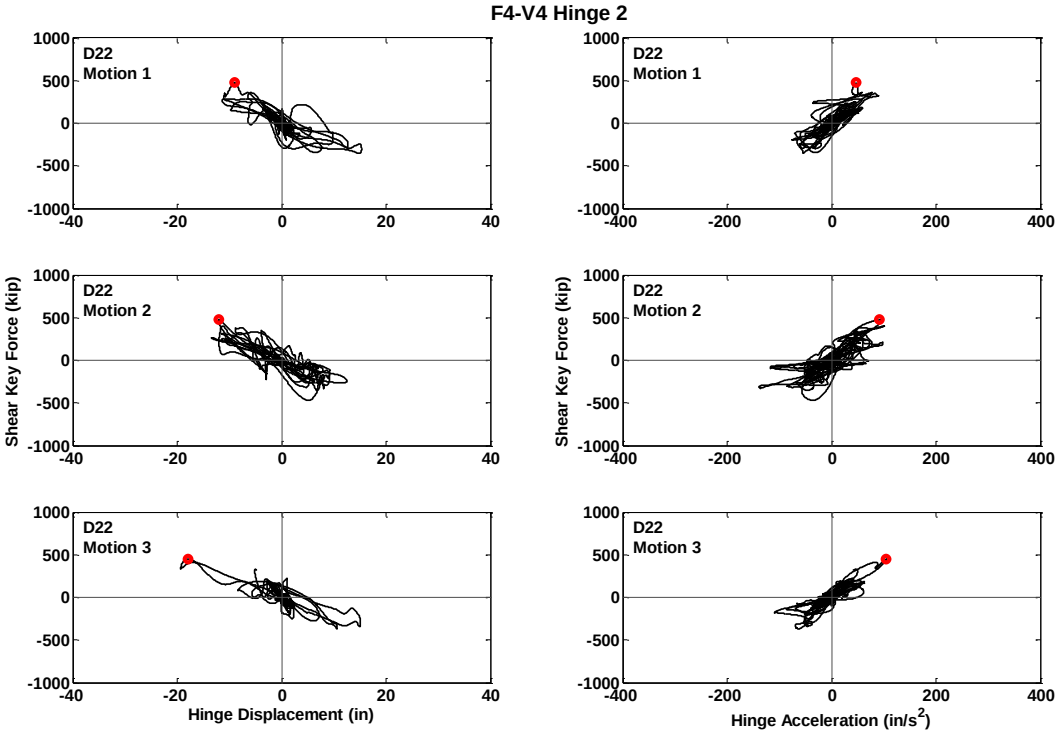

Figure C.193 Hysteresis Curves for Prototype F4-V4, Hinge 2, Motions D22

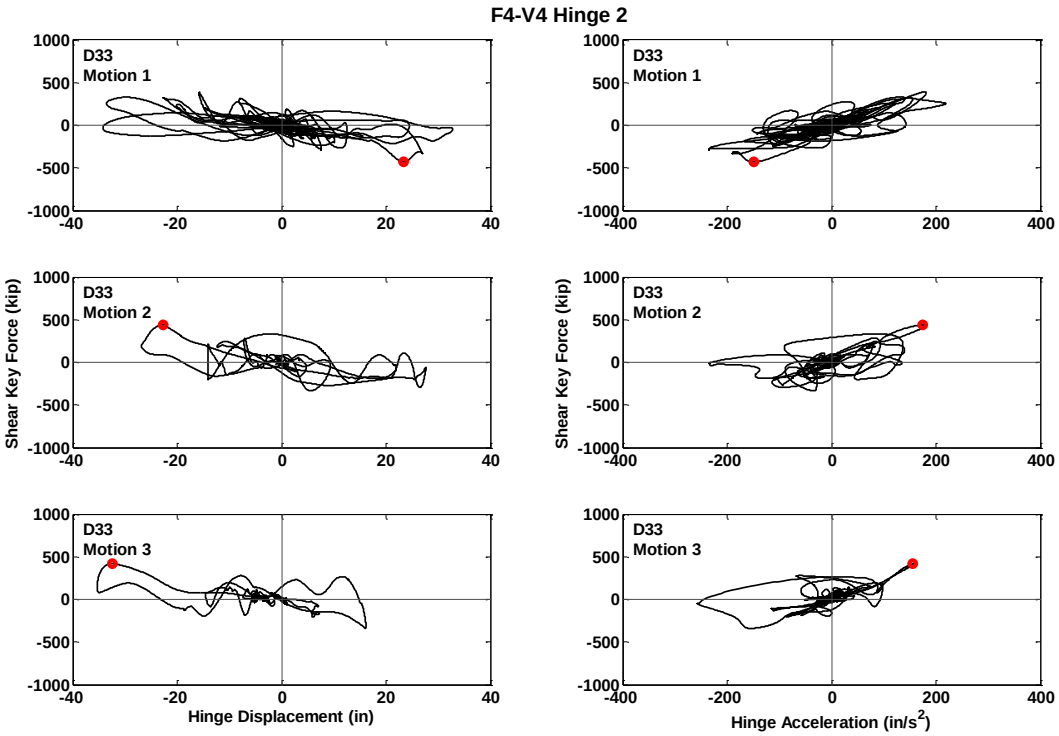

Figure C.194 Hysteresis Curves for Prototype F4-V4, Hinge 2, Motions D33

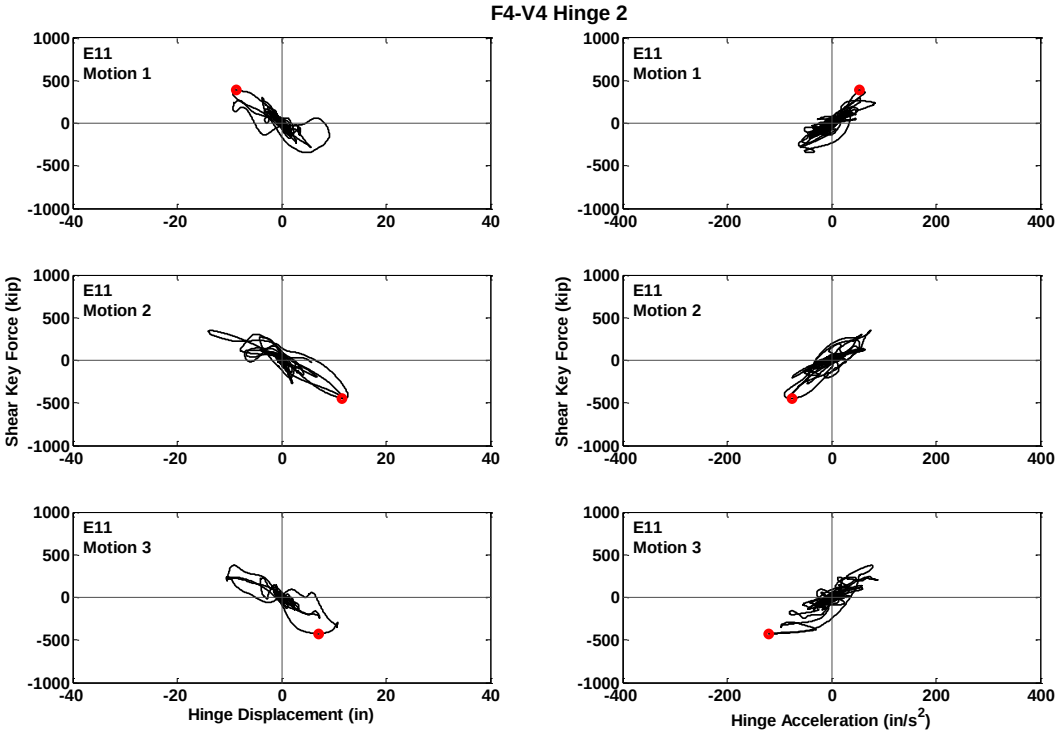

Figure C.195 Hysteresis Curves for Prototype F4-V4, Hinge 2, Motions E11

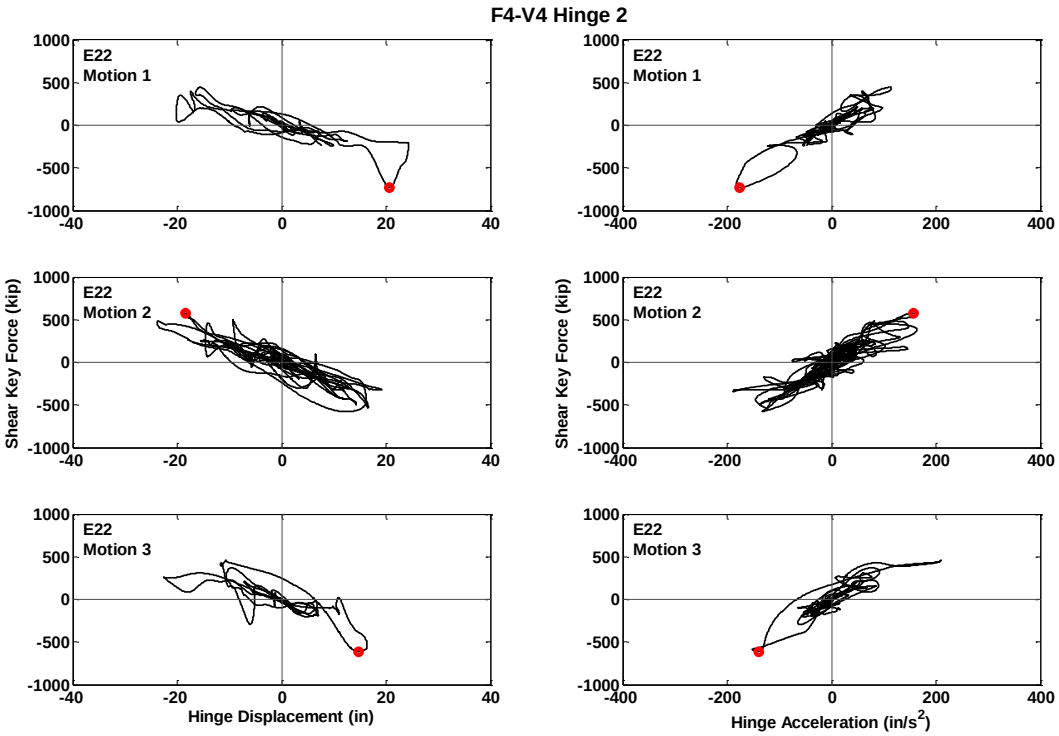

Figure C.196 Hysteresis Curves for Prototype F4-V4, Hinge 2, Motions E22

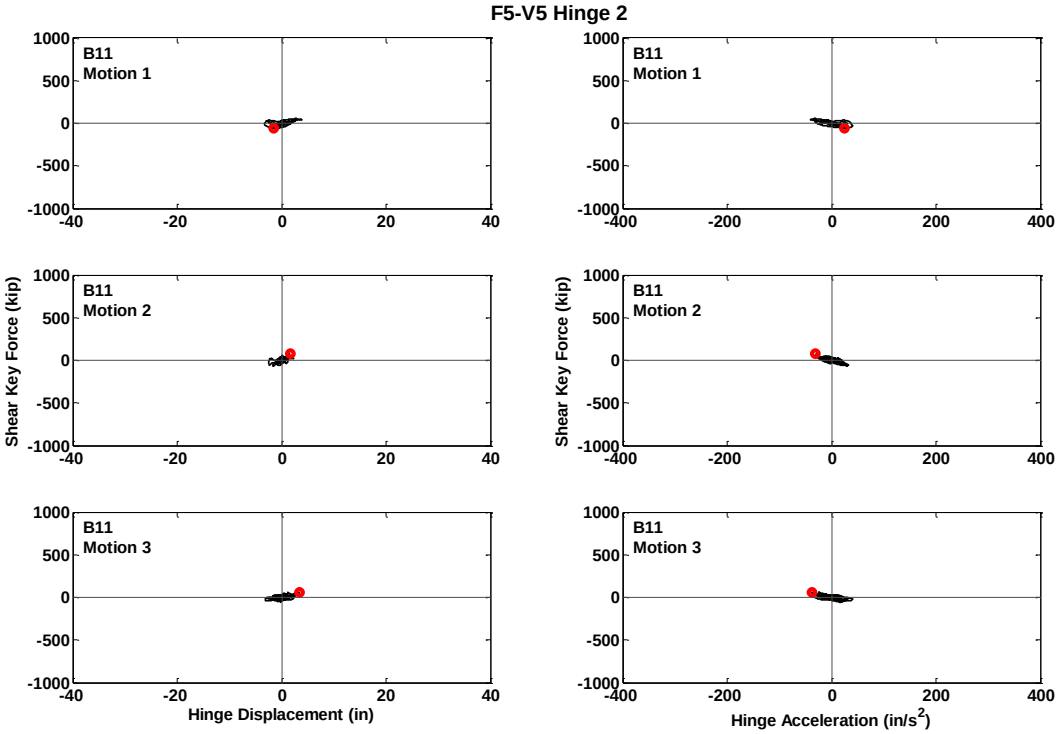

Figure C.197 Hysteresis Curves for Prototype F5-V5, Hinge 2, Motions B11

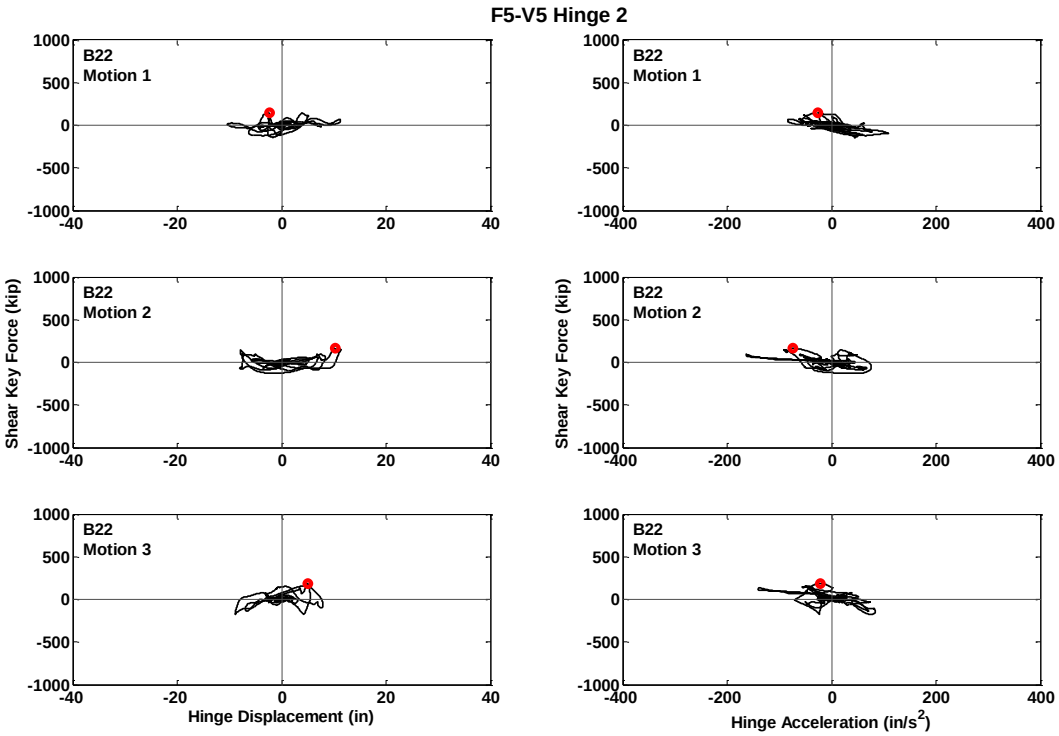

Figure C.198 Hysteresis Curves for Prototype F5-V5, Hinge 2, Motions B22

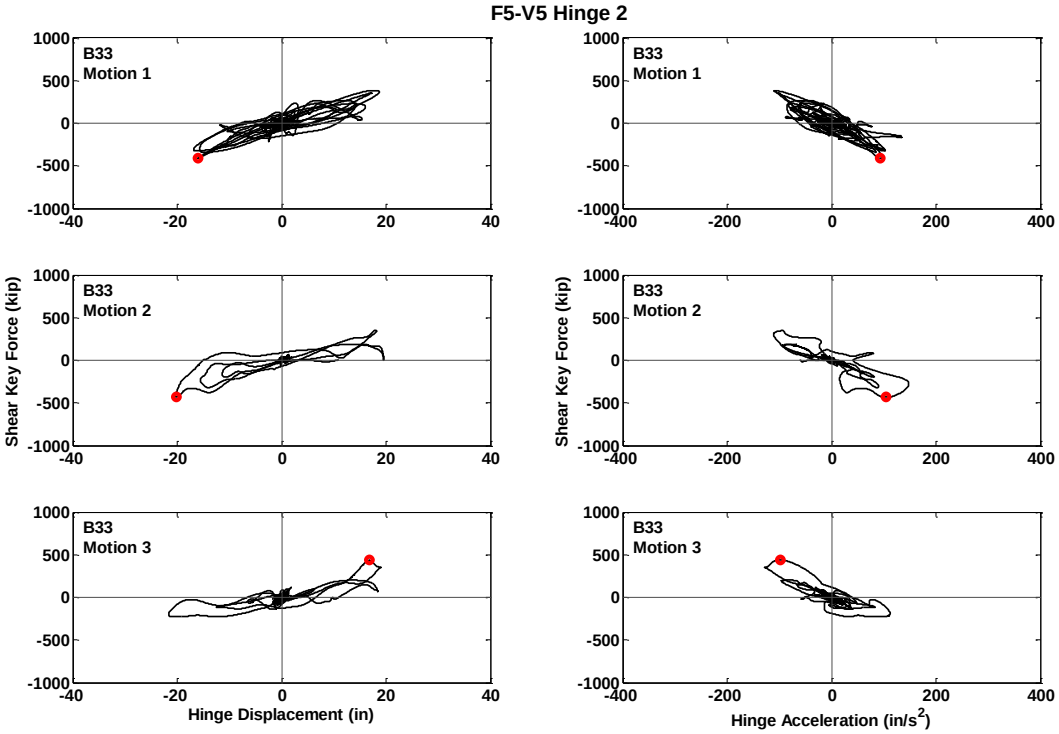

Figure C.199 Hysteresis Curves for Prototype F5-V5, Hinge 2, Motions B33

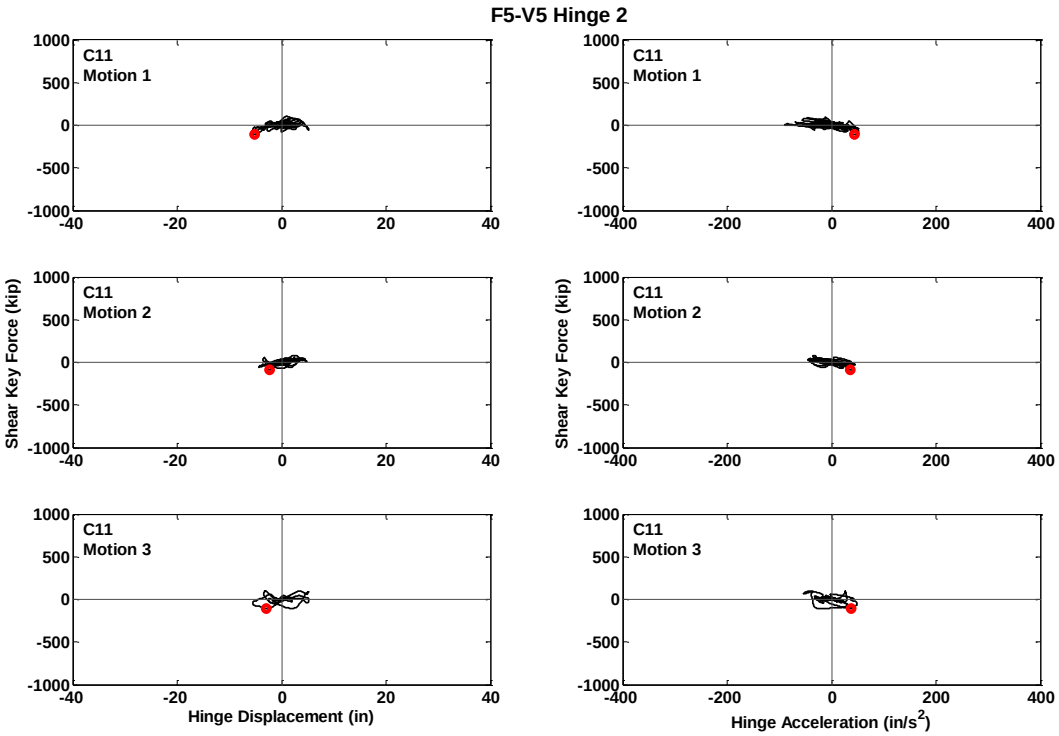

Figure C.200 Hysteresis Curves for Prototype F5-V5, Hinge 2, Motions C11

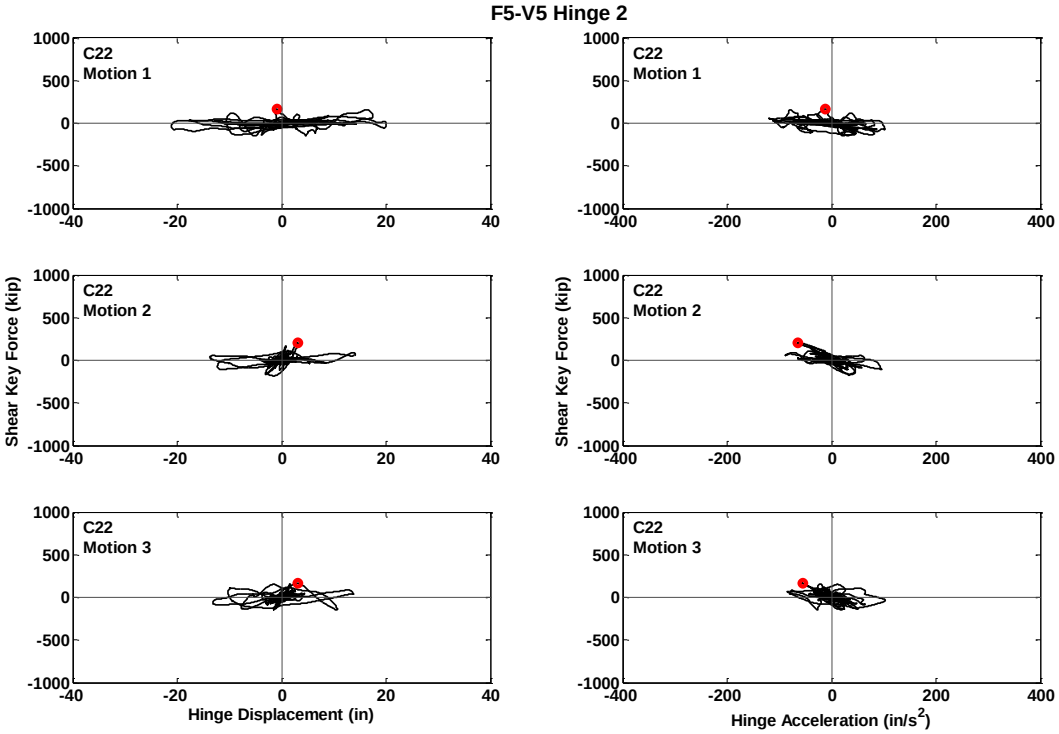

Figure C.201 Hysteresis Curves for Prototype F5-V5, Hinge 2, Motions C22

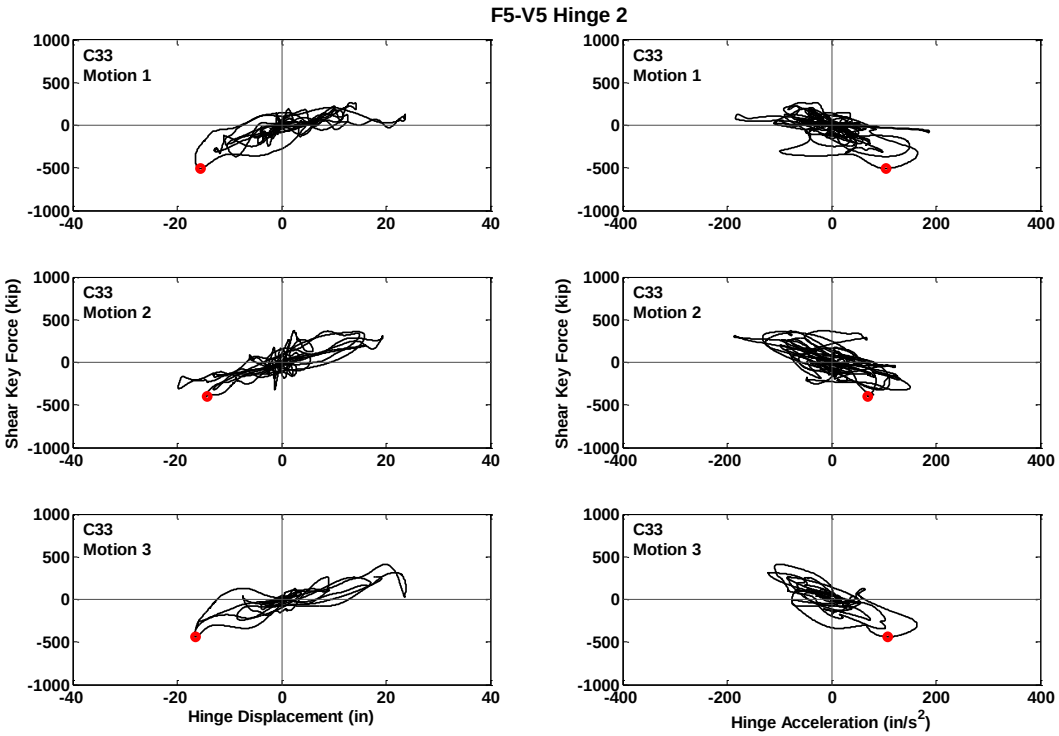

Figure C.202 Hysteresis Curves for Prototype F5-V5, Hinge 2, Motions C33

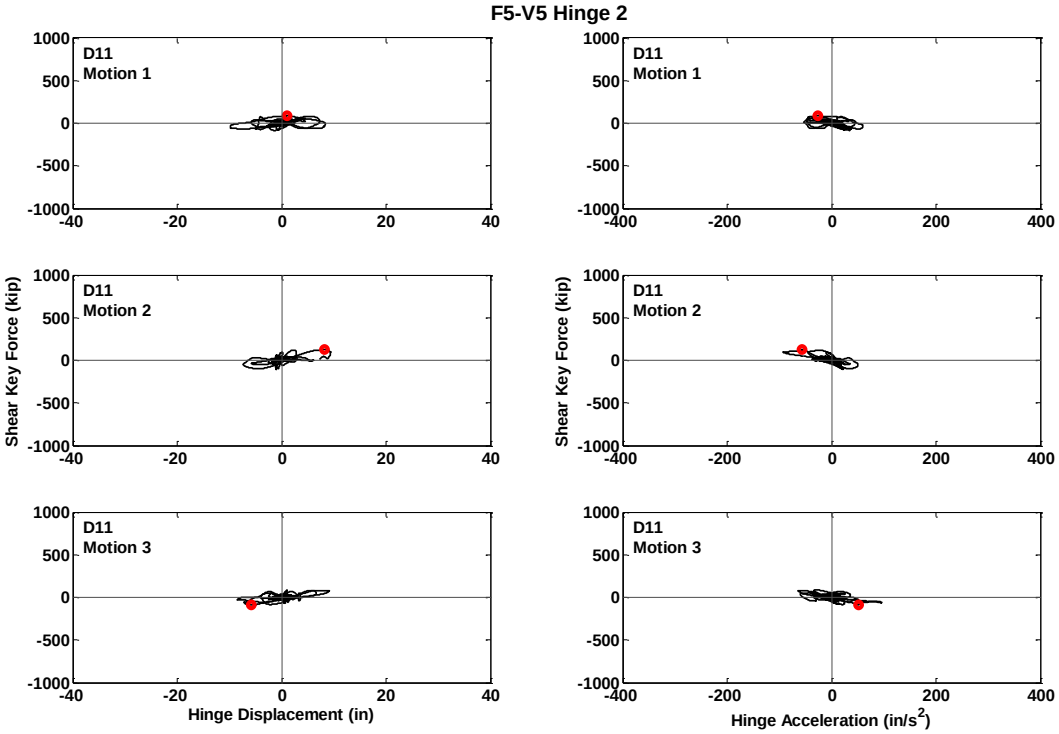

Figure C.203 Hysteresis Curves for Prototype F5-V5, Hinge 2, Motions D11

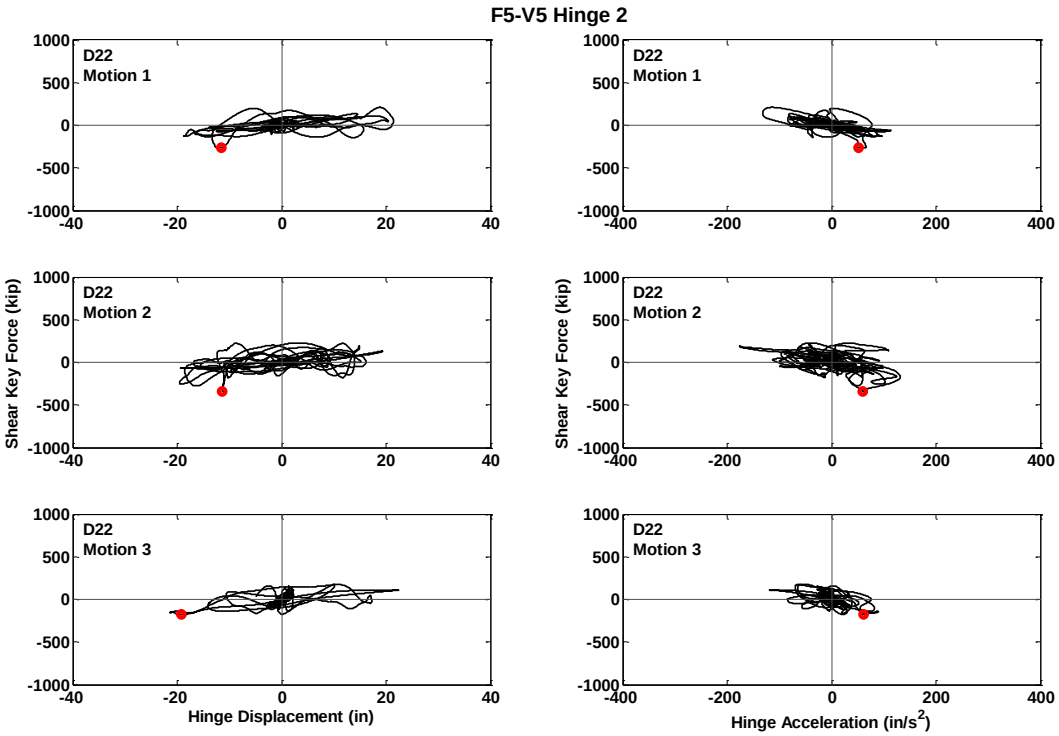

Figure C.204 Hysteresis Curves for Prototype F5-V5, Hinge 2, Motions D22

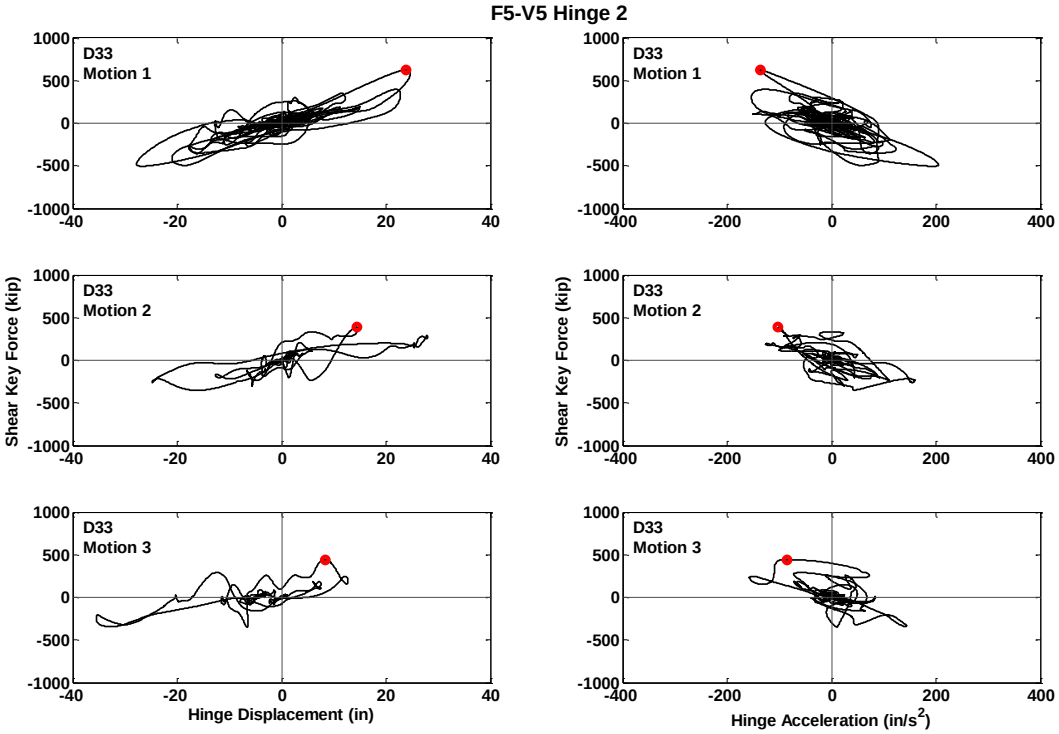

Figure C.205 Hysteresis Curves for Prototype F5-V5, Hinge 2, Motions D33

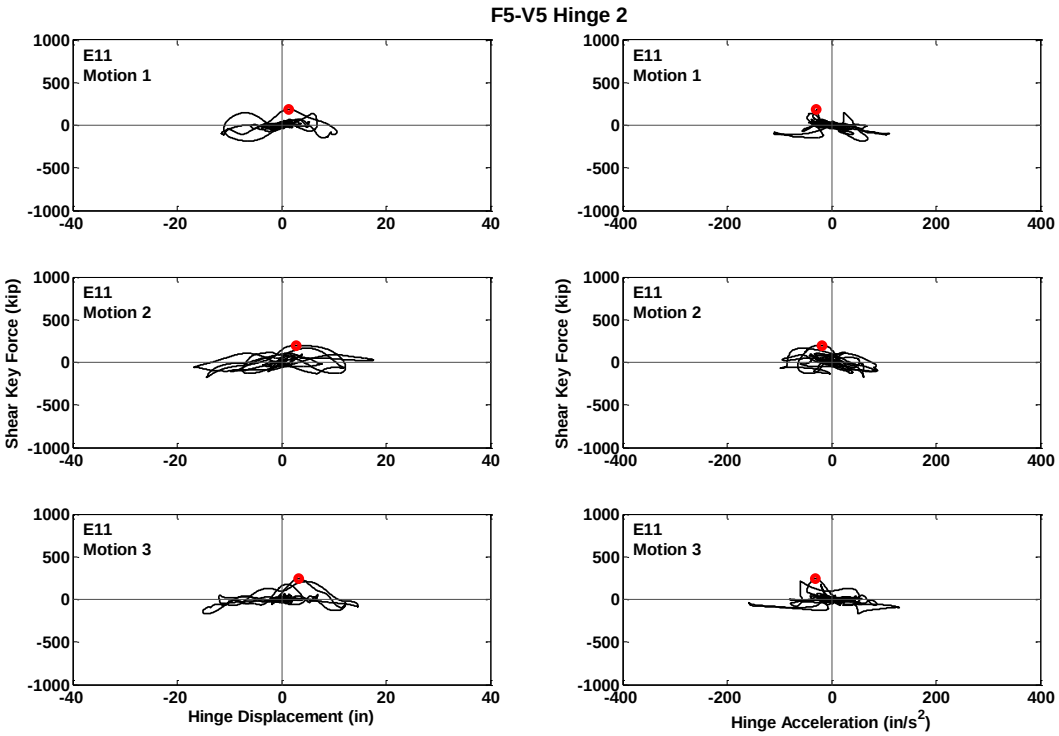

Figure C.206 Hysteresis Curves for Prototype F5-V5, Hinge 2, Motions E11

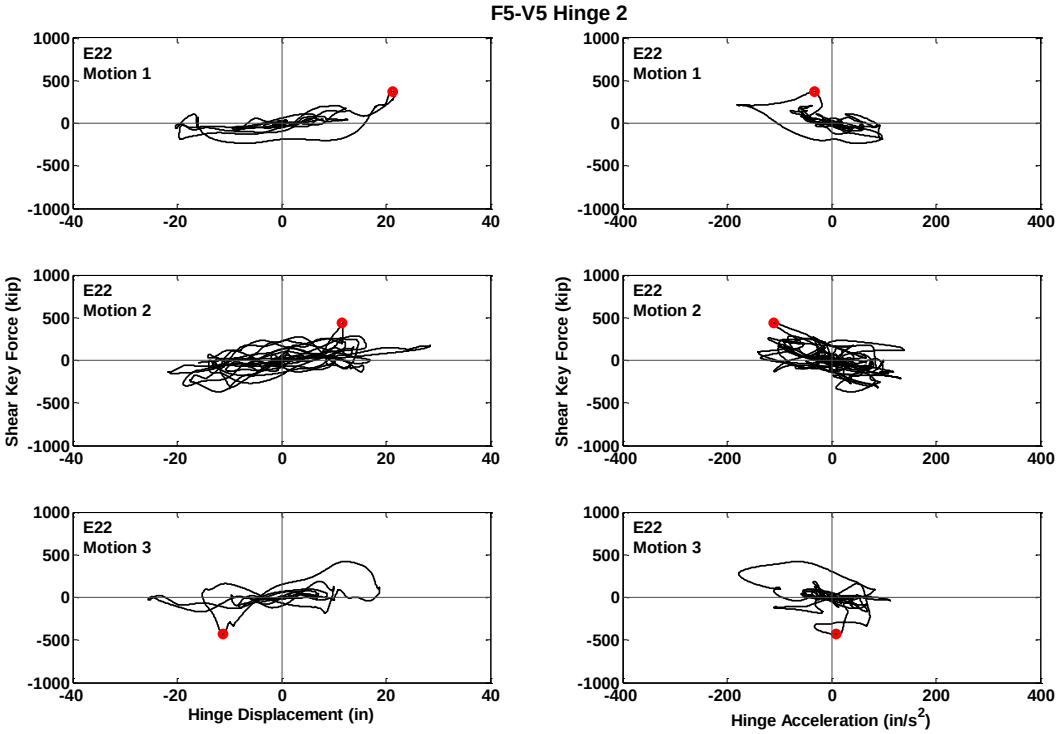

Figure C.207 Hysteresis Curves for Prototype F5-V5, Hinge 2, Motions E22

PART-3b: Hysteresis Curves for Two-Column Bent Prototypes.

Shear Key Force vs. Transverse Displacement and Shear Key Force vs. Transverse Acceleration.

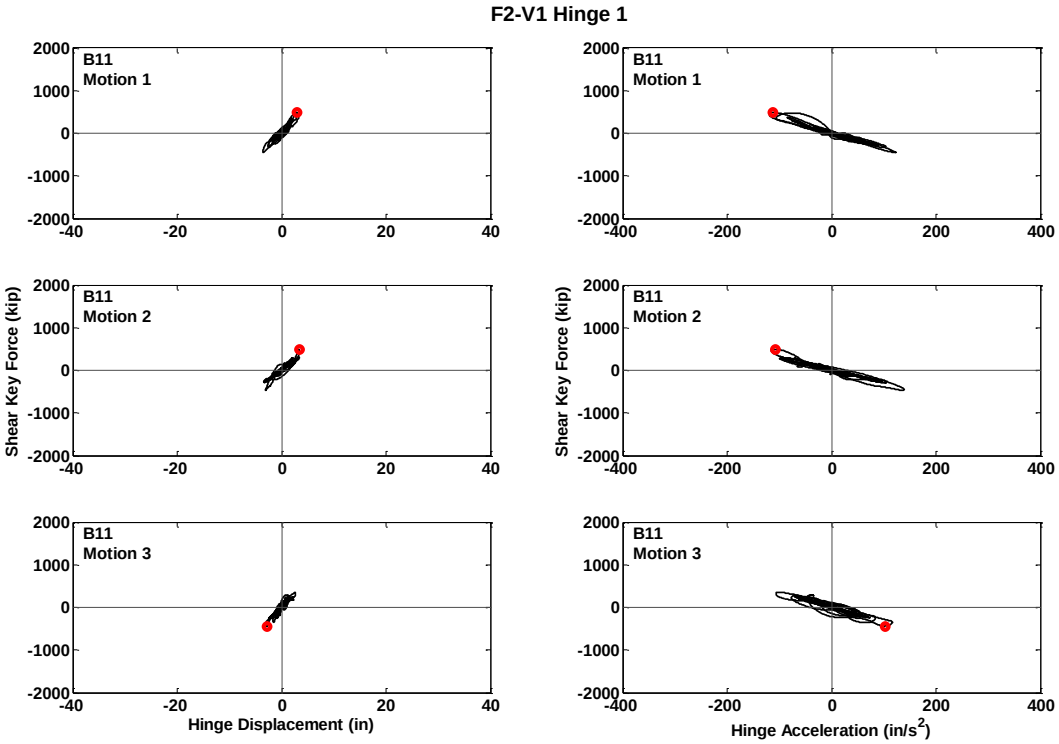

Figure C.208 Hysteresis Curves for Prototype F2-V1, Hinge 1, Motions B11

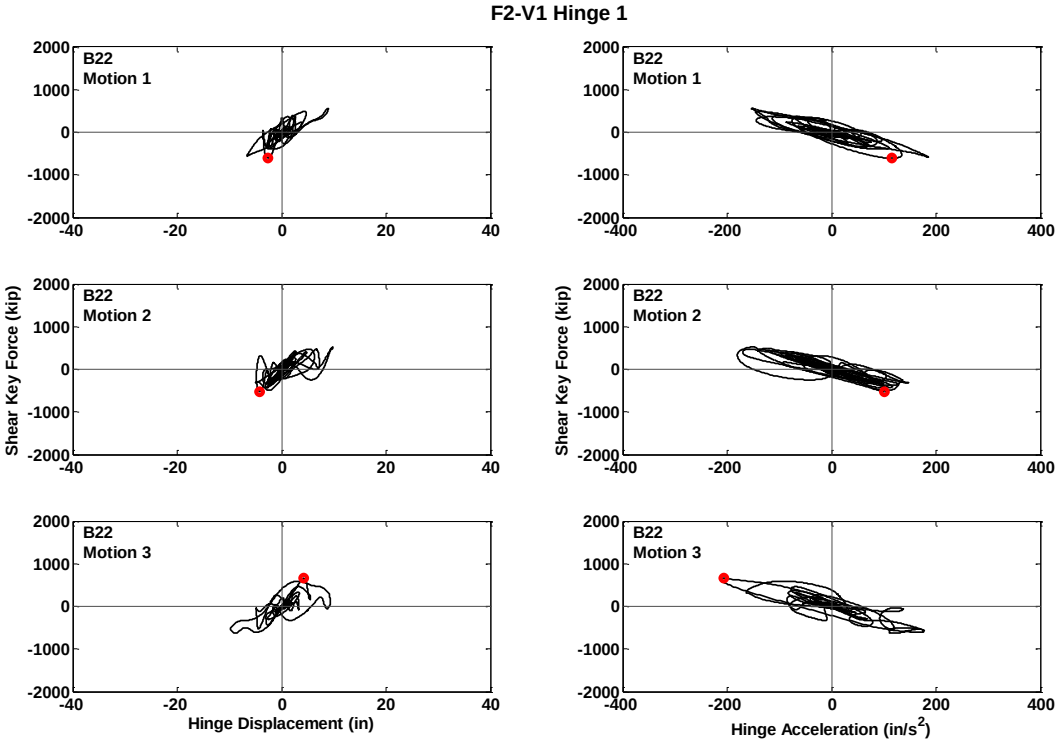

Figure C.209 Hysteresis Curves for Prototype F2-V1, Hinge 1, Motions B22

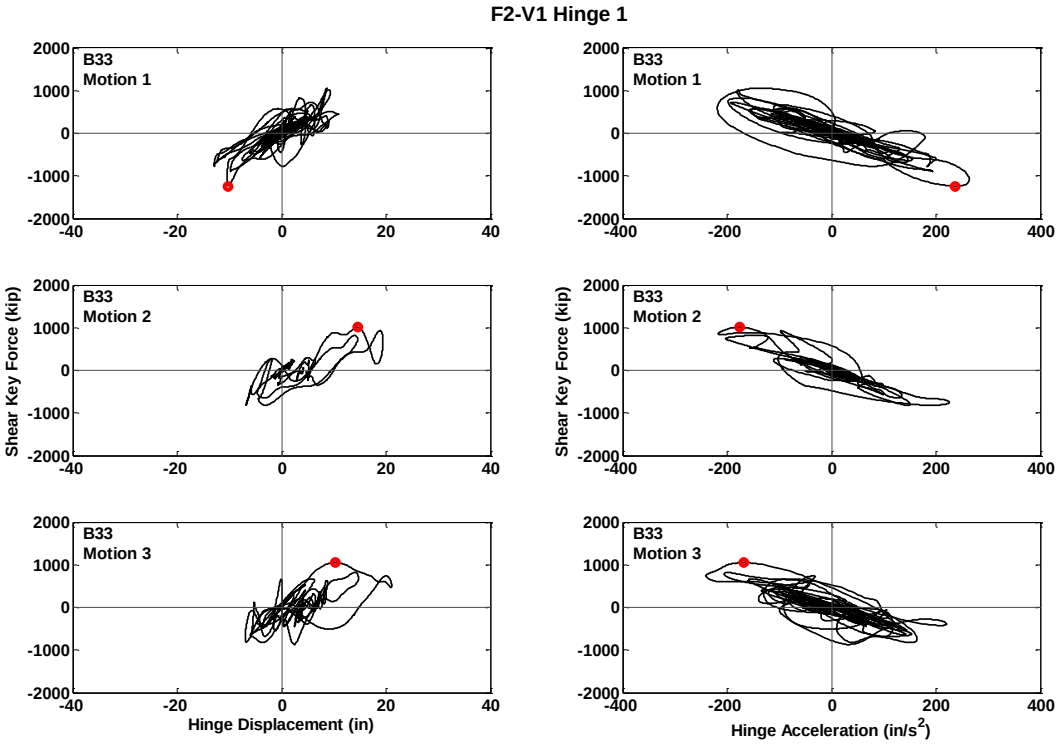

Figure C.210 Hysteresis Curves for Prototype F2-V1, Hinge 1, Motions B33

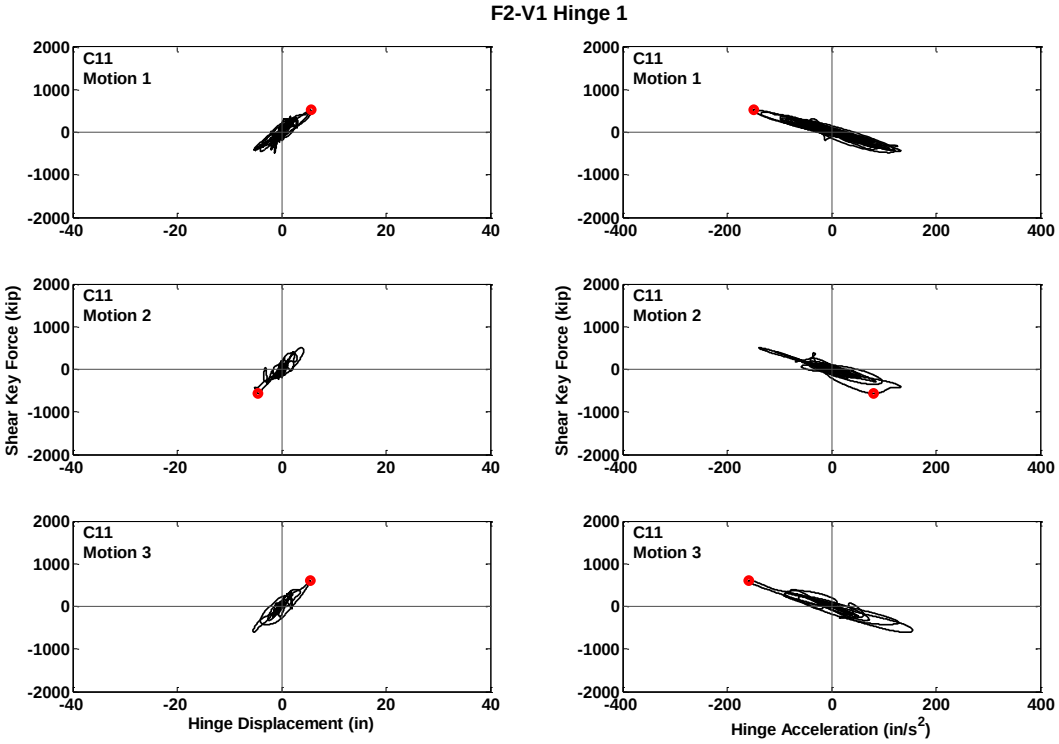

Figure C.211 Hysteresis Curves for Prototype F2-V1, Hinge 1, Motions C11

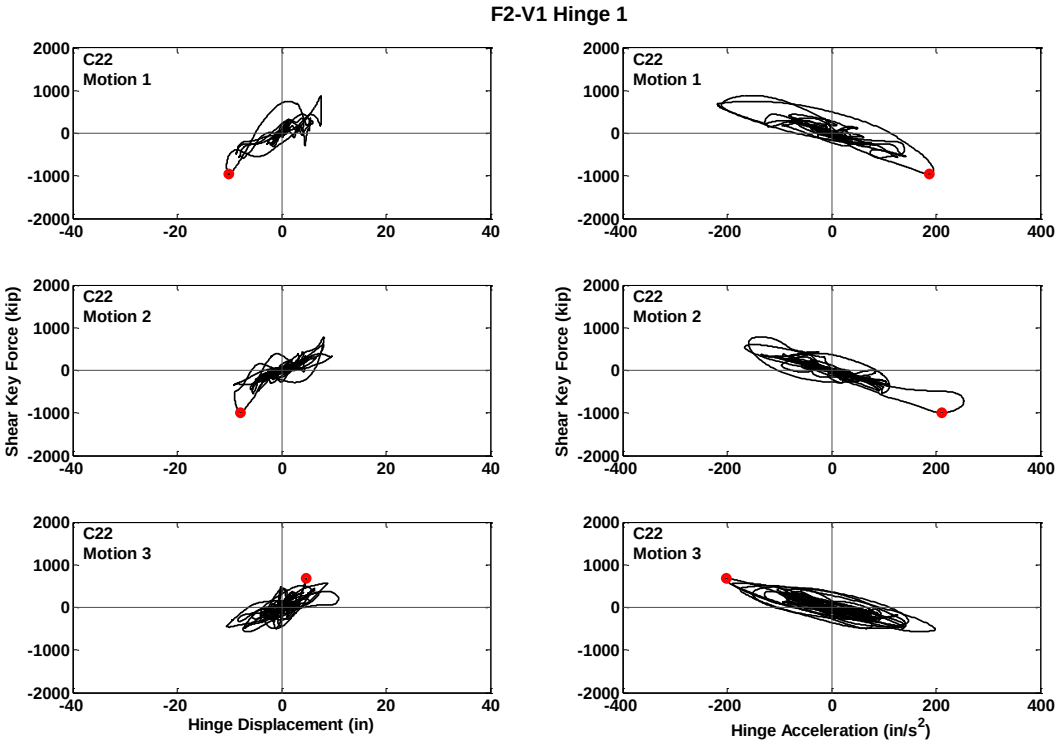

Figure C.212 Hysteresis Curves for Prototype F2-V1, Hinge 1, Motions C22

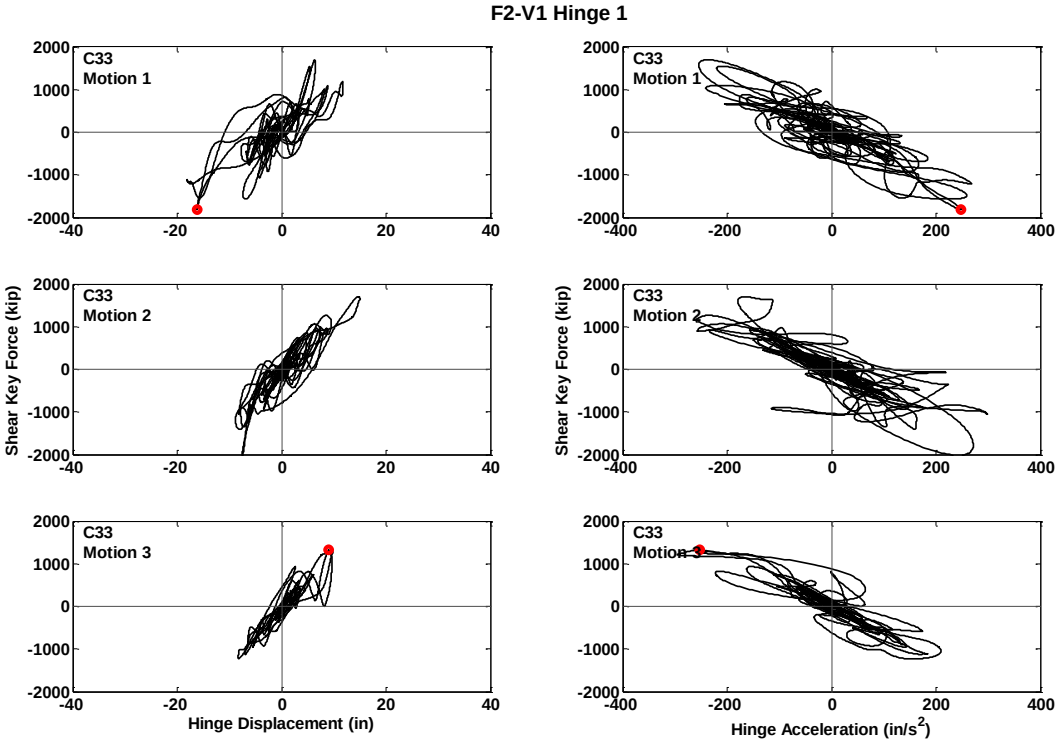

Figure C.213 Hysteresis Curves for Prototype F2-V1, Hinge 1, Motions C33

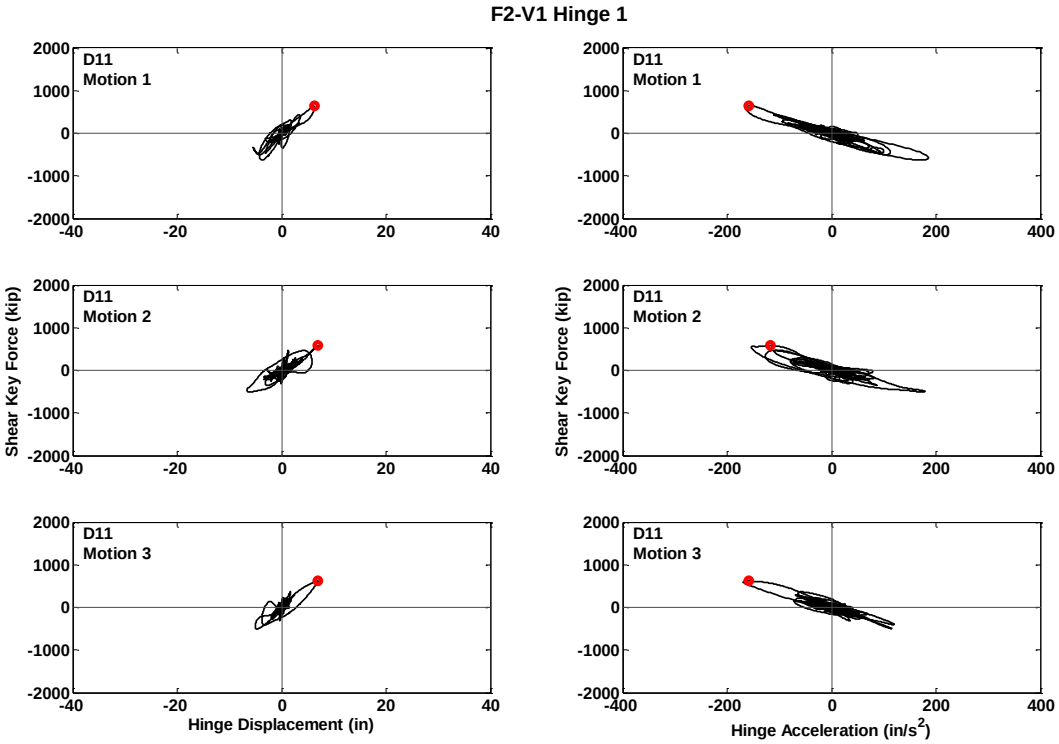

Figure C.214 Hysteresis Curves for Prototype F2-V1, Hinge 1, Motions D11

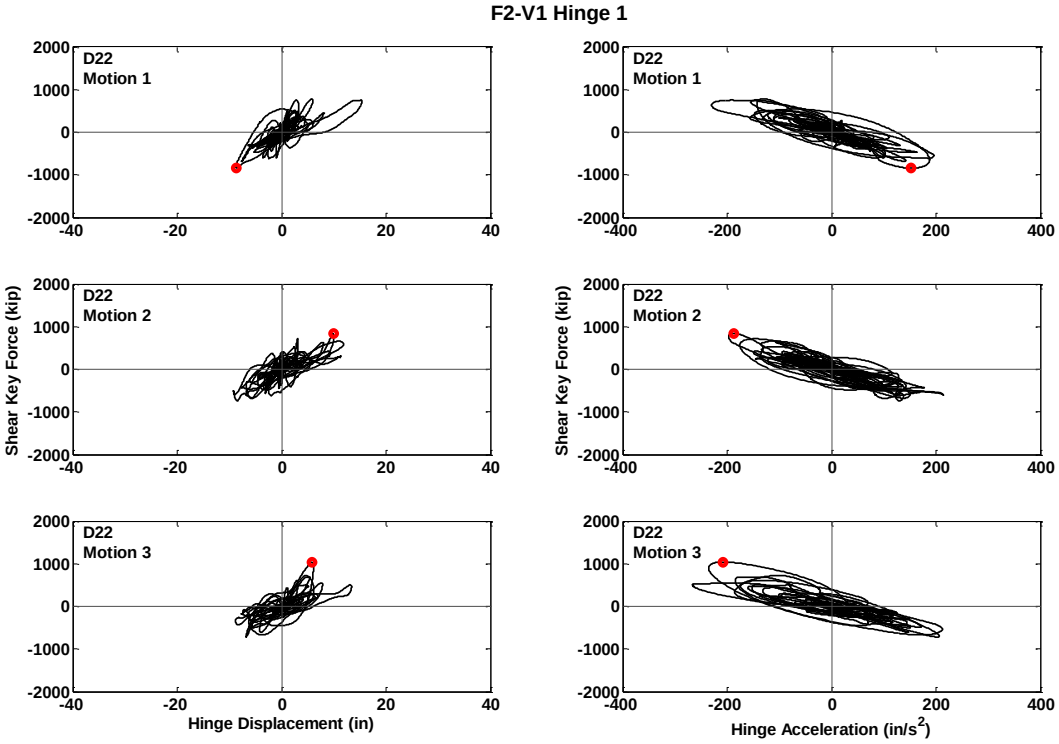

Figure C.215 Hysteresis Curves for Prototype F2-V1, Hinge 1, Motions D22

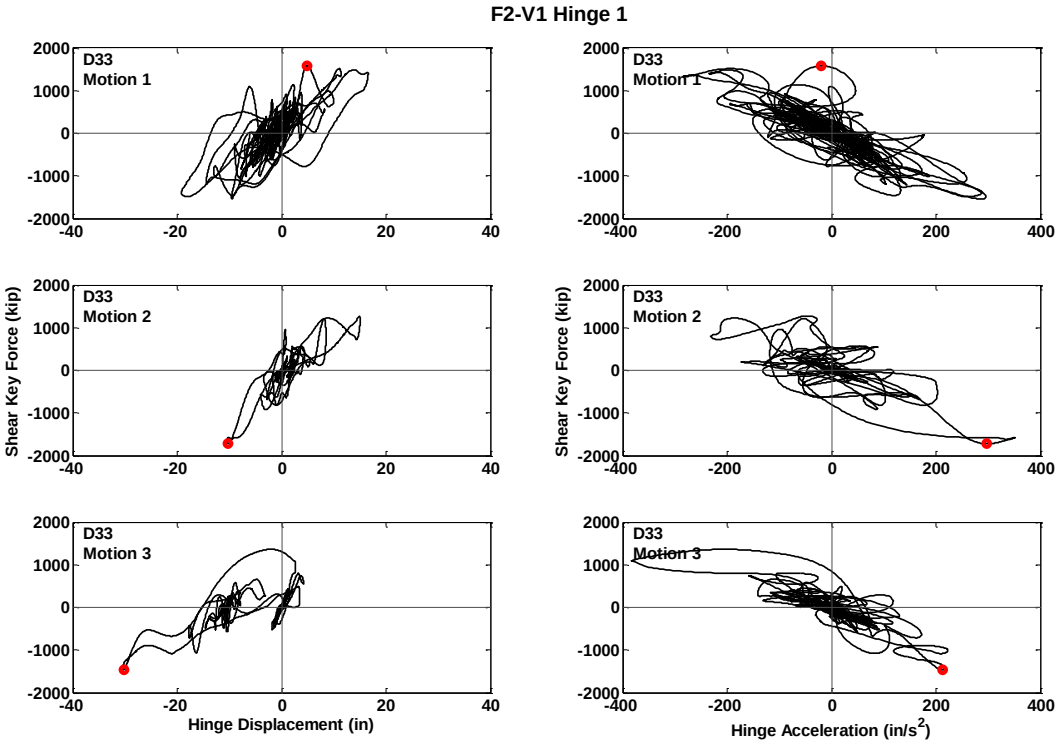

Figure C.216 Hysteresis Curves for Prototype F2-V1, Hinge 1, Motions D33

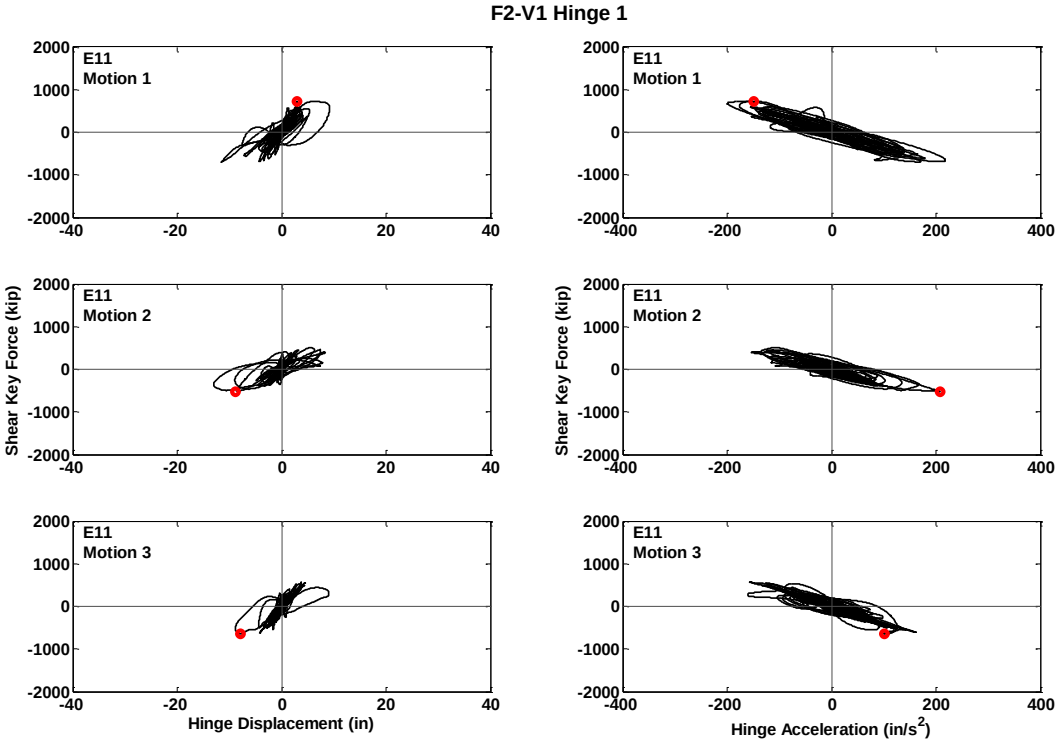

Figure C.217 Hysteresis Curves for Prototype F2-V1, Hinge 1, Motions E11

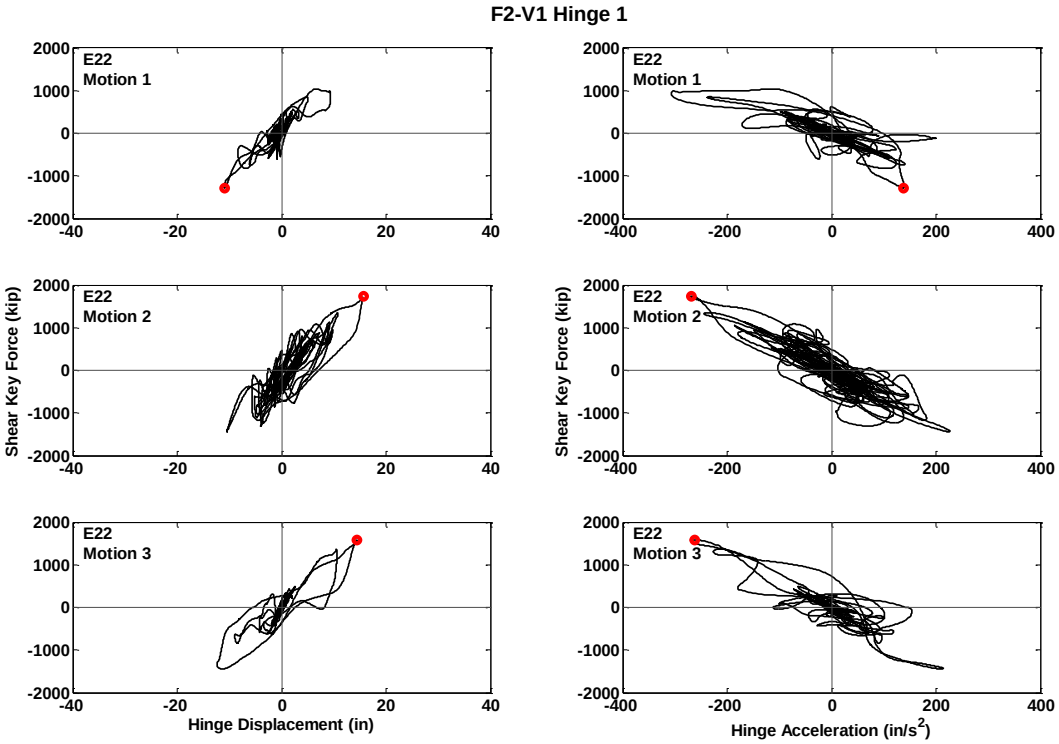

Figure C.218 Hysteresis Curves for Prototype F2-V1, Hinge 1, Motions E22

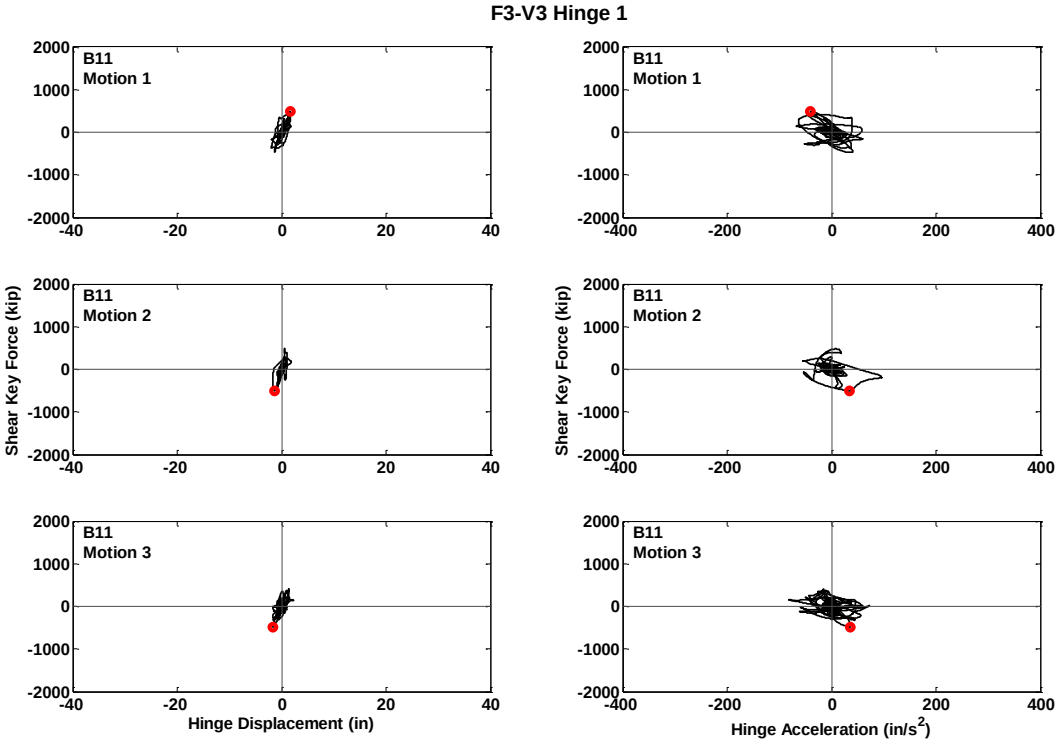

Figure C.219 Hysteresis Curves for Prototype F3-V3, Hinge 1, Motions B11

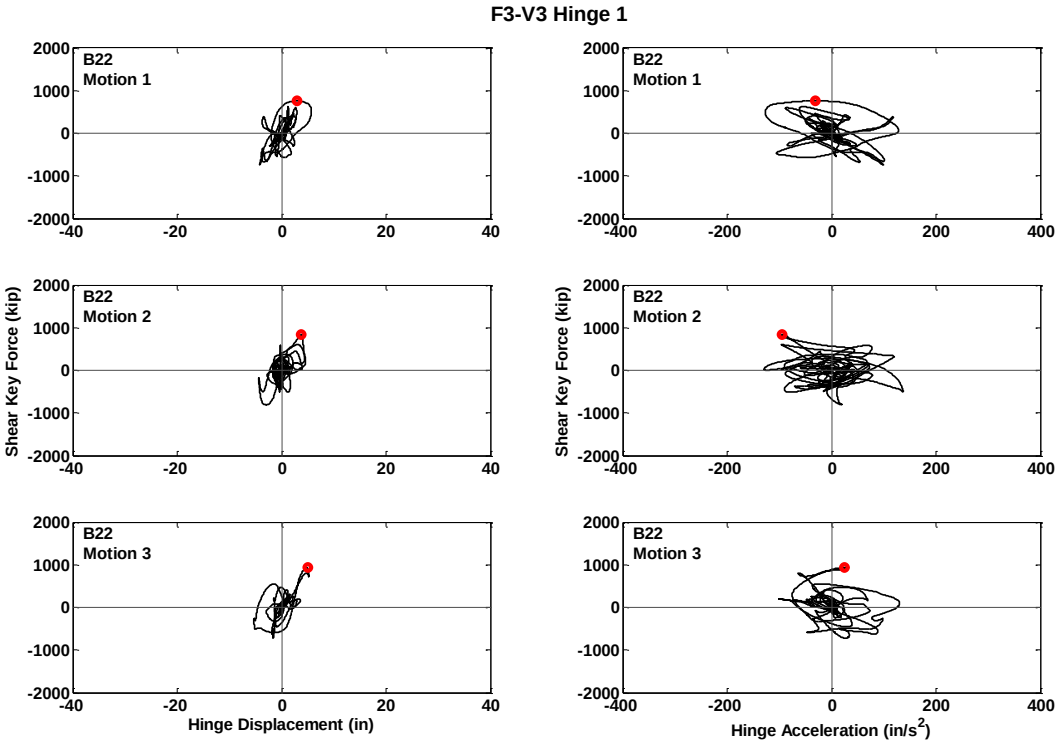

Figure C.220 Hysteresis Curves for Prototype F3-V3, Hinge 1, Motions B22

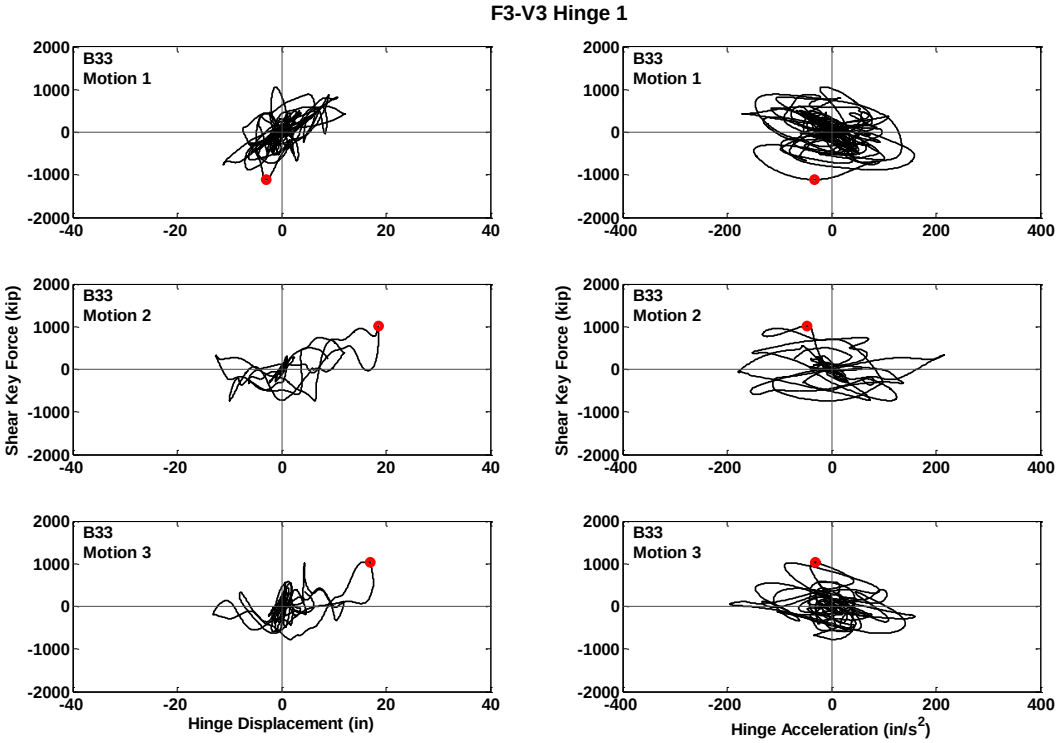

Figure C.221 Hysteresis Curves for Prototype F3-V3, Hinge 1, Motions B33

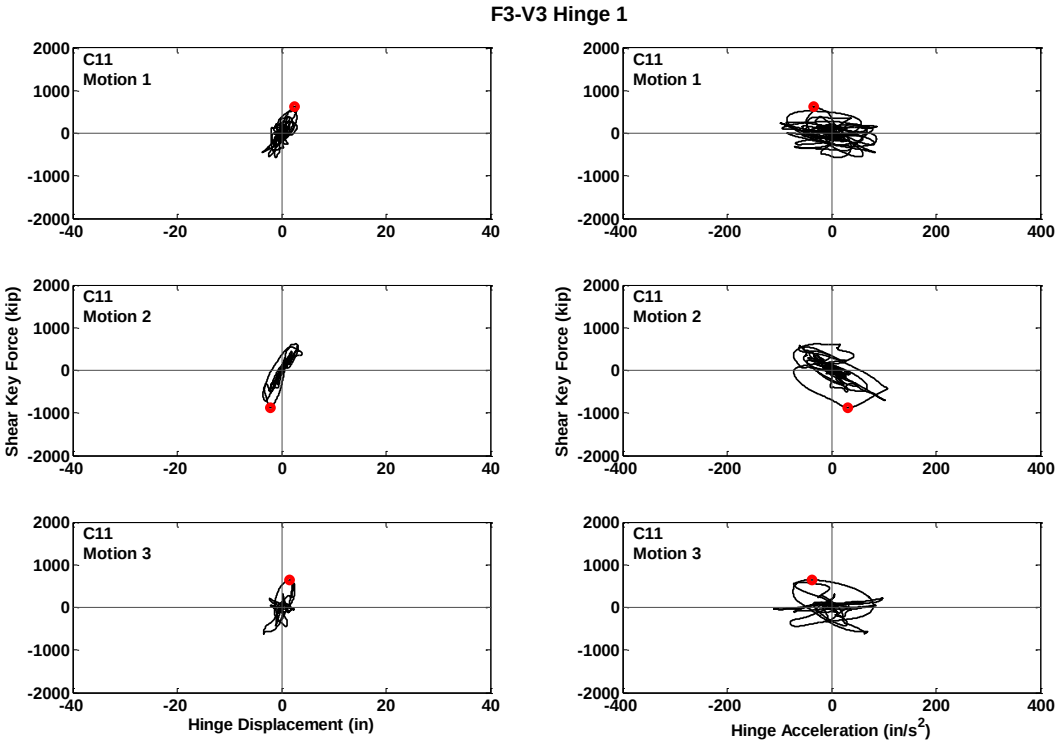

Figure C.222 Hysteresis Curves for Prototype F3-V3, Hinge 1, Motions C11

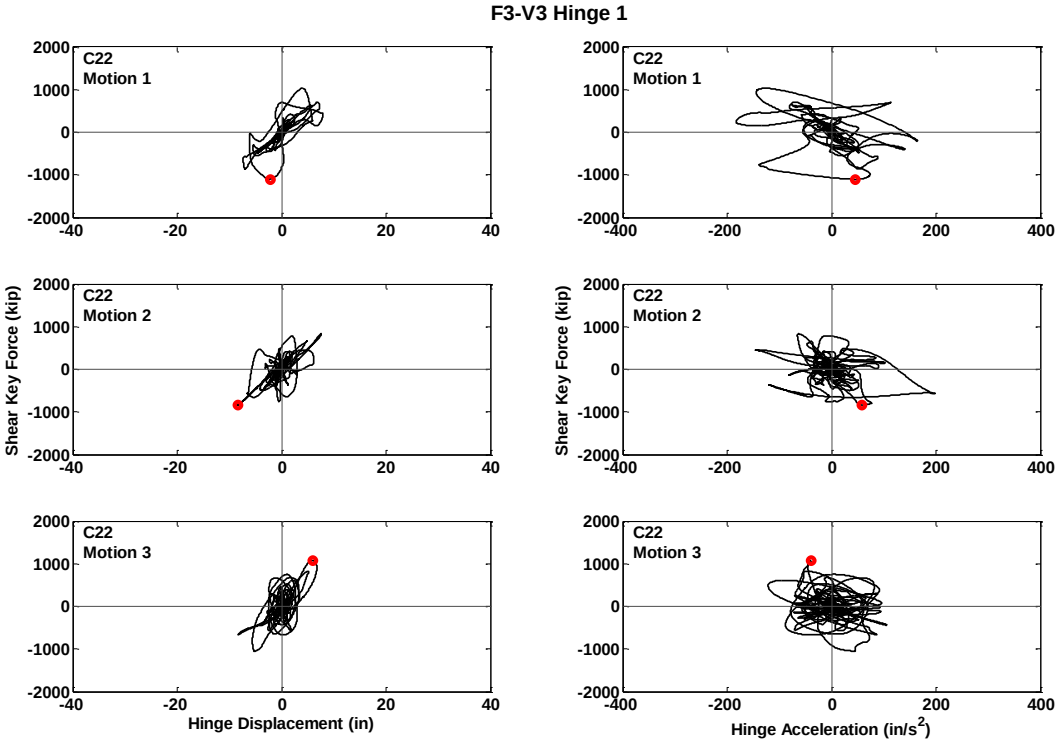

Figure C.223 Hysteresis Curves for Prototype F3-V3, Hinge 1, Motions C22

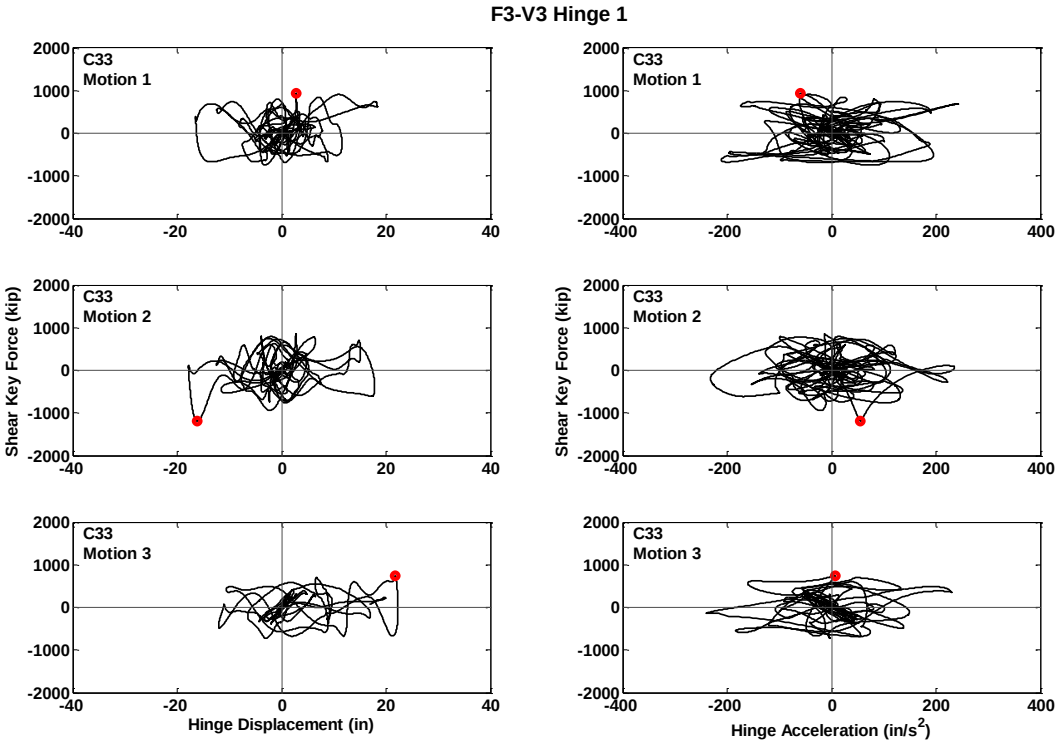

Figure C.224 Hysteresis Curves for Prototype F3-V3, Hinge 1, Motions C33

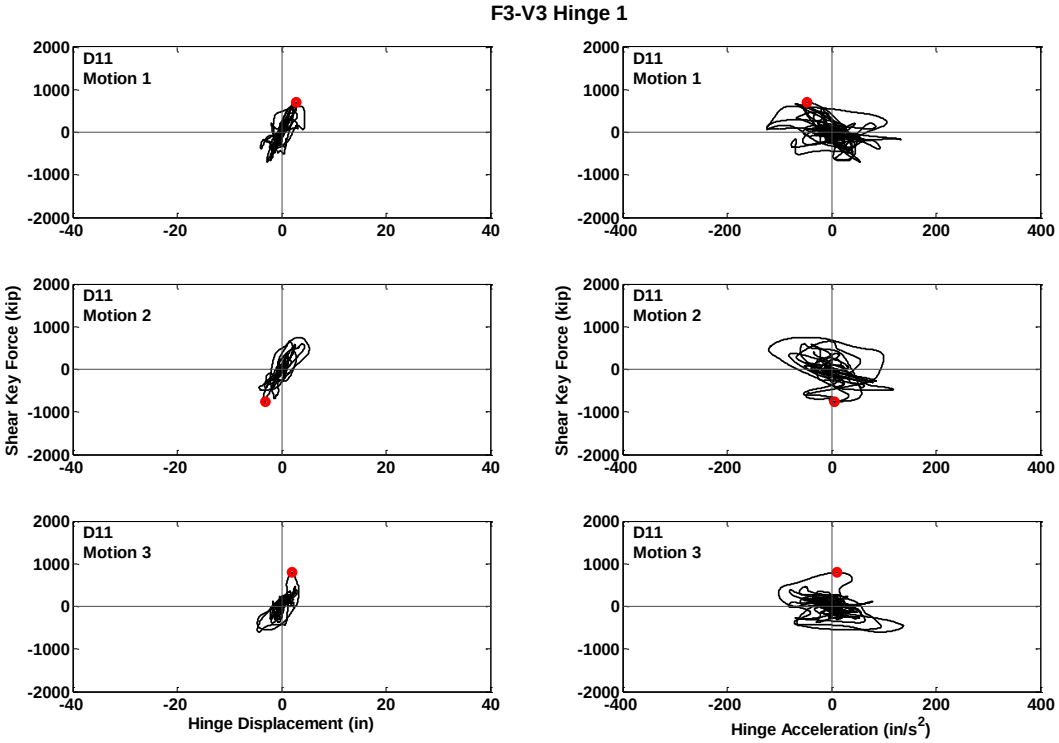

Figure C.225 Hysteresis Curves for Prototype F3-V3, Hinge 1, Motions D11

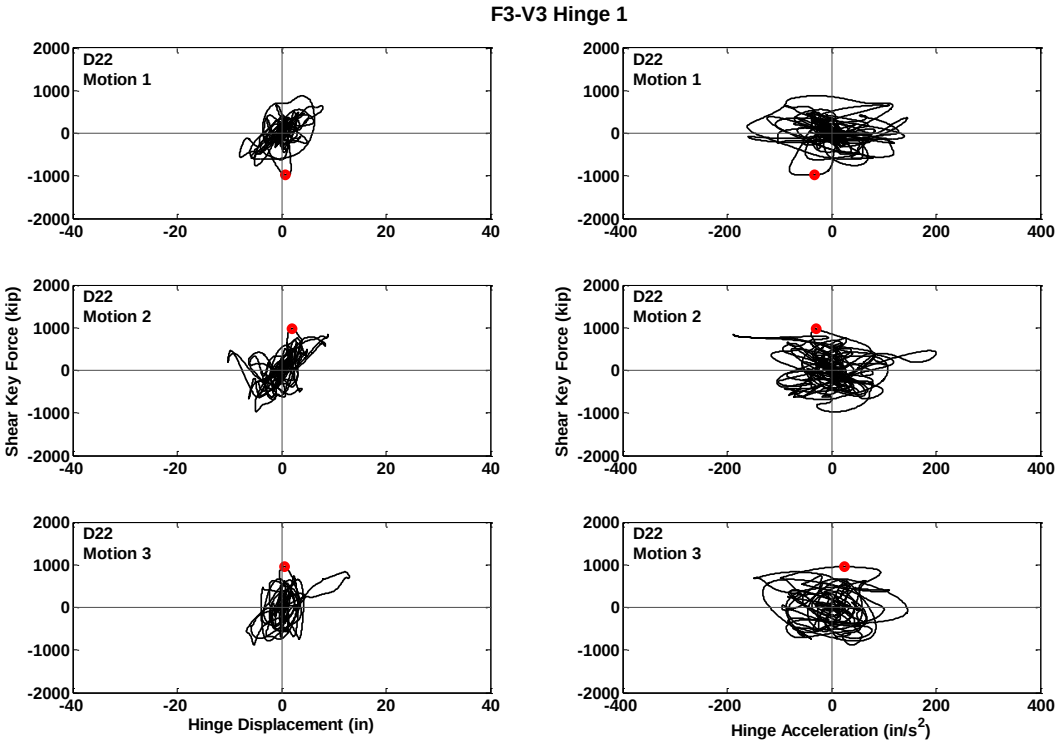

Figure C.226 Hysteresis Curves for Prototype F3-V3, Hinge 1, Motions D22

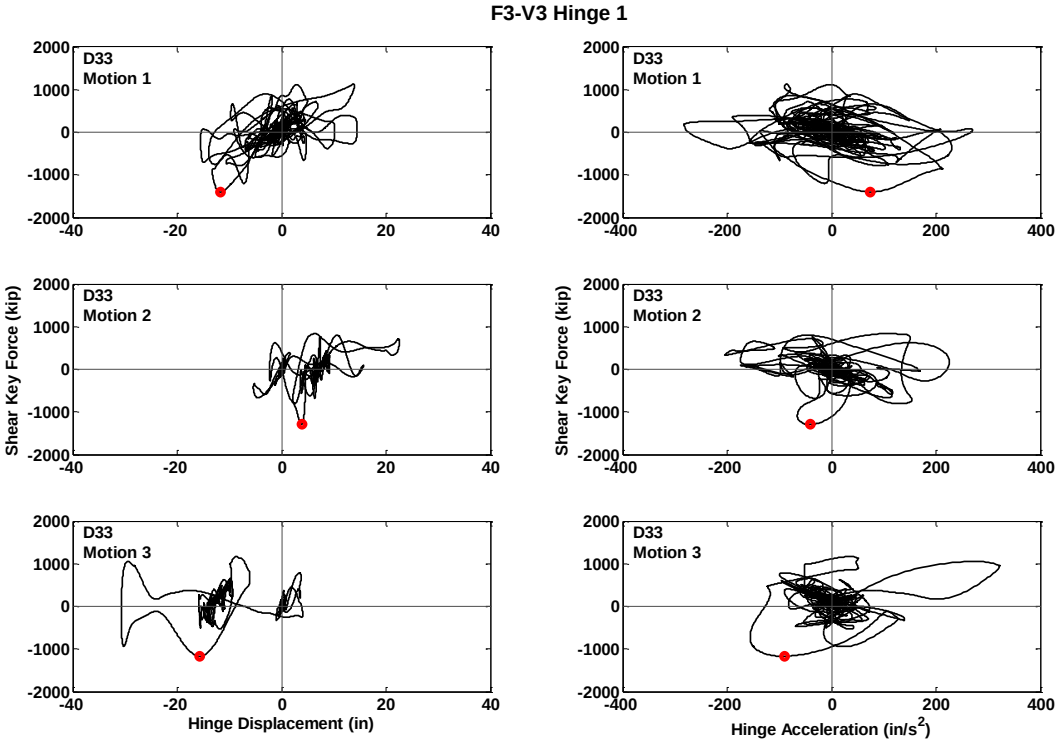

Figure C.227 Hysteresis Curves for Prototype F3-V3, Hinge 1, Motions D33

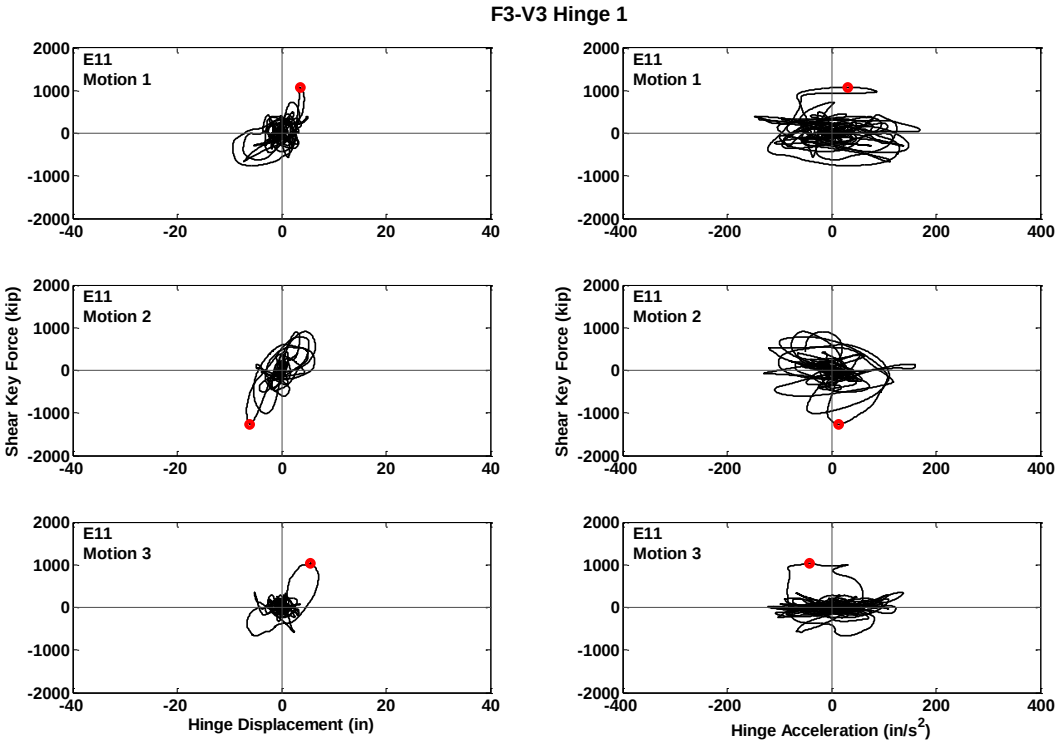

Figure C.228 Hysteresis Curves for Prototype F3-V3, Hinge 1, Motions E11

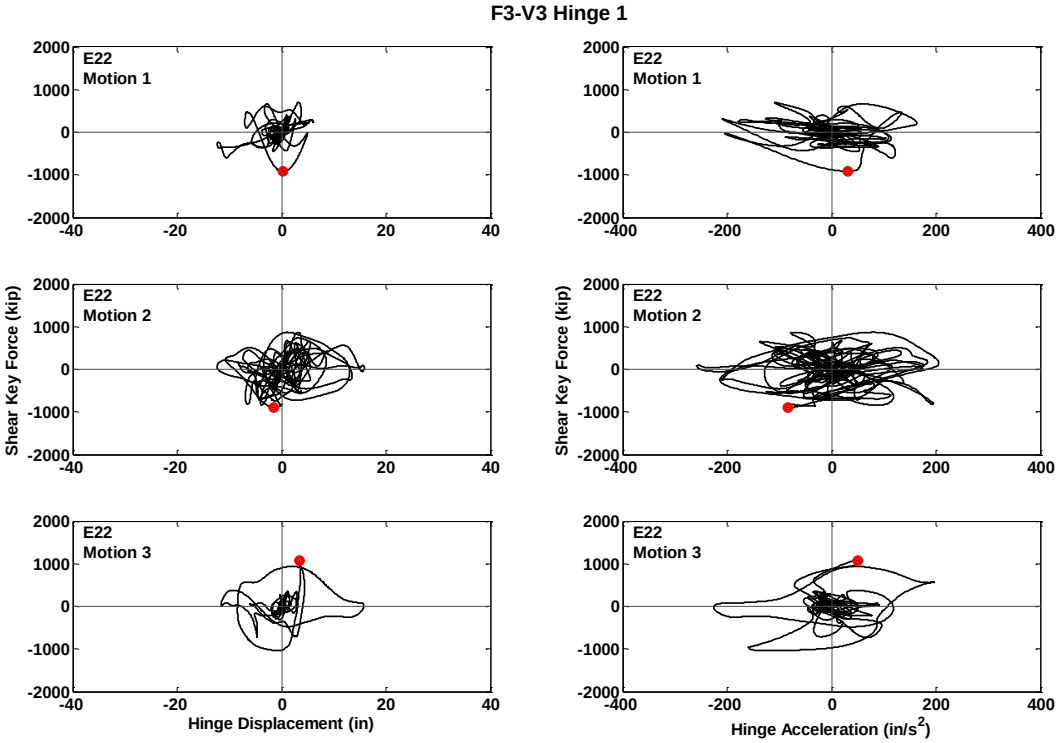

Figure C.229 Hysteresis Curves for Prototype F3-V3, Hinge 1, Motions E22

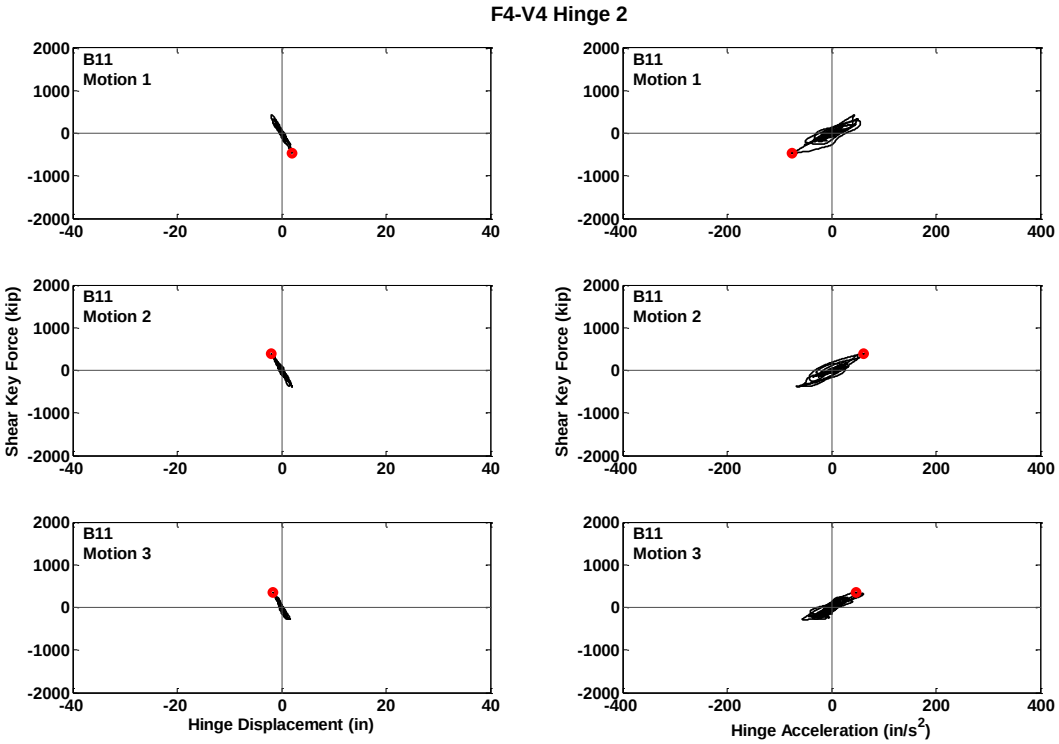

Figure C.230 Hysteresis Curves for Prototype F4-V4, Hinge 2, Motions B11

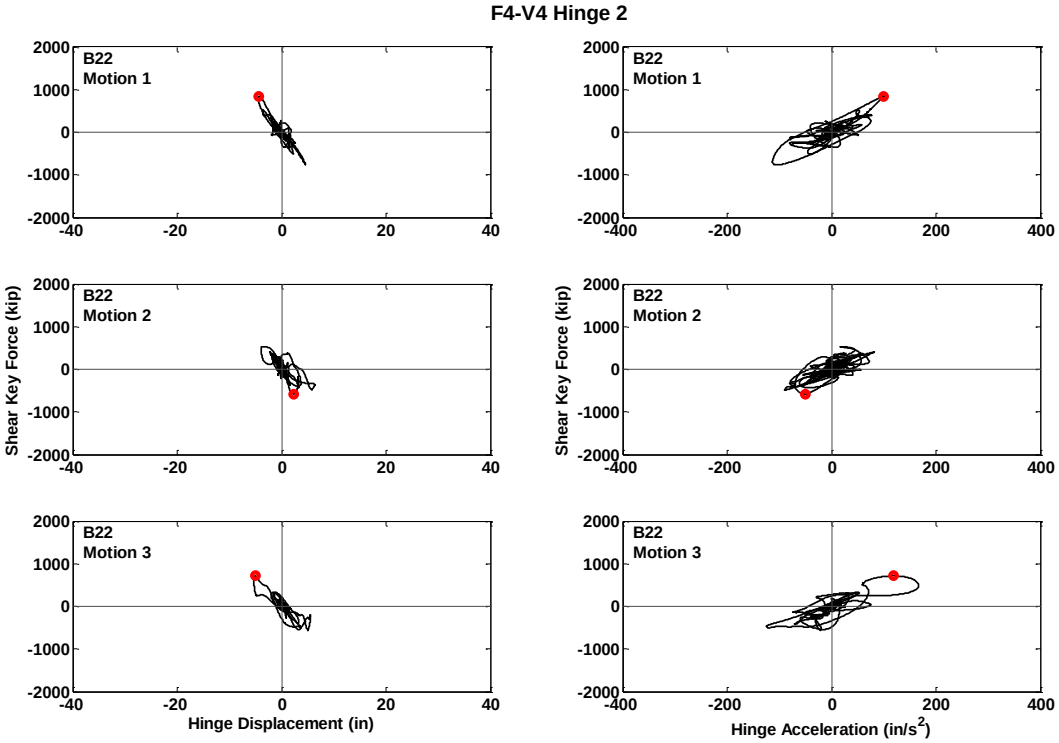

Figure C.231 Hysteresis Curves for Prototype F4-V4, Hinge 2, Motions B22

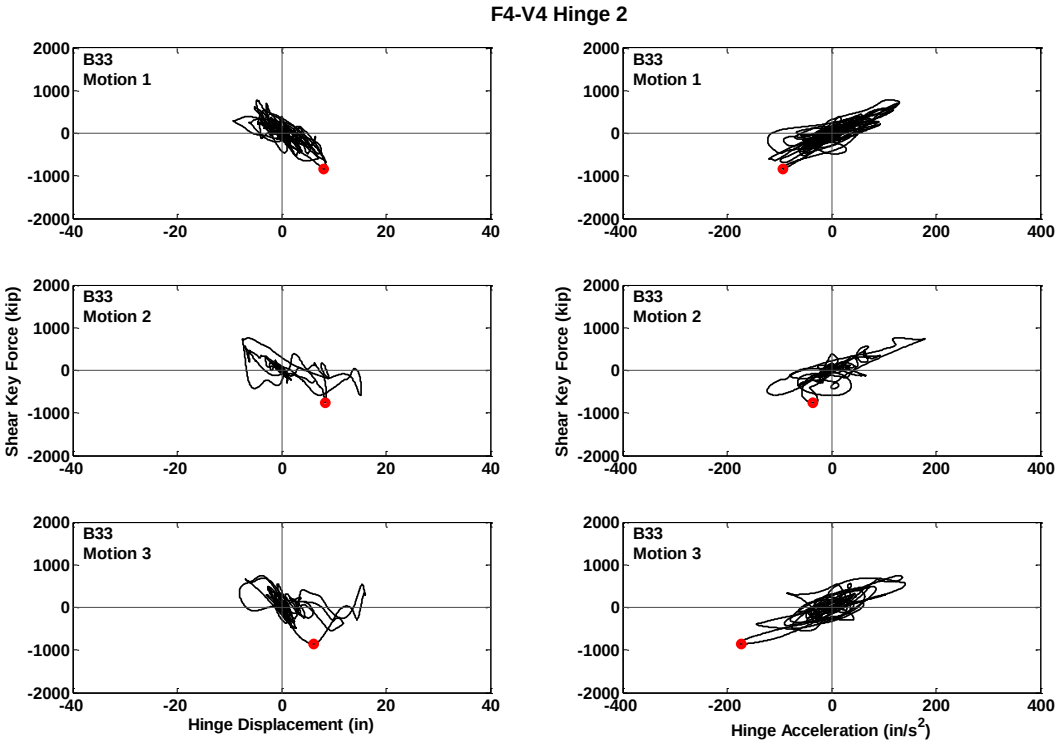

Figure C.232 Hysteresis Curves for Prototype F4-V4, Hinge 2, Motions B33

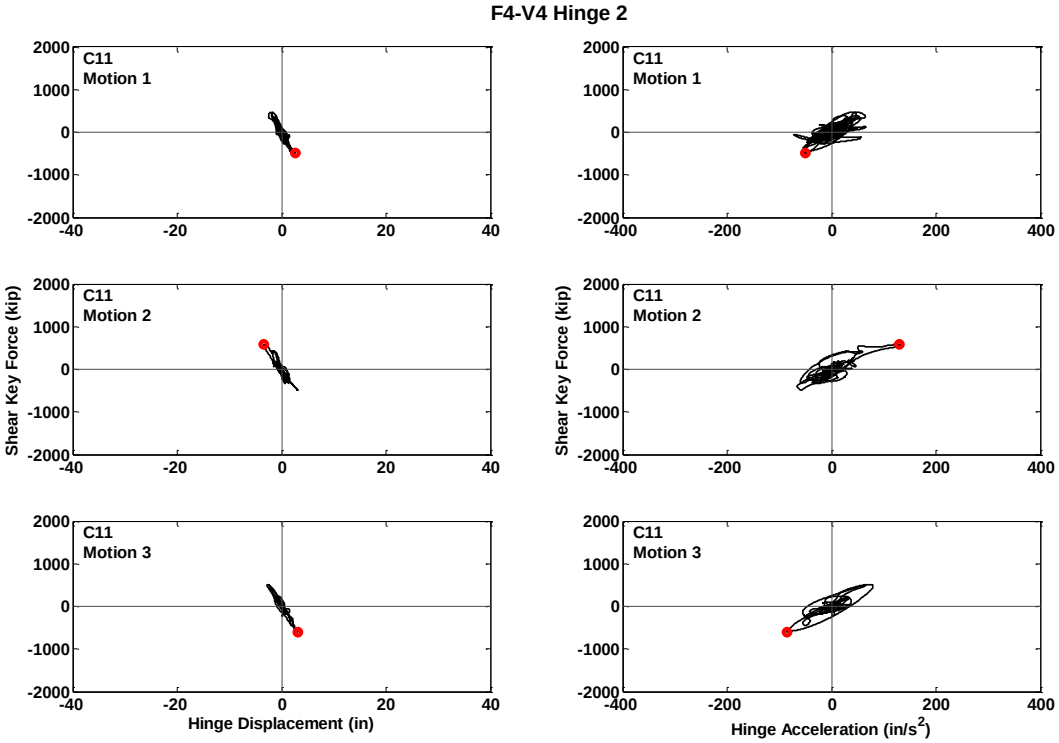

Figure C.233 Hysteresis Curves for Prototype F4-V4, Hinge 2, Motions C11

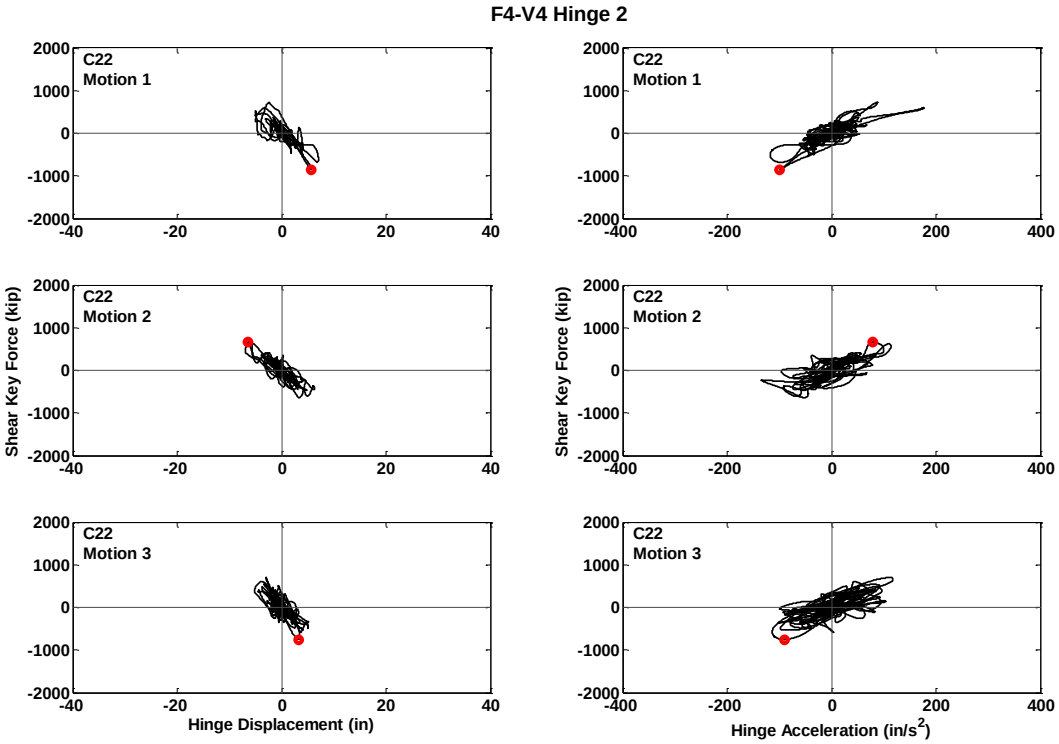

Figure C.234 Hysteresis Curves for Prototype F4-V4, Hinge 2, Motions C22

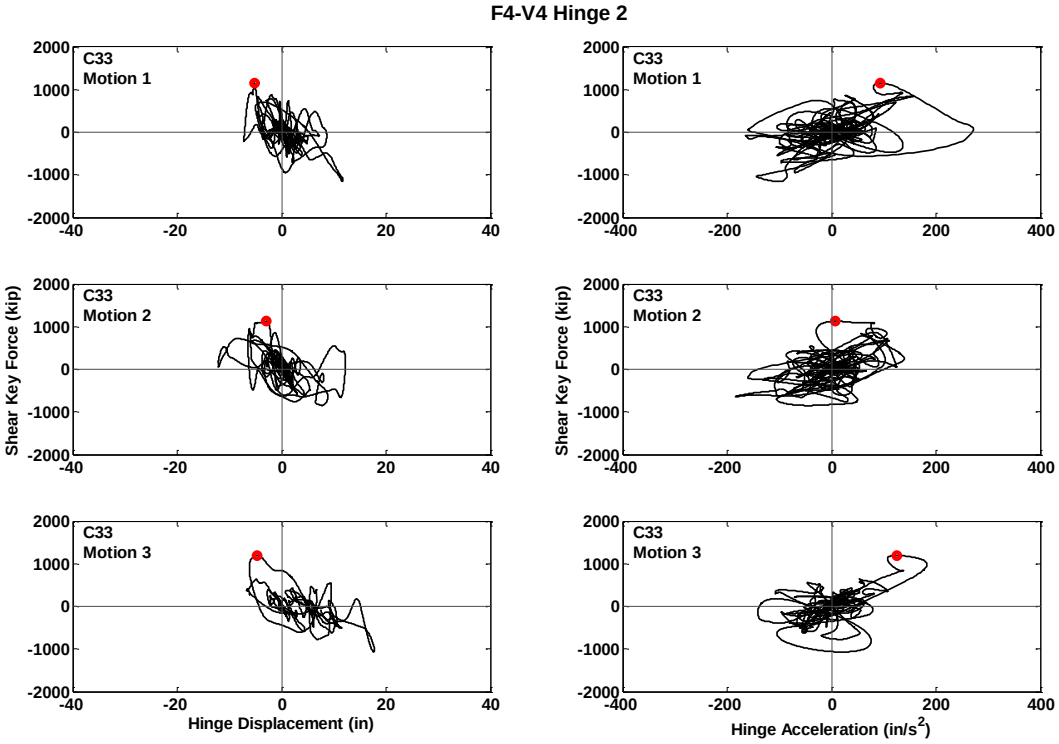

Figure C.235 Hysteresis Curves for Prototype F4-V4, Hinge 2, Motions C33

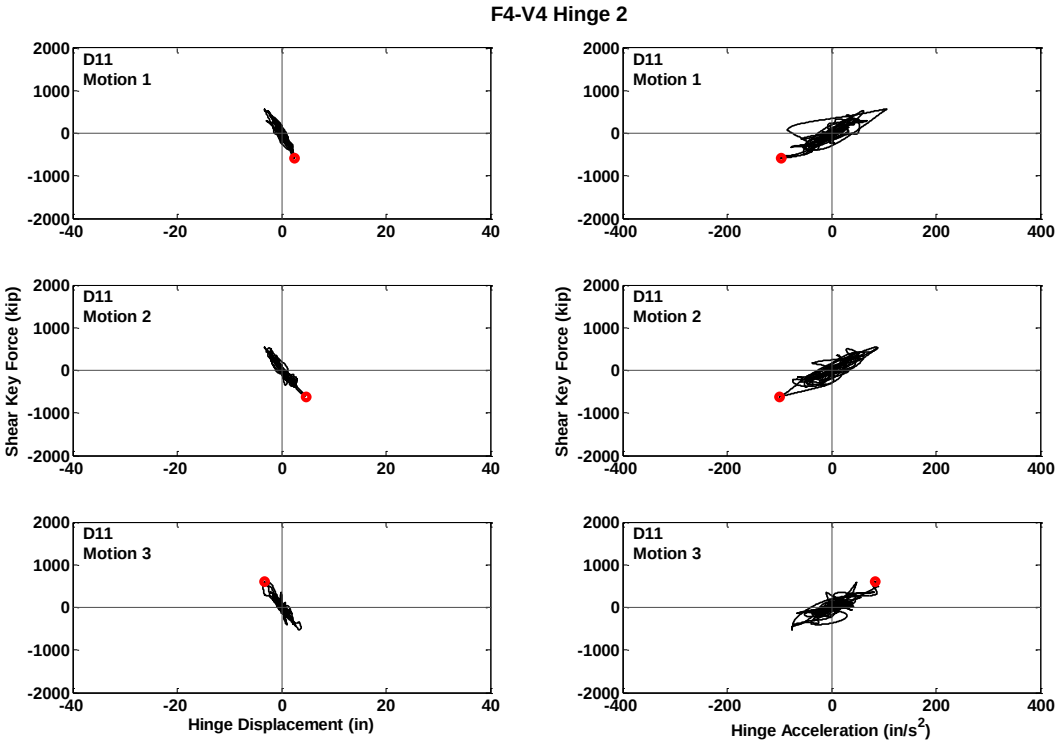

Figure C.236 Hysteresis Curves for Prototype F4-V4, Hinge 2, Motions D11

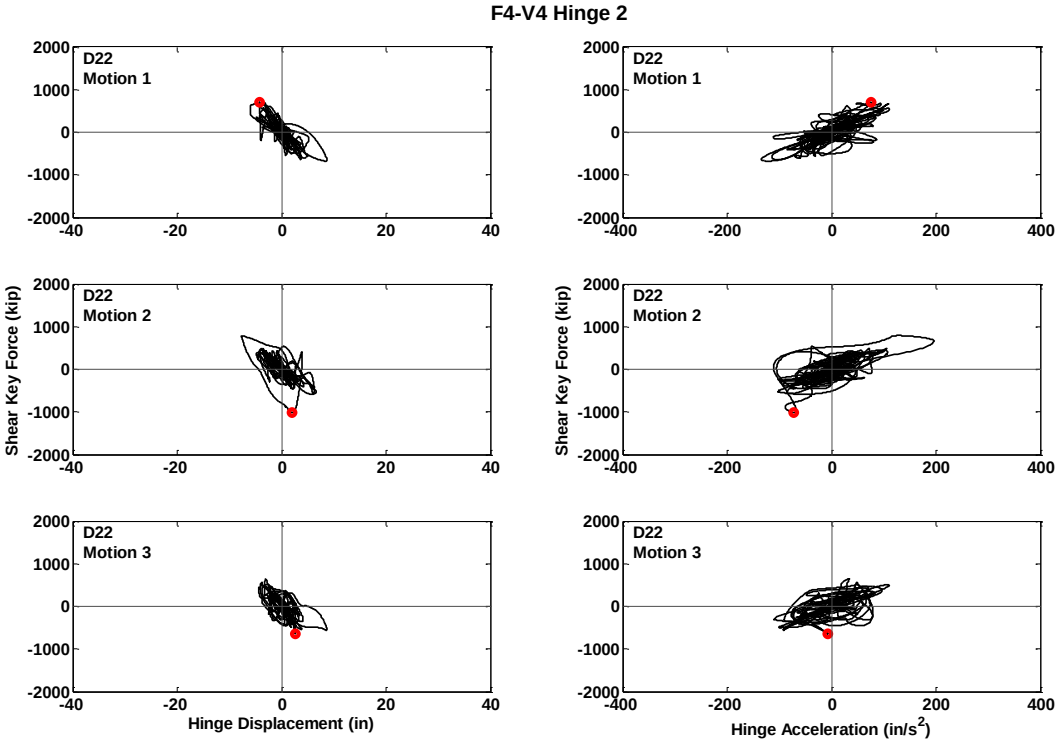

Figure C.237 Hysteresis Curves for Prototype F4-V4, Hinge 2, Motions D22

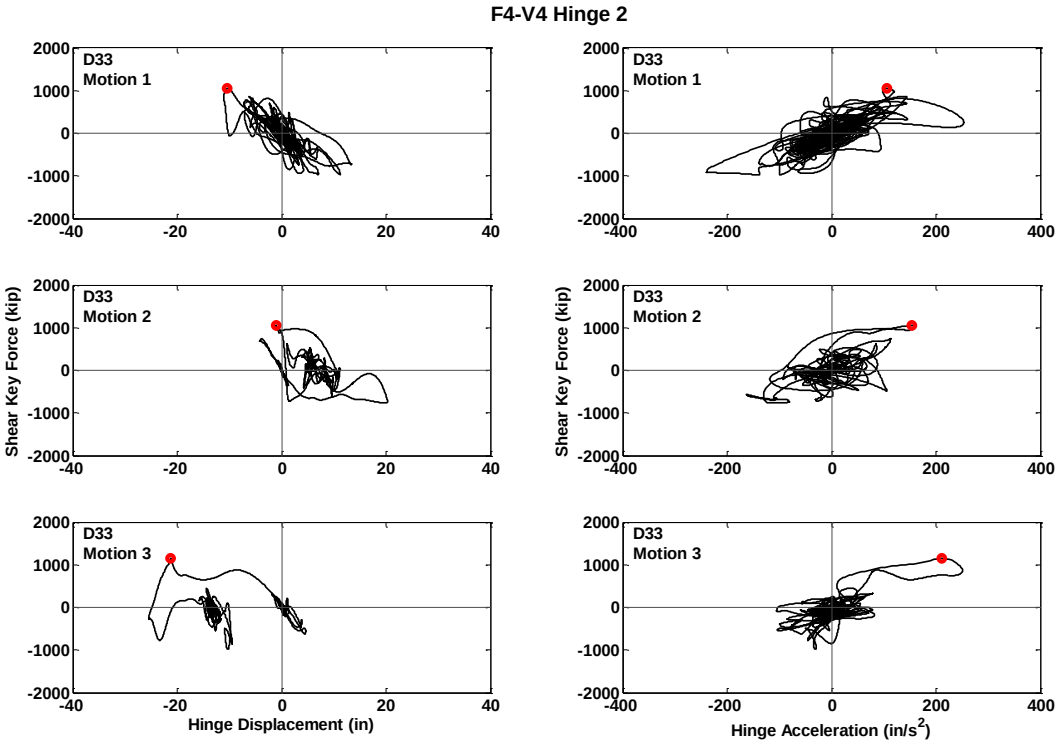

Figure C.238 Hysteresis Curves for Prototype F4-V4, Hinge 2, Motions D33

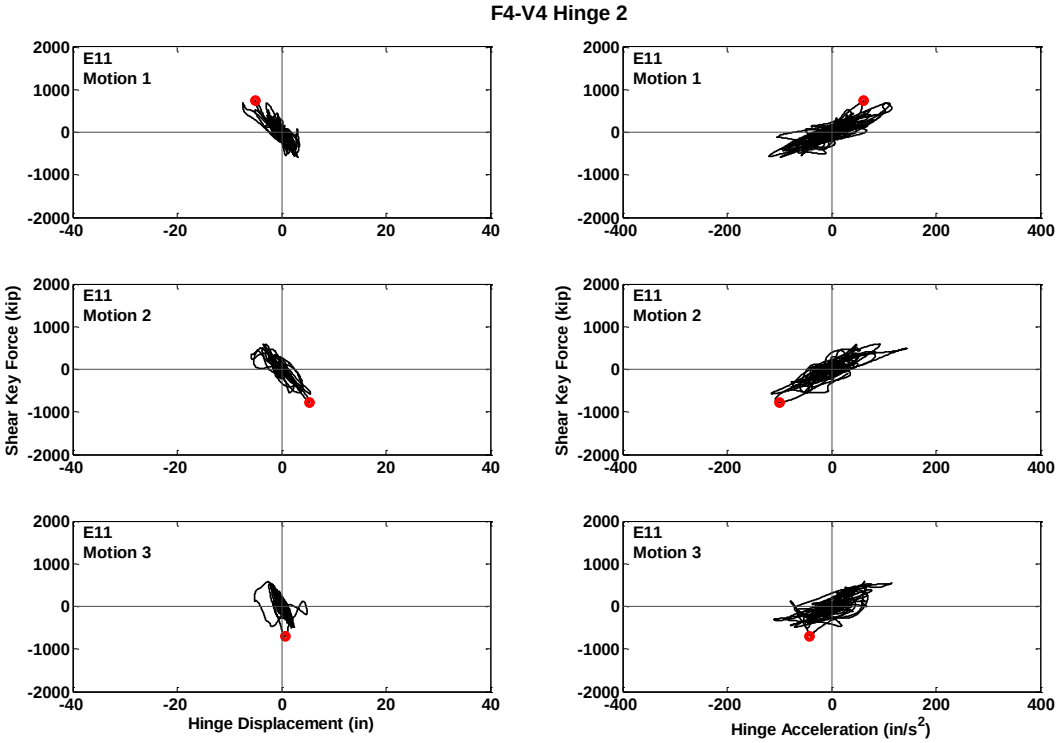

Figure C.239 Hysteresis Curves for Prototype F4-V4, Hinge 2, Motions E11

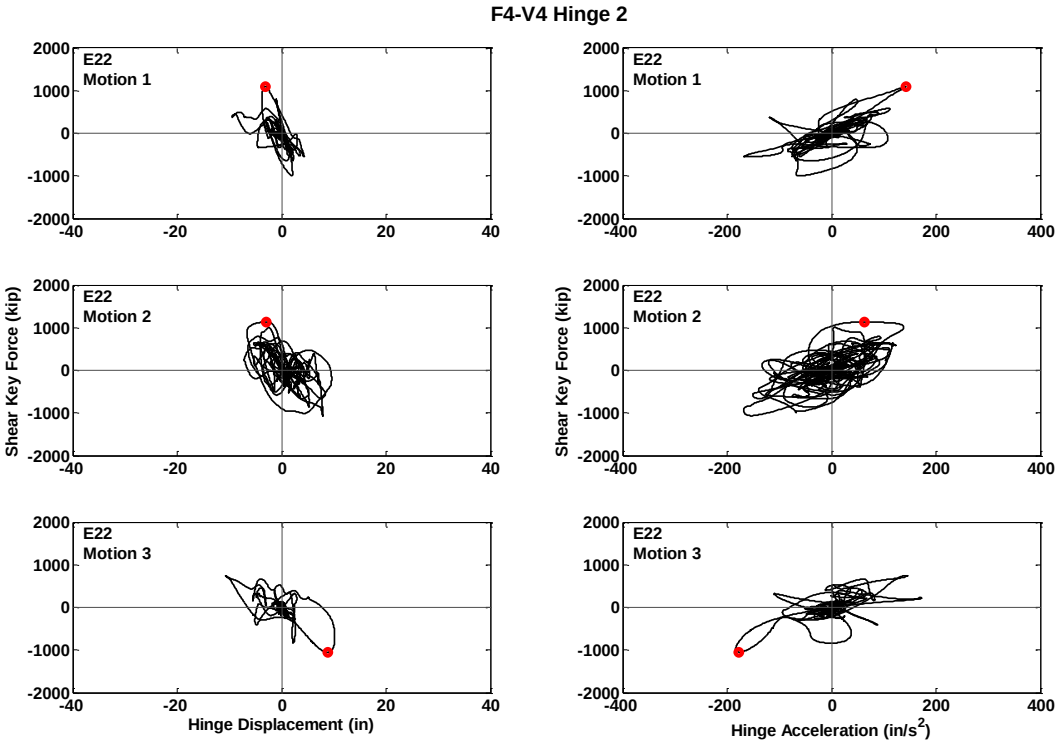

Figure C.240 Hysteresis Curves for Prototype F4-V4, Hinge 2, Motions E22

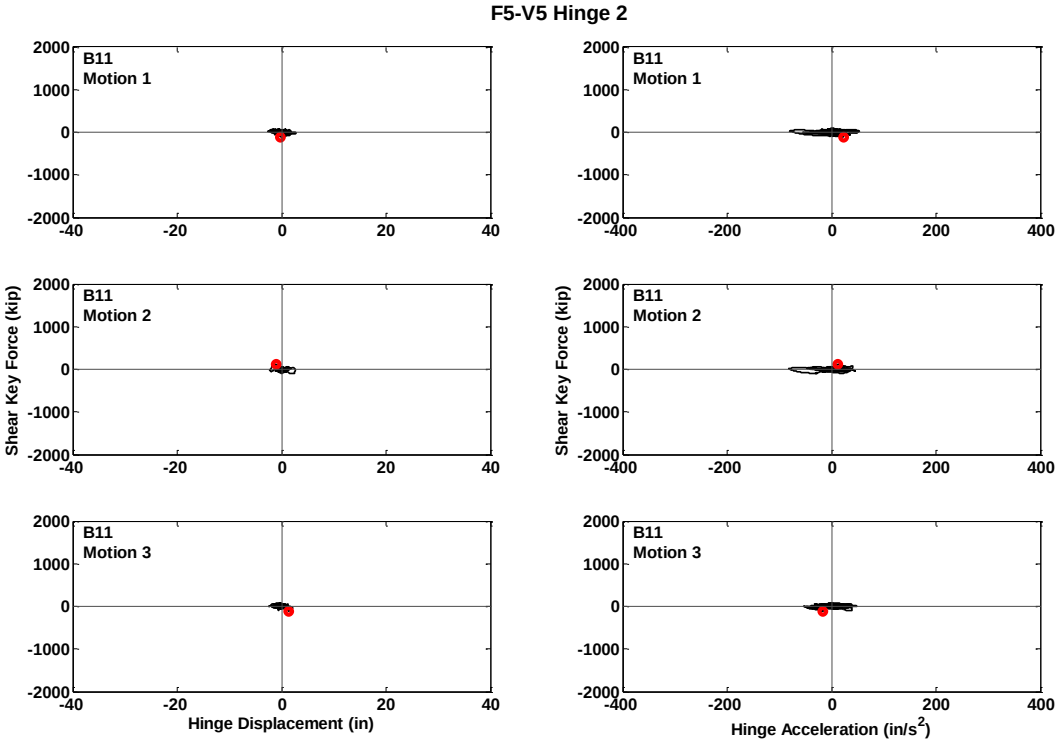

Figure C.241 Hysteresis Curves for Prototype F5-V5, Hinge 2, Motions B11

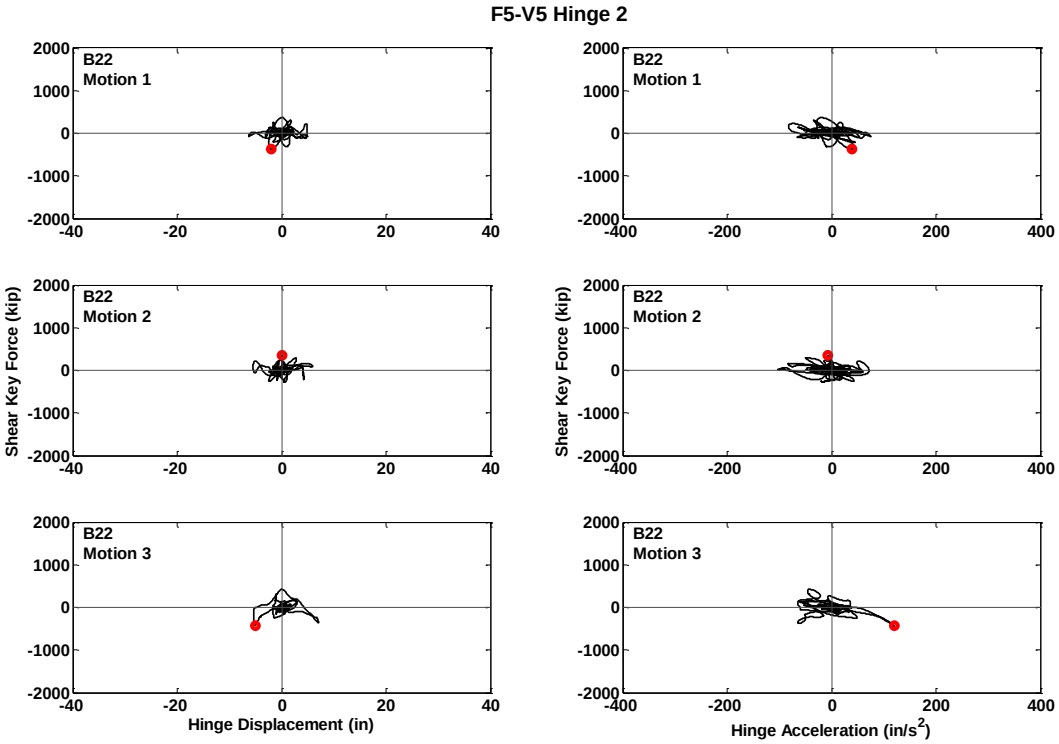

Figure C.242 Hysteresis Curves for Prototype F5-V5, Hinge 2, Motions B22

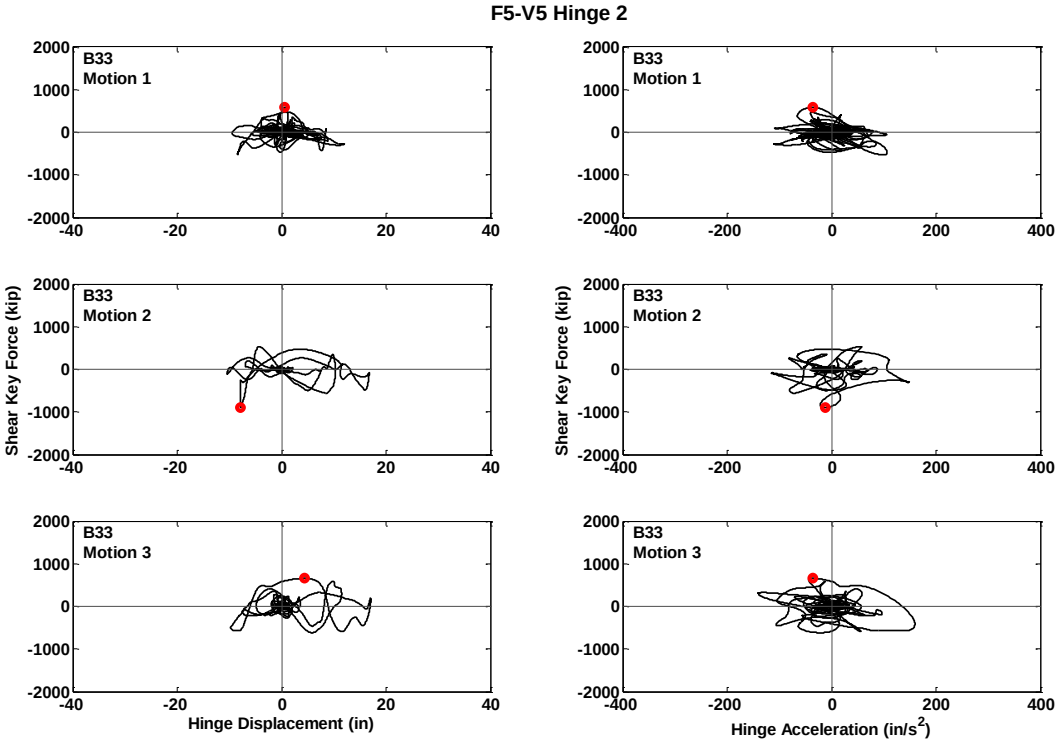

Figure C.243 Hysteresis Curves for Prototype F5-V5, Hinge 2, Motions B33

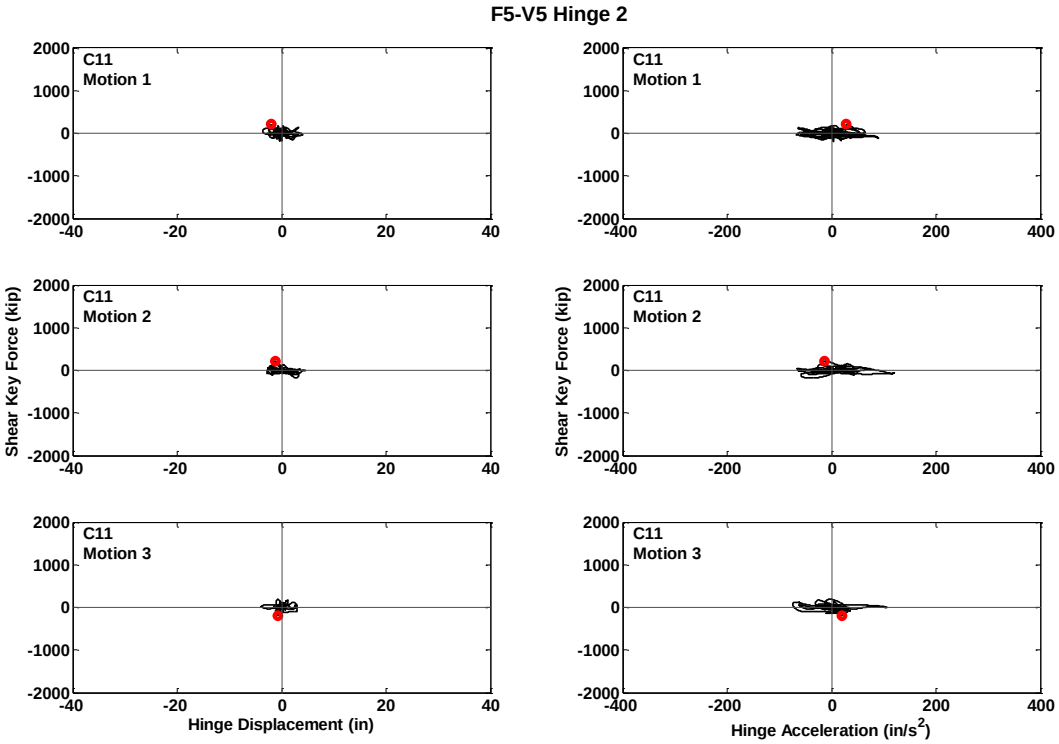

Figure C.244 Hysteresis Curves for Prototype F5-V5, Hinge 2, Motions C11

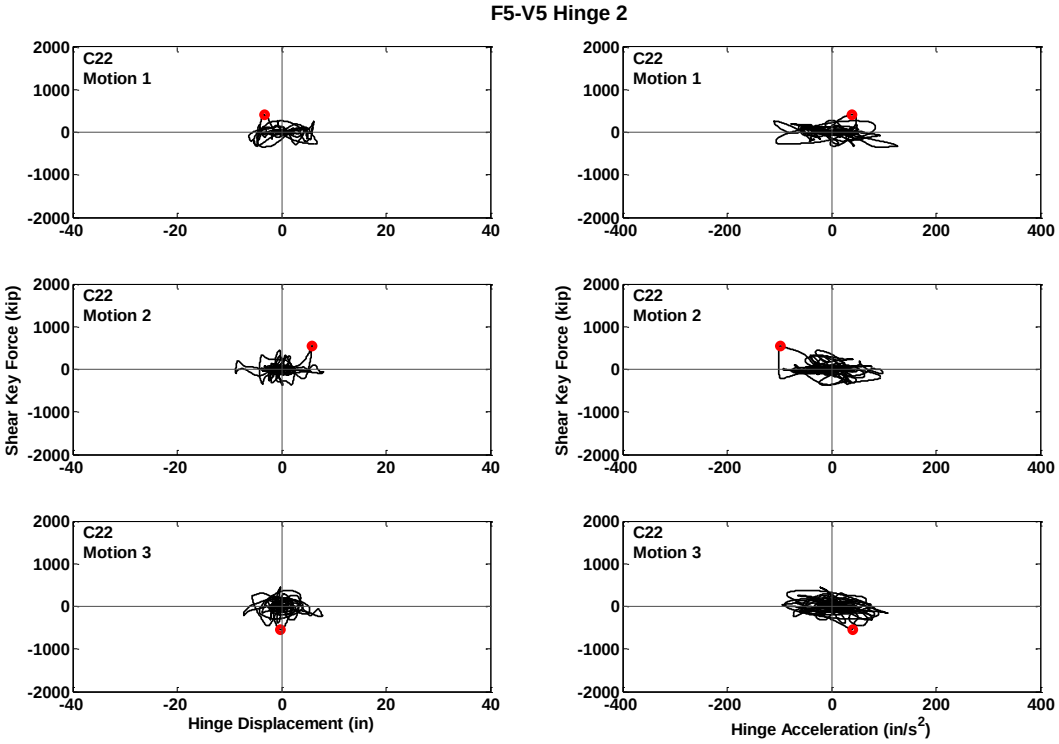

Figure C.245 Hysteresis Curves for Prototype F5-V5, Hinge 2, Motions C22

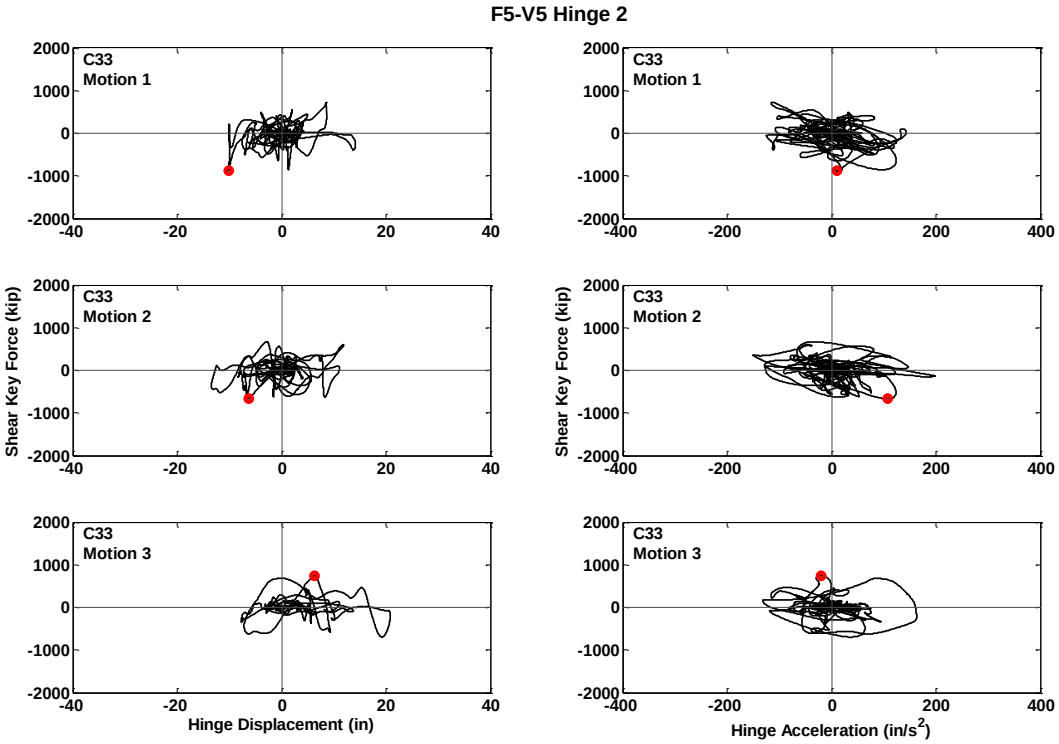

Figure C.246 Hysteresis Curves for Prototype F5-V5, Hinge 2, Motions C33

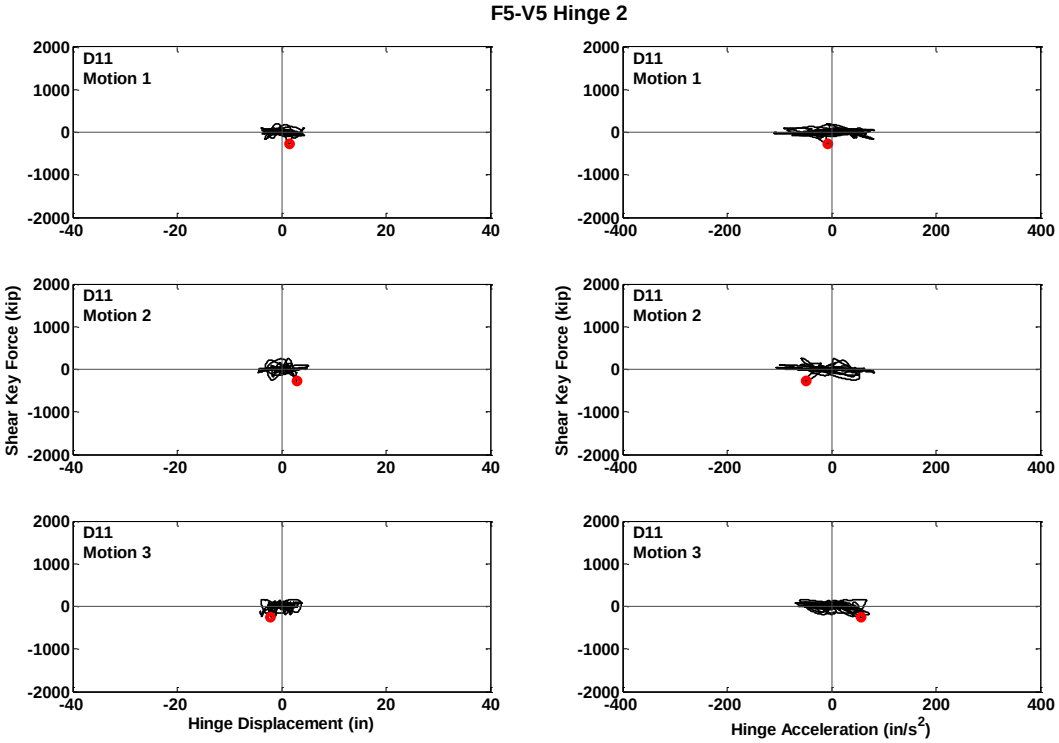

Figure C.247 Hysteresis Curves for Prototype F5-V5, Hinge 2, Motions D11

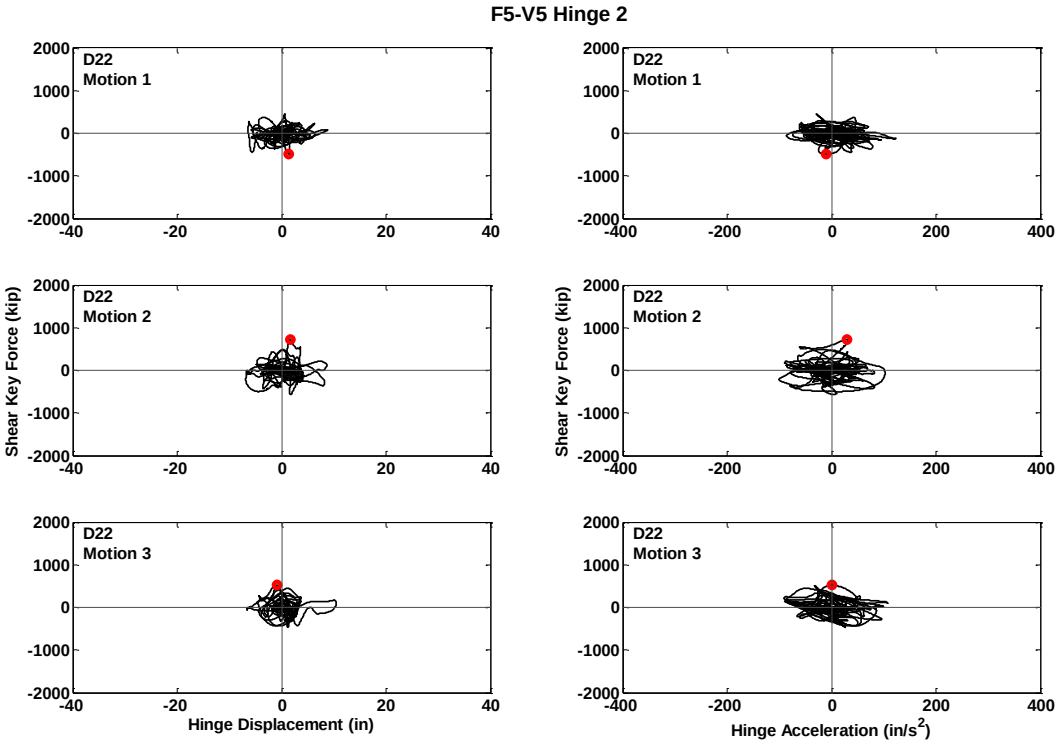

Figure C.248 Hysteresis Curves for Prototype F5-V5, Hinge 2, Motions D22

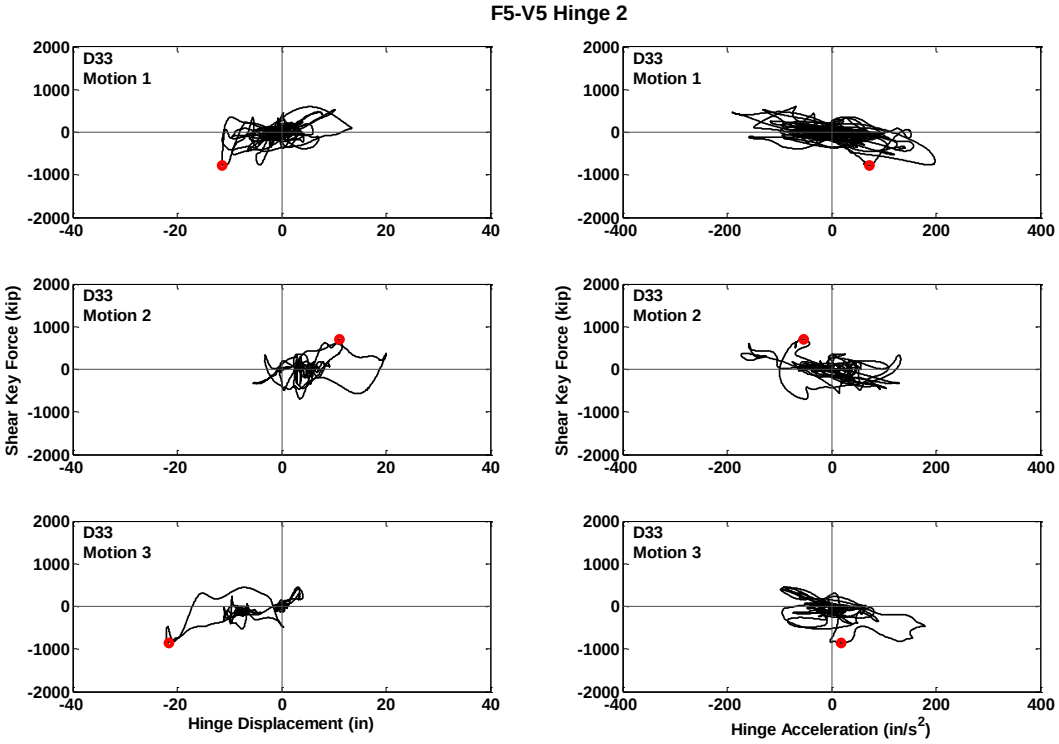

Figure C.249 Hysteresis Curves for Prototype F5-V5, Hinge 2, Motions D33

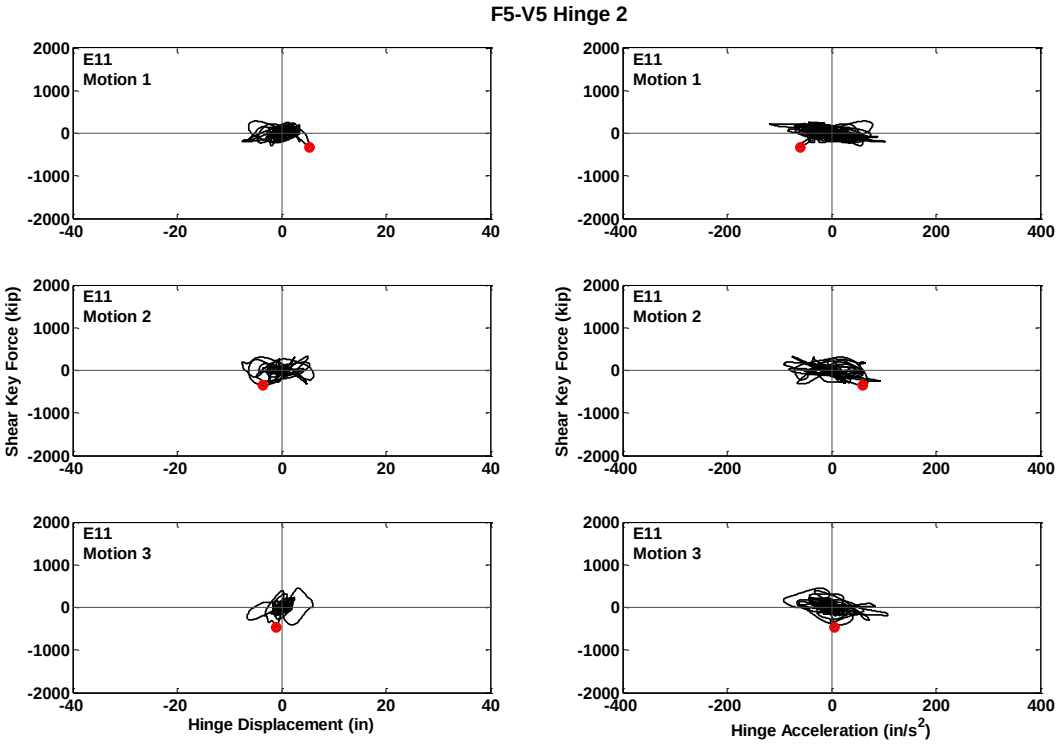

Figure C.250 Hysteresis Curves for Prototype F5-V5, Hinge 2, Motions E11

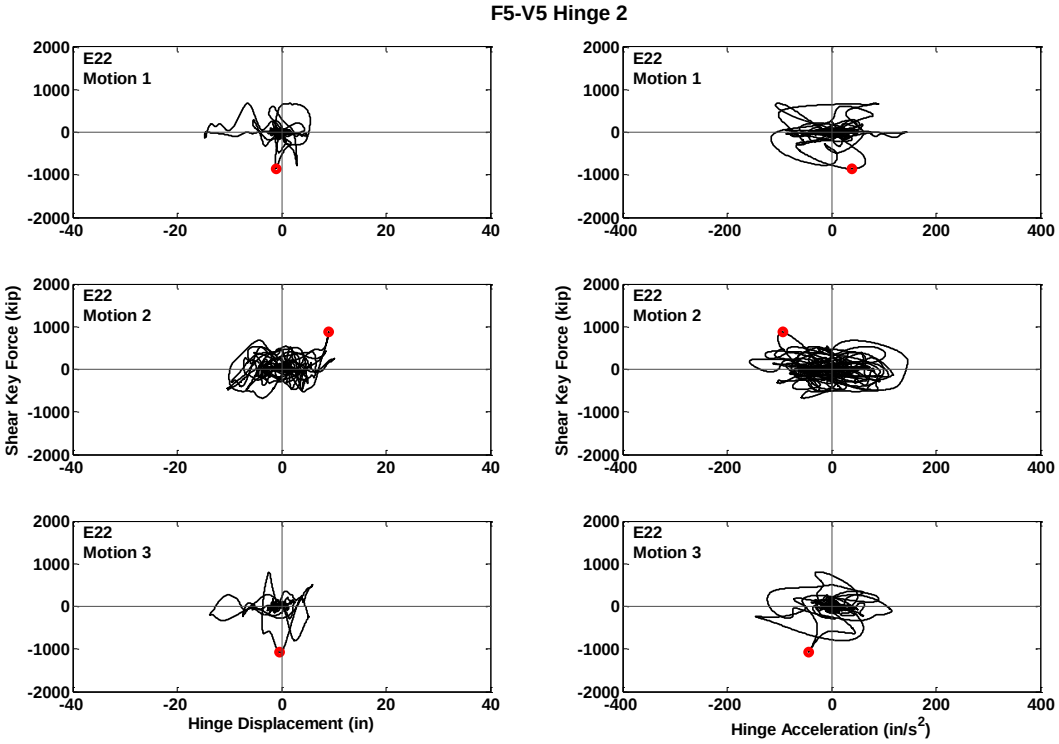

Figure C.251 Hysteresis Curves for Prototype F5-V5, Hinge 2, Motions E22

PART-4a: Single-Column Bent Prototypes
System State at the Time of the Maximum Shear Key Forces.

Legend:

Solid Black = Displacements

Dash line = Accelerations

Gray =Design Displacement Demands

Red Stem = bent capacities

Black Stem = base reactions

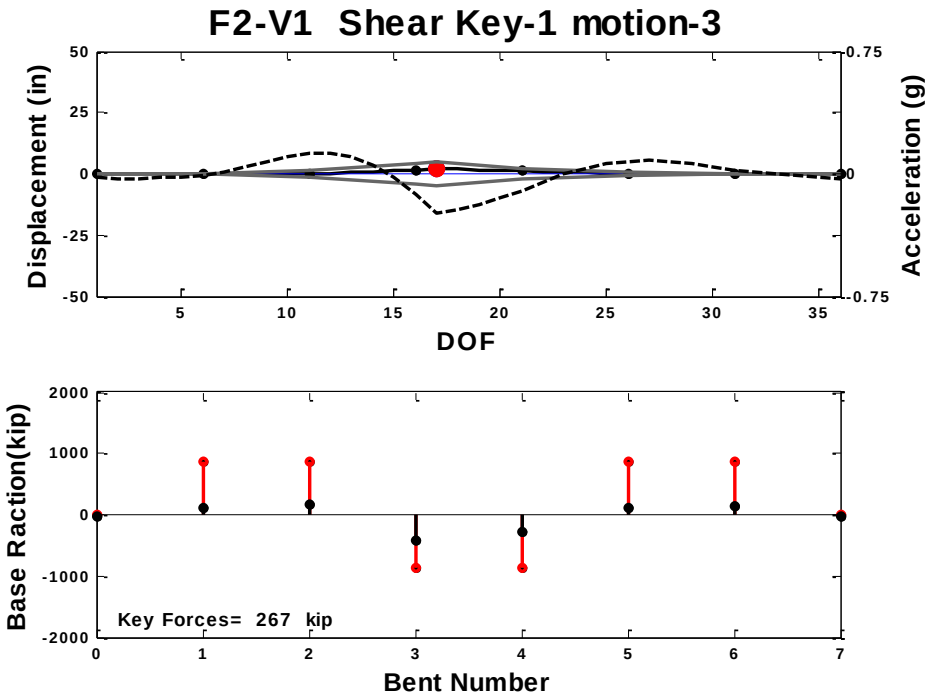

Figure C.252 System State at Maximum Force, Prototype F2-V1, motion-3

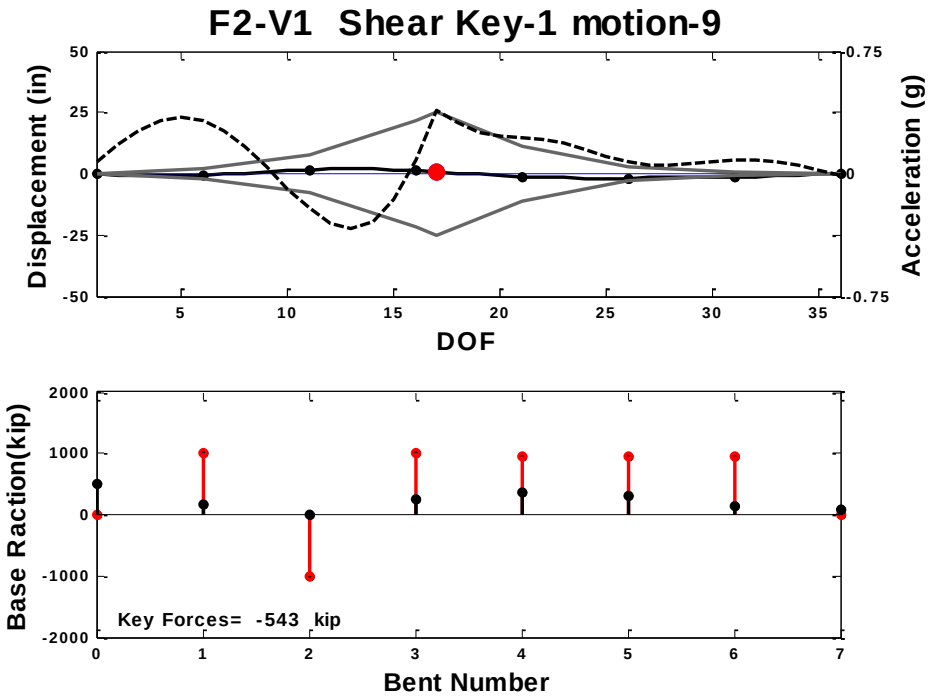

Figure C.253 System State at Maximum Force, Prototype F2-V1, motion-9

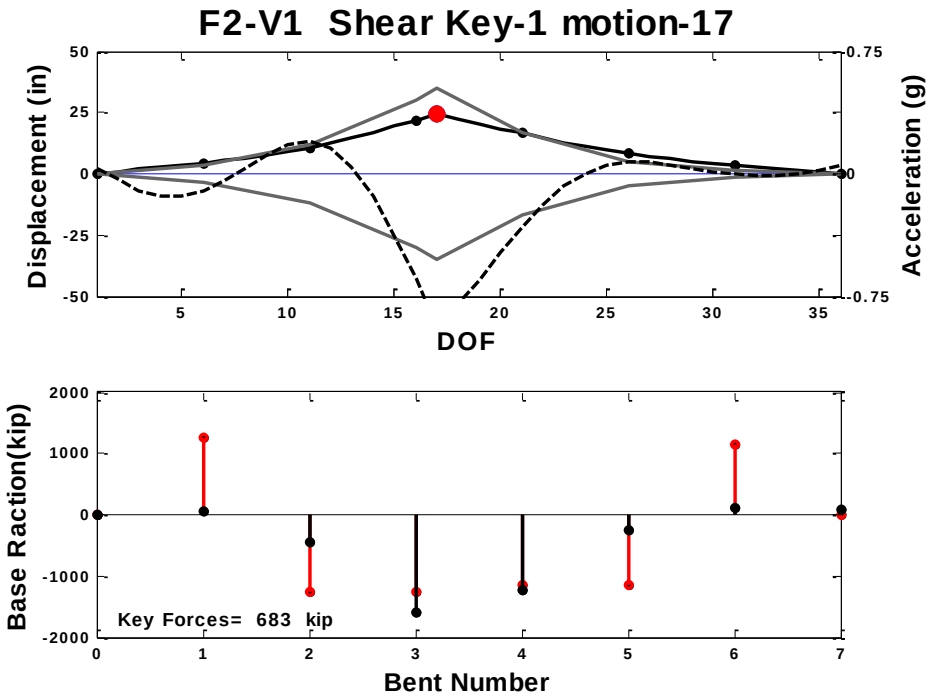

Figure C.254 System State at Maximum Force, Prototype F2-V1, motion-17

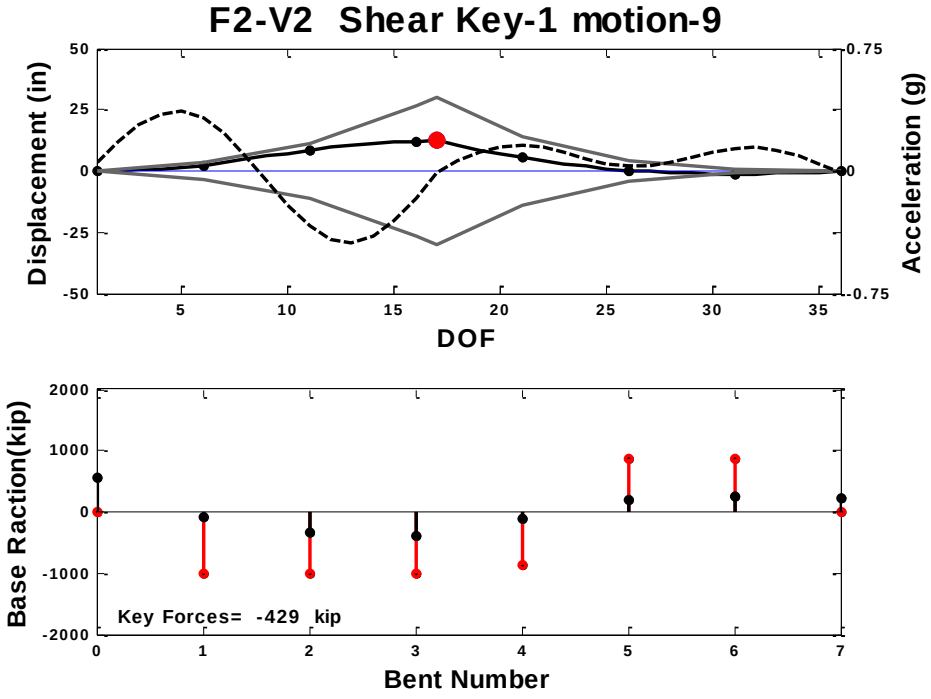

Figure C.255 System State at Maximum Force, Prototype F2-V2, motion-9

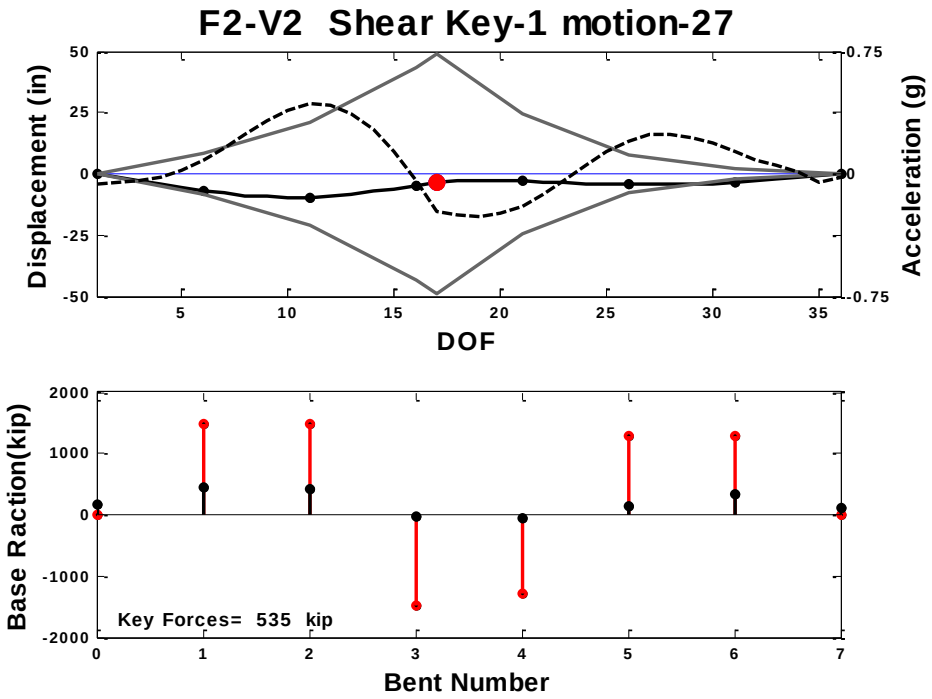

Figure C.256 System State at Maximum Force, Prototype F2-V2, motion-27

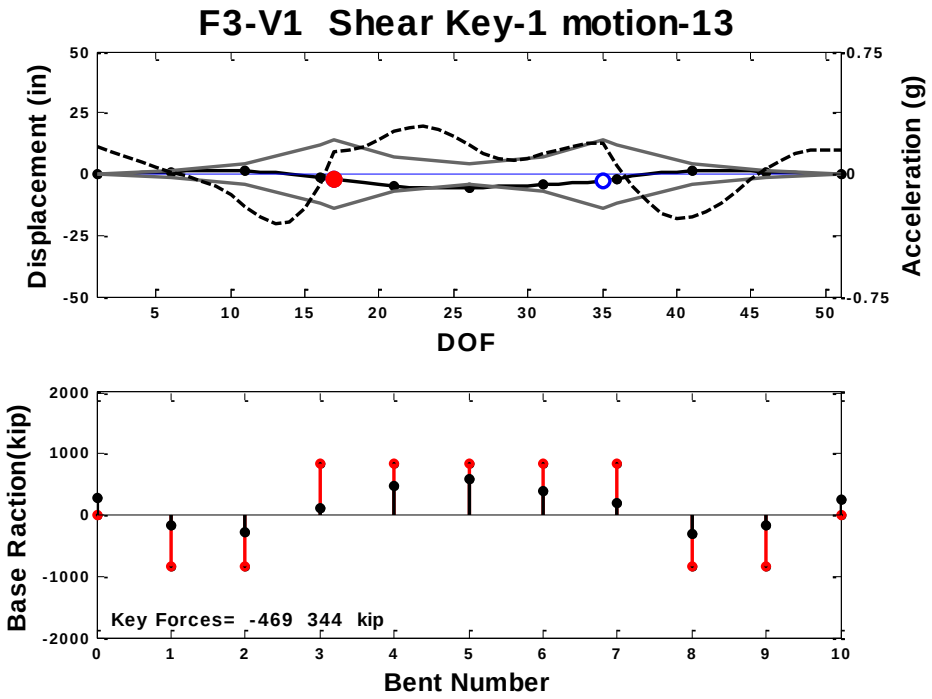

Figure C.257 System State at Maximum Force, Prototype F3-V1, motion-13

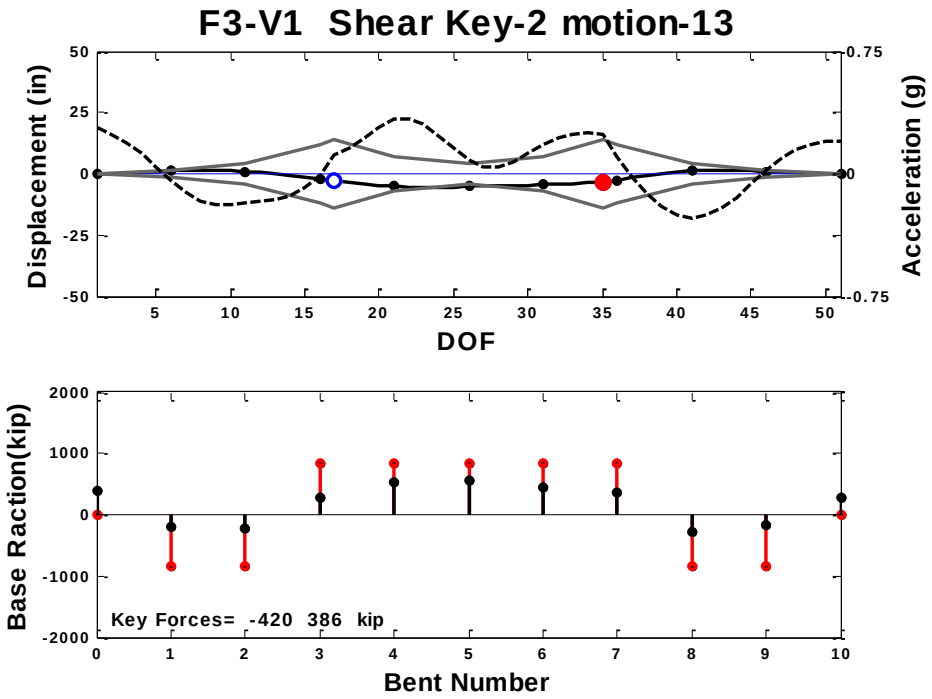

Figure C.258 System State at Maximum Force, Prototype F3-V1, motion-13

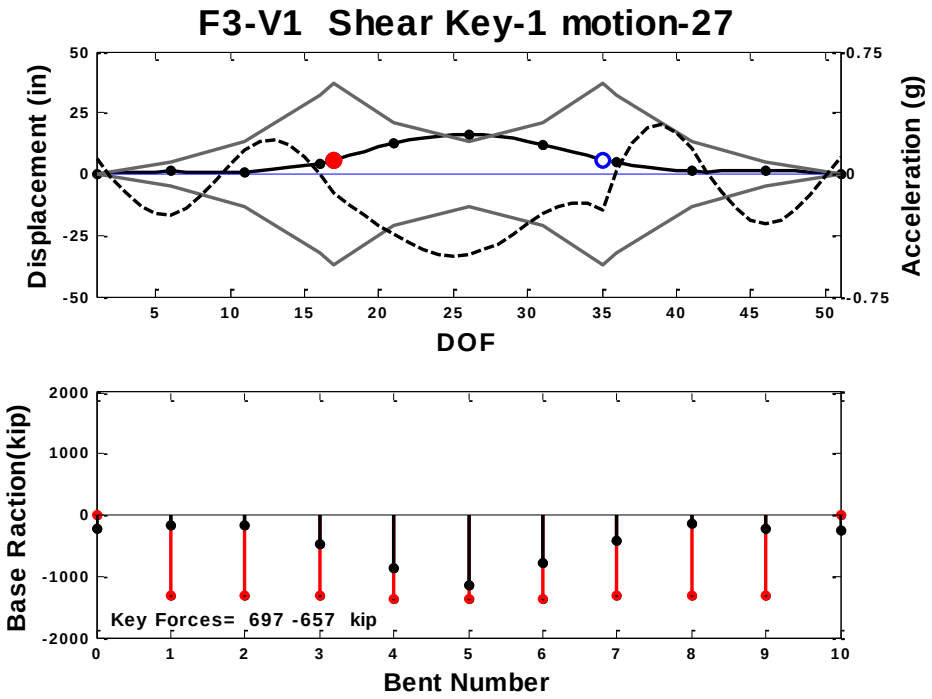

Figure C.259 System State at Maximum Force, Prototype F3-V1, motion-27

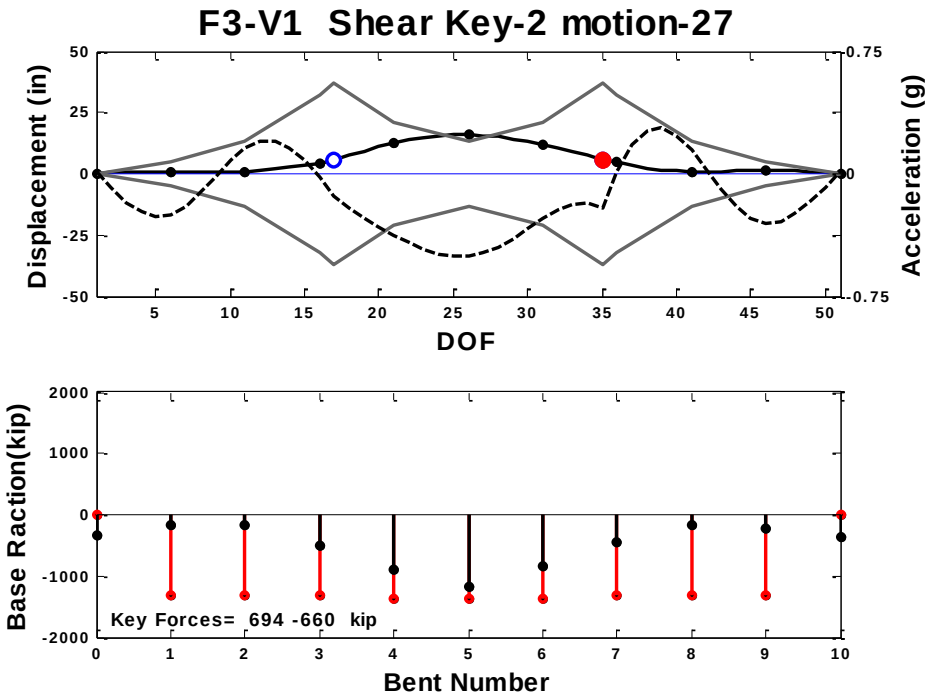

Figure C.260 System State at Maximum Force, Prototype F3-V1, motion-27

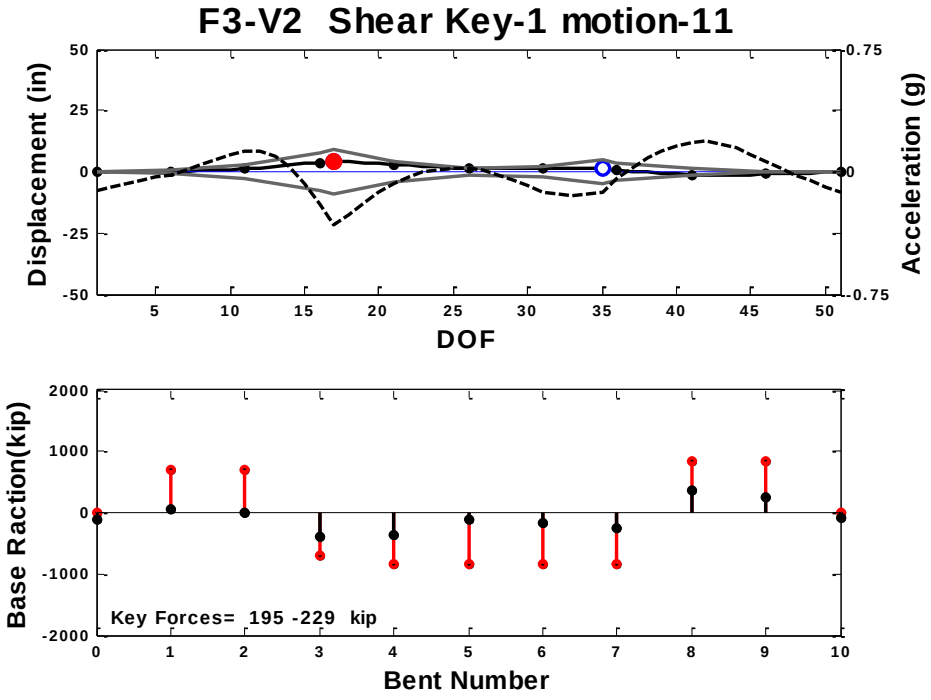

Figure C.261 System State at Maximum Force, Prototype F3-V2, motion-11

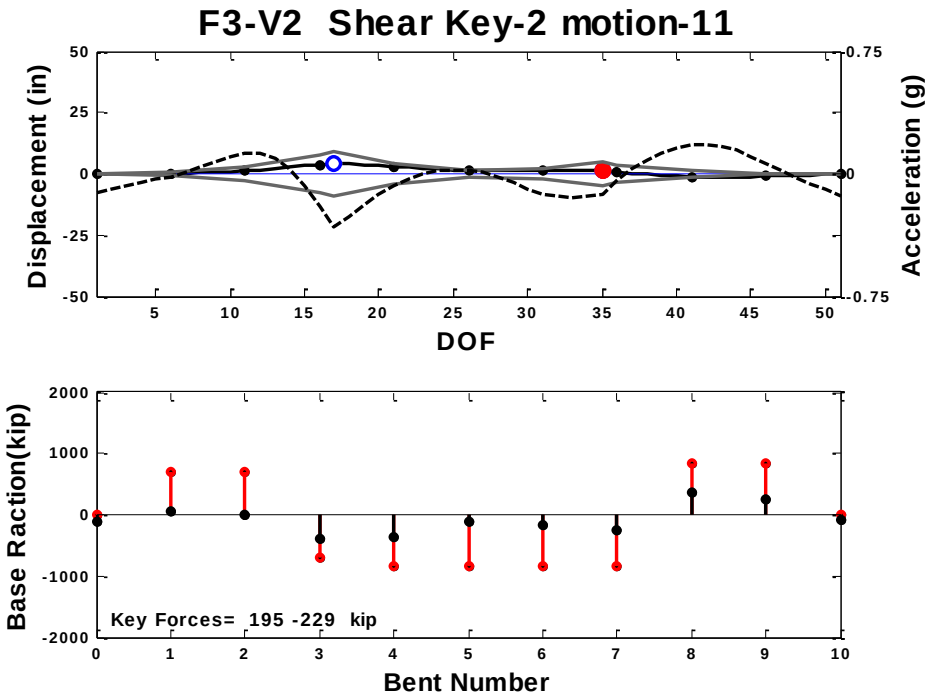

Figure C.262 System State at Maximum Force, Prototype F3-V2, motion-11

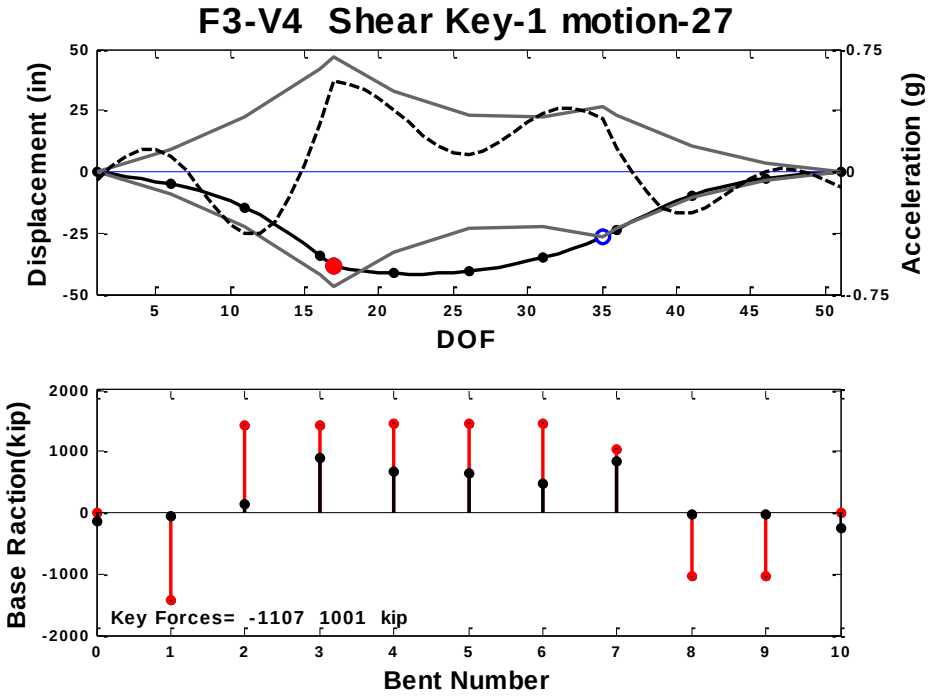

Figure C.263 System State at Maximum Force, Prototype F3-V4, motion-27

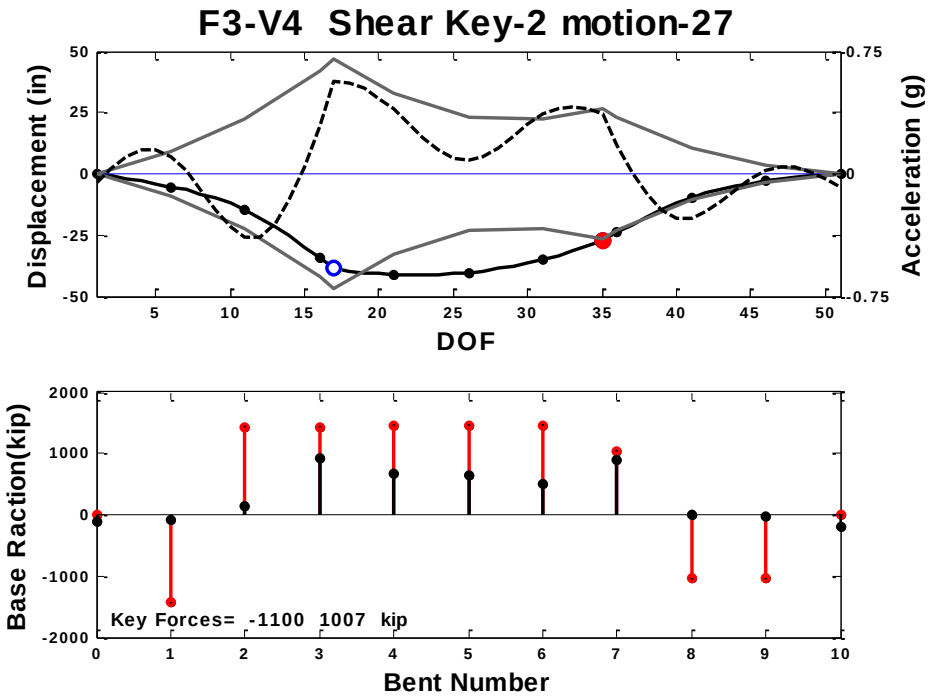

Figure C.264 System State at Maximum Force, Prototype F3-V4, motion-27

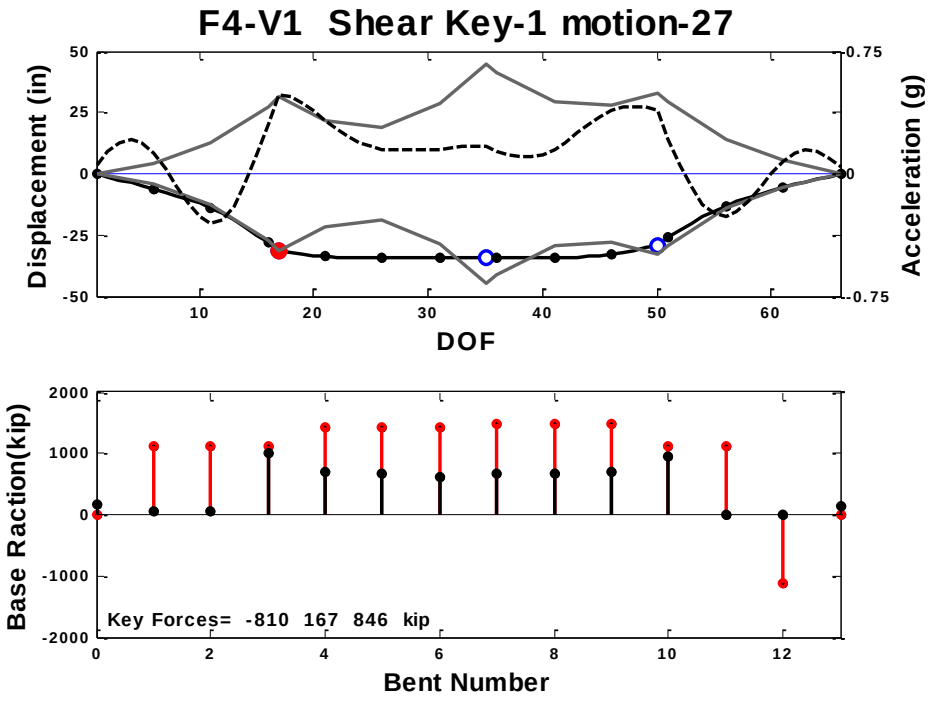

Figure C.265 System State at Maximum Force, Prototype F4-V1, motion-27

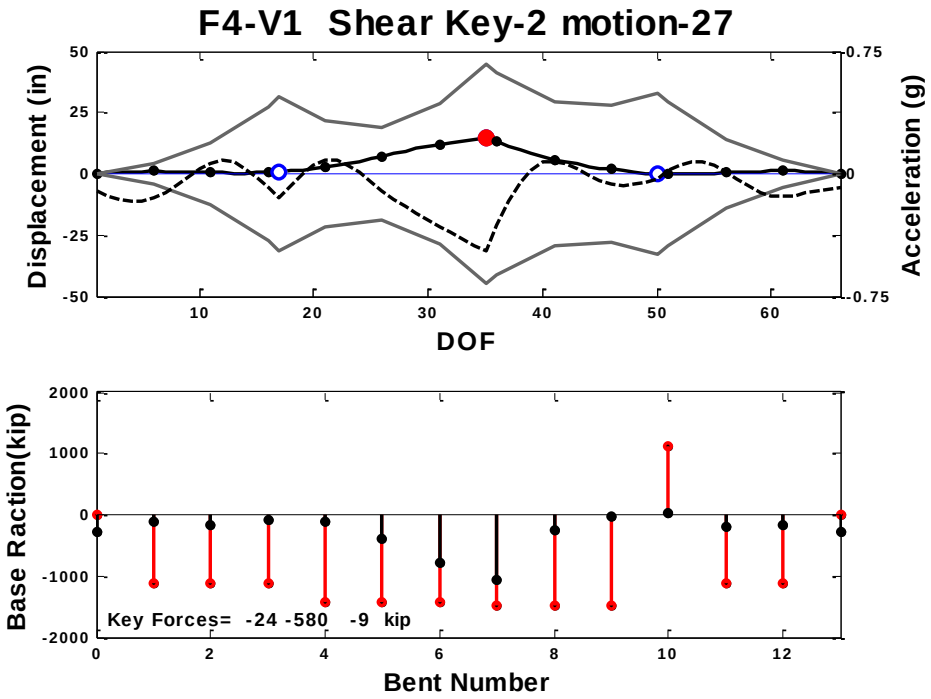

Figure C.266 System State at Maximum Force, Prototype F4-V1, motion-27

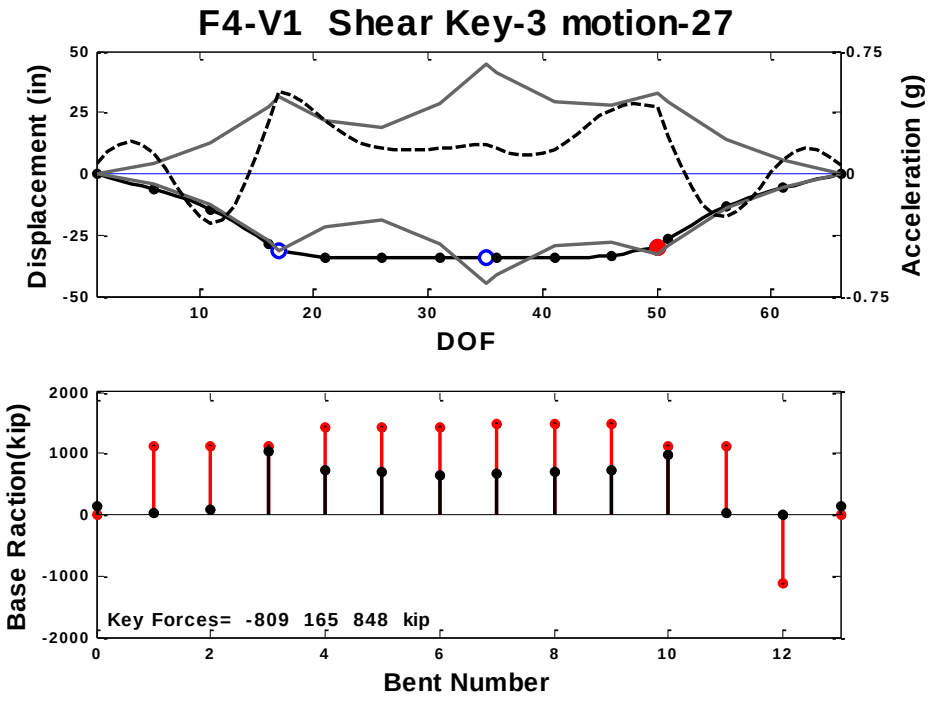

Figure C.267 System State at Maximum Force, Prototype F4-V1, motion-27

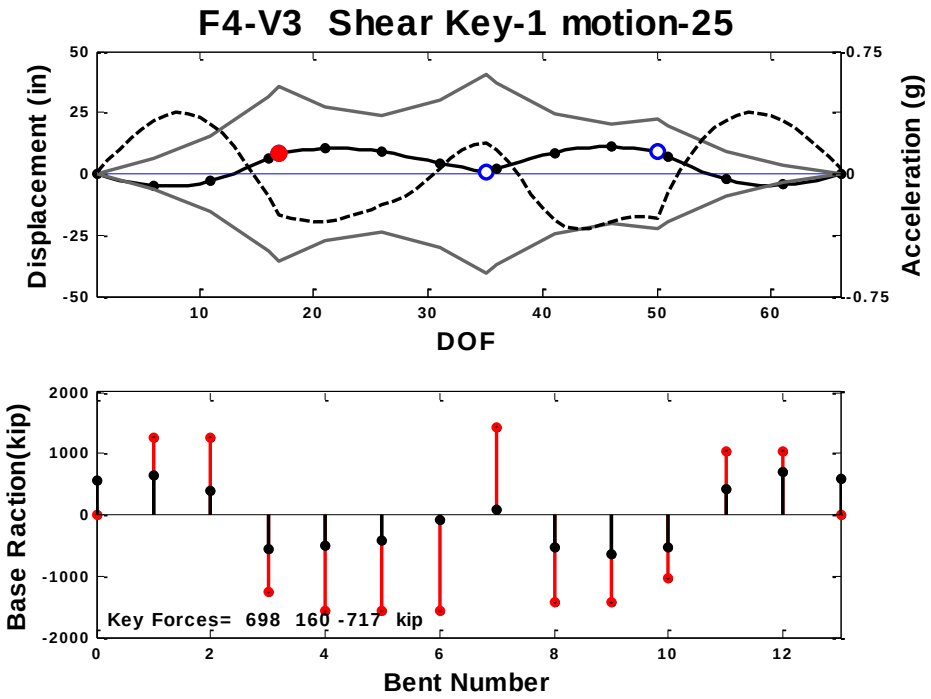

Figure C.268 System State at Maximum Force, Prototype F4-V3, motion-25

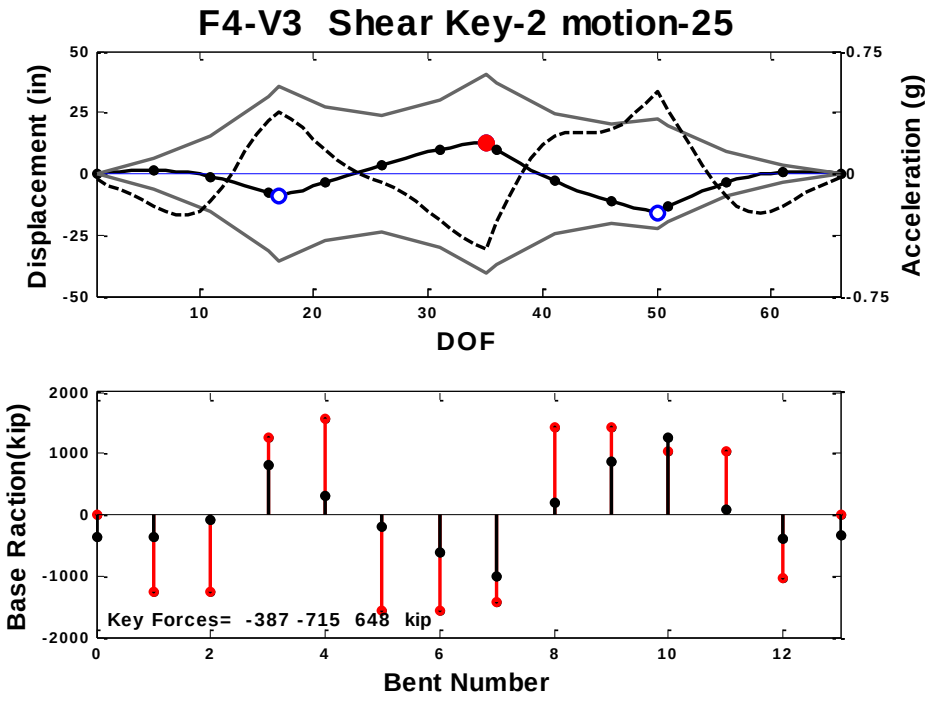

Figure C.269 System State at Maximum Force, Prototype F4-V3, motion-25

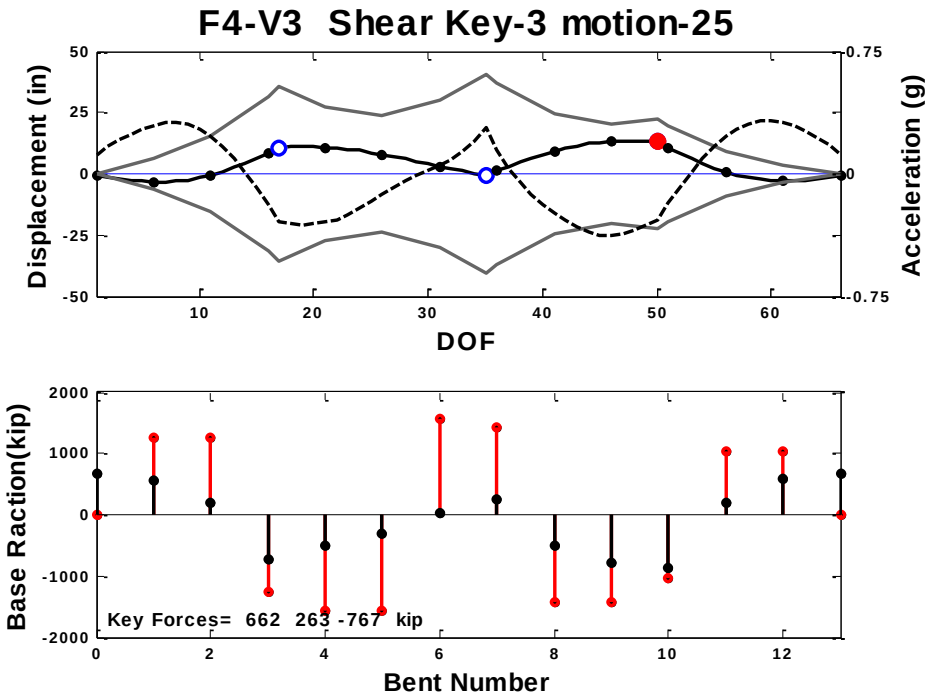

Figure C.270 System State at Maximum Force, Prototype F4-V3, motion-25

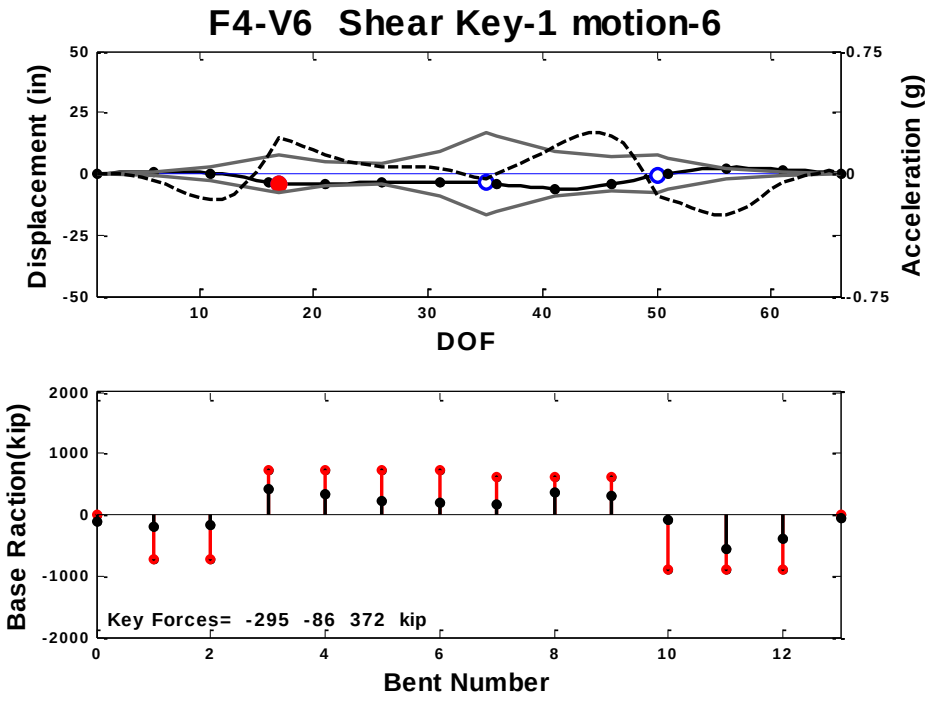

Figure C.271 System State at Maximum Force, Prototype F4-V6, motion-6

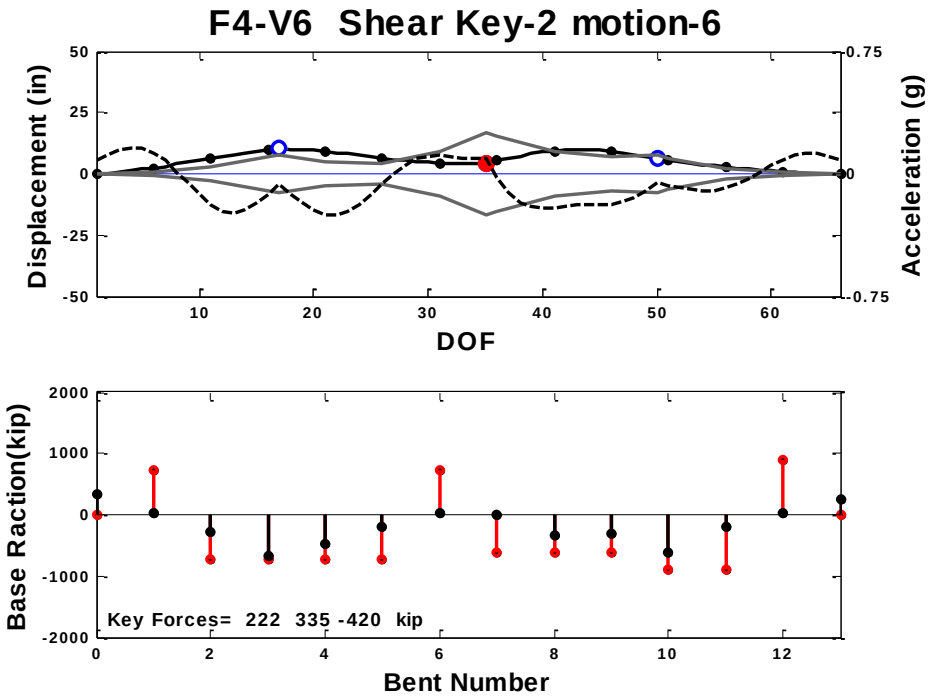

Figure C.272 System State at Maximum Force, Prototype F4-V6, motion-6

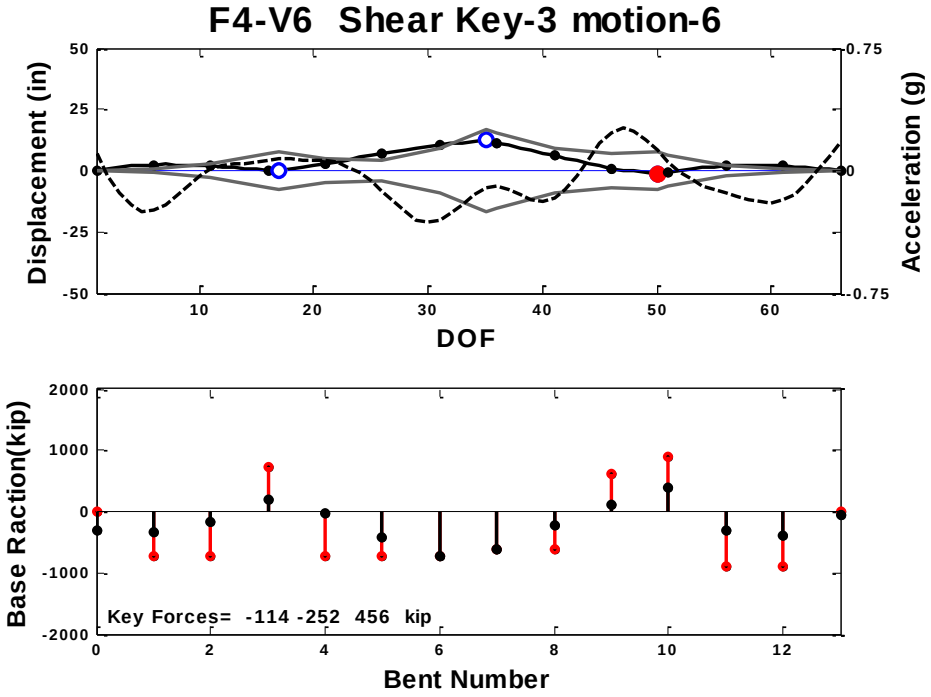

Figure C.273 System State at Maximum Force, Prototype F4-V6, motion-6

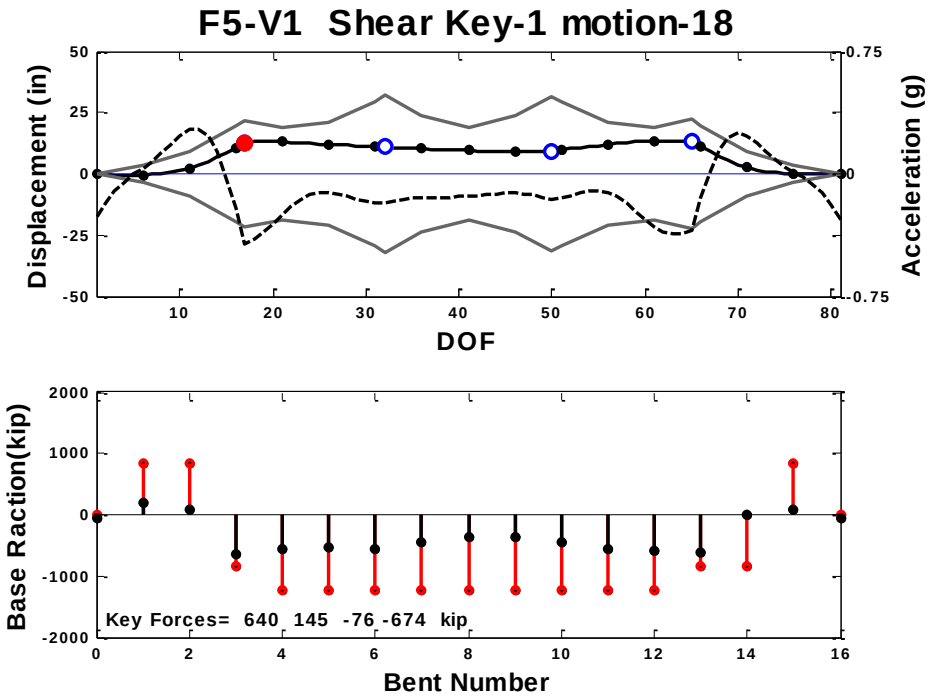

Figure C.274 System State at Maximum Force, Prototype F5-V1, motion-18

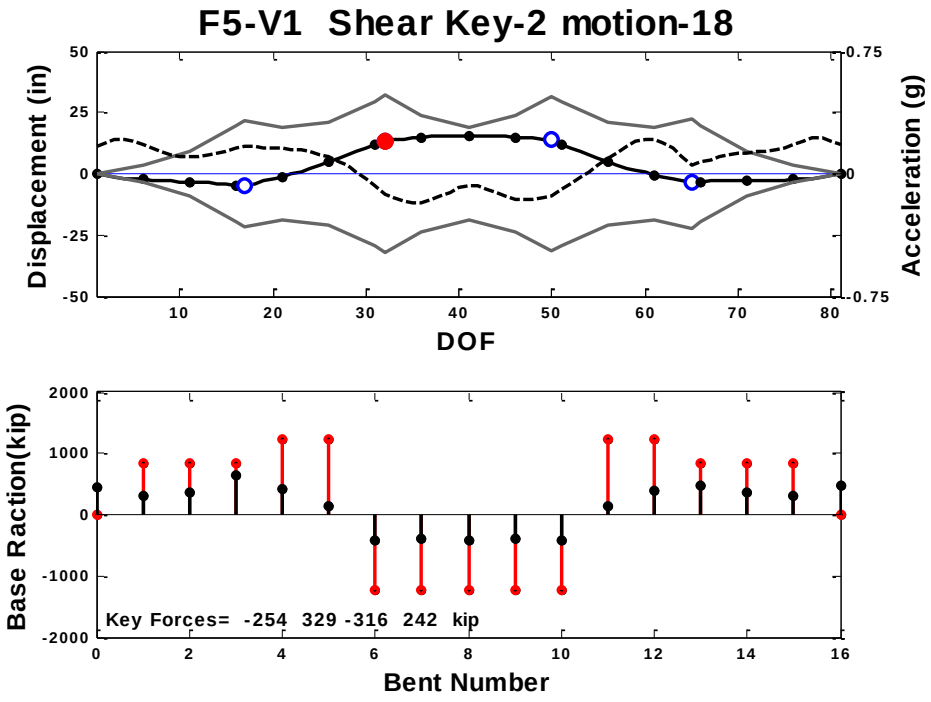

Figure C.275 System State at Maximum Force, Prototype F5-V1, motion-18

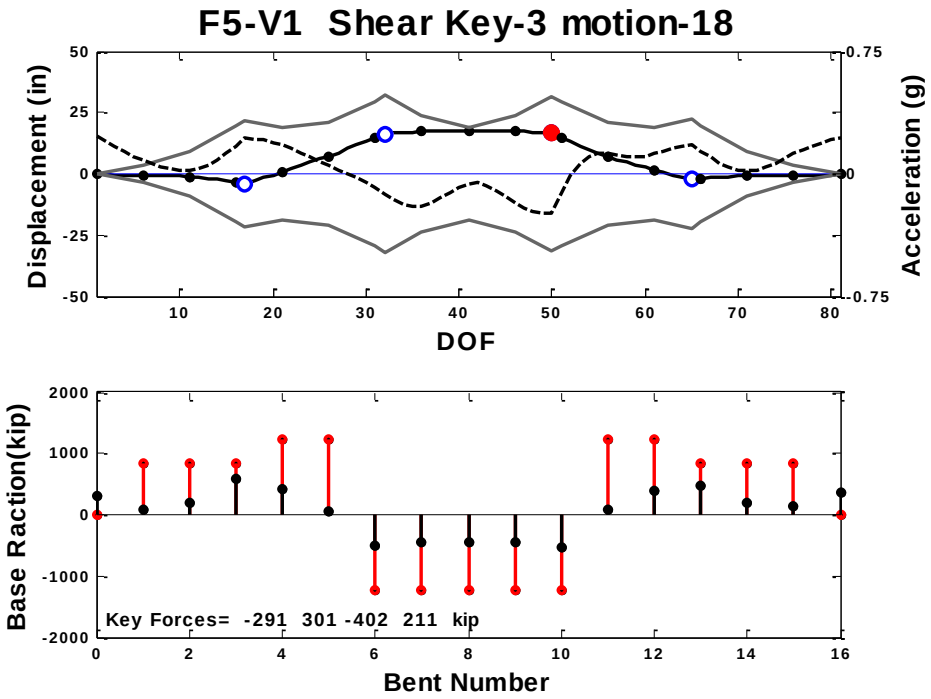

Figure C.276 System State at Maximum Force, Prototype F5-V1, motion-18

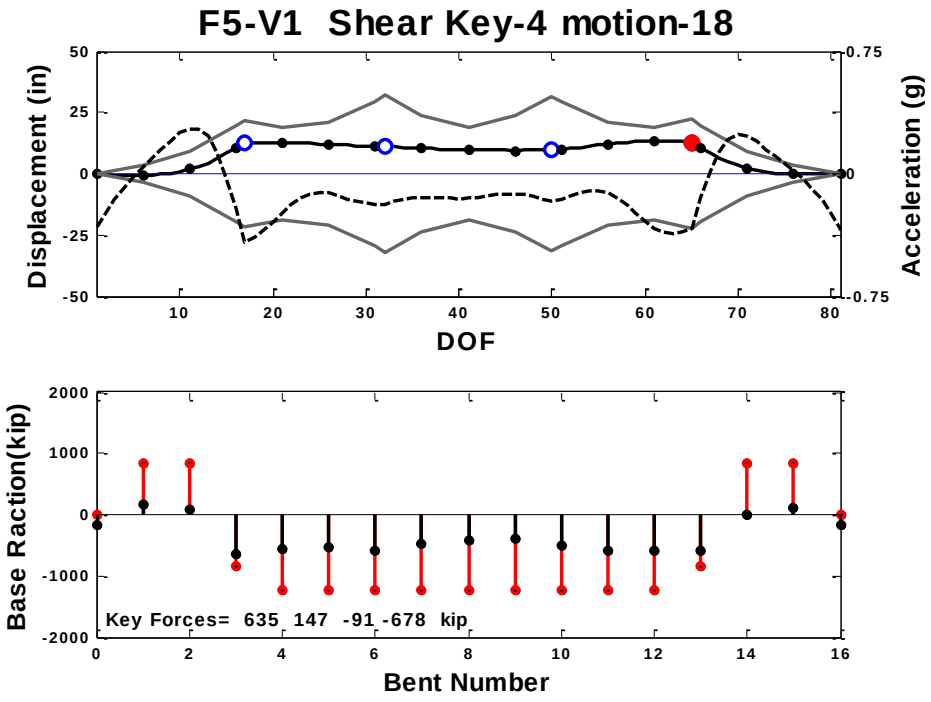

Figure C.277 System State at Maximum Force, Prototype F5-V1, motion-18

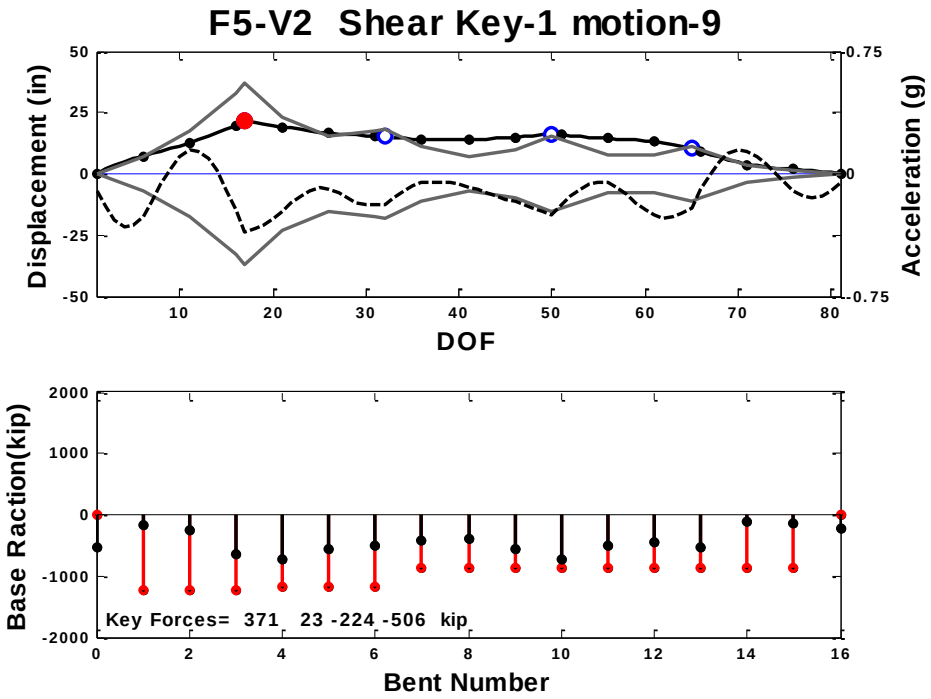

Figure C.278 System State at Maximum Force, Prototype F5-V2, motion-9

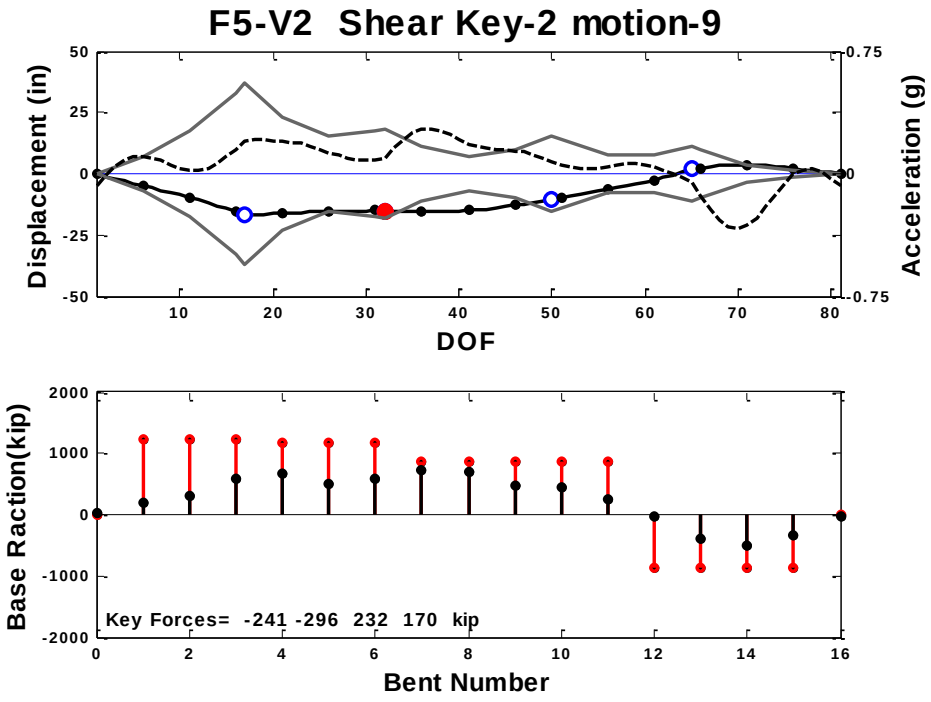

Figure C.279 System State at Maximum Force, Prototype F5-V2, motion-9

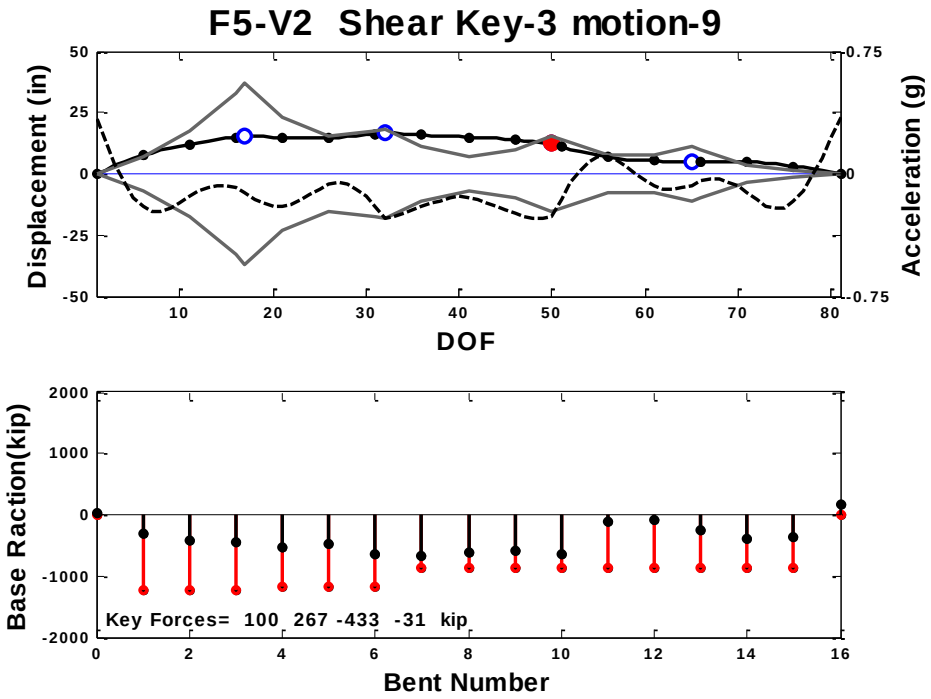

Figure C.280 System State at Maximum Force, Prototype F5-V2, motion-9

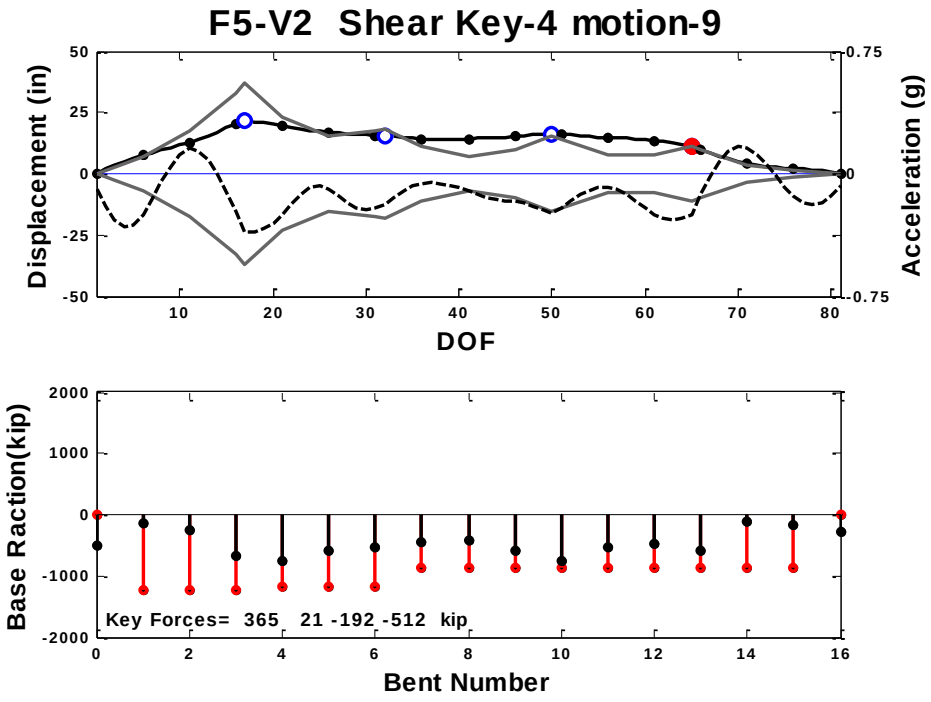

Figure C.281 System State at Maximum Force, Prototype F5-V2, motion-9

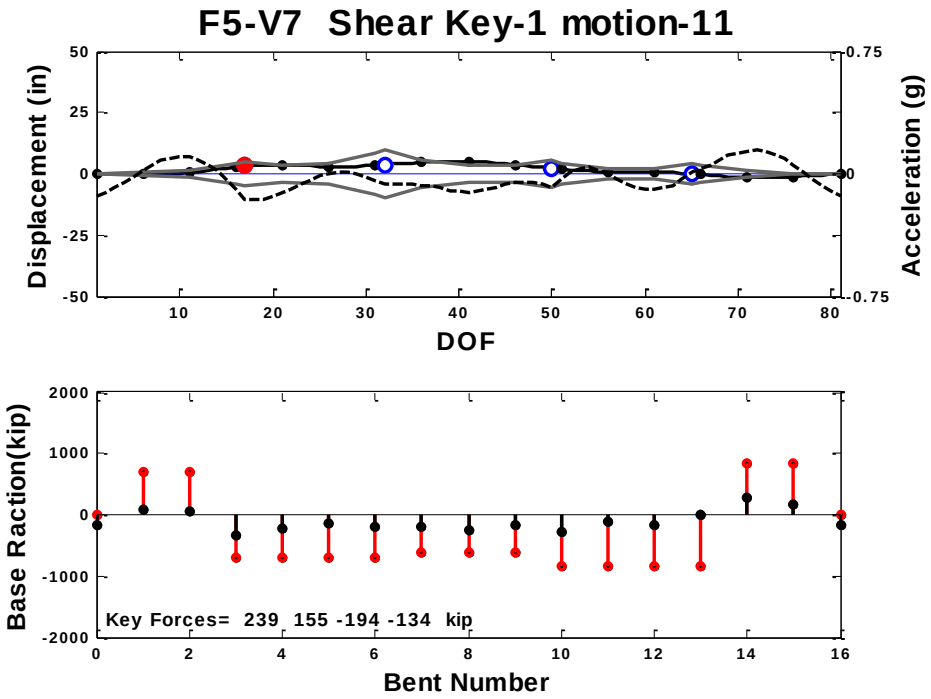

Figure C.282 System State at Maximum Force, Prototype F5-V7, motion-11

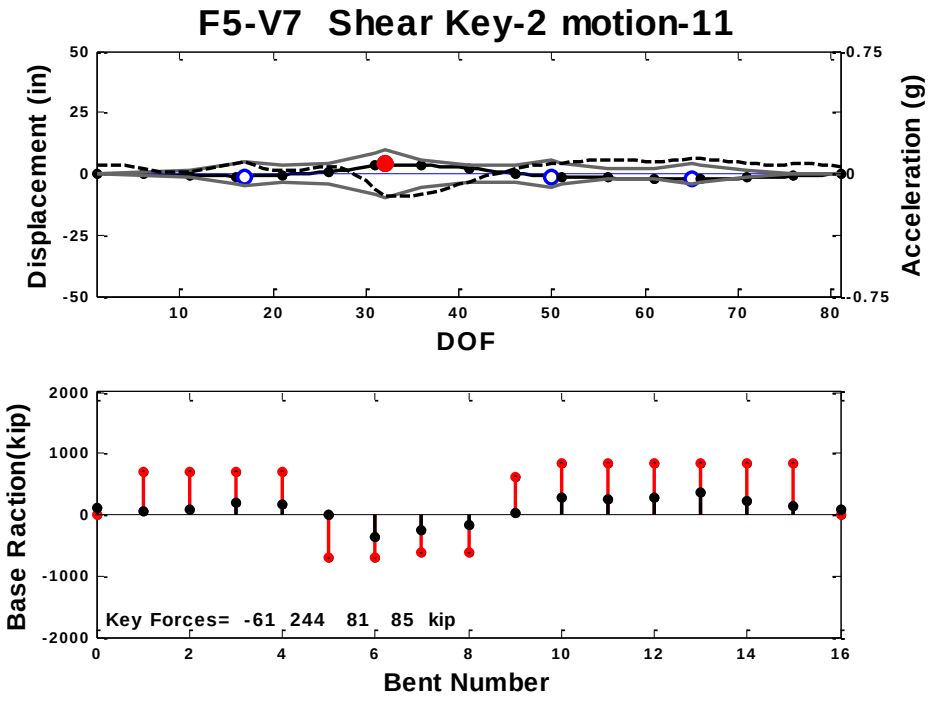

Figure C.283 System State at Maximum Force, Prototype F5-V7, motion-11

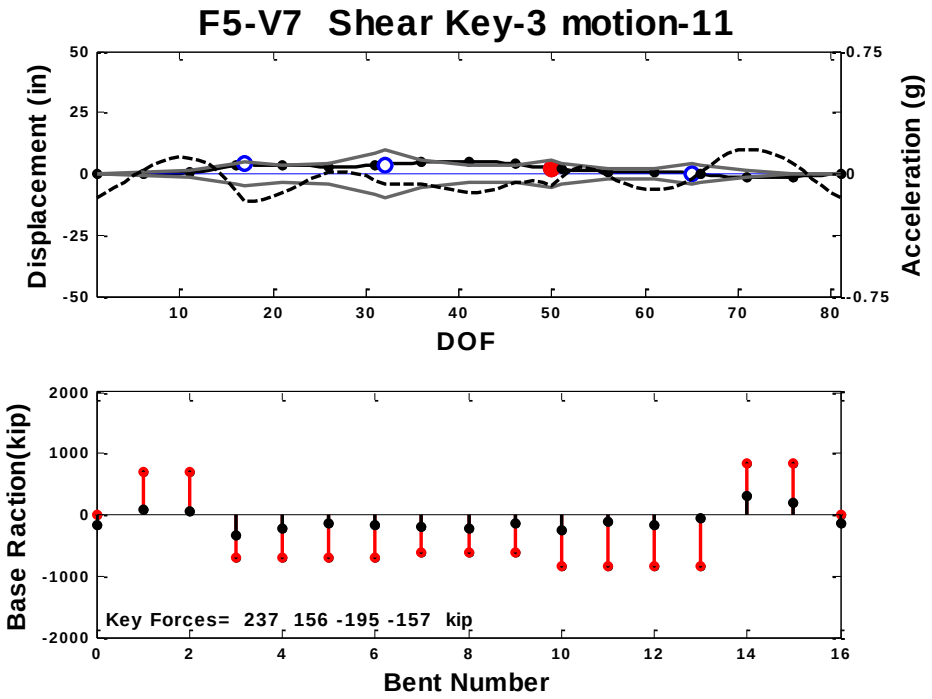

Figure C.284 System State at Maximum Force, Prototype F5-V7, motion-11

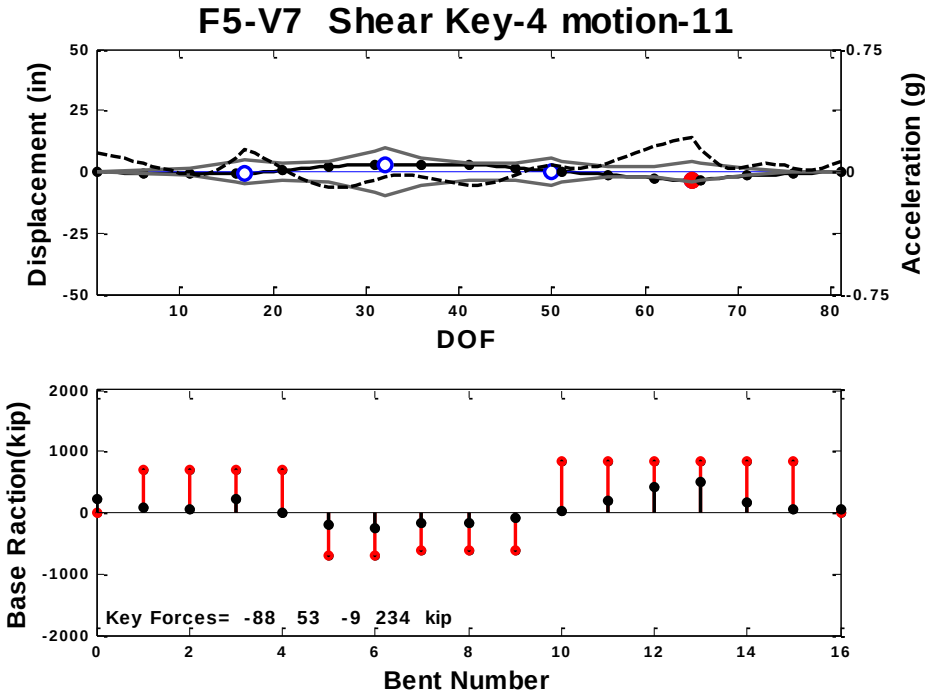

Figure C.285 System State at Maximum Force, Prototype F5-V7, motion-11

PART-4b: Two-Column Bent Prototypes
System State at the Time of the Maximum Shear Key Forces.

Legend:

Solid Black = Displacement

Dash line = Acceleration

Gray = Design Displacement Demand

Red Stem = bent capacity

Black Stem = base reaction

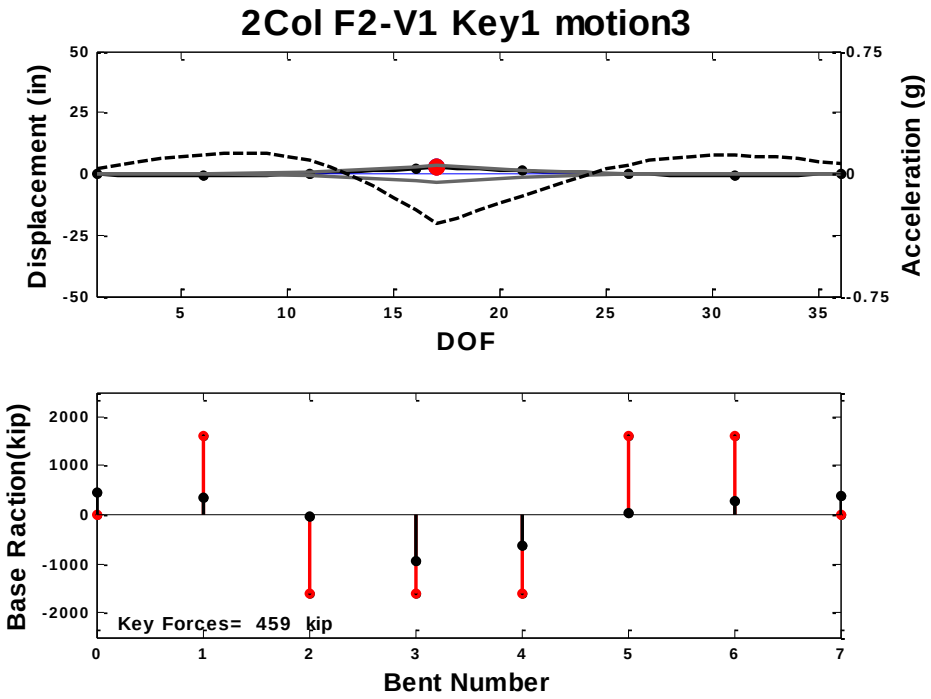

Figure C.286 System State at Maximum Force, Prototype F2-V1, motion-3

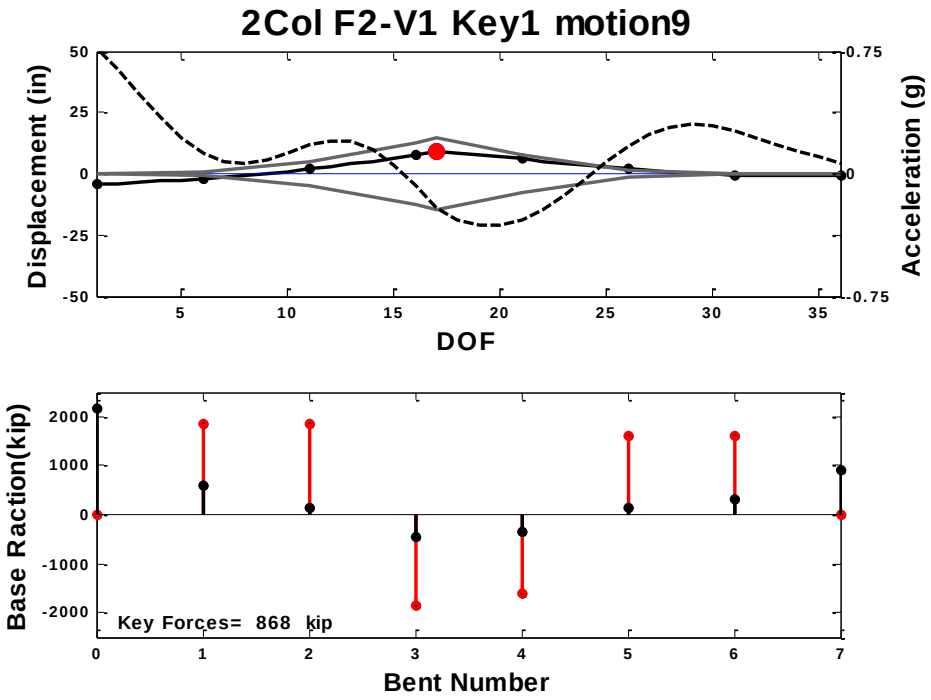

Figure C.287 System State at Maximum Force, Prototype F2-V1, motion-9

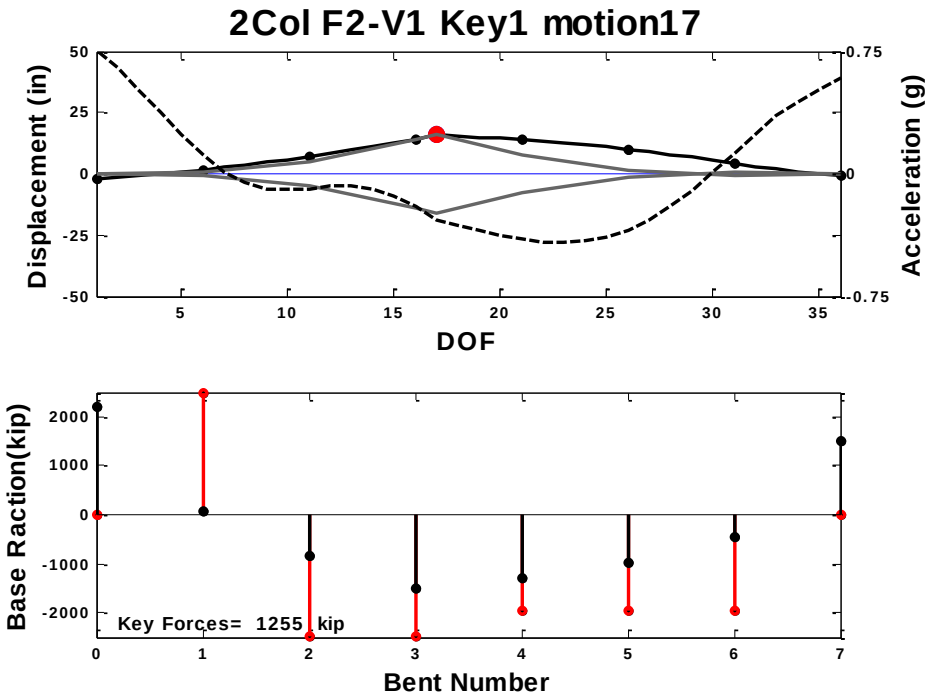

Figure C.288 System State at Maximum Force, Prototype F2-V1, motion-17

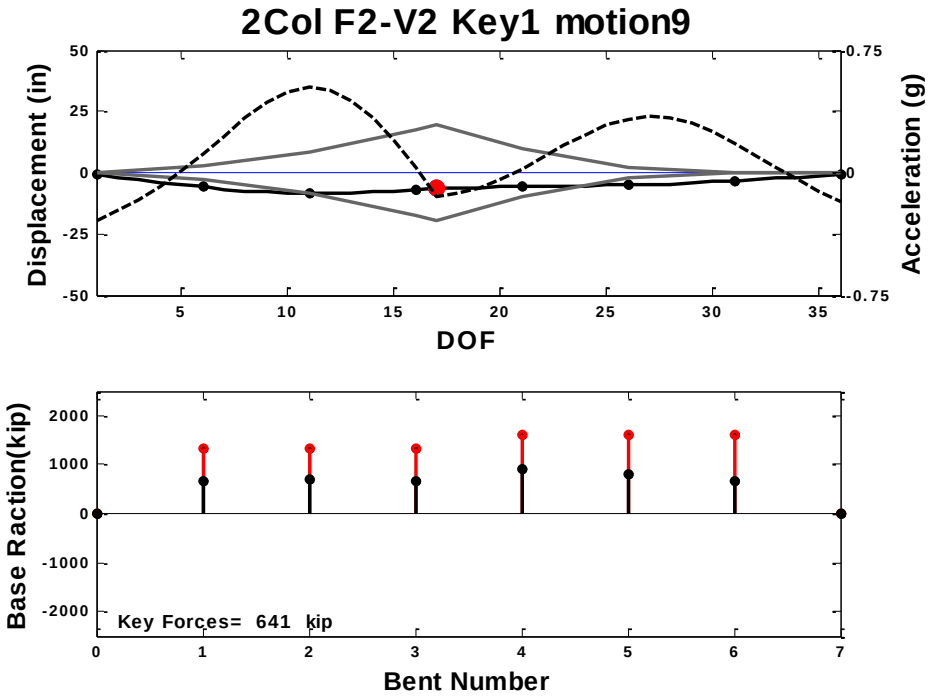

Figure C.289 System State at Maximum Force, Prototype F2-V2, motion-9

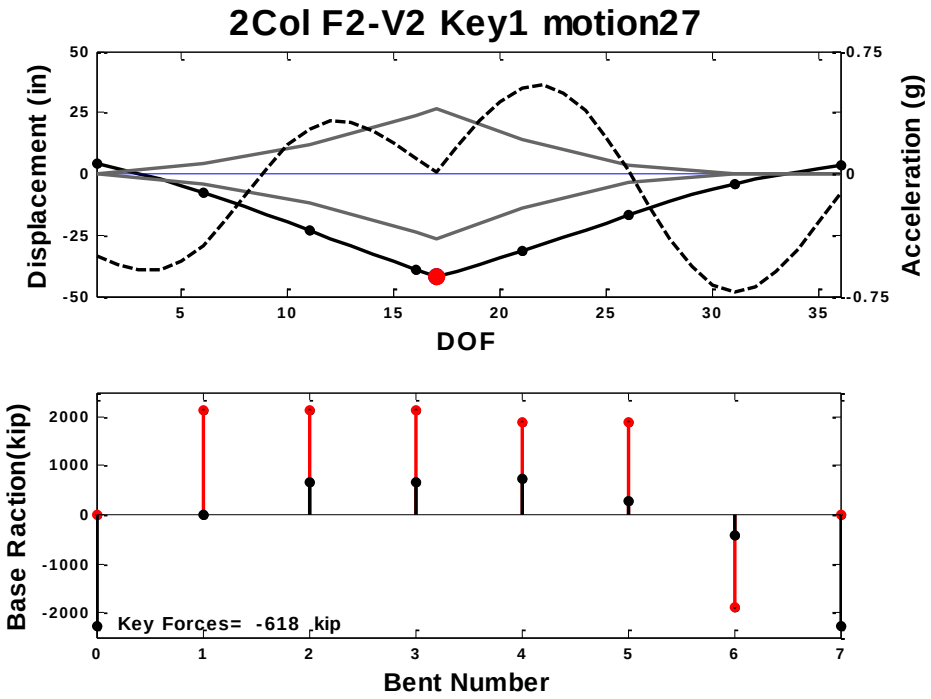

Figure C.290 System State at Maximum Force, Prototype F2-V2, motion-27

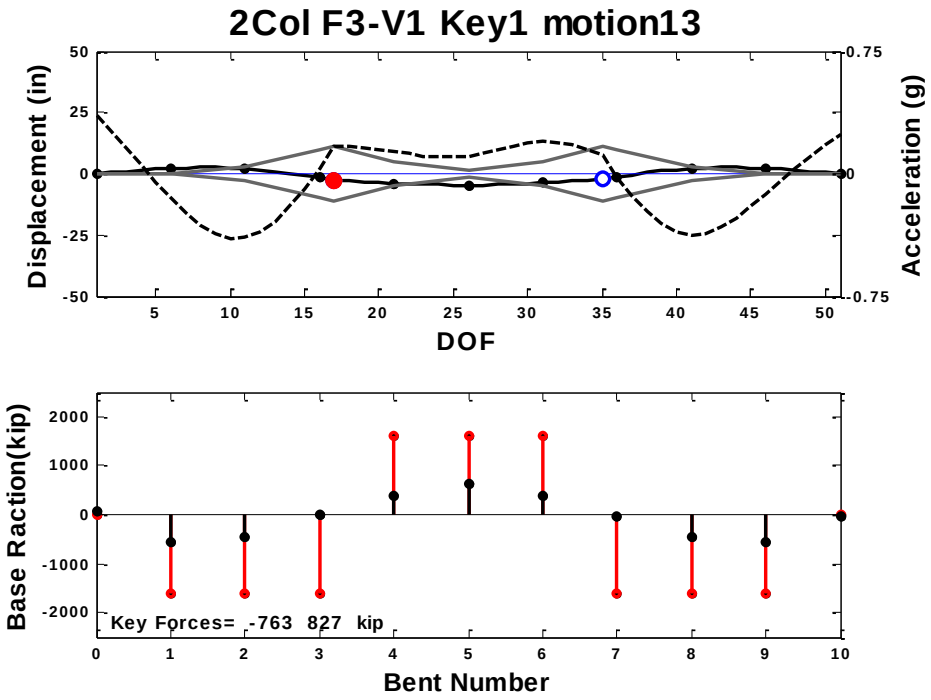

Figure C.291 System State at Maximum Force, Prototype F3-V1, motion-13

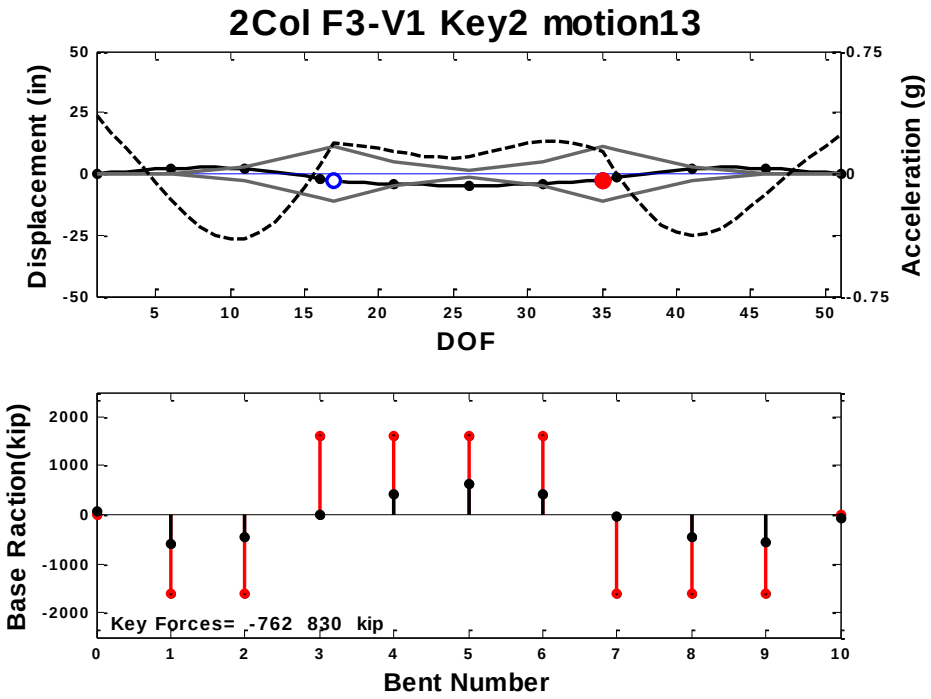

Figure C.292 System State at Maximum Force, Prototype F3-V1, motion-13

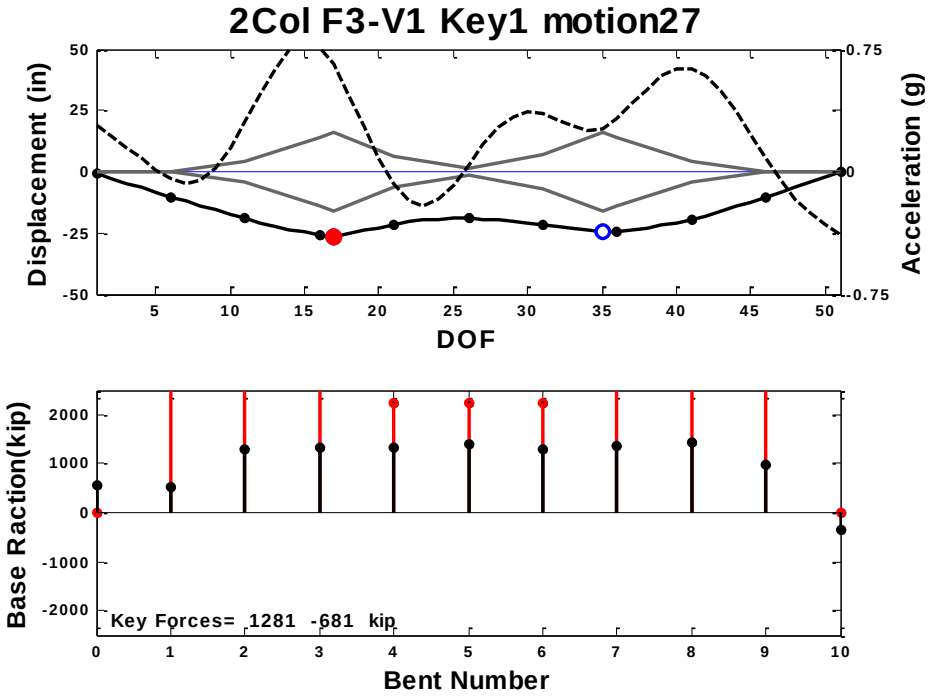

Figure C.293 System State at Maximum Force, Prototype F3-V1, motion-27

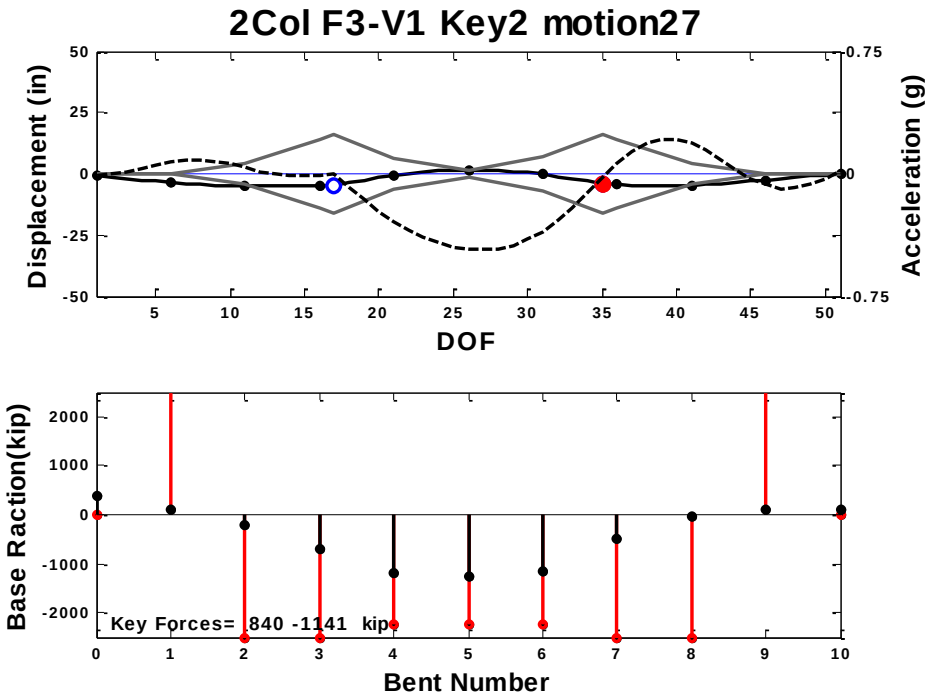

Figure C.294 System State at Maximum Force, Prototype F3-V1, motion-27

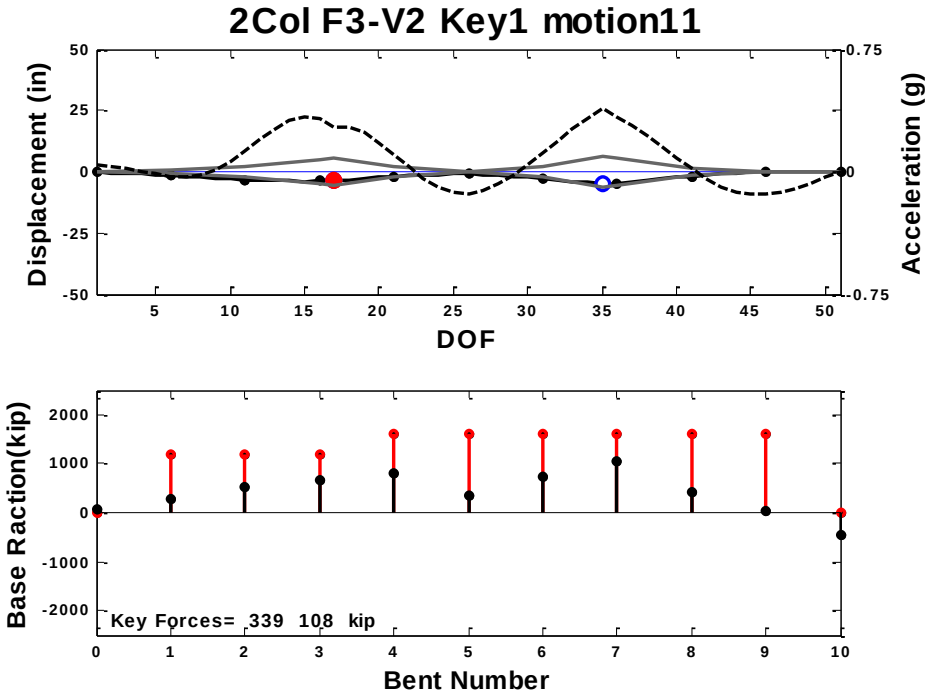

Figure C.295 System State at Maximum Force, Prototype F3-V2, motion-11

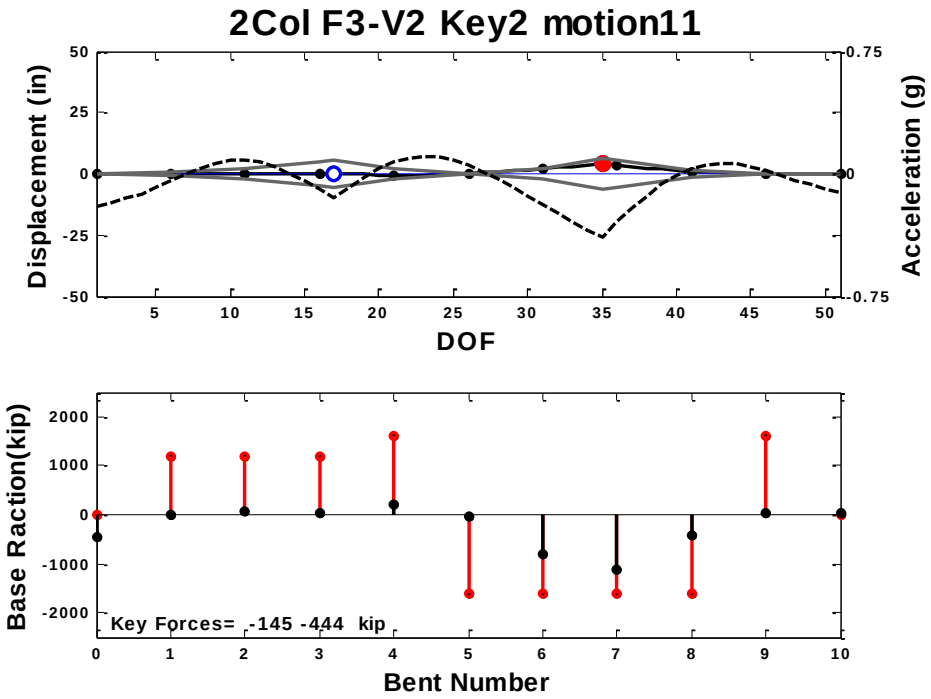

Figure C.296 System State at Maximum Force, Prototype F3-V2, motion-11

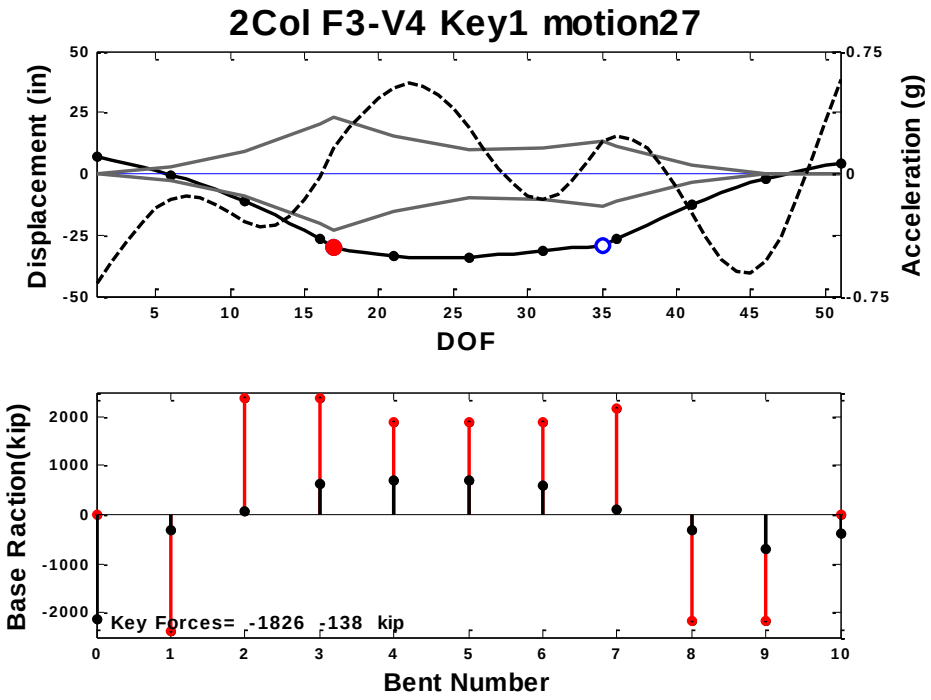

Figure C.297 System State at Maximum Force, Prototype F3-V4, motion-27

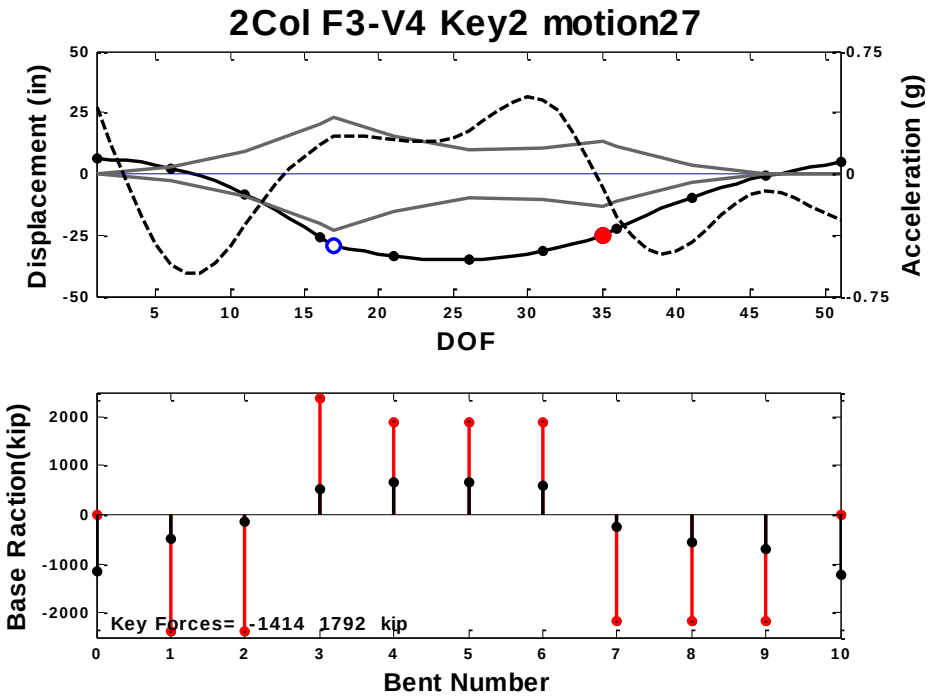

Figure C.298 System State at Maximum Force, Prototype F3-V4, motion-27

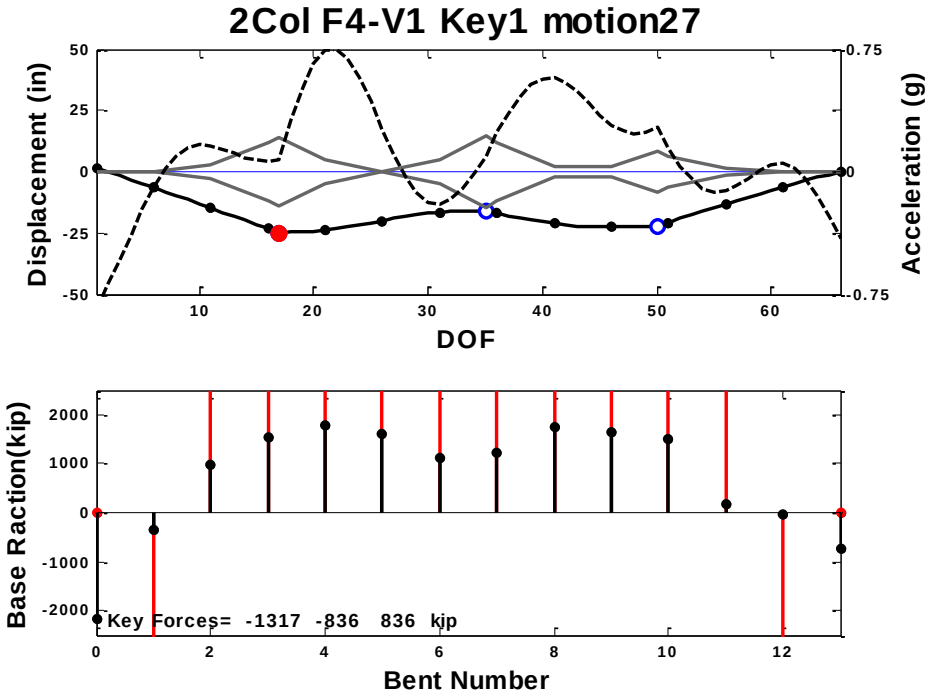

Figure C.299 System State at Maximum Force, Prototype F4-V1, motion-27

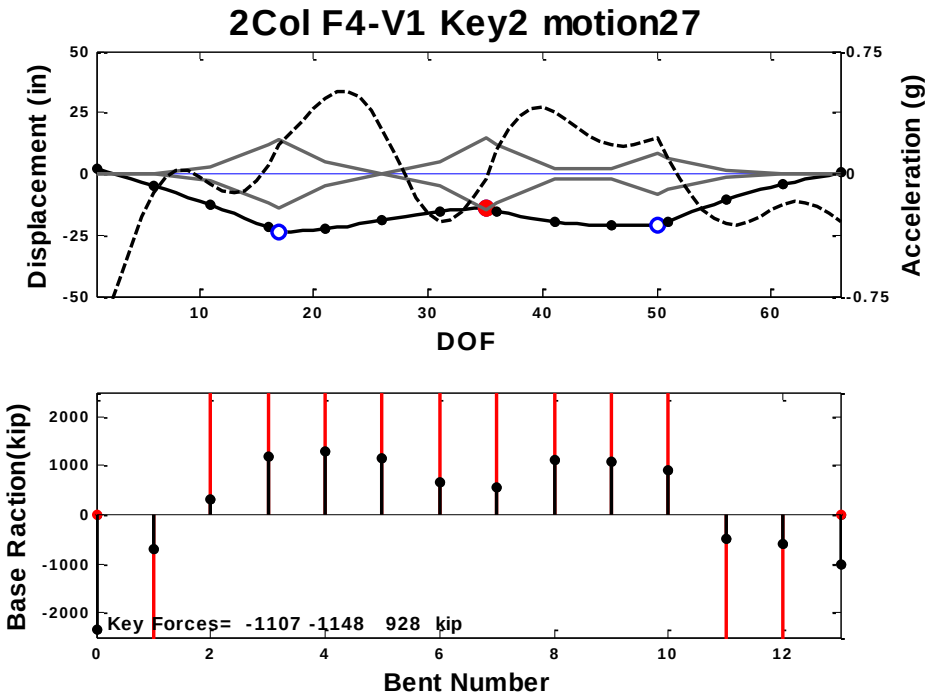

Figure C.300 System State at Maximum Force, Prototype F4-V1, motion-27

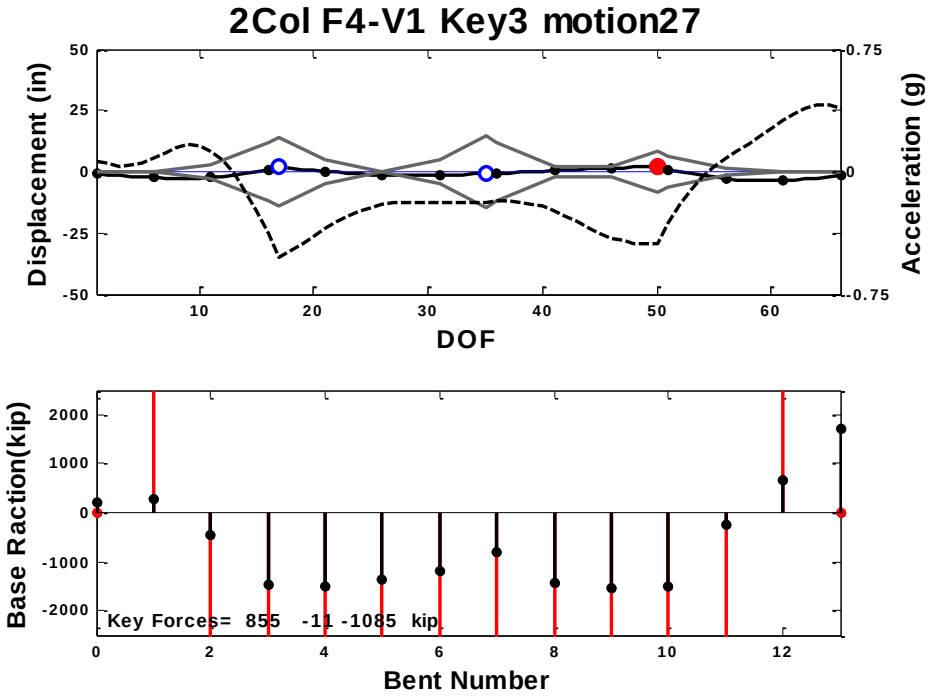

Figure C.301 System State at Maximum Force, Prototype F4-V1, motion-27

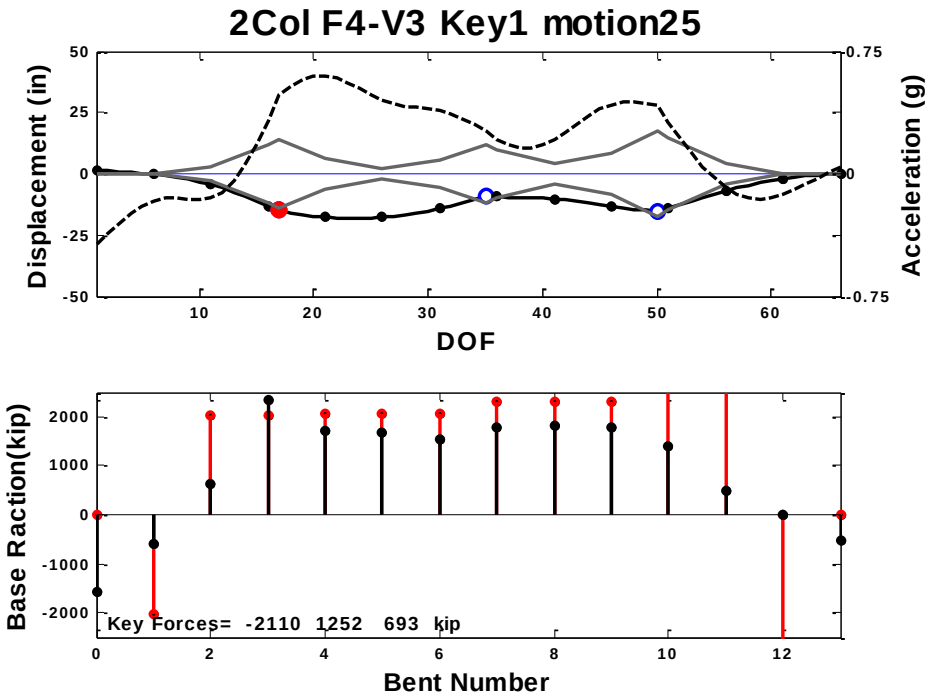

Figure C.302 System State at Maximum Force, Prototype F4-V3, motion-25

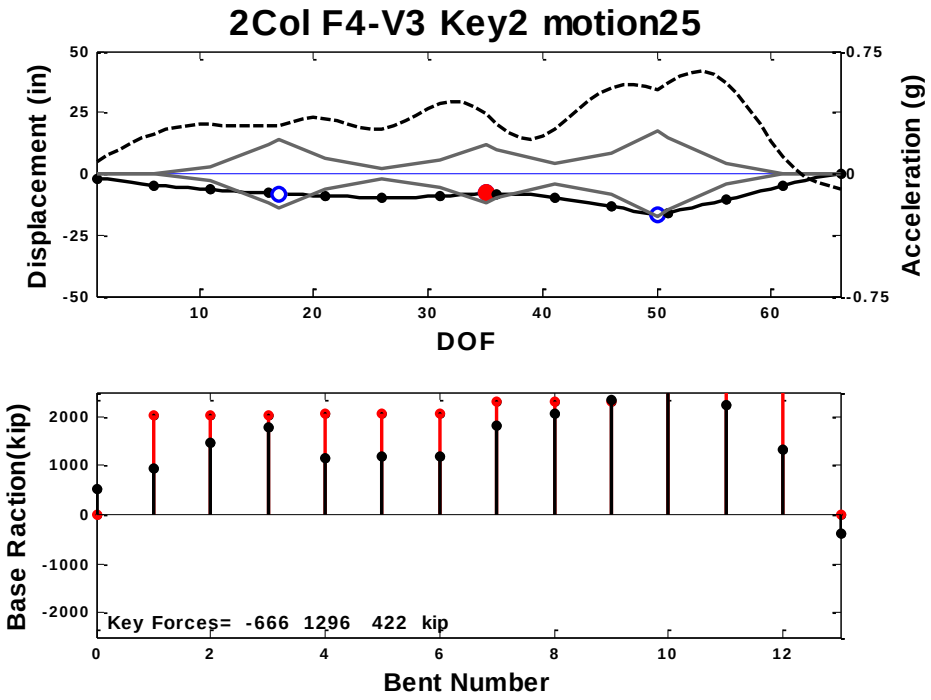

Figure C.303 System State at Maximum Force, Prototype F4-V3, motion-25

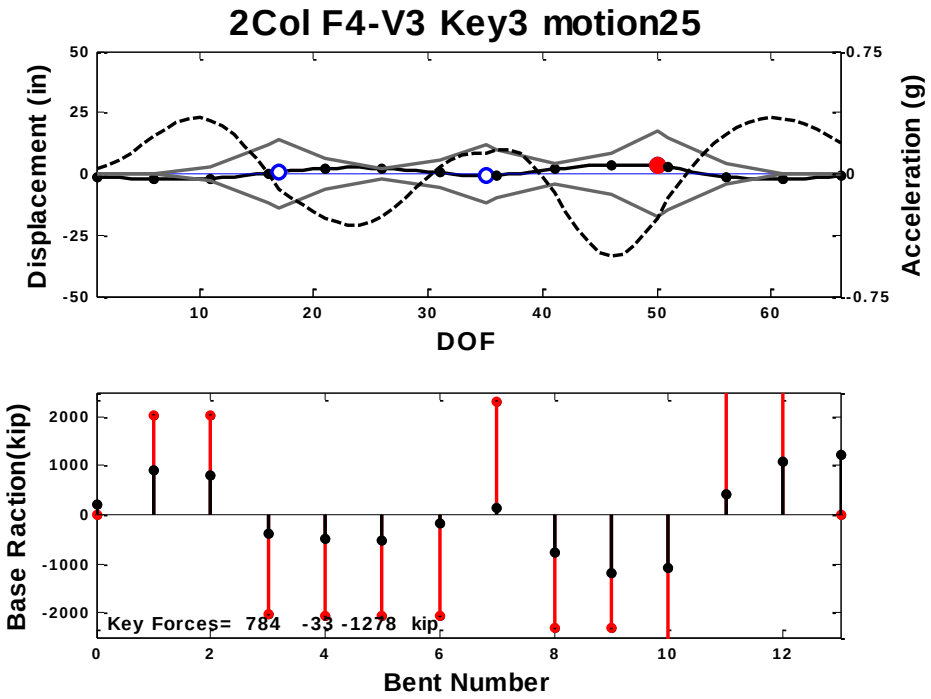

Figure C.304 System State at Maximum Force, Prototype F4-V3, motion-25

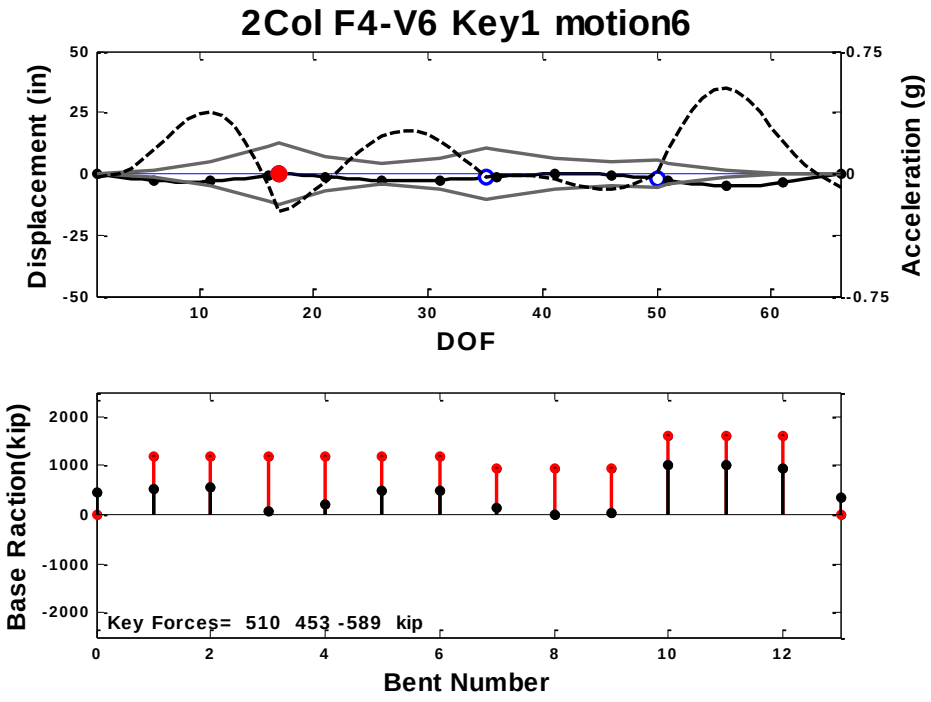

Figure C.305 System State at Maximum Force, Prototype F4-V6, motion-6

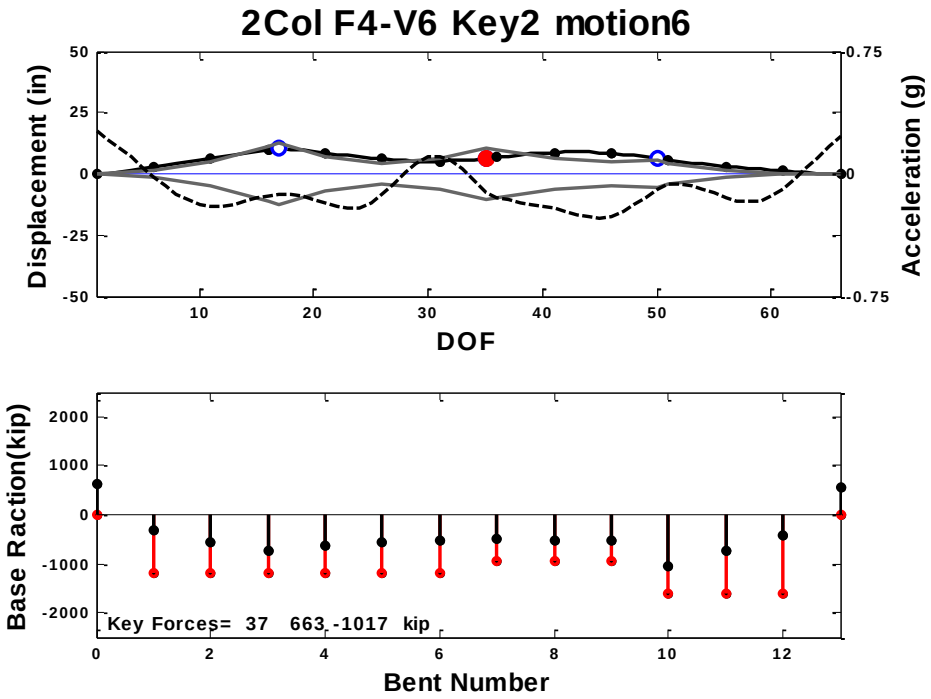

Figure C.306 System State at Maximum Force, Prototype F4-V6, motion-6

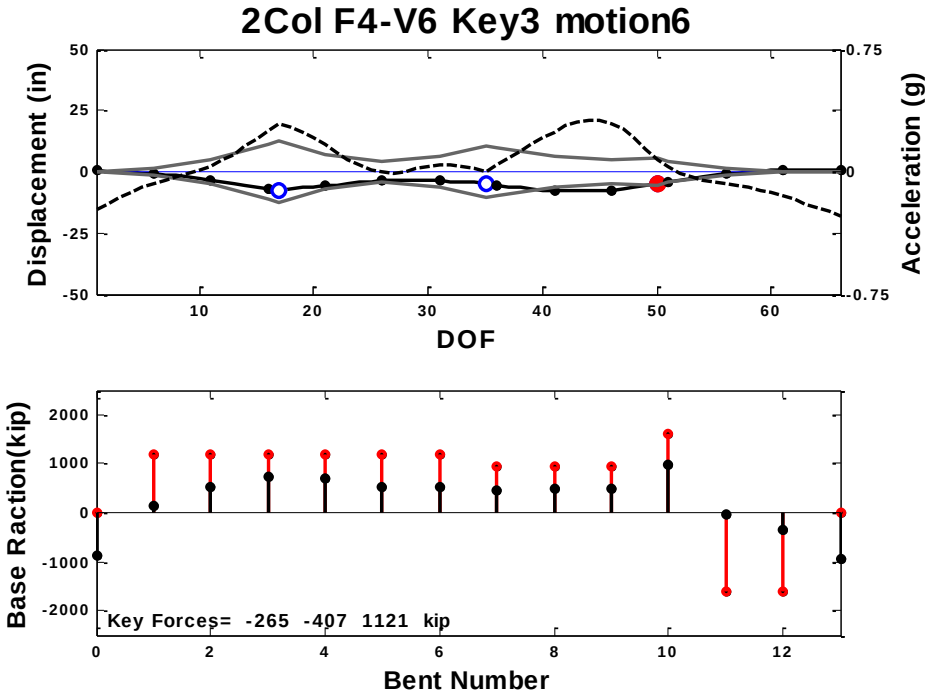

Figure C.307 System State at Maximum Force, Prototype F4-V6, motion-6

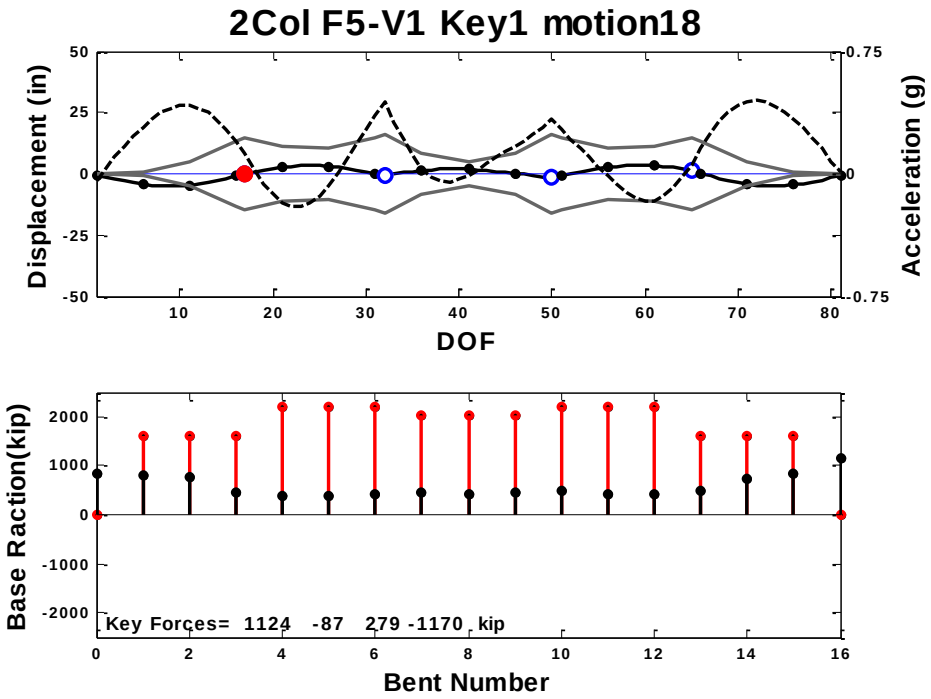

Figure C.308 System State at Maximum Force, Prototype F5-V1, motion-18

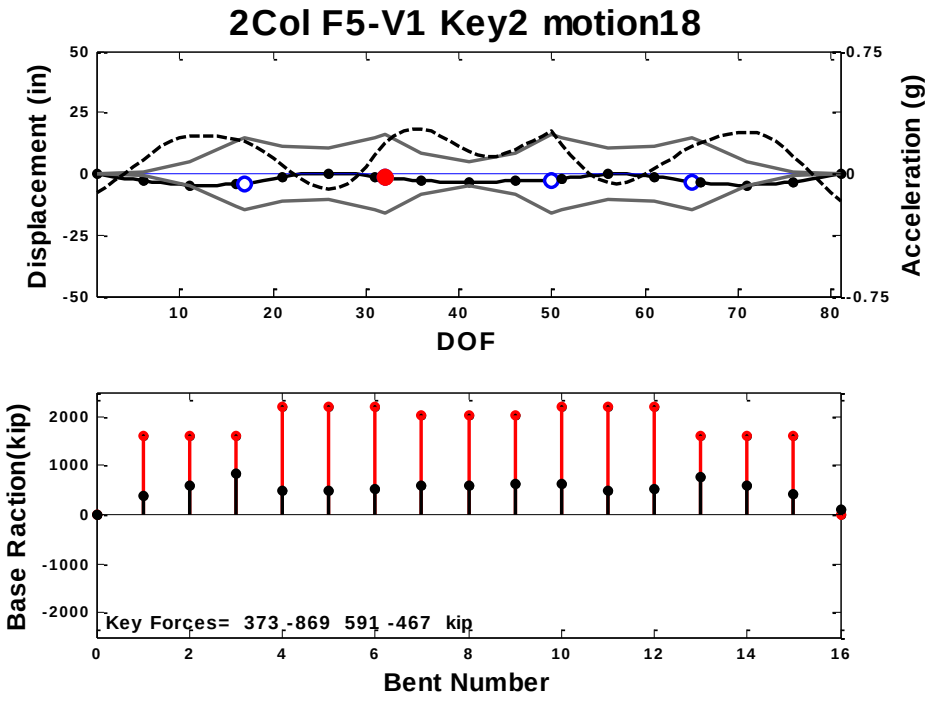

Figure C.309 System State at Maximum Force, Prototype F5-V1, motion-18

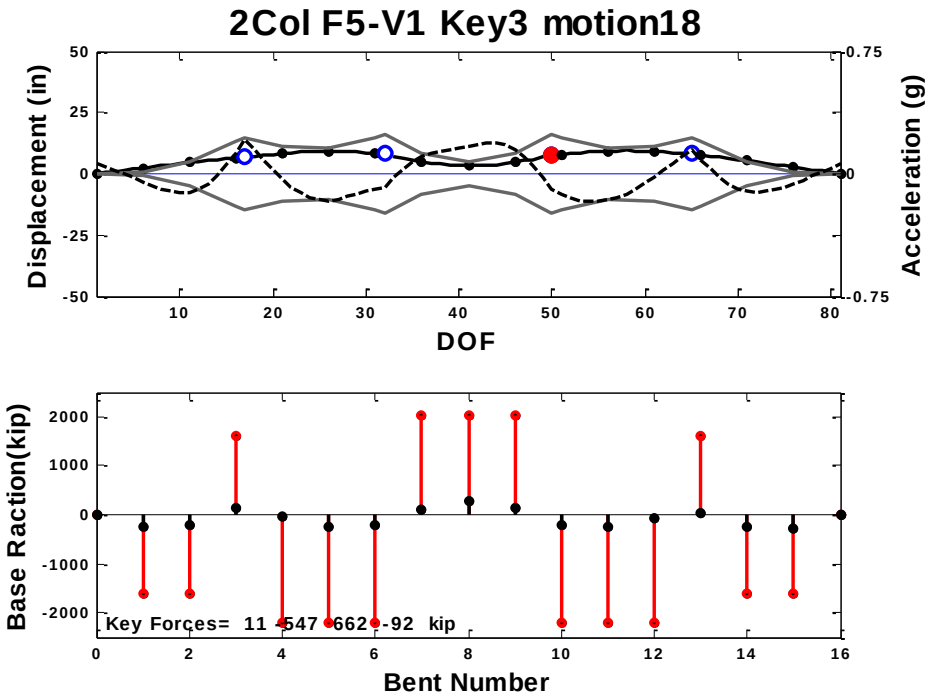

Figure C.310 System State at Maximum Force, Prototype F5-V1, motion-18

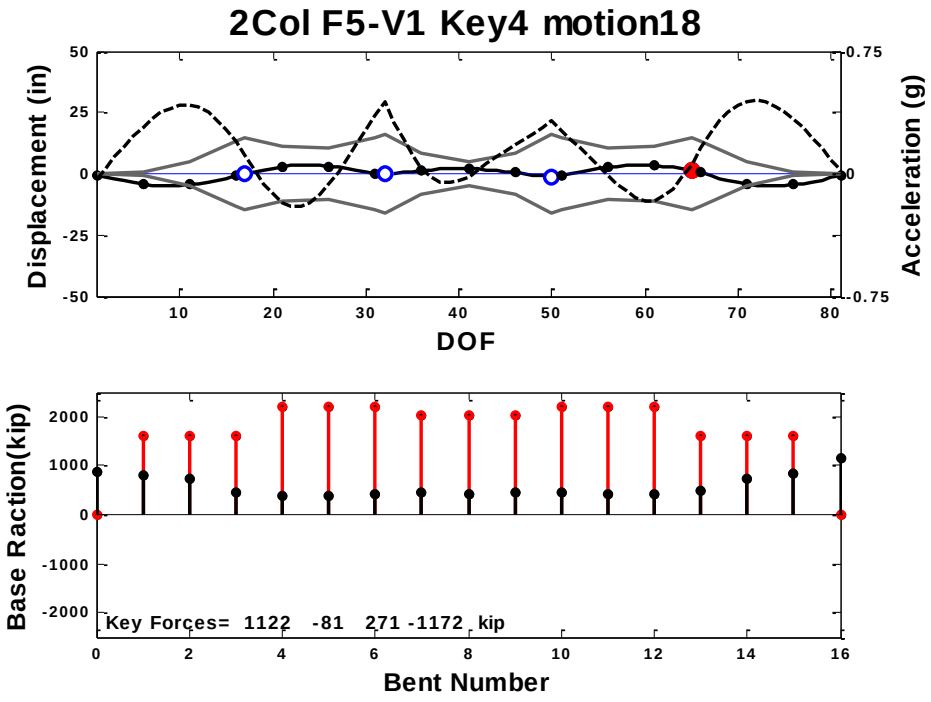

Figure C.311 System State at Maximum Force, Prototype F5-V1, motion-18

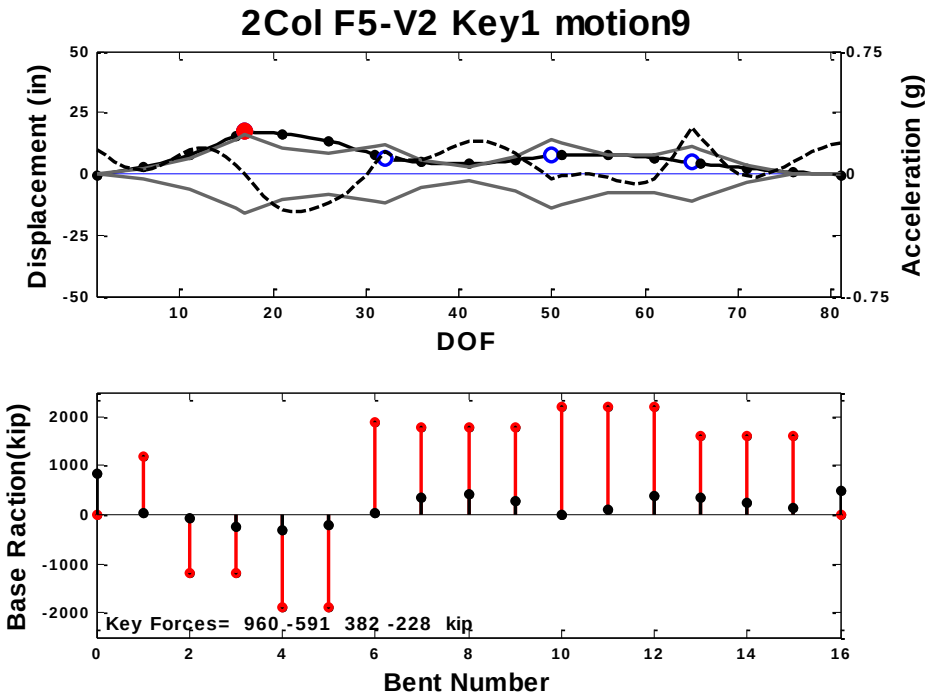

Figure C.312 System State at Maximum Force, Prototype F5-V2, motion-9

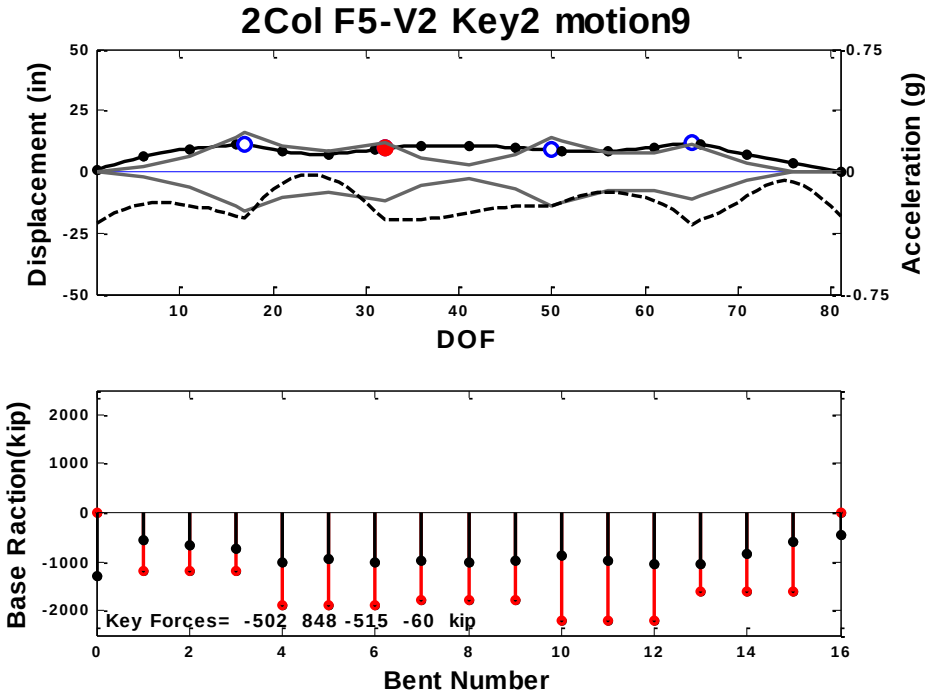

Figure C.313 System State at Maximum Force, Prototype F5-V2, motion-9

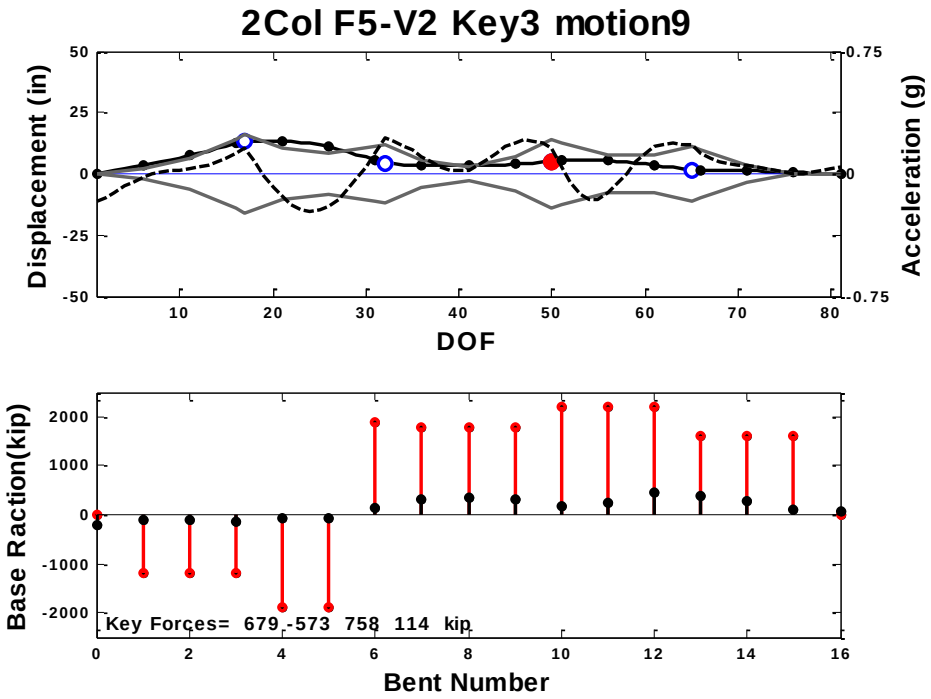

Figure C.314 System State at Maximum Force, Prototype F5-V2, motion-9

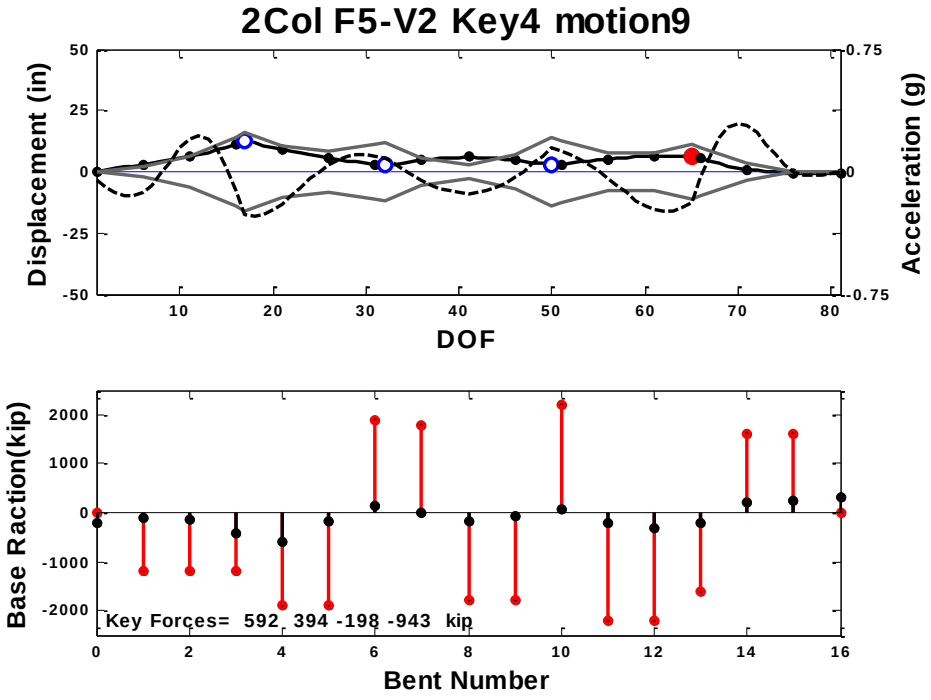

Figure C.315 System State at Maximum Force, Prototype F5-V2, motion-9

PART-5a: Single-Column Bent Prototypes

Shear Key Force Responses w/ and w/o Transverse Gap

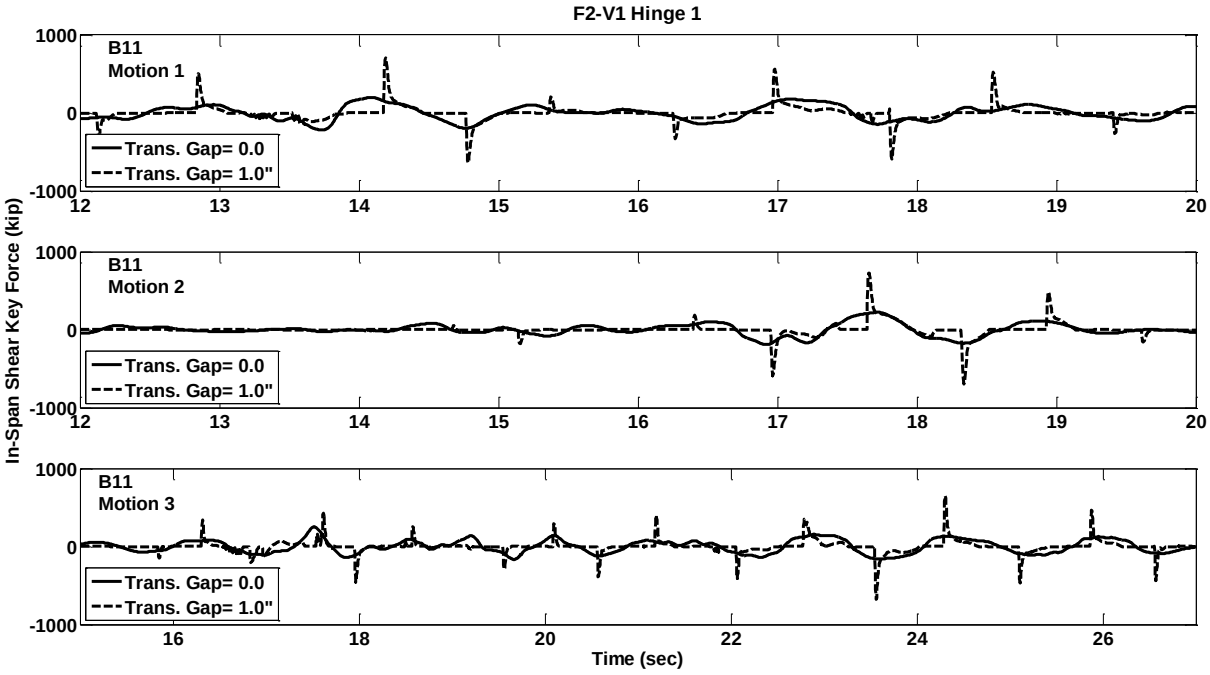

Figure C.316 Shear Key Force Response w/ and w/o Gap, Prototype F2-V1, Hinge-1, Motions B11

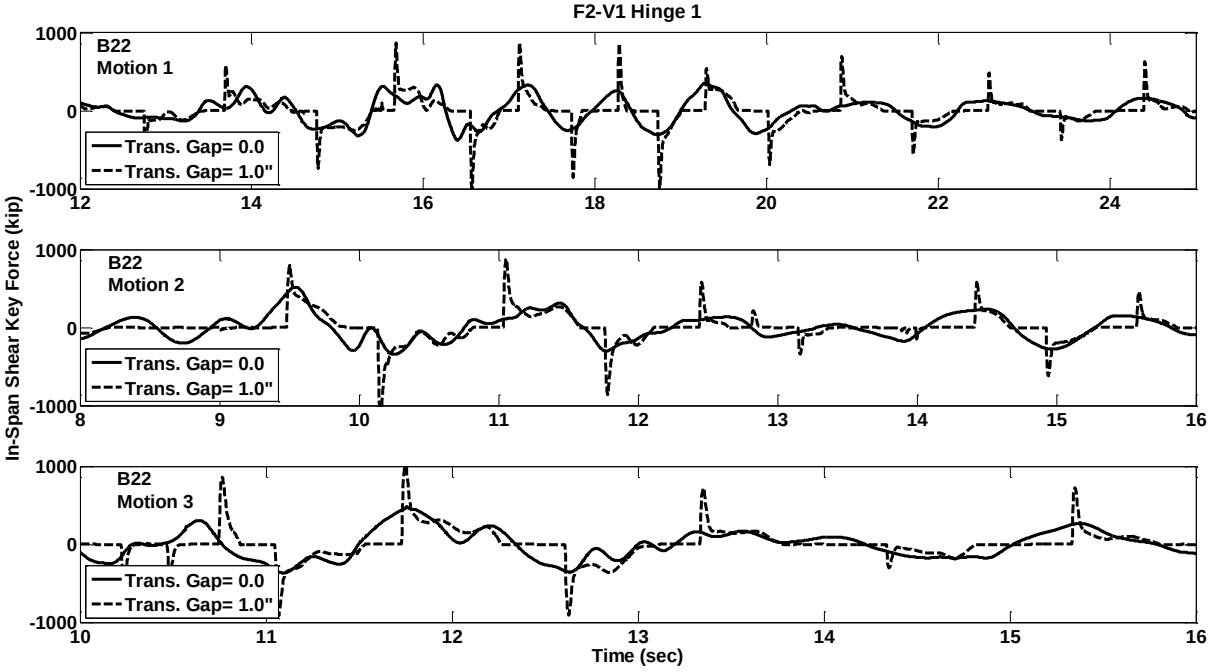

Figure C.317 Shear Key Force Response w/ and w/o Gap, Prototype F2-V1, Hinge-1, Motions B22

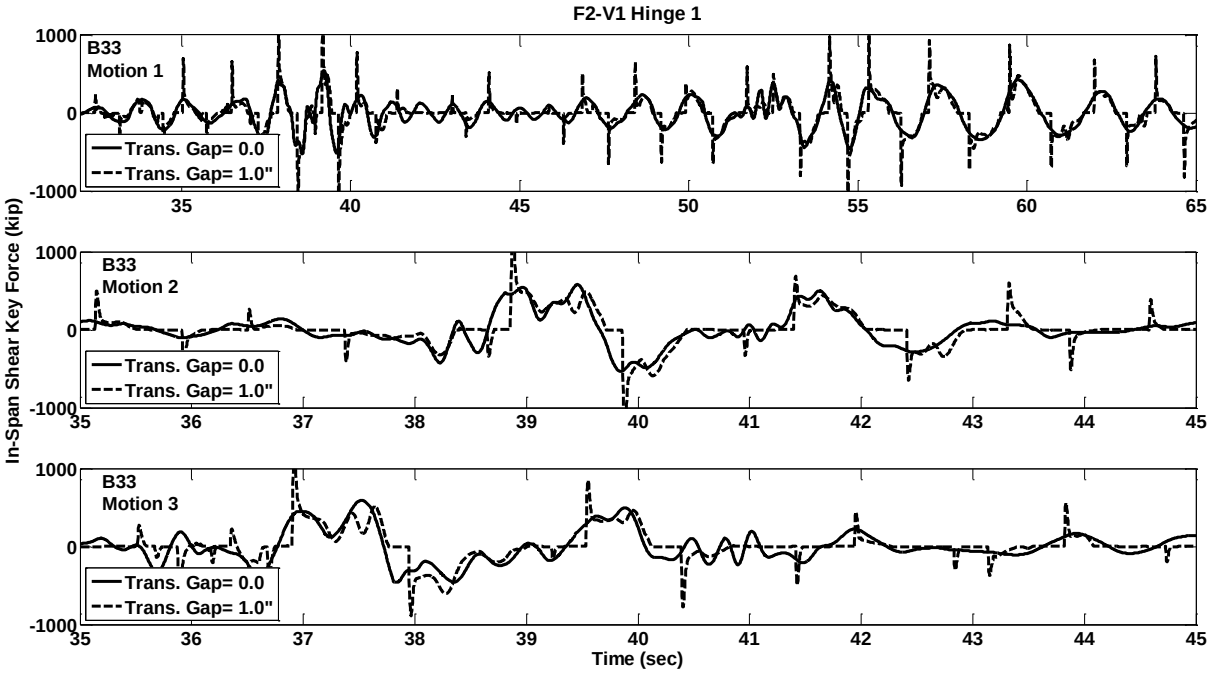

Figure C.318 Shear Key Force Response w/ and w/o Gap, Prototype F2-V1, Hinge-1, Motions B33

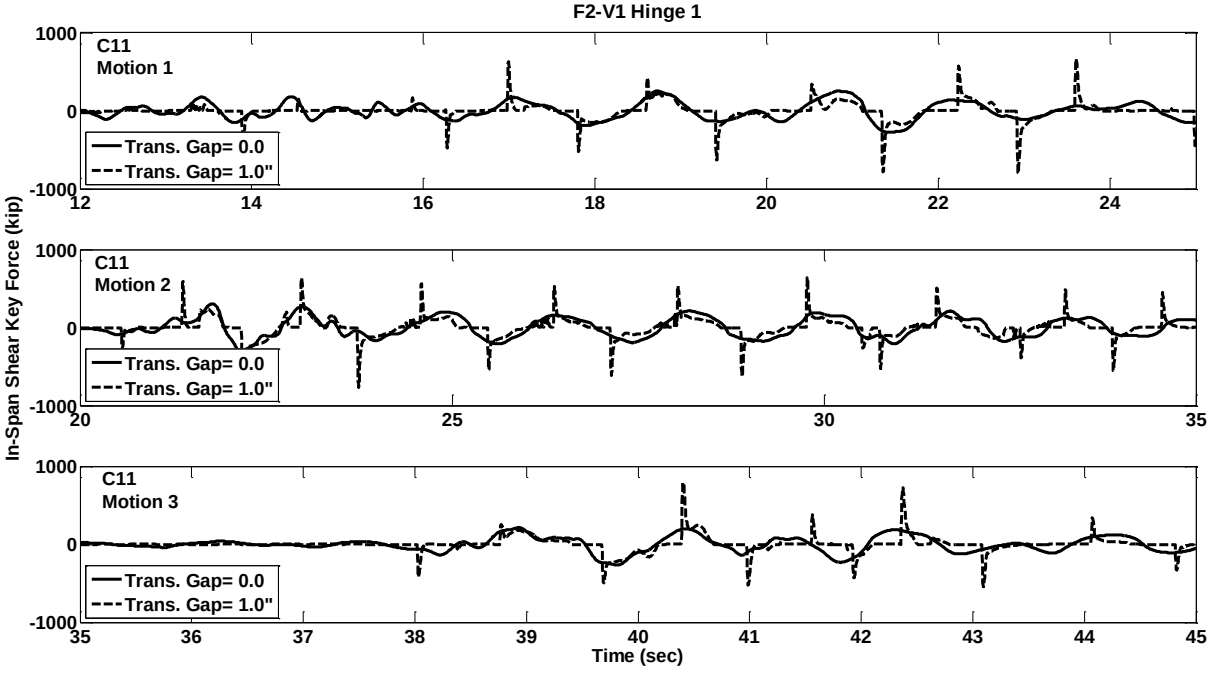

Figure C.319 Shear Key Force Response w/ and w/o Gap, Prototype F2-V1, Hinge-1, Motions C11

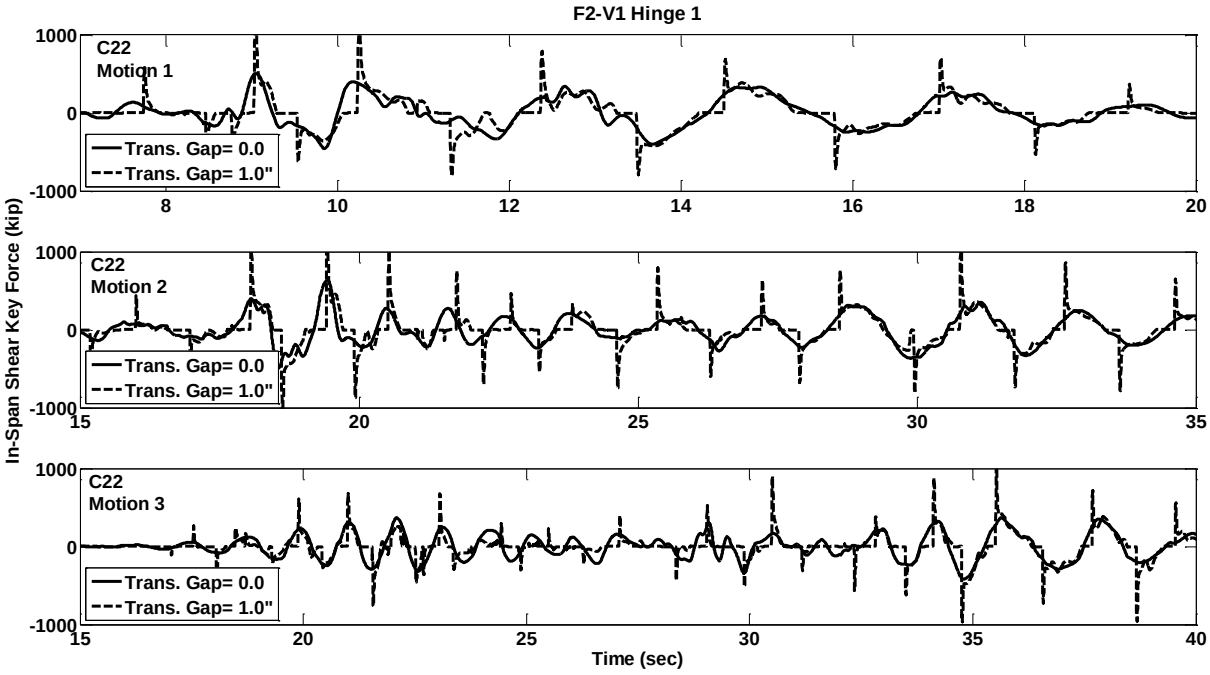

Figure C.320 Shear Key Force Response w/ and w/o Gap, Prototype F2-V1, Hinge-1, Motions C22

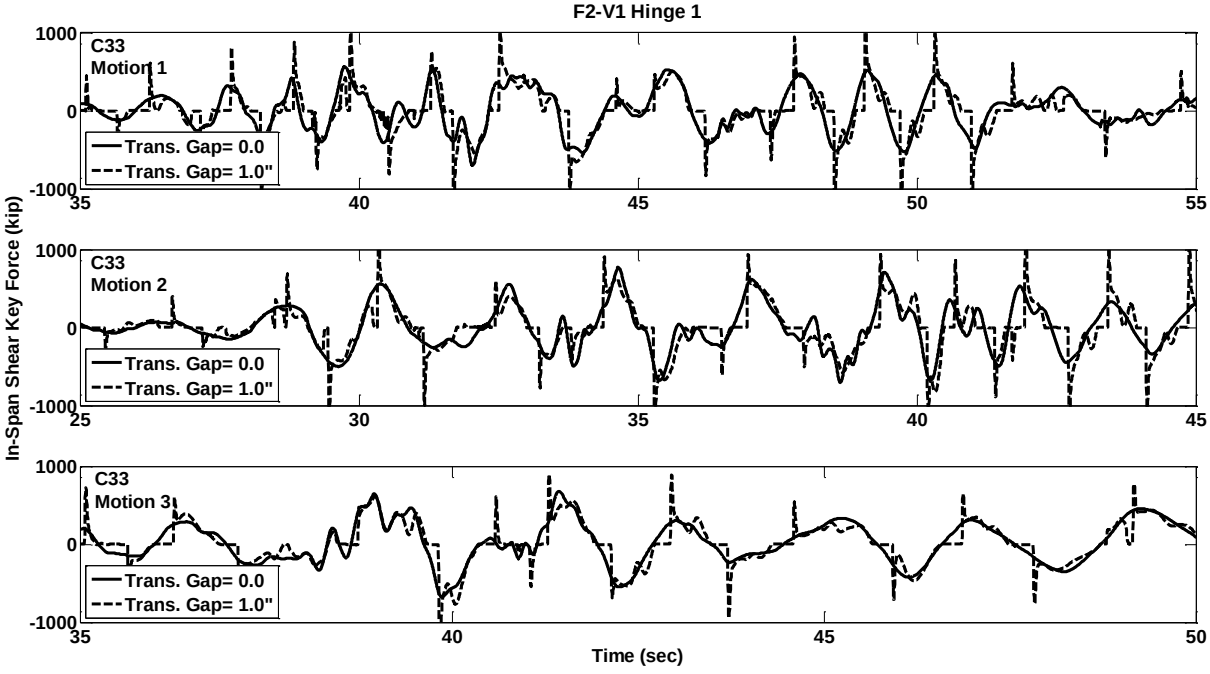

Figure C.321 Shear Key Force Response w/ and w/o Gap, Prototype F2-V1, Hinge-1, Motions C33

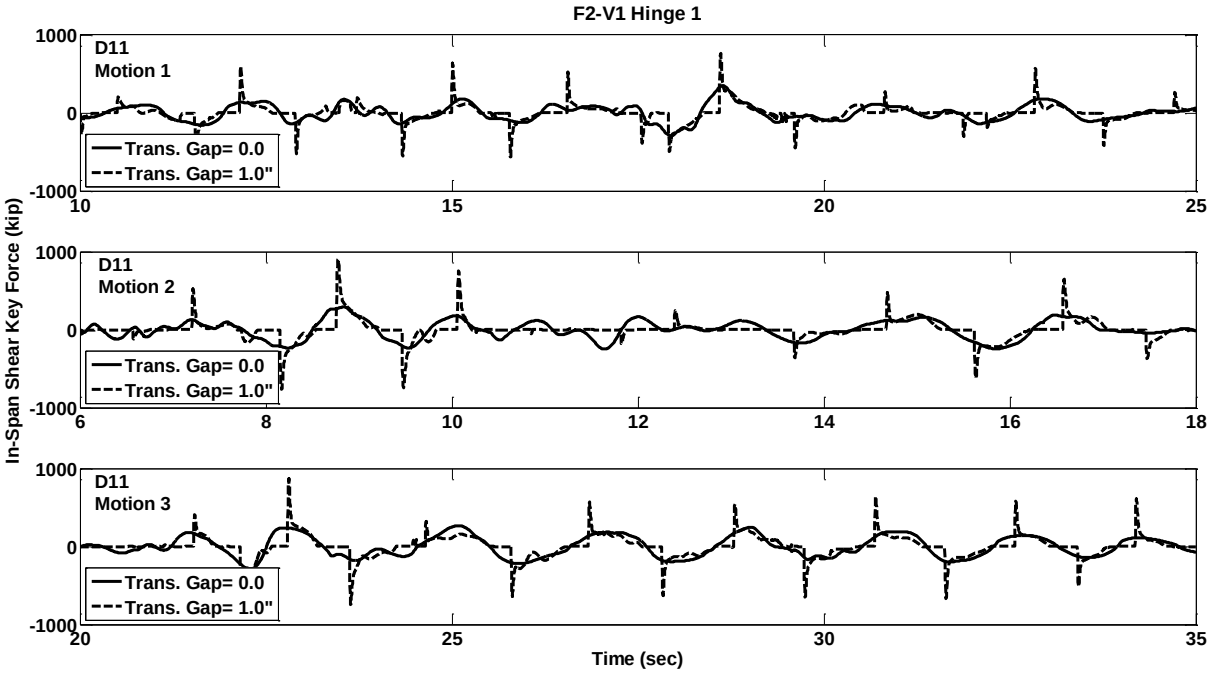

Figure C.322 Shear Key Force Response w/ and w/o Gap, Prototype F2-V1, Hinge-1, Motions D11

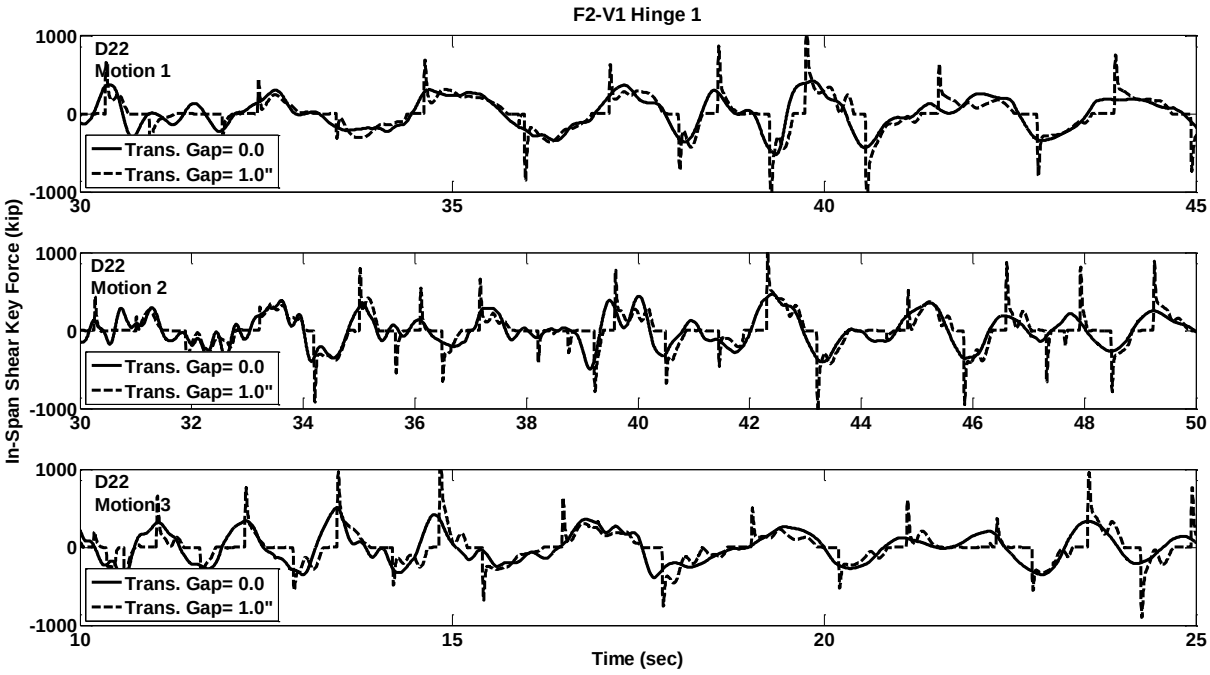

Figure C.323 Shear Key Force Response w/ and w/o Gap, Prototype F2-V1, Hinge-1, Motions D22

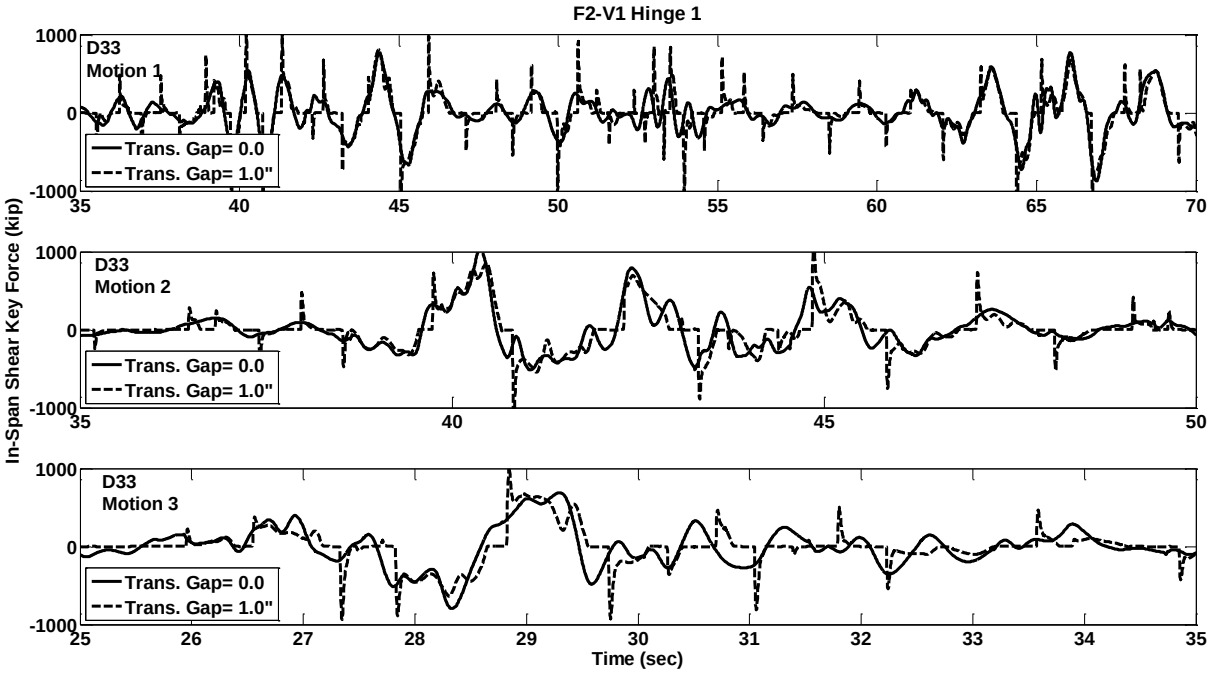

Figure C.324 Shear Key Force Response w/ and w/o Gap, Prototype F2-V1, Hinge-1, Motions D33

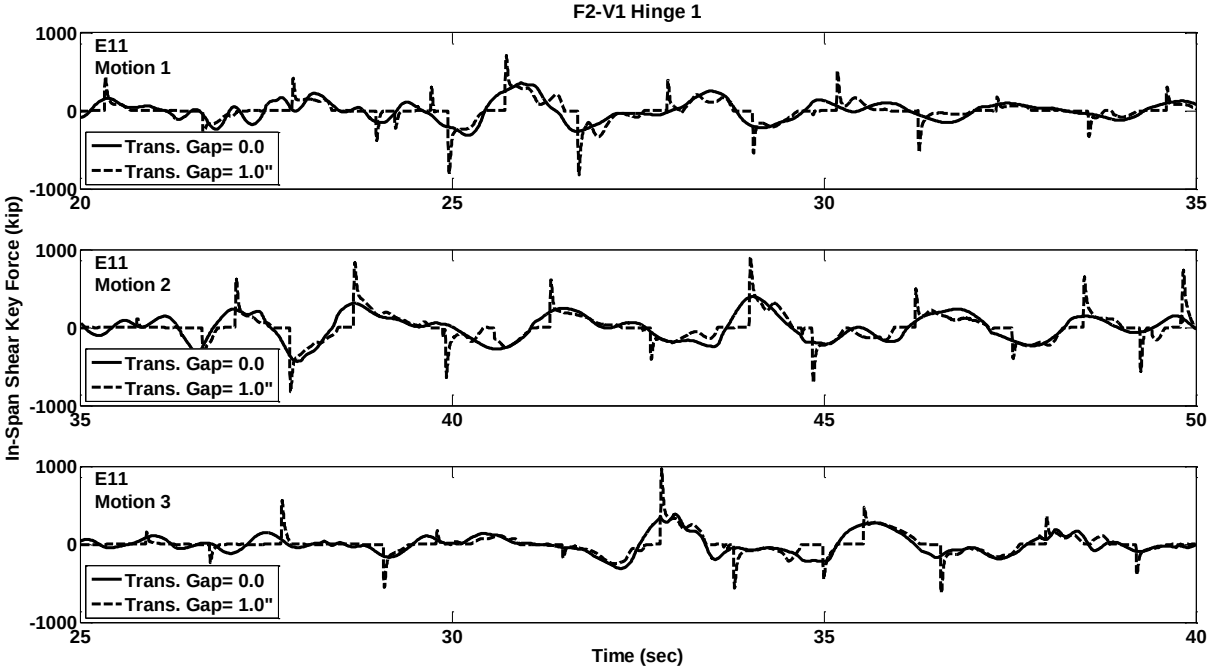

Figure C.325 Shear Key Force Response w/ and w/o Gap, Prototype F2-V1, Hinge-1, Motions E11

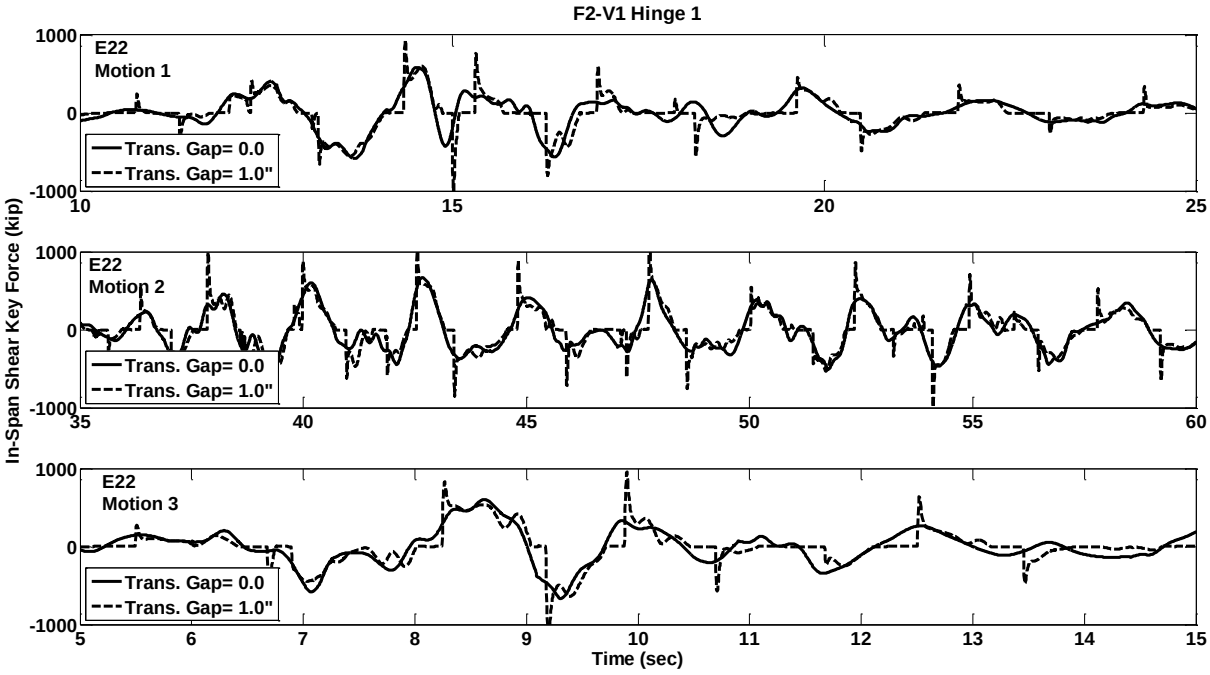

Figure C.326 Shear Key Force Response w/ and w/o Gap, Prototype F2-V1, Hinge-1, Motions E22

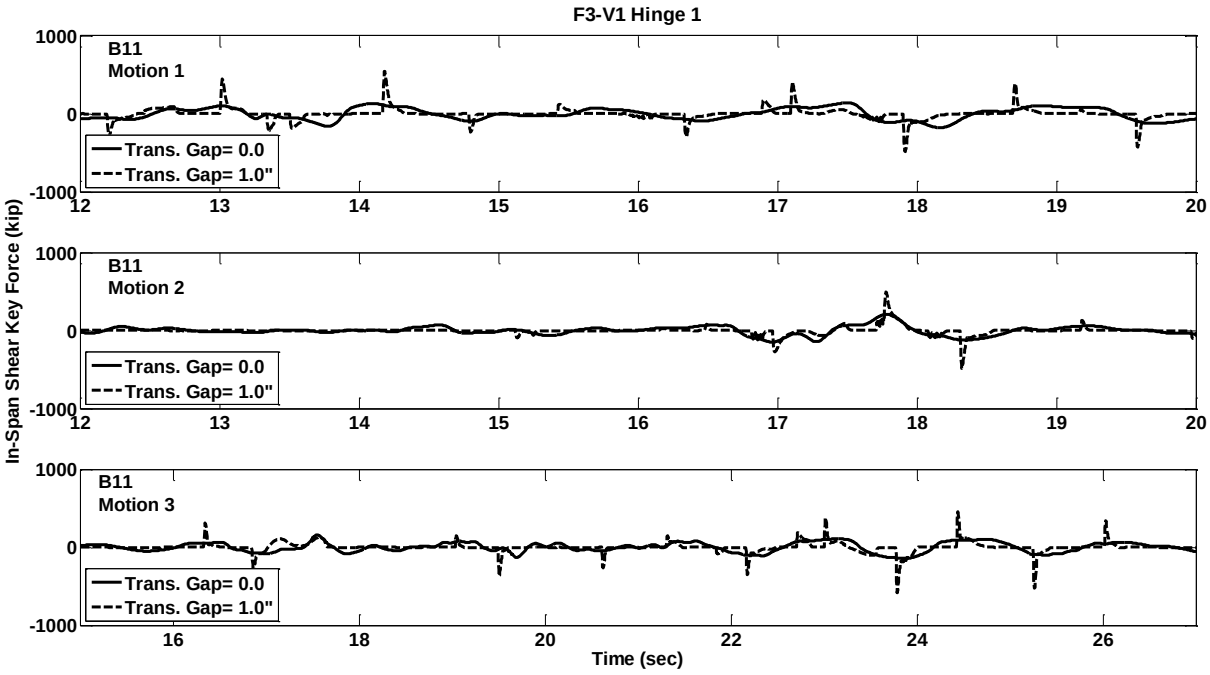

Figure C.327 Shear Key Force Response w/ and w/o Gap, Prototype F3-V1, Hinge-1, Motions B11

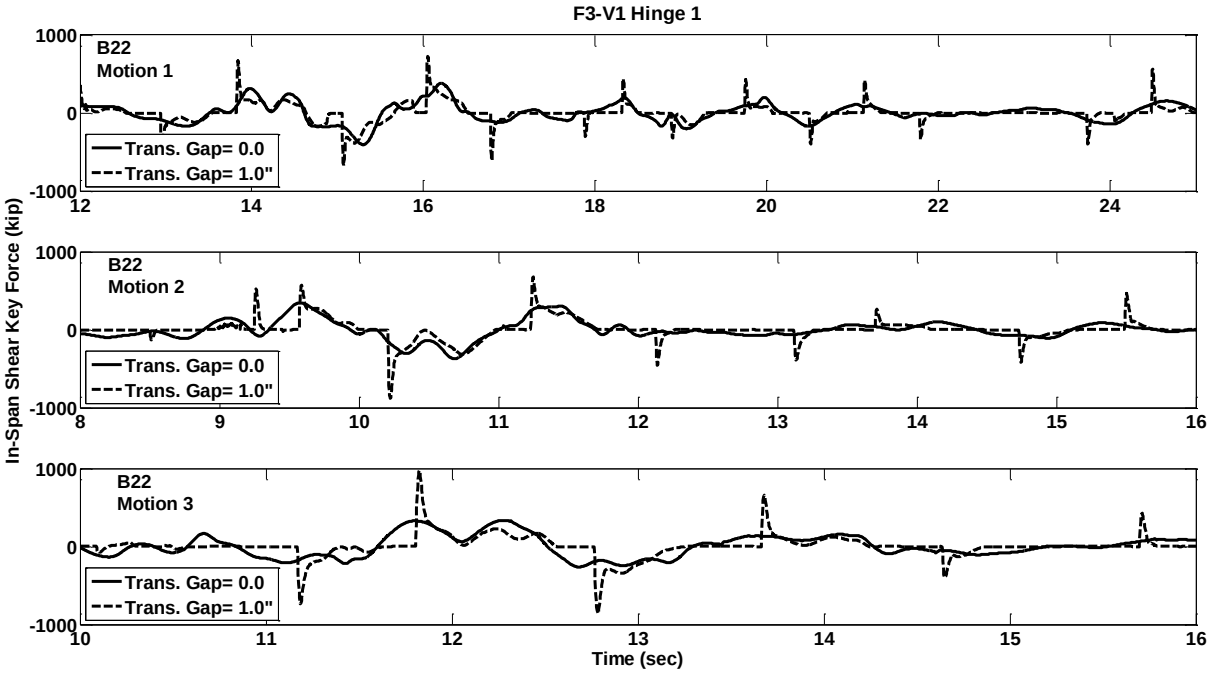

Figure C.328 Shear Key Force Response w/ and w/o Gap, Prototype F3-V1, Hinge-1, Motions B22

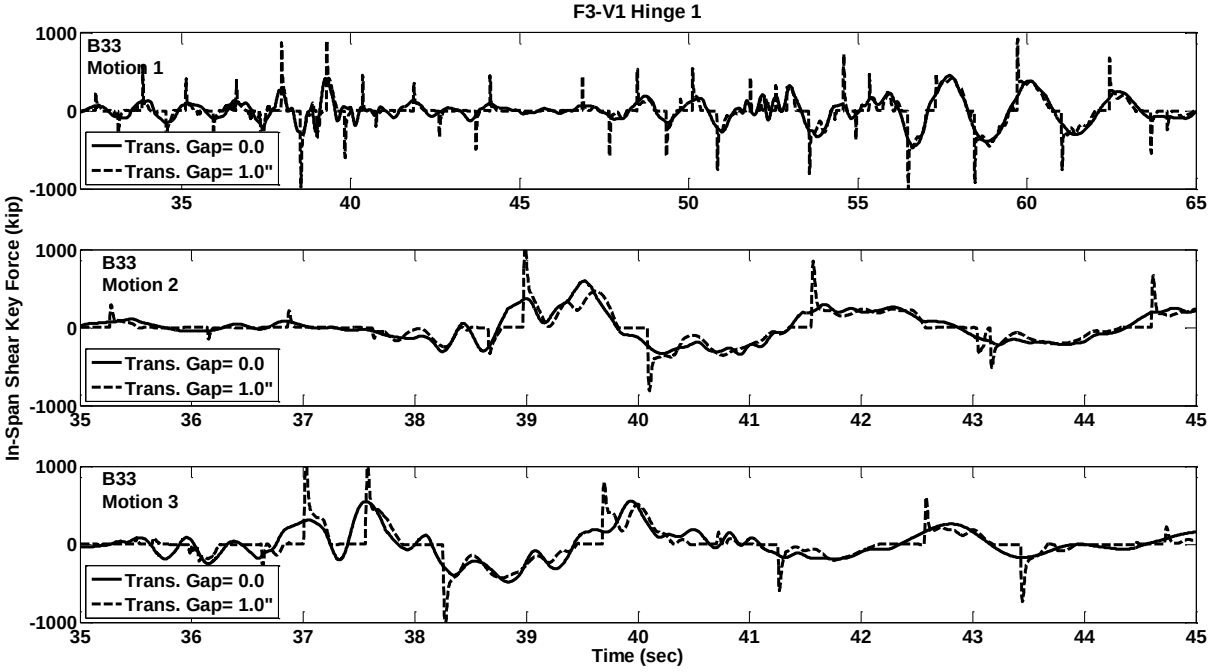

Figure C.329 Shear Key Force Response w/ and w/o Gap, Prototype F3-V1, Hinge-1, Motions B33

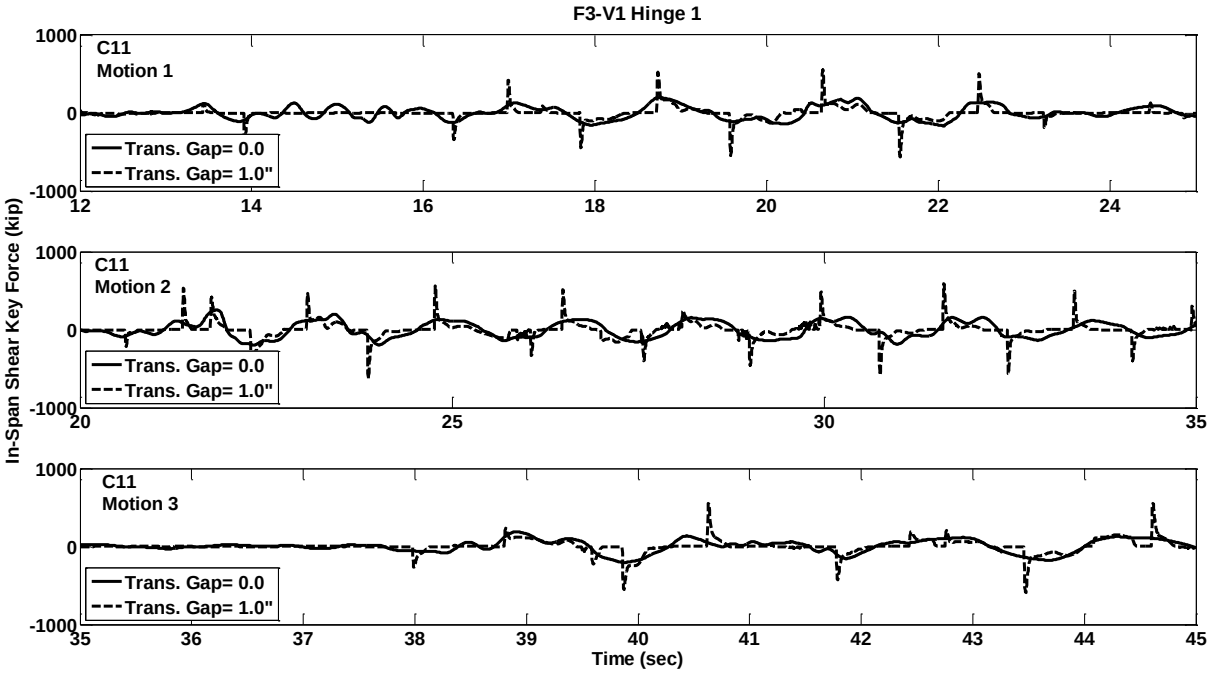

Figure C.330 Shear Key Force Response w/ and w/o Gap, Prototype F3-V1, Hinge-1, Motions C11

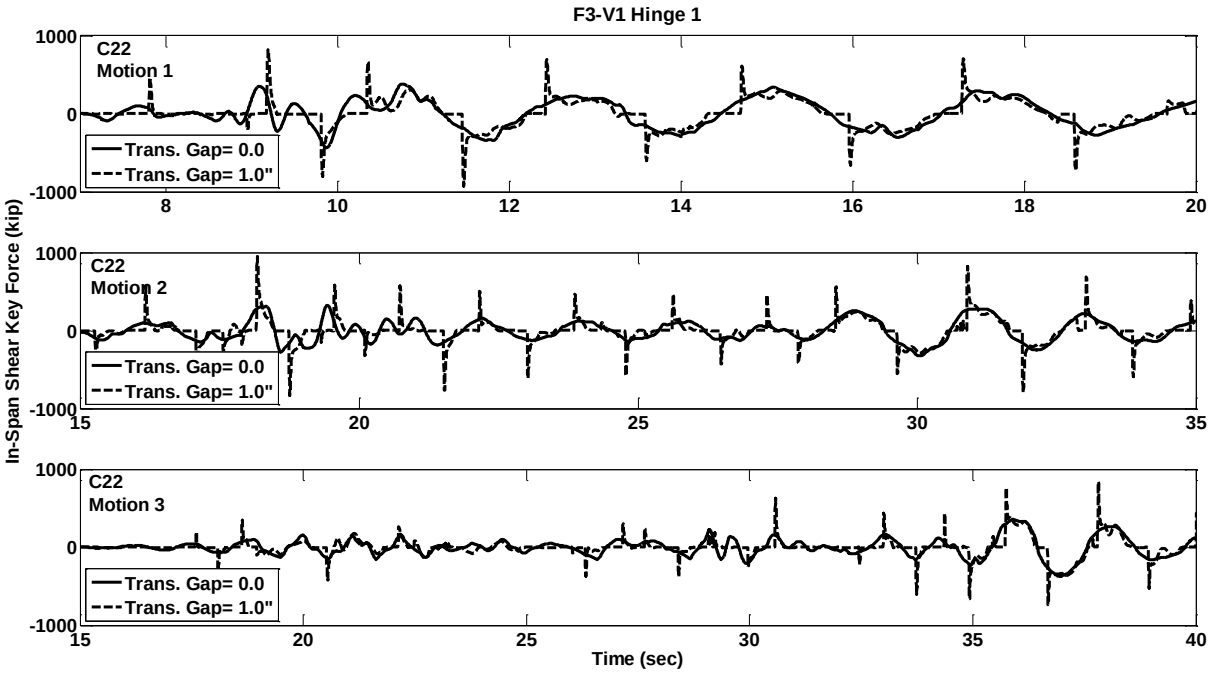

Figure C.331 Shear Key Force Response w/ and w/o Gap, Prototype F3-V1, Hinge-1, Motions C22

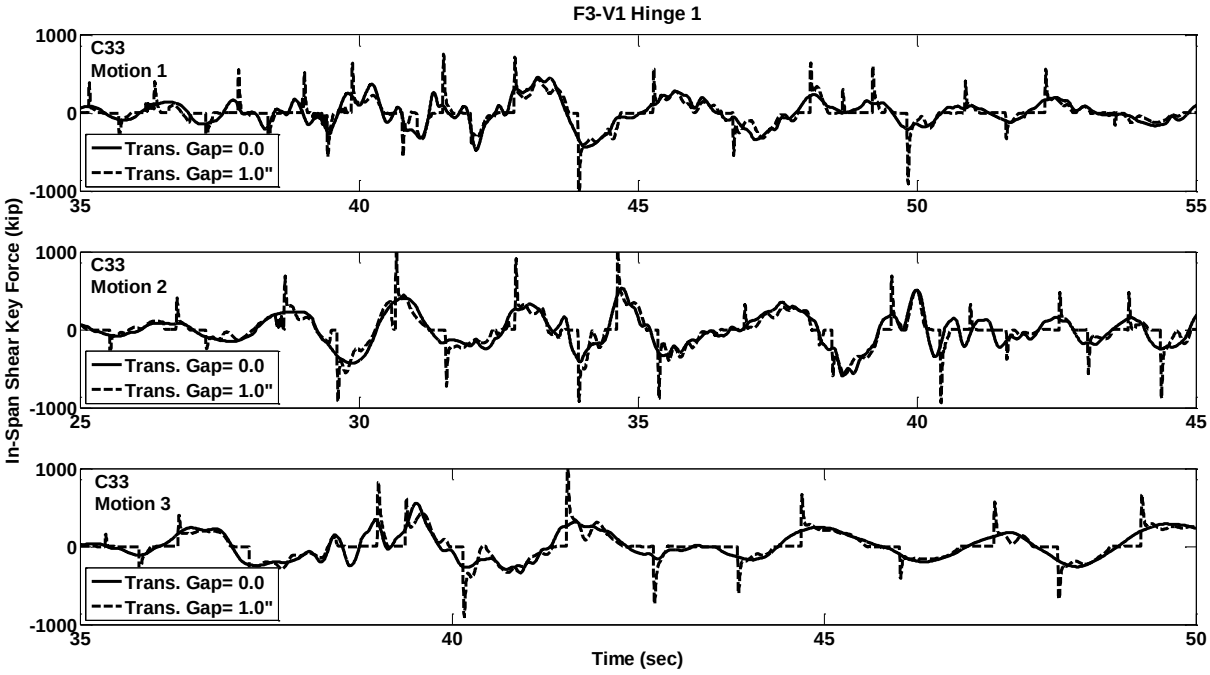

Figure C.332 Shear Key Force Response w/ and w/o Gap, Prototype F3-V1, Hinge-1, Motions C33

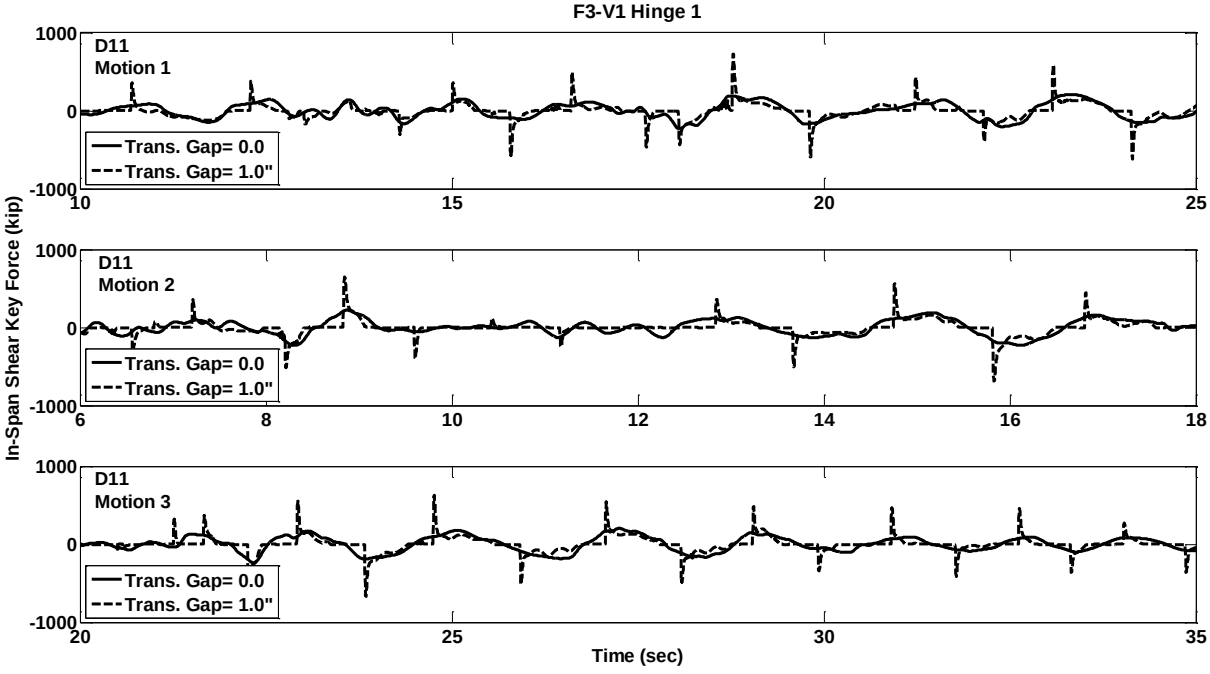

Figure C.333 Shear Key Force Response w/ and w/o Gap, Prototype F3-V1, Hinge-1, Motions D11

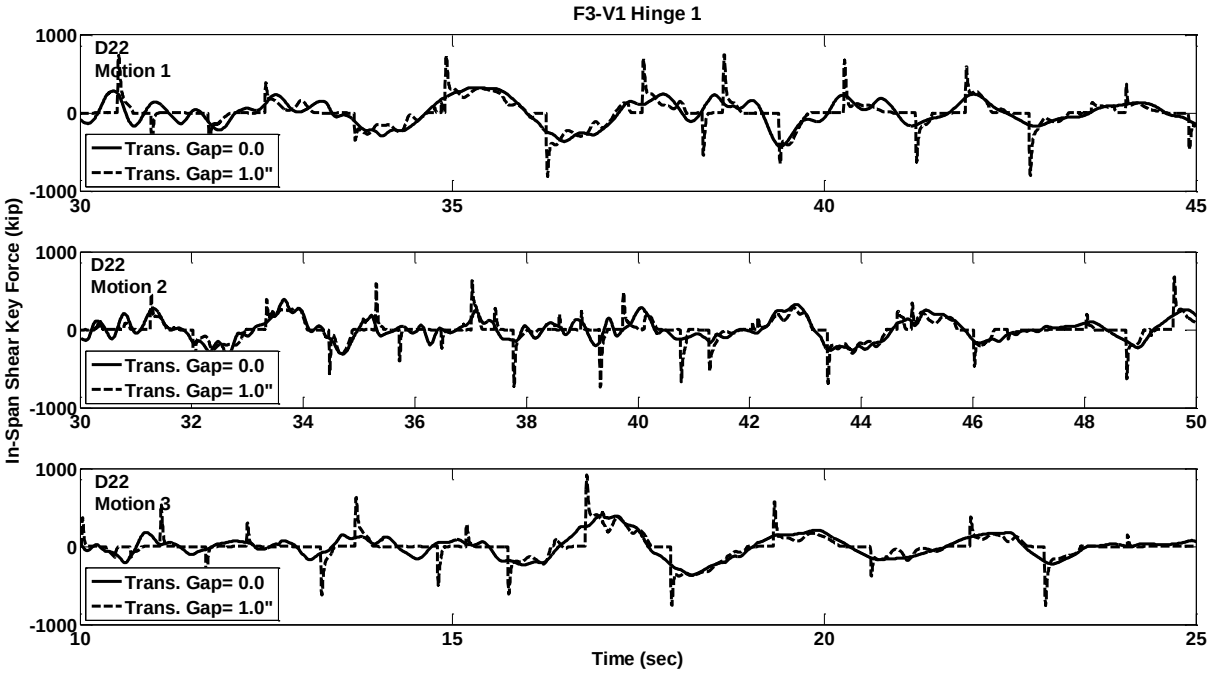

Figure C.334 Shear Key Force Response w/ and w/o Gap, Prototype F3-V1, Hinge-1, Motions D22

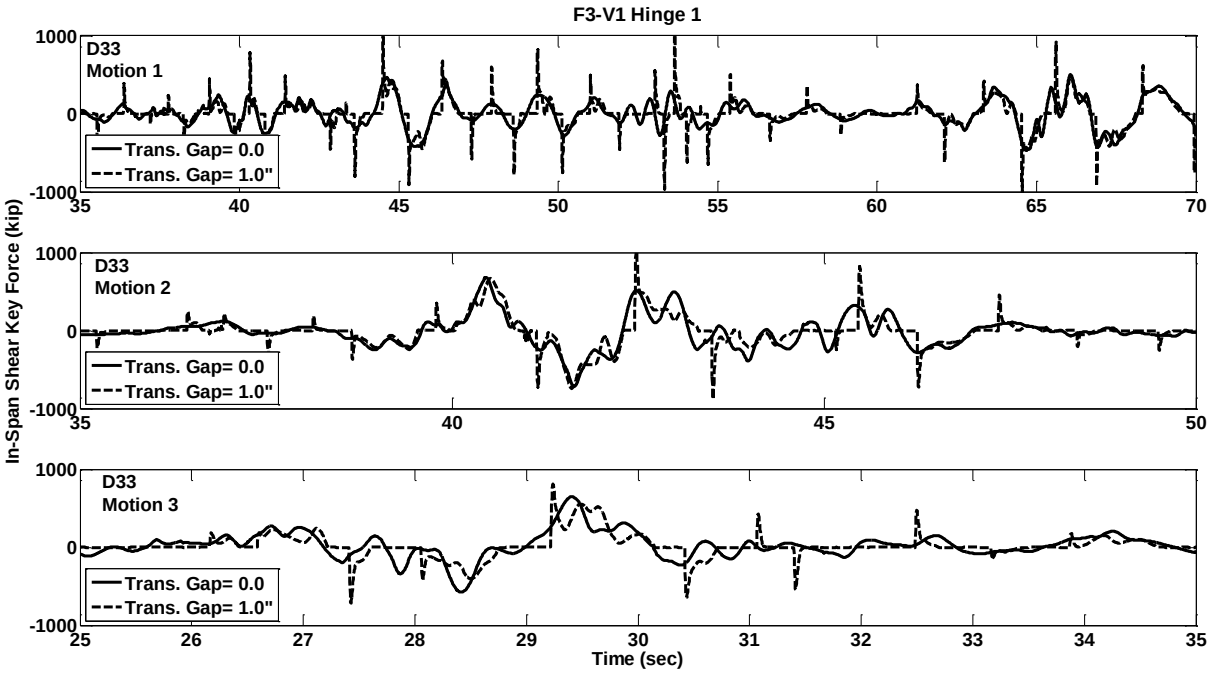

Figure C.335 Shear Key Force Response w/ and w/o Gap, Prototype F3-V1, Hinge-1, Motions D33

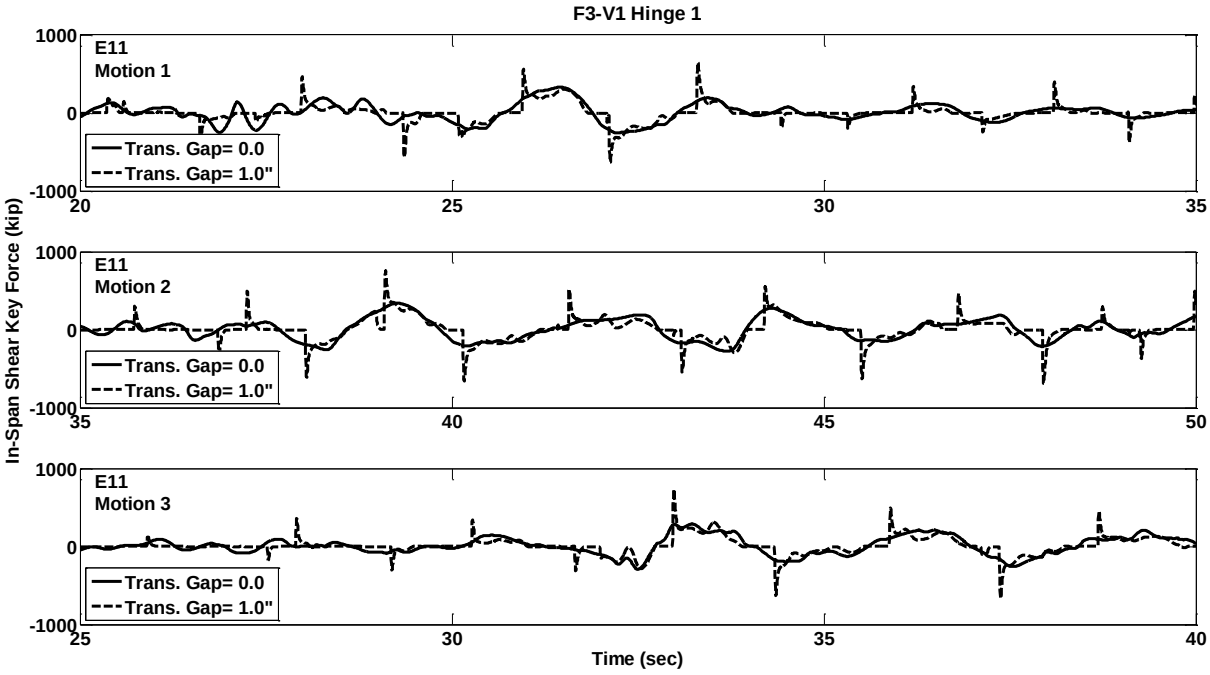

Figure C.336 Shear Key Force Response w/ and w/o Gap, Prototype F3-V1, Hinge-1, Motions E11

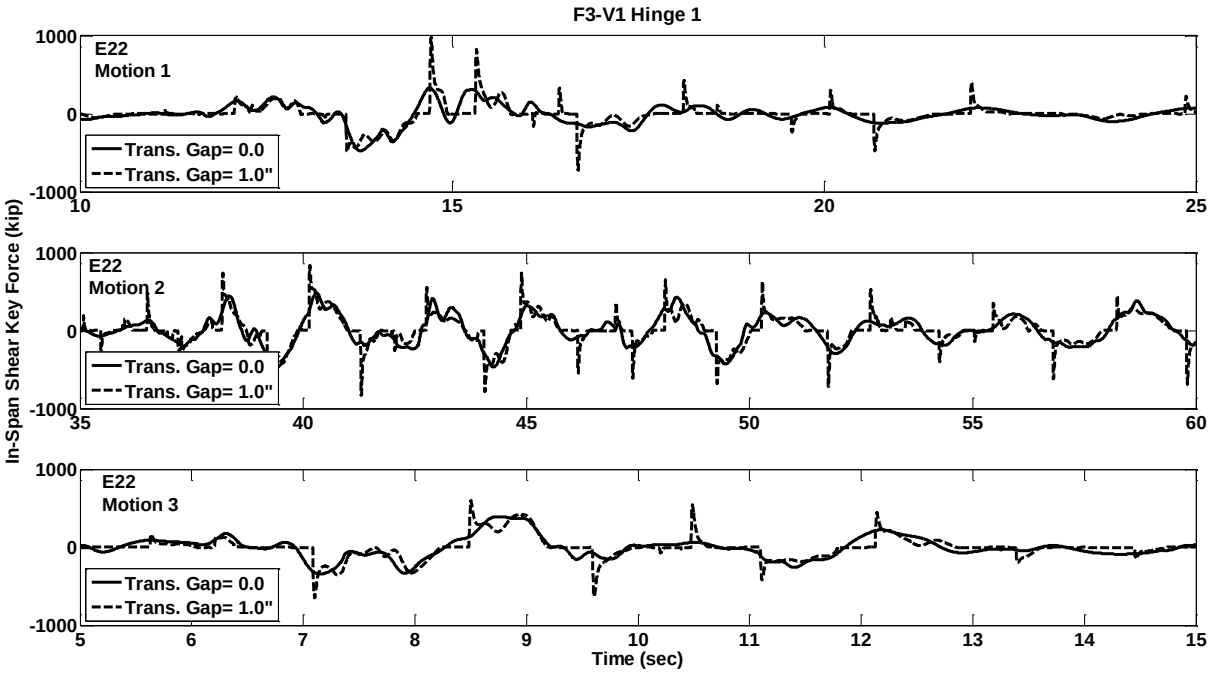

Figure C.337 Shear Key Force Response w/ and w/o Gap, Prototype F3-V1, Hinge-1, Motions E22

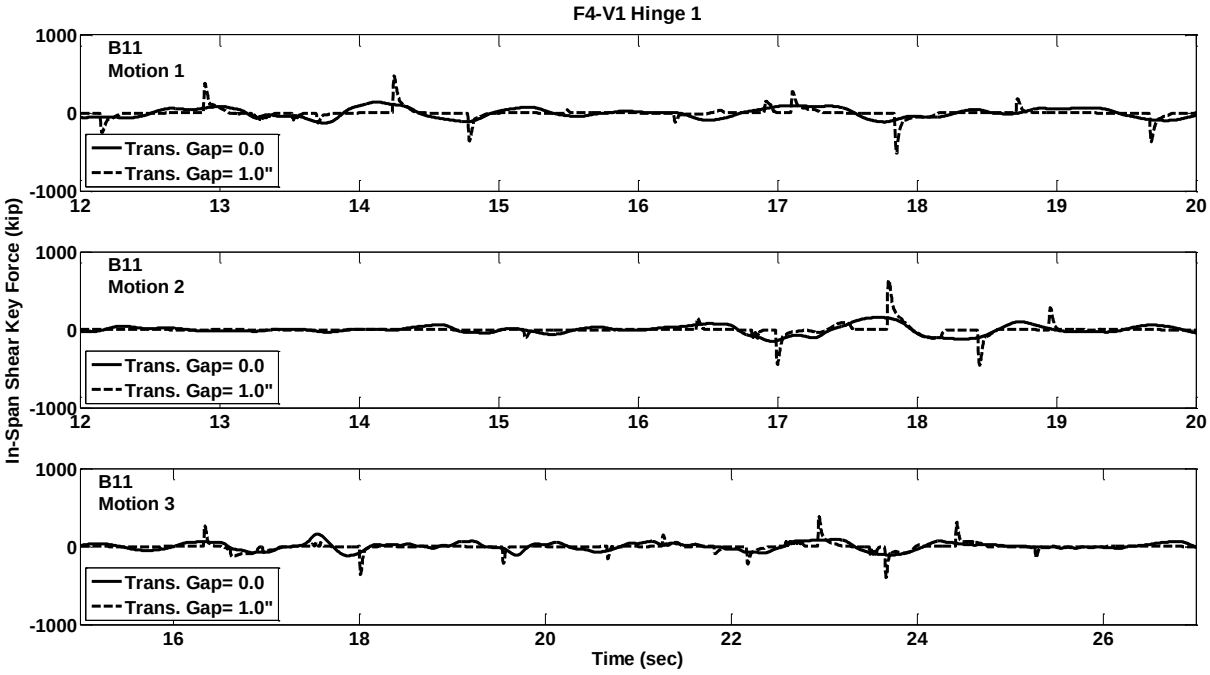

Figure C.338 Shear Key Force Response w/ and w/o Gap, Prototype F4-V1, Hinge-1, Motions B11

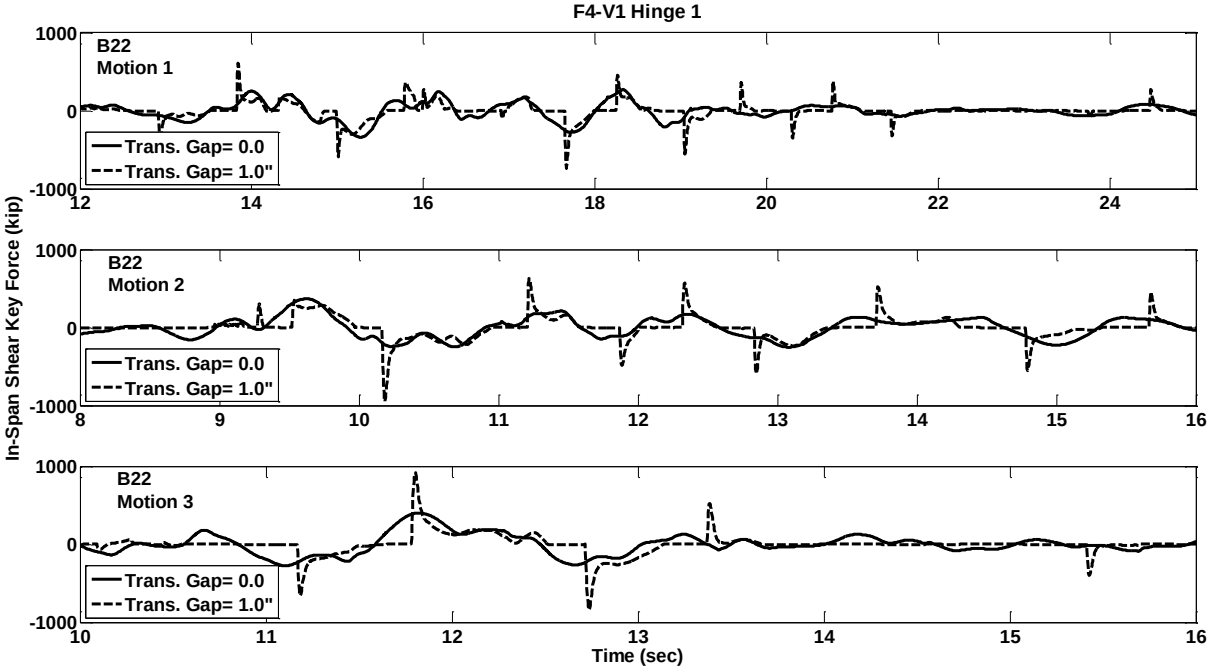

Figure C.339 Shear Key Force Response w/ and w/o Gap, Prototype F4-V1, Hinge-1, Motions B22

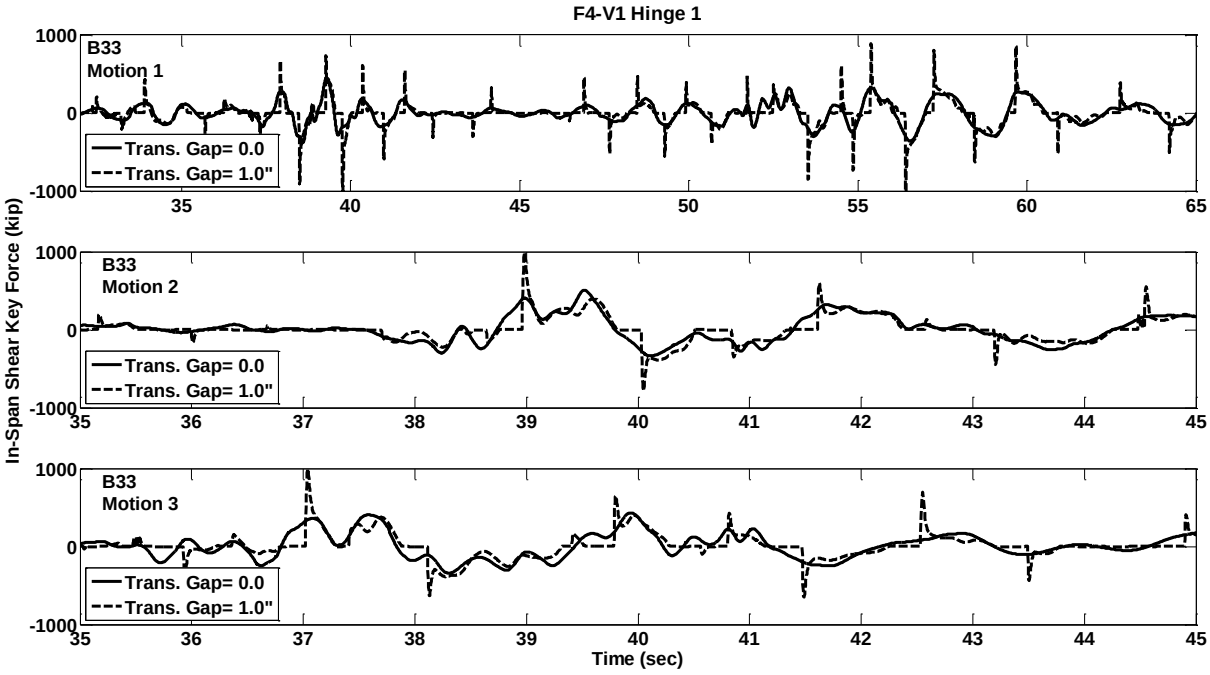

Figure C.340 Shear Key Force Response w/ and w/o Gap, Prototype F4-V1, Hinge-1, Motions B33

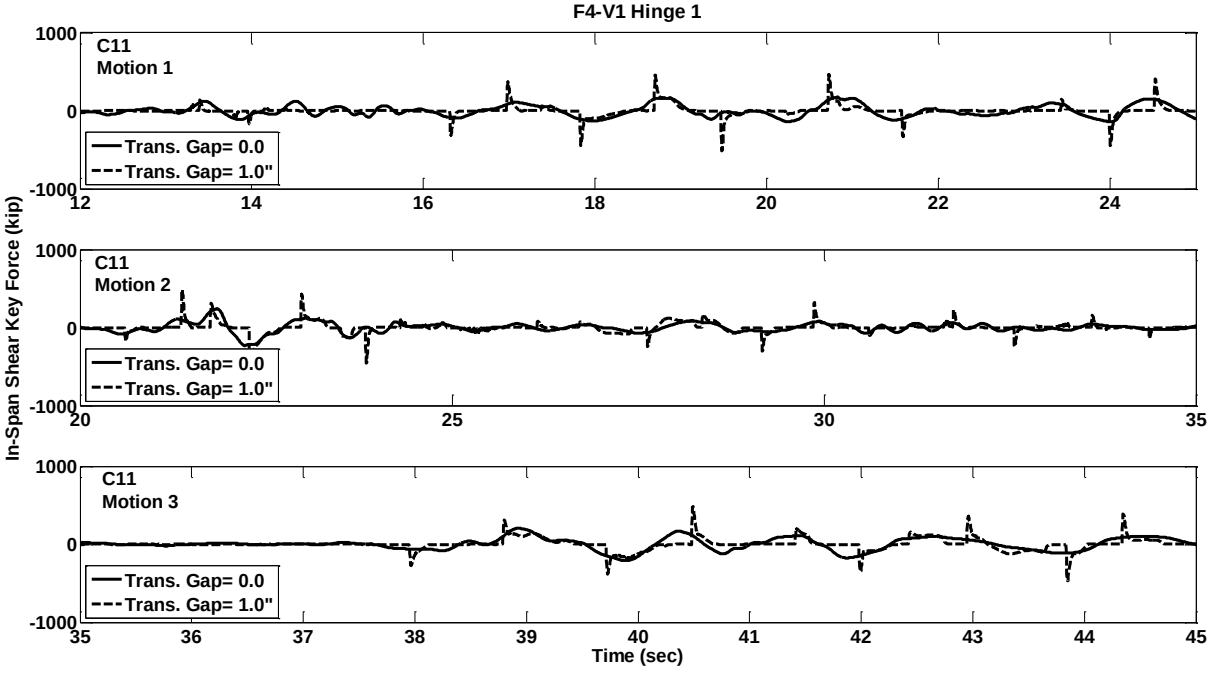

Figure C.341 Shear Key Force Response w/ and w/o Gap, Prototype F4-V1, Hinge-1, Motions C11

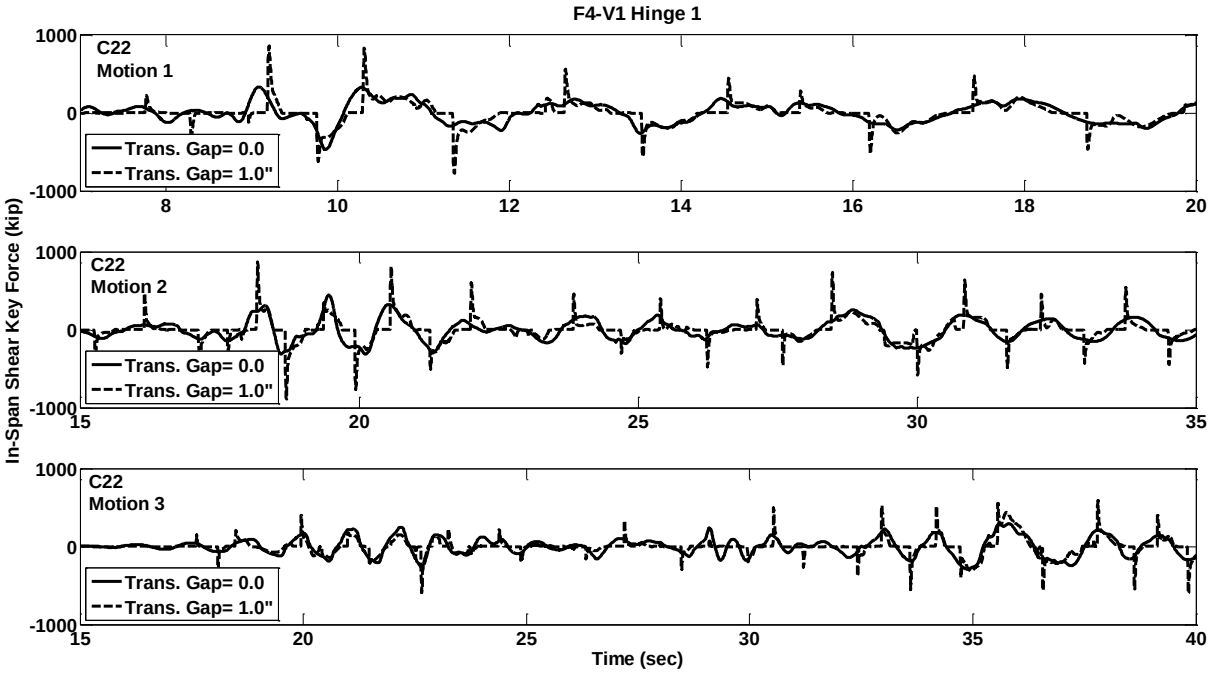

Figure C.342 Shear Key Force Response w/ and w/o Gap, Prototype F4-V1, Hinge-1, Motions C22

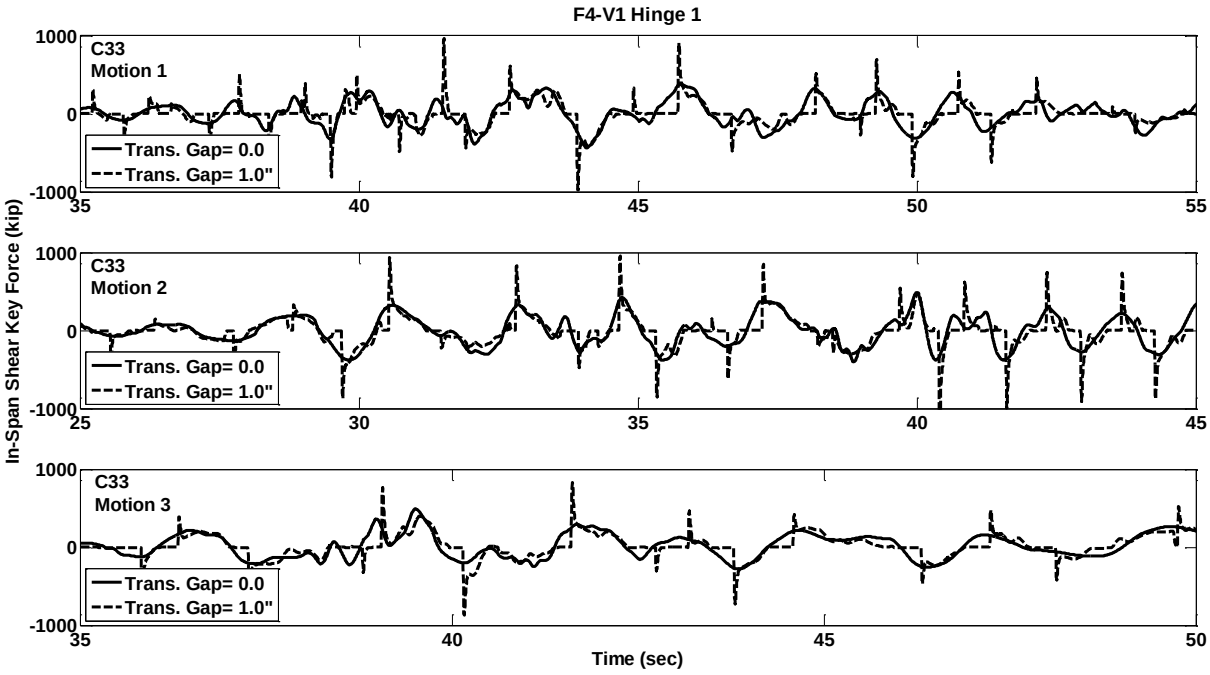

Figure C.343 Shear Key Force Response w/ and w/o Gap, Prototype F4-V1, Hinge-1, Motions C33

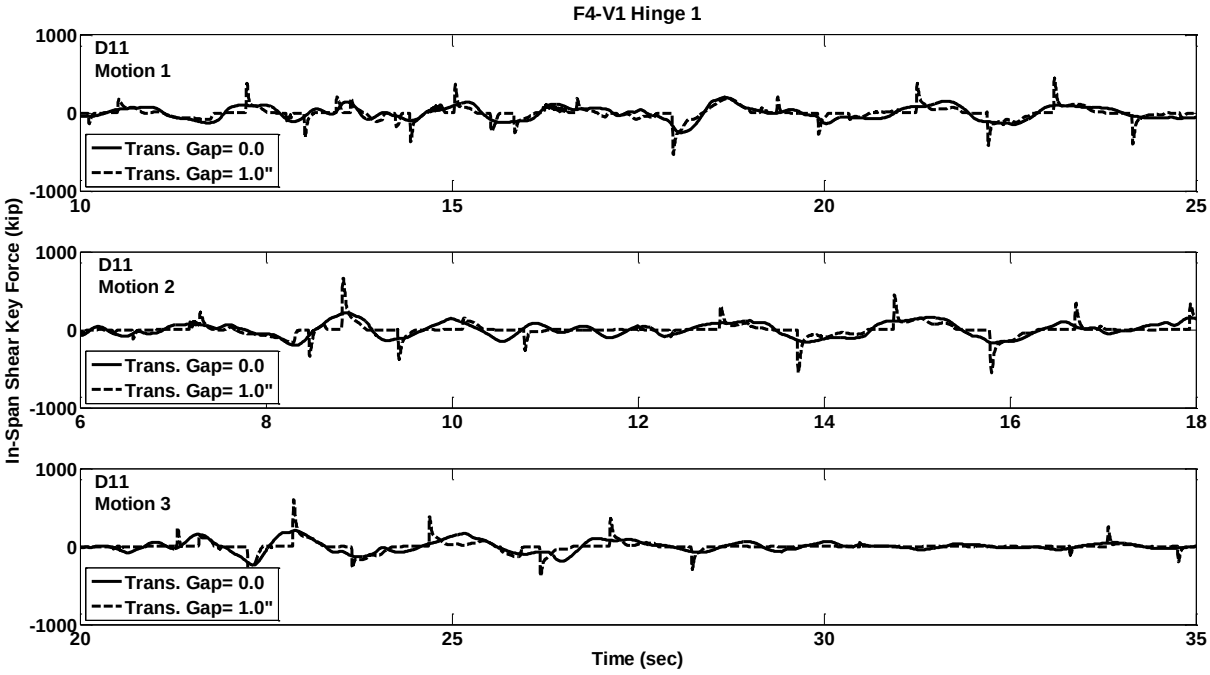

Figure C.344 Shear Key Force Response w/ and w/o Gap, Prototype F4-V1, Hinge-1, Motions D11

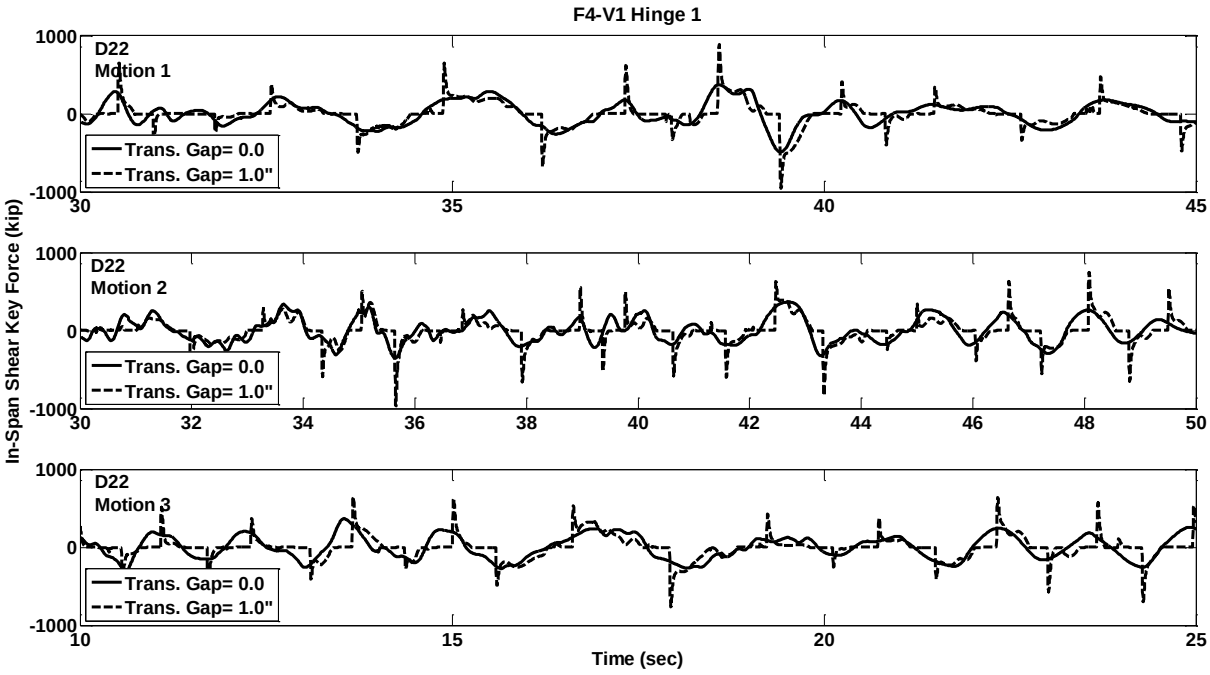

Figure C.345 Shear Key Force Response w/ and w/o Gap, Prototype F4-V1, Hinge-1, Motions D22

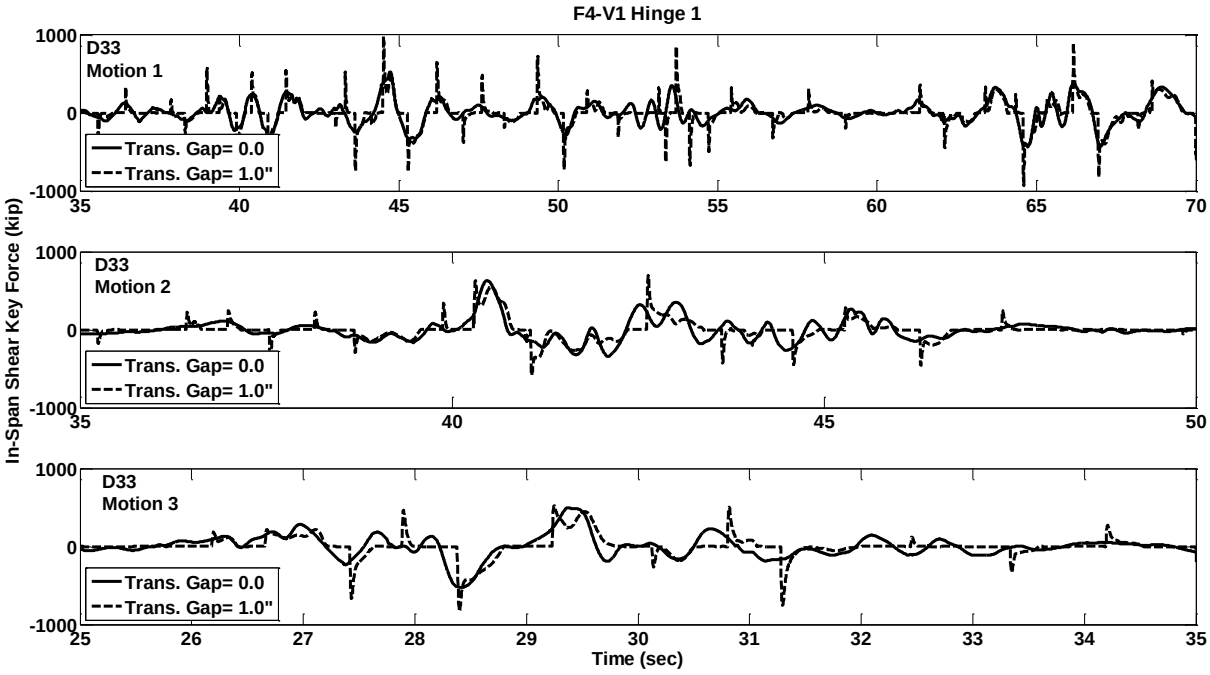

Figure C.346 Shear Key Force Response w/ and w/o Gap, Prototype F4-V1, Hinge-1, Motions D33

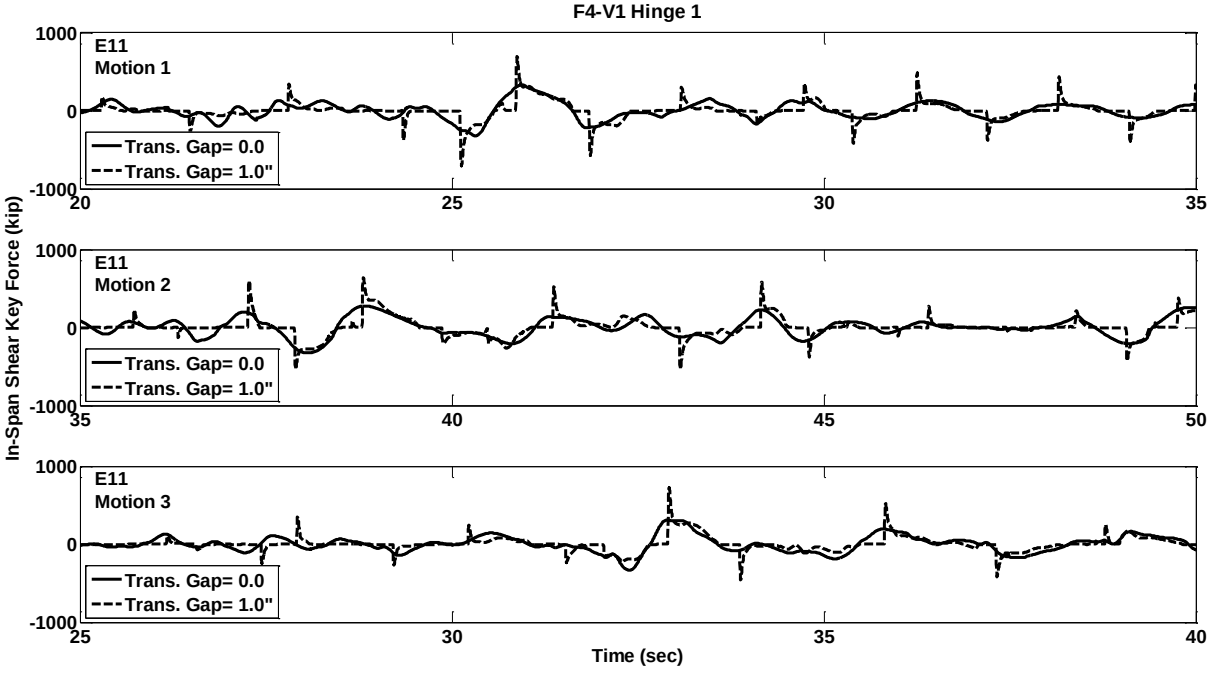

Figure C.347 Shear Key Force Response w/ and w/o Gap, Prototype F4-V1, Hinge-1, Motions E11

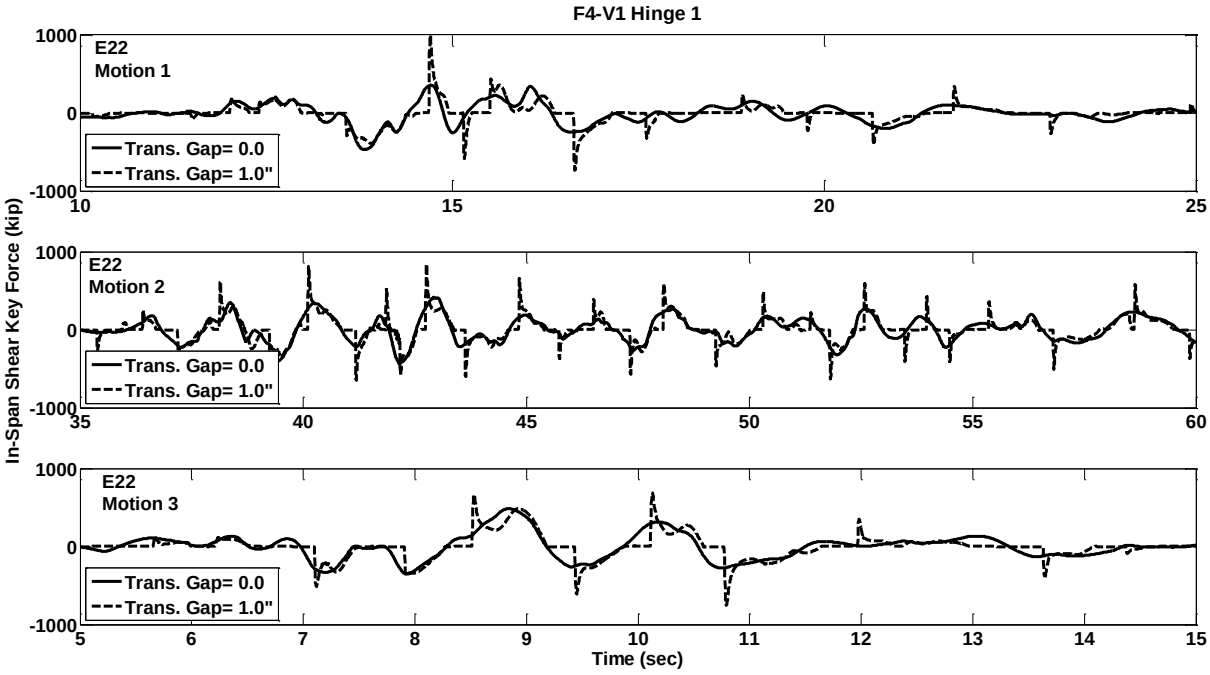

Figure C.348 Shear Key Force Response w/ and w/o Gap, Prototype F4-V1, Hinge-1, Motions E22

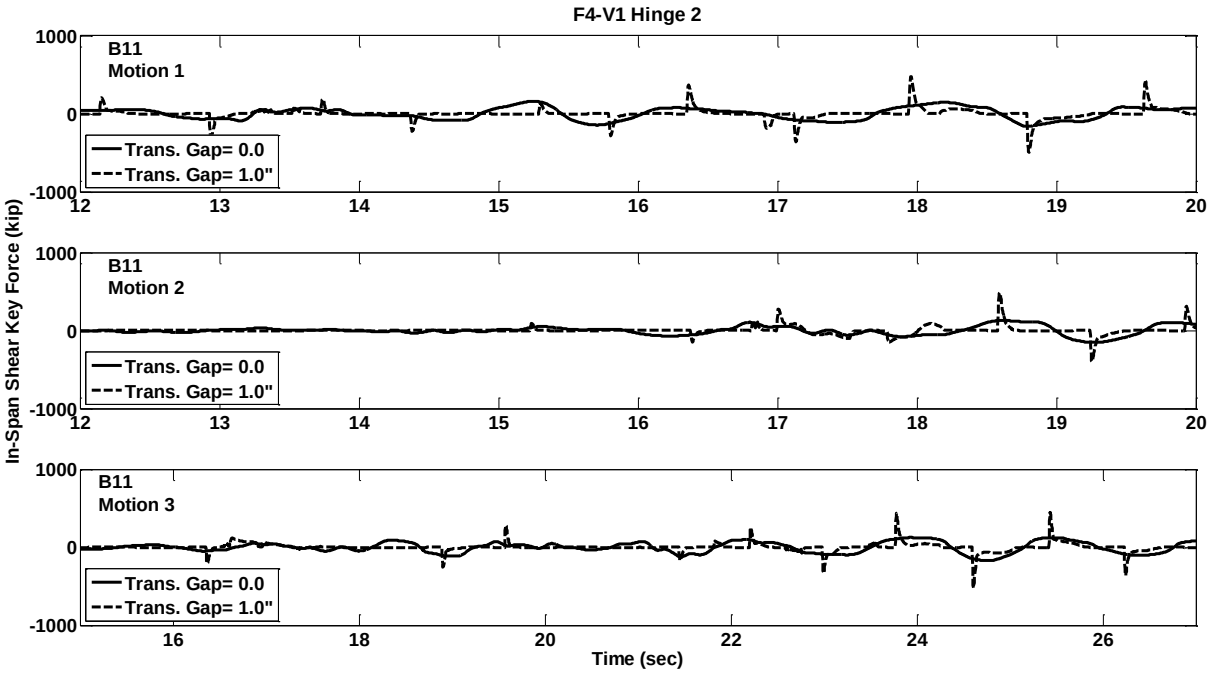

Figure C.349 Shear Key Force Response w/ and w/o Gap, Prototype F4-V1, Hinge-2, Motions B11

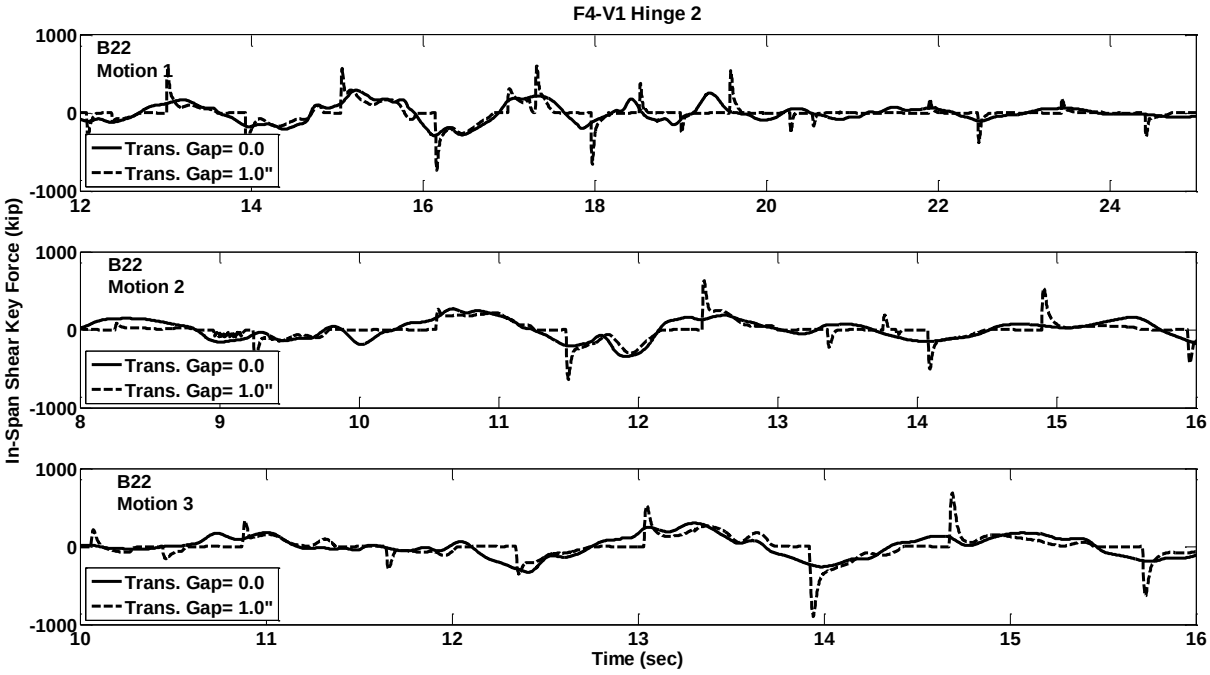

Figure C.350 Shear Key Force Response w/ and w/o Gap, Prototype F4-V1, Hinge-2, Motions B22

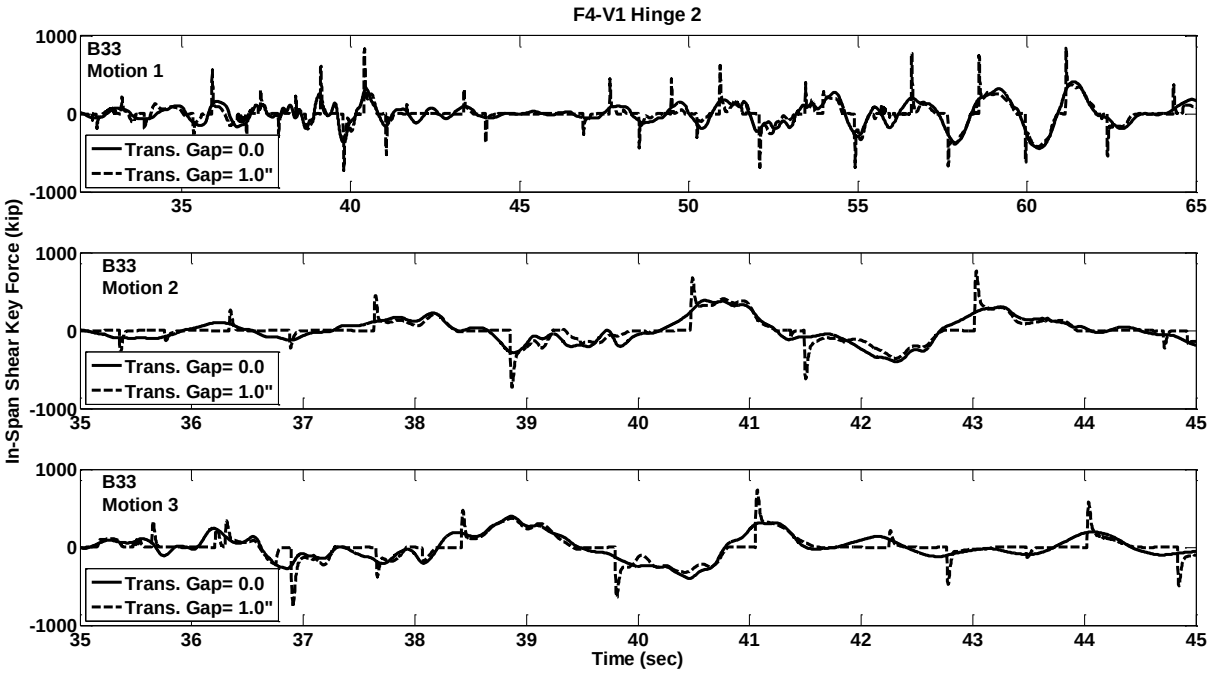

Figure C.351 Shear Key Force Response w/ and w/o Gap, Prototype F4-V1, Hinge-2, Motions B33

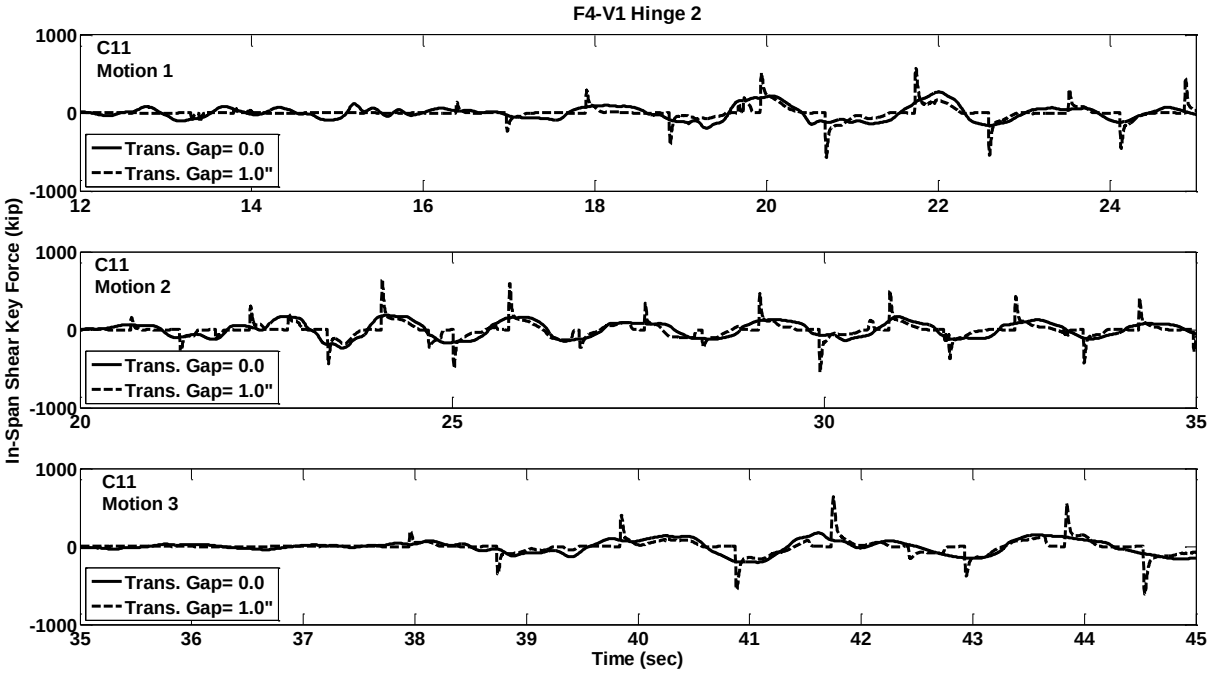

Figure C.352 Shear Key Force Response w/ and w/o Gap, Prototype F4-V1, Hinge-2, Motions C11

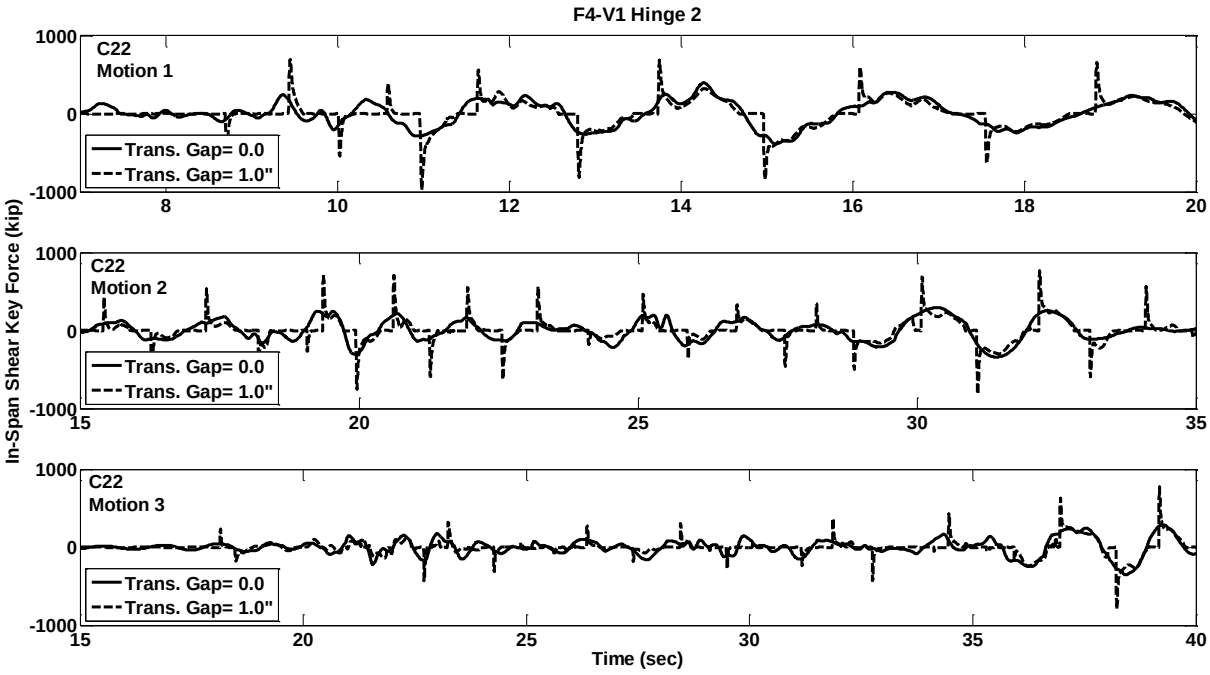

Figure C.353 Shear Key Force Response w/ and w/o Gap, Prototype F4-V1, Hinge-2, Motions C22

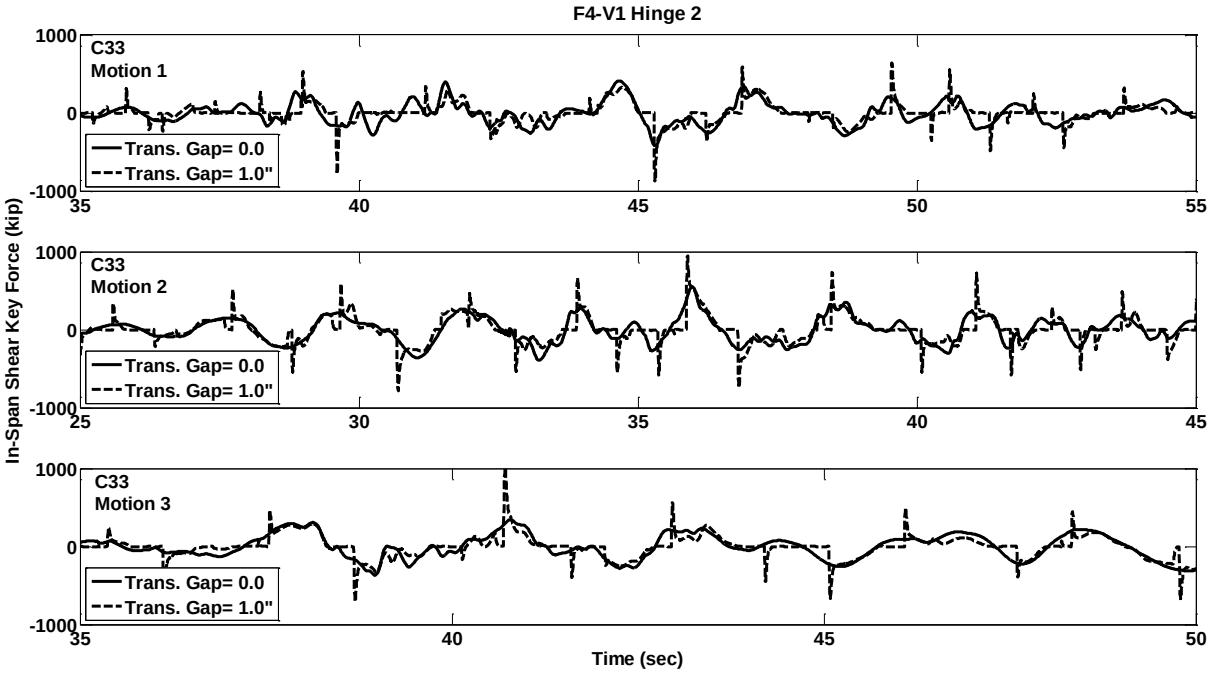

Figure C.354 Shear Key Force Response w/ and w/o Gap, Prototype F4-V1, Hinge-2, Motions C33

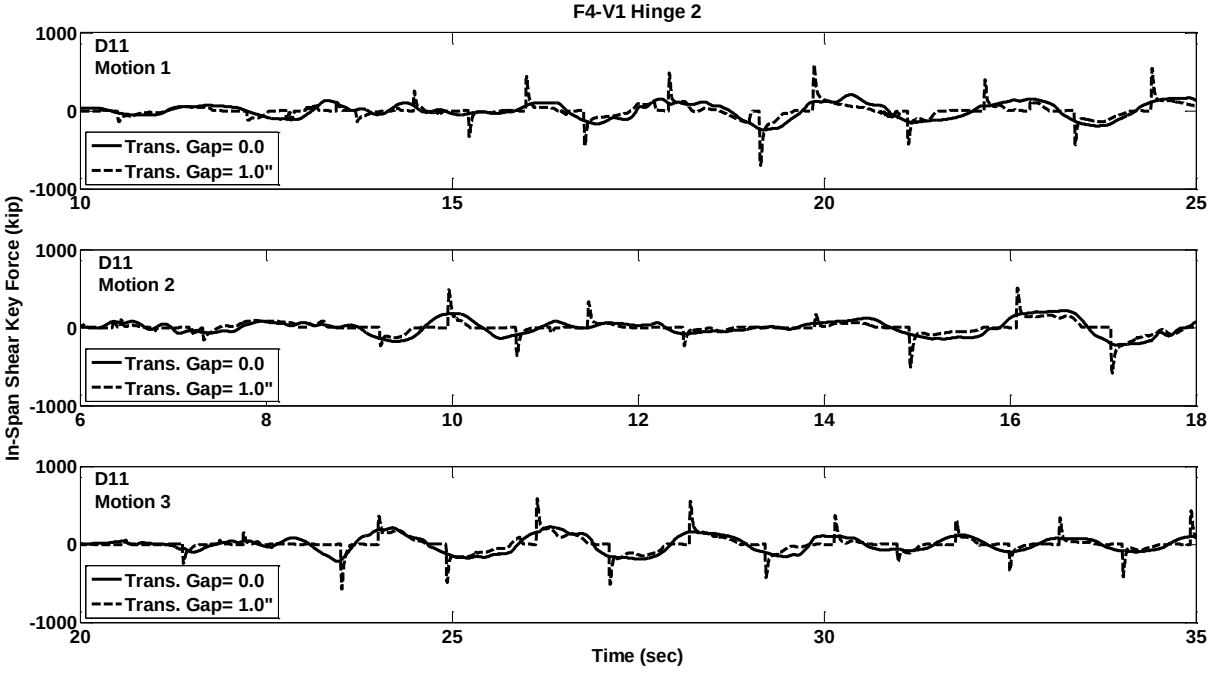

Figure C.355 Shear Key Force Response w/ and w/o Gap, Prototype F4-V1, Hinge-2, Motions D11

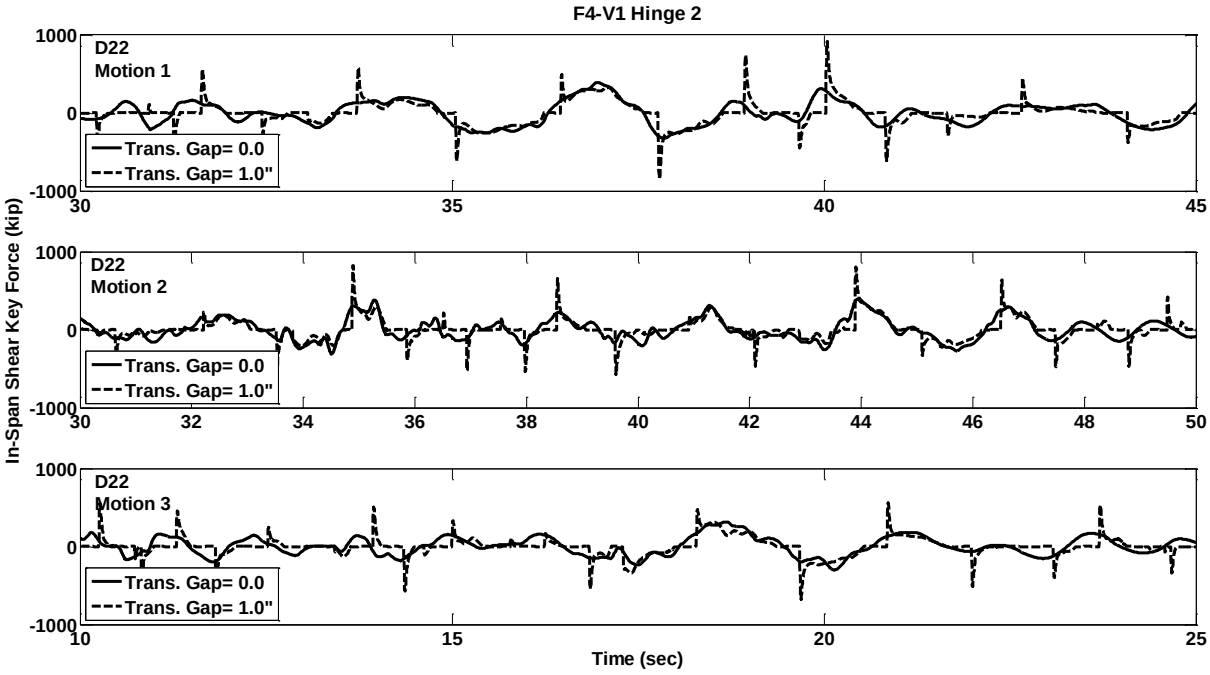

Figure C.356 Shear Key Force Response w/ and w/o Gap, Prototype F4-V1, Hinge-2, Motions D22

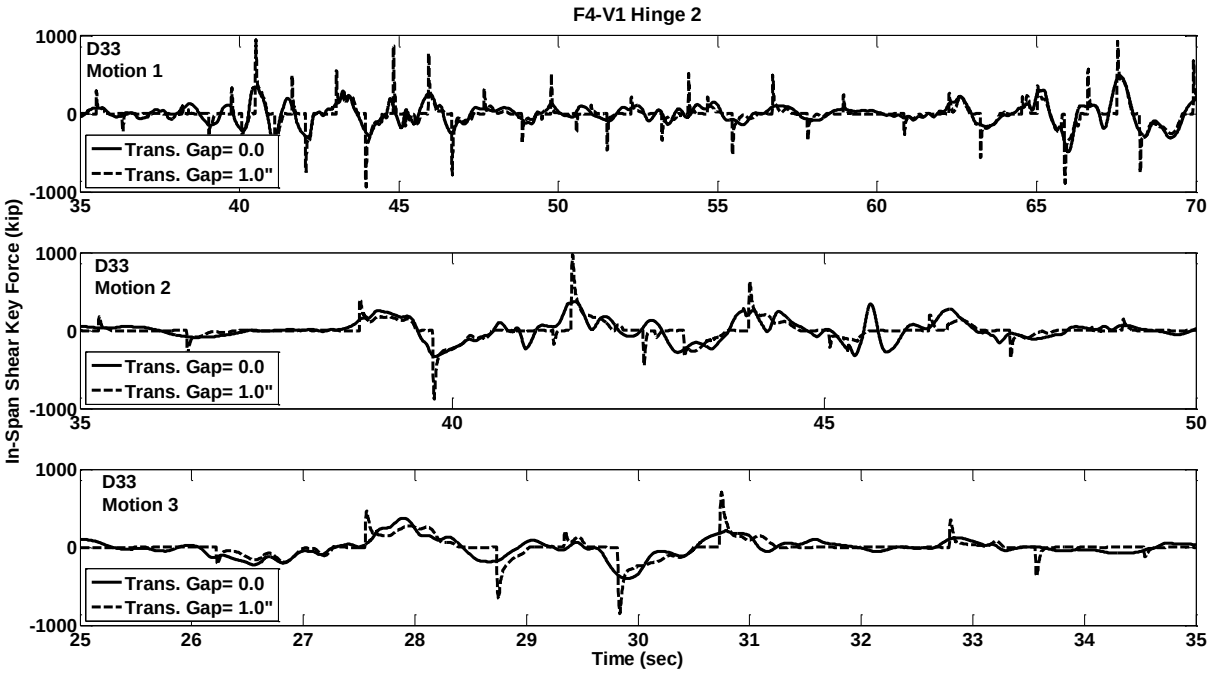

Figure C.357 Shear Key Force Response w/ and w/o Gap, Prototype F4-V1, Hinge-2, Motions D33

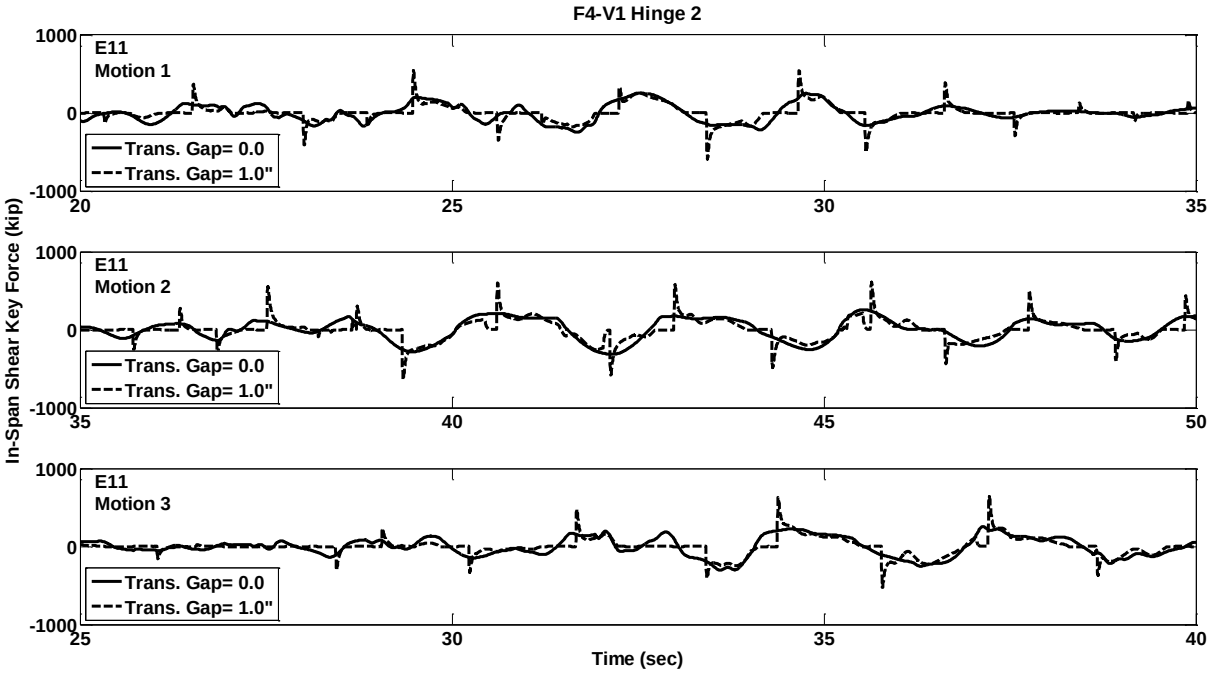

Figure C.358 Shear Key Force Response w/ and w/o Gap, Prototype F4-V1, Hinge-2, Motions E11

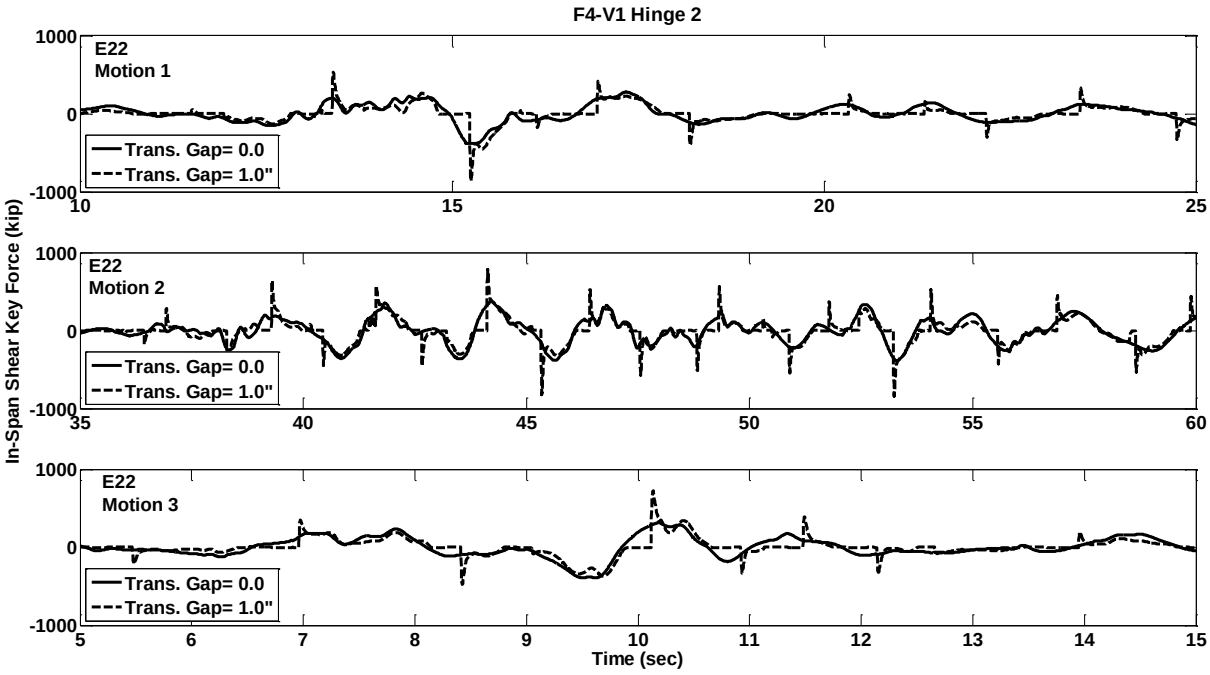

Figure C.359 Shear Key Force Response w/ and w/o Gap, Prototype F4-V1, Hinge-2, Motions E22

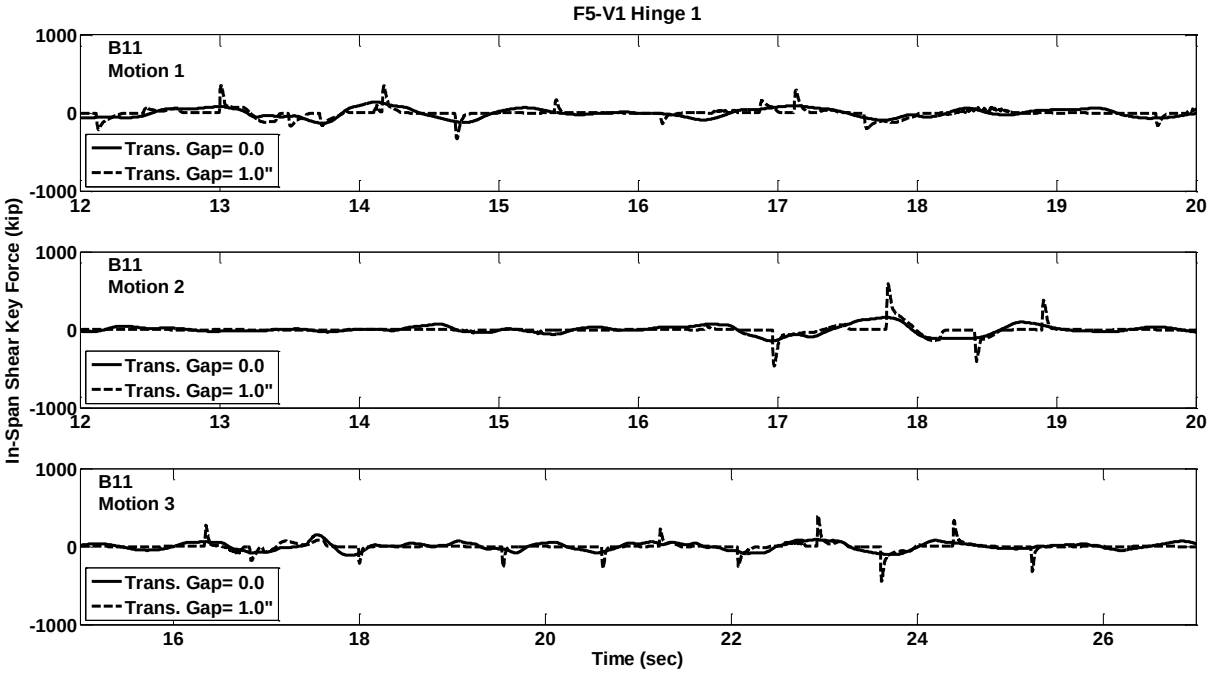

Figure C.360 Shear Key Force Response w/ and w/o Gap, Prototype F5-V1, Hinge-1, Motions B11

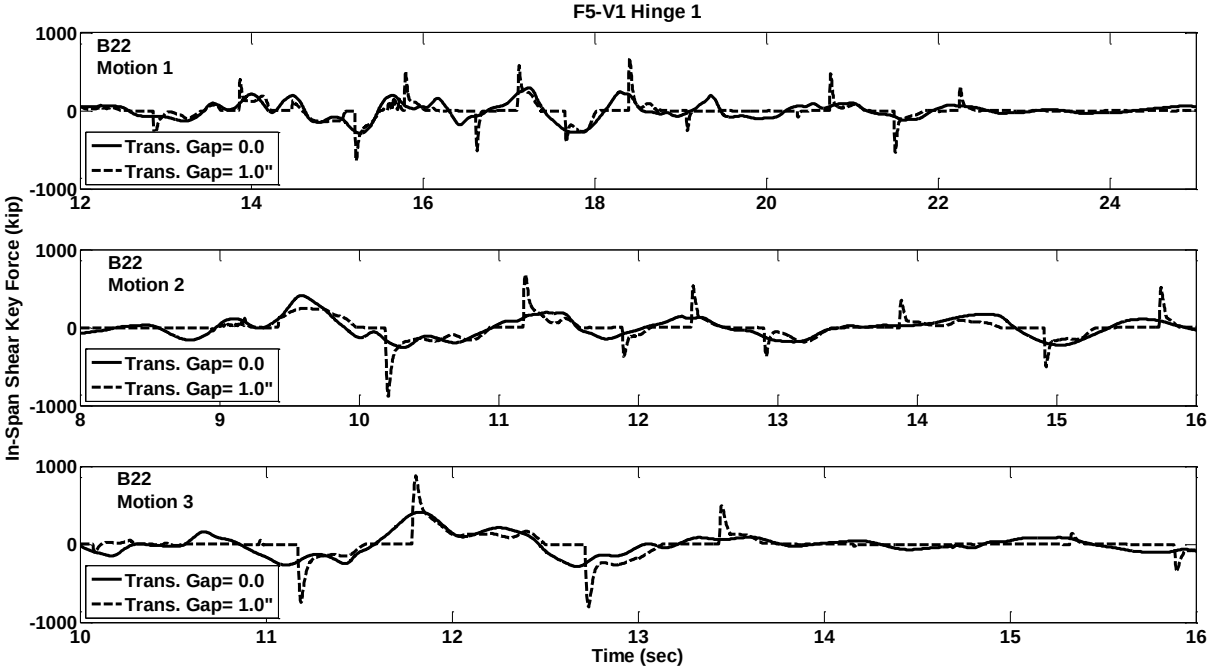

Figure C.361 Shear Key Force Response w/ and w/o Gap, Prototype F5-V1, Hinge-1, Motions B22

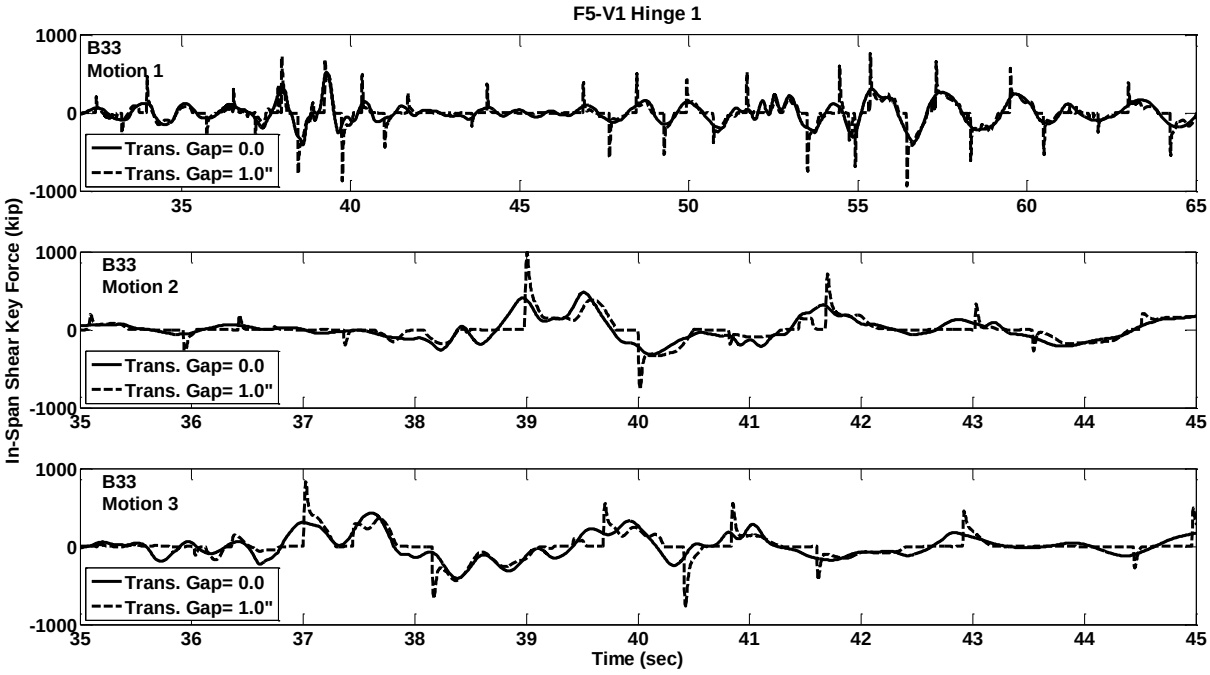

Figure C.362 Shear Key Force Response w/ and w/o Gap, Prototype F5-V1, Hinge-1, Motions B33

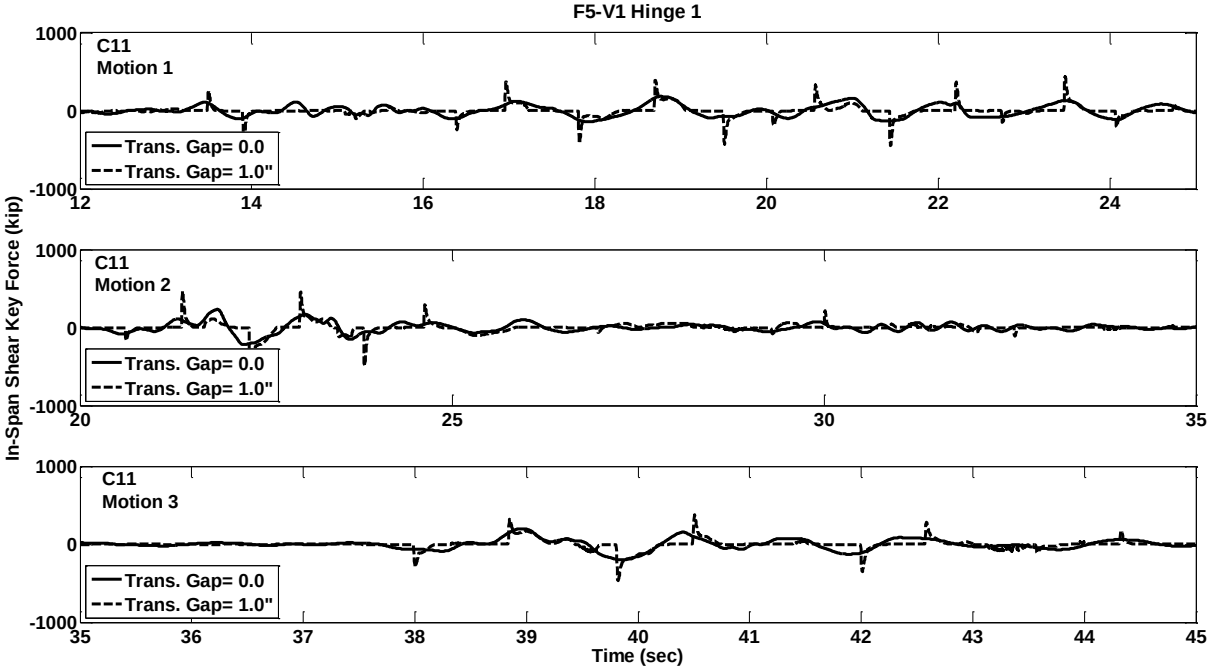

Figure C.363 Shear Key Force Response w/ and w/o Gap, Prototype F5-V1, Hinge-1, Motions C11

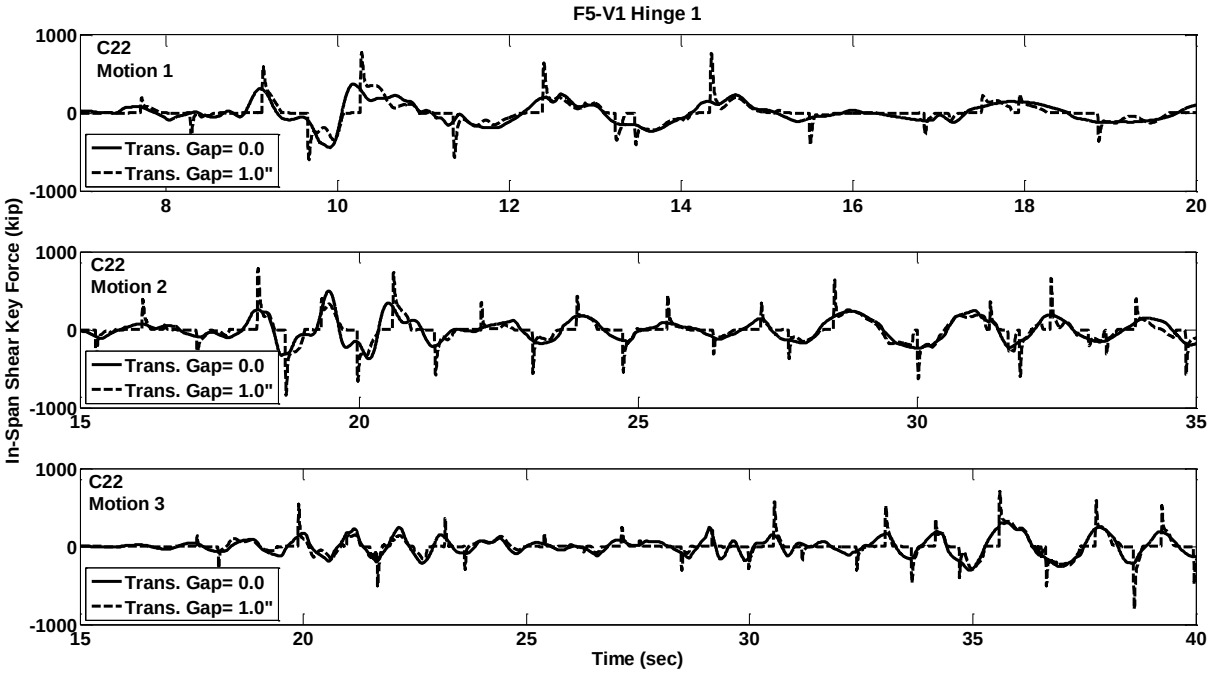

Figure C.364 Shear Key Force Response w/ and w/o Gap, Prototype F5-V1, Hinge-1, Motions C22

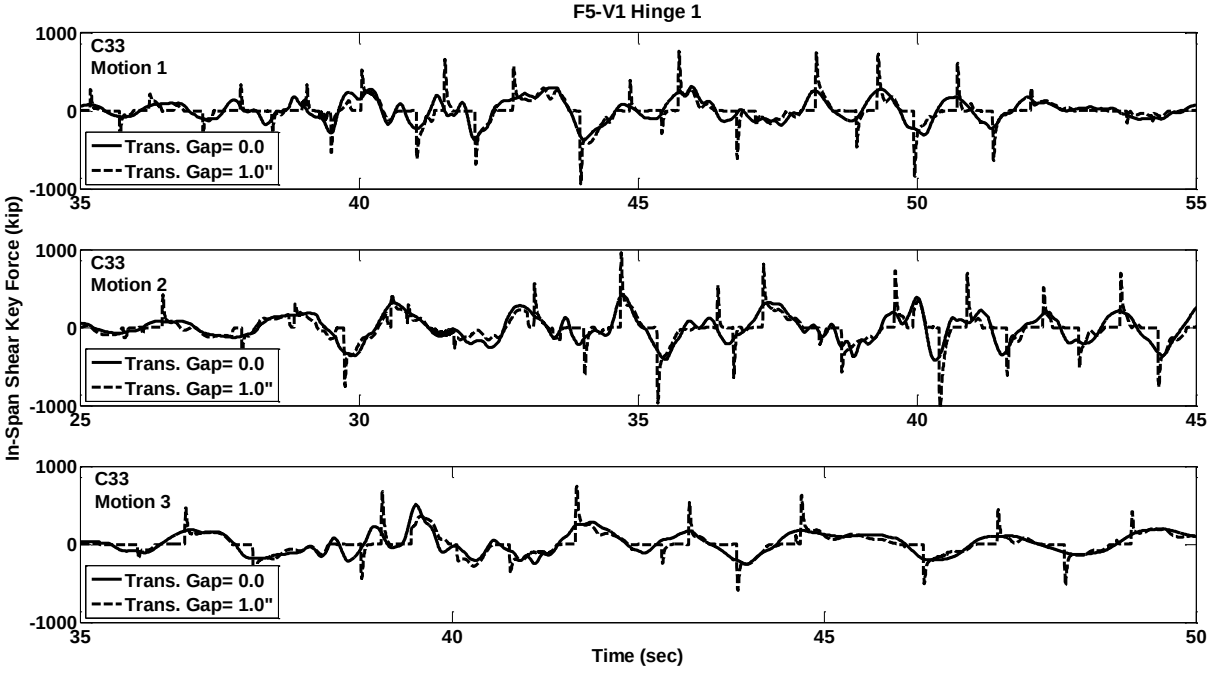

Figure C.365 Shear Key Force Response w/ and w/o Gap, Prototype F5-V1, Hinge-1, Motions C33

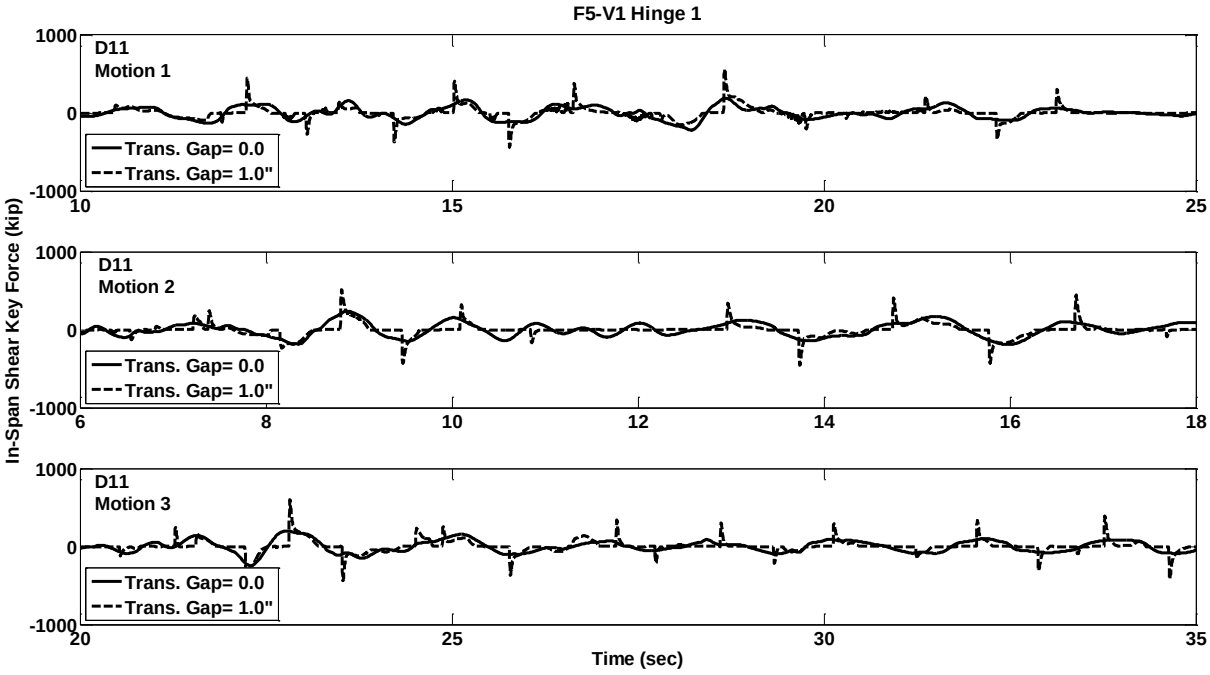

Figure C.366 Shear Key Force Response w/ and w/o Gap, Prototype F5-V1, Hinge-1, Motions D11

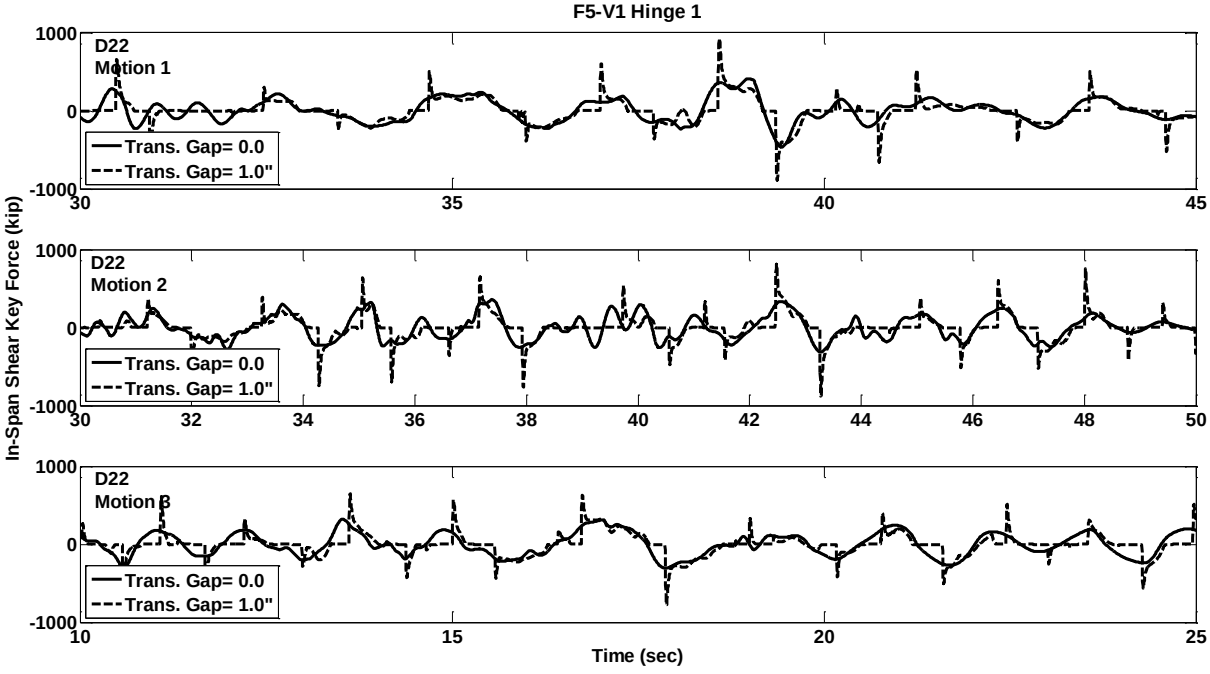

Figure C.367 Shear Key Force Response w/ and w/o Gap, Prototype F5-V1, Hinge-1, Motions D22

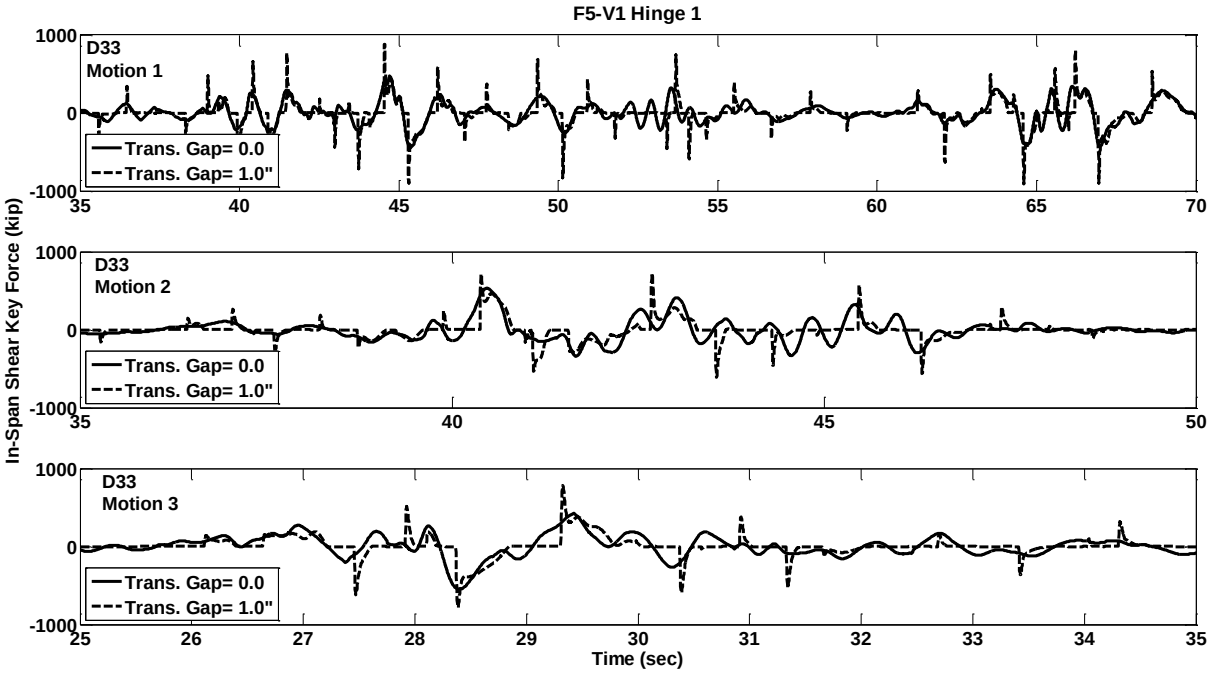

Figure C.368 Shear Key Force Response w/ and w/o Gap, Prototype F5-V1, Hinge-1, Motions D33

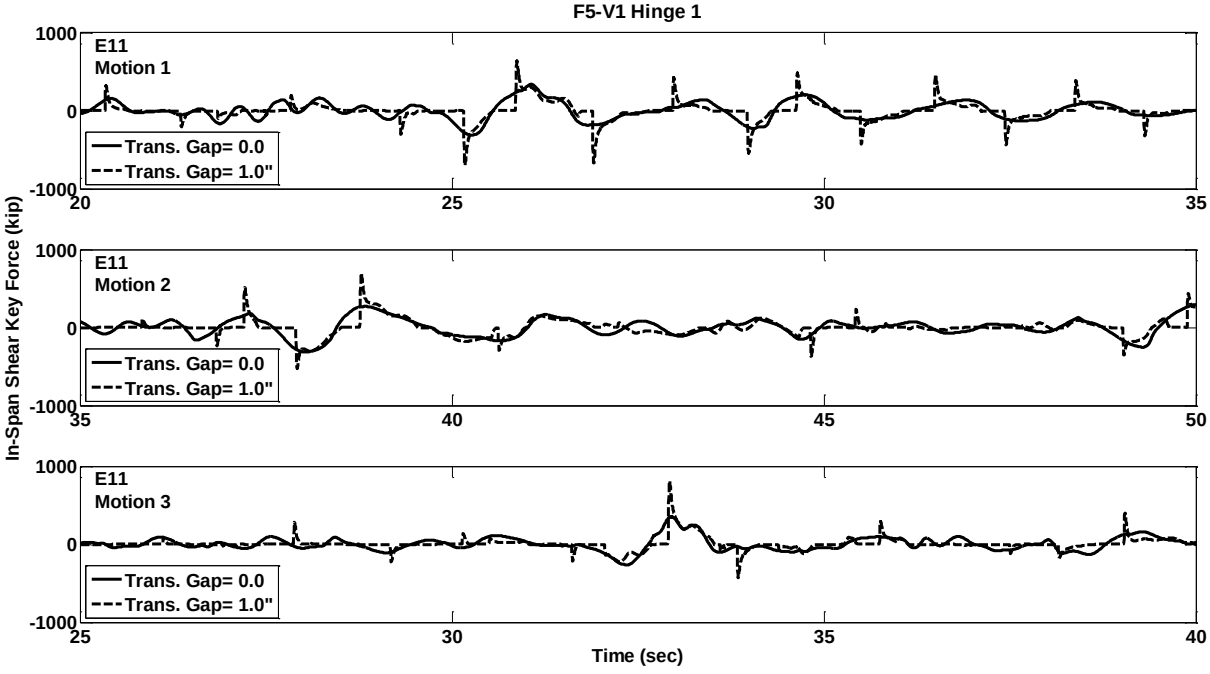

Figure C.369 Shear Key Force Response w/ and w/o Gap, Prototype F5-V1, Hinge-1, Motions E11

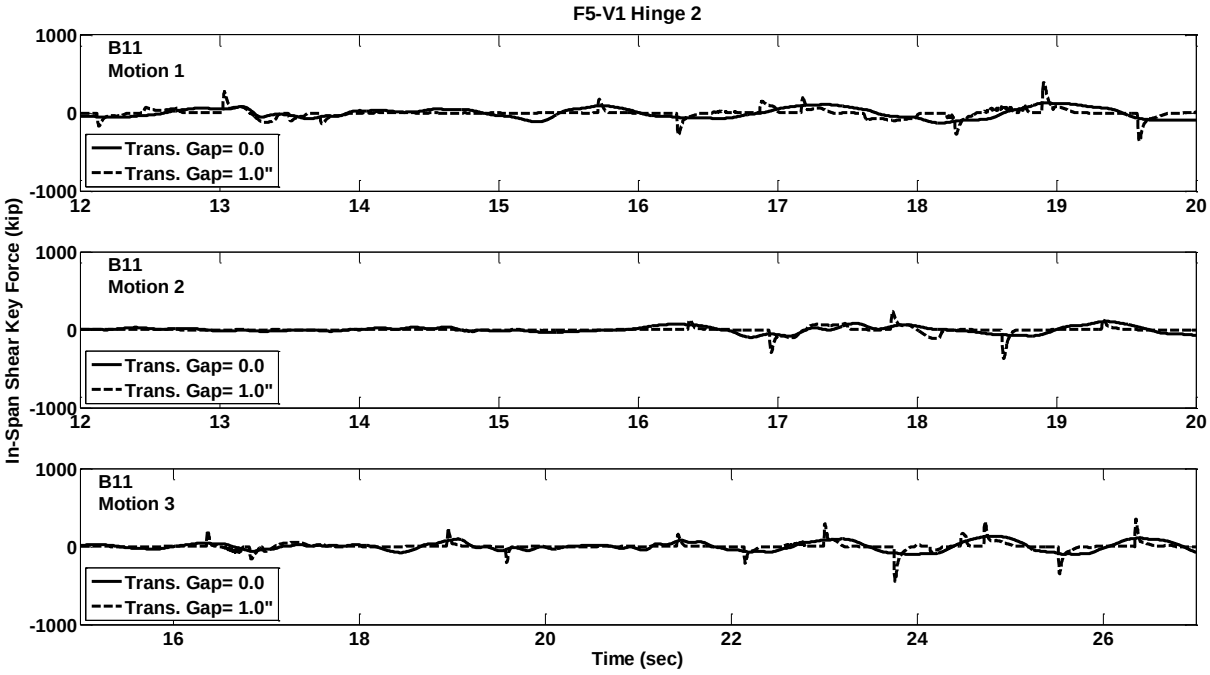

Figure C.370 Shear Key Force Response w/ and w/o Gap, Prototype F5-V1, Hinge-2, Motions B11

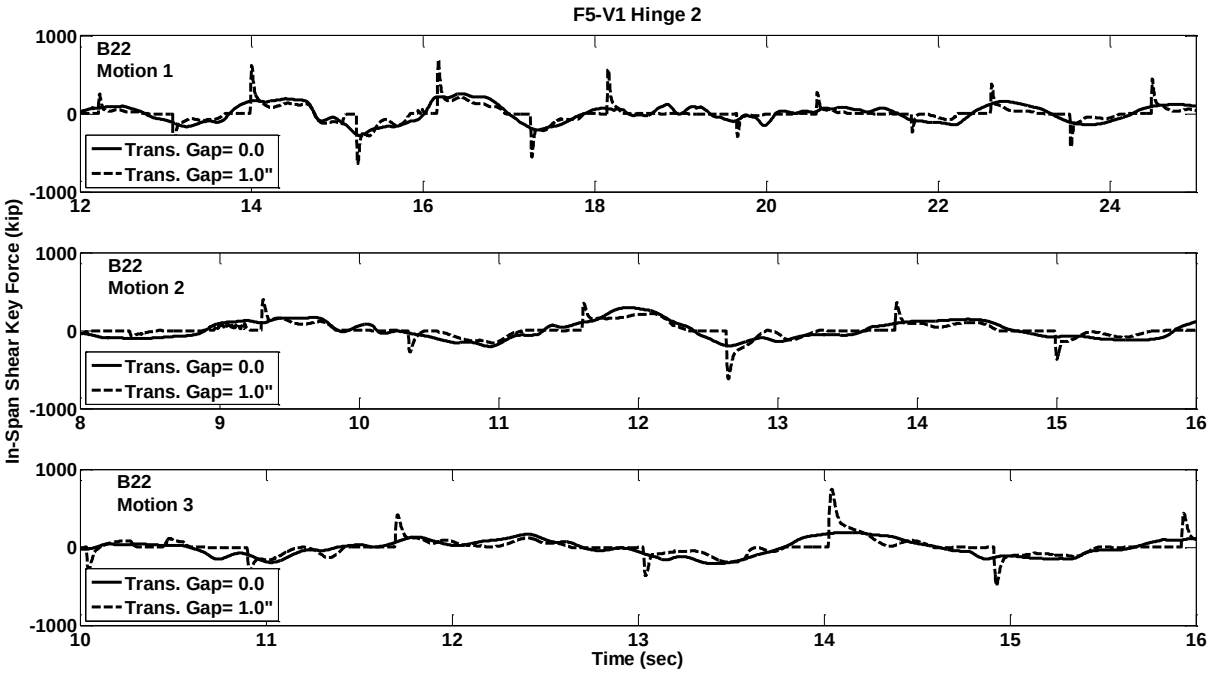

Figure C.371 Shear Key Force Response w/ and w/o Gap, Prototype F5-V1, Hinge-2, Motions B22

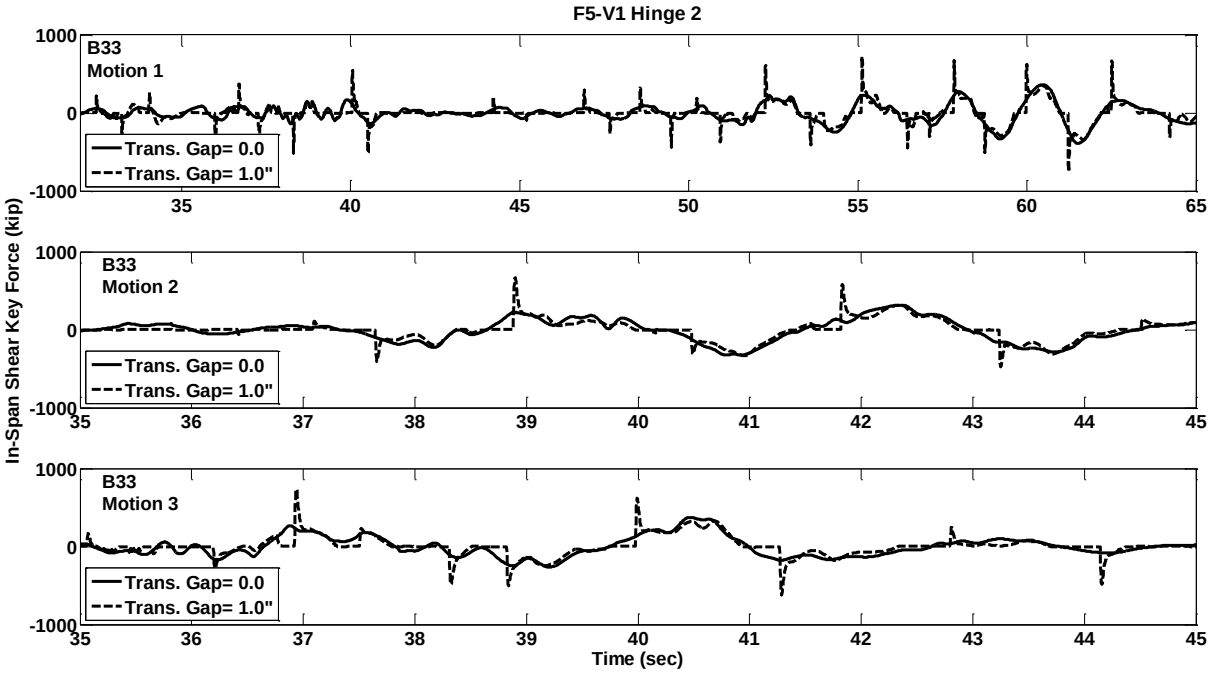

Figure C.372 Shear Key Force Response w/ and w/o Gap, Prototype F5-V1, Hinge-2, Motions B33

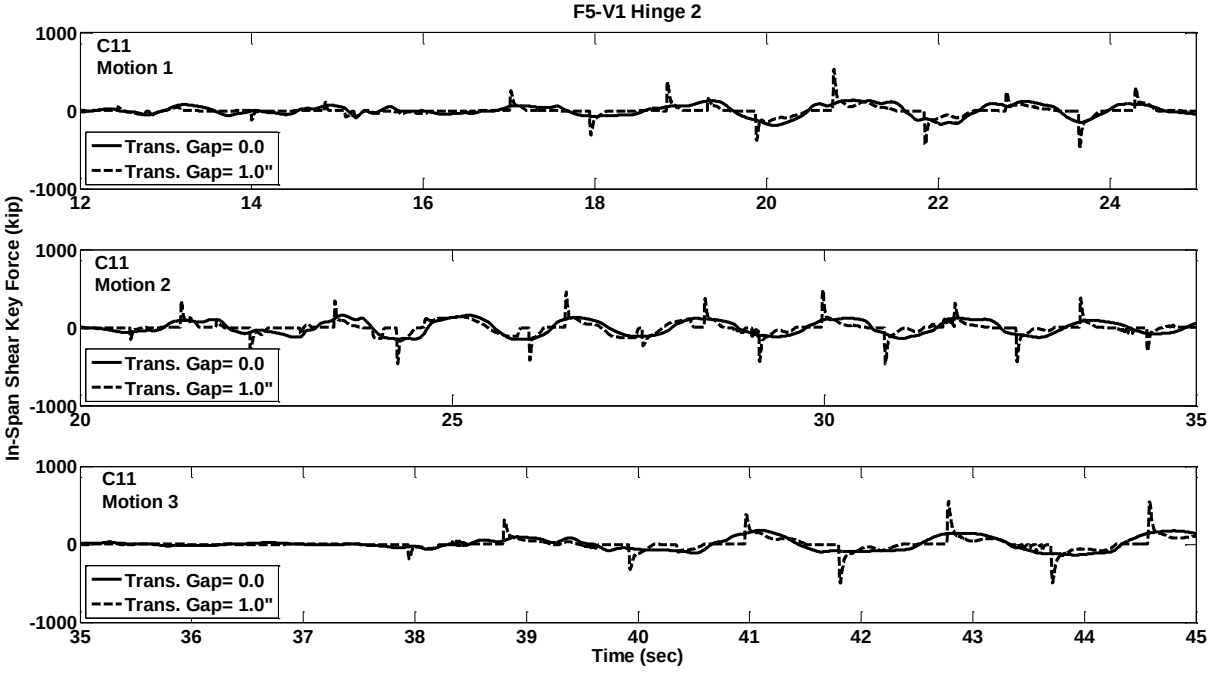

Figure C.373 Shear Key Force Response w/ and w/o Gap, Prototype F5-V1, Hinge-2, Motions C11

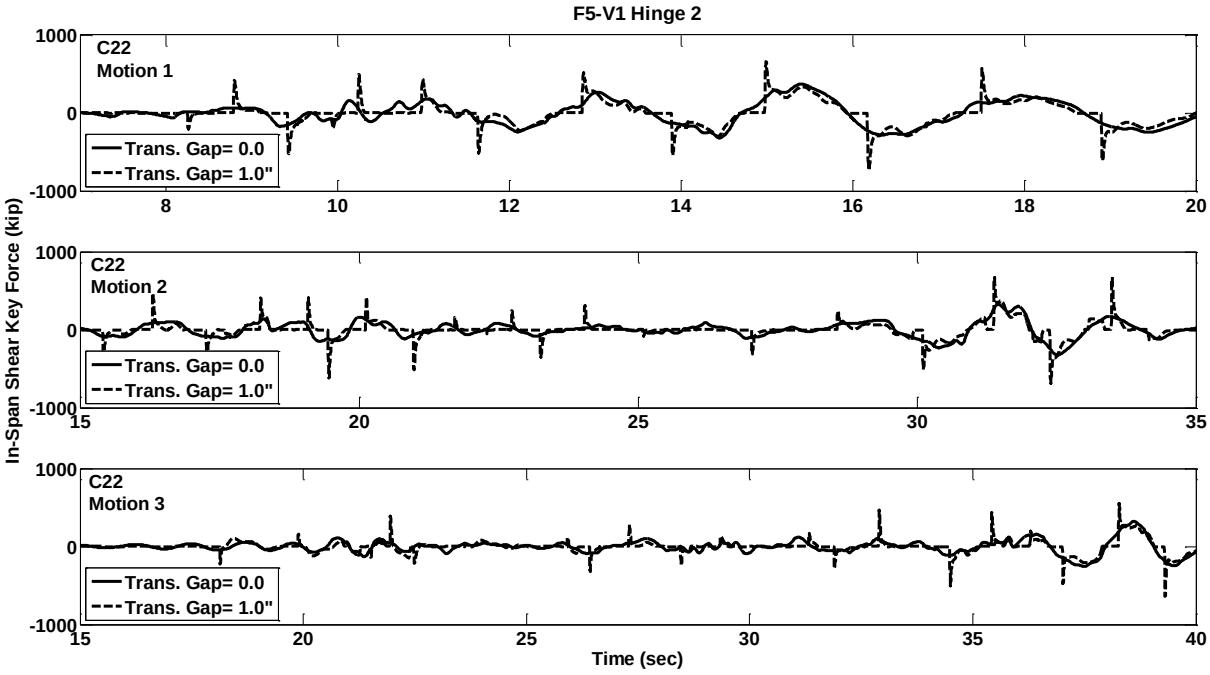

Figure C.374 Shear Key Force Response w/ and w/o Gap, Prototype F5-V1, Hinge-2, Motions C22

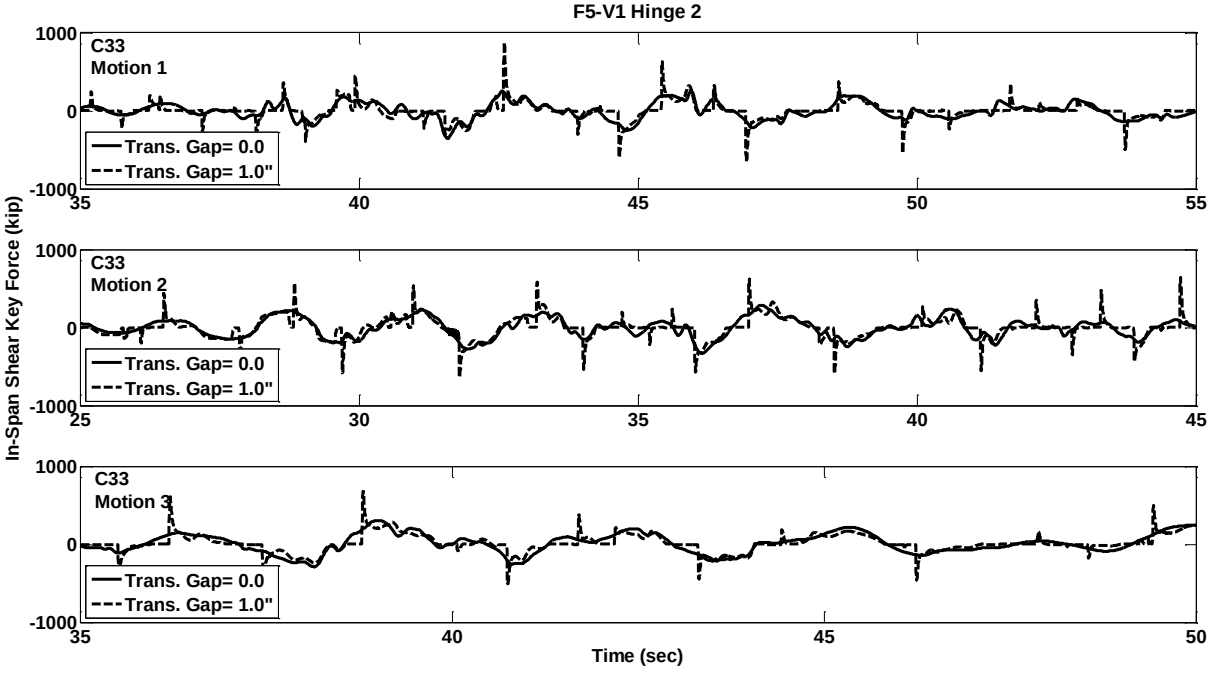

Figure C.375 Shear Key Force Response w/ and w/o Gap, Prototype F5-V1, Hinge-2, Motions C33

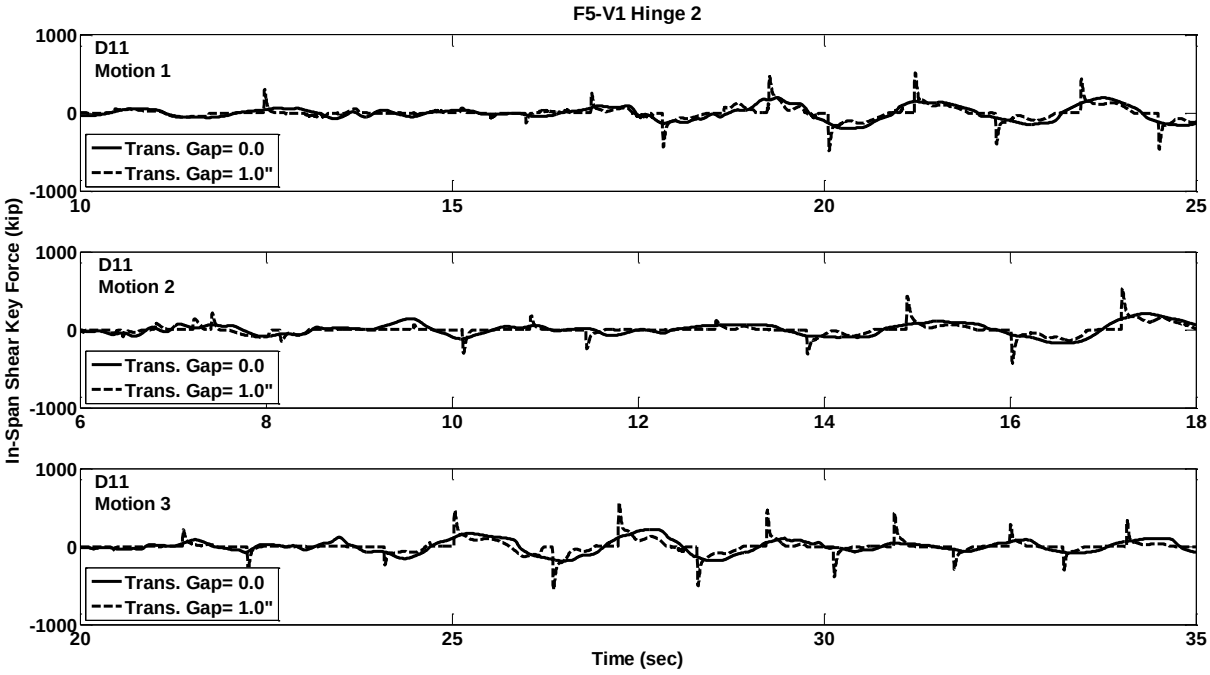

Figure C.376 Shear Key Force Response w/ and w/o Gap, Prototype F5-V1, Hinge-2, Motions D11

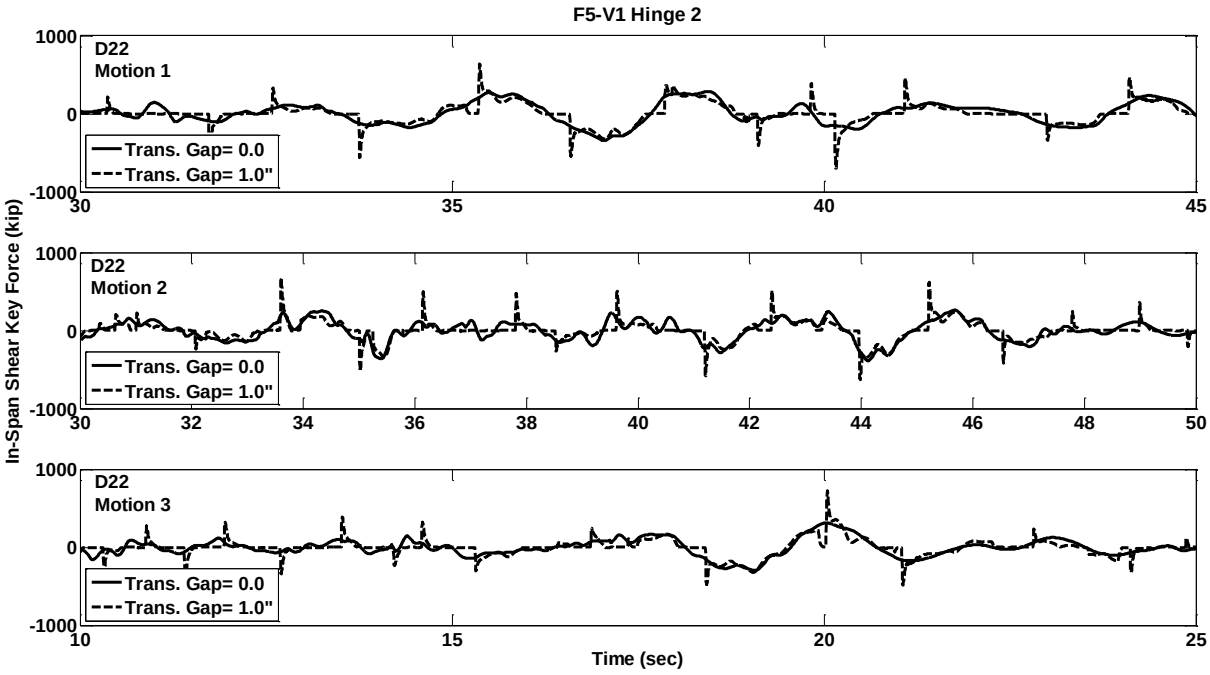

Figure C.377 Shear Key Force Response w/ and w/o Gap, Prototype F5-V1, Hinge-2, Motions D22

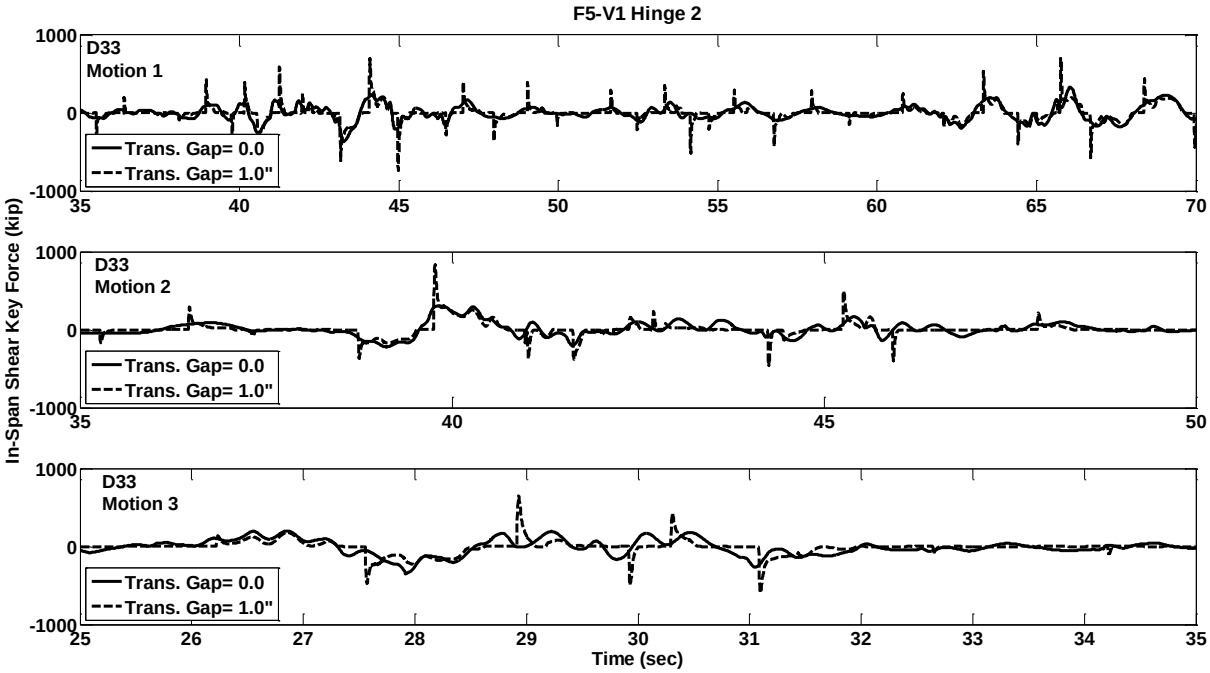

Figure C.378 Shear Key Force Response w/ and w/o Gap, Prototype F5-V1, Hinge-2, Motions D33

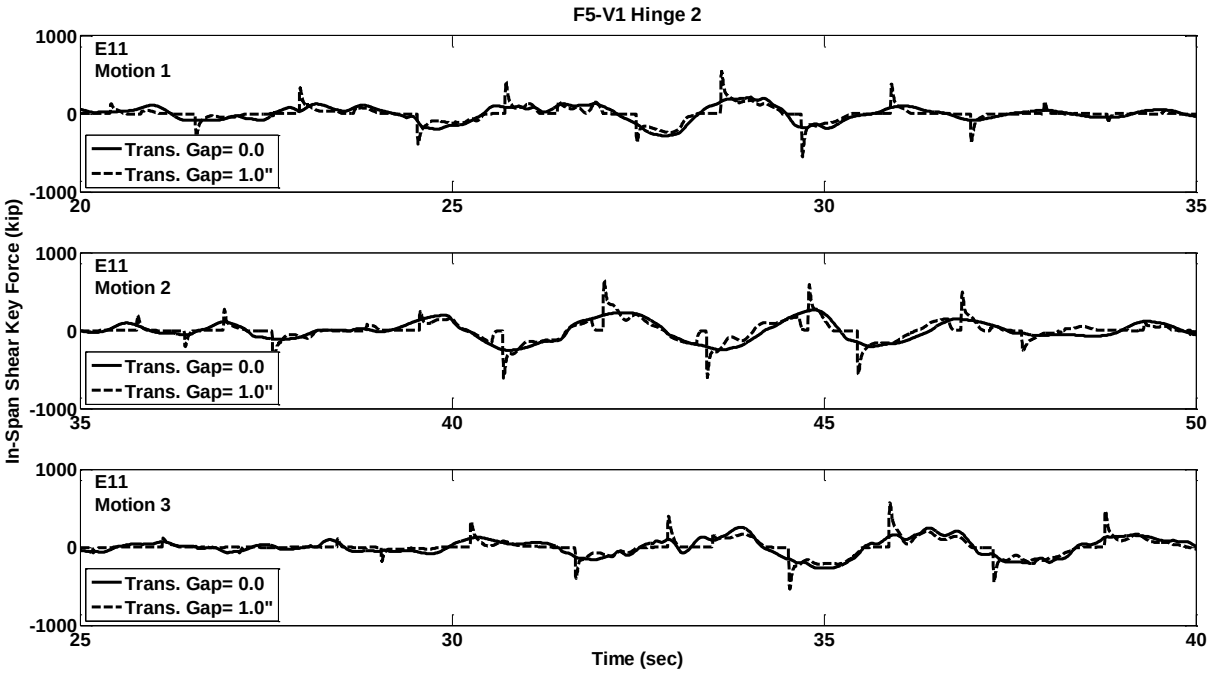

Figure C.379 Shear Key Force Response w/ and w/o Gap, Prototype F5-V1, Hinge-2, Motions E11

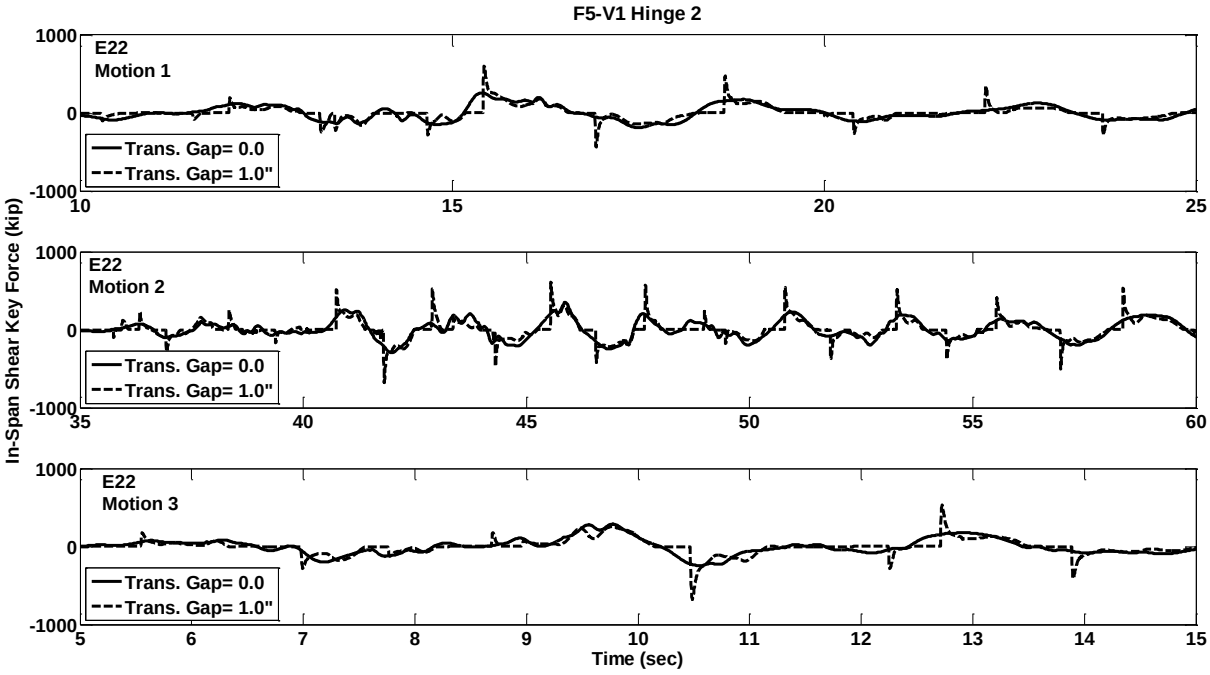

Figure C.380 Shear Key Force Response w/ and w/o Gap, Prototype F5-V1, Hinge-2, Motions E22

PART-5b: Two-Column Bent Prototypes

Shear Key Force Responses w/ and w/o Transverse Gap

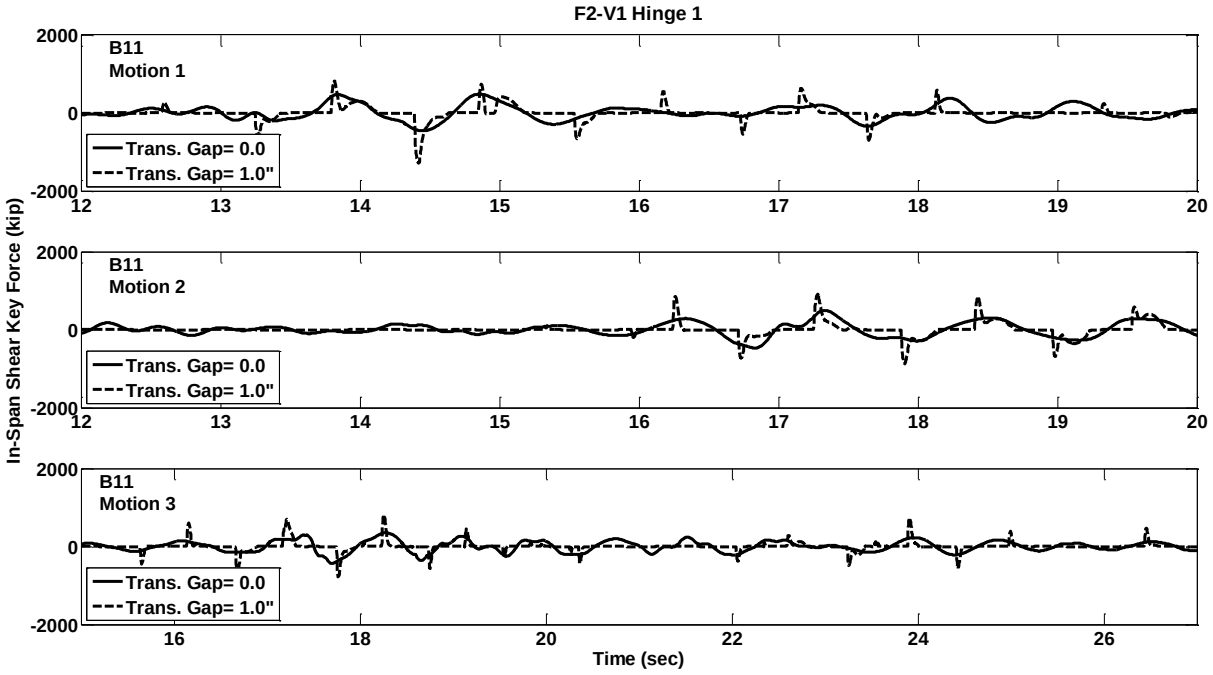

Figure C.381 Shear Key Force Response w/ and w/o Gap, Prototype F2-V1, Hinge-1, Motions B11

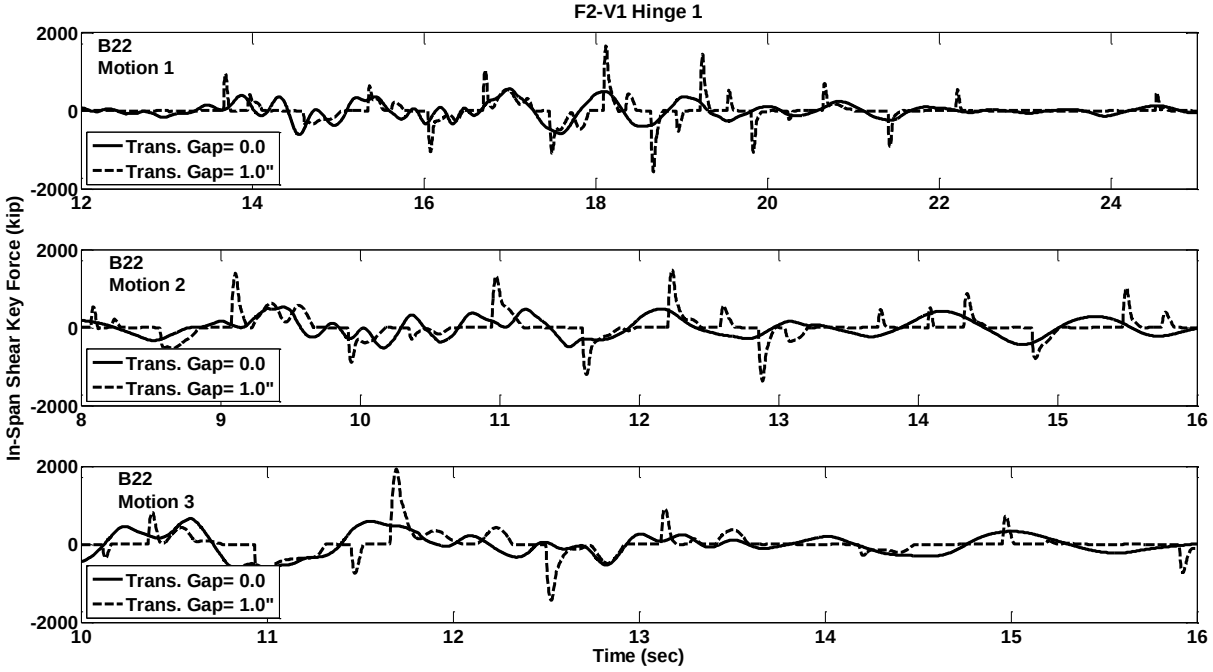

Figure C.382 Shear Key Force Response w/ and w/o Gap, Prototype F2-V1, Hinge-1, Motions B22

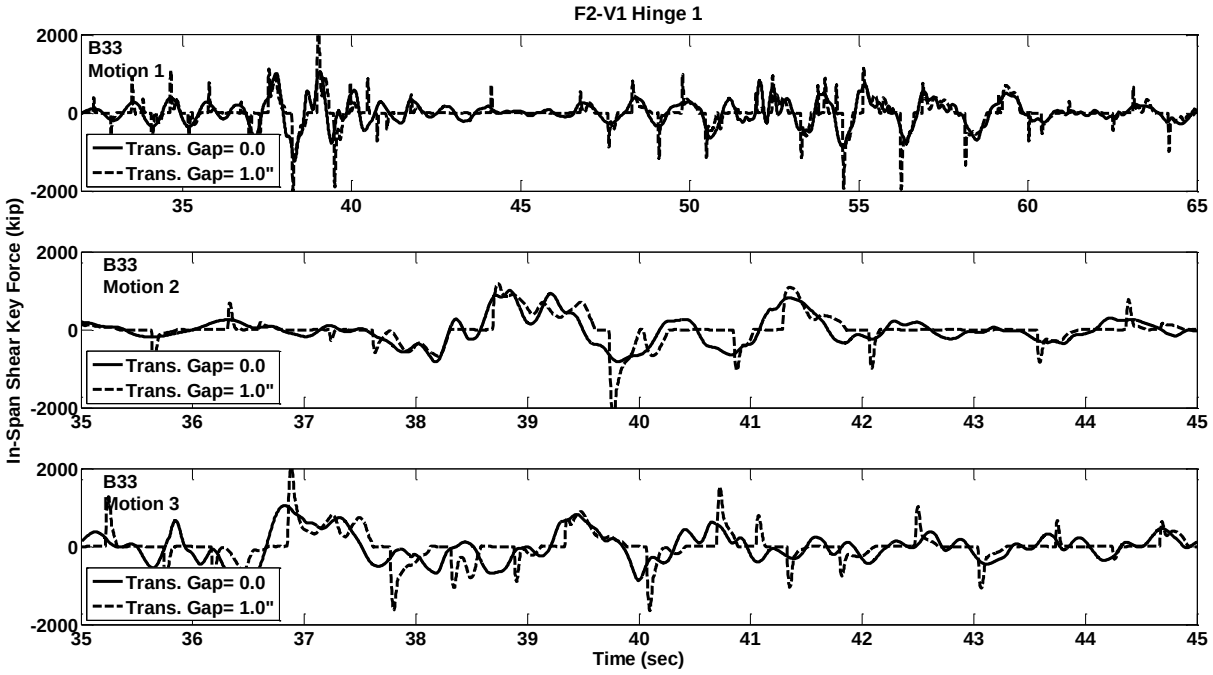

Figure C.383 Shear Key Force Response w/ and w/o Gap, Prototype F2-V1, Hinge-1, Motions B33

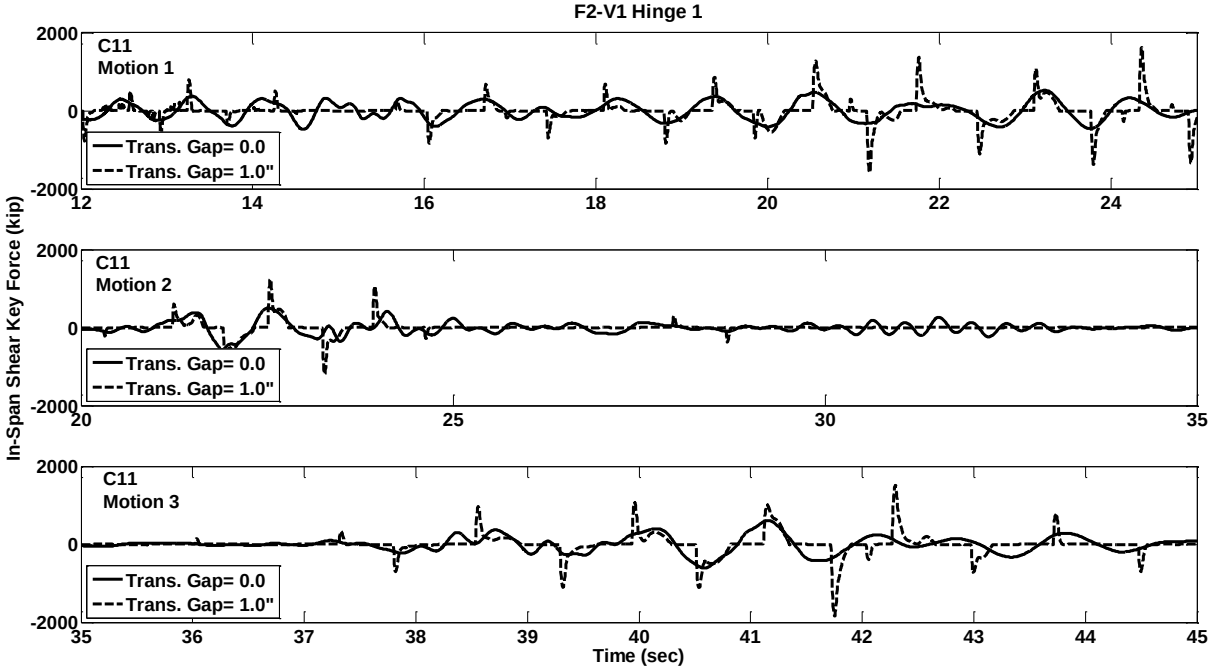

Figure C.384 Shear Key Force Response w/ and w/o Gap, Prototype F2-V1, Hinge-1, Motions C11

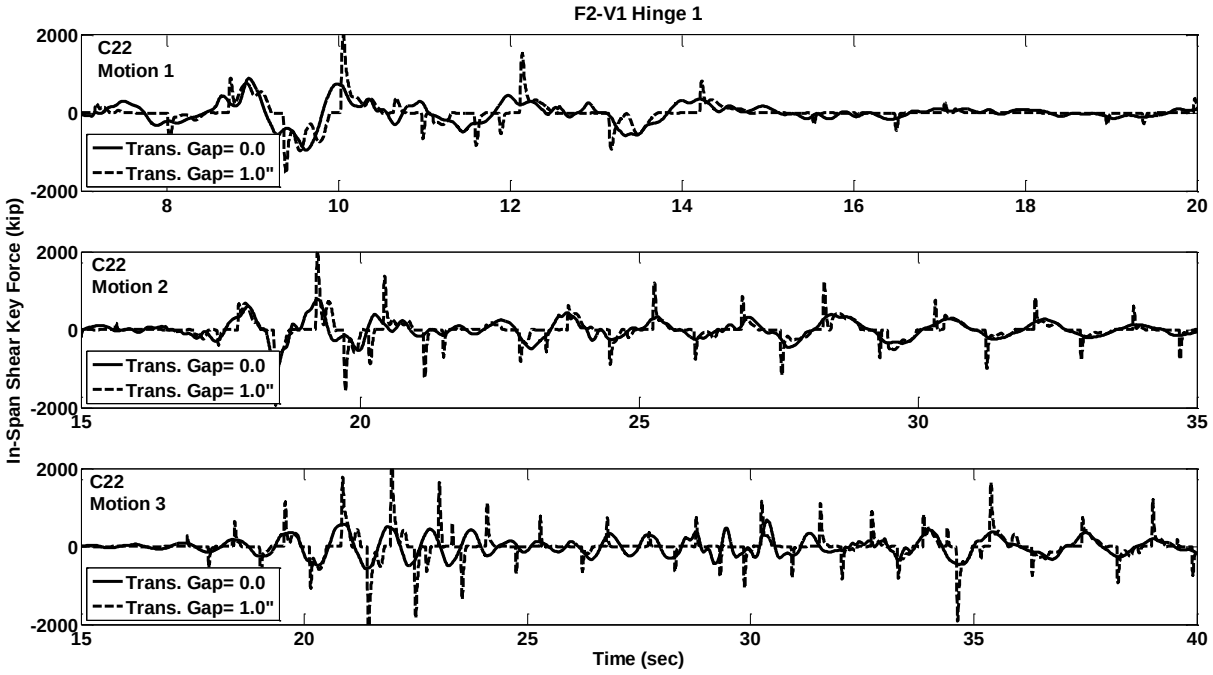

Figure C.385 Shear Key Force Response w/ and w/o Gap, Prototype F2-V1, Hinge-1, Motions C22

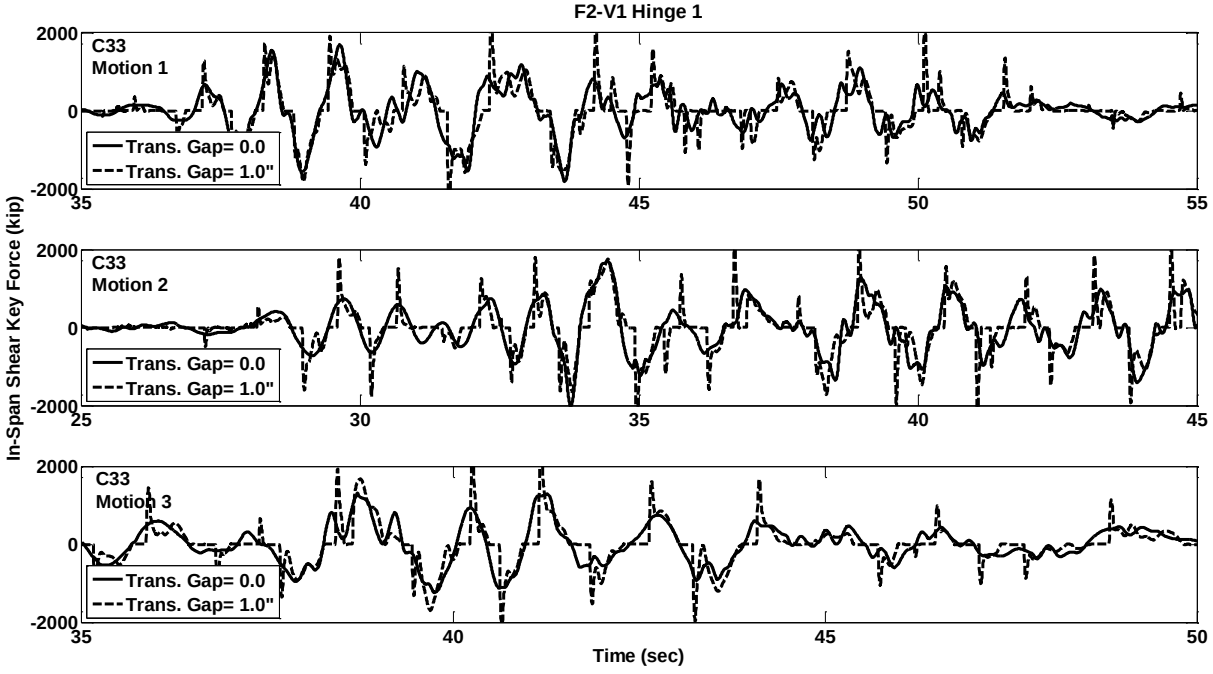

Figure C.386 Shear Key Force Response w/ and w/o Gap, Prototype F2-V1, Hinge-1, Motions C33

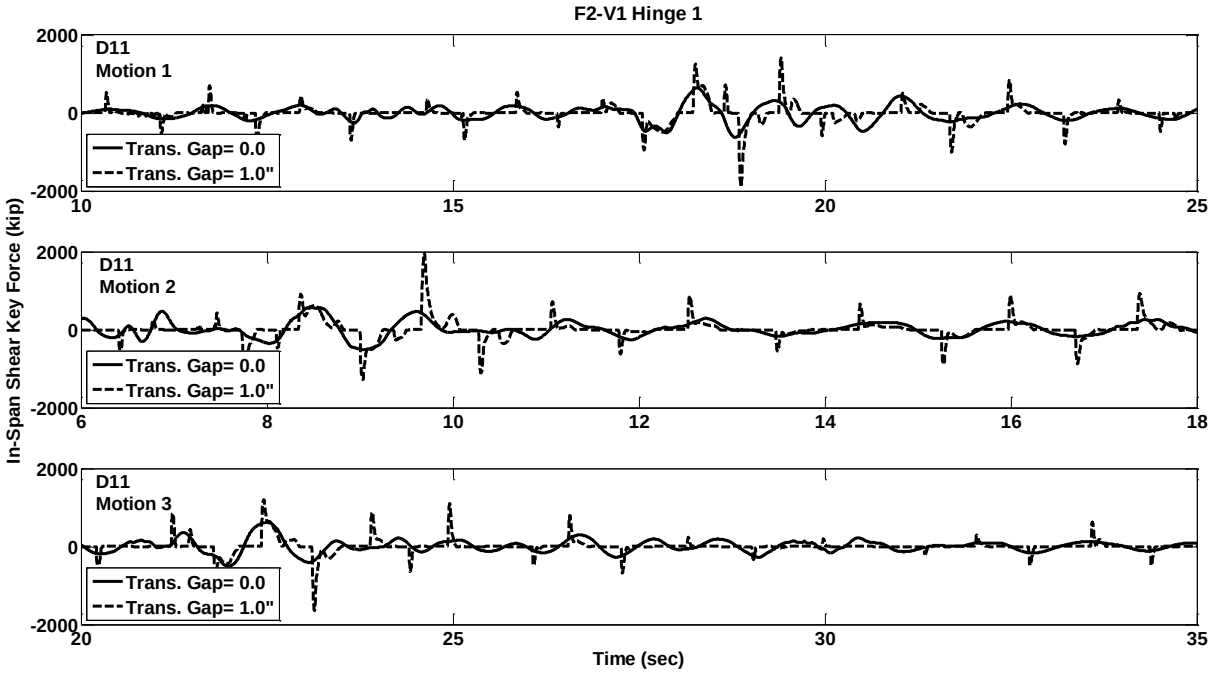

Figure C.387 Shear Key Force Response w/ and w/o Gap, Prototype F2-V1, Hinge-1, Motions D11

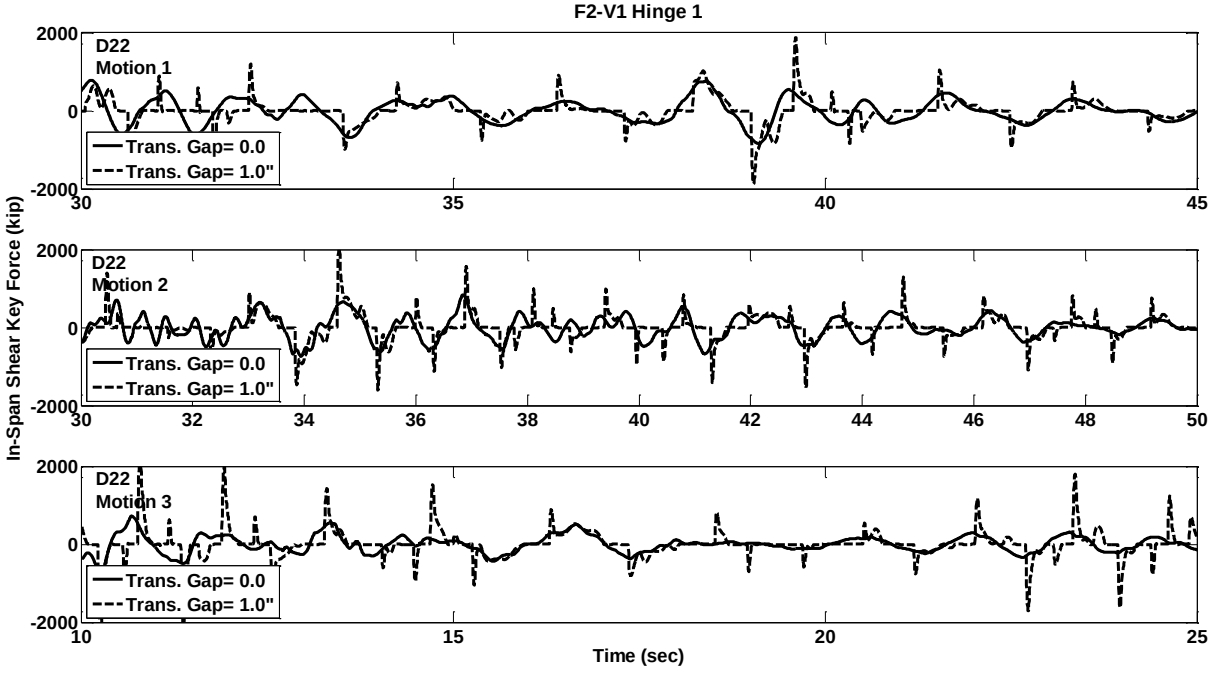

Figure C.388 Shear Key Force Response w/ and w/o Gap, Prototype F2-V1, Hinge-1, Motions D22

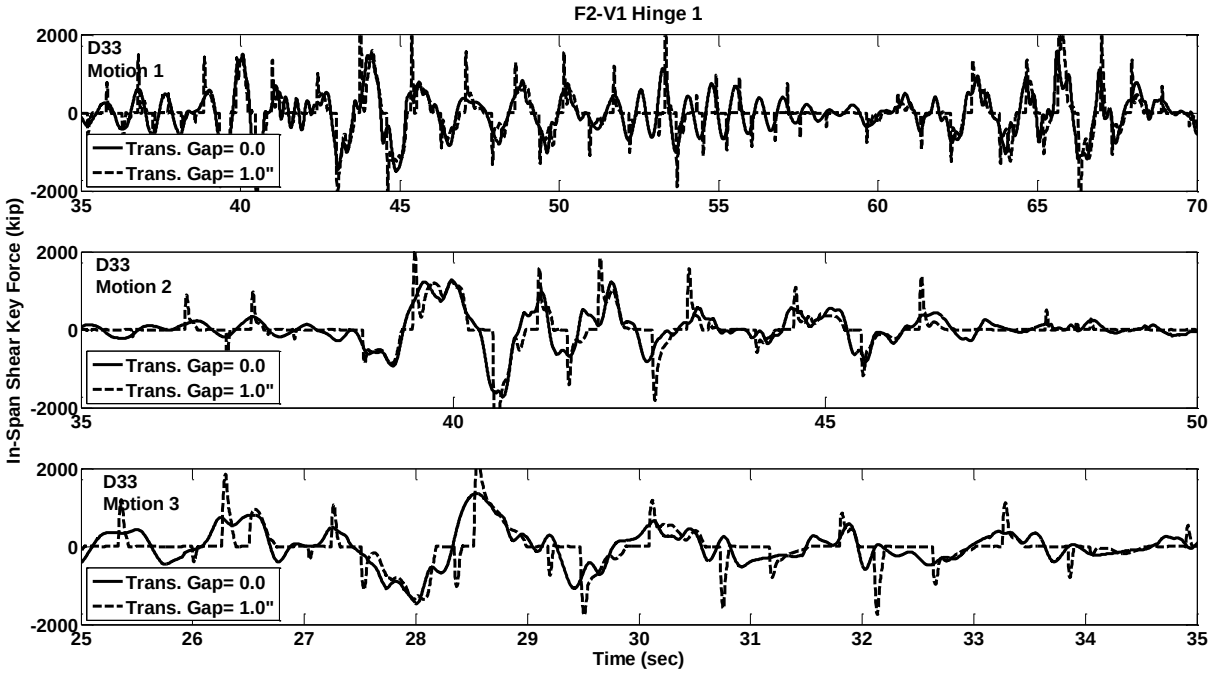

Figure C.389 Shear Key Force Response w/ and w/o Gap, Prototype F2-V1, Hinge-1, Motions D33

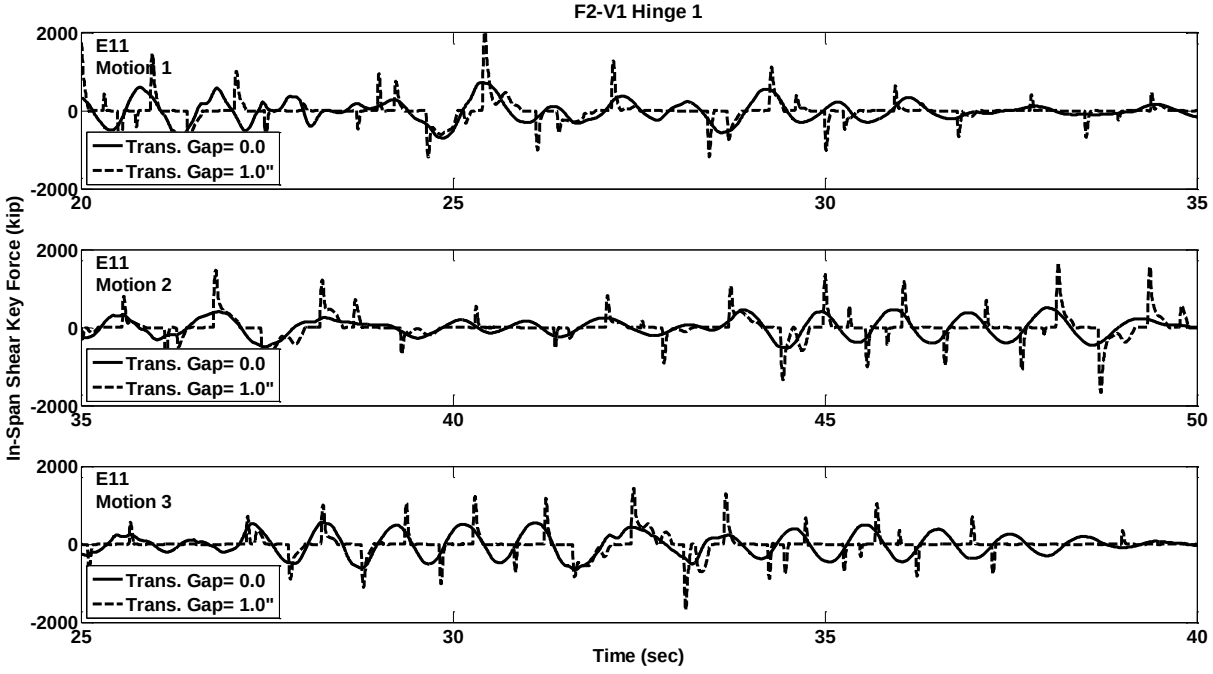

Figure C.390 Shear Key Force Response w/ and w/o Gap, Prototype F2-V1, Hinge-1, Motions E11

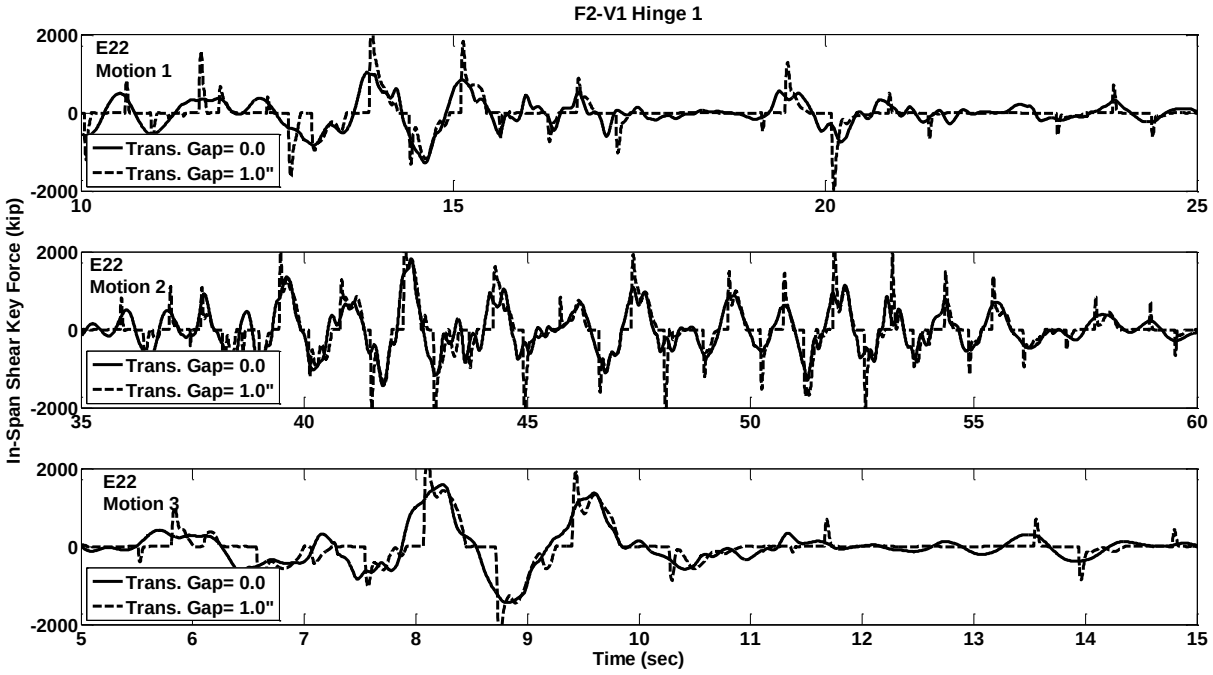

Figure C.391 Shear Key Force Response w/ and w/o Gap, Prototype F2-V1, Hinge-1, Motions E22

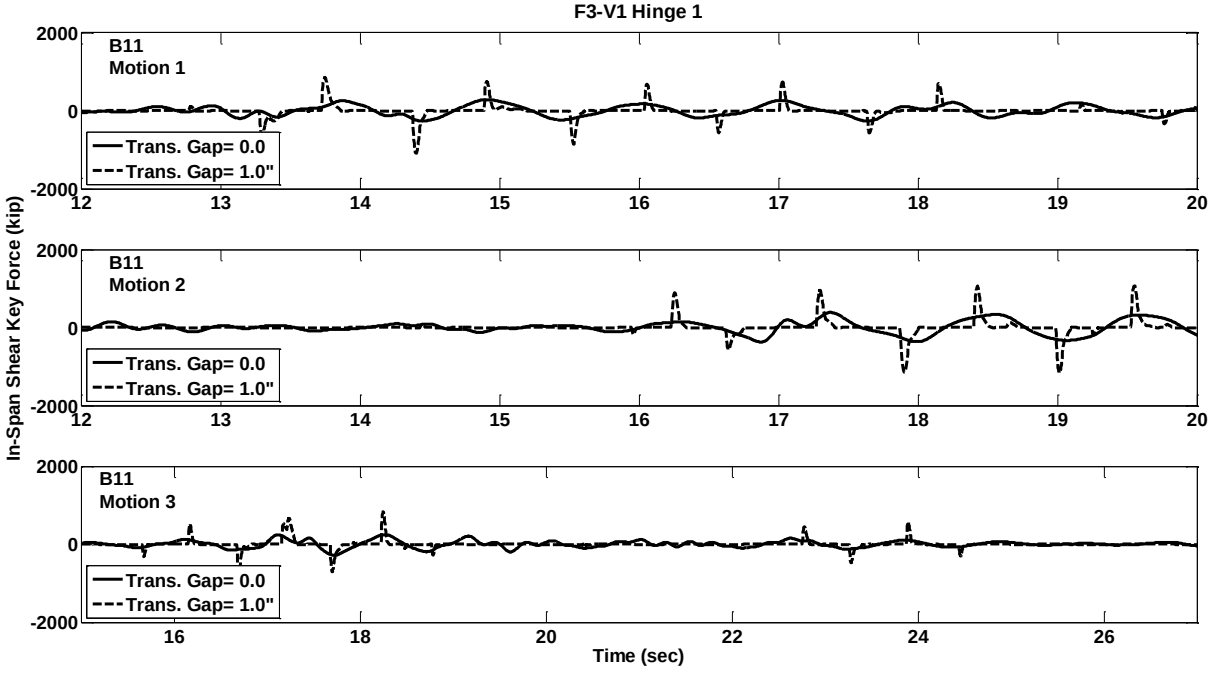

Figure C.392 Shear Key Force Response w/ and w/o Gap, Prototype F3-V1, Hinge-1, Motions B11

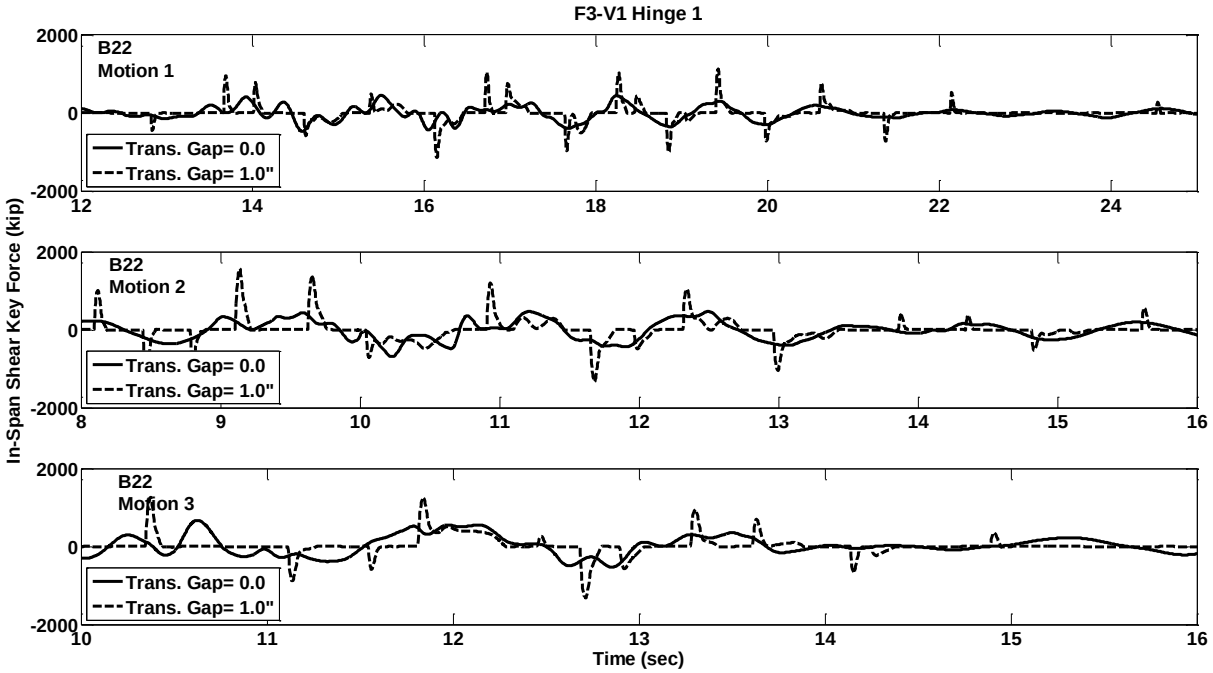

Figure C.393 Shear Key Force Response w/ and w/o Gap, Prototype F3-V1, Hinge-1, Motions B22

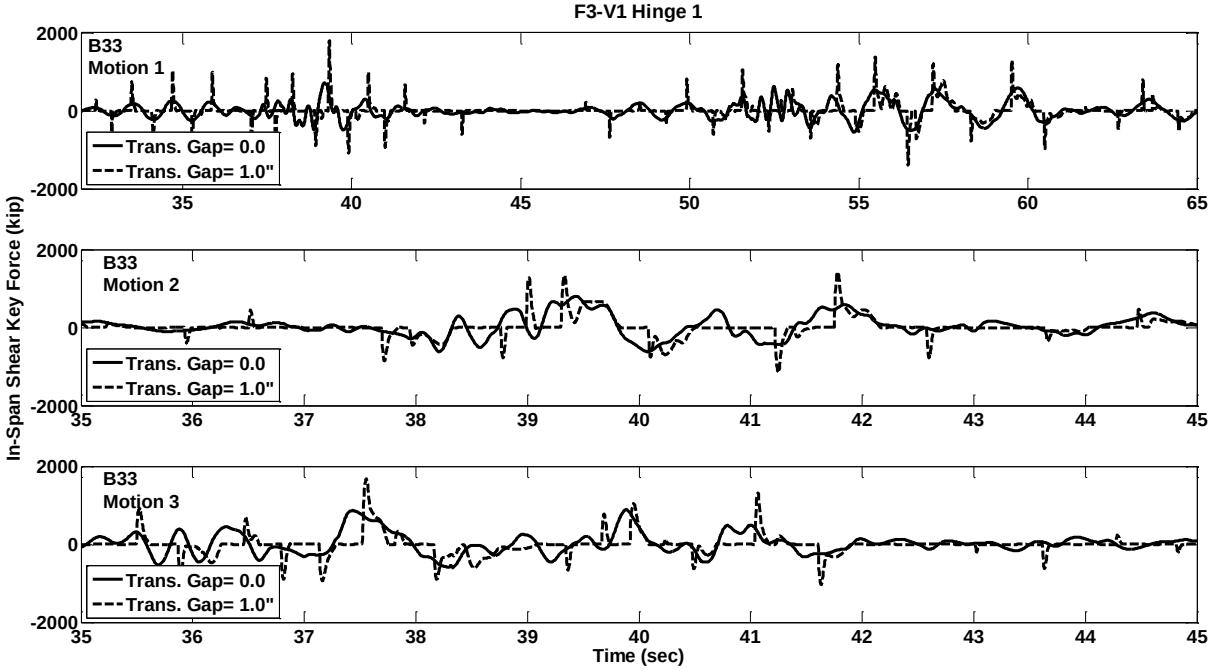

Figure C.394 Shear Key Force Response w/ and w/o Gap, Prototype F3-V1, Hinge-1, Motions B33

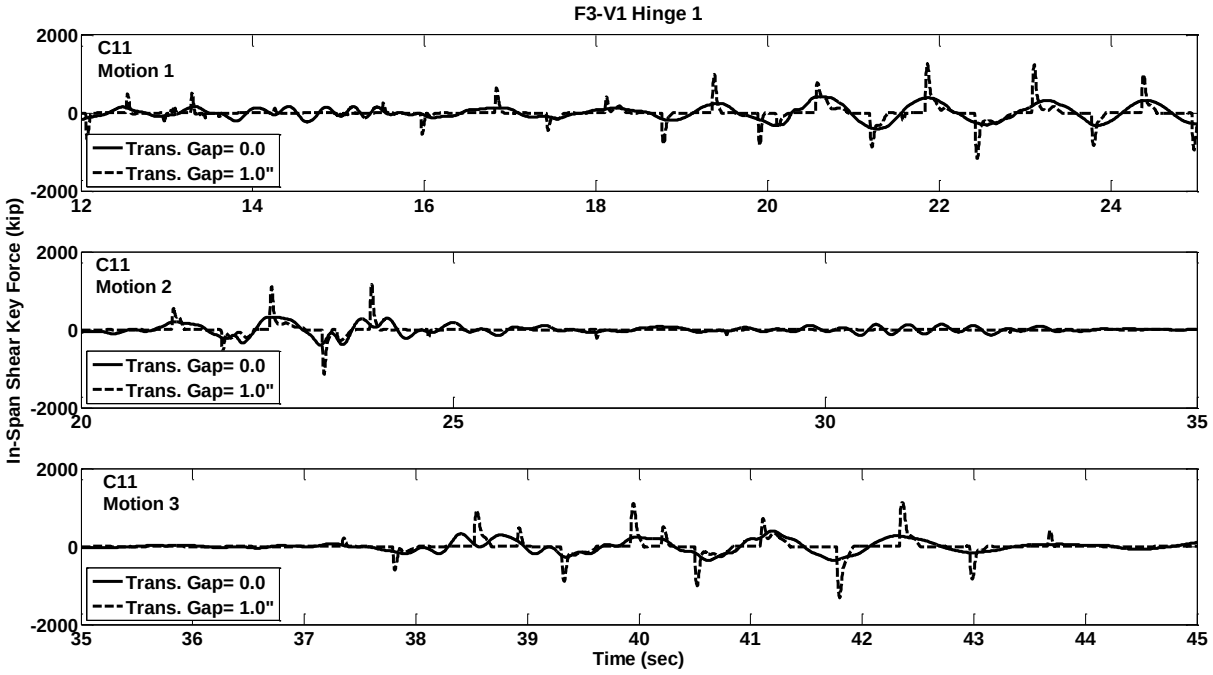

Figure C.395 Shear Key Force Response w/ and w/o Gap, Prototype F3-V1, Hinge-1, Motions C11

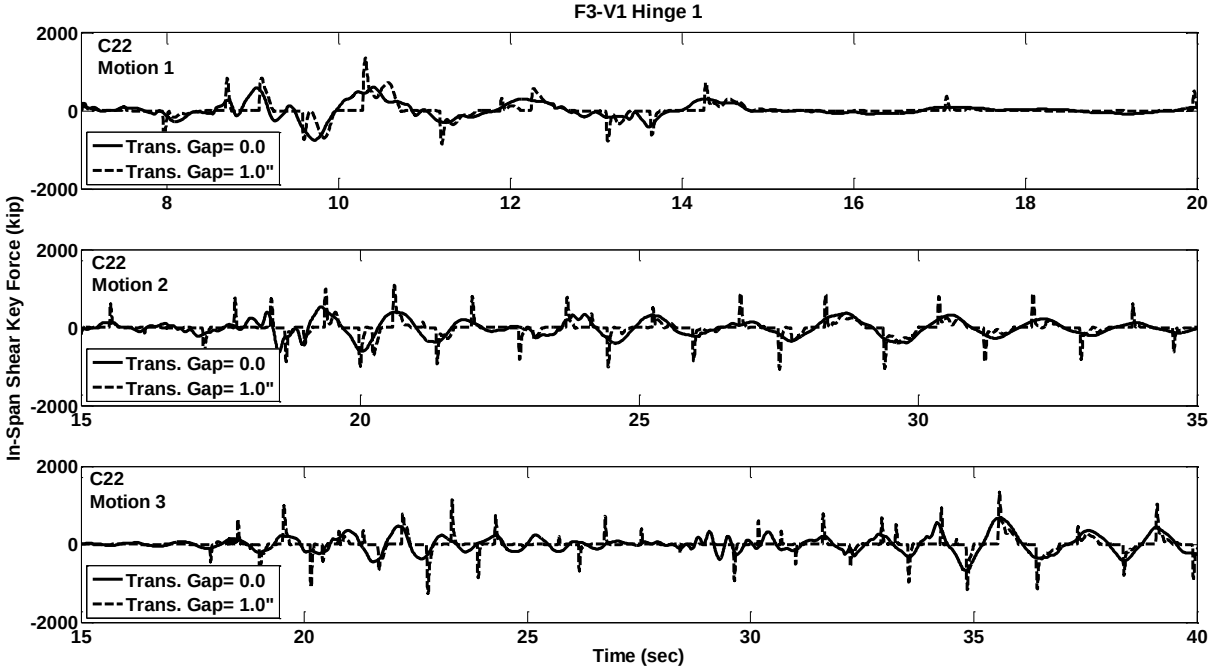

Figure C.396 Shear Key Force Response w/ and w/o Gap, Prototype F3-V1, Hinge-1, Motions C22

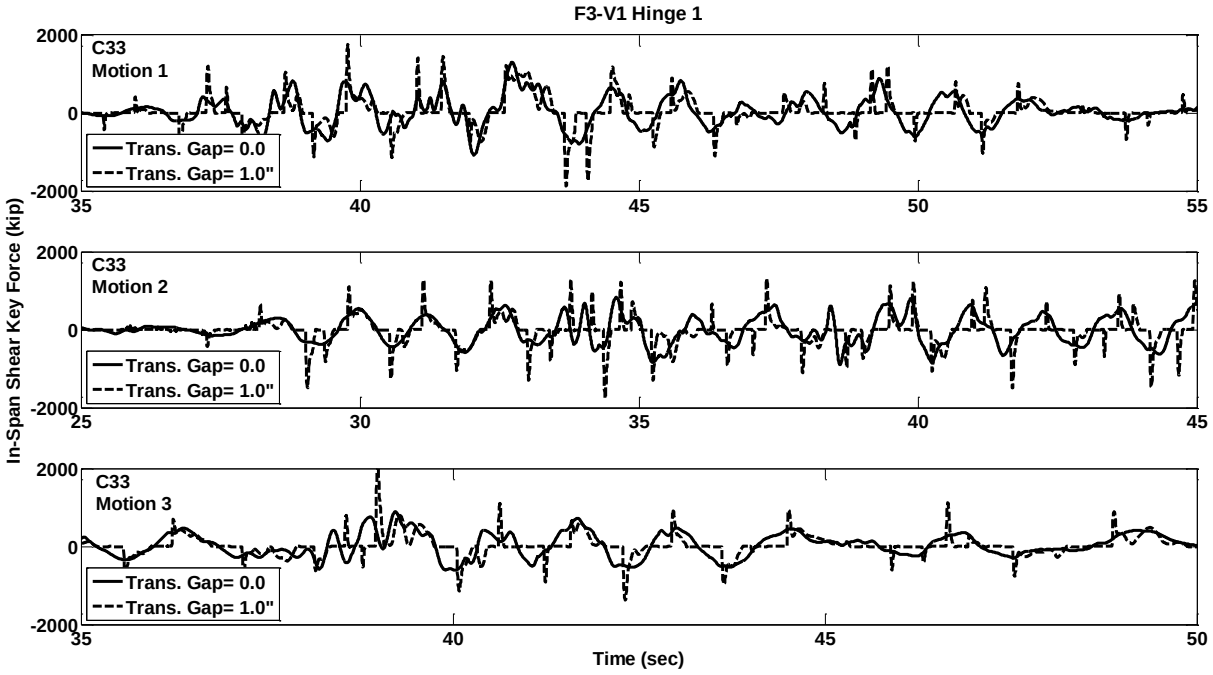

Figure C.397 Shear Key Force Response w/ and w/o Gap, Prototype F3-V1, Hinge-1, Motions C33

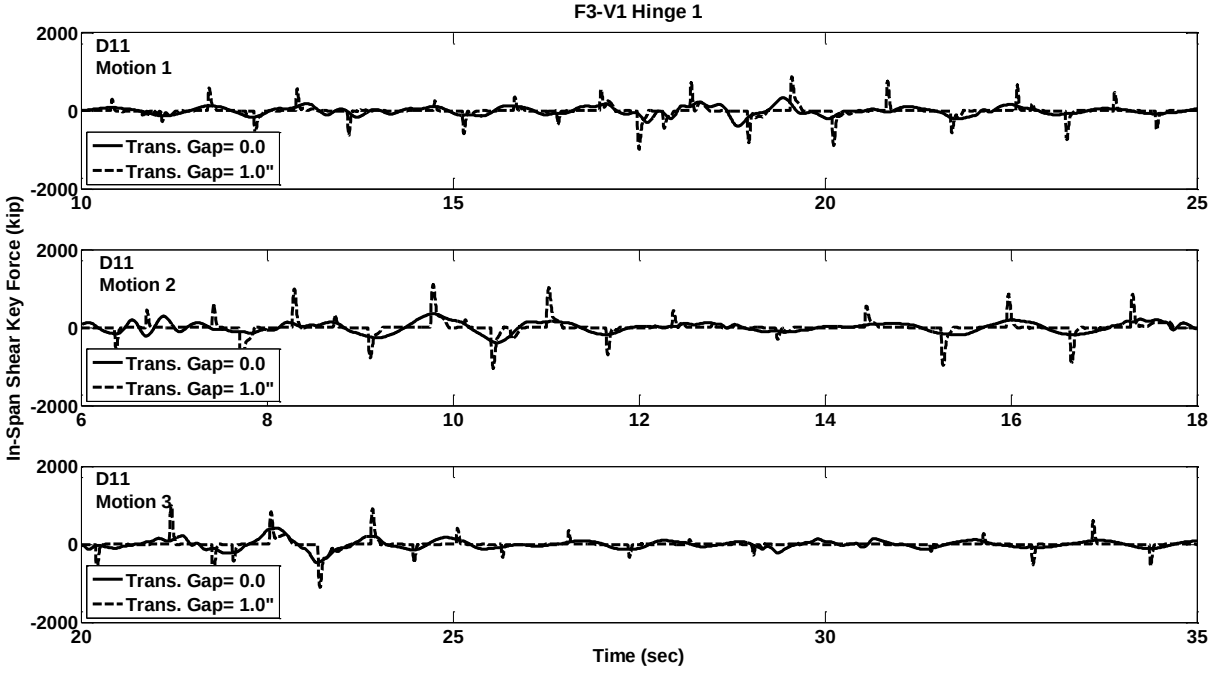

Figure C.398 Shear Key Force Response w/ and w/o Gap, Prototype F3-V1, Hinge-1, Motions D11

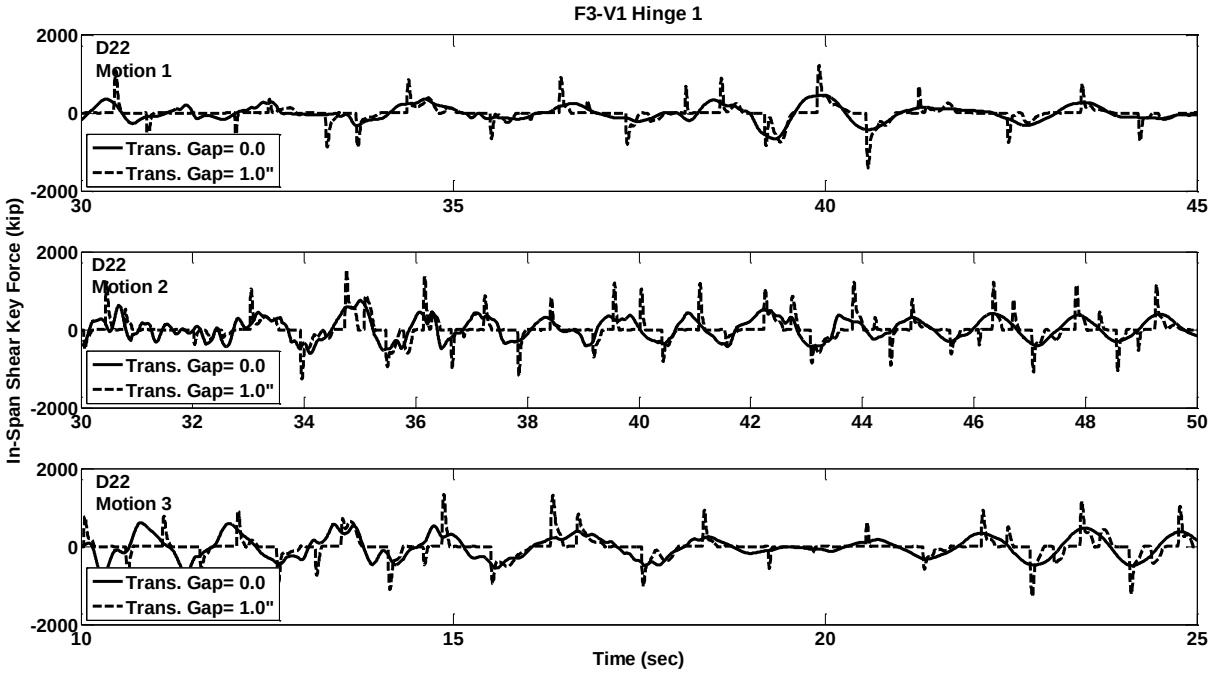

Figure C.399 Shear Key Force Response w/ and w/o Gap, Prototype F3-V1, Hinge-1, Motions D22

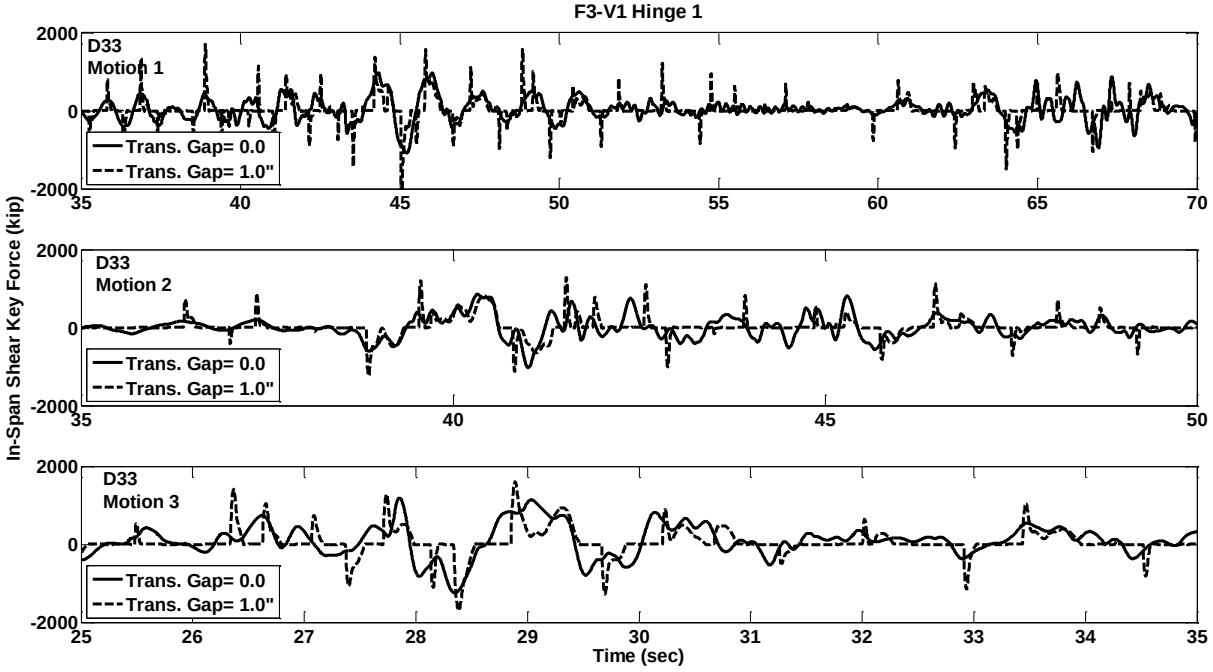

Figure C.400 Shear Key Force Response w/ and w/o Gap, Prototype F3-V1, Hinge-1, Motions D33

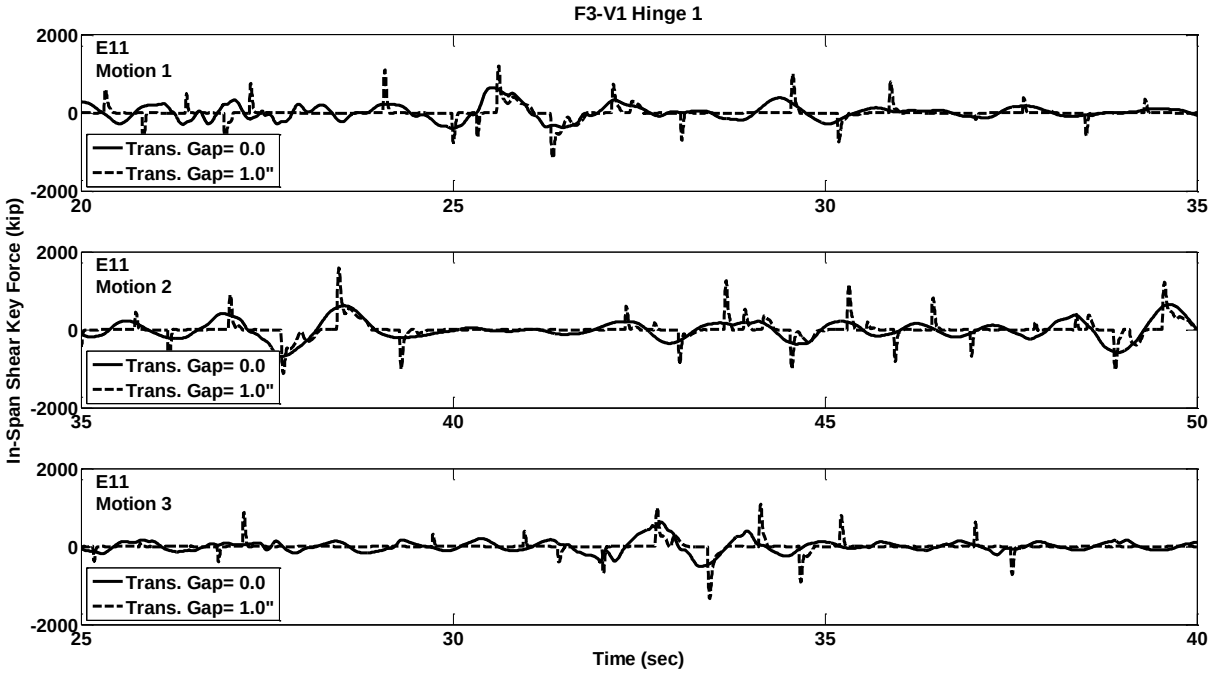

Figure C.401 Shear Key Force Response w/ and w/o Gap, Prototype F3-V1, Hinge-1, Motions E11

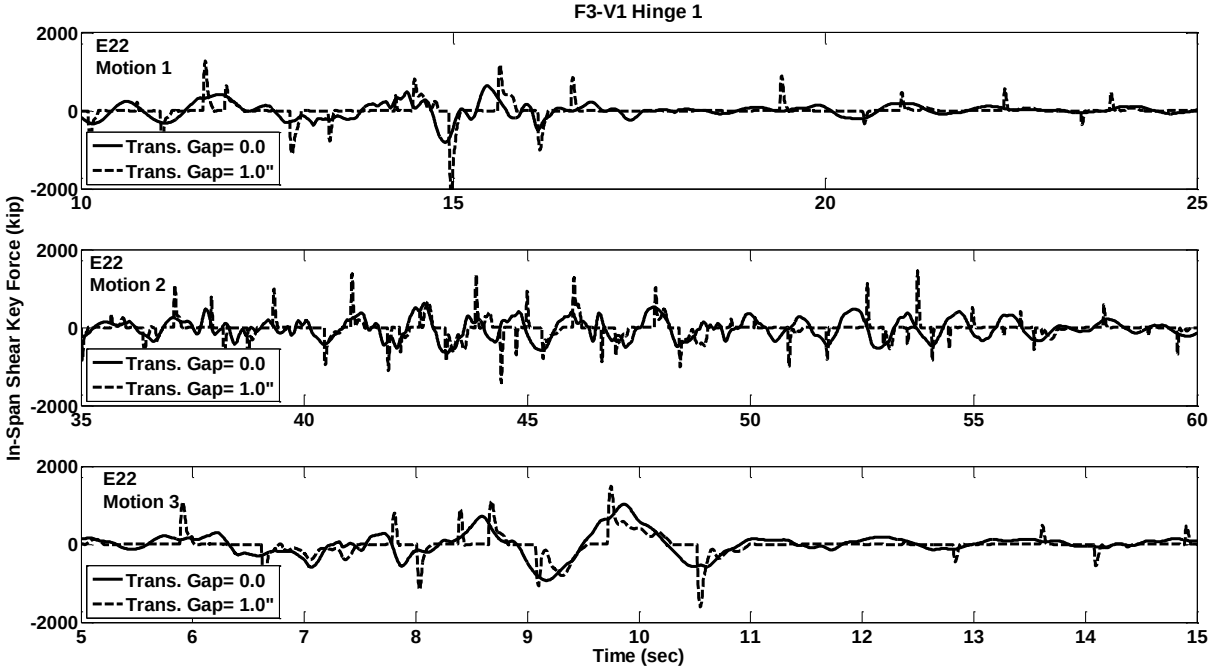

Figure C.402 Shear Key Force Response w/ and w/o Gap, Prototype F3-V1, Hinge-1, Motions E22

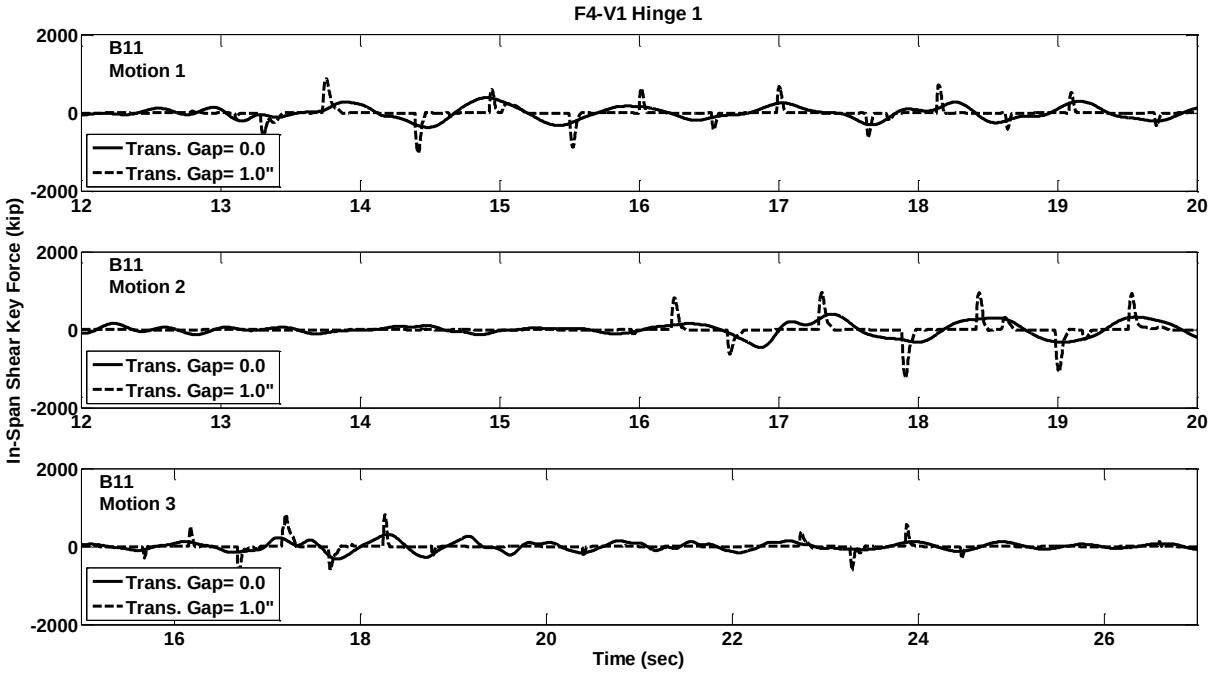

Figure C.403 Shear Key Force Response w/ and w/o Gap, Prototype F4-V1, Hinge-1, Motions B11

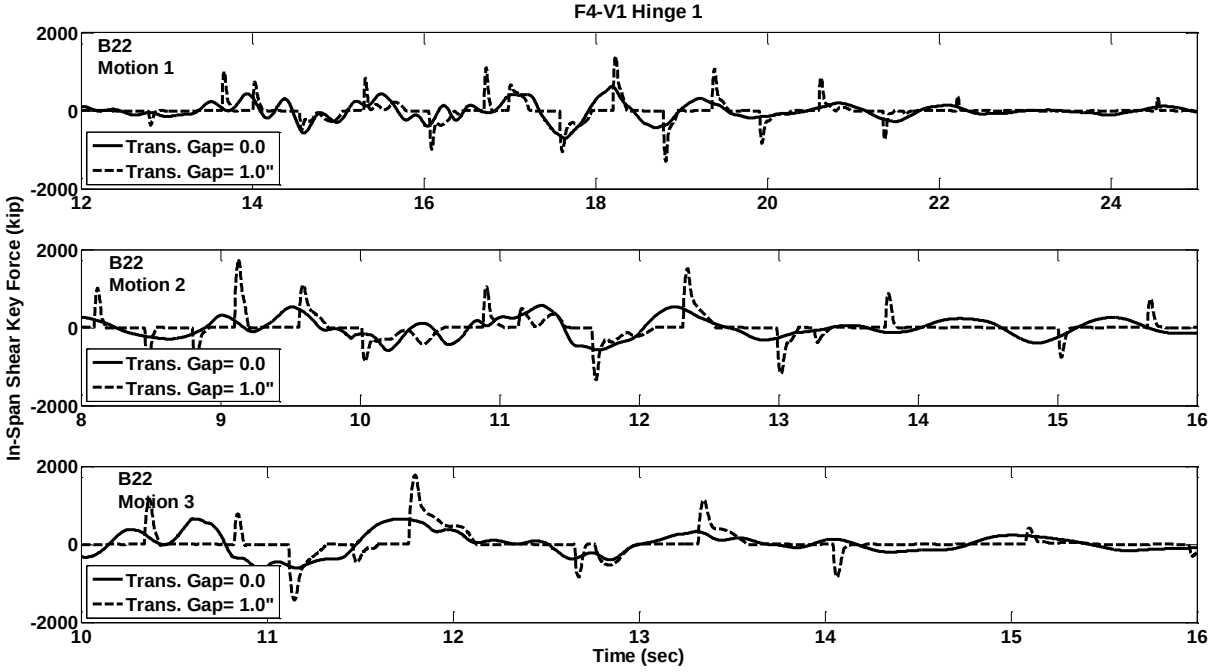

Figure C.404 Shear Key Force Response w/ and w/o Gap, Prototype F4-V1, Hinge-1, Motions B22

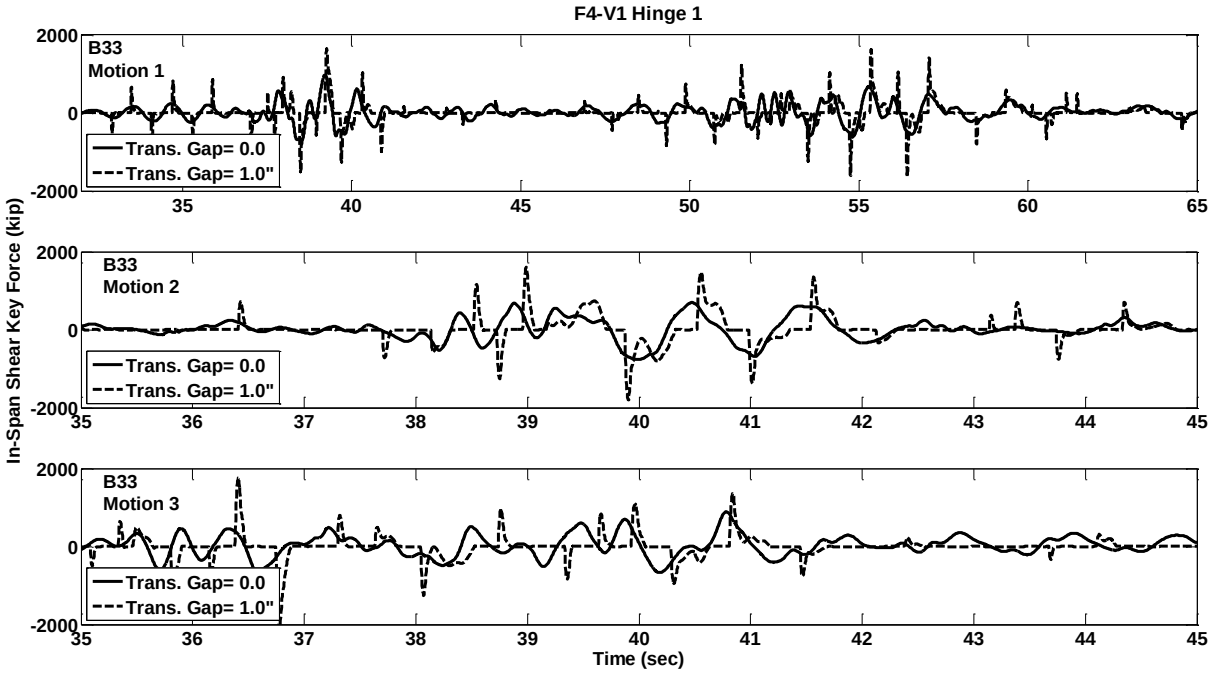

Figure C.405 Shear Key Force Response w/ and w/o Gap, Prototype F4-V1, Hinge-1, Motions B33

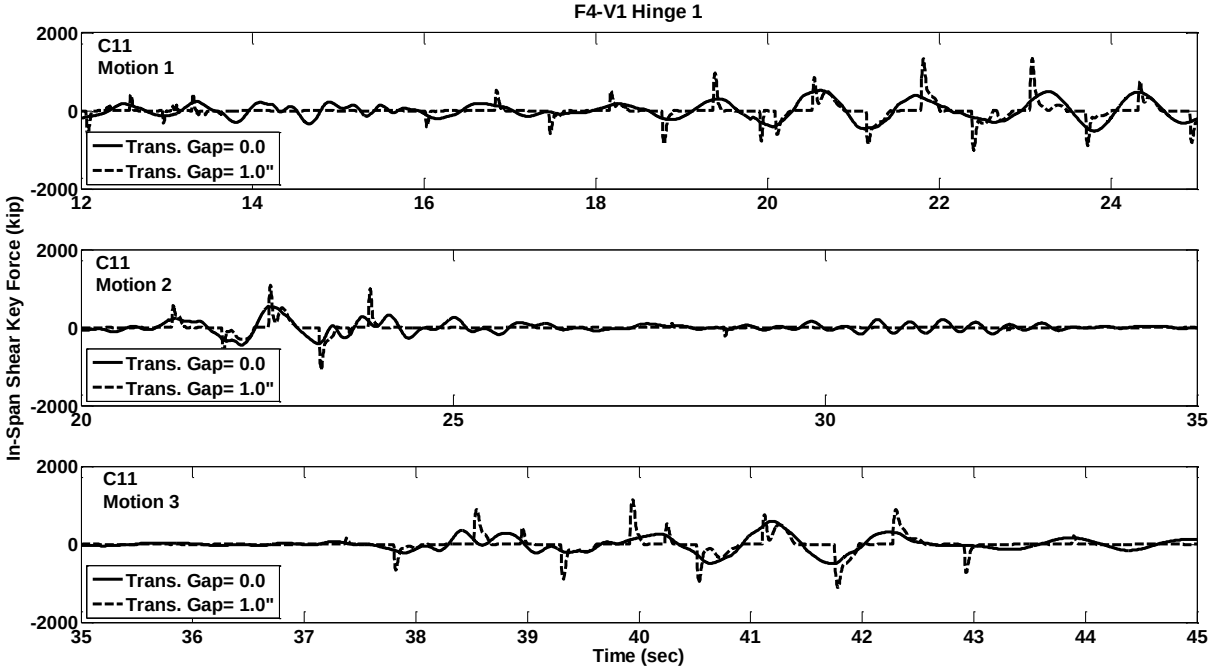

Figure C.406 Shear Key Force Response w/ and w/o Gap, Prototype F4-V1, Hinge-1, Motions C11

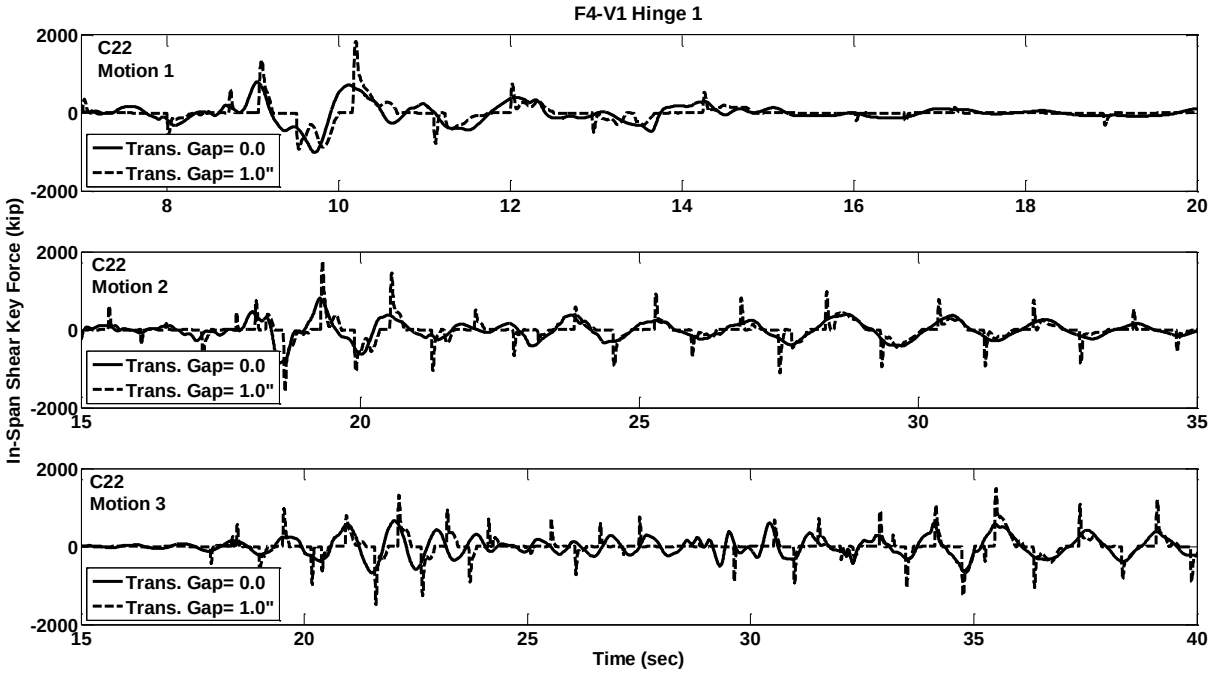

Figure C.407 Shear Key Force Response w/ and w/o Gap, Prototype F4-V1, Hinge-1, Motions C22

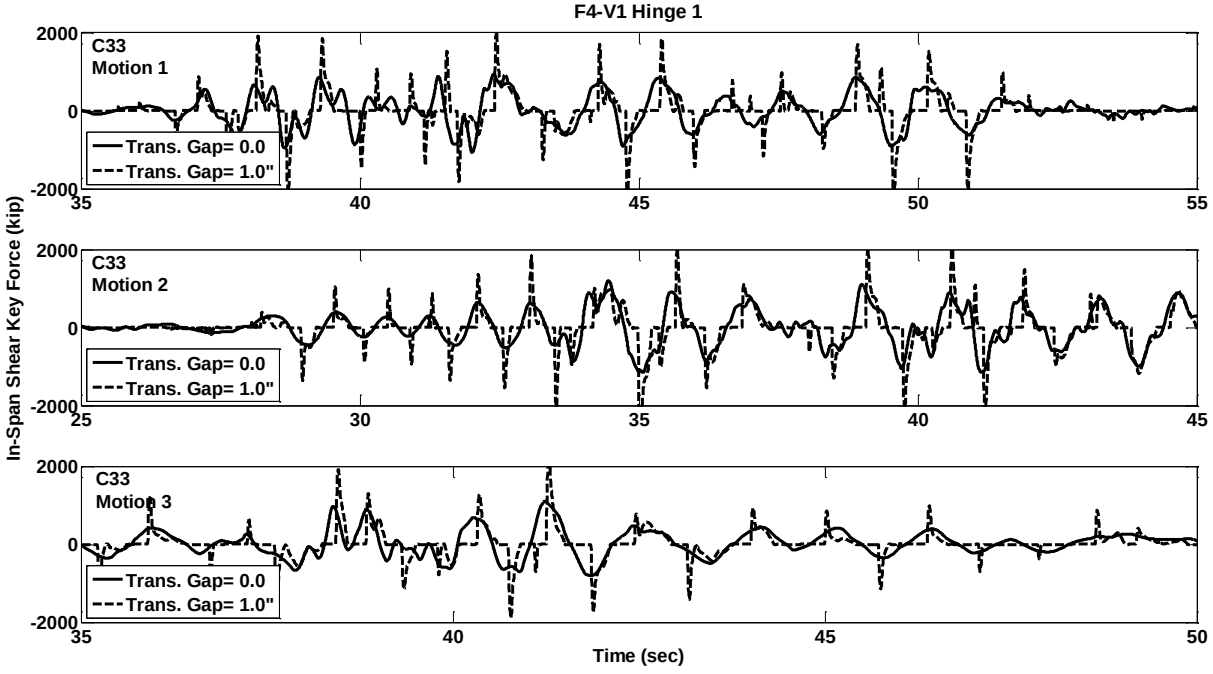

Figure C.408 Shear Key Force Response w/ and w/o Gap, Prototype F4-V1, Hinge-1, Motions C33

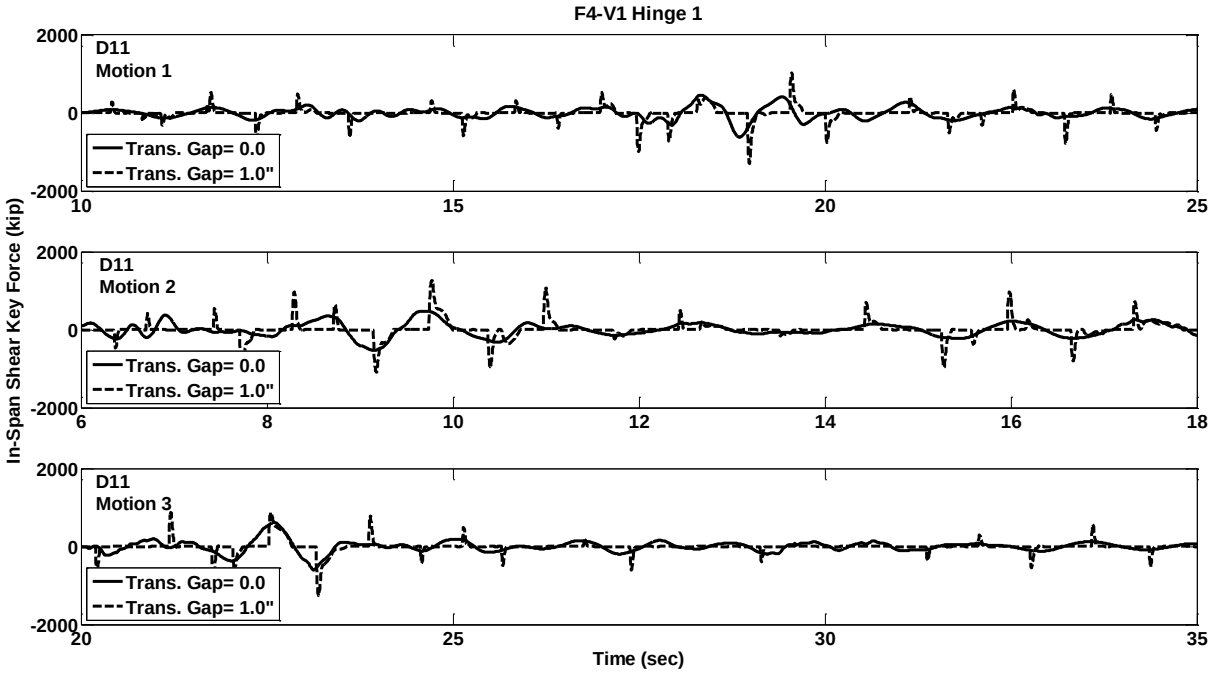

Figure C.409 Shear Key Force Response w/ and w/o Gap, Prototype F4-V1, Hinge-1, Motions D11

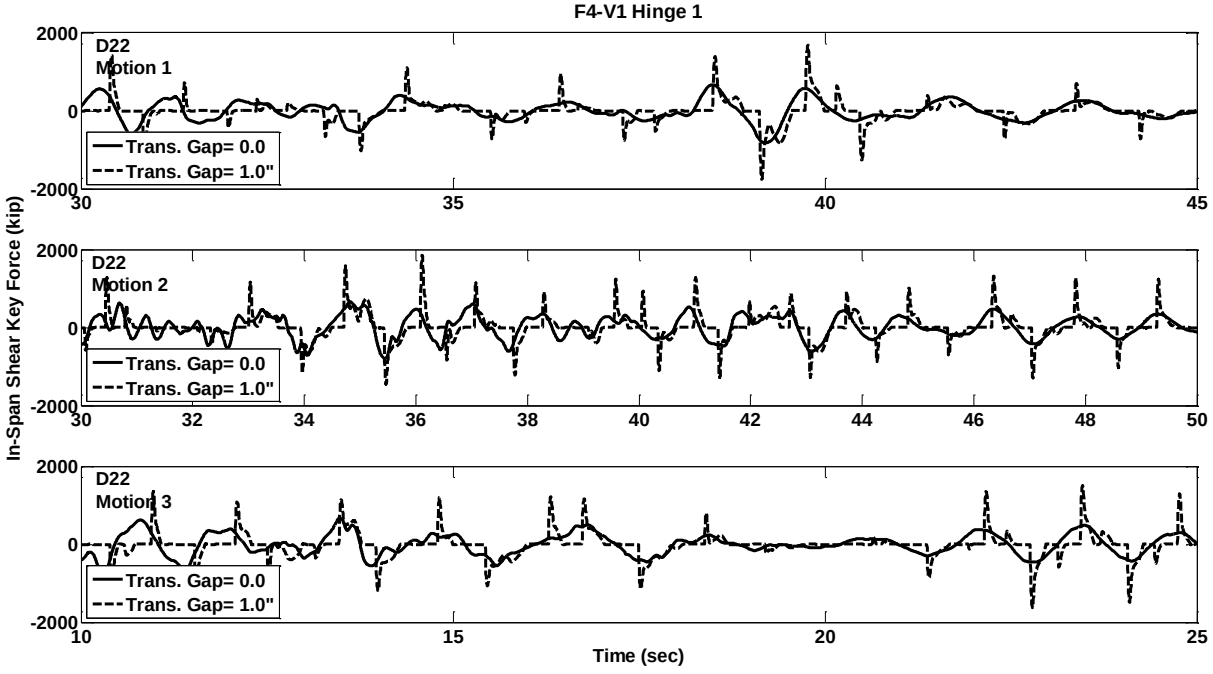

Figure C.410 Shear Key Force Response w/ and w/o Gap, Prototype F4-V1, Hinge-1, Motions D22

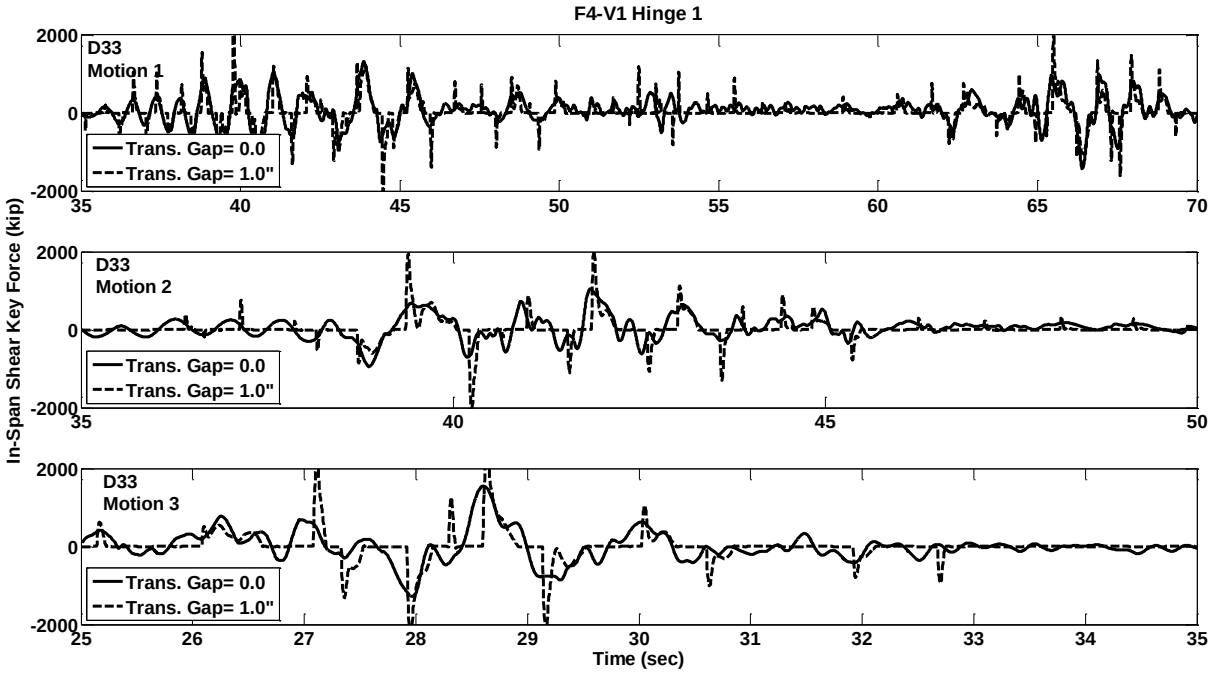

Figure C.411 Shear Key Force Response w/ and w/o Gap, Prototype F4-V1, Hinge-1, Motions D33

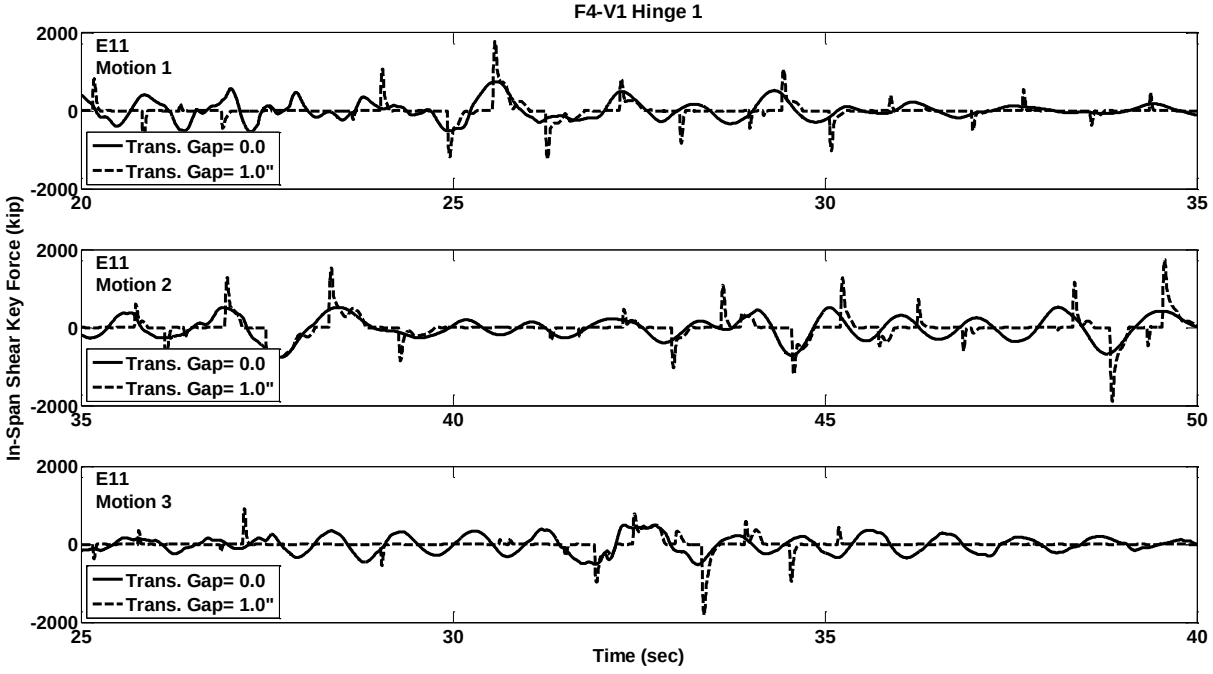

Figure C.412 Shear Key Force Response w/ and w/o Gap, Prototype F4-V1, Hinge-1, Motions E11

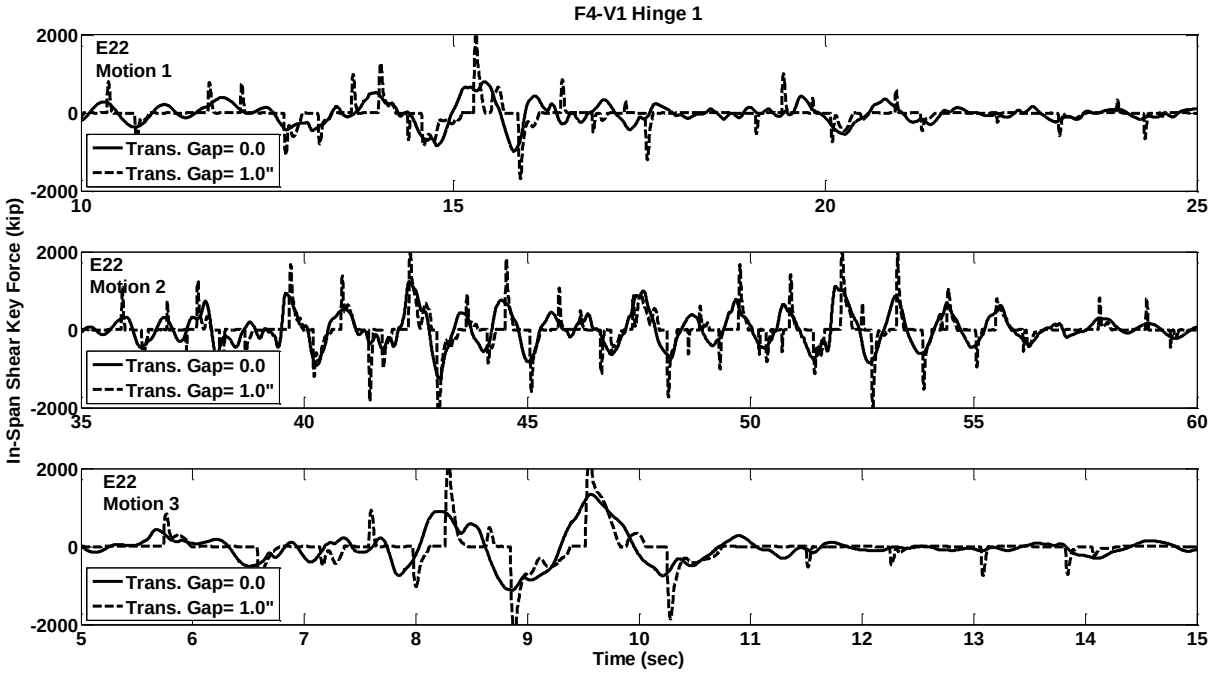

Figure C.413 Shear Key Force Response w/ and w/o Gap, Prototype F4-V1, Hinge-1, Motions E22

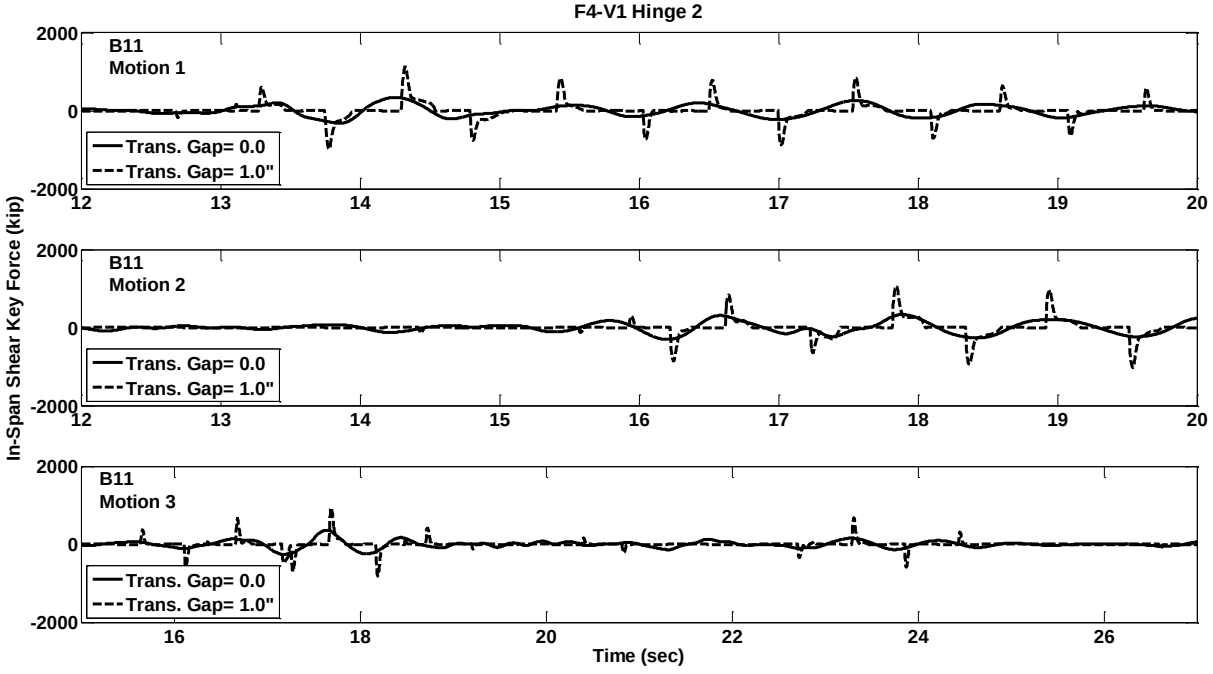

Figure C.414 Shear Key Force Response w/ and w/o Gap, Prototype F4-V1, Hinge-2, Motions B11

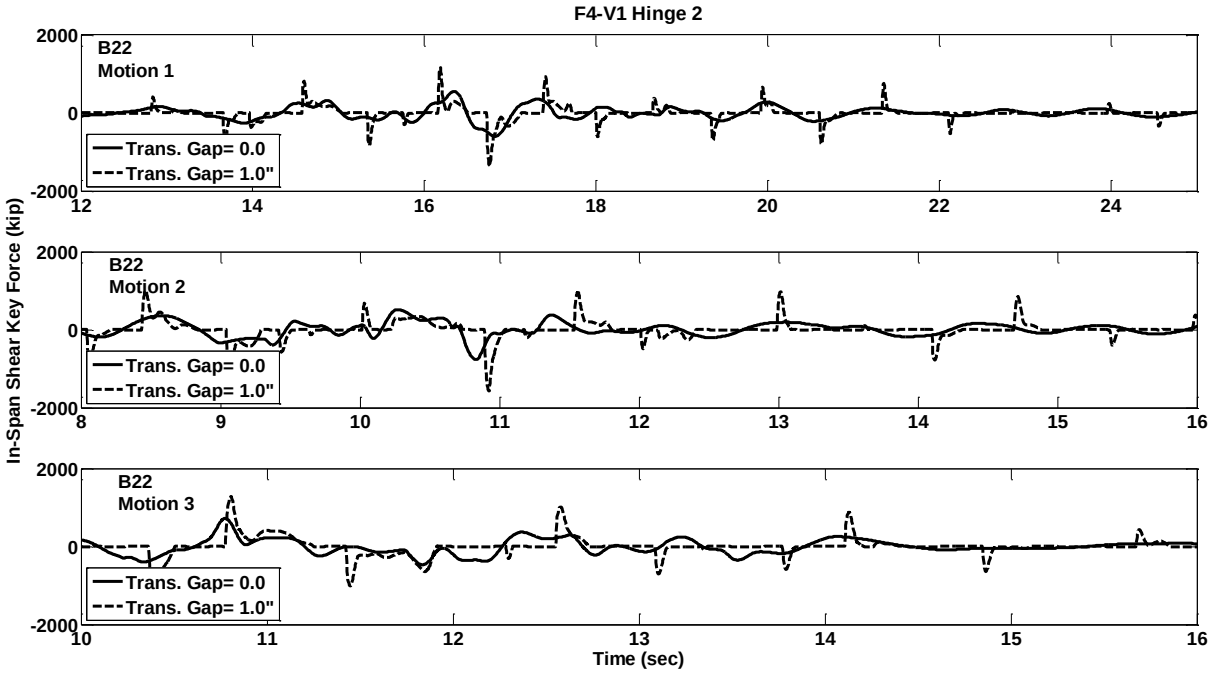

Figure C.415 Shear Key Force Response w/ and w/o Gap, Prototype F4-V1, Hinge-2, Motions B22

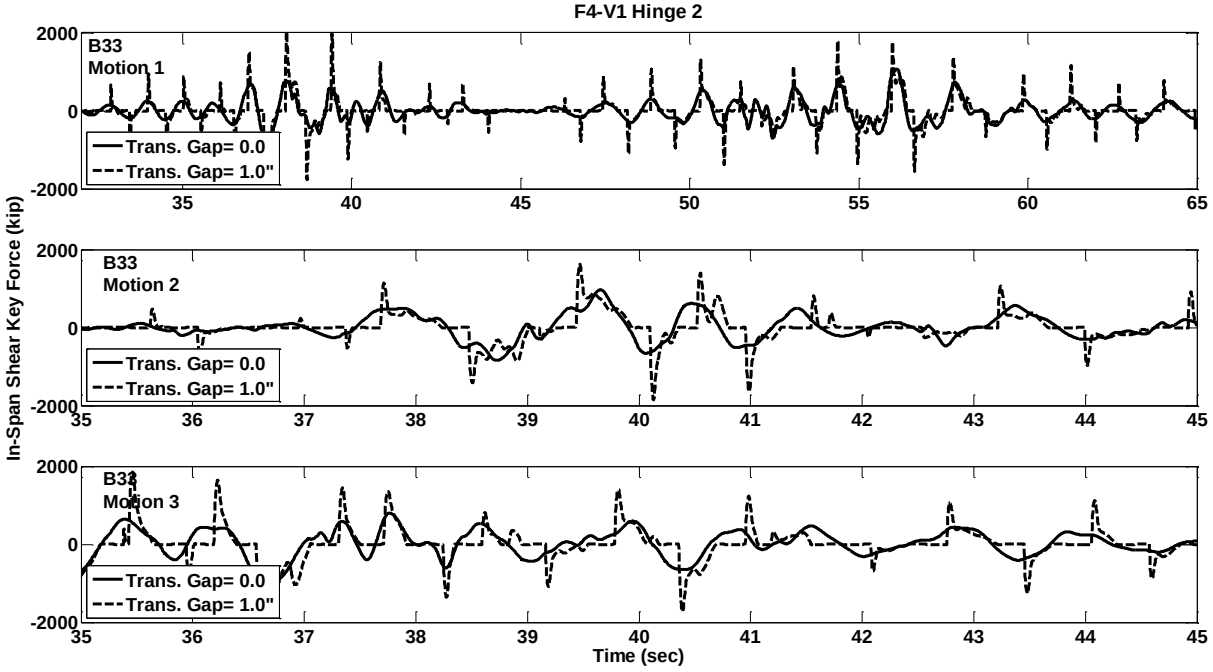

Figure C.416 Shear Key Force Response w/ and w/o Gap, Prototype F4-V1, Hinge-2, Motions B33

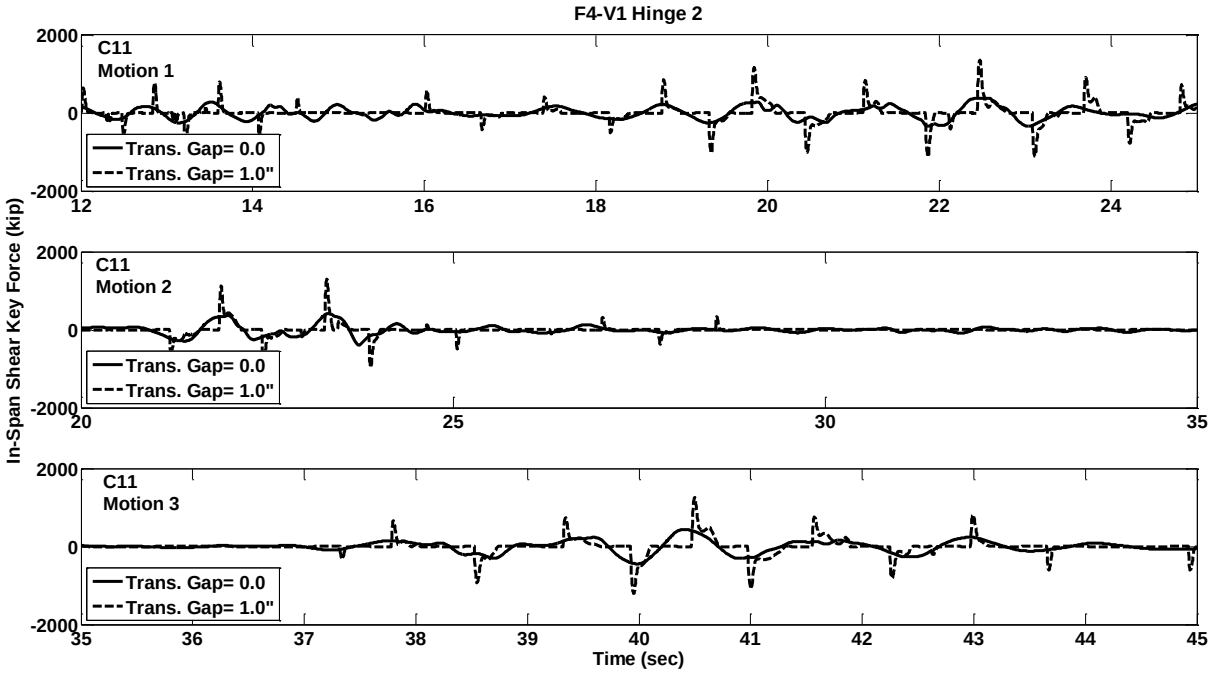

Figure C.417 Shear Key Force Response w/ and w/o Gap, Prototype F4-V1, Hinge-2, Motions C11

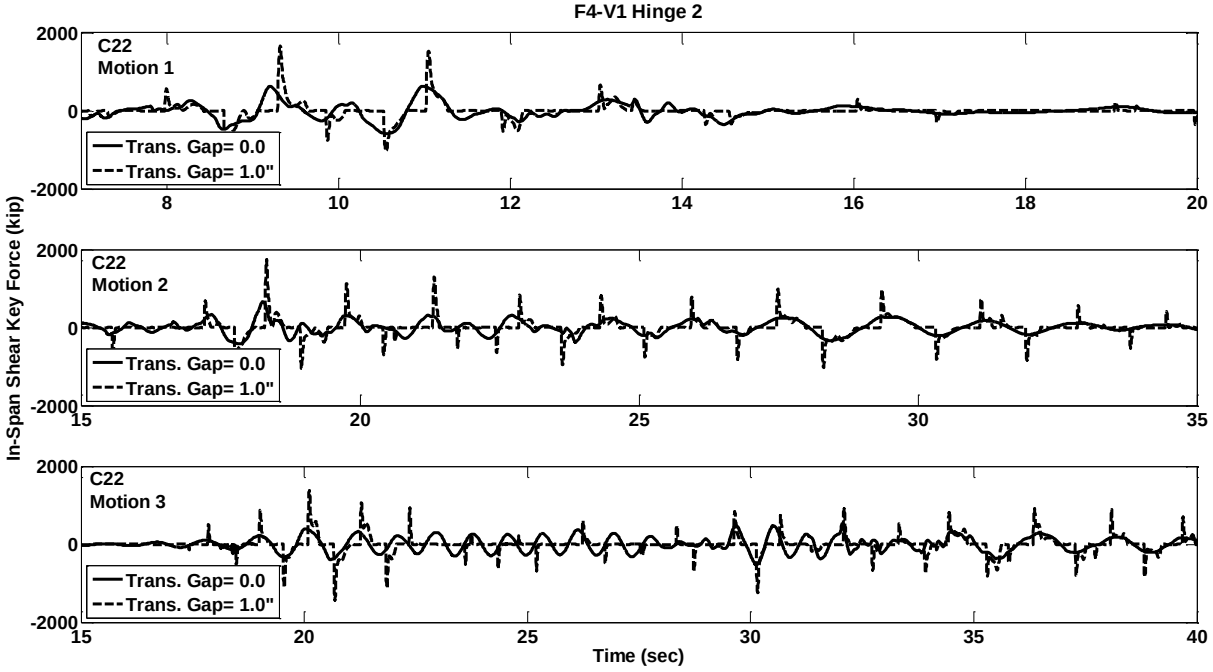

Figure C.418 Shear Key Force Response w/ and w/o Gap, Prototype F4-V1, Hinge-2, Motions C22

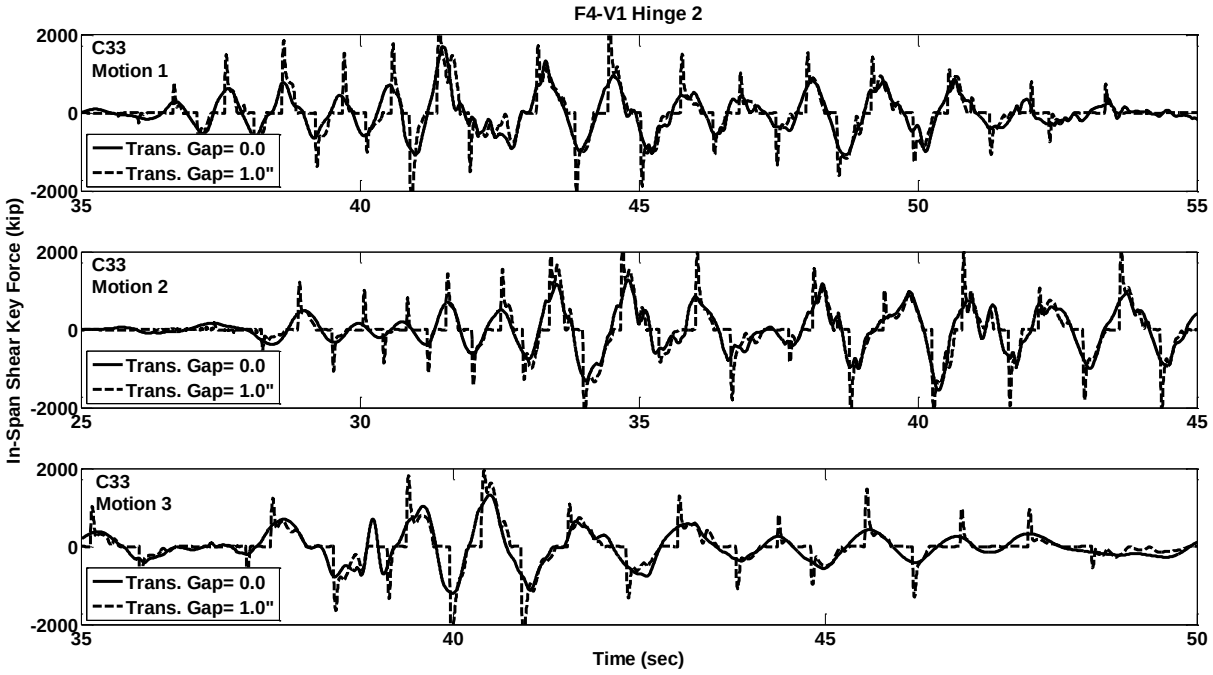

Figure C.419 Shear Key Force Response w/ and w/o Gap, Prototype F4-V1, Hinge-2, Motions C33

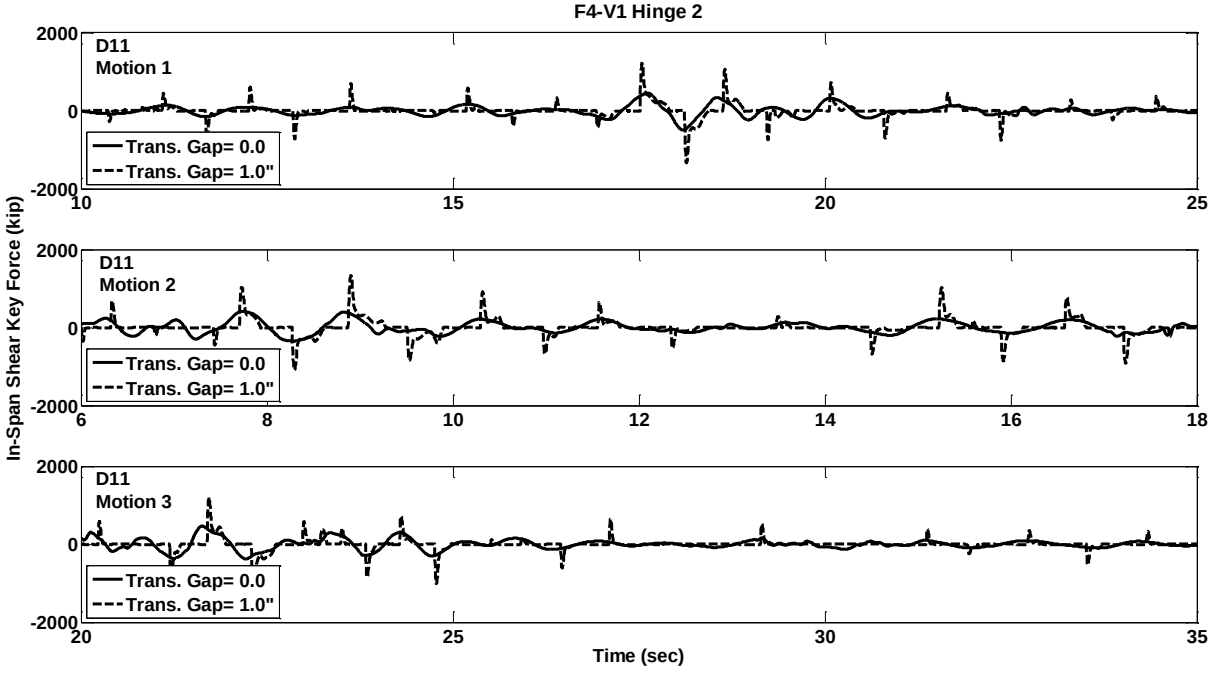

Figure C.420 Shear Key Force Response w/ and w/o Gap, Prototype F4-V1, Hinge-2, Motions D11

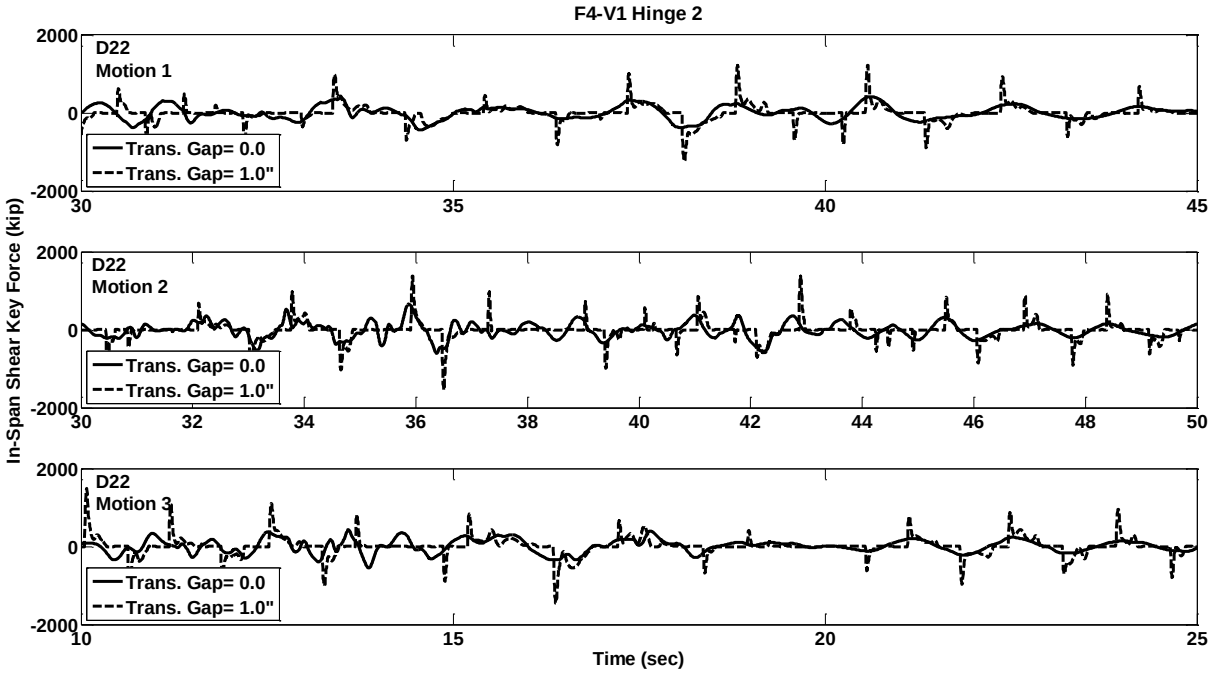

Figure C.421 Shear Key Force Response w/ and w/o Gap, Prototype F4-V1, Hinge-2, Motions D22

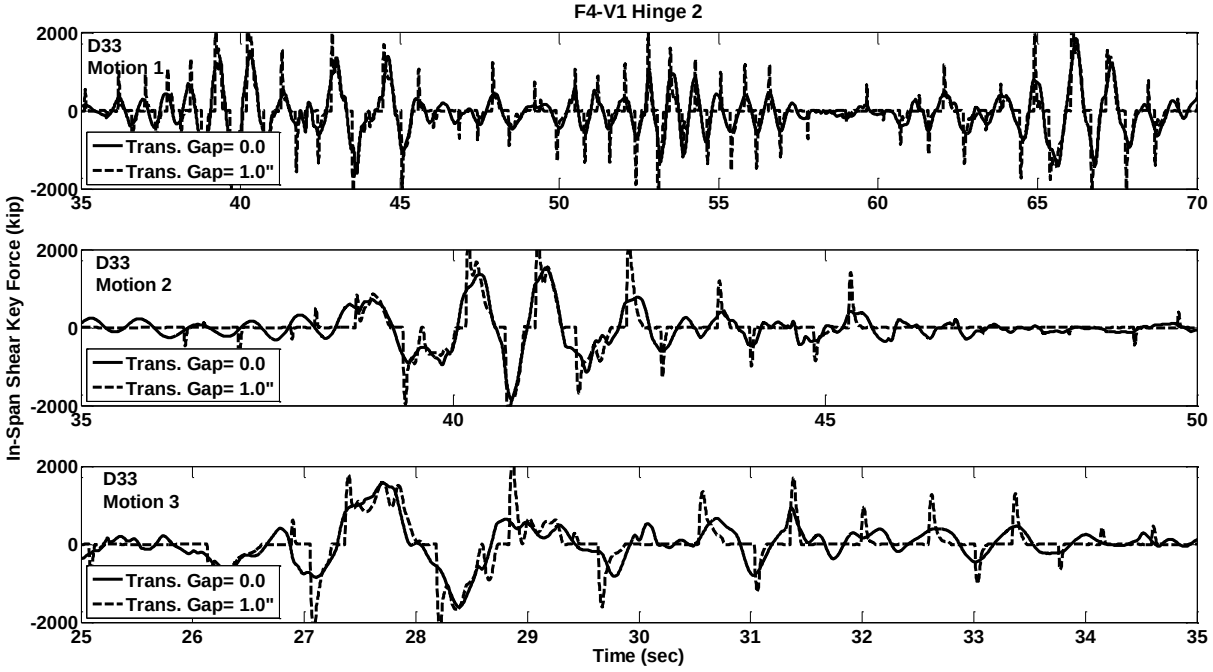

Figure C.422 Shear Key Force Response w/ and w/o Gap, Prototype F4-V1, Hinge-2, Motions D33

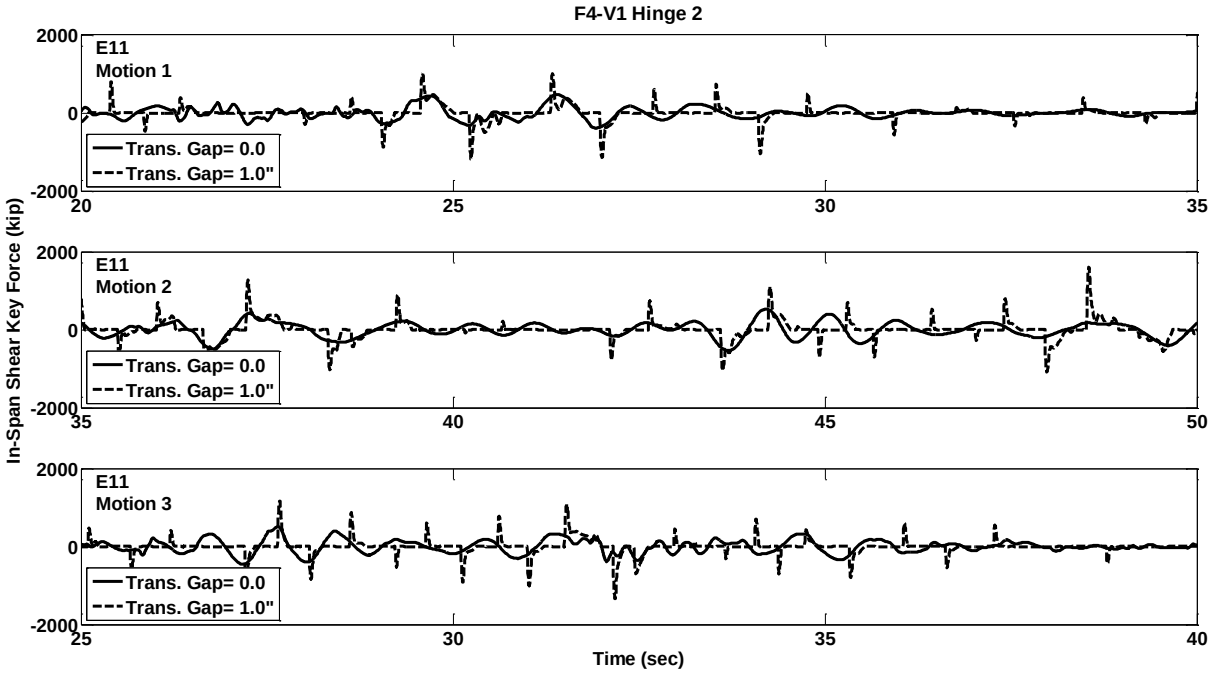

Figure C.423 Shear Key Force Response w/ and w/o Gap, Prototype F4-V1, Hinge-2, Motions E11

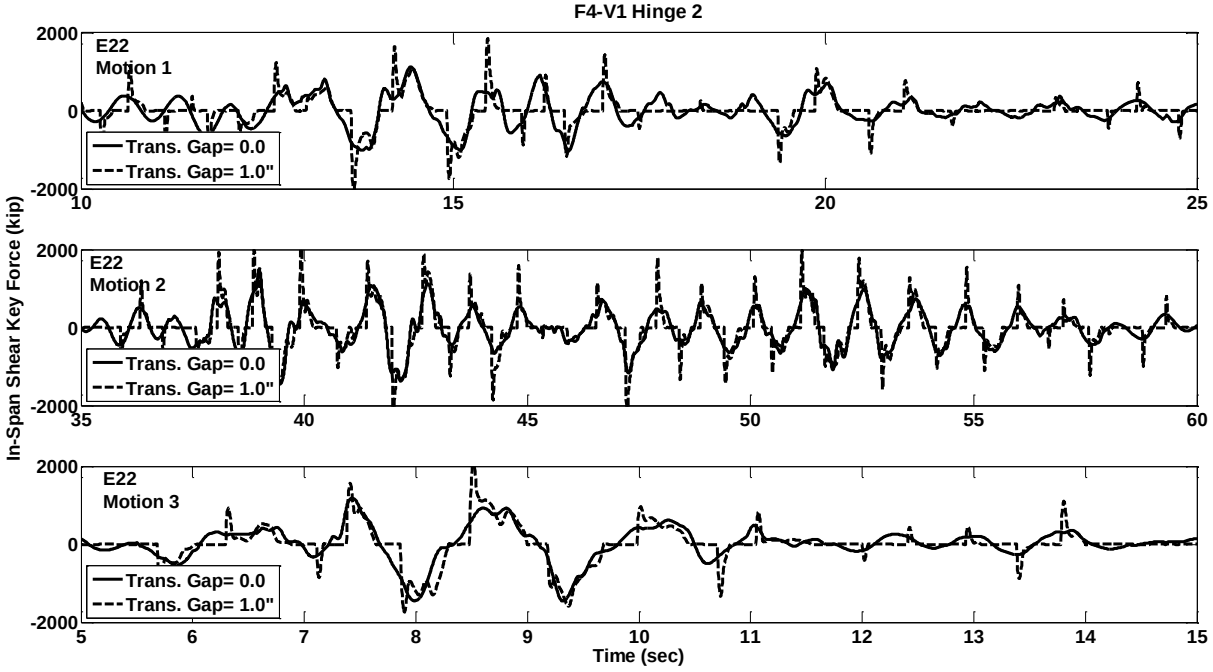

Figure C.424 Shear Key Force Response w/ and w/o Gap, Prototype F4-V1, Hinge-2, Motions E22

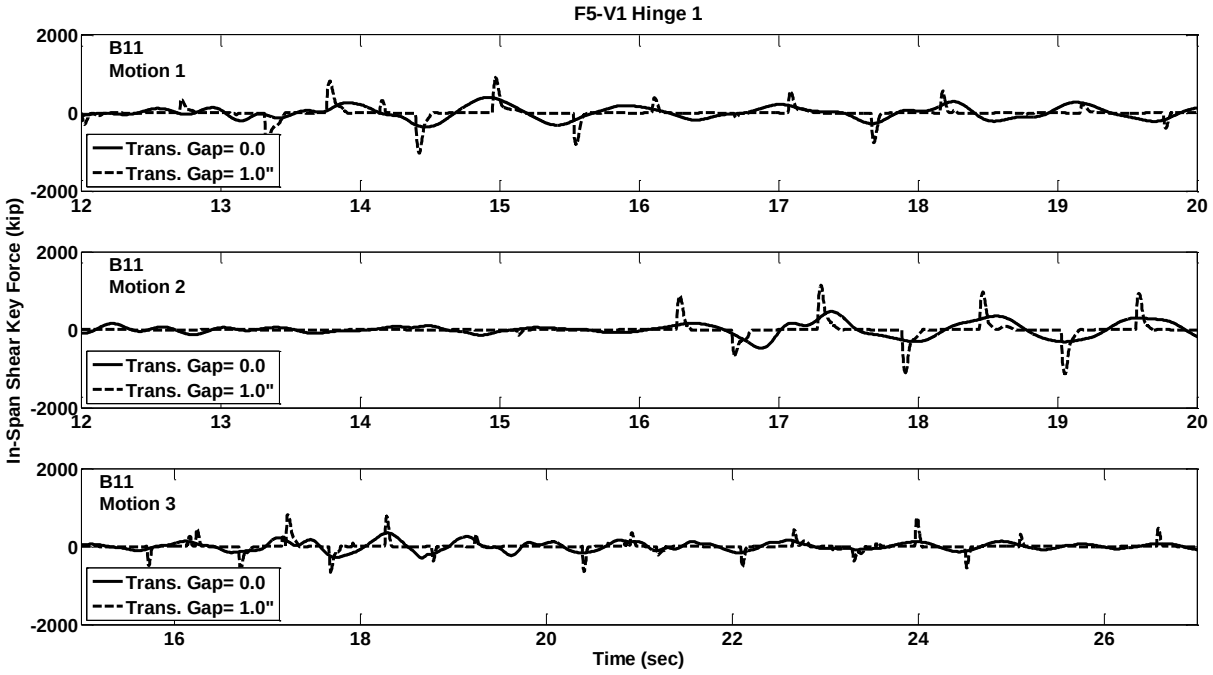

Figure C.425 Shear Key Force Response w/ and w/o Gap, Prototype F5-V1, Hinge-1, Motions B11

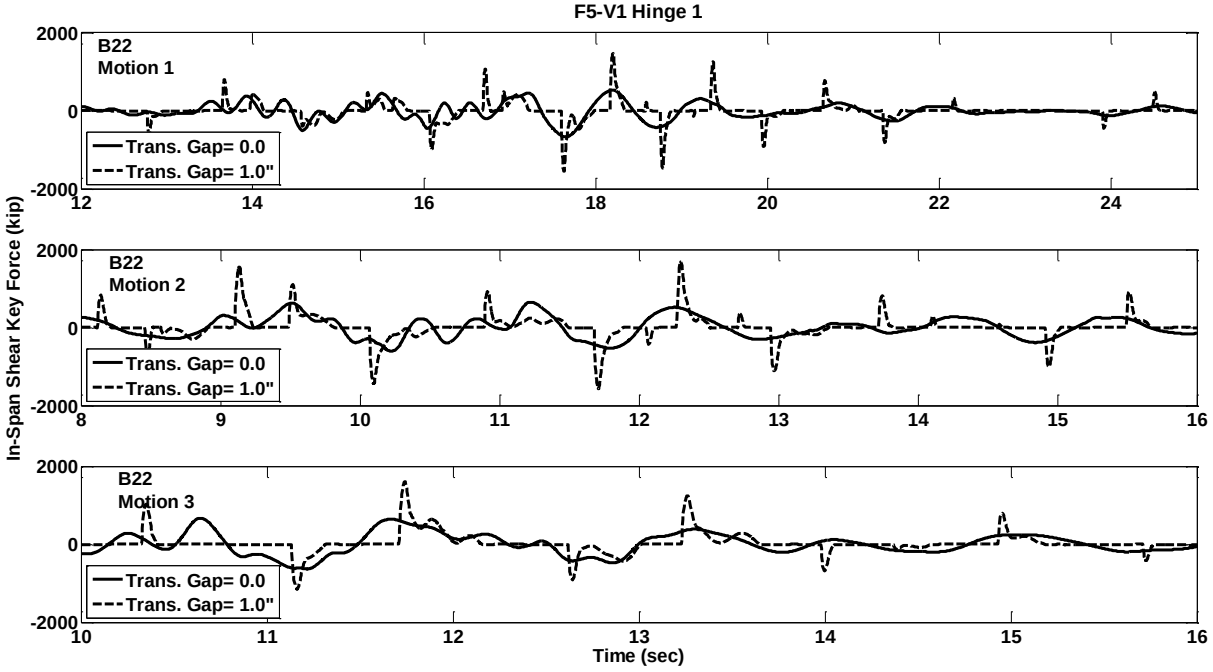

Figure C.426 Shear Key Force Response w/ and w/o Gap, Prototype F5-V1, Hinge-1, Motions B22

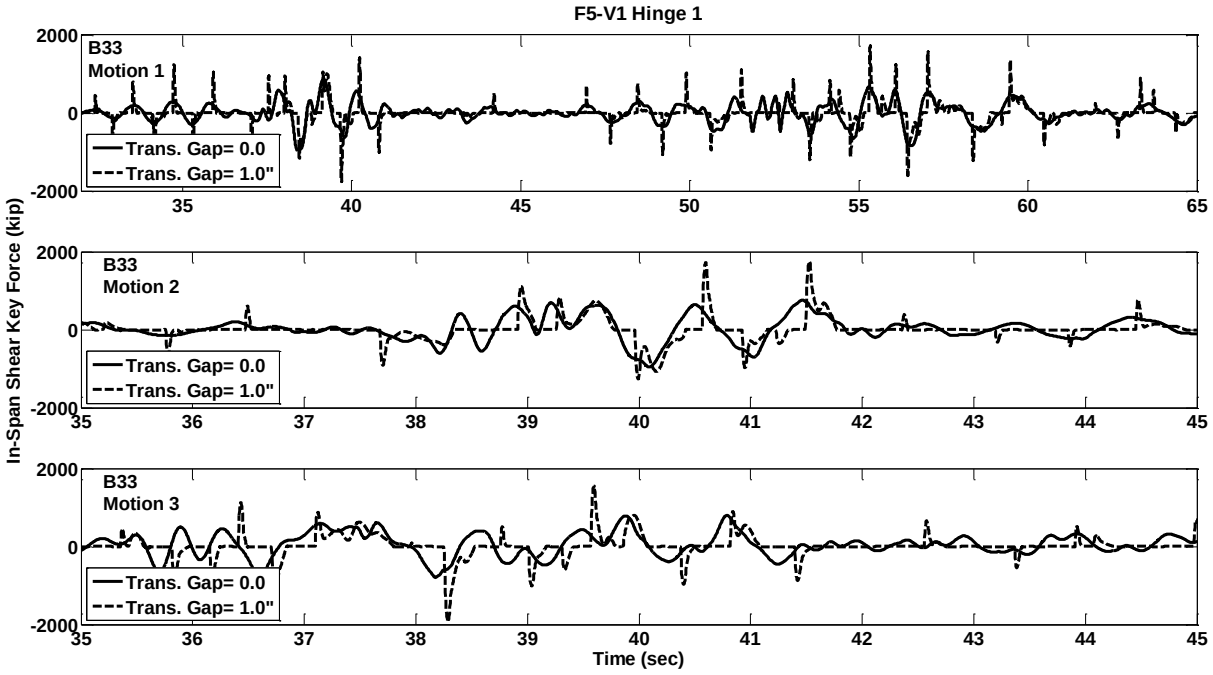

Figure C.427 Shear Key Force Response w/ and w/o Gap, Prototype F5-V1, Hinge-1, Motions B33

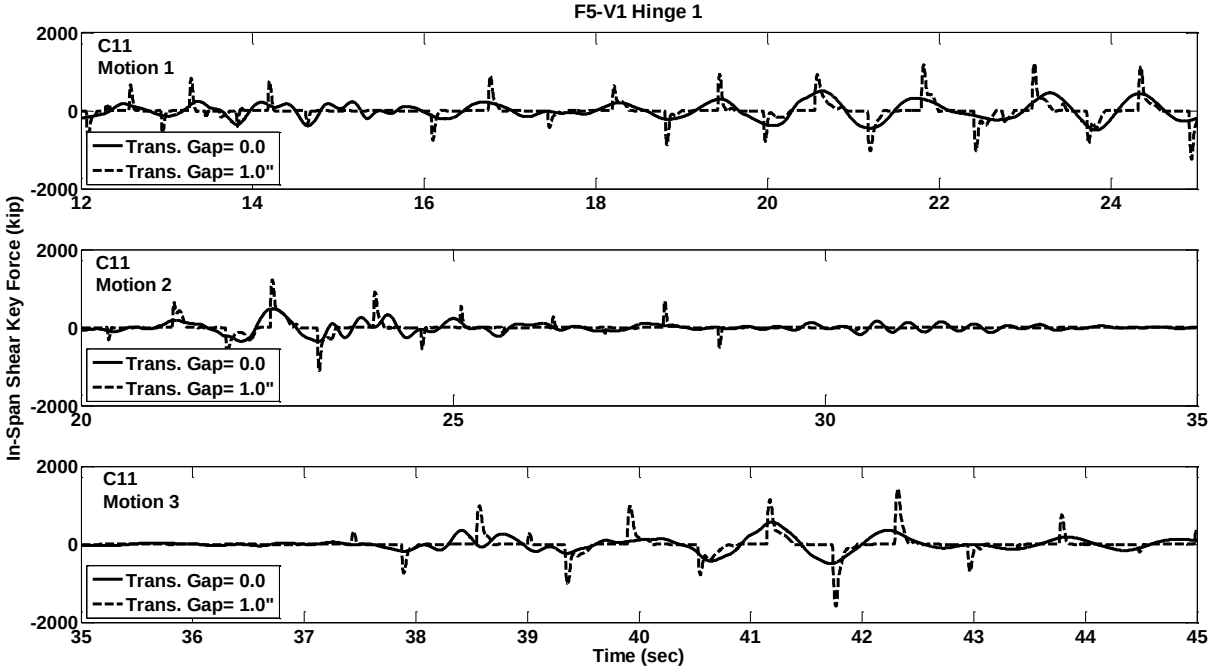

Figure C.428 Shear Key Force Response w/ and w/o Gap, Prototype F5-V1, Hinge-1, Motions C11

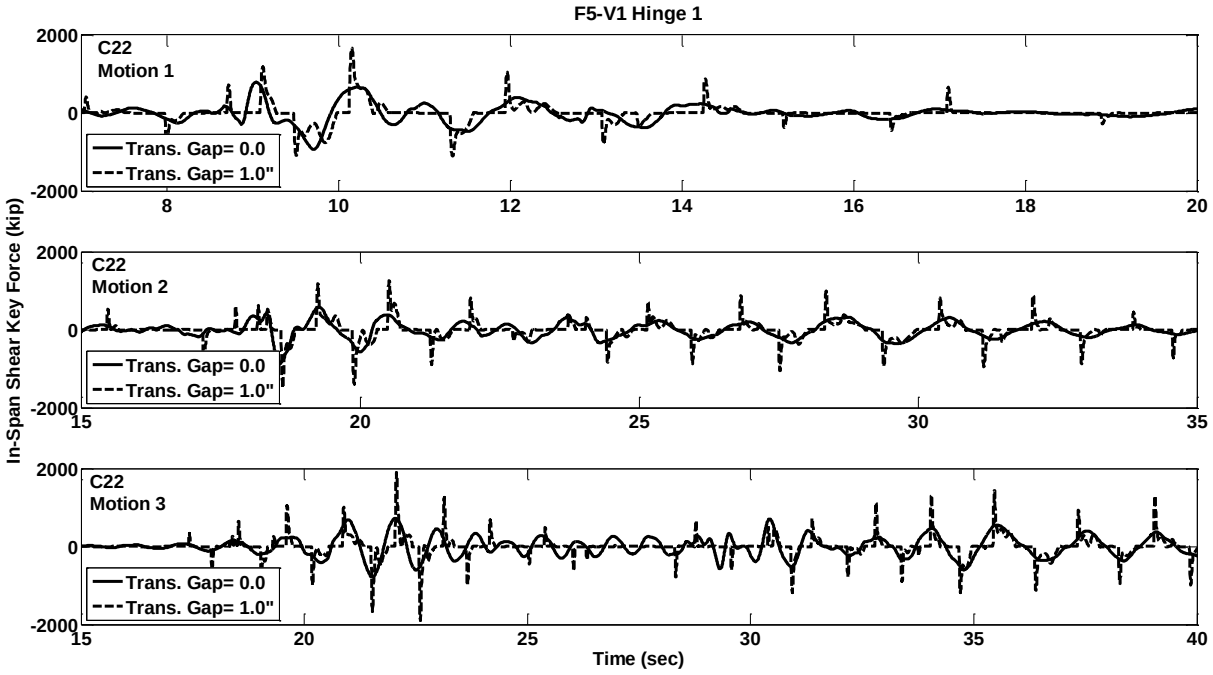

Figure C.429 Shear Key Force Response w/ and w/o Gap, Prototype F5-V1, Hinge-1, Motions C22

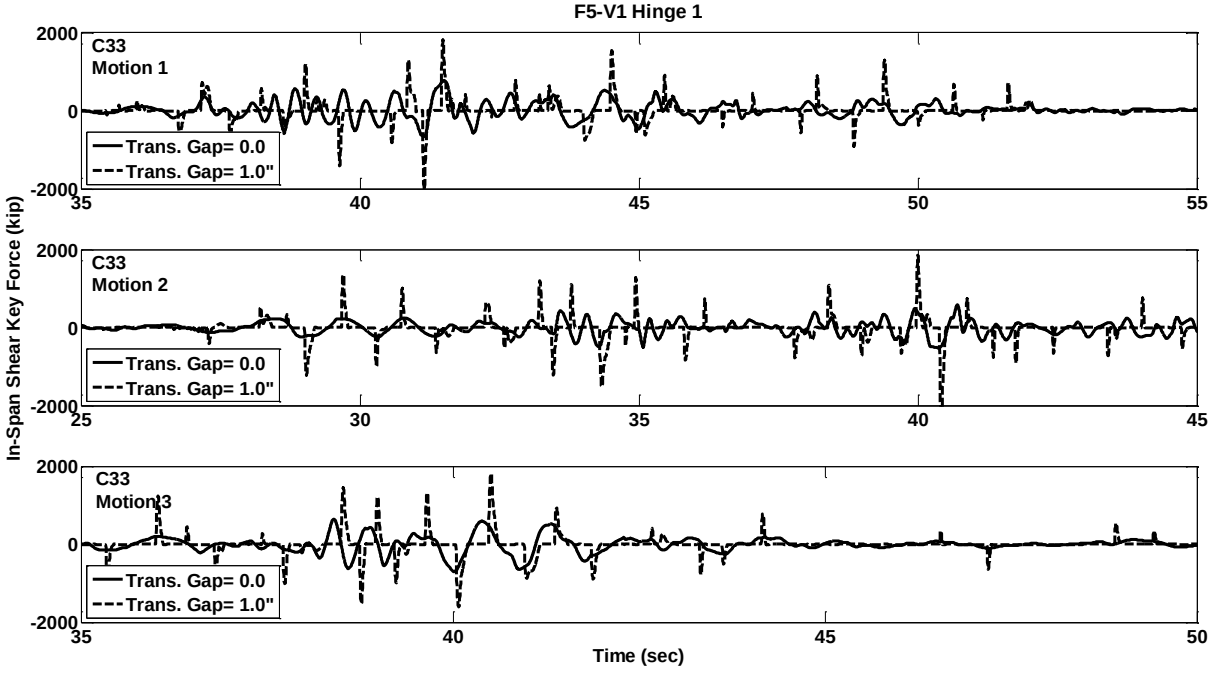

Figure C.430 Shear Key Force Response w/ and w/o Gap, Prototype F5-V1, Hinge-1, Motions C33

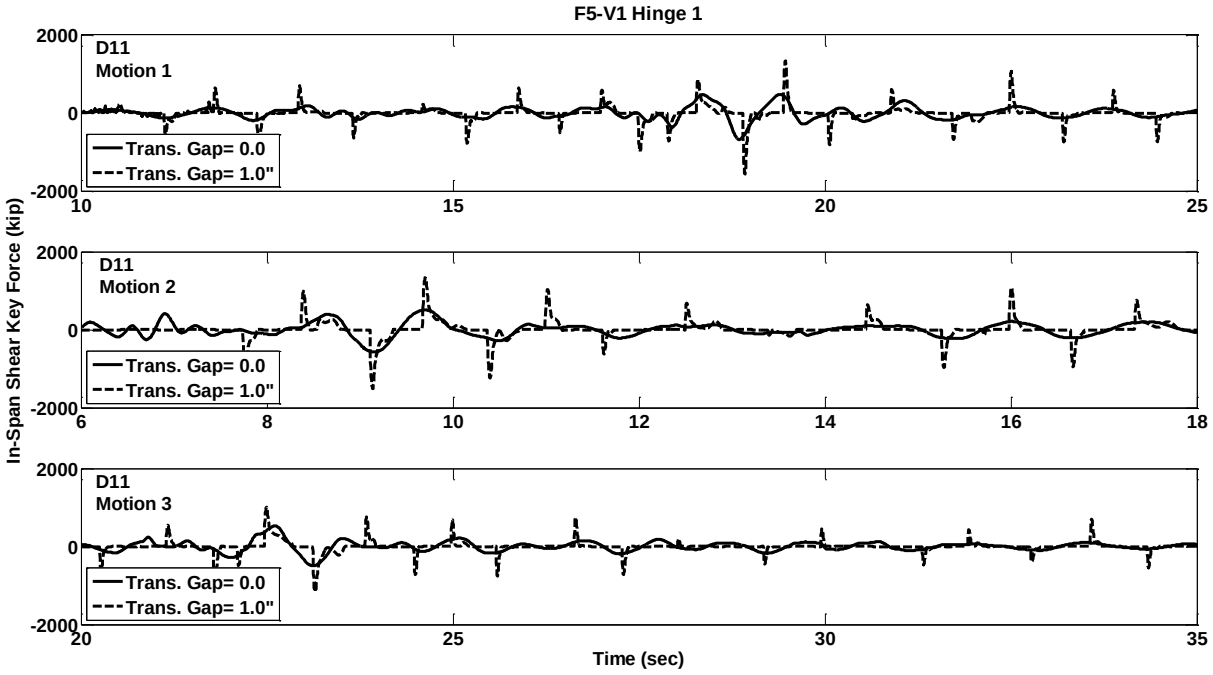

Figure C.431 Shear Key Force Response w/ and w/o Gap, Prototype F5-V1, Hinge-1, Motions D11

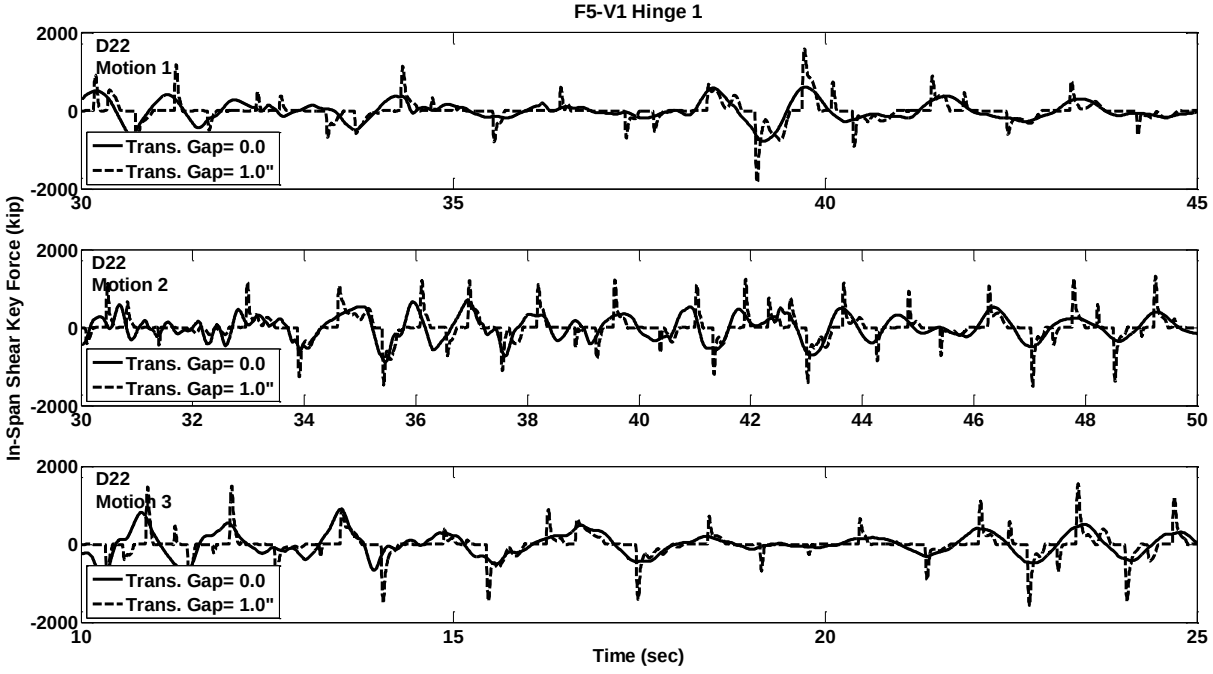

Figure C.432 Shear Key Force Response w/ and w/o Gap, Prototype F5-V1, Hinge-1, Motions D22

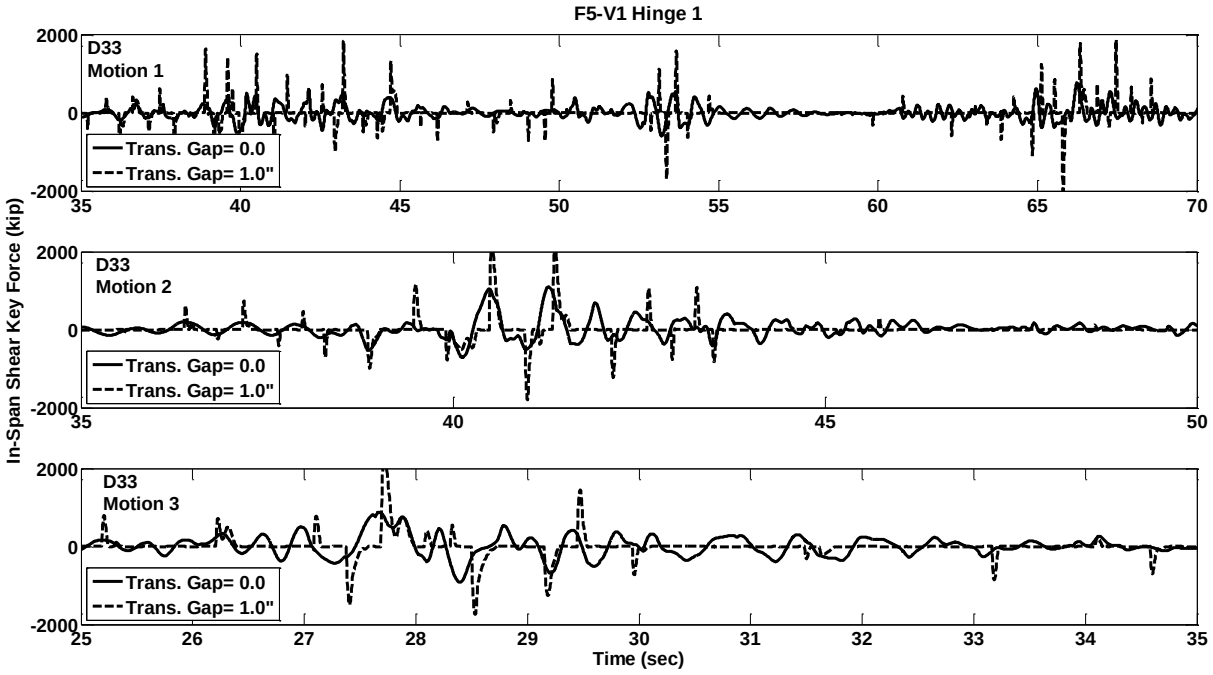

Figure C.433 Shear Key Force Response w/ and w/o Gap, Prototype F5-V1, Hinge-1, Motions D33

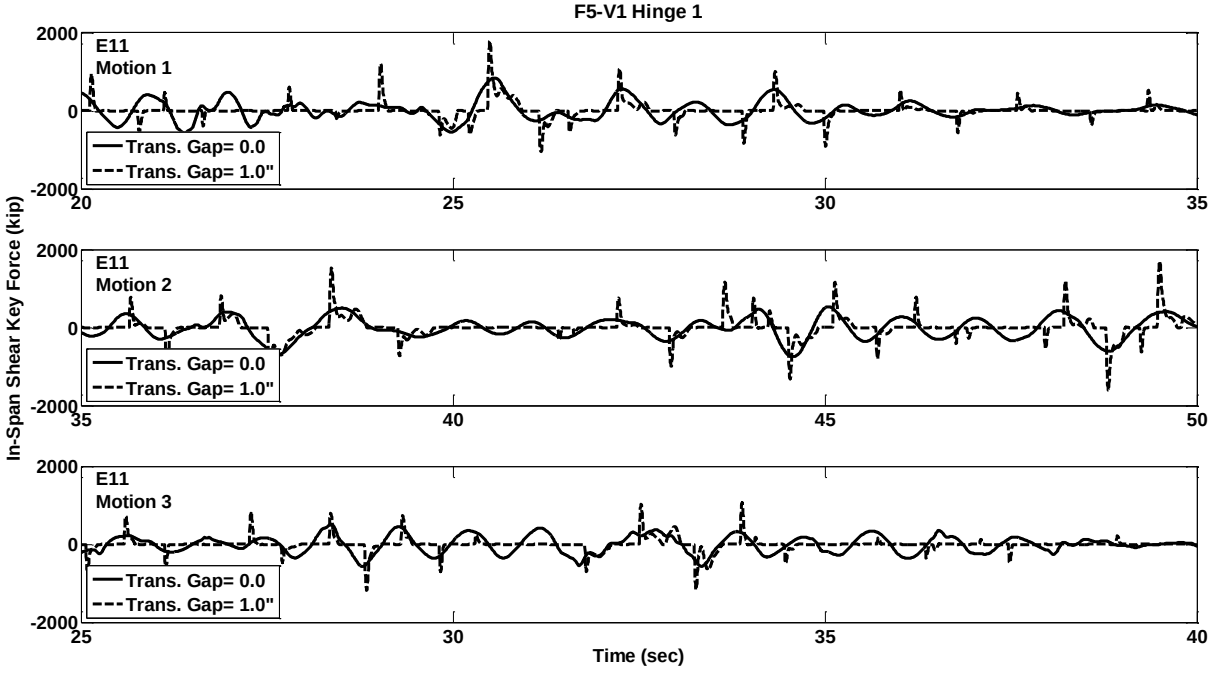

Figure C.434 Shear Key Force Response w/ and w/o Gap, Prototype F5-V1, Hinge-1, Motions E11

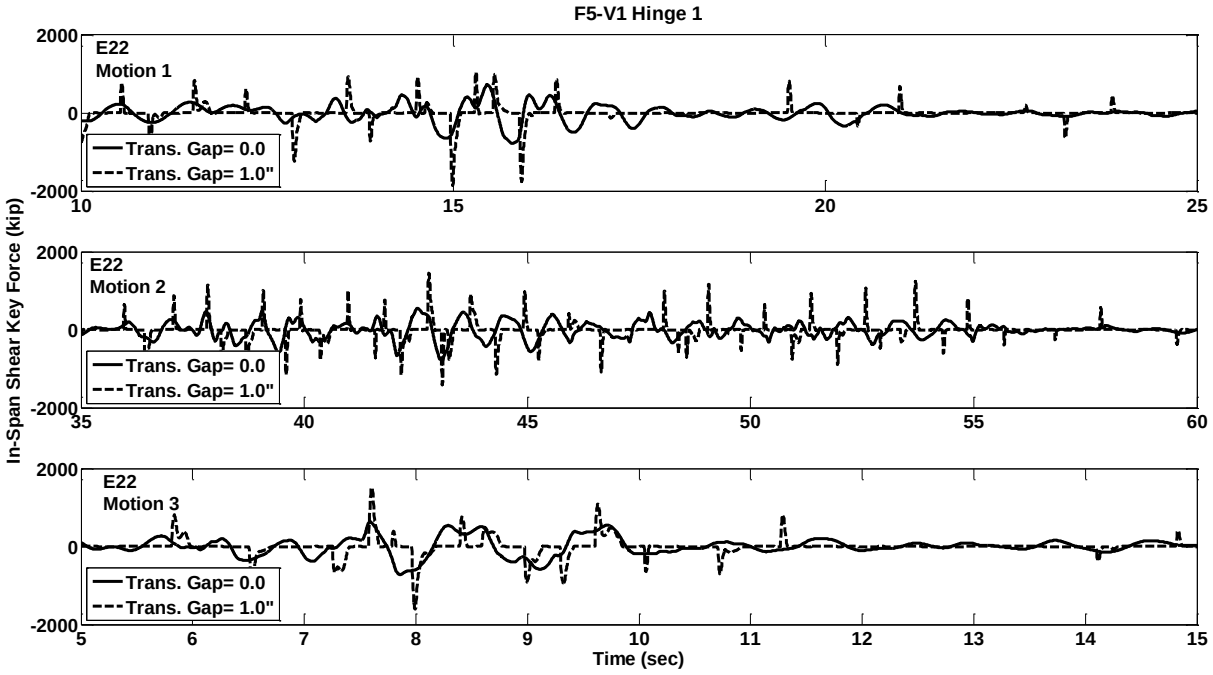

Figure C.435 Shear Key Force Response w/ and w/o Gap, Prototype F5-V1, Hinge-1, Motions E22

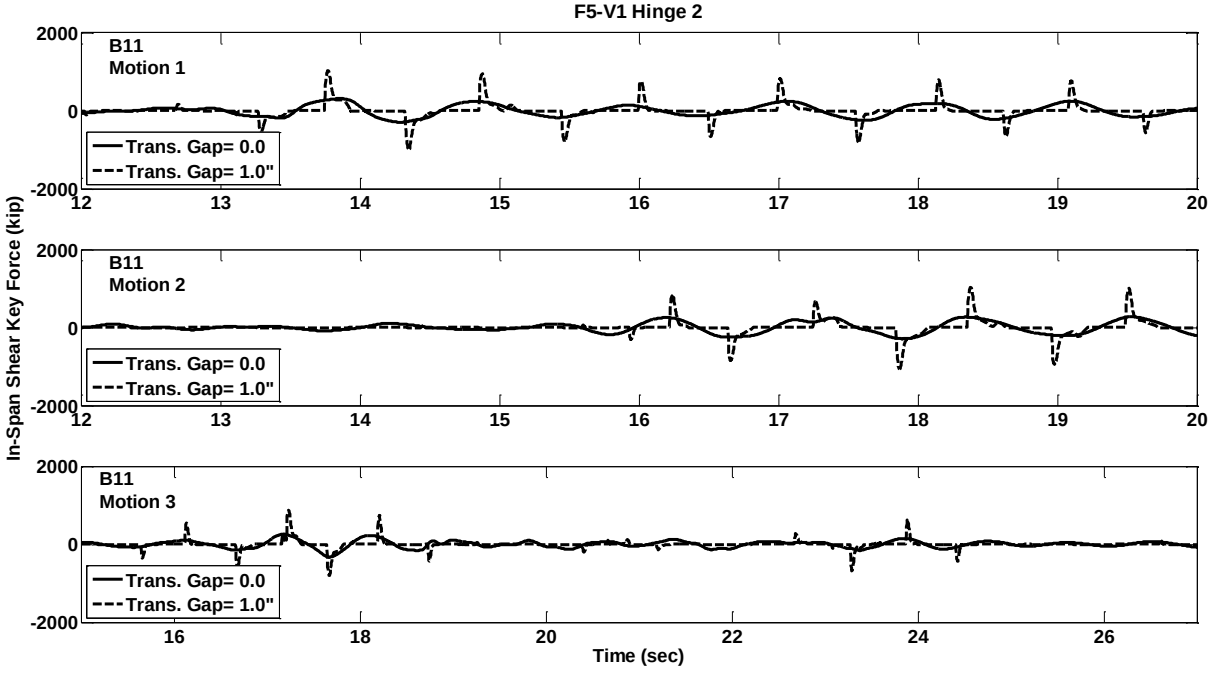

Figure C.436 Shear Key Force Response w/ and w/o Gap, Prototype F5-V1, Hinge-2, Motions B11

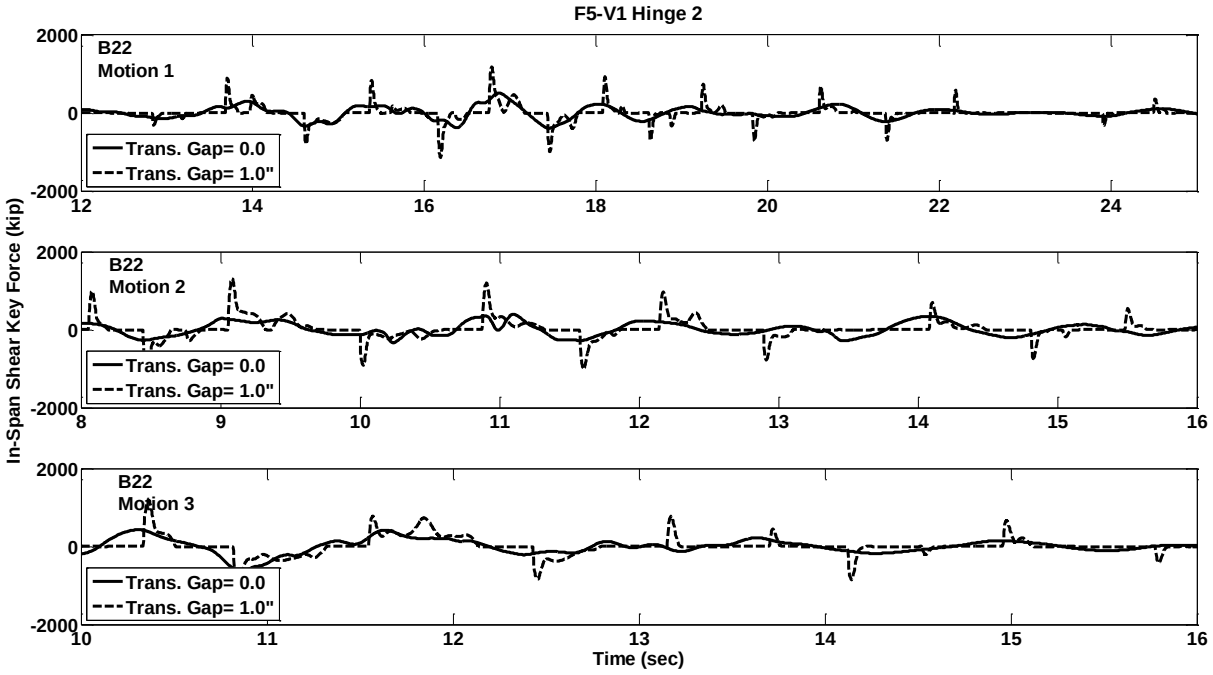

Figure C.437 Shear Key Force Response w/ and w/o Gap, Prototype F5-V1, Hinge-2, Motions B22

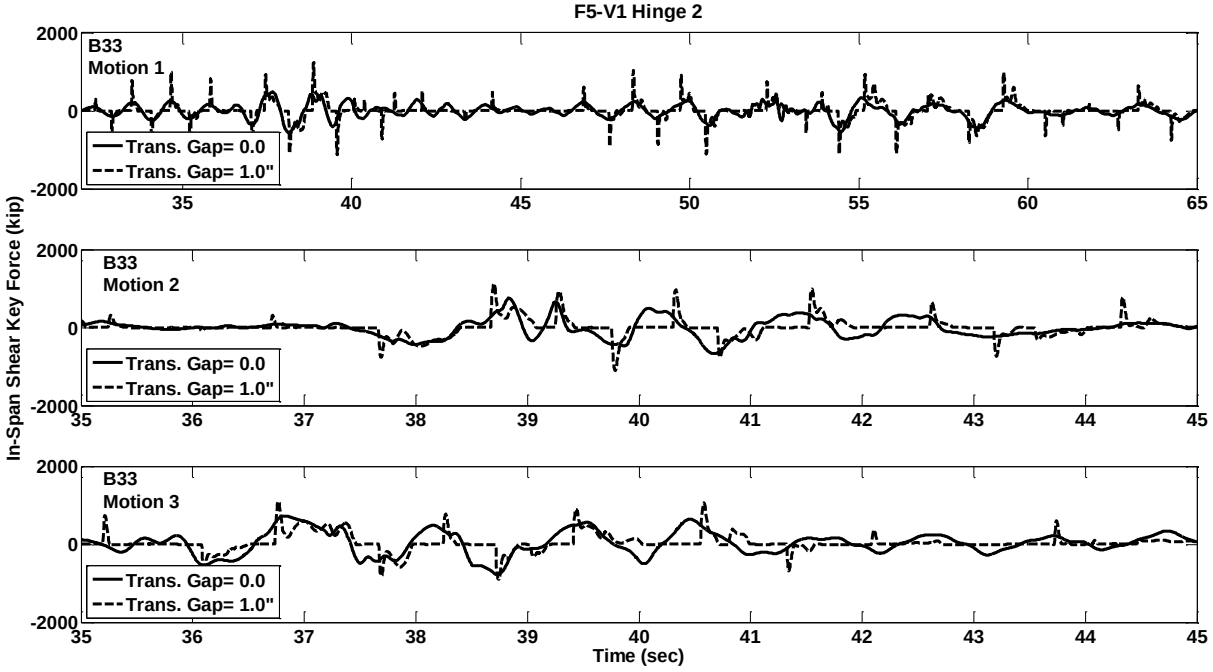

Figure C.438 Shear Key Force Response w/ and w/o Gap, Prototype F5-V1, Hinge-2, Motions B33

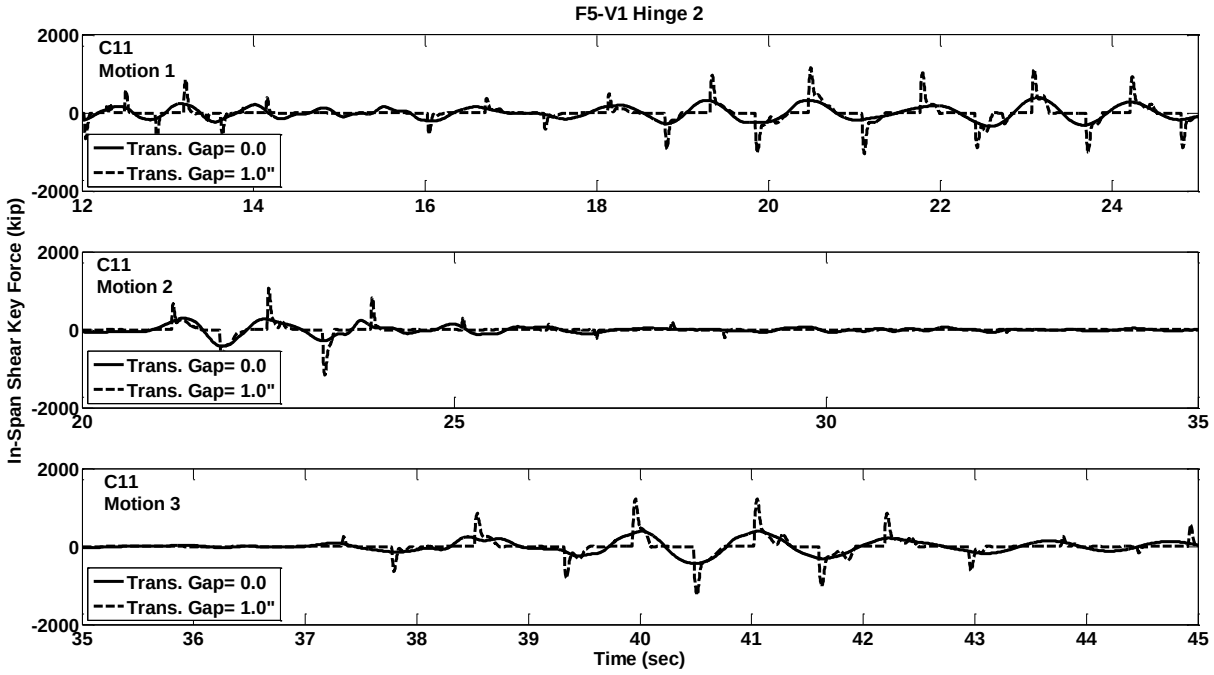

Figure C.439 Shear Key Force Response w/ and w/o Gap, Prototype F5-V1, Hinge-2, Motions C11

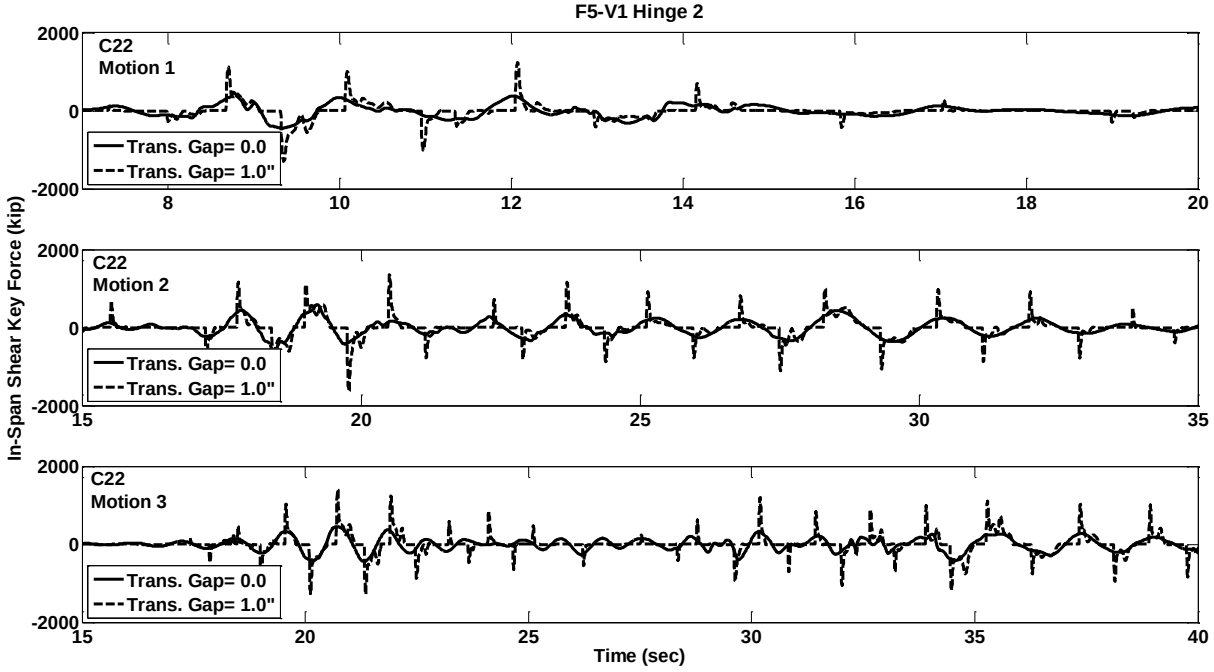

Figure C.440 Shear Key Force Response w/ and w/o Gap, Prototype F5-V1, Hinge-2, Motions C22

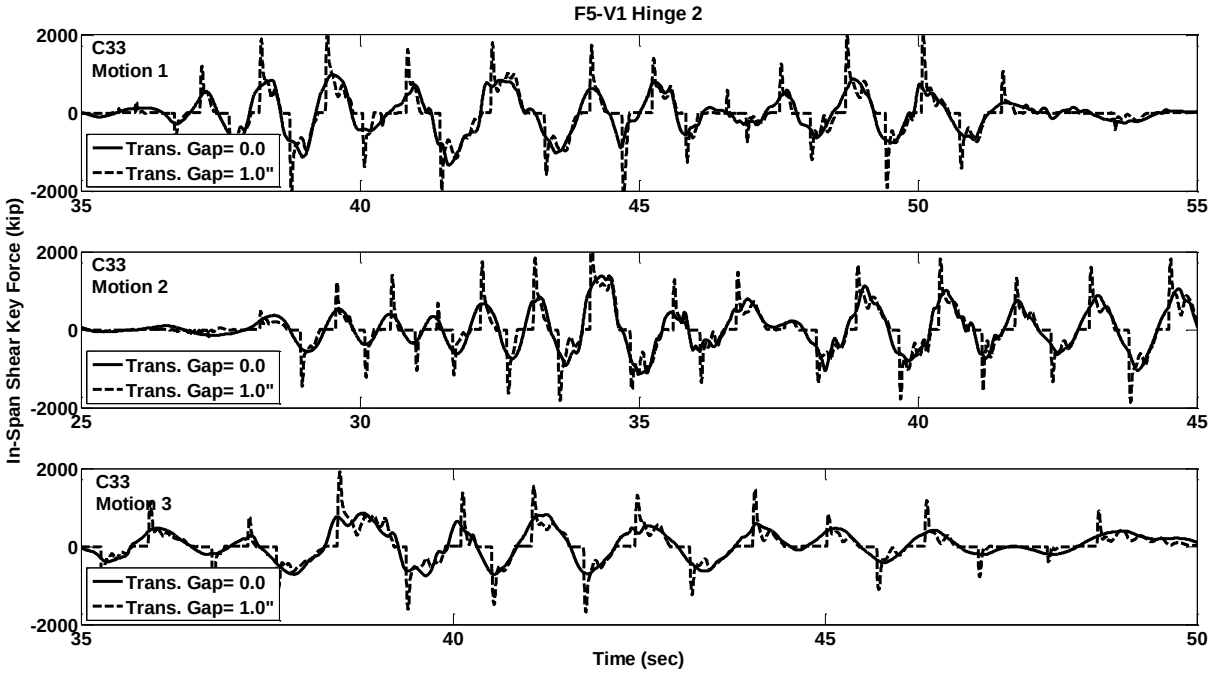

Figure C.441 Shear Key Force Response w/ and w/o Gap, Prototype F5-V1, Hinge-2, Motions C33

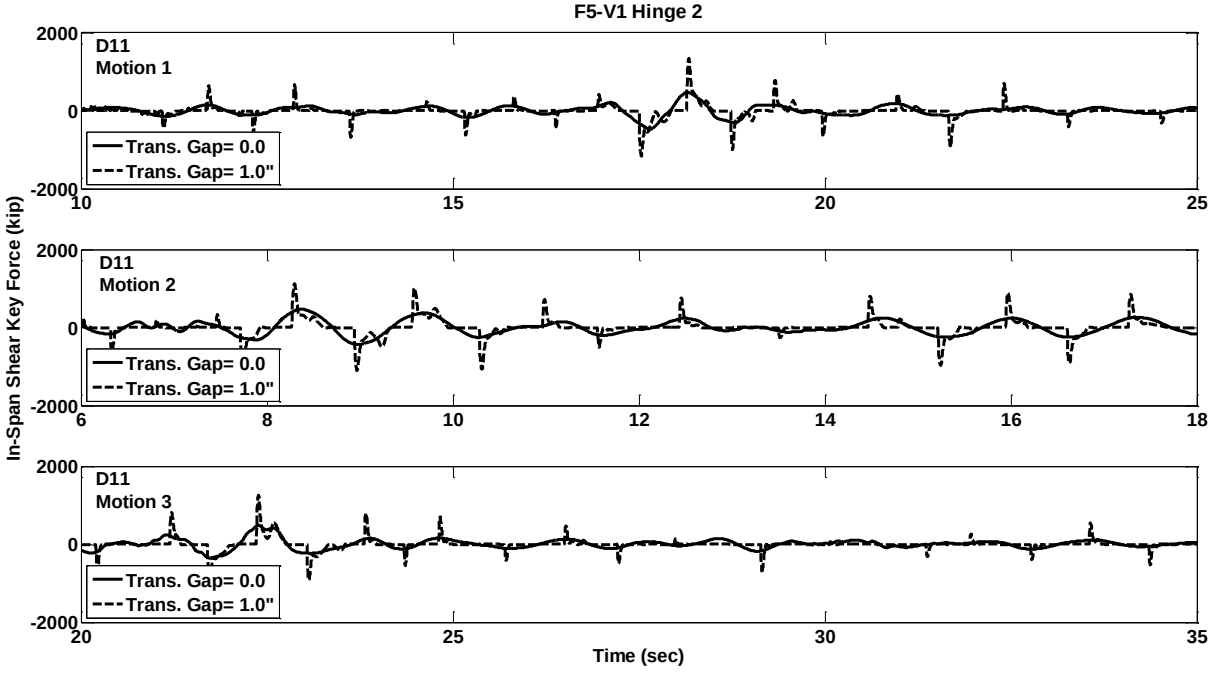

Figure C.442 Shear Key Force Response w/ and w/o Gap, Prototype F5-V1, Hinge-2, Motions D11

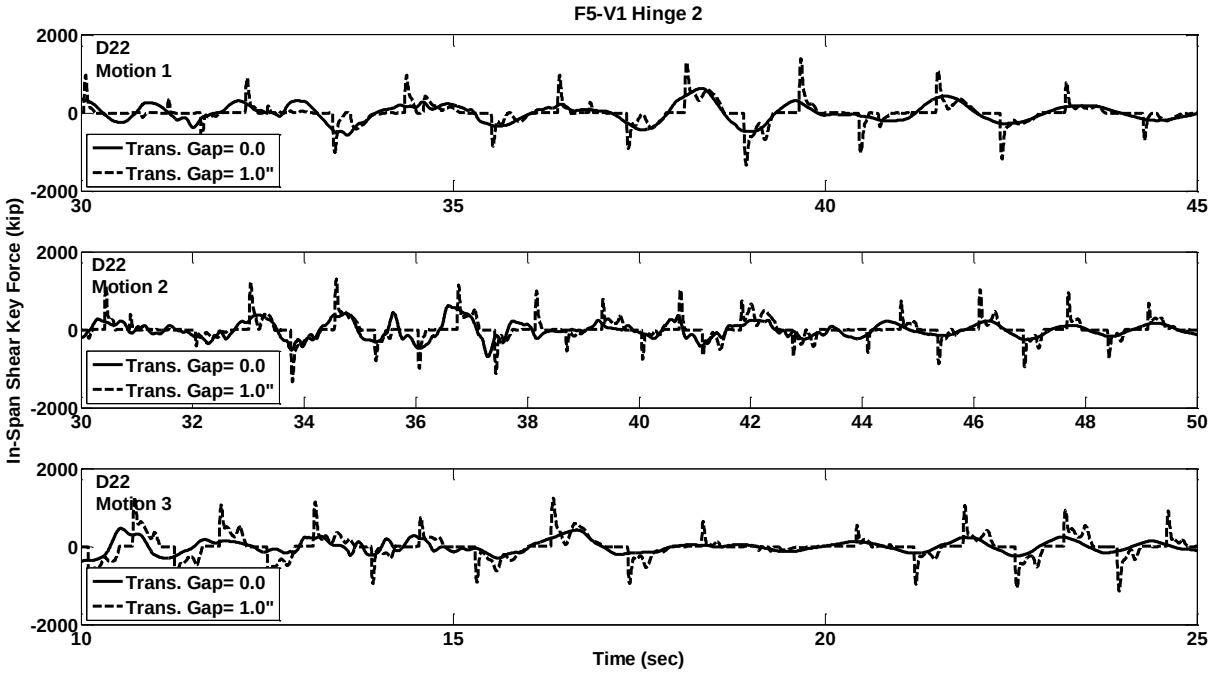

Figure C.443 Shear Key Force Response w/ and w/o Gap, Prototype F5-V1, Hinge-2, Motions D22

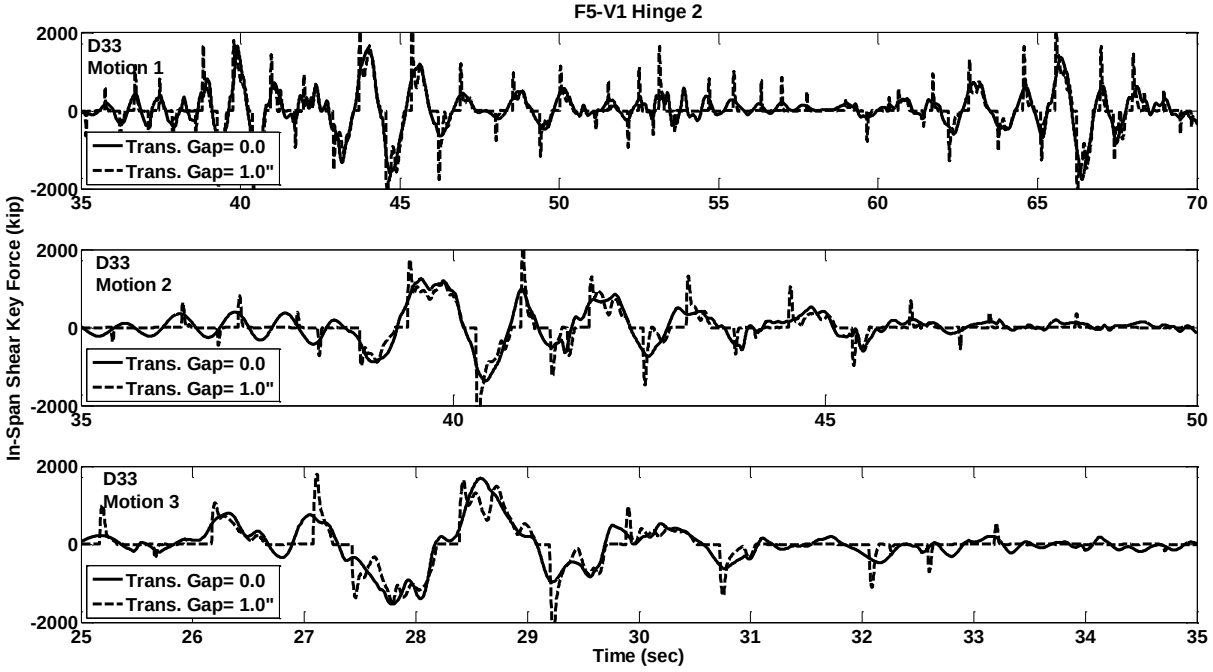

Figure C.444 Shear Key Force Response w/ and w/o Gap, Prototype F5-V1, Hinge-2, Motions D33

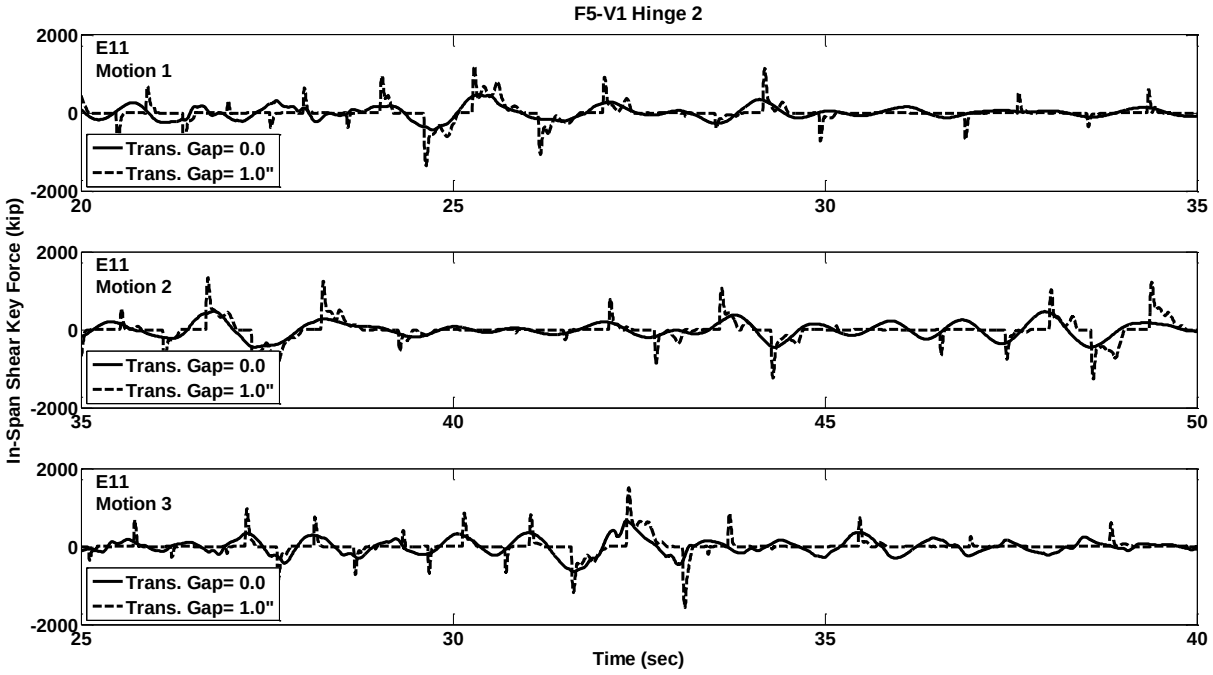

Figure C.445 Shear Key Force Response w/ and w/o Gap, Prototype F5-V1, Hinge-2, Motions E11

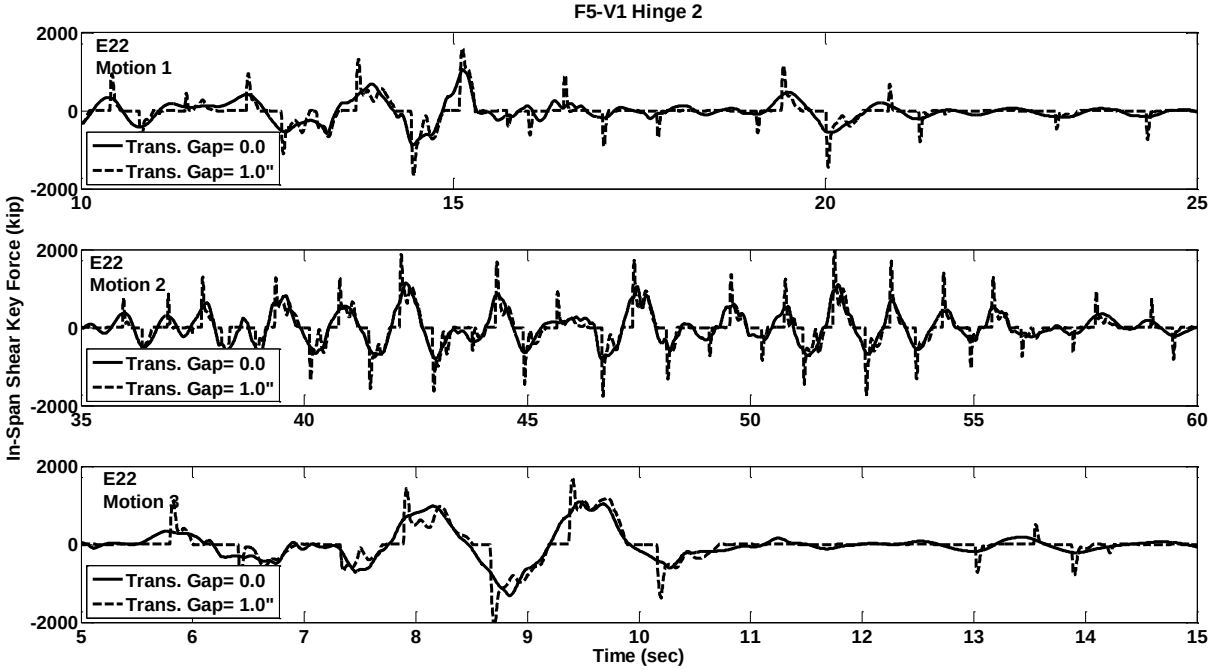

Figure C.446 Shear Key Force Response w/ and w/o Gap, Prototype F5-V1, Hinge-2, Motions E22

APPENDIX D.
MATLAB SCRIPTS FOR DATA PROCESSING

Data Loading and Processing Algorithm

1) Open and read the txt files generated by OpenSees.
2) Process the data; extract the target information such as maximum displacement, maximum force and etc.
3) Place them in a pre-allocated 2D matrix. Each matrix row is related to one prototype due to one ground motion, and matrix columns are corresponding target parameters.
4) For modal responses a 3D matrix is formed: matrix rows are same as before, matrix columns are corresponding modal response for mode 1 to n, and the third dimension is related to different responses (force, period, participation factors, etc.)
5) Close the txt file, repeat steps 1-5 for all prototypes and motions.
6) Multiple other scripts are developed to try different methods for prediction of shear key force and for parametric study.
7) A few functions and scripts are developed for plotting the processed results. Three of them are presented as following.

Script-1: plot actual and log-normal distribution bar chart and CDF.

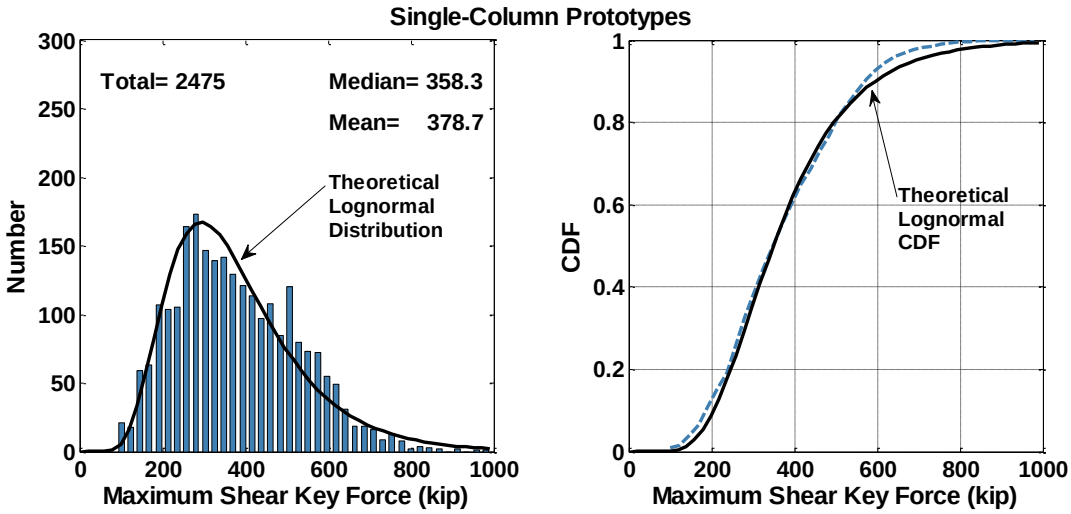


```
% Input Variables:
Input is the designated variable or array.
BinNo is desired number of bins for bar chart.
AxisLimitx is horizontal axis limit.
AxisLimity is vertical axis limit.
XLable is desired label sting for x axis.
bentType is substructure type; 1.0 for Single-Column and 2.0 for Two-Column bents.

Example: PDFCDF(NTH_ShearKeyForce, 50, 1000 ,300 ,'Maximum Shear Key Forces
(kip)',1.0)

function PDFCDF(Input, BinNo, AxisLimitx,AxisLimity,XLable,bentType)
axisLableSize =12.5;
axisFontWeight=  'bold'
lableFontWeight=  'bold'
```

```
h1FaceColor =[0.25 0.50 0.70];
lineWidth = 1.45;
figure('Position',[100 500 1100 450]);
subplot(1,2,1)
parmhat = lognfit(Input);
[H,Bin]=hist(Input,BinNo);
h1=bar(Bin,H); hold on
xt=0:max(Input)/50:max(Input);
scale=sum((Bin(2)-Bin(1)).*H);
plot(xt,scale*lognpdf(xt,parmhat(1),parmhat(2)), 'LineWidth', 2.5,  'color' ,'k');
str= ['Median= ' num2str(median(Input))]; ht =text(AxisLimitx*.6,AxisLimity*.9,
str(1:13)) ; set(ht, 'rotation',  0
,'FontName','Arial','FontSize',1.2*axisLableSize,'FontWeight',lableFontWeight)
str= ['Mean=    ' num2str(mean(Input))]; ht =text(AxisLimitx*.6,AxisLimity*.8,
str(1:14)) ; set(ht, 'rotation',  0
,'FontName','Arial','FontSize',1.2*axisLableSize,'FontWeight',lableFontWeight)
str= ['Total= ' num2str(length(Input))]; ht =text(AxisLimitx*.05,AxisLimity*.9, str) ;
set(ht, 'rotation',  0
,'FontName','Arial','FontSize',1.2*axisLableSize,'FontWeight',lableFontWeight)
set(h1,'facecolor',h1FaceColor,'LineWidth', lineWidth', 'BarWidth',0.6) % use color
name
set(gca,'FontName','Arial','FontSize',1.2*axisLableSize,'XScale','linear','YScale','li
near' ,'FontWeight', axisFontWeight);
xlabel( XLable , 'FontName','Arial','FontSize',1.3*axisLableSize,'FontWeight',
lableFontWeight);
ylabel( 'Number','FontName','Arial','FontSize',1.3*axisLableSize,'FontWeight',
lableFontWeight); %
axis([0 AxisLimitx 0 AxisLimity]);
ht =text(AxisLimitx*.6,AxisLimity*0.6, {'Theoretical' ; 'Lognormal' ; 'Distribution'})
; set(ht, 'rotation',  0
,'FontName','Arial','FontSize',1.0*axisLableSize,'FontWeight',lableFontWeight)
if bentType== 1; str= 'Single-Column Prototypes'; else  str='Two-Column Prototypes';
end
ht =text(AxisLimitx*.75,AxisLimity*1.06, str) ; set(ht, 'rotation',  0
,'FontName','Arial','FontSize',1.3*axisLableSize,'FontWeight',lableFontWeight)
subplot(1,2,2)
PDF=H./length(Input); CDF_R=cumsum(PDF);
CDF = cdf('Lognormal',xt,parmhat(1),parmhat(2));
plot(Bin, CDF_R, 'LineStyle' , '--','LineWidth', 2.5,  'color' , h1FaceColor) ; hold
on
plot(xt, CDF, 'LineStyle' , '-','LineWidth', 2.5,  'color' , 'k') ; hold on
set(gca,'FontName','Arial','FontSize',1.2*axisLableSize,'XScale','linear','YScale','li
near' ,'FontWeight', axisFontWeight);
xlabel( XLable , 'FontName','Arial','FontSize',1.3*axisLableSize,'FontWeight',
lableFontWeight);
ylabel( 'CDF','FontName','Arial','FontSize',1.3*axisLableSize,'FontWeight',
lableFontWeight); %
ht =text(AxisLimitx*.65,0.57, {'Theoretical' ; 'Lognormal' ; 'CDF'}) ; set(ht,
'rotation',  0
,'FontName','Arial','FontSize',1.0*axisLableSize,'FontWeight',lableFontWeight)
axis([0 AxisLimitx 0 1]);
grid on;
 end
```

Script-2: Scatter Plots with Coefficient of Correlation and Number of Data Points

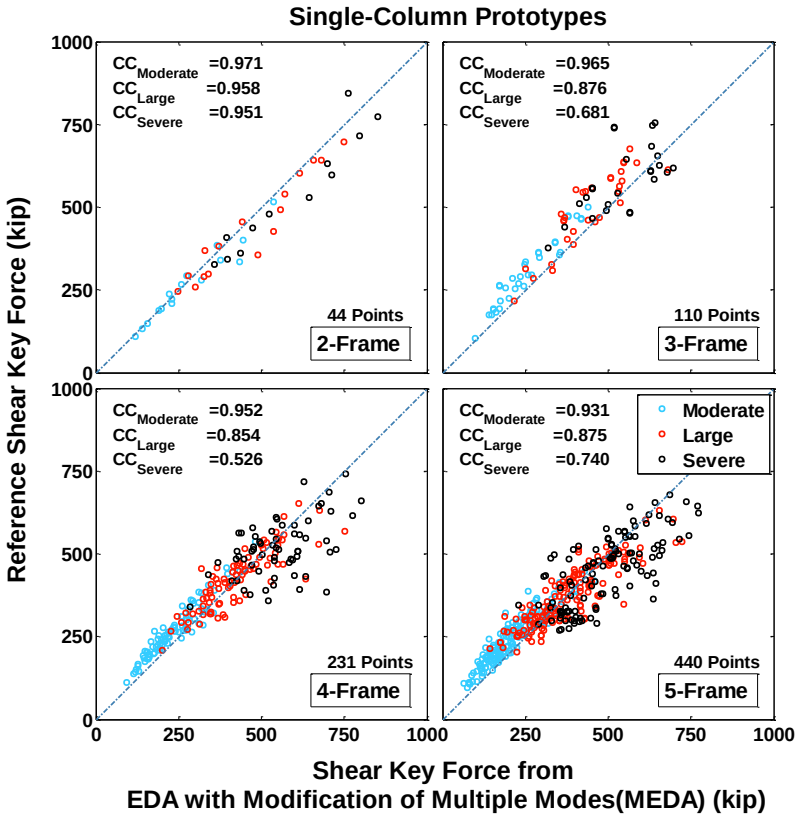


```
figure('Position',[10 50 950 950]);
margin1=0.12; margin2=0.0195; W=(1-margin1-4*margin2)/2;
positionVector(1,1:4)=[margin1, margin1+margin2+W, W, W];
positionVector(2,1:4)=[margin1+margin2+W, margin1+margin2+W, W, W];
positionVector(3,1:4)=[margin1, margin1, W, W];
positionVector(4,1:4)=[margin1+margin2+W, margin1, W, W];
markerShape = [ 's' 'd' '^' 'o' ];
axisFontWeight=  'bold';
lableFontWeight=  'bold';
axisLableSize =12.5;


for pro = 2 : 5   ;

% Input Variables:
X_moderate ,  Y_moderate , X_large, Y_large , X_severe , Y_severe are desired
processes variables for three seismic hazard levels.
bentType is substructure type; 1.0 for Single-Column and 2.0 for Two-Column bents.

plot(X_moderate ,  Y_moderate,  markerShape(4) ,'LineWidth',2.2,'MarkerEdgeColor',[.2
.8 1] ,'MarkerSize',4.5);hold on; %
plot(X_large ,  Y_large,  markerShape(4) ,'LineWidth',2.2,'MarkerEdgeColor',[1 .1 0]
,'MarkerSize',4.5);hold on; %
plot(X_severe ,  Y_severe, markerShape(4)  ,'LineWidth',2.2,'MarkerEdgeColor',[0 0 0],
'MarkerSize',4.5);hold on;


CC = corrcoef(X_moderate, Y_moderate); cc = CC(1,2);
str_cc_moderate = [ 'CC =' num2str(cc) ]; %
CC = corrcoef(X_large, Y_large); cc = CC(1,2);
str_cc_moderate = [ 'CC =' num2str(cc) ]; %
```

```
CC = corrcoef(X_severe, Y_severe); cc = CC(1,2);
str_cc_moderate = [ 'CC =' num2str(cc) ]; %

AxisLimity= 1000 * bentType ;
AxisLimitx= AxisLimity;

ht =text(AxisLimitx*.05,AxisLimity*.925, str_cc_moderate(1:21)); set(ht, 'rotation',
0 ,'FontName','Arial','FontSize',1.2*axisLableSize,'FontWeight',lableFontWeight)
ht =text(AxisLimitx*.05,AxisLimity*.925, str_cc_large(1:21)); set(ht, 'rotation',  0
,'FontName','Arial','FontSize',1.2*axisLableSize,'FontWeight',lableFontWeight)
ht =text(AxisLimitx*.05,AxisLimity*.925, str_cc_severe(1:21)); set(ht, 'rotation',  0
,'FontName','Arial','FontSize',1.2*axisLableSize,'FontWeight',lableFontWeight)

str_datapoint = [num2str(length(X)) ' Points'   ];%
ht =text(AxisLimitx*.7,AxisLimity*.175,str_datapoint); set(ht, 'rotation',  0
,'FontName','Arial','FontSize',1.2*axisLableSize,'FontWeight',lableFontWeight)

axis equal;
axis([0 AxisLimitx 0 AxisLimity]);
h1=line([0 AxisLimitx], [ 0  AxisLimity]);
set(h1, 'LineStyle' , '-.','LineWidth', 2.0,  'color' , [0.25 0.50 0.70]); %

if pro==2;      set(gca,'xtick',[0 AxisLimitx/4 AxisLimitx/2 3*AxisLimitx/4
AxisLimitx], 'xticklabel', [], 'ytick',[0 AxisLimity/4 AxisLimity/2 3*AxisLimity/4
AxisLimity] );
elseif pro==3;  set(gca,'xtick',[0 AxisLimitx/4 AxisLimitx/2 3*AxisLimitx/4
AxisLimitx], 'xticklabel', [], 'ytick',[0 AxisLimity/4 AxisLimity/2 3*AxisLimity/4
AxisLimity], 'yticklabel', [] );
elseif pro==4;  set(gca,'xtick',[0 AxisLimitx/4 AxisLimitx/2 3*AxisLimitx/4
AxisLimitx], 'ytick',[0 AxisLimity/4 AxisLimity/2 3*AxisLimity/4 AxisLimity]);
elseif pro==5;  set(gca,'xtick',[ AxisLimitx/4 AxisLimitx/2 3*AxisLimitx/4
AxisLimitx], 'ytick',[0 AxisLimity/4 AxisLimity/2 3*AxisLimity/4 AxisLimity],
'yticklabel', [] );
end

set(gca,'FontName','Arial','FontSize',1.3*axisLableSize,'XScale','linear','YScale','li
near','FontWeight', lableFontWeight);

str_f= [ num2str(pro) '-Frame'    ];
TxBxPosVec= [ positionVector(pro-1,1)+.65*W , positionVector(pro-1,2)+.015, .12, .04];
annotation('textbox', TxBxPosVec,'String', str_f,
'FontName','Arial','FontSize',1.5*axisLableSize,'FontWeight',lableFontWeight)

end; % pro

legend('Moderate', 'Large', 'Severe');
ax=axes('Units','Normal','Position',[.6*margin1 .8*margin1 0.95
0.85],'Visible','off','tag','suplabel');

set(get(ax,'Title'),'Visible','on')
if bentType== 1;
title('Single-Column
Prototypes','FontName','Arial','FontSize',1.75*axisLableSize,'FontWeight',
lableFontWeight);
else
title('Double-Column
Prototypes','FontName','Arial','FontSize',1.75*axisLableSize,'FontWeight',
lableFontWeight);
end

set(get(ax,'XLabel'),'Visible','on')
xlabel({'Shear Key Force' ; 'from EDA with Modification of Multiple Modes(MEDA)
(kip)'},'FontName','Arial','FontSize',1.75*axisLableSize,'FontWeight',
lableFontWeight);
set(get(ax,'YLabel'),'Visible','on')
```

```
ylabel('Reference Shear Key Force
(kip)','FontName','Arial','FontSize',1.75*axisLableSize,'FontWeight',
lableFontWeight);
```

Script-3: Plotting System State of the Bridge at the Instance of Peak Shear Key Force

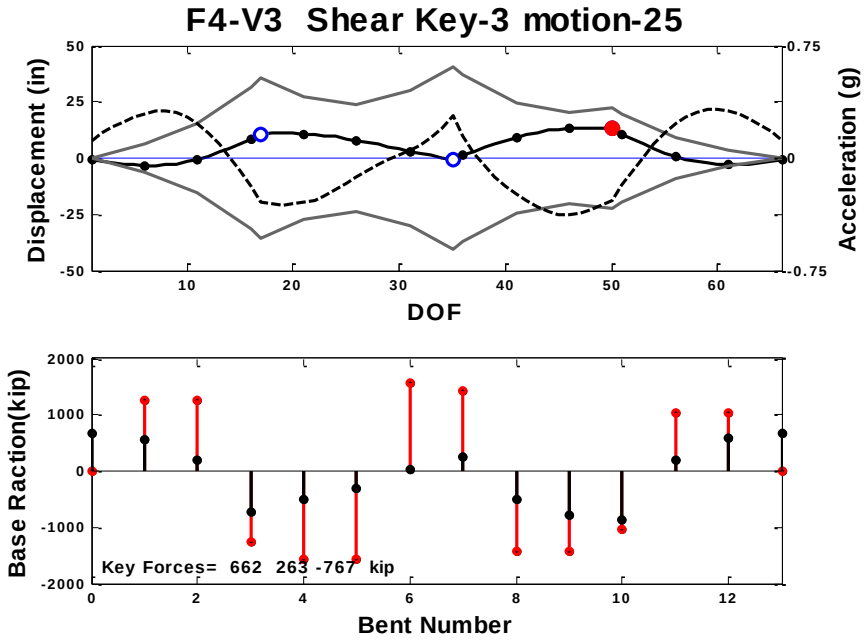


```
% Input Variables:
DispProfile is displacement time history of all nodes along the length of the bridge,
loaded from txt file.
AcclProfile is acceleration time history of all nodes along the length of the bridge
loaded from txt file.
AllKEY_Th is shear key force time history Response Histories of  all shear keys
within the bridge loaded from txt file.
DemandDispProfile is design displacement demand of all nodes along the length of the
bridge loaded from txt file.
BaseReactions is columns reaction time history in 3 directions: longitudinal,
transverse and vertical loaded from txt file.
BentCapacity_All is overstrength shear capacity for all columns loaded from txt
file.
Key is designated hinge number in multi-frame bridge.
bentType is substructure type; 1.0 for Single-Column and 2.0 for Two-Column bents.

valleyTag = [ 4 5 7 10 ]; % Number of valley shapes for two-, three-, four- and
five-frame prototypes;
[ TH_KeyForce,TH_KeyForce_index] = max( abs( AllKEY_Th(:,key+3) ) );

deformedShape= DispProfile(TH_KeyForce_index,2:end);
Acceleration= AcclProfile(TH_KeyForce_index,2:end) / g ;

DemandDisp = DemandDispProfile(end,2:end);
if bentType == 1;
BaseReactions= BaseReactions(TH_KeyForce_index,3:3:end);
signSet = BaseReactions ./ abs(BaseReactions);
else
BaseReactions_double= BaseReactions(TH_KeyForce_index,3:3:end);
clear BaseReactions;
BaseReactions(1)=BaseReactions_double(1);
for i=2:length(BaseReactions_double)/2
BaseReactions(i) =  BaseReactions_double(2*i-2)+BaseReactions_double(2*i-1);
end
BaseReactions(i+1)=BaseReactions_double(end);
signSet = BaseReactions ./ abs(BaseReactions);
```

```
end

BentCapacity_frame = BentCapacity_All(3:4:end) ; %  only for Single-Column
AllKeysForce= round( AllKEY_Th(TH_KeyForce_index,4:4+pro-2));

clear BentCapacity;
if valley ~= valleyTag(end);
j=1;
for i=1:3*pro
if i > 3*j ; j=j+1 ; end;
BentCapacity(i) = BentCapacity_frame(j);
end
BentCapacity =  signSet .* [0  BentCapacity 0 ];

else
BentCapacity =  signSet .* [0 BentCapacity_frame 0] ;
end

figure;
subplot(2,1,1);

X= 1:length(deformedShape);
[ax, h1, h2] =  plotyy(X,deformedShape, X, Acceleration, 'plot' , 'plot');hold on

set(h1, 'linestyle', '-' , 'LineWidth', 1.8,   'color' , 'k') % use color name
set(h2, 'linestyle', '--' , 'LineWidth', 1.9,  'color' , 'k') % use color name
set(ax(1), 'xlim', [ 1 X(end)] , 'ylim', [-50  50] ,  'YTick',[-50 -25 0.0 25 50],
'FontName','Arial','FontSize',0.7*axisLableSize,  'FontWeight',axisFontWeight
,'YColor','k' ) %  'YTickLabel', [  78 84 90 96 102 108 114 120] ,

set(ax(2), 'xlim', [ 1 X(end)] , 'ylim', [-0.75 0.75] , 'YTick',[-0.75 0.0 0.75] ,
'FontName','Arial','FontSize',0.7*axisLableSize,  'FontWeight',axisFontWeight
,'XTickLabel',[] ,'YColor','k') %

line([0 X(end)], [   0 0 ], 'LineWidth', 1.25, 'color' , 'b');
%ylim([-1 1]);    ;
xlim([ 1 X(end)])

x_demand=[];
for node=1: length(X)

if  ismember(node, HingeIndex) ==1  ;
plot(X(node), deformedShape(node),'
o','MarkerSize',7,'MarkerEdgeColor','b','MarkerFaceColor','w','LineWidth',1.5 )
x_demand=[x_demand node];
 end
if node == HingeIndex(key) ;
plot(X(node), deformedShape(node),'
o','MarkerSize',7,'MarkerEdgeColor','r','MarkerFaceColor','r','LineWidth',1.5 )

end
if fix((node-1)/5) == (node-1)/5 ;
plot(X(node), deformedShape(node),'
o','MarkerSize',4,'MarkerEdgeColor','k','MarkerFaceColor','k','LineWidth',1.5 )
 x_demand=[x_demand node];
end
end

plot(x_demand,DemandDisp, 'linestyle', '-' , 'LineWidth', 1.5 , 'color' , [ 0.4 0.4
0.4] );hold on
plot(x_demand,-DemandDisp,'linestyle', '-' , 'LineWidth', 1.5 , 'color' , [ 0.4 0.4
0.4] );hold on

title([ num2str(bentType) 'Col ' 'F' num2str(pro) '-V' num2str(valley)    ' Key'
num2str(key) ' motion'  num2str(e) ]
```

```
,'FontName','Arial','FontSize',0.8*titleSize,'FontWeight',lableFontWeight ) %  '-V'
num2str(valley) ' ShearKey ' num2str(key)

set(get(ax(1), 'Ylabel'), 'String', {'Displacement
(in)'},'FontName','Arial','FontSize',axisLableSize,   'FontWeight',axisFontWeight);
set(get(ax(2), 'Ylabel'), 'String', 'Acceleration (g)'
,'FontName','Arial','FontSize',axisLableSize , 'FontWeight',axisFontWeight);


xlabel('DOF','FontName','Arial','FontSize',axisLableSize,'FontWeight',lableFontWeight)
;

subplot(2,1,2);
x=0:length(BentCapacity)-1;
stem(x,BentCapacity, 'LineWidth', 1.8 , 'Color' , 'r',  'MarkerSize', 2.75,
'MarkerFaceColor', 'k' );hold on
stem(x,BaseReactions,'LineWidth', 1.8 , 'Color' , 'k' , 'MarkerSize', 2.75,
'MarkerFaceColor', 'k');
set(gca, 'FontName','Arial','FontSize',0.7*axisLableSize, 'FontWeight',axisFontWeight,
'YColor','k'  )

str=[ 'Key Forces=  ' num2str(AllKeysForce) 'kip'];
if bentType == 1;
ylim([-2000 2000]); xlim([ 0 x(end)]);
h =text(0.2,-1700,str); set(h, 'rotation',  0
,'FontName','Arial','FontSize',0.75*axisLableSize,'FontWeight',lableFontWeight)
else
ylim([-2500 2500]); xlim([ 0 x(end)]);
h =text(0.2,-2200,str); set(h, 'rotation',  0
,'FontName','Arial','FontSize',0.75*axisLableSize,'FontWeight',lableFontWeight)
end

ylabel('Base
Raction(kip)','FontName','Arial','FontSize',axisLableSize,'FontWeight',lableFontWeight
);

xlabel('Bent
Number','FontName','Arial','FontSize',axisLableSize,'FontWeight',lableFontWeight);
```